ELEVENTH INTERNATIONAL CONFERENCE ON COMPOSITE MATERIALS

Gold Coast, Queensland, Australia
14th - 18th July 1997

PROCEEDINGS

VOLUME V

TEXTILE COMPOSITES AND CHARACTERISATION

Editor
Murray L. Scott

AUSTRALIAN COMPOSITE STRUCTURES SOCIETY
WOODHEAD PUBLISHING LIMITED

TABLE OF CONTENTS

Textile Composites

Environmental Effects

Mechanical Properties

Test Methods

THE EFFECT OF STRAIN GAGE SIZE ON MEASUREMENT ERRORS IN TEXTILE COMPOSITE MATERIALS

Eric J. Lang[1] and Tsu-Wei Chou[2]

[1] The Why Not Corp., 743 W. Sparrow Rd., Springfield, OH 45502, USA
[2] Center for Composite Materials, and Department of Mechanical Engineering, University of Delaware, Newark, DE 19716 USA

SUMMARY: The heterogeneous nature of textile composites on the microstructural scale leads to variation in the local strain field within the unit cell. This variation can result in inaccurate measurement of the average global strain when using strain gages of insufficient size. A statistical model for sensor error is presented which leads to expressions for sensor variance. The model includes the effects of unit cell size, gage length, gage width, microstructural defects and irregularities, and instrument error. The proposed model is verified experimentally using a plain woven graphite-epoxy composite material and strain gages of various lengths. The experimental results are compared with analytical predictions. A set of guidelines for the use of strain gages on textile composites has been developed.

KEYWORDS: textile composites, statistics, microstructure mechanical properties, strain gage

INTRODUCTION

Consider the problem of determining the average macroscopic strains on the surface of a heterogeneous material using a relatively compact strain gage. This problem arises, for instance, when determining the bulk material properties of a textile composite material by mechanical testing.

The area of the strain gage is smaller than the macroscopic area and therefore, if the strain distribution is not constant, the sensor output and the macroscopic strain may not be in agreement. The gage averages the strain over the gage section. If the gage is located in a region of below average strain, the sensor output will be lower than the average macroscopic strain. Conversely, if the gage is located in a region of above average strain, the sensor output will be higher than the average macroscopic strain. In general, it is not known whether a strain gage is in a region of above average strain, average strain, or below average strain. Thus, the sensor output tends to be a random variable with some probability distribution around the true macroscopic strain. Ideally, this probability distribution is closely centered around the actual macroscopic strain value. In practice, the distribution depends on factors such as gage size and unit cell size.

A non-uniform strain distribution may be caused by random defects or material irregularities introduced during manufacturing. Alternatively, the heterogeneous microstructure of the

material can cause variation in the local strain field. This microstructurally induced strain variation has been predicted analytically and measured experimentally using Moiré Interferometry methods[1]. The magnitude of the strain variation is predicted to be a function of the relative stiffnesses of the fiber and matrix material as well as the fiber architecture. The greater the difference in stiffness, the larger the strain variation.

Moiré interferometry also shows distinct variation in the strain field due to the microstructure in various textile composite materials. While these variations may not be significant if the tows are relatively small in comparison to the gage size, when the tows are large, the variation is likely to lead to measurement errors. Some textile composite materials such as through-the-thickness, multi-layer weaves and 3-dimensional braids [2-4] have quite large unit cells -- in some cases exceeding one or more inches.

The purpose of this paper is to investigate the effect strain gage size has on the accuracy of strain measurements made on periodically heterogeneous materials. A statistical model for sensor output including the effects of unit cell size, strain variation within the unit cell, gage length, gage width, material defects and irregularities, and instrument error is proposed. The model is verified experimentally using a plain weave graphite-polyester composite. The details of the theoretical analysis and experimental verification can be found in Refs. [5, 6].

DEFINITIONS AND PROBLEM FORMULATION

Let us decompose the strain $\varepsilon_{ij}(x,y)$ at a point on the surface of a heterogeneous material with a periodically repeated microstructure or unit cell into a constant component $\bar{\varepsilon}_{ij}$ which represents the macroscopic average strain, a random component $\varepsilon_{ij}^{d}(x,y)$ which represents the effects of material defects and irregularities, and a periodic component $\varepsilon_{ij}^{u}(x,y)$ which represents the local strain variation within the unit cell caused by the textile microstructure. The actual strain at a point is the sum of these three components, or

$$\varepsilon_{ij}(x,y) = \bar{\varepsilon}_{ij} + \varepsilon_{ij}^{d}(x,y) + \varepsilon_{ij}^{u}(x,y) \tag{1}$$

with

$$\bar{\varepsilon}_{ij} \equiv \frac{1}{A}\iint_{A} \varepsilon_{ij}(x,y)\,dA \quad E\left[\varepsilon_{ij}^{d}(x,y)\right] \equiv 0 \quad \iint_{A_u} \varepsilon^{u}(x,y)\,dA \equiv 0 \tag{2}$$

where A is some macroscopic area, $E[\ ]$ denotes the statistical expectation[7], and A_u is the area of a unit cell.

Each component of the unit cell strain is, in general, a function of all the components of global average strain as well as position within the unit cell. Assuming linear elasticity, the effects on the unit cell strain of each component of macroscopic strain can be superposed. The unit cell strains are related to the global average strains by an equation of the form

$$\varepsilon_{ij}^{u}(x,y) = F_{ijkl}(x,y)\bar{\varepsilon}_{kl} \tag{3}$$

Symmetry of the strain tensor requires,

$$F_{ijkl} = F_{jikl} = F_{ijlk} \tag{4}$$

which reduces the maximum number of independent constants in F_{ijkl} to thirty-six. It should be remembered that the components of F_{ijkl} are functions of position in the unit cell and have periodicity conditions. For simplicity, we will consider the case of rectangular unit cells in which F_{ijkl} and $\varepsilon^u_{ij}(x,y)$ must satisfy the following periodicity conditions

$$F_{ijkl}(x^*+m\lambda_x, y^*+n\lambda_y) = F_{ijkl}(x^*,y^*) \quad \begin{cases} m=1,2,\ldots. \\ n=1,2,\ldots. \end{cases} \tag{5}$$

$$\varepsilon^u_{ij}(x^*+m\lambda_x, y^*+n\lambda_y) = \varepsilon^u_{ij}(x^*,y^*) \quad \begin{cases} m=1,2,\ldots. \\ n=1,2,\ldots. \end{cases} \tag{6}$$

where λ_x and λ_y are the lengths of the unit cell in the x and y directions and (x^*,y^*) is any point in the unit cell. Similar periodicity conditions can be derived for unit cells of different shapes.

Strain gages are usually placed on the surface of a material where there are only three non-zero strains. Thus, in practical situations, the nontrivial components of Eqn 3 can be represented by

$$\begin{Bmatrix} \varepsilon^u_{xx} \\ \varepsilon^u_{yy} \\ \varepsilon^u_{xy} \end{Bmatrix} = \begin{bmatrix} f_{11} & f_{12} & f_{13} \\ f_{21} & f_{22} & f_{23} \\ f_{31} & f_{32} & f_{33} \end{bmatrix} \begin{Bmatrix} \bar{\varepsilon}_{xx} \\ \bar{\varepsilon}_{yy} \\ \bar{\varepsilon}_{xy} \end{Bmatrix} \quad \text{or} \quad \{\varepsilon^u\} = [F]\{\bar{\varepsilon}\} \tag{7}$$

Similarly, the strain at a point due to material defects is given by

$$\begin{Bmatrix} \varepsilon^d_{xx} \\ \varepsilon^d_{yy} \\ \varepsilon^d_{xy} \end{Bmatrix} = \begin{bmatrix} g_{11} & g_{12} & g_{13} \\ g_{21} & g_{22} & g_{23} \\ g_{31} & g_{32} & g_{33} \end{bmatrix} \begin{Bmatrix} \bar{\varepsilon}_{xx} \\ \bar{\varepsilon}_{yy} \\ \bar{\varepsilon}_{xy} \end{Bmatrix} \quad \text{or} \quad \{\varepsilon^d\} = [G]\{\bar{\varepsilon}\} \tag{8}$$

In the previous equations, we use an upper case letter to denote a matrix and a lower case letter to denote the elements of the matrix. The tensor F_{ijkl} should not be confused with the matrix F.

The components of G are assumed to be random variables, independent of each other and independent from one point to the next in space. The expected value for each component is zero, and, for the purposes of this analysis, the variance is assumed to be the same for all components and all positions in the unit cell. We will denote this variance by σ^2_δ and it is defined by,

$$\sigma^2_\delta \equiv E\left[\frac{1}{A}\iint_A g^2_{ij}(x,y)dA\right] \tag{9}$$

SENSOR OUTPUT EQUATIONS

On the surface of a material, there is the possibility of three independent strain components. However, a strain gage gives only one measurement output. Most gages are designed to have very low sensitivities to transverse and shearing strains and the contribution of these strains to the gage output is neglected in the following analysis. The output of the sensor depends on

the orientation of the sensor relative to the global coordinates, and the strain in the global coordinates.

Figure 1 shows the coordinate system used to describe the position and orientation of the strain gage. Primes are used to denote the gage coordinates. The lower left-hand corner of the gage is located at a position (X,Y) and the sensing direction of the gage is rotated in the counter-clockwise direction to an angle ϕ relative to the global coordinate system x-y.

Following Eqn 1, the strain in the direction of the strain gage is

$$\varepsilon_g(x,y,\phi) = \bar{\varepsilon}_g + \varepsilon_g^d(x,y,\phi) + \varepsilon_g^u(x,y,\phi) \tag{10}$$

where

$$\begin{aligned}
\bar{\varepsilon}_g &= \cos^2(\phi)\bar{\varepsilon}_{xx} + \sin^2(\phi)\bar{\varepsilon}_{yy} + 2\cos(\phi)\sin(\phi)\bar{\varepsilon}_{xy} \\
\varepsilon_g^d(x,y,\phi) &= \cos^2(\phi)\varepsilon_{xx}^d(x,y) + \sin^2(\phi)\varepsilon_{yy}^d(x,y) + 2\cos(\phi)\sin(\phi)\varepsilon_{xy}^d(x,y) \\
\varepsilon_g^u(x,y,\phi) &= \cos^2(\phi)\varepsilon_{xx}^u(x,y) + \sin^2(\phi)\varepsilon_{yy}^u(x,y) + 2\cos(\phi)\sin(\phi)\varepsilon_{xy}^u(x,y)
\end{aligned} \tag{11}$$

Foil strain gages currently in common usage consist of a single thin strip of metal which traverses back and forth across the gage area. In this analysis, we will treat the strain gages as areal sensors. Areal sensor measure the average strain over an area. With this assumption, the results of the present analysis can also apply to strain gages made from piezoelectric materials.[8]

In most cases a strain gage is positioned without any knowledge of its location relative to the underlying unit cell. Therefore, the variables X and Y shown in Fig. 1 are assumed to be uniformly distributed random variables with the following probability density functions:

$$f_X(X) = \begin{cases} 0 & X < 0 \\ 1/\lambda_x & 0 \le X \le \lambda_x \\ 0 & \lambda_x < X \end{cases} \qquad f_Y(Y) = \begin{cases} 0 & Y < 0 \\ 1/\lambda_y & 0 \le Y \le \lambda_y \\ 0 & \lambda_y < Y \end{cases} \tag{12}$$

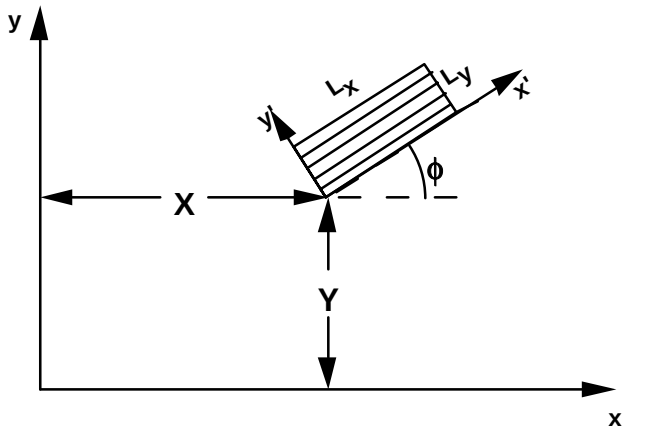

Fig. 1: Coordinate system detailing the position of the strain gage

The strain at a point (x,y) can be written as a function of (x', y', X, Y) by making the substitution

$$\begin{Bmatrix} x \\ y \end{Bmatrix} = \begin{bmatrix} \cos(\phi) & -\sin(\phi) \\ \sin(\phi) & \cos(\phi) \end{bmatrix} \begin{Bmatrix} x' \\ y' \end{Bmatrix} + \begin{Bmatrix} X \\ Y \end{Bmatrix} \tag{13}$$

Using this change of variables and the assumption of an areal sensor, the measured strain, ε_m, is given by

$$\varepsilon_m(X,Y,\phi) = \bar{\varepsilon}_m + \varepsilon_m^d(X,Y,\phi) + \varepsilon_m^u(X,Y,\phi) \tag{14}$$

where

$$\begin{aligned} \bar{\varepsilon}_m &= \bar{\varepsilon}_g \\ \varepsilon_m^d(X,Y,\phi) &= \frac{1}{A_g}\int_{L_y}\int_{L_x} \varepsilon_g^d(x',y',X,Y,\phi)dx'\,dy' \\ \varepsilon_m^u(X,Y,\phi) &= \frac{1}{A_g}\int_{L_y}\int_{L_x} \varepsilon_g^u(x',y',X,Y,\phi)dx'\,dy' \end{aligned} \tag{15}$$

where A_g is the area of the gage.

Let us define the apparent strain, which is the strain actually recorded by the data acquisition system, as

$$\varepsilon_a \equiv \varepsilon_m + \varepsilon_I \tag{16}$$

where $\in_m$ is the actual average strain on the gage section, and $\in_I$ is the random error introduced by all other sources such as gage defects, instrument errors (calibration, gain, gage factor, etc.), and interference. To detect the error components we must analyze the variation in gage output. Since the errors are statistically independent, the variance in the apparent strain is the sum of three variances :

$$\sigma_a^2 = \sigma_u^2 + \sigma_d^2 + \bar{\varepsilon}_g^2\sigma_I^2 \tag{17}$$

where σ_a^2 is the apparent or measured sensor output variance, σ_u^2 is the variance due to the microstructure, σ_d^2 is the variance due to the material defects, and $\bar{\varepsilon}_g^2\sigma_I^2$ is the variance due to instrument error.

A SPECIFIC EXAMPLE

In this section some assumptions are made about the relationship between unit cell strain and macroscopic strain which allow us to find closed form expressions for σ_u^2. We will consider a balanced plain weave material. The width, spacing, and density of the yarns are the same in both the warp and weft directions. The only geometric parameter important in this study is the microstructure wave length λ, which is the distance it takes for the microstructure to repeat itself in either the warp or weft direction.

In order to find the contribution of unit cell strain to the overall variance, it is necessary to specify the probability distributions of X and Y. Here, we consider the case of random position of a gage on the unit cell for $\phi = 0$. Using the definitions,

$$\alpha \equiv \frac{L_x}{\lambda} \quad \beta \equiv \frac{L_y}{\lambda} \quad \gamma \equiv \frac{\kappa}{\pi\lambda} \tag{18}$$

the variance is given by

$$\sigma_u^2 = \frac{1}{A_g^2} I_2 = \frac{\gamma^2}{\alpha^2\beta^2} \sin^2(\pi\alpha)\sin^2(\pi\beta)\bar{\varepsilon}_{xx}^2 \tag{19}$$

where κ is a parameter which defines the magnitude of the displacement perturbations caused by the microstructure for a given material
Figure 2 shows $\sigma_u / \bar{\varepsilon}_g$ as a function of α and β with $\gamma \equiv 1$. It is clear that $\sigma_u / \bar{\varepsilon}_g$ generally decreases as the sensor gets longer or wider. Also, if the sensor length or width is a integer multiple of the unit cell length $\sigma_u / \bar{\varepsilon}_g$ is zero. In fact, the error is almost zero whenever the gage is wider and longer than the unit cell. Conversely, gages smaller than the unit cell can have large errors.

EXPERIMENTAL METHODS

In order to validate the theory developed in the previous sections, a series of experiments was performed. Coupons with multiple strain gages were tested in uniaxial tension. The variance in gage output was calculated for each coupon. These observed variances are used to determine which components of the sensor error model are significant.

A graphite-polyester composite material was chosen for the test material in order to maximize the ratio of the stiffness of the reinforcement to the stiffness of the matrix, thereby maximizing the magnitude of the microstructurally induced strain perturbations. A plain

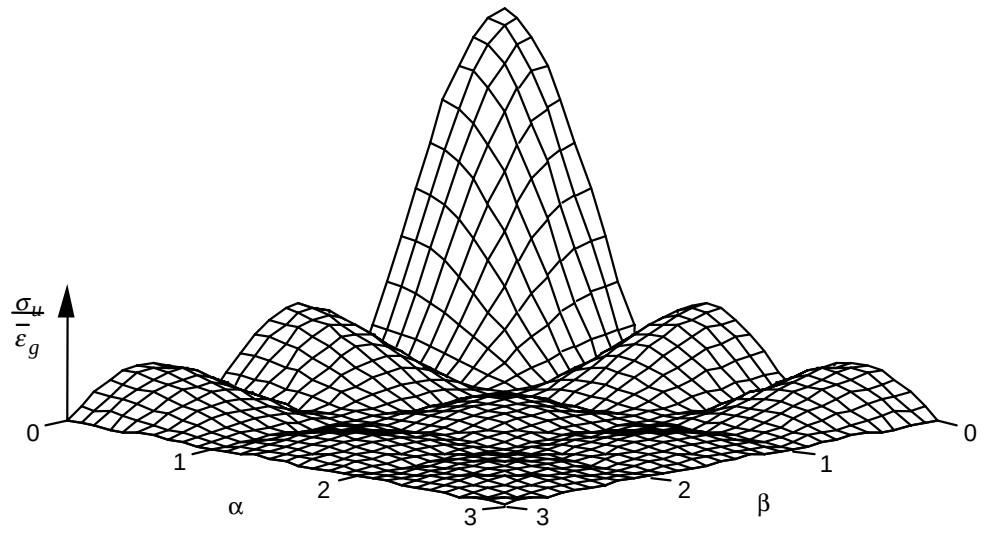

Fig. 2 σ_u/ε_g vs function of gage dimensions α and β

weave was the textile form chosen since it has the smallest unit cell size for a given yarn size and thereby minimizes the maximum required gage size. The chosen preform material had 8 warp yarns per 25.4 mm (1") and 8 weft yarns per 25.4 mm (1") giving it microstructure repeat period, λ, of 6.35 mm (0.25"). A four layer laminate was made.

After cure, the material was end-tabbed and cut into 25.4 mm (1") wide and 508 mm (20") long coupons using a diamond tipped blade on a polishing table. This technique allowed accurate parallel cuts to be made. The multiple strain gages were mounted on both sides of eight coupons. The largest gage had a gage length of 12.7 mm (0.5") and an overall length of 20.3 mm (0.8"). Therefore, the gages were placed 25.4 mm (1") apart nominally. The set of gages was centered in the gage section of the coupon. However, in order to properly randomize the test, a random offset in the range of 0.00-6.35 mm (0.00-0.25") was added to the 25.4 mm (1") nominal starting position of the gages. After the random off-sets were generated, the clearance gap between adjacent gages was checked to make sure that two adjacent gages would not overlap. Chance would have it that none of the gages overlapped. Thus, the starting position of each gage was at a randomly assigned position along the tow.

All coupons except Coupon 6 had 7 gages on each side. On one side (6A) of Coupon 6, ten gap-centered gages were mounted while on the other side (6B), ten tow-centered gages were mounted. The nominal length and width of gages for Coupon 6B are 1.575 mm (0.062") and 3.048 mm (0.120"), respectively.

The coupons were loaded to a nominal 0.15 percent strain and the output of each gage was recorded. A plot of gage reading versus average gage reading for Coupon 6B are shown in Fig. 3. Notice how widely dispersed the readings are for Coupon 6B, which has small tow-centered gages, and thus microstructurally induced variation. The results dramatically demonstrate the importance of considering gage size relative to unit cell size.

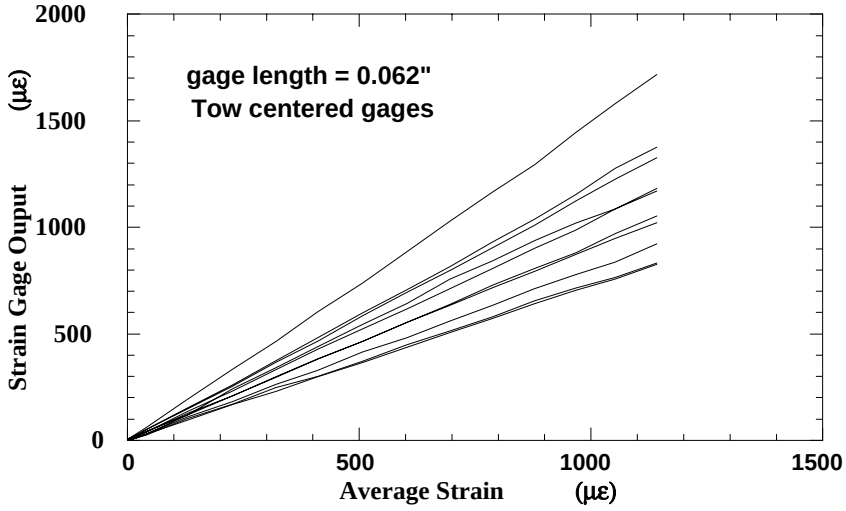

Fig. 3: Gage output vs average - Coupon 6B

CONCLUSIONS

The variation in strain caused by the microstructure of a textile composite can have a significant effect on the output of strain gages. If gages of the proper size are used, the effect of microstructurally induced variation is essentially eliminated. However, if the gages are too small the measurements can be inaccurate. In fact, with very small gages and composites made of a polymer matrix and a textile preform consisting of a high modulus fiber such as graphite, the magnitude of the error is so large that the measurements are almost worthless. Thus, even though strain gages are usually idealized as "point sensors", their distributed nature can play an important role with regard to their accuracy. A set of guidelines for the use of strain gages on textile materials has been presented in Refs. [5, 6].

REFERENCES

1. Post, D., Han, B. and Ifju, P., "Textile Composites," in *High Sensitivity Moire - Experimental Analysis for Mechanics and Materials*, Springer-Verlag, New York, 1994, pp. 313-328.

2. Byun, J. H. and Chou, T. W., "Modelling and Characterization of Textile Structural Composites: A Review," *J. Strain Analysis*, Vol. 24, No. 4, 1989, pp. 253-262.

3. Byun, J. H. and Chou, T. W., "Processing-Microstructural Relationships of 2-Step and s4-Step Braided Composites," *Comp. Sci. Tech.*, Vol. 56, No. 3, 1996, pp. 235-251.

4. Chou, T. W., *Microstructure Design of Fiber Composites*, Cambridge University Press, Cambridge, UK, 1992.

5. Lang, E. J., *Intelligent Textile Composite Materials Containing Lineal Strain Sensors*, Ph.D. dissertation, University of Delaware, Newark, Delaware, 1996.

6. Lang, E. J. and Chou, T. W., "The Effect of Strain Gage Size on Measurement Errors in Textile Composite Materials," *Comp. Sci. Tech.*, submitted for publication.

7. Montgomery, D. C., *Design and Analysis of Experiments*, Third ed., John Wiley & Sons, New York, 1991.

8. Tsou, H. S. and Hollkamp, J. J., "Collocated Independent Modal Control with Self-Sensing Orthogonal Piezoelectric Actuators" - Paper AIAA-94-1737-CP, *AIAA/ASME Adaptive Structures Forum*, Hilton Head, SC, AIAA, 1994.

ACKNOWLEDGMENTS

This work was supported by the U. S. Army Research Office under the University Research Initiative program at the University of Delaware. We also thank Teddy Yong of the Imperial College, UK for his assistance with the experimental work.

COMPRESSION STRENGTH OF TEXTILE COMPOSITES

Kunigal N. Shivakumar

Center for Composite Materials Research, Department of Mechanical Engineering
North Carolina A&T State University, Greensboro, NC 27411, USA

SUMMARY: Compression strengths of 3-D braided, 3-D orthogonal woven, and 3-D braided with pultruded rods composites were measured. The average strength of braided, woven, and braided with pultruded rod composites was 262.7, 373.6, and 268.3 MPa, respectively. The data scatter was reasonable for woven and braided with pultruded rod composites but it was large (about ±17%) for 3-D braided composites. Micrographic studies concluded that the natural waviness of fiber tows in textile composites lead to buckling and shear kinking fracture of fibers. The tow collapse model, which incorporates this phenomenon, accurately predicted the compression strength of all three textile preform composites. The compression strength was found to be strongly dependent on the axial tow misalignment angle. The use of pultruded rods in place of axial braider tows reduced the manufacture process induced tow misalignment and hence increased the compression strength of braided composites.

KEYWORDS: textile preform composites, compression strength, microbuckling, tow collapse model, braided composite, woven composite, pultruded rod

INTRODUCTION

Advances have been made in laminated composite materials to build structures that are lighter, stiffer, and stronger than their metallic counterparts. Further developments are being in reducing the manufacturing cost, sometimes at the expense of performance. Textile preform composites are one such development. The interlocked fiber architecture increases the delamination resistance of the composites, but the natural waviness of fibers can significantly reduce its compression strength. Some innovative ways of selectively reinforcing composite structural components have been experimented in helicopter industries. However more studies are needed to improve the compression properties of textile preform composites. In addition, analytical compression strength models would help in understanding the influence of various parameters that contribute to the strength and developing innovative processing and fabrication techniques to improve the strength. In this direction, Shivakumar and Emehal[1,2] developed a simple compression strength model, referred to as the “tow collapse model” for multiaxial laminates and textile preform composites. This model is an extension of unidirectional fiber microbuckling (or kinking) models of Argon’s[3], Budiansky[4], and Fleck and Budiansky[5]. The objective of this paper is to verify the tow collapse model through experimentation on 3-D triaxial braided and woven composites. Then, evaluate the use of pultruded axial rods to enhance the compression strength of textile preform composites.

MATERIAL SYSTEM

The textile preform composite panels were made of BASF G30-500, 6k graphite fibers and Dow Chemicals' Tactix 123 resin. Three types of textile architecture were used, namely, 3-D braid, 3-D orthogonal weave, and 3-D braid with pultruded rods (referred to as braid with pultruded rods). In the third case, the axial tows were replaced by pultruded rods, which are straight like an arrow. Fabric architecture is designated by the orientation of the fiber tows about the load axis. Braids are represented by $0/\pm\beta$, where β is the braid angle and the weave is represented by 0/90/90. The 0 deg represent the axial direction and the two 90 deg represents the two orthogonal axis on the plane normal to the weaving direction. Flat panels of 300x300 mm were fabricated using the resin transfer molding process. Specimens of 125x19 mm and 5.5 mm thickness with 25 mm gage length were extracted for compression tests. Table 1 lists preform architecture and the fiber volume fraction (V_f) of the specimens.

Table1 1: Measured and calculated compression strength of textile preform composites.

		Compression strength, MPa				
	Fiber volume fraction	Test data		Tow collapse model		
		Uncorrected	Corrected for SCF			
Braids				$6^o/\pm17^o$	$7^o/\pm17^o$	$8^o/\pm17^o$
B1	0.45	218.6	242.6	311.9	282.5	260.8
B2	0.33	235.1	261.0	232.8	211.0	194.6
B3	0.35	277.2	307.7	245.4	222.4	205.2
B4	0.41	215.8	239.5	283.2	256.6	236.8
Average	0.38	236.7	262.7	268.3	243.1	224.3
Weaves				$3^o/\pm90^o$	$4^o/\pm90^o$	$5^o/\pm90^o$
W1	0.43	367.1	414.9	482.2	374.2	309.6
W2	0.46	396.7	448.2	521.9	405.0	335.1
W3	0.42	408.3	461.4	473.2	367.2	303.9
W4	0.44	322.2	364.1	500.4	388.2	321.3
Average	0.44	373.6	422.1	494.4	383.7	317.5
Braids with pultruded rods				$2^o/\pm37^o$	$3^o/\pm37^o$	$4^o/\pm37^o$
PR2	0.25	242.4	269.1	381.2	266.1	208.7
PR3	0.35	249.5	276.9	548.6	382.9	300.3
PR4	0.25	244.2	271.1	389.0	271.5	212.9
PR5	0.26	230.7	256.1	409.1	285.6	223.9
Average	0.28	241.7	268.3	432.0	301.5	236.5

Note that the axial fiber orientation of composites was different for different types of textile architectures. Axial fiber tow orientations ranged from 6-8 deg for 3-D braids, 3-5 deg for weaves, and 2-4 for braid with pultruded rods. Note that the pultruded rod's panel was fabricated with low lateral pressure so that the rods are not broken during the fabrication. This resulted in a low fiber volume fraction (average V_f =0.28).

TOW COLLAPSE MODEL

The tow collapse analysis[1,2} is an extension of microbuckling analysis of Argon[3], Budiansky[4], and Fleck and Budiansky[5] for unidirectional composites. Because of natural waviness of fiber tows in textile preform composites (see Fig. 1) and the wave angle is reasonably large no distinction is made between the misalignment and kink angles. The natural

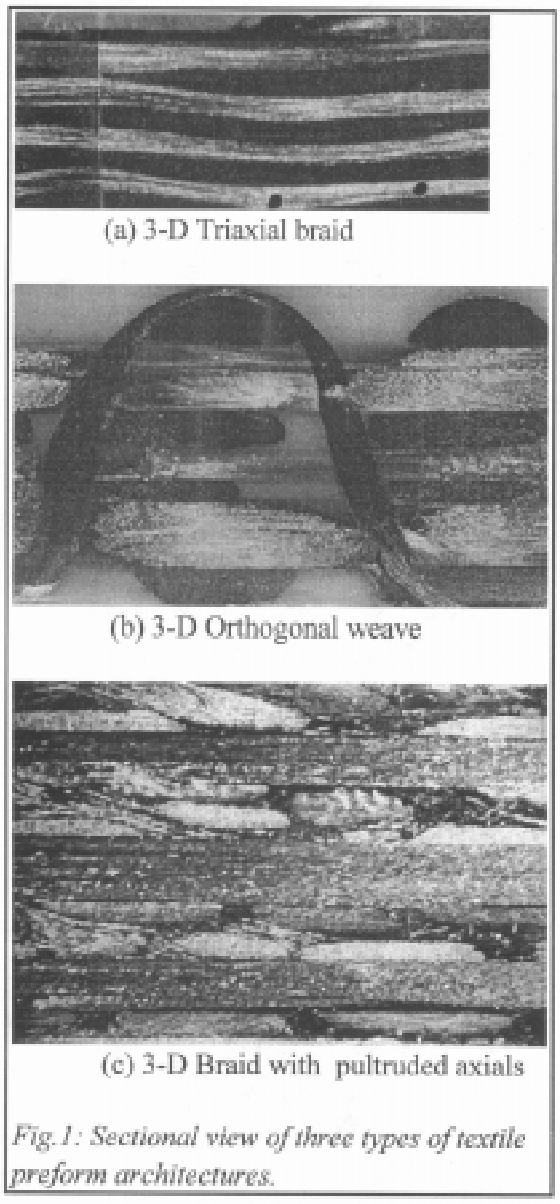

Fig.1: Sectional view of three types of textile preform architectures.

waviness is introduced during the fabric manufacturing and consolidation process. In the tow collapse model the textile composite is assumed to be an assemblage of N set of inclined fiber tows. The compression strength of the composite is the weighted sum of strengths of the N sets of fiber tows. The load carried by each set of tows is a function of tow inclination (ϕ_i) to the load, tow cross-sectional area fraction (A_i), total fiber volume fraction (V_f), transverse yield strength of the composite (σ_{tys}), and the shear yield strength (τ_{ysm}) of the matrix in the presence of fiber constraint. The expression for the compression strength (σ_c) is given by:

$$\sigma_c = \left(\frac{V_f}{V_{fRef}}\right)\tau_{ysm}\sum_{i=1}^{N} A_i \sqrt{\frac{1}{\tan^2\phi_i} + \left(\frac{\sigma_{tys}}{\tau_{ysm}}\right)^2}$$

The reference fiber volume fraction V_{fRef} is assumed to be 0.6 based on the linear relationship derived from Greszczuk[8] experimental data for unidirectional composites. Values of σ_{tys} and τ_{ysm} used in the present analysis were 127.6 and 63.8 MPa, respectively. The area fractions of 3-D braids were A_1=0.46, A_2=A_3=0.27, for the weaves were A_1=0.5, A_2=A_3=0.25, and for braids with pultruded rods were A_1=0.46, A_2=A_3=0.27.

COMPRESSION TEST

Test Specimen

Modified IITRI test specimen[6,7] with and without tapered cross-ply glass/epoxy tabs was used in the present study. Figure 2 shows the details of the specimen configuration with two types of tabs. The specimen width was 19 mm, thickness was 5.5 mm, and the unsupported length was 25 mm. The global buckling stress for simply-supported end conditions was about 101 MPa for textile composites for G=2.8 GPa and E=55.2 GPa. This buckling stress is about three times the expected compression strength of the textile composites. All specimens were strain gaged in both the axial and transverse directions on top and bottom faces of the specimen to measure both bending and membrane strains.

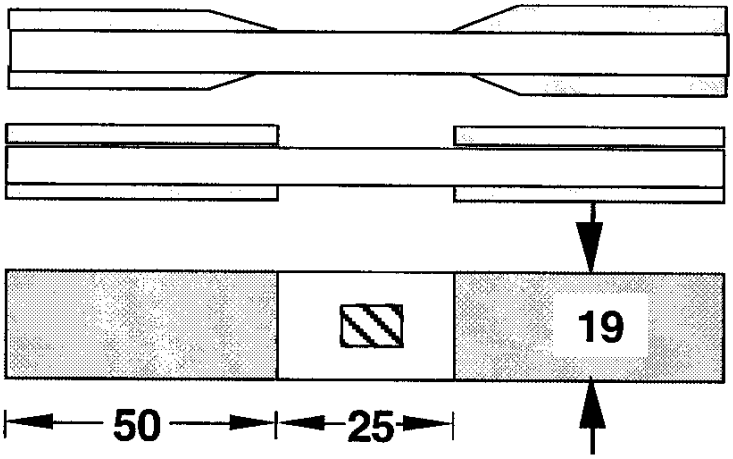

Fig. 2: Test specimen configuration.

Test Procedure

The specimens were tested in compression using the IITRI test fixture in a universal testing machine. A displacement controlled load was applied at a constant rate of 0.5 mm/minute. Stroke displacement, load, and strains were recorded at every two second interval in an automatic data acquisition system. The test was stopped immediately after the ultimate load. The ultimate load was used for calculating the compression strength of the material. During the test, the specimens were visually monitored and failure processes were monitored. After

the test, the failed regions of the specimens were inspected through a microscope and the relevant areas were photographed.

RESULTS AND DISCUSSIONS

Test Results

Figures 3 and 4 show stress-displacement response of 3-D braided and braided with pultruded rods specimens, respectively. Results of woven specimens were similar to that of braided composites, hence it is not shown. Almost all specimens failed by sudden fracture with little damage progression. An evaluation of back and front strain gages showed that the specimen bending was small and the bending strain was less than 10% of membrane strains immediately before the fracture. Visual monitoring of specimens during the test showed that the failure in braided specimens initiated as a surface tow buckling (out-of-plane buckling of tows) followed transverse shear fracture (see Fig. 5(a)). The buckled surface tows spanned between the two consecutive tows interlocks. The transverse shear failure can be characterized as the shear kinking of fibers or tow collapse. Unlike in braided specimens, woven and braided with pultruded rod specimens exhibited no out-of-plane buckling of surface tows. Tow kinking in woven composites is very clearly seen in Fig 5(b).

The ultimate load was used to calculate the compression strength. Table 1 lists the compression strengths of all the specimens. Examination of fractured specimens revealed that stress concentration due to tabs caused the specimens to fail near the tabs. A separate 3-D finite-element analysis of test specimens was conducted and found that the stress concentration factor (SCF) to be 1.11 for braided specimens (tapered tabs) and 1.13 for woven specimens (no taper tabs). Compression strength after applying this correction (refer to data after applying SCF) is also given in the Table 1. The average strength, after applying the SCF correction, is 262.7, 373.6, and 268.3 MPa for braided, woven, and braided with pultruded rod composites, respectively. The data scatter was ±17% in braided, (-14%/9.3%) in woven, and (-4.3%/3.2%) in braided with pultruded rod composites. The average V_f of braided, woven, and braided with pultruded rod composites were 0.38, 0.44, and 0.28, respectively. Contrary to one's expectation the strength of braided with pultruded rod composites has not improved from that of the braided composites because of its low V_f (0.28).

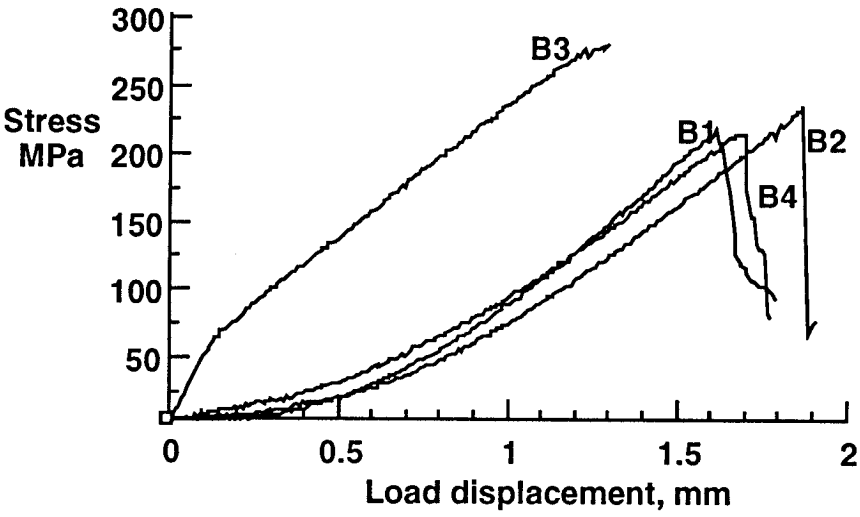

Fig. 3: Stress versus displacement of 3-D braided composites.

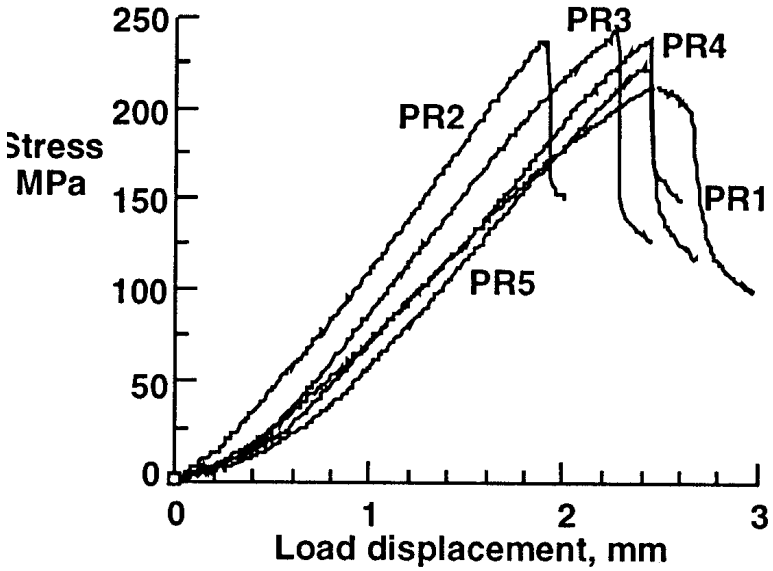

Fig. 4: Stress versus displacement of 3-D braided composites with pultruded rods.

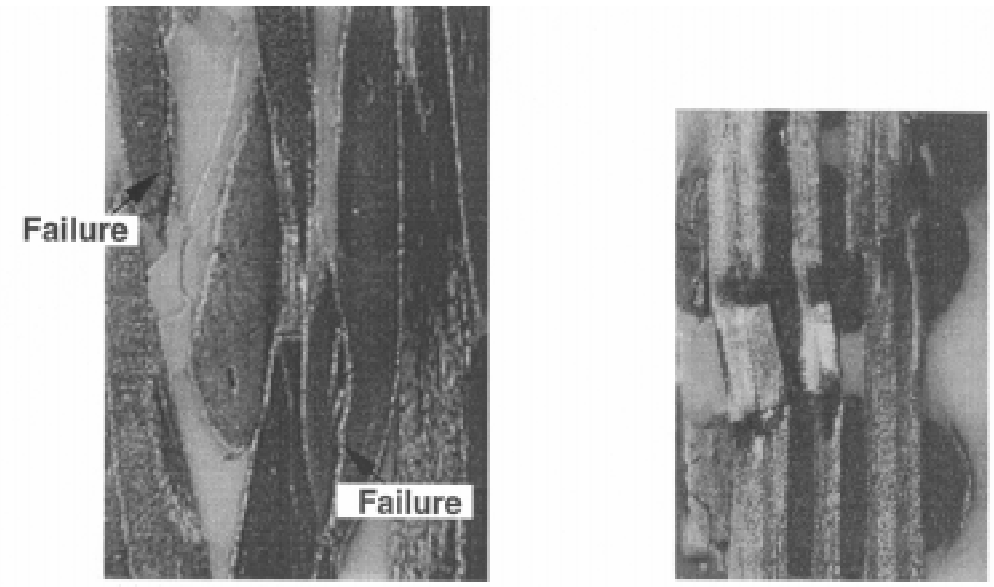

Fig. 5: Sectional view of the failed braided and woven composites.

Comparison of Analysis with Test

Calculated compression strength from the tow collapse model for all three composites is given in Table 1. Because the axial tow orientation was different from specimen to specimen and location to location, calculations are made for a range of angles: 6-8 deg for braids, 3-5 deg for weaves, and 2-4 deg for braids with pultruded rods. Fiber volume fractions of respective specimens were used in the calculation. Calculated strengths for $7^o/\pm17^o$ braided, $3.5^o/90^o/90^o$ woven, and $3.5^o/\pm37^o$ braided with pultruded rod specimens agree with the respective test data. Figure 6 shows the comparison of analysis with test data for various angle of axial tow orientations. For all three composites the analytical results agree well with the test data. Because the values of V_f were different for different composites, the advantage

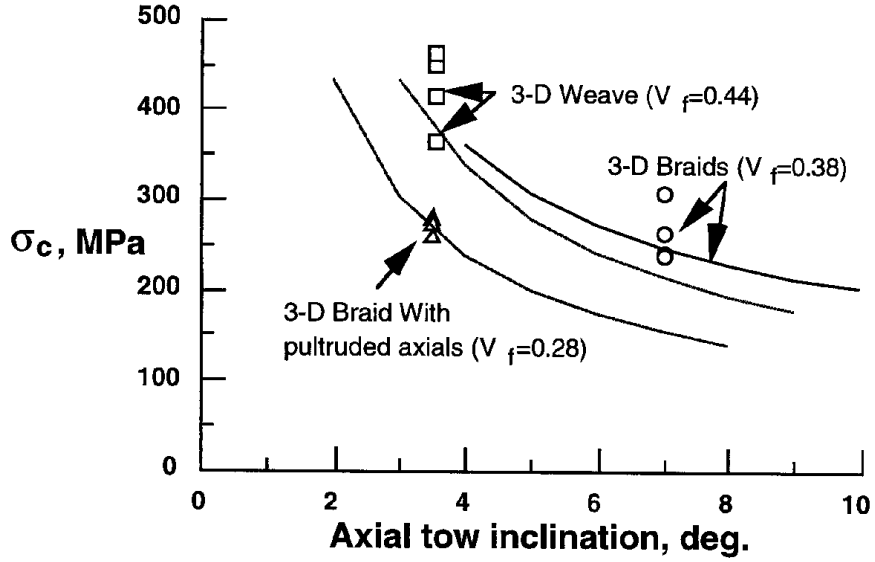

Fig. 6: Comparison of predicted and experimental compression strength.

of using the pultruded is not apparent. The figure 7 shows the normalized plot of Fig. 6. All the strengths are normalized by average V_f (0.38) of the braided composites. Normalized compression strength of braid with pultruded rod composites is 327.1 MPa about 38% larger than the bare 3-D braids (262.7 MPa). This strength increase is attributed to smaller misalignment angle of pultruded rods. It is apparent from the tow collapse model equation that the lower misalignment angle gives higher compression strength of braided composites. Therefore, the use of pultruded rods as axial tows can increase the compression strength. Noted here that any process modification to increase V_f might change the axial tow orientation. In the case of woven composites, because the axial tows were held in tension during weaving, it had the lower misalignment angle. Finally, the tow collapse model has all the important parameters to predict the compression strength of textile composites.

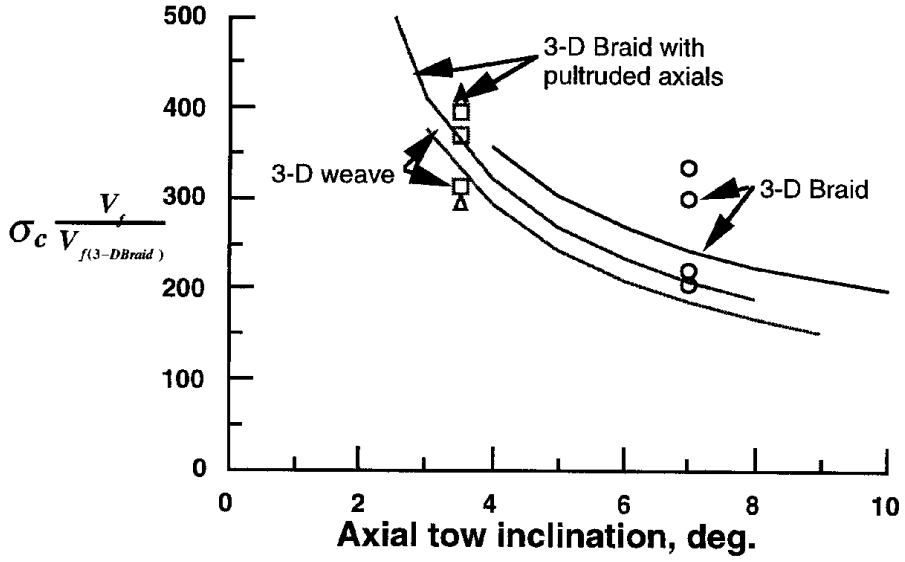

Fig. 7: Normalized compression strength of the three composites.

CONCLUDING REMARKS

Three types of textile preform composites were made from BASF G30-500 6k graphite yarns and Dow Chemicals Tactix 123 matrix, using a resin transfer molding technique. The preform architectures were 3-D braid ($7^o/\pm17^o$), 3-D orthogonal weave ($3.5^o/90^o/90^o$), and 3-D braid with pultruded rods ($3.5^o/\pm17^o$). In the last preform the axial tows were replaced by pultruded rods. Compression tests were conducted using the IITRI test fixture. The average compression strength of braided, woven, and braided with pultruded rod composites was 262.7, 373.6, and 268.3 MPa, respectively. The data scatter was reasonable for woven and braided with pultruded rod composites but it was large (about ±17%) for 3-D braided composites. Micrographic studies concluded that the natural waviness of fiber tows in textile composites lead to buckling and shear kinking fracture of fiber tows. The tow collapse model, which incorporates this phenomenon, accurately predicted the compression failure of all three textile preform composites. The compression strength was found to be strongly dependent on the axial tow misalignment angle. A small variation in the axial tow orientation can have a significant change in the compression strength. Braid with pultruded rods had small misalignment angle, consequently it had high compression strength. Similar trend was noticed also in woven composites, wherein the axial tows were held in tension during the weaving. Therefore the use of pultruded rods in place of axial tows can improve the compression strength of braided composites.

REFERENCES

1. Shivakumar, K. N., Emehel, T. C., Avva, V. S., and Sadler, R. L., "Compression Strength and Failure Mechanisms of 3-D Textile Composites," AIAA Paper 95-1159, 1995.

2. Emehel, T. C. and Shivakumar, K. N., "Tow Collapse Model for Compression Strength of Textile Composites," Proc. of ASC 10th Technical Conference, Santa Monica, Ca. October 18-20, 1995.

3. Argon, A. S., “Fracture of Composites,” *Treatise of Materials Science and Technology*, Vol. 1, Academic Press, New York, 1972.

4. Budiansky, B., "Micromechanics,” *Computers and Structures*, Vol. 16, No.1, 1983.

5. Fleck, N. A. and Budiansky, B., “Compressive Failure of Fibre Composites due to Microbuckling.” *Proc. IUTAM Symp. on Inelastic Deformation of Composite Materials*, Troy, New York, May 29-June 1, 1990, ed. J. Dvorak, pp. 235-273.

6. ASTM Standards 1993 Annual Book, Section 15, Vol. 15.03, American Society for Testing and Materials, Philadelphia, Pa.

7. Minguet, P. J., Fedro, M. J., and Gunther, C. K., “Test Methods for Textile Composites,” *NASA CR-4609*, July 1994.

8. Greszczuk, L. B., “Microbuckling Failure of Circular Fiber-Reinforced Composites,” *AIAA Journal*, Vol. 13, No. 10, 1975, pp. 1311-1318.

PREFORMS FOR COMPOSITE PARTS MADE BY TAILORED FIBRE PLACEMENT

D. Feltin, K. Gliesche

Institute for Polymer Research Dresden, Hohe Str. 6, D-01069 Dresden, GERMANY

SUMMARY: A special characteristic of fibre reinforced composites is their anisotropic properties. The maximum of the mechanical properties exist only along the fibre direction. The Institute of Polymer Research developed a new textile process for the production of reinforcing structures. This process allows the consequent transfer of calculated results into textile reinforcements, so that the reinforcement has locally varying fibre orientations and quantities. This paper reports on the technology of tailored fibre placement, the advanteges and the possibilities of this technology by means of demonstrator parts.

KEYWORDS: composite material, fibre preforming, tailored fibre placement, application

INTRODUCTION

Different structures for reinforced composite parts today are well known. These are produced for instance by weaving, knitting or braiding [1-4]. For the reinforcement of highly loaded composite components the fibres should be arranged in the following way:

- stretched (without waves and twists)
- aligned to the stress field
- constant stress (the cross-section of the component corresponding to the local load)

Common textile structures can sometimes attend this requests in an economical way.

That is why in the Institute of Polymer Research developed a new textile process for the production of reinforcing structures [5,6]. This process allows the consequent transfer of calculated results into textile reinforcements, so that the reinforcement has locally varying fibre orientations and quantities.

ANISOTROPIC MATERIAL BEHAVIOUR

A special characteristic of fibre reinforced composites is their anisotropic properties. This means the properties, especially the mechanical properties like strength or stiffness are dependent on direction. The maximum of these properties exist only along the fibre direction. If the fibre direction differs from that of the applied stress the mechanical properties are reduced. If the angle between the fibre and the load direction differs only 10 degrees then the strength is reduced to 20% of the maximum (see Fig.1) [7].

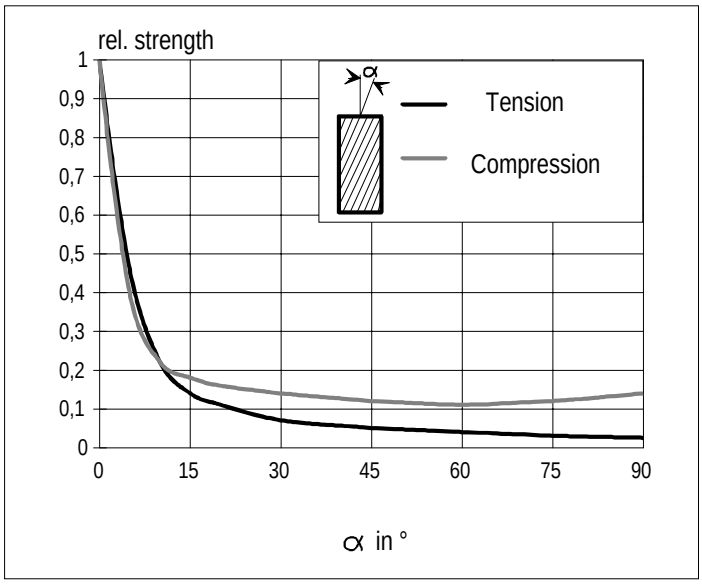

Fig.1: Relative strength of carbon fibre UD reinforced composite with epoxy resin dependence on the angle between the load and the fibre direction

That is why is the agreement of fibre and the load direction is very important for the properties of a component. Through the maximum exploitation of the fibres very light weight structures are possible. Requirements for this are:

- exact knowledge of the load cases
- small number of load cases
- is it possible to produce textile structures with the necessary fibre orientations?
- can the textile structures be processed to composite components?

TAILORED FIBRE PLACEMENT (TFP)

With tailored fibre placement it is possible to produce reinforcing structures with stress field aligned fibre orientations. This process is based on the well known embroidery technology, which is currently used for decorating fabrics. The principle of the production process is shown in Fig. 2.

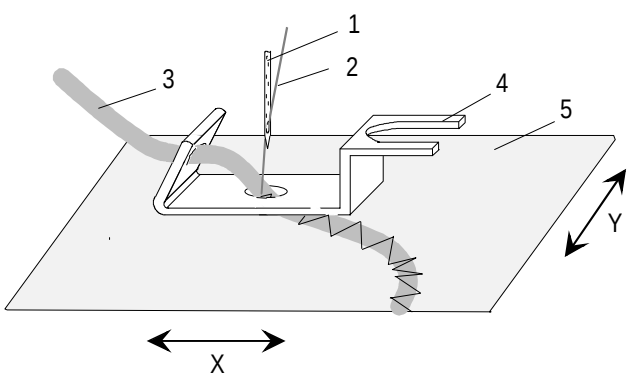

1 - Needle
2 - Needle thread
3 - Carbon roving
4 - Hold down device
5 - Base material
X,Y - possible move directions

Fig. 2: Principle of tailored fibre placement

A roving is fixed through stitches on a base material. Between the stitches the base material can be moved by numeric control in the X,Y direction. The roving is placed on the base material by zig-zag stitches either side of the roving. The roving can be made of carbon, glass fibres or other types of fibres. The base material can be a fabric or a nonwoven. Suitable is a thin glass fibre fabric. In most cases the needle yarn is made of polyester.

Fig. 3 shows the working unit of the fibre placement machine.

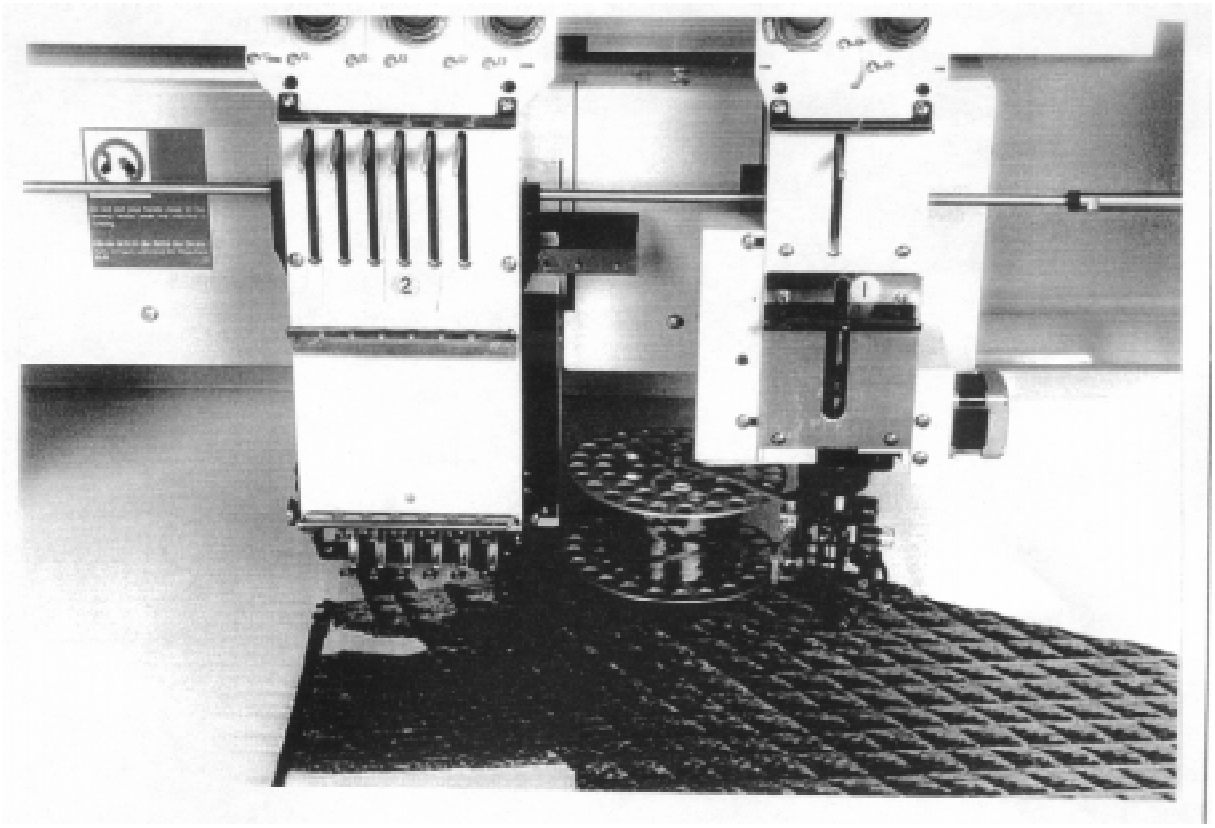

Fig.3: Tailored fibre placement machine

The main advantage, compared to the common textile technologies, is the ability to arrange reinforcing fibres in every direction of the reinforcing area from an angle of 0° to 360°. Accumulation of fibres can be achieved by stitching several times across the same area.

MECHANICAL PROPERTIES

Table 1 shows mechanical properties of UD and 0°/90° reinforced composites made by TFP. It can be seen that this composite reaches the usual values.

APPLICATIONS

Brake Booster

The brake booster is a component that is used to support the bicycle brake. This component is fixed in front of the brake and prevents deformations of the brake shoe holder devices. The principle function is shown in Fig. 4.

Table 1: Mechanical properties of UD and 0°/90° reinforced composites made by TFP

Bending Test					
fibre	matrix	structure	fibre volume fraction (%)	σ_{max} (MPa) (coefficiet of variation)	E (GPa) (coefficiet of variation)
carbon fibre (Tenax HTA)	epoxy	UD	53	1440 (2,2 %)	103,2 (5,9 %)
carbon fibre (Tenax HMS 40)	epoxy	UD	53	1059 (5,0 %)	154,1 (3,3 %)
carbon fibre (Tenax HTA)	epoxy	0°/90°	52	912 (3,2 %)	71,8 (0,7 %)
glass fibre (commingling yarn)	PA6	UD	50	781 (3,6 %)	28,4 (2,0 %)
Tension Test					
carbon fibre (Tenax HTA)	epoxy	UD	48	1438 (3,0 %)	115,0 (1,9 %)
glass fibre (EC 17-1200-G52)	epoxy	UD	53	904 (3,8 %)	42,0 (0,5 %)

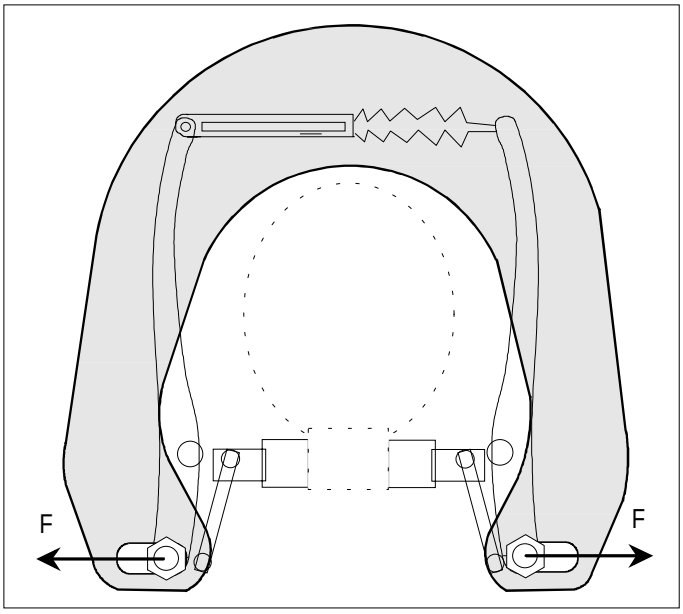

Fig. 4: Principle function and load case of the brake booster

Because the brake booster is used as a curved cantilever beam the stress field of this component for the represented load case is easy to determine. The outer areas will be loaded in compression, the inner areas in tension and the middle in shear stress. Therefore the fibres in the outer and in the inner areas should be a in 0° direction and the middle in an angle of +45°/-45°. Fig. 5 shows 3 different types of brake boosters.

A brake booster, made of aluminium, is tested as reference for the composite components. The first component type is produced through the use of a special fibre bundle. This fibre bundle, existed of 4 carbon rovings (4 x 12K), held together by axial threads around it. The cross section of this fibre bundle is circular and is fixed on the base material by stitches through the reinforcing fibres.

The second brake booster type is produced though the fixing of a carbon roving (12K) directly on the base material by zig-zag stitches either side of the reinforcing fibres. The used quantity of carbon fibres is the same as for the component type II.

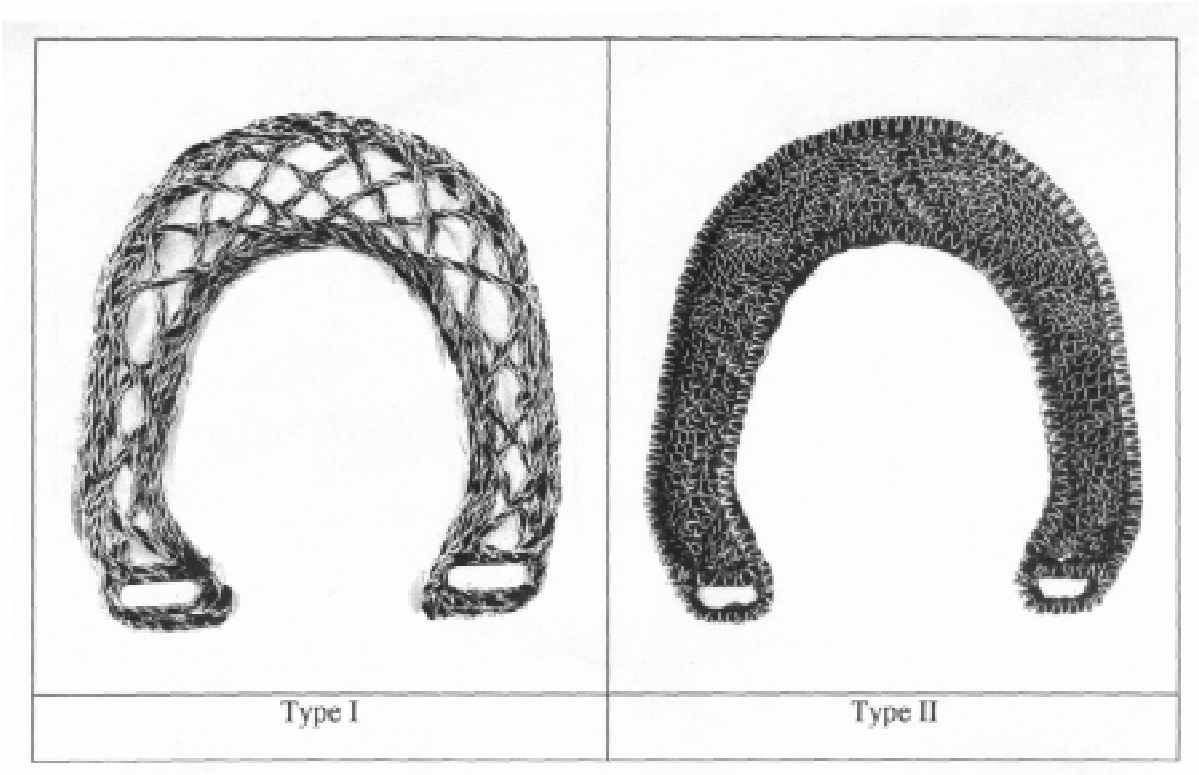

	Aluminium	*Type I*	**Type II**
Stiffness in [(N/mm)/g]	1,77	4,06	6,49

Fig. 5. Brake boosters (real size 130 mm x 135 mm) and their properties

RESULTS

Fig. 5 shows furthermore the stiffness depending on the component weight of the brake boosters at the beginning of the loading. The second brake booster shows the best results. The

values for the first component are not so very good, due to follow causing. On the cross points in the middle area (loaded in shear stress) this bundle creating a deviation of the fibre-axis in the third dimension.

The advantage of using a fibre bundle is a higher production rate compared to the second brake booster.But both the first and the second component shows better properties than the aluminium brake booster and it can be seen that the tailored fibre placement gives the possibility of very light weight constructions.

Link Plate

This component is used for full suspension bikes and transmits impulses from the back wheel over struts to the spring unit. The principle function and the load case are shown on Fig. 6

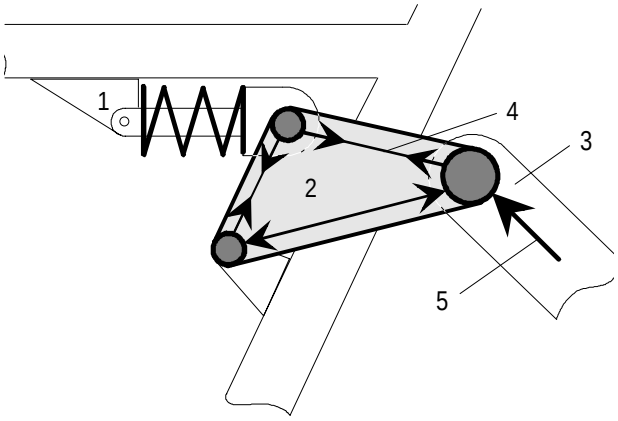

1 - Spring unit
2 - Link plate
3 - Strut to the back wheel
4 - main compression load
5 - impulses from the back wheel

Fig. 6 Principle function and load case of the link plate

The main load is the compression load in the represented area but the requirement is a compression and a tension part from hole to hole. Fig. 7 shows the optimized preform and the component.

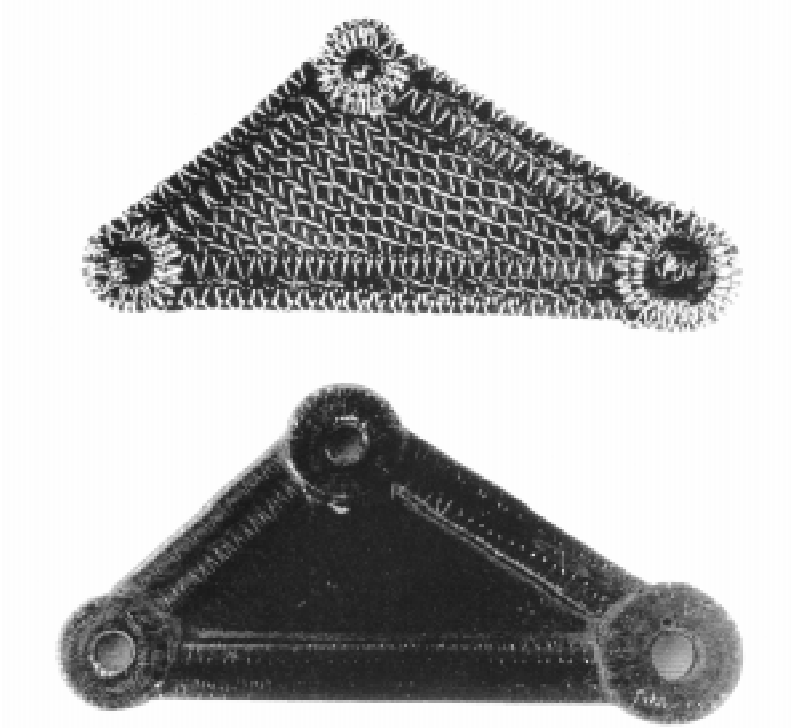

Fig.7: Preform and component (real size 115 mm x 60 mm)

The necessary fibres for the compression and tension load are in the outer area and in the middle in UD structure. This UD-structure move to a direction of 30° to the main loaded compression part and prevent the bend of this part. The weight of this link plate is only 27g and the maximum transmitted force is higher than 10 kN (determined in an experiment). The result of this force is a compression stress over 1000 MPa in the main loaded area. In the testing phase it was not possible to introduce higher loads, because the load was introduced through a bolt with a diameter of only 6 mm and this bolt failed at higher loads.

Bicycle Frame

One of the most interesting components for bicycles is the frame. The requirements, such as maximum loads, drive comfort and minimum production costs on a carbon frame are very high. The frame of a bicycle will be mainly loaded in torsion in one direction and in bending in two directions.

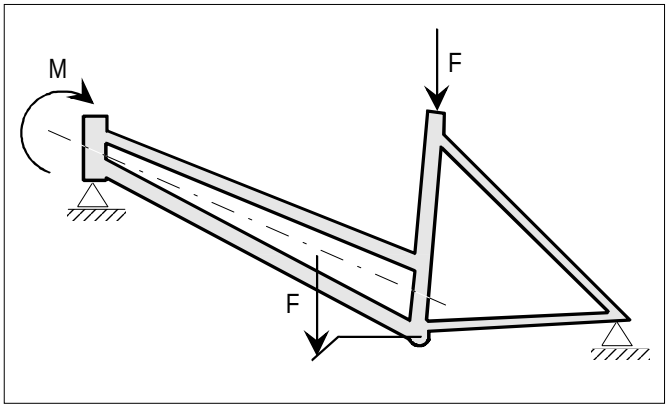

Fig. 8: Main load directions in a bicycle frame

The next figure shows the developed frame.

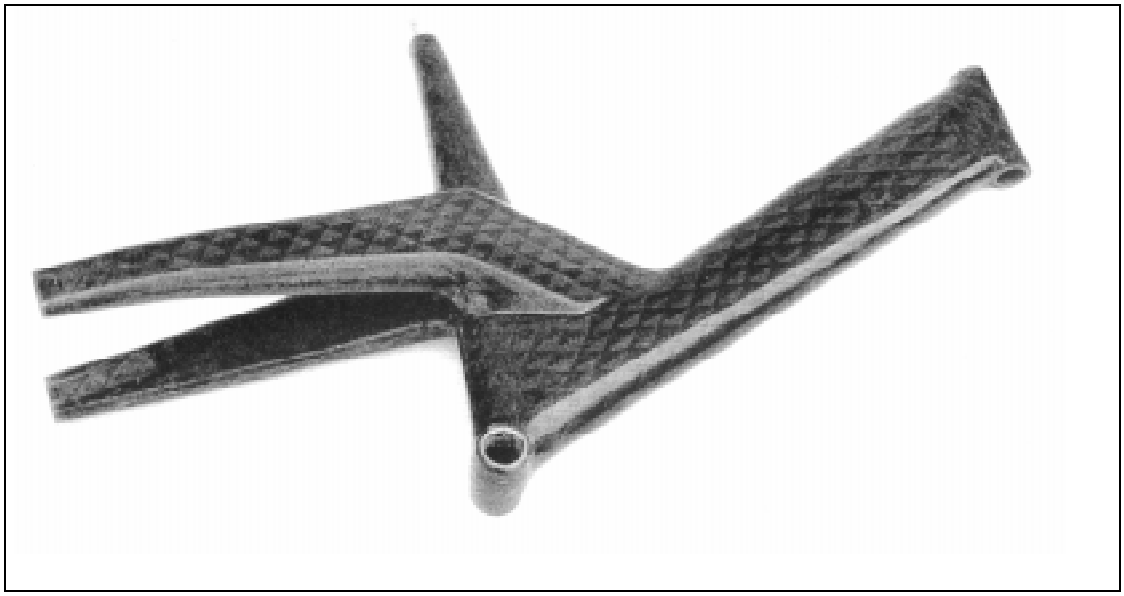

Fig. 9: Carbon bicycle frame

One of the main problems of this frame is the ordered design of this frame. In the area from the seat to the pedal crankcase, this frame has a very complex shape, so that it is not possible to place the reinforing fibres optimal on this contour. That is why we developed a reinforcing structure with 4 walls in this area (see Fig 10).

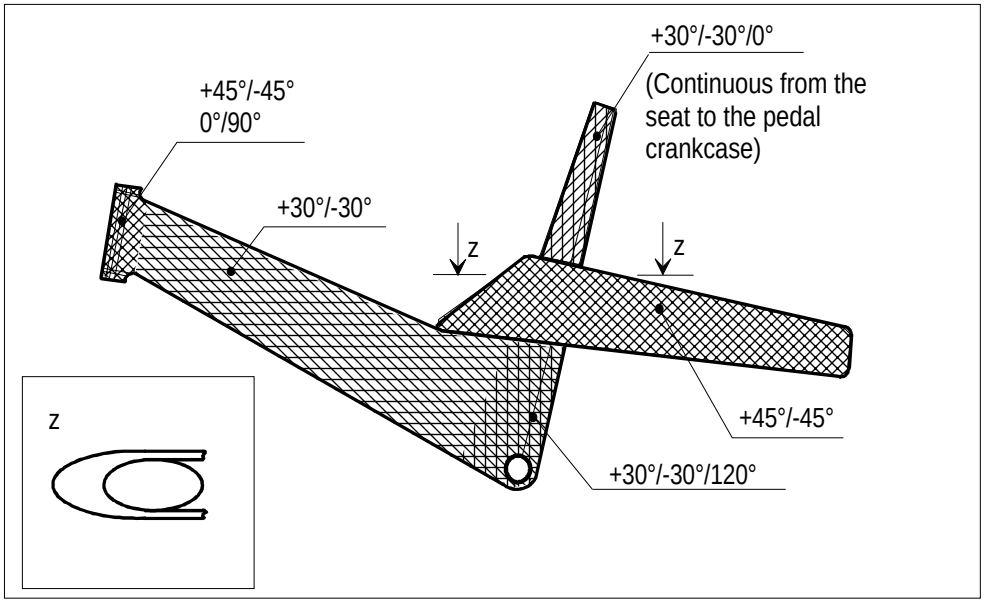

Fig. 10: Reinforcing structure of the frame

In this way it is possible to place the carbon fibres in this area in a straight line. Most fibres in this area are placed in 0° direction (direction from seat to pedal crankcase). Fig. 10 shows the directions of the fibres in the other areas. In the part from the steering unit to the pedal crankcase the fibres are placed in an angle of +/- 30°. This fibre orientation is a good

compromise compared with the optimal orientations for the torsion load and both bending loads. The fiber orientation in the rear end is +/- 45°. This is the best fibre orientation for torsion load but not the best for bending forces. This reinforcement improves the drive comfort due to reduced the bending stiffness. That is why this part can partly absorb high impulses from the back wheel.

Properties of the Frame

The weight of the carbon part of the developed bicycle frame is about 1600 g and for the necessary inserts 500 g. The inserts are made of steel and not optimized for minimum weight. One importent criterion for the quality of a frame is the torque stiffness. For the determination of this value the frame is fixed at the back wheel axis and the steering unit is loaded in torsion. The force per degree of deformation is the value for the torque stiffness of the frame. This carbon frame reaches a torque stiffness of 55 N per degree. So, despite the difficult design this frame shows good mechanical properties.

ADVANTAGES OF TAILORED FIBRE PLACEMENT

In combination with innovative design and production techniques, TFP show excellent potential for a great variety of textile preforms with stress field aligned fibre placement and reinforcment in the third dimension. Its base on well established automated design and production technologies ensures the short time from design initiation to preform production and makes the TFP an exceptionally fast prototyping technique. Reproducebility is excellent.

FINAL REMARK

This paper reports on the technology of tailored fibre placement. By means of demonstrator parts the advanteges and the possibilities of this technology are shown.

A seperate paper reports on the design methodologies which promise the best exploitations of the TFP technology. Several of these methodologies were tested in their abilities to relieve a stess concentration in a notched composite. The manufacturing of these components, the testing setups used and results are presented in the seperate paper.

REFERENCES

1. G. Niederstadt; “Leichtbau mit kohlenstoffaserverstärkten Kunststoffen”; Kontakt & Studium Band 167

2. W. Michaeli, M. Goedel; “Stationen der Herstellung von FVK-Bauteilen am Beispiel des FVK-Rades”; Fachtagung “Industrielle Anwendung der Faserverbundtechnik” an der RWTH Aachen, 1992

3. P. Offermann, G. Franske; “Beanspruchungs- und konfektionsgerechte Textilkonstruktionen für Hochleistungsverbunde”; Meliand Textilberichte, Mai 1991

4. K. Drechsler; “Beitrag zur Gestaltung und Berechnung von Faserverbundwerkstoffen mit dreidimensionaler Textilverstärkung”; Dissertation an der Universität Stuttgard; 1992

5. K. Gliesche, D. Feltin; “Automatisierte Herstellung von Langfaser (Endlosfaser) - Preforms für Faserverbund-Bauteile”; Vortrag zur 35. Internationalen Chemiefasertagung, Dornbirn 1996

6. K. Gliesche; “Sticken und Nähen verstärkender Fasern”; Spectrum der Wissenschaften, Februar 1996

7. A.H.J. Nijhof; “Ontwerpen in verzelversterkte Kunststoffen”; TH Delft, 1983

EFFECT OF WEAVE STRUCTURE ON MODE I INTERLAMINAR FRACTURE BEHAVIOUR OF PLAIN GLASS WOVEN FABRIC COMPOSITES AS A FUNCTION OF THE INTERFACE: REPORT OF A ROUND ROBIN TEST II

H.Saidpour & M.Sezen, *Bournemouth University, UK*
Y.J.Dong, H.S.Yang, Y.L.Bai & T.X.Mao, *Chinese Academy of Science, China*
C.Bathias, *CNAM/ITMA, France*
P.Krawczak, R.Bequignat & J.Pabiot, *Ecole des mines de Douai, France*
S.Pinter & G.Banhegyl, *Furukawa Electric Institute of Technology, Hungary*
J.K.Kim & M.L.Sham, *Hong Kong University of Science & Technology, Hong Kong*
I.Verpoest, *Katholike University of Leuven, Belgium*
H.Hamada, Y.Hirai & K.Fujihara, *Kyoto Institute of Technology, Japan*
C.Y.Yue & K.Padmanabhan, *Nanyang Technological University, Singapore*
Y.Suzuki, *Nitto Boseki Co.Ltd, Japan*
T.Tanimoto, *Shonan Institute of Technology, Japan*
K.Schlute, *Technical University Hamburg - Harburg, Germany*
J.K.Karger-Kocsis, *University of Kaiserslautern, Germany*
W.J.Cantwell & R.Zulkifli, *University of Liverpool, UK*
L.Ye, *University of Sydney, Australia*
A.Lowe, *Australia National University, Australia*
S.V.Hoa, *Concordia University, Canada*
V.V. Smirnov, *Metal - Polymer Resarch Institute BAS, Belarus*
L.T.Drzal, *Michigan State University, USA*
W.R Brougntor, *National Physical Laboratory, UK*
J.J.Lesko, *Virginia Polytechnic Institute and State University, USA*

SUMMARY: Short beam shear tests and mode I interlaminar fracture toughness tests are performed in a Round Robin Test (RRT) programme proposed by the Society of Interfacial Materials Science (SIMS) to characterize the interlaminar fracture behavior of E-glass woven fabric reinforced vinylester composites. Twenty institutions worldwide have participated in this programme. No specific guidelines are given for the details of the test and the data reduction schemes, so that the participating laboratories perform the tests in their own ways. Only the fiber orientations relative to the specimen length are specified i.e. warp and weft fiber specimens. The first report of this programme to be presented at the 11th International Conference on Composite Materials (ICCM-11) focuses mainly on the effect of silane coupling agent on mode I interlaminar fracture toughness tests and the stability of crack propagation. In this report, the focus is placed on the influence of weave structure of reinforcement on interlaminar fracture behavior.

KEYWORDS: e-glass woven fabric reinforced vinylester composites; silane coupling agents; interface; interlaminar shear strength; mode I interlaminar fracture toughness; weave structure.

INTRODUCTION

The interphase of composite materials is a key part which plays an important role in determining the mechanical, chemical and degradation properties in composite materials. Hence, evaluations of the interphase properties in composite materials have been performed actively [1~4]. For instance, several testing methods (e.g. fiber fragmentation tests [3], embedded single fiber tests [4] etc.) have been developed to measure the bond quality at the interphase between the fiber and matrix resin. There are also other testing methods to evaluate the interphase using the bulk composite laminates based on short beam shear tests [5,6] and interlaminar fracture toughness tests [7,8].

E-glass woven fabric reinforced composites have been widely used in commercial application, such as printed circuit boards, water tanks and fishing boats. It is well known that surface treatment is generally performed on the glass surface with silane coupling agents to improve the bonding with the matrix resin. The structure of interphase in glass fiber reinforced composites is very complex chemically and physically, and there are many factors which affect the mechanical properties of the composites made therefrom. On performing surface treatment of glass fibers, optimum conditions in order to get good adhesion between the fiber and matrix resin were reported [9].

The Society of Interfacial Materials Science (SIMS) was established in 1993 to promote the understanding of composite interphases of various kinds as an interdisciplinary problem from the perspectives of chemistry, physics, material science and engineering mechanics. As part of its activities, the SIMS has organized the RRT programme to study the mechanical properties of E-glass woven fabric reinforced composites. The aim of the programme is to exchange the experiences between the participants and enhance the fundamental understanding of the composite interphase. In the first RRT (RRT-I) programme, the tensile and bending tests were performed by ten institutions. It was found that both tensile and bending strengths increased with increasing the concentration of methacryl silane. In the present second RRT (RRT-II) programme short beam shear tests and mode I interlaminar fracture toughness tests have been performed by twenty institutions. The first part of the report presents the results on the effect of surface treatment on mode I interlaminar fracture toughness. In this paper which is the second part of the report on the present RRT programme, a focus is placed on the effect of weave structure on interlaminar shear strength (ILSS) and mode I interlaminar fracture toughness. It is aimed to contribute to further understanding of interphase properties which are vital to mechanical properties of composite materials.

EXPERIMENTAL PROCEDURE

Material

Glass woven fabrics of 44 (warp) x 34 (weft) strands count per 2.5 cm x 2.5 cm were used as reinforcement (Nitto Boseki Co. Ltd., Japan). Fig.1 schematically illustrates the elements of

weave structure in glass woven fabric which are used in this study. The distance between the center of fiber strands was longer in the warp direction than in the weft direction, due to the difference in density of fiber strands. Surface treatment was performed on the glass fiber fabric by using γ - methacryloxypropyltrimethoxysilane (A-174, Nippon Unicar, Co., Japan) and γ-glysidoxypropyltrimethoxysilane (A-187, Nippon Unicar, Co., Japan), which are called methacryl silane and epoxy silane, respectively. The concentrations of silane agents were 0.01, 0.4, 1.0 wt% methacryl silane, 0.4 wt% methacryl silane washed with methanol solvent and 0.4 wt% epoxy silane. The aqueous solution of silane coupling agent was acidified with acetic acid at ph = 4.0. The glass fiber fabrics were dipped into the silane aqueous solutions. They were squeezed by rollers and dried at 110 degree C for 10 min. Vinylester resin (R-806, Syowa High Polymer, Japan) was polymerized with 0.7 phr methyl-ethyl-ketone-peroxide. Composite laminates were fabricated by hand lay-up technique. A 40 μm thick polytetrafluoroethylene (PTFE) was inserted as an initial crack during the lay-up at the mid-plane of the laminates for mode I interlaminar fracture toughness tests.

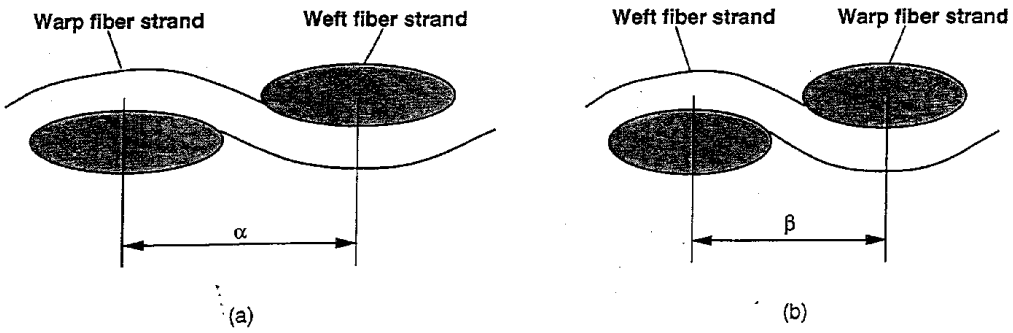

Fig.1 Schematic diagram of weave structure of glass woven fabrics: (a) warp specimens, (b) weft specimens.

Specimen Geometry and Test Condition

The SIMS fabricated and supplied the composite laminates whose thicknesses were specified by the individual participating laboratories. The participating laboratories decided the test speed, specimen geometry and so on. Typical specimen geometry for measuring interlaminar shear strength by short beam shear test was given in Fig.2 (a). The specimen was cut parallel and perpendicular to the warp strand direction, designating warp and weft specimens, respectively. Table 1 gives the details of the specimen dimensions and test conditions used by each laboratory. Short beam shear tests were performed on the specimens with all five surface treatments. The interlaminar shear strength (ILSS) was calculated according to specification BS2782 and ASTM D 2344:

$$\tau = 3P_{max} / 4wh \qquad (1)$$

where P_{max} is the applied maximum load, w and h are the specimen width and thickness, respectively.

Mode I interlaminar fracture toughness tests were performed using double cantilever beam (DCB) specimens. Specimens finished 0.01 and 0.4 wt% methacryl silane were used. Typical geometry and details dimension of DCB specimen are shown in Fig.2 (b) and Table 2. Either aluminium blocks or piano hinges were bonded to the specimen edges to allow loading in tension. Mode I interlaminar fracture toughness, G_{IC} and G_{IR}, were calculated

according to data reduction scheme chosen by the individual laboratories. The details are reported in the first part of this report [10].

Table 1 Specimen dimensions and data reduction schemes on interlaminar shear strength test.

List number	Affiliations	Width W	Thickness h	Length L	Span length D	Cross-head speed (mm/min)	Data reduction scheme*
1.	B.U.	10	3	18	15	1.0	BS2782
4.	E.M.D.	10	3	18	15	1.0	ASTM D 2344
6.	H.K.U.S.T.	6.4	4	28	20	1.3	ASTM D 2344
9.	N.T.U.	10	2.95 ± 0.05	24	15	1.2	ASTM D 2344
12.	U.K.	10	4	28	19	1.0	ASTM D 2344

Table 2 Specimen dimensions and data reduction schemes on mode I interlaminar fracture toughness test.

List number	Affiliations	Width W*	Thickness 2h*	Length L*	Crack length a	Cross-head speed (mm/min)	Data reduction scheme*
4.	E.M.D.	20	3	125-180	25-80	1.0	A
5.	F.E.I.T.	10	3	270	20	5.0	A and F
6.	H.K.U.S.T.	20	4	130	20	1.0	A
8.	K.I.T.	25	4	100	20	1.0	B
9.	N.T.U.	12.5, 25	3	125	25	1.0	C
11.	T.U.H.H.	20	5	200	55	2.0	A
14.	U.S.	25	3.8	170	65	0.5	D and E

*A = corrected beam theory (ESIS Protocol); B = modified compliance method (JIS K7086); C = load method; D = modified compliance method (ASTM 5528 - 94a); E = displacement method; F = area method.

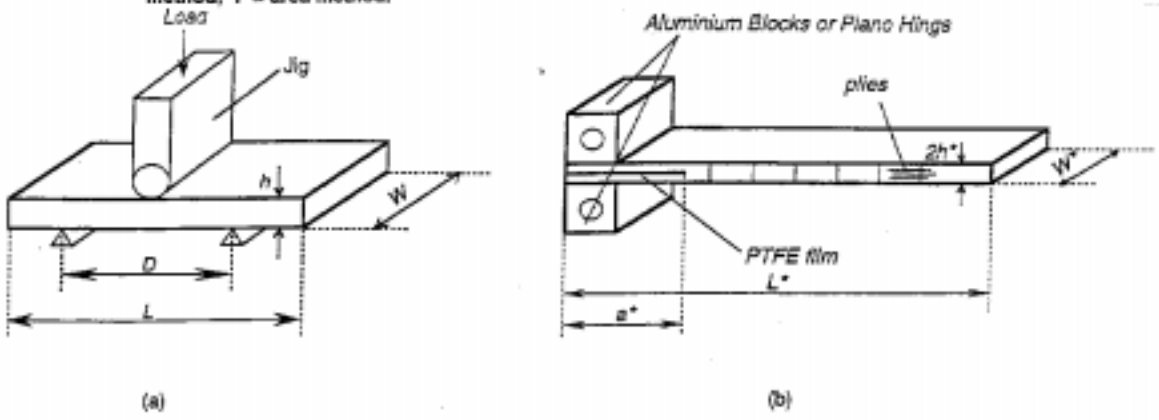

Fig.2 Schematic geometry of the specimen for ILSS test:(a) and mode I interlaminar fracture toughness test:(b).

RESULTS AND DISCUSSION

Short Beam Shear Test

Fig. 3 shows the ILSS values for composites with five different surface treatments. It can be noted here that the ILSS increased 10%~30% with increasing concentration of methacryl silane, regardless of the fiber orientation (warp or weft directions). This appears clearly on Fig.4. It is also noted that the ratio of increasing ILSS is slightly 20% higher in the weft direction than in the warp direction. This is probably related to the weave structure of the woven fabric used in this study. But in general the amplitude of the variations observed remain very low and lower than those observed between materials with different interface qualities. This suggests that the contribution of the fiber orientation is very small and could be perhaps neglected in regard to the contribution of the interface quality.

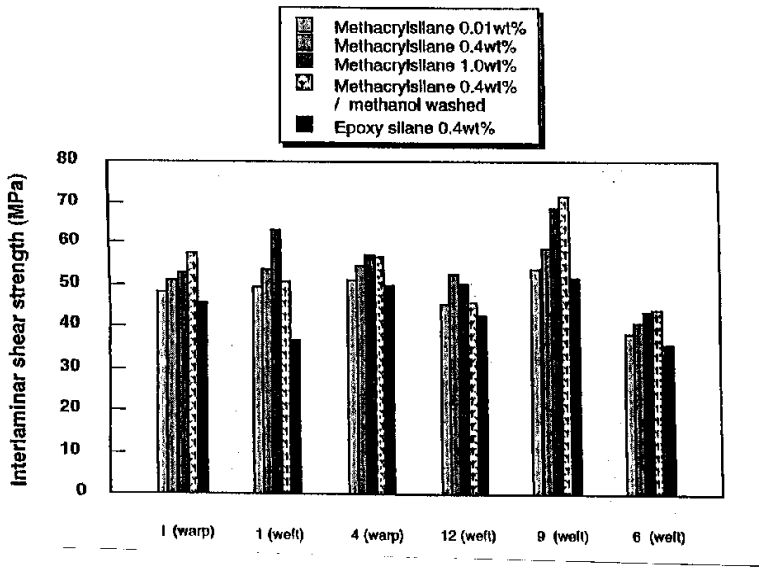

Fig.3 Interlaminar shear strength with five different surface treatments.

For a majority of laboratories, methanol washed specimen showed an increase in ILSS by 5%~20% in comparison with unwashed specimen. For 0.4 wt% epoxy silane finished specimens the lowest ILSS values were obtained among the composites with different surface treatments from all the participating laboratories. Regarding the effects of surface treatment on ILSS (nature of silane, methanol washing and amount of silane), it is finally interesting to note that the same general trends have been found previously on the basis of tensile and bending tests (strength values) [10].

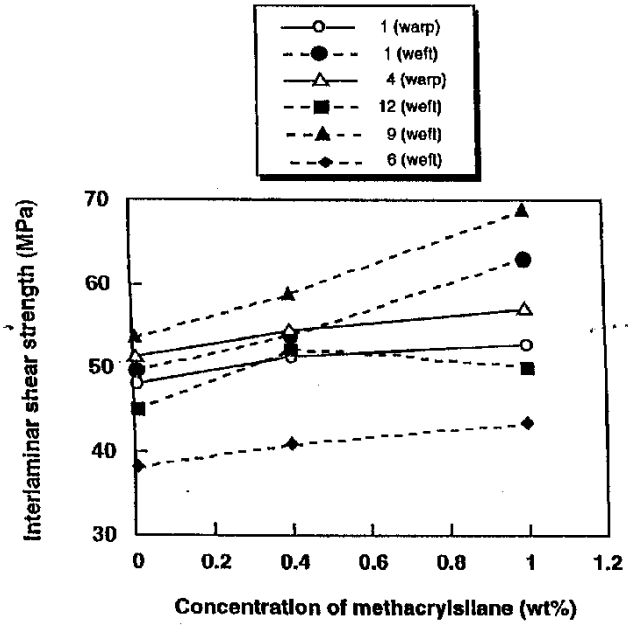

Fig.4 Interlaminar shear strength of warp and weft specimens with concentration of methacrylsilane.

Mode I Interlaminar Fracture Toughness Test

Fig.5 shows typical load - displacement curves for warp and weft specimens with finished by 0.01 and 0.4 wt% methacryl silane. In the case of 0.01 wt% specimens, the load increased to the maximum load linearly, and decreased gradually after the maximum, with stable crack propagation. The maximum loads obtained from the weft specimen was higher than the warp specimen. On the other hand, the load-displacement curve displayed saw teeth like behavior for 0.4 wt% specimens. The load dropped suddenly after reaching the maximum load, and crack propagated unstably at fast speed for both the warp and weft specimens.

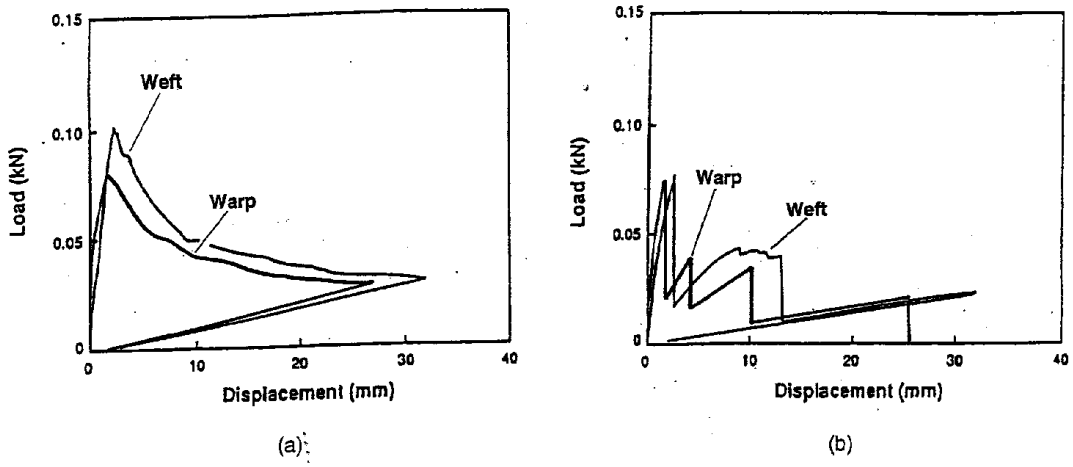

Fig.5 Typical load - displacement curves for warp and weft specimens: (a) 0.01wt% methacryl silane, (b) 0.4wt% methacryl silane.

Initiation values of mode I interlaminar fracture toughness G_{IC}, are shown in Fig.6. It is generally found that the weft specimens showed slightly higher G_{IC}, than the warp specimens,

for both silane concentrations, 0.01 and 0.4 wt%, except those reported from two laboratories. Especially, there was more difference between the weft and warp specimens in the 0.01 wt% specimen relative to the 0.4 wt% specimen. Unstable fracture occurred in the 0.4 wt% specimens so that the propagation value G_{IR}, could not be obtained. Fig.7 gives a comparison of the propagation values, G_{IR} calculated for 0.01 wt% specimens. Most laboratories reported that the propagation values, G_{IR}, were higher for the weft specimens than the warp specimens. It was also noted that the propagation values, G_{IR}, were higher than the initiation values, G_{IC}.

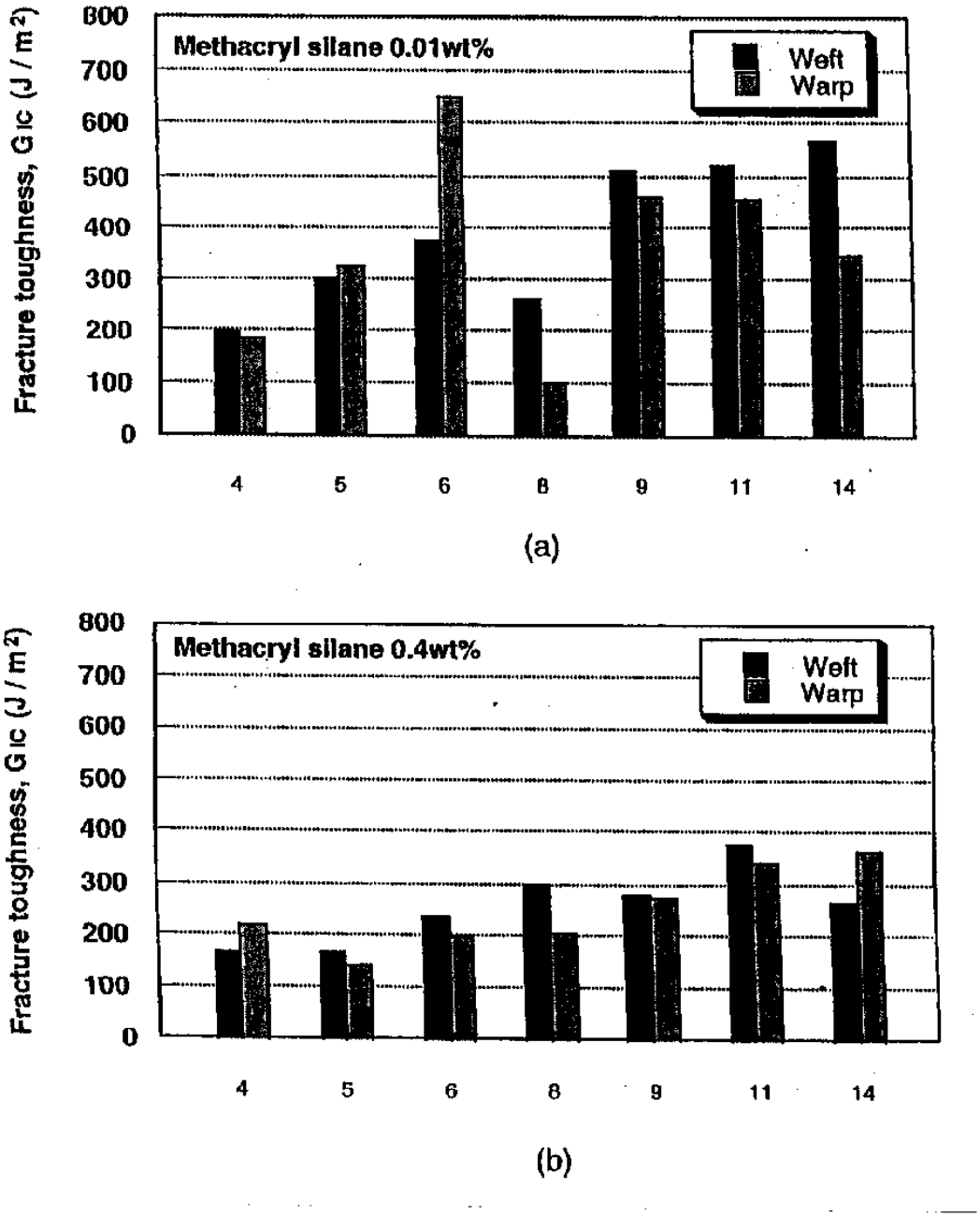

Fig. 6: Initiation values of mode I interlaminar fracture toughness of warp and weft specimens: (a) 0.01 wt% methacryl silane, (b) 0.4 wt% methacryl silane

The weft specimens had higher strands density in the longitudinal direction than the warp specimens as noted from Fig.1. As such, it is thought that crack propagation along the length of weft specimens may need more energy than along the warp direction. Accordingly, both

the initiation values G_{IC}, and propagation values G_{IR}, for the weft specimens were higher than the warp specimens. Concerning the increase of fracture toughness with crack propagation i.e., $G_{IR} > G_{IC}$, which is considered due to fiber bridging. Many researchers reported that fiber bridging gives rise to higher mode I interlaminar fracture toughness [11,12]. According to our observation, the fiber bridging builds up gradually with crack propagation.

Just as for ILSS results, the results obtained on the basis of mode I tests show that the influence of fiber orientation is far less than the influence of interface quality[10]. As over 100% variation was observed on G_{IC} initiation values with different surface treatments, only 10~20 % variation is noted when changing the fiber orientation. This confirms the fact that the interface quality plays here a role of prime importance on the damage mechanisms of such composites. The role of fiber orientation is less important.

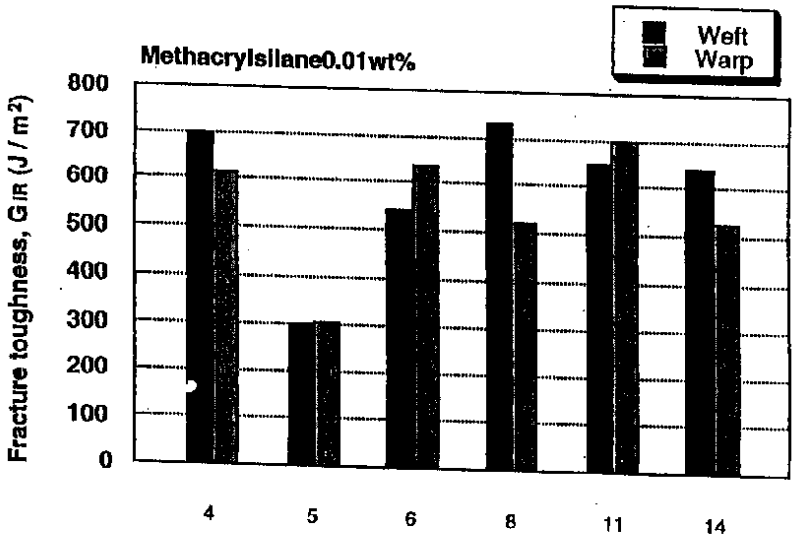

Fig. 7 Propagation values of mode I interlaminar fracture toughness of the specimens finished with 0.01wt% methacryl silane.

CONCLUSIONS

The second Round Robin Test was carried out with twenty laboratories having participated globally to study the interlaminar fracture behavior of glass woven fabric vinylester composites with five different silane coupling agents. Short beam shear tests and mode I interlaminar fracture toughness tests were performed with the specimens whose directions were both weft and warp fiber orientations. Regarding the influence of the surface treatment, it could also be noted that in general the same trends previously observed for tensile and bending strengths are obtained for ILSS. A slight increase in both the initiation and propagation G_{IC} values was generally noted when changing the fiber orientation from warp to weft direction. Finally it is interesting to note that the amplitude of the variation of the properties (ILSS or mode I) is higher when modifying the surface treatment than when modifying the orientation of the fibers. This means that the purely interfacial effects are influencing more the damage mechanisms than the weave structure effects (at least for the glass / vinylester composite materials studied here).

ACKNOWLEDGMENTS

The organizers of the 2nd round robin test programme wish to thank all the participants who completed the test as instructed and submitted the results in time. A special gratitude is due to Dr. Y.Suzuki of Nitto Boseki Co. Ltd, Japan for supplying the glass woven fabrics used in this study.

REFERENCES

1. H.Hamada, N.Nishida, Z.Maekawa & N.Ikuta, Journal of Material Science, **29**, 352 (1994).
2. P.S.Chua & M.R.Piggot, Composite Science and Technology, **22** pp.33-42 (1987).
3. G.Dorey & J.Harvey, Interfaces in Polymer Ceramic and Metal Matrix Composites, pp.694 (1988).
4. L.T.Drzal, 28th National SAMPE Symposium, pp.1051 (1983).
5. E.Fitzer, K.H.Geigl, W.Huttner & W.Weiss, Carbon, **18** pp.389-393 (1980).
6. T.Norita, J.Matsui & H.S.Matsui, Composite Interfaces, pp.213-232 (1980).
7. Y.Suzuki, Z.Maekawa, H.Hamada, M.Kibune, M.Hojo & N.Ikuta, Journal of Material Science, **27** pp.6782-6790 (1992).
8. P.Krawczak & J.Pabiot, Jornal of composite materials, **29** pp.2230-2253 (1995).
9. Y.Nakanishi & N.Ikuta, Journal of Society Material Science, **45** pp.1307-1315 (1996).
10. H.Saidpour, M.Sezen, Y.J.Dong, H.S.Yang, Y.L.Bai, T.X.Mao, C.Bathias, P.Krawczak, R.Bequignat, J.Pabiot, S.Pinter, G.Banhegyl, J.K.Kim, M.L.Sham, I.Verpoest, H.Hamada, Y.Hirai, K.Fujihara, C.Y.Yue, K.Padmanabhan, Y.Suzuki, T.Tanimoto, K.Schlute, J.K.Karger-Kocsis, W.J.Cantwell, R.Zulkifli, L.Ye, A.Lowe, S.V.Hoa, V.V Smirnov, L.T.Drzal, W.R Brougntor & J.J.Lesko, to appear in Proc.ICCM-11.
11. M.Hojo & T.Aoki, ASTM STP 1156 pp.281-298 (1993).
12. X.Z.Hu & Y.W.Mai, Composites Science and Technology, **46** pp.147-156 (1993).

TENSILE BEHAVIOUR AND DAMAGE PROGRESSION IN MULTILAYER WOVEN GLASS/VINYL ESTER COMPOSITES

P. Callus [1], F. Coman [2], K. H. Leong [3], I. Herszberg [1], M. Bannister [3]

[1] Sir Lawrence Wackett Centre for Aerospace Design, Royal Melbourne Institute of Technology, GPO Box 2476V, Melbourne, Victoria, 3001, Australia.
[2] Department of Manufacturing Systems and Engineering, Royal Melbourne Institute of Technology, GPO Box 2476V, Melbourne, Victoria, 3001, Australia.
[3] Cooperative Research Centre for Advanced Composite Structures Limited, 506 Lorimer Street, Fishermens Bend, Victoria, 3207, Australia.

SUMMARY: Preforms containing orthogonal, normal layered interlock and offset layered interlock architectures were woven in E-glass and consolidated with vinyl ester resin. Tensile specimens were prepared, in the warp and weft directions, then tested to failure. The stress-strain response of most specimens were trilinear, with a primary softening of 20-30 % at 2500-3500 με and a secondary softening of 0-15 % at 10000-17000 με. The difference in the elastic modulus and strength of all structures was within experimental scatter, provided the fibre content in the testing direction was accounted for. The strain to failure was similar for all specimens. Selected specimens were illuminated with transmitted light and photographed during testing. Cracks occurred within the tows oriented both perpendicular and parallel to the testing direction. Structures containing more heavily crimped warp tows also exhibited disbonding local to the warp tow/binder crossover point. The softening events were attributed to these cracks.

KEYWORDS: multilayer weave, modulus, tensile strength, strain to failure, softening, transmitted light photography, damage progression, crack distribution

INTRODUCTION

The mechanical behaviour of textile composites can be predicted with reasonable reliability using a number of models [1-3]. The most critical variable in prediction is the orientation of tows relative to the loading axis. In all but the simplest approximations [3], these models must be experimentally calibrated with “real” structures, either by measuring the distribution of tow orientations in consolidated [1], or dry [4], preforms, or by calibrating models with experimental results from composites containing known fibre orientations [1].

Extensive pre-test and post-failure examinations have been used to develop these prediction models [1]. The mechanisms for load transfer and damage progression have had to satisfy both the stress-strain behaviour and the observed damage. While such work has proved extremely useful it does not precisely establish the progression of damage during loading. Interrupted testing, where specimens were unloaded prior to failure and then examined, provides definitive evidence of the progression of damage and has been used in the

development of predictive models, however it is a very laborious technique. A more convenient method would be to continuously monitor the specimen during testing. Damage accumulation would then be observed explicitly, and subsequent interrupted testing targeted to more closely examine critical events.

This paper describes the preliminary results for composites containing multilayer woven glass preforms in vinyl ester resin. Damage was monitored during testing by photographing specimens that had been illuminated with transmitted light, then post-failure by examining polished cross-sections. Detailed examination of the critical damage features reported in this work, using interrupted testing, is underway and will be presented in the future.

Weave Architectures

The multilayer woven fabrics evaluated in this work consisted of alternate layers of warp and weft tows linked with weft binders. The three binder architectures shown in Fig. 1 have been investigated at the Cooperative Research Centre for Advanced Composite Structures Limited due to their potential for good in-plane properties, since warp and weft tows were nominally straight, and improved impact tolerance, due to the presence of through thickness binders.

The idealised orthogonal architecture shown in Fig. 1 (a) contained reinforcing binders perpendicular to, and spanning the entire thickness of, the preform. It was found that, rather than remaining perpendicular to the preform, the binders tended towards a sine wave profile because they were pulled as part of the weaving process [5]. This separated the outer layers of warp tows and produced large resin rich channels. It was suspected that these channels would act as flaws, providing sites for easy crack initiation, especially under impact loading.

Alternative architectures were therefore designed to reduce the volume of the individual resin rich zones. The normal layered interlock structure, shown in Fig. 1 (b), contained three sets of binders. By reducing the distance that each binder spanned in the through thickness direction then, for the same binder tension as an orthogonal preform, the volume of the resin rich zone was reduced. However the binder configuration in the normal layered interlock structure produced a crimping effect on the warp tows which was expected to reduce the in plane properties [6]. The offset layered interlock structure, in which the central binder was offset by half a unit cell as shown in Fig. 1 (c), was introduced to reduce warp tow crimping through a more uniform distribution of binders.

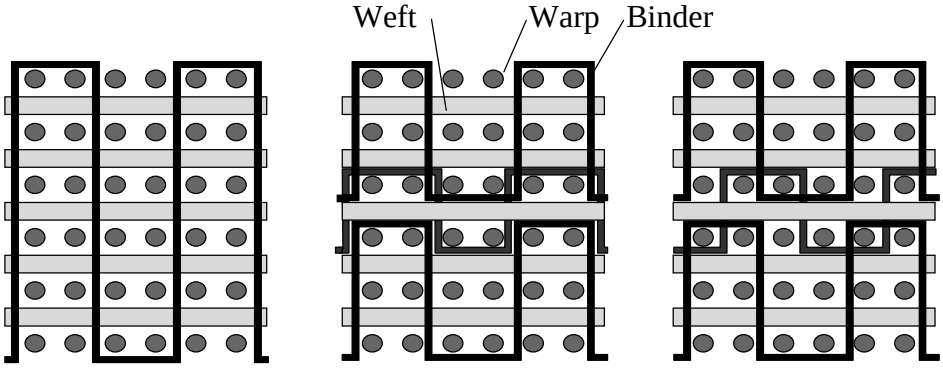

Fig. 1: Idealised binder distributions in multilayer woven structures. (a) Orthogonal interlock, (b) normal layered interlock, and (c) offset layered interlock

EXPERIMENTAL TECHNIQUES

Preform and Specimen Production

The processing and postcure conditions for these panels have been described elsewhere [7] and are summarised in Table 1. One orthogonal preform and two preforms containing both normal layered interlock and offset layered interlock architectures were woven from E-glass with a mechanical hand loom. Each preform contained six layers of 1440 tex warp tows, five layers of 1200 tex weft tows, and 68 tex weft binders. The preforms were consolidated with Derakane vinyl ester resin using resin transfer moulding. Straight sided, 200 mm x 40 mm with 120 mm gauge length, specimens were cut from the panels in the warp and weft directions. Specimen lengths were limited by material availability, and width was that recommended in ref. [8] to ensure that an adequate number of complete unit cells would be tested and the results representative of the composite.

Table 1: Specimen manufacture details

Panel number	Architecture	Resin	Postcure	No. of specimens	
				Warp	Weft
1	Orthogonal	411-C-50	100 °C/3 h	5	5
2	Normal layered Offset layered	411-45	Room temperature	10 6	2 2
3	Normal layered Offset layered	411-C-50	100 °C/3 h	2 2	5 5

Tensile Testing

Tests were conducted in a 100 kN MTS servo hydraulic testing machine using the configuration shown in Fig. 2. A light source was positioned to the rear of the specimen and a 35 mm camera mounted in front. Photographs were taken, with the specimen illuminated by transmitted light, at load increments of approximately 2 kN.

An open weave abrasive cloth (Screenbak) was placed between the specimens and serrated grip faces to soften the gripping interface. This permitted specimens to be tested without tabs but with failure still occurring inside the gauge length.

Specimens were loaded at 0.5 mm min^{-1} until failure while strain was measured using an MTS 632-12C extensometer modified to a 100 mm gauge length. The increased extensometer gauge length ensured that the effects of damage, which occurred uniformly over the entire specimen gauge length, were measured up to specimen failure. After testing the failed specimens were sectioned, polished and a microstructural examination performed.

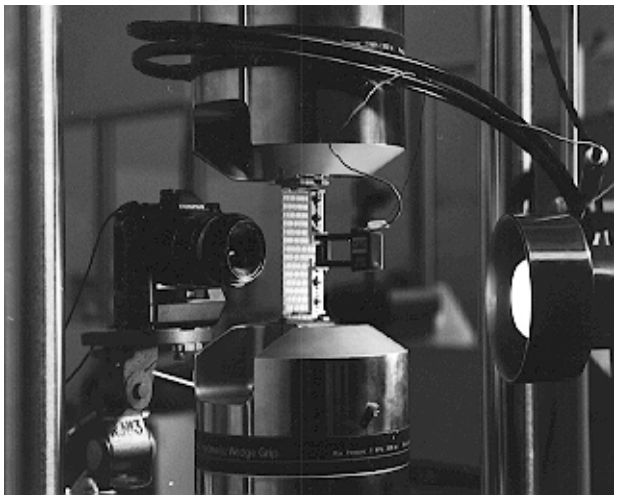

Fig. 2: Test configuration showing the specimen, light source, camera, and extended gauge length extensometer

RESULTS AND DISCUSSION

Mechanical Properties

The elastic moduli, evaluated between 1000 and 3000 με, tensile strength and strain to failure are plotted in Fig. 3. The most important parameter controlling mechanical properties was found to be the volume fraction of fibres in the test direction. This was different for each of the specimens due to local variations in architecture, panel thickness and size of the unit cells in the woven preform. Data was therefore normalised to the nominal fibre content for each panel/architecture combination and is shown as the light columns in Fig. 3. The average nominal fibre contents for all architectures was calculated to be 33.3 vol. % in the warp direction and 30.4 vol. % in the weft direction. The contribution of binders to the weft fibre content was ignored. Strength and modulus data were further normalised to these fibre contents and are shown as the dark columns in Fig. 3.

The properties of all architectures in the warp direction and the strain to failure in the weft direction was within the experimental scatter. It was considered valid to compare tests in the warp direction, from Panels 2 and 3, with those in the weft direction, Panel 3 only, since the differences in warp direction modulus and strength between Panels 2 and 3 were typically less than 10 %. The strain to failure of the offset layered interlock, in the warp direction, was 20 % lower in Panel 2, however this was not considered sufficient to invalidate comparisons since this data was still within the overall scatter for all tests.

In the weft direction the data for each panel, light columns, suggested a reduction in modulus and strength as architecture changed from orthogonal to normal layered interlock to offset layered interlock. These differences were reduced to within experimental scatter once the data had been normalised to the standard weft fibre contents, dark columns.

Damage Progression

The form of the stress-strain plot and the features observed in transmitted light photographs were similar for all architectures tested in both directions. These features and behaviours are

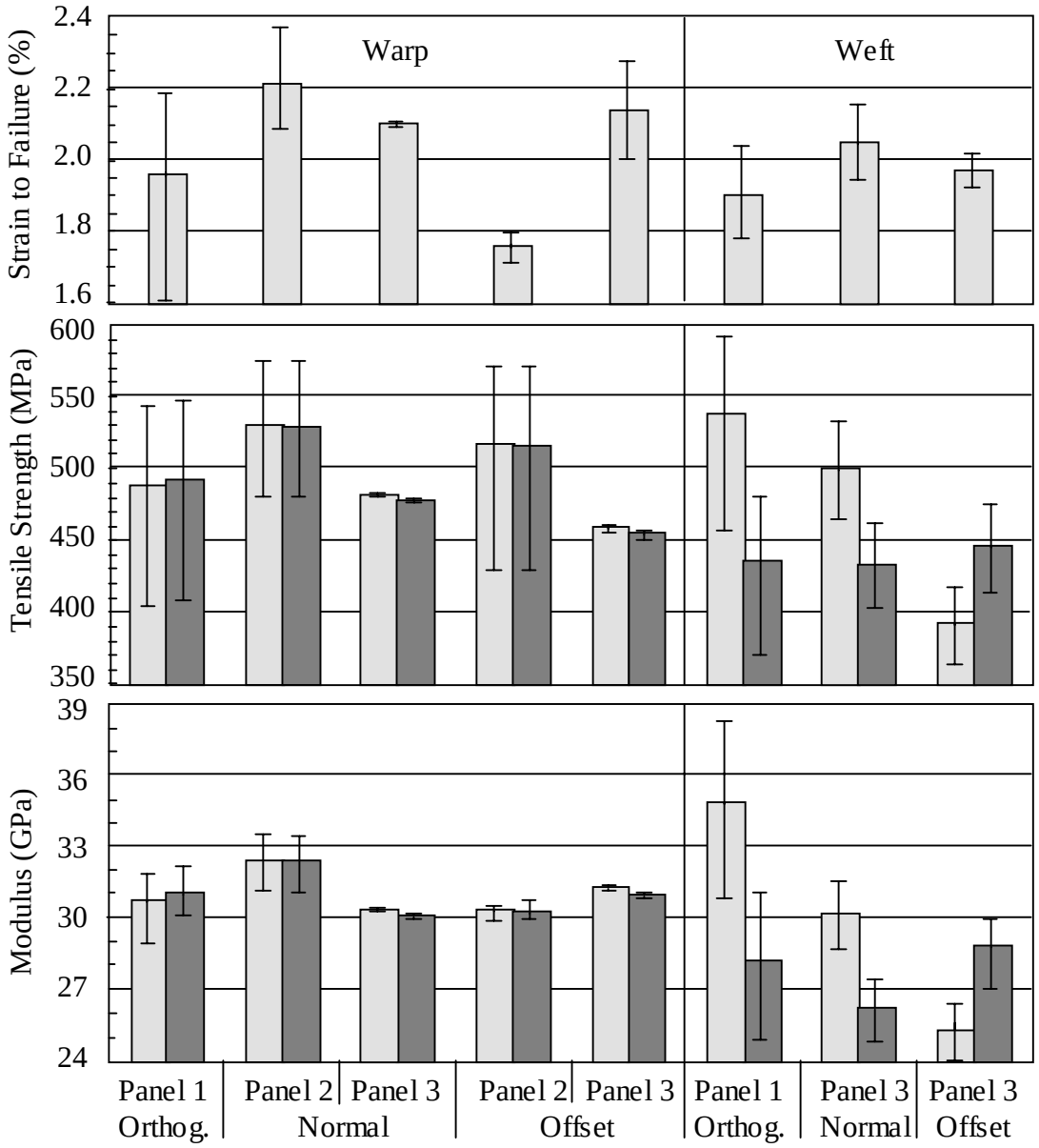

Fig. 3: Effect of architecture on; modulus, tensile strength and strain to failure. Light columns show data for each panel and dark columns show data standardised for the fibre content in the test direction. Error bars indicate the range of data

summarised in Fig. 4 and Table 2. Inspection of Table 2 reveals that in some cases the features either occurred in a different order to that shown in Fig. 4, or were not observed at all.

Elastic Range

The unloaded appearance of all specimens was similar to that shown in Fig, 5 (a), with wide warp tow columns separated by thinner resin rich channels. On some specimens the surface legs of the binders were observed, Fig. 5 (e), permitting easy identification of the unit cells.

Preliminary analysis indicates that, in agreement with ref. [1], the elastic modulus of these multilayer woven architectures can be predicted with reasonable accuracy using orthotropic laminate theory. The results of this investigation will be reported during the conference.

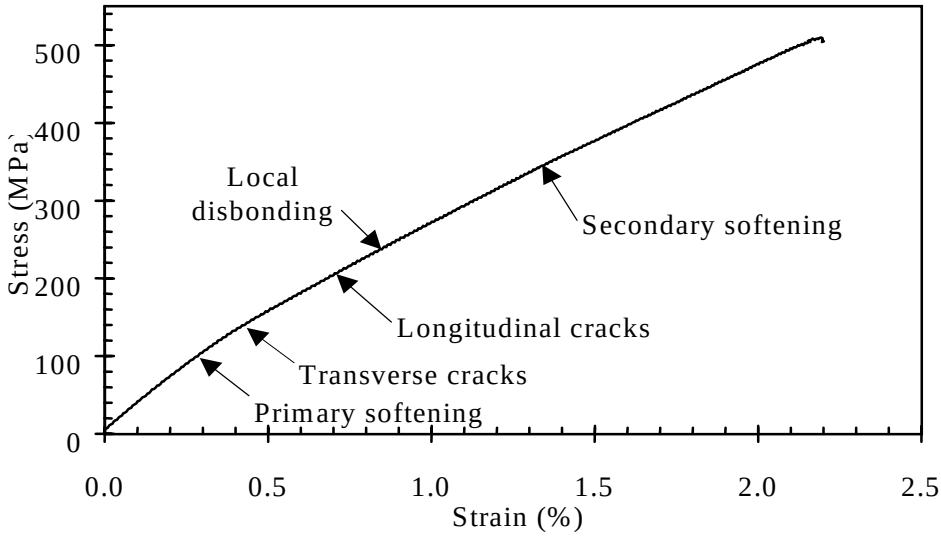

Fig. 4: Generalised stress-strain response showing all mechanical behaviour and damage features observed for these architectures and test directions

Table 2: Average strain at which stiffness changes and damage features were observed

Damage or property feature	Orthogonal		Normal layered		Offset layered	
	Warp	Weft	Warp	Weft	Warp	Weft
Primary softening (με)	3340	3530	3090	2540	2990	3130
Modulus drop (%)	26	25	29	19	*	22
Appearance of transverse cracks (με)	6810	5250	3800	5940	4870	4110
Appearance of longitudinal cracks (με)	None	None	8220	14900	6860	15050
Appearance of local disbonding (με)	None	None	13200	None	6850	None
Secondary softening (με)	10610	12280	16730	10670	*	11080
Modulus drop (%)	8	5	13	5	*	14

* Data unavailable

Primary Softening

A 20 to 30 % reduction in stiffness was observed for all specimens at approximately 3000 με. It is most likely that this drop was due to transverse cracking, ie. cracks within the tows oriented perpendicular to the test direction. These cracks were observed in transmitted light photographs and are discussed in the next section. Although the transverse cracks were

observed well after softening had occurred it is probable that the cracks were present earlier but not detected. Interrupted testing will be performed to confirm that this was the case.

Transverse Cracking

Transverse cracks, as shown in Fig. 5 (b), initiated between 3040 and 7160 με and occurred in all specimens. Cross-sections, such as Fig. 5 (c), show that these cracks were confined exclusively to the tows transverse to the testing direction and did not extend into the surrounding resin rich zones. The number and length of individual cracks increased with load until, at approximately 50 % of failure load, saturation occurred. At this stage cracks spanned most of the specimen width and were uniformly spaced along the full gauge length, similar to the transverse cracks that appear in cross ply laminates.

Load was transferred from tows parallel to the test direction to tows perpendicular to the test direction by shearing of the matrix at the interface between parallel/perpendicular tows. The efficiency of this transfer was probably enhanced by the presence of through thickness binders. Cracking occurred when stress in the perpendicular tows exceeded the matrix tensile strength. It is proposed that this cracking reduced the contribution of perpendicular tows to the load bearing capacity of the composite and so caused the primary softening. Models relating the spacing of transverse cracks and the degree of softening in cross-ply laminates [9] probably apply to the multilayer woven composites used in this work.

When testing in the warp direction the cracks in the weft tows were very clear, appearing straight in orthogonal and normal layered interlock specimens but wavy in offset layered interlock specimens. Most property models account for out of plane tow deviations, however Fig. 5 (e) shows that if the weaving or RTM processes have not been optimised, then in plane deviations, of similar magnitude to out of plane deviations could occur. Figure 3 shows that the effect of weft tow waviness on the specimens tested in this work was not significant.

Secondary Softening

In most specimens a second change in stiffness was observed at higher strains. The response of the specimens that did not display this behaviour; two orthogonal warp, one orthogonal weft and two normal layered interlock warp, were either bilinear or continuously curved.

The resin for the secondary softening is unknown. It is possible that, in normal layered interlock specimens tested in the warp direction, this softening was caused by easier straightening of load bearing tows afforded by the presence of longitudinal cracking and local disbonding. In all other cases the transmitted light photographs either did not detect cracks, or cracks were observed after softening. Again interrupted testing will be performed to determine the precise order of events.

Tow lock-up in the woven architecture has been proposed as a mechanism to explain softening at high loads and very large strain to failure for woven carbon/epoxy composites [1]. However in this work the secondary softening occurred as low as 9000 με and 250 MPa. It is very unlikely that tow failure would commence at such low strains.

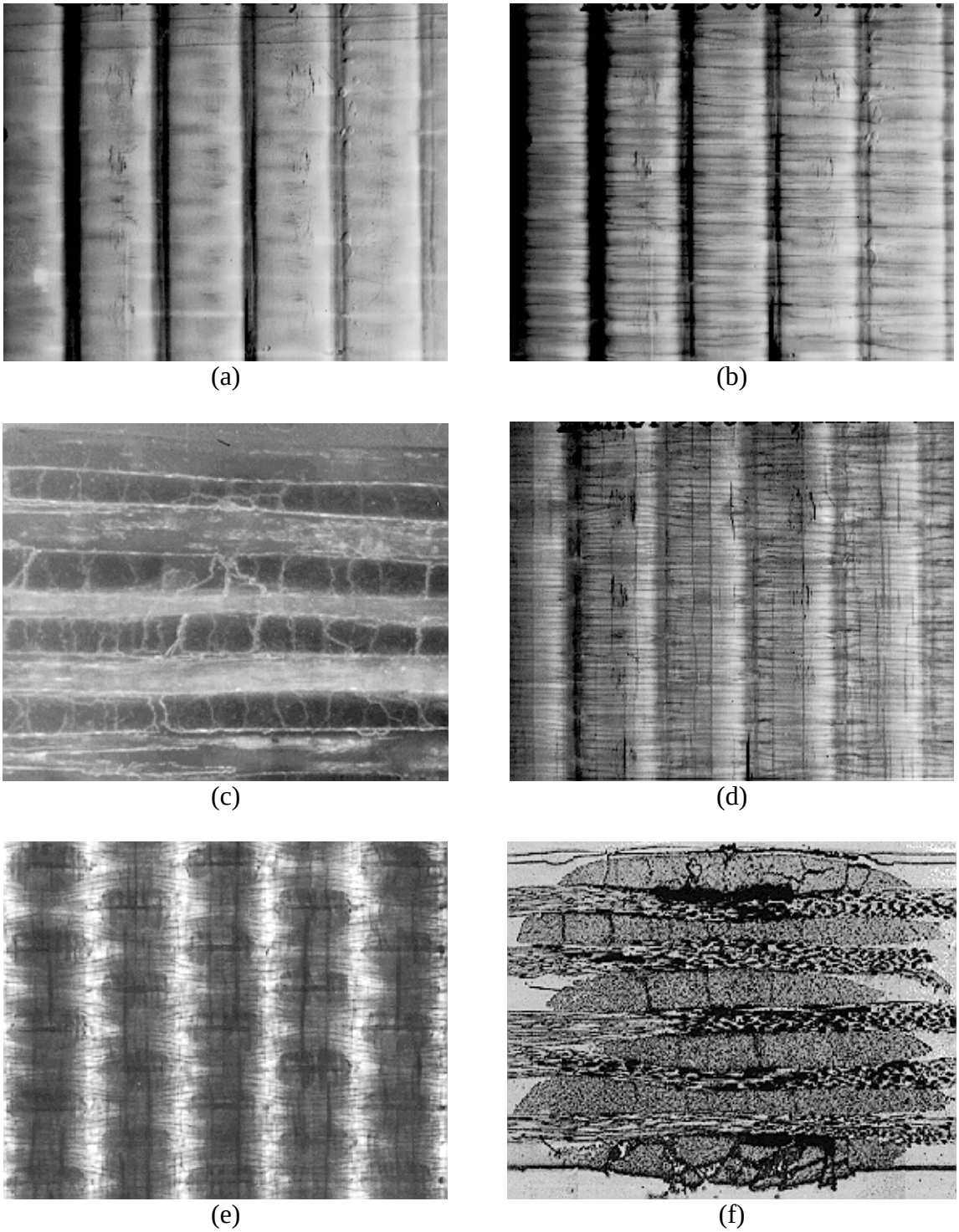

Fig. 5: Transmitted light photographs and cross-sectional micrographs of various specimens indicating the progression of damage. (a) A specimen prior to testing. (b) Transverse cracks. (c) Micrograph showing transverse cracks occurred wholly within perpendicular tows. (d) Longitudinal cracks. (e) Local disbonds. (f) Micrograph showing disbonds as circumferential cracks around the outer tows

Longitudinal Cracking

Longitudinal cracks, as shown in Fig. 5 (d), appeared at intermediate loads within tows parallel to the loading direction. Cracks appeared to initiate under the binder/warp tow crossover point then propagate within the tow to almost the full specimen gauge length.

The most likely cause of these cracks originated during weaving of the preform. Tension in the binders crimped the warp tows at the warp tow/binder crossover point. In the consolidated composite under load, these crimped warp tows tended to straighten and return to their original cross-sectional shape. This produced a tensile stress perpendicular to the tow and cracking if the resin strength was exceeded. This mechanism assumes that, although binders exert considerable restraint on warp tows, they cannot completely prevent all lateral movement.

Local Disbonding

Local disbonding was observed when testing the offset layered interlock specimens, and to a lesser extent the normal layered interlock specimens, in the warp direction. As shown in Fig. 5 (e) disbonding occurred in the region immediately surrounding the warp tow/binder crossover point and was initiated where a short longitudinal crack had reached the surface of a warp tow. Figure 5 (f) showed that these disbonds were restricted to the surface tows, where crimping in the warp tow by the weft binder was most severe.

Disbonding occurred in the most severely crimped regions of tows when the stress at the warp tow/matrix interface, generated by tow straightening, exceeded the tow/matrix interfacial shear strength. Disbonding was confined to the crimped region and crack size depended on the severity of the crimp. Disbonds were much larger in the offset layered interlock specimens, supporting the observations that the tows in this structure were more wavy than those in the other architectures. This increased tow waviness was caused by high binder tension during weaving and is discussed below.

Additional Comments

The extent of crimping in tows parallel to the loading direction controlled the appearance of longitudinal cracks and local disbonds. This crimp was generated not only by the weave architecture, but also by the weaving process, in particular the binder tension. The preforms in this work were woven on a manual loom, with control over binder tension provided by the operator. Due to the difficulties in exerting close control over binder tension it is likely that the degree of crimp in any one preform, let alone between preforms, was variable. In fact the ideal architectures were probably never achieved, however test results indicate that provided this variation was less than 5 to 10° the effect on tensile properties was minimal.

The resin rich channels did not appear to contribute to crack formation. Strains within these channels were very close to the overall specimen strain, and specimen failure strains of 1.6 to 2.4 % were well within the resin capacity of 5 to 6 % [10]. The strain within tows, magnified due to the close packing of glass fibres, was sufficient to cause extensive local cracking [11].

Architectural differences are expected to play a much more significant role when the composites are subjected to compression and impact loading. In these situations two

competing factors will influence performance. The first is the volume of the resin rich zones, increasing of which will reduce performance, and the straightness of tows, where more crimped tows will decrease performance. The volume of resin rich zones decreased from orthogonal to normal layered interlock to offset layered interlock, while tow straightness was controlled by architecture and weaving technique. The effect of each factor must be determined experimentally.

CONCLUSIONS

There was no significant difference in the elastic modulus, strength and strain to failure of glass/vinyl ester orthogonal, normal layered interlock and offset layered interlock architectures when tested in the warp and weft directions, provided the effect of fibre content in the testing direction was accounted for.

Five features were identified during the tensile loading of these materials; (i) primary softening, (ii) cracks within tows transverse to the testing direction, (iii) secondary softening, (iv) cracks within tows parallel to the testing direction, (v) local disbonding at the warp tow/binder crossover. The softening events were probably caused by cracking and disbonding.

Transmitted light photography is a useful technique for characterising damage accumulation in translucent composite specimens during testing. It has contributed to an understanding of failure mechanisms and assisted in more detailed examination of these materials.

ACKNOWLEDGMENTS

The authors acknowledge the contribution of the following colleagues to this work; A. Nicolaidis - preparation of woven preforms, K. Houghton - resin transfer moulding, M. Finch and M. Wilson - testing, R. Chuah - data analysis, and K. Dixon - assistance throughout.

REFERENCES

1. Cox, B., “Failure Models for Textile Composites”, NASA CR-4686, Langley Research Center, August 1995.

2. Vandeurzen, P., Ivens, J. and Verpoest, I., “ A Critical Comparison of Analytical and Numerical (FEM) Models for the Prediction of the Mechanical Properties of Woven Fabric Composites”, TEXComp 3, Aachen, December 9-11, 1996, pp 12/1-12/11.

3. Falzon, P.J., PhD Thesis, Royal Melbourne Institute of Technology, Department of Aerospace Engineering, To be submitted.

4. Gommers, B, Verpoest, I., and Van Houtte, P., “On the use of Orientation Tensors in the Analysis of Knitted Fabric Reinforced Composites”, TEXComp 3, Aachen, December 9-11, 1996, pp 8/1-8/18.

5. Bannister, M. K., Herszberg, I., Coman, F., Raper, H., Curiskis, J., “Manufacture and Analysis of Multilayer Woven Preforms”, Ninth Technical Conference of the American Society for Composites, Newark, Delaware, U. S. A., September 20-22, 1994.

6. Coman, F., Herszberg, I., Bannister, M., John, S., “A Realistic Computer Simulation of Multilayer Woven Preforms for the Analysis of Composite Structures”, CADCOMP 96, Udine, Italy, July 1-3, 1996.

7. Callus, P., Dixon, K., Leong, K.H., Herszberg, I. and Bannister, M., “Damage Visualisation During the Tensile Testing of Multilayer Woven Glass/Vinyl Ester Composites”, To be presented at the International Aerospace Congress IAC97, Sydney, Australia, February 25-27, 1997.

8. Minguet, P. J., Fedro, M. J., Gunther, C. K., “Test Methods for Textile Composites”, NASA CR-4609, Langley Research Center, July, 1994.

9. Highsmith, A.L. and Reifsnider, K. L., “Stiffness-Reduction Mechanisms in Composite Laminates”, Damage in Composite Materials, ASTM STP 775, K. L. Reifsnider, Ed., American Society for Testing and Materials, 1982, pp. 103-117.

10. “Derakane Epoxy Vinyl Ester Resins, Product and Usage Guide”, Dow Plastics, September, 1994, 20 pp.

11. Kies, J.A., “Maximum Strains in the Resin of Fibreglass Composites”, U.S. Naval Research Laboratory, Ballistics Branch, Mech. Div., NRL Report 5752, March 26, 1962.

INTERLAMINAR DELAMINATION TOUGHNESS AND STRENGTH OF 3-D ORTHOGONAL INTERLOCKED FABRIC COMPOSITE

Yasuyo Tanzawa[1] , Naoyuki Watanabe[2] and Takashi Ishikawa[3]

[1] Graduate Student, Department of Aerospace Engineering
Tokyo Metropolitan Institute of Technology, 6-6, Asahigaoka, Hino, Tokyo 191, JAPAN
[2] Associate Professor, Department of Aerospace Engineering
Tokyo Metropolitan Institute of Technology
[3] Section Head, Airframe Division, National Aerospace Laboratory
6-13-1 Ohsawa, Mitaka, Tokyo 181, JAPAN

SUMMARY: The double cantilever beam (DCB) tests were executed for interlaminar fracture toughness of 3-D orthogonal interlocked fabric composite. The jagged load-deflection curves caused by unstable crack propagation were obtained. The strain energy release rate for 3-D composite becomes far higher even if the volume fraction of z-direction fiber is small, and becomes higher as the volume fraction becomes high. The observation of the specimens revealed that z-direction fibers made the fracture more complex and caused many characteristic phenomena: debondings of the z-direction fiber from in-plane layer; its failure or pull-out and bridging of z-direction fiber; crack branching, deviation and secondary crack almost in front of the crack tip. They may increase the absorbed fracture energy. The double-notched shear (DNS) tests were carried out to estimate the interlaminar shear strength of the present composite. The shear strength were nearly equal for different distance between the notches at least for tested cases.

KEYWORDS: 3-D orthogonal interlocked fabric composite, tabbed DCB test, DNS test, mode I strain energy release rate, fiber bridging

INTRODUCTION

Fiber reinforced composite materials have many advantages and are frequently used in many kinds of fields [1], but most of them are two-dimensional (2-D) laminated composites, so interlaminar delamination is the weakest failure mode in these materials. In fact, the delamination is considered to be the most prevent life-limiting growth mode in composite structures [2]. Various techniques have been introduced to enhance the interlaminar strength. One way is a usage of thermoplastic or toughened thermoset matrices. One of the most effective way is three-dimensional (3-D) fabric construction technique [3], [4] such as braiding, weaving, knitting or stitching process. Among them, the orthogonal interlocked fabric composite provides fiber architecture aimed at retaining in-plane performance while enhancing out-of-plane properties, by including a small amount of through-the-thickness reinforcement [5]. It is important to investigate quantitatively the influence of the z-direction reinforcement on the material performances to assess fully the trade-off study between in-

plane and interlaminar properties in the design of fabric composite structures. Until now, several experimental studies about interlaminar toughness have been done for 3-D fabric composites [6] - [8]. On the other hand, to the authors' knowledge, few analyses have been carried out about the material [9]. The authors modified the model used in Ref. 9 and carried out the analyses [10].

In this paper, two kinds of the experiments related to the interlaminar properties of 3-D orthogonal interlocked fabric composite are performed. The DCB tests were executed for Mode I interlaminar fracture toughness and the results were compared with those of unidirectional composite. The effect of z-direction fiber bundle on the interlaminar fracture behavior of the material is discussed. From the observation of the specimen after the test, the fracture mechanism of the material is discussed. To estimate the interlaminar shear strength of the 3-D composite, the double-notched shear (DNS) tests were carried out in compression.

EXPERIMENTS

Material Systems and Properties

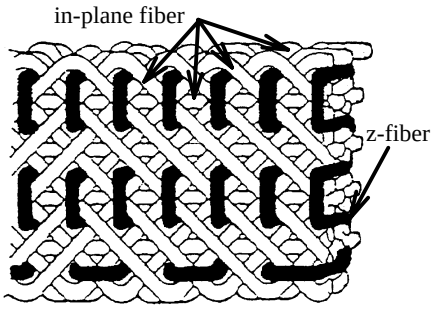

Fig. 1: Fiber structure of five-axes 3-D orthogonal interlocked fabric composite

The orthogonal interlocked fabric composites used in our experiments were made of CF/Epoxy, which were manufactured in Nagoya Aerospace Systems Division, Mitsubishi Heavy Industries, Co. Ltd. (MHI). The fiber architecture of 3-D composite used here is given in Figure 1. It was composed of five axes fiber yarns: four of them were in-plane and the other was z-direction. To fabricate the composites, resin transfer molding (RTM) process was adopted. The stacking sequence was $[\pm 45/0/90]_{3S}$ thus the total number of plies is 24. Detailed data of the properties of 3-D composite used here is given in Table 1. Carbon fiber TR40 was used for in-plane fiber in all the specimens. There were three types of the specimens: C1 and C2 were reinforced in z-direction by carbon fiber TR40 and K is reinforced in z-direction by aramid fiber K49. The z-direction fiber tows were 1K or 3K, respectively in C1 and C2, thus volume fraction of fibers running in the z-direction wss different. The unidirectional composite with heat resistant thermoplastic resin, CF/PI-SP, was also tested as a reference. The properties of PI-SP are as follows: T_g = 254 [°C], the tensile strength = 91.2 [MPa] and the tensile modulus = 2.65 [GPa].

Table 1: Properties of 3-D orthogonal interlocked fabric composite

Type		C1	C2	K
fibers	in-plane	TR40 - 12K (carbon fiber)		
	z-direction	TR40 - 1K	TR40 - 3K	K49 - 768
distance between z-fibers [mm]		3.9 Å~ 3.9		
fiber volume fraction [%]	total	54.2	54.7	54.5
	0°	20.6	20.4	20.5
	- 45°	29.2	28.9	29.0
	+45°	29.2	28.9	29.0
	90°	20.6	20.4	20.5
	z-direction	0.5	1.4	1.1

Testing Procedure for DCB Test

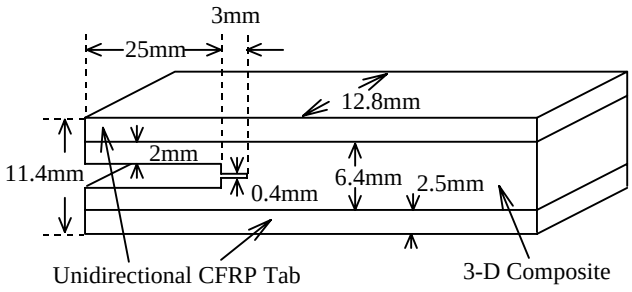

Fig. 2: Geometry of tabbed DCB specimen

The DCB test is a common method for Mode I interlaminar fracture toughness. This method has been applied to 2-D composite laminate successfully. However classical DCB specimen cannot be used in the test for 3-D composites. Because this material has high interlaminar strength, usually it fails first at the root of the DCB beam by a bending moment with no interlaminar fracture toughness data. To avoid this difficulty, several methods have been contrived recently. For example, Guenon *et al*. developed one method by using the tabbed DCB specimen [5]. Another test method developed in National Aerospace Laboratory by Ishikawa *et al*. [7].

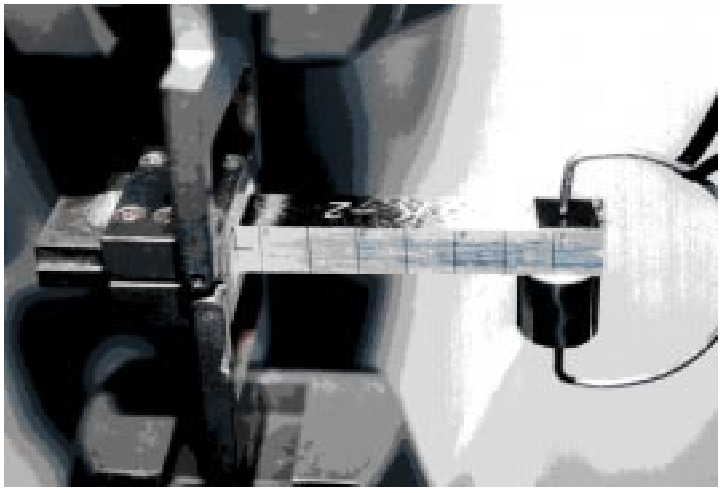

Fig. 3: Test configuration of tabbed DCB specimen

Figure 2 shows the specimen design and dimensions used in this study, which have been developed by Ishikawa *et al*. This specimen is cut out to insert the jig useful when the load to extend the delamination is high. Figure 3 shows the feature of the specimen using unidirectional CFRP tab. Initial crack was given in this specimen artificially by machining. The width of the specimen was measured at three points and initial artificial crack length was measured on both sides. The DCB specimen was loaded in tension by the INSTRON 4502 screw-driven testing machine in a displacement-controlled mode with 0.25 [mm/min] cross-head speed.

Figure 4 illustrates the schematic load-deflection curve for the present 3-D composite. The specimen was loaded till the load decreased suddenly at the point A, then the machine was stopped to measure the crack length. For the current 3-D composites, it is uncertain whether

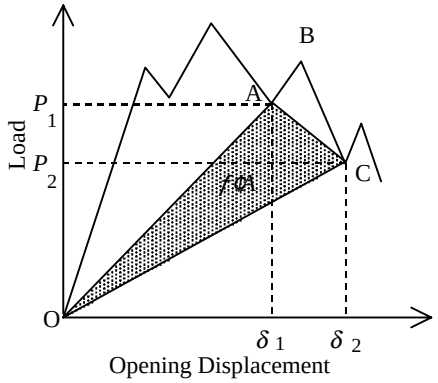

Fig. 4: Schematic load-deflection curve of 3-D composite

the geometry of crack is similar to that of initial states or not. Therefore, the crack length was measured on both sides and the averaged value was employed. This average was used in calculation of the strain energy release rate, G_I, under the assumption of a straight tip line. The curve of load versus crack opening displacement, which is assumed to be identical with cross head displacement, had been plotted during the experiment. After the experiment, loads and opening displacements at the instances when the load suddenly dropped were picked up. With these data, G_I was calculated by the area method, which is based on energy consideration and suitable to estimate it for the 3-D composites. The first load drop point was neglected and other data after the second drop were utilized to calculate G_I because the first drop is affected by a dull artificial crack tip.

Testing Procedure for Shear Tests

The interlaminar shear strength was evaluated with the DNS tests. The geometry of the specimen is shown in Figure 5. The specimen has two alternate notches with interval of L whose depths are half of the thickness of the specimen. Restricting the thickness-wise deformation, the specimen was compressed up to failure between the notches by the INSTRON 4505 screw-driven testing machine in a displacement-controlled mode with 1.0 [mm/min] cross-head speed. The tests were conducted for two types of the specimen of different distances between the notches 6.4 [mm] and 12.7 [mm].

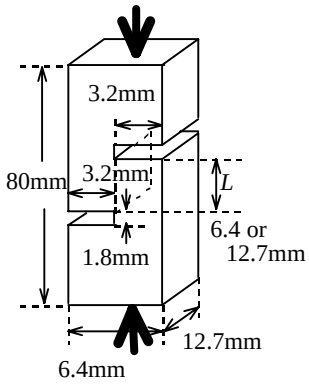

Fig. 5: Geometry of DNS specimen

RESULTS AND DISCUSSIONS

DCB Tests

The DCB tests were carried out for three types of the materials, namely C1, C2 and K. As for C1 series, five specimens were tested, and three specimens were tested for C2 and K series. As for unidirectional CF/PI-SP composite, six specimens were tested.

Load-Deflection Curve for 3-D Fabric Composite

Figure 6 shows the typical load-deflection curve of C2 series where the cross-head displacement is assumed as the crack opening displacement. Similar curves were obtained for other materials in the tests. At the beginning of loading procedure, the load increases almost linearly, then drops abruptly when the crack extends. The crack extends step by step and unstably in a manner so-called stick-slip behavior. This behavior is presumably ascribed to the existence of the z-direction fiber. The load drops every time when the crack extends, and the load drop step is generally independent of the crack opening displacement. The peak load decreases gradually as the crack extension.

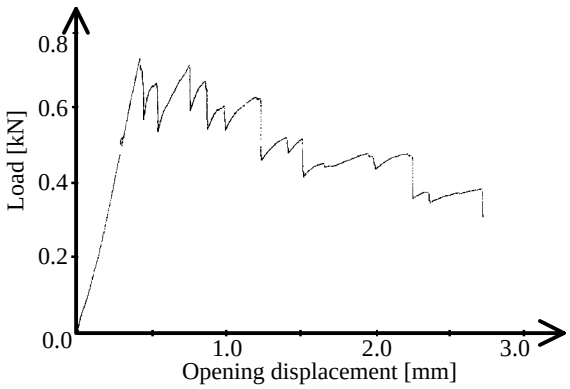

Fig. 6: Typical load-deflection curve for C2 series

Effect of z-direction Fibers

Figure 7 shows the Mode I strain energy release rate G_I, for C1 series as a function of normalized crack growth length. The normalized crack growth length is defined as (a - a_0) / a_0, where a is an instant crack length and a_0 is an initial crack length. The averaged values of G_I for all the specimens are listed in Table 2. The values for #1 and #2 are distributed in a narrow region, from 0.69 [kN/m] to 1.54 [kN/m] for #1 and from 0.75 [kN/m] to 1.54 [kN/m] for #2. The averaged values for #1 and #2 are 0.99 [kN/m] and 1.33 [kN/m], respectively, as listed in Table 2. On the other hand, the values of G_I for #3, #4 and #5 are distributed widely, for example, from 0.45 [kN/m] to 4.73 [kN/m] for #5. Most values for these three specimens are higher than those for #1 and #2, with the higher average of 1.42 [kN/m] for #3, 1.86 [kN/m] for #4 and 1.55 [kN/m] for #5. On the whole, the G_I values remain in particular region from 0.8 [kN/m] to 2.0 [kN/m] with a few exception, exhibiting the average for C1 series of 1.43 [kN/m].

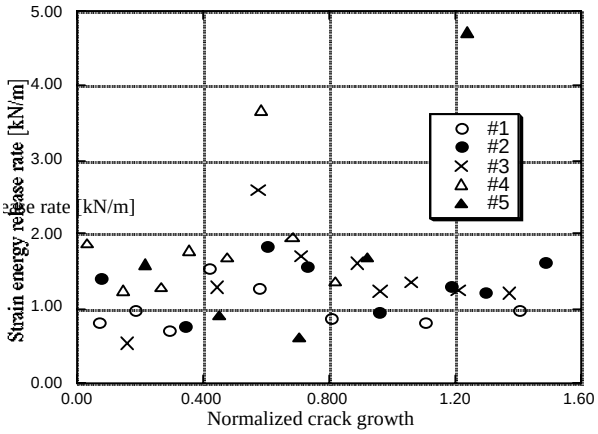

Fig. 7: Strain energy release rate for C1 series as a function of normalized crack growth length

Table 2: Strain energy release rate of 3-D orthogonal interlocked fabric composite

Strain energy release rate [kN/m]						
Type	**Specimen**					**average**
	#1	**#2**	**#3**	**#4**	**#5**	
C1	0.99	1.33	1.42	1.86	1.55	1.43
C2	6.18	4.95	3.79			4.98
K	3.43	2.75	3.25			3.14

The averaged strain energy release rates of unidirectional CF/PI-SP for all the specimens are listed in Table 3. The values are nearly constant with the average of the whole values of 0.64 [kN/m], which is considerably lower than that of C1 series. In Ref. 11, it was reported that G_I for conventional unidirectional CF/Epoxy composite was 0.094 [kN/m] and that for unidirectional CF/PEEK composite was 1.82 [kN/m]. Comparing with these results, the value of G_I for C1 series is high enough, although this composite system with normal epoxy resin contains only 0.5% of z-direction fibers.

Table 3: Strain energy release rate of unidirectional CF/PI-SP composite

Strain energy release rate [kN/m]						
Specimen						average
#1	#2	#3	#4	#5	#6	
0.53	0.62	0.68	0.63	0.70	0.66	0.64

Effect of the Volume Fraction of z-direction Fibers

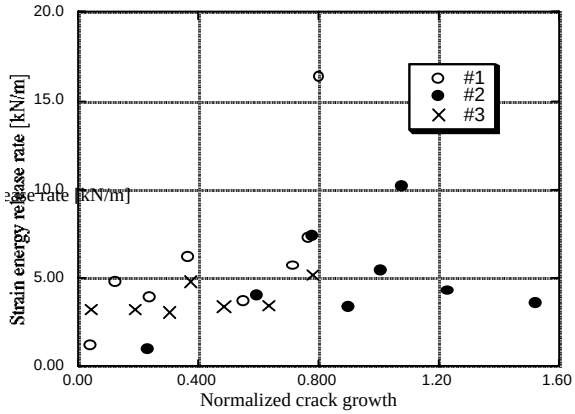

Fig. 8: Strain energy release rate for C2 series as a function of normalized crack growth length

Figure 8 shows the G_I for C2 series as a function of normalized crack growth length and their average are also listed in Table 2. The values of G_I for #1 and #2 are distributed widely, from 1.23 [kN/m] to 16.36 [kN/m] for #1 and from 0.99 [kN/m] to 10.22 [kN/m] for #2 with the average for #1 and #2 being 6.18 [kN/m] and 4.95 [kN/m], respectively. In the case of #3, G_I are distributed in a narrow region, from 3.23 [kN/m] to 5.14 [kN/m] with 3.79 [kN/m] in average. The averaged value for whole C2 series is obtained as 4.98 [kN/m]. Figure 9 shows the results for K series as a function of normalized crack growth length. The averaged values for each specimen are 3.43 [kN/m] for #1, 2.75 [kN/m] for #2 and 3.25 [kN/m] for #3 with the whole average of 3.14 [kN/m], as listed in Table 2. Note that the values of G_I for each specimen disperse widely again, for example, from 0.33 [kN/m] to 7.83 [kN/m] for #3. A tendency that G_I becomes high with crack growth is observed.

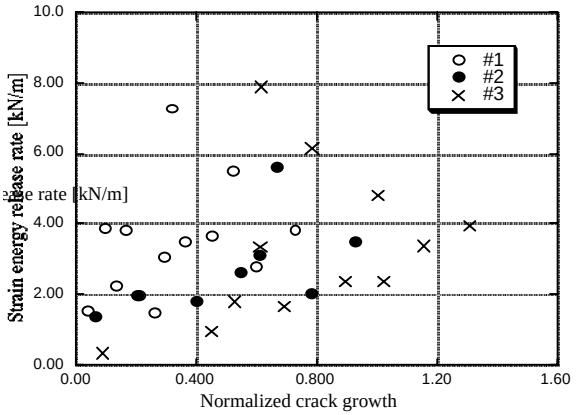

Fig. 9: Strain energy release rate for K series as a function of normalized crack growth length

In summary, the whole average are 1.43 [kN/m] for C1, 4.98 [kN/m] for C2 and 3.14 [kN/m] for K, respectively, as listed in Table 2. To compare with one another, it is considered that the strain energy release rate and its scatter become more serious as the volume fraction of z-fiber yarn becomes higher.

Fracture Mechanisms in 3-D Composite

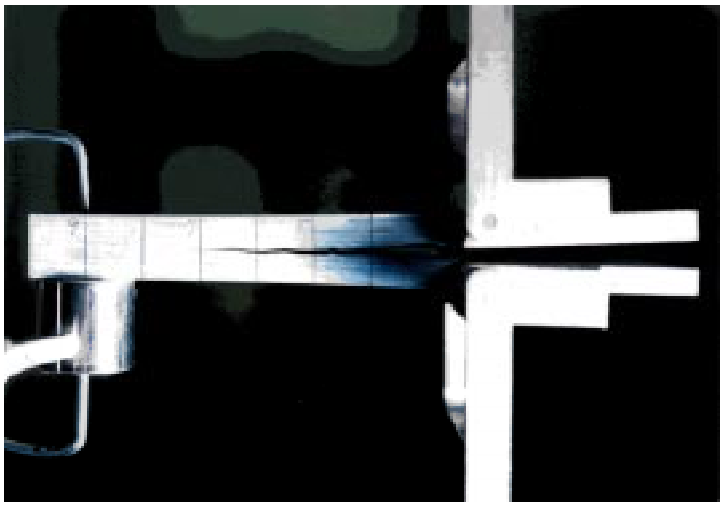

(a)

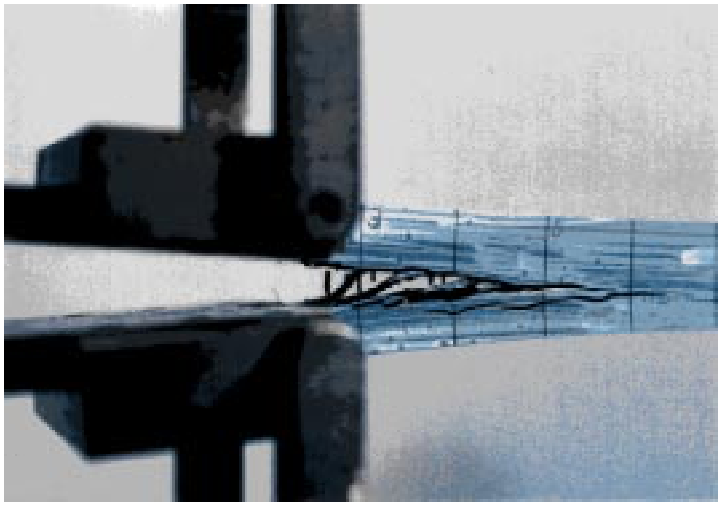

(b)

Fig. 10: Typical failure modes of 3-D orthogonal interlocked fabric composite after DCB test: (a) C1 series, and (b) C2 series

As stated earlier, the crack propagated in an unstable stick-slip manner. Stable crack propagation in the matrix was seldom observed. Figure 10(a) shows the photograph of the typical fracture mode in C1 series after the DCB test. The lines seen on the side were written in 1 [cm] distance by pencil for an assistance of crack length measurement. Although AE data were also acquired by a sensor as shown in this photograph, they would not be discussed here. Nevertheless many fracture behavior such as z-fiber bridging and pull-out, crack branching and deviations were observed in this specimen, they were not significant in

comparison with C2. The in-plane fiber bridging and pull-out were also observed. Figure 10(b) shows the photograph of the typical fracture mode in C2 series where it is indicated that the secondary cracks were created and they generally ran parallel to the main crack. The z-fiber bridging and pull-out were prominently observed in this specimen. In addition, failure in most z-direction fibers did not occur in the plane of crack propagation but occurred in the region near the surface where a stress concentration could be expected in the manufacturing process. Based on comparison of the fracture mode between C1 and C2, it is dearly understood that the mechanisms of fracture becomes more complex as z-fiber volume fraction increases. While the load supported by the z-direction fiber increases as z-fiber volume fraction increases, the crack deviation or branching become serious because of the existence of z-fiber.

From these observations, various kinds of fracture phenomena could be found in 3-D composite toughness tests: debondings of z-direction fiber from in plane layers; its failure or pull-out, and bridging by z-direction fiber; crack branching, deviation and secondary crack almost everywhere in front of the crack tip. In addition, the crack branching and deviation may lead to bridging by in-plane fibers. Because these phenomena can be considered to increase the absorbed fracture energy, the crack propagation is apt to be arrested.

Interlaminar Shear Tests

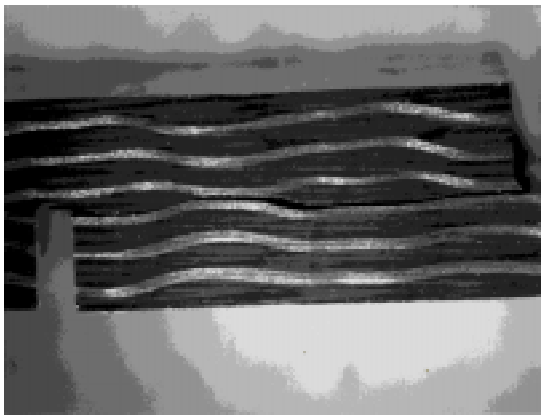

Fig. 11: Typical fracture modes of 3-D orthogonal interlocked fabric composite after the DNS tests

The short beam shear (SBS) test in three-point bending is often used as a simple and convenient method. Although these tests were carried out, the results exhibited serious dependency on the distance between the supporting points. Therefore, the interlaminar shear strength was evaluated with the DNS tests in compression. These tests were carried out only for C2 series specimens by two types of the distances between the notches, 6.4 [mm]: A and 12.7 [mm]: B. The number of specimens was five for each type. The interlaminar shear strength for Type A and Type B were distributed from 86.85 [MPa] to 114.22 [MPa] for Type A and from 92.34 [MPa] to 102.21 [MPa] for Type B. The pitch of z-direction fibers is 3.9 [mm] in the present composite, thus only one or two z-fiber exist between the notches for Type A, while there are three or four z-fibers between the notches for Type B. Therefore, the interlaminar shear strength obtained with Type A depends on the state of the specimen and its scatter becomes serious. On the other hand, the results of Type B exhibit lower scatter than those of Type A. The interlaminar shear strength average were 99.80 [MPa] for Type A and

97.13 [MPa] for Type B with only 2.7% difference between them, although their scatter level were different each other. Therefore, no dependency of the interlaminar shear strength on the distance between the notches was found so far as tested. Figure 11 shows the failure mode of type B after the tests. Only single delaminaton was observed between the notches along 0° axis fiber yarn, which could be regarded as the result of almost pure-shear fracture.

CONCLUSIONS

The interlaminar fracture toughness and strength of the 3-D orthogonal interlocked fabric CF/Epoxy were evaluated by using the tabbed DCB specimen and the interlaminar shear tests. The area method was used in calculation of the strain energy release rate. The interlaminar shear tests were carried out with the DNS test in compression. The conclusions are given as follows:

1) The DCB tests were carried out for C1, C2 and K series with the volume fractions of z-direction fiber being 0.5% for C1, 1.4% for C2 and 1.1% for K. The obtained strain energy release rate averages were 1.43 [kN/m] for C1, 4.98 [kN/m] for C2 and 3.14 [kN/m] for K, respectively.

2) The value of the strain energy release rate for 3-D orthogonal interlocked fabric composites was compared with those for tougher unidirectional composites. Although the volume fraction of z-direction fiber is only 0.5%, the strain energy release rate of 3-D CF/Epoxy is fifteen-fold greater than that of the UD composite of similar resin without z-direction reinforcements.

3) The difference of the strain energy release rate due to the difference of z-fiber volume fraction was also discussed. The strain energy release rate comes to higher as the z-fiber increases. Moreover, serious scatter was found in the results of the strain energy release rate, and the scatter became more serious with increasing the volume fraction of z-direction fiber.

4) The load-deflection curves of 3-D composite were much different from those of unidirectional composites. The jagged curve was obtained for 3-D due to unstable stick-slip crack propagation.

5) During and after the DCB tests, the interlaminar crack propagation processes were observed and fracture mechanisms were contemplated. They are far more complicated than those in unidirectional composites. The presence of z-direction fibers causes many characteristic phenomena: debondings of z-direction fiber from in-plane layers; its failure or pull-out, and bridging by z-direction fiber; crack branching, deviation and secondary crack almost everywhere in front of the crack tip. The bridging by in-plane fibers may occur because of the crack branching and deviation. These phenomena increases the absorbed fracture energy and the crack propagation tends to be arrested.

6) The interlaminar shear strengths obtained by the SBS test exhibited strong dependency on the distance between the supporting points. On the contrary, those by the DNS tests exhibited almost no dependency on distance between the notches at least for tested cases. It is concluded at present that the DNS test is suitable to evaluate the interlaminar shear strength of the 3-D orthogonal interlocked fabric composite.

ACKNOWLEDGMENTS

The authors thank Mr. Y. Hayashi and Mr. M. Matsushima, Composite Structure Section, Airframe Division, National Aerospace Laboratory, for their help in the experiments. The authors also thank Mr. Y. Shinya, Nagoya Aerospace Systems Division, Mitsubishi Heavy Industries, Co. Ltd., for fabrication of the materials used in the experiment.

REFERENCES

1. Mallic, P. K., *Fiber-Reinforced Composite; materials, manufacturing, and design*, 2nd ed., Marcel Dekker Inc., 1993.
2. Whitney, J. M., "Experimental Characterization of Delamination Fracture," *Interlaminar Response of Composite Materials*, Composite Material Series 5, Pagano, N. J. Ed., Elsever Science Publishers B.V., 1989.
3. Ko, F. K., "Three-Dimensional Fabric For Composite," *Textile Structural Composite*, Chou, T. W. and Ko, F. K. Ed., Elsivier Publisher, New York, 1989.
4. Chou, T. W., *Microstructural Design of Fiber Composites*, Cambridge University Press, New York, 1992.
5. Guenon, V. A. F., Chou, T. W and Gillespie, J. W., "Toughness Properties of a Three-Dimensional Carbon-Epoxy Composite," *Journal of Material Science*, Vol.24, 1989, pp.4168 - 4175.
6. Guenon, V. A. F., "Interlaminar Fracture Toughness of a Three-Dimensional Composite," *Master Thesis of Applied Science in Mechanical Engineering, University of Delaware*, 1987.
7. Ishikawa, H., Ji, M., Anahara, M. and Yasui, Y., "The Estimation of Fracture of Orthogonal Three-Dimensional Fiber-Reinforced Composite By DCB Testing," *Proceedings of 71th Ordinary General Meeting of the Japan Society of Mechanical Engineers*, 1994, pp.455-457. (in Japanese).
8. Ishikawa, T., Matsushima, M., Bansaku, K., Watanabe, N. and Sunakawa, M., "Experimental Results of Interlaminar Fracture Toughness and In-Plane Strength of 3-D Woven CF/Epoxy Plates," *Proceedings of Seminar of the Japan Society for Composite Materials*, 1996, pp.51-52. (in Japanese).
9. Byun, J. H., Gillespie, J. W. and Chou, T. W., "Mode I Delamination of a Three-Dimensional Fabric Composite," *Journal of Composite Materials*, Vol.24, 1990, pp.497-518.
10. Watanabe, N. and Tanzawa, Y., "Delamination Analysis of 3-D Orthogonal Interlocked Fabric Composite," *Proceedings of 37th AIAA SDM Conference*, April 1996, AIAA-96-1418.
11. Matsushima, M., Ishikawa, T., Hayashi, Y. and Kobayashi, S., "Experimental Investigation of Interlaminar Fracture Toughness of Carbon Fiber/Thermoplastic and Carbon Fiber/Thermosetting Composite by DCB Specimens," *Report of National Aerospace Laboratory*, TR-1096, 1991, pp.3-16. (in Japanese).

DAMAGE DEVELOPMENT IN PLAIN WEAVE GFRP

C.I.C. Manger[1], S.L. Ogin[1], P.A. Smith[1] and R.P. Greaves[2]

[1] Department of Materials Science and Engineering, University of Surrey, Guildford, GU2 5XH, UK
[2] Rolls-Royce Plc., PO Box 31, Derby, DE24 8BJ, UK

SUMMARY: Damage development in a two layer plain weave glass/epoxy system under quasi-static loading has been investigated. The damage comprised matrix cracking and delamination. Three distinct types of damage morphology were found and were related to the relative shift of the fabric laminae with respect to each other. The tortuous path of the transverse cracking and repeat of damage patterns were found to depend upon tow and weave characteristics, respectively.

KEYWORDS: plain weave, GFRP, damage development, lamina shift.

INTRODUCTION

Over recent years there has been a renewed interest in woven composite materials. Although woven composites exhibit slightly (approximately 5-10 %) lower moduli and strength than equivalent cross-ply laminates they offer some specific advantages. They have very good drapability, especially the common eight harness satin weave. Manufacturing costs can be reduced as one layer of cloth replaces two unidirectional plies, resulting in easier handling and shorter lay-up times. They also have better impact resistance as the nature of the weave localises the damage.

The theoretical modelling of the elastic behaviour of woven fabric composite materials is now well developed. This includes both closed form analytical models building on the early research of Chou and co-workers, e.g. [1], and finite element methods such as those of Whitcomb [2]. However, due to the nature of the fibre architecture and the associated complex damage morphology, work concerned with characterising and predicting damage onset and growth, together with the effect of damage on residual properties, is more limited. Present models require extensive computational effort and involve many simplifications, e.g. [3]. The aim of the present work is to address these issues making use of a model (transparent) GFRP system in order to facilitate damage observation.

Marsden et al. [4-6] characterised the damage in an eight harness satin weave glass/epoxy composite under both quasi-static and fatigue loading. Damage development was found to be a function of tow and weave architecture. It is clear from the work of Marsden et al. [4-6] and Boniface et al. [7] that cracking damage in woven GFRP and CFRP has a complex morphology and that this morphology needs to be understood before the effect of damage can be modelled. The present paper studies the damage initiation and development in a plain weave glass/epoxy composite.

In the present work a laminate assembled from two layers of plain weave fabric was used. A particular feature of interest has been the effect of the shift of the fabric layers relative to one another on the damage pattern which develops. The effect of this shift on material properties has been considered analytically by other workers. The models of Naik and Shembekar [8] report

optimum elastic properties for configurations out of phase with one another, i.e. fabric layers shifted relative to each other. Yurgartis and Maurer [9] suggest that relative lamina shift, along with weave configuration and stacking sequence, influence interlaminar shear strength.

MATERIALS AND EXPERIMENTAL METHODS

The reinforcement used was an E-glass plain weave fabric with similar warp and weft tows consisting of three finer bundles twisted together (Fig. 1). The cloth has a weight of 182 g/m^2 and thickness of 0.15 mm. It was marginally unbalanced with 142 and 126 tow ends in the warp and weft directions, respectively. The matrix used was an Epikote 828 epoxy resin with an NMA curing agent and Ancamine K61B accelerator. Laminates were fabricated using a two layer wet lay up process, in which resin was introduced into cloths which had been carefully marked out to ensure alignment and stacked so as to maintain overall maintain symmetry about the mid-plane. The laminates were cured at 100^{o}C for 3 hours and post-cured at 150^{o}C for a further 3 hours.

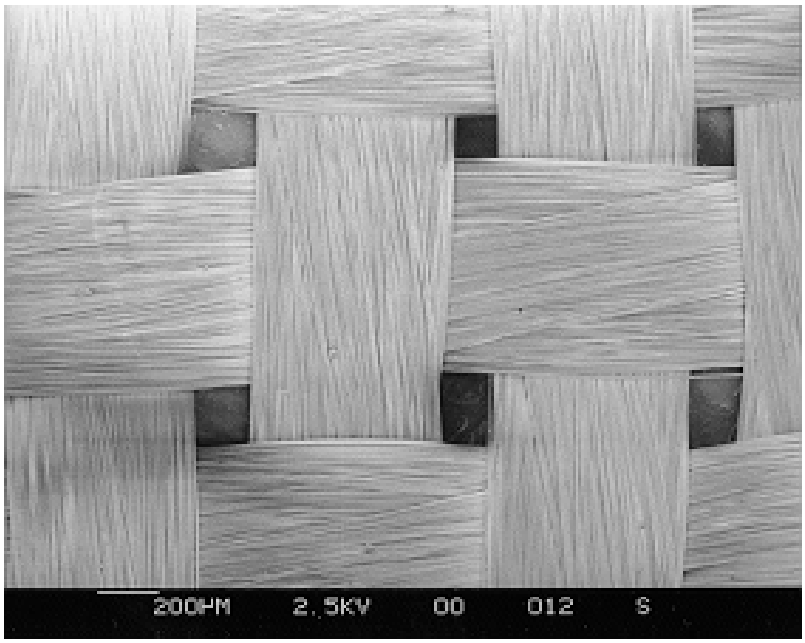

Figure 1. SEM photomicrograph of plain weave cloth

Test coupons (20 mm x 200 mm) were cut using a water cooled diamond saw. Aluminium end tags of dimensions 20 mm x 50 mm were bonded to the coupons leaving a 100 mm gauge length at the centre of which were bonded strain gauges. Quasi-static mechanical testing was performed using an Instron 1175 machine at a crosshead speed of 0.5 mm/min. Data was recorded using a PC-based data-logger package. A linear regression analysis of the stress-strain curve between 1000 and 4000 microstrain was carried out to obtain moduli data.

Observations of damage accumulation were facilitated by the transparent nature of the GFRP, which allowed the plan view damage development to be observed by in situ photography. Samples were unclamped from the grips of the testing machine prior to being photographed. Polishing longitudinal edge sections allows the through thickness profile of the damage to be studied, following the method of Marsden et al. [6]. With accurate measurements during sample preparation, a plan view array of cracks may be located and viewed in cross section.

RESULTS

Laminate Properties

Laminate properties are given in Table 1. The number in brackets denotes the number of samples tested. Crack initiation and failure strains are comparable to those found by Marsden et al. [6] on a similar eight harness satin material. The relatively low volume fraction of 36 % is attributed to the open nature of the weave and low pressure used in fabrication. The variation in modulus is largely attributable to local variations in laminate thickness due to nesting and the thin nature of the cloth.

Table 1: Laminate properties

E_0 (GPa)	18.7 ± 1.4 (12)
σ_{TS} (MPa)	260
ε_i (%)	0.6
ε_f (%)	2.1
V_f (%)	36
Thickness (mm)	~0.4

Damage Development

Under quasi-static loading short transverse cracks of approximately 1 mm in length initiate in the weft tows at an initiation strain, εi, of approximately 0.6 %. Photographs of edge sections show the initial damage occurs near the tow centre (Fig.2a). The crack path is often complicated and is diverted at the interfaces of the three twisted bundles within each tow. At higher levels of strain further cracking initiates towards the tow ends (Fig 2b). The damage tends to saturate, resulting in a reasonably regular spacing within the tows of approximately twice the tow thickness (Fig.2c). The damage is confined to the tows and does not extend into the matrix.

Plan view photomicrographs show that the transverse cracking is aligned at approximately 5 - 10^{o} to the horizontal weft tows which is a result of the cracks following the line of the twist within the tows. The average crack length at saturation is roughly equivalent to the inter-crimp distance which is much less than the laminate width.

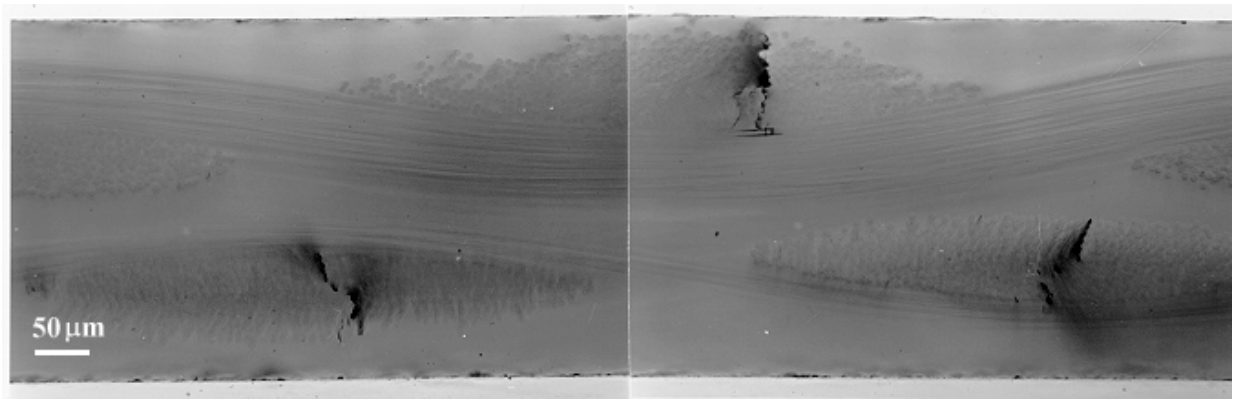

(a)

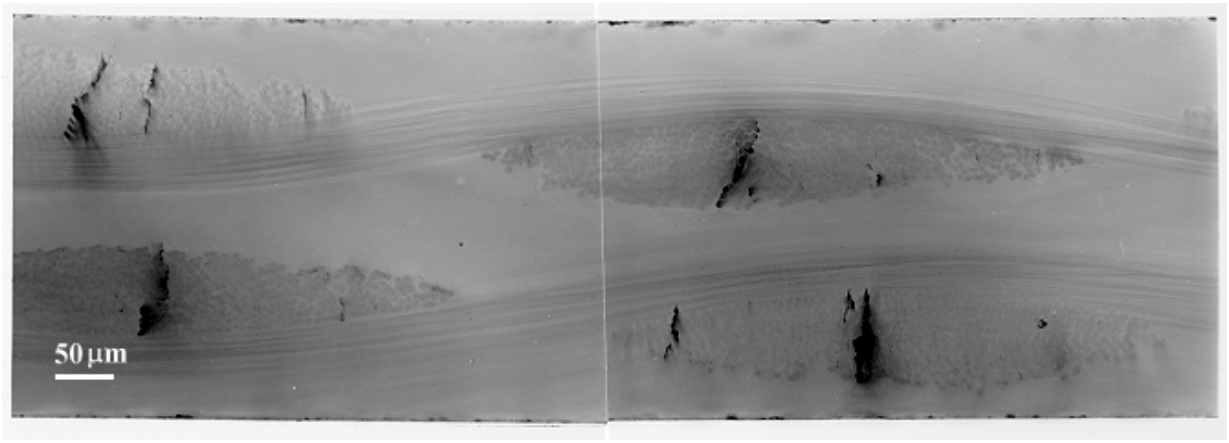

(b)

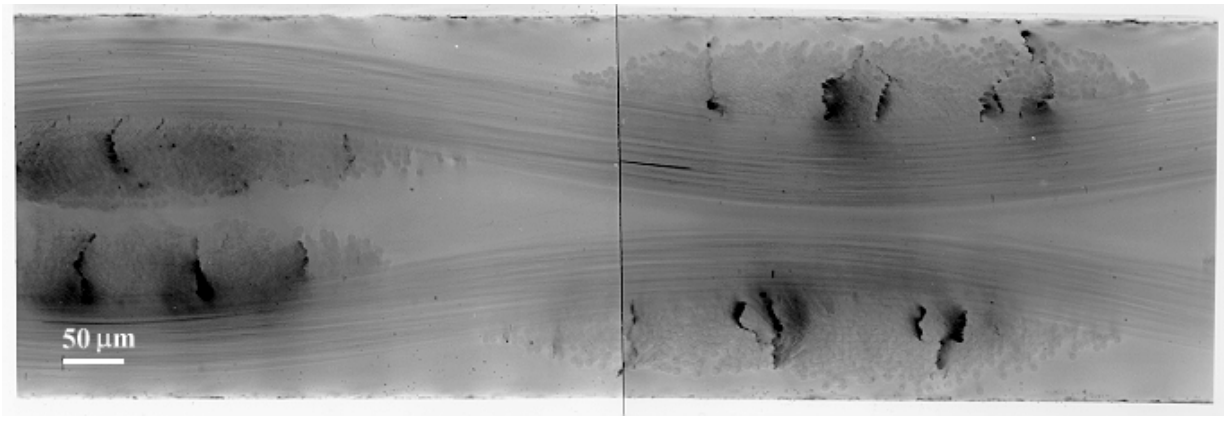

(c)

Figure 2: Polished edge section photomicrographs of damage at (a) 1.0 % strain, (b) 1.2 % strain and (c) 1.6 % strain.

Interestingly, there are three types of damage morphology that may be found in any one laminate. The use of edge sections to study the local relative position of the cloths has shown the morphologies to be as follows.

Banded transverse cracking in weft tows.

The plan view here shows damage to be contained in horizontal bands, perpendicular to the loading direction, P, which are composed of transverse cracks in the weft tows (Fig 3a). The loading direction indicated applies to parts (a), (b) and (c) of the figure. This damage morphology occurs when the two cloths lie in phase with one another as shown in Fig. 3b and indicated schematically in Fig. 3c. The two weft tows are superimposed resulting in damage free resin rich bands.

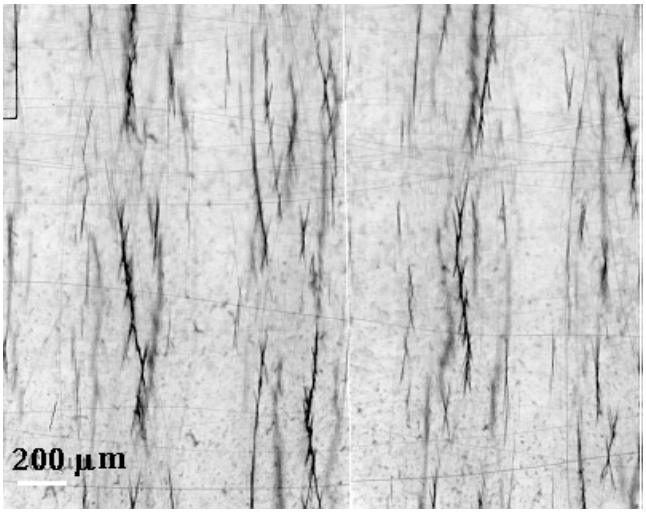

(a) ← P →

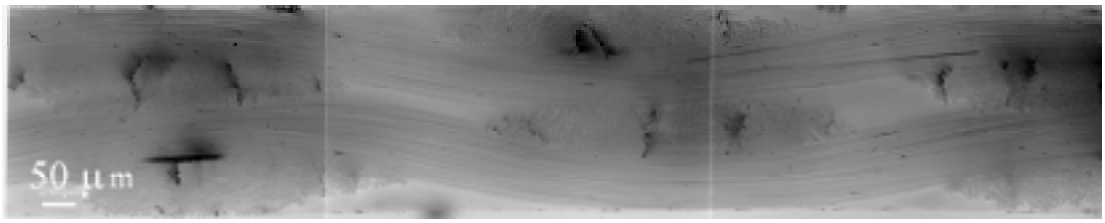

delamination

(b)

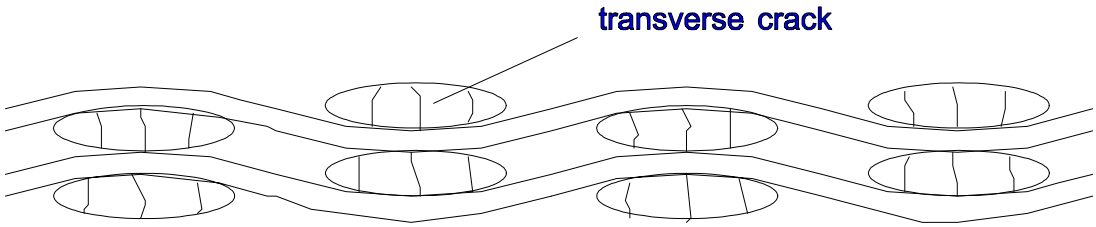

(c)

Figure 3: Damage morphology of case A, (a) plan view photomicrograph, (b) polished edge section photomicrograph and (c) schematic representation of edge section

Banded transverse cracking in weft tows with a regular array of delaminations.

In this damage morphology the plan view damage is similar to case A but with additional delaminations orientated in the loading direction (Fig. 4a). These delaminations initiate at approximately 1.5 % strain. In this case the two cloths are symmetrical about the mid-plane, i.e. 180° out of phase (Fig. 4b and Fig. 4c) and the transverse cracking is arranged in bands as in case A. The delaminations occur at sites where two warp tows touch, i.e. every 180°. This leads to a delamination at every other warp / weft cross over point. The delaminations are dependent on laminate consolidation and are found only if the warp tows are touching.

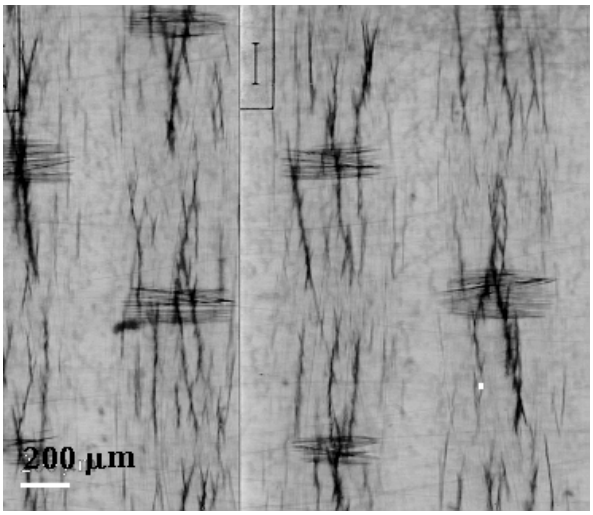

(a) ← P →

(b)

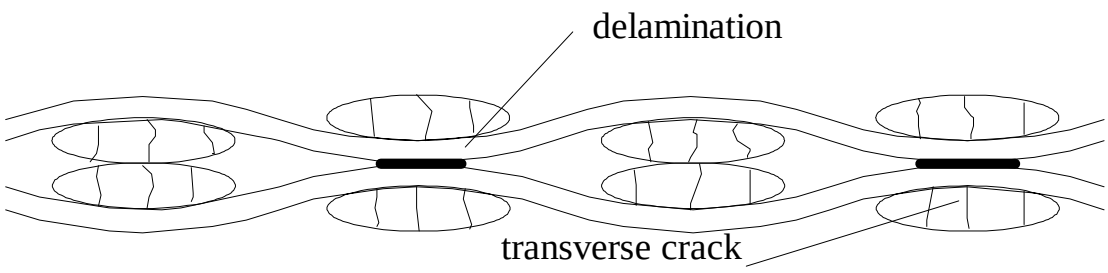

(c)

Figure 4: Damage morphology of case B, (a) plan view photomicrograph, (b) polished edge section photomicrograph and (c) schematic representation of edge section

Regularly distributed plan view transverse cracking in weft tows.

This is shown in plan view in Figure 5a and results when the cloths are at some intermediate phase between the above two cases (Fig. 5b and Fig.5c). The adjacent weft tows are no longer superimposed and overlap when viewed in plan view, resulting in no through-thickness resin rich regions.

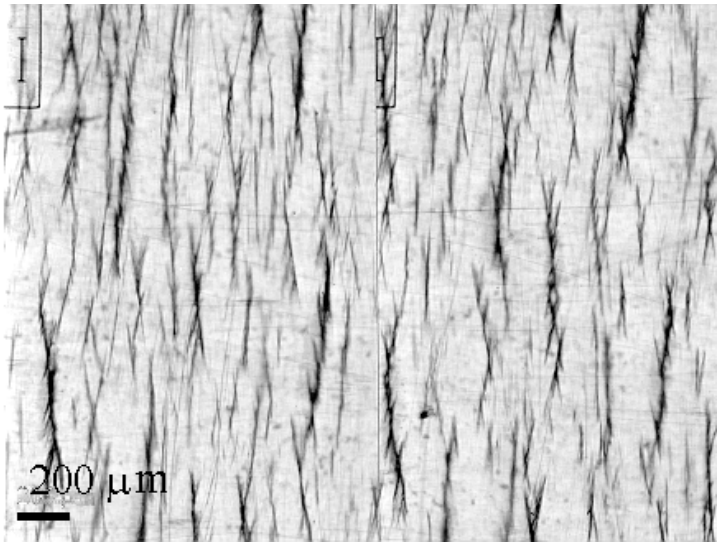

(a) ← P →

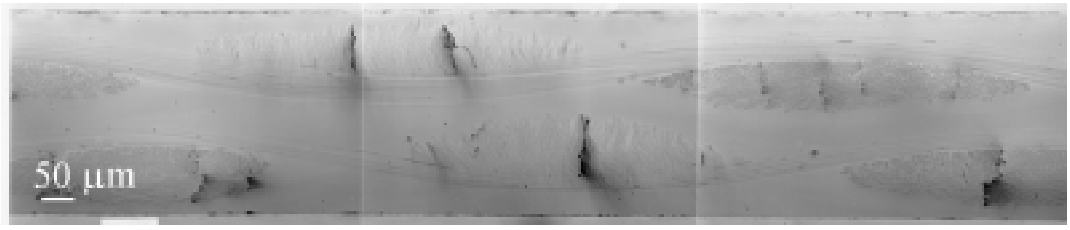

(b)

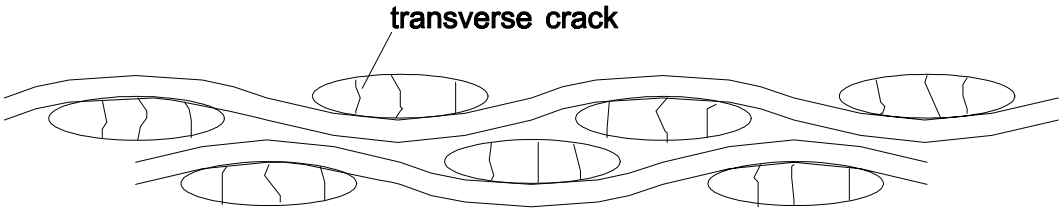

(c)

Figure 5: Damage morphology of case C, (a) plan view photomicrograph, (b) polished edge section photomicrograph and (c) schematic representation of edge section

Similarities in cracking morphology can be found for all three cases. Transverse cracking appears to be more pronounced at cross over points between the warp and weft tows. This can clearly be seen in both cases A and B. Delaminations may be found in cases A and C at high damage densities, although the delaminations do not appear with the regularity seen in case B. Such a delamination is shown in Figure 3b, located at the interface of a warp and weft tow. Of the three crack morphologies the banded plan view damage morphology (case A) was found to be dominant, suggesting that the open nature of the plain weave cloth encourages nesting of the cloths on one another during consolidation.

In this study it has been shown that the relative shift of adjacent cloths influences damage morphology, in addition to the previously reported influence on mechanical properties [4-5]. These findings should be considered in any subsequent detailed modelling of the effect of damage development on mechanical properties of woven composite materials.

CONCLUSIONS

The damage morphology seen in a plain weave GFRP laminate under quasi-static loading was found to be dependent on tow characteristics, weave geometry and relative cloth shift. The transverse cracking morphology, both plan view and through thickness, was strongly influenced by the twist of individual tows, whilst the macroscopic cracking patterns were determined by the weave geometry and relative cloth shift. A regular array of delaminations between fabric layers was found to result for relative cloth shifts of 180^{o}, when the laminate was symmetrical about its mid-plane. Transverse cracking initiated near the tow centre and, at saturation, developed a reasonably regular saturation spacing within the tows of approximately twice the tow thickness.

ACKNOWLEDGEMENTS

The authors would like to thank Reg Whattingham for his technical assistance and also Rolls-Royce plc and the EPSRC for funding a CASE studentship for C. Manger.

REFERENCES

1. Ishikawa, T., Chou, T.-W., "Stiffness and Strength Behaviour of Woven Fabric Composites", J. Mat. Sci., Vol. 17 (1982) pp.3211-3220.

2. Whitcomb, J.D., “Three-Dimensional Stress Analysis of Plain Weave Composites”, Composite Materials Fatigue and Fracture, Volume 3, T. K. O’Brien, ed., ASTM.STP 1110, Philadelphia: American Society for Testing and Materials, pp. 417-438.

3. Whitcomb, J., Srirengan, K., "Effect of Various Approximations on Predicted Progressive Failure in Plain Weave Composites", NASA Conference Publication 3311 Part 2, Mechanics of Textile Composites Conference, (1995) pp. 665-681.

4. Marsden, W. M., Boniface, L., Ogin, S. L., Smith, P. A., "Quantifying Damage in Woven Glass/Epoxy Laminates", Proc. FRC 94, Newcastle (1994) 32/ pp.1-9.

5. Marsden, W. M., Boniface, L., Ogin, S. L., Smith, P. A., Greaves, R. P., "Matrix Cracking and Stiffness Reduction in Woven Fabric Composites", Proc. ICCM 10, Eds. A. Poursartip and K. Street, published by The Tenth Int. Conf. On Comp. Materials Society, Woodhead Publishing Ltd., Vancouver (1995) Vol. 1, pp. 431-438.

6. Marsden, W.M. "Damage Accumulation in a Woven Fabric Composite", Phd. Thesis. Department of Materials Science and Engineering, University of Surrey, Guildford, UK (1996).

7. Boniface, L., Gao, F., Marsden, W. M., Ogin, S. L., Smith, P. A., "Matrix Cracking Phenomena in Glass and Carbon Woven Fabric Composites", Proceedings of 3rd International Conference on Deformation and Fracture of Composites (1995) pp.317-325.

8. Naik, N. K., Shembekar, P. S., "Elastic Behaviour of Woven Fabric Composites: II - Laminate Analysis", J. Composite Mat., Vol. 26 (1992) pp.2226-2246.

9. Yurgartis, S. W., Maurer, J. P., "Modelling Weave and Stacking Configuration Effects on Interlaminar Shear Stresses in Fabric Laminates", Composites, Vol. 24 (1993) pp.651-658.

A FLEXIBLE 3D FEA MODELLING APPROACH FOR PREDICTING THE MECHANICAL PROPERTIES OF PLAIN WEAVE UNIT CELL

P. Tan, L. Tong and G. P. Steven

Department of Aeronautical Engineering, University of Sydney, NSW 2006 Australia
Cooperative Research Center for Aerospace Structures, P.O.Box 30, 351 Milperra Road, Bankstown, NSW 2200, Australia.

SUMMARY: A finite element analysis (FEA) modelling approach was developed for predicting the mechanical properties of plain weave graphite/epoxy fabric-reinforced composites. 3D FEA models for a single layer plain weave fabric were generated by interfacing an in-house computer code with the FEA software Strand6 using 8-node brick and 6-node wedge elements. The paths of the impregnated tow (or yarn) within the composite materials were chosen to be sinusoidal, and a lenticular cross-section formed by two sinusoidal curves was utilised in the models. Pure tension and shear loading were applied. Results from FEA models were in good agreement with the present test results and those reported in the literature. In addition, a parametric study illustrated the effects of the geometrical dimensions of a unit cell on its mechanical properties.

KEYWORDS: woven fabric-reinforced composite, mechanical properties, finite element analysis (FEA) model

INTRODUCTION

Fibre reinforced woven fabric has been widely adopted in aerospace structures. To effectively utilise this material, it is necessary to evaluate its mechanical properties for a wide range of weave architecture parameters and to tailor the composite to the specified requirements of its role in practical structures [2]. Measurements of these properties are difficult and can be very expensive when investigating the effects of some manufacturing and geometrical parameters. Fortunately, theoretical and FEA modelling provide a cost-effective alternative for determining these properties. However, modelling the architecture of woven fabric-reinforced composite material in detail is difficult. Part of this difficult is due to the complicated architecture of the woven fabric composite materials when viewed at the same scale as the weave geometry [3]. Hence, most of research workers developed the models based on the simplified geometry of woven fabric composites. Earlier work was carried out by Ishakawa and Chou [4-7] who developed one-dimensional models for woven fabric-reinforced composites. Later, various analytical and FEA models for predicting the mechanical properties of woven fabrics were proposed and developed, including the one-dimensional models [8]; two-dimensional models [9-11] and three-dimensional models [12-15].

In this study a flexible 3D FEA modelling approach is proposed for determining the mechanical properties of plain weave fabric-reinforced composite materials. The models created are capable of producing a 3D representation and visualisation of any plain weave unit

cell. The approach was validated by comparing with the test results. In addition, a parametric study was conducted to investigate the effects of geometric dimensions of a unit cell on its mechanical properties.

DEVELOPMENT OF FEA MODEL FOR A PLAIN WEAVE UNIT CELL

When developing the computer model of a plain weave unit cell, it is predefined that the model should be general and capable of further development and refinements. Thus, a general model, capable of producing any required weave geometry, and not restricted to any particular geometry or to a particular textile description, is required. For easy construction of any plain weave unit cell model, a flexible modelling approach is necessary. In addition, in order to evaluate the mechanical behaviour, a representation of a plain weave which is suitable for finite element meshing and analysis is required [2]. In this section, the details of the geometry for a woven fabric unit cell, the boundary conditions and loadings chosen will be discussed. The procedure for developing the 3D FEA models and the relevant assumptions will be described.

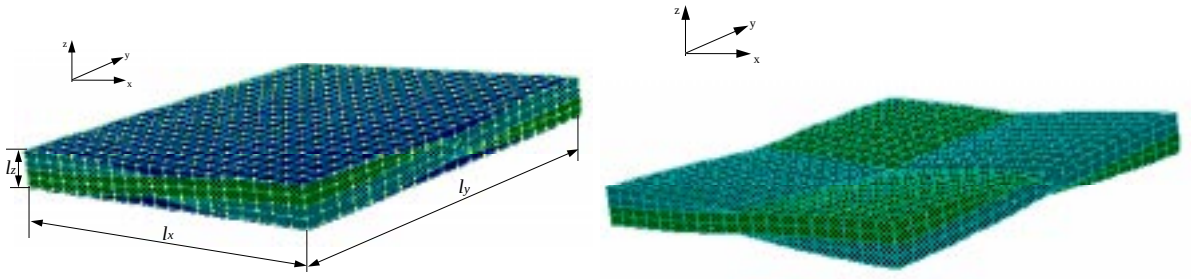

(a) with resin (b) without resin

Fig. 1: 3D FEA model for plain weave unit cell

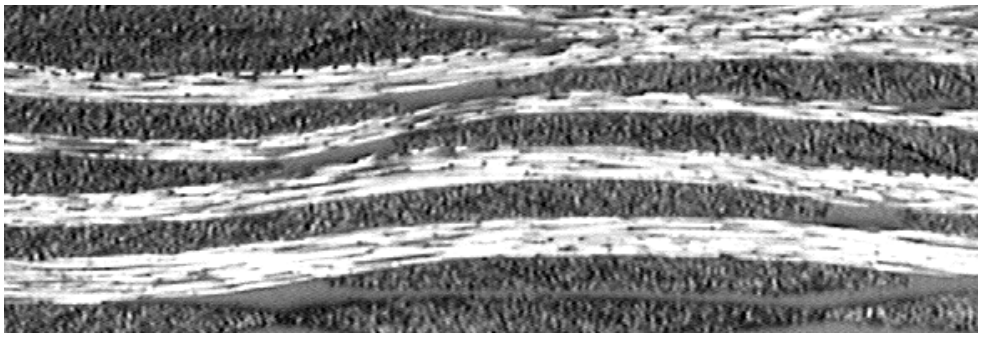

Fig. 2: Photomicrograph of a section of T300/934 plane weave laminate

Geometry and Assumptions for Plain Weave Unit Cell

Due to the complicated architecture of woven fabrics, it is difficult to describe the 3D unit cell geometry at the same scale as the woven fabric micro geometry. Hence, the geometrical model for a plain weave unit cell was established at the yarn level. Each yarn contains a few thousand fibres, and all fibres in each yarn are assumed to follow the same path which is

chosen to be sinusoidal. Also, a strictly lenticular cross-section formed by two sinusoidal curves is utilised in the model (see Fig. 1(a) with resin and (b) removing the resin from the model). The 3D FEA models are easy to be created by interfacing an in-house computer code with the FEA software Strand6 [1]. These models include some of the major parameters affecting the mechanical properties of composite, ie. impregnated yarn orientation, fibre volume fraction, mechanical properties of composite constituents. They can be evaluated from the scan of real weave fabric geometry (see Fig. 2), which was obtained by using an image analysis system together with the Iphoto Plus software. The mechanical properties for the composite constituents in a plain weave unit cell are considered to be homogeneous and isotropic for the resin but orthotropic for the impregnated fibre yarns with the respect to the principle material axis (or local coordinate system).

Boundary Conditions and Loadings

To evaluate the stiffness constants for a plain weave unit cell, six separate strain vectors are respectively applied to the relevant unit cell model using the Lagrange Multipliers Method. Six separate FEA cases need to be run respectively on the same FEA model for the corresponding six separate strain vectors (ε_x=0.001, ε_y=0.001, ε_z=0.001, γ_{xy}=0.001, γ_{yz}=0.001, γ_{zx}=0.001), and the relevant boundary conditions for each case are listed in Table 1.

Table 1: Boundary conditions for cases (a)-(f)

Case	Boundary conditions
a	$DX\|_{x=lx}=0.001l_x$, $DX\|_{x=0}=0$, $DY\|_{y=0}=DY\|_{y=ly}=0$, $DZ\|_{z=0}=DZ\|_{z=lz}=0$
b	$DY\|_{y=ly}=0.001l_y$, $DY\|_{y=0}=0$, $DX\|_{x=0}=DX\|_{x=lx}=0$, $DZ\|_{z=0}=DZ\|_{z=lz}=0$
c	$DZ\|_{z=lz}=0.001l_z$, $DZ\|_{z=0}=0$, $DX\|_{x=0}=DX\|_{x=lx}=0$, $DY\|_{y=0}=DY\|_{y=ly}=0$
d	$DX\|_{y=ly}=0.0005l_y$, $DX\|_{y=0}=0$, $DY\|_{x=lx}=0.0005l_x$, $DY\|_{x=0}=0$, $DZ\|_{z=0}=DZ\|_{z=lz}=0$
e	$DY\|_{z=lz}=0.0005l_z$, $DY\|_{z=0}=0$, $DZ\|_{y=ly}=0.0005l_y$, $DZ\|_{y=0}=0$, $DX\|_{x=0}=DX\|_{x=lx}=0$,
f	$DX\|_{z=lz}=0.0005l_z$, $DX\|_{z=0}=0$, $DY\|_{y=0}=DY\|_{y=ly}=0$, $DZ\|_{x=lx}=0.0005l_x$, $DZ\|_{x=0}=0$

Considering the boundary conditions and strain vectors selected above, the required mechanical properties can be evaluated from the relevant equations [16].

EXPERIMENTAL VERIFICATION

In order to investigate the validity of the developed FEA models, 18 tests were carried out. The specimen preparation, testing procedure, experimental results and comparisons between the predicted and testing results are discussed in this section.

Specimen Preparation and Testing Procedure

In this experimental investigation, plain weave graphic/epoxy fabric reinforced composite materials T300/934 (3K-70-PW) were used.

Eight layers (or plies) of prepreg woven fabrics were laminated. The stacking sequence of laminate specimens is balanced and symmetric so that the bending coupling stiffness and shear coupling stiffness terms are zero, and the torsion coupling stiffness is relatively low;

close to their minimum due to the fine ply distribution [19]. The lay-up sequence and the thickness of the laminate specimens are listed in Table 2.

Table 2: Lay-up sequence and thickness of laminate specimens

Specimen group	Stack sequence	Thickness of laminates (mm)	Purpose	Number of specimens
A	$[0]_8$	1.75	Test for E_1, ν_{12}	6
B	$[90]_8$	1.75	Test for E_2, ν_{12}	6
C	$[+45/-45]_{4s}$	1.75	Test for G_{12}	6

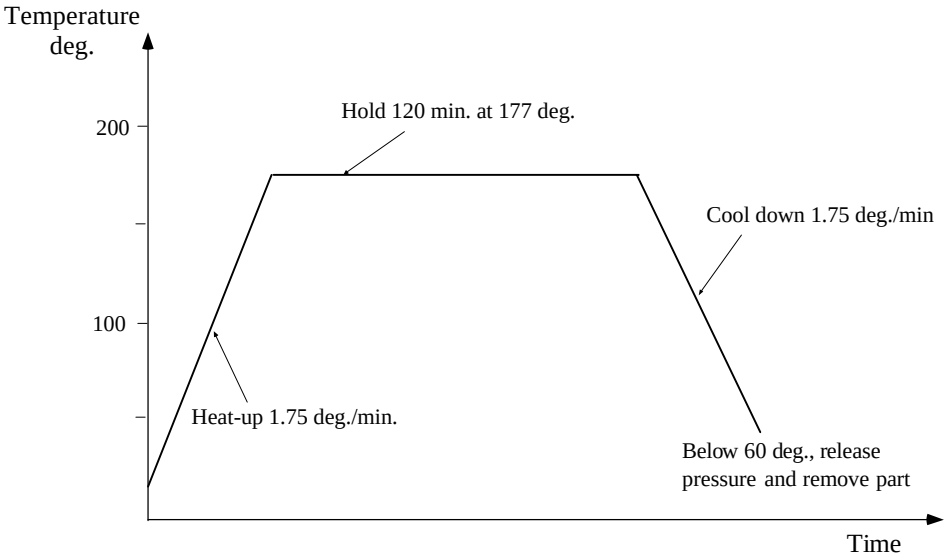

Fig. 3: Autoclave curve cycle

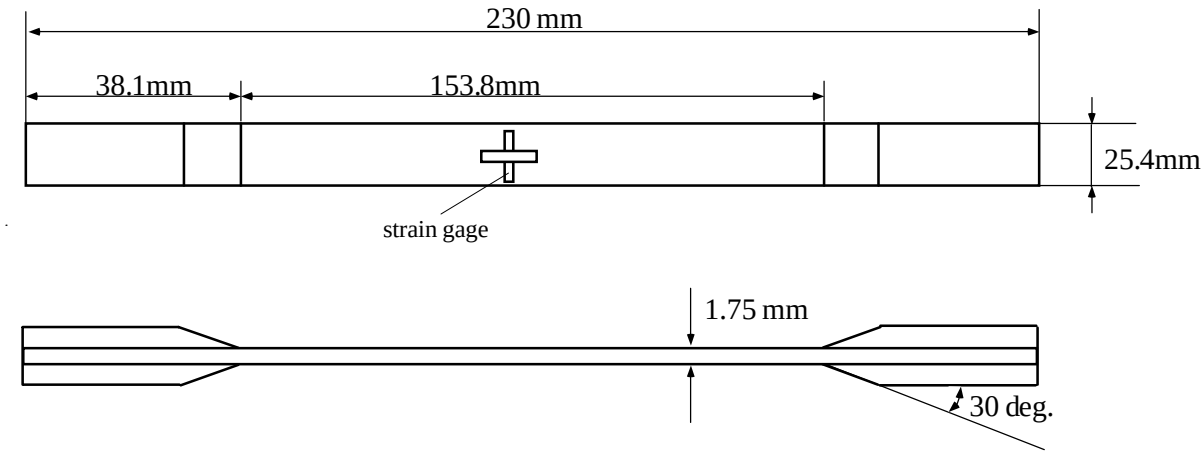

Fig. 4: The geometry of test specimen

All specimens were laminated from prepreg plain weave fabric sheets and cured in an autoclave following a curing cycle shown in Fig. 3 [20]. The configuration of the specimens is in accordance with the ASTM D 3039-76 and is shown in Fig. 4 [19, 21-23]. Strain gauges with 120±0.3 Ω gauge resistance and 2.13± 1% gauges factor were located at the mid length of a specimen. These strain gauges can be used for measuring the strains in both longitudinal

and transverse directions. Static tension tests were performed by Instron machine. The specimens were tested at a room temperature (26°C) and at a cross-head speed of 1mm/min. Two computer data acquisition systems were used in the test for collecting the relevant data, eg., the loading, displacement and the strains. These two systems were driven by the software packages Instron Merlin and Labview respectively, which were operated via an user interface menu.

The geometrical parameters for a plain weave unit cell interested were obtained from the photomicrograph of a specimen section and listed in Table 3.

Table 3: Geometrical dimensions and fibre volume fraction

models	l_x (mm)	l_y (mm)	l_z (mm)	V_f^o (%)
ModEXP	2.1	2.1	0.22	50.1

The overall fibre volume fraction V_f^o was evaluated using the following equation

$$V_f{}^o = \frac{N \times \rho_A}{T \times D} \tag{1}$$

where N is the number of ply for the laminate specimen, ρ_A is fibre areal weight (g/m^2), D is fibre density (g/cc) and T is the thickness of laminate specimen [24].

Table 4 lists the mechanical properties for the T300 carbon fibre and the 934 resin epoxy as well as the mechanical properties for the impregnated tow (T300/934) that were calculated using the following micromechanics equations proposed by Chamis [18]

$$E_{11} = V_f' \times E_{1f} + V_m' \times E_m \tag{2}$$

$$E_{22} = E_{33} = \frac{E_m}{1 - \sqrt{V_f'} \times (1 - E_m / E_{2f})} \tag{3}$$

$$G_{12} = G_{31} = \frac{G_m}{1 - \sqrt{V_f'} \times (1 - G_m / G_{12f})} \tag{4}$$

$$G_{23} = \frac{G_m}{1 - \sqrt{V_f'} \times (1 - G_m / G_{23f})} \tag{5}$$

$$\nu_{12} = \nu_{13} = V_f' \times \nu_{12f} + V_m' \times \nu_m \tag{6}$$

$$\nu_{23} = \frac{E_{22}}{2 \times G_{23}} \tag{7}$$

Using the data given in Table 4, the mechanical properties for a T300/934 plain weave unit cell were predicted with the aid of the relevant 3D FEA models and are tabulated in Table 5. The predicted values are compared with those reported by the Boeing company [25], and the present experimental results which were obtained following the ASTM test standards ASTM D 3096-76 and ASTM D3518-76.

In Table 5, the differences between the predicted and experimental results are 4.9% for the in-plane Young's moduli E_1 and E_2, 12.2% for the in-plane Poisson's ratio ν_{12} and 1.7% for the in-plane shear modulus G_{12}, while the differences between predicted results and the average values reported by the Boeing company are 0.7% for the in-plane Young's moduli E_1 and E_2,

14% for the in-plane Poisson's ratio ν_{12} and 8% for the in-plane shear modulus G_{12}. Thus it is noted that the predicted mechanical properties for a T300/934 plain weave unit cell are generally in good agreement with the present experimental results and those obtained by the Boeing company. However, the FEA results tend to be lower than the measured mechanical properties. One reason for this could be that equation (1) may underestimate the overall fibre volume fraction.

Table 4: Mechanical properties of constituents and impregnated tow for T300/934 composite materials

Item	Material	E_{1*} (GPa)	E_{2*} (=E_{3*}) (GPa)	G_{12*} (=G_{13*}) (GPa)	G_{23*} (GPa)	ν_{12*} (=ν_{13*})	ν_{23*}
Fibre	(T300)	220	13.8	11.35	5.5	0.2	0.25
Matrix	Epoxy resin (934)	4.1	4.1	1.454	1.454	0.41	0.41
Impregnated tow	(T300/934)	173.11	10.84	6.361	4.165	0.2456	0.3019

* Subscripts 1, 2 and 3 indicate the quantities in longitudinal, transverse and through-the-thickness directions respectively.

Table 5: The comparisons of the mechanical properties for T300/943 plain weave composites

Item	E_1 (GPa)	E_2 (GPa)	E_3 (GPa)	ν_{12}	ν_{13}	ν_{23}	G_{12} (GPa)	G_{13} (GPa)	G_{23} (GPa)
FEA model V_f^o=50.1%	56.5	56.5	10.18	0.043	0.45	0.45	4.28	2.86	2.86
Test	59.4	59.4	N/A	0.049	N/A	N/A	4.353	N/A	N/A
NASA [25]	53.09-60.67	53.09-60.67		0.05			3.1-6.205		

PARAMETRIC STUDY

Four unit cell models with different geometrical dimensions were developed for the plain weave composite, and they are referred as ModA, ModB, ModC and ModD. Based on the results of these models, the effects of some geometrical parameters on the mechanical properties were discussed. The mechanical properties predicted from model ModA will be compared with those available in the literature.

In all calculations in this section, the overall fibre volume fractions for all four models were chosen to be the same and equal to 58.46%. The relevant geometrical dimensions of unit cells are given in Table 6, in which l_x, l_y and l_z are the length, width and thickness of a unit cell (see Fig. 1).

Table 6: Geometrical parameters for all four models

models	l_x (mm)	l_y (mm)	l_z (mm)
ModA	2.1	2.1	0.19
ModB	2.8	2.8	0.19
ModC	2.1	2.1	0.25
ModC	3	1.5	0.19

Table 7: Mechanical properties of constituents for T300/GY260 composite materials

Material (GPa)	E_1	E_2 (=E_3)	ν_{12} (=ν_{13})	ν_{23}	G_{12} (=G_{13})	G_{23}	V_f (%)
Fibre (T300) [17]	220	13.8	0.2	0.25	11.35.	5.5	58.46
Resin (GY260) [17]	3.252	3.252	0.355	0.355	1.2	1.2	41.54
Impregnated tow (T300/GY260)	202.038	12.134	0.2128	0.2704	8.358	4.776	

Table 7 gives the mechanical properties for the T300 carbon fibre, the GY260 epoxy and the impregnated yarn (T300/GY260). It should be mentioned that each impregnated tow (or yarn) in the plain weave composite material was modelled as a unidirectional prepreg. The mechanical properties of the unidirectional fibre yarn were calculated using equations (2) to (7).

Same strain vectors and boundary conditions were applied for the four unit cell models, and the mechanical properties were then obtained following the same procedure as described in the previous sections. Table 8 presents the mechanical properties for all four plain weave unit cell models.

Table 8: Mechanical properties for all four plain weave models

Model	E_1 (GPa)	E_2 (GPa)	E_3 (GPa)	ν_{12}	ν_{13}	ν_{23}	G_{12} (GPa)	G_{13} (GPa)	G_{23} (GPa)
ModA	65.68	65.68	8.60	0.032	0.364	0.364	5.23	2.71	2.71
ModB	67.10	67.10	8.60	0.032	0.358	0.358	5.26	2.67	2.67
ModC	63.77	63.77	8.60	0.032	0.371	0.371	5.25	2.76	2.76
ModD	67.32	63.23	8.60	0.032	0.356	0.372	5.25	2.67	2.77

By studying the data listed in the first three rows in Table 8, it is noted that when the unit cell dimensions increase in both the warp (*x*) and the weft (*y*) directions or decreases in the *z* direction, the in-plane Young's moduli E_1, E_2 increase, while the out-of-plain Poisson's ratios ν_{13}, ν_{23} and the shear moduli G_{13}, G_{23} decrease. The variations of dimensions in all three directions almost do not affect the out-of-plane Young's modulus E_3, the in-plane Poisson's ratio ν_{12}, and the shear modulus G_{12}. For model ModD, the in-plane Young's modulus in the warp direction (ie. with longer unit cell dimension) E_1 is greater than that in the weft direction (ie. with shorter unit cell dimension) E_2, the out-of-plane Poisson's ratio ν_{23} and shear modulus G_{23} are larger than ν_{13} and G_{13} respectively. It is believed that variations of fibre

orientation could be an important contributing factor to these changes in mechanical properties.

The mechanical properties for model ModA can be compared with those given in Ref. [17], as model ModA was established based on the same geometry reported in Ref. [17]. Table 9 lists the mechanical properties predicted by the present model, and those predicted and measured in Ref. [17]. It is noted that the in-plane Young's modulus E_1 and E_2 obtained from ModA are close to the experimental results and those evaluated from UB's models. The differences between the results of model ModA and the experimental ones are less than 2% for the in-plane Young's modulus E_1 (or E_2). However, the differences for the in-plane Poisson's ratio and the shear modulus are 34% and 20% respectively.

Table 9: Comparison of Mechanical properties between presented and those in Ref [17]

Item	ModA	LB-1 [17]	LB-2 [17]	UB-1 [17]	UB-2 [17]	Test [17]
E_1 (GPa)	65.68	42.97	55.71	67.35	66.44	66.12
E_2 (GPa)	65.68	42.97	55.71	67.35	66.44	66.84
E_3 (GPa)	8.58	8.41	8.44	8.44	8.50	N/A
G_{12} (GPa)	5.23	3.996	N/C	3.98	N/C	4.357
G_{13} (GPa)	2.71	N/C	N/C	N/C	N/C	N/A
G_{23} (GPa)	2.71	N/C	N/C	N/C	N/C	N/A
ν_{12}	0.032	0.323	0.150	0.027	0.0299	0.0476
ν_{13}	0.364	0.257	0.323	0.38	0.4101	N/A
ν_{23}	0.364	0.257	0.323	0.38	0.4101	N/A

CONCLUSIONS

This paper presented a 3D FEA modelling approach for predicting the mechanical properties of plain weave fabric composites. The present modelling approach was validated by comparing the predicted results with the experimental ones. This modelling approach can be used to model various plain weave composite materials with different geometrical parameters and mechanical properties of composite constituents. The parametric study demonstrated that some mechanical properties, eg, E_1 and E_2, ν_{13} and ν_{23}, G_{13} and G_{23} are sensitive to the changes in dimensions of a unit cell while others, eg, G_{12}, ν_{12}, and E_3, are less sensitive or not sensitive.

ACKNOWLEDGMENTS

P.Tan is supported by an Australian Postgraduate Award (APA) and a Supplementary Scholarship in the Aeronautical Engineering Department of the University of Sydney. She would like to thank Mr Radu Turcanu for the assistance provided in the test.

REFERENCES

1. "STRAND6 Reference Manual and User Guide," G+D Computing Pty Ltd, Sydney, Australia, September, 1993.

2. Hewitt, J.A., Brown, D. and Clarke, R.B., "Computer Modelling of Woven Composite Materials," *Composites*, Vol. 26, 1995, pp.134-140.

3. Blackketter, D.M., Walrath, D.E. and Hansen, A.C., "Modeling Damage in a Plain Weave Fabric-Reinforced Composite Material," *Journal of Composites Technology & Research*, 1993, pp.136-142.

4. Ishikawa, T. and Chou, T.W., "Elastic Behaviour of Woven Hybrid Composites", *Journal of Composite Material*, Vol. 16, No. 1, 1982, pp. 2-19.

5. Ishikawa, T. and Chou, T.W., "In-Plane Thermal Expansion and Thermal Bending Coefficients of Fabric Composites", *Journal of Composite Material*, Vol. 17, No. 2, 1983, pp. 92-104.

6. Ishikawa, T and Chou, T.W. "One-dimensional Micromechanical analysis of Woven Fabric Composites," *AIAA Journal*, Vol. 21, No.12, 1983, pp. 1714-1721.

7. Ishikawa, T. and Chou, T.W., "Nonlinear Behaviour of Woven Fabric Composites", *Journal of Composite Material*, Vol.17, No. 5, 1983, pp 399-413

8. Zhang, Y.C. and Harding, J. "A Numerical Micromechanics Analysis of the Mechanical Properties of a Plain Weave Composite," *Computer and Structures*, vol. 36, No. 5, 1990, pp.839-844.

9. Naik, N. K. and Shembekar, P. S. "Elastic Behaviour of Woven Fabric Composites: I-Lamina Analysis," *Journal of Composite Material*, Vol. 26, No. 15, 1992, pp. 2197-2225.

10. Shembekar, P. S. and Naik, N. K., "Elastic Behaviour of Woven Fabric Composites: II-Laminate Analysis," *Journal of Composite Material*, Vol. 26, No. 15, 1992, pp. 2226-2246.

11. Naik, N. K. and Shembekar, P. S. "Elastic Behaviour of Woven Fabric Composites: III-Laminate Design," *Journal of Composite Material*, Vol. 26, No. 17, 1992, pp. 2523-2541.

12. Woo, K and Whitcomb, J.D., "Three-Dimensional Failure Analysis of Plain Weave Textile Composites Using a Global/Local Finite Element Method," *Journal of Composite Materials*, Vol. 30, No.9, 1996, pp. 984-1003.

13. Whitcomb, J.D., "Three-Dimensional Stress Analysis of Plain Weave Composites," *NASA report*, NASA TM-101672, 1989.

14. Hewitt, J.A., Brown, D. and Clarke, R.B., “Computer Modelling of Woven Composite Materials,” Composites, Part A Vol. 26, No. 2, 1995, pp. 134-140.

15. Cox, B.N., Carter, W.C. and Fleck, N.A. “A Binary Model of Textile Composites-I. Formulation”, Acta Metall. Mater., Vol.42, No.10, 1994, pp. 3463-3479.

16. P.Tan, L.Tong and G.P.Steven, “A 3D Modelling Technique for Predicting the Linear Elastic Properties of Opened-Packing Woven Fabric Unit Cell,” to be presented at the 9th International Conference on Composite Structure, Paisley, Scotland, 8th-10th, Sep. 1997.

17. Falzon, P.J. and Herszberg, I., “Three-Dimensional Finite Element Analysis of a Plain Woven Composite,” CRC-AS report, CRC-AS TM 95001, December,1994.

18. Chamis,C.C., “Simplified Composite Micromechanics Equations for Hygral, Thermal, and Mechanical properties,’ *SAMPE Quarterly*, pp.14-23, April 1984.

19. Isaac, M. Daniel and Ori Ishai “Engineering Mechanics of Composite Materials,” Oxford University Press, 1994.

20. Anonymous, “ICI Fiberite Material Handbook” Tempe, Arizona, USA, March, 1989.

21. Anonymous, "Annual book of ASTM Standards. Section 15, General Products, Chemical Specialties and End Use Products,” Vol.15.03, Philadelphia, DA: ASTM, 1985.

22. Whitney, J.M., Daniel, I.M. and Pipes, R.B., “Experimental Mechanics of Fibre Reinforced Composite Materials,” The Society for Experimental Stress Analysis, U.S.A., 1982.

23. Carlsson, L.A. and Gillespie, J.W., “Dalaware Composites Design Encyclopedia”, Technomic Pub. Co., 1992.

24. “Composite Manufacturing of Tooling,” CRC-AS Short Course note, 1994

25. BOEING Advanced Composites Handbook, 1986.

OPTIMISATION OF IN-PLANE AND BENDING PROPERTIES OF WOVEN FABRIC LAMINATE CONFIGURATIONS

R. W. Stewart, V. E. Verijenko, S. Adali

University of Natal, Durban, South Africa

SUMMARY: The properties of a satin weave glass/carbon hybrid composite lamina are established according to the theory in [1-3]. This is extended to a multi-layered solution where the main focus is on the behaviour of 3-layered symmetric laminates. Various angular orientations are imparted to each layer according to the standard transformation equations [4]. Vertical shifts are allocated to each layer to fix its position in the lay-up. Once the describing matrices have been determined, the deflection characteristics of a simply supported rectangular plate can be found according to [5,6]. Through changing the thickness and geometry of the various layers, changes to the angle of the various laminae and of the whole plate to the simple supports, the influence of each of the parameters on the plate deflection can be determined. It is also possible to show an optimal solution for minimum deflection of the plate.

KEYWORDS: woven fabric, deflection, in-plane, satin weave

INTRODUCTION

The properties of a satin weave glass/carbon hybrid composite lamina are established according to the theory in [1-3]. The in-plane properties predicted by the parallel-series scheme in [1] have been shown to agree well with experimental data. The investigation is extended here to include bending properties. It has been found, although not presented here, that there is a significant difference between the results obtained ignoring weave structures and those obtained considering them. The focus of this study is therefore to investigate the influence of weave structure on the deflection of a plate.

In order to extend the theory to a laminated plate, the summation of the various matrices that describe each lamina is done at the end of the unit cells. It is therefore possible to change the angular orientation of each layer, which could not be achieved previously. The in-plane properties of each constituent layer are determined to show the influence of this on the behaviour of the laminate. It will be shown that although the in-plane properties are not used directly for the determination of deflection characteristics, these properties are closely related.

THEORY

Material Properties

The material properties of each woven fabric lamina were first established. This involved defining shape functions for the weave structure. These shape functions can be found in [1-3].

The relevant stiffness parameters could be found as presented in [1], [3]. Relevant dimensions and terms can be seen in Fig. 1.

The satin weave under consideration consists of carbon fibre reinforcement in the *Warp* direction and glass fibre reinforcement in the *Fill* direction. The assumed properties of the carbon, glass and resin are presented in Table 1.

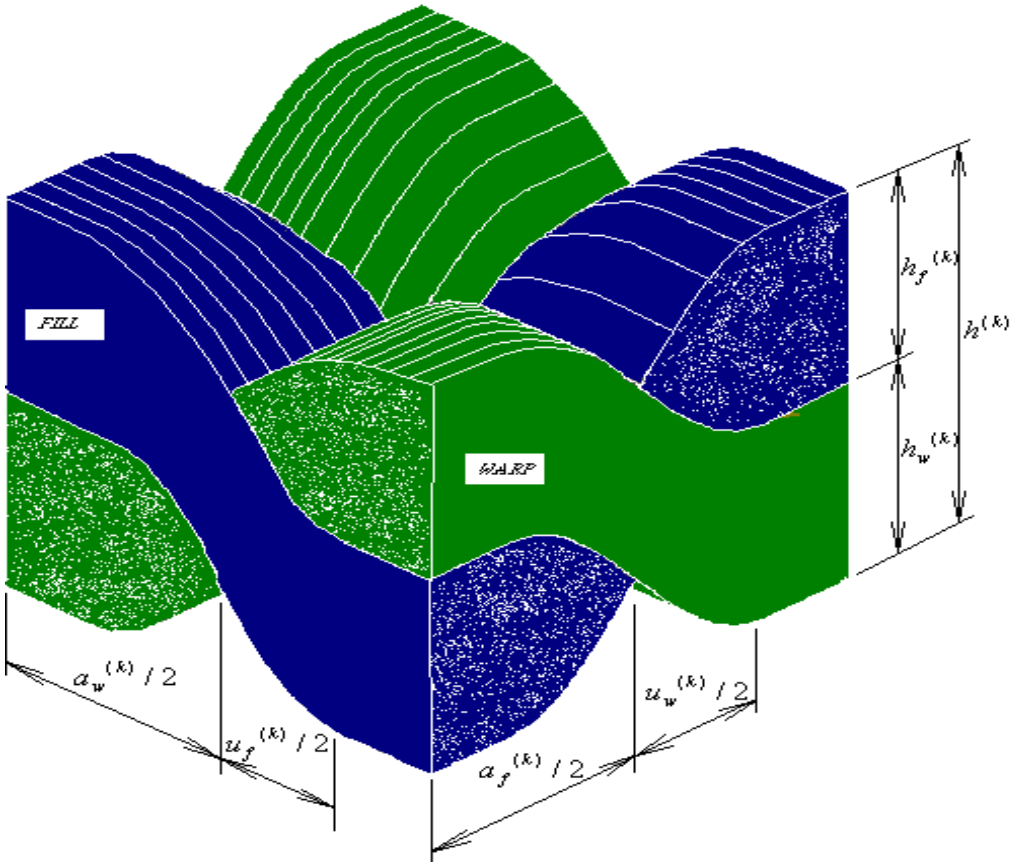

Fig. 1: Unit cell of weave structure and relevant dimensions

Model Details

The weave under consideration was a satin weave where the thickness $h^{(k)}/a_w^{(k)}$ could be varied. It was assumed that the gap between adjacent yarns is so small that it is insignificant. A three-layer laminate configuration (Fig. 2) was assumed and the overall thickness of this laminate was kept constant. The proportionate thickness of each of the component layers was, however, varied. It was assumed that the two outer laminae were identical in terms of thickness and orientation. For the middle layer (here termed layer 1), $h^{(1)}$ was varied while $a_w^{(1)}$ was kept constant. This changed the ratio $h^{(1)}/a_w^{(1)}$, which changed the shape of the weave and hence affected the properties. For the outer layers (each termed layer 2), $h^{(2)}/a_w^{(2)}$ was kept constant as the value of $h^{(2)}$ was varied. The properties of the outer layers thus remained constant and were subject only to variation under off-axis loading.

The properties of the outer layers were kept constant throughout the investigation in order to establish how the weave structure of the middle layer would affect the behaviour of the laminated plate, particularly under bending loads.

Table 1: Constituent material properties

	E_L	E_T	G_{LT}	G_{TT}	ν_{LT}
Glass	71.5	71.5	27.5	27.5	0.29
Carbon	210.0	39.6	24.0	14.3	0.26
Resin	3.5	3.5	1.3	1.3	0.35

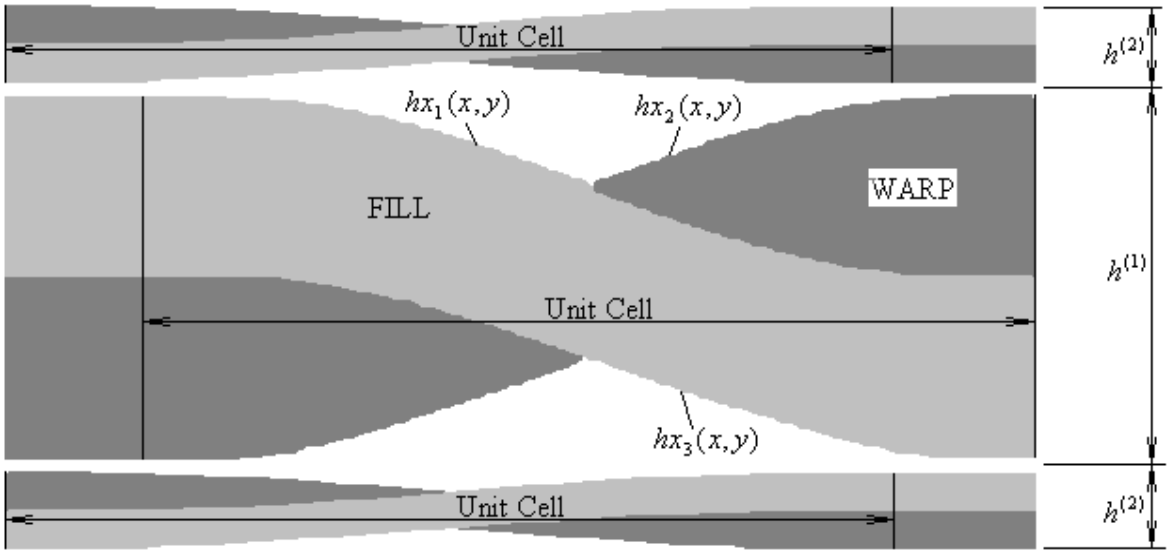

Fig. 2: Stacking of unit cells for determination of stiffness parameters

Stiffness Parameters

Finding the bending resistance of each layer involves finding the elements of the D-matrix. The following relationship from [7] is commonly used to describe the behaviour of a plate where material and geometric nonlinearities are small:

$$\begin{Bmatrix} \{N\} \\ \{M\} \end{Bmatrix} = \begin{bmatrix} [A] & [B] \\ [B] & [D] \end{bmatrix} \begin{Bmatrix} \{\varepsilon^0\} \\ \{\kappa\} \end{Bmatrix} \quad \text{[none]} \tag{1}$$

where [A] gives the in-plane stiffness, [D] the coupling stiffness and [B] gives the coupling terms of the stiffness matrix. $\{N\}, \{\varepsilon^0\}$ are in-plane forces and mid-surface strains respectively and $\{M\}, \{\kappa\}$ are bending moments and curvatures respectively. It shall be shown later that we do not need to find the elements of the [B] matrix. The in-plane stiffness matrix [A] can be found from:

$$\begin{aligned} A^{(k)}(x,y) = {} & Q^M [hx_3{}^{(k)}(x,y) + h_u{}^{(k)} - h_l{}^{(k)} - hx_2{}^{(k)}(x,y)] \\ & + Q^W(x,y)[hx_2{}^{(k)}(x,y) - hx_1{}^{(k)}(x,y)] \\ & + Q^F(x,y)[hx_1{}^{(k)}(x,y) - hx_3{}^{(k)}(x,y)] \end{aligned} \tag{2}$$

and the bending stiffness from:

$$\begin{aligned} D^{(k)}(x,y) = {} & Q^{M}[hx_3{}^{(k)}(x,y)^3 - (h_u{}^{(k)}/2)^3 + (h_l{}^{(k)}/2)^3 + hx_2{}^{(k)}(x,y)^3] \\ & + Q^{W}(x,y)[hx_2{}^{(k)}(x,y)^3 - hx_1{}^{(k)}(x,y)^3] \\ & + Q^{F}(x,y)[hx_1{}^{(k)}(x,y)^3 - hx_3{}^{(k)}(x,y)^3] \end{aligned} \tag{3}$$

where Q^M, $Q^W(x,y)$, $Q^F(x,y)$ are the Q matrices of the *Matrix*, *Fill* and *Warp* yarns respectively; and $h_u{}^{(k)}$ and $h_l{}^{(k)}$ are the upper and lower limits of the lamina, the extreme points of its thickness $h^{(k)}$.

In order to account for the different angular orientation of each layer, the matrices for each are transformed according to the standard orthotropic transformation equations given in [4]. The transformed matrices are simply added together to find the overall matrices for the laminate. It can be shown that if the laminate is symmetrical, the terms of the [*B*] matrix cancel when this addition is made, leaving no coupling between bending and in-plane forces. This simplifies the investigation significantly.

It is assumed, as in [5], that the applied load on the plate at is given by:

$$q = \sum_{m=1}^{\infty}\sum_{n=1}^{\infty} q_{mn} \cos\frac{m\pi x}{a} \sin\frac{n\pi y}{b} \tag{4}$$

A rectangular plate, simply supported at the edges, is the focus of this study. In order to apply simply supported boundary conditions to the plate boundaries shown in Fig. 3, the following expressions apply:
For x = 0,a

$$w = 0,\ M_x = B_{16}\left(\frac{\partial u^0}{\partial y} + \frac{\partial v^0}{\partial x}\right) - D_{11}\frac{\partial^2 w}{\partial x^2} - D_{12}\frac{\partial^2 w}{\partial y^2} = 0 \tag{5}$$

$$u^0 = 0,\ N_{xy} = A_{66}\left(\frac{\partial u^0}{\partial y} + \frac{\partial v^0}{\partial x}\right) - B_{16}\frac{\partial^2 w}{\partial x^2} - B_{26}\frac{\partial^2 w}{\partial y^2} = 0 \tag{6}$$

For y = 0,b

$$w = 0,\ M_y = B_{26}\left(\frac{\partial u^0}{\partial y} + \frac{\partial v^0}{\partial x}\right) - D_{12}\frac{\partial^2 w}{\partial x^2} - D_{22}\frac{\partial^2 w}{\partial y^2} = 0 \tag{7}$$

$$v^0 = 0,\ N_{xy} = 0 \tag{8}$$

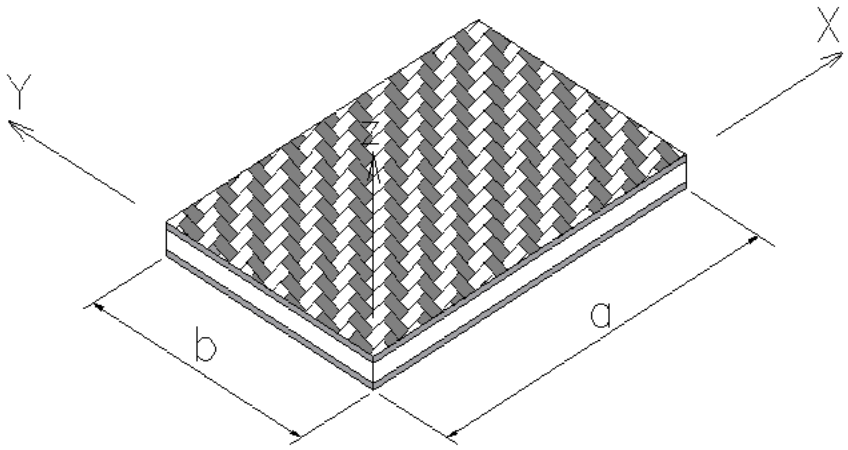

Fig. 3. Laminated plate dimensions

The deflection at each point on the plate is then given by the expression:

$$w(x,y) = \frac{R^4 b^4}{\pi^4} \sum_{m=1}^{\infty} \sum_{n=1}^{\infty} q_{mn} \frac{\sin\dfrac{m\pi x}{a} \sin\dfrac{n\pi y}{b}}{\left[D_{11}m^4 + 2(D_{12} + 2D_{66})m^2 n^2 R^2 + D_{22} n^4 R^4\right]} \tag{9}$$

where the maximum deflection will occur in the centre of the plate for a uniformly distributed load. From [6], it can be seen that m = 1,3,5,..... and n = 1,3,5,..... The series achieves rapid convergence and it in practice m and n were summed to 99, which yields a very small error in the results. The plate is assumed to be square for the purposes of the investigation. This means that the value of the aspect ratio R in equation (8) is 1.

The properties of the each of the layers and the overall plate model as entered for computation by the model are as follows:

- Plain satin weave, $a_w^{(k)} = a_f^{(k)}$
- Undulation, $u^{(k)} / a_w^{(k)} = 0.6$
- Fibre volume content = 0.6
- Size of plate $a / a_w^{(1)} = 100.0$ and $b / b_w^{(1)} = 100.0$.

RESULTS

The maximum deflection for a layer of core material with $h^{(1)} / a_w^{(1)} = 1.0$ and with infinitely thin outer layers is given in Fig. 4a. It can be seen that there is considerable variation in the maximum deflection as the orientation of the plate is altered. The maximum deflection is $w / h = 0.26 \times 10^{-3}$ and occurs when the 0/45/0 laminate is orientated at 90^o to the simple supported boundary of the plate. Note that $h = h^{(1)} + 2h^{(2)}$. The configuration with the lowest variation is the 0/0/0 laminate. The maximum deflection occurs at a load angle of 60^o, which is a feature repeated in later results.

The maximum deflection of a plate with $h^{(1)} / a_w{}^{(1)} = 0.9$ can be seen to be $w/a = 0.17 \times 10^{-3}$ from Fig. 2b. This occurs in the 0/60/0 laminate for an orientation angle of 75^0. The variation in the behaviour of the different configurations is substantially reduced.

Fig. 2c displays an interesting occurrence. All the laminate configurations begin to display a similar pattern for maximum deflection when $h^{(1)} / a_w{}^{(1)} = 0.7$. In almost all cases max. $w/a = 0.14 \times 10^{-3}$ at on orientation angle of 60^o. It is clear from this point on that the middle layer (layer 1) does not influence the behaviour of the laminate significantly when $h^{(1)} / a_w{}^{(1)} \leq 0.7$. Only the magnitude of deflection is affected by the ratio of middle layer thickness to overall thickness.

It is found that under the conditions chosen here, the minimum deflection is achieved when $h^{(1)} / a_w{}^{(1)} = 0.5$. For this case, maximum $w/a = 0.125 \times 10^{-3}$ at an orientation angle between 45^o and 60^o for almost any laminate configuration.

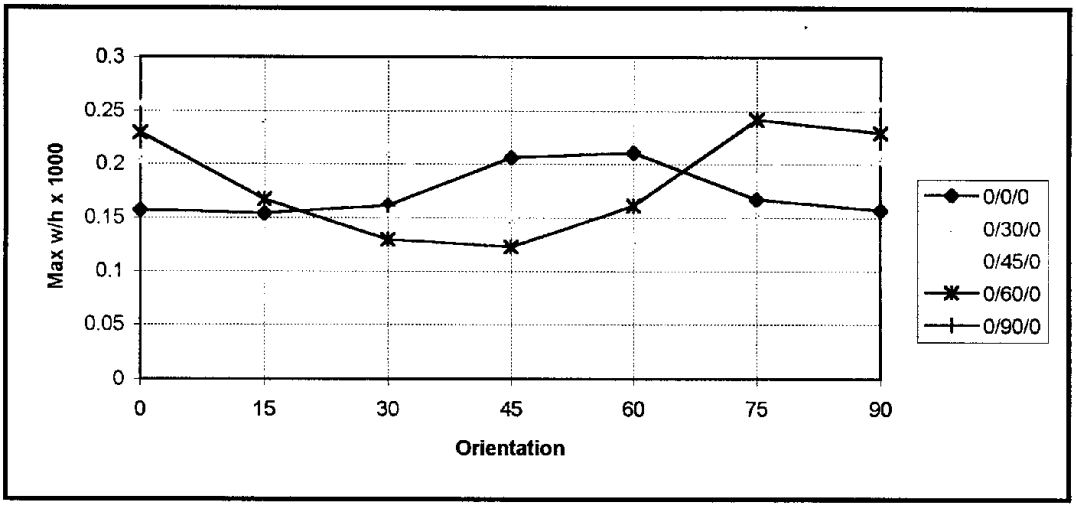

Fig. 4a: Max. $w/h \times 10^3$ for plate with $h^{(1)} / a_w{}^{(1)} = 1.0$

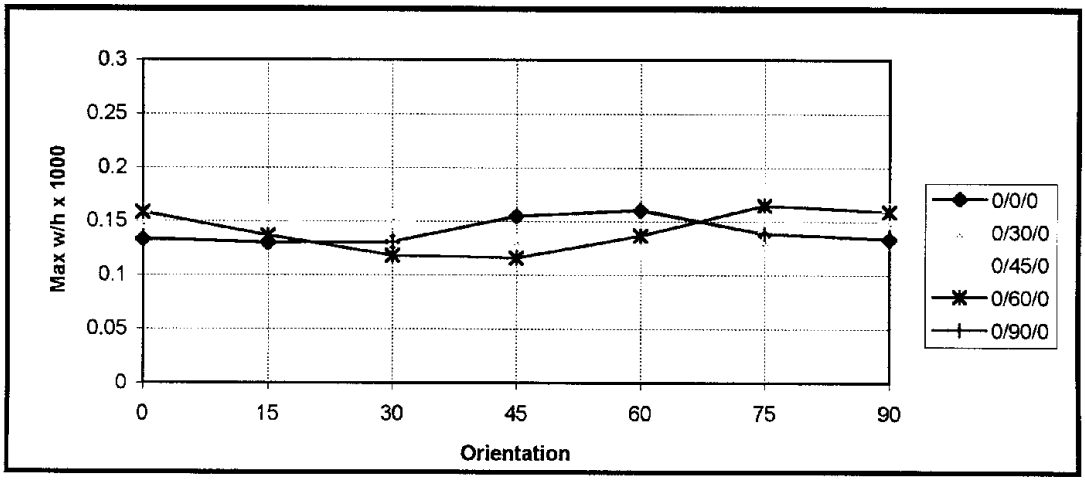

Fig. 4b: Max. $w/h \times 10^3$ for plate with $h^{(1)} / a_w{}^{(1)} = 0.9$

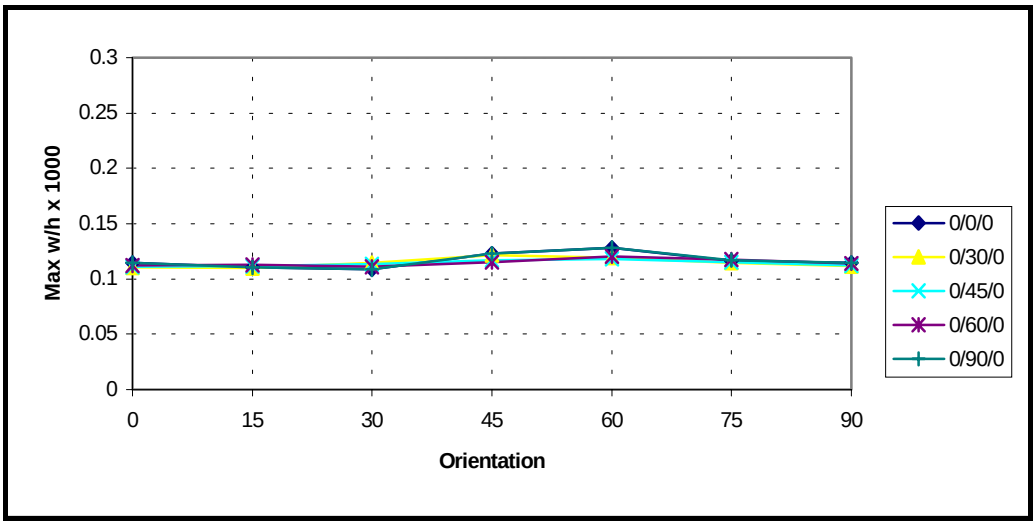

Fig. 4c: Max. $w/h \times 10^3$ *for plate with* $h^{(1)} / a_w^{(1)} = 0.7$

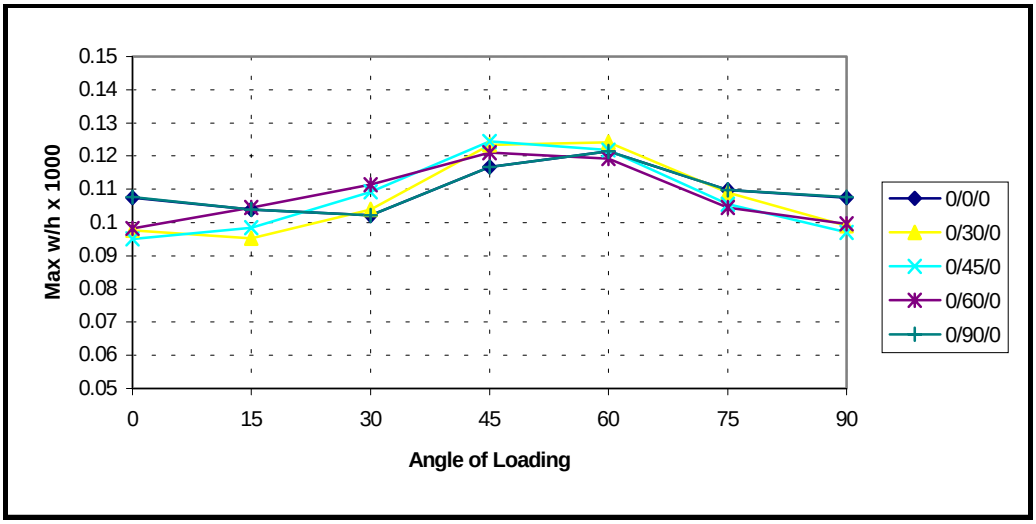

Fig. 4d: Max. $w/h \times 10^3$ *for plate with* $h^{(1)} / a_w^{(1)} = 0.5$

Although it can be seen from equation (9) that only elements of the *D*-matrix influence the calculated deflection under the current method, it is still possible to explain deflections in terms of in-plane stiffness' (which are properties of the A-matrix). This is because it can be seen from equations (2) and (3) that the *A* and *D* matrices are very closely related. A high value in the *A*-matrix will usually mean a high value in the corresponding D-matrix.

There is also a dependency of the terms of the D-matrix on the value of the h-parameters. These effectively position the laminate. It is therefore possible to see how in-plane stiffness terms can indirectly affect the deflection of the lamina.

Fig. 5a shows the effect of orientation on the in-plane properties of the middle lamina, layer 1. It can be seen that there is clear orthotropic behaviour, with the lowest stiffness achieved at an orientation angle of 45^0. As the ratio h^1 / a_w^1 is increased, the change in shape of the weave structure causes the in-plane stiffness to drop.

Fig. 5b also shows clear orthotropic behaviour with the Bulk modulus having its highest value at an orientation of 45^0. It can be seen that the value drops as the ratio h^1 / a_w^1 is increased in the same way as Fig. 5a.

Figs. 5a and 5b show a clear drop in in-plane stiffness parameters as the thickness of the middle layer is increased. The drop is attributable to increasing fibre undulation, which causes the load direction to occur along a line which is not optimal for the fibre stiffness. It should also be noted that due to the orthotropic nature of the material, the lowest stiffness occurs at an orientation angle of 45^0. However, the stiffness at a load angle of 60^0 is not much greater. This phenomenon can explain why the greatest deflection for the various plates occurred at an orientation angle of between 45^0 and 60^0.

The two outer laminae (Layers 2) only show change in material properties with orientation. This is because the thickness ratio of the unit cell, $h^{(2)} / a_w^{(2)}$ is fixed, as described earlier. The behaviour of the X and Y direction Young's moduli are shown in Fig. 5c. Again the lowest Young's modulus occurs at an orientation angle of between 45^0 and 60^0 for E_x.

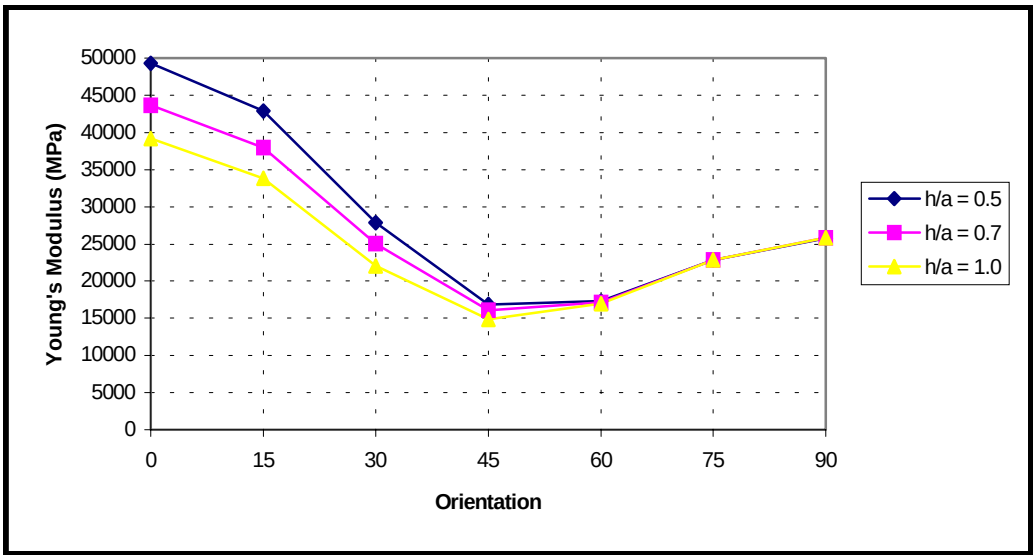

Fig. 5a: Young's modulus vs. orientation for Layer 1

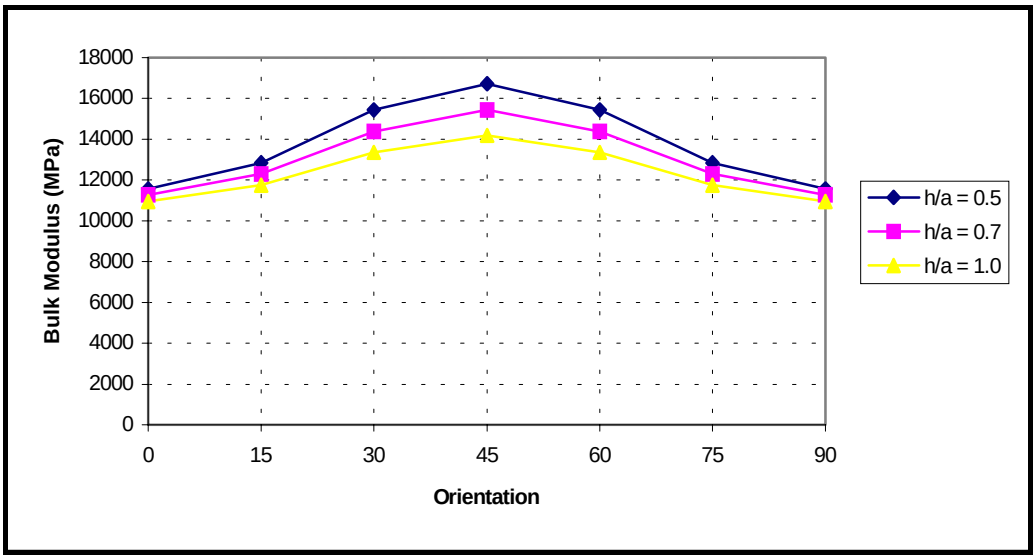

Fig. 5b: Bulk modulus vs. orientation for Layer 1

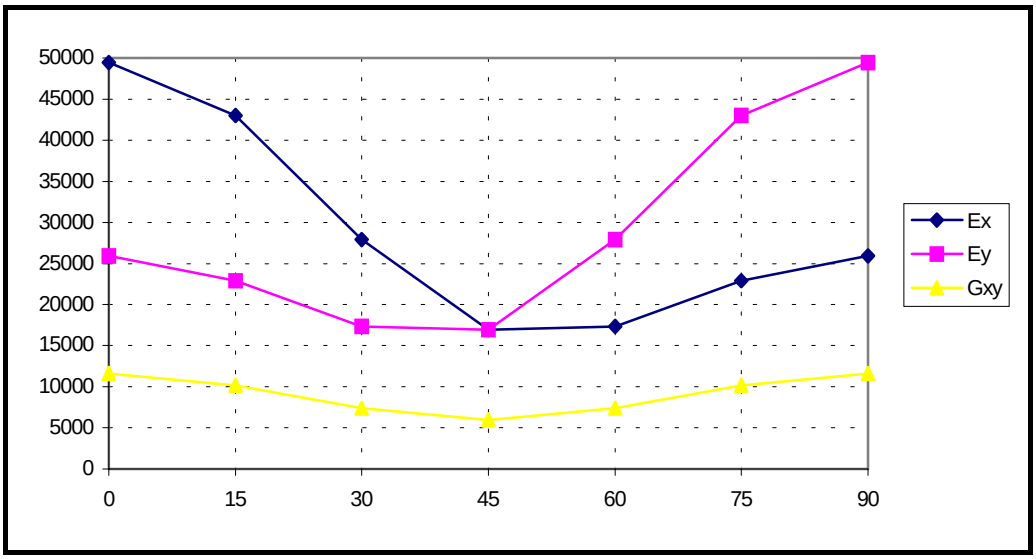

Fig. 5c: In-plane properties for Layer 2

CONCLUSIONS

The best resistance to bending is achieved when the thickness of the middle layer, $h^{(1)} / a_w{}^{(1)} = 0.5$. The orientation of the middle layer did not have much influence at this thickness ratio. In-plane stiffness of the laminae has a large influence on the bending stiffness of the laminate. Maximum deflection typically occurs for the laminates considered at an orientation angle of between 45^0 and 60^0, depending on the lay-up sequence and thickness.

REFERENCES

1. Naik K, “Woven Fabric Composites”, Technomic Publishing, 1994.

2. Shembekar P.S., Naik K., “Elastic Analysis of Woven Fabric Laminates: Part 1. Off-axis Loading”, Journal of Composites Technology and Research, Vol. 15, No. 1, 1993.

3. Stewart R.W., Verijenko V.E., Adali S, “Analysis of In-Plane Properties of Hybrid Glass-Carbon Woven Fabric Composites”, Proceedings of 1st International Conference on Composite Science and Technology, pp509-514, 1996.

4. Jones R.M., “Mechanics of Composite Materials”, McGraw-Hill, 1975.

5. Whitney J.M., “Structural Analysis of Laminated Anisotropic Plates”, Technomic, pp177-185, 1987.

6. Vasiliev V.V., Jones R.M., “Mechanics of Composite Structures”, Taylor and Francis, pp 281-284, 1993.

7. Pedersen, Pauli, “Mechanical Behaviour of Composites and Laminates”, Elsevier Applied Science, 1987.

DEVELOPMENTS IN MULTIAXIAL WEAVING FOR ADVANCED COMPOSITE MATERIALS

J.I. Curiskis[1], A. Durie[2], A Nicolaidis[3] and I. Herszberg[4]

[1] Department of Textile Technology, University of New South Wales, Sydney 2052, New South Wales, Australia.
[2] Department of Aviation and Technology, University of Newcastle, University Drive, Callaghan 2308, New South Wales, Australia
[3] Department of Fashion and Textile Design, Royal Melbourne Institute of Technology, City Campus, GPO Box 2476V, Melbourne 3001, Victoria, Australia.
[4] Sir Lawrence Wackett Centre for Aerospace Design Technology, Royal Melbourne Institute of Technology, GPO Box 2476V, Melbourne 3001, Victoria, Australia.
This work has been carried out as part of a CRC-ACS research program.

SUMMARY: There is an increasing demand within the composites industry for integrally-manufactured three-dimensional preform structures. Using and extending the basic principles of conventional weaving processes has allowed a wide range of such structures to be developed, as briefly summarised in this paper. Such integrally-woven preforms, however, lack reinforcing fibre in the bias directions (eg. $\pm$45°) intermediate between the warp and weft. A detailed review of recent developments to overcome this limitation is presented in this paper, together with the type of integrally-woven multiaxial structure (eg. 5-axis) achievable. Although the details of implementation differ, these multiaxial weaving developments utilise the principles of lappet weaving, triaxial weaving, and cross-laying.

KEYWORDS: multiaxial, weaving, lappet, triaxial, cross-laying, bias, three-dimensional.

INTRODUCTION

The use of textile technology in the manufacture of preforms for advanced composite materials has and continues to be under intense investigation due to the potential of these processes, together with resin infusion techniques such as resin transfer moulding (RTM), to produce low-cost high-quality structures with improved mechanical performance. Perhaps foremost among these textile processes is weaving technology.

Using the basic principles of conventional weaving processes, as discussed below, a wide range of integrally-woven preform structures have been developed for the composites industry. Such structures, however, are generally limited to at most three directions of fibre reinforcement, viz. the orthogonal directions of warp, weft and through-thickness (binder) yarns. Inclusion of fibre reinforcement in the in-plane "bias" direction (eg. $\pm$45°) still requires formation of a laminate structure. This restriction has led to interest in the use of multiaxial weft-inserted warp-knitted/stitch-bonded structures which can be manufactured on appropriate commercially available machinery. Such structures, however, suffer from limitations as regards potential channelling in the fibre architecture and the use of thermoplastic knitting threads to provide through-thickness reinforcement, as well as limited versatility for three-dimensional shaping during preform manufacture.

Recent years, however, have witnessed new developments in multiaxial weaving to overcome the above limitations. These developments are reviewed in this paper. Included in this is a brief outline of two special weaving techniques in which bias yarns can be introduced intermediate between the warp and weft directions in a woven fabric.

CONVENTIONAL WEAVING PROCESSES

Weaving is perhaps the oldest fabric-forming technology, with a rich history of technological development both in terms of machinery and fabric structures. It is essentially the action of producing a fabric by the interlacing of two sets of yarns (warp and weft) as schematically illustrated in Figure 1. The warp yarns run in the machine direction and are provided in a parallel sheet array, either from one or more warp beams or from individual warp yarn packages located in a frame known as a creel. The weft yarns run in the cross-machine direction and are typically introduced singly or in looped double-pick form. Weaving is characterised by three primary motions:

1. shedding - the separation of the warp sheet into an upper and lower layer, thereby creating a tunnel known as the shed;
2. picking - the insertion of the weft yarn (pick) into the shed;
3. beating-up - the consolidation of the inserted weft yarn into the edge of the fabric (known as the cloth fell).

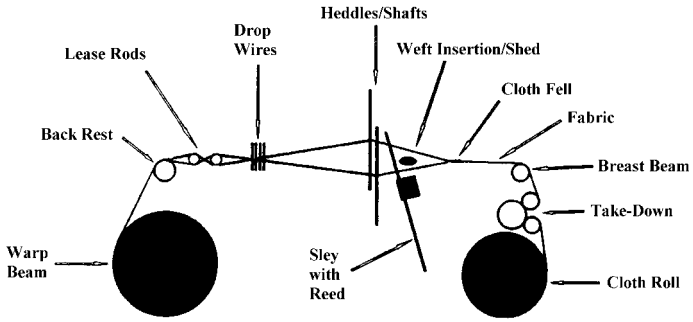

Fig. 1: Principles of conventional weaving

Secondary motions required for power weaving are warp let-off and cloth take-up. The former is the release of the warp yarn from its supply as weaving progresses, and the latter is the withdrawal of the fabric from the weaving zone as it is produced and its subsequent storage (eg. on a cloth roll). Additional auxiliary motions are associated with the continuity (and selection) of the weft yarn supply and the provision of various stop motions in the event of yarn breakage or other malfunctions; in the case of shuttleless weaving, selvedge forming devices are also required. Ideally, both yarn sets are under controlled tension regimes during the weaving cycle. Fundamental to the conventional weaving process is the use of heddles to effect shedding for individual warp yarns and of the reed to achieve beating-up; heddles are essentially (vertical) wires with an eye in the centre through which a warp yarn is threaded, while the reed is a comb-type device across the width of the machine - further, both devices maintain the lateral position of the warp yarns in the sheet array. Various mechanisms have been developed to implement and extend these motions and texts are available for the interested reader [eg. 1]. From these basic principles, an amazing array of woven fabric structures have been developed to satisfy various aesthetic and functional requirements for apparel, furnishing, and technical/industrial end-uses [eg. 2].

Extension to Textile Composite Preforms

Simple woven structures (eg. satin weaves) found early application as preforms in laminate structures. The poor impact performance and delamination resistance of such structures has

led to the use of stitching techniques borrowed from clothing technology; in addition, the weave crimp is often considered to reduce the mechanical efficiency of the reinforcing fibres. The development of multilayer plate structures is a natural progression well within the scope of conventional weaving - indeed, they form the compound weave category of woven structures. Typical examples of such 3D woven fabrics are the simple angle interlock, warp interlock and orthogonal structures, which utilise binder warp and/or weft to provide through-thickness reinforcement and structural integrity to (ideally) straight warp and/or weft primary load-bearing yarns. In the patent literature there are various other plate-type structures developed for moulding into curved 3D surfaces [eg. 3] and for stiffened panels, including beams with various cross-sections [eg. 4]. In addition, the technique of face-to-face weaving, traditionally employed in the manufacture of cut-pile woven carpets, can be used to manufacture sandwich structures in which the "pile" yarn traverses between the two "backing" fabrics [eg. 5]. Further, this basic technique has been extended to manufacture core-type structures in which fabric "ribs" join the two surface layers [eg. 6]. Finally, the technique of contour or shape weaving has been utilised to weave 3D shell-type structures [eg. 7].

While recognisable weaving developments such as the above have been reported, other developments yielding structures sometimes referred to as 3D nonwoven orthogonal fabrics have also been undertaken [eg. 8]. Where the three primary motions of weaving are recognisable, such processes are in fact weaving developments. A typical example is the use of binder warp to provide structural integrity in an otherwise non-interlaced orthogonal array forming composite beams of various cross-sectional shapes [eg. 9].

MULTIAXIAL WEAVING PROCESSES

The inclusion of bias yarns at an angle (eg. $\pm$45°) intermediate between the warp and weft directions for the development of multiaxial multilayer integrally woven preforms (eg. 5-axis 3D structures) requires that the constraints imposed by the heddles and reeds in conventional weaving be overcome. Before proceeding to such preform developments, it is instructive to first consider two special weaving techniques in which the same problems were encountered.

Lappet Weaving

Lappet weaving is a special technique in which extra warp threads are introduced traditionally to develop isolated design motifs on an open weave background [2]. Figure 2 illustrates the principles of the technique, which requires the use of a lappet (or needle) bar (D) positioned between the reed (V) and the cloth fell (A). The extra warp yarns (W) are threaded through the eyes of the needles of the lappet bar and do not pass through the reed; the extra warp is usually supplied from a separate warp beam to the normal warp (X), which is controlled by heddles (Y) in the usual way. The lappet bar has two directions of movement: a lateral (shogging) movement in the weft direction, thereby controlling the angular position of the extra warp yarns with respect to the principal directions of the fabric; and a vertical movement which allows the lappet bars to form a shed for weft insertion and to be clear of the reed during beat-up - the lappet bar can be considered similar to a guide bar in warp knitting. In principle, a standard weaving loom can be modified to incorporate the lappet system.

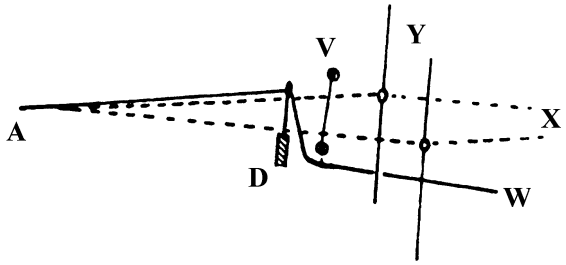

Fig. 2: Principles of lappet weaving

Clearly, lappet weaving has potential to manufacture integrally-woven multiaxial multilayer preform structures for composite materials. The extra warp yarns can be made to run at virtually any angle between (and including) the warp and weft directions, and can therefore be considered as bias yarns. These bias yarns are interlaced with the weft but held in position by the adjacent pair of normal warp yarns, and float on one surface of the fabric between successive weft interlacing points. Further, the bias yarns can be interlaced with weft yarns at any position within a multilayer structure, with the two extremes corresponding to the weft yarns at the same or opposite fabric surface; the latter would provide through-thickness reinforcement using bias yarns. However, such structures would have two main limitations: the location of the bias yarns would be limited to the outer surfaces of the preform structure; at some stage the lappet bars must reverse the direction of their shogging movement, thus limiting the extent to which an individual bias yarn can traverse the fabric width. The latter limitation, however, can be overcome with modification of the lappet system.

Triaxial Weaving

Triaxial weaving is another special weaving technique in which two sets of warp yarns and one set of weft yarns are interlaced in such a way that the three sets of threads form a multitude of triangles. Figure 3(a) illustrates a simple triaxial weave in which equilateral triangles can be seen as well as reversal of the (bias) warp yarns at the fabric selvedges. The latter ensures the continuity of an individual warp yarn across the full width of the fabric. Further, it clearly indicates that an individual warp yarn during one traverse (left-to-right, say) will be a member of one set of warp yarns but on the return traverse (right-to-left) will be a member of the opposite set of warp yarns.

The first specific patent of which the authors are aware was published in 1921 [10]. However, Mooney [11], in an excellent review of triaxial structures and manufacturing techniques, traces the history to the early 19th century. Interest in triaxial weaving was renewed in the 1960s due to its potential to manufacture stable fabric structures with excellent burst and tear resistance and with near-isotropic in-plane mechanical performance. Indeed, the 1960s and 1970s was a period of intense activity in which many patents describing structures and manufacturing techniques appeared [eg.

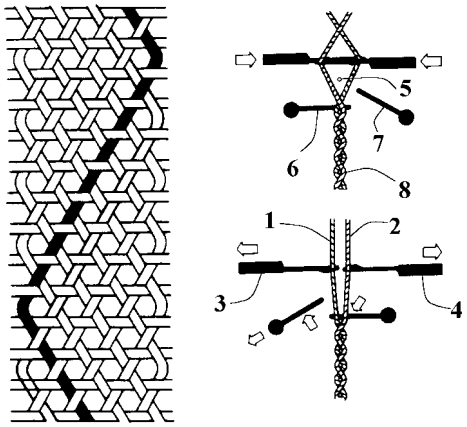

(a) Weave (b) Primary motions
Fig. 3: Principles of triaxial weaving

12,13] as well as various research papers describing mechanical properties [eg. 14]. The following summarises the basic features required in the triaxial weaving process, and as exemplified in the Barber-Colman TW-2000 triaxial loom [15].

In order to achieve transverse positioning of the two opposing sets of warp yarns (1,2 in Figure 3(b)), including yarn transfer at the fabric selvedges, special heddles (3,4) circulating around a racetrack-type circuit [10,12] are used. These heddles are also used to form a shed for weft (5) insertion via a rigid rapier. The warp yarns are supplied on beams or individual yarn packages mounted on a rotating carousel [16]; alternate approaches are to use a warp beam in which the yarns form a flattened spirally wrapped sleeve [17] or to maintain the warp supply stationary and to rotate the machine. Beat-up is usually achieved through the use of two open reeds (6,7) working sequentially, with the fabric (8) formed in the same plane as the warp sheet. One reed maintains the position at the cloth fell of the traversing warp sets for the previous pick, while the second reed beats-up the newly inserted pick; the first reed is withdrawn immediately before the second reed reaches the cloth fell. On the next pick, the two open reeds reverse roles.

The potential of triaxial fabric structures for composite materials has been recognised with respect to their in-plane mechanical performance [18], conformability to curved surfaces [19], and a recent machine development for composite applications in shell-type structures [20]. It is clear from Figure 3 that inclusion of axial warp yarns as a third warp set in the basic triaxial process has some potential for the development of multilayer triaxial fabrics. However, modifying the conventional triaxial weaving process to incorporate such yarns would be a major engineering task. Rather, modifying the yarn guides to operate in a lappet weaving mode would be a simpler task - one which would overcome the second limitation of a traditional lappet weaving system as described in the previous section.

Multiaxial Developments for Textile Composite Preforms

The patent by Ruzand and Guenot [21] is the first patent to indicate how a standard loom can be modified for multiaxial weaving. Figure 4(a) illustrates the type of structure that can be obtained. The bias yarns (3a,3b) run across the full width of the fabric in two opposing layers on the top and back surfaces of the fabric, although they can be inserted on one surface only if desired. The bias yarns are held in position by selected weft yarns (2) interlaced with warp binding yarns (1) on the two surfaces of the structure. The intermediate layers between the two surfaces are composed of other warp (1) and weft (2) yarns which may be interlaced (as illustrated) or not.

The basis of the technique is an extension of lappet weaving in which pairs of lappet bars (6a and 6b, 6c and 6d) are utilised on one or both sides of the fabric, as schematically illustrated in Figure 4(b). The lappet bars are segmented and of a length greater than the fabric width by one segment length. Each pair of lappet bars move in opposite directions, with no reversal in the motion of a segment until it fully extends past the opposite fabric selvedge. When the latter situation is reached, the segment is detached from the lappet bar, its yarns gripped between the selvedge and the guides and cut near the selvedge. The detached segment is then transferred to the opposite side of the fabric where it is reattached to the lappet bar and its yarns subsequently connected to that fabric selvedge. Since a rapier is used for weft insertion, the bias yarns can be consolidated into the selvedge by an appropriate selvedge-forming device employed for shuttleless weaving. The bias warp supply for each lappet bar segment

must be independent of all other segments and not interfere with the yarns from other segments.

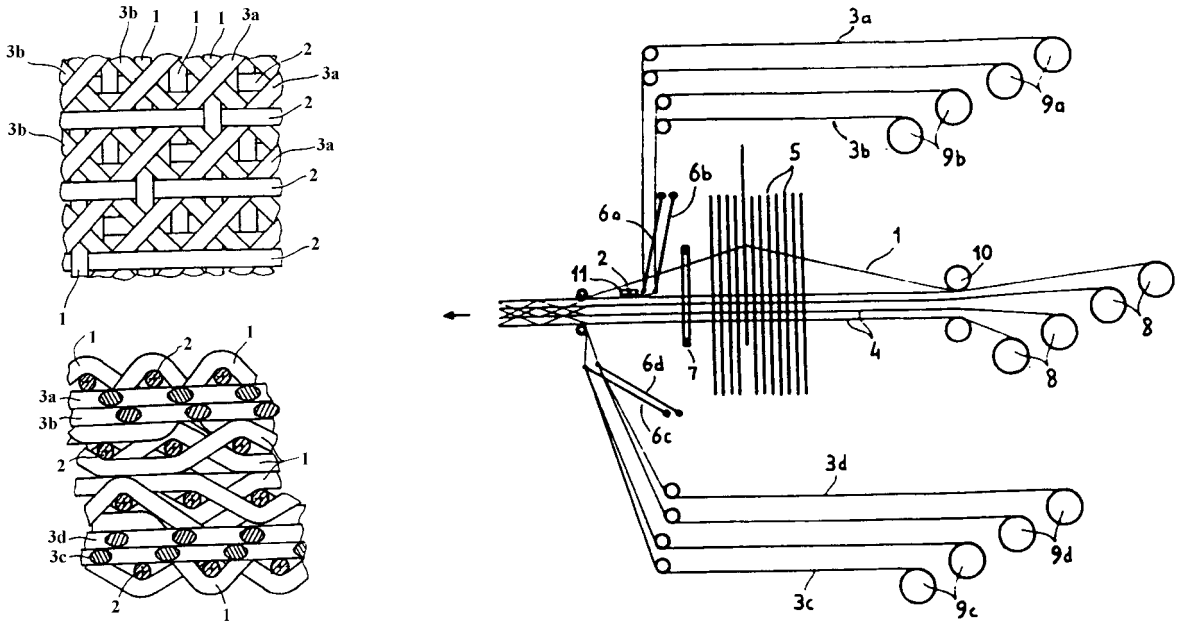

(a) Example weave *(b) Schematic illustration of loom cross-section*

Fig. 4: Multiaxial weaving development by Ruzand and Guenot [21]

Another approach utilising lappet weaving principles has been described by Farley [22]; Figure 5 shows relevant aspects of his invention. In this case the lappet bars comprise slotted needles (34) positioned in transversely moveable needle holders (20) mounted on racks (22) placed in an assembly (18) which is positioned in front of a shedding mechanism (16); the latter controls the normal warp (14) which is drawn from warp beams or a creel supply (12). The bias yarns (24) are positioned in the slotted eyes (36) of the needles, with the yarn supply (eg. individual spools) attached to the needle holders; there is a plurality of such needle holders on any rack. The needle holders, and thus bias yarns, are moved transversely (F1) across the fabric width. At desired transverse positions, the needles are moved vertically to form a shed into which the weft yarn (38) is inserted by a special rapier (26) which also achieves beat-up through an attached inflatable membrane, thus negating the need for a reed. At the end of the traverse, a needle holder assembly is removed from its rack and repositioned at the opposite side (start) of the rack. The protruding ends of the bias yarns can be woven into the fabric selvedge or attached to a suitable clamping system moving parallel to the selvedge. According to the patent, a rack can be split into two halves so that each half can be separately withdrawn to opposite sides of the fabric to facilitate the weaving of complex preform structures, such as stiffened panels, without disrupting the continuity of the bias yarns. Examples of such preform structures, however, are not given, although it should be noted that the positioning of the lappet system together with bias yarn supply on racks permits the inclusion of bias yarn layers at any vertical position in the through-thickness direction.

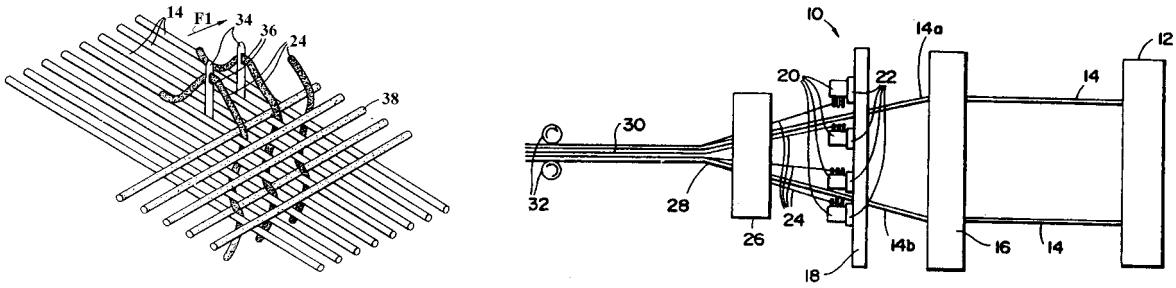

(a) Lappet weaving principles. *(b) Schematic illustration of loom cross-section*

Fig. 5: Multiaxial weaving development by Farley [22].

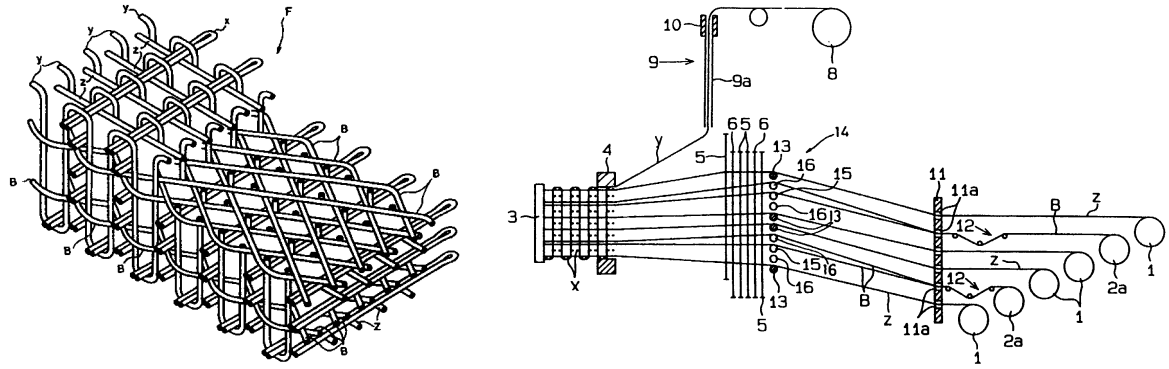

(a) Example weave Indexing screw-shaft system

(b) Schematic illustration of loom cross-section.

Fig. 6: Multiaxial weaving development by Anahara et al [23]

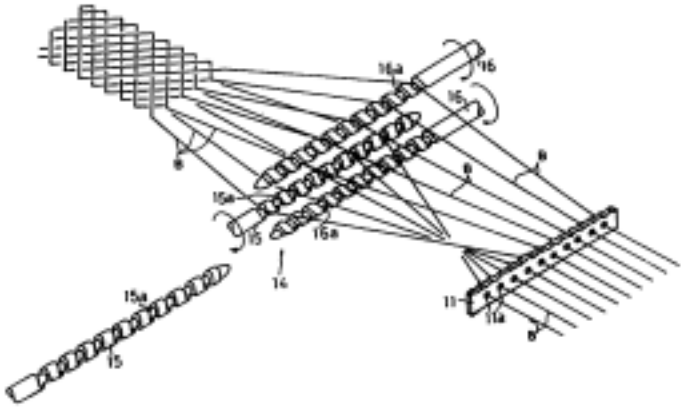

A multiaxial multilayer structure together with the manufacturing principles described by Anahara et al [23] is illustrated in Figure 6. The normal warp (z), bias (B) and weft (x) yarns are held in place by vertical binder yarns (y). The weft yarns are inserted as double picks using a rapier needle (not shown) which also performs beat-up. Weft insertion requires the normal warp and bias yarn layers to form a shed via shafts (5,6) which do not use heddles but rather have horizontal guide rods to maintain the vertical separation of these yarn layers. The binder yarns are introduced simultaneously across the fabric width by a vertical guide bar assembly (10) comprising a number of pipes with each pipe controlling one binder yarn. The bias yarns are continuous throughout the fabric length and traverse the fabric width from one selvedge to the other in a cross-laid/folded structure, as shown in Figure 6(a). Lateral positioning and cross-laying of the bias yarns is achieved through use of an indexing screw-shaft system (15,16), shown in Figure 6(c). As the bias yarns are folded downwards at the end of their traverse, there is no need to rotate the bias yarn supply as in triaxial weaving. Consequently, the bias yarns can be supplied on conventional warp beams (2a) or from a warp creel, but they

must be appropriately tensioned (12) due to path length differences at any instant of weaving, although total yarn consumption will be equal for all bias yarns within a folded structure. It should be noted, however, that the folded structure of the bias yarns results in each layer having triangular sections which alternate in the direction of the bias angle about the normal warp direction due to bias yarn interchange between adjacent layers.

In total, Anahara's patent describes eight variations, in which the fabric structure achieved is the main emphasis. However, two of these variations also describe an alternate approach based on triaxial weaving principles. The bias yarns are threaded through individual guide blocks which are controlled by a special shaft to circulate in one direction around a rectangular path. Clearly, this also requires rotation of the bias yarn supply.

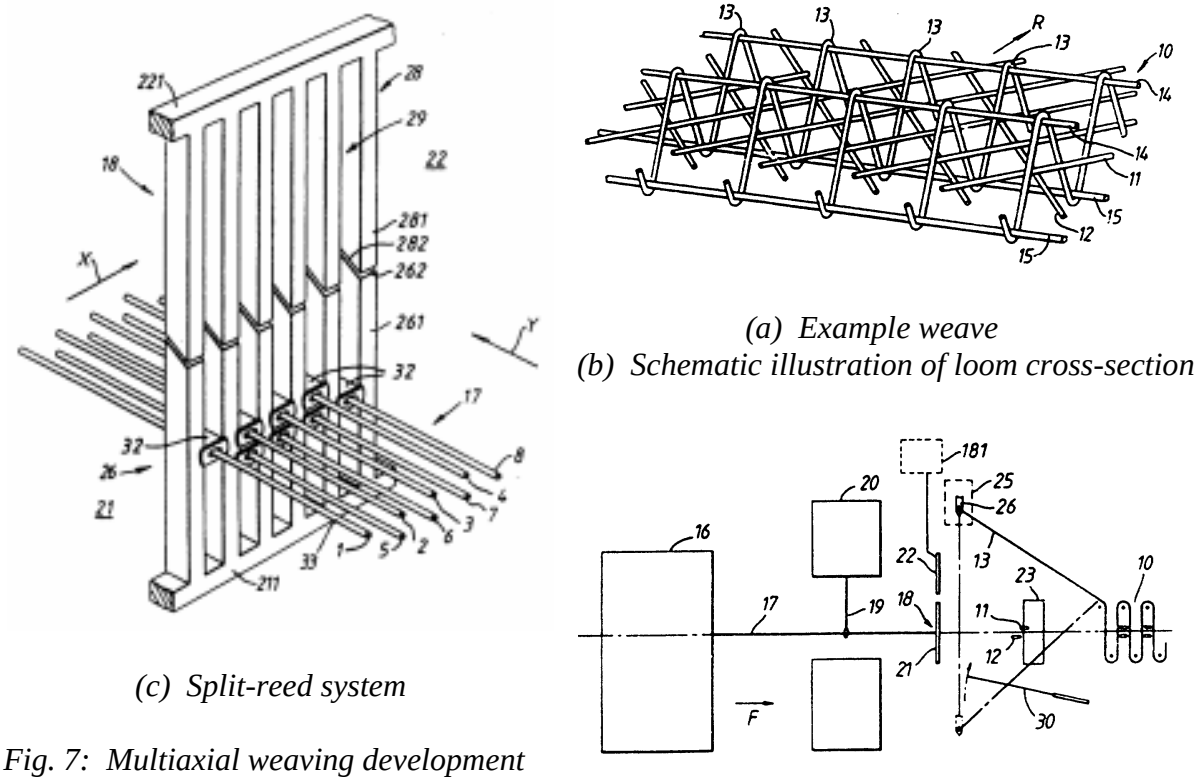

(a) Example weave
(b) Schematic illustration of loom cross-section
(c) Split-reed system

Fig. 7: Multiaxial weaving development by Addis [25]

Another approach is presented by Mood and Mahboubian-Jones [24] and extended by Addis [25]. While there are differences in detail, the prime features in these patents for control of the bias yarns are the use of special split-reeds together and a jacquard shedding mechanism with special heddles. Figure 7 illustrates the system developed by Addis together with an example of the type of structure that can be produced; the latter comprises bias yarns (11,12) sandwiched between weft yarns (14,15) with structural integrity provided by warp binding (13). A creel (16) supplies bias warp yarns in a sheet (17) to the special heddles (19) connected to the jacquard head (20). The bias yarns then pass through the split-reed system (18) which includes an open upper reed (22) and an open lower reed (21) together with guides (32) positioned in the reed dents. The lower reed is fixed while the upper reed can be moved in the weft direction. The jacquard head is used to position selected bias yarns in the dents of the upper reed so that they can be shifted transverse to the normal warp direction; it should be noted that correct positioning of the bias yarns requires a series of such lifts and transverse displacements and must ensure that there is no entanglement of the warp. A shed is formed

by the warp binding yarn (13) via a needle bar system (25) and the weft is inserted at the weft insertion station (23), with beat-up performed by another open reed (30).

The earlier patent [24] utilised two split-reed systems, positioned on either side of the jacquard head, and required the bias yarns to be detachably engaged by the special heddles (eg. latch needles) for selective raising and lowering of yarn. Normal warp yarns were also controlled by the jacquard head and beat-up could be performed by the open lower reed of the split-reed system. It would appear that the yarn guides (32) in the later system were introduced to overcome problems of yarn abrasion and other failures. Nevertheless, the basic approach described in these two patents appears to have potential for the manufacture of unique structures, due to the use of the jacquard head, but clearly requires further exploration. However, as the warp supply is not rotated, reversal in the direction of the bias yarns must be governed by "cross-laying/folding" considerations which are not discussed in the patents.

A multiaxial multilayer nonwoven (non-interlacing) development has also been described in a second patent by Anahara et al [26]. The aim is to ensure that such structures are symmetrical about an imaginary central plane. The various layers are assembled from individual yarns laid around perpendicular pins in a frame. The pins are subsequently replaced by vertical binding yarn in a stitching action.

CONCLUDING REMARKS

The textile industry has a rich history of innovation and invention to meet consumer demands and increase productivity through automation of fibre/yarn manipulation processes - indeed, the development of a Dutch 12-piece ribbon loom in 1604 was, according to Karl Marx, the harbinger of the Industrial Revolution. The composites industry is one consumer of growing importance to the textile industry. The need for integrally-woven three-dimensional preform structures for advanced composites has seen many developments in recent years extending conventional weaving processes, as briefly summarised in the early part of this paper. The increasing demand for integrally-woven multiaxial structures (eg. 5-axis reinforcement), in which bias yarns complement the orthogonal directions of warp, weft and through-thickness binder reinforcement, has been the main focus of this paper. Developments in this area were reviewed in detail, together with the special techniques of lappet weaving and triaxial weaving. It is clear that lappet weaving principles have been incorporated in two of these developments [21,22] while a third patent [23] has offered a number of variations based on triaxial weaving principles and cross-laying principles. The fourth development [24,25] would appear to have potential for the manufacture of unique structures through the use of a jacquard shedding mechanism but this requires further exploration as cross-laying is implicit for bias yarn traverse across the full width of the fabric. The fifth development [26] is not a weaving technique but combines the assembly of non-interlaced yarn layers with subsequent binding via stitching. The authors are currently considering the feasibility of alternate weaving developments to the above and will report the principles of these in the near future.

REFERENCES

1. Marks R. and Robinson A.T.C., “Principles of Weaving”, Textile Institute, Manchester, 1976.

2. Grosicki Z.J., “Watson’s Textile Design and Colour”, Newnes-Butterworth, London, 1975.

3. Rouhling J.A., “Deformable Fabric for composite materials”, European Patent 0-439-274-A1, 31 July 1991, Scapa Group PLC.

4. Muller J., Zulliger A. and Dorn M., “Economic production of composite beams with 3D fabric tapes”, Textile Month, Sept 1994, 9-13.

5. Bompard B. and Lamarie J-P., “Laminated material reinforced by a multi-dimensional textile structure and method for producing the same”, US Patent 5,021,281, 4 June 1991, Brochier S.A.

6. Sawko P.M., Calimito D.P. and Jong A., “Flexible ceramic thermal protection system resistant to high aeroacoustic noise comprising a three-dimensional woven-fiber structure having a multilayer top fabric layer and an intermediate rib fabric layer”, US Patent 5,451,448, 19 Sept 1995, NASA.

7. Busgen A., “Shape weaving - new invention for producing 3D-shaped woven shells”, Technische Textilien/Technical Textiles, vol.38, Sept 1995, 129-132 (E28-E29).

8. Khokar N., “An experimental uniaxial noobing device: working principle and important features”, *Proc 77th Annual World Conference of the Textile Institute*, Niches in the World of Textiles, Tampere, Finland, 21-24 May 1996, vol.2, 303-304.

9. Mohamed M.H. and Zhang Z-H., “Method for forming variable cross-sectional shaped three dimensional fabric”, US Patent 5,085,252, 4 Feb 1992, NCSU.

10. Stewart F.H., “Woven fabric”, US Patent 1,368,215, 8 Feb 1921.

11. Mooney D.R., “Triaxial weaves and weaving: an exploration for hand weavers”, Ars Textrina, vol.2, 1984, 9-68.

12. Kulczycki K. and Burns D., “Triaxial weaving machine with heddle transfer and method”, US Patent 4,013,103, 22 March 1977, Barber-Colman Co.

13. Dow N.F., “Triaxially woven fabrics of uniform compliancy and porosity”, US Patent 3,874,422, 1 April 1975, N.F. Doweave Inc.

14. Schwartz P., “Complex triaxial fabrics - cover, flexural rigidity, and tear strength”, Textile Res. J., vol.54, 1984, 581-584.

15. Trost W.C., “The triaxial weaving machine”, Canadian Textile Journal, July 1977, 55-59.

16. Helton M., Dow F., Dow R.M. and Hillebrand M.J., “Triaxial fabric forming machine and components therefor”, US Patent 4,015,637, 5 April 1977, N.F. Doweave Inc.

17. Dow N.F., “Warp beam for triaxial weaving”, US Patent 3,884,429, 20 May 1975, N.F. Doweave Inc.

18. Fujita A., Hamada H. and Maekawa Z., “Tensile properties of carbon fiber triaxial woven fabric composites”, J. Comp. Mat., vol.27, no.15, 1993, 1428-1442.

19. Trost W.C., “Triaxial fabric”, US Patent 4,438,173, 20 March 1984, Barber-Colman Co.

20. Fukuta K., Hatta H., Hiroshima N., Murayama K. and Sugano T., “Triaxial fabric of interlaced oblique yarns”, US Patent 5,070,914, 10 Dec 1991, Mitsubishi Denki Kabushiki Kaisha, and Agency of Industrial Science and Technology.

21. Ruzand J-M. and Guenot G., “Multiaxial three-dimensional fabric and process for its manufacture”, International Patent WO 94/20658, 15 Sept 1994, Etablissements Cotton Freres et Cie.

22. Farley G.L., “Method and apparatus for weaving a woven angle ply fabric”, US Patent 5,224,519, 6 July 1993, NASA.

23. Anahara M., Yasui Y. and Omori H., “Three-dimensional textile and method of producing the same”, European Patent 0-426-878-A1, 15 May 1991, Kabushiki Kaisha Toyoda Jidoshokki Seisakusho.

24. Mood G.I. and Mahboubian-Jones M.G.B., “Multi-axial weaving”, International Patent WO 92/14876, 3 Sept 1992, Bonas Machine Co. Ltd.

25. Addis S.R., “A bias yarn assembly forming device”, International Patent WO 96/06213, 29 Feb 1996, Short Brothers PLC.

26. Anahara M., Yasui Y., Sudoh M. and Nishitani M., “Three-dimensional fabric with symmetrically arranged warp and bias yarn layers”, US Patent 5,270,094, 14 Dec 1993, Kabushiki Kaisha Toyoda Jidoshokki Seisakusho, and Kawasaki Jukogyo Kabushiki Kaisha.

CREEP AND CREEP RUPTURE OF STITCHED COMPOSITES

Feiyi Pang[1], C. H. Wang[2] and R. G. Bathgate[1]

[1] School of Engineering and Technology, Deakin University, Geelong, Australia
[2]Aeronautical and Maritime Research Laboratory, Melbourne, Australia

SUMMARY: Plain woven composites have been found to exhibit significant creep at ambient temperature with low to medium stress levels. One effective means to improve the creep resistance of woven composites is to introduce through-thickness stitching. Experiments were conducted using specimens stitched with different threads at various densities prior to resin injection. The results showed that stitching can significantly reduce delamination and hence enhance creep resistance, provided the stitches are aligned in the direction of loading. The effectiveness of stitching was found to increase with stitch density and thread modulus.

KEYWORDS: creep, creep testing, creep rupture, temperature creep, tensile testing, woven composite, stitched composite, fibers

INTRODUCTION

Woven composite materials are extensively used in a wide range of applications, including aerospace structures, infrastructures, etc, and frequently these structures are designed to carry static and fatigue loads. Due to the presence of a viscous matrix, e.g., epoxy, and the architecture of these materials, woven composites may exhibit significant creep as a function of stress, temperature and time [1,2,3,4]. Furthermore, the ultimate failure loads may also depend on the time period over which the load is applied. While metallic components normally have negligible creep at ambient temperature, creep and creep rupture are of great importance in the design and application of composites with a viscous phase which has a low glass transient temperature. Engineering designs, based on static properties without considering time dependent degradation of composite materials may lead to and eventually cause catastrophic disasters, especially when the design load is high when compared with the failure strength. In this regard, creep rupture of composites is a serious concern.

Since real time experimental testing and evaluation of the creep behaviour of large scale structures is very difficult and time consuming, considerable efforts have been devoted to the characterisation of creep using analytical or semi-empirical approaches. Earlier attempts include a power law constitutive relation by Norton [5]. Lilholt [6] showed the creep of off-axis unidirectional composites, can be predicted by using the law of mixture, taking into account the different creep properties of the constituents. These studies, however, have so far been concerned mainly with extensional creep of various fiber lay-up angles [7], or randomly oriented fiber composite [8]. Very little is known about the creep and creep rupture behaviours of woven composites, with or without stitching.

The objective of this paper is to present an experimental study of the creep rupture behaviour of woven composites at ambient temperatures. Through-thickness stitching was investigated as a promising means of improving the creep resistance of composites.

MATERIALS AND EXPERIMENTS

A two-dimensional woven fiber composite was manufactured using a standard resin injection technique. Five layers of bi-directional carbon fibre cloth were placed in between two layers of glass fibre fabric which was bi-directional E-glass cloth (top and bottom). The fabric was stitched through the thickness to obtain the preform, using a modified lock stitching method [2,3,4]. When the stitching process was completed, a standard resin injection procedure was applied to obtain the stitched composite. The resin used was Epocast 50-A, mixed with hardener 946 at a ratio of 100:15 by weight. Finally the composite was cured three days at room temperature followed by a post curing process of 2 hours at 80°C. The resulting composites had a volume fraction of approximately 0.5, half of which was aligned parallel to the axis of the specimens and the rest aligned perpendicular to the specimen axis. Table 1 shows the specifications of cotton and carbon threads used in the present work.

Table 1: Characterisation of stitch yarn

	cotton yarn (Tex=300)	carbon yarn (Tex=200)	thick carbon (Tex=800)
Tensile strength (MPa)	350	3400	3400
Modulus(GPa)	2.857	238	238

The stitching process was repeated along the loading direction as shown in Fig.1. The manual stitching process was achieved with a high level of control and repeatability to provide evenly distributed stitch points throughout the hybrid fabric preform.

Tensile Static and Creep Testing

The size of the specimen was 200mm long, 15 mm wide and 1.5 mm thick. The two stitching lines were symmetry to the centre. At each end, 50mm of the specimen was held in the grips, leaving a test area of 100mm long and 15mm wide.

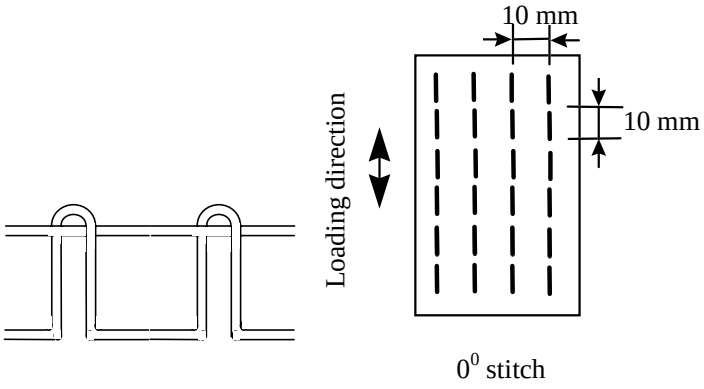

(a) (b)

Fig.1 (a) Lock stitching pattern and (b) loading direction.

Static tensile tests were conducted to quantify the mechanical properties of the unstitched and stitched woven composites, with particular attention to the effect of stitching on the in-plane tensile strength and elastic modulus. As shown in Table 2, both the Young's Modulus and the tensile strength increased as a result of stitching, suggesting that stitching of the preforms did not result in any loss of in-plane stiffness and strength. Tensile creep tests were conducted using a workshop constructed lever arm system. Constant load was applied to each specimen, corresponding stress levels ranging from 10% to 90% of the respective tensile strength. At least two specimens were tested at each condition to assess the variations between specimens.

Table 2: Mechanical properties of non-stitch and stitched. Stitch threads and density

Static Properties	non-stitch composite	Stitched			
		cotton pitch=5mm	cotton pitch=10mm	carbon pitch=5mm	carbon pitch=10mm
Tensile strength (MPa)	279	309	297.5	340	333
Elastic Modulus (GPa)	53.5	59.1	51.6	78.1	73.2

RESULTS AND ANALYSIS

Stitch Threads and Density

The experimental creep curves for specimens without stitch are shown in Figure 2(a), where the creep strains measured at various constant applied stress are plotted against time. Here the strains are the total longitudinal strain, ε, recorded using an extensometer. It is clear that very little creep occurred at stress level equal to or below 50 MPa, roughly one fifth of the ultimate tensile strength of the unstitched specimens.

Fig.2(b) shows the creep behaviour of specimens stitched with cotton threads at a pitch=5mm along the loading direction. Comparison with the unstitched specimens reveals that higher stress was required to induce the same amount of creep at a given time. The creep response of high density (pitch=5mm) carbon thread stitched composites are shown in Fig.2(c). As comparing with the cotton thread stitched composites (same pitch) even more reduction in the creep strain at a given stress level was observed. To further examine the influence of thread stiffness on creep, experiments have also been carried out for specimens stitched with a thicker carbon thread. The results are shown in Fig.2(d).

For a given stitching thread, the density of stitching was also important, as evidenced in Fig.3(a) and (b). The experimental results showed that the smaller the stitch pitch, the more effective was the stitching. The different creep behaviours of unstitched and stitched composites can be better seen in Fig.4, where the specimens were tested at an identical stress level. It is evident that for the same pitch, thick carbon thread was clearly the most effective in terms of reducing creep.

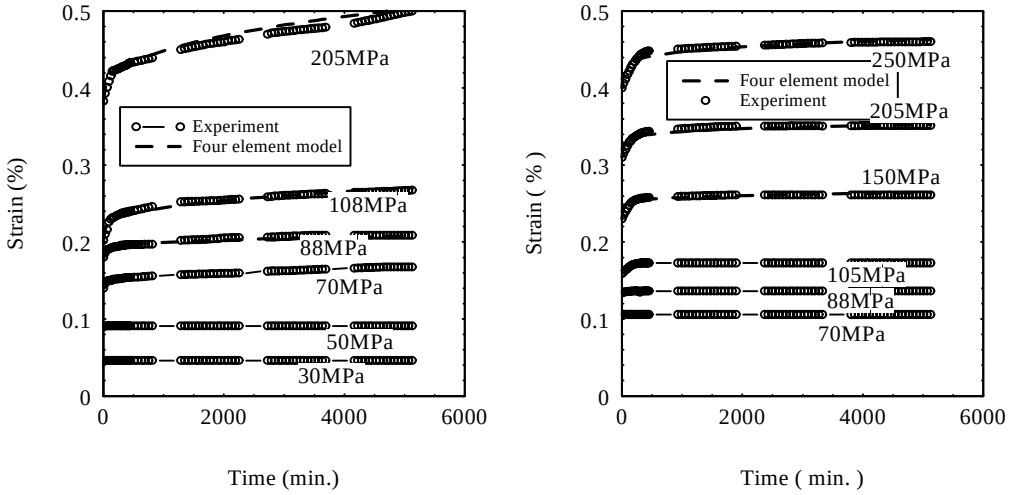

Fig.2: Creep responses of (a) unstitched composite (b) cotton

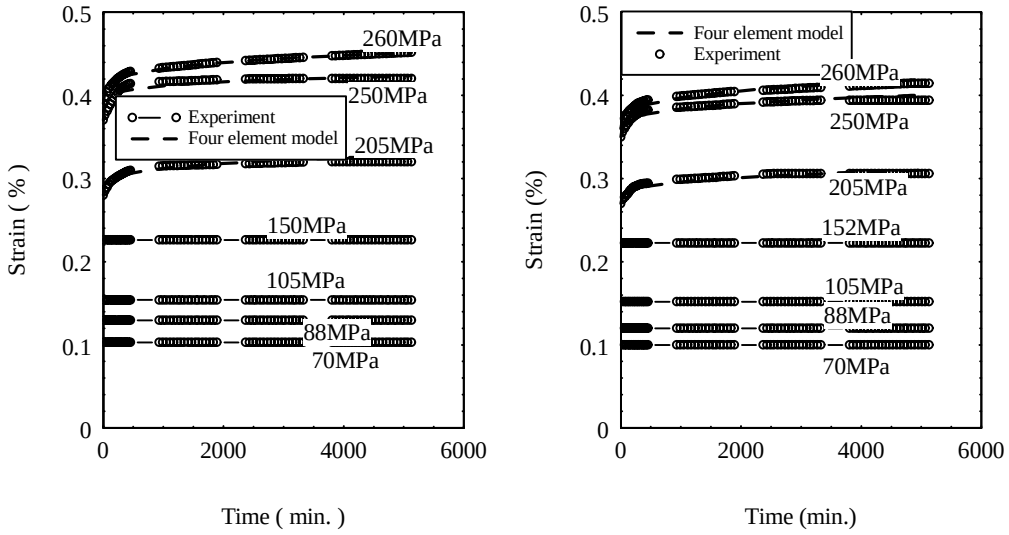

(c) carbon *(d) thick carbon composite*

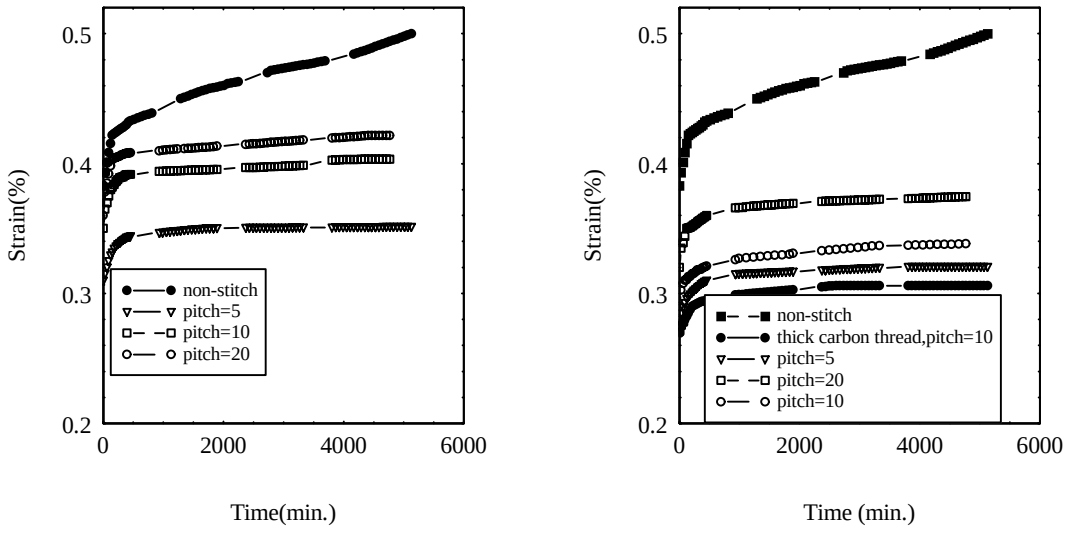

Fig.3: Effects of stitching density on creep behaviour (a) cotton thread (205MPa) *(b) carbon thread (MPa).*

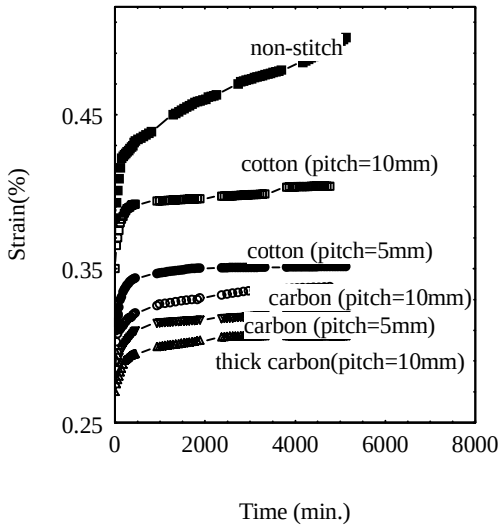

Fig.4: Effects of stitching and type of stitch fiber on creep behaviour (205MPa)

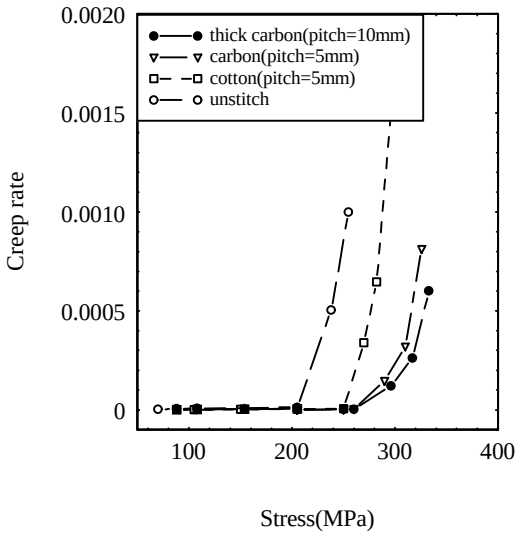

Fig.5: Variation of the creep rate for different stress levels

The relationships between the creep rate and the stress are shown in Fig.5. It was found that the creep rate increased nearly linearly with increase of stress at low and medium stress levels. This suggested that the unstitched and stitched woven composites could be considered as linear viscoelastic materials. An accurate description for stitched and unstitched composites can be obtained by using linear viscoelastic theory. In the present the four-element, Burger's model was adopted to characterise the creep behaviour. The total strain at time *t* is equal to the sum of the following strains:

$$\varepsilon = \varepsilon_1 + \varepsilon_2 + \varepsilon_3 \tag{1}$$

The relationship between σ and ε for Burger's model were considered as[9]:

$$\sigma + \left(\frac{\eta_1}{R_1} + \frac{\eta_1}{R_2} + \frac{\eta_2}{R_3} \right) \dot{\sigma} + \frac{\eta_1 \eta_2}{R_1 R_2} \ddot{\sigma} = \eta_1 \dot{\varepsilon} + \frac{\eta_1 \eta_2}{R_2} \ddot{\varepsilon} \tag{2}$$

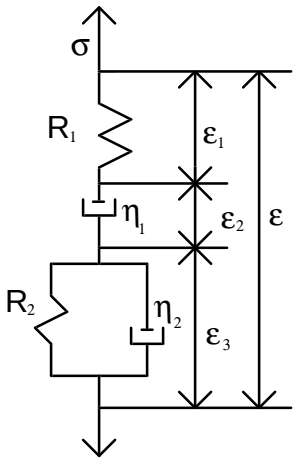

Fig.6: Burgers Model

The predictions of Burger's model are compared with the experimental results obtained at ambient temperatures, and, as shown in Fig.2, the correlation was very good. It was found that good agreement between theory and experiment was illustrated for the linear viscoelastic response characterised. The error in both estimates was approximately 4%. The accuracy of Burger's model has been illustrated for such materials [9]. The results of the present investigation indicate that Burger's model has the potential to accurately predict the linear viscoelastic response of stitched and unstitched woven composites.

Creep Rupture

The experimental results obtained for stage I and II regions represent the behaviour that would occur under service conditions with low to medium applied stresses. As the applied stress increases, failure in the form of creep rupture may result, even at ambient temperature. If composite materials are to be used reliably for extended periods of time, it is important to know not only how much the material deforms but if and when the material will fail. To this end, experiments were carried out by increasing the applied stress level to between 85% and 95% of the tensile strength. The results for unstitched, cotton stitched, carbon stitched and thick carbon stitched are shown in Fig.7(a)-(d). Compared with un-stitched composite under the same stress level, stitched specimens generally took longer to fail. The creep curves for all specimens appeared to be rather similar, exhibiting some stage III creep prior to rupture. A comparison of specimens stitched with different threads is shown in Fig.8, clearly demonstrating the effectiveness of stitching to increase creep rupture stress level for a given time or increasing creep rupture life for a given stress level.

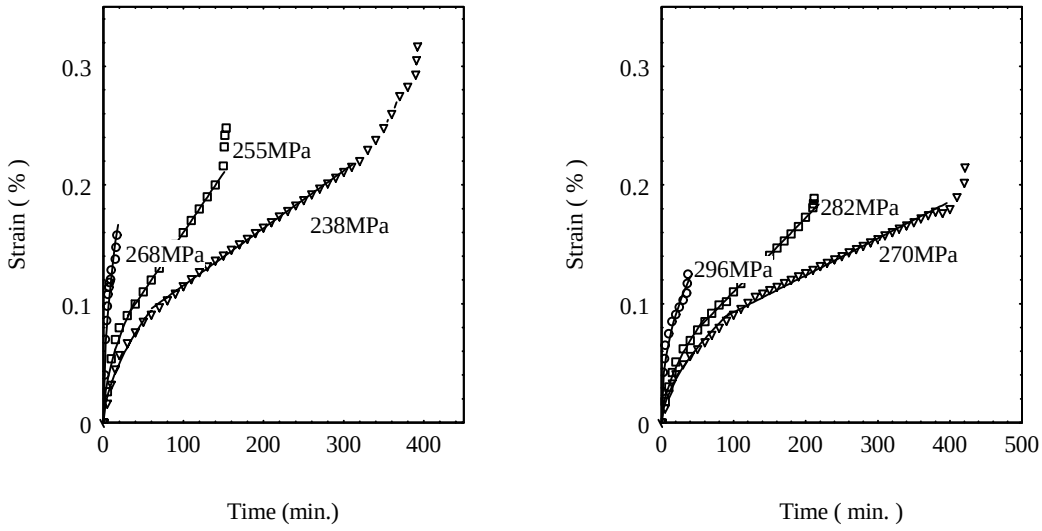

Fig.7: Rupture behaviour of (a) unstitched composite *(b) cotton stitched composite*

It can also be observed that the creep strain at failure, as shown in Figs.7(a)-(d), decreases as the applied stress increases, indicating a gradual transition towards a more brittle behaviour. It has been suggested that the creep lifetime of many materials can be correlated using a Monkman-Grant (see e.g., Service [10]) type of relationship which relates the failure time t_f to the creep rate $\dot{\varepsilon}$

$$t_f = C\dot{\varepsilon}^{-m} \tag{3}$$

Where *C* and *m* are material and environmental constants. An exponent of m=1 implies a constant strain at failure and assumes that creep in the primary and tertiary stages is negligible, whereas an exponent greater than unity means that the failure strain should increase as the strain rate decreases. The failure creep strain for unstitched and stitched specimens are plotted versus the failure time in Fig.9. The creep rates for the unstitched and stitched composites are shown in Fig.10 against the time to failure, at two different temperatures. It can be seen that there exists a universal relationship between the creep strain rate and the time to failure, thus providing a creep rupture criterion that can be identified relatively easily, as *C, m* are independent of temperature, stitching method and stitching density.

For practical application purpose, a relationship that gives the time to failure for any given applied stress and temperature would be more useful. Since the results of this study have shown that for a given creep strain rate the time to failure is independent of the temperature and stitching, Norton law and (3) can be combined to provide an expression that gives the time to failure as a function of the applied stress:

$$t_f = CA^{-m}\sigma_a^{-mn} \tag{4}$$

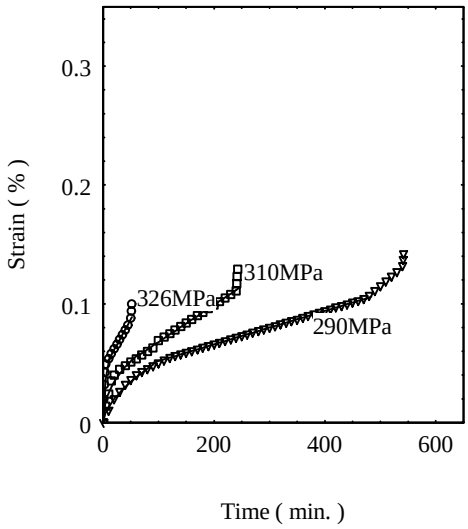

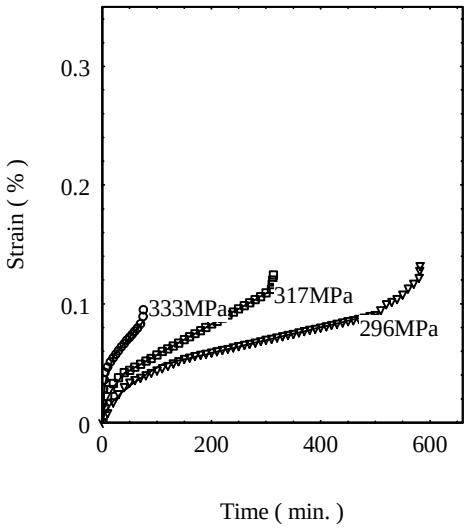

Fig. 7(c) carbon stitched composite *Fig. 7(d) thick carbon stitched composite.*

Where C and m are constants, independent of geometry and temperature, A and n are dependent on temperature and stitching threads and pitch.

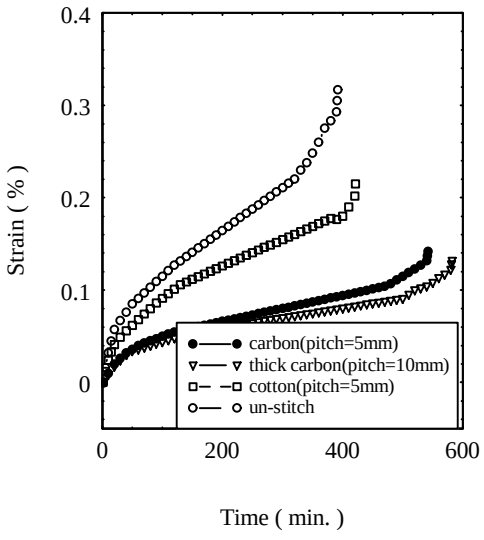

Fig.8: Effects of stitching and type of stitch stitched composite.

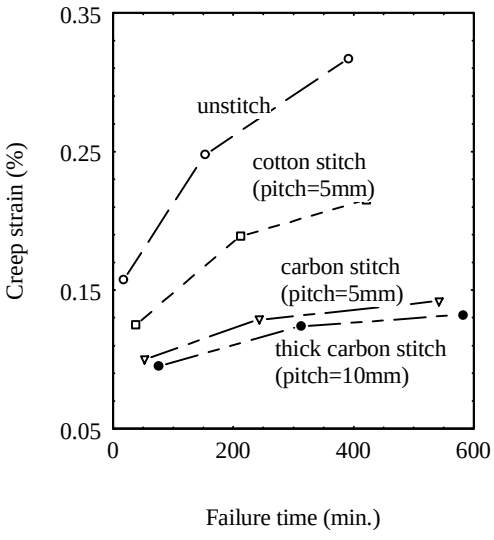

Fig.9: Creep failure strain as a function of failure time.

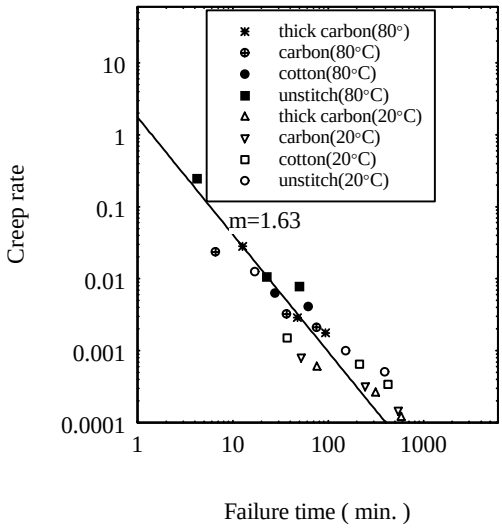

Fig.10: Master rupture curves for woven and stitched composites

CONCLUSION

1. Stitching, with the stitches being parallel to the dominant loading direction, has been found to be very effective in slowing down creep the process and enhancing creep rupture strength.

2. Under uniaxial tension, unstitched composites would fail due to creep rupture at stress levels less that 80% of the static tensile strength and ambient temperature within a relatively short period of time.

3. The density of stitching also plays an important role, as the smaller the stitch pitch, the more effective is the stitching

4. The application of Burger's model was adopted in this investigation to predict the creep response of stitched and unstitched woven composites.

ACKNOWLEDGMENTS

Authors are grateful to Mr. G. Giles for assistance in constructing the testing facilities.

REFERENCES

1. Shen, S. Z., "Prediction of long-term behaviour of fibre reinforced plastic", *In proceedings of the international Conference on Composite Materials,* Vol. 2, Guangzhou, China, 1989, pp. 1-5.

2. Pang, F., Wang, C. H. and Bathgate, R. G., "A creep study on stitched fiber/resin composite", proceedings of *1st Australasian Congress on Applied Mechanics,* Institution of Engineers Australia, 1996, pp:357-361.

3. Pang, F., Wang, C. H. and Bathgate, R. G., "Creep response of woven fiber composites: effect of stitching", accepted by *Composite Science and Technology.*

4. Pang, F., Wang, C. H. and Bathgate, R. G., "Effects of stitch thread and density on the creep behaviour of woven composites", submitted to *Journal of Composite Materials.*

5. Norton, F. H., "The creep of steel at high temperature", *New york : McGrawHill.* 1929.

6. Lilholt, H., "Models for creep of fibrous composite materials", *Materials Forum.* Vol.11, 1988, pp. 133-139.

7. Chung I., Sun C. T. & Chang I. Y., "Modelling creep in thermoplastic Composites", *Journal of Composite Materials,* Vol. 27, No. 10, 1993, pp. 1009-1029.

8. Wang Y. R. & Chou T. W., "Analytical modelling of creep behaviour of short fibre reinforced ceramic matrix composites", *Journal of Composite Materials,* Vol. 26, No. 9, 1992, pp.1269-1287.

9. Findley W. N., Lai J. S. & Onaran K., "Creep and relaxation of nonlinear viscoelastic materials", *North-Holland Publishing Company.*

10. Service T. H., "Creep rupture of a phenolic-alumina particulate composite", *Journal of Materials Science* 28, 1993, pp : 6087-6090.

MODELING OF DISCRETE RADIAL REINFORCEMENT IN CURVED POLYMER MATRIX COMPOSITE LAMINATES

Ming Y. He[1], Brian N. Cox[2] and Keith T. Kedward[1]

[1] Materials Department and Department of Mechanical & Environmental Engineering, University of California, Santa Barbara CA 93106
[2] Rockwell Science Center, 1049 Camino Dos Rios, Thousand Oaks CA 91360

SUMMARY: The problem of how through-thickness reinforcement opposes the opening of delamination cracks in curved laminar structures is examined theoretically. Finite element calculations have been performed to show how the through-thickness reinforcement modifies the energy release rate of a delamination crack. Solutions are found for perfectly bonded and debonded cases. Energy conservation arguments are then used to define constitutive laws for equivalent continuous bridging springs acting on the delamination fracture surfaces. This step allows the immediate application of useful concepts from the literature on bridged cracks. Results are summarized for convenient use and trends are highlighted by relating the exact numerical results to analytical approximations for the perfectly bonded and debonded cases.

KEYWORDS: polymer matrix composite, stitch, laminate, delamination, finite element, bridging traction, bridged crack.

INTRODUCTION

In previous publications [1,2] simple approaches for predicting the amount of through thickness reinforcement required to suppress delamination in polymer matrix composites have been presented. A curved configuration originally defined by Kedward et al [3] and used for conventional curved composite laminates was adopted for the theoretical development of these prediction methods. Further evaluation of the adequacy of these simple methods is now accomplished through finite element analyses.

From a practical viewpoint a relatively small percentage of through thickness reinforcement has been proven to be effective in suppressing the propagation of delamination in impact damaged panels and at stepped transitions associated with local changes in laminate thicknesses. Similarly, it is anticipated, but as yet unproved experimentally, that delamination tendencies in curved structures subjected to bending loads, that tend to increase with the radius of curvature, can be suppressed by stitching.

One major incentive for the present work is the substantiation of the simple methods advanced by Cox et. al [1] enabling estimation of the minimum percentage of stitch reinforcement in the radial direction of curved laminates, necessary to suppress delamination in curved laminates subjected to static or fatigue loading. These simple methods can then be adopted by structural designers in their efforts to select prudent stitch densities and evaluate

the relative merits of a range of stitch formulations, i.e. fiber type and number of filaments per tow. The designer can then avoid the penalty of in-plane property degradation that can be created by fiber damage and distortion with excessive percentage of through thickness (stitch) reinforcement. In addition the closed form relationship developed can facilitate estimation of the type, area fraction and distribution of stitches that would represent effective percentages for various skin thickness and/or curvatures.

Other constraints are imposed by the textile machinery available and used by the fabricators of fiber preforms and the subsequent polymer matrix composites. Hence the contribution of the analysis tools developed and validated herein, which serve the designers in the vital interactions with the manufacturing activities. Typically the processes involved in the fabrication of stitched composites consist of some form of resin infiltration technique such as Resin Film Infusion (RFI) or Resin Transfer Molding (RTM).

The following development addresses the categories of well bonded and debonded interfaces between the stitch tow and surrounding matrix. This is shown to represent strong differences in performance and effectiveness of the through thickness reinforcement and therefore the selection can be influenced by both the reinforcing fiber and its surface characteristics.

THE DELAMINATION AS A BRIDGED CRACK

Consider the uniformly curved laminate depicted in Fig. 1, subject to opening bending moments, i.e. moments of such a sense that the through-thickness stresses developed, σ_r are tensile. The laminate has total thickness 2h and the radius of curvature of its mid-plane is denoted r_m. When the curvature is modest ($h/r_m < 0.2$), σ_r takes its maximum value in the uncracked laminate near the mid-plane. It will be assumed in the following that all delaminations occur exactly on the mid-plane. This will be reasonable for studying delaminations caused solely by the through-thickness stress acting on naturally occurring flaws.

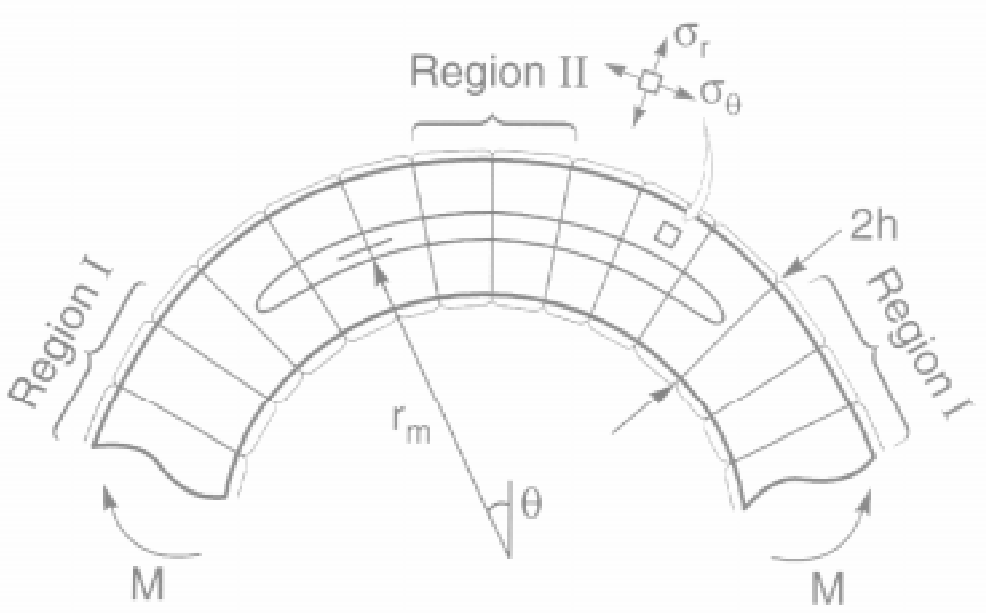

Fig. 1: A delamination crack in a curved structure under opening bending moments, with bridging stitches indicated schematically

Attention is also restricted here to delamination cracks that initiate and propagate far from the ends of the curved structure or any holes. With this condition, Mode II sliding displacements are expected to be negligible. The problem can therefore be treated by examining purely Mode I opening.

When a delamination crack begins to propagate, it will be bridged by the stitches, as depicted in Fig. 1. The axial stresses in the stitches will be transferred to the laminate, tending to close down the delamination crack and reducing the crack tip stress intensity factor, K_{tip}. This closure effect can be represented by a system of bridging tractions acting on the fracture surfaces. The bridging traction will usually increase as the delamination crack opening increases, at least until the stitches fail. This enables the possible existence of a steady state mode of delamination crack propagation, in which the critical value, σ_c, of σ_r required to cause propagation of the delamination crack reaches a constant value, σ_1, independent of the delamination crack length.

To enable concepts from the literature on bridged cracks to be invoked, an analogue with continuous bridging traction is now sought to the discrete unit cell model shown in Fig. 2a. The continuous model will be formulated to be energetically equivalent to the discrete model.

The unit cell with continuous bridging traction, *p*, acting on the delamination fracture surfaces is sketched in Fig. 2b. The laminate and stitch have been replaced by a homogenous orthotropic medium. The models of Figs. 2a and 2b will be called the "discrete" and "continuous" models, respectively.

For the continuous model, the linear bridging traction law is given by

$$p=\beta u \tag{1}$$

where 2u is the total crack opening, β the bridging stiffness parameter.

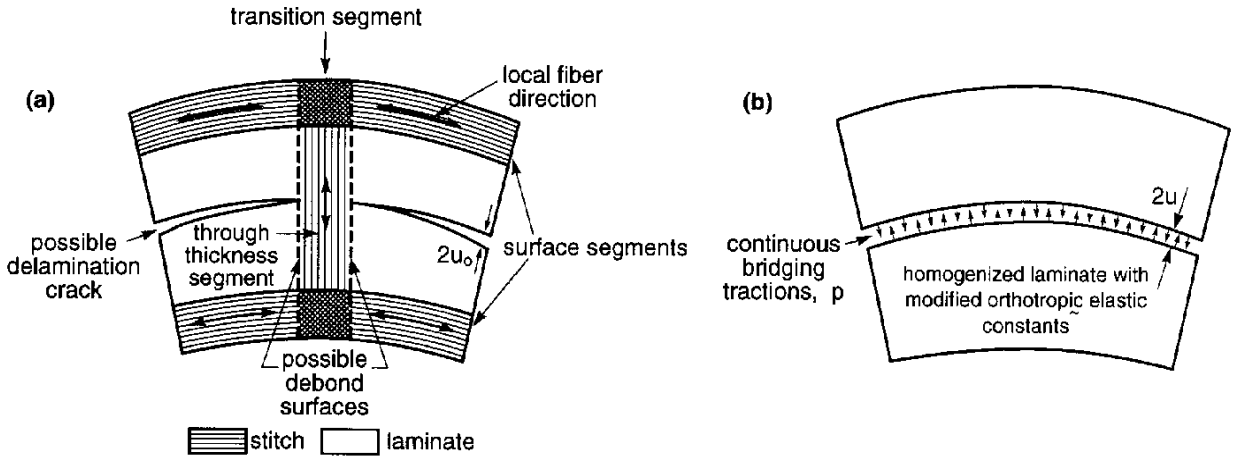

Fig. 2: (a) Detail of the geometry assumed for modeling a stitched laminate. (b) Analogue of continuous bridging tractions acting on an homogenized laminate

The fracture properties of the continuous model have already been analyzed in Refs. 1,4 and 5. From these prior works, the steady-state cracking stress, σ_1 is given by

$$\sigma_1 = \sqrt{\beta \Gamma_c} \tag{2}$$

where Γ_c is the intrinsic Mode I fracture energy of the stitched laminate. A fair estimate of Γ_c is

$$\Gamma_c = (1\text{-}c_s)\, \Gamma_m \tag{3}$$

where c_s is the area fraction of stitches, Γ_m is the fracture toughness of the unstitched laminate. More generally, Γ_c refers to the delamination resistance arising from crack tip processes. Given Eq. (3) or some other estimate or measurement of Γ_c, σ_1 is fully determined by the bridging stiffness parameter, β.

ESTIMATION OF THE BRIDGING STIFFNESS PARAMETER β

Shear Lag Approximation

The problem of a cylindrical inclusion (here the through-thickness segment of the stitch) being pulled out of a semi-infinite half space (here one half of the laminate with the boundary being the crack plane) to which it is well bonded was analyzed by Budiansky, Hutchinson, and Evans (BHE) using shear lag methods [6]. While BHE assumed isotropy in the cylinder and the half-space, it will serve to equate Young's modulus for their inclusion to the axial modulus of the stitch, E_s, here; and the through-thickness and shear moduli of their half-space to the through-thickness and shear moduli of the laminate, E_z and G_{zx} here. Integrating the stress fields of BHE's Eq. (25) yields displacements at the fracture surface and thence an estimate, β_{BHE}, for β:

$$\beta_{BHE} = \frac{\rho c_s E_s}{r_s} \tag{4a}$$

where

$$\rho = \left[\frac{2G_{zx}}{E_z} \left(\frac{c_s}{1-c_s} + \frac{E_z}{E_s} \right) \frac{-4(1-c_s)^2}{2\log c_s + (1-c_s)(3-c_s)} \right]^{1/2} \approx \eta c_s^{1/2} \tag{4b}$$

and r_s is the radius of the stitch, η is a dimensionless factor of order unity. The shear lag analysis of BHE yields axial stresses in the stitch which fall exponentially with distance from the fracture plane with a characteristic length r_s/ρ. Thus if

$$h < r_s / c_s^{1/2} \tag{5}$$

$$\varepsilon_s = \frac{u_o}{h} = \frac{\sigma_o}{E_s} \tag{6}$$

where u_o is defined in Fig. 2a and σ_o is the average stress in the stitch on the crack plane. Assigning $u=u_o$ (in this approximation only) and recalling that $p=c_s\sigma_o$, the estimate, $\beta^{(1)}_{unif}$, of β follows as

$$\beta^{(1)}_{unif} = c_s E_s / h \quad . \tag{7}$$

This was the estimate used for β in Reference 1. As pointed out in [2], the load from the stitch will deform the laminate, creating a dimple at the transition zones. This increases the crack opening, which decreases β. With laminate deformation taken into account, an improved estimate, $\beta^{(2)}_{unif}$, of β is given by

$$\beta^{(2)}_{unif} = \frac{c_s E_s}{h} / [1 + \frac{(1-\nu) r_s E_s}{h G_{zx}}] \tag{8}$$

Results from Finite Element Model

Numerous calculations were performed by finite element methods in reference [2] for the discrete cell model (Figure 2a) for two material systems:

System 1: a quasi-isotropic carbon/epoxy laminate stitched with carbon fibers;
System 2: the same laminate stitched by glass fibers;

Values of β deduced from the FEM results for well bonded stitches are presented in Fig. 3. The FEM results have been normalized by the estimate β_{BHE} derived from the BHE model. The abscissa shows the ratio h/r_s.

Figure 3a shows calculations for material system 1 for c_s = 0.008 (a relatively low volume fraction of stitches); and three values of the curvature measure r_m/h. Results for r_m/h= 200 will be very close to the limit obtained for vanishing curvature. The case r_m/h= 5.7 represents the maximum degree of curvature that this work will recommend in designing stitched laminates. For large h/r_s solutions for all r_m/h approach a constant value, not far from unity. For small h/r_s, β falls well below β_{BHE}. The cut-off occurs near the expected condition, Eq. (5), i.e., near h/r_s = 11 for material system 1. For $h/r_s > c_s^{1/2}$ (the regime where BHE is appropriate), there is some separation of curves for different r_m/h, but the dispersion is moderate for curvatures in typical structures ($5 < r_m/h < 10$).

For $h/r_s < 5$, the BHE derived approximation seriously overestimates β, which would lead to nonconservative designs. This is the regime of thin laminates, which can deform very easily by buckling without significant axial displacement of the stitches. The regime $h/r_s < 5$ must be avoided by designers.

Figure 3b shows results of the same form for fixed curvature, r_m/h = 9; up to three representative stitching area fractions, c_s = 0.008 (low), 0.02 (moderate), and 0.06 (relatively high); and for the same two material systems. All curves show similar trends, being almost constant for $h/r_s > 10$ and low for $h/r_s < 5$. For these material systems, β/β_{BHE} is not far from

unity for $h/r_s > 10$. As Fig. 3 summarizes, the estimate β_{BHE} is fairly accurate for highly anisotropic materials (polymer composites).

Figure 4 shows FEM results for the case of debonded stitches for the two material systems with $c_S = 0.008$ and $r_m/h = 5.7$. The bridging stiffness parameter, β, is now normalized against the estimate, $\beta^{(1)}_{unif}$, derived by assuming uniform axial strain in the stitch (Eq. (15)). All the curves lie significantly below the ordinate unity, indicating that $\beta^{(1)}_{unif}$ is a nonconservative estimate. The discrepancy is associated with the contribution of laminate deformation and its effect on stitch compliance which was ignored in the formulation for $\beta^{(1)}_{unif}$. The dashed curve shows $\beta^{(2)}_{unif}/\beta^{(1)}_{unif}$ where $\beta^{(2)}_{unif}$ is the estimate of Eq. (8), which includes an approximate estimate of laminate deformation. This curve reproduces the magnitudes and trends with h/r_s quite well. Just as for well bonded stitches, designing structures with $h/r_s < 5$ is not recommended, because β becomes very small (ineffective stitching).

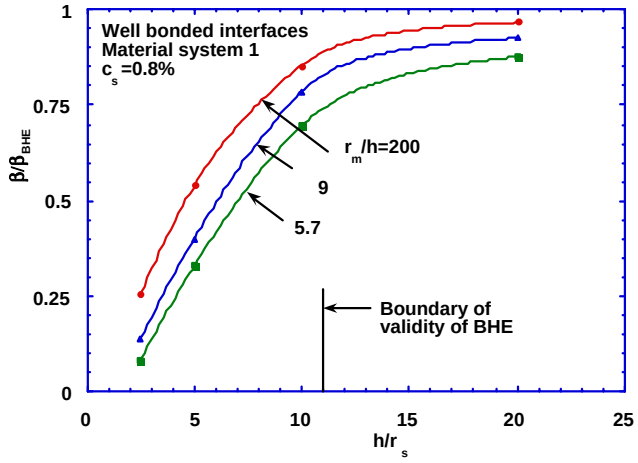

(a)

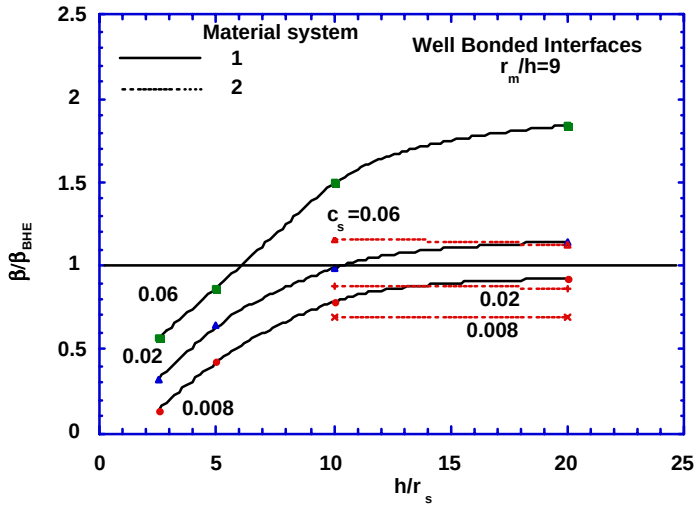

(b)

Fig. 3: Numerical results for the bridging stiffness parameter, β normalized against the estimate derived from the BHE model vs. the ratio of the laminate half-thickness to the stitch radius. Well bonded stitches. (a) Three different curvatures; material system 1. (b) Different stitch area fractions for two material systems.

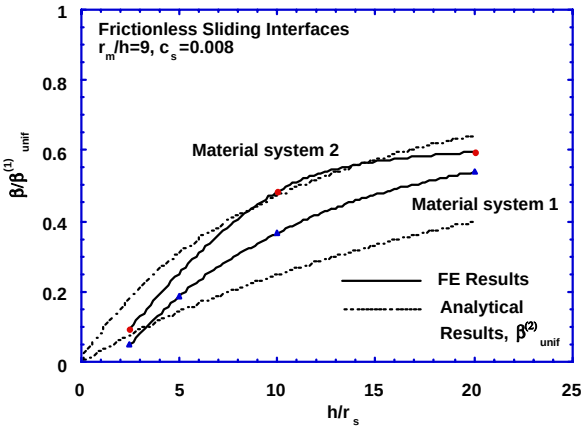

Fig. 4: Numerical results for the bridging stiffness parameter, β, for the continuous model normalized against the estimate derived by assuming uniform axial strain in the stitch vs. the ratio of the laminate half-thickness to the stitch radius. Debonded, frictionless stitches.

Bounds for β

The bonded and debonded, frictionless cases for which solutions have been computed by finite element methods provide upper and lower bounds for β. Let $\beta^{(max)}$ denote the upper bound and $\beta^{(min)}$ denote the lower bound. Any case of intermediate debonding or nonzero friction must lie between these bounds.

For the well bonded case,

$$\beta^{(max)} \approx \chi(E_s / E_z)\beta_{BHE} \tag{9}$$

where χ is given by [2]

$$\chi(E_s / E_z) \approx 0.23 + \frac{1}{14} E_s / E_z - \frac{1}{450}(E_s / E_z)^2 \tag{10}$$

For the debonded case,

$$\beta^{(min)} \approx \beta^{(2)}_{unif} \tag{11}$$

The upper and lower bounds for the steady-state cracking stress, $\sigma_1^{(max)}$, and $\sigma_1^{(min)}$, can be determined from the bounds for β and Γ_c by Eq. 2. Figure 5 shows representative values for the carbon-epoxy system as functions of the area fraction of stitches, c_s. The intrinsic fracture energy was assigned the value 1 kJm^{-2}.

MINIMUM AREA FRACTION OF STITCHES REQUIRED TO SUPPRESS DELAMINATION

In Ref. 1 it was proposed that a practical criterion for an adequate density of stitching was the requirement that delamination occur at a higher external load than that required for failure by some other mechanism. In most cases, the other mechanism will be failure on the compressive (outer) surface of the laminate, usually by kink band formation [1,7]. Let the critical in-plane compressive stress for kinking failure be denoted σ_c. The compressive stress on the outer surface, $\sigma^{(o)}$, is related to the maximum radial stress, $\sigma_r^{(a)}$ which arises near the mid-plane, by [1,4]

$$\sigma_r^{(a)} / \sigma^{(o)} = \frac{h}{2r_m} \xi[h / r_m, E_z / E_x] \qquad (12)$$

where E_X is the in-plane Young's modulus of the laminate; and ξ is close to unity. A fitted approximation to ξ can be found in [1]. In the following, it will be assumed that $5 < r_m/h < 10$, so that $\sigma_r^{(a)}/\sigma_r^{(o)}$ For typical carbon-epoxy laminates, in-plane failure occurs by kinking on the compressive side when $\sigma^{(o)} = \sigma_c \approx 500$MPa. Thus for the assumed curvature range, one requires σ_1 in the range $25 < \sigma_1 < 50$ MPa. This range is marked in Figure 5. If the stitches remain well bonded, the area fraction of stitching c_s for stitches of common denier ($r_s \leq 0.5$ mm) required to achieve high enough σ_1 to suppress delamination never exceeds 4%. If the stitches are assumed to debond, the required area fractions are much higher and care would have to be taken to select a suitably fine stitch denier. A stitch of radius 0.125 mm would support the top of the range for σ_1 when $c_s = 0.06$. Nevertheless, this is the most conservative outlook for what is probably an extreme case. Stitching densities of a few percent with a stitch spacing of at least several mm are likely to represent common and practicable conditions.

CONCLUSIONS

The problem of a delamination crack bridged by discrete stitches in a curved structure has been mapped onto an analogue in which the crack is bridged by continuous crack face tractions. Solutions for well bonded and debonded, frictionless stitches form bounds to the general case. The bounds can be expressed as estimates of the critical stress for delamination, from which bounds for the volume fraction of the stitching required to suppress delamination can be deduced. For polymer composites, stitch area fractions below 5% will be enough to suppress delamination. Another important conclusion of this study is that the ratio of the laminate half-thickness to the stitch radius should not be allowed to fall below 5. Stitching is ineffective in suppressing crack opening and therefore in raising the delamination fracture energy for laminates that are thinner than this.

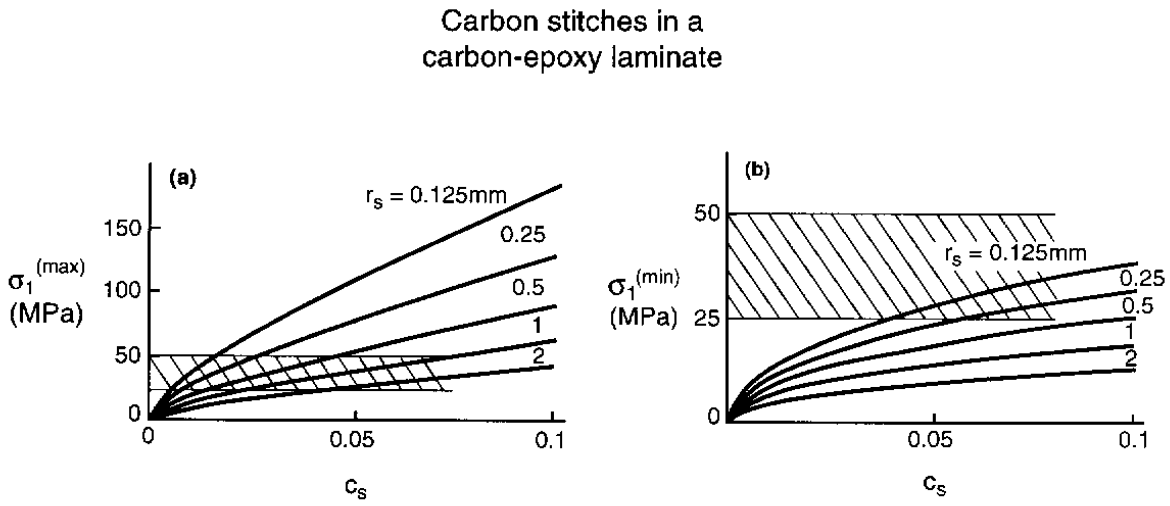

Fig. 5: Bounds for the design stress σ_1. The shaded bands indicate values required for representative values of the relative curvature and the critical stress for failure

REFERENCES

1. Cox, B. N., Massabò, R., and Kedward, K. T., "The Suppression of Delaminations in Curved Structures by Stitching," *Composites*, part A 1996, **27A**, 1133-8.

2. He, M. Y., and Cox, B. N., " Crack Bridging by Through-Thickness Reinforcement in delaminating Curved Structures", submitted to *Composites*,. part A, 1996.

3. Kedward, K. T., Wilson, R. S., and McLean, S. K., "Flexure of Simply Curved Composite Shapes," Composites J. **20**, 1989, 527-536.

4. Lu, T. J., Xia, Z. C., and Hutchinson, J. W., "Delamination of Beams under Transverse Shear and Bending," *Mater. Sci. Engng* 1994, **A188**, 103-112.

5. Lu, T. J., and Hutchinson, J. W., "The Role of Fiber Stitching in Eliminating Transverse Fracture in Cross-Ply Ceramic Composites," *J. Amer. Ceram. Soc.*, 1995, **78**, 251-3.

6. Budiansky, B., Hutchinson, J.W., and Evans, A.G., "Matrix Fracture in Fiber-Reinforced Ceramics," *J. Mech. Phys. Solids*, 1986, **34**, 167-189.

7. Cox, B. N., Dadkhah, M. S., Morris, W. L., and Flintoff, J. G., "Failure Mechanisms of 3D Woven Composites in Tension Compression and Bending," *Acta Metall. Mater.*, 1994, **42**, 3967-84.

INTERLAMINAR FRACTURE PROPERTIES OF STITCHED FIBREGLASS COMPOSITES

A.P. Mouritz[1] and L.K. Jain[2]

[1] Department of Defence, DSTO, Aeronautical and Maritime Research Laboratory, P O Box 4331, Melbourne, Victoria, AUSTRALIA 3001
[2] Cooperative Research Centre for Advanced Composite Structures Ltd. (CRC-ACS), 361 Milperra Road, Bankstown, New South Wales, AUSTRALIA 2200

SUMMARY: This paper assesses the ability of two theoretical models to predict the Mode I and Mode II interlaminar fracture toughness properties of fibre reinforced polymer composites reinforced by through-the-thickness stitching. The models were used to calculate R-curves and steady state energy release rates for stitched glass fibre reinforced polymer (GFRP) composites. The GFRP was stitched in two orientations with Kevlar® thread to two densities. The Mode I model predicted a significant increase in the delamination resistance of the stitched composites, and the magnitude of this improvement was confirmed experimentally using the double cantilever beam (DCB) test. Scanning electron microscopy (SEM) showed that this toughening was caused by stitches bridging the delamination and, to a lesser extent, by crack tip deflection and by stitch pull-out processes. The Mode II model predicted that stitching would only provide a small improvement in delamination toughness, and this was in reasonable agreement with experimental results determined with the end notch cantilever (ENC) test which showed no appreciable change in toughness as a result of stitching. SEM was used to observe the failure mechanisms of the stitches under Mode II loading, and it appears that the ability of stitching to improve the delamination resistance was masked by the unusually high toughness of the unstitched GFRP laminate. This study shows that the theoretical models can predict with reasonable accuracy the delamination resistance of stitched GFRP loaded in translaminar tension or shear.

KEYWORDS: glass fibre reinforced polymer (GFRP) composite, stitching, mode I and mode II interlaminar fracture toughness, modelling

INTRODUCTION

Fibreglass composites are used in a wide variety of sporting goods, civil structures, automotive and aerospace components, and marine vessels. For example, these composites are used in sporting equipment such as fishing rods, javelins, pole vault poles and tennis rackets while in automobiles they have been used in structural chassis components such as drive shafts, springs and road wheels. Fibreglass is used in marine structures ranging in size from masts and radomes to racing yachts, fishing trawlers and minehunting ships. Despite the widespread use of glass fibre reinforced polymer (GFRP) composites, their use in other applications has been restricted by low mechanical, fracture toughness and impact resistant properties in the through-thickness direction. This is a result of the two-dimensional (2-D) laminate structure, in which glass fibres do not extend in the through-thickness direction.

Since the mid-1980s there has been great interest in reinforcing composites by through-the-thickness stitching. Interlaminar fracture toughness studies reviewed by Dransfield *et al.* [1] show that stitched composites possess higher delamination resistance under Mode I and Mode II loading than traditional 2D laminates. For example, Jain [2] reports that the Mode I steady state energy release rate (G_{IRs}) required for crack propagation for a stitched carbon fibre reinforced polymer (CFRP) composite was 16 times higher than the unstitched CFRP laminate, while under Mode II loading the steady state values (G_{IIRs}) for CFRP composites was increased up to fourfold by stitching.

As a result of these improvements in interlaminar fracture toughness, stitched composites are being used in new structural applications such as the wings and fuselage of some aircraft [3]. An important requirement for assessing potential applications for stitched composites is a capability to accurately predict the improvement in delamination resistance resulting from stitching without the need for costly and time-consuming fracture toughness testing. Jain and Mai [4,5] have recently developed theoretical models for predicting the delamination crack growth resistance (R) curves of stitched composites under Mode I and Mode II loading. Jain [2] found that these models predicted the R-curves for a stitched CFRP composite with reasonably good accuracy when compared with experimentally measured R-curves. Despite this agreement, the models have not been rigorously tested for other types of stitched composite, and therefore the aim of this paper is to assess their accuracy against experimentally measured Mode I and Mode II R-curves for a GFRP composite stitched with Kevlar thread.

INTERLAMINAR FRACTURE TOUGHNESS MODELLING OF STITCHED COMPOSITES

Mode I Interlaminar Fracture Model

The model developed by Jain and Mai [4] for calculating the Mode I interlaminar toughness is based on Euler-Bernoulli linear elastic beam theory applied to a stitched composite with a double cantilever beam (DCB) geometry, as shown in Fig 1a. The model can be used to determine the effect of various stitching parameters (*eg.* stitch density, stitch modulus, thread diameter) on the R-curve behaviour of composites. However, the influence of stitching orientation cannot be determined. Jain and Mai [4] show that the Mode I delamination resistance in terms of stress intensity factor, $K_{IR}(\Delta a)$, of a composite with continuous through-the-thickness stitching can be calculated from the expression:

$$K_{IR}(\Delta a) = Y \frac{P}{\sqrt{H}} f\left(\frac{a_o + \Delta a}{H}\right) \tag{1}$$

where: a_o is the initial crack length
Δa is crack growth characterised by the stitch bridging zone length
f(.) is a geometric factor
H is the half-thickness of the DCB specimen
P is the crack propagation load at a known length $a_o + \Delta a$, and
Y is an orthotropic correction factor.

These and the following parameters are defined in detail in Ref. [4]. The crack propagation load, P, is obtained from the following crack propagation condition:

$$K_{IR}(\Delta a) \;=\; Y\frac{P}{\sqrt{H}}f\left(\frac{a_o+\Delta a}{H}\right) \;=\; K_{IC}+Y\int_{t=0}^{\Delta a}p(t)\frac{1}{\sqrt{H}}f\left(\frac{t}{H}\right)dt \qquad (2)$$

where: K_{Ic} is the critical stress intensity factor of the (unstitched) composite
p(t) is the closure traction due to bridging stitches, and
t is the distance from the crack tip to the specimen end.

Once the crack propagation load is known, the fracture toughness, $K_{IR}(\Delta a)$, can be calculated using equation 1, and the fracture toughness in terms of energy release rate, $G_{IR}(\Delta a)$, may be obtaining using:

$$G_{IR}(\Delta a)=\frac{K_{IR}^2(\Delta a)}{E_o} \qquad (3)$$

where E_o is the orthotropic elastic modulus of the composite [4].

Mode II Interlaminar Fracture Model

The Mode II interlaminar fracture toughness model by Jain and Mai [5] was derived using first order shear deformation laminated plate theory and Griffith's energy release rate approach. Models have been developed for stitched composites subjected to shear loading using the end notched flexure (ENF) or end notched cantilever (ENC) test methods. Fig 1b shows a diagram for the ENC specimen geometry, and the energy release rate available for crack propagation for this specimen is given by the following expression [5]:

$$G_{II}=\frac{A^*}{\cosh^2(\lambda\Delta a)}\left\{\tau\left(\frac{\sinh(\lambda\Delta a)}{\lambda}+a_o+\alpha H\right)-\frac{\lambda}{A^*}\left(\frac{\alpha_1}{\alpha_2}\right)\sinh(\lambda\Delta a)\right\}^2 \qquad (4)$$

where: τ is the shear stress and is related to the applied load P
is the correction factor to include shear deformation
α_1 & α_2 are stitching parameters and
is related to material properties through A* and α_1.

The expressions for τ, A^*, α, α_1, α_2, and λ may be found in Ref. [5]. Using the crack propagation condition, $G_{II} = G_{IIc}$, where G_{IIc} is the critical energy release rate for the unstitched composite, the shear stress τ required for crack propagation can be determined. The energy release rate can then be calculated from:

$$G_{IIR}=A^*\tau^2(a+\alpha H)^2 \qquad (5)$$

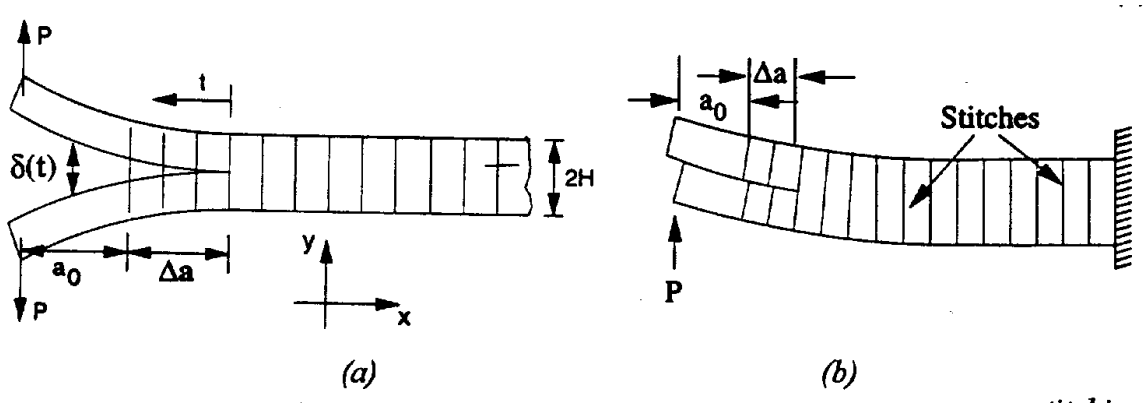

Fig. 1: The (a) DCB and (b) ENC specimen geometry with through-the-thickness stitching used as a basis for the modelling of Modes I and II interlaminar fracture toughness

MATERIALS AND EXPERIMENTAL TECHNIQUES

Stitched GFRP Composites

Fibreglass composites were made with E-glass and a cold-curing vinyl ester resin. Two types of fibreglass, made by ACI Fibreglass Pty. Ltd., were used in each composite: a plain woven roving fabric (with an areal density of 0.6 kg/m^2) and a chopped strand mat (0.3 kg/m^2). These fibreglass materials were layered in an alternating sequence to 14 plies. This choice of material and layup was selected because it is used in many GFRP composite structures. Some of the fibreglass preforms were stitched using a modified lock stitch with 40 tex (2 x 20 tex) spun Kevlar®-49 yarn, which had a diameter of 0.16 mm. The stitching was performed in straight parallel rows along the length or across the width of the fracture toughness specimens (Fig. 2) to a density of 3 or 6 stitches/cm^2.

The preforms were resin transfer moulded with Derakane® 411-45 vinyl ester resin, which is produced by the Dow Chemical Company. The resin content of the composites was about 40% by weight, and the resin was cold-cured under ambient conditions (~20^{o}C) for several weeks before fracture toughness testing.

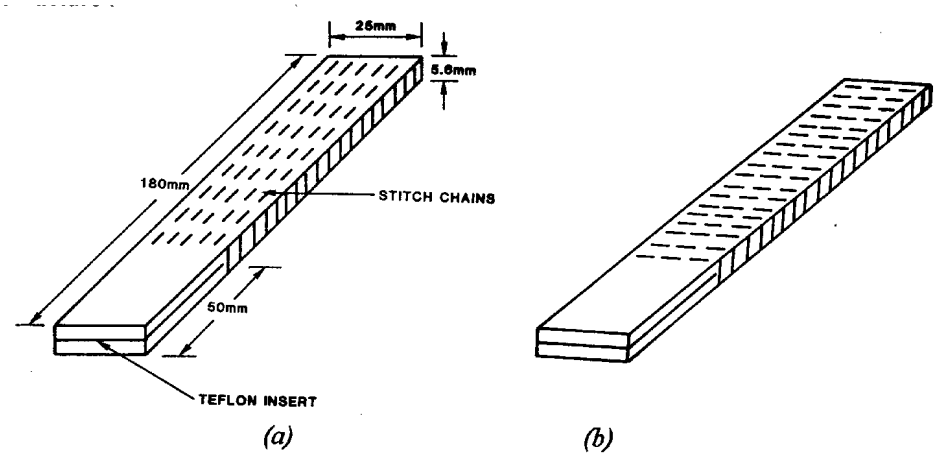

Fig. 2: Geometry of the DCB specimens stitched in the (a) parallel and (b) normal directions

Interlaminar Fracture Toughness Testing

The Mode I interlaminar fracture toughness was measured using the DCB method in accordance with ASTM D5528-94a. The specimen geometry is shown in Fig 2. A 50 mm long Teflon film was located between the mid-thickness plies at one end of the specimen to initiate the delamination. End blocks were attached to this end of the specimen. Load was applied at a cross-head speed of 2 mm/min until the crack grew by 4-6 mm, and at this point the load (P) and cross-head displacement (δ) were recorded and the crack length (a) was measured using a travelling optical microscope before the specimen was unloaded and then reloaded until the crack grew by a further 4-6 mm. This process was repeated 12 times in a DCB test, which caused the delamination to grow by an average of 80 mm. Five DCB tests were performed on each composite. The Mode I energy release rate required for crack propagation was calculated using the elastic beam equation derived by Hashemi, Kinloch and Williams [6]:

$$G_{IR} = \frac{3P\delta}{2b(a + \chi H)} \tag{6}$$

where b is the specimen width and χ is a constant to correct for deflection and rotation effects at the crack tip, and is calculated using equations in Ref [6].

The Mode II fracture toughness was measured using the ENC method. The ENC specimen geometry was similar to the DCB specimens (Fig 2) except the pre-crack and specimen lengths were about 70 and 135 mm, respectively. The ENC specimens were loaded at a cross-head speed of 2 mm/min until the delamination grew a short distance (usually within 10 mm of the pre-crack). The load, cross-head displacement and crack length were then measured before the specimen was unloaded and reloaded. This process was repeated 8 times during a ENC test, which caused the delamination to grow by an average of 60 mm. Each composite was tested 5 times, and the Mode II energy release rate causing crack propagation was calculated from the expression [6]:

$$G_{IIR} = \frac{9P^2a^2}{4b^2H^3E_{11}} \tag{7}$$

where E_{11} is the Young's modulus of the composite.

RESULTS AND DISCUSSION

Mode I Interlaminar Fracture Properties

Fig. 3 compares R-curves measured for the stitched composites under Mode I loading against theoretical R-curves calculated using equation 3. Also shown is a typical R-curve measured for the unstitched GFRP. The theoretical model is seen to calculate the Mode I interlaminar fracture toughness of the stitched composites with reasonably good accuracy. The theoretical R-curves predict a rapid increase in fracture toughness within the first 8 mm of crack growth. This is due to the formation of a stitch bridging zone behind the delamination crack front (as

represented in Fig. 1 as the region Δa). Once this zone has fully developed, the model predicts steady-state delamination growth where the G_{IR} value remains constant with further crack growth. The measured R-curves show however that the G_{IR} value does not remain constant,

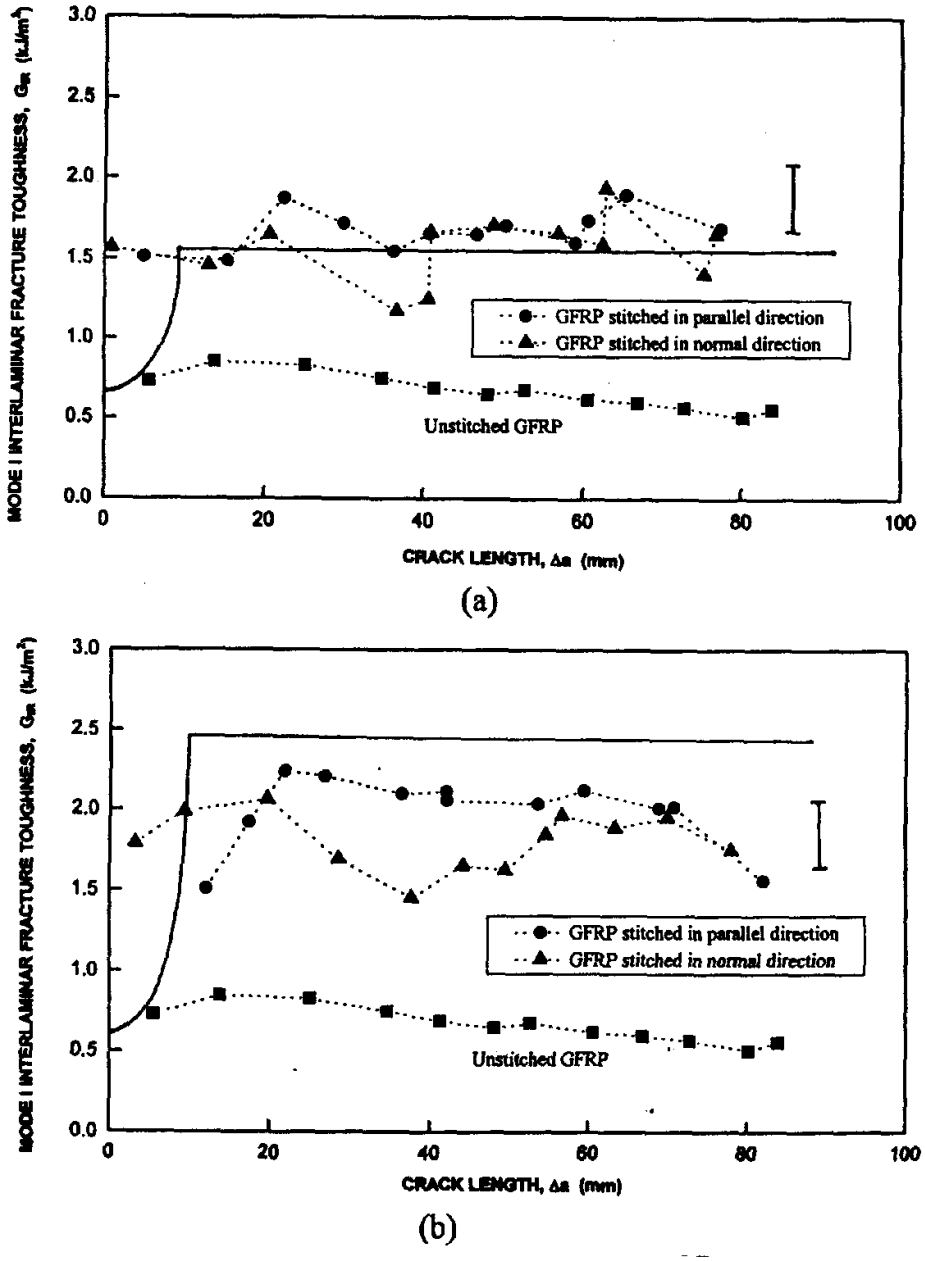

Fig. 3: Theoretical and measured Mode I R-curves for the GFRP composites stitched to a (a) low and (b) high stitch density. The theoretical R-curves are shown by the solid line

and this is because the delamination grew in a slip/stick process. In the DCB tests it was observed that when the delamination approached a row of stitches the crack growth speed was slowed until some of the stitches bridging the delamination failed under a higher load. This then allowed the delamination to propagate rapidly to the next row of stitches where the process repeated itself. This slip/stick fracture process contributed to the scatter in the G_{IR} values of the stitched composites, which is represented by the error bars in Fig. 3.

A comparison of the measured and calculated G_{IRs} values is presented in Table 1. The calculated toughness values are the same for stitching in the parallel and normal directions because the model does not account for stitch orientation. The measured values, however, show that stitch direction has a negligible influence on toughness. Good agreement is seen between the measured and predicted G_{IRs} values, although the model predicts a slightly higher value for the high stitch density composites.

Table 1: Comparison of theoretical and experimental G_{IRs} values

COMPOSITE	THEORETICAL	MEASURED
Unstitched GFRP	-	0.67 ± 0.11 kJ/m^2
GFRP stitched to low density in parallel direction	1.55 kJ/m^2	1.73 ± 0.20 kJ/m^2
GFRP stitched to low density in normal direction	1.55 kJ/m^2	1.63 ± 0.12 kJ/m^2
GFRP stitched to high density in parallel direction	2.45 kJ/m^2	2.27 ± 0.21 kJ/m^2
GFRP stitched to high density in normal direction	2.45 kJ/m^2	1.90 ± 0.13 kJ/m^2

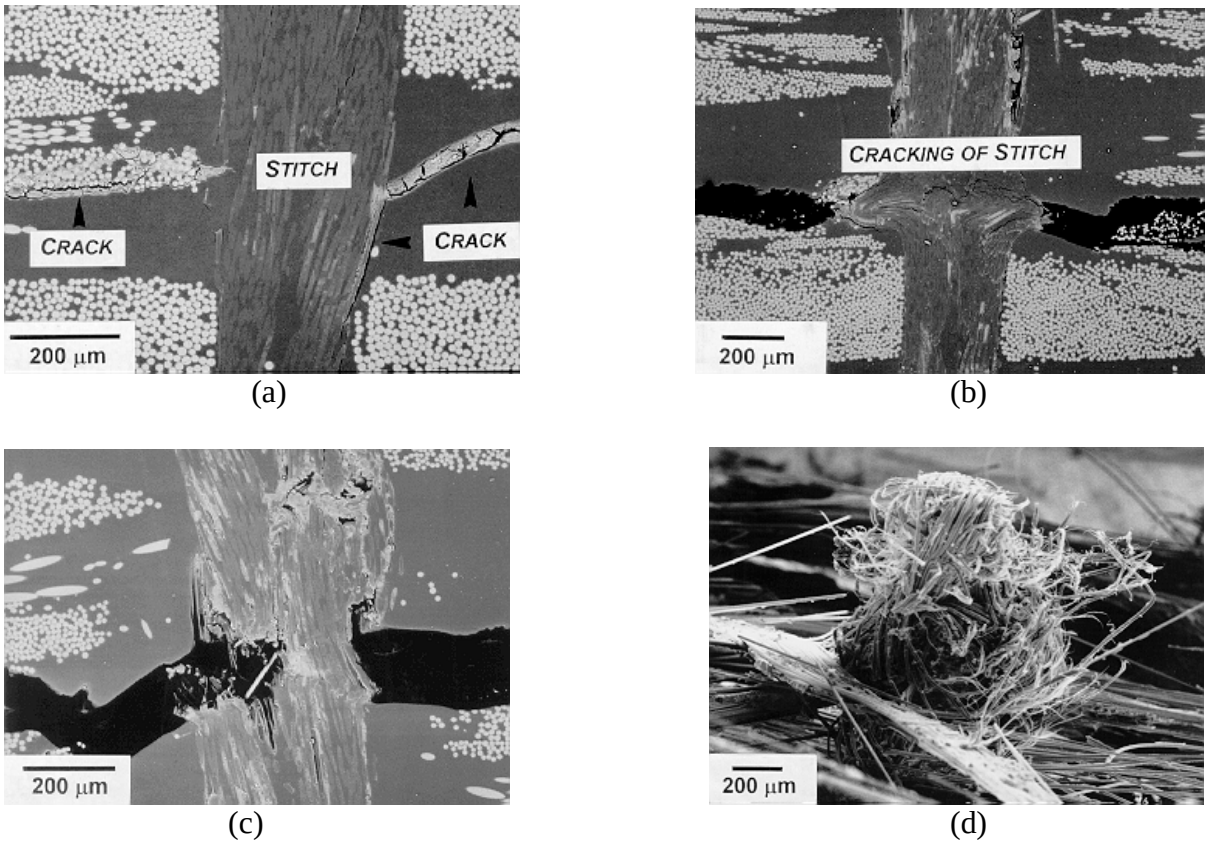

Fig. 4: SEM micrographs of stitches located (a) 2.5 mm, (b) 10 mm and (c) 25 mm behind the crack front as well as (d) a broken stitch on the fracture surface of a DCB specimen. The direction of crack growth is to the left

The fractured DCB specimens were examined in cross-section using scanning electron microscopy (SEM) to observe the delamination crack growth process and the failure mechanisms of the stitches. The delamination grew along the chopped glass mat layer at the mid-plane of the DCB specimen, and this promoted pull-out and bridging of these fibres

behind the crack front. This toughening process is responsible for the relatively high interlaminar fracture toughness of the unstitched GFRP. When the delamination reached a stitch it was deflected along the stitch/GFRP interface for 1-2 mm (Fig. 4a). This appeared to arrest the crack until a higher load caused the delamination to grow around the stitch without causing any damage to the Kevlar®. From this observation it appears that the crack tip deflection process contributes to the toughening of the GFRP by stitching. The undamaged stitches formed a crack bridging zone which extended for ~6 mm and 10-15 mm in the composites stitched to the low and high densities, respectively. The length of the bridging zone is the same or slightly longer than that predicted by the model (Δa = 8 mm). Towards the end of the bridging zone the Kevlar® filaments began to fail (Fig. 4b) shortly before complete tensile fracture of the stitch (Fig. 4c). Examination of the fracture surfaces revealed that filaments from the broken threads were pulled-out (Fig. 4d), and this is expected to contribute a small amount to the toughening of the stitched composites.

Mode II Interlaminar Fracture Properties

Fig. 5 compares R-curves for the stitched composites experimentally measured under Mode II loading against the theoretical R-curves calculated using equation 5. It is important to note that R-curves measured for the same composite showed considerable scatter, and this is represented in the figure by error bars. The theoretical R-curves are characterised by a small increase in G_{IIR} within the first 8 mm of crack growth, and then a steady-state crack growth condition exists for longer crack lengths. The measured R-curves also show an initial rise in G_{IIR}, which occurs over the first 15-20 mm. This is mainly from the bridging effect caused by the in-plane glass fibres of the chopped glass mat layer. The experimental curves then show a region where G_{IIR} remains constant or declines gradually with increasing crack length. This region is due to near steady-state crack growth, and the G_{IIRs} values measured from this region are compared with theoretical values in Table 2. This Table and Fig. 5 show that neither the stitch density nor stitch direction influenced the measured Mode II delamination toughness of the GFRP. The model, on the other hand, predicted a small improvement in toughness with increasing stitch density. However, considering the large amount of scatter with the measured G_{IIR} values, the model predicted the Mode II delamination toughness with reasonably good accuracy.

Table 2: Comparison of theoretical and experimental G_{IIRs} values

COMPOSITE	THEORETICAL	MEASURED
Unstitched GFRP	-	6.2 ± 0.4 kJ/m^2
GFRP stitched to low density in parallel direction	6.9 kJ/m^2	5.9 ± 0.4 kJ/m^2
GFRP stitched to low density in normal direction	6.9 kJ/m^2	6.0 ± 0.9 kJ/m^2
GFRP stitched to high density in parallel direction	7.6 kJ/m^2	6.6 ± 0.6 kJ/m^2
GFRP stitched to high density in normal direction	7.6 kJ/m^2	5.9 ± 0.4 kJ/m^2

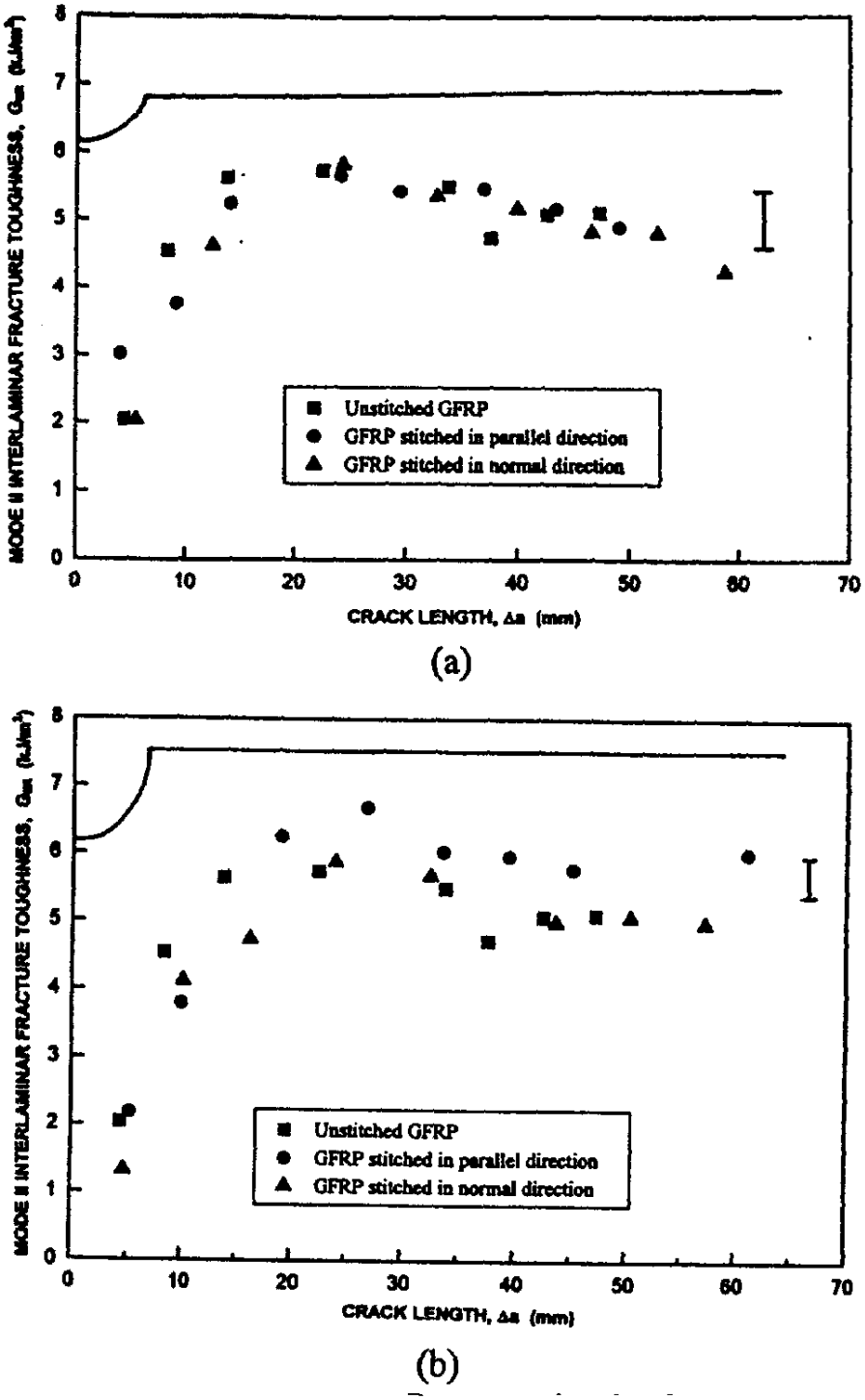

Fig. 5: Theoretical and measured Mode II R-curves for the GFRP composites stitched to a (a) low and (b) high stitch density. The theoretical R-curves are shown by the solid line

The inability of stitching to improve the Mode II fracture toughness was probably due to the intrinsically high toughness of the unstitched GFRP laminate. SEM examination of this composite after ENC testing showed that delamination crack growth occurred along the chopped glass mat layer located at the mid-plane of the specimen. This promoted extensive bridging of the chopped glass fibres across the opposing fracture surfaces behind the crack front. High shear forces would be needed to pull-out and break these fibres, causing a

substantial improvement in interlaminar toughness. Another feature of the fracture surfaces was their reasonably high roughness caused by the delamination weaving through the chopped glass mat layer. In the ENC tests it was observed that this roughness often caused the opposing fracture surfaces to interlock at high asperities, and increased loading was needed to shear these asperities before crack growth could continue. This toughening caused by surface traction combined with fibre bridging appear to be responsible for the high delamination resistance of the unstitched GFRP. The modelling reveals that the contribution to toughening from stitching was much less, and as a result the delamination resistance of the stitched composites were similar to the unstitched laminate.

Interlaminar fracture studies using the end notched flexure (ENF) test report that the Mode II delamination resistance of unidirectional CFRP composites is improved by stitching [2,7,8]. The G_{IIc} values of unstitched CFRP composites (~1.5 kJ/m^2) are much lower than the unstitched GFRP (6.2 kJ/m^2). This is because unidirectional laminates do not experience large amounts of fibre bridging and surface traction under shear loading. Stitching is then able to improve the fracture toughness by forming a bridging zone behind the crack front. For example, Jain [2] found that the G_{IIc} value for an unstitched CFRP laminate was 1.3 kJ/m^2, and this increased to 5.2 kJ/m^2 after stitching with Kevlar® yarn to a density of 12 stitches/cm^2. While this improvement in delamination resistance is considerable, the toughness of the stitched CFRP composite is still lower than the unstitched GFRP. As a result, the ability of stitching to improve the already tough GFRP laminate is lower than for a unidirectional CFRP composite.

After the ENC tests the stitched specimens were examined by SEM to identify the failure mechanism of the Kevlar® stitches under shear loading. Fig. 6 shows the stitches at various distances behind the crack front. When the delamination reached a stitch it was deflected along the interface between the thread and surrounding GFRP, and this fracture process was similar in appearance to that observed under Mode I loading (Fig. 4a). The crack then spread around the stitch without causing any damage. At a short distance (Δa = 6 mm) behind the crack front the stitches began to split along their length (Fig. 6b). This splitting spread across the stitch (Fig. 6c) leading to complete failure (Fig. 6d). The length over which the stitches bridged the delamination was observed to be ~20-25 mm for the two stitch directions and stitch densities. This stitch bridging zone was longer than that predicted by the model (~8 mm), but it corresponds to the region on the measured R-curves where the G_{IIR} increased with crack length for the first ~25 mm. It appears, therefore, that the initial increase in the R-curves is due to the formation of the stitch bridging zone as well as the chopped glass fibre bridging zone. It is worth noting that other Mode II delamination toughness studies [2,7,8] on stitched composites have used the ENF test method rather than the ENC technique. A limitation of the ENF method is that the crack can only be grown for ~25-30 mm, which is slightly longer than the length of the stitch bridging zone. In comparison, the maximum crack length with the ENC test is about 70-90 mm, and for this reason the ENC method is a better technique for measuring the steady state fracture toughness of stitched composites.

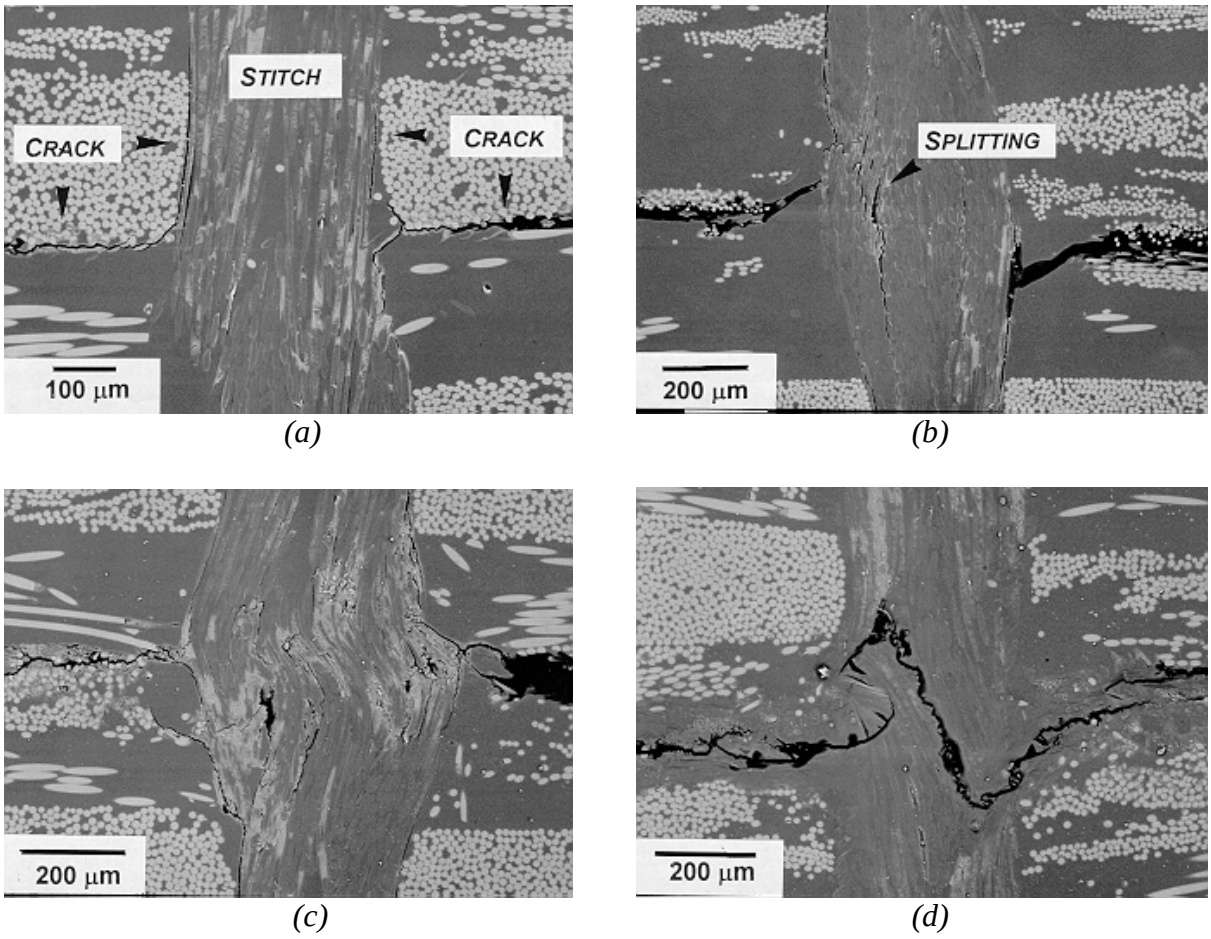

Fig. 6: Scanning electron micrographs showing increasing amounts of shear-type damage to the Kevlar stitches at distances (Δa) of (a) 3.5 mm, (b) 6 mm, (c) 15 mm and (d) 25 mm. The direction of crack growth is to the left

CONCLUSIONS

Theoretical models developed by Jain and Mai have been shown experimentally to calculate the Mode I and Mode II interlaminar fracture properties of stitched GFRP composites with reasonably good accuracy. The models are capable of predicting various fracture parameters, including the length of the stitch bridging zone, the shape of the R-curve, and the G_{IRs} and G_{IIRs} values. The Mode I fracture toughness of the GFRP composites was improved by stitching because of three toughening mechanisms: stitch bridging zone, crack deflection at the stitches, and pull-out of broken filaments from the stitches. The Mode II delamination was not improved appreciably by stitching because of the intrinsically high toughness of the unstitched GFRP laminate.

ACKNOWLEDGMENTS

The authors thank the Cooperative Research Centre for Advanced Composite Structures Ltd. (CRC-ACS) for manufacturing the specimens.

REFERENCES

1. Dransfield, K., Baillie, C. and Mai, Y.-W., "Improving the Delamination Resistance of CFRP by Stitching - A Review", *Composite Science and Technology*, Vol. 50, 1994, pp. 305-317.

2. Jain, L.K., "Improvement of Interlaminar Properties in Advanced Fibre Composites with Through-Thickness Reinforcement", Cooperative Research Centre for Aerospace Structures Ltd., Report CRC-AS TM 94012, 1994.

3. Jackson, A.C., Barrie, R.E., Shah, B.M. and Shulka, J.G., "Advanced Textile Applications for Primary Aircraft Structures", *Proceedings of Fiber-Tex 1992*, October 27-29, 1994, NASA Conference Publication 3211, pp. 325-352.

4. Jain, L.K. and Mai, Y.-W., "On the Effect of Stitching on Mode I Delamination Toughness of Laminated Composites", *Composite Science and Technology*, Vol. 51, 1994, pp. 331-345.

5. Jain, L.K. and Mai, Y.-W., "Determination of Mode II Delamination Toughness of Stitched Laminated Composites", *Composite Science and Technology*, Vol. 55, 1995, pp. 241-253.

6. Hashemi, S., Kinloch, A.J. and Williams, J.G., "The Analysis of Interlaminar Fracture in Uniaxial Fibre-Polymer Composites", *Proceedings of the Royal Society of London*, Vol. A427, 1990, pp. 173-199.

7. Ogo, Y., "The Effect of Stitching on In-Plane and Interlaminar Properties of Carbon Epoxy Fabric Laminates", University of Delaware, CCM-87,17, 1987.

8. Sharma, S.K. and Sankar, B.V., "Effect of Stitching on Impact and Interlaminar Properties of Graphite/Epoxy Laminate", *Proceedings of the Ninth American Society for Composites Annual Technical Conference*, September 20-22, 1994, pp. 700-708.

QUALITY ASSESSMENT DURING STITCHING OF REINFORCING TEXTILES FOR COMPOSITES

K-U. Moll, B.Wulfhorst

Institut für Textiltechnik der RWTH Aachen, University of Technology, Aachen (ITA), Eilfschornsteinstraße 18, D-52062 Aachen, Germany

SUMMARY: During stitching of reinforcing textiles the stitching parameters should be set for optimal reinforcing results in the manufactured composite. The damages of the sewing thread and the reinforcing textile should be minimized. The architecture of the sewing thread should be load bearing. For optimal results measurement devices were developed which are suitable to watch the relevant parameters (presser foot distance, needle thread tension) during the stitching process. This measurement devices allow a reproducable setting of the sewing machine. A test stand for the simulation of the loads of a sewing thread is also presented which is necessary to determine the damages of the sewing thread during the stitching process.

KEYWORDS: stitching of reinforcing textiles, composites, stitching parameters, measurement, machine settings, thread damages

INTRODUCTION

Since a very long time stitching is used for joining textile parts. It is the traditional way to manufacture clothes from woven or knitted textiles. There are a lot of requirements on the stitching process during the manufacturing of clothes. But the main aim is to manufacture stitching rows which cause no buckling of the textile and possess a high elasticity. The materials and the requirements differ completely from the demands which are relevant in the area of composites. Even at non-reinforcing technical textiles, like airbags, belts and others, the requirements are not to be compared with those in the area of composites.

Stitching reinforcing textiles for composites means that a reinforcing material should be introduced in the third dimension of the textile structure. For this the sewing thread should be placed in a load bearing geometry and its damages during the stitching process should be as low as possible. The reinforcing textile should also not be damaged by the stitching process. No additional crimp should be introduced by the sewing thread.

In the past investigations of stitching reinforcing textiles have been done in America [1, 2, 3], Asia [4, 5, 6], Australia [7, 8] and Europe [9]. Nearly always stitching has been performed by using conventional sewing machines. The machine settings were fixed in a way like they would have been fixed for stitching clothes, too. Improvements of the delamination resistance, the peeling resistance and the interlaminar shear strength of the manufactured composites have been measured. In this presentation new methods for exactly reproducable settings of the sewing machines and for an instant control of the stitching process are shown.

AIMS OF STITCHING REINFORCING TEXTILES FOR COMPOSITES

A lot of methods exist for the manufacturing of composites. These methods are mainly distinguishable by the way of wetting the reinforcing textiles with the matrix material. Nearly all these methods start with the placing of layers of reinforcing textiles in a mould. In most cases woven textiles are used. These layers are bonded together by the matrix material. Most matrix materials, especially the thermoset matrix materials, are very brittle. Their mechanical properties are worse in comparison with the reinforcing materials. Therefore the reinforcement of composite materials in z-direction is poor. As a result the mechanical properties in z-direction are not as high as in-plane. In z-direction the matrix material is mainly loaded and therefore the delamination resistance, the interlaminar shear strength and the peeling resistance are low.

In the past a lot of investigations have been made to manufacture three-dimensional reinforcing textiles. Examples for this textiles are multi-layered fabrics, knitted structures for the production of sandwich panels and three-dimensional braids. They all have a three-dimensional geometry and a three-dimensional fibre architecture. Using these textiles for the production of single parts or structures leads to high mechanical properties in z-direction which are caused by three-dimensional fibre orientation. The in-plane properties are reduced by some fibres of the x-y-plane guided into z-direction. Additionally this textiles must often be joined to flat structures. One prominent example for this are stringer stiffened panels. The joining of two different composites structures is often done by adhesives. Therefore the joining zone is non-reinforced again and its properties in z-direction are low. For the optimal transmission of loads from one structure to the other the joining zone should content reinforcements which might be loaded by shear and peeling loads. For manufacturing such reinforcements, stitching is a suitable process. The reinforcing textiles should be stitched together before the wetting process.

Manufacturing complex shapes from conventional (2-D) reinforcing textiles means that every single one has to be draped and deformed. The preforming of several layers in advance is difficult because the single layers are slipping. Stitching is a good alternative for a fixation of single layers. Additionally by a combination of stitching and folding processes new 3-D preforms might be manufactured which are reinforced in discrete regions by the reinforcing sewing thread and the handling properties of the preform are improved by this fixation.

Therefore several investigations are described in literature for an improvement of these mechanical properties by stitching reinforcing textiles. Some other advantages of stitched joining zones might be mentioned. Bonded joining zones which are manufactured by an adhesive are influenced by temperature. Most adhesives are getting soft by increasing temperature and their brittleness increases rapidly with decreasing temperature. They may show their best mechanical properties only in a very narrow range of temperature. Using stitching as a joining method the properties in the joining zone are changed by the temperature in the same way as in-plane.

The use of adhesives to join two composite parts means that the separate parts have to be prepared for the bonding process. The quality of a bonded joining area depends on the thickness of the bonding zone. Bonding together two plain parts will not cause any problems, but if the separate parts are curved it is necessary to manufacture these two parts with exactly

the same curvature. This is not always possible. During stitching the textiles are fixed together before the wetting process. They might be bended after the stitching process.

But also the stitching process must be controlled for getting highest performing joining zones. Possible control mechanisms are shown in this presentation.

PARAMETERS TO BE CONTROLLED DURING STITCHING REINFORCING TEXTILES

Some parameters might be set for the stitching process at the sewing machine. One very important parameter is the geometry of the needle, but the selection of an useful needle for stitching reinforcing textiles can be done in pre-tests. If we are investigating the parameters of a lock-stitch sewing machine further parameters are the turning speed of the main shaft, the pressure of the presser foot and the tensions of the needle thread and the lower thread.

The range of tensions of the lower thread is very narrow for a non-critical stitching process. The tension of the needle thread influences the position of the knot in z-direction because a equilibrium of forces between both the two thread tensions and the friction with the stitched textile is working. As a result of a very low tension of the needle thread the knot will be positioned at the bottom of the stitched textile. At a very high tension of the needle thread the knot will lay on top of the stitched textile. Despite the fact that the position of the knots for clothing textiles is only an asthetical aspect, it is very important for technical textiles, especially reinforcing textiles. The position of the thread will influence the mechanical properties of the whole composite part.

A suitable pressure of the presser foot influences the trouble-free tightening of the knot. As the knot is tightened during the upward movement of the needle, it is important to prevent an upward displacement of the top layers. That is done by the presser foot, too. At lock-stitch sewing machines the pressure is also necessary for a reliable transport of the stitched textiles which is responsible for regular stitch-lengths. Therefore the pressure is also in general an important parameter for stitching. This pressure is suitable for a compression of the reinforcing textiles during the stitching process.

During the consolidation process additionally a compression of the reinforcing textiles happens. It is possible to calculate the thickness t [mm] of the composite by knowledge of the areal weight of a reinforcing textile m_a [g/m²], the aimed fibre volume fraction of the composite to be manufactured φ_F, the density of the fibre material ρ_F [g/cm³] and the number of layers of the reinforcing textile with help of equation 1.

$$t = \frac{n * m_a}{\rho_F * \varphi_F * 1000}. \qquad (1)$$

If the reinforcing textiles are compressed during stitching to a thickness which is bigger than t the reinforcing sewing thread might be crimped during the consolidation process. Thereby it looses its load bearing architecture (see figure 1). If the pressure is too high the structure of the composite will be deeply disturbed in the area of the stitching row (see also figure 1). From this point of view it is not important to control the pressure itself but its effect concerning the thickness of the stitched textile.

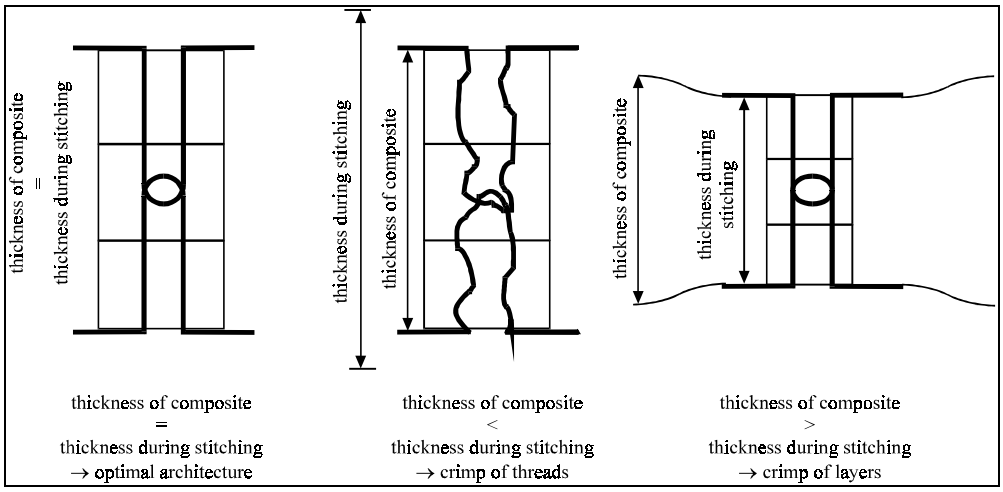

Fig. 1: Effects of different pressures on composite structures

MEASUREMENT OF THE PARAMETERS DURING THE STITCHING PROCESS

For the measurement of the above described parameters a measurement device has been adapted at a lock-stitch sewing machine. An incremental optical encoder has been mounted on the main shaft. Its output signal is a rectangular voltage between 0 and 5 V. It has a resolution of 480 partitions. That means that at every turning angle of 0.75° of the main shaft a measurement of the parameters is triggered.

The lock-stitch sewing machine possesses a triple feed system (unison feed). Besides the drop feed the needle movement describes an elliptical curve. That means that the needle supports the feeding action by the feed-synchronized needle motion. Additionally a top feed is installed, which consists of two presser feet. One of these feet moves only upwards and downwards, the other one moves up and down and additionally in the horizontal direction. Therefore this is the third transport mechanism of the stitching machine. The movement of the presser feet happens in a alternating way. Therefore the textile is always in contact with at least one presser foot, and is always compressed. One of the presser feet rests on the needle plate, the other one on the drop feed if no textile is stitched. During stitching a textile the distance between the presser feet and the needle plate respectively the drop feed is the thickness of this textile loaded by the presser feet. The unison transport is shown in figure 2.

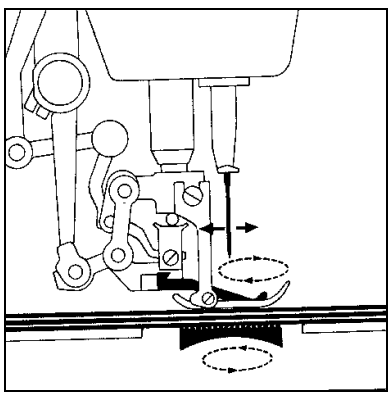

Figure 2: Unison feed of the used lock-stitch sewing machine

At each presser foot a distance encoder has been fixed. Their signal is set to zero if the presser feet are resting on the needle plate or the drop feed. With the textile between the presser feet and the drop feed respectively the needle plate the thickness of the compressed textile is measured. The measurement of the thickness is triggered by the signals of the incremental optical encoder. That means that 480 signals are derived from each presser foot per turn of the main shaft of the sewing machine respectively per stitch cycle. They are on-line stored and analysed by a computer. They are also set in relation to the turning angle of the main shaft. The sensors possess also a very high resolution. It is possible to measure differences smaller than one micron.

A RES measurement device is integrated in the run of the needle thread. It is responsible for the measurement of the needle thread tension. The measurement of the needle thread tension is also triggered by the incremental optical encoder and the signals are set in relation to the turning angle of the main shaft of the machine.

A schematic view of the measurement systems is shown in figure 3. The systems allow the control of the parameters as well as the reproduction of settings of the machine. Both aspects allow the assessment of the quality during stitching reinforcing textiles for composites. This is shown in an example in the following paragraph.

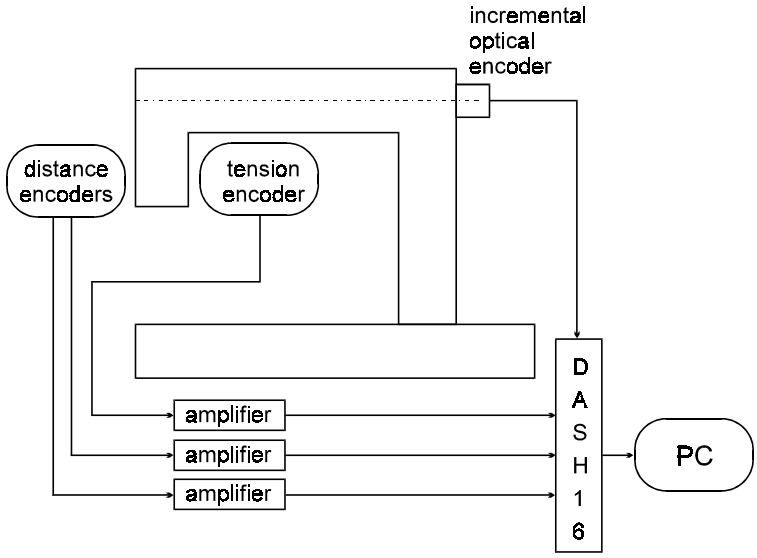

Figure 3: Schematic view of the measurement system

If 18 layers of a woven glass fabric with an areal weight of

$$m_a = 163 \text{ g/m}^2 \tag{2}$$

should be used for the production of a composite the fibre volume fraction might be assumed as

$$\varphi_F = 50 \text{ \%}. \tag{3}$$

With this the thickness of the resulting composite can be calculated as

$$t = 2.3 \text{ mm}. \tag{4}$$

Therefore the pressure of the presser feet should be fixed in a way that the textile layers are compressed to a thickness of 2.3 mm during the stitching process. The measurement of the thickness during the stitching process has never been done before, but it is a convenient method to measure a very important parameter during the process.

The measurement of the tension of the needle thread is also important for the quality assessment during stitching reinforcing textiles. It might be a parameter which is important for later calculations of the mechanical properties of the composites. Both measurements are shown in figure 4.

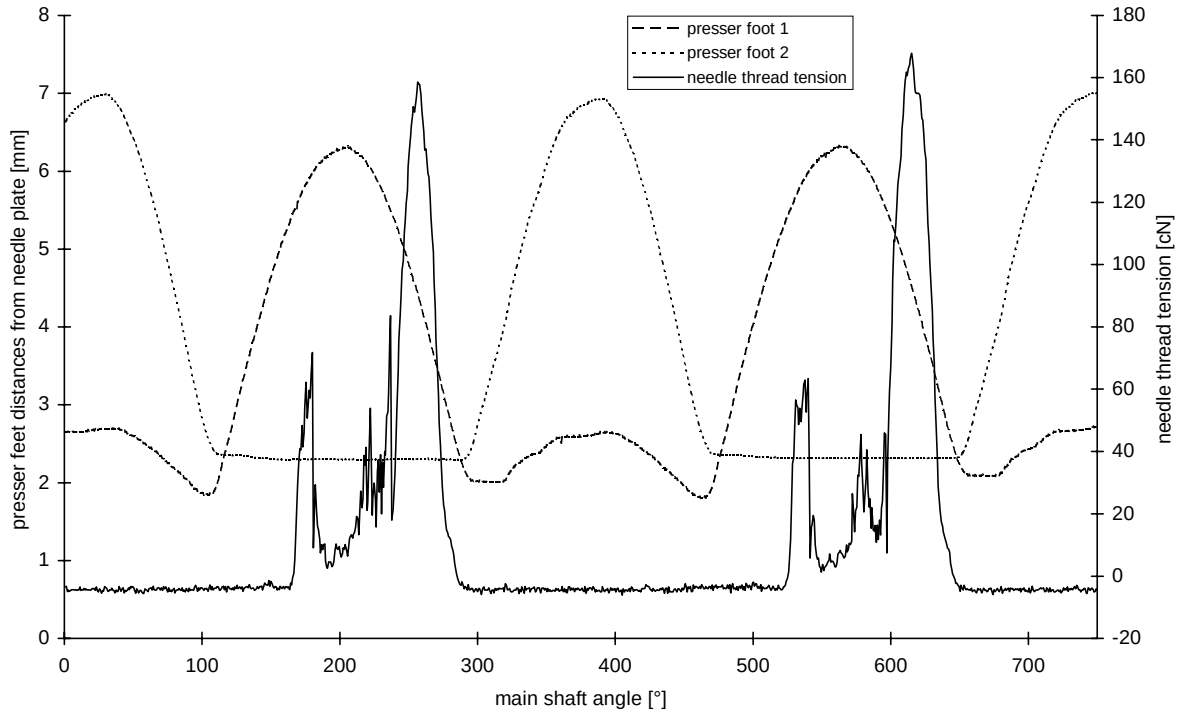

Fig. 4: Measurement of presser feet distances from the needle plate and needle thread tensions

The needle thread tension is also responsible for thread damages. For this reason the measurement of the tension is important.

MEASUREMENT OF THREAD DAMAGES

Up to now it was not possible to evaluate exactly the thread damages occuring during the stitching process. As in stitching clothing textiles typically polyester threads are used which are not very brittle this topic is not as relevant there as in stitching reinforcing textiles. Using a carbon or glass thread during stitching reinforcing textiles can cause thread damages because of their high brittleness and the small bending curvatures combined with the abrasive-loads which are working on the threads during the stitching process.

It is not possible to dissect the thread out of the stitched textile and do some tensile tests with it. During the preparation of this tests additional damages are caused. It is not possible to determine the amount of this damages.

The needle thread carries the highest loads at a lock-stitch sewing machine. The thread passes the needle hole many times before it is brought into the seam. The aim was to design a test stand at which the loads are simulated.

At a sewing machine with a drop feed the needle thread is teared off the bobbin during the feeding movement. The drawing off is induced by the movement of the stitched textile. This happens when the needle is above the needle plate. At a sewing machine with an unison feed the drawing off also happens during the feeding of the textile, but then the needle actually penetrates the textile. No relative movements between the textile and the thread occur, because the needle and the thread are moving in the same direction with the same velocity. The feeding happens during a defined turning angle of the sewing machine. First it is important to know this angle during which the feeding happens.

To copy all the brakes and all the machine parts which are in friction with the thread and bending it would be very complex. Therefore a drawing off system was adapted to the lock-stitch sewing machine.

The thread passes all machine parts like in the usual stitching process. The process is done without a lower thread. That means that the small friction between the needle thread and the lower thread is not considered. The needle and the needle thread are not passing a textile which is fed by the machine but the needle thread is guided to a bobbin. The bobbin turns with the same velocity and about the same length like the textile would be fed by the unison feed. That means that the drawing off of the bobbin and relative movements between the needle thread and the machine parts are completely the same like during stitching a textile. That moment at which the drawing off starts is given by a signal of the incremental optical encoder. A computer takes this signal as a triggering and outputs a signal to a stepping motor. This stepping motor is connected with a bobbin which takes the thread on. The system is shown schematic in figure 5.

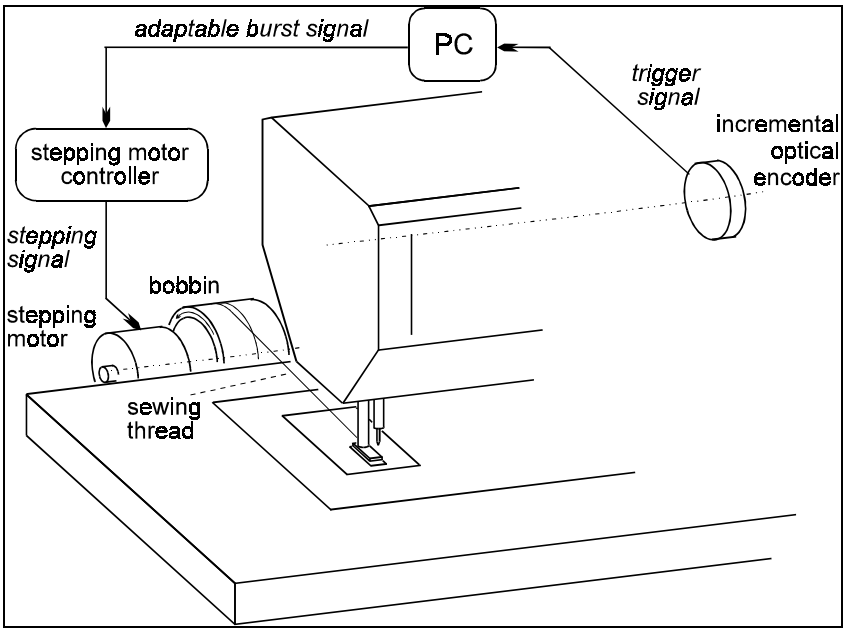

Figure 5: Take up mechanism for the sewing threads loaded during the sewing process

With the thread which is wound on the bobbin tensional tests can be performed. The measured tensile strength is a sign for the filament damages of the sewing thread. With this results the stitching parameters and especially the needle thread tension might be optimized to perform a stitching process with as low as possible filament damages of the sewing thread. This investigations are necessary to make use of the full performance of the threads.

The investigations have been done with a glass filament thread with a total fineness of 138 tex. In these tests the sewing machine ran with a speed of 180 tpm. Higher speeds are possible. The measurement of the needle thread tension is similar to that shown in figure 4. The statistical results of the tensile tests are given in table 1.

Table 1: Tensile strengths of loaded and non-loaded glass filament sewing thread, sewing machine speed for loading the thread: 180 tpm

	thread non-loaded	thread loaded during stitching process
tensile strength [N]	60,72	47,21
standard deviation [N]	4,75	5,06

The results documented in table 1 show that a damage of the glass filament sewing thread occurs. Even with the very low turning speed of 180 tpm the damage occurs. With higher turning speeds and other stitch lengths more damages will occur.

POSITIVE NEEDLE THREAD FEED

The used sewing threads are typically manufactured from reinforcing filaments. They are wound on bigger bobbins than typical sewing threads, e.g. polyester sewing threads. The yarns are very slippery. Therefore their single windings are falling down if the bobbin is placed vertically for the sewing process. Filament damages and a wide range of needle thread tensions are the results. Covering the bobbin with a cloth prevents the falling down of the single windings, but the neddle thread tension changes thereby in a very wide range depending on the actual position of the thread. Therefore a mechanism was developed in which the bobbin is placed horizontally on the shaft of a stepping motor. During each stitching cycle the stepping motor turns as far as needle thread is necessary for a perfect performance of the stitch. Thereby the tension of the needle thread is always the same during all stitching cycles.

The positive needle thread feed is a similar system to the mechanism which draws on the needle thread as described before. Its development is a result of the investigations which are done with the measurement systems and reduces thread damages. Therefore it belongs to the area of quality assessment methods during stitching.

CONCLUSIONS

The presented measurement systems are a new and necessary way to improve the quality of composites manufactured from stitched reinforcing textiles. They allow to set the sewing

machine in an optimal way to produce composites with load bearing structures of the sewing threads. They also allow to reproduce the settings of a machine and to show correlations between the stitching parameters and the mechanical properties of the composites.

With the measurement of thread damages a new method has been developed which gives the possibility to examine the properties of sewing threads after the stitching process. This has not been necessary in the area of clothing textiles because of the low brittleness of the sewing threads. Using now glass and carbon threads for the stitching process makes the new information useful. Especially for the calculations or simulations of the mechanical properties of stitched joining zones in a composite it is necessary to assume the mechanical properties of the sewing thread.

This shows that the typical measurement systems of textile technology might be useful for new results in stitching reinforcing textiles for composites.

The paper gives an overview over the methods used for the improvement of the properties of composites manufactured of stitched reinforcing textiles. First tests with the systems have been done. The complete results will be shown during the oral presentation of the paper.

REFERENCES

1. Mignery, L.A., Tan, L.M., Sun, C.T.: The use of stitching to suppress delamination in laminated composites. Johnson, W.S. (ed.): Delamonation and Debonding of Materials, ASTM STP 876, Philadelphia/USA: ASTM, 1985, 371-385.

2. Sawyer, J.W.: Effects of stitching on the strength of bonded composite single lap joints. AIAA Journal 23 (1985), 1744-1748.

3. Portanova, M.A., Poe, C.C., Whitcomb, J.D.: Open hole and post-impact compression fatigue of stitched and unstitched carbon/epoxy composites. NASA TM 102676, 1990

4. Du, X., Xue, F., Gu, Z.: Experimental study of the effect of stitching on strength of a composite laminate. International Symposium on Composite Materials and Structures (Beijing 10-13/06/1986). Proc., Lancaster/PA/USA: Technomic, 1986, 912-918

5. Liu, D., Kim, Y.G., Hong, S.: Stitching as joint in woven composite plate. ASM/ED: 3rd Annual ASM/ESD Adv. Comp. Conf. (Detroit/MI/USA 15-17/09/1987), 343-347

6. Matsuhisha, Y, Hiramatsu, T., Nishimara, A: Z-directional laminate reinforcing material. High performance Torayca carbon stitching thread. SAMPE: 33rd Int. SAMPE Symposium and Exhibition (Anaheim 07-10/03/1988)

7. Herszberg, I., Bannister, M.K.: Tensile properties of thin stitched carbon/epoxy composites. Cooperative Research Centre for Aerospace Structures: 5th Australian Aerospace Conference (09/1989), Proc. ACN 059048770, Victoria: CRC-AS Ltd., 1993

8. Herszberg, I., Bannister, M.K.: Compression and compression-after-impact properties of thin stitched carbon/epoxy composites. Cooperative Research Centre for Aerospace Structures: 5th Australian Aerospace Conference (09/1989), Proc. ACN 059048770, Victoria: CRC-AS Ltd., 1993

9. Mc Illhagger, R., Hill, B.J., McLaughlin, P.: Flexural properties of sewn carbon-fibre composites. Journal of the Textile Institute 83 (1992), 614-620

OPEN HOLE FATIGUE OF STITCHED AND UNSTITCHED CARBON/EPOXY LAMINATES

I. Herszberg[1], A. Loh[1], M.K. Bannister[2], H.G.S.J.Thuis[3]

[1] The Sir Lawrence Wackett Centre for Aerospace Design Technology, Department of Aerospace Engineering, Royal Melbourne Institute of Technology, P.O. Box 2476V, Melbourne, VIC, 3001, Australia.

[2] Cooperative Research Centre for Advanced Composite Structures (CRC-ACS), 506 Lorimer Street, Fishermens Bend, VIC 3207, Australia

[3] Advanced Composites Structures Department, National Aerospace Laboratory, P.O.Box 153, 8300 AD Emmeloord, The Netherlands.

SUMMARY: Tension-compression open hole fatigue tests were conducted to determine the effect of stitching on the delamination damage progression and fatigue life of notched carbon/ epoxy laminates. The specimens were made from uniweave fabric stitched with Kevlar or Dyneema thread at various stitch densities and subsequently impregnated by resin transfermoulding. The specimens had a 6 mm hole drilled at their centre and were supported by anti-buckling plates with a 25 x 62 mm window surrounding the hole. They were cycled, up to a maximum of 100,000 cycles, between the tension and compression loads required to achieve, far-field strains of ± 0.35%. It was concluded that the low density Kevlar stitched specimens had better fatigue resistance than the unstitched specimens and the low density stitched Dyneema specimens had even better fatigue resistance. On the other hand, the fatigue resistance of the high density stitched Kevlar specimens was inferior to that of the unstitched specimens.

KEYWORDS: open hole fatigue, stitched composites, carbon/epoxy composites, delamination progression

INTRODUCTION

The manufacture of composites from stitched woven carbon cloth and impregnated by a liquid moulding techniques, such as Resin Transfer Moulding (RTM), has the potential to produce low cost high quality components with improved resistance to delamination. The increase in damage tolerance and resistance of such stitched composite depends on many parameters such as laminate thickness and stitching yarn properties and density. A major motivation for stitching preforms is the potential to greatly reduce the cost of component manufacture by reducing RTM tooling costs and to reduce the number of components in the structure, hence reducing the assembly costs. Consequently, stitched preforms may be used solely for manufacturing considerations, even for configurations which do not benefit from increased damage tolerance. To facilitate the use of such materials in aircraft production, it is essential that their mechanical properties are characterised.

To this end, a collaborative program between The Cooperative Research Centre for Advanced composite Structures (CRC-ACS), and National Aerospace Laboratory, The Netherlands (NLR) was undertaken to explore the mechanical properties of carbon/epoxy laminates stitched with Kevlar or Dyneema. Preliminary results of the static properties have been

reported by Thuis and Bron [1]. This follows previous studies at the CRC-ACS on the tension [2], compression [3] and compression-after-impact [3-5] of Kevlar stitched carbon/epoxy laminates. An extensive review of the effect of stitching on the in-plane mechanical properties of fibre reinforced plastics has been conducted by Mouritz et. al. [6] where they summarise the limited amount of work which has been reported to date on the fatigue properties of stitched composites.

Most reported fatigue studies of stitched composites involved compression-compression loading. Lubowinsky and Poe [7] found that stitching improved fatigue life, despite the local damage and fibre distortion caused by stitching. On the other hand, others (eg Furrow et al. [8]) found that stitching did not effect the fatigue performance. In particular Portanova and Poe [9] found open hole fatigue performance was unaffected by stitching. Shah Khan and Mouritz [10] have studied the fatigue performance of stitched and unstitched GFRP under zero-to-tension cycling and they report a substantial reduction in fatigue life due to stitching. This was attributed, in part to damage caused by stitching. Xiao and Bathias [11] have conducted tension fatigue tests on unstitched notched (open hole) and unnotched woven glass/epoxy laminates and they have reported that the notched and un-notched laminates had the same ratios of fatigue strength to ultimate tensile strength.

An investigation has been undertaken to determine the effect of stitching on the open-hole fatigue performance of carbon/epoxy laminates subject to tension-compression cyclic loading. In particular the effect of stitching on the progression of delamination has been studied. This paper presents preliminary results of this investigation.

SPECIMENS MANUFACTURE AND DEFINITION

The test specimens used for the present study were machined from panels produced by impregnating stitched and unstitched woven carbon preforms with epoxy resin, using the Resin Transfer Moulding (RTM) process.

The preforms were manufactured from 17 layers of Ciba Composites GU-230-E01 uniweave fabric with a lay-up of [45, -45 ,45 , 0, -45, 90, 45, -45, 0, -45, 45, 90, -45, 0 , 45, -45, 45]. The warp tows were 3K T300 (or equivalent) and they formed 90% of the fibres. The weft included special yarns to facilitate resin infusion by RTM. The fabric had a fine surface spray of partially cured epoxy which facilitated preforming.

Some of the preforms were stitched, respectively, with a twisted 40 tex (2×20) Kevlar thread or a twisted 16.5 tex (3 x 5.5) Dyneema thread. A modified lock-stitch was used, where the knot was adjusted to lie within the top fabric layer. The stitch rows were oriented at 0°, with a stitch pitch of 3.6 mm and spacing of 7.0 mm to produce a stitch density of four stitches per cm^2. A high density stitching of ten stitches per cm^2 was achieved by spacing the stitch rows at 3.5 mm and reducing the stitch pitch to 2.9 mm. Further details of the stitch geometry are presented by Leong et al. [5]

The preforms were impregnated, using the closed mould RTM process, with Ciba Composites LY 5052 epoxy resin, in conjunction with HY 5052. They were cured for four hours at 55°C. The nominal panel thickness was 3.5 mm, giving a fibre volume fraction (carbon only) of 60%. In fact, the specimens had an average thickness of 3.66 mm (standard deviation 1.6%) with a corresponding fibre volume fraction of 57%.

The specimens, of dimension 50 x 250 mm and described in Fig. 2, were cut from the panels so that the stitch rows were parallel to their loading direction. A 6.0 mm hole was drilled in their centre and left in the as-drilled condition. Steel end tabs and aluminium clip-gauge tabs, as shown in Figs. 1 and 2, were bonded to the specimens using Redux 420A/B adhesive and cured for 4 hours at 50°C. The aluminium clip-gauge tabs, of dimension 5 x 10 mm were located so that their centreline was 10 mm to one side of the centre of the hole and the gap between them was 14 mm to accommodate the clip-gauge extensometer (MTS model 632.03C-02).

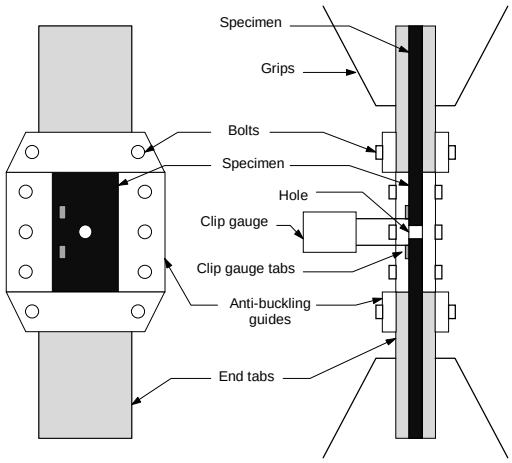

Fig. 1: Schematic of fatigue test showing anti-buckling guides, clip gauge and clip gauge tabs

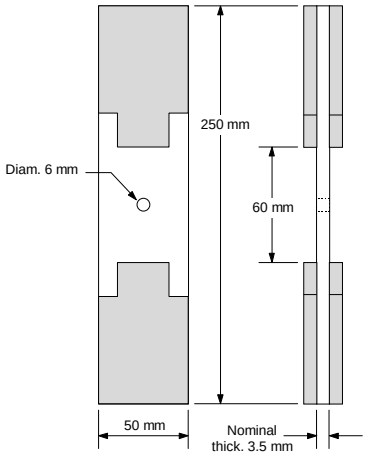

Fig. 2: Fatigue specimens and steel tab lay-out

TEST PROCEDURE

Four specimens were tested, of each of the four stitch configurations, which were: unstitched, low density Kevlar stitching, high density Kevlar stitching and low density Dyneema stitching. Specimen details and their uncycled static ultimate tensile (UTS) and compressive (UCS) are summarised in Table 1. Each of the specimen was allocated a four digit identification number. The first two digits define the specimen type and the following two digits allowed discrimination among individual specimens. For example, specimens 1217 and 1220 are two of the Kevlar low density stitched specimens.

Table 1: Specimen details and static strengths

Specimen Type	Stitching		No. Cycled	Ultimate Strength (MPa)	
	Type	Density /cm^2		Tension	Compression
11	unstitched		4	335	223
12	Kevlar 40 tex	4	4	323	226
13	Kevlar 40 tex	10	4	321	n/a
15	Dyneema 16.5 tex	4	4	326	243

Each specimen was loaded, at room temperature, in tension/compression fatigue at a frequency of 5 Hz under load control, between the tension and compression loads required to achieve, respectively, far-field strains of +/- 0.35% in the uncycled specimen. During the test these strains increased considerably. Those specimens which did not fail sooner, were subjected to 100,000 cycles, after which their residual compressive strength was measured. At the beginning of the test and at 10,000 cycle intervals the specimens were subject to visual inspection, an ultrasonic inspection and a strain survey. During cycling the specimen was constrained from buckling by antibuckling guides. Details of the test procedure and equipment are presented below.

Fatigue Cycling

The tests were conducted at room temperature (18°C to 24°C) using a 100 kN MTS servo-hydraulic test machine fitted with hydraulic grips and controlled by a MTS Teststar control and data acquisition system, which was also used for data acquisition.

The specimens were cycled, under load control, with constant amplitude at a frequency of 5Hz to a maximum of 100,000 cycles. The maximum and minimum loads were chosen to correspond, respectively to a far-field strain of +/- 0.35% in the uncycled specimen. They were typically 20 kN and 19 kN respectively. Such high strain levels were chosen so that significant fatigue damage would occur, in order to assess the effects of stitching. This level was in fact appropriate as evidenced by the fact that five of the sixteen specimens tested failed at fewer than 100,000 cycles. The tests were interrupted at 10,000 cycle intervals in order to conduct strain surveys and allow inspection of the specimen.

In order to determine the load limits, one specimen for each type had a strain gauge located 25 mm above the centre of the hole which measured the far-field strain. This specimen was loaded in tension, under load control, at a rate of 125 N/sec until a strain of 0.35% was reached, at which time the test was terminated. The corresponding load was used as the maximum load for subsequent cycling. The test was repeated in compression in order to determine the minimum load. The same fatigue profile was used for all specimens of one type.

Anti-Buckling Guides

The specimens, prior to testing, were fitted with an anti-buckling guide so as to leave an unsupported region of 60 mm x 25 mm around the hole. The configuration of these guides is shown in Fig. 1. To accommodate the compressive strain, there was a 1 mm gap between the top and bottom of the guides and the respective end-tabs. The specimen was clamped between the specimen with the aid of bolts which were adjusted until finger-tight. At each 1,000 cycle inspection interval the guides were removed and refitted before subsequent testing.

The out-of-plane deflection of a number of specimens was measured during a number of strain surveys with the aid of an LVDT located close to the hole. In the worst case an out-of-plane displacement of 0.04 mm was measured at a load of 22 kN, which corresponds to a maximum bending stress of less than 2% of the total compressive stress. This demonstrated that the guides were effective.

In-Situ Ultrasonic C-Scan

An in-situ ultrasonic scanner, based on the time of flight technique, was used to monitor damage growth without the necessity to remove the specimen from the test machine. The system uses a semi-impervious membrane and water couplant to transmit the signals from a 10 MHz focused ultrasonic transducer and it has a resolution of 1 mm^2. A description of the system, its operation, calibration and validation is reported by Galea and Saunders [12].

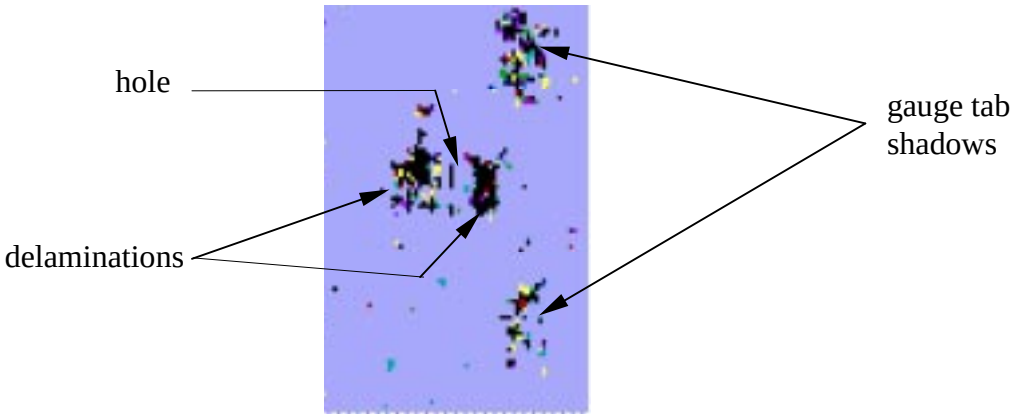

Fig. 3: C-Scan of stitched specimen 1320 after 30,000 cycles

At each inspection interval the antibuckling-guide was removed and the specimen was C-scanned. Fig. 3 is an example of such a C-Scan which clearly shows the damage area extending laterally from the hole. The clip-gauge tabs caused interference which resulted in the apparent damage pattern at the top and the bottom of the right hand side of the hole.

Strain Surveys

The strain surveys which were conducted at intervals of 10,000 cycles, involved loading the specimen progressively, at a rate of 500N/sec, up to the maximum load then decreasing the load, at the same rate, down to the minimum load (compression) and again increasing the load to zero. Data was recorded, at 0.25 second intervals, for applied load and strain from the clip gauge. The slope of the resulting load vs strain plot, called the load/strain parameter (LSP) was monitored. The change in the LSP is a manifestation of the extent of material degradation which caused a loss of stiffness in the region of the hole and a consequential redistribution of the load path. The load/strain ratio (LSR) was defined as the ratio of the LSP to its value for the uncycled specimen.

RESULTS AND DISCUSSION

For all specimens delamination cracks were visible in the sides of the hole after the first 10,000 cycles. These cracks progressed laterally from tool marks in the wall of the hole. In

most cases the initial rapid growth of the delamination reached a plateau and subsequently resumed its growth (eg Fig.4[a]). The load/strain ratio followed a similar, but inverse, progression (eg Fig.4[b]). A total of five of the 16 specimens tested failed at fewer than 100,000 cycles. As is to be expected from fatigue test there was considerable scatter in the data. However, there are indications that the low density Kevlar stitched specimens had better fatigue resistance than the unstitched specimens and the low density stitched Dyneema specimens had even better fatigue resistance. On the other hand, the fatigue resistance of the high density stitched Kevlar specimens was inferior to that of the unstitched specimens.

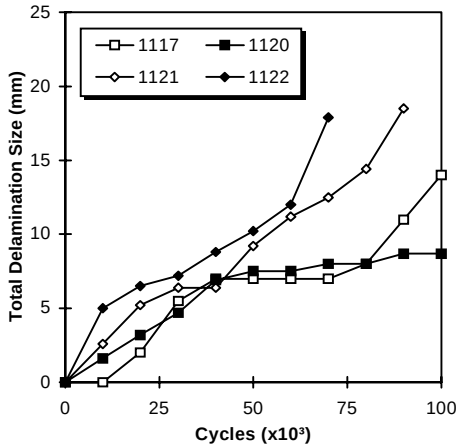

Fig. 4[a]: Delamination progression unstitched specimens

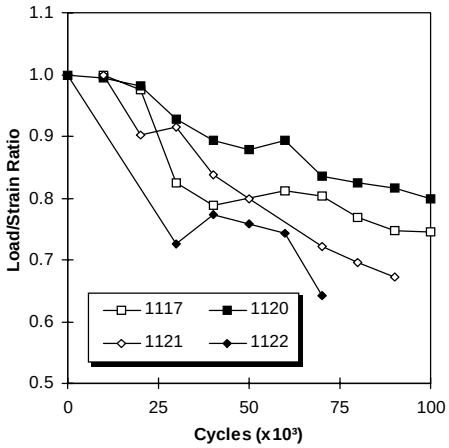

Fig. 4[b]: Progression of load/strain ratio unstitched specimens

Damage Progression

Various forms of damage were manifest as the cycling progressed these included: delamination, transverse cracks, matrix and fibre pulverisation and stitch debonding. There were indications that delamination and transverse crack growth were arrested for a while at the stitch rows, however, they were not conclusive.

Delamination damage growth was monitored via C-Scan and the progression of changes in the load strain ratio gave an indication of general damage accumulation and growth. Figs. 4[a] to 7[a] describe the behaviour of the delamination growth where, typically, the initial rapid growth reached a plateau and subsequently resumed its growth. Figs. 4[b] to 7[b] describe the progression of the LSR, which is a manifestation of the extent of material degradation. It, typically, followed a similar, but inverse, progression to the delamination growth.

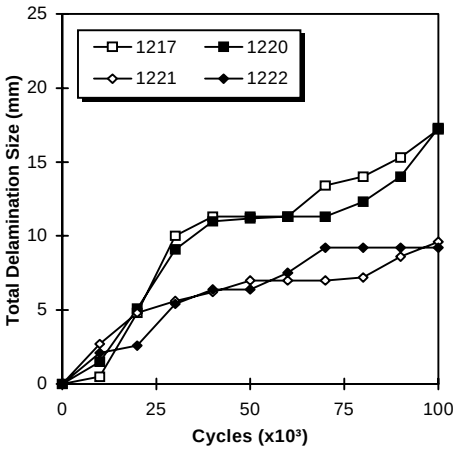

Fig. 5[a]: Delamination progression Kevlar low density stitched specimens

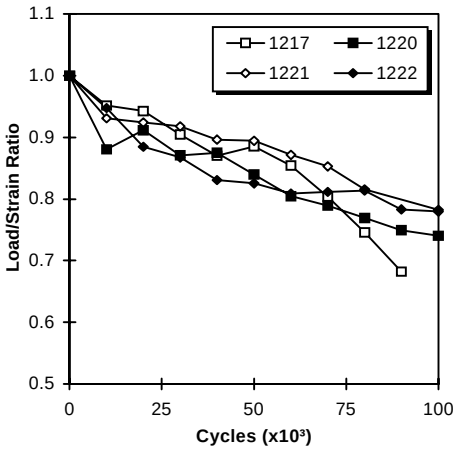

Fig. 5[b]: Progression of load/strain ratio Kevlar low density stitched specimens

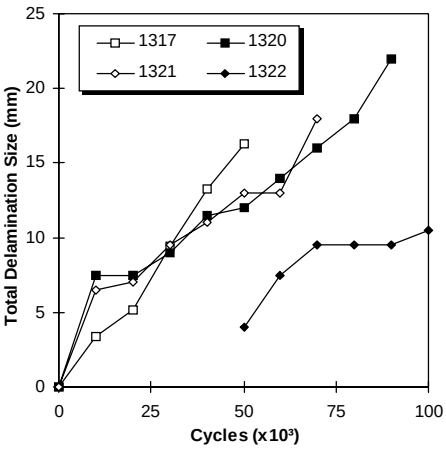

Fig. 6[a]: Delamination progression Kevlar high density stitched specimens

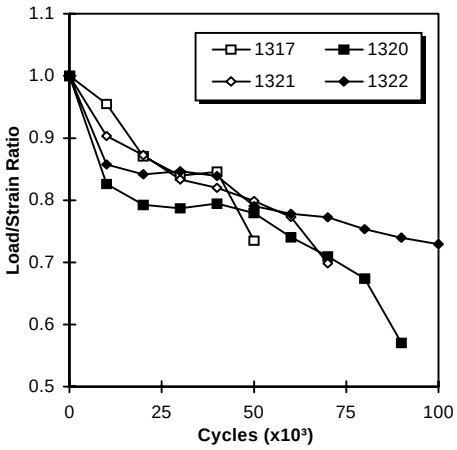

Fig. 6[b]: Progression of load/strain ratio Kevlar low high density stitched specimens

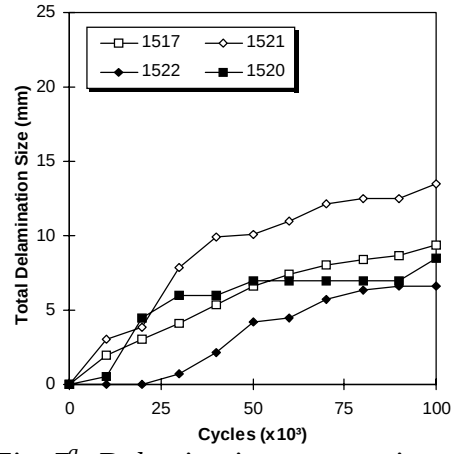

Fig. 7[a]: Delamination progression Dyneema low density stitched specimens

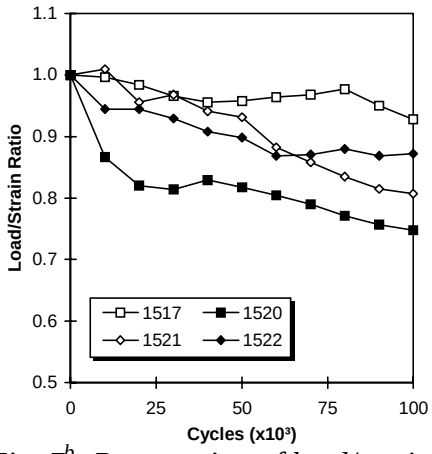

Fig. 7[b]: Progression of load/strain ratio Dyneema low density stitched specimens

Visual Inspection

Fig. 8 shows an example of a delamination crack in the rim of the hole initiating from a tool mark. Such cracks were seen in all specimens at the first inspection interval. The number and extent of such delamination cracks increased as the tests progressed. This delamination, on both sides of the hole, was also manifest in sublaminate buckling, which was observable during cycling and first appeared at about 20,000 cycles. The buckling region grew in an intermittent fashion for both stitched and unstitched specimens. There was a qualitative impression that the progression of this buckling was arrested by the stitch rows. However, an attempt to quantify this was inconclusive. Debonding of stitches at the surface was evidenced by slight relative motion of stitches to the surface of the specimen. This appeared as early as 20,000 cycles and appeared to be associated with and preceded the sublaminate buckling.

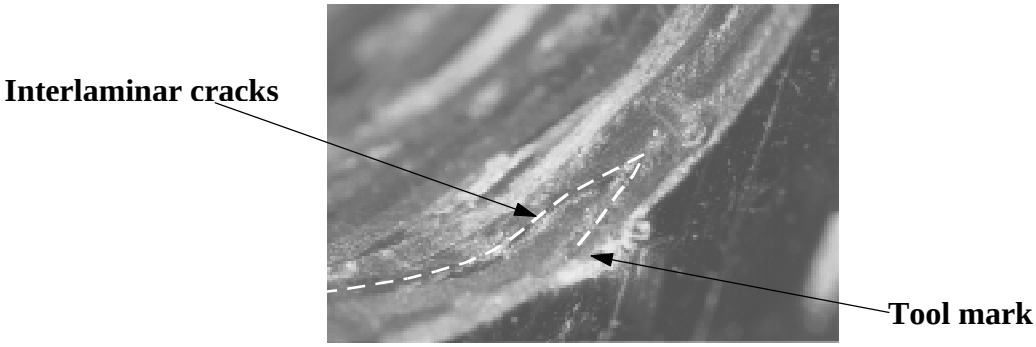

Fig. 8: Delamination crack in hole rim

Transverse cracks were observed on the surface of the specimens. These cracks originated at the three o'clock and nine o'clock positions at the rim of the hole and progressed at 45° along the direction of the surface warp tows. In most cases only one crack formed in each direction but occasionally there were two. Matrix crazing subsequently appeared close to the cracks. After 100,000 cycles these cracks were between 5 mm and 15 mm long for the various specimens. As was the case with the delaminations, these cracks grew in an intermittent fashion for both the stitched and unstitched specimens. Again, there was a qualitative impression that their progression was arrested by the stitch rows. However, an attempt to quantify this was inconclusive.

After about 50,000 cycles, debris comprising both black and white particles were evident and the surface of the specimen, in the vicinity of the damage, became rough. These are indications that pulverisation of both the matrix and fibres had occurred. A microscopic examination of the cycled specimens has yet to be conducted.

C-Scan

The progression of delamination width is presented in Figs. 4^a to 7^a. The value plotted is the sum of the widths of the delaminations on each side of the hole, measured between the edge of the hole to the lateral extent of the C-Scan plot. As mentioned earlier the resolution of the C-Scan plot was 1 mm and it is estimated that the accuracy of the measurements was ± 1 mm.

The window in the anti-buckling guide was 25 mm wide, consequently, sublaminate buckling would have been constrained for delamination widths greater than 19 mm. The maximum

width for specimens which survived 100,000 cycles was 17 mm for specimens 1217 and 1221. The specimens that failed did so within 10,000 cycles after the delamination width reached the window. This indicates that sublaminate buckling was not the sole failure mechanism.

The delamination width grew in an intermittent fashion for both the stitched and unstitched specimens. An attempt to correlate the position of the plateaux with the stitch line positions was inconclusive.

Load/Strain Ratio

The progression of the load/strain ratio (LSR) for each of the specimens is presented in Figs. 4^b to 7^b. The LSP is not only a measure of the stiffness of the material in the region of the clip gauge, but it also a measure of load redistribution due to damage and consequent changes in local stiffness in other regions of the material. In particular a local reduction in stiffness in the region of the hole which does not extend to the location of the clip gauge will nevertheless cause a reduction in the LSP and consequently the LSR. Delamination damage, particularly when sublaminate buckling occurs, will cause such a reduction in stiffness. However, other forms of damage, such as microcracking, will also cause a stiffness reduction. The fact that the LSR follows the same (inverse) progression as that of the delamination damage does not necessarily mean that delamination was the dominant damage mode, since the other forms of damage may have progressed at a similar rate. The second change in slope of the LSR curve may be due to the delamination, on the clip-gauge side, passing the clip-gauge position. A comparison of the number of cycles at which these two events occurred showed good correlation. This is not always evident from Figs. 4^a to 7^a, because they record the total of the delamination widths on each side, which were not always equal. A more extensive discussion of these issues will be presented elsewhere.

Table 2: Fatigue life or damage at 100,000 cycles

Specimen	Stitching		Load Range (kN)		Fatigue Life (cycles)	At 100,000 cycles	
	Type	Density	Tens.	Comp.		Delamination width (mm)	Load/Strain Ratio
1117	unstitched		21.8	20.3	$100{,}000^{+*}$	14	0.74
1120					$100{,}000^{+}$	8	0.80
1121					96,260	-	-
1122					74,354	-	-
1217	Kevlar	Low	20.8	19.7	$100{,}000^{+*}$	17	0.65
1220					$100{,}000^{+*}$	9	0.72
1221					$100{,}000^{+}$	17	0.78
1222					$100{,}000^{+}$	9	0.78
1317	Kevlar	High	21.8	20.2	53,236	-	-
1320					92,500	-	-
1321					74,404	-	-
1322					$100{,}000^{+}$	10	0.72
1517	Dyneema	Low	20.2	18.9	$100{,}000^{+}$	9	0.92
1520					$100{,}000^{+}$	16	0.73
1521					$100{,}000^{+}$	13	0.81
1522					$100{,}000^{+}$	6	0.88

*fatigue life < 110,000 cycles estimated on the basis of damage progression

Effects of Stitching

As may be seen from the data presented in Table 2, the fatigue performance of the high density Kevlar stitched specimens was inferior to that of the unstitched specimens. None of the low density Kevlar and Dyneema stitched specimens failed below 100,000 cycles indicating a superior fatigue performance to that of unstitched specimens. However, this may have been influenced by the slightly lower (about 5%, see Table 2) cycling load range. As described earlier, the load range was chosen, for each specimen type, to give a strain range of ± 0.35% for the uncycled specimens. In order to facilitate the comparison of fatigue performance, it would perhaps have been preferable to use the same load range for all specimen types.

A comparison of the damage progression for the low density Kevlar and Dyneema stitched specimens (Figs. 5 and 7) shows that the Dyneema stitched specimens have superior fatigue performance. This is particularly evident from a comparison of the progression of their LSRs (Figs. 5^b and 7^b). This may be related to the higher compressive strength measured for the Dyneema stitched specimens compared to the unstitched and low density Kevlar stitched specimens (Table 1). Unfortunately the compressive test results for the high density stitched specimens is unavailable for comparison. The improved compressive and fatigue performance may be due to the smaller diameter (~20%) of the Dyneema thread which would lead to less fibre distortion due to stitching.

From visual observations there were indications that the stitch rows provided some resistance to the growth of transverse cracks and sublaminate buckling, however an attempt to quantify this effect was inconclusive. No correlation was found between the positions of stitches and the plateaux in the progression of delamination damage. This may be because the length scale of the damage is such as to preclude steady-state crack bridging.

From the above results, the indications are, that the through-thickness reinforcement effect of stitching does enhance fatigue performance to some extent. On the other hand, the fibre misalignment caused by stitching degrades compression and compressive fatigue performance. It would appear that there is an optimum combination of stitch density and fibre diameter which will maximise the fatigue performance.

CONCLUSIONS

Tension-compression open hole fatigue tests were conducted on carbon/ epoxy laminates made from uniweave fabric stitched with Kevlar or Dyneema thread at various stitch densities. Four specimens from each type were cycled up to a maximum of 100,000 cycles.
Based on the limited number of specimens tested, the following conclusions may be made on the effect of stitching on their open hole fatigue performance.

- The fatigue performance of the high density Kevlar stitched specimens was inferior to that of the unstitched specimens.

- The fatigue performance of the low density Kevlar stitched specimens was inferior to that of the low density Dyneema stitched specimens. This is possibly because of the smaller diameter of the Dyneema thread.

- There are strong indications that the fatigue performance of both, the low density Kevlar and Dyneema stitched specimens, was superior to that of the unstitched specimens.

- For all specimens there was evidence of delamination after the first 10,000 cycles.

- There was no evidence that stitching arrested the progression of delamination damage.

- There were indications, based on visual examination, that the stitch rows temporarily arrested the propagation of transverse cracks and sublaminate buckling. However, attempts to quantify this were inconclusive.

ACKNOWLEDGMENTS

The authors gratefully acknowledge the assistance of Mr Paul Falzon of the CRC-ACS and Dr Paul Callus of RMIT, who contributed to the testing and the analysis of the results.

REFERENCES

1. Thuis, H.G.S.J. and Bron, E. "The Effects of Stitching Density and Laminate Lay-up on the Mechanical Properties of Stitched Carbon Fabrics", National Luct-en Ruimtevaart-laboratorium, Report NLR CR 96126L, 1996
2. Herszberg, I. and Bannister. M. K. "Compression and Compression-after-Impact Properties of Stitched Carbon/Epoxy Composites", Cooperative Research Centre for Aerospace Structures CP-93001, 1993.
3. Herszberg, I., and Bannister M.K., "Tensile Properties of Thin Stitched Carbon/Epoxy Composites", *Proceedings, 5th Aeronautical Conference*, Melbourne. September 1993.
4. Leong, K.H., Herszberg, I., and Bannister, M.K., "Impact Damage Resistance and Tolerance of Stitched Carbon Epoxy Laminates", *Proceedings, 2nd Pacific International Conference on Aerospace Science & Technology*, Melbourne, March 1995.
5. Leong, K.H., Herszberg, I., and Bannister, M.K., "An Investigation of Fracture Mechanisms of Carbon Epoxy Laminates Subjected to Impact and Compression-After-Impact Loading", *I J Crash*, Vol 1 No 3, 1996, pp 285-293.
6. Mouritz, A.P, Leong, K.H, Herszberg, I. "A Review of The Effects of Stitching on The In-Plane Mechanical Properties Of Fibre-Reinforced Polymer Composites", in-press *Composites.*
7. Lubeowinski, S.J. and Poe, C.C. "Fatigue Characterization of Stitched Graphite/Epoxy Composites", *Proceedings. Fibre-Tex 1987*, NASA Conf. Pub. 3001, 1987, pp 253-271.
8. Furrows, K.W., Loos, A.C. and Can, R.J. "Environmental Effects on Stitched RTM textile Composites" *J Rein Plast Comp*, Vol 15, 1996, pp 378-419.
9. Portanova, M.A. Poe, C.C. and Whitcomb, J.D. "Open hole and Post-Impact Compressive Fatigue of Stitched and Unstitched Carbon-Epoxy Composites" *Composite Materials: Testing and Design* (Tenth Volume), ASTM STP 1120, Glenn, G.C. ed, American Society for Testing and Materials, Philadelphia, 1992 pp 37-53.
10. Shah Khan, M.Z. and Mouritz, A.P. "Fatigue Behaviour of Stitched GRP Laminates" Comp Sci & Tech, Vol 56, 1996, pp 695-701.
11. Xiao, J. and Bathias, C. "Fatigue Behaviour of Unnotched and Notched Woven Glass/Epoxy Laminates", Comp Sci & Tech Vol 50, 1994, pp 141-148.
12. Galea, S.C. and Saunders, D.S. "In-Situ Ultrasonic C-Scanner", Australian Department of Defence, DSTO, ARL-TR-4, 1992

THE RESIDUAL COMPRESSION STRENGTH OF STITCHED AND UNSTITCHED PLAIN-WEAVE CARBON/EPOXY LAMINATES AFTER IMPACT AND HYGROTHERMAL CYCLING

B. Qi[1], I. Herszberg[2], A.A. Baker[3] and M.K. Bannister[4]

[1]The Sir Lawrence Wackett Centre for Aerospace Design Technology, RMIT. Now with CRC-ACS

[2]The Sir Lawrence Wackett Centre for Aerospace Design Technology, Dept of Aerospace Engineering, Royal Melbourne Institute of Technology, P.O. Box 2476V, Melbourne, Vic. 3001, Australia

[3]Airframes and Engines Division, Aeronautical and Materials Research Laboratory, 506 Lorimer Street, Fishermens Bend, Vic, 3207, Australia

[4]Cooperative Research Centre for Advanced Composite Structures (CRC-ACS), 506 Lorimer Street, Fishermens Bend, Vic. 3207, Australia

SUMMARY: Damage effects due to hygrothermal cycling were experimentally studied for thin (~1mm) Carbon /Epoxy laminates containing various levels of impact damage. T300/GY260 laminates were made by Resin Transfer Moulding from plain woven fabric with various densities of through-the-thickness stitching using Kevlar threads. The cycling was conducted, on impacted and non-impacted wet specimens, over a temperature range from -30°C to +100°C with ambient humidity ranging from low to 99%. Stitching did not significantly affect the damage resistance of the laminates, nor their residual compressive strength after impact (CAI strength). The cycled specimens were only slightly more resistant to damage than the dry specimens and the saturated specimens showed further slight improvement. Hygrothermal cycling slightly decreased the CAI strength and decreased the undamaged strength.

INTRODUCTION

The use of post-buckling design in composites has raised interest in the performance of stitched thin-skinned composites. Through-the-thickness stitching is a simple technique and can be combined with liquid moulding techniques such as Resin Transfer Moulding (RTM) to potentially produce low cost and high quality components with improved resistance to delamination [1, 2].

Tada and Ishikawa [3] evaluated the effects of stitching on compression strength of holed carbon fibre laminates in which Kevlar 49 threads were stitched around the hole. They found that stitching could prevent crack initiation and/or propagation at initial failure stage but had little effect on compression strength. Herszberg et. al [4] showed that Kevlar transverse stitching did not affect the residual compression strength of thin woven fabric laminates. While stitching was generally reported to improve Mode I fracture toughness [5, 6], Ogo [5] found that stitching had negligible effect on Mode II delamination toughness, while Jain and Mai [7] reported a significant increase due to stitching.

Hygrothermal cycling is a significant factor in the long term performance of polymer matrix composites for aircraft structures. Under hygrothermal cycling, interlaminar and intralaminar cracking may occur within composite structures. In particular, impact damage may spread as a result of hygrothermal cycling due to the freeze-thaw or boiling cycle of any moisture absorbed in the damaged region [8, 9]. This could affect their impact resistance and tolerance. Most work done on hygrothermal effects to date has concentrated on laminates made from unidirectional prepreg tape. Hygrothermal cycling 100 times between -54°C and 93°C caused no significant microstructural cracking of a quasi-isotropic T300/5208 laminate as detected by optical microscopy [10]. Brandt [11] reported that moisture absorbed in 24-ply T300/914C laminates did not affect significantly their residual compressive strength after impact. Birger [12] concluded that the ageing of carbon/epoxy composites at 50 and 95% relative humidity (RH) for 960 hours, although resulting in a drop in their glass transition temperature, hardly affected the mechanical properties of the material. However, other studies showed that thermal spiking to 135°C of wet XAS/914C laminates caused matrix cracking and affected the rate of subsequent moisture uptake [13, 14]. Previous results [15] showed that extensive intralaminar cracking surrounding the impacted-induced damage area due to hygrothermal cycling did not affect the residual compression strength of tape laminates.

Very few studies examined the effect of hygrothermal cycling on textile composites. Furrow and Loos [16] studied the hygrothermal effect on AS4/3501-6 stitched uniweave laminates. They found that after 160 cycles the static compression strength of the Kevlar 29 stitched uniweave laminate was reduced by nearly 10% (-55~60^{o}C with varying degree of RH). When exposed to 60°C and 95% RH for 80 days and then saturated in 70°C water, the material lost 19% of their baseline compression strength. Mitrovic and Carman [17] studied the influence of tensile fatigue damage on residual compression strength of 8 harness satin woven composites. Their results showed that residual compression strength of the material was significantly influenced by the amount of damage induced during tension-tension fatigue.

This paper reports the combined effects of hygrothermal cycling and low velocity impact (up to 6 J) on the impact resistance and residual compressive strength of thin carbon/epoxy laminates made from plain-weave fabric stitched with different stitching densities.

SPECIMEN MANUFACTURE

The test specimens, produced from Ciba Composites G1051 plain weave fabric, comprising 3K T300 tows, had a layup sequence of $[0_2,45]_s$. They were then stitched with Kevlar 49 (40 Tex) and then impregnated with Ciba Composites GY260 epoxy resin HY917/DY070 by RTM. They are cured at 80°C for 4 hours and postcured at 160^{o}C for 4 hours. Their cured thickness was 1.1 ± 0.05 mm. Three stitch densities of 0, 4 and 8 stitches/cm^2 were employed. The unstitched, low density stitched and high-density stitched panels were respectively designated PW, LDST, HDST. Figure 1 shows the stitch configuration.

The test specimens, of dimension 91 x 117 mm, were cut from the panel so that their long dimension was in the 0° (warp) direction. The specimens were C-scanned to ensure general quality and they were examined by optical microscope to check for any microcracking.

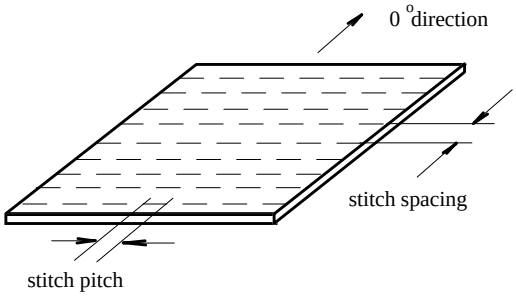

Fig. 1: Configuration of stitched woven fabric laminate

EXPERIMENTAL TECHNIQUES

Four groups of specimens were tested, each with a different sequence of impact and hygrothermal cycling. Each group comprised a number of specimens from each stitch configuration, ie., PW, LDST and HDST. The specimens from the various designations were damaged by impacting at energy levels ranging from 0 to 6 J. Before testing all specimens were dried in an oven at 70°C until constant weight was reached. The edges of the test specimens were not sealed during conditioning since minor local edge effects would not affect the impact performance. The testing sequence for each group is outlined below and summarised in Table 1 which also includes moisture content in the non-impacted specimens and their measured glass transition temperature (T_g).

- Group A specimens were impacted at different energy levels, then compression tested.
- Group B specimens were immersed in water at 70°C until their weight reached an equilibrium (constant conditioning), then impacted at different energy levels and subsequently compression tested.
- Group C specimens were immersed in water for constant conditioning. Impact test were then performed before 810 standard hygrothermal cycles (SHC). After that some of them were subjected to constant conditioning for moisture reabsorption. The others were subsequently compression tested.
- Group D specimens were subjected to 810 standard hygrothermal cycles after constant conditioning, then impact and subsequently compression tested.

Table 1: Test matrix

Group	Test sequence	Number of specimens	Moisture content*(%)		T_g (°C)	
			at Impact	at CAI	At Impact	at CAI
A	Dry→Imp→CAI	PW: 13 LDST: 33 HDST: 17	<0.2	<0.2	146	146
B	Wet→Imp→CAI	PW: 4 LDST: 4 HDST:	0.62	0.62	125	125
C	Wet→Imp→SHC→CAI	PW: 6 LDST: 9 HDST: 7	0.62	0.52	125	114
D	Wet→SHC→Imp→CAI	PW: 4 LDST: 4 HDST: 5	0.52	0.52	114	114

*for non-impacted specimens

Standard Hygrothermal Cycle – SHC

The temperature ranges was -30°C to +100°C (measured at the specimen surface) with relative humidity ranging from low to 99% RH. The average heating rate was 1.1°C/min. The temperature range chosen is based on the general temperature profile for a commercial aircraft (see Ref. [18] for more detail).

Moisture Absorption and Glass Transition Temperature

Moisture absorption behaviour before and after cycling was determined by using water immersion at 70°C. Selected specimens were redried and their moisture reabsorption characteristics determined. Details on measuring weight, and determination of the effect of absorbed moisture on T_g of composite materials using dynamic mechanical thermal analysis (DMTA) have been reported previously by Qi et al. [18].

Impact and CAI tests

Impact test were conducted at six different incident impact energy levels from 0 to 6 J. Compression after impact tests were conducted at room temperature using the CRC-ACS test rig. The specimen was constrained by anti-buckling plates which contained a circular cut-out of diameter 40 mm to allow any damage growth and local buckling within this window. Details of those testing and test procedures have been reported by Qi et al. [19].

Damage Characterisation

Tetrabromoethene enhanced X-ray radiography was employed to characterise the initiation and growth of microcracking (after SHC) and damage (after impact and CAI). Through transmition C-Scan was also used to determine the projected impact damage area. Optical microscopy was employed to study surface damage and failure mode and SEM was also used to investigate the fracture morphology.

RESULTS AND DISCUSSION

Plain Woven Fabric Structures

Cross-sections of a plain-weave specimen revealed tow waviness, due to the weave structure, such that fibre tows were at out-of-plane angles of up to 8.2°. Stitching cause further out of plane crimping of the tows and also local in-plane distortion of the yarns such that diamond shaped resin-rich areas were formed in the vicinity of each stitch. No distortion of the stitch loops was found due to RTM consolidation process. This fibre/tow waviness is a major factor affecting in-plane mechanical properties of this type of laminate, especially for their undamaged compression strength [1, 4]. Dow [1] has shown that stitched flat laminates have compression strength about 20% lower than the strength of comparable unstitched laminates which may be attributed to crimping and fibre displacement and damage due to stitching.

Hygrothermal Effect

A variety of damage modes were manifest for the various specimens subsequent to cycling. These have been previously reported by Qi et al [18]. Short transverse matrix cracks and surface debonding between resin and tow fibres were observed. These microcracks grew along fibres in the tows and they were arrested in the interlacing zone of warp and weft tows. Some delamination was found in the interlacing tows of the surface plies. Figure 2 is an X-ray radiograph and shows some small dark zones at the interlace points on the surface ply. Cross-sectional microscopic inspection revealed that these were delamination cracks occurring between surface warp tows and weft tows. Stitched specimens developed cracks in the resin rich areas associated with the stitching and there was evidence of debonding at the stitch

interface. However, they were far less susceptible to the surface ply delamination cracks, as may be seen from Figure 3. This may be because the hygrothermal stresses had been relieved by the cracking in the stitch region.

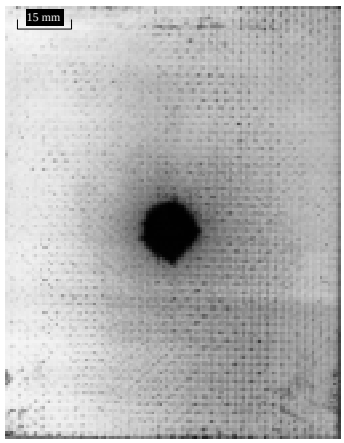

Fig. 2: Matrix cracking of PW specimen, shown by short dark lines and delamination in the interlacing area (SHC; X-ray)

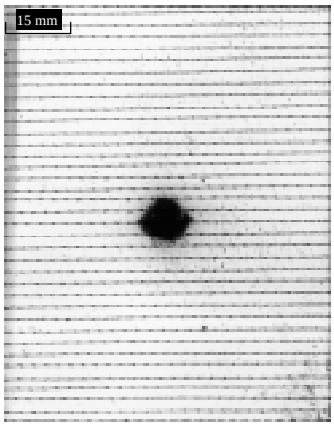

Fig. 3: Matrix cracking and stitch thread debonding of a HDST specimen (SHC; X-ray)

Impact Resistance

The impact damage resistance, as measured by the decrease in damage area due to impact, is shown in Fig. 4 for dry, cycled and wet PW specimens. Those data points are best fitted to linear lines. The damage resistance of the cycled specimens (Group D) was found to be higher than for the dry specimens (Group A) and the wet specimen (Groups B & C) even greater. It appears that constant water exposure enhanced matrix toughness, probably due to plasticisation of the matrix with moisture absorption. These results are consistent with the degree of moisture absorbed by the various specimens (Table 1). Similar results were found for the various stitched configurations and tape laminates [19].

Stitching did not significantly change the impact resistance, in terms of impact damage area, of dry, cycled or wet specimens. As an example, Fig. 5 presents the results for dry PW, LDST and HDST specimens.

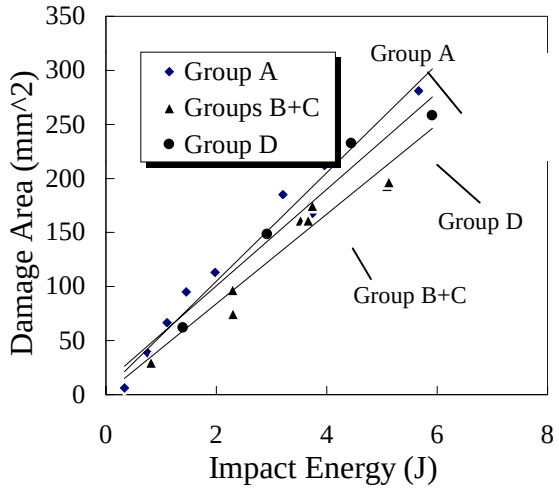

Fig. 4: Impact performance of PW under different conditions

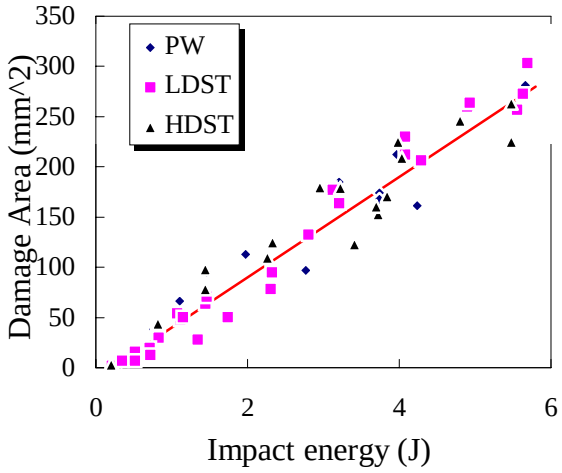

Fig. 5: Comparison of impact resistance between dry PW, LDST & HDST specimens

Impact Damage Mode

The projected impact damage area was circular for both non-stitched and stitched specimens. Fig. 6 shows a cross-section of dry PW specimen impacted at 4.5 J. It is interesting to note that at the maximum impact energy, the area ratio of the damage zones, measured on the back and impacted surfaces respectively, was less than 3, whereas for tape specimens this ratio is typically greater than 10. The impact damage comprised: fibre breakage, transverse matrix cracking, and tow separation. This contrasts with the large rear ply delamination areas formed in impacted tape laminates. This more localised damage and high impact resistance for the woven composite compared to conventional tape laminates, is attributed to the wavy tow structure providing greater resistance for crack propagation.

By counting the number of stitches in the impact damage area, it was found that the effective stitch density was less than the nominal stitching density. This is obviously dependent on stitching pattern. For example, for a HDST specimen, with a nominal stitch density of 8 stitches per cm^2, at an impact energy level of 5J, there were only nine stitches in the failure area giving an effective stitch density of only 4 stitches per cm^2.

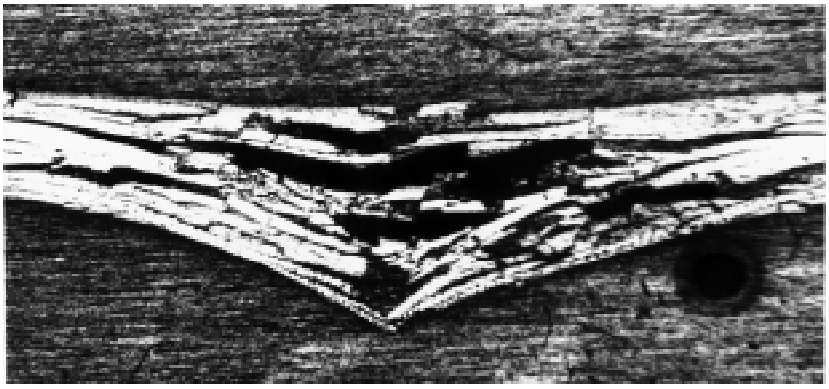

Fig. 6: Cross-section view of impacted PW specimen (Group A, impacted at 4.5J)

Damage Tolerance

Failure mode

Inspection of edges and surfaces of failed specimens after CAI revealed that significant warp tow barrelling occurred and failure mode was transverse shear cracking. Further cross-sectional inspection, see Fig. 7, showed that kinking of warp tows occurred on the crack path. Since fibre kinking is a type of fibre microbuckling, it was assessed that this preceeded the final shear failure. The failure mode was similar for both stitched and unstitched specimens.

In progressive loading tests the impact induced damage area was not observed to spread (Fig. 8). This contrasts with tape laminates where the impact damage region spreads under compessive loading as a result of sublaminate buckling.

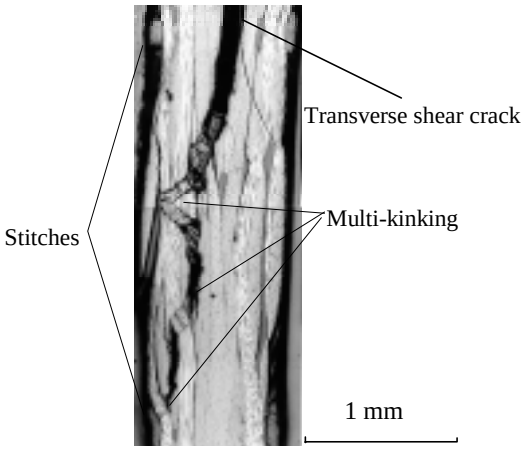

Fig. 7 Kinking bands in warp tows of a HDST specimen after CAI (Group D, impacted at 3.84 J)

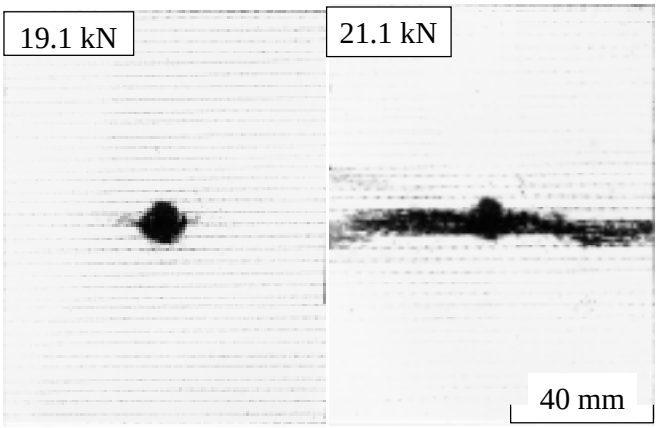

Fig.8 Compression failure of an impacted HDST specimen during stepped loading (Group A, X-ray , impacted at 4.5 J)

Residual Compression Strength

As may be seen from Figs. 9-12, which show the influence of damage width on residual compression strength of the various laminates, stitching did not significantly affect residual compression strength of the woven fabric laminates. This is despite the fact that stitching reduced the undamaged compressive strength [4].

No significant difference was found in the residual compressive strength, between the uncycled Group A (dry) and Group B (wet) specimens (see eg Fig. 10), indicating that plasticisation of the matrix due to moisture absorption did not affect residual compression strength. This confirms the findings of other researchers (Guild et al. [20] and Dost et al. [21]) that resin toughness has little effect on the relationship between CAI and damage diameter.

As may be seen from Figs. 10-12, Group D (cycled then impacted) specimens had a lower residual compressive strength than that of uncycled (A and B) specimens. The CAI strength for group C (impacted then cycled) specimens was intermediate. The compressive strength for undamaged cycled specimens was also lower than for the uncycled specimens. This may be because of the placement of load-bearing (0°) plies on the surface. The degradation of the matrix at the surface due to hygrothermal cycling would reduce the support to the warp tows resulting in a lower compression strength.

It was expected that the impact damage area in the Group C (impacted then cycled) specimens would grow due to cycling as a result of the freeze-thaw effect of moisture trapped in the damage area. No such damage growth was observed and the CAI strength of the Group C specimens was in fact higher than that of the Group D (cycled then impacted) specimens. This may be because for group C specimens, the impact-induced crack tips were blunted by the hygrothermal cycling.

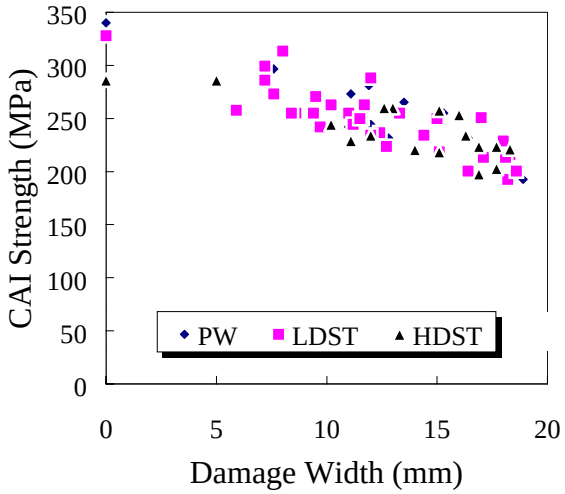

Fig. 9 CAI strength of Influence of dry PW, LDST and HDST specimens

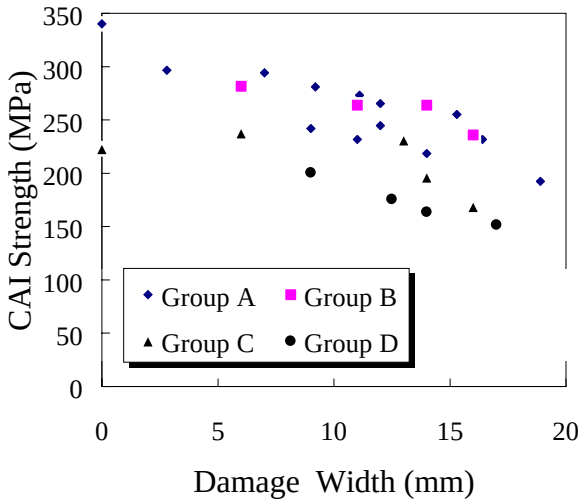

Fig. 10 Influence of damage induced by hygrothermal cycling on CAI strength for cycled and non-cycled PW specimens

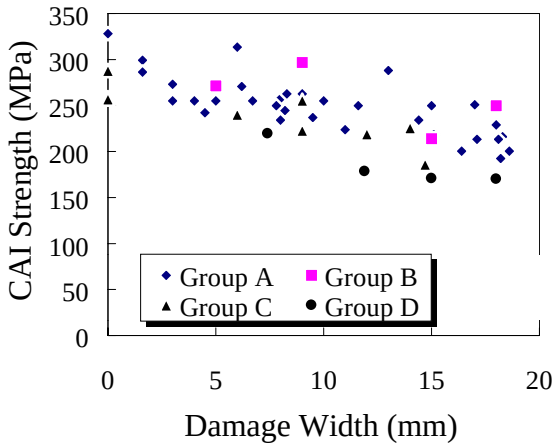

Fig. 11 Influence of damage induced by hygrothermal cycling on CAI strength for cycled and non-cycled LDST specimens (Group A, B C and D)

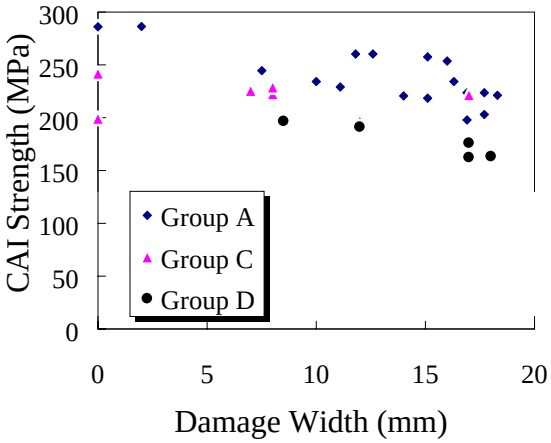

Fig. 12 Influence of damage induced hygrothermal cycling on CAI strength for cycled and non-cycled HDST specimens (Group A, C and D)

Stitching Effect

In the present study, it was found that stitching did not affect significantly the residual compressive strength. This has been atributed to the fact that, as reported above, both stiched and unstitched specimens exhibited similar failure modes. The nestling of adjacent plies in the RTM fabric composite was sufficient to inhibit the sublaminate buckling which is manifest in the failure of prepreg tape laminates. The failure mode for the fabric specimens was kink band formation followed by transverse shear cracking. Such failure was not greatly influenced by stitching.

Failure analysis showed the failure projected area, as schematically shown in Fig. 13 and summarised in Table 2, was similar for PW, LDST and HDST specimens. This was

confirmed by X-ray radiography and visual inspection on the failed specimens. Table 2 showed that for LDST specimens almost no stitches were involved in the failure process, since cracks propagated between two stitching rows, while only 4 stitches per cm^2 were involved in the failure region for HDST specimens.

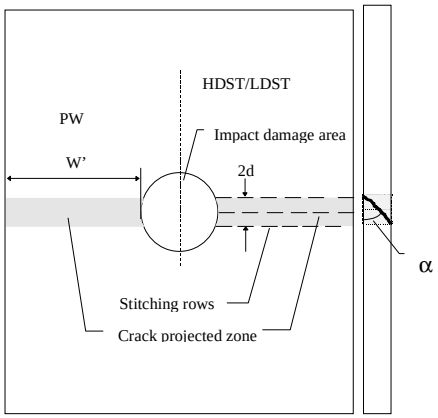

Fig. 13: A sketch showing damage propagation, the projected failure area and transverse shear crack on the edge for PW, LDST and HDST specimens

Table 2: Estimated failed stitch density during CAI

Nominal stitching density (st/cm^2)	Estimated projected failure area (cm^2)	Estimated number of stitches failed	Estimated effective stitch density ($st/c\ m^2$)
0	2 x (2d x W')	0	0
4	2 x (2d x W')	0	0
8	2 x (2d x W')	2 x (1 + W'/d)	4.1

Components of shear force would be expected to act on the through-the-thickness stitches because of the shear type failure mode. The shear properties of Kevlar/epoxy is poor compared to that of carbon/epoxy [22]. SEM photographs of a broken stitch thread, showing evidence of shear and pull-out failure, are presented in Figs. 14 and 15.

An important factor in the failure mechanism was the friction caused by the relative movement between two fractured surfaces during the transverse shear cracking. Friction may be a potential energy dissipation mechanism during mode II fracture [7]. The contribution of the stitches to resist such crack propagation was much lower than the neighbouring carbon fibres because of their small volume fraction and lower shear properties.

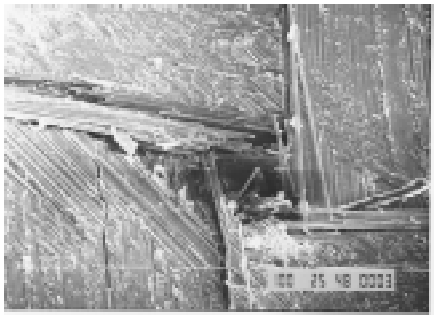

Fig. 14 Breakage of a stitch thread in a HDST specimen after CAI (Group D, SEM)

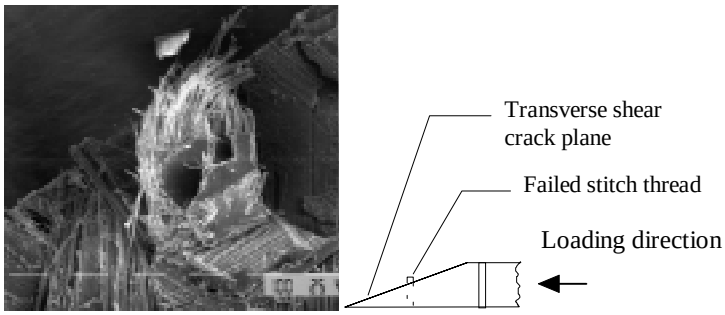

Fig. 15 Breakage of a stitch thread in a failed HDST specimen after CAI (SEM)

CONCLUSIONS

For the thin carbon/epoxy specimens studied, which were stitched with kevlar thread and subject to the combined effect of hygrothermal cycling and impact damage, the following conclusions were reached:

- Stitching did not increase their damage resistance or improve the residual compressive strength.
- Hygrothermal cycling caused a reduction in undamaged compressive strength and the CAI strength of both stitched and unstitched specimens. The reduction manifest in cycled then impacted specimen was greater than for impacted and cycled specimens.

ACKNOWLEDGMENT

The assistance of Mr K Houghton in the manufacture of the specimens, and Mr H. Morton in the use of X-ray radiography are gratefully acknowledged.

REFERENCE

1. Dow, M. B., Smith, D. L. “Damage-Tolerant Composite Materials Produced by Stitching Carbon Fabrics", *21st International SAMPE Technical Conference*, Sept. 25-28, 1989
2. Farley, G. L. and Dickinson, L. C. "Mechanical response of Composite materials with through-the-thickness Reinforcement", *NASA CR*- ? 1991
3. Tada, Y. and Ishikawa, T. “Experimental evaluation of the effects of stitching on CFRP laminate specimens with various shapes and loading”, *Key Engineering Materials* Trans tech Publications, Switzerland, Vol.37, 1989, pp.305-316
4. Herszberg, I. and Bannister. M. K. “Compression and Compression-after-Impact Properties of Stitched Carbon/Epoxy Composites”, 5th Australian Aerospace Conference, Melbourne, Sept., 1993, also published in Cooperative Research Centre for Aerospace Structures CP-93001, 1993.
5. Ogo, Y. “The effect of stitching on in-plane and interlaminar properties of carbon /epoxy fabric laminates”, MSc. Thesis, Uni. Of Delaware, Newark, Delware, May, 1987

6. Morales, A. “Structural stitching of textile preforms”, *Proc. 22nd SAMPE Tech. Conf.*, 6-8 Nov. 1990, pp.1217-1230
7. Jain, L. K. and Mai, Y. W. “Analysis of stitched laminated ENF specimens for interlaminar Mode II fracture toughness”, International J. of Fracture, Vol. 68, 1994, pp.219-244
8. Ashford, L.W. "Analysis and Test of Carbon/Bismaleimide Laminates Subjected to Internal Pressures Resulting from Trapped Moisture", *18th International SAMPE technical Conference*, Oct. 7-9, 1986
9. Stansfield, K.E. and Pritchard, G. "Damage generation and healing during composite thermal spikes", *21st International SAMPE Conference*, pp.120-129, Sept. 1989.
10. Crossman, F.W., Mauri, R.E. and Warren, W.J., "Hygrothermal Damage Mechanisms in Graphite-Epoxy Composites", *NASA Contractor Report 3189*, 1979
11. Brandt, J. and Warnecke, J. "Influence of material parameters on the impact performance of carbon-fibre-reinforced polymers", *High Tech - The Way Into The Nineties*, Ed. Brunsch, K., *et al.* Elsevier, Amsterdam, 1986, pp. 251-260
12. Birger, B. Moshonov, A. and Kenig, S. "The effects of thermal and hygrothermal ageing on the failure mechanisms of graphite-fibre epoxy composites subjected to flexural loading," *Composites.*, Vol. 20, No. 4, 1989 p.341.
13. Bohlman, R.E. and Derby, E.A., "Moisture Diffusion in G/E Laminates-Experimental and Predicted", *Proc. of Structures, Structural Dynamics and materials Conference*, March 1997, pp.219-226.
14. Clark, G., Saunders, D.S., van Blaricum, T.J. and Richmond, M. "Moisture Absorption in Graphite/Epoxy Laminates", *Composites Science and Technology*, 1990 pp. 355-375
15. Qi, B., Herszberg, I., Baker, A. A. and Bannister, M., "The Effects of Hygrothermal Cycling on the Impact Resistance and Tolerance of Quasi-Isotropic T300/914C Laminates", *1st Australasian Congress on Applied Mechanics*, Melbourne, 21-23 Feb., 1996, pp. 371-376
16. Furrow, K. W., Loos, A. and Cano, R. J. “Environmental effects on stitched RTM textile composites”, *J. of Reinforced Plastics and Composites*, Vol. 15, 1996, pp.378-419.
17. Mitrovic, M. and Carman, G. P. “The influence of tensile fatigue damage on residual compression strength of woven composites”, *Proc. of the American Society for Composites, Tenth Technical Conference*, Oct. 18-20, 1995, pp. 633-643.
18. Qi, B., Herszberg, I., Baker, A. A. and Bannister, M., "Damage Effect of Hygrothermal Cycling on Carbon/Epoxy Laminates”, PICAST2-AAC6, Melbourne 20-23 March, 1995, pp. 585-592
19. Qi, B., Herszberg, I., Baker, A. A. and Bannister, M., "The Effects of Moisture and Impact on Ultimate Compressive Strength of G/E Composites", in *Proc. 5th Australian Aeronautical Conference*, Melbourne, 14 Sept, 1993.
20. Guild, F.J., Hogg, P.J. and Prichard, J.C. "A model for the reduction in compression strength of continuous fibre composites after impact damage", *Comp*, 24 (4), 1993 p. 333.
21. Dost, E. F. Ilcewicz, L. B. and Gosse, J. H. “Sublaminate stability based modeling of impact damage composite laminates”, Proc. Of the American Society for Composites - *Third Technical Conference*, ASC, 1988
22. Clements, L. L. and Moore, R. L. *SAMPE Quart*, Vol.9, No.1. 1977, p.6
23. Morgan, R. J. and Allred, R. E. “Aramid Fibre Reinforcements”, in *Reference Book for Composites Technology* Vol. 1, edited by S. M. Lee, 1987 pp.143-166

SIMULATION OF THE SHAPING OF WOVEN FABRICS

Roger Blanlot

Aerospatiale, Common Research Center Louis Blériot
Département Ingénierie et Procédés Composites,12, Rue Pasteur BP.76
92152 Suresnes Cedex, France

SUMMARY: This paper is a second part of a general reflection aiming to the definition of the mechanical behaviour of prepreg woven fabrics used for the manufacture of undevelopable composite parts by lay-up as well as by extension by any shaping processes. We present a finite element formulation based on anisotropic hypoelastic constitutive equations. This formulation has been achieved by considering the need for obtaining an industrial design tool. The present formulation corresponds to the objective rigid-body rotation frame with an up-dating of the warp and weft yarn directions of the fabric. The hypothesis is assumed that the evolution of these directions is quasi-identical to the evolution of the principal directions of strain. The constitutive equations of the fabric behaviour are identified at each increment. The numerical model is integrated in the ABAQUS finite element software. Firstly we have studied the simple shear test with different orientations of the fabric. In a second part we have simulated an example of forming.

KEYWORDS: woven fabrics, prepreg, simulation, constitutive equations, finite strains, finite element method, laying-up

INTRODUCTION

The increasing use of composite materials over the last few decades, more particularly in the field of aerospace, has implied the improvement of design rules and consequently, has lead the industries to look into the automation of the different manufacturing processes. In the case of automation of the classical laying up forming process, specific automated machines have been now in use for several years in different countries such as U.S.A., or France. But they were originally designed for developable or slightly undevelopable composite parts. In the case of undevelopable parts, automation was generally not considered. Several kinds of different systems in processing aids were achieved without taking various mechanical aspects of the fabric into account.

The present study is concerned with a general research pattern pertaining to the definition of the mechanical behaviour of prepreg fabrics used for the manufacture of undevelopable composite parts by laying-up as well as its extension for stamping process.

Generally, two different approaches can be used for this type of problems: one way favours the geometrical aspect of the warping, the other one its mechanical aspect. Our research is based on the mechanical approach.

The behaviour of prepreg fabrics with resin in the non-polymerized phase during the manufacture of undevelopable composite parts by lay-up, depends on various parameters which can be grouped into two sets as:

the parameters associated to the dry fabric
- materials constituting warp and weft yarns (type and mechanical characteristics)
- the method of preparation of the yarn (size, thickness, section shape, etc...)

the weaving technique (fabric weave, fabric structure)

the parameters associated to the resin
- the average resin content
- the mechanical characteristics

the fabric impregnation method.

These parameters were identified experimentally after carrying out a whole range of mechanical tests, on the prepreg fabric, and the resin, separately and respectively.

A micro-structural finite element model developed earlier [1] was validated by comparing it to the results obtained from tests. This study has brought out that the most important factor for the shaping process is the fabric ability to allow for a relative rotation of the yarns associated with the plane shear of the resin [2].

In this paper, we present a finite element formulation based on anisotropic hypoelastic constitutive equations. This formulation has been achieved by considering the need to obtain an industrial design tool. We have also developed a macro-mechanical model, which substitutes an homogeneous continuous material to the discrete nature of fabric. The homogenisation has been obtained through an iteration in the computation procedure.

The continuous variation of the geometric positions of fabric yarns is taken into account by incorporating the velocity of particles in the formulation, thus allowing the evolution of anisotropy during the transformation. We have used Green-Nadghi's formulation associated with rigid body rotation derived from polar decomposition. The evolution of the orthotropic hypoelastic law is there determined by the location of the bisectors of the warp and weft directions identified at each instant of the transformation.

PRELIMINARIES

Kinematic of the Transformation

Let us consider the motion of the different material points, called particles, of a deformable body. The motion of a particle P relative to a reference frame R, associated to a orthonormal basis in a Euclidean space of three dimensions, is described by the time locus of its position vector $\mathbf{x}$ (P, t). This locus is the path trajectory of P in R. This particle can be identified by its position vector $\mathbf{X}$(P) in R at a reference time (t_0). At this time the different particles occupy the reference configuration C(t_0) or C_0. The motion of this particle P is described by the vector function :

$$\mathbf{x} = f(\mathbf{X}, t)$$

The position of different particles at a given time (t) corresponds to the current configuration C(t) or C.

The transformation of an infinitesimal element d**X** in C_0 into an infinitesimal element d**x** in C, is defined by the *deformation gradient* tensor **F**.

$$d\mathbf{x} = \mathbf{F}.d\mathbf{X}$$

This tensor which is continuously differentiable has a strictly-positive determinant, and hence admits the polar decomposition

$$\mathbf{F} = \mathbf{R}.\mathbf{U} = \mathbf{V}.\mathbf{R}$$

U(t) and **V**(t) describe the local deformation of the element and are referred to as the right and left stretch tensor respectively. These tensors are symmetric and positive-definite. **R**(t) is the proper orthogonal tensor and characterises the rigid body rotation with $\mathbf{R}^T = \mathbf{R}^{-1}$.

The material time rate of change of the body deformation is described by the velocity gradient tensor **L**.

$$\mathbf{L} = \text{grad}\,\dot{\mathbf{x}} = \dot{\mathbf{F}}.\mathbf{F}^{-1}$$

The symmetric part **D** is called the stretching tensor,

$$\mathbf{D} = \text{sym}\,\mathbf{L} = \frac{1}{2}\left(\mathbf{L} + \mathbf{L}^T\right)$$

and the anti symmetric part **W** the spin tensor,

$$\mathbf{W} = \text{skw}\,\mathbf{L} = \frac{1}{2}\left(\mathbf{L} - \mathbf{L}^T\right)$$

This completes the sketch of basic kinematics essential for this presentation.

Change of Frame and Objectivity

For pure homogeneous deformations, an orthogonal triad, composed of the principal axes which remain orthogonal throughout the deformation, can be identified. Furthermore, its material derivative equals the deformation rate tensor. Only for homogeneous (not pure) deformations is the deformation gradient tensor unsymmetric, and there is no triad which remains orthogonal throughout. For this reason, finite strain formulations which involve stress rate must compensate for the material rotation by using objective derivatives [5], [6]. These objective derivatives are divided into two types : the convective derivatives and those which eliminate the parasitic rotations by changing frame. For the latter, a lot of objective tensor rates are proposed in literature.

Let $\{e_i(t)\}$ be a smooth, time-dependent orthonormal basis. The corresponding twirl tensor **Ω** is the skew tensor function defined by

$$\dot{e}_i = \Omega.e_i$$

Given a smooth tensor function **B**, the time derivative of **B** measured by an observer rotating with $\{e_i(t)\}$ can be written as

$$\overset{\nabla}{\mathbf{B}} = \dot{\mathbf{B}} + \mathbf{B}.\Omega - \Omega.\mathbf{B}$$

Green-Nagdhi's (Mc Innis or Dienes) derivative corresponds to the case of $\{e_i(t)\}$ associated with the rotation experienced by the material yarns and coinciding with the principal directions of strain since the initial time.

Sowerby-Chou's (Hill) derivatives corresponding to the case of $\{e_i(t)\}$ are the rotations of the principal directions of **U** and **V** tensors.

Another important notion is Jaumann's derivative $\overset{J}{\mathbf{B}}$ given by

$$\overset{J}{\mathbf{B}} = \dot{\mathbf{B}} + \mathbf{B}.\mathbf{W} - \mathbf{W}.\mathbf{B}$$

in which **W** is the spin. This derivative corresponds [4] to the corotationnal frame where, for each time, the materials yarns that coincide with the principal axes of deformation have no angular velocity.

Application to a Non-Up-Dated Behaviour Law for Simple Shear

The simple shear test can be described by the figure below :

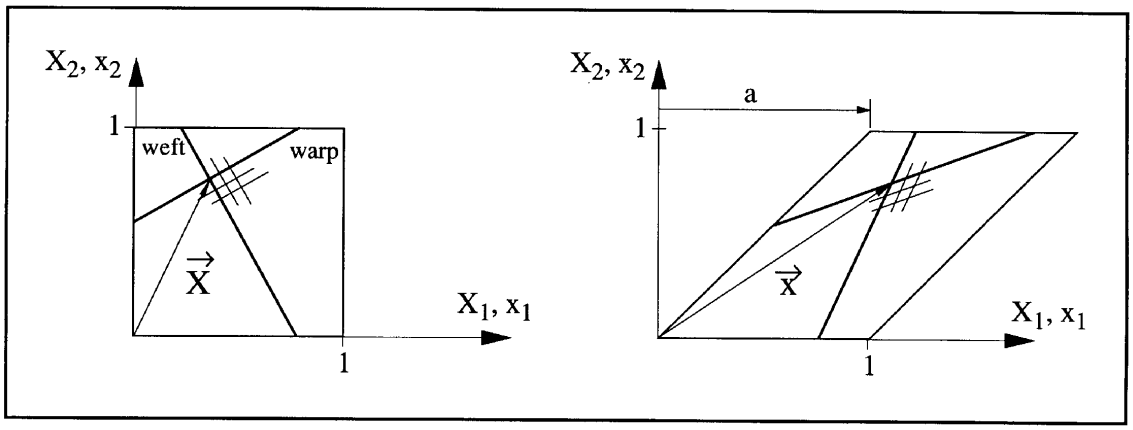

Fig. 1. Simple shear test

A Green-Nagdhi's formulation is used with an orthotropic hypoelastic behaviour law. The orthotropic axes are assumed to rotate with the rigid body frame. The overbars and greek subscripts denote the writing of equations in the rotating frame.

$$\begin{Bmatrix} \dot{\overline{\sigma}}_{\alpha\alpha} \\ \dot{\overline{\sigma}}_{\beta\beta} \\ \dot{\overline{\sigma}}_{\alpha\beta} \end{Bmatrix} = [\overline{C}_{\alpha\beta}].[\overline{D}] = \begin{bmatrix} C_{\alpha\alpha\alpha\alpha} & C_{\alpha\alpha\beta\beta} & 0 \\ C_{\beta\beta\alpha\alpha} & C_{\beta\beta\beta\beta} & 0 \\ 0 & 0 & C_{\alpha\beta\alpha\beta} \end{bmatrix} . \begin{Bmatrix} \overline{D}_{\alpha\alpha} \\ \overline{D}_{\beta\beta} \\ 2\overline{D}_{\alpha\beta} \end{Bmatrix} \text{ with } \overline{D}_{\alpha\beta 3} = \begin{bmatrix} \frac{\dot{a}}{2}\sin(2\theta) & \frac{\dot{a}}{2}\cos(2\theta) & 0 \\ \frac{\dot{a}}{2}\cos(2\theta) & \frac{-\dot{a}}{2}\sin(2\theta) & 0 \\ 0 & 0 & 0 \end{bmatrix}$$

and $\theta = \arctan\left(\frac{-a}{2}\right) + \theta_0$, θ_0 represents the initial angle (e_1, e_α) between the shearing direction and one of the orthotropic directions. The integration of these equations in the rotating local basis gives

$$\overline{\sigma}^{R}_{\alpha\alpha} = -\overline{\sigma}^{R}_{\beta\beta} = (C_{\alpha\alpha\alpha\alpha} - C_{\alpha\alpha\beta\beta}).\left[\left\{2\arctan\left(\frac{a}{2}\right) - \frac{a}{2}\right\}.\sin(2\theta_0) - \ln\left(1+\frac{a^2}{4}\right).\cos(2\theta_0)\right]$$

$$\overline{\sigma}^{R}_{\beta\beta} = (C_{\alpha\alpha\beta\beta} - C_{\beta\beta\beta\beta}).\left[\left\{2\arctan\left(\frac{a}{2}\right) - \frac{a}{2}\right\}.\sin(2\theta_0) - \ln\left(1+\frac{a^2}{4}\right).\cos(2\theta_0)\right]$$

$$\overline{\sigma}^{R}_{\alpha\beta} = 2C_{\alpha\beta\alpha\beta}.\left[\left\{2\arctan\left(\frac{a}{2}\right) - \frac{a}{2}\right\}.\cos(2\theta_0) + \ln\left(1+\frac{a^2}{4}\right).\sin(2\theta_0)\right]$$

The next figures indicate the evolution of the Cauchy's stress components in the rigid body frame.

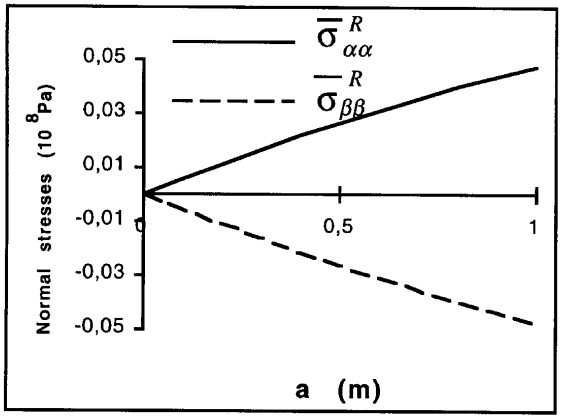

Fig. 2. Normal stresses in the rigid body frame

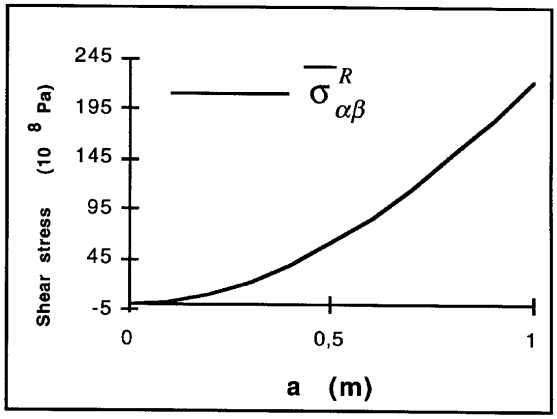

Fig. 3. Shear stresses in the rigid body frame

$C_{\alpha\alpha\alpha\alpha} = C_{\beta\beta\beta\beta} = 100010$ MPa ; $C_{\alpha\alpha\beta\beta} = 6.8$ MPa ; $C_{\alpha\beta\alpha\beta} = 4.4$ MPa, $\theta_0 = 0°$

OUR STUDY

Basic Assumptions

The basic assumptions of our model are given as follows:

1. on the macroscopic scale, the fabric has a plane of symmetry coinciding with the median plane of the fabric, and the material considered is a perfectly balanced fabric,
2. the thickness of the fabric is small so that the stress vector components orthogonal to the median plane of the fabric are zero,
3. deformations due to warping shrinkage are neglected. An average modulus is assigned to each of the warp and weft directions.
4. the behaviour of the fabric is assumed to be orthotropic along the directions of the bisectors of the warp and weft roving. The components of the behaviour law then vary as functions of the relative rotation of these directions.

The latter assumption results from the kinematics study of two material segments, e.g. as in fig. 4, which are initially perpendicular to an arbitrary initial position. This study compares the bisector rotation of the dihedron formed by these segments to the rotation of the rigid body derived from the polar decomposition. This assumption is permissible within the transformation range applicable for the studied process as it can be seen at the fig. 5.

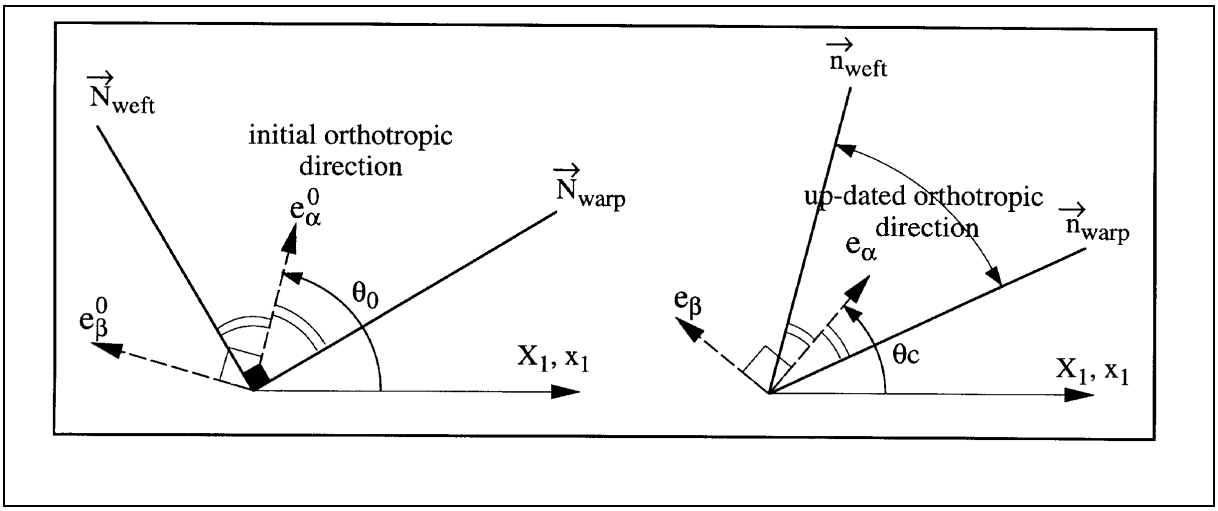

Fig. 4. Rotation of the warp and weft yarns

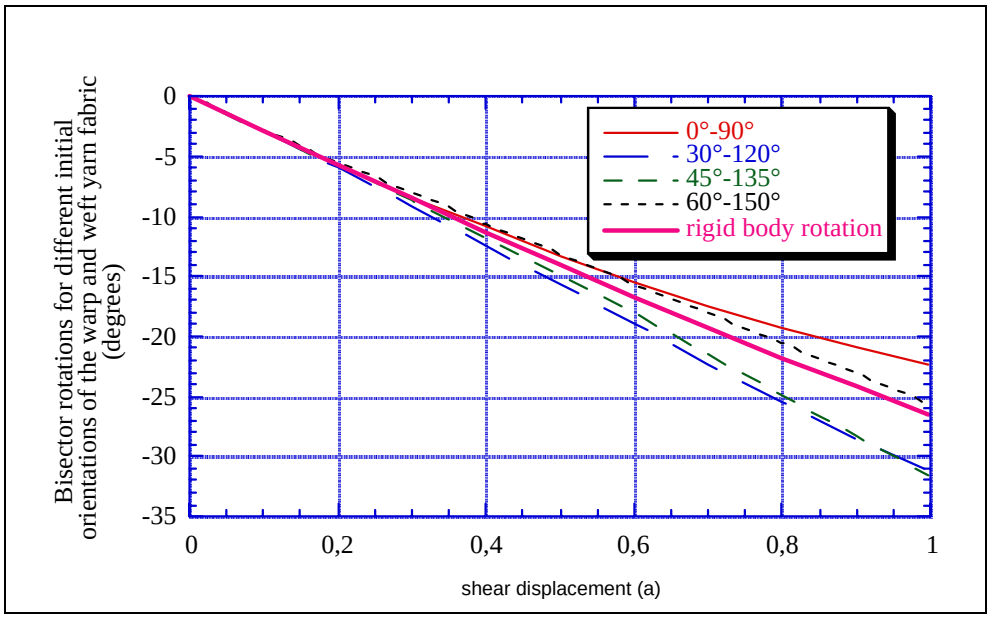

Fig. 5. Comparison between rotation of bisectors obtained from real rotations of warp and weft yarns and the rigid body rotation

The variation of the behaviour law in the mobile coordinate system (e_α,e_β) corresponding to the rigid body rotation can then be monitored in order to ensure that the formulation is objective. Actually, one way to obtain an objective behaviour law for our material with material symmetry is to express it in a frame which rotates with the material. An orthotropic behaviour law will thus stay within it. Among those frames and according to our hypothesis, the rigid body frame, initially coinciding with the directions of the warp and weft yarns angle bisectors remains in coincidence throughout the transformation. Furthermore, as the deformations in the yarn directions are infinitesimal compared to the finite shear deformations in the fabric plane, the behaviour law remains orthotropic in this frame but evolves with the variation of the angle between warp and weft yarns. Only the variation of this orthotropy needs to be considered.

Constitutive Equations

We have chosen to work with a hypoelastic law, representative of the constitutive law of carbon yarns. The viscoelasticity of the resin is thus neglected and it is given an elastic modulus. We can write the law in the rotating frame as follow :

$$\left[\dot{\bar{\sigma}}\right] = \left[\mathbf{C}(\bar{\sigma})\right].\left[\bar{\mathbf{D}}\right] \quad \text{where } \left[\bar{\mathbf{D}}\right] \text{ is the strain rate, expressed in this frame.}$$

We will then use this frame together with the rigid body rotation to formulate strains and stresses at velocity to benefit from the objectivity of magnitudes manipulated in it, and we can write :

$$\bar{\sigma}(t+\Delta t) = \bar{\sigma}(t) + \int_{t}^{t+\Delta t} \dot{\bar{\sigma}}(\tau)d\tau \qquad \text{in this rotating frame.}$$

In our incremental numeric formulation, taking the behaviour law variation into account, we assume that the rotation of the main elongation directions is zero on an increment. Furthermore, we assume that the behaviour law is constant for this increment. Note that this assumption is particularly justified for very small increments.
Therefore, we obtain:

$$\bar{\sigma}(t+\Delta t) = \bar{\sigma}(t) + \bar{C}_{\alpha\beta}(t).\Delta\bar{\varepsilon}^{R}$$

The $\bar{C}_{\alpha\beta}$ tensor of the behaviour law is calculated from the geometric positions of the two yarn directions which are up-dated at the end of the increment. Let N_{warp} and N_{weft} be the respective direction vectors of a warp or weft yarn at the beginning of an increment. During this increment, those directions are transformed into n_{warp} and n_{weft} by :

$$n_{warp} = \frac{1}{\left\|\Delta\mathbf{F}.N_{warp}\right\|}.\Delta\mathbf{F}.N_{warp} \text{ and } n_{weft} = \frac{1}{\left\|\Delta\mathbf{F}.N_{weft}\right\|}.\Delta\mathbf{F}.N_{weft} .$$

So we can express the angle between those two vectors and so recalculate the angle $\theta(t+\Delta t) = \frac{1}{2}\left(\hat{n}_{warp}, n_{weft}\right)$ between them and the bisector.

The behaviour law is obtained for the next increment by integrating the local behaviour of the warp and weft networks (assumed to be independent) associated with the pre impregnation resin, across the thickness of the fabric, using the law $\bar{C}_{\alpha\beta} = \frac{1}{h}\int_{h}(C_{\alpha\beta}^{warp}(-\theta) + C_{\alpha\beta}^{weft}(+\theta))dz$ where $C_{\alpha\beta}^{warp}(-\theta)$ and $C_{\alpha\beta}^{weft}(+\theta)$ are the initial orthotropic homogenised behaviour laws for the warp or weft networks, expressed in a basis rotated from respectively $-\theta$ and $+\theta$. The rotation of the bisector being comparable to the rigid body rotation, the orthotropic behaviour law is objective.

BASIC TESTS

In order to validate our algorithm, we have implemented it in the ABAQUS industrial software by writing a "VUMAT" map, a subroutine used to define a specific behaviour law. Here below we present some results in comparison with a non up-dated material.

Simple Shear Test

This test has been described previously. The results obtained with a material which is a carbon satin are presented in Fig. 6 and 9.

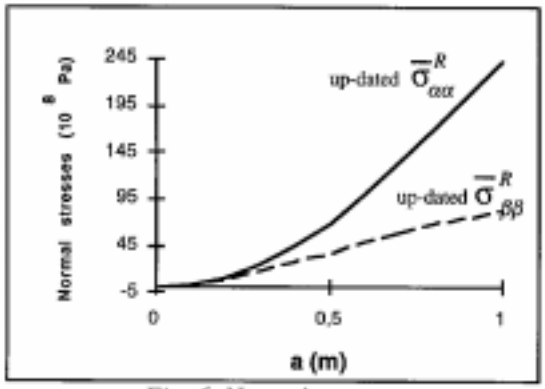

Fig. 6. Normal stresses in the rigid body frame

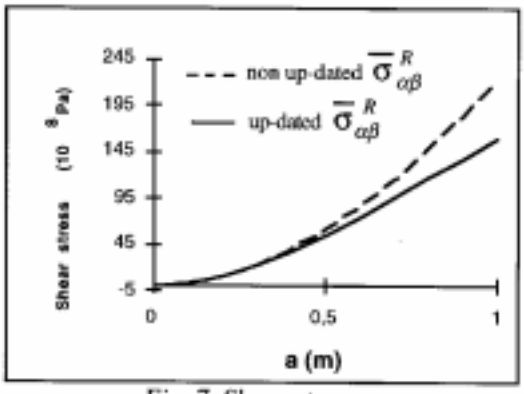

Fig. 7. Shear stresses in the rigid body frame

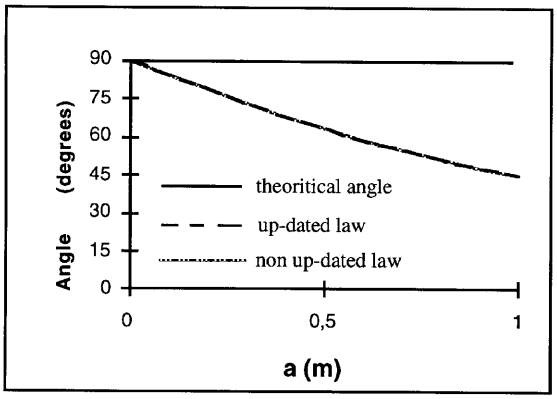

Fig. 8. Angle between the warp and weft directions

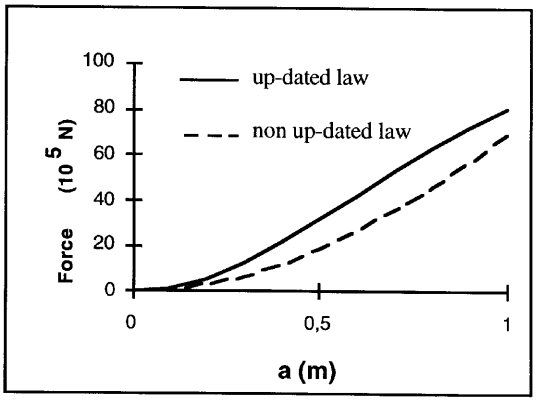

Fig. 9. Resulting force in x and y directions

Behaviour law of one network of yarns:

C_{1111} = 100003 MPa ; C_{2222}= 7.62 MPa ; C_{1122} = 3.4 MPa ; C_{1212} =2.2 MPa, θ_0= 0°

The non up-dated normal stresses being insignificant compared to the up-dated stresses, they are not indicated in Fig. 6.

Simple Tensile Test

This test has been performed in order to test the kinematic of deformation obtained with this algorithm. We have imposed a displacement on a sample with a 45° initial angle of the warp yarns, as the width of a real sample of fabric becomes 1/2 of the initial width. For this test the angle between yarns that we have to obtain is 41.4 degrees. We have found 42.2 degrees with our model and a width of 0.507, whereas the sample with non up-dated behaviour law is near 62 degrees with a width of 0.756 .

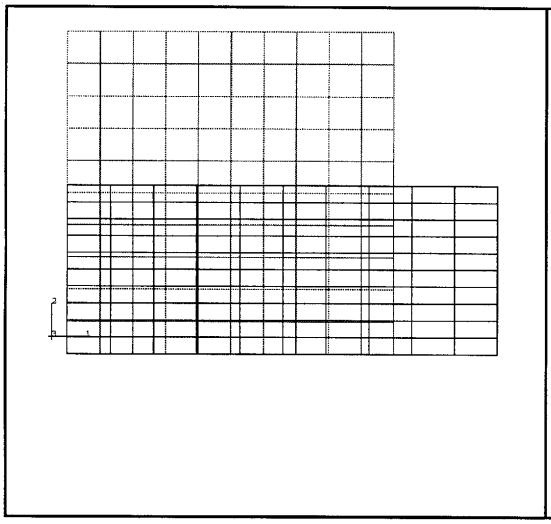

Fig. 10. Up-dated behaviour law

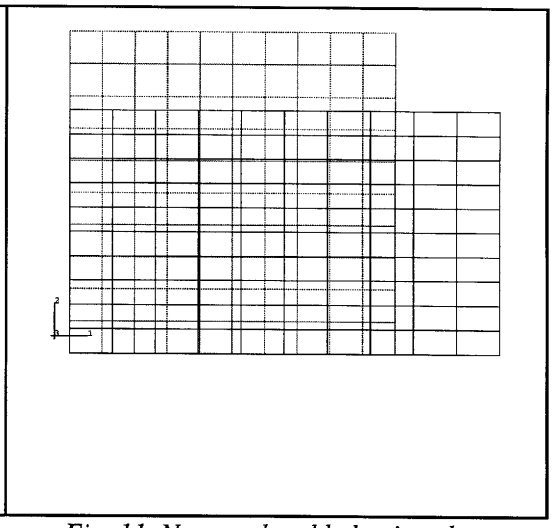

Fig. 11. Non up-dated behaviour law (ABAQUS)

EXAMPLE

The example of shaping process which is presented in this paper corresponds to a automated laying-up of a hemispherical part with a woven fabrics with yarns oriented at +-45° (directions of fibers along the diagonals of the fabric pattern).

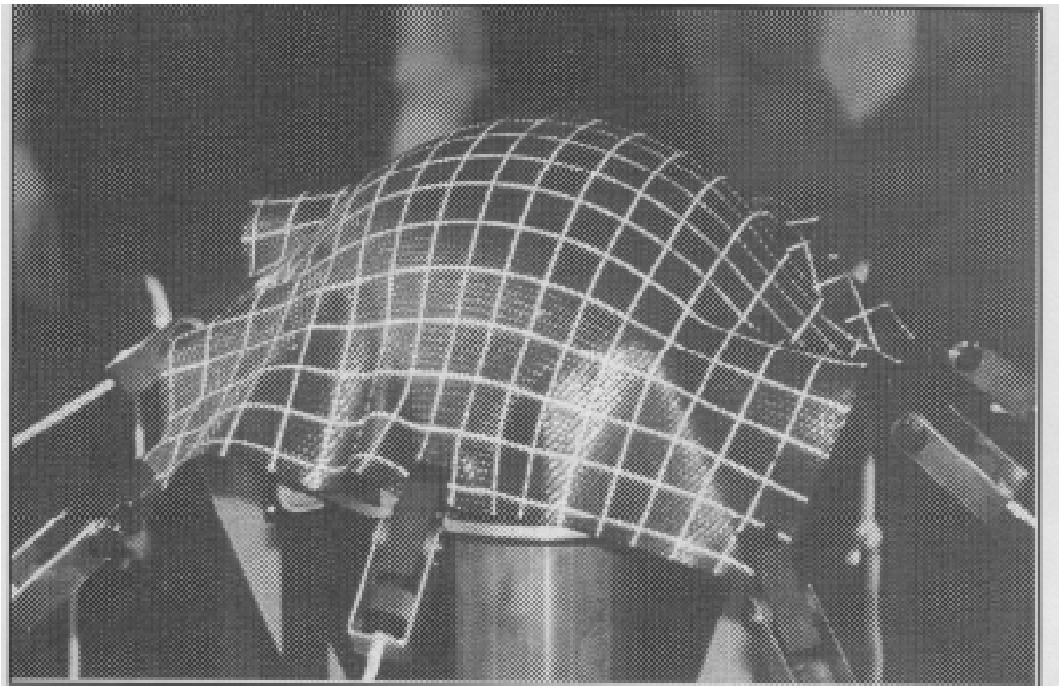

Fig. 12 Laying up on a hemisphere
Fabrics at +-45°

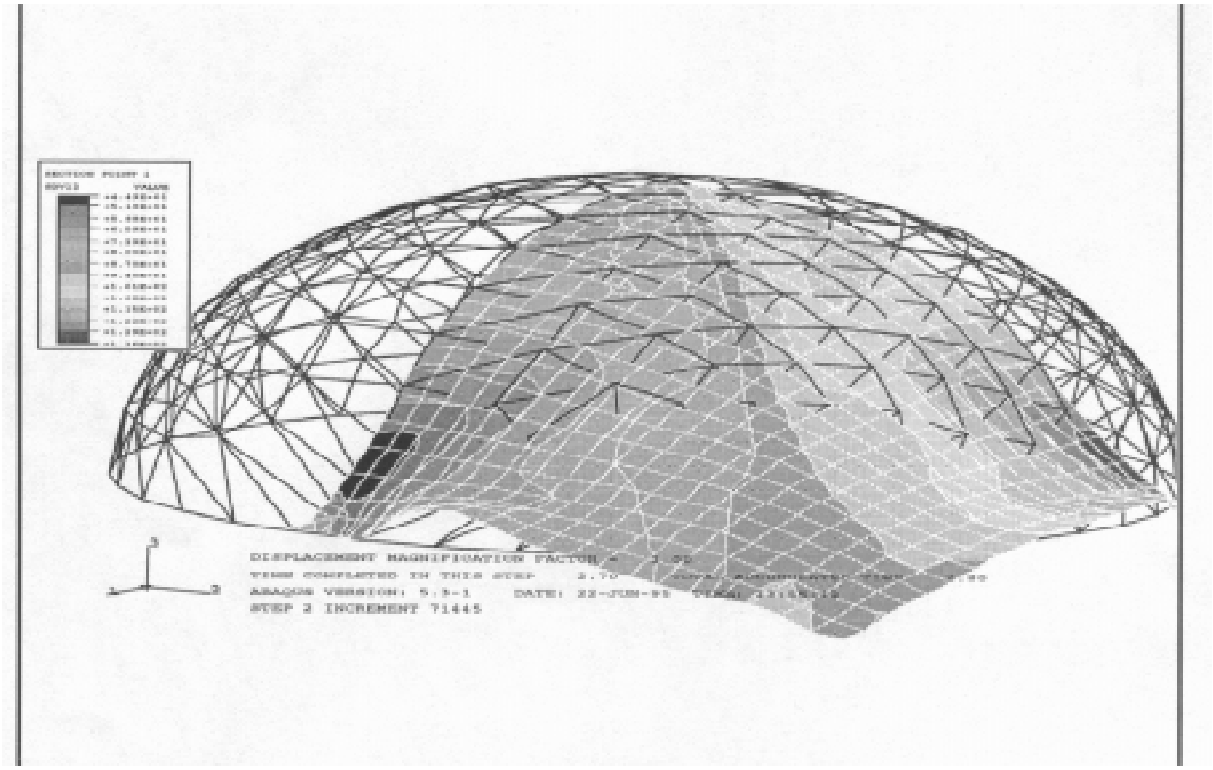

Fig. 13 Simulation of taying up on a hemisphere
Fabrics at +-45°
Angles between yarns

A comparison with simulation is performed and show a very agreement with experiment.

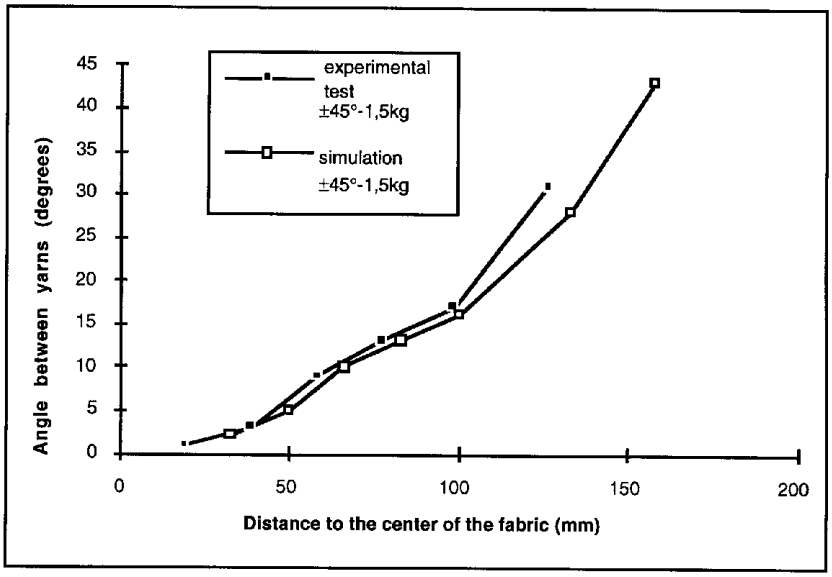

Fig. 14 Comparison between experimental test and simulation
Angles between yarns

CONCLUSIONS

This study is the first part of a numerical model of the laying-up for non-developable composite parts. We must now introduce the viscoelastic behaviour in the constitutive equations to obtain an industrial aided design tool.

ACKNOWLEDGMENTS

This study was performed in collaboration with M. Billoët from ENSAM PARIS.

REFERENCES

1. BLANLOT R. BILLOET J.L. "Modélisation en grandes transformations de milieux à anisotropie évolutive - Modeling of large transformations in bodies with variable anisotropy)." *Internal Report", ENSAM PARIS* 1995 .

2. BLANLOT R. BILLOET J.L. GACHON H. "Study of the non-polymerized prepreg fabrics in off-axes tests", *ICCM9 - Volume 4, Madrid* 1993.

3. GELIN "Modélisation en grandes transformations de milieux à anisotropie évolutive - Modeling of large transformations in media with variable anisotropy)." *Internal Report",*.

4 GILORMINI P. "Sur les référentiels locaux objectifs en mécanique des milieux continus - (About objective local frames in mechanics of continuous media)" - Acad. Sci. Paris report T. 318, Series II, pp 1153-1159, 1994.

5. SOWERBY R., CHOU E. "Rotations, stress rates and strain measures in homogeneous deformation processes" - Int. J. Solids Stuctures, Vol. 20, No. 11/12, pp. 1037-1048, 1984

6 SZABO L. - BALLA M. "Comparison of some stress rates " - Int. J. Solids Stuctures, Vol. 25, No. 3, pp. 279-297, 1989

NUMERICAL MODELLING OF ENERGY ABSORPTION IN WOVEN COMPOSITES

Louis Dagba[1], Christian Wielgosz[2]

[1]*Laboratoire de Mécanique et Matériaux, Ecole Centrale de Nantes*
1 Rue de la Noë, 44072 Nantes Cedex 03, France
[2] *Laboratoire de Génie Civil de Nantes St - Nazaire, Ecole Centrale de Nantes - Université de Nantes, 2 Rue de la Houssinière, 44322 Nantes Cedex 03, France*

SUMMARY: The aim of the paper is to submit experimental and numerical results on energy absorption behaviour of woven composite plates submitted to high dynamic tensile. The hybrid woven plate (glass - kevlar - epoxy) is clamped at one end and impacted at the other end in order to obtain damage and failure of the sample. Usual finite element method programs with damage theories are unable to give a correct numerical answer to this problem. We show that a modified Chang's ([1], [2], [3]) progressive damage theory including new post failure rules can be used to compute the response of the sample and to obtain good numerical results on the energy absorbed by the sample.

KEYWORDS: hybrid woven composite, dynamic, failure, energy absorption

INTRODUCTION

The use of composite materials in crashworthy structures offers significant weight and cost reduction relative to metal structures. In the last decade, several authors ([4], [5], [6]) have shown by crushing tests on composite tubes the ability of composite materials to absorb energy. In spite of the considerable work done in experimental studies, reliable numerical models are not yet available to predict the energy absorption behaviour of composite structures. The aim of this study is to simulate this phenomenon in the case of composite plates by using a dynamic finite element software [7]. The woven composite constitutive law is obtained from an experimental study. Dynamic behaviour is described and the typical load displacement curve shows the ability of the woven to absorb energy. A first finite element model based on Chang's theory shows that the failure rules are inadequate to describe energy absorption. New damage rules are introduced to solve failure progression in the plate. It is shown that load carried capacity of the plate is in good agreement with experimental results.

EXPERIMENTAL PROCEDURE

Material data

The material used in this investigation is a glass - kevlar- epoxy woven composite. The tested structure is made of height ply of twill weave as shown on Fig 1.

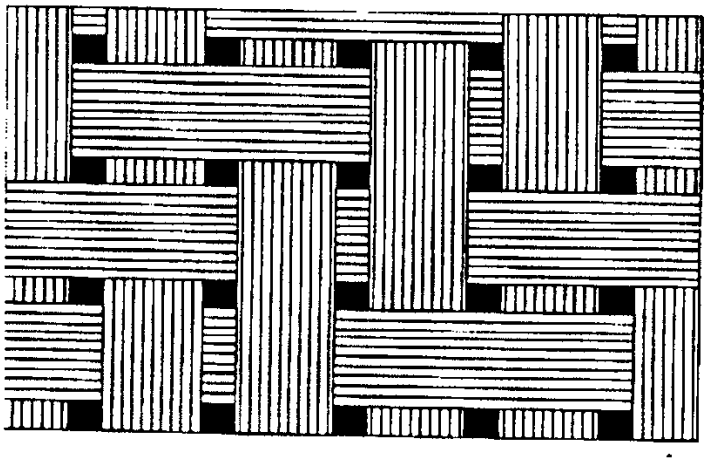

Fig.1: Twill weave.

The samples (Fig.2) are cut from twill panels and submitted to quasi-static tensile load in order to derive in-plane elastic constitutive law [8]. Table 1 sumarizes fiber volume fraction and elastic properties of the studied structure.

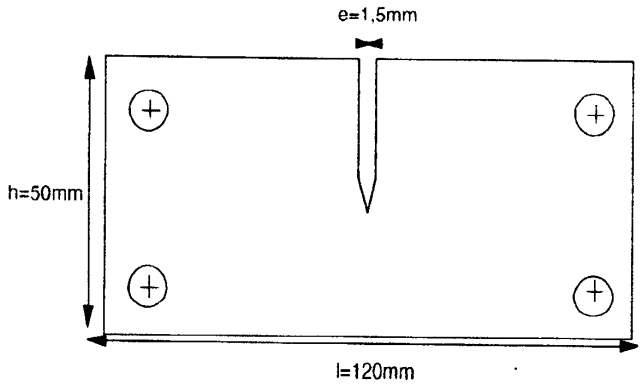

Fig. 2 : geometry of the studied sample.

E_{11}	σ^r_{11}	ε^r_{11}	ν_{12}	G_{12}
13400 MPa	156 MPa	1.16 %	0.20	2040 MPa

Table 1

Dynamic Tensile Test.

The dynamic test on the sample was carried on the cutted sample [8]. One end is clamped and the other end is impacted by a rigid body with velocity V (Fig 3).

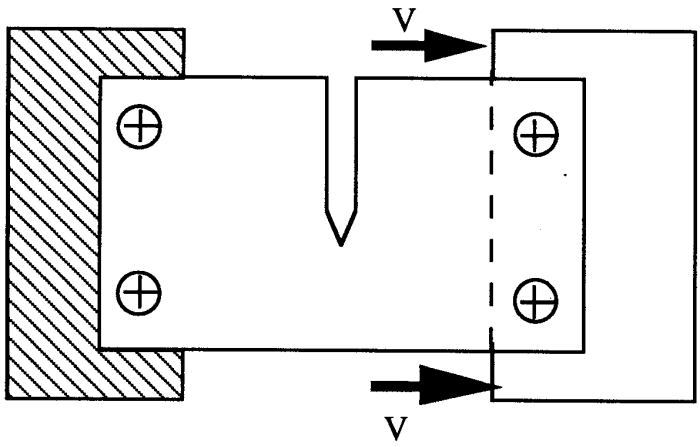

Fig.3: Schematic view of testing machine.

Velocity is choosen to obtain damage and the final breaking of the structure. Different values of the velocity (10.5, 15, 20.5, 25 m/s) were applied to the rigid body. We have only deal with the third case of velocity.

Experimental Results.

Displacement is recorded at one end of the sample whereas load carried by structure is at the other end. The pattern of failed sample and the load displacement curve are shown in Fig 4 and Fig 5. The scheme of Fig 4 shows that damage occurs only in a localised zone behind initial cutting.

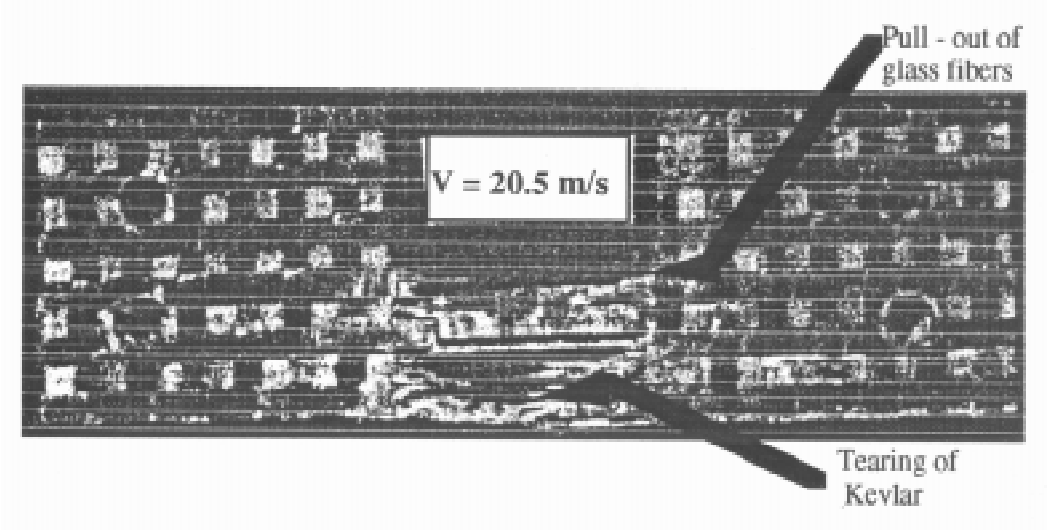

Fig. 4: Failed sample with localised damage zone

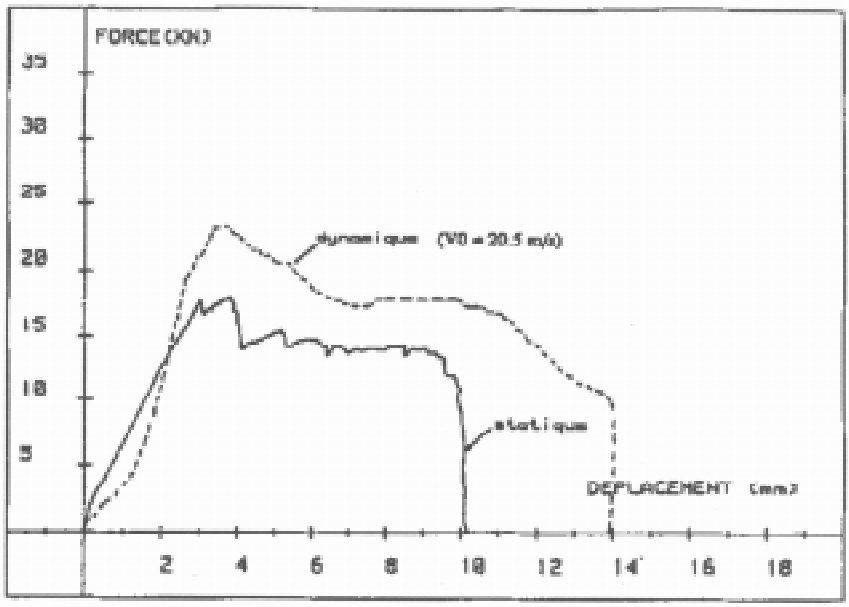

Fig.5: Load - displacement curves for static and dynamic experiments.

NUMERICAL RESULTS

Constitutive Relations of Laminates.

The woven structure is considered to have an inelastic behaviour. As described by ([9],[10],[11],[12]), the non linearities between shear stresses and shear strains are more important than non linearities between normal stresses and normal strains. This behaviour is taken into account by the following relation suggested by Tsaï [11]:

$$2\varepsilon_{12} = \frac{\tau_{12}}{G_{12}} + \alpha . \tau_{12}^{3} \qquad (1)$$

where ε_{12} and τ_{12} are respectively strain and shear components, G_{12} is the shear modulus and α is a material constant. We assume plane stress state in this study and use the usual laminated theory to derive constitutive equations of the plate which are given by

$$\begin{Bmatrix} \varepsilon_{11} \\ \varepsilon_{22} \\ \gamma_{12} \end{Bmatrix} = \begin{bmatrix} S_{11} & S_{12} & 0 \\ S_{21} & S_{22} & 0 \\ 0 & 0 & S_{66} \end{bmatrix} \begin{Bmatrix} \sigma_{11} \\ \sigma_{22} \\ \tau_{12} \end{Bmatrix} \text{ or, } \{\sigma\} = [S]^{-1}\{\varepsilon\} = [Q]\{\varepsilon\} \qquad (2)$$

with,

$$Q_{11} = \frac{E_1}{1 - \nu_{12} . \nu_{21}} \qquad Q_{22} = \frac{E_2}{1 - \nu_{12} . \nu_{21}} \qquad (3)$$

$$Q_{12} = \frac{E_1 \cdot \nu_{21}}{1 - \nu_{12} \cdot \nu_{21}} = \frac{E_2 \cdot \nu_{12}}{1 - \nu_{12} \cdot \nu_{21}} = Q_{21}, Q_{66} = G_6 \qquad (4)$$

thus:

$$\begin{Bmatrix} \sigma_1 \\ \sigma_2 \\ \sigma_6 \end{Bmatrix} = \begin{bmatrix} Q_{11} & Q_{12} & 0 \\ Q_{21} & Q_{22} & 0 \\ 0 & 0 & Q_{66} \end{bmatrix} \begin{Bmatrix} \varepsilon_1 \\ \varepsilon_2 \\ \varepsilon_6 \end{Bmatrix} \qquad (5)$$

Chang's degradation rules are used to take into account progressive failure in composites.

Finite element model and numerical results with Chang's model.

The finite element discretization uses Belytschho [13] shell elements. Several computations were done and the results on the mesh size have shown that the optimum number of shells was about 480. Numerical results with Chang's damage rules are given on Fig 6:

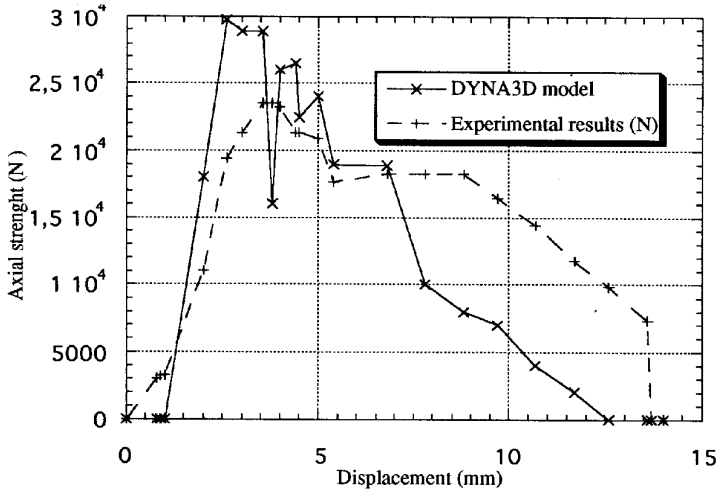

Fig. 6 : First numerical and experimental results for the sample

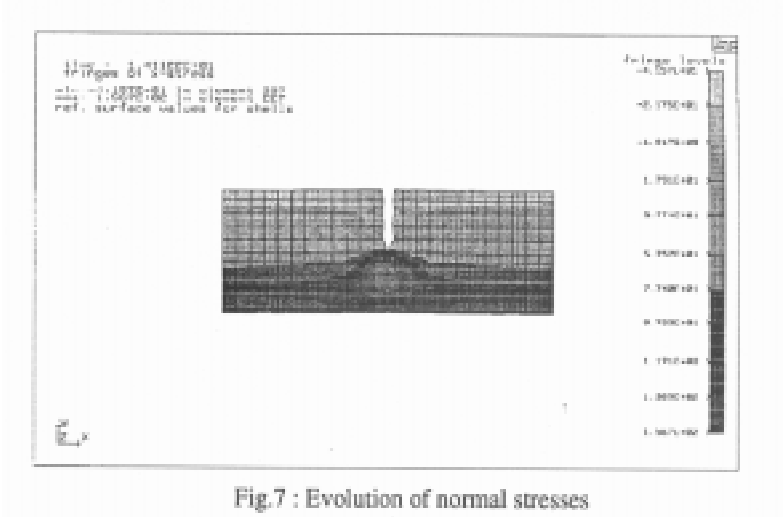

Fig.7 : Evolution of normal stresses

The load curve versus displacement shows pic values which are similar to experimental results, but maxima values of stresses are too high and energy absorbeb is not completely described.

A new theory of damage and post failure in woven composites.

Since Chang criterion tends to overload the strength of the woven composite in the case of dynamic loading and to undervalue energy absorption, we have implemented in LS-DYNA3D software [7], a maximum stress limit and new post degradation rules which are based on the hypothesis that the failure of fibers in tensile is the predominant mode of failure. The loss of woven stiffness in filler and stuffer weavers is governed by two different parameters a_c and a_t. The usual constitutive relations

$$\begin{bmatrix} \frac{E_{xx}}{1-\nu_{xy}\,\nu_{yx}} & \frac{E_{yy}\,\nu_{xy}}{1-\nu_{xy}\,\nu_{yx}} & 0 \\ \frac{E_{xx}\,\nu_{yx}}{1-\nu_{xy}\,\nu_{yx}} & \frac{E_{yy}}{1-\nu_{xy}\,\nu_{yx}} & 0 \\ 0 & 0 & G_{xy} \end{bmatrix} \qquad (6)$$

are replaced by the new law:

$$\begin{bmatrix} a_c.E_{xx} & a_t.E_{yy} & 0 \\ 0 & 0 & 0 \\ 0 & 0 & G_{xy} \end{bmatrix} \qquad (7)$$

Numerical results are now closely connected with experimental data (Fig.8). Let us tell that our results are here given without any filter. We can therefore state that post failure behaviour of woven composite structures can be numerically taken into account in the treatment of crash response of energy absorption components.

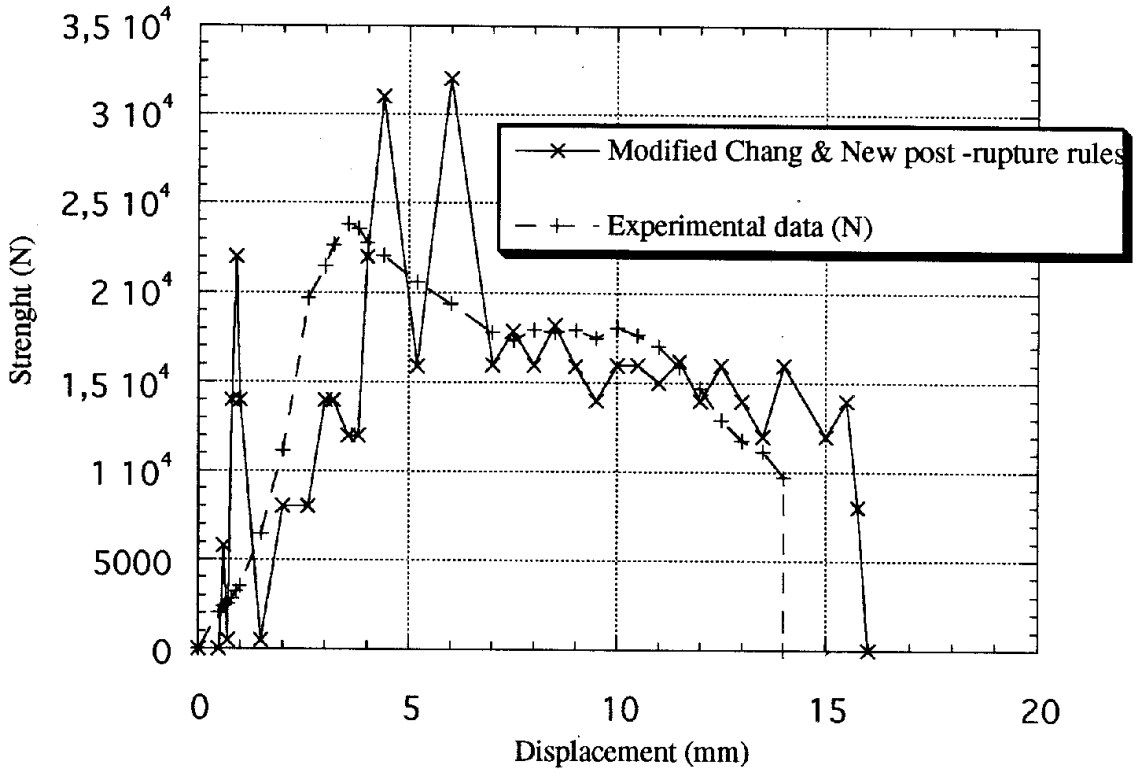

Fig.8 : Carried load versus displacement

CONCLUSION

Behaviour up to failure in woven composites subjected to high dynamic tensile can be well modelled by a modified Chang's progressive damage theory. Numerical results concerning an hybrid woven composites (glass - kevlar - epoxy) are in good agreement with experimental data. The post-failure behaviour of composite structures can be numerically obtained by using finite element method. Numerical solutions can be taken into account in the treatment of crash response of energy absorption components.

REFERENCES

1. Chang, F. K., K.Y.Chang, A Progressive Damage Model for Laminated composites Containing Stress Concentrations,*Journal of Composite.Materials.*, Vol 21, 1987, pp. 834-855.

2. Chang, F. K., R. A. Scott, G. S. Springer, Failure Strength of Nonlinearly Elastic Composite Containing a Pin Loaded Hole,*Journal of Composite.Materials.*, Vol 18, 1984, pp. 464-477.

3. Chang, F. K., Post-Failure Analysis of Bolted Composite Joints in Tension or Shear-out Mode Failure, *Journal of Composite.Materials.*, Vol 21, 1987, pp. 809-833.

4. Farley, G. L., The effects of Crushing Speed on the Energy-Absorption capability of Composite Tubes, *Journal of Composite.Materials.*, Vol 26, 1992, pp. 1314-1329.

5. Farley, G. L., Relationship between Mehanical - Property and Energy Absorption Trends for Composite Tubes, *NASA Report,* L- 17087, 1992.

6. Kindervater, G. L., Composite Strength and Energy Absorption as an Aspect of Structural Crash Resistance, In *Structural Crashworthiness and Failure*, ed. N. Jones, T. Wierzbicki, Elsevier, 1993, pp. 189-235.

7. Hallquist, J. O., DYNA3D User's Manual (Non Linear Dynamic Analysis of Structures in three Dimensions), Lawrence National Laboratory, 1992.

8. Zeitouni, R., Contribution à l'étude de l'Absorption d'énergie par Mécanisme de Déchirure des Matériaux Composites, *E.C.N.*, Ph D Thesis, 1992.

9. Hahn, H. T., Nonlinear Behavior of Laminated Composites, *Journal of Composite Materials.*, Vol 7, 1973, pp. 257-271.

10. Sims, F. D., Nonlinear Elastic Behavior of Unidirectional Composite Laminae, *Journal of Composite Materials.*, Vol 7, 1973, pp. 103-108.

11. Tsai, S. W., Hahn, T. H., Nonlinear Elastic Behavior of Unidirectional Composites Laminated, *Journal of Composite.Materials.*, Vol 7, 1973, pp. 102-118.

12. Yamada, S. E., Analysis of Laminate Strength and its Distribution, *Journal of Composite.Materials.*, Vol 12, 1978, pp. 275-284.

13. Belytschko, T. W., Chiang, H. Y., Improvements in Low-order Shell Elements for Explicit Transient Analysis, *Analytical and Computational Models of Shells,* A. K. Noor and Belytschko, T. W., ASME - CED, **3** , pp. 383-398 (1989).

ANALYSIS OF SHEAR DEFORMATION AND STRENGTH AT FIBER CROSSING PART IN TEXTILE COMPOSITES

Asami Nakai[1], Hiroyuki Hamada[2] and Nobuo Takeda[3]

[1]Graduate student, The University of Tokyo, 4-6-1 Komaba, Meguro-ku, Tokyo 153, Japan
[2]Faculty of Textile Science, Kyoto Institute of Technology
Matsugasaki, Sakyo-ku, Kyoto 606, Japan
[3]Center for Collaborative Research (CCR), The University of Tokyo

SUMMARY: Woven, knitted and braided fabric, in spite of differences on fabrication process and mechanical behavior, are fabricated by intertwining the fiber bundle and the whole structure consists of repeat of crossing fiber bundles. Clearly the deformation and fracture behavior at fiber crossing part control the mechanical behavior of textile composite, so that it is important to understand the behavior at fiber crossing part quantitatively. In this study, for the purpose of investigating the behavior at fiber crossing part in textile composites, the evaluation method of the interface between fiber bundles was examined by numerical approaches. The effects of fiber undulation and modulus of interface between fiber bundles on shear deformation and strength at fiber crossing part was examined. Finally, a new attempt was performed that the strength of interface was calculated by combining the numerical and experimental approach.

KEYWORDS: textile composite, fiber crossing part, finite element method, interface property, crimp ratio, fiber bundle pull-out test

INTRODUCTION

Traditionally, advanced composite structures have been fabricated from tape prepregs which were systematically stacked to form a laminate. Two limitations of laminated composites provide much of the drive for the interest in "textile composite". First, the laying up of pre-preg has been difficult to automate and it still an expensive and time consuming task. Second, the strength of some laminated structures is dominated by a relatively weak resistance to transverse shear, which is governed primarily by the matrix. Various forms of textile composites, which are reinforced with woven, knitted and braided fabric preform, have been considered through much of the modern composite history. It is believed that a properly designed textile composite would be relatively easy to automate and have a greater transverse strength than a laminated composite.

Woven, knitted and braided fabric, in spite of differences on fabrication process and mechanical behavior, are fabricated by intertwining the fiber bundle and the whole structure consists of repeat of crossing fiber bundles. Therefore, the fiber crossing is an invariable structure in textile composites. Because of the fiber crossing in textile composites, the undulation (crimp) of fiber bundles is generated and the particular transmission mechanism of force between fiber bundles is produced. The stress applied to one fiber bundle is transmitted

to another fiber bundle at the fiber crossing part. The deformation and fracture behavior at fiber crossing part control the mechanical behavior of textile composites, so that it is important to understand the behavior at fiber crossing part quantitatively. However, the architecture of a textile fabric in textile composite is complex and, therefore, the parameters controlling the behavior at fiber crossing part become numerous. Moreover, the behavior at fiber crossing part is dependent on the properties of interface between fiber and matrix.

Hamada et al have proposed a evaluation method of the interface between fiber bundles in woven fabric composite experimentally [1]. In the special experimental method, the shear strength of interface between warp fiber strand and weft fiber strand in a plain woven fabric with different concentration of silane coupling agents was obtained.

In this study, for the purpose of investigating the deformation and fracture behavior at fiber crossing part in textile composites, the evaluation method of the interface between fiber bundles was examined by numerical approaches. Firstly, the concept of modeling and numerical analysis model for textile composite is proposed. Second, the evaluation method proposed by Hamada et al. [1] was introduced as a background. The numerical analysis model was applied to the evaluation method. In this paper, the effects of fiber undulation and modulus of interface between fiber bundles on shear deformation and strength at fiber crossing part was examined. Finally, a new attempt was performed that the strength of interface was calculated by combining the numerical and experimental approach.

MODELING FOR TEXTILE COMPOSITES

In the case of textile composites, fiber orientation angle, crimp, continuity of fiber and stress transmission system between fibers greatly affect the mechanical behavior. So, the analytical model has to represent the weaving structure faithfully. Moreover, various range of fractures from microscopic fracture to macroscopic fracture in the composite have to be considered. It might be difficult to represent all ranges of fracture in a single model. In conformity with the concept, we have established an unified method from micro model to macro model [2-4]. Figure 1 shows the five modeling steps for simulating the mechanical behaviors of the braided composite precisely. Basically, results obtained from micro models are used in the analyses of macro models. According to this system, macroscopic analysis can be performed considering microscopic phenomena. Hereafter, specific characteristics of each model are described.

"Fiber bundle model" represents the fiber bundle impregnated with resin. This model does not consider the undulation of fiber bundle, although micro fracture in the fiber bundle can be considered by using the model. This model might consider micro phenomena such as the effects of surface treatment, filament diameter and number of filaments.

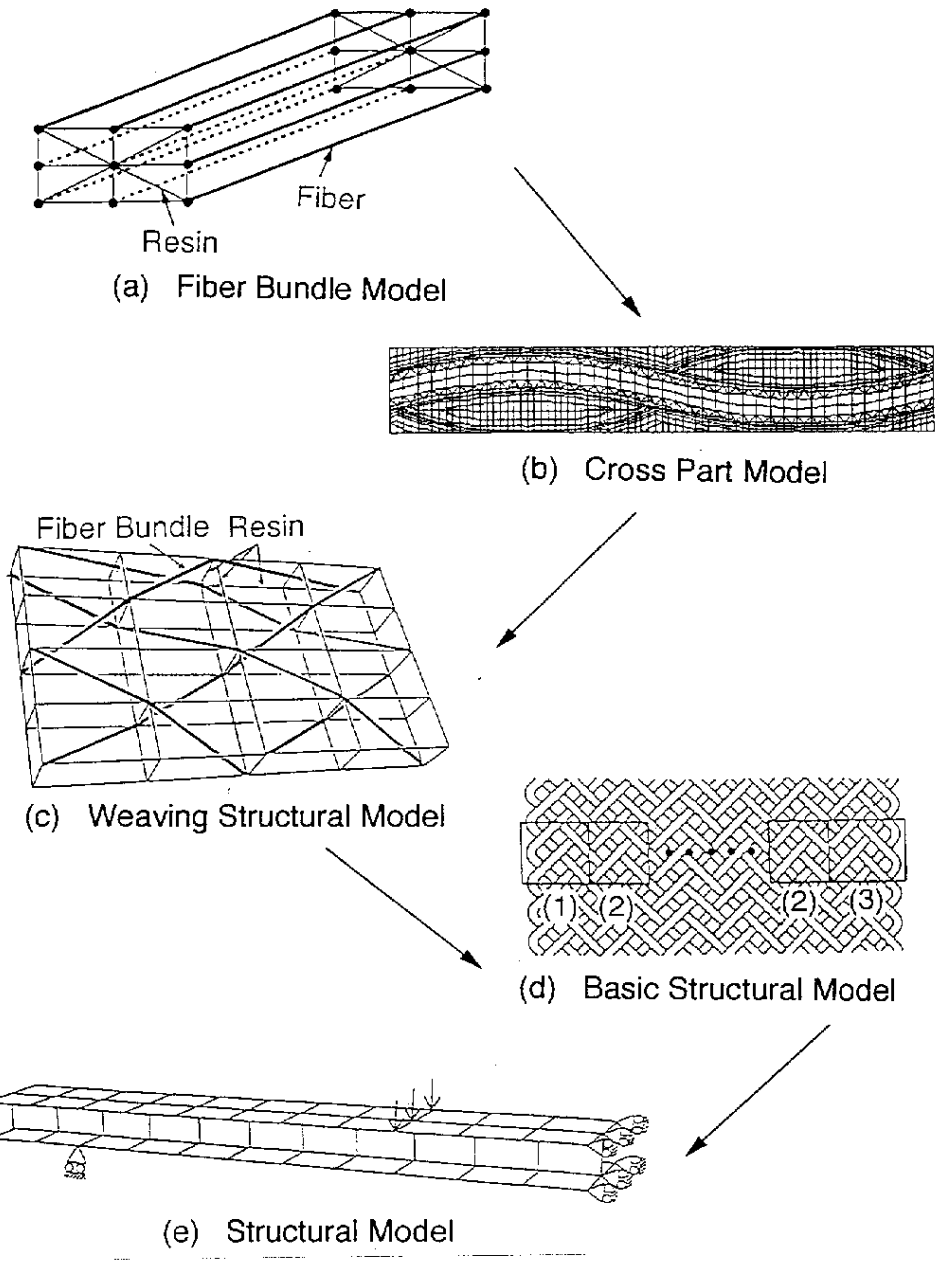

Fig.1 Five modeling steps for simulating mechanical behaviors of braided composites.

"Cross part model" represents the cross part between fiber bundles to consider the effects of the contact between undulated fiber bundles and interface between fiber and matrix. This model might consider the cross sectional shape of fiber bundle, weaving structure and interfacial properties at the cross part between fiber bundles.

"Weaving structural model" represents the weaving structure to consider its effect on the mechanical behavior of braided composites. The braided composites are recognized as an aggregation of the resin impregnated fiber bundle and resin region. The weaving structure of the braided composites is expressed as connections to beam elements. Resin existing between crossing fiber bundles is set by using beam element because of considering transmission of force at crossing point between the fiber bundles and the material constants of

the resin element will be obtained by analysis of "Cross part model". The resin elements are also set up in both surfaces of textile composite since the resin exists at surface of the textile composite except for between crossing fiber bundles.

"Basic structural model" represents the basic braided composite such as flat or tubular braided composite. The mechanical behavior of the basic braided composites can be predicted by using the numerical results of the weaving structural models as material constants and failure criteria. Finally "Structural model" represents the whole structure of braided composite. Numerical results of the weaving structural models or basic structural model, can be used as material constants of each element in the structural model. This analytical method can be applied to predict the various mechanical properties of braided composite, by selecting and combining these models according to the analytical objects.

BACKGROUND - FIBER BUNDLE PULL-OUT TEST -

Hamada et al have proposed a new evaluation method of the interface between fiber bundles in textile composites, called “Fiber bundle pull-out test” [1]. Through the fiber bundle pull-out test, the shear strength at fiber crossing part in textile composites should be obtained.

The schematic diagram of the specimen for fiber bundle pull-out test is shown in Fig.2(a). Figure 2(b) shows the magnification of warp/weft fiber crossing part. In order to cause the pull-out of warp fiber strand at the fiber crossing part, notches are introduced as shown in Fig.2. Moreover, to apply the shear force only to the fiber crossing part, a plate made by epoxy resin is placed on the both sides of fiber crossing part as shown in Fig.2(a). The geometry of the specimen was decided by finite element analysis in consideration of the stress components at fiber crossing part.

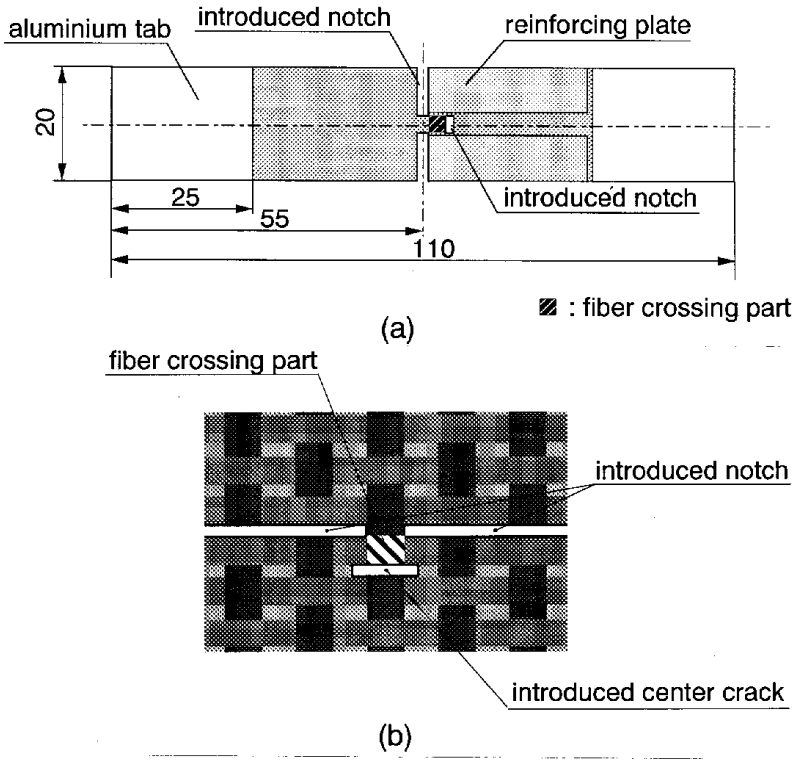

Fig.2 Schematic diagram of specimen for fiber bundle pull-out test.

Figure 3 shows the fracture process of fiber crossing part in fiber bundle pull-out test. Applying a load to the specimen, initial crack was occurred in the vertical direction to the load as shown in Fig.3. As the displacement increased, the delamination of fiber bundle progressed from the initial crack, and then the pull-out of warp fiber strand was observed. The fracture progress was independent of the concentration of silane coupling agents on a plain woven fabric. The strength of fiber crossing part was obtained by dividing the load at which initial crack occurred by the area of fiber crossing part.

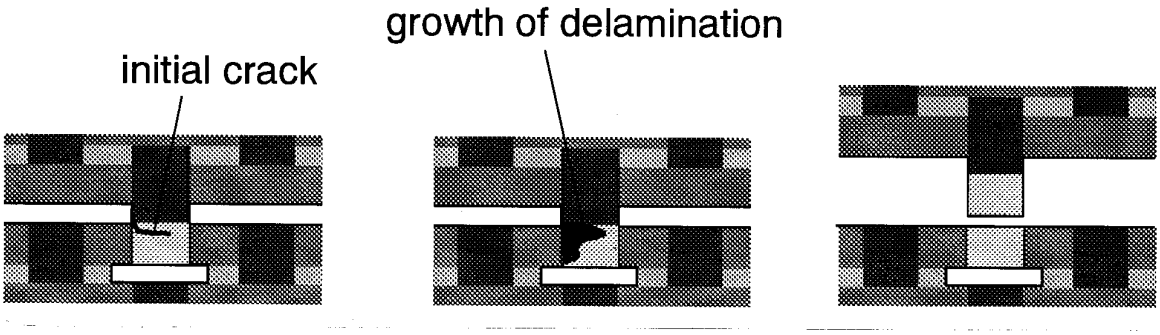

Fig.3 Fracture process of fiber crossing part in fiber bundle pull-out test.

ANALYTICAL MODEL AND METHOD

In order to clarify the effects of fiber undulation and modulus of interface between fiber bundles on the shear deformation and strength at fiber crossing part, numerical analysis was performed by finite element method. Cross part model which represent the fiber crossing part was employed to consider the contact between undulated fiber bundles and the interface properties.

Figure 4 shows the finite element division for a fiber bundle pull-out test specimen and the boundary condition. The load was applied to one side of warp fiber strand as shown in Fig.4. In this study, three types of FE model with different crimp ratio were chosen. Crimp ratio is a unique characteristic in textile fabric which represent the degree of the fiber undulation and clearly the crimp ratio affects the mechanical behavior of textile composites. The FE model was composed of warp fiber strand, weft fiber strand, resin and interface elements. Two dimensional plain strain element was used in all elements. The material constants used in the model are shown in Table 1. The material constants of the fiber elements were calculated by Rule of Mixture since the fiber bundle was impregnated with the resin. The resin elements possess the properties of an epoxy resin. However, the material constants of the interface elements are unknown, because this relates to the interfacial properties between the fiber and matrix. Therefore, the elastic modulus of interface were changed on the basis of resin property, 1/10, 1 and 5 times as shown in Table 1. After all, nine kinds of analytical model with different crimp ratios and moduli of interface were examined as shown in Table 2. Hereinafter, abbreviated names in Table 2 is employed to express each model.

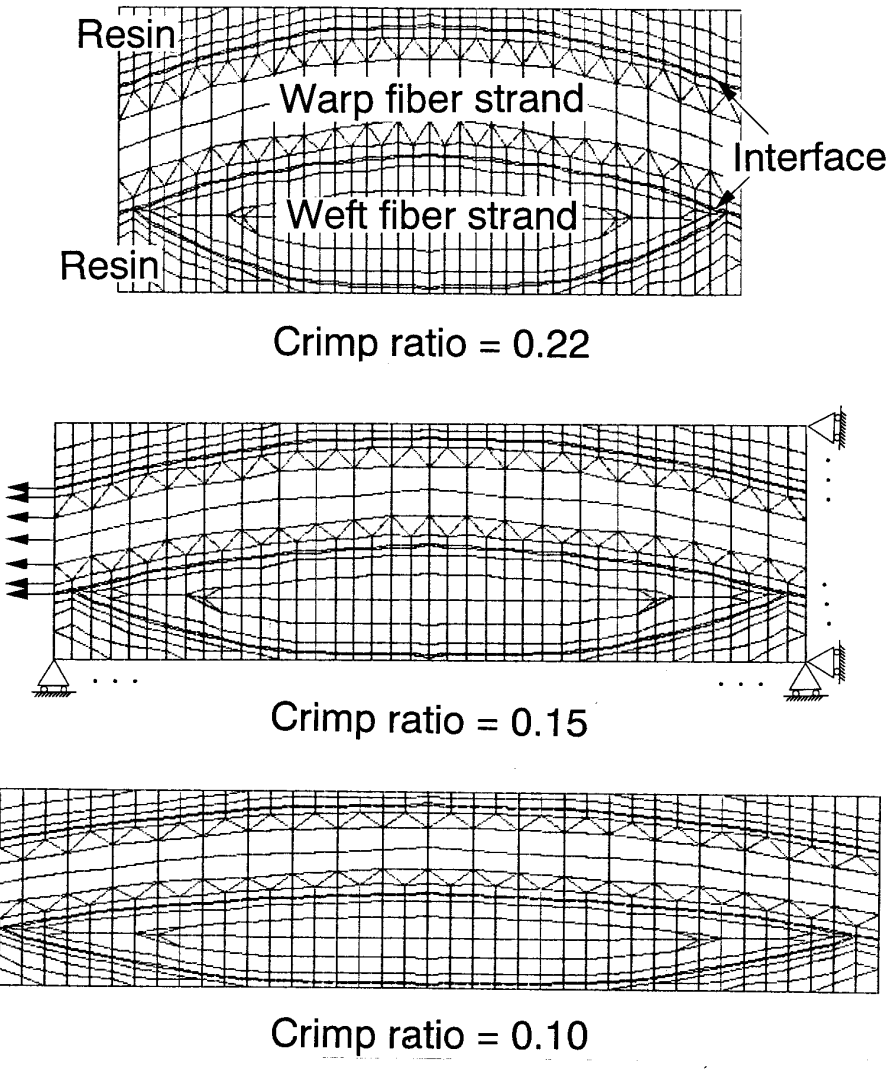

Fig.4 Finite element division for fiber bundle pull-out test specimen.

Table 1 Material constants used in FE model.

	Elastic Modulus (GPa)	Poisson's Ratio
Warp Fiber Strand	58.8	0.30
Weft Fiber Strand	17.0	0.03
Resin	3.4	0.33
Interface	0.34 / 3.4 / 17.0	0.33

Table 2 Analytical model with different crimp ratios and moduli of interface.

Crimp ratio \ Elastic modulus of interface (GPa)	0.34	3.4	17.0
0.22	BL	BM	BH
0.15	ML	MM	MH
0.10	SL	SM	SH

RESULTS AND DISCUSSIONS

Figure 5 shows the deformation states of the MM model and ML model. In the case of the model with lower elastic modulus of interface than resin, the transmission of the strain of warp fiber strand through interface was smaller and the deformation of resin became smaller than that in the case of the model with higher elastic modulus of interface. The tendency was independent of the crimp ratio of the model.

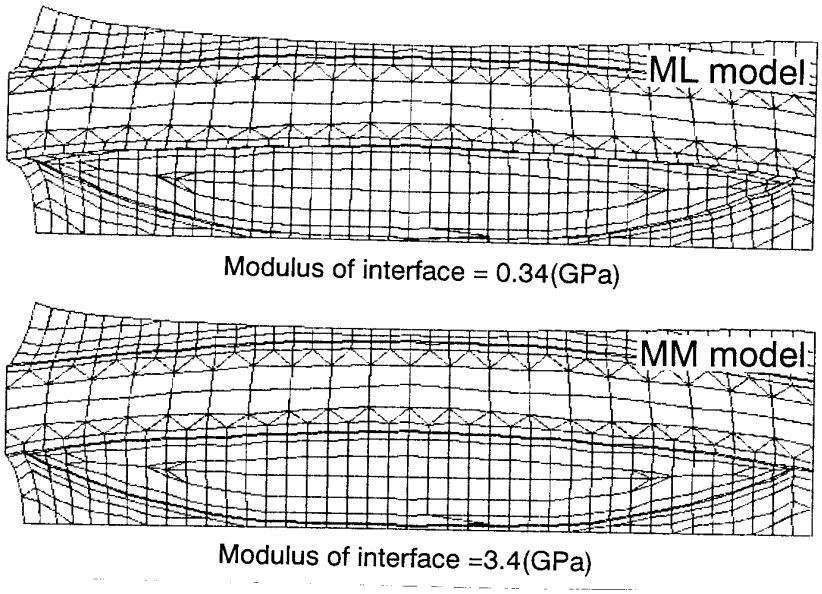

Fig.5 Deformation states of ML model and MM model.

Second, initial fracture stress of the each model was investigated. Upon investigation of stress distribution on each element, clearly the initial fracture occurred at interface element. Figure 6 shows the initial fracture position at interface elements. The initial fracture position was changed with the crimp ratio and the modulus of interface elements. Figure 7 shows the relation between the normalized maximum stress at the interface and modulus of interface on each model with different crimp ratios. In this figure, the calculated maximum (von Misses) stress at the interface was normalized by dividing the applied stress to the warp fiber strand at each model. The normalized stress was also changed with the crimp ratio and the modulus of

interface elements. The maximum stress at the interface increased with increase either crimp ratio or modulus of interface.

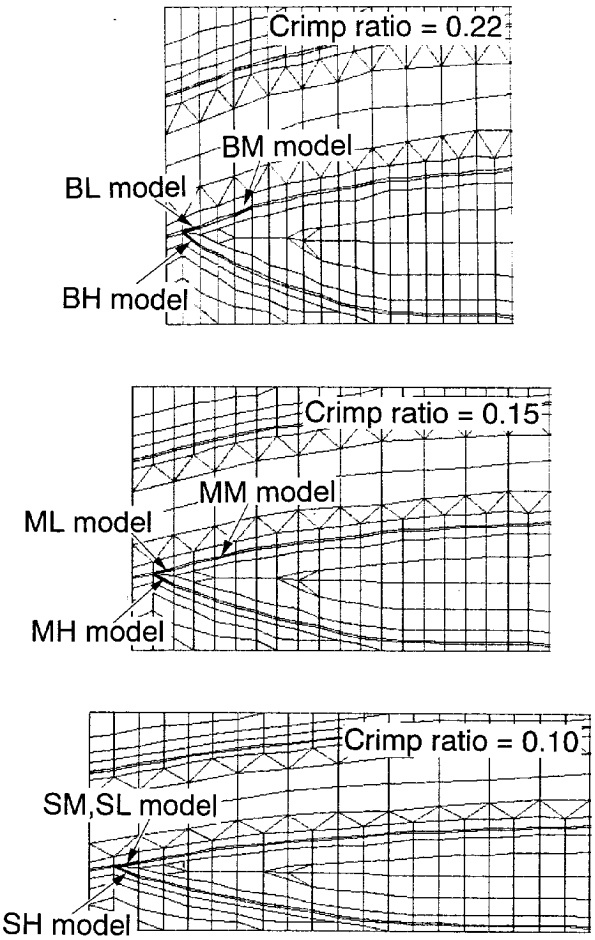

Fig.6 Initial fracture position at interface elements.

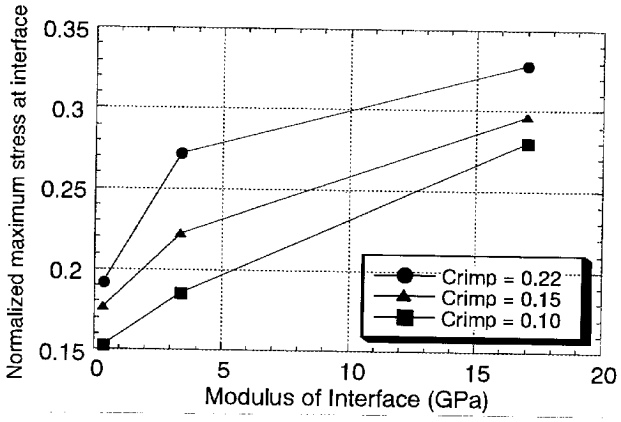

Fig.7 Relation between normalized maximum stress at the interface and modulus of interface.

Finally, a new attempt was performed that the strength of interface was calculated by combining the numerical and experimental approaches. From the above numerical approach, the relation between the applied stress to the warp fiber strand and the calculated stress at the interface could be clarified. On the one hand, the shear strength of fiber crossing part could be obtained by experimental approach. In conjunction with the shear stress at which initial fracture occurred in experiments and the applied stress to the warp fiber strand in analysis, the stress calculated at the interface when the initial fracture occurred was obtained. This stress, indeed, is the strength of the interface.

The shear strength of fiber crossing part obtained by experiments with different concentration of silane coupling agents was ranging from 11.5 to 21.1 MPa. By using the strength, the strength of the interface was calculated with each model. Figure 8 shows the relation between modulus of interface and calculated strength of interface. In this case, since the crimp ratio and modulus of interface were unknown quantities, the strength could not be specified but the range of reasonable modulus and strength of interface could be clarified. Within the range, a proper combination of the modulus and strength should be fixed according to each interfacial treatment on fiber strand.

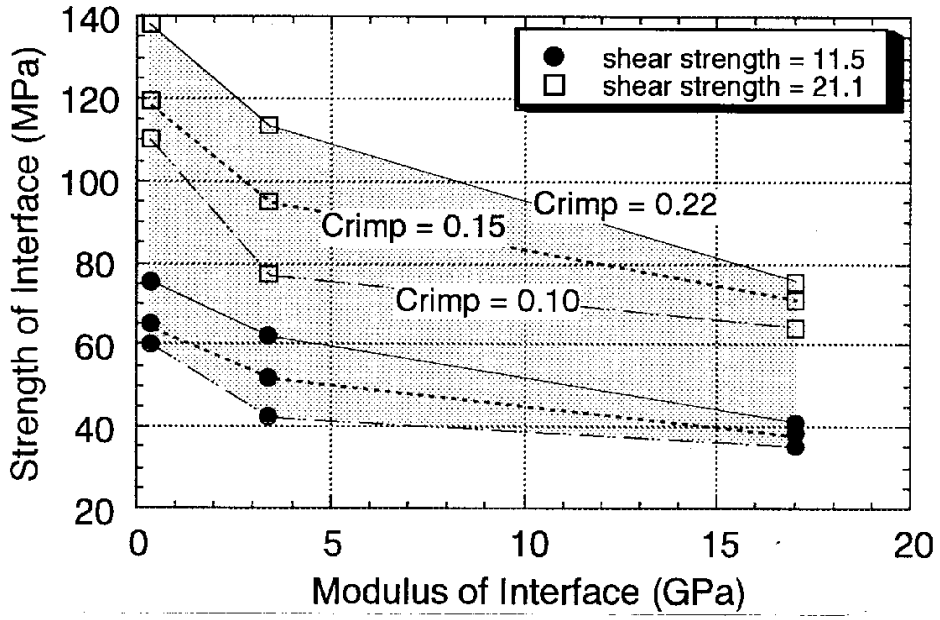

Fig.8 Relation between modulus of interface and calculated strength of interface.

CONCLUSIONS

In this study, in order to study the deformation and fracture behavior at fiber crossing part in textile composites, an evaluation method of the interface between fiber bundles was examined by numerical approaches. The concept of modeling and numerical analysis model for textile composite was proposed and applied to fiber bundle pull-out test. The effects of crimp ratio and modulus of interface between fiber bundles on shear deformation and the stress at fiber crossing part was clarified. Finally, the strength of interface was calculated in conjunction with the shear stress at which initial fracture occurred in experiments and the applied stress to the warp finer strand in analysis. The introduced analytical model should be useful for investigation of the behavior at fiber crossing part in textile composites and further the determination the material constants of interface.

REFERENCES

1. Hamada, H., Kotaki, M., Kadomoto, S., Harada, T., “Evaluation of interfacial properties of intersection part between warp and weft fibers in glass woven fabric composites”, Proc. of Annual meeting in Kansai section of JSME (Japan Society of Mechanical Engineers), 1996.21-22 March, pp.348-349 (in Japanese).

2. Hamada, H., Nakai, A., Fujita, A., Maekawa, Z., Yokoyama, A. and Uozumi, T., “CAE in Integrated Braided Composite”, Journal of Science and Engineering of Composite Materials, Vol.4, No.2, 1995, pp.109-120.

3. Nakai, A., Fujita, A., Yokoyama, A. and Hamada, H., “Design Methodology for a Braided Cylinder”, Composite Structures, Vol.32, 1995, pp.501-509.

4. Nakai, A. and Hamada, H., “Bending Properties of Multi-layered Braided Composite Tube”, Journal of Science and Engineering of Composite Materials, (in submitting).

CLOSED FORM PREDICTIONS OF MACROSCOPIC THERMOMECHANICAL PROPERTIES OF ORTHOGONAL 3-D WOVEN FABRIC COMPOSITES

Takashi Ishikawa [1], Naoyuki Watanabe[2], Kazuhiro Bansaku[3] and Yoshinobu Ono[2]

[1] Section Head, Airframe Division, National Aerospace Laboratory
6-13-1 Ohsawa, Mitaka, Tokyo 181,JAPAN
[2] Aerospace and Systems Dept., Tokyo Metropolitan Institute of Technology
6-6 Asahigaoka, Hino-shi, Tokyo 191, JAPAN
[3] Research Center for Advanced Science and Technology, Tokyo University
4-6-1 Komaba, Meguro-Ku, Tokyo 153, JAPAN

SUMMARY: A simple mechanical model for describing elastic moduli and coefficients of thermal expansion of composites using orthogonal 3-D woven fabric reinforcement is proposed in the present work based on the constituent material properties. The theoretical procedure consists of two phases: the first phase is a property description of unidirectional composites as the element of 3-D fabric composites and the second is a description of the whole. Although the emphasis is placed on the second phase, simple but expedient closed form formulae are also developed for predicting E_T and G_{LT}. The second phase is constructed by combination of parallel and serial linkage of the UD composite blocks. The predicted elastic modulus, in-plane shear modulus and coefficient of thermal expansion of Tyranno® /epoxy 3-D composite system were compared with experimental results and numerical results obtained from homogenization finite element analysis. An agreement between them are basically excellent. A simple method to predict elastic and thermal expansion behavior of 3-D composites is established.

KEYWORDS: mechanical modeling, serial and parallel linkage, elastic modulus, coefficient of thermal expansion, experiments, homogenization finite element

INTRODUCTION

Three dimensional woven fabric composites have attracted an engineering interest of composite community in recent years. They can provide higher translaminar properties, and imply a potential of low-cost processing of polymer composite structures. Another role of 3-D fabric composites is a reinforcement of ceramic matrix composites (CMC) including carbon/carbon materials. In these composites, because matrices are brittle, functions of translaminar (z) yarns are enhanced. However, such z yarns make gaps between load carrying in-plane (x and y) yarns and deteriorates in-plane mechanical properties. According to this background, simple prediction formulae of mechanical properties of 3-D woven composites are needed more strongly than before in order to establish a quick loop of optimization in material design. Literature survey revealed that no simple closed form formulae had not been proposed yet for description of elastic moduli and coefficients of thermal expansion (CTE) of

3-D woven composites although some pioneering research work (e.g.: Ref.. 1, 2, 3 and 4) had been conducted.

The purpose of the present paper is first to establish a simple mechanical modeling for description of thermomechanical behavior of orthogonal 3-D fabric composites, and secondly to provide simple full closed form equations for predicting the above-mentioned constants based on the established model. In order to comprehend the structure of the problem at a glance, Table 1 is provided here. Required baseline inputs are constituent material properties of 3-D composites, i. e., Young's moduli, Poisson's ratios, coefficients of thermal expansion (CTE) of fiber and matrix, fiber volume fraction, and geometrical parameters of 3-D fabrics. Theoretical procedures are divided into two phases; the first phase consists of a prediction of properties of unidirectional (UD) composites as a component of a unit cell of 3-D fabric, and the second phase consists of a prediction of 3-D fabric composite properties based on the established model. For the first phase, a simple and useful closed formula based on a similar mechanical concept to the second phase is proposed, which is another focal point of the present paper. A reliability of this formula was checked by using previous semi-numerical method[5] developed by one of the author (TI). The second phase procedures are constructed by combinations of parallel and serial linkage of the constituent blocks.

Table 1 Explanation for Construction of the Theoretical Procedure

Phase for Prediction of UD-Composites
Required Data: E_f, ν_f, (G_f), α_f, E_m, ν_m, (G_m), α_m
Fiber Volume Fraction in UD; V_{Fu}
Methods: Closed Form Formula in Sec. 2 or Ref.5
Outputs: E_L, E_T, ν_L, G_{LT}, G_{TT}, (ν_{TT}), α_L, α_T
Phase for Prediction of 3-D Fabric Composites
Model Concept and Geometry of 3-D Fabric Composites
Required Data: above outputs and Width of Yarn, b_T & b_F
Methods: Two Approx. Formulae, PSA & SPA in Sec.3
Outputs: E_{X1}, G_{XY1}, α_{X1} for PSA solution, etc.

The calculated results through closed form paths were compared with numerical results by homogenization finite element analysis (HFEA). They were also compared with the corresponding experimental results for Tyranno®/Epoxy 3-D fabric composites. Agreements of the closed form results with HFEA results and experimental values will be shown to be very good in general.

PREDICTION OF MECHANICAL PROPERTIES FOR UD COMPOSITES

This sort of problems were concern of the early time composite mechanics research and hundreds of papers were published, which were reviewed in, e.g., Ref.6. Of course, there is no problem to predict longitudinal modulus and CTE, E_L and α_L, and major Poisson's ratio, ν_L. Transverse properties like modulus and CTE, E_T, ν_{TT} and α_T, and longitudinal shear modulus G_{LT} were considered to be difficult at first. After cumulative research work, composite community regards these problems as almost solved until some time in 1970's except for the corresponding part to random fiber packing. Some famous formulae like Halpin & Tsai[7] are quoted in student textbooks. However, it should still be noted that many of those formulae require some semi-empirical factors like contiguity, C. This sort of factors always cause an ambiguity at application. One of the authors (TI) also proposed a semi-numerical method[5] based on a combination of Fourier expansion of stress functions and point collocation. Its results could be regarded as very close to the exact solution because of an

excellent agreement with preceding numerical analysis and because some mathematical conditions about symmetry were satisfied. One disadvantage of this method was that no closed form expression was obtained. Thus, there remain a necessity for the simplest closed-form formula for predicting particularly E_T and G_{LT}. However, an expediency will be imposed as a penalty of the simplicity.

A sectional geometry of the conceived model at this phase is shown in Fig. 2. According to Ref.5, the hexagonal fiber packing is selected here. One bold simplification introduced here is to employ the hexagonal fiber section. This assumption makes the solution very simple. Note that fiber volume fraction in UD(V_{fu}) is given by $(a/b)^2$. Let us consider the case where $1/2< b/a<1$ corresponding to V_{fu} over 25% and where $0<T_1/b<1-a/b$, in the left region. It is assumed that the model is subjected to the tensile force in the T_2 direction and that so-called mechanics of materials approach is adopted after early References of 8 and 9. If the model is cut along the force direction with a width of dT_1 and the force uniformity is assumed, then the modulus in the T_2 direction is obtained as follows using the position of fiber edge $F(T_1)$:

$$E_{T2} = E_f E_m / \{E_m F(T_1)/\sqrt{3}\, b + E_f (1 - F(T_1)/\sqrt{3}\, b)\} \qquad (1)$$

Because the fiber edge is a slant straight line, Equation 1 can be modified into the following form:

$$E_{T2} = E_f E_m / \{E_m (2a/3b - T_1/3b) + E_f (1 - 2a/3b + T_1/3b)\} \qquad (2)$$

In the region where $1-a/b<T_1/b<1/2$, one expedient assumption is introduced. Although the true distance of two fibers is $4(a-b)/\sqrt{3}$, it is assumed to be half in order to account stress concentration. If we admit this assumption, E_{T2} becomes constants in this region as follows:

$$E_{T2} = E_f E_m /\{E_m (1/3 + 2a/3b) + E_f (2/3 - 2a/3b)\} \qquad (3)$$

If we do not introduce such an expediency, the results are always smaller than the calculated results by the method of Ref.5. In other words, the above distance reduction is considered to be one empirical parameter by which the results can be adjusted to fit the exact solutions. The averaged E_{T2} , namely aimed value of E_T, can be obtained by integrating these equations in the T_1 direction and divided by $b/2$, leading to the following natural logarithmic function :

$$E_T = 6 E_f E_m /(E_f - E_m) \propto n [(E_f - E_m)(1 - a/b) /\{3E_f - 2a/b(E_f - E_m)\} + 1] + 3 E_f E_m (2a/b - 1) / \{E_m (1 + 2a/b) + 2E_f (1 - a/b)\} \qquad (4)$$

The second expedient compromise have to be introduced next: The distance reduction truly means an increase of fiber area, which is written in the following form of V_{fu} change:

$$dV_{fu} = 4/3 (1- a/b)(1-1/2/(a/b)) \qquad (5)$$

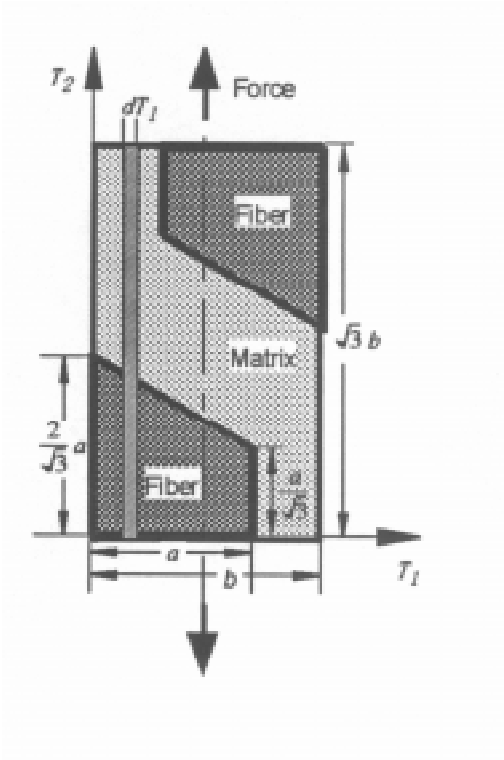

Fig. 1: Model for UD Prediction Phase

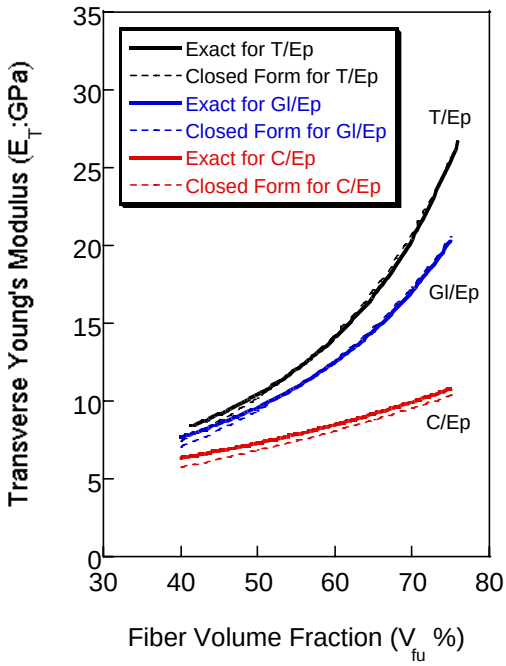

Fig. 2: Comparison in predictions of E_T in unidirectional composite phase

However, this V_{fu} change should be neglected, in other words, the initial $V_{fu} = (a/b)^2$ is assumed to be maintained. Otherwise, the results do not coincide with the exact solution curves. According to these strong assumptions, the present solution is regarded as expedient.

The calculated curves based on Eq. 4 are shown in Fig.2 for three cases of composite, Tyranno®/Epoxy, glass/epoxy and carbon/epoxy. As it is well known, former two fibers are isotropic and the last is anisotropic. For carbon/epoxy case, E_f is assumed as $E_{fT} = \kappa E_{fL}$ where κ is an anisotropic factor of carbon fiber and *where* E_{fL} is a longitudinal modulus of carbon fiber.

The used material values are : E_f = 185GPa for Tyranno®, E_f = 68.6GPa for glass and E_{fL} = 187GPa and κ = 0.084 for carbon fibers. For isotropic fibers, agreements of the present results with exact solutions are fairly good particularly in practical V_{fu} regions. For carbon/epoxy, an agreement becomes slightly worse. Although a description is omitted here, similar equations for G_{LT} and calculated results were obtained. Comparison indicates that the prediction by the closed formula is getting worse than E_T. However, it could be still used if we consider the fact that the hexagonal array provides slightly lower prediction than reality for UD composites due to random fiber packing. Thus, the present formulae are correlated with exact solutions with confidence. We can use them in 45 to 65% V_{fu} if we admit a few percent errors. To meet a need in the next section, E_T of Tyranno®/ Epoxy with V_{fu} = 59.7%, and above material values was determined as 14.1GPa, where exact solution provides 13.9GPa. E_L and ν_L were obtained as 112 GPa and 0.26 upon ν_m=0.38 and ν_f = 0.2.

PREDICTION OF MECHANICAL PROPERTIES FOR 3-D FABRIC COMPOSITES

Let us proceed into the aimed phase, prediction of mechanical properties of orthogonal 3-D fabric composites. The first step is to establish a mechanical model. Figure 1 depicts the geometry of the model constructed upon micro-observation of an actual composite piece. The model is based on a possible repeating unit cell. Transparent volume denotes regions filled with pure matrix materials. Other regions consist of unidirectional (UD) composite bricks, namely 12 elements in total. Thickness, h_t, and width of yarns, b_F , of fill and warp are assumed to be identical in this model. Width of translaminar (z) yarns is denoted by b_T. Thus, a relationship between local volume fraction in UDC, V_{fu}, and total volume fraction of 3-D composites, $V_{fT,}$ can be written as follows considering pure matrix regions:

$$V_{fT} = V_{fu}\{(b_F + b_T)\, b_F + b_T^2/2\} / (b_F + b_T)^2 \qquad (6)$$

Actual values of b_F and b_T for the present SCL type orthogonal Tyranno®/Epoxy were measured to be 1.043 and 0.5153 mm respectively. Then, the factor for V_{fu}would be 0.724. The same epoxy resin with E_m = 3.43GPa and ν_m=0.38 as UDC, Epicote 828, is used. As stated in the previous section, baseline UDC material properties were already obtained.

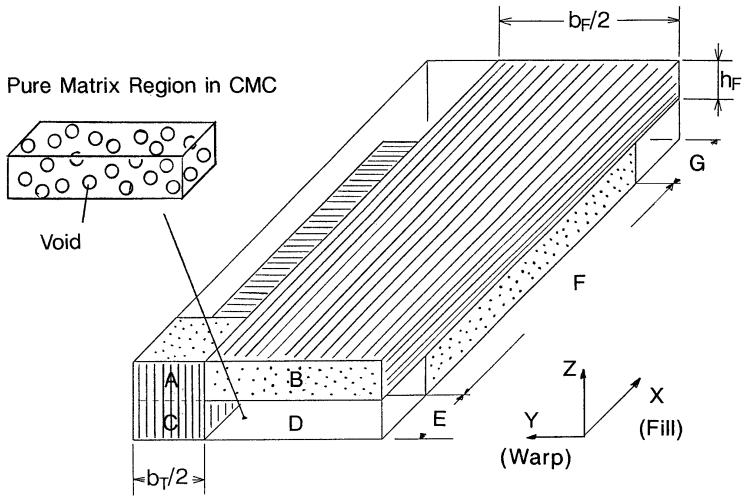

Fig.3: Schematic of the mechanical modeling

It is assumed that voids which are inevitable factor in ceramic matrix composites exist only in pure matrix regions. However, since this paper treats only polymer matrix composites, an effect of voids is neglected according to a sectional observation as void free.

Hereafter, we go into the core of the present procedure, development of closed-form formulae for 3-D composite phase. The first one is referred to as the Parallel-Serial approach (PSA) where the parallel volume average of rule of mixture (ROM) type is conducted first and then serial average of Reuss type is conducted. The first ROM style average in regions with label E gives:

$E_{x(E)} = \{ b_T E_T + (E_L + E_m) b_F/2 \} / (b_F + b_T)$ where suffix *x* denotes the x direction. *(7)*

In the regions AF, BF, CF, and DF, and also AG, BG, CG, and DG, the same procedure gives:

$$E_{x(F)} = \{ (b_F + b_T)E_T + b_F E_L + b_T E_m \} / \{2(b_F + b_T)\} \quad (8)$$

$$E_{x(G)} = \{ b_F E_L + (b_F + 2b_T) E_m \} / \{2(b_F + b_T)\} \quad (9)$$

By connecting these three moduli in Reuss estimate style, we have an approximate modulus:

$E_{x1} = 2(b_F + b_T)/(b_T/E_{x(E)} + 2b_F/E_{x(F)} + b_T/E_{x(G)})$ where suffix 1 denotes PSA solution. *(10)*

The second procedure is referred to as the Serial-Parallel approach (SPA) where the order of average is reversed. For example, serial linkage is counted first in regions with labels A to D as:

$$E_{x(A)} = 2(b_F + b_T) / \{ b_T/E_T + (2b_F + b_T) / E_m \}, \quad E_{x(B)} = E_L \quad (11)$$

$$E_{x(C)} = 2(b_F + b_T) / \{(2b_F + b_T)/E_T + b_T/E_m \}, \quad E_{x(D)} = (b_F + b_T) / (b_F/E_T + b_T/E_m) \quad (12)$$

Finally, the total average of the modulus in the x-direction, denoted by E_{x2}, is obtained by ROM:

$$E_{x2} = (b_T E_{x(A)} + b_F E_{x(B)} + b_T E_{x(C)} + b_F E_{x(D)}) / \{2(b_F + b_T)\} \quad (13)$$

Thus, two approximating closed-form formulae are obtained.

In the previous section, only a little discussion about in-plane shear modulus, G_{LT}, was given and discussion about coefficients of thermal expansion (CTE) was skipped. Because solutions for these properties are also key purpose of the present paper, they will be given below only for the PSA case. Equations for in plane shear modulus can be written as follows for the ROM part:

$$G_{xy(E)} = \{ b_T G_{TT} + (G_{LT} + G_m) b_F /2 \} / (b_F + b_T)\} \quad (14)$$
$$G_{xy(F)} = \{ (2b_F + b_T)G_{LT} + b_T G_m \} / \{2(b_F + b_T)\} \quad (15)$$
$$G_{xy(G)} = \{ b_F G_{LT} + (b_F + 2b_T) G_m \} / \{2(b_F + b_T)\} \quad (16)$$

where G_{TT} denotes transverse shear modulus of the constituent UD composite bricks.

Overall averaged in-plane shear modulus by the PSA procedure, G_{xy1} , is obtained as:

$$G_{xy1} = 2(b_F + b_T) / (b_T /G_{xy(E)} + 2b_F /G_{xy(F)} + b_T /G_{xy(G)}) \quad (17)$$

For calculating CTE, a concept of a modulus modified ROM average should be introduced instead of common ROM average in a parallel linkage. The harmonic mean, Reuss estimate, should be substituted by a simple summation of thermal deformation. If we understand these modifications, CTE in the x direction can be obtained as follows, for the first parallel linkage:

$$\alpha_{x(E)} = \{ b_T E_T \alpha_T + (E_L \alpha_L + E_m \alpha_m) b_F /2 \} / \{ b_T E_T + (E_L + E_m) b_F /2\} \quad (18)$$
$$\alpha_{x(F)} = \{ (b_F + b_T) E_T \alpha_T + b_F E_L \alpha_L + b_T E_m \alpha_m \} / \{ (b_F + b_T) E_T + b_F E_L + b_T E_m \} \quad (19)$$
$$\alpha_{x(G)} = \{ b_F E_L \alpha_L + (b_F + 2b_T) E_m \alpha_m \} / \{ b_F E_L + (b_F + 2b_T) E_m \} \quad (20)$$

Overall averaged CTE in the x direction by PSA procedure, α_{x1}, is obtained as:

$$\alpha_{x1} = (\alpha_{x(E)} b_T /2 + \alpha_{x(F)} b_F + \alpha_{x(G)} b_T /2) / (b_F + b_T) \quad (21)$$

Thus, the aimed closed form solutions of E_x, G_{xy}, and α_x are all determined.

Some comments about α_T predictions for UD phase should be stated here. Although It is well known to us that α_T is affected by matrix Poisson's ratio[10,5], equations in the previous section can not handle such behavior. Thus, one possible and again expedient way is to incorporate a law given in Ref.10 and a similar formula to Eq. 4) in a manner of the average where the true distance between fibers is adopted here. Although a presentation of equations and results is omitted, such formula provides reasonable α_T within a few percent error from the solution of Ref.5. So far as checked by a reliable result, such crude formulae could be practically applied.

PREDICTED RESULTS FOR 3-D FABRIC COMPOSITES AND DISCUSSIONS

Figure 4 indicates a comparison between calculated and experimental elastic moduli in the x-direction for Tyranno®/Epoxy 3-D fabric composites. The objective solution here is the PSA

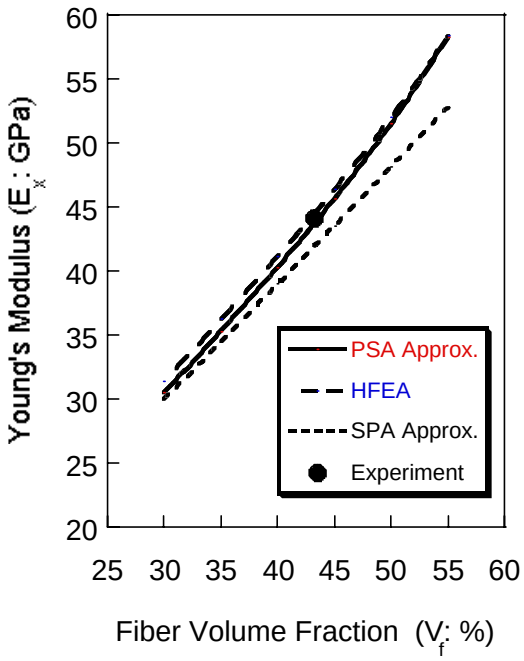

Fig. 4: Relationships between elastic moduli and fiber volume fraction (V_{fT})

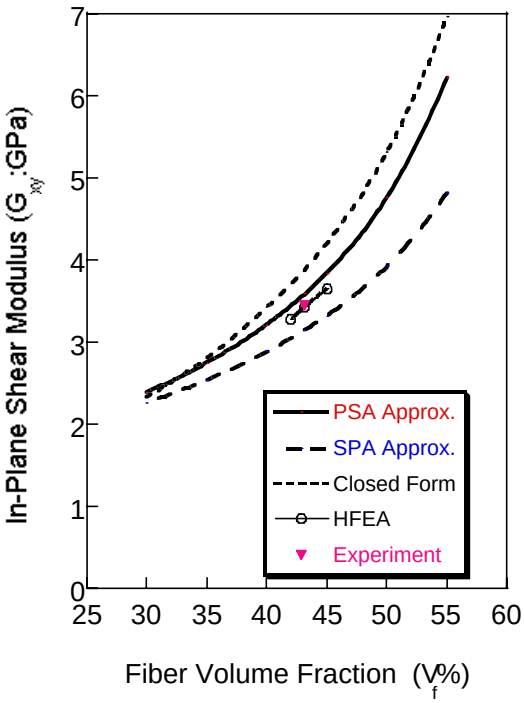

Fig.5: Relationships between in-plane shear moduli and fiber volume fraction (V_{fT})

approximation indicated by a solid curve. Because the baseline UD moduli obtained through Eq.4) and the method of Ref.5 are very close to each other, the current plot is based on the exact solution and an indication of PSA based on Eq.4) is omitted. It can be observed that an agreement between the present PSA solution and the results of homogenization finite element analysis is very favorable. They also coincide with the experimental elastic modulus. Note that a brief description about experimental procedure will be given in the next section. The SPA approximate solution provides slightly lower values than those from PSA. If we consider the simplicity of the analysis and predictability, it can be concluded that the present closed form solution for prediction of 3-D fabric composites is applicable so long as E_x concerned.

The results concerning another aimed modulus, G_{xy}, are shown in Fig.5. A solid line indicates PSA solution based on the exact UD composite input. A discrepancy from the HFEA solution tends to be greater than the previous Young's modulus case. In the case of the closed form formula, one difficulty arises to predict transverse shear modulus, G_{TT}. For solving this point, a transverse Poisson's ratio is assumed to 0.5 and transverse isotropy relation is utilized. Full closed form solution based on this simplification is indicated by a chain curve, where a discrepancy from HFEA becomes much larger than exact-UD/PSA solution. However, if we consider a simplicity and easy handling, this sort of solution could be used for some purpose. It should be noted that the experimental result fall between exact-UD/PSA and HFEA curves, being closer to the latter. Exact-UD/SPA solution provides the lowest prediction among all. So, if we pursue expediency, a combination of closed form UD and SPA might be the best.

Predicted results for coefficient of thermal expansion (CTE) and the experimental value are shown in Fig.6 where HFEA solution has not been obtained yet. As stated earlier, the closed form solution for UDC was the poorest in CTE case, the indicated results are for combinations of exact-UD and PSA/SPA formulae. Mutual relations between two approximations are similar to the previous modulus cases, whereas an agreement between PSA and the experimental value is again excellent.

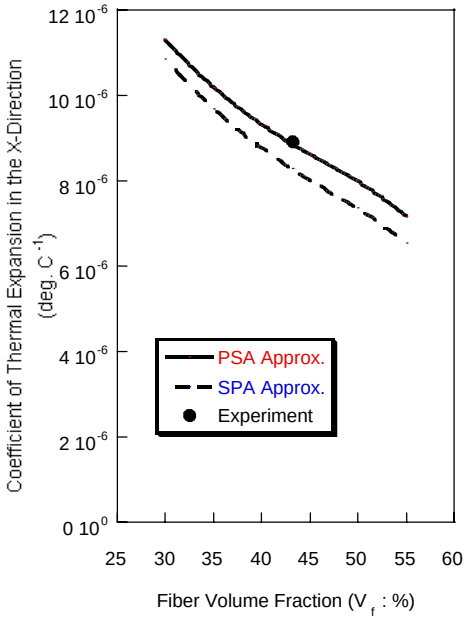

Fig. 6: Relationships between in-plane CTE and fiber volume fraction (V_{fT})

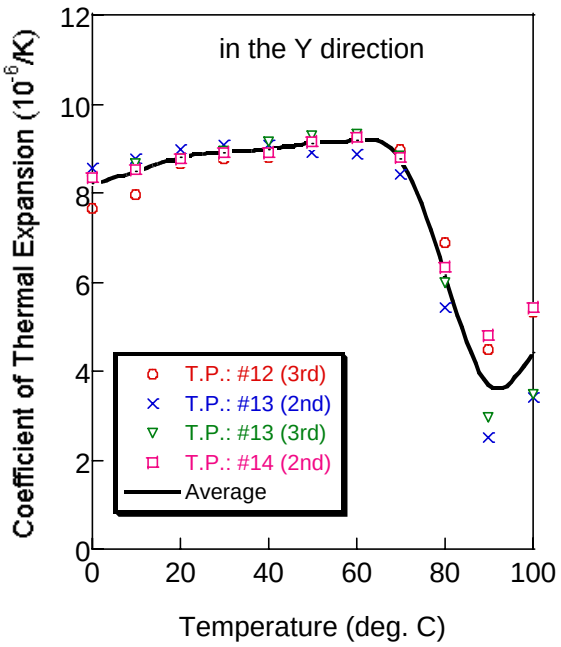

Fig.7 Measured Results of CTE in the Y Direction by Laser Dilatometer

OUTLINES ABOUT EXPERIMENTAL PROCEDURES

Some outline descriptions about both experimental procedures of elastic modulus and CTE measurements are given here. Selected material system was Tyranno®(standard) /Epoxy (Epicote 828) woven into SCL style 3-D fabric which contains 17 and 16 layers in the x and y directions, and consolidated through an RTM method. Volume fraction values were V_{fT} = 43.2% by experiment and V_{fu} = 59.7% calculated by Eq.6 using b_F =1.043mm and b_T=0.5153mm.

Coupon specimens of 140 mm in length for the x and y directions and 180 mm in length for the 45 degree direction were used for elastic moduli. Nominal width and thickness for all specimens were 12.7mm and 5mm, respectively. Stain data up to 800×10^{-6} were employed for modulus calculation. There was found little difference in the results between the x and y directions. For obtaining in plane shear modulus, Poisson's ratios in the 45 direction were measured and the following well known formula which is only valid in the x, y and 45 directions was used:

$$G_{xy} = E_{45} / \{2 (1+ \nu_{45})\} \qquad (22)$$

where E_{45} is a moduli measured for these 45 degree specimens. Average values of 5 specimen data were calculated and plotted in Figs. 4 and 5.

Coefficients of thermal expansion were measured by a dilatometer using laser interferometry whose pictures are indicated in the other paper in this conference volume[11)]. A specimen which cut out of the source plate was a short block and its ends were ground to be round for a point contact.

A typical example of the measured data in the y-direction is shown in Fig.7 where the data for the second and third measurements are chosen for avoiding hygroscopic effect. An average at 25°C was adopted for an indication in Fig.6.

CONCLUSIONS

It can be mentioned that the present closed form solution in the second estimation phase of 3-D fabric composite properties, particularly PSA approach, provides excellent predictions of in-plane Young's modulus in spite of its simplicity if the elastic moduli of the constituent UD composite are properly estimated. Its reliability is confirmed by agreements with homogenization finite element predictions and experimentally obtained modulus. In-plane shear modulus by the PSA equation also shows a good agreement with HFEA and experimental results if the exact UD moduli are available. In the case of coefficient of thermal expansion, again the PSA solution provides good predictions only if the result of UD prediction phase is reliable. Thus, the main aim of the present paper to develop closed form formulae for predicting 3-D composite thermo-mechanical properties is almost fulfilled with the PSA solution.

Some imperfection in the first phase, a long-lasting classic problem of UD composite property prediction by simple closed formulae, still remains unsolved within this paper. If some expedient assumptions are allowed, a candidate equation using a logarithmic form of $a/b(= V_{fu}^{1/2})$ is proposed here for a prediction of E_T, which gives favorite curves for isotropic fiber PMCs. However, because of its expediency, the same form for G_{LT} leads to higher estimations and the equation for α_T derived based on the same idea provides much smaller values than exact calculations. Although another compromising formulae are possibly described for these two properties, persuasiveness of the concept will be degraded seriously. Thus, a conclusion about this phase is summarized as follows: A closed form solution for E_T with expedient handling of fiber distance can be formulated and it can predict a favorable value under a recognition of its limitation.

A practical goal of this research program is an application of the simple solutions to estimation of the matrix elastic modulus of CMC, which is very hard to measure. Because of the length and consistency in the discussion, description of this part is omitted in the present paper and Reference 12 should be referred for that purpose.

ACKNOWLEDGEMENT

This work is supported by funding of STA of Japanese Government for establishing technologies of Japanese Space Transportation System, HOPE. The authors also wish to thank Mr. Sunao Sugimoto for his assistance in preparation of graphical work.

REFERENCES

1. Yang, J.M., Ma, C.L. and Chou, T.W., "Fiber Inclination Model of Three-Dimensional Textile Structural Composites", *Journal of Composite Materials*, Vol.20, No.9, 1986, pp.472-484.

2. Whitney, T.J. and Chou, T.W., "Modeling of 3-D Angle Interlock Textile Structural Composites", *Journal of Composite Materials*, Vol.23, No.9, 1989, pp.890-911.

3. Nagai, K., Yokoyama, A., Hamada, A., Maekawa, Z., and Noguchi, Y., "The Study of Analytical Method for Three-Dimensional Composite Materials (1st Report: Evaluation of Tensile Elastic Modulus) (in Japanese)", *Journal of Japan Society of Mechanical Engineers*, Part A, Vol.58, No.555, 1992, pp.2099-2103.

4. Gu, P. and Mohamad, M., "Structure and Properties of 3-D Woven Carbon/Epoxy Composites", *Proceedings of 9th International Conference on Composite Materials*, Madrid, Spain, July 12-16, 1993, Vol. IV.: Composites Design, Miravete, A., Eds., pp.568-575.

5. Ishikawa, T., Koyama, K., and Kobayashi., S., "Thermal expansion Coefficients of Unidirectional Composites", *Journal of Composite Materials,* Vol.12,No.2, 1978, pp.153-168.

6. Chamis, C.C., and Sendeckyj, G.P., "Critique on Theories Predicting Thermo-Elastic Properties of Fibrous Composites", *Journal of Composite Materials*, Vol.2, 1968, pp.332.

7. Halpin, J.C. and Tsai, S.W., "Environmental Factors in Composite Materials Design", *AFML-TR-66-190*, Air Force Materials Laboratory, 1966.

8. Greszczuk, L.B., "Theoretical and Experimental Studies on Properties and Behavior of Filamentary Composites", *Proceedings of 21st SPI Conference*, Chicago, Illinois, 1966, Sect.8-A.

9. Uemura, M., and Yamada, N., "Elastic Constants of Carbon Fiber Reinforced Plastic Composites (in Japanese)", *Zairyo (Materials), Journal of Japan Society of Materials*, Vol.24, No.257, 1975, pp.156-163.

10. Shapery, R.A., "Thermal Expansion Coefficients of Composite Materials Based on Energy Principles", *Journal of Composite Materials*, Vol.2, 1968, pp.380.

11. Sugimoto, S, and Ishikawa, T., "Calibration of Infrared Stress Measurement Technique for CFRP Composites and Its Application", *Proceedings of 11th International Conference on Composite Materials*, Gold Coast, Australia, July 14-18, 1997, Scott, M.L., Eds.

12. Ishikawa, T. Bansaku, K., Watanabe, N., Nomura, Y., Shibuya., M., and Hirokawa, T., "Experimental Stress-Strain Behavior of Si-Ti-C-O Fiber/SiC Matrix Composites and Estimation of Matrix Elastic Modulus", *Composite Science and Technology*, in printing.

THE EFFECTS OF DEFORMING KNITTED GLASS PREFORMS ON THE TENSILE PROPERTIES OF RESULTANT COMPOSITE LAMINATES

K. H. Leong[1], M. Nguyen[2] & I. Herszberg[2]

[1]*Cooperative Research Centre for Advanced Composite Structures Ltd. (CRC-ACS), 506 Lorimer Street, Fishermens Bend, VIC 3207, AUSTRALIA.*
[2]*The Sir Lawrence Wackett Centre for Aerospace Design and Technology, RMIT, GPO Box 2476V, Melbourne, VIC 3001, AUSTRALIA.*

SUMMARY: The effects of deforming knitted fabrics on the tensile properties of their resultant composites have been evaluated. The properties were studied for both the course and wale directions for composite laminates with fabrics that had been deformed in either of the two directions. It was found that as the amount of deformation in the fabrics was increased tensile stiffness and strength of the laminates improved markedly in the direction which the knitted fabrics had been deformed. When the laminates were loaded normal to the direction in which the fabric had been deformed, it was found that deformation in the wale and course directions resulted in improvement and deterioration of tensile properties, respectively. The relative orientation of the fracture planes with respect to the loading axis was also found to be dependent on the degree of deformation that had been induced in the knitted fabric.

KEYWORDS: knitted preforms, textile composites, tensile properties, deformation, fracture mechanisms

INTRODUCTION

The use of knitting technology with advanced fibres, such as glass, carbon and aramid, to produce near-net-shape fabrics, or "socks", has in recent years received increasing interest from the composite materials community. In conjunction with a suitable liquid moulding technique, such as Resin Transfer Moulding (RTM), the fabrics have the potential to be used for production of a wide variety of composite structures with complex shapes [1,2]. Whilst such fabrics are obviously advantageous in terms of reducing production cost as a result of minimum material wastage and reduced labour time, the development of a suitable "sock" for a particular structure is often a time consuming, and hence an expensive task. Therefore, unless such costs are justified, an alternative cheaper method would be to impregnate flat knitted fabrics in a forming tool to obtain the required shape of the component [3].

During the process of forming a flat knitted fabric (*e.g.* during deep drawing), it is inevitable that the fabric would be deformed due to stretching so that optimum conformibilty to the shape of the component is achieved. The highly looped fibre architecture of the knitted fabric easily affords such deformation, and hence its excellent forming characteristics. However, the exercise results in distortion to the knit structure which could result in tearing and/or isolated

bunching of the fabric [3]. The distortion would also cause a degree of fibre orientation in the direction of stretching which, in turn, would affect the mechanical properties of the resultant composite [4,5]. In addition, previous investigations carried out on composite materials manufactured from knitted glass and carbon fabrics have revealed that the mechanical properties of knitted composites are anisotropic [4,6-9], and they are dependent on factors such as the number of layers of fabric [4,5,10], stitch density (which is a measure of the tightness of the knit) [7], knit architecture [8] and fibre volume fraction [9-11].

Whilst knitted composites generally have inferior in-plane strength and stiffness compared with materials such as woven composites, they are superior in terms of impact resistance and retention of post-impact properties [12], with comparable bearing capabilities [9,12]. Consequently, these positive attributes partly account for the increasing effort to develop this technology for niche applications [13,14].

In the present study, the effects of deformation of knitted fabrics on the tensile properties of resultant composites have been investigated for the weft knitted Milano rib fibre architecture. The properties were investigated for both the course and wale directions for composites with fabrics deformed in either of the two directions. This study was also supported by fractographic studies using stereooptical microscopy. It is noteworthy that the research reported in this paper is an auxiliary part of a larger project that is currently undertaken at the Cooperative Research Centre for Advanced Composite Structures Ltd. (CRC-ACS). The project involves the development of a more cost-effective technique for producing a non-structural helicopter component which is currently being manufactured using the tape layup method [3].

EXPERIMENTAL

Materials and Manufacture

The test panels used in this experimental programme were manufactured via RTM and using up to 7 layers of weft knitted Milano rib fabric (see Figure 1 for loop structure) and Derakane 411-C50 vinyl ester resin/Triganox T-239 catalyst/CoNap promoter/2, 4-P inhibitor. A 10-gauge, flat bed knitting machine was employed to produced a fabric of nominal areal weight of 730g m^{-1} (undeformed) using 2 × 68tex multi-filament glass fibre.

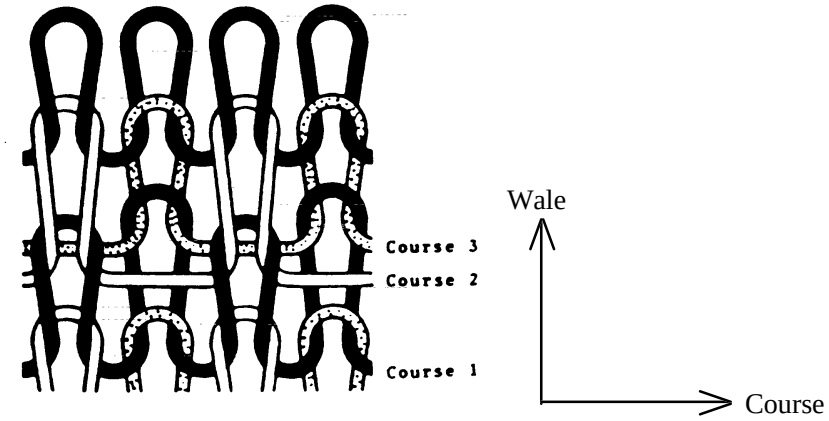

Fig. 1: Schematic diagram of the Milano rib structure.

A rig, details of which are given elsewhere [15], was developed and built to afford systematic deformation to the knitted fabrics. In the course direction, the fabrics were deformed to 20%, 35% and 45% (maximum achievable) while in the wale direction to 20%, 30% and 40% (maximum achievable). Undeformed (0%) fabrics were also considered.

The fibre volume fractions (V_f) of the laminates were maintained fairly constant at approximately 55% by varying the number of knitted fabric layers to isolate the effect of V_f on strength. Further, a reasonably uniform resin flow pattern and, hence, quality in terms of porosity and wetting, between the different laminates could also be maintained. Hence, between 6 and 7 fabric layers were used to produce the laminates. It is noteworthy that earlier studies [9,14] have established the relative insensitivity of tensile strength and stiffness of the Milano rib structure to the number of fabric layers used in a composite; what is in fact more important is the fibre volume fraction.

Coupon Tests

Straight-sided tensile test specimens of 3mm × 25mm × 210mm nominal dimensions were used throughout the programme. Tensile tests were conducted using an Instron 50kN screw-driven mechanical testing machine under displacement control at a nominal rate of 0.5mm min^{-1}. A gauge length of 120mm was used leaving 45mm on each end of the specimens which were gripped in the testing machine. An open weave emery cloth (Screenbak™) was used instead of tabs in the gripped areas of the specimens and this appeared to be effective in promoting failure to occur within the gauge length of the specimens. Specimens of both deformed and undeformed fabrics were tested in the wale and course directions. No less than 5 specimens were considered for each case.

RESULTS AND DISCUSSION

Introduction

To facilitate the presentation of the results, discussion and conclusions, the following abbreviations are used in the rest of this paper.

- δWW = deformed and tested in the wale direction;
- δCC = deformed and tested in the course direction;
- δWC = deformed in the wale direction and tested in the course direction; and
- δCW = deformed in the course direction and tested in the wale direction;

where δ represents the amount of deformation.

Stress-Strain Behaviour

Figure 2 shows a typical stress-strain curve for the 45CW laminate. It reveals that the laminate initially exhibited linear behaviour but then transformed to pseudo-plastic in the latter stages of loading before a maximum stress (defined as the tensile strength) was reached, after which a rather gradual reduction ensued. The transition in linear to non-linear behaviour generally corresponded to the onset of matrix cracking. The stress-strain behaviour described above was generally observed to be similar for all the specimens, irrespective of the direction and degree of fabric deformation or the relative loading axis of the laminates.

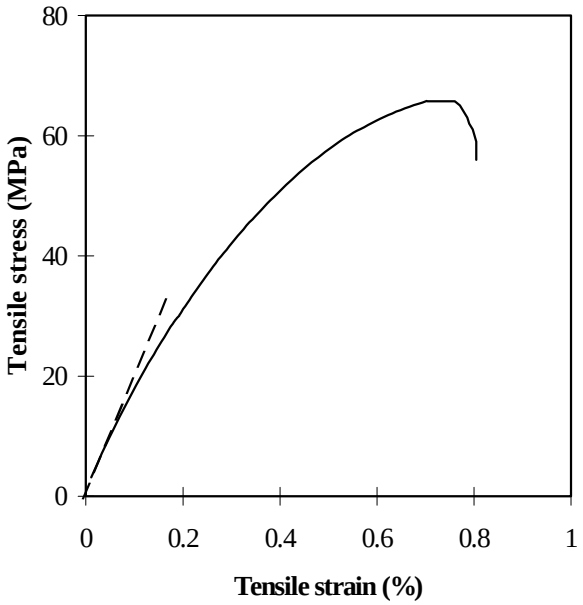

Fig. 2: Typical stress-strain curve of the knitted composite under study.

Tensile Strength and Stiffness

The fibre content of the different laminates varied between 52% and 57% and therefore, to afford comparison, the experimental results of each set of laminates have been normalised to a constant V_f of 55% and presented in Figures 3 and 4 for strength and stiffness, respectively.

From Figures 3 and 4, it will be noted that when the fabrics had not been deformed, the resultant composite laminates displayed higher strength and stiffness in the wale than in the course direction. Although no systematic measurements have been carried out, it is clear from qualitative assessments that the content of fibres oriented in the wale direction is higher, which would account for the better tensile properties along that axis.

As the amount of deformation in the fabrics was increased, the tensile strength and stiffness of the laminates improved markedly in the direction which the fabrics had been deformed. It is interesting to note that this behaviour is consistent with the results of Ha *et al.* [5] for composites derived from deformed and undefomed plain weft knitted carbon fabrics. This improvement in strength and stiffness with the degree of deformation is attributed to an increase in the content of fibres oriented along the loading axis as the knitted fibres were increasingly drawn and straightened in the direction of stretch. The present results also imply that the fibres were not significantly pre-stressed (*i.e.* the yarns were straightened along the stretch axis but not elongated), if at all, when the fabrics were deformed within the levels considered in this study. If the fibres were significantly pre-stressed, then there would be a deterioration in tensile strength with increased fabric deformation which was not observed. In addition, the improvements in tensile properties with increased deformation were revealed to be considerably more pronounced for strength (40WW = 72.4%; 45CC = 89.9%) than they are for stiffness (40WW = 17.5%; 45CC = 38.5%). This is not unexpected since a slight misalignment in fibre orientation from the loading axis (up to ~25°) is known to have a more significant influence on strength than on stiffness [16].

When loading normal to the direction of stretch, Ha *et al.* [5], on plain weft knitted carbon composite laminates, have shown that tensile properties deteriorated with the degree of

deformation in the knitted fabric. This degradation in tensile properties is believed to be attributed to a reduction in content of fibres oriented in the course direction as the fabric was deformed along the wale, and *vice versa*. This is consistent with the simultaneous increase in the content of fibres oriented in the direction of stretch which accounts for the improved WW and CC properties mentioned earlier.

For the laminates considered in the present work, however, loading normal to the direction of fabric deformation resulted in an improvement and a deterioration in the WC and CW tensile properties, respectively. Inspection of fabrics subjected to various amounts deformation suggests that the opposing trends observed for the WC and CW laminates are due to the manner in which the Milano rib structure changes with deformation in the wale and course directions.

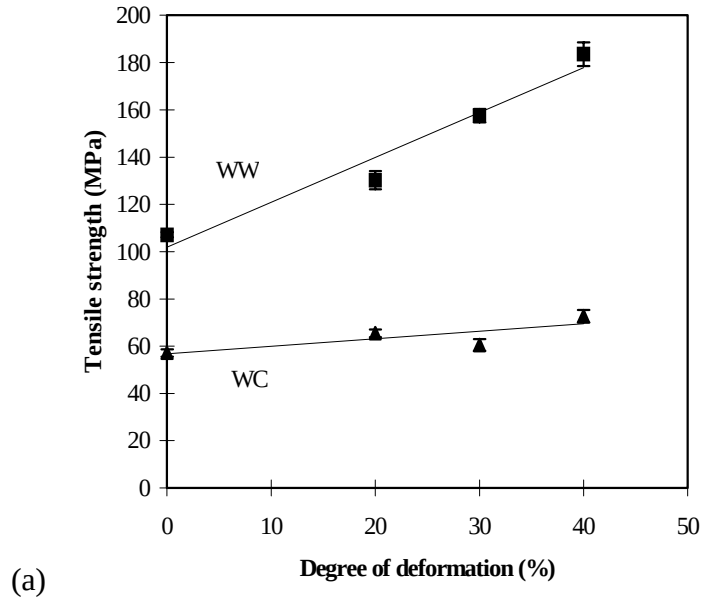

(a)

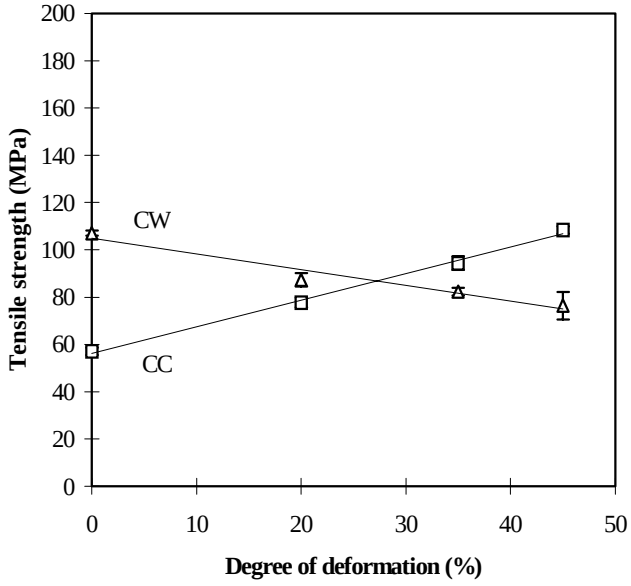

(b)

Fig. 3: The influence of deformation of the knitted fabric on composite strength.

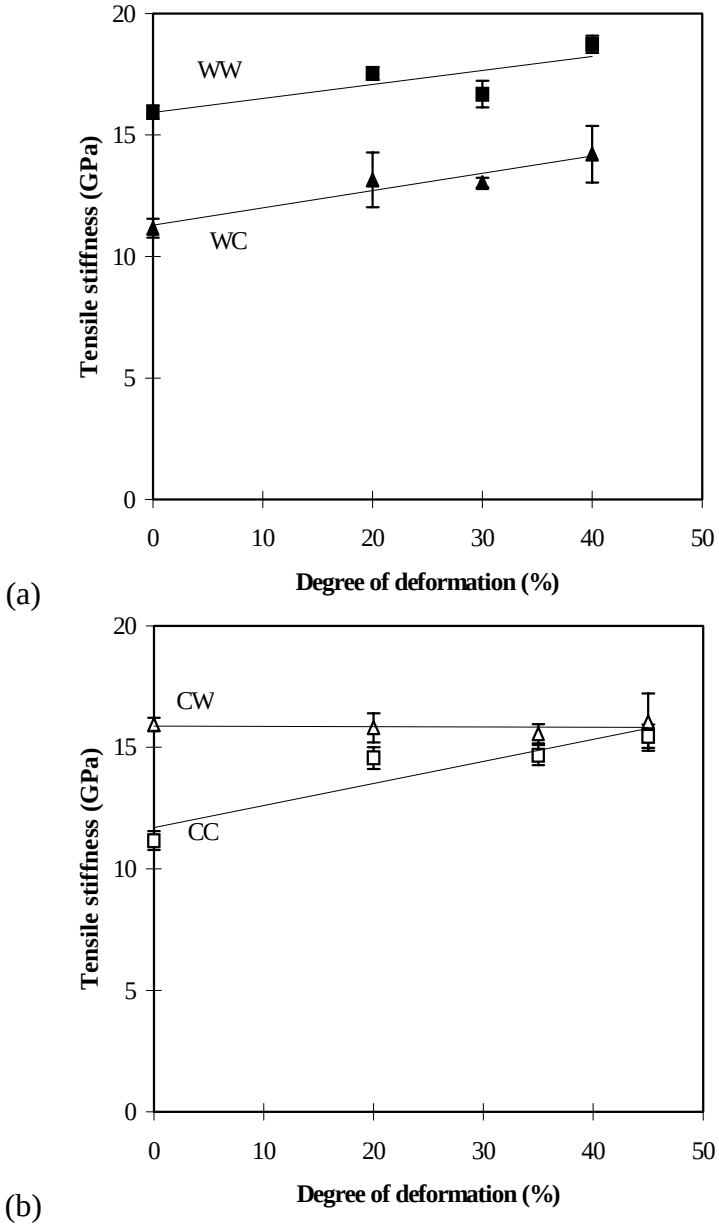

Fig. 4: The influence of deformation of the knitted fabric on composite stiffness.

It is clear from Figures 5d and 5e that when the fabric was deformed in the course direction, the individual courses were simply drawn closer together, as would be in a plain weft knit structure, thus effectively reducing the amount of fibres that contribute to the wale-wise properties. Consequently, the tensile properties of the CW laminates deteriorated with the amount of fabric deformation. It is interesting to observe that the "loopy" nature of the knit structure was increasingly diminished with deformation of the fabric in the course direction.

However, as illustrated in Fugures 5b and 5c, when the fabric was deformed in the wale direction, the "loopy" nature of the knit structure was retained. The legs of the loops (see Figure 6) not only remained oriented at an angle to the two principal axes, *i.e.* wale and course, so that these fibre components contribute to the tensile properties in both the directions. The enhancement of strength and stiffness of the WC laminates is in fact attributed to the increasing straightening of these fibre components with deformation.

Close examination of Figure 5 further revealed that the fibres are much straighter in the course-deformed fabrics than in the wale-deformed ones, and this is probably the reason for the steeper rate of increase both in strength (WW = 1.81% per unit stretch; CC = 2.00% per unit stretch) as well as in stiffness (WW = 0.43% per unit stretch; CC = 0.86% per unit stretch) for the former compared with the latter laminates.

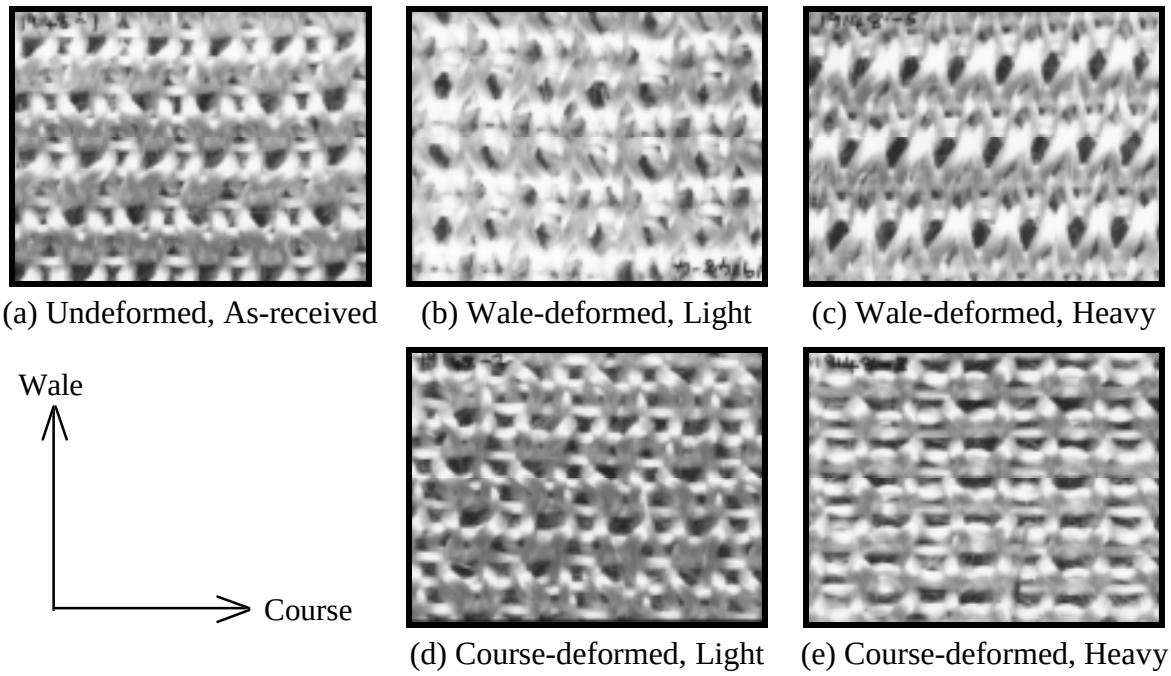

(a) Undeformed, As-received (b) Wale-deformed, Light (c) Wale-deformed, Heavy

(d) Course-deformed, Light (e) Course-deformed, Heavy

Fig. 5. The effects of deformation on the effective fibre architecture of the Milano rib fabric.

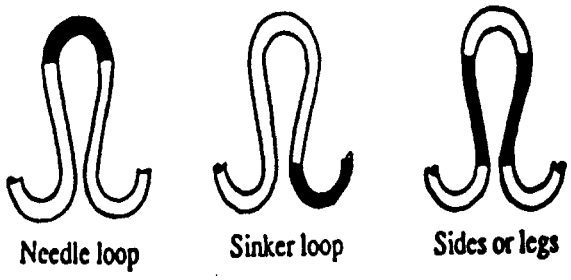

(a) (b) (c)

Fig. 6: Components of a weft knitted loop.

Fracture Mechanisms and Failure Modes

Irrespective of the amount of deformation in the fabric, and the relative loading direction, the first discernible damage in the specimens was observed to be matrix cracking (see Figure 7), which increased in intensity with loading until final failure of the specimen intercepted. It will be noted that this microcracking appeared macroscopically as whitened areas in the specimens. The locations of the microcracks within the gauge section were initially relatively random, but as loading progressed and more microcracks formed, they appeared to coalesce together to form regular rows of matrix cracks that span the whole width of the specimens (see Figure 7). Earlier work by Leong *et al.* [9] have revealed that the microcracks do not actually span the whole thickness of the laminates but are arrested by the complex array of fibres that came about through the intermeshing between the different fabric layers.

They also pointed out that the matrix crack spacings were of the order of the distances between the loop components in the fabric (see Figure 6), depending on the loading axis.

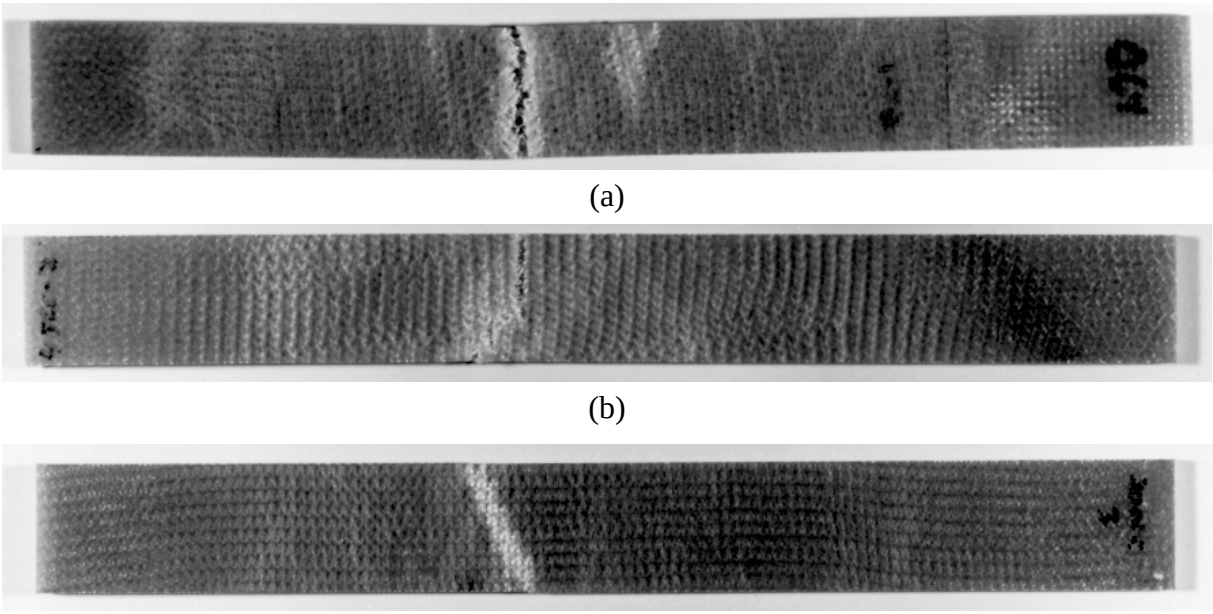

(a)

(b)

(c)

Fig. 7: Typical fractured specimens made from (a) undeformed, and (b & c) deformed, fabrics.

In the present work, ultimate failure is defined as the point at which there was an appreciable drop in the load-carrying capacity of the specimen. In most cases, when this happened, the specimens were not completely broken whereby the matching fracture surfaces was bridged by a ligament of fabric material. It is noteworthy that the gradual drop in stress after reaching a maximum, as depicted by the stress-strain curve in Figure 2, suggests that groups of fibres within the fracture plane had failed sequentially so that if a test were terminated before all the fibres within the plane had failed a ligament of fabric material would remain. Consistent with this fracture behaviour, ultimate failure for the knitted composites was not catastrophic. It is believed that the appreciable drop in the load-carrying capacity, and hence ultimate failure, of the laminates occurred with the onset of gross fibre fracture, *i.e.* breakage of the first fibre bundles.

The amount of deformation that the fabric had undergone was also observed to have an influence on the fracture mode of the resultant composite laminates. By referring to Figure 7, it can be seen that the laminates had failed in one of three modes with respect to the relative orientation of the fracture plane to the loading axis. More precisely, the specimens of undeformed (and lightly deformed) fabric failed in a plane normal to the loading axis (see Figure 7a) whilst the specimens of more heavily deformed fabrics generally failed at an angled plane of approximately 20° to 30° (see Figure 7c). It has been noted that the angles of the fracture planes on the whole increased with the amount of deformation of the fabrics. In some intermediate cases, the specimens failed in a combination of both modes, usually beginning at angle and finishing up normal, to the loading axis (see Figure 7b).

Post-failure examination of the fracture surfaces, using an Olympus ZHS stereooptical microscope, confirmed that ultimate failure of the specimens was indeed dictated by the capacity of the fibres to withstand loading after matrix cracking. As expected the fibre

breakages occurred in a fashion very similar to that observed by Ramakrishna and Hull [10] for their plain weft knitted carbon samples, whereby the fracture plane coincided with the plane of lowest local fibre content. In other words, wale-tested specimens tended to have fibres breaking at the legs of loops, and course-tested ones at the needle/sinker loops. It will be noted that, as in the specimens that failed in a plane normal to the loading axis, fibre breakages in the wale- and course-tested specimens that failed at an angled plane also occurred predominantly at legs of loops and needle/sinker loops, respectively. These latter fibre breakages were however not confined to a single row of wale of course but, instead, they consistently moved to adjacent rows causing large matrix cracks to form along the way.

CONCLUSIONS

In the present work, the effects of deforming knitted fabrics on the tensile properties of their resultant composites have been evaluated. The properties were studied for both the course and wale directions for composite laminates with fabrics that had been deformed in either of the two directions. It was revealed that as the amount of deformation in the fabrics was increased tensile stiffness and strength of the laminates improved markedly in the direction which the knitted fabrics had been deformed. This improvement in strength and stiffness with the degree of deformation is attributed to an increase in the content of fibres oriented along the loading axis as the knitted fibres were increasingly drawn and straightened in the direction of stretch. When the laminates were loaded normal to the direction in which the fabric had been deformed, it was revealed that deformation in the wale and course directions resulted in improvement and deterioration of tensile properties, respectively. The opposing trends observed for the CW and WC laminates is accounted for by a difference in the nature of distortion to the Milano rib structure when it is deformed in the two principal directions.

The orientation of fracture planes with respect to the loading axis appeared to be also dependent on the degree of deformation that had been induced in the knitted fabric. Specimens of undeformed (and lightly deformed) fabric failed in a plane normal to the loading axis whilst the specimens of more heavily deformed fabrics generally failed at an angled plane of approximately 20° to 30° depending on the amount of fabric deformation. In some intermediate cases, the specimens failed in a combination of both modes, usually beginning at angle and finishing up normal, to the loading axis. Nevertheless, irrespective of the amount of deformation in the fabric, ultimate failure of the wale- and course-tested specimens was attributed to fibre breakages occurring predominantly at the legs of loops and needle/sinker loops, respectively.

ACKNOWLEDGEMENTS

The authors are grateful to P.J. Falzon for useful discussions, and K. Houghton for assistance in specimens preparation.

REFERENCES

1. Epstein M. and Nurmi S. (1991) "Near net shape knitting of fiber glass and carbon for composites", (Proc. Conf.) 36th Int. SAMPE Symposium., April 15-18, 1991, pp 102 - 113.

2. Raz S. (1994) "Advanced knitted structures for composites : an outlook", (Proc. Conf.) TEXCOMP2 - New textiles for composites, May 17-19, 1994, Leuven, Belgium, Eds. I. Verpoest & F.K. Ko, 20pp.
3. Qi, B., Kruckenberg, T. and Raju, J. (1996) Resin transfer moulding of a non-structural component using a glass knitted fabric reinforcement, *Submitted to Comp. Sci. Tech.*
4. Verpoest I. & Dendauw J. (1992) "Mechanical properties of knitted glass fibre/epoxy resin laminates", (Proc. Conf.) 37th Int. SAMPE Symp., March 9-12, 1992, pp 369-377.
5. Ha S-W., Mayer J., De Haan J., Petitmermet M. & Wintermantel E. (1993) "Knitted carbon fibers reinforced biocompatible thermoplastics, mechanical properties and structure modelling", (Proc. Conf.) ECCM-6, September 20-24, 1993, Bordeaux, France, eds. A.R. Bunsell, A. Kelly, A. Massiah, pp 637-642.
6. Verpoest I. & Dendauw J. (1993) "Mechanical properties of knitted glass fibre/epoxy resin laminates", (Proc. Conf.) ECCM-6, September 20-24, 1993, Bordeaux, France, eds. A.R. Bunsell, A. Kelly, A. Massiah, pp 927-932.
7. Wu, W.L., Hamada, H., Kotaki, M. & Maekawa, Z. (1995) "Design of knitted fabric reinforced composites", *J. Rein. Plast. Comp*., **14**, 1032.
8. Chou, S., Chen, H.-C. & Lai, C.-C. (1992) "The fatigue properties of weft knitted fabric reinforced epoxy resin composites", *Comp. Sci. Tech.*, **45**, 283.
9. Leong, K.H., Falzon, P.J., Bannister, M.K. and Herszberg, I. (1996) "An investigation of the mechanical performance of weft knitted Milano rib glass/epoxy composites, *Submitted to Comp. Sci. Tech.*
10. Ramakrishna, S. & Hull, D. (1994) "Tensile behaviour of knitted carbon-fibre-fabric/epoxy laminates - Part I : Experimental", *Comp. Sci Tech.*, **50**, 237.
11. Ramakrishna, S. & Hull, D. (1994) "Tensile behaviour of knitted carbon-fibre-fabric/epoxy laminates - Part II : Prediction of tensile properties", *Comp. Sci Tech.*, **50**, 249.
12. Herszberg, I., Falzon, P.J., Leong, K.H. & Bannister, M.K. (1996) "Bearing strength of glass/epoxy composites manufactured from weft-knitted E-glass fabric", (Proc. Conf.) 1st Australasian Congress on Applied Mechanics, 21-23 February, 1996, Vol. 1, pp. 279-284.
13. Bannister, M.K. and Herszberg, I. (1995) "The manufacture and analysis of composite structures from knitted preforms", (Proc. Conf.) 4th Int. Conference on Automated Composites, 6-7 September 1995, Nottingham, U.K., Vol. 2, pp. 397-404.
14. Herszberg, I., Bannister, M.K., Leong, K.H. & Falzon, P.J. (1996) "Textile composites research at the Cooperative Research Centre for Aerospace Structures Ltd. (CRC-AS)" (Proc. Conf.) TEXCOMP3 - New textiles for composites, December 9-11, 1996, Aachen, Germany, ed. Wulfhorst, B., pp. 3/1-3/20.
15. Nguyen, M. (1996) "Investigation on the mechanical properties of stretched composite panels", Final Year Project Dissertation, Royal Melbourne Institute of Technology.
16. Hull, D. (1981) "An introduction to composite materials", Cambridge University Press.

OPTIMISING THE MECHANICAL PROPERTIES OF 3D-KNITTED SANDWICH STRUCTURES

Dirk Philips [1], Ignaas Verpoest [2] and Joris Van Raemdonck [3]

[1,2] Department of Metallurgy and Materials Engineering, KU Leuven, de Croylaan 2, B-3001 Leuven, Belgium
[3] IPA, Waaslandlaan 38, B-9160 Lokeren, Belgium

SUMMARY: In this paper an overview is given of the newest developments on 3D-knitted composites. The main effort has been focussed on overcoming the problems of translating the knittings from a textile environment to the field of composites. The major developments are going on in the development and use of complex yarns. Also, the first results of bending tests on different kinds of 3D-knitted composites are presented. The main parameters seem to be the orientation of the beam elements and the areal density of the composite. However, it is not easy to compare all results since a lot of parameters are involved. To overcome this, a new normalisation method will be necessary and more tests results are required.

KEYWORDS: knittings, sandwich, preforms

INTRODUCTION

In the last few years the interest for composites based on knittings has increased significantly due to the extremely good drapability of knitted prepregs and because complex parts can be shaped quite easily even with a reduced number of processing steps.

The new material described in this paper is based on two existing types of composite. It combines the advantages of the integrally 3D-woven sandwich structures[1] with the deformability and handleability of knitted preforms[2]. It is thought that this approach can have some advantages compared to the more traditional sandwich structures.

Currently, most sandwich structures are produced by bonding together two skins onto a core material. However, core materials with high specific properties such as honeycombs and some special types of foam are very expensive and hence, the complete sandwich becomes quite expensive as well. In the case of textile reinforcements such as the 3D-knitted and 3D-woven sandwich fabrics, the cost can be significantly lower because of the well-known textile technologies and the low cost mass production of these textiles[3].

Another typical problem which is difficult to solve with classical sandwich structures is the delamination of the skins, especially when the sandwich has been damaged. By using integral 3D-knitted and 3D-woven sandwich composites, this problem can be prevented.

One of the main advantages of these 3D-knitted structures is that double-curved sandwich panels can be produced easily. This is not really possible with the current sandwich materials and thus 3D-knitted sandwich composites bring a new feature to this class of materials.

CONCEPT & PRODUCTION OF 3D-KNITTINGS

Concept

3D-knitted sandwich fabrics consist of two skins [4], which look like a grid of knitted beam elements in a hexagonal or a rhombic configuration. The top and bottom skin of the knit are attached to each other by pile fibers standing vertical to the fabric plane. These pile fibers act as a core for the sandwich structure. Their length can be adjusted to modify the fabric thickness and hence also the composite properties.

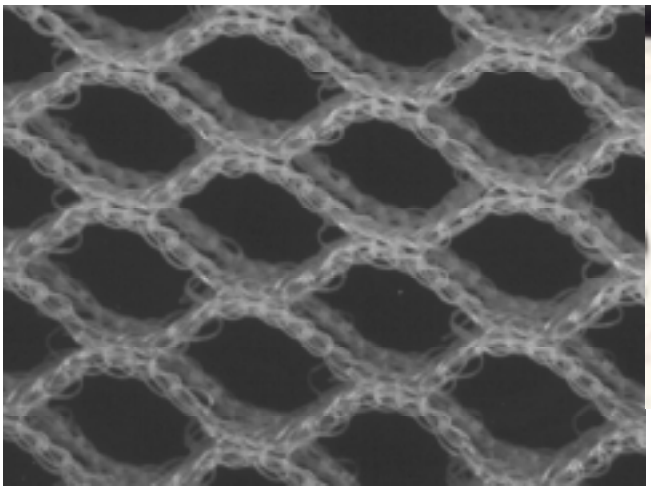

Fig. 1: Hexagonal grid structure of a 3D-knitting

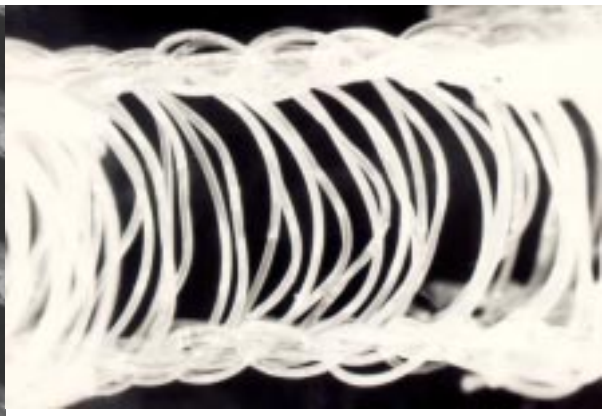

Fig. 2: Close look at the pile fibers

Production

The production of 3D-knittings is very similar to that of flat knittings. Only here, in principle, two knitting machines are put back to back in order to produce the top and the bottom skins of the sandwich fabric simultaneously. In practice, a double-bed rashell knitting machine is used for this purpose. This machine has two needle beds that can be controlled independently.

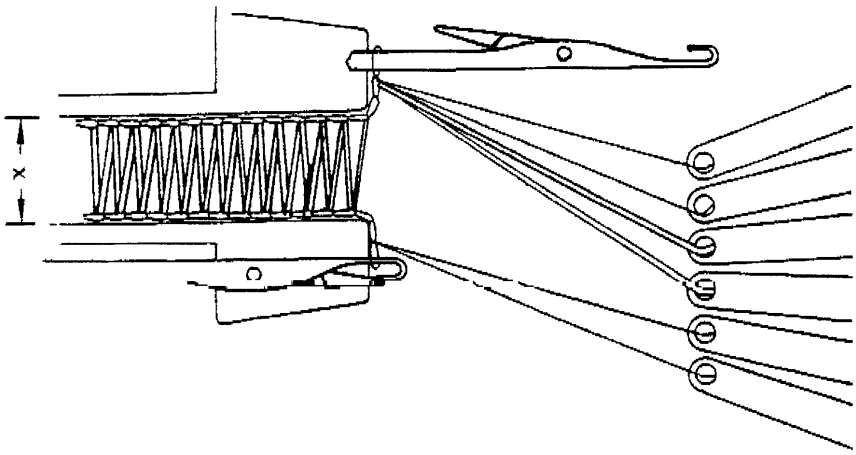

Fig. 3: Schematic drawing of the knitting process

During the knitting process the skins are being connected with pile fibers. These fibers not only constitute the core of the fabric but they are also part of the skins. This can be seen in Fig. 3 where it is shown how the piles are knitted into the top skin of the fabric. In the next

production step, the pile fibers will be drawn downwards and they will be used together with the skin yarns to knit one more loop of the bottom skin. It is clear that the pile fibers make up an integral part of the skins and it will be difficult to delaminate the skins from the core.

OPTIMISING THE KNITTINGS FOR COMPOSITE APPLICATIONS

Basic problems

The open 3D-knittings which were first used for producing composite samples are types that have been developed for textile applications only. These samples were all knitted with PET-monofilament yarns and after some exploratory investigation it became clear that these plain PET-monofilament knittings needed some adaptation before being qualified for composite applications.

First of all, there is already a contradiction for selecting the right yarns for knitting. From a knitting point of view, a flexible yarn is needed to produce small but complex loops with high curvature. In this case a multifilament yarn is recommended. However, when this knit has to be impregnated and draped over a complex surface. It has to keep a stable geometry and the skins need to stay at a distance from each other in order not to loose the sandwich effect. So in this case a stiffer monofilament yarn is required although this yarn may not be too stiff or the needles will break during knitting.

The picture becomes more complex when impregnation characteristics are considered too. Multifilaments can be impregnated better, easier and more homogenous than monofilaments as can be clearly seen in Fig. 4 and Fig. 5.

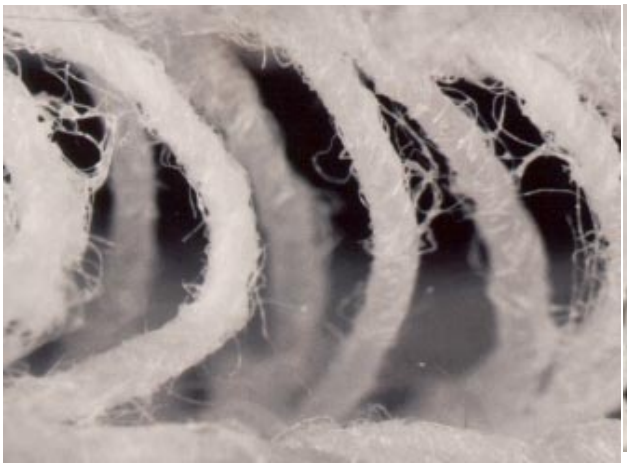

Fig. 4: Homogenous impregnation of pile fibers

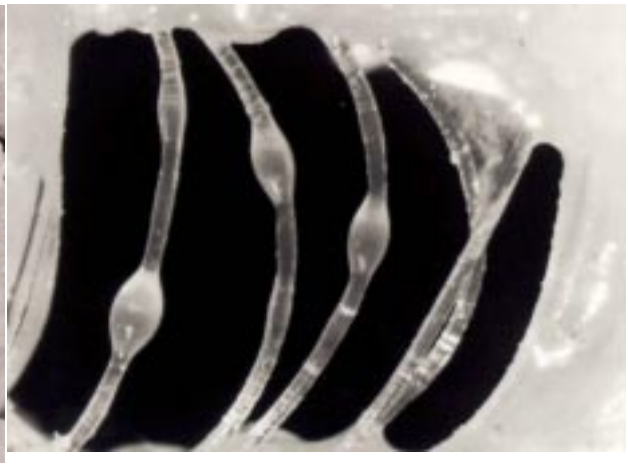

Fig.5: Poor impregnation of pile fibers

All these problems can be solved by combining multi and monofilament yarns. The basic idea is the following. One central thin PET-monofilament is wrapped with lots of other fibers so that the combined fiber is still very flexible for knitting The central monofilament provides the geometrical stability of the knit during impregnation while the multifilaments improve the impregnation quality but they can also increase the mechanical properties of the composite if stiffer fibers like glass or ramie are used. The multifilaments can have two effects on the resin. The network of cavities between the fibers can take up a lot of resin because of capillarity while the some fibers can absorb resin by themselves (i.e. ramie).

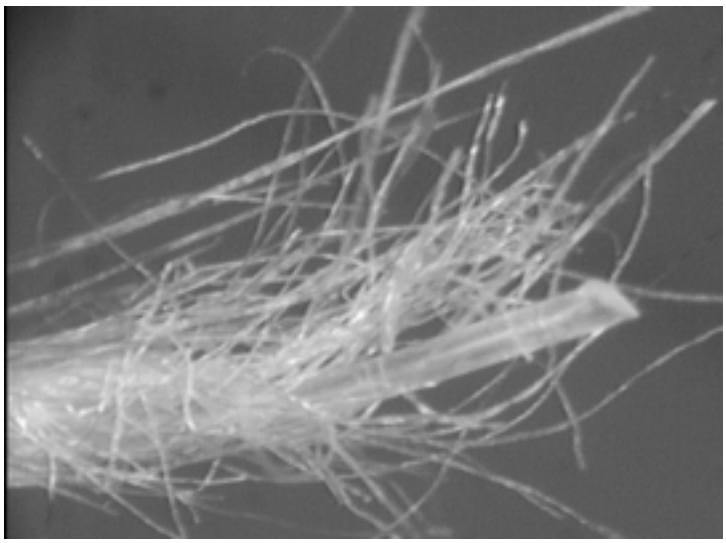

Fig. 6: Combined PET/ramie-viscose yarn ***Improving the mechanical properties***

Bending properties

Because of the very open structure we cannot expect the mechanical properties of the knitted sandwich composite to be extremely high. Nevertheless, the material performance can be optimised and several options are available to reach this goal.

First of all, the geometry can be adapted by changing the type of unit cell. Cell size can be reduced also to increase the effective surface area of the fabric and to increase the amount of material in the skins. Consequently this will increase the density of the material too. Another possibility is to stretch the knit before impregnating, so that the beam elements in the fabric become more oriented in one direction (Fig. 7, Fig. 8). Of course this will make the composite behave more anisotropic.

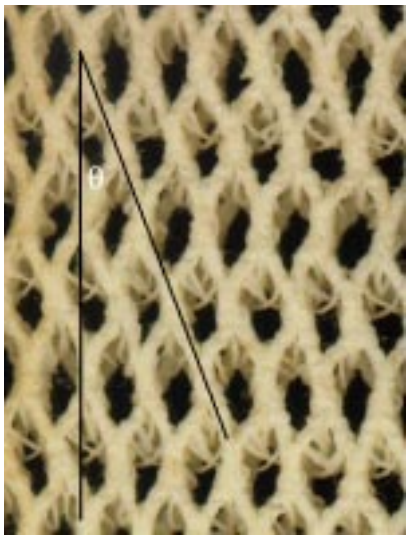

Fig. 7: Higly stretched knitted composite (18°)

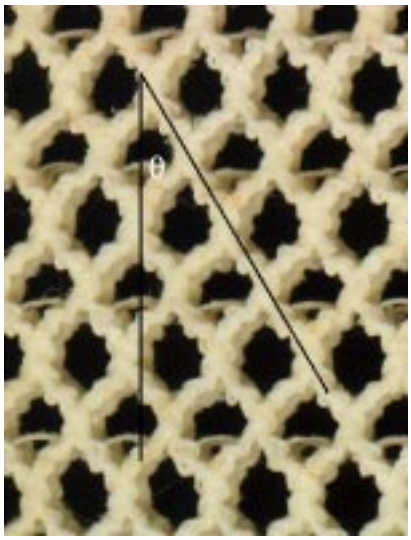

Fig. 8: Less stretched knitted composite (33°)

A second alternative is to make the composite stiffer by using stiffer yarns. This was first done by introducing ramie-viscose into the skins. The next step was to include glass fibers but knitting glass into the skins is already much more difficult. The glass fibers easily break

because of the high tension on the knitting yarns and because of high curvatures inside the knitting loops. Another option is not to knit the glass but to insert the glass fibers as straight bundles in the skins.

Compression & impact

To increase the compression and impact resistance of the composite, the load bearing capacity of the pile fibers has to become higher. This means that the buckling resistance of each single pile has to get better. With the introduction of combined yarns for pile fibers a major improvement has been realised.
By increasing the density of pile fibbers the load experienced by a single pile can be reduced so that the overall compression and impact properties of the composite can improve.

BENDING PROPERTIES

Description of the fabrics used

Table1: Description of 3D-knittings

Knit	Geometry	Pile Fiber	Skin Fiber	Skin Inserts
H10	Hexagonal	PETmonofil	PETmonofil	-
R7	Rhombic	PETmonofil	PETmonofil	-
Hr1	Hexagonal	PET/ramie-viscose	PETmonofil	-
Hr2	Hexagonal	PET/ramie-viscose	PETmonofil	-
Hr3	Hexagonal	PET/ramie-viscose	PETmultifil	-
Hpg1	Hexagonal	PET/polyester	PETmultifil	204 tex glass knitted
Hpg2	Hexagonal	PET/polyester	PETmultifil	68 tex glass inserted

In Table 1, three families of materials can be distinguished. The first two types of knits are the plain PET-monofilament knittings as produced for textile applications. The newly developed Hr-types all have PET/ramie-viscose pile fibers, while the Hpg-types have PET/polyester piles and extra glass fibers in their skins. Two versions of Hpg-knits are available: one with the glass knitted into the skins while the other version has the glass inserted as straight bundles.

It is clear that the knits with combined yarns will have higher mechanical properties because they can be impregnated better, especially the pile fibers.

Production of composite samples

Two types of resin systems have been used for the production of composite samples. Resin1 is a sheet like resin that has to be cured in an oven for 60 minutes at 125°C. The other one, resin2 is a solvent based resin which cures at room temperature in open air after evaporation of the solvent. This second type gives better homogenisation of the resin.
All composite samples have a thickness around 7mm. Only the samples Hpg2-a and Hpg2-b are thinner (5.5mm).

Bending properties

In Fig. 9, the apparent bending modulus of 3D-knitted composites has been shown. The main orientation angle of the beam elements (which is in fact the main fiber orientation) and the resin content are mentioned. In this figure, two groups of composites can be distinguished. The samples on the left hand side of the figure have been impregnated with resin1, the others with resin2.

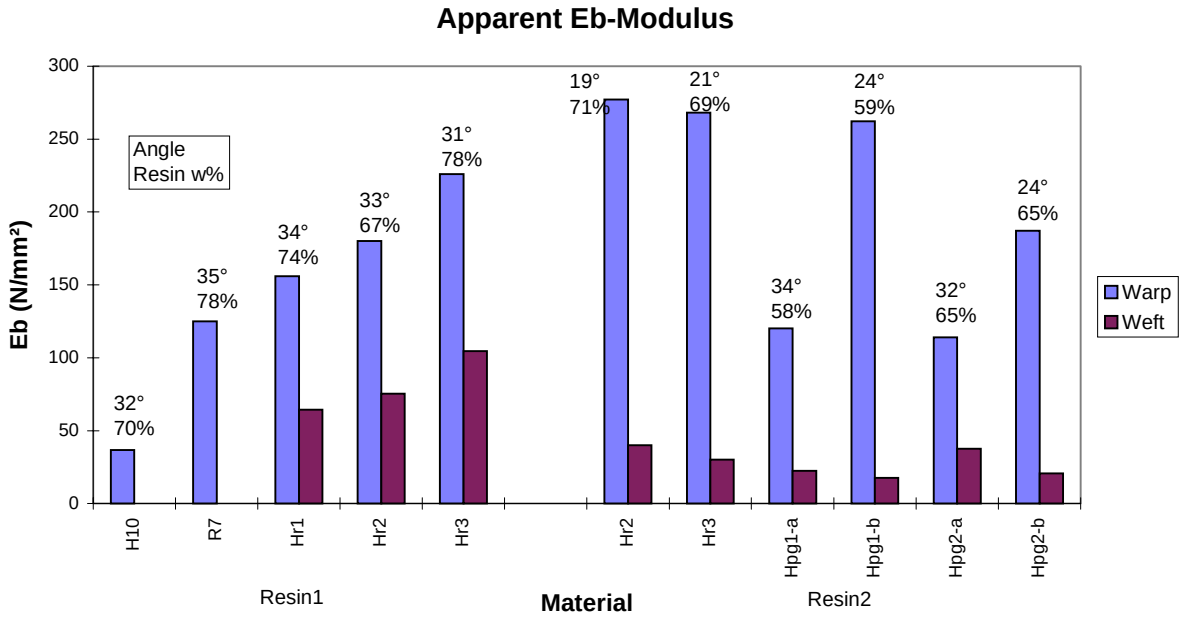

Fig. 9: Bending modulus of 3D-knitted composites

In the left group all samples have about the same degree of stretching so that they are comparable in this respect. Samples H10 and R7 are the first generation of 3D-knitted composites: they are knitted from plain PET-monofilaments which are difficult to impregnate properly. This is also the reason why the modulus of H10 is low: the pile fibers are barely impregnated.

The value for R7 is already much higher because the sample has a high resin content. In this case the skins are well impregnated and on some spots even over-impregnated, while the pile fibers of R7 are getting impregnated as well due to the abundance of resin. As a consequence of this, resin walls between the piles are being formed. This drastically increases the stiffness of the composite. Resin lumps in the corners between the piles and the skins have the same effect.

Samples Hr1, Hr2, Hr3 are all based on PET/ramie-viscose pile fibers which means that the core is much better impregnated and the properties are higher. However, these three types of samples, especially Hr1 and Hr3 have been over-impregnated. The corners between beam elements and the corners between piles and skin have been filled with resin, which drastically increases the stiffness.

Comparing these three samples with Hr2 and Hr3 impregnated with resin2 shows that the latter are somewhat stiffer despite the lower resin content. The reason for this is that they have been stretched more. However, one would expect the difference to be bigger, but this is not so

because of over-impregnation of the samples with resin1 and because resin1 is stiffer than resin2.

The effect of stretching the knittings becomes more clear in the Hpg-samples. They are all impregnated with the same resin2 but also, the resin content for samples made from one type of knit is constant (58 or 65w%) for both the stretched and the unstretched versions. The stretched samples (~21°) clearly are stiffer, they have a stiffness of about double that of the less stretched ones (~33°).

In Fig. 10 the apparent bending modulus versus the density of the composite is visualised. All available samples have been put into two categories, although there is some variation in the measured angle. There is a group of samples which are highly stretched (~21°) and samples which are less stretched (~33°). Both the warp and weft direction are presented.

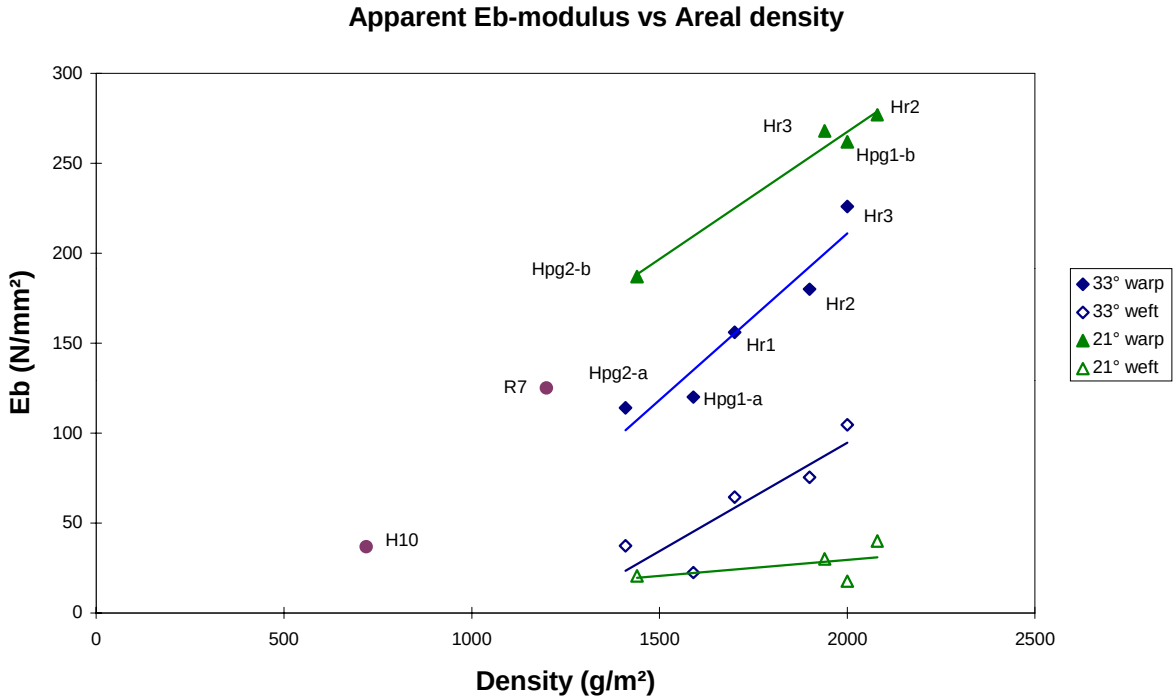

Fig.10: Apparent bending modulus versus composite density

For each group of samples a linear relationship between modulus and density is observed. Modulus goes up with increasing density of the composite but also depends on the degree of stretching. The type of knitting yarn does not seem to have a lot of influence nor does the resin. This would suggest that the stiffness is mainly dependent on the geometry of the unit cells and on the density, just like foam materials. Of course, all results presented here are the first findings based on just a small number of samples. It is still to early to draw general conclusions.

However, one limitation of the current analysis is the artificial division of the composite samples into two categories. A more correct way is to perform a normalisation for the degree of stretching and to have a look at more samples that only differ in angle.

A variation of a few degrees was recorded when characterising the samples. This will not have such a big influence on the samples that have their beam elements at an angle of 33°. However, it becomes much more critical for samples that are more stretched. This is probably

the reason why the extra glass in the skins of Hpg-knits seems to be inefficient at first sight. Another reason is that part of the glass fibers are broken because of knitting and these broken fibers could be seen on the sample. It is also obvious that if the Hpg-samples with 24° would have been normalised to an angle of about 20°, the apparent E_b-modulus would be higher.

CONCLUSIONS

1. 3D-knitted fabrics are being adapted to satisfy specific needs of composites and new types of complex yarns are under investigation.

2. Stretching the fabric can be used to control the stiffness of the composite.

3. A reliable method for comparing test specimen with different degrees of stretching is necessary.

REFERENCES

1. Van Vuure, A.W., Ivens, J., Verpoest, I., “Sandwich fabric panels”, Proceedings 40th Int. SAMPE Symposium, Anaheim, USA, May 8-11, 1995

2. Verpoest, I., Dendauw, J., “Mechanical properties of knitted glass fiber/epoxy resin laminates”, 37th Int. SAMPE Symposium, March 9-12, 1992, pp. 369-377.

3. Verbrugge, K., Ivens J., Verpoest, I., Van Der Vleuten, P., “Foamed 3D-fabric sandwich structures”, Proceedings of the 12th European SAMPE Conference, Maastricht (NL), 1991, pp. 417-425

4. Philips, D., Verpoest, I., Van Raemdonck, J., “3D-knitted fabrics for composite structures”, Proceedings TEXCOMP 3, Aachen, Germany, December 9-11, 1996

ACKNOWLEDGEMENTS

We would like to thank the following organisations and institutions:

Part of this research has been financed with a specialisation grant of the Flemish Institute for the Promotion of Scientific and Technological Research in Industry (IWT).

This text presents research results of the Belgian programme on Interuniversity Poles of attraction initiated by the Belgian State, Prime Minister’s Office, Science Policy Programming. The scientific responsibility is assumed by its authors.

NOTCHED STRENGTH OF KNITTED FABRIC COMPOSITES

J. de Haan[1], K. Kameo[2], A. Nakai[2], A. Fujita[2], J. Mayer[1], E. Wintermantel[1], H. Hamada[2]

[1]Chair of Biocompatible materials Science and Engineering, Swiss Federal Institue of Technology Zurich, Wagistrasse 23, 8952 Schlieren, Switzerland
[2]Kyoto Institute of Technology, Matsugasaki, Sakyo-ku, Kyoto606, Japan

SUMMARY: Holes in composite materials generally lead to a reduction in strength of the remaining cross section. In former study on knitted carbon fibre-PEEK composites, however, it was observed that forming-in of holes lead to an increase in strength of the remaining cross section [1]. In this paper two other types of holes are tested on knitted aramid fibre / epoxy composites, tested in tension: knitted and drilled holes. The difference between both holes is, that for the latter the fabric is only deformed but further remains unchanged, whereas in case of knitted holes one loop is placed on the neighbouring needle, thus leaving a free space at its original position and doubling the number of fibres on the neighbouring needle. The effect of this technique on specimen with holes tested in tension is, that the strength of the remaining cross section increases. Experiments were carried out in both principal directions of the knitted fabric (course and wale), with a hole of 6 mm and a variable specimen width. An interesting characteristic is observed for the drilled holes: for small widths the tensile strength of the remaining cross section appeared to be higher than the strength of the unnotched cross section, although no special strengthening effect is apparent. For higher specimen widths this effect disappeared and the strength values approached closely.

KEYWORDS: knitted fabric composites, open hole tension, elastic properties, strength properties, monolayer model composites

INTRODUCTION

In composite structures, drilling of holes leads to local fracture of the area around the cutting plane, when the structure is loaded. This fracture is considered to cause final failure when the load on the structure is increased. To prevent structures from weakening due to cracks induced by cutting, the area around the hole should be strengthened. This strengthening effect is obtained in knitted fabrics when holes are formed or knitted in the fabric.

The versatility of the knitting technique allows the textile manufacturer to produce knitted fabrics with knitted-in holes by placement of one or more loops on neighbouring needles. Another possibility to obtain holes in knitted fabrics is the forming in of holes by placement of a bolt inside the loop of a normal knitted fabric and subsequently a widening the (existing) loop. The advantage of this type of holes is that the area around the hole is strengthened by an increased fibre density (especially in monolayer composites, where fibre rich areas are alternated with matrix rich areas) and an improved orientation of the fibres circumferentially to the hole. This strengthened area forms a buffer for the effects of stress peaks due to the presence of a hole.

The experiments in this study were carried out with plain weft knitted fabrics made from aramid fibres. One single layer of this fabric was impregnated with epoxy and consolidated. In this way, a model composite was produced. This material is a model for multilayer knitted composites, since it detects failure sources (due to the small deformability of the epoxy matrix) and shows mechanisms (due to the transparency of the epoxy). In studies on knitted composites with thermoplastic PEEK matrix [1], the failure sources could not be detected for two reasons: the inner layers in multilayer laminates are not visible when non transparent fibre or matrix materials are used and when the thermoplastic matrix allows high deformation due to which strain concentrations in the matrix do not necessarily lead to failure.

MATERIALS AND METHODS

Two series of fabrics with an intermediate stitch density (18 loops per square cm) were knitted with aramid fibres: the first series without holes and the second series with knitted-in holes with the size of a single loop, which agrees with a hole of approximately 6 mm diameter.

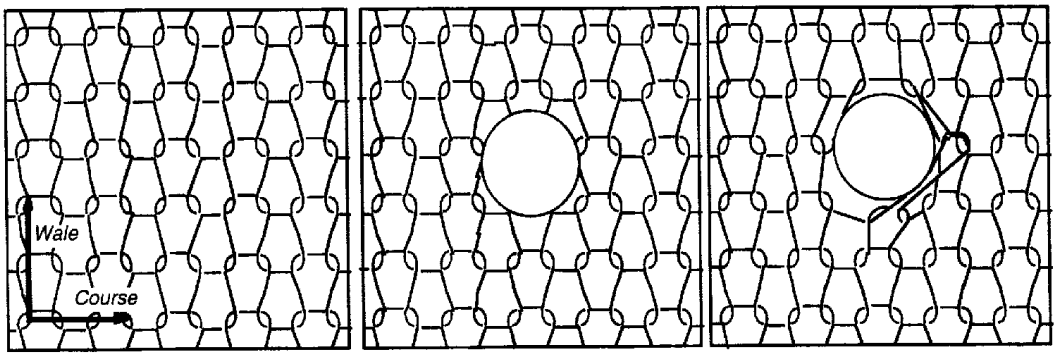

Fig. 1: *Schematic drawing of the knit structure (left), structure with drilled hole (middle), structure with knitted hole (right). It is observed in the case of the knitted hole, that at one side of the hole an extra loop contributes to the tensile strength. On the other side, there is squeezing of fibres which are formed around the hole. This way, a non symmetric fibre distribution occurs.*

The aramid fibres (Kevlar 49, Du Pont) were knitted on a flat knitting machine. The fabric was impregnated with epoxy (Epikote 828, Yuka Shell Epikote Co.), degassed in a vacuum chamber and subsequently panels of 300 x 300 mm^2 were manufactured by hand lay-up. The panels were cured at 50° C for 1 hour and postcured for 2 hours at 100°C. The thickness of the composite panels was approximately 0.8 mm, which corresponded with a overall fibre volume fraction of 20 %. Finally specimen of 250 x 25 mm^2 were cut from the panels by circular saw and aluminium end-tabs were placed on the specimen in such a way that a free testing length of 150 mm remained (see Fig. 2). Altogether, three types of specimen were produced: the first type was unnotched, the second type with knitted holes and the third type with drilled holes. All types were produced both in wale and in course direction of the knitted fabric (Fig. 1)

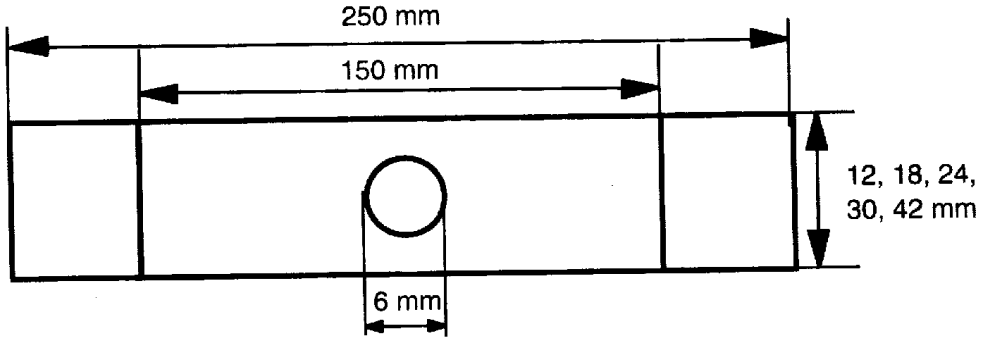

Fig. 2: *Geometry of the specimen and placement of the hole and the end-tabs.*

In this study, the tensile strength of single layer aramid fibre / epoxy composites with drilled holes was compared with the strength of composites made from fabrics with knitted-in holes and with a reference specimen made from unnotched material. For the experiments the hole diameter was kept constant, whereas the specimen width was varied to obtain different values for the ratio (W/D) of specimen width (W) to hole diameter (D).

Tensile tests were performed on an Instrom universal testing machine, with a crosshead rate of 0.1 mm/min. The deformation was measured by the displacement of the crosshead, whereas the forces were measured by a load cell.

RESULTS

The knitted monolayer aramid fibre / epoxy laminate is characterised by the heterogeneity of the fibre / matrix distribution: the fibres are localised in the fibre bundle, whereas the matrix is accumulated in between the knitted loop. This heterogeneity has strong consequences for the stress-strain behaviour of the composite.

Stress-strain behaviour

The stress-strain behaviour of the knitted aramid fibre reinforced epoxy can be regarded as linear up to first failure of the specimen (Fig. 3). After the failure, the stress-strain behaviour can be regarded as a series connection of a composite share with a large volume and a fibre share with a low volume. Similar stress-strain behaviour was found on unnotched specimen by Ramakrishna [2] on monolayer carbon / epoxy laminates and Fujita [3] on aramid /epoxy.

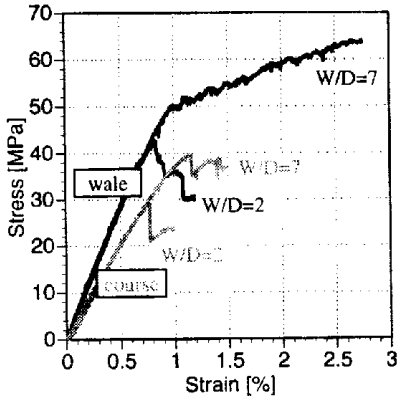

Fig. 3: Stress-strain curves in wale (black) and in course (grey) direction for small (W/D = 2) and wide specimen (W/D = 7) with knitted holes.

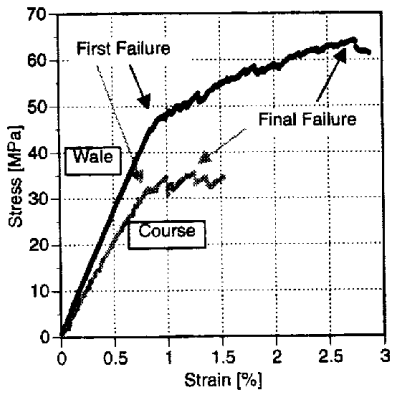

Fig. 4: Stress-strain curves in wale (black) and in course (grey) direction for wide specimen (W = 42 mm) without holes. Indicated are the points of initial and final failure.

Another characteristic, which can be observed in Fig. 3, is the slope of the linear part. The stress-strain curves shown, were taken from one single panel. The slope, e.g. the Young's modulus of the specimen, is equal for the specimen tested in the same direction of the knit structure (wale / course). This equivalence of the slope implies, that the influence of the hole region is rather small. This can be explained by the fact that the hole region has a small volumetric share relative to the whole specimen (D = 6 mm, l = 150 mm).

Failure behaviour

The failure behaviour of the knitted aramid fibre / epoxy composites was characterised by two types of failure: first failure and final failure (Fig. 4). Initial cracks were predominantly formed in the interlacing points. First failure for strength analysis was defined as the point in the stress-strain curve at which the drop exceeds 2 % of the tensile stress. Both in course and in wale direction the first failure occurred at low strain levels. In case of W/D = 2 the first failure was also final failure, whereas for W/D > 2 a failure path was found in the stress-strain curve: due to a matrix crack the stress dropped and after continued macroscopic deformation the stress was built up again. This failure mechanism was repeated until the aramid bundles broke; the final failure. The failure mechanism between first and final failure was attended by large strains in comparison with the strain up to first failure. Observations during testing showed, that for

W/D < 7 the matrix cracks progressed completely through the width of the specimen. For the widest specimen with a W/D ratio of 7, the failure behaviour was different: here the matrix cracks were preferably initiated at one side of the specimen and they alternately stopped and grew with increasing macroscopic deformation.

Strength values

The strength values for first failure were only compared for W/D>2. The reason that the data for W/D = 2 were not taken into account was that for those specimen first failure was also final failure and, therefore, the fracture sequence did not occur.

In Fig. 5 the first failure stress and strain values are shown. The strength of specimen with W/D = 3 is low. It can be expected that this low value is caused by the side effects due to cutting of the specimen: the cracks which are formed this way have a strong effect on the stress in the specimen, since the remaining cross section is relatively small. With increasing width of the specimen, the influence of the side effect reduces. However, for large specimen again a drop in first failure stress values is found. The observations discussed in the preceding section showed, that the crack distribution was not symmetric. Since only averaged stresses are calculated it is expected that the real stresses at the cracked side are higher than the measured stress and, therefore, the value for first cracking in the wide specimen is lower than the real stress at first failure. For drilled holes, the values for first failure are on a lower level, which is due to the absence of reinforcing bundles at the hole. Therefore, the stress concentrations around the hole cause increase the probability of first cracking at the hole.

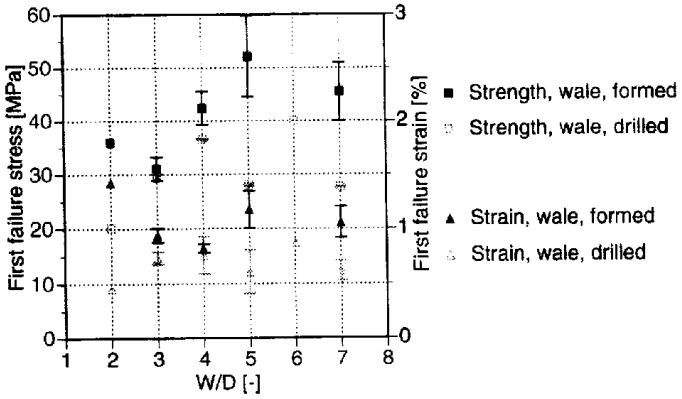

Fig. 5: First failure stress and strain values in wale direction for knitted and drilled holes

In course direction the first failure stress values for small specimen are on the same level as for small specimen in wale direction (Fig. 6), whereas for increasing W/D ratios the strength of the specimen remains on a similar level. Since the strength of unnotched specimen in wale direction is higher than the strength of unnotched specimen in course direction, this indicates that the strength directly around the hole is on the same level for both principal directions (the number and the orientation of the bundles should in that case be equal in course and in wale direction).

The stress levels for wider specimen are on the same level as for smaller specimen, the decrease which is found for specimen in wale direction with W/D = 7 is not observed. This could be caused by a smaller bending moment (not systematic failure) or could indicate a smaller sensitivity for misorientations.

In the figures 5 and 6 the values for the strain are given, but will further not be discussed in this context.

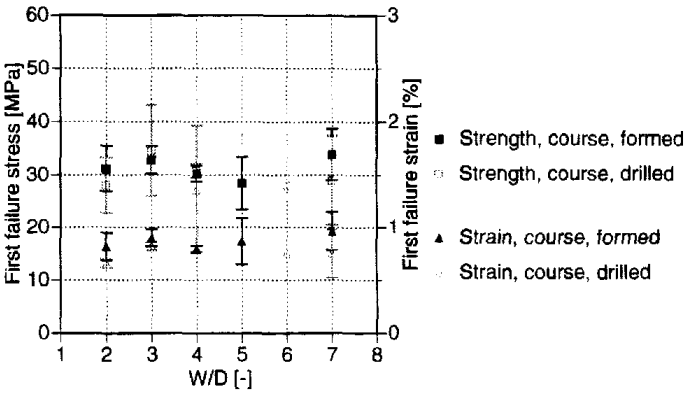

Fig. 6: First failure stress and strain in course direction for knitted and drilled holes

The second failure type, the final failure, occurred after progressive failure of the matrix. The progressive failure consisted of a sequence of matrix cracking with unloading and reloading of the specimen. After reaching a certain stress, the fibre bundles in one of the cracking planes broke and caused final failure. For specimen with knitted holes two types of final failure were observed: failure of the hole region and failure outside the hole region. The first type of failure occurred at small specimen, where the remaining area after the forming-in of the 6 mm hole was to small to redistribute the increased stresses around the hole. For wider specimen the remaining cross section was large enough to redistribute the increases stresses and, therefore, final failure did not necessarily occur at the hole. Both types of fracture were recorded on the specimen with knitted holes (Fig.7).

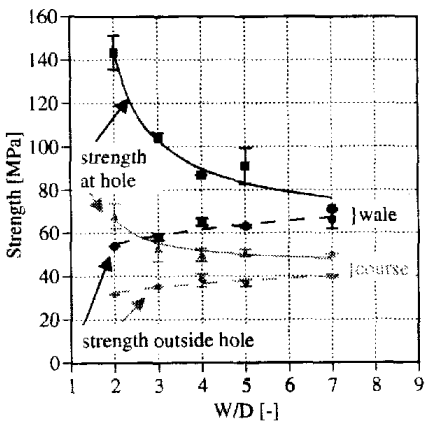

Fig. 7: Strength at the knitted hole (in case failure occurs at the hole) and strength outside the knitted hole (in case failure occurs outside the hole region) in wale (black) and course (grey) direction

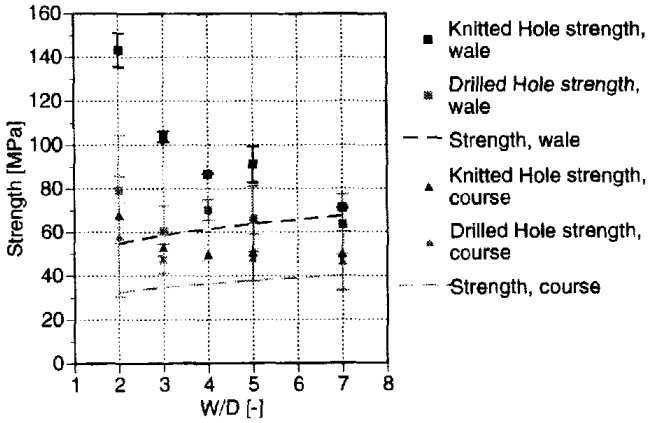

Fig. 8: Strength for knitted and drilled holes and for unnotched specimen in wale (black) and in course (grey) direction

For the strength outside the hole, the trendline is shown in Fig. 7 and 8. The lower strength for small specimen is expected to be caused by cutting defects at the specimen sides. For the strength at the hole the line was fitted according to the following considerations for the apparent strength σ_{app}:

$$\sigma_{app} = \frac{S_1 x + S_2 (W - D - x)}{W - D} \qquad (1)$$

where S_1 is the strength around the hole, where the fibre density and thus the composite strength is increased and S_2 is the strength outside the hole region, which coincides with the strength of an unnotched specimen. x is the width of the area around the hole with the increased

fibre density and W and D are the specimen width and the hole diameter respectively. Expression (1) can be rewritten as:

$$\sigma_{app} = \frac{C_1}{\left(\frac{W}{D}\right) - 1} + C_2 \tag{2}$$

where C_1 and C_2 are the fitting parameters, with

$$C_1 = \frac{1}{6} S_1 x - \frac{1}{6} S_2 x \tag{3}$$

and

$$C_2 = S_2 \tag{4}$$

For the fitting parameters the following values were found:

	C_1	$C_2=S_2$
Wale	80.7	62.9
Course	22.3	44.2

Table 1: Fitting parameters for the open hole strength for failure at the hole

From this fitting procedure only the unnotched strength is found directly: for specimen tested in wale direction the unnotched strength is 62.9 MPa and in course direction the strength is 44.2 MPa, the value represents the limit of the curve for W/D → ∞. In Fig. 6 this asymptote is located in between the values of W/D 7 for unnotched specimen and specimen with knitted holes. The strength at the hole is dependent on the size of the area (the width) with improved strength and, therefore, the size of this area should be estimated, before the value can be calculated.

DISCUSSION

The stress-strain and failure behaviour of the investigated knitted aramid fibre / epoxy composite are dominated by the (brittle) matrix: up to first failure the stress-strain behaviour can be regarded as linear. This is expected to be inherent to the epoxy matrix, which is highly linear up to failure, whereas the knitted fibre structure is strongly non-linear. Besides, the fibre volume fraction is low (<20%), so that the influence of the fibres is rather small. Also at first failure the matrix was dominant, since cracks were formed in the matrix. Final failure, on the other hand, was caused by failure of the aramid bundles. The failure mechanism appeared to be dependent on the specimen width. For small specimen (W/D = 2), the first failure was at the same time final failure. For wider specimen (W/D > 2) the load in the fracture region was transferred by the fibres after the first matrix crack had progressed through the width of the specimen. With increasing macroscopic deformation, the specimen was reloaded above the stress level of the first fracture and new fracture planes were formed, positioned apparently arbitrary on the length of the specimen, but at least two loops away from the old fracture plane(s). For specimen with W/D = 7 the cracks progressed less fatal: cracks were stopped and subsequently new cracks were initiated or existing cracks grew.

Characteristic for the first failure strength values is the large scatter in results. A possible explanation for this is, that the epoxy materials are sensitive for imperfections, which are introduced by the bundles. On the other hand, the knit structure is irregular; in wale direction the loops are not completely aligned, but show a zigzag pattern. During tensile testing it was observed, that due to this pattern some interlacing points are preferred points for initiation of fracture. A third explanation is the definition of the first failure. Since the first failure was defined as the point at which the first drop in stress occurs, small changes in stress are not taken into account. A more reliable method would be to measure the first failure by acoustic emission.

Ramakrishna [2] used the approach of acoustic emission to detect the point of first failure and found, that this point was accompanied by a knee point in the tensile curve. This knee point, however, was not explicitly observed in the study presented here.

At the location of the fracture, the fibres obtain a larger freedom due to the absence of matrix material. Besides, the fibre part which sticks in the matrix starts shearing in the cavity of the fibre bundle, as a cause of the weak interface. Therefore, the deformation in the fracture region is accompanied by large strains. Although the volume this fracture region represents is relatively small in comparison with the specimen size, the large strains have a significant influence on the macroscopic deformation of the composite and thus, implicitly, on the slope of the stress-strain curve. In the experiments it is observed, that after each matrix crack, the slope decreases.

Concerning the final failure, it was observed that for all (unnotched, knitted hole, drilled hole) small specimen loaded in wale direction the strength was low. It is expected, that for small specimen the region influenced by cutting defects at the specimen sides is large compared to the specimen width.

For wide specimen the effect of a loads which are not uniformly divided over the width of specimen due to a imperfect clamping increases. In this way, a bending moment is added to the tensile force, due to which cracking is preferred at one side of the specimen. For wide specimen the effect of this bending moment causes higher stress differences than for small specimen, which could be an explanation for the decreasing strengths.

Another interesting aspect of the drilled and the knitted holes in knitted structures is, that the strength ratio r_s is larger than 1.

$$r_s = \frac{S_{hole}}{S_{unnotched}} \tag{5}$$

where S_{hole} = strength at hole and $S_{unnotched}$ = strength of unnotched specimen.

In general it is observed, that the strength of the remaining cross-section in a structure is reduced when a hole. However, in knitted composites with holes (see also [1]) the strength of the remaining cross-section is not reduced (Fig. 8). For small specimen the improvement is large, whereas the values for wider specimen the ratio approaches 1. This effect is also observed in specimen with drilled holes, although there the ratio is smaller, but for all values of W/D the ratio is larger than 1. Since strength factors are higher than 1 it can be concluded, that the investigated knitted composites are insensitive to notches.

CONCLUSIONS

Tensile tests on single layer, knitted aramid fibre / epoxy composites were carried out to clarify the failure mechanisms in knitted composites. The tests carried out on specimen with drilled and knitted holes, showed a strengthening of the remaining cross-section around the hole in comparison with the unnotched cross section. For specimen with drilled holes, the region around the hole always caused final failure, whereas for composites with knitted-in holes, in case of specimen with values of the ratio W/D>2, the region around the hole did not necessarily lead to final failure. Although sometimes cracking occurred in the hole region, final failure of the majority of specimen with knitted holes occurred outside the hole region. It was found that the strength of the area around the hole was up to two times higher than the strength of unnotched specimen. In specimen with drilled holes, failure occurred at the hole. The strength ratio was only slightly higher than 1, which was to small to prevent the structure from cracking at the hole.

An addition to this study, finite element calculations with a model which represents the wearing structure around a hole were carried out. The model consisting of beam elements can describe the initial linear behaviour and the progressive failure behaviour, when the load is redistributed after initial failure has occurred. According to the proposed model the notched strength was calculated. The model, as well as a more detailed fracture study, will be presented in a separate work.

It can be concluded, that open holes in single layer knitted aramid fibre / epoxy composites tested in tension, do not necessarily lead to final failure if the holes are knitted-in and the ratio w/d is larger than two. This, and the damage tolerant failure aspect of net-shape manufacturing of knitted composites might be interesting for the application in constructions. An example of such an application is an osteosynthesis plate for bone support, where the volume share of the holes is large in comparison with the volume of the complete plate (Wintermantel [4]).

REFERENCES

[1] de Haan, J., Schmitz, S., Mayer, J., Wintermantel, E., Open hole tension of knitted carbon fibre reinforced PEEK composites, *Texcomp-3 Proceedings*, Aachen, Germany, Dec. 9-11,

[2] Ramakrishna, S., Hull, D., Tensile behaviour of knitted carbon-fibre-fabric / epoxy laminates-Part I: experimental, *Composite Science and Technology*, 50, 1994, p. 237-247

[3] Fujita, A., Numerical Modelling for Textile Structural Composites, Ph. D. Thesis, Kyoto Institute of Technology, Kyoto, 1995, p. 222-258

[4] Wintermantel, E., Mayer, J., Anisotropic biomaterials: strategies and developments for bone implants, *Encyclopic handbook of biomaterials and bioengineering*, Marcel Dekker Inc., New York, 1995, p. 3-42

NEW LOW COST TEXTILE PREFORMS AND SHORT CYCLE PROCESSING TECHNIQUES FOR THERMOPLASTIC COMPOSITES

Sofie Baeten [1], Ignaas Verpoest [1], Hauke Stumpf [2], Karl Schulte [2], Walter Zäh [3], Edith Mäder [4], Toni Pisanikovski [5], Carl-Håkan Andersson [5], Kjell Eng [6]

[1] Department of Metallurgy and Materials Engineering, Katholieke Universiteit Leuven, de Croylaan 2, B-3001 Heverlee, Belgium
[2] Technical University Hamburg-Harburg, Polymer and Composites section, Denickestrasse 15, D-21071 Hamburg, Germany
[3] Karl Mayer, PB 1120, 63166 Obertshausen, Germany
[4] Institut für Polymerforschung, PF 12.04.11, 01005 Dresden, Germany
[5] Lund University, LTH-Mat.Eng-PB 118, 22100 Lund, Sweden
[6] Engtex, PB 83, 56522 Mullsjö, Sweden

SUMMARY: Weft-inserted warp knitting is chosen for its low production cost to produce a novel thermoplastic textile preform, containing both the non-crimp reinforcing fibres and the thermoplastic matrix ribbons. The composite structures are obtained by simple hot pressing the textile preform without any further addition of the matrix. Special glass sizings and low viscosity matrix materials are developed to ensure a good wetting out of the reinforcement and an easy, thus fast impregnation. This new SPLIT-WARPKNIT structure reveals a high potential for a good mechanical performance while it remains cost-competitive with other commercial materials, already available on the market. An extensive mechanical and physical analysis, of which the evaluation of the impregnation quality and the global fibre distribution, is carried out to determine the optimal processing window for two different fast processing techniques, while the flow of the highly viscous thermoplastic matrix through the fibre bundles is modelled.

KEYWORDS: textile preforms, thermoplastic, glass fibres, fast processing, impregnation quality, flow behaviour, automotive

INTRODUCTION

Improved safety standards and extended luxury demands have tremendously increased the weight of vehicles. With the urge of weight reduction in the automobile industry for minimising fuel consumption and exhaust emissions, fibre reinforced composite materials offer, besides Al and Mg, a significant light weight potential in structural body parts of vehicles [1]. Due to some severe disadvantages of thermoset composites, like high production cycle times, limited recyclability, constrained storage time as well as storage requirements, engineering composites based on thermoplastics have been investigated in recent years. Despite a promising cost decrease when using thermoplastic matrix composites, the price level is far away from that of competing light weight materials, such as Al. A decrease in the fabrication cost of thermoplastic composite parts can be obtained if the separate impregnation step can be eliminated, by means of a 'dry impregnation' [1]. It seems that textile preforms are

particularly well suited due to the experience of the textile industry with low-cost production and optimal textile processes.. Hence a considerable decrease of the part cost is only achieved by significantly lowering the cost of pre-impregnated thermoplastic textile preforms [5].

However, major difficulties are encountered during the processing of thermoplastic matrix composites and include the impregnation due to the high viscosities and low shear flow rates. To overcome these problems, several alternative methods of combining the fibres and the matrix have been developed to reduce the mass transfer distance of the matrix to the fibres during processing , e.g. the use of several types of "combined yarns", where the reinforcing fibres are intensily mixed with the matrix fibres [2]. A new cost-effective thermoplastic textile preform has been developed [3]. The advantages of this new class of thermoplastic split-warpknit textile preform are [4][5]:

- low production cost of the textile structure
- preform shows a good drapability
- increased mechanical properties due to the non-crimp textile structure
- one textile structure is composed of different layers, with different orientations of the reinforcing fibres
- short cycle processing time is possible
- as the hybrid yarn structure determines the homogeneity of the distribution of the reinforcing fibres in the polymer matrix and thus the mechanical performance, a good composite part can be made

SPLIT-WARPKNIT TEXTILE PREFORM

A new thermoplastic textile preform, both containing the reinforcing fibres and the thermoplastic matrix ribbons is developed. The thermoplastic ribbon, which will later form the matrix, is either used as knitting yarn or laid down parallel to the glass fibres, forming a hybrid yarn.

Material Selection

The characteristics required for the novel pre-impregnated textile structure are versatile and demand special research [4][5]. The main requirements are:

- Good compatibility between the reinforcing fibres and the thermoplastic matrix
  - good adhesion
  - good wetting behaviour, giving an overall good impregnation quality
- Low melt viscosity of the polymer matrix to achieve an easy flow during processing
- Good processibility of the film, when using a thermoplastic grade with a high MFI
- Adequate splitting behaviour of the film
- Adequate knitting behaviour of fibres and matrix ribbons

A thorough market survey pointed out that the commercially available thermoplastic films are not suited for composite applications. They do not contain the required antioxidants, stabilisers and coupling agents and are often coated. The glass fibres were also not available with the suited sizings for good adhesion and textile processing and of necessary fineness.

Therefore, special glass sizings and low viscosity PP matrix materials were selected and modified in a laboratory scale aimed at a good wetting of the glass fibres and an easy impregnation. After optimization, a commercially available PP grade (Shell XS 6500 S) has been stabilized and modified with a maleic anhydride grafted PP during film extrusion.

The glass fibres with the optimized sizing have been produced by Glasseiden GmbH Oschatz, Germany as cost-effective direct roving of 300 tex fineness. The material selection and development of PET-matrices and corresponding sized glass fibres revealed continuous amorphous film of Hoechst AG best suited for the new processing technique. PET-compatible glass fibres have been also produced by Glasseiden GmbH Oschatz, Germany.

Textile Preform

Weft-inserted warp knitting is selected to produce the split-warpknit textile preform [4][5] (see fig 1 and 2).

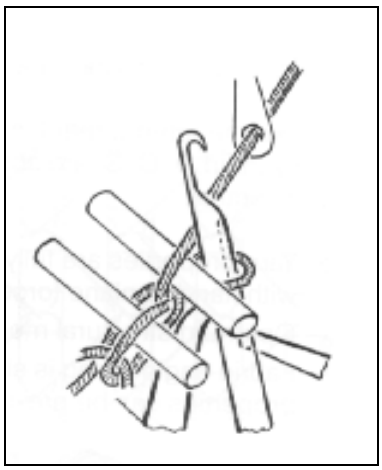

Figure 1: Warp knitting with weft inserts

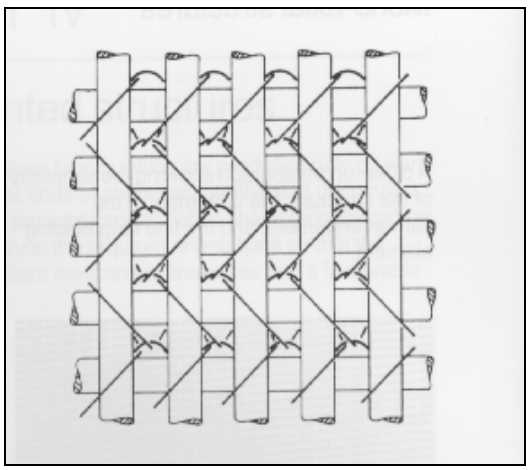

Figure 2: Split-warpknit textile

During the first knitting trials of *a co-knitted split-warpknit* uni-axial structure, where the matrix ribbons are knitted around glass fibres (fig 3), several problems occurred:

- a polymer mixture with a high MFI (10 times more than commercially used) was taken to produce the film
- the film was not oriented in the width direction
- the film showed a high brittleness
- the thermoplastic tape has a too low elongation
- the low resistance of the ribbons lead to untwisting and tearing of the tapes
- during rewinding of the bobbins the stretch ratio in the length direction increased
- the glass rovings were too heavy and too open to use a E 18 gaugeknitting machine: a change to 12 needles per inch was necessary
- tubular guides had to be used for the glass rovings
- the production of the glass beams should be eliminated by using creels

After evaluation of the produced composite laminates, more questions arose that were linked to further material optimisation. The insufficient composite properties could be due to bad wetting of the fibres or due to the bad impregnation homogeneity caused by the textile structure. However, the kinetics of wetting single fibres by thermoplastic melts showed immediate wetting of the sized glass fibres, in contrary, the co-knitted textile structure, with

the thermoplastic ribbons knitted around the glass fibres, resulted in a composite material with a highly non-uniform fibre distribution surrounded with unreinforced matrix rich zones. Hence lower mechanical properties were obtained. One possibility to improve the impregnation homogeneity is to reduce the flow path by using of a new textile structure where the thermoplastic ribbons are inserted in the glass fibre bundles, forming a hybrid yarn, and sewed together with a non-meltable stitching yarn. This led to the hybrid split-warpknit material where the thermoplastic ribbons are laid down parallel to the glass fibre bundles and a PET stitching yarn is used to form the textile preform (fig 4). Another preform is now being developed where a meltable, compatible stitching yarn is used.

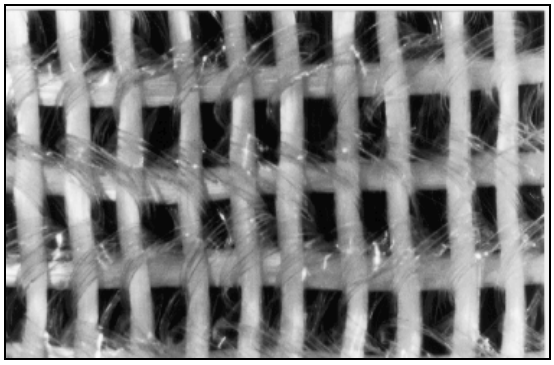

Figure 3: Co-knitted split-warpknit

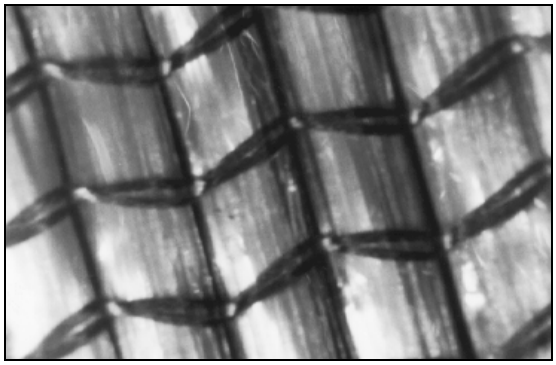

Figure 4: Hybrid split-warpknit

Short Cycle Processes

Given the apparent potential for the application of thermoplastic fabric composites in high volume manufacturing, the conflicting demands of process cycle time and laminate quality require to be resolved.

In all material developments, focusing on mass applications, the processability under industrial conditions, is an important issue. When considering thermoplastic composites, the minimum cycle time to consolidate the preform is of primary importance [4].

The process cycle involves preheating the matrix polymer above its melting point, followed by a compaction to wet out the reinforcement and cooling the laminate to below the polymer crystallisation temperature [2]. Before the matrix will flow it must be heated sufficiently above its melting point to reduce the viscosity for full fibre impregnation. While overheating will degrade the polymer, the preheating stage is critical and can be achieved in two ways.
In the classical hot pressing *in-mould heating and cooling* method, a loose stack of textile layers is placed in a cold mould, heated, pressed and cooled down in the mould to produce a pre-compacted sheet. It involves high heating energy flow to and from the forming equipment, resulting in longer cycle times and higher operating costs. This classical process is hence far too expensive for industrial use. During an alternative production method, the fabric is preheated separately in an external oven prior transfer to the forming equipment, which is at a temperature below T_g. This technique is well established in the traditional *GMT processing* and eliminates the need to cycle the mould temperature, avoiding large cycle times. The major difference between processing continuous reinforced materials and classical GMTs is that generally no bulk or large scale flow is thought to occur [2].

Highly oriented thermoplastic split-film ribbons will, when heated up, shrink considerably. So, it is necessary to support the textile preform throughout the heating phase to prevent an uncontrolled shrinkage and curling of the fabric. Note that the classical GMT process does not fulfil this requirement. Hence, alternative processing techniques have to be developed for the fast and cost-effective composite production when using the new thermoplastic split-warpknit textile preform.

Quicktemp Concept

In the alternative method, the mould has to go through the same thermal history as the part, which immediately poses a heat transfer problem. Conventional moulds are usually made of steel and it is virtually impossible to cool them down in a sufficiently short time. An improvement can be obtained using diaphragma forming, which is however expensive due to the use of special film material.

A new concept for cycle time reduction has been conceived [4][5]:

1. The surface temperature of the mould on the cavity side is the quantity of primary interest to the part. Other domains of the mould can be kept at a different temperature.
2. A large temperature difference between two media (or two domains of one mould) can be used to enhance the heat transfer.
3. The duration of the heating phase is the bottleneck when optimising the cycle time. Water cooling of the composite is fast enough.

This concept has been incorporated in a new mould design. The mould is mainly made of a material with a low temperature conductivity (steel) while only the small part, close to the mould surface, consists of a material with a high temperature conductivity. The first region is held at a very high temperature and acts as a heat storage while the second region, equipped with heating and cooling systems to adjust the temperature, is the forming region and is in contact with the part. During the heating phase, additional heat is flowing from the heat storage into the forming region due to the large temperature gradient.

Adapted GMT Process

To reduce the cycle times, the idea rose to modify the GMT process (Glass mat reinforced thermoplastics), where the pile of textile layers is externally heated and transferred to a mould at constant temperature below the melting temperature of the thermoplastic matrix. If the mould is kept at a low temperature, cycle time is reduced drastically because the heating and the cooling of the massive equipment is no longer needed [4].

However, any alteration of the ideal, uneconomical hot pressing method has an influence on the impregnation and distribution of the fibres throughout the composite. While in the classical process the impregnation time is a programmable parameter, this is no longer the case for the GMT based production process.

Problems also rise during the external heating and transfer of the pile of molten textile layers from the oven to the press. Because a loose stack of split-warpknit textile layers contains about 80% of air, the stack of textiles should be precompacted to remove as much air as possible in order to accelerate the heating. During convective heating trials it was observed that the textile exhibited a high amount of shrinkage, preferentially in one direction, distorting

the fibre architecture and resulting in an uncontrolled waviness of the fibres. To provide a degree of constraint, the loose pile of textiles was heated by conduction between two steel platens of a hot press, where teflon sheets were used to prevent sticking of the molten layers to the platens. In industry however, it is possible to precompact the loose stack of textile layers with a kind of calendering rolls in a continuous way. The actual preheating could be carried out by radiative heating in an inert atmosphere to prevent the oxidation and degradation of the textiles. If radiative heating can be applied, the composite can be produced without the use of Teflon foils. It is also worth trying to use a mould with a lower thermal conductivity to slow down the cooling speed and further improve the impregnation.

MECHANICAL TEST DATA FOR DIFFERENT PROCESSING TECHNIQUES

Classical Hot Pressing

Before going into the different short cycle processes, laminates were manufactured using various split-warpknit textile preforms with the classical hot pressing technique, resulting in optimal mechanical properties.

Two different types of a glass fibre reinforced polypropylene split-warpknit textile preform were examined:

1. *co-knitted split-warpknit* preform where the thermoplastic matrix ribbons are knitted around the glass fibre bundles: mono-axial and bi-axial structure
2. *hybrid split-warpknit* preform where the thermoplastic matrix ribbons are laid down parallel to the glass fibres and sewed together with a PET yarn: mono-axial structure

The properties are also compared to "Twintex" based material.

The mono-axial hybrid split-warpknit preform has a higher fibre volume fraction than the mono-axial co-knitted split-warpknit preform but analogous tensile properties (table 1).
The bending properties of the hybrid split-warpknit laminates are significantly better than those of the co-knitted split-warpknit laminates, probably due to the more homogeneous fibre distribution. No matrix rich zones, which could cause interlaminar shear failure during transversal three point bending are present in the new hybrid split-warpknit preform structure. The properties of the new split-warpknits are well comparable to the ones of competitive co-mingled yarns, already commercially available (Twintex).

Adapted GMT Process

The main goal of this study was to investigate whether it is possible to use a GMT based production process for the split film co-knitted composites. Furthermore, an optimisation of the production parameters was carried out. Considering the process of external heating under slight pressure, transferring the molten material to the cold mould and consolidating under pressure, several parameters are examined:

Preheating temperature and heating method
Mould temperature
Pressure of consolidation
Holding time at pressure

Table 1: Tensile properties of the first and the second generation split-warpknit laminates, compared to Twintex co-mingled yarn (Vetrotex).
Processing parameters (optimal classical cycle): 25 bar, 220°C during 5 min

	Mono-axial co-knitted	Mono-axial hybrid	Bi-axial co-knitted	Bi-axial hybrid	Twintex TPP 60650
Fibre volume fraction (%)	22	37	39	36	46
Tensile strength (MPa)	297*	289*	360**	320**	317*
Young's modulus (GPa)	14.5*	16.5*	18**	17.5**	16.6*

**: related to a fibre volume fraction of 20%*
***: related to a fibre volume fraction of 40%*

The experimental results showed that the only parameter of major importance for the tensile behaviour of cross ply laminates of the bi-axial co-knitted split-warpknit textile, where the matrix ribbons are knitted around the glass fibres, oriented in the 0° and 90° direction, was the *preheating temperature*, the temperature to which the material is externally heated in an oven before it is transferred to the press to be formed in a cold mould. This temperature greatly influences the viscosity of the thermoplastic matrix and hence the ease of wetting out and flow through the closely packed fibre bundles. This is even more pronounced when studying the shear modulus during ±45 tensile tests (fig 5). The pressure and the mould temperature influence the shear modulus to a lower extent.

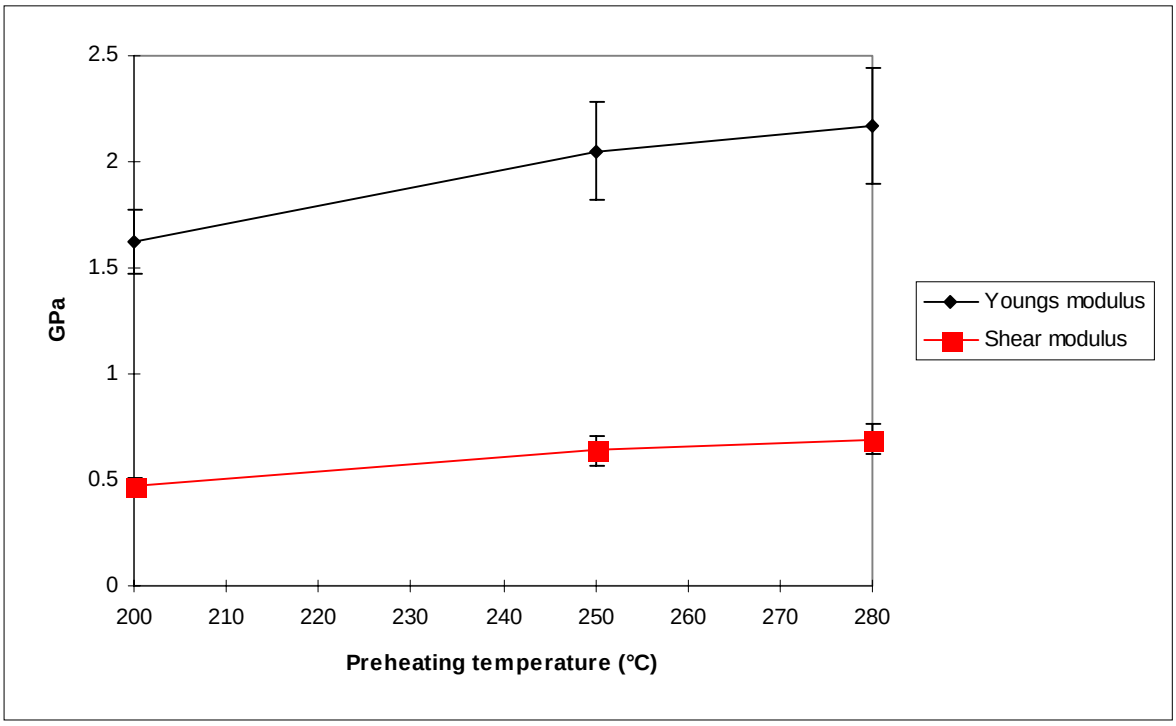

Figure 5: The influence of the preheating temperature on the shear properties of cross ply laminates of the bi-axial co-knitted split-warpknit, tested at 45°. The shear modulus is given by: $G_{xy} = \frac{E_{45}}{2(1+\nu_{xy})}$

The optimal process parameter set is:
- Pre heating temperature = 280°C
- Mould temperature = 125°C
- Pressure = 48 bar
- Holding time = 300 sec.

resulting in optimal mechanical properties for GMT-produced bi-axial co-knitted split-warpknit aminates :
- Tensile modulus: 15.92 GPa
- Tensile strength: 305.4 MPa
- Shear modulus: 0.69 GPa
- ± 45° tensile modulus: 2.17 GPa
- Poisson coefficient: 0.58

The optimal properties for the conventional hot pressing method and the adapted GMT processing technique are compared in table 2 for cross ply symmetric laminates of the bi axial co-knitted split-warpknit textile.

The lowest void fraction and the highest fibre volume fraction is found for the classical production cycle, resulting in a better impregnation homogeneity and thus an overall better mechanical performance of the composite. However, the classical production cycle is much more time consuming and economically non-competitive and further optimisation of the adapted GMT process is still possible.

Table 2: Comparison of the mechanical properties of the biaxial co-knitted split-warpknit

	Hot pressing	*Adapted GMT*
Fibre volume fraction (%)	48.0	46.6
Void fraction (%)	3.2	5.4
Matrix volume fraction (%)	48.8	48
Tensile strength (correcred to 50% fibre volume fraction) (MPa)	361.5	327.3
Tensile modulus (corrected to 50% fibre volume fraction) (GPa)	21.25	17.06
Shear modulus: ±45° tensile testing(GPa)	1.73	0.69

Prototype Development

A dome-type part has been manufactured with a lab-scale mould, using the "Quicktemp" principle. Figure 6 shows a shoesole, produced with an adapted GMT process, using existing industrial equipment. These preliminary prototype trials could already show the industrial processability of the new thermoplastic split-warpknit preform.

An industrial tool for the production of an automotive upper washer spring seat has been recently manufactured incorporating the new "Quicktemp" fast heating concept (see fig 7). This tool will be operated in an industrial environment.

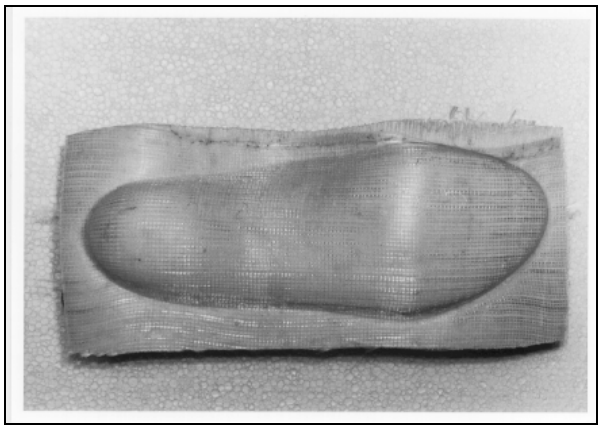

Figure 6: Shoesole, GMT, bi-axial co-knitted split-warpknit

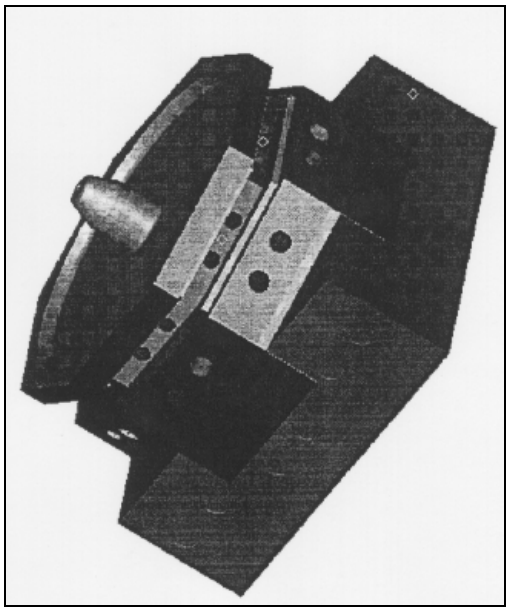

Figure 7: "Quicktemp" mould for upper washer spring seat

Modelling of the Impregnation

The main issue during the production of thermoplastic composites is the impregnation, controlled by the velocity and the ease of flow of the thermoplastic matrix through the closely packed fibre bundles.

The flow of a polymer matrix through a regular array of reinforcing fibre bundles is often described by Darcy's law as a flow through a porous medium [8][9][12]:

$$q_i = \frac{K_{ij}}{\mu} \frac{\partial p}{\partial x_j} \tag{1}$$

with K_{ij} the permeability tensor and μ the viscosity.

While the permeability tensor is mostly experimentally determined, the capillary model is one of the mostly used geometric approaches to calculate the permeability of a porous medium, given by the Carman-Kozeny equation [6][7][8][12]. However, because this equation is developed for a packed bed of ellipsoids, the permeability is isotropic which can not be valid for a UD reinforcement where the transverse flow is much more difficult than the flow along the fibre bundles. Gutowski et al. did propose a modified equation which forces the transverse permeability (K becomes anisotropic) to approach zero as the fibre volume fraction reaches a theoretical maximum value, depending on the stacking pattern of the fibres [9][12][14].

While Darcy's law for the flow through a porous medium is a good model to describe the relative flow of a low viscous thermoset matrix through a regular array of fibre bundles, it can not be valid for modelling the flow in thermoplastic matrix composites. The flow under pressure of the melted thermoplastic matrix through the reinforcing fibres, should be modelled as a squeeze flow of a viscous, compressible medium [10][11].

Since in the *conventional hot pressing*, a sufficiently high pressure is already applied during the heating phase, the stacked textile layers are strongly compacted before the polymer melts and the originally round fibre bundles become elliptical. When however, the material is externally heated (*GMT like process*), the molten polymer will surround the fibre bundles and under influence of the surface tension force them to take up a circular cross section..

The model, which is currently under development, predicts the impregnation quality as a function of the production parameters and can be subdivided in three different levels [14]:

1. a *micro scale model*, where the fibre diameter is a typical length unit. The description of the flow on a micro scale, allows to trace the influence of deviations of the ideal stacking pattern of the fibres (missing of a fibre, displacement with regard to the ideal stacking, variation in fibre diameter...), on the permeability.
2. an *intermediate scale model*, where the fibre bundle diameter is chosen as a typical length. The radial flow in the fibre bundles is described by the equation of Brinkman and the permeability is given by Gebart [13][14]. For the flow along the fibre bundles, the equations of Navier Stokes are used.
3. a *macro scale model*, where the length unit is much larger than the bundle diameter and where the reinforcement can be considered as a continuous porous medium.

However, the development will be focused on the micro and intermediate scale model.

ACKNOWLEDGEMENTS

This research is suppported by the European Community Research Programme Brite-Euram, Project no BE7256-93, Contract number BRE2-CT94-0552. The authors gratefully acknowledge the financial contribution by the commission. Part of this research has been financed with a specialisation grant of the Flemish Institute for the Promotion of Scientific and Technological Research in Industry (IWT). This text presents research results of the Belgian programme on Interuniversity Poles of attraction initiated by the Belgian State, Prime Minister's Office, Science Policy Programming. The scientific responsibility is assumed by its authors.

REFERENCES

1. Singkofer R. Mehn R., "Advanced Thermoplastic Composites based on Knitted Fabrices with Weft Insertion - Economical Application in Highlu Loaded Vehicle Components", Proc. 17th Intern Sampe Conference, Basel, Switzerland, May 28-30 1996.

2. Wakeman M.D., Cain T.A., Rudd C.M., "Optimisation of the Flexural Stiffness of Compression Moulded Co-mingled Glass and Polypropylene Composites, Proc. ECCM 7, London, May 14-16, 1996

3. Mäder E., "New Hybrid Yarns for Continuous Fibre-reinforced Thermoplastics", Proc 35th Intern man-Made Fibres Congress, Dornbirn, Austria, September 25-27, 1996

4. Stumpf H., Mäder E., Baeten S., Pisanikovski T., Zäh W., Eng K., Andersson C.-H., Verpoest I., Schulte K., "New Thermoplastic Composite Preforms based on Split-film Warp Knitting", Proc. TexComp Conf, Aachen, Germany, December 9-11, 1996

5. Stumpf H., Mäder E., Schulte K., Zäh W., "New Thermoplastic Composites Made from Low-cost Textile Preforms and Specialized Processing Techniques for Short Cycle Times", Proc. 17th Intern? Sampe Conference, Basel, Switserland, May 28-30, 1996

6. Ye L., Klinkmüller V., Friedrich K.: Impregnation and Consolidation in Composites made of GF/PP Powder Impregnated Bundles, Journal of Thermoplastic Composite Materials, vol 5, p 32-48, 1992

7. Seo J.W., Lee W.I.: A Model of the Resin Impregnation of Thermoplastic Composites, Journal of Composite Materials, vol 25, p 1127-1142, September 1991

8. PP, Structure, Blends and Composites, Vol 3, Composites, edited by J. Karger-Kocsis, Chapman and Hall, 1995

9. Klinkmüller V., Um M.K., Friedrich K., Kim B.S.: Impregnation and Consolidation of different GF/PP Commingled Yarns, Proc. of ICCM-10, Whistler B.C., Canada, August 1995, vol III, p 397-404

10. Balasubramanyam R., Jones R.S, Wheeler A.B.: Modelling Transverse Flows of Reinforced Thermoplastic Materials, Composites vol 20, no 1, p 33-37, January 1989

11. Ranganathan S., Advani S.G., Lamontia M.A.: A Non-isothermal Process Model for Consolidation and Void Reduction during In-situ Tow Placement of Thermoplastic Composites, Journal of Composite Materials, vol 29 no 8, p 1040-1061, 1995

12. Vol 10, Composite Materials Series: Flow and Rheology in Polymer Matrix Composites Manufacturing, Editor Suresh G. Advani, Series Editor R.B. Pipes, Elsevier, 1995

13. Gebart B.R.: Permeability of Unidirectional Reinforcements for RTM, Journal of Composite Materials, vol 26, no 8, p 110-1133, 1992

14. Lundström T.S., Gebart B.R.: Effect of Perturbation of Fibre Architecture on Permeability inside Fibre Tows, Journal of Composite Materials, vol 29, no 4, p 424-443, 1995

EXPERIMENTAL ANALYSIS OF FABRIC DEFORMATION MECHANISMS DURING PREFORM MANUFACTURE

A. C. Long[1], C. D. Rudd[1], M. Blagdon[1] and M. S. Johnson[2]

[1] Department of Mechanical Engineering, University of Nottingham, University Park, Nottingham NG7 2RD, UK
[2] Cooporative Research Centre for Advanced Composite Structures Ltd, 506 Lorimer Street, Fishermens Bend, Victoria, 3207, Australia

SUMMARY: In recent years, a number of fabric drape models have been developed, which are usually based on a kinematic algorithm in which deformation is restricted to inter-fibre shear. However relatively little experimental evidence has been reported to support this approach, and it is widely recognised that a number of other deformation mechanisms exist. The objective of this study was to investigate the formability of a range of non-crimp fabric reinforcements, both to validate the kinematic model and to quantify the effects of fabric construction on formability. The first stage involved analysing fabrics during pure shear, which showed that the fabric construction can greatly affect both the fabric shear stiffness and fibre locking angle. Fabric samples were then deformed using a hemispherical punch, with an automated strain analysis system used to measure the resulting fibre distribution. The predicted and measured fibre patterns agreed well up to the fibre locking angle, with fabric shear stiffness apparently having a negligible effect.

KEYWORDS: preforms, drape modelling, fabric shear, non-crimp fabrics, RTM, SRIM

INTRODUCTION

Liquid composite moulding processes, including resin transfer moulding (RTM) and structural reaction injection moulding (SRIM), are now finding widespread applications in the automotive and aerospace industries. These processes involve the impregnation of a fibre preform with a liquid thermosetting resin, which is then cured to produce a rigid component. Preforms are usually produced in a separate manufacturing process, with a wide range of techniques available for their manufacture. Whilst a number of textile based techniques can be used to produce preforms directly from yarns or rovings, these are usually limited to specific component geometries such as regular or prismatic sections and it is often necessary to produce preforms by forming or stamping of reinforcement mats or fabrics. However the formability of the reinforcements, which are often woven or stitch-bonded “non-crimp” fabrics, is limited by their construction. In particular fabric wrinkling can occur in areas with complex curvature, which would lead to rejection of the preform on grounds of quality. Another associated problem is that the resulting variations in fibre volume fractions and orientations can lead to a non-uniform distribution of both preform permeability and component mechanical properties, thus making preform design strategies based on flow simulation and structural analysis somewhat problematic.

To overcome some of the difficulties outlined above, in recent years a number of simulations have been developed for fabric deformation during preform manufacture. These are usually based on a kinematic mapping of an idealised fabric to an arbitrary surface, assuming the reinforcement to be analogous to a pin-jointed net. However it is widely recognised that a number of other deformation mechanisms exist, although relatively little experimental work has been reported to quantify these. The objective of this study was to establish the formability of a range of reinforcement fabrics and to investigate the validity of the kinematic model. The first stage was to examine the behaviour of the fabrics during shearing to establish both the shear stiffness and fabric locking angle. An automated strain analysis system, originally developed to characterise sheet metal formability, was then used to measure the fibre distribution within three-dimensional preforms. This allowed the relative importance of fabric deformation mechanisms to be established, and highlighted the limitations associated with the kinematic model.

Materials

A number of non-crimp (stitch-bonded) glass fabrics were used in this study. These are summarised in Table 1, which includes tow linear density in Tex (g/km), tow pitch (distance between centre lines) and fabric superficial density for each material. Examples of fabrics from the two manufacturers are shown in Fig. 1. The TT material (Fig. 1(a)) is held together using a tricot stitch, with the stitch oriented at $\pm 45^{o}$ to the fibres. The BUC materials (Fig. 1(b)) contain a similar tricot stitch, with an additional chain stitch used to maintain each layer of unidirectional fibres within the fabric. Although the BUC materials were intended to be $\pm 45^{o}$, the samples actually had a ply angle of approximately $\pm 55^{o}$ due to fabric relaxation.

Table 1: Material data for Tech Textiles (TT) and Flemmings (BUC) non-crimp fabrics

Code	Tow linear density (Tex)	Tow pitch (mm)	Superficial density (g/m^2)
TT/936	600	1.3	936
BUC/403	408	2.0	403
BUC/440	408	1.8	440
BUC/545	408	1.5	545
BUC/600	408	1.3	600
BUC/682	408	1.2	682
BUC/784	900	2.3	784
BUC/800	600	1.5	800
BUC/1200	900	1.5	1200

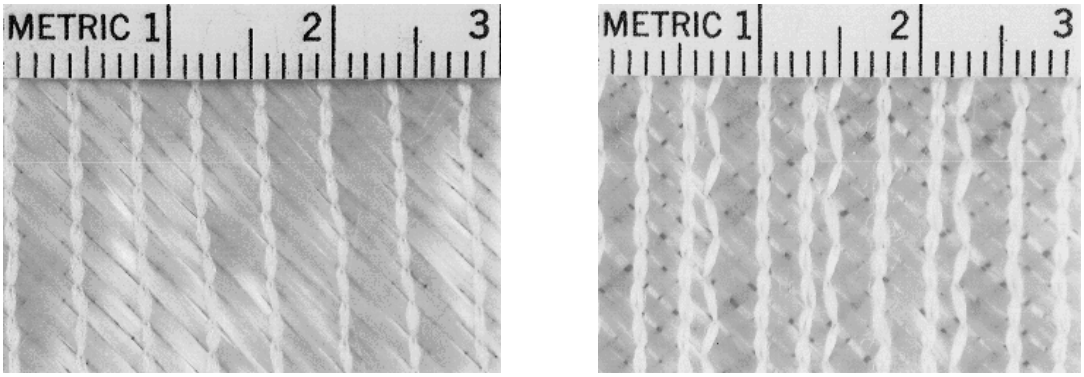

(a) Tech Textiles (TT/936) *(b) Flemmings (BUC/800)*

Fig. 1: Non-crimp fabric constructions

FABRIC DRAPE MODELLING

Deformation Mechanisms

Reinforcement fabrics based on high modulus fibres can conform to non-developable surfaces via a number of mechanisms (as discussed in detail by Potter [1]). The most important mechanisms can be summarised as follows:

1. Inter-fibre shear—fibres rotate about their crossover points (stitch or weave centres) up to the limit of shear deformation (known as the “locking angle”).
2. Inter-fibre slip—fibres move relative to each other at the crossovers, so that the fabric is effectively stretched locally.
3. Fibre buckling—when the fabric is subjected to local in-plane compression, resulting in folds or wrinkles in the preform (likely to occur at the limit of shear/slip deformation).

The relative importance of each of the above mechanisms is likely to be fabric specific, and may be characterised experimentally using a number of techniques as described later in this paper.

Kinematic Drape Model

The majority of models of fabric deformation are based on a relatively simple approach, assuming that deformation is restricted to inter-fibre shear. This allows a kinematic mapping to be used to determine the deformed fibre architecture, and has been applied by a number of researchers to simulate the deformation of both fabric reinforcements and prepregs [eg. 2-4]. Fabric wrinkling may be anticipated by comparing the predicted local deformation to the measured fabric locking angle, thus allowing such problems to be accounted for at the design stage. Although in practice other deformation mechanisms may also occur, this simplified approach provides a useful design limit in which the effects of deformation on fibre orientations and volume fraction are maximised. Starting with two intersecting fibre paths, which determine the initial orientation of the material, each fibre crossover or “node” is located by solving the equations of intersection between the fabric and the surface. These equations can be solved explicitly if the surface is represented using flat patches (using the method described by Long & Rudd [4]).

FABRIC SHEAR TESTING

Whilst the modelling approach described above can be used to provide a rapid indication of the fibre architecture within the preform, it has no way of distinguishing different fabrics other than in the specification of the deformation limit (locking angle). The behaviour of fabrics subjected to shearing can be measured experimentally to determine the effective shear compliance. As well as providing a measure of the fabric locking angle, such tests can also be used to provide data for a mechanistic deformation model (eg. [5]). Fabric shear testing can be carried out in a parallelogram fixture (as shown in Fig. 2), in which the fabric sample is clamped on either two or four sides. The shearing force is applied in the bias direction while measuring the axial displacement using an instrumented loading frame.

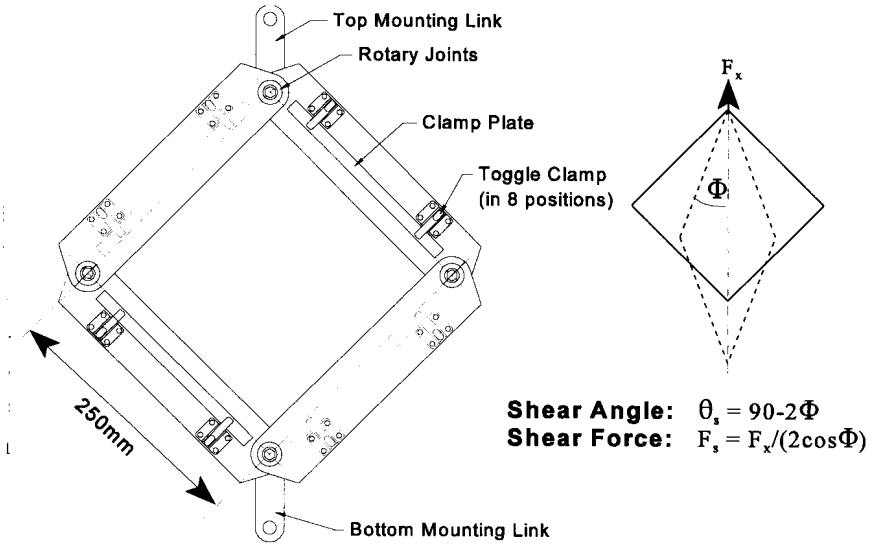

Fig. 2: Parallelogram fixture for fabric shear testing

Typical results for a stitch-bonded (non-crimp) fabric reinforcement are shown in Fig. 3. Results are presented for specimens loaded both parallel and perpendicular to the stitching thread (as indicated in the inset figure). It is clear that this particular material exhibits significantly greater resistance to shear when loaded parallel to the stitch, which is under increasing tension throughout the test. The rapid increase in shear force as the shear angle approaches 60^o is thought to indicate the onset of fibre locking, as wrinkles were clearly visible on fabric specimens towards the end of the tests. These results were produced at a crosshead speed of 100mm/min, although similar results were obtained at other rates in the range 68 to 1020 mm/min.

To establish the effect of fabric construction on shear properties, tests were carried out using a number of non-crimp fabrics with a range of tow spacings and linear densities (the BUC materials listed in Table 1). As has already been mentioned, these materials were actually $\pm 55^o$, so shear tests were carried out with samples clamped on two parallel sides with one set of fibres aligned in the direction of shear. For all materials, it was found that fibre locking occurred at a very low shear angle (approximately 15^o) when loaded parallel to the tricot stitch, with shear forces typically double those measured with a perpendicular stitch. Fig. 4 shows the relationship between shear force and shear angle for specimens loaded perpendicular to the stitch. It is clear that an increase in tow linear density with constant pitch

(Fig. 4(a)) results in an increase in shear force. Similarly for constant linear density tows a decrease in pitch results in increased resistance to shear (Fig. 4(b)).

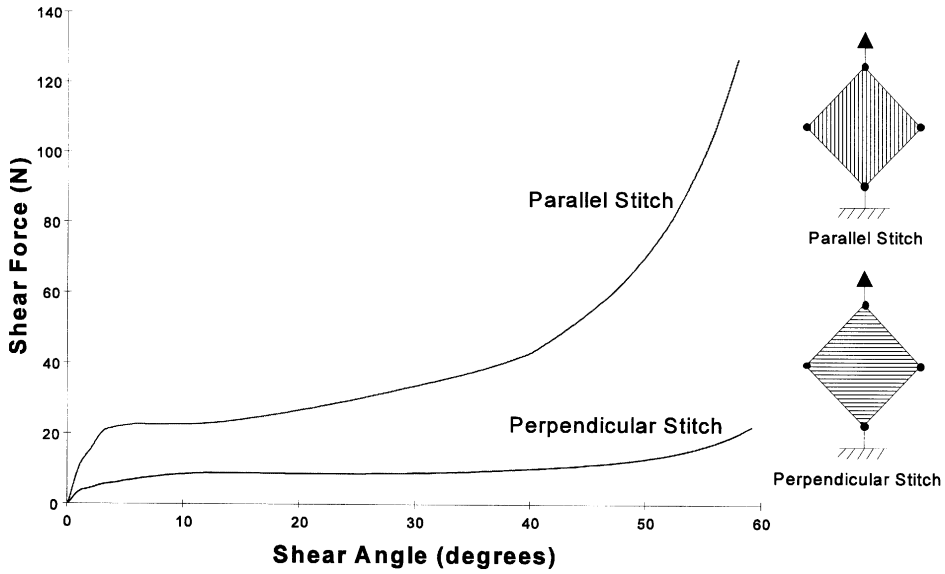

Fig. 3: Shear force versus shear angle for TT/936 non-crimp fabric

Skelton [6] defined the fabric shear stiffness as the ratio between shearing couple per unit area and shear angle. However as the graph of shear force versus angle is non-linear, a direct application of this relationship leads to a variation in shear stiffness throughout the test. It is more appropriate to calculate the shear stiffness over the linear portion of the graph using:

$$S = \frac{1}{l}\frac{d F_s}{d \theta_s} \tag{1}$$

where l is the length of fabric in the direction of shear (250mm for these tests). This relationship was applied to the data presented in Fig. 4 over the range 8 to 32^o shear. According to Skelton [6], the resistance to shear of a fabric is governed by friction at the tow crossovers, and should be proportional to the number of tow crossovers per unit area. However, whilst this may be applicable to materials with the same tow properties, when the linear density is varied it is more realistic to consider the effective area of each of the tow crossovers. Thus it may be expected that resistance to shear should be proportional to the area of tow crossovers per unit area of fabric. This is confirmed by Fig. 5, which shows that fabric shear stiffness varies almost linearly with the relative crossover area (calculated on the basis of a tow aspect ratio of 3:1). However whilst this is interesting it should not be considered critical to preform design, as the forces required to deform the fabrics were small in all cases.

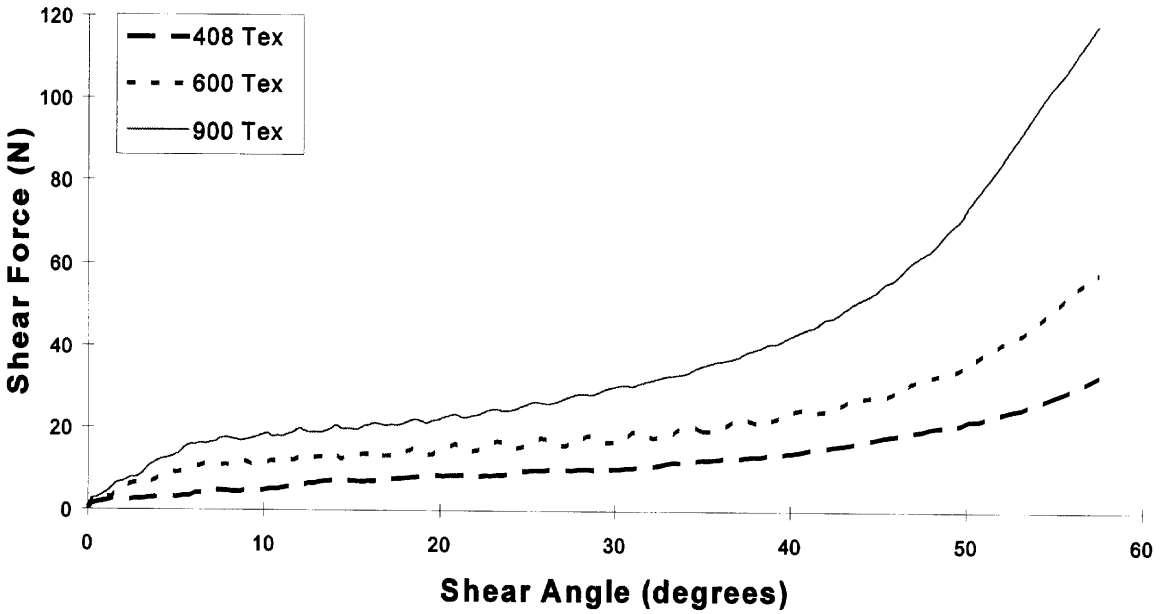

(a) Varying tow linear density (16.9mm pitch)

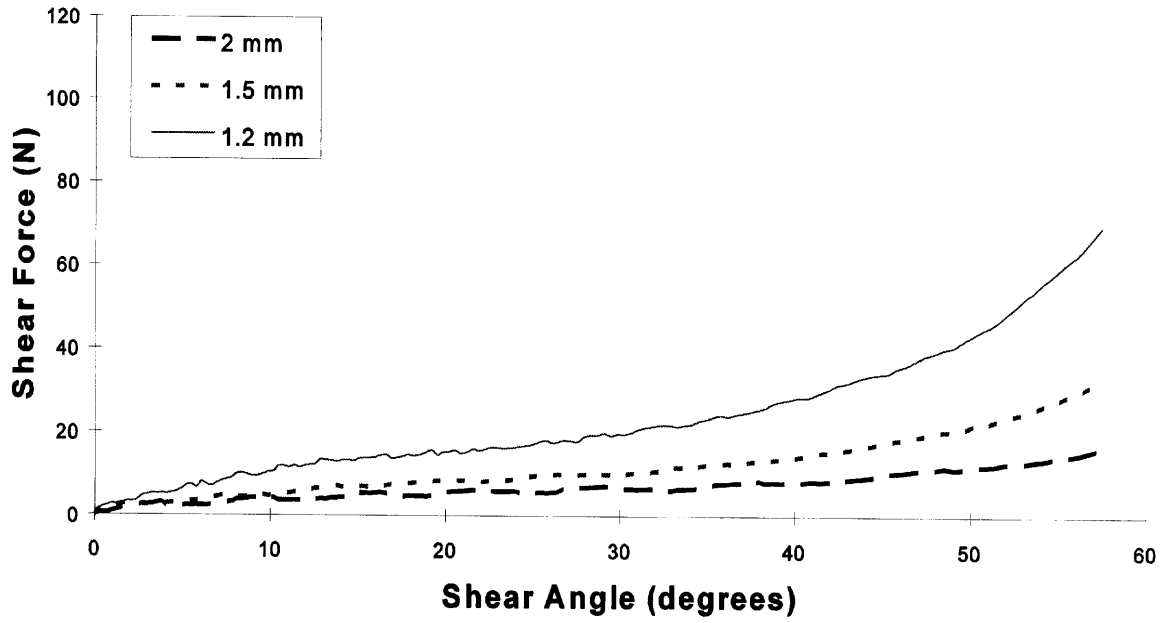

(b) Varying tow pitch (408 Tex)

Fig. 4: Effect of fabric construction on shear force versus shear angle relationship

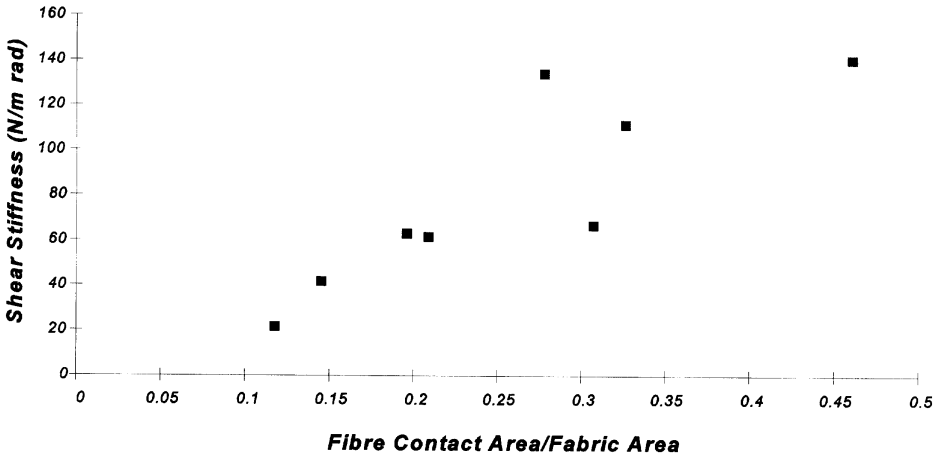

Fig. 5: Variation in shear stiffness with proportion of fibre crossovers for Flemmings fabrics (loaded perpendicular to stitch).

AUTOMATED STRAIN ANALYSIS

Although the above method can be used to examine the formability of fabrics during shearing, other deformation mechanisms are excluded by the nature of the test. To study the deformation of reinforcements during three-dimensional forming operations, a technique is required to measure the positions and orientations of fibres within a preform. Such a technique can be used to assess the relative importance of the available deformation mechanisms, and also provides a method for validating the drape model described earlier. To this end a method developed by Ford Motor Company to characterise sheet metal formability has been adapted to measure fabric deformation. This involves measuring the deformation of a square grid on the material surface, and is known as the CAMSYS Automated Strain Analysis and Measurement Environment (as shown schematically in Fig. 6). This can be used to determine the position of each grid intersection, from which local shear and slip data can be obtained (as described in our earlier paper [7]).

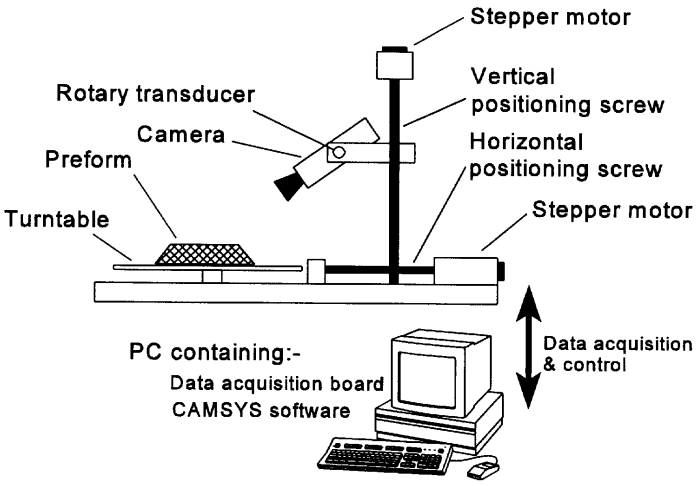

Fig. 6: Automated strain analysis and measurement environment schematic

To apply this technique to reinforcements, fabric samples were formed using a 100mm diameter punch mounted on a hydraulic press. Specimens were formed to a depth of 65mm at a punch velocity of 65mm/s, with constant clearance maintained at the clamped periphery to allow edge draw during forming. Deformed specimens were then rigidised using an aerosol varnish prior to analysis using the CAMSYS system. In each case, specimens were considered in four quadrants, two of which were effectively deformed parallel to the stitching thread and two perpendicular. Typical results for a non-crimp fabric are shown in Fig. 7, which compares the measured fibre pattern with the distribution predicted using the kinematic drape model. In both cases the surface is shaded to represent local shear, whilst for the measured pattern fibre segments are also shaded to indicate inter-fibre slip (calculated as percentage strain between intersections). On a qualitative level, it is clear that the predicted and measured fibre distributions agree reasonably well.

A quantitative comparison is made in Fig. 8, which shows the predicted and measured inter-fibre angles along the axis of maximum deformation (as indicated on the inset figure). There is generally a good agreement between the predicted and measured values, particularly for quadrants sheared parallel to the stitch. The predicted level of shear is slightly lower (ie. higher inter-fibre angle) for quadrants which were sheared parallel to the stitching thread, which may be due to the increased resistance to shear in this direction as demonstrated in Fig. 3. Minimum inter-fibre angles of 41^o and 51^o were measured respectively for deformation parallel and perpendicular to the stitch. These may be considered to be the effective locking angles for this material, as wrinkles were clearly visible around the base of the specimens. Inter-fibre slip of up to 10% was recorded in the same areas, suggesting that the pure shear assumption may be unsatisfactory in the most highly deformed regions.

The same technique was applied to the range of BUC fabrics (as described in Table 1). Typical inter-fibre angle data is compared with the kinematic model prediction in Fig.9. As noted in the previous section, these materials lock at a very low level of shear when deformed parallel to the stitching thread. In this case, the maximum shear angle measured in this direction was 12^o. For the quadrants which were sheared perpendicular to the stitch, the measured level of shear was slightly greater than predicted by the drape simulation. This demonstrates that the significant deformation was restricted to 2 quadrants during the forming operation. Similar measurements made with various fabric constructions showed little or no effect on the deformed fibre distribution. This would suggest that the important parameter in simulating fabric drape is the fibre locking angle. Differences in fabric shear stiffness may be of relevance if forming loads are of concern, although in practice these are likely to be significantly lower than the forces generated during reinforcement compaction.

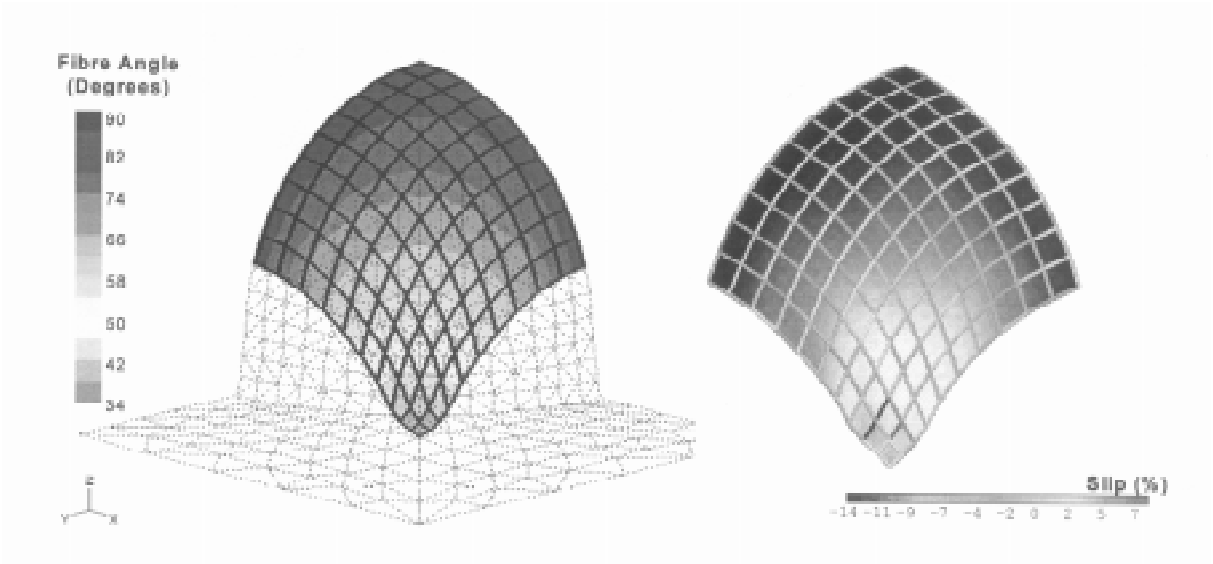

Fig. 7: Predicted (left) and measured (right) fibre patterns for hemisphere draped with TT/936

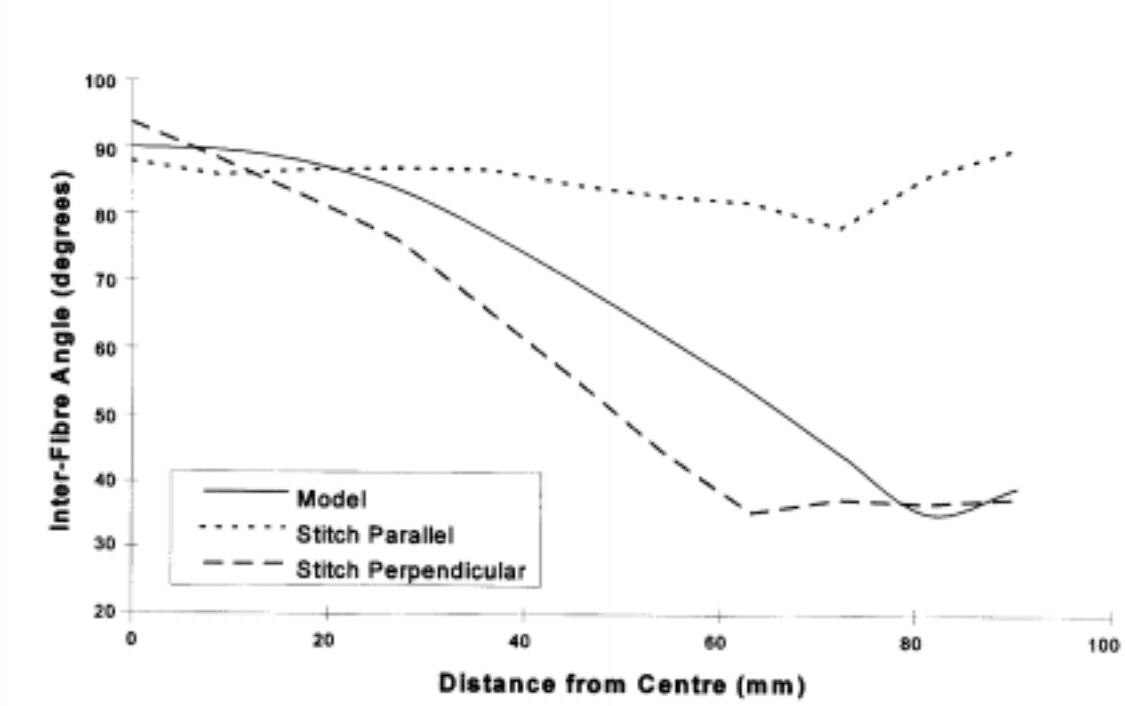

Fig. 8: Comparison of predicted and measured fibre angles for TT/936

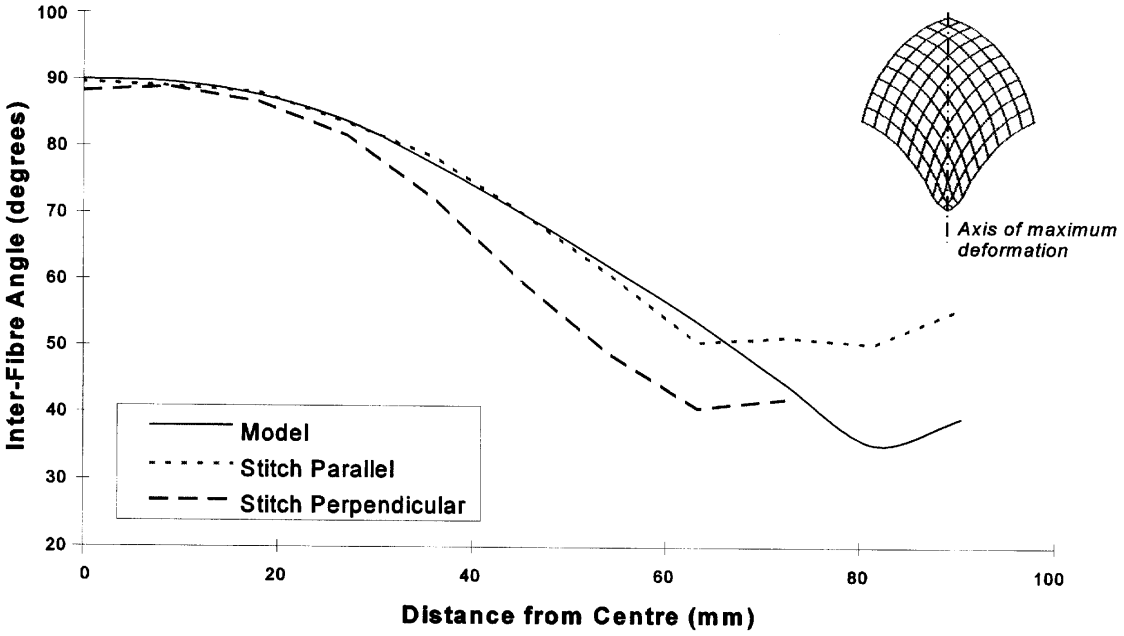

Fig. 9: Comparison of predicted and measured fbre angles for BUC/800

CONCLUSIONS

This study has demonstrated two methods which can be used to characterise reinforcement formability. Fabric shear testing can be used to determine the effective shear stiffness, and may also indicate the fabric locking angle. However the latter is very much subject to interpretation, and in particular there is no obvious way to deduce the deformation limit from the shear force variation measured during the test. An automated strain analysis technique, adapted from sheet metal formability, can be used to measure the fibre distribution within a three-dimensional preform. This method allows a wider range of deformation mechanisms to be characterised, and also provides a quantitative method for validating a fabric drape simulation.

Each of these methods was applied to a range of non-crimp fabrics with various constructions. Stitch orientation, tow linear density and tow pitch were all found to have a significant affect on fabric shear stiffness, although only stitch orientation appeared to affect the fabric locking angle. The stitching thread also had a significant affect on the fibre distribution during three-dimensional forming, whereas other factors which influence fabric shear stiffness were not found to be significant. From these results it may be concluded that the most important parameter in characterising fabric formability is the locking angle, although it should be recognised that this may depend on the direction of shear deformation.

ACKNOWLEDGEMENTS

The work described in this paper continues to be funded by Ford Motor Company, and the authors would particularly like to thank Ken Kendall and Carl Johnson for their support. Flemmings Industrial Fabrics are also thanked for supplies of raw materials and technical advice.

REFERENCES

1. Potter, K.D. "The influence of accurate stretch data for reinforcements on the production of complex structural mouldings", *Composites*, Vol. 10, 1979, pp. 161-167.

2. Van West, B.P., Pipes, R.B., Keefe, M. and Advani, S.G. "The draping and consolidation of commingled fabrics", *Composites Manufacturing*, Vol. 2, 1991, pp. 10-22.

3. Bergsma, O.K. "Computer simulation of 3D forming processes of fabric reinforced plastics", *Proc. 9th Int. Conf. on Composite Materials*, Madrid, Spain, July 1993, Vol. IV, pp. 560-567.

4. Long, A.C. and Rudd, C.D. "A simulation of reinforcement deformation during the production of preforms for liquid moulding processes", *Proc. I.Mech.E. Journal of Engineering Manufacture*, Vol. 208, 1994, pp. 269-278.

5. Boisse, P., Cherouat, A., Gelin, J.C. and Sabhi, H. "Experimental study and finite element simulation of a glass fibre fabric shaping process", *Polymer Composites*, Vol. 16, 1995, pp. 83-95.

6. Skelton, J. "Fundamentals of fabric shear", *Textile Research Journal*, December 1976, pp. 862-869.

7. Long, A.C., Rudd, C.D., Blagdon, M., Kendall, K.N. and Demeri, M. *Proc.10th Int. Conf. on Composite Materials*, Whistler, B.C., Canada, August 1995, Vol. III, pp. 205-212.

NEW TEXTILE PREFORMS AND PROCESSING CONCEPTS FOR THE MANUFACTURE OF LOW-COST THERMOPLASTIC COMPOSITE COMPONENTS

H. Stumpf, T. Otto, K. Schulte

Technical University Hamburg-Harburg, Polymer & Composites Section
Denickestrasse 15, D-21071 Hamburg, Germany

SUMMARY: Newly developed thermoplastic textile preforms for composite production containing matrix material and reinforcement fibers in a non-impregnated form appear very favorable in view of the general urge for cost reduction. An attempt has been made to develop tools for predicting the forming behavior of a weft-inserted warp knitted sample textile of this type. Good agreement was found between experiment and simulation for in-plane deformation, where even the loading-unloading hysteresis could be modeled. Moreover, the molding concept QUIKTEMP is presented shortly. It allows for the conduction of the whole composite part production in one mold, while being economically reasonable.

KEYWORDS: textile preform, warp knitting, split-film, weft inserts, drapeability, shaping, shear deformation, modeling, QUIKTEMP mold, fast heating and cooling

INTRODUCTION

A strong urge to reduce the weight of transportation vehicles can currently be observed in the automotive, aerospace and railway industry, respectively. At the same time the market conditions and the available budgets put tight limits on the acceptable cost. In particular, any design that is more costly than the conventional ones is not likely to progress into large scale applications.

Composites appear to belong to the materials of choice when replacers for the state-of-the-art steel constructions are discussed. As far as the mass applications are concerned only thermoplastic matrix composites will be able to compete. The requirements of the respective industries in regard to the maximum cycle time in mass applications apparently cannot be met with the currently available thermoset resins.

As pointed out above only composite material solutions with a considerably lowered cost have a chance in the tough competition. For this reason, several recent developments focused on the reduction of the material cost, when compared to the composite materials that have been known mainly from aerospace applications in the past two decades. Two principal approaches can be observed: On the one hand, work is directed towards the use of less costly fibers and matrix materials, respectively, such as glass fibers and polypropylene matrices, for instance. On the other hand efforts are undertaken to reduce the processing cost all along the

way from the constituent production to the composite part. Particularly the development of new textile preforms has attracted much interest.

Since it is hardly economical to place single fibers in order to produce a composite part, it is evident that in most cases some kind of preform will be employed. When continuous fiber reinforced composites are considered textile preforms have been proven in the past to be very favorable. Textile manufacture and processing has been known for centuries and can be applied in mass production at a very low cost and high productivity, respectively.

"DRY IMPREGNATED" TEXTILE PREFORMS - MATERIALS AND PROCESSING

In this paper we are concerned with textile preforms that contain both the reinforcement fibers and the matrix material of the composite to be made. However, unlike in many other preforms such as pre-impregnated sheets, in the cases considered the material is unconsolidated and the matrix polymer is present merely in its original form, i.e. as textile yarn, as powder that adheres to the textile or similar. It should be noted that the matrix yarns can have any cross sectional shape (that is, also split-films are covered by this term, which will be explained later) or length. The textile can thus be seen as a "dry mixture" of the reinforcement fibers and the matrix.

According to the underlying philosophy, impregnation of these textile preforms would be achieved when the final composite part is produced. The processing of the material (after the textile manufacture) would thus be reduced to one step to be conducted in a press. This bears a considerable technical and economical potential:

- reduced preform material cost, since no impregnation of the preform is needed
- reduced production cost, due to the absence of pre-consolidation and other intermediate steps
- availability of the full drapability of the dry textile preform, which facilitates the production of complex shapes

As far as the second point is concerned it should be noted that conventional thermoplastic prepregs are usually pre-compacted in a double-belt press in order to obtain organosheets and to complete the pre-impregnation. This machinery needs a very high invest, while the production rate is not of infinite magnitude. Efforts to significantly reduce the cost of the thermoplastic prepreg-material thus suffer from inherent, tight constraints.
Various techniques to combine matrix material and reinforcement fibers in a textile without pre-impregnation have been considered in the past:

1. Techniques that combine matrix and reinforcement fiber before the manufacture of a textile
   - commingled rovings incorporating thermoplastic staple yarns (air-textured, friction-spun etc. [1]) processed with any textile technique
   - commingled rovings incorporating continuous thermoplastic yarns (on-line assembled) processed with any textile technique
   - FIT ('fibres impregnées thermoplastiques': powder coated reinforcement yarns)
   - other
2. Techniques that combine matrix and reinforcement yarn by the textile processing
   - co-woven structures (conventional thermoplastic yarns or other)
   - co-knitted structures (conventional thermoplastic yarns, thermoplastic split-film etc.)
   - other (stitch-bonding of nonwovens etc.)

The first group cited usually gives a more homogenous distribution of matrix and reinforcement fibers, respectively, already in the textile preform. This most likely yields an even fiber distribution in the eventual composite. It should be noted at this point that during most processes (impregnation/consolidation) the fibers do not move over long distances, especially when short cycle times are considered, due to the viscosity of the molten matrix and the absence of a driving pressure gradient. Especially the now commercially available TWINTEX-roving (by Vetrotex S.A.) has recently attracted interest. Textile structures produced with this roving were transformed to composite parts without substantial problems in many applications. Minor potential problems arising from the shrinkage of the thermoplastic constituents of the roving are pointed out in [2].

The second group of techniques usually is favorable for the lower preform cost achievable with it, since yet one processing step less is needed. However, care has to be taken in order to ensure adequate impregnation when short cycle times are considered. The selection of fiber-matrix-systems with low melt viscosity and good wetting behavior is thus mandatory. It is also necessary to optimize the textile architecture for an even fiber distribution i.e. without matrix rich regions in the composite.

A development falling in the second group is currently carried out by the authors together with multiple partners in the context of an international consortium. While the presentation of this project is not the aim of the current paper, a short introduction should be given, since the deformation behavior of a type of material like developed there shall be considered. A comprehensive report can be found elsewhere [2, 3].

The basic idea is to produce a preform that combines both the matrix material in the form of split-film and the reinforcement rovings. Split-film is a special term for continuos thermoplastic film that has been cut lengthwise into tapes of small cross section. The resultant yarn is much less expensive than conventional (i.e. spun) fibers, but nevertheless well-suited to classical textile operations. Warp knitting of split-film only has been known for a long time as a favorable technique to produce low-cost net-type textile structures in large volumes. Warp knits also exhibit a great drapability. For this reason it was intended to combine warp knitting with weft-inserted reinforcement fibers to obtain a structure like the one displayed in figure 5 (see third section), hence a non-crimp fabric. In the (uniaxial) version shown the loops are made from split-film and melt away during composite production. This textile comprised a tricot loop-structure of polypropylene split-film and weft-inserted glass-rovings with a commercial composite sizing.

DEFORMATION BEHAVIOR OF THE TEXTILE PREFORM

As described above, one fundamental treat of the intended processing route is that the dry, non-molten fabric be inserted in the final compression step where the composite part is formed. Clearly, this gives a much larger formability of the fabric when being compared to a pre-consolidated organosheet. This is especially true when the melting of the matrix thermoplastic does not take place before the material is put in the mold in order to be formed to the final part shape. The latter is incorporated in a process according to the QUIKTEMP concept as described below.

Nevertheless, it is crucial that the textile is not susceptible to wrinkling in large deformation states. The occurrence of folds and wrinkles constitutes a process limit, since this is not acceptable in terms of part quality. Hence, special attention has to be given to this subject.

At this point it should be noted that complex shaping operations nearly always involve large local shear deformations. This deformation mode is likely to yield wrinkling of the fabric [4] and, therefore, needs to be examined in depth. Figure 1 shows the classical deformation of a rectangular piece of fabric by deep-drawing with a spherical punch. As indicated, extensive shear deformation is encountered in the corners of the textile. This example is to show that virtually all deforming processes of initially flat materials into doubly curved surfaces yield large-angle shearing.

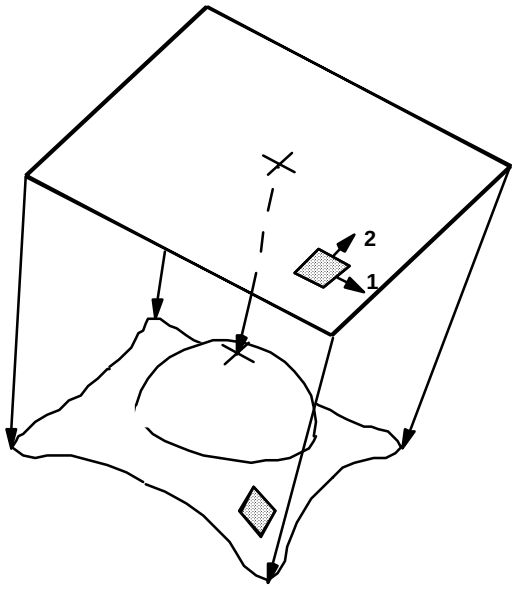

Fig. 1: Shaping of a piece of fabric over a spherical surface; large local shear deformation is encountered

In-plane axial deformations, on the other hand, are often not so critical, since substantial pre-tensioning is usually applied by clamps at the fabric edges or other devices. The resulting biaxial stress states then merely exhibit positive stress values (tension) in both directions and thus exclude wrinkling, which is mainly caused by the presence of zero or compressive stresses/strains in the respective directions.

It should also be mentioned that the reinforcement textiles in questions often exhibit a shear rigidity of some two or three orders of magnitude lower than the axial stiffnesses in the direction of the reinforcement fibers, due to a large content of oriented yarn portions in the textile. Inevitably, in deformations without severe constraints that prescribe the local strains (i.e. far away from the clamped edges) the shear mode is much easier activated than the axial deformation modes. This underlines the necessity to be especially concerned with the shear behavior of these textiles. It should be defined more clearly that this reasoning addresses the shearing obtained by the relative rotation one or more initially inclined (to each other) fiber families about the cross-over points. This mode is, for instance, encountered in a lattice-like textile architecture in trellis shear or similar.

For completeness also the bending of the textile preform should be addressed. It is very difficult to access the behavior of fabrics in this deformation mode. Moreover, the bending radii in technical shaping operation are rarely so small that they fall into the range where buckling-out of the textile constituents (i.e. reinforcement rovings) is a problem. Since the biaxial curvature loadcases to a large extent result in local shear as already pointed out, we choose to neglect the bending rigidity and to assume a membrane-like behavior for the moment.

The deformation behavior of the preforms certainly is largely dependent on the specific textile architecture. Figure 2 shows a warp knitted structure in comparison to a woven. Generally it can be said that knitted fabrics are less susceptible to wrinkling than wovens, since their loop structure can accommodate large deformations much more easily [2, 4]. This seems to apply even for uni- or multiaxial weft-inserted warp knits (as shown in figure 3), where the biaxial versions (not shown explicitly) resemble woven structures to a certain extent. Apparently the absence of interlocking of the reinforcement rovings in these non-crimp fabrics is favorable especially in regard to the shear behavior [4]. Ongoing work of the authors is directed to this aspect.

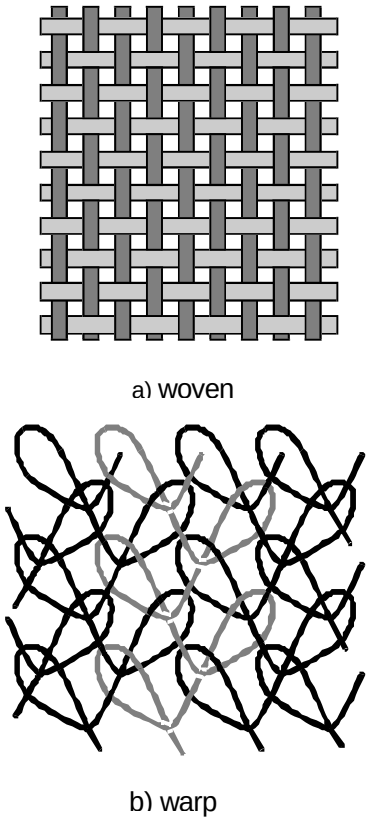

Fig. 2: Woven (a) vs. warp knitted fabric (b)

As a consequence of the above we are mainly concerned with the shear behavior of the textile preforms in question. For the simplicity of the experimental setup we choose to deal with the trellis shear mode (compare the schematic sketch of the device in figure 4). It should be stressed at this point that this mode has to be clearly distinguished from both pure shear and simple shear, as indicated e.g. by Hearle et al. [5]. Only for small deformations the respective shear resistances might be coincident. Our eventual objective is to develop a model that can be employed to predict the forming behavior. However, for this purpose the trellis shear test is just as good as another one, since the specific setup can be incorporated in a finite element model and the textile model parameters then be adjusted to fit the experimental curve.

Nevertheless, in the case of a trellis shear test care has to be taken that the reinforcement fiber families in the textile are exclusively parallel to the ankles of the trellis, when the resistance to relative rotation of the fiber families is to be measured. Otherwise a considerable axial stretch of at least one family of fibers would be the consequence (compare e.g. [6]), resulting in a greatly increased deformation force that is rarely encountered in practical three-dimensional forming operations. This would prohibit the measurement of the shear resistance as intended. Hence, the trellis shear test with the current objective is only applicable to uniaxially and biaxially reinforced textiles such as wovens or warp knits with uni- or biaxial weft-insertion. For multiaxially weft-inserted warp-knits a setup as proposed by Hörsting [4] is needed.

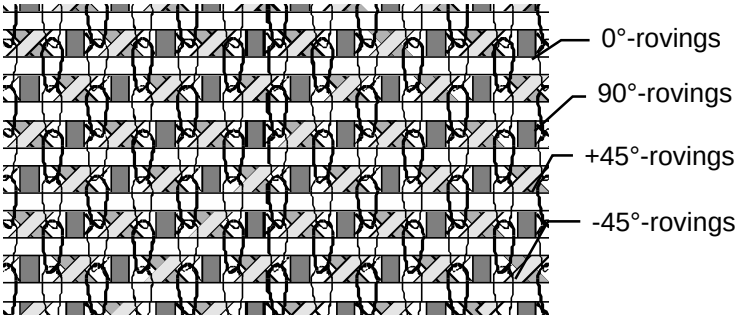

Fig. 3: Weft-inserted warp knit for composite applications; straight inserts are reinforcement rovings; 90°-direction is weft

Figure 5 shows the fabric considered in this study in the initial and in a deformed state. This very fabric is actually not a development of the cited project. It is, however, of very similar type and was used for the experiments reported here. It is clearly visible that the rovings come close to each other as the deformation progresses. Like in the shearing of other (woven and weft-inserted) fabrics, this leads to blocking of the deformation from a certain shear angle on, which depends on the very textile structure. From this critical shear angle on a sharp rise of the deformation force is usually observed [4].

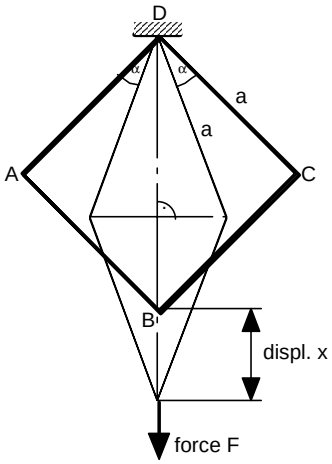

Fig. 4: Trellis shear setup, schematic sketch

The resulting force-deformation curves of the trellis shear test carried out are given together with the simulation results in the next section's figures. Due to the specific setup at the time of the conduction of the experiments only positive displacements x of the trellis load lower joint (versus the upper support) could be achieved. In figure 7, for example, the loading and unloading curve are given. An extensive hysteresis identifies a considerable inter-loop and loop-roving friction during shear deformation. The contribution of the respective effects will hardly be separable and are, therefore, only accounted for in a cumulative manner in the modeling.

Aside from the shear experiments uniaxial tensile tests were conducted to explore the in-plane axial stiffnesses. However, the experiments were limited to the direction perpendicular to the reinforcement rovings in order to measure the stiffness of the thermoplastic loops. The textile stiffness along the rovings is basically determined by the reinforcement fiber modulus and can easily be obtained by taking into account the fineness of the rovings and the number of rovings per unit length.

MODELING THE TEXTILE IN TRELLIS SHEAR AND IN TENSION

An attempt was made to model the in-plane deformation behavior of a sample textile, where a uniaxial weft-inserted warp knit was chosen for this work. One major objective was to model also the hysteresis in the shear deformation properly. The out-of plane behavior, that is to say the behavior in 3-dimensional deformations, will be subject of future activities. However, no

principal problems should arise in using the same model, since apart from the out-of-plane bending the fundamental deformation modes are equal.

We will at first be concerned with the adequate representation of the shear behavior and then show that the model with the same set of parameters is also valid for the tensile test in the loop direction (warp). Standard finite element techniques are applied in all cases. For convenience the ankles of the trellis shear tester were modeled by very stiff beams in order to prescribe the trellis shear kinematics. Since a homogeneous deformation field was found in the experiments it was chosen for the sake of a low numerical expense to model only a smaller portion of the textile (square of size 10x10 mm^2 in, while the shear tester was a square of ca. 170x170 mm^2).

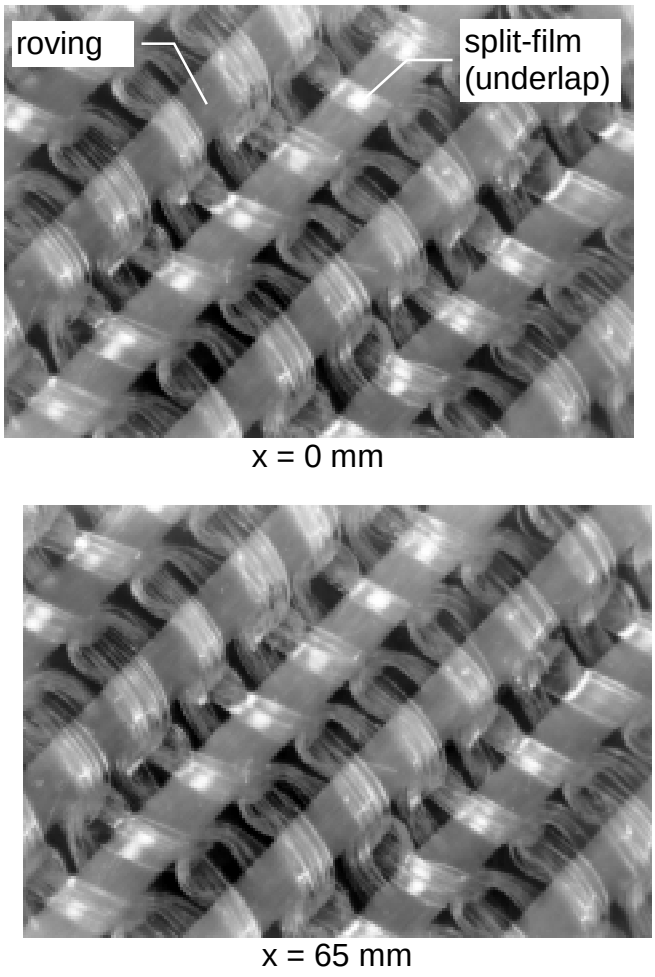

Fig. 5: Undeformed (x=0 mm) and deformed (x=65 mm) fabric state; loops from polypropylene split-film, weft-inserted glass rovings (inital spacing: 1.9 mm)

In the setup chosen the reinforcement rovings are represented by standard Euler-Bernoulli beam elements. Figure 6 shows the model. Apparently substantial friction is encountered in the loops and between loops and rovings as the deformation progresses (compare the experimentally observed hysteresis in figure 7). The thermoplastic loops were thus modeled by rods with non-linear force-extension behavior. Since the numerous friction effects occurring can hardly be separated it was decided to represent the loop volume between the reinforcement rovings by pairs of mutually orthogonal elastic-plastic rods with a certain work hardening rule, all inclined with respect to the roving direction (compare figure 6, where only half of the rods is actually elastic-plastic; the rest is elastic for the sake of computation time reduction).

In the case currently considered the location and orientation of the rods must not necessarily coincide with the loop yarns. The elastic-plastic material parameters were adjusted so that the macroscopically observed non-linear force-displacement curve with hysteresis was met. However, during this process it was found that the rather steep slope of the curve at large shear angles could never be modeled. Hence, when the small-angle shear part of the curve was fit, the rigidity given by the model was much to low for large shear angles, whereas a fitting of the large-angle shear resulted in considerably larger rigidity predictions in the low range than given by the experimental values.

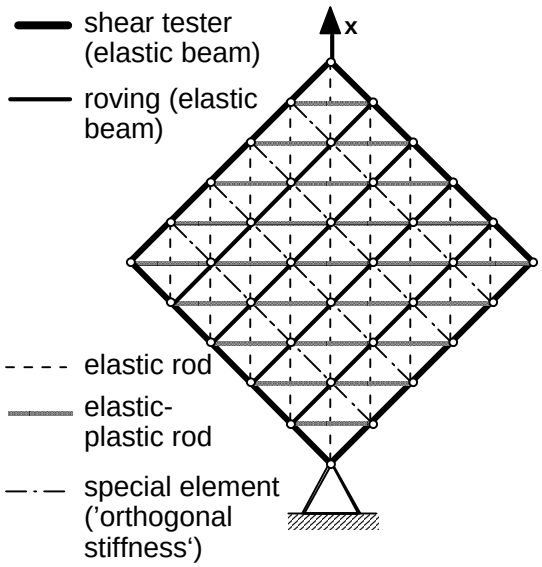

Fig. 6: Finite element model assembled from linear elastic beams, elastic-plastic (and linear elastic) rods and an especially developed 'orthogonal stiffness' element

Physically this effect is related to the compression of the loop system (and to a certain extent to the compression of the rovings, dependent on the textile's parameters), that yields 'blocking' of the deformation when the rovings come very close to each other at large shear angles, as pointed out already above. However, any rod that is fixed to nodes on the beam elements representing the reinforcement rovings, regardless of the original orientation, cannot display this increase of stiffness orthogonal to the rovings. The projected stiffness of the rod in this direction will rather decrease, since a continuos inclination takes place as the shear progresses. This is a fundamental conflict resulting from the formulation of a finite element model with the available standard elements.

Therefore, a special finite element was developed, which, in a qualitative manner, precisely displays the compressional stiffness of the loop volume orthogonal to the rovings. With proper parameters this element can also display the tension behavior of the loop system. The representation of the axial stiffness orthogonal to the rovings is then exclusively taken over by the 'orthogonal stiffness' element, whereas the elastic-plastic rods are adjusted so that the model as a whole is in accordance with the textile's shear behavior. The tensile behavior of the textile in the roving direction is represented by the axial stiffness of the respective beam elements. Details on the 'orthogonal stiffness' element will be given in a detailed publication which is currently being prepared [7].

Figure 7 shows the results of experiment and simulation in one diagram. Apparently the agreement is very good, even for the unloading curve, which is subject to extensive hysteresis. The model with identical parameters was also tested for its behavior in tension orthorgonal to the roving direction. The predicted force-displacement curve is shown in figure 8 together with the corresponding experimental curve. Again, experiment and simulation agree very well. In this example, the stiffness value of the 'orthogonal stiffness' elements accumulated over the specimen width was close to the rigidity of the real specimen in this direction, hence these elements represented the major part of the model tensile stiffness orthogonally to the rovings and at the same time modeled the loop compression in shearing properly.

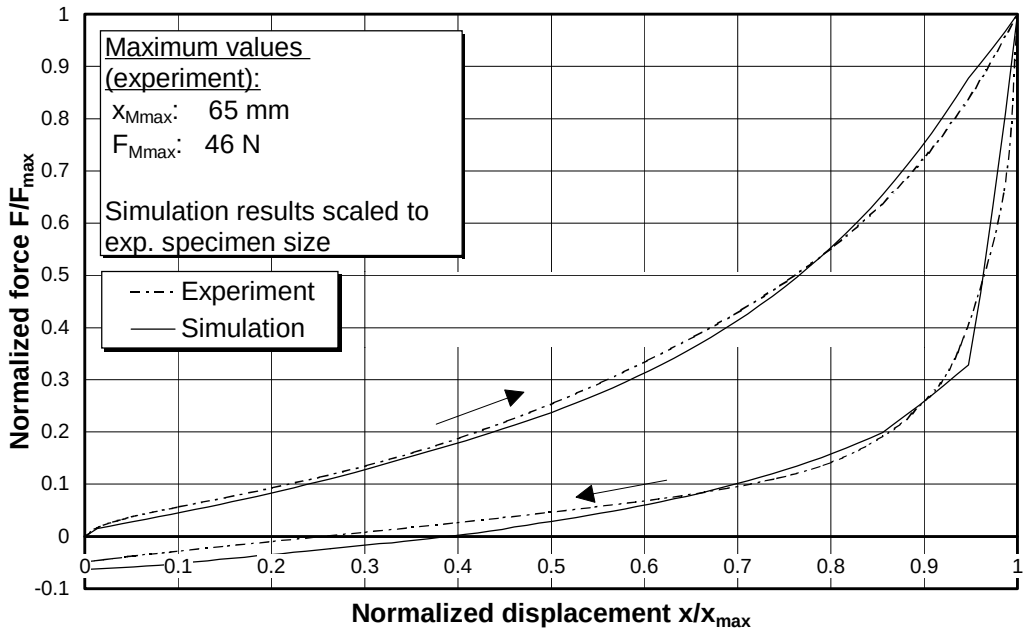

Fig. 7: Loading and unloading force-displacement curve in trellis shear; experiment and simulation in comparison

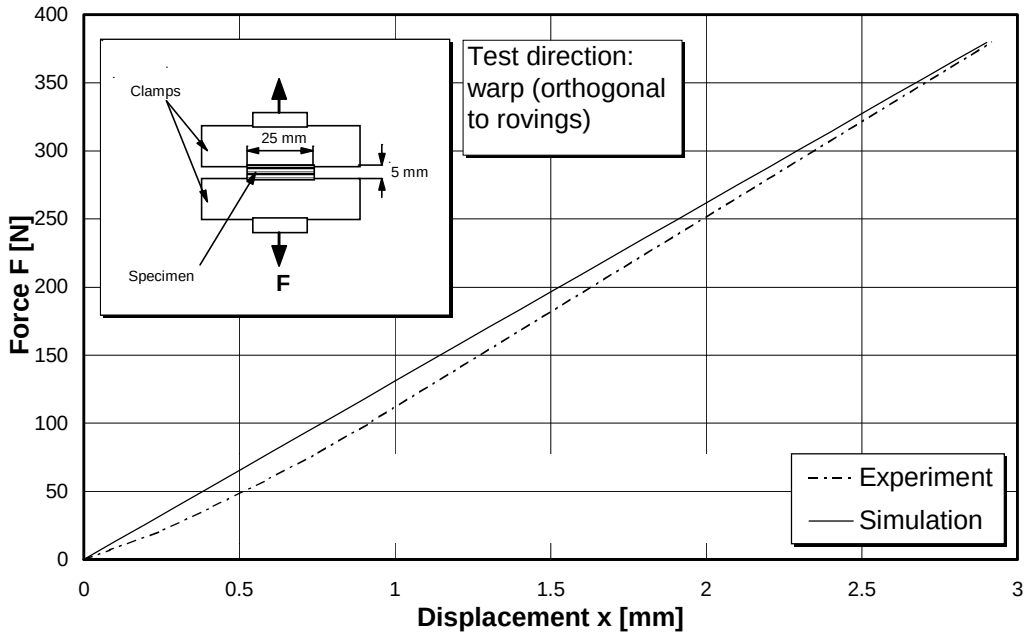

Fig. 8: Fabric in uniaxial tension orthogonal to the rovings; load-displacement curve of experiment and simulation in comparison

For obvious reasons it would be favorable to have a continuous representation (i.e. shell or membrane finite elements) of the fabrics considered. However, with the high degree of anisotropy, in particular the extremely low shear rigidity and a poisson contraction behavior that is typically far from anything known from continuous solids, at this points it seems questionable to the authors whether this will be achievable in the near future, when not some of the accuracy requirements are dropped. The combined beam/truss representation on the other hand appears to be an interesting alternative. The incorporation into larger models and complex shaping simulations have to be investigated in the near future.

FAST HEATING AND COOLING OF THE MATERIAL IN MASS PRODUCTION: THE QUIKTEMP CONCEPT

Thermoplastic composites are usually processed by heating the material up externally and then pressing it in a cold mold. An uncontrolled, quick cooling of the part is inevitable, which may limit the quality of impregnation and might result in a material with poor mixing of the constituents. On top of that the transfer from the preheating station to the press may cause trouble particularly with 'dry' textile preforms. They may suffer from shrinkage of the thermoplastic constituents and increased void formation in the ready part, as there is no lateral pressure or mechanical support during transfer [3].

Hence, favorably the complete process would be conducted in one mold. This, however, would require the mold to go through the same thermal history as the part, which is not feasible with state-of-the-art molds due to their excessive thermal inertia. The consequence would be cycle times on the order of hours which are prohibitive in mass production.

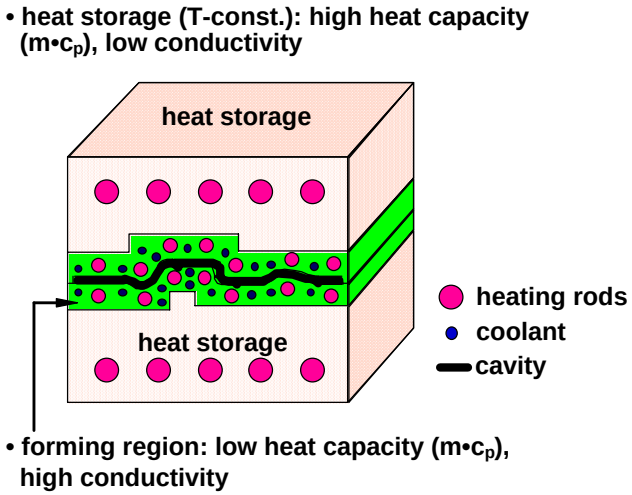

Fig. 9: QUIKTEMP - Newly developed mold design for fast heating and cooling

The design shown in figure 9 incorporates the finding that domains of the mold volume other than the cavity surface region can be of different temperature. Hence, the mold consists of a large volume made of a material with high thermal inertia (e.g. steel) and a smaller volume of very low thermal inertia.

While the first region acts as a heat storage and is held at a very high temperature level (e.g. 300 or 400 °C) the second region - termed "forming region" - is in contact with the part. It comprises heating and cooling systems which adjust the temperature of the cavity surface to the desired value. During the heating phase there will be an additional heat flux from the heat storage into the forming region as a significant temperature gradient exists in this direction. This boosts the heating.

During cooling the heat storage tends to decelerate the temperature change. However, as the cooling is by far more effective this is not really of concern when considering the total cycle time. Potential problems can be overcome by raising the coolant volume flux.

The newly developed QUIKTEMP concept works properly, which was shown by tests with a lab-scale mold [3]. It allows for heating and cooling rates up to 200°C per minute. Merits of

QUIKTEMP are i.e. the continuous application of pressure throughout the whole cycle and the free choice of the temperature history, while reasonable cycle times on the order of minutes can be maintained. Many of the problems mentioned above can thus be avoided. For a detailed presentation of the concept, compare [3].

CONCLUSIONS

Non-impregnated textiles incorporating both matrix material and reinforcement fibers that are suitable to be processed in one step in order to obtain a composite are very attractive costwise when compared to conventional thermoplastic prepregs. They are especially well suited to accommodate complex part shapes without substantial wrinkling, where their low shear resistance seems of fundamental importance.

A finite element model for the simulation of one textile of this kind, a weft-inserted warp knit, in fundamental in-plane deformation modes was presented. The model fits corresponding experimental results very well. The QUIKTEMP concept for fast heating and cooling of molds was presented. It can favorably be applied also in mass applications in conjunction with the textile preforms considered.

ACKNOWLEDGEMENTS

The authors would like to thank Engtex AB, Mulsjö, Sweden, for providing the textile material. The material was taken from a preliminary test production for the Brite-Euram Project BE7256-93 before its actual start. That project is funded by the European Comission under the Contract No. BRE2-CT94-0552. The financial contribution is gratefully acknowledged.

REFERENCES

1. Kaldenhoff, R., Wulfhorst, B., Franzke, G., Diestel, O., Offermann, P., Mäder, E., *Proc. 39th Int. SAMPE Symposium*, Anaheim, USA, April 11-14, 1994, pp. 3036-3050
2. Stumpf, H., Mäder, E., Baeten, S., Pisanikovski, T., Zäh, W., Eng, K., Andersson, C.-H., Verpoest, I., Schulte, K., "New thermoplastic composite preforms based on split-film warp-knitting", submitted to *Composites Part A*
3. Stumpf, H., Mäder, E., Schulte, K., Zäh, W., *Proc. Europ. SAMPE Symposium*, Basel, Switzerland, May 28-30, 1996, pp. 327-339
4. Hörsting, K., "Rationalisierung der Fertigung langfaserverstärkter Verbundwerkstoffe durch den Einsatz multiaxialer Gelege" (in German), *PhD Thesis RWTH Aachen*, Germany, 1994
5. Hearle, J.W.S., Grosberg, P., Backer, S., *Structural mechanics of fibers, yarns, and fabrics*, Vol. 1, Wiley Interscience, New York, 1969, pp. 371-381
6. Sabhi, H., "Etude expérimentale et modélisation mécanique et numérique du comportement des tissues de fibres de verre lors de leur preformage" (in French), *PhD Thesis Université de Franche-Compte*, France, 1993
7. Stumpf, H., Otto, T., Schulte, K., "Assessment of the deformation behavior of weft-inserted warp-knitted composite preforming textiles", to be submitted to *Composites Part A*

THE EFFECT OF WEFT BINDER PATH LENGTH ON THE ARCHITECTURE OF MULTI-LAYER WOVEN CARBON PREFORMS

B. Lee[1], I. Herszberg[2], M. K. Bannister[3], J. I. Curiskis[4]

[1] Royal Melbourne Institute of Technology (RMIT), Department of Fashion and Textile Design, City Campus, GPO Box 2476V, Melbourne, 3001, Australia.
[2] Royal Melbourne Institute of Technology, Department of Aerospace Engineering, The Sir Lawrence Wackett Centre for Aerospace Design Technology, GPO Box 2476V, Melbourne, 3001, Australia.
[3] Cooperative Research Centre for Advanced Composite Structures, 506 Lorimer St. Fishermens Bend, Vic. 3207, Australia.
[4] School of Fibre Science and Technology, The University of New South Wales, Sydney, 2052, NSW Australia.

SUMMARY: Multilayer woven preforms were manufactured from 12K carbon tows and 1K binder yarns with orthogonal weft binder. The effects of weft binder path before and after liquid moulding compaction were examined. A theoretical study analysed the effect of weft binder path length on the geometry of multi-layer woven carbon preforms. A differential warp yarn tension model was established to indicate the required warp yarn tension during weaving in order to produce a uniform weave architecture. It was found that the creation of a defined binder path length would ensure a uniform preform structure with minimum resin rich areas, and weaving with the optimal binder path length would ensure the production of a multilayer preform of acceptable quality.

KEYWORDS: weft binder, nominal binder length, minimal binder length, binder locking length, differential warp tension

INTRODUCTION

The use of fibre reinforced composite structures has been limited by their high cost of production and their poor resistance to damage. Using well developed textile technologies, such as multilayer weaving, structural preforms with three-dimensional fibre architectures may be produced [1,2]. Liquid moulding techniques may then be used to impregnate the preform with resin. These highly automated processes have the potential to produce low-cost, reliable composite structural components of complex shapes [3]. Due to the three-dimensional nature of the fibre architecture such structures are less prone to delamination and their impact resistance is significantly increased [4].

Glass and carbon fibre yarns are highly rigid and inextensible. Unlike textile fibres, these high-performance fibre yarns have to be controlled individually over their warp yarn tension during weaving. Due to the complex nature of warp and weft interaction over their interlacing points, it is difficult, but important to predict the fibre architecture in the preform

and the composite, which will determine the mechanical behaviours of the composite. The influence of the weaving parameters upon the fibre orientation is significant, and must be quantified in order to design and manufacture successful composite structures [2].

The idealised fibre arrangements in a preform structure would provide full straightness of tows and therefore would enhance the in-plane mechanical properties of the composite. One of the commonly used three-dimensional woven architectures has a lattice of non-crimped warp and weft yarns held in place by a relatively thin binder yarn which provides through-thickness interlacing and which forms the basis of the through-thickness strength. Traditionally, these binder yarns have been warp binders. More versatility in the design of the architecture may be achieved by using weft binders. However, early preforms produced using weft binders had non-uniform architectures and resin rich zones, and this was probably due to the irregular binder path length placement across the width of the fabrics.[2]

This paper describes a preliminary study on the effect of weft binder path length on the preform architecture for an 11 layer (6 warp, 5 weft) multilayer woven preform with orthogonal weft binders. The preforms were woven from 12K carbon tows and 1K binder yarns. A theoretical analysis is presented to study the relationship between binder path length and resin rich area. A differential warp yarn tension model is also presented.

SPECIMEN PRODUCTION

Multilayer preforms were produced with different binder path lengths on a 16 shafts table loom. They were constructed from carbon yarn of 12k tows with six layers of warp and five layers of weft in an orthogonal woven structure. Weft binders (1k tows) were used to interlace the lattice of warps and wefts in a through-thickness and alternatively offset fashion. A schematic diagram of the generic architecture is shown on Fig. 9.

After preform manufacture, samples of the fabric were cut out and moulded into composite panels by using RTM process and RTM 6 resin. Composite thickness upon RTM was 3.2mm and Fibre Volume Fraction was 60%. Specimens were sectioned along both the binder and warp directions, and the sections were examined through an optical microscope. To examine the fibre architecture directly after weaving, the preform was wet out with epoxy resin by hand and then cured at room temperature for 24 hours without applying consolidation pressure.

RESULTS AND DISCUSSION

Figs. 1 and 2 are microphotographs of warp and weft sections respectively, of a composite produced with a short weft binder length.

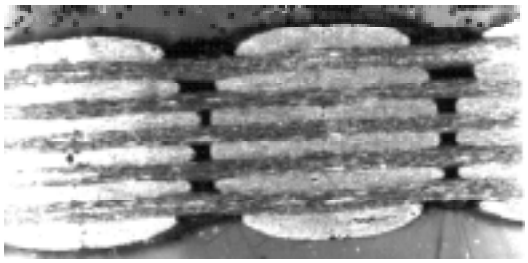

Fig. 1: Multilayer woven structure with a short binder length, consolidated without pressure (sectioned along binder direction)

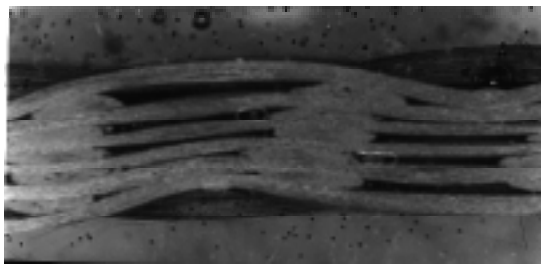

Fig. 2: Multilayer woven structure with a short binder path length, consolidated without pressure (sectioned along warp direction)

As shown on Fig. 1, the weft binder followed a wavy path and impeded warp yarns from spreading evenly, causing resin rich zones outside the binder loop. The cross-sectional shape of a warp column became elliptical. From Fig. 2, It may be observed that weft yarns were pushed away from the binder and warp yarns were forced to crimp. The resulting weft was uneven and of low density allowing extensive resin rich regions.

Figs. 3, 4 and 5 are microphotographs of composites made from preforms with optimal weft binder length. Figs. 3 and 4 depict warp and weft sections, respectively, of the composite consolidated without compaction pressure and hence gives an indication of the preform architecture. Fig. 5 depicts a warp section of the composite consolidated under a compaction pressure of 276 kPa. Fig. 3 shows that a near 'square shape' binder path may be achieved which allows a uniform distribution of warp yarns and minimises the extent of resin-rich areas. As may be seen from Fig. 4 the wefts are uniform and tightly packed. Fig. 5 shows that when consolidated under compaction pressure a uniform structure with straight wefts and vertical binder yarns may be achieved.

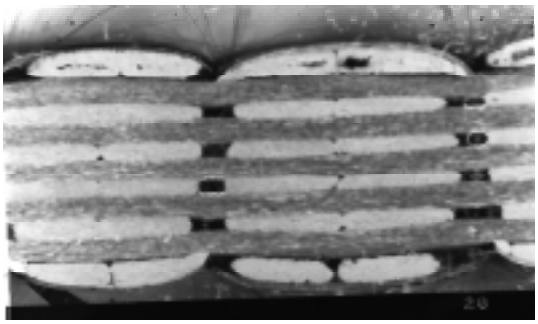

Fig. 3: Multilayer woven structure with a near 'square shape' binder path, consolidated without pressure (sectioned along binder direction)

Fig. 4: Multilayer woven structure with a 'near square shape' binder path, consolidated without pressure (sectioned along warp direction)

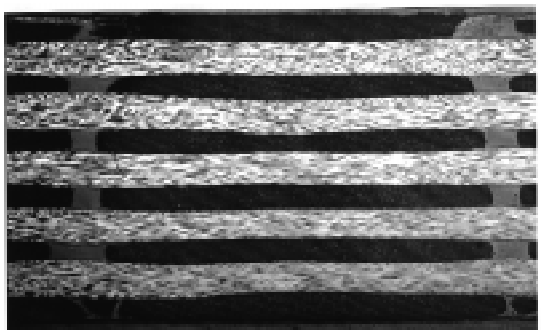

Fig. 5: Multilayer woven structure with a near 'square shape' binder, consolidated with pressure (sectioned along binder direction)

Compressed and consolidated composite structures were shown on Fig. 5 and Fig. 6. The composite architecture in Fig. 5 was achieved with a near 'square shape' binder path. It demonstrated that the resin rich areas were kept to a minimum. The binder path length of this structure has an optimal length, leading to straight tows of a composite architecture with minimal resin rich areas.

Fig. 6 shows a composite structure with a slightly longer than the nominal binder path length. The sign of binder buckling occurred within the layers after consolidation, due to the extra binder path length. Fig. 7 demonstrates the longer than the nominal binder path structure without applying consolidating pressure.

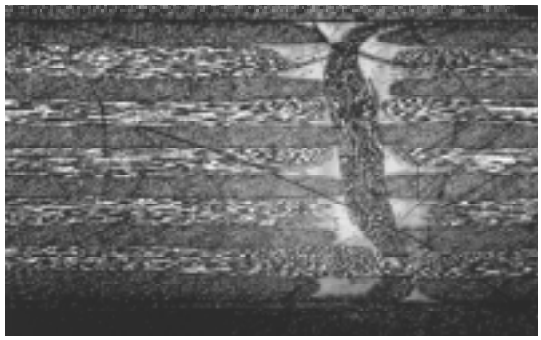

Fig. 6: Multilayer woven structure with long binder length, consolidated with pressure (sectioned along binder direction)

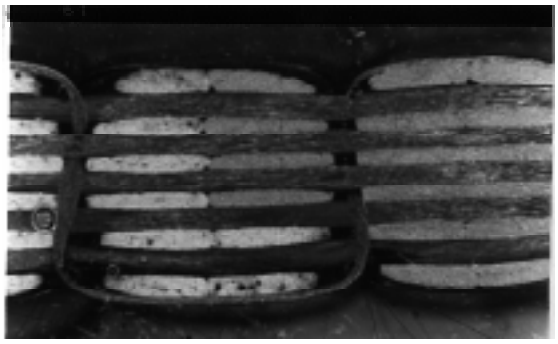

Fig. 7: Multilayer woven structure with long binder length, consolidated without pressure (sectioned along binder direction)

The above examples indicate that there is an optimal binder path length, which is sufficient to reduce warp yarn crimping and pinching to an acceptable level and yet, is not so long as to cause instability in the preform during compaction.

THEORETICAL APPROACHES

The design and manufacturing objective for a multi-layer preform is to achieve a lattice of non-crimp warp and weft yarns in the preform architecture with minimum resin rich area. It has been shown that one of the keys to ensure a successful composite structure is to provide the exact binder length required to interlace with the warp and weft. It is difficult to achieve an architecture which requires a long path length for a weft binder because of the locking effect, due to yarn friction, during shed closure.

Nominal Architecture

The nominal architecture is described in Fig. 8. this architecture will not be achieved in practice because of yarn bunching and crimping due to the interactions among the warp, weft and binder yarns. The object of the analysis is to determine the process parameters which will lead to an architecture as close as possible to the nominal (see Fig. 5).

It consists of a multi-layer structure (six layers of warp and five layers of weft) with a rectangular shaped weft binder passing over and under two columns of warp alternatively. This geometric structure is defined as a nominal orthogonal weave structure, and the unit binder path length of the rectangular shape is defined as the nominal binder length.

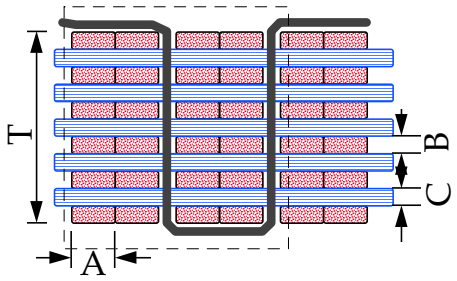

Fig. 8: A nominal orthogonal weave structure

As shown on Fig. 8, the nominal binder path length can be expressed as

$$L_n = 4*A + 2*T \quad (1)$$
$$B.C.R. = T/2A \ (\%)$$

where A is the width of warp yarn; T is the preform thickness; B.C.R. is binder crimping rate.

The thickness of the preform is

$$T = 6*B + 5*C \ (mm) \quad (2)$$
$$A*B = \text{Yarn linear density / fibre density } (* 10^{-3} \text{ mm}^2)$$

where B is the thickness of warp yarn; C is the thickness of weft yarn.

The Fibre Volume Fraction is

$$F.V.F. = V_f / V_T \quad (3)$$
$$V_f = W_f / \rho$$

where ρ is the fibre density; W_f is the unit weight of fibre yarn.

Warp Yarn Pinching and Minimal Binder Path Length

When a binder path length was shorter than the nominal binder length, the binder path could no longer be kept rectangular. As shown on Fig. 1 and Fig. 9, the binder would force the warp yarn to change its cross-sectional shape. It was assumed that 1) the two neighbouring columns of warp yarns were on the same horizontal axis plane; 2) the warp ends were not crimped under the tension of weft binders. With the cross-sectional area of warp and weft yarn being constant, the binder path would decrease to a minimal length in order to maintain its structural stability. A minimal binder path is defined as the binder path length which is shorter than the nominal length, but not short enough to cause warp yarn to crimp.

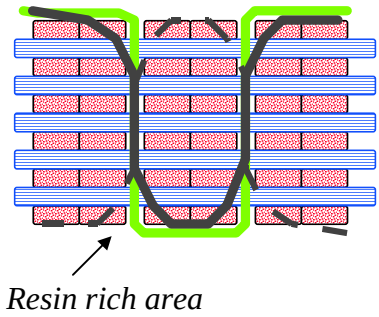

Fig. 9: A schematic diagram of binder forced resin rich area

The wavy minimal binder path (see Fig. 1) may be modelled as a series of ellipses and the path length may be expressed as:

$$L_{\min} = 2\pi\sqrt{\frac{A^2 + (T'/2)^2}{2}} \tag{4}$$

where T' is the fabric thickness when the binder is in an elliptical path.

The cross sectional area of the confined warp column is constant:

$$S_a = 1/4 * \pi * A * T'/2 = T/2 * A$$

This leads to an expression for the preform thickness:

$$T/T' = \pi/4 \tag{5}$$

If A = 2.5 mm, T = 3.2 mm;
then, T' = 4.1 mm; L_n = 16.4 mm and; L_{min} = 14.3 mm.

This indicates that a shorter binder length will lead to a thicker fabrics.

As shown earlier, the warp tows would be forced to bunch-up when the binder path length is shorter than the nominal length. For a minimal length binder, the warp yarns would be forced into an elliptical shape. If the binder length is further reduced, crimping of the warp yarns will occur and neighbouring warp columns may move vertically with respect to one-an-other.

Resin Rich Area

As shown on Fig. 9, the short binder path forced the warp tows to bunch-up and generated a v-shaped gap between tow warp columns. After resin infusion, this area formed a resin rich channel, which may become a microcrack initiation site [2]. The cross-sectional area of this resin rich channel is given by:

$$\text{Resin rich area} = A * T' - 2S_a \tag{6}$$

Using the data given by the above example, the resin rich area would be 2.2 mm^2.

Warp Yarn Crimping

When the binder is further shortened beyond the minimal length, the top and bottom layers of warp would be forced to crimp in order to accommodate the reduced binder length. The resulting decrease of the crimp rate of the binder would be at the expense of the crimp generated in the warps.

Following Lord 1980 [5]; assuming the warp yarn being forced into a sinusoidal path and ignoring yarn stiffness and the frictional effect between the binder and the warps, the relationship between the tensions in the warps, binders and their crimp amplitude may be described as

$$A_b/A_w \approx (\lambda_b/\lambda_w) * (t_w/t_b) \quad (7)$$

where A_b is the crimp amplitude of the binder; A_w is the crimp amplitude of the warps; λ_b is the pitch of the binder; λ_w is the pitch of the warp yarns; t_b is the tension in the binder and t_w is the tension in the warps.

From Eqn. (7) it may be seen that the crimp amplitude in the warp is dictated by the tension and spacing of the yarns. If the binder is kept at low tension (i.e. longer path length) whilst the tension in the warp direction is high, then there will be very little crimp in the warp and considerable crimp in the binder. Although the warp has bending stiffness which is much higher than that of the binder, and will consequently resist crimping, this effect may be neglected because the friction between the binder and warp yarns induces high binder tension during shed closure.

Weft Density

Once warp crimping occurs there is a severe restriction on the extent to which the weft yarns may be beat into the fabric. The resulting weft density is consequently lower and the distribution of warp tows is uneven leading to resin rich regions. An exreme example of this may be seen in Fig. 2.

Fibre Volume Fraction

From Eqn (3), F.V.F can be further expressed as:

$$F.V.F. = V_f / V_T = [(D_w*N_w + D_f * N_f) * Y_y / \rho + (D_f / \lambda_{b)} * (Y_b / \rho)] / T \quad (8)$$

where D_w is warp density; N_w is the number of warp layers; D_f is weft density; N_f is the number of weft layers; Y_y is the warp/weft yarn linear density and Y_b is the binder yarn linear density.

Binder Buckling

Longer binder path length would generate binder buckling during preform compaction as may be seen in Fig. 6. This will reduce the effectiveness of the binders in providing delamination resistance.

DIFFERENTIAL WARP TENSION SET-UP APPROACH

In a weaving machine, a proper tension control over warp yarn may produce the required binder path. As shown on Fig. 10, the shed closure of warp yarns forces the weft binder to increase its path length (crimp). However, the friction between the binder and warp yarns would impede such an increment. The frictional force on the weft binder is of the greatest in the central region and gradually decreases toward the edges according to Amonton's law of friction: $T_2 = T_1 e^{\mu\theta}$ assuming the binder being perfectly flexible. This indicates that a differential warp tension set-up on the loom is crucial to achieve an uniform architecture across the width of the fabric. The higher the tension in the warps, the longer the binder path length may be achieved. However, due to the practical restriction of the shedding height, the width of the fabric and also the adverse effect of higher tension on the quality of warp yarns (i.e. fibre damage), there exist a maximum achievable unit binder length. This specific binder length may be defined as a "locking length". If the locking length is longer than the minimal binder length, then warp yarn crimp may not occur, and vice versa.

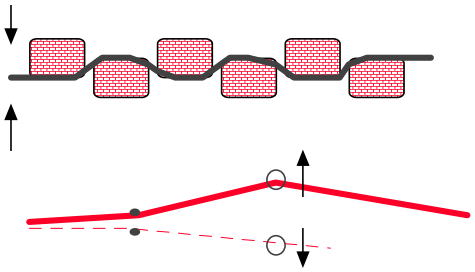

Fig.10: A schematic diagram of binder/warp yarn interaction

CONCLUSION

Multilayer woven carbon preforms have been produced. The fibre architecture examination and theoretical analysis indicated that the creation of a defined binder path length will ensure an uniform preform structure with minimum resin rich areas and full straightness of warp yarns. The high tension induced in the binder due to the shed closure and the friction between the binder and warp yarns may cause bunching of the warp yarns within the binder loops which would lead to undesirable resin-rich channels in the resulting composite. The binder might further cause the warp yarns to crimp and so reduce the mechanical properties in the composite.

An optimal binder path length can be used in the production of an acceptable quality of multilayer preforms. It was around the nominal binder path length, and not less than the minimal length, which was sufficiently long to reduce crimping and pinching to an acceptable level and yet, was not too long so as to cause instability in the preform during compaction. Differential warp yarn tension set-up across the width of the fabric would ensure the realisation of such an uniform path length. Due to the practical limitation on warp tension, there is a restriction on the control of binder path length, the binder "locking length" defines the basic ability of a loom to produce a multilayer preform with acceptable quality.

ACKNOWLEDGMENTS

We would like to thank Ms F. Coman for the assistance of preparing the photographs, Mr K. Houghton for the technical support in the RTM process.

REFERENCES

1. Hill, B. J., McIllhager R. and McLaughlin P., "Weaving multilayer fabrics for reinforcement of engineering components"**,** *Composites Manufacturing* No 4 1993, pp227-232.

2. Bannister, M.K., Herszberg, I., Coman, F., Raper, H., and Curiskis, J.I., "Manufacture and Analysis of Multilayer woven Preforms"**,** *American Society of Composites Ninth Technical Conference*, Delaware 1994.

3. Farley, G.L., Smith, B.T., Maiden, J., **"**Compressive Response of Thick Layer Composite Laminates with Through-The-Thickness Reinforcement", *Journal of Reinforced Plastics and composites*, Vol 11 July 1992.

4. Broslus, D., Clarke, S., **"**Textile preforming techniques for low-cost structural composites", *Advanced Composite Materials: New Developments and Applications Conference Proceedings*, Detroit, Sept. 30 - Oct. 3, 1991, pp 1 - 10. Lord, P., Mohamed, M.H., "Weaving: Conversion of Yarn to Fabric", 2nd edition, Merrow Publishing Co. Ltd 1982.

THE DESIGN PRINCIPLE AND WEAVING TECHNOLOGY OF THREAD-LINKED BOX-BEAM PREFORM

Yang Caiyun, Li Wenzhang, Guo Wenping

Department of Textiles,Tianjin Institute of Textile Science and Techonlogy, Chenglinzhuang Road, Hedong Distric, Tianjin, 300160, P.R. China

SUMMARY: Thread-linked box-beam preform is a new structure textile. There are many threads between one pair opposite walls and these threads are woven together with the walls to form a three dimensional integrated structure. These threads not only link the two opposite walls but also keep them apart from a certain distance. The paper explores the principle of fabric forming and the weave structure developed by us, introduces the weaving process in detail and also discusses some problems which should be noticed in weaving with this new structure textile. It will certainly have a great value in developing and producing a new type of textile composites.

KEYWORDS: box-beam preform, thread-linked, design principle, weaving technique, woven, centre-weft-stitching, stitching place, fabric specifications

INTRODUCTION

Thread-linked box-beam preform is a new structure of textile preform. The tradional woven hollow fabric only has four connected walls which form a rectangle cross section. In this new structure, there are many threads between one pair opposite walls and these threads are woven together with the walls to form a three dimentional integrated structure. These threads not only link the two opposite walls but also keep them apart from a certain distance. The preform can be designed for specific applications such as a passage, a filter of gases or liquids, and a filling with sand, foam and so on, and its properties are varied by means of the material, fabric structure and thread arrangement.It can contain up to 160,000 thread stitching places per m^2 and can be produced with the spacing up to 1000 mm.The fabrics can also be coated, rubberised and cured to form a composite product.

The paper explores the principle of the fabric forming and the weave structure developed by us in three topic, intruduces the weaving process in detail and also discusses some problems which should be noticed in weaving with this new structure.

PUT THE THREAD-LINKED DOUBLE-WALL PREFORM TO TRIAL BY USING FACE-TO-FACE FORMING PRINCIPLE OF WARP PILE FABRICS

Up to now, it seems that there are some common character between the forming principle of warp pile fabrics produced on the face-to-face principle and the thread-linked box-beam preform.

The typicle product of warp pile fabrics are velvet-plain and high-pile fabrics. Figure 1 shows the vertical section of velvet-plain before cutting pile.It can be seen that two separate ground fabrics with a space between them, each of which with its own warp and weft, are woven on the unstitched double-cloth principle, while the pile warp threads interlace alternately with the picks of both fabrics and thus link them together. Through cutting pile, two cloths are thus formed -the bottom cloth with the pile facing up, and the top cloth with a similar pile facing down.The distance between the ground fabrics is regulated according to the required length of pile. For example, 2 mm for velvet-plain, 10 mm for high-pile fabrics. One of the keys is how to control regularly the threads length between double-cloth, which can be the length from 10 mm to 1000 mm, and even above while we put the thread-linked box-beam preform to trial by using the forming principle of warp pile fabrics produced on the face-to-face principle. So, we make a weaving on a hand-loom, adopting the follow methods:(1) hand-lengthen threads between cloths;(2) changing the order of pile interlacing. The results have shown that:

The threads length between the face cloth and the back cloth is not regular, there is a wide variation.

The number quantity of pile interlacing places is too small for utility box-beam preform.

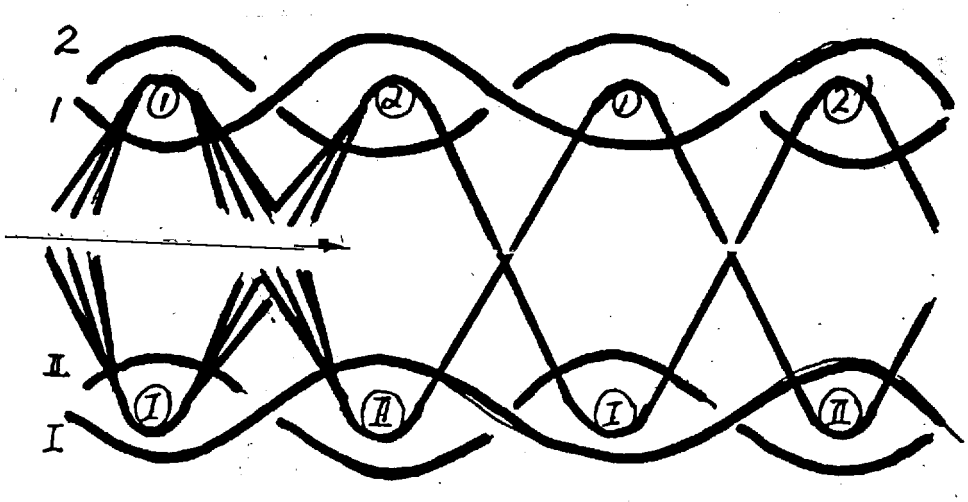

Figure 1: The vertical section of velvet-plain

PUT THE THREAD-LINKED DOUBLE-WALL CLOTHS TO TRIAL BY USING VARIED FORMING PRINCIPLE OF CENTRE-WEFT STITCHED DOUBLE CLOTHS

There are five basic structures for double cloths to be stitched or tied together. (a). self-stitched double cloths. (b). centre-stitched double cloths. (c). double cloths stitched by threads interchange. (d). double cloths stitched by cloth interchange. (e). althernate single-layer and

double-layer construction. Centre-stitching can be classified into two, centre-warp-stitching and centre-weft-stitching. The basic principle of centre-wef- stitching is introducing the third system of weft whose whole function is to stitch the two otherwise separate layers of cloth together.The centre-weft lie between the face and the back cloth which is for the purpose of stitching occasionlly at a regular interval between the inter-layer cohesion.

The thread-linked double-wall cloths we want to weave is charactered not only integrated by stitching but seprated a distance from 10 mm to 1000 mm or even above. So, it is imposible to use the principle of centre-weft- stitching entirely. Thus we modify the principle of centre-weft-stitching. Firstly, the number of stitching places is designed only two for every one centre-weft, one of two stitching the face cloth, the other stitching the back cloth. Secondly, the two stitching places are arranged lang distance apart. Figure 2 shows the cross section. After removing the fabric, levelly moving the face cloth layer toward left until the two stitching places near by, then toward up until the link threads vertical, a hollow thread-linked double cloths appears. The height of the double-wall cloths is the distance between two stitching places, and the linked threads of between the two opposite walls are the centre-weft. It should be noticed that the stitching places of the every centre-weft should be different unless finishing a repeat.

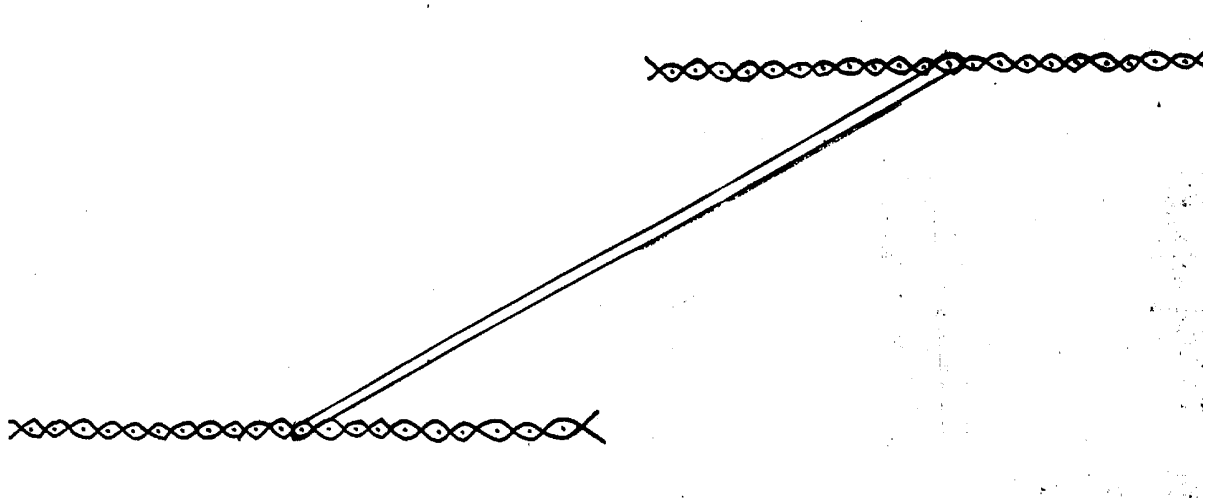

Figure 2 Cross section of double-wall cloths

PUT THE THREAD-LINKED BOX-BEAM PREFORM TO TRIAL BY COMBINING THE FORMING PRINCIPLE OF THE TRADITIONAL WOVEN HOLLOW FABRIC WITH THE FORMING PRINCIPLE MENTIONED ABOVE

As mentioned earlier, thread-linked double-wall cloths can be obtained by using above varied forming principle of the centre-weft stitched double cloths, but this is not our ultimate purpose that is obtaining thread-linked box-beam or thread-linked four connected walls with a rectangle cross section.How to get both sides of the thread-linked double-wall cloths? There are two ways.The one is sewing a single-layer structure cloth on to thread-linked double-wall cloths to form thread-linked box-beam preform.The other is weaving both sides cloth with thread-linked double-wall cloths simultaneously to form a three dimensional integrated thread-linked box-beam preform. It is obviously that, the integrated property and outware appearence quality of the later is better than former because of sewing. So, we try to develop integrated thread-linked box-beam preform by means of combining the forming principle of the traditional woven hollow fabric with the above forming principle of thread-linked double-wall cloths.

The basic forming principle of the hollow fabric is no stitching while double fabric forms and the face weft and the back weft insert cloth fell in proportion of 1:1 strictly. We produce out thread-linked box-beam preform on power loom, as show in figure 3.

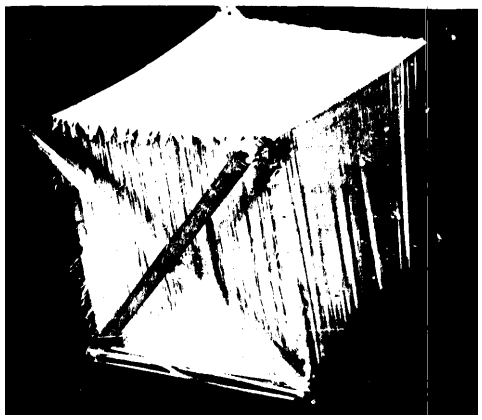

Figure 3: The photograph of thread-linked box-beam preform

THE WEAVING TECHNIQUES OF THREAD-LINKED BOX-BEAM PREFORM

The weaving technique of thread-linked box-beam preform are different between hand loom and power loom. We made a lot of experiments about affecting factor such as choosing of yarns, designing of fabric specifications as well as winding, warping, warp sizing, drawing-in and weaving, and obtained reasonabler weaving techniques and technique parameters of thread-linked box-beam preform on a power loom.

Choice of Yarns

What yarns are chosen is depended on the ultimate uses of the thread-linked box-beam preform. If it is used as a general filter fabric, then cotton yarn can be chosen. If it is used as a high temperature filter fabric, then polyester yarn or filament yarn even cavlar can be chosen. If it is used in building, municipal works and so on, then high tenacity polyester yarn or polypropylene fibre yarn can be chosen. The purpose of this paper is to study the priciple and find out the weaving technique of the thread-linked box-beam preform, so we choose $32^{s}/2$ general mid-fiber-length yarn, the weaving properties of which are better,the preform can be used as a filter fabric.

Design of fabric specifications

Design of cover factor

The degree of cover factor must be appropriate; if too low, the fabric is loose, and link threads are not firm, as a result, its using scope will be limited; if too high, ends breaking often takes place, shed cling, as a result, the weaving is very difficult.According to the experiment, the suitable scope of warp cover factor is 100%-120%, the ratio of wefe to warp is 0.80-0.95. In this way, the fabric is close and weaving is easy.The warp count and weft count of the thread-linked box-beam preform we weave on power loom are 45.8/cm and 37.0/cm respectively.

Design of weaves

(1) The choosing of base veave. On principle, the base weaves may be plain weave, twill weave, satin weave and filling rib weave and so on, but plain weave is the best, since it has the highest number of interlacings compared to other weaves which cause it to be the firmest and the fastest when as the fix link threads. So we choose plain weave as base weave.

(2) The way and the pattern of centre-weft-stitching. The fabric is composed of two system of warp threads, the face warp threads and the back threads, and three series of weft threads, the face weft threads and back weft threads as well as centre-weft. The face warp with the face weft interlace each other and the back warp with the back weft interlace each other to form four walls of thread-linked box-beam preform. The centre-weft with the face warp and the back warp interlace respectively forming stitching threads to combine the centre-weft with the four walls and make the centre-weft an long link threads of the threads-linked box-beam preform.The way of the stitching may be "V"style, in which centre-weft are bound in by one end only at a place, or "W"style, in which centre-weft are bound in by three ends at a place. So, "W" style stitching is termed a 'fast' stitching, "V" as a 'loose' stitching. It is evident that 'W'style stitching is more suitable for thread-linked box-beam preform. In this way, more steady link threads can be obtained.

In weaving, a stitching place is completed and a link thread of thread-linked box-beam preform is formed during inserting a pick. It is therefore necessary that the stitching places distribate in some patterns to make the link threads of thread-linked box-beam preform have the same length and even density. In this paper, a restangle pattern of stitching places is designed. There are 17 face ends (or back ends) and 16 face picks (or back picks) between near stitching places. As a result, the density of up to 80,000 stitching places per m^2 is obtained. Of couse, the density of stitching places can be changed by varying the number of face ends and face picks between near stitching places.

(3) The yarns ratio and the yarn number of complete weave repeat. The ratio is a very important factor to secure quality of the perform. In this paper, both ratios of face to back ends and face to back picks are 1:1, the ratio of base to centre-weft is 16:200.

For the warp number of complete weave repeat, concerning to warp set, loom width and weave continuative on selvedge of hollow fabric and so on, 4401 ends are in the final beam. This value is not only the yarn number of complete weave repeat but also the total number of warp ends. On the basis of the pattern of stitching places distribute, the weft number of complete weave repeat is 432.

Table 1 gives the summary of fabric specifications of threads-linked box-beam preform.

Table 1: Fabric specifications

yarn	base weave	warp count	weft count	width	total ends
$32^s/2$	1/1 plain	45.8/cm	37.0/cm	96cm	4401

The techonological process and the choosing of production equipment

The techonological process of the thread-linked box-beam preform is given in Figure 4.

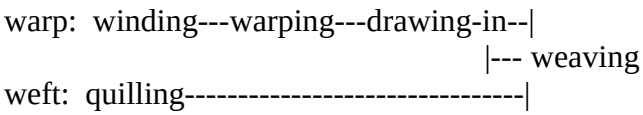

Figure 4: Techonological process

According to the design principle and specifications of the fabric, the production equipment employed are 1332M winding machine, G122 drum warping, G191 quilling machine, 1515M power loom (fitted with JK202 jacquard attachment).

The main points of weaving process

1 In the weaving process, the warp yarns are subjected to rubbing seriously, which lead to ends breakage and shedding indistinctly. To minimize this problem, slashing is chosen. It is the key of weaving fluently that the wearability of warp yarns is increased. In addition, a wax stick can be put at the back of loom to reduce friction, the warp sheet is kept close to its face moving forward, or talcum powder can be used to reduce friction.

2 According to the require of construction design, let-off stop motion and take-up stop motion must be mounted. During inserting base picks, the let-off and the take-up are activated on the basis of pick density. However, during inserting centre-weft, the let-off stop motion and the take-up stop motion work, the let-off and the take-up are not activated, and weaving goes on only accompanyed with shedding, filling insertion, and beat-up until 200 centre-weft are inserted, and loom motions become regular.

3 The weaving of the preform is similar to the weaving of the hollow fabric in some way. The weaving main points of the hollow fabric are very useful, Also it is very important that two shuttles must be used, one for base picks, the other for centre-weft.

4 In the weaving process, the fell of cloth floats up and down seriously. Consequently the shed is not clear. This appearance is more serious during inserting centre-weft. This problem must be solved by improving weaving technique. Otherwise, interlace disorders even flying shuttle occurs. The horizontal incresing pressure motion is equiped near shed, to minimize floating range.

5 Picking power and pick tension should be controled strictly. If they are higher, centre-weft drags the stitching ends aside,the appearance of fabrics emerges small holes. If picking power is lower, the shuttle can’t arrive opposite box. If pick tension is lower, the centre-weft in cloth is looser and longer than other centre-weft.

CONCLUDING REMARKS

Through exploring for the structure and technique of the thread-linked box-beam preform, we obtain the dedign principle and the keys of weaving technology of the fabric. The principle of fabric forming and the weave structure developed by us is new. It will certainly have a great value in developing and producing a new type of textile composites.

REFERENCES

1. Cai Bixia,"Weave Struture and Design", Textile Industrial Publishing House.

2. Chen Yuanpu, "Weaving Technology and Equipment", Textile Industrial Publishing House.

PERFORMANCE CHARACTERIZATION OF POLYMERIC COMPOSITE IMPLANT ROD SUBJECTED TO TORSION

Kh. G. Schmitt-Thomas, Zhen-Guo Yang and T. Hiermer

Institute of Applied Materials Engineering
Technical University of Munich, Arcisstraße 21, 80333 Munich, Germany

SUMMARY: This study was aimed at characterizing the shear performance and failure behavior of polymeric composite implant rod subjected to torsion load. Three kinds of molding processes for manufacturing the rod were investigated: hot-pressing process, winding process, and combination process of winding and braiding. The properties for two types of rod configurations were carefully analyzed: one with a braided-fabric and other without a braided-fabric. Shearing fracture tests were conducted with a special loading facility which integrates newly-developed torsion tester with Instron universal testing machine. The effect of loading rate on shear performance of the rod was taken into account when failure behavior and morphology associated with torsion load were investigated. Experimental results show that owing to three-dimensional reinforcing effect of the braided-fabric, the comprehensive performance for the rod with a braided-fabric could be better improved as compared to its counterpart without a braided-fabric.

KEYWORDS: torsion test, implant rod, biomaterial, epoxy/carbon, molding process, braided-fabric, loading rate, failure analysis.

INTRODUCTION

Implants for load-bearing body prostheses usually consist of either metal materials, polymer composites or materials with combination of metals and polymers. The use of metal is largely dependent on the need of sufficient strength. However, there exist a number of deficiencies in metal materials, although they possess excellent mechanical properties and fracture toughness. The mismatch between the elastic modules of their alloys and body bone is obvious [1]. It is the incompatibility of mechanical and physical properties between metal material and human body that results in one of the main reasons of artificial implant failures. In addition, some interference diagnostic problems exist for the metal implants while determining implant quality with non-destructive testing such as X-radiography, magnetic resonance, and ultrasonic inspection [2]; another problem is the corrosion of the metal implant. In view of these, development of advanced polymeric composite with both suitable mechanical properties and physical compatibility has been receiving great attention since the beginning of the 1980's [3-6].

As laminated composites have been widely applied to aerospace and other industries, there are some disadvantages relating to them; among those are lack of sufficient damage tolerance and low interlaminar shear strength. In comparison with the laminated composites, woven-

fabric reinforced composites seem to display more advantages, such as improved damage tolerance, higher shear-resistance property, dimensional stability as well as balanced mechanical property [7]. For those reasons, polymeric composites reinforced with braided-fabric are increasingly attractive to researchers.

However, test and characterization for woven-fabric composites subjected to torsion load have not been identified well because of their inherent difficulty and anisotropy in property. Even with unidirectional-fiber reinforced composites applied by torque parallel to the fiber, different position results in each fiber to be deformed differently [8]. As a component to be used for fixing spine in human body, the implant rod is inevitably subjected to twist load, which might be one of the main forces for causing its failure. Therefore, how to effectively anticipate its shear performance and failure behavior under the condition of torque is currently a new challenge. For this purpose, as a preliminary investigation, the present study will mainly focus on some experiment details relevant to torsion test of the implant rod and corresponding property characterization. Full consideration of the experimental results will be addressed in future publications.

EXPERIMENTAL PROCEDURE

Material

The matrix material studied was a biocompatible epoxy resin with the designation MEPOMAN, which was developed by MAN Ceramics Company, Germany. For the reinforcement, fiber with a diameter of 5.2 μm, called T800H, was supplied by Toray Industries Inc., Japan. The fibers are processed into roving containing 12000 filaments. All unidirectional carbon-fiber reinforced polymer (CFRP) rods investigated during testing are composed of a fiber content of 60 vol. % . The associated material properties are listed in Table 1.

Table 1: Fundamental properties of materials

Material specification	Tensile Strength (MPa)	Tensile modulus (GPa)	Density (g/cm^3)	Strain to failure (%)
Epoxy resin, MEPOMAN	100	3.1	1.30	4.50
Carbon-fiber, T800H	5590	294	1.81	1.90
CFRP-Plate, UD	3000	170	1.60	1.55

Fabrication of the rod

The CFRP rods used for experiment were produced with three kinds of molding processes: the first was hot-pressing process, the second was winding process, and the last was a combination of winding and braiding. The related fabrication process are illustrated in Fig.1.

For the hot-pressing process several plies of unidirectional prepregs were stacked together and then pressed into a CFRP-plate through pressure and heating in the mould (Fig. 1a). This material was simplified as UD_{press} plate. As to the winding process, fiber-rovings impregnated by resin were wound on a rotating, heated steel plate. After curing under a condition of temperature of about 160 °C, the material, which is simplified as UD_{wind}

plate, was cut at the edge of the steel-pate and so two CFRP-plates were made (Fig. 1b). Next, both kinds of CFRP-plates are machined into several quadrangular bars, and then those bars are ground with a conventional machining method into cylindrical rods (Fig. 1c).

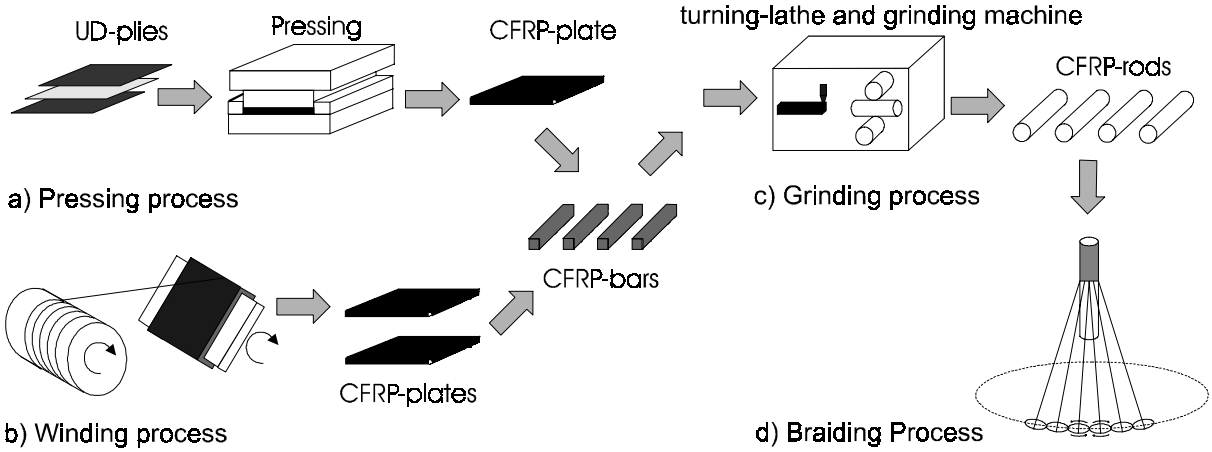

Fig. 1: Schematic illustration for fabricating CFRP-Rod

Finally, the surface of the rod fabricated by the winding process was wound with a layer of resin-impregnated roving through a rotary and braiding molding equipment which was employed for producing fabric with different braiding-angles (Fig. 1d) and so CFRP-rod with a braided-fabric, namely $UD_{braided}$-rod, was made. The angle and thickness of braided-fabric investigated are respectively 45° and 1 mm.

Preparation of the samples

For a preliminary study three kinds of rods were tested, that is, UD_{press}-rod and UD_{wind}-rod with a diameter of 4 mm, as well as $UD_{braided}$-rod with a diameter of 7.3 mm. The rods were embedded in two steel cartridges with a mixture of epoxy resin and aluminum powder to get the samples for the experiment. During preparation the rods bonded by embedding-mixture were carefully fixed in a special equipment so they were aligned in the center of both cartridges. The whole length of the sample was 110 mm, in which each cartridge has a length of 40 mm and the gauge length is 30 mm, as depicted in Fig. 2.

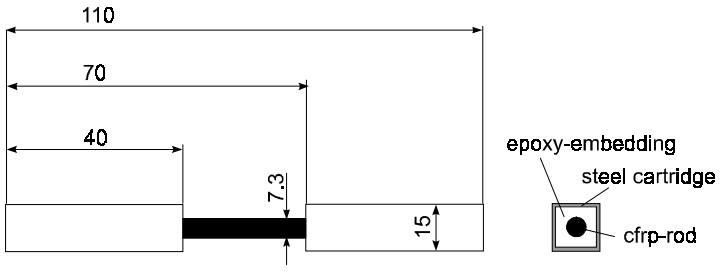

Fig. 2: Sketch of the $UD_{braided}$ sample

Test facility and procedure

A torsion loading facility shown in Fig. 3, which integrates torsion tester with an Instron universal testing machine, was specially developed, so that one can easily measure torque and angle of twist of the sample.

The fundamental principle is described as follows: first, two sensors for measuring torque and angle of twist were set to be zero before testing; a sample was then put in clamp holders; next a nylon rope in the torsion tester moved up vertically through loading of Instron universal testing machine. The rope caused a hoisting drum to rotate around the shaft and apply torque to the sample; finally, analogous signals received by the sensors were transmitted to two amplifiers which sent data to an analog/digital card installed in a computer. After acquisition of the data, a personal computer automatically constructed a torque-angle-curve on its screen through special software.

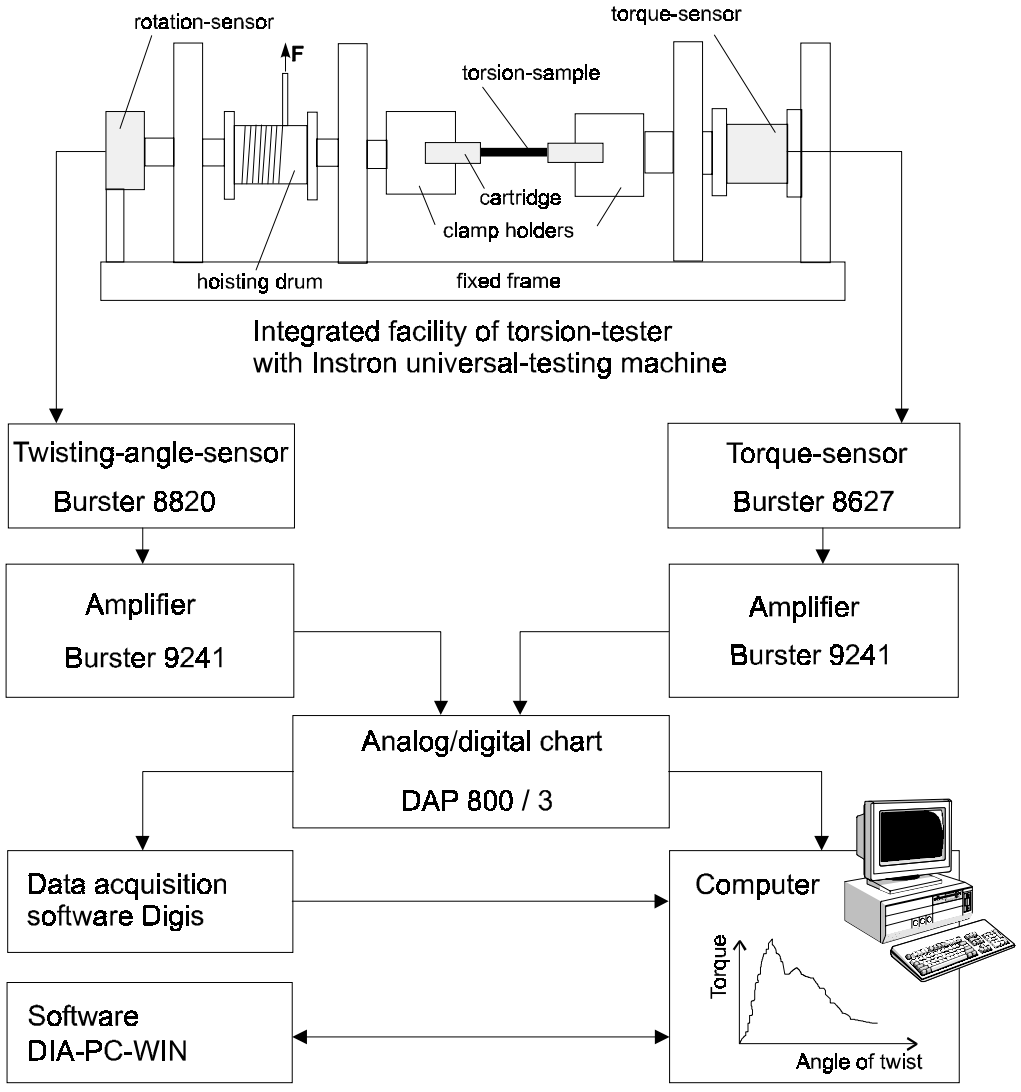

Fig. 3: Torsion loading facility

RESULTS AND DISCUSSIONS

Microstructure details

Figure 4 shows optical micrographs about transverse and longitudinal cross-section profile of the rod braided with an angle of 45^0. It clearly displays some manufacture flaws such as voids, macropores, and delaminations existing in the rod. These flaws have a certain distribution law. Voids usually lie at the transverse cross-section of the rod (Fig. 4b) and rarely appear in the longitudinal direction; macropores, called resin starvation, exist within the areas of braid intersection and interface between braided-fabrics and unidirectional plies; and delaminations appear between some plies (Fig. 4a). It is these existing flaws that affect stability of the material property of the rod. In general, these flaws are mainly resulted form either raw material or molding process. Some flaws like voids and delaminations, which are caused by residual moistures during curing, could be avoided or be diminished greatly by improving quality of raw resin and fiber, for example, minimizing moisture in the resin by vacuum drying. However, for macropores, which have greater impact on shearing property of the rod, it is very difficult to reduce them because of limitation of the current manufacture technology of composite. Obviously, this issue is a challenge to modern manufacture technology.

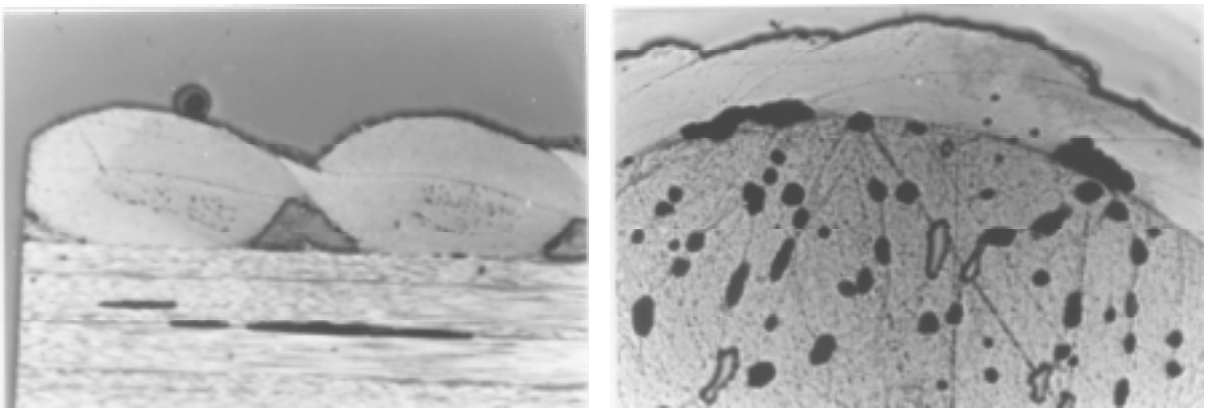

a) Longitudinal section (20x) *b) Transverse section (15x)*

Fig. 4: Cross sections of the rod with a braided woven-fabric angle of 45^0

Characterization of shearing properties

Shear deformation behavior of the rod

In order to analyze experimental data, some fundamental relationships are necessary. Let us assume the rod has a geometrical size of length L, diameter D, polar inertia moment of the circular cross-section area J, shear modulus G, and is subjected to torsion load T at its end, then maximum shear stress and corresponding angle of twist of the rod can be calculated as follows:

$$\tau = G\gamma \text{ , and } \tau = \frac{TD}{2J} \text{ , } \gamma = \frac{D\theta}{2} \qquad (1)$$

$$\theta = \frac{TL}{JG} \quad , \quad \text{and} \quad J = \frac{\pi D^4}{32} \tag{2}$$

where τ denotes shear stress, γ shear strain and θ angle of twist of the rod.

Based on Eqs. (1) and (2), the associated shear properties of the rods manufactured with different molding processes were computed against a loading rate of 10 mm/min. and the corresponding values are given in Table 2.

Table 2: Shear performance for three kinds of rods

Molding process	UDpress	UDwind	UDbraided
Shear modulus, MPa	4408	4902	5008
Failure shear stress, MPa	54.7	70	194
Angle of twist at failure, °	31.4	34.8	36.5
Relative twist angle, °/mm	0.71	0.83	1.22

Note: the $UD_{braided}$-rod has a diameter of 7.3mm and both UD_{press} and UD_{wind} rod*s* have a diameter of 4 mm.

As predicted, the material properties for $UD_{braided}$ rod were best among three of them, especially for largely increasing the relative twist angle and failure shear stress. Those indicate that due to braided a layer fabric, the global performance resistant to shear deformation of the rod has been improved.

For the sake of comparison, Figs. 5 and 6 further illustrate torque-angle plot for $UD_{braided}$-rod with braided-fabric angle of 45^0 and UD_{wind}-rod at the loading rate of 10 mm/min.

It can be seen from Figs. 5 and 6 that before approaching to maximum torque value, the angle of twist linearly increases with the applied torque for both kinds of rods without appreciable pop-up of curve slope. Obviously, in this case, the bonding between braided-fabric and unidirectional-fibers of $UD_{braided}$-rod is good although there are some macropores existing in their interfaces shown in Fig. 4. The applied torque continues to rise to the limit torque of the material, after which the load-bearing capability of the rod collapses immediately. The torque of $UD_{braided}$-rod drops significantly, which is much larger than its counterpart without a braided-fabric. The main reason for accounting for this is that the interfacial situation between woven-fabric and the unidirectional plies occurs fully debonding, which causes shear stiffness of the rod along the transverse direction diminish dramatically. However, the reduction for load-bearing capability of the UD_{wind}-rod is mainly resulted from cracking of the matrix and delamination of the plies. Another distinctive feature between $UD_{braided}$-rod and UD_{wind}-rod lies at the variation of the subsequent applied torque with the angle after initial breaking. For the $UD_{braided}$-rod, its applied torque displays tendency of a little going up with the angle (Fig. 5), and the torque for the UD_{wind}-rod always decreases with the angle(Fig. 6). This is because the former needs further cracking of the matrix and delamination of the plies, just as the latter did previously. Consequently, the $UD_{braided}$-rod, in fact, undergoes more than two times the fracture processes.

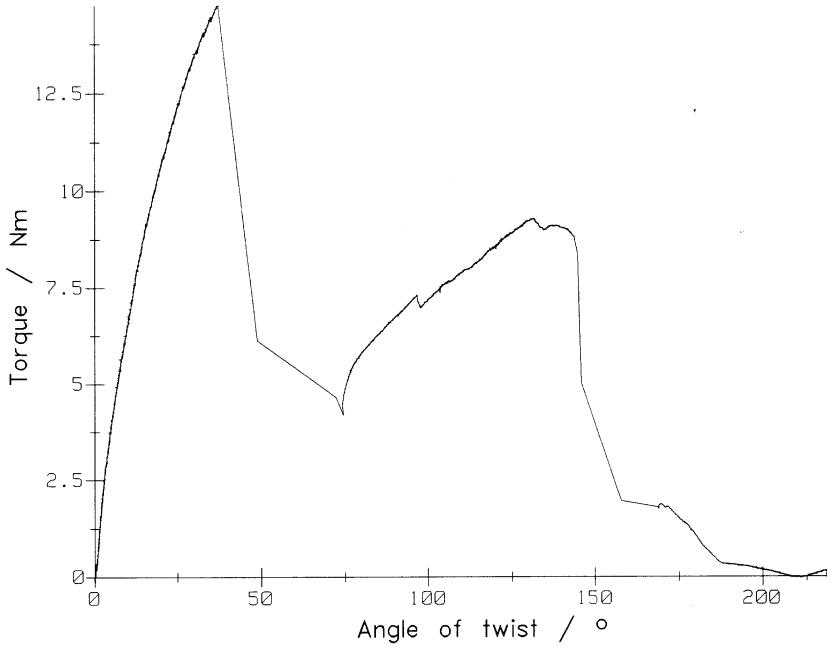

Fig. 5: Torque-angle plot for $UD_{braided}$-rod with braid angle of 45°

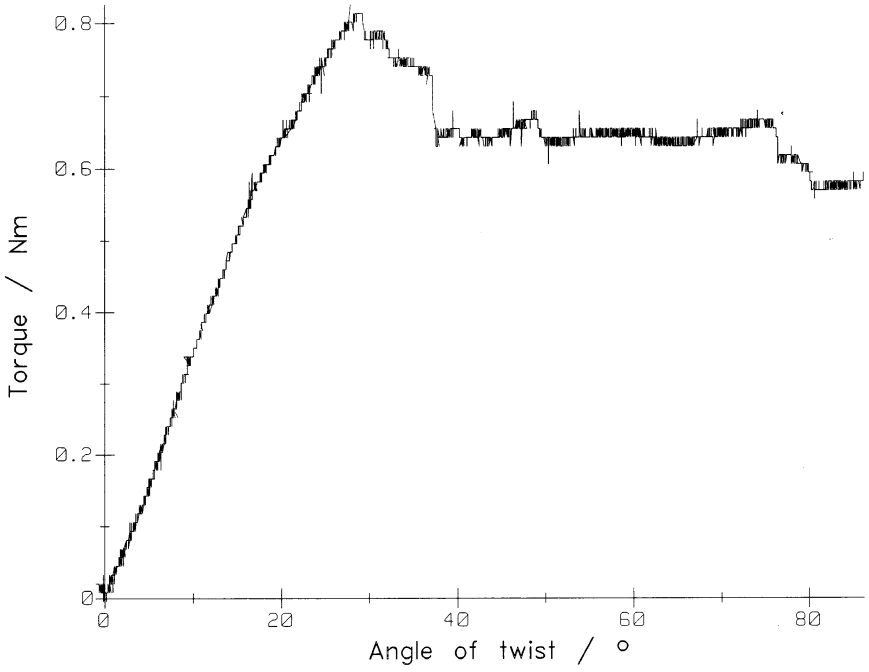

Fig. 6: Torque-angle plot for UD_{wind}-rod

Loading rate effect

The properties of composite materials are often influenced by some experimental parameters like loading rate etc. It is therefore necessary to repeat standard tests over a range of suitable

test condition. Table 3 shows some data related to shearing performance of the $UD_{braided}$-rod with loading rate ranging from 10 mm/min. to 1000 mm/min.

Table 3: The variation of shearing performance with loading rate

Loading rate, mm/min.	10	50	100	200	1000
Twist rate, °/min	22.9	114.6	229.2	458.0	2292.0
Shear modulus, MPa	5008	5204	4621	4935	4938
Failure shear stress, MPa	194	194	187	188	180
Angle of twist at failure, °	36.5	35.1	38.2	36.0	34.2
Relative twist angle, °/mm	1.22	1.17	1.27	1.20	1.14

It is shown that all material properties such as shear modulus, failure shear stress, angle of twist as well as relative twist angle were not influenced by the loading rate. The error among data was less than 5 %, which is allowable from the sense of engineering. As a result, the effect of the loading rate on static material strength of the rod can be neglected. But it should be worthwhile to note here that for other kinds of rods such as braided-fabric angles of 60^0 and 70^0, something was a little different due to the molding process, which will be discussed in an another paper.

Failure behavior

Figure 7 shows fractographs of $UD_{braided}$-rod and UD_{wind}-rod after torsion test, in which the final fracture position of all rods were far away from the grip of the cartridge. Typical fractographic morphologies are illustrated in Figs. 8-9. Several fracture characteristics can be recognized from these SEM photos.

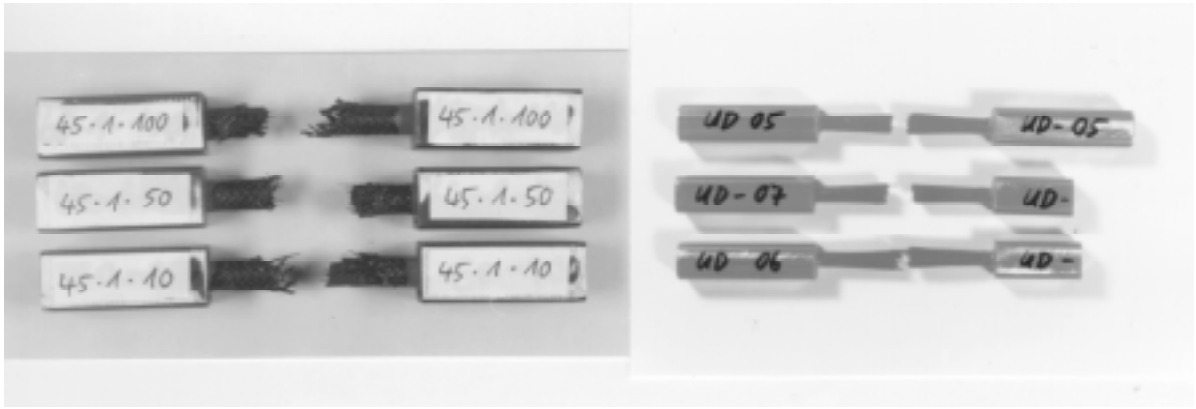

a) $UD_{braided}$-rod *b) UD_{wind}-rod*

Fig. 7: Fractographs of $UD_{braided}$-rod and UD_{wind}-rod after torsion test

It is clearly shown in Fig. 8a and Fig. 9a that the number of delamination for $UD_{braided}$-rod is obviously smaller than that for UD_{wind}-rod; many brittle cracking layers appear on the outer surface of the UD_{wind}-rod. This indicates that apart from increasing shear properties of the rod, the reinforcement of braided-fabric was also able to repress the brittle fracture process to some extent. This may be very significant for both design of fracture-resistance for polymer composite rod and enhancing residual service life of the rod containing some flaws.

8a)

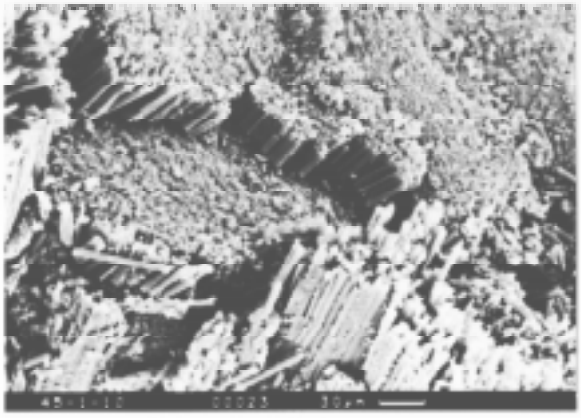

8b)

8c)

Fig. 8: SEM photographs of $UD_{braided}$-rod

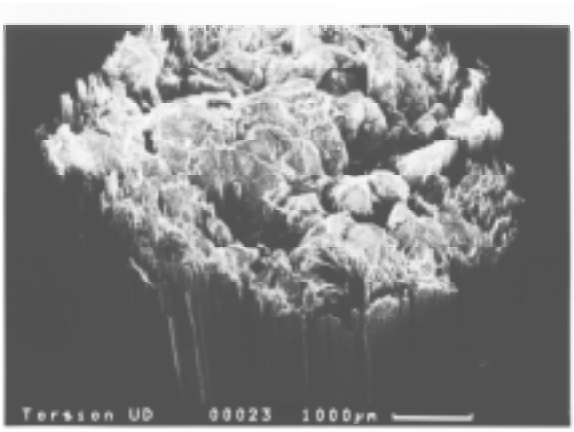

9a)

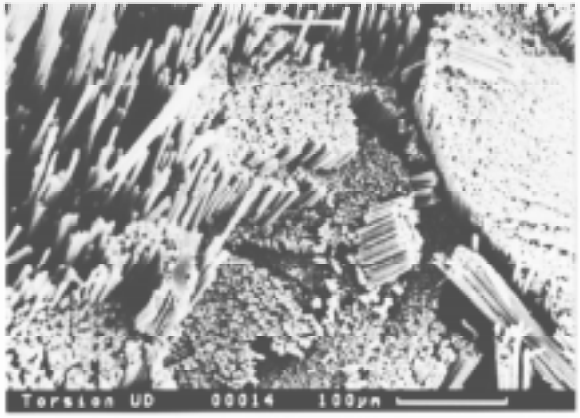

9b)

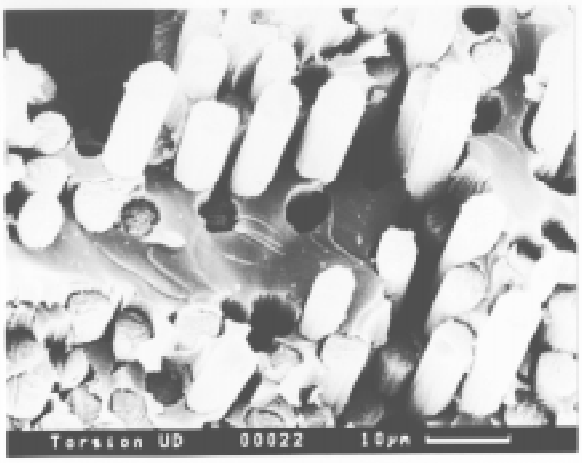

9c)

Fig. 9: SEM photographs of UD_{wind}-rod

Referring to Fig. 8b and Fig. 9b, it is easy to find that fractographs of both rods have a similar feature: their morphologies have a terrace shape. This three-dimensional fracture behavior has a close relation with torsion load. The main reason for producing this special morphology was that the rod experienced secondary and multi-fracture with further twisting, which is implied from the curve of torque-angle illustrated in Fig. 5. However, carefully comparing

Fig. 8c with Fig. 9c, one is able to be aware that the number of fiber pull-outs for $UD_{braided}$-rod was less than that for UD_{wind}-rod; this meant that the braided-fabric can also improve axial property of the rod besides shear stiffness of transverse direction and thus produce three-dimensional reinforcement effect. In addition, the fractured surface of the $UD_{braided}$-rod was full of a lot of powders; by contrast, the fractured surface of UD_{wind}-rod looks very clean and corresponding matrix displays brittle cracking characteristics. This further exhibits that the braided-fabric reinforcement has a function of avoiding formation of brittle fracture.

CONCLUSIONS

1. The torsion loading facility, which integrates specially-designed torsion tester with Instron universal testing machine, was developed. The facility can be used not only for evaluating failure behavior of the implant rod subjected to torsion load, but also effectively measuring shear performance of the material.

2. The reinforcement with a braided-fabric is beneficial for reducing brittle fracture in the rod in addition to enhancing transverse shear property; moreover, the comprehensive performance of the rod with a braided-fabric, such as shear modulus, critical shear stress, angle of twist, and relative twist angle, are improved compared to its counterpart without a braided-fabric.

3. A terrace-like morphology represents the most common failure characteristic corresponding to torsion load, which is mainly caused by repeated twist fractures.

4. Under the certain range from 22.9 °/min. to 2292 °mm/min., the effect of loading rate on shear property of the rod can be ignored.

REFERENCES

1. Jamison, R.D., *Biomechanics Symposium 1989*, 3rd Joint ASCE/ASME Mechanics Conference, AMD (Symposium Series), **98**, 1989, pp. 195-199

2. Matthew, R.M. et al, *J. of Biomedical Materials Research*, **28**, 1994, pp. 1221-1231

3. Akay, M. and Aslan, N., *J. of Biomedical Materials Research*, **31**, 1996, pp. 167-182

4. Ruffieux, K. et al, *Textiles and Composites'92*, Finland, 1992, pp. 326-332

5. Deger, C., Jadhav, T. and Jadhav, B., *Progress in Biomedical Polymers*, Plenum Press, 1990, pp.239-248

6. Williams, D.F., McNamara, A. and Turner, R.M., *J. Mater. Sci. Letters*, **6**, 1987, pp. 188-190

7. Hoa, S.V., *Comptuer-Aided Design of Polymer-Matrix Composite Structures*, Marcel Dekker, Inc., 1995, pp.137-138

8. Gong, X.L. et al, *J. Reinforced Plastics and Composites*, **14**, 1995, pp. 29-44

THE MANUFACTURE AND TESTING OF 3D MULTILAYER WOVEN I-BEAMS

G. P. Kamp[1], M. K. Bannister[1], I. Herszberg[2], A. Nicolaidis[1]

[1]Cooperative Research Centre for Advanced Composite Structures Limited
506 Lorimer Street, Fishermens Bend, Victoria, 3207, Australia
[2]Sir Lawrence Wackett Centre for Aerospace Design Technology, Royal Melbourne Institute of Technology, GPO Box 2476V, Melbourne, Victoria, 3001, Australia

SUMMARY: Composite I-beams were manufactured from E-glass and vinyl ester resin. The glass preforms for the I-beams were produced using advanced multilayer weaving techniques and consolidation of these preforms was carried out via Vacuum Assisted Resin Injection (VARI). The design requirements for the beams were based upon those for a cross-member in a typical footbridge. Three- and four-point tests demonstrated that the composite beams achieved the required structural performance except for a 5% reduction in expected bending stiffness. This was thought to be due to a reduction in the anticipated flange thickness. The use of multilayer woven preforms also demonstrated improved manufacturability of the beams when compared to standard 2D glass fabric.

KEYWORDS: FRP I-beam, multilayer weaving, mechanical performance, vacuum assisted resin injection

INTRODUCTION

For most of their existence, modern-day composite materials have been intimately related to the aerospace industry. Their high specific strength and stiffness have made them the material of choice for an increasing number of aerospace components and it is only relatively recently that composite materials have begun to be used as major structural components in civil engineering projects. Although the mechanical performance and corrosion resistance of composites have always been of interest to civil engineers, the high cost of raw materials and labour intensive production methods have limited their use.

Increasingly, however, it is becoming apparent that as the cost of materials is reduced and improved manufacturing processes are developed a potentially huge market for composites is forming in the construction industry. In the USA alone, the problems associated with ageing infrastructure is costing the economy billions of dollars annually with recent estimates stating that around 230,000 of the 575,000 bridges in the US are either structurally deficient or functionally obsolete [1].

Composites can be used in a number ways to overcome the infrastructure problems currently facing the USA and many other countries. They have the potential to help repair existing problems [2] through techniques such as wrapping of concrete support columns [3], which is particularly relevant in earthquake-prone areas, and strengthening of concrete beams with

bonded composite plates [4,5]. Composite materials have also been used in the manufacture of a number of pedestrian and road bridges, including those at Aberfeldy (Scotland) [6], Stroud, Gloucestershire (UK) [6] and Russell, Kansas (USA) [7]. To date, hundreds of composite footbridges have been manufactured, with the choice of composite materials being made for reasons which include; ease of construction and maintenance, corrosion resistance, nearly inaccessible locations, environmental concerns and aesthetics. In particular, one major factor for the choice of composites in footbridges is the desire to reduce the overall weight of the bridge as this is a substantial proportion of the total load.

As mentioned earlier, the use of composites in large civil engineering projects has been limited by the high material costs and the labour-intensive methods required for composite component production. With the advent of relatively low-cost, commercially available, large carbon fibre tows the problem of high material cost is beginning to be addressed, however, forming these tows into the required shapes is still a matter of concern. Pultrusion [8] is a method of producing composite structural components in the large volumes that are needed in civil engineering and has certainly been an important technique used in the production of most of the composite bridges currently standing. The supply of fibre in the pultrusion process is generally in the form of individual tows or two dimensional woven fabric. This can result in a costly set-up stage for large components, due to the large number of fibre sources that need to be fed into the equipment to build up the final component. Utilising advanced textile manufacturing processes it is possible to produce a single fibre preform in the desired structural configuration. These techniques have been shown to produce components with improved performance at a reduced cost [9].

This paper reports on initial work, conducted at the Cooperative Research Centre for Advanced Composite Structures, which investigated the potential of using advanced weaving techniques to produce three-dimensional fibre preforms for composite I-beams.

DESIGN OF I-BEAM

Performance Requirements

There are numerous applications for I-beams within the civil engineering field, each of which will dictate their own particular performance requirements upon the structural member. For the purpose of this investigation a specific use for the I-beam had to be determined in order that dimensions and mechanical properties could be calculated. Due to the increasing use of composite materials in footbridges it was decided to design the beams as generic cross-members in such an application.

The generic footbridge structure consists of two longitudinal beams upon which the cross-members are placed with the bridge deck on top of these cross-members (Fig. 1). The load on the bridge is the weight of the people times a safety factor plus the dead weight of the bridge structure itself. For this investigation it was assumed that the width of the bridge was 2 metres with the longitudinal supporting beams placed 1 metre apart. Standard design requirements stipulate a maximum of 9 people, each weighing 100 kg will fit in a square metre. This gives a uniformly distributed load on the bridge of 8.8×10^{-3} MPa. If a safety factor of three is applied this becomes 30×10^{-3} MPa, which also allows for approximately 120 kg/m^2 of structural weight. It was assumed that the deck will distribute the load evenly to the cross-members, therefore reducing the bridge design to a two-dimensional problem of a simply

supported beam with a distributed load. If the distance between the cross-members is taken to be 1 metre a distributed load on each cross-member of 30 N/mm is obtained.

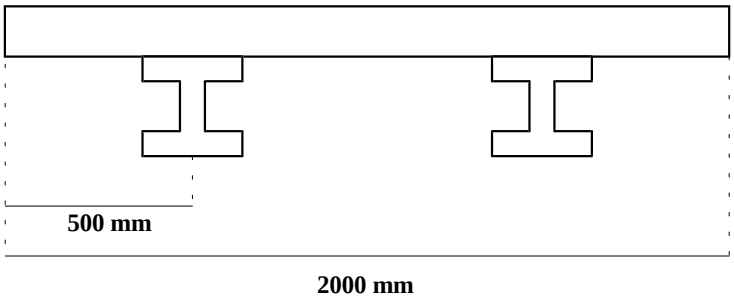

Fig. 1: Illustration of generic footbridge used for design of I-beams

With these dimensions and calculated loads, simple beam theory gives the maximum bending moment and shear load in the cross-members as 3.75 kNm and 18.75 kN respectively. The bending stiffness of the beam is determined by the maximum allowable deflection of the bridge deck, which is limited to $1/80^{th}$ of the deck width. This restriction yields a required minimal bending stiffness of $EI = 4.69 \times 10^{10}$ Nmm^2 for the beam. With these performance parameters in mind a multilayer woven preform was then designed for use as the I-beam.

Weave Architecture

For this investigation the materials for the I-beam were chosen on the basis of their cost and ease of use. The cost of E-glass is substantially lower than the higher performance carbon fibres and is less susceptible to damage during the weaving process than carbon. Vinyl ester was chosen as the resin material as it is relatively cheap and cures at room temperature thus removing the need for expensive curing cycles and high temperature tool materials.

The preforms were woven at the CRC-ACS on a dobby hand loom (for initial trials) and an advanced electronic jacquard loom (for the production of full size preforms). The use of these looms restricted the manufacture and style of the preform in a number of ways. Firstly, the majority of weaving looms are incapable of producing material with fibres in the ±45° direction as well as the normal 0° and 90° directions. It is possible to manufacture material with fibres in all 4 directions on special looms but this material is not widely available. This restriction of only 0° and 90° fibres in the web and flanges will result in having to increase the thickness of the web in order to obtain the required shear strength. It would be possible to add additional material to the web at ±45° but for the purpose of this investigation the design was restricted to only multilayer 0/90 fabric.

Due to the set-up of the looms, which were also being used for the manufacture of preforms for other investigations, there were restrictions placed upon the types of preforms that could be produced. This meant that the weave architecture had to be, essentially, identical in the web and the flange even though the performance requirements for both areas are very different. Thus, for the purpose of this initial work, the selection of weave architecture was based upon previous work performed at the CRC-ACS which examined critical factors in the manufacturability and weave architecture of multilayer woven preforms [10]. This selected weave architecture contained fibre distributions of 54% and 46% for the longitudinal (along the length of the beam) and transverse direction respectively with the total fibre volume

fraction of the beam predicted to be 50%. It should be noted that in commercial production of preforms for composite I-beams, a loom would be initially set-up to produce the required material as a single preform with optimised weave architectures for both the flange and web.

Dimensions of I-beam

The I-beam contains four independent dimensional variables, namely; the web height (H), the flange width (W), the web thickness (t_w) and the flange thickness (t_f). These dimensions will be determined by the performance requirements of the beam and the mechanical properties of the materials used.

The Young's moduli of E-glass fibres and vinyl ester are 72 GPa and 3.4 GPa respectively. For a composite containing a 54% - 46% distribution of fibres in the longitudinal - transverse directions and a 50% final fibre volume fraction the estimated Young's moduli [11] in the longitudinal and transverse direction are;

$$E_1 = 25.6 \text{ GPa}$$
$$E_2 = 23.4 \text{ GPa}$$

In order to adequately determine the beam dimensions shear tests were performed upon the multilayer woven composite. These tests produced the following mechanical properties;

Maximum Shear Stress $\tau_{max} = 40$ MPa

Shear modulus, $G_{12} = 4.5$ GPa

The web area of the beam was calculated from the maximum shear load capacity required by the beam (18.75 kN) and the maximum shear stress that the multilayer woven composite material will be allowed to carry. This allowable shear stress was set to be 30 MPa, giving a safety factor of 1.3. Using this data, the web area was given by the relation;

$$Area_{web} = \frac{ShearLoad}{\tau_{average}} \tag{1}$$

which yielded a required web area of 625 mm^2.

For the bending properties of the I-beam it is desirable to place the flanges as far apart as possible, but increasing this distance decreases the web thickness and increases the chance of the web becoming unstable in lateral/torsional buckling. With this in mind and also taking into account the range of preform dimensions that could be produced on the loom, the web height and thickness were chosen to be 102 mm and 6.1 mm respectively.

The minimum moment of inertia of the beam is dictated by the required bending properties. The required bending stiffness depends directly on the moment of inertia. With a predicted Young's modulus of 25.6 GPa in the longitudinal direction of the multilayer woven composite, the stiffness requirements demand a minimum moment of inertia of;

$$I_{yy} = \frac{EI}{E_1} = 1.8 \times 10^6 \ mm^4 \tag{2}$$

The required bending moment capacity is linked to the moment of inertia via the following relation;:

$$\sigma_x = \frac{M \cdot z}{I_{yy}} \tag{3}$$

where σ_x is the maximum allowable stress in the longitudinal direction and z is the level where this stress acts (this stress will occur at the outer flange surfaces). Previous tests upon the multilayer woven composite had measured the minimum strength of the material to be 320 MPa in tension. Applying a safety factor of 1.3 the maximum allowable stress in the flanges was assumed to be 250 MPa. From Eqn. 3 this results in a minimum moment of inertia of approximately 7.7 x 10^5 mm^4. Comparing the two values obtained for the moment of inertia shows that the bending stiffness requirement is the major factor in dictating the minimum moment of inertia and thus the flange area as well. The moment of inertia can be expressed in terms of beam dimensions,

$$I_{yy} = \tfrac{1}{12} \cdot \left[W \cdot H^3 - (W - t_w) \cdot (H - 2 \cdot t_f)^3 \right] \tag{4}$$

Substitution of the known parameters leads to the following relation between the flange thickness and width.

$$t_f = 51 - \tfrac{1}{2} \cdot \sqrt[3]{\frac{W \cdot 102^3 - 12 \cdot 1.8 \times 10^6}{W - 6.1}} \tag{5}$$

The flange width and thickness were chosen to prevent flange buckling at the design loads and to conform with the range of preforms that could be produced by the loom. A buckling analysis of the flange lead to the selection of a flange width of 62 mm and a flange thickness of 4.8 mm. The required dimensions of the I-beam were therefore;

Web height (H) = 102 mm	Flange width (W) = 62 mm
Web thickness (t_w) = 6.1 mm	Flange thickness (t_f) = 4.8 mm

MANUFACTURE OF I-BEAM

Weaving of preforms

Initial weaving trials were conducted upon a 24 shaft dobby hand loom and the resultant preforms produced were used to manufacture specimens for three-point bend tests. These tests were conducted to determine whether the weave architecture and dimensions of the web, that was based upon earlier rail-shear tests, would in fact provide adequate shear strength.

Full scale specimens for 4-point bend tests were manufactured upon an automated, electronically controlled, jacquard loom. This loom was used not only because it could produce samples of the required size but also to demonstrate the manufacture of advanced textile preforms, that are suitable for composite structures, on an industry standard production loom.

As mentioned earlier, the decision to use these two looms restricted the manufacture of preforms in a number of ways. One important restriction was that it was not possible to manufacture the I-beam as a single preform with the loom set-up that was in operation at that time. The looms could have been reset in order to produce a single preform but this would have been a time-consuming and very costly process. Therefore, in the interests of speed and cost reduction, the I-beam was manufactured as 2 preforms that were consolidated as shown in Fig. 2.

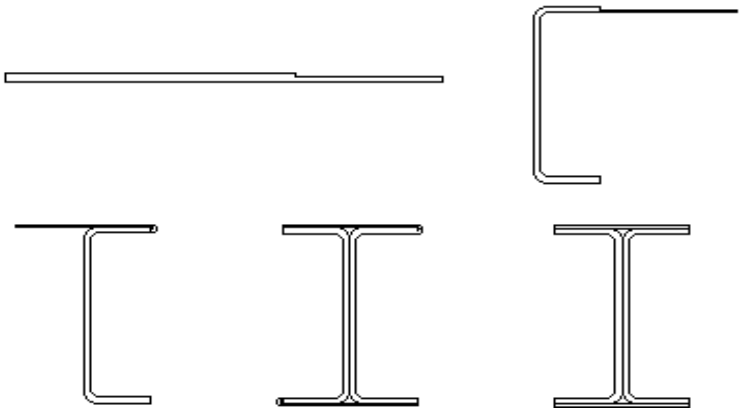

Fig. 2: Illustration of preform consolidation

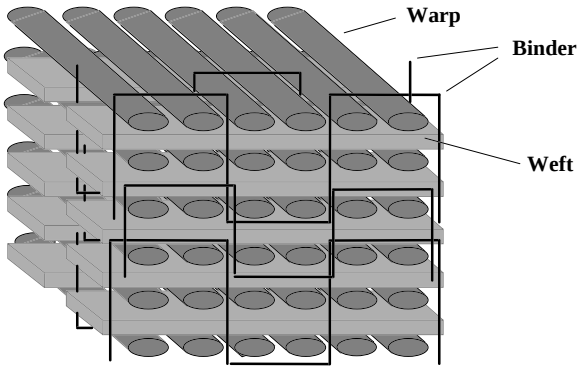

Fig. 3: Example of an idealised multilayer weave architecture

Due to the fact that two looms were used in the production of specimens, there were some slight differences in the preforms produced. In the samples from the dobby handloom the longitudinal and transverse yarns in the multilayer structure were essentially uncrimped. The various layers of yarns were kept in place by a low percentage of a very fine E-glass yarn that travelled in the preform thickness direction, binding the yarn layers together and providing the preform with adequate handling characteristics. It is expected that this binder yarn will not significantly contribute to the in-plane mechanical performance of the I-beam. An idealised representation of this type of weave architecture is shown in Fig. 3 and the proportions of the various yarn types in the final composite I-beam is listed in Table 1. The preforms produced by jacquard loom differ slightly from this in that they do not have a separate binder yarn holding the layers together, this job is done by a small percentage of the transverse yarns. This difference resulted in a more rapid production rate than using a different binder yarn but produced an architecture in which the longitudinal and transverse yarns were slightly crimped. It is thought that this crimping may lead to a small reduction in the stiffness of the I-beam.

Table 1 again lists the proportions of yarns in the final composite I-beam for the jacquard preforms.

Table 1: Details of critical I-beam dimensions, fibre proportions and overall composite fibre volume fractions

Loom	I-beam Dimensions H, t_w, W, t_f (mm)	Longitudinal (%)	Transverse (%)	Binder (%)	Fibre vol. frac. (%)
Dobby	99, 6.0, 62, 3.9	56.4	41.2	2.4	51
Jacquard	99, 6.3, 62, 4.2	55.8	44.2	-	52

Consolidation

The preforms manufactured by both loom types were consolidated with vinyl ester resin by a process known as Vacuum Assisted Resin Injection (VARI). Generally, this process relies on drawing resin through the preform by applying vacuum at one end with a resin reservoir at the other end (Fig. 4). Unlike resin transfer moulding techniques, where resin flow between inlet ports and outlets is primarily through the preform itself, in the VARI method the primary resin flow is through a carrier which distributes the resin over the surface of the preform after which the secondary flow is through the preform thickness. The resin therefore has less distance to travel through the preform and thus resin injection pressures do not need to be as high. These factors generally allow cheaper, more easily managed tooling to be used thus saving on production costs. One disadvantage is that a smooth tool surface on the finished component is not possible on the surface that was in contact with the carrier material, although this was not a critical consideration for this work.

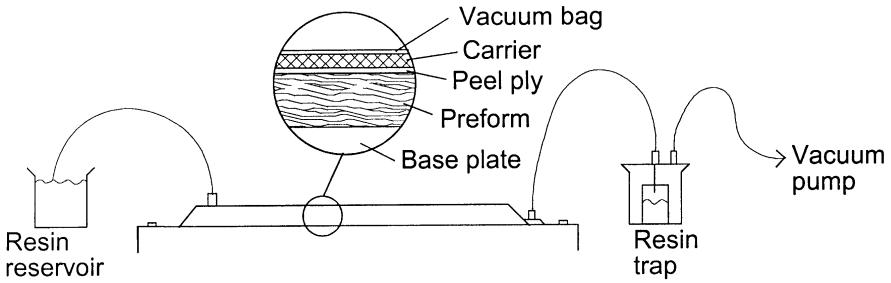

Fig. 4: Illustration of the Vacuum Assisted Resin Injection technique

The VARI tooling set-up for the I-beams is illustrated in Fig. 5. This tooling was enclosed in a vacuum bag, which was necessary for the VARI process to work and also compacted the preforms to achieve the required fibre volume fractions. It was found that the best results were obtained when the carrier material was placed next to the flanges. The fillet space at the junction of the C-channels and the flanges was filled with uniaxial E-glass yarn to prevent premature failure at this point. I-beams produced with this arrangement were found to be free of voids with dimensions and fibre volume fractions very similar to the design values (Table 1) although the flange thicknesses were less than the design values due to the restrictions placed by the set-up of the loom. The small differences in thickness between the two preform types was thought to be due to the slight changes in preform architecture and fibre volume fraction.

Initial trials with the tooling were conducted with standard 2D glass fabric. It was found that cutting to size and accurately maintaining the position of the large number of fabric layers required for the I-beams was very complicated and time-consuming and occasionally lead to defects in the consolidated beams. The use of the multilayer woven preforms significantly decreased the time required for the setting up of the preform in the tooling by more than 50%. This demonstrates the potential advantages that can be gained in the production of complex-shaped components by the use of multilayer preforms that are woven to the required shape.

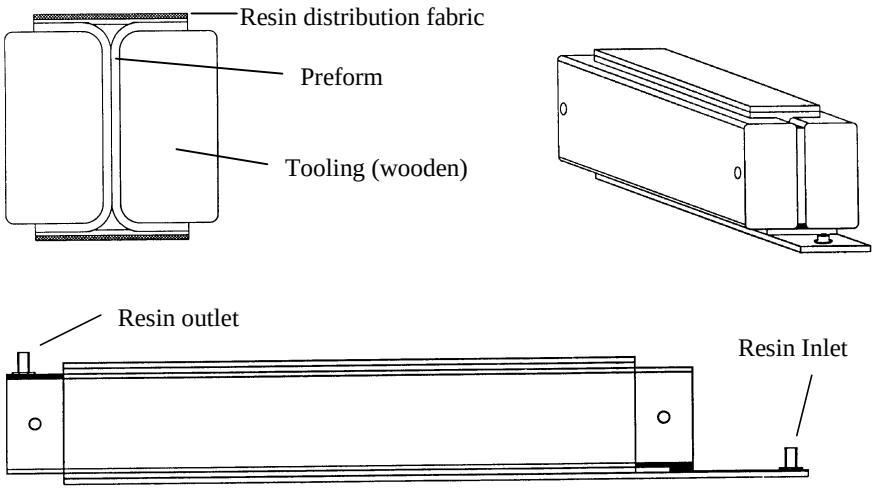

Fig. 5: Illustration of the tooling used for consolidation of the I-beams

TESTING OF I-BEAM

Shear Tests

Three preforms produced on the dobby handloom were consolidated into I-beams and tested in three point bend to determine the maximum shear load capacity of the weave architecture and beam dimensions selected during the design phase. Table 1 lists the dimensions of the I-beam cross-section whilst the test span used was 370 mm. To ensure failure of the web via shear, wooden blocks were placed inside the I-section on the points where the load was introduced to reinforce these areas and to prevent premature failure of the beam. These blocks were of the same timber used for the tooling and were glued into place using vinyl ester resin of the same composition as the resin in the beam.

Measurements of load and neutral axis displacement were made throughout the tests and the failure load was used to calculate the shear load capacity of the I-beam. Table 2 shows the experimentally measured shear load capacity (average of all three beams) compared with the shear load required by the design conditions. The results show that the weave architecture and dimensions chosen for the I-beam can adequately accommodate the maximum shear load required by the original design. The measured average shear load of the beams (23.5 kN) gives a shear strength for the composite material of 37.6 MPa, which is a very similar result to the strength obtained earlier by rail shear tests.

Bend Tests

The automatic jacquard loom was used to produce three I-beam preforms which were consolidated and tested in four-point bending in a pure bending rig [12] to determine their bending stiffness and bending moment capacity. Table 1 lists the dimensions of the I-beam cross-section whilst the inner and outer spans of the test rig were 678 mm and 1292 mm respectively. In a similar fashion to the previous three-point bend tests, wooden blocks were glued inside the I-section of the beam to provide reinforcement at the loading points and thus ensure failure of the beam within the inner span.

Table 2 again shows the results of the tests (average of all three beams) and compares them with the design requirements. It is clear that the I-beams have a more than adequate bending moment capacity, almost twice that required. However, the flange dimensions, which control the beam's moment of inertia, were selected to just satisfy the required minimum bending stiffness calculated during the design phase. The experimental results for bending stiffness were found to be approximately 5% less than the design requirements. This shortfall is thought to be due to the actual thickness of the flange being less than the design value. This difference would lower the bending stiffness of the I-beam below the design requirements.

Table 2: Mechanical properties of I-beams

	Design	**Experimental**
Shear Load Capacity (kN)	18.75	23.5 ± 2
Bending Stiffness (10^{10} Nmm^2)	4.69	4.47 ± 0.2
Bending Moment Capacity (kNm)	3.75	7.32 ± 0.7

DISCUSSION AND CONCLUSIONS

The test results presented in the preceding section show that the I-beam manufactured by advanced weaving and liquid moulding techniques successfully achieved the majority of its design requirements. The one exception was a slightly lower bending stiffness that was thought to have resulted from a reduction in the flange thickness. It should be noted that due to the restrictions placed upon the beam design by the available looms, this design was far from optimised for its end use as a footbridge cross-member. The addition of ±45° fibres to the web area to improve its shear performance would have allowed a reduction in the web cross-section and thus the weight of the beam. Similarly, if the initial set-up of the loom had allowed a variation in the weave architecture between the flange and the web, a higher proportion of longitudinal fibres could have been placed in the flange thus improving the beam's bending performance. The placement of higher modulus carbon fibres in the flange would also have improved the bending performance of the I-beam whilst at the same time allowing a reduction in the weight of the beam.

Initial trials in utilising the VARI method to manufacture the I-beams had demonstrated the difficulty of maintaining accurate positioning of the large number of layers of standard 2D glass fabric required for the beams. The use of a smaller number of fabric pieces (multilayer woven preforms) was observed to lead to a significant improvement in manufacturability. An optimal loom set-up would have allowed the preform to be manufactured as a single piece of

multilayer fabric which would help reduce the set-up costs inherent in production methods, such as pultrusion.

It is therefore clear that advanced weaving techniques, coupled with improved processes for resin infiltration, have the ability to manufacture composite structural components to specified design requirements. The use of multilayer weaving also demonstrated the potential advantages that could be gained by processes such as pultrusion by using single preforms that have been woven to the required shape.

REFERENCES

1. "Cable news…", *Advanced Materials News,* Millbank, P., Ed., No. 82, April 1996, pp 1-8.

2. McConnell, V. P., "Can composites rebuild America's infrastructure?", *Advanced Composites,* November/December 1992, pp. 22-31.

3. Brooks, N., "GRP wraps up bridge repairs", *Reinforced Plastics*, July/August 1995, pp 30-32.

4. Zou, R. D., Jones, R., Hanna, S., Lam, Y. C., "An investigation on strengthening of concrete beam with GFRP laminates", *First Australasian Congress on Applied Mechanics*, Melbourne, Australia, 21-23 February, 1996, Vol 1, Grzebieta, R., Wong, A., Marco, J., Lam, Y., Eds., pp 461-466.

5. Weaver, A., "Carbon plate stops the cracks", *Reinforced Plastics*, July/August 1995, pp 34-37.

6. Weaver, A., "Hybrid bridges exploit composites durability", *Reinforced Plastics*, July/August 1995, pp 24-29.

7. *Composite News: Infrastructure*, No. 59, 16 December, 1996, Loud, S., Ed. Composites Worldwide, Inc., 1996, pp 6-8.

8. Strong, A. B., "Versatility in pultrusion", *Composites Fabrication*, June 1996, pp 9-13.

9. Müller, J., "The extension of advanced composites into the machine industry", *4th International Conference on Automated Composites"*, Nottingham, UK, September 6-7, 1995, The Institute of Materials, pp 499-509.

10. Bannister, M., Herszberg, I., Nicolaidis, A., Coman, F., Leong, K.H., "The manufacture of glass/epoxy composites with multilayer woven architectures", *to be published in Composites Part A: Applied Science and Manufacturing.*

11. Halpin, J., Tsai, S., "Effects of environmental factors on composite materials", *AFML-TR67-423*, June 1969.

12. Cimpoeru, S., "The modelling of the collapse during roll-over of bus frames consisting of square thin-walled tubes" *Ph.D. thesis*, Monash University, Melbourne, Australia, December, 1992.

STIFFNESS AND STRENGTH PROPERTIES IN 3D BRAIDED STRUCTURAL COMPOSITES

A.S.D. Wang and Amrita Kumar

Department of Mechanical Engineering and Mechanics
Drexel University, Philadelphia, PA 19104 USA

SUMMARY: Structural beam members of square and rectangular cross-sections are braided three-dimensionally with continuous yarns; these are then consolidated with an epoxy matrix. The consolidated composites are tested under 4-point bending load. Local and global deformation responses, including load-induced damage initiation and progression, are studied along with established analysis models.

Under 4-point bending, the load-deflection response of the composites exhibited a linearly elastic regime until a critical load is reached. At that load, spontaneous damages in the yarn-matrix interfaces occurred due to compression in the pure-bending zone. After the critical load, a slow progression of the damages ensued, precipitating a prolonged inelastic response regime.

In this paper, we examine the bending response of the beams up to and including the critical load. In particular, we examine the pertinent mechanisms that caused the sudden and proliferate damages in the yarn-matrix interfaces in the compressive zone. Based on the observed global failure modes and the local damage mechanisms, an interface shear-induced damage initiation criterion is proposed.

KEYWORDS: 3D-braided composites, 4-point bending, damage modes and mechanisms, yarn-matrix interface, local and global analyses, shear-induced damage initiation criterio

INTRODUCTION.

With a proper design of the yarn-carrier pattern and movements, 3D braiding can produce integrated fabric preforms that have the prescribed shape and the desired yarn architecture. After consolidation with a selected matrix material, the resulting fiber-reinforced composites can serve as load-carrying members with unusual properties. This particular fabrication technology has the potential to produce structural and other functional members in one integrated process.

In an on-going study, the authors have fabricated a series of 3D braided composites, which are intended as bending members suitable for use in helicopter structures. Specifically, preforms of solid square and rectangular cross-sections were braided using 12K E-glass yarns and 12K AS-4-G2 graphite yarns; these preforms were consolidated with the PR-500 epoxy resin following a resin-transfer-molding (RTM) procedure. The consolidated composites were tested under 4-point bending, where local and global load-response data were collected and analyzed

with the aid of pertinent mechanics models. The global load-deflection response exhibited a linearly elastic regime until a critical load is reached; at which point, spontaneous damages in the yarn-matrix interfaces occurred suddenly throughout the compression side of the pure-bending zone. The beam then underwent a slow damage progression as it continued to carry the applied load.

In what follows, we begin with a brief presentation on the pertinent yarn structures in the composites and the associated mechanics models for extracting their elastic properties; we then examine the mechanisms responsible for the observed sudden initiation of yarn-matrix interface failures at the critical load. With the aid of a series of photomicrographs taken from selected sections of the tested specimens, a shear-induced damage initiation criterion is proposed.

YARN STRUCTURES AND PROPERTY MODELS.

The cross-sectional shape of a braided preform is dictated by the particular yarn-carrier pattern laid on the braiding machine, while the general yarn architecture in the braided preform is determined by the yarn-carrier movement in each repetitive braiding cycle. Wang, et. al. [1] developed a "control space" approach to geometrically describe the yarn structure topology based on the yarn-carrier movement alone; the exact yarn structure in the matrix-consolidated composite can then be defined by it's external dimensions.

Braiding and Yarn Architecture.

The 3D braids studied in this paper were fabricated using the popular 4-step 1x1 braiding procedure [1]. For preforms of solid square or rectangular cross-sections, a typical physical look of the preform exterior is shown in Fig.1a. Note the distinct yarn patterns on the bounding surface and at the corner. However, as one cannot see the yarn structure inside the preform from the exterior, it can be determined using the "control space" method first outlined in [1]. Geometrically, the interior yarn structure is composed of two groups of parallel plates (labeled α and $-\alpha$ in Fig.1b) which crisscross at the angle 2α (α is measured from x-axis). The $\pm\alpha$-plates are formed by two groups of parallel yarns which crisscross with the angle 2γ (γ is measured from z-axis), as shown in Fig.1c. Normally, the $\pm\alpha$-plates are 90^{o} from each other; but this orthogonality could be somewhat distorted during to matrix consolidation. A linear scale, known as the braiding pitch h, represents the preform length braided during each cycle. Thus, the interior yarn structure is geometrically characterized by the three free parameters: α, γ and h.

Fig.1d is a section cut along the α-plane of a matrix-consolidated [11x11] E-glass specimen; the interior yarn structure compares fully with that sketched in Fig.1b and 1c.

The yarn structure on the bounding surface of the preform is a thin layer which is composed of two groups of parallel yarn segments as shown in Fig.1e; the crisscrossing yarn segments orient at the angle $\pm\theta_s$ with the braiding axis-z. Since there are two pairs of surfaces, so $\theta_s = \theta_x$ on surfaces in the x-axis and $\theta_s = \theta_y$ on surfaces in the y-axis. These are related to the interior angles α and γ [1]:

$$\tan\theta_x = (1/2)\tan\gamma\sin\alpha \quad \tan\theta_y = (1/2)\tan\gamma\cos\alpha \tag{1}$$

Similarly, at each of the four corners, a group of parallel yarn segments exists with the angle θ_c, see Fig.1f. Again, θ_c is related to the interior angles by:

$$\tan\theta_c = (1/6)\tan\alpha\tan\gamma \qquad (2)$$

Therefore, the cross-section of the preform can be treated as an area composed of the interior core, the four bounding surface layers and the four corner areas; each has its own unique yarn structure; and all can be characterized by the three free parameters α, γ and h.

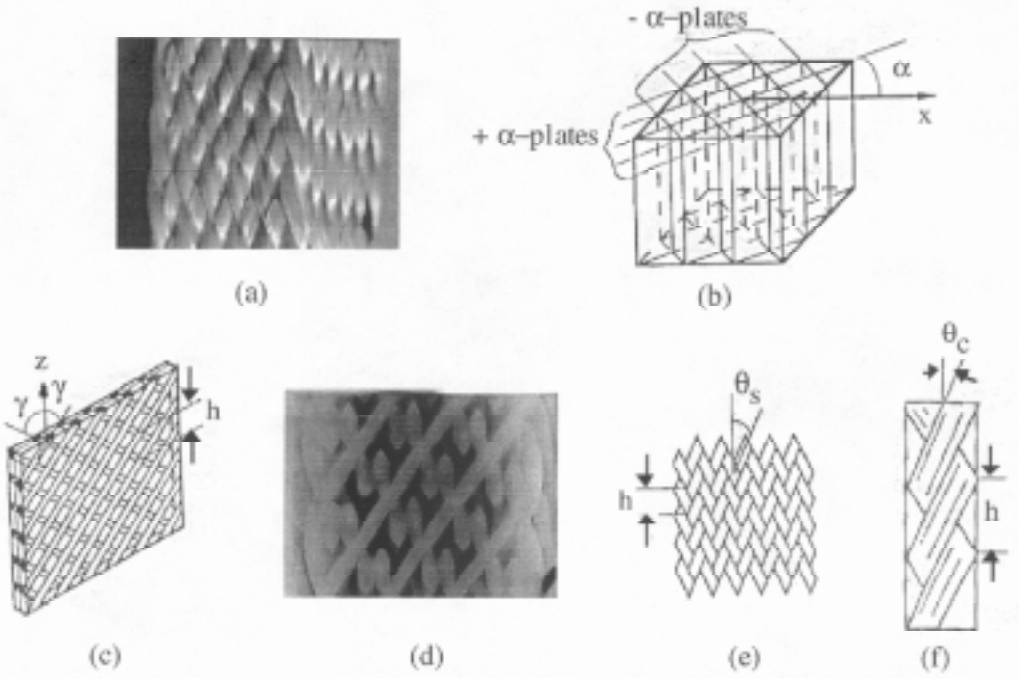

Fig. 1: (a) Exterior look of the braided specimen; (b) Interior intersecting plates structure; (c) Yarn topology of the α-plate; (d) An actual section of the α-plate; (e) Yarn topology of the braided surface; (f) Yarn topology of the braided corner.

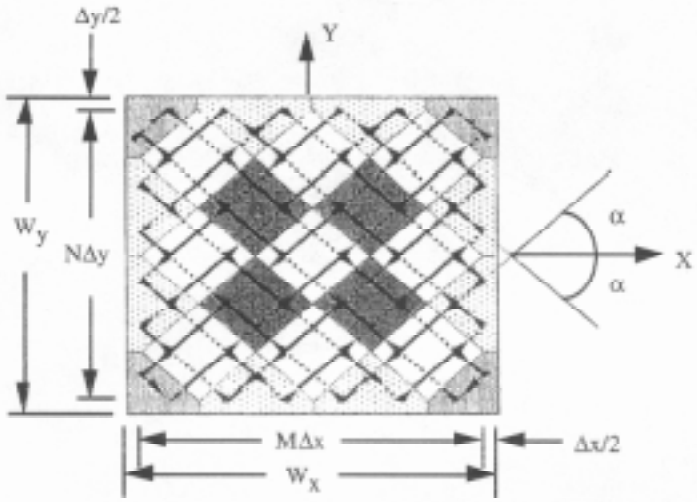

Fig. 2: Rectangular cross-section of the braided specimen, showing the geometric relationships among the interior, surface and corner areas.

Once the preform is consolidated, the braiding pitch h is measured from the exterior surface; so are the dimensions of the cross-section: W_x and W_y (as denoted in the sketched in Fig.2). Then, we can define:

$$\Delta x = W_x/(M+1) \qquad \Delta y = W_y/(N+1) \tag{3}$$

where M and N are, respectively, the number of yarn carriers in the x-track and the y-track of the original braiding setup (see [1]). It follows that the surface yarn angles are defined by:

$$\tan\theta_x = \Delta x/h \qquad \tan\theta_y = \Delta y/h \tag{4}$$

Consequently, the interior angles α and γ are found by (1) and the corner angle θ_c by (2).

Fiber Volume Fractions.

From Fig.2, we approximate the interior core area as $(N-1)(M-1)\Delta x\Delta y$; the corner area as $(3/2)\Delta x\Delta y$; the surface layer areas as $2(M-1)\Delta x\Delta y$ and $2(N-1)\Delta x\Delta y$ with the normal in x-axis and the y-axis, respectively. Then, the fiber volume fractions of the interior (V_i), the surface layers (V_x and V_y) and the corner area (V_c) can be determined as:

$$V_i=A_f/(\Delta x\Delta y\cos\gamma) \quad V_x=[A_f\sqrt{(h^2+\Delta x^2)}]/(h\Delta x\Delta y) \quad V_y=[A_f\sqrt{(h^2+\Delta y^2)}]/(h\Delta x\Delta y)$$
$$V_c = [2A_f\sqrt{(9h^2+\Delta x^2+\Delta y^2)}]/(9h\Delta x\Delta y) \tag{5}$$

where A_f is the solid cross-sectional area of the yarn.

Elastic Property Models.

The interior core is composed of the $\pm\alpha$ plates as explained before. One simple approach is to model the plates individually as a $[\pm\gamma]$ angle-plied laminate: the $[+\gamma]$ lamina is modeled first as an off-axis unidirectional (UD) ply with the fiber volume fraction V_i. Given the properties of the fiber and the matrix, the elastic constants of the UD ply can be found, for instance, by the model of Chamis [2] who considers the UD ply as a transversely isotropic material. In its principal coordinates (L,T,z), the five independent elastic constants of the UD ply are:

$$E_L=V_iE_f+(1-V_f)E_m \quad E_T(=E_z)=E_m/[1-(1-E_m/E_f)\sqrt{V_i}] \quad G_{LT}=G_m/[1-(1-G_m/G_f)\sqrt{V_i}]$$
$$\nu_{LT} = V_i\nu_f + (1-V_i)\nu_m \qquad \nu_{Tz} = [E_T/(2G_{LT}) -1] \tag{6}$$

The elastic constants of the $[\pm\gamma]$ angle-plied laminate can subsequently be found by a model such as given by Pagano [3] (the detail of which is omitted here); the elastic constants of the the $+\alpha$ or $-\alpha$ plate in the global coordinates (x,y,z) are found by a proper rotation about the z-axis. This last step furnishes the elastic constants for the interior core. Similarly, the surface layers can individually be modeled as cross-plied $[\pm\theta_s]$ laminates, using the proper fiber volume fraction V_s. As for the corners, they are modeled as an off-axis lamina with the off-axis angle θ_c

and the fiber volume fraction V_c. All constants must be properly transformed to the global co-ordinates (x,y,z) of the total specimen.

With the above, any global response of the composite under a given load can, at least logically, be forecasted by treating the beam as one composed of the core, surface layers and corner areas according to Fig.2. By the rule of mixture, the fiber volume content of the whole composite is:

$$V_{fc}=(V_iA_i+V_sA_s+V_cA_c)/A \tag{7}$$

with A_i, the core area; A_s the 4-surface layers area; and A_c the 4-corners area; $A=A_i+A_s+A_c$.

If the composite is under axial tension in the z-direction, for instance, the axial tensile modulus E_{tz} can be estimated as:

$$E_{tz} = (E_iA_i+E_sA_s+E_cA_c)/A \tag{8}$$

If the composite is under pure bending, the flexural modulus E_{fl} of the beam is:

$$E_{fl} = (E_iI_i+E_sI_s+E_cI_c)/I \tag{9}$$

where I_i, I_s, I_c are the area moments of inertia (with respect to the bending axis) of the core, surface and corner areas, respectively; and $I=I_i+I_s+I_c$.

EXPERIMENT AND ANALYSIS RESULTS.

Braiding, Preform Consolidation and Test Specimens.

Six preforms were braided by the 4-step 1x1 method; three of which were braided using the AS4-G2 12K graphite yarn with the respective braiding sizes of [11x11], [11x7] and [11x3]; and the other three were braided using a 12K E-glass yarn with the braiding sizes of [11x11], [8x8] and [4x4], respectively. The relevant properties of the yarns are:

Yarn	E_f (axial)	ν_f	A_f
Graphite	235.0 GPa	0.22	0.48 mm^2
E-glass	72.4 GPa	0.20	2.12 mm^2

These preforms were all RTM-processed with the PR-500 epoxy. The epoxy in the bulk has the base-line properties:

$$E_m=4.5 \text{ GPa} \quad \text{and} \quad \nu_m= 0.38.$$

The consolidated preforms were cut into 16 specimens suitable for 4-point bending test: the E-glass [11x11] and [8x8] each yielded two specimens of 305 mm in length; the E-glass [4x4] and all the graphite ones each yielded three specimens of 203 mm in length. For each of the 16 specimens, the braiding pitch h and the cross-section W_x,W_y were measured; the character-

izing parameters α and γ were computed using (1-4); the fiber volume fractions of the core, surface and corner areas are computed via (5). The average over 2 or 3 replicates in each case is listed below:

Specimen	W_x, mm	W_y, mm	h, mm	α	γ	V_i, %	V_s, %	V_c, %
GR. [11x11]	12.17	12.33	3.41	45.4^o	40.2^o	60	48	31
GR. [11x7]	14.61	7.90	3.81	39.1	39.5	52	42	27
GR. [11x3]	13.70	4.60	3.61	45.2	41.9	49	38	25
GL. [11x11]	26.63	23.51	8.30	41.5	35.6	60	50	32
GL. [8x8]	18.92	17.50	7.77	42.8	36.4	64	53	35
GL. [4x4]	11.07	10.50	6.36	43.5	43.8	63	48	31

In the above, it is noted that the computed $V_x \approx V_y \approx V_s$.

Each specimen was strain-gaged with a pair of 90^o-rosettes, one mounted on the tensile side and one on the compression side of the pure bending section; strains up to 1.5% were recorded in real-time. In addition, the maximum bending defection at the center of the beam was recorded up to 6 mm by a dial gage; and a CCTV camera (zoomed up to 200x) was placed near the center section of the beam during the entire test.

Global Responses.

The global response of the beam under loading is first studied from it's load-deflection (F-δ) curve recorded from the dial-gage. Fig.3a is the F-δ curve taken from a graphite [11x11] specimen and Fig.3b is one taken from an E-glass [11x11] specimen. The curves show a linear elastic regime up to the critical load (point A), whereby a sudden drop in the load occurs. Beyond this point, the beam continues to bear load and undergoes a prolonged inelastic deformation. From the CCTV video recording and other in-situ inspections, it was found that the beam is essentially damage-free in the linear regime. At the critical load, however, spontaneous damages suddenly occur in the compression zone of the entire pure bending length. This rather proliferate damage state is associated with the observed load-drop at point A.

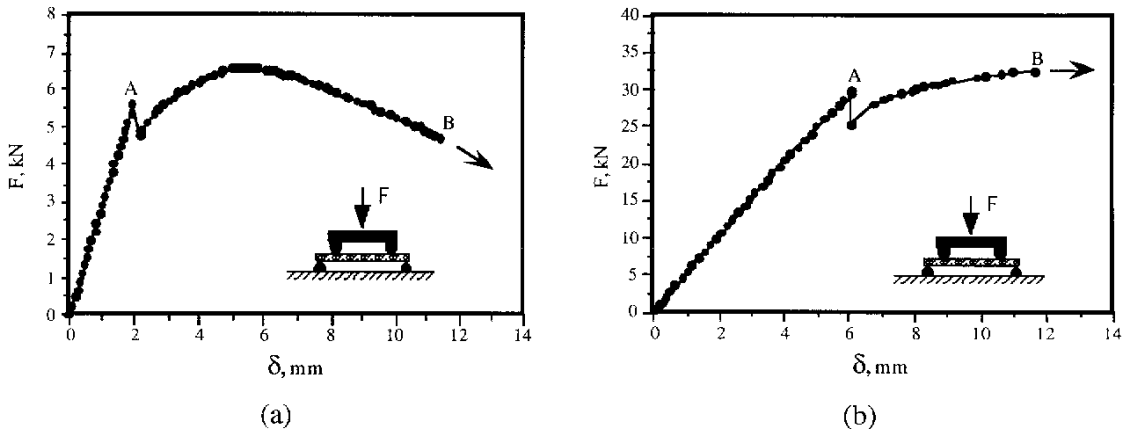

Fig.3: Load-deflection data for (a) graphite [11x11]; (b) E-glass [11x11].

In the linear response regime, the strain-gage readings provide a measure of the flexural strain ε_{fl} and the Poisson ratio ν_{zx} on the specimen's top and bottom surfaces. These measurements (average of 2 or 3 replicates) are listed below:

Specimen	$\varepsilon_{fl}(+)$, $\mu\varepsilon$/(N-m)	$\varepsilon_{fl}(-)$, $\mu\varepsilon$/(N-m)	$\nu_{zx}(+)$	$\nu_{zx}(-)$
GR. [11x11]	76.70	83.91	0.66	0.67
GR. [11x7]	179.00	165.86	0.80	0.80
GR. [11x3]	655.56	717.24	0.52	0.50
GL. [11x11]	14.31	15.35	0.43	0.40
GL. [8x8]	39.01	38.68	0.43	0.40
GL. [4x4]	234.83	232.37	0.46	0.46

In the above, $\mu\varepsilon = 10^{-6}$; the (+) sign refers to the tensile side and (-), the compressive side of the beam.

From the measured surface strain ε_{fl}/(N-m), the flexural modulus E_{fl} of the beam can be estimated by means of the mechanics models outlined previously, where the beam is composed of a core, four surface layers and four corner areas. Omitting the details in the calculation, we simply state that the surface stress corresponding to the surface strain ε_{fl} per unit applied moment (N-m) is:

$$\sigma_{fl}/(\text{N-m}) = W_y/2I \tag{10}$$

where $I=I_i+I_s+I_c$ as before. It then follows that $E_{fl} = \sigma_{fl}/\varepsilon_{fl}$.

Independently, the linear portion of the F-δ curves from the dial-gage reading also provides an estimate for the flexural modulus E_{fl}. At the same time, a theoretical estimate for E_{fl} is provided by (9). Thus, omitting the detailed calculation, a comparison between the experimental (average over 2-3 replicates) and the theoretical E_{fl} is given below:

Specimen	E_{fl}, strain-gage	E_{fl}, dial-gage	E_{fl}, theoretical
GR. [11x11]	41.3 GPa	37.2 GPa	38.0 GPa
GR. [11x7]	36.6	31.4	37.2
GR. [11x3]	30.5	23.7	29.8
GL. [11x11]	27.6	25.5	25.4
GL. [8x8]	26.7	26.0	27.1
GL. [4x4]	21.3	25.4	23.2

Note the relative range of agreement or disagreements in the above results.

Damage Modes and Mechanisms.

For each beam loaded to it's critical load, the compressive zone along the pure bending length suffers a sudden collapse. The associated damage modes can be explained from the photographs in Fig.4 below:

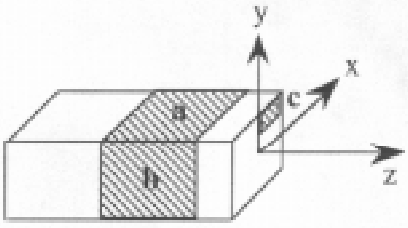

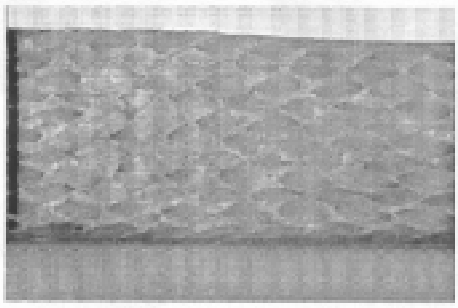

(a)

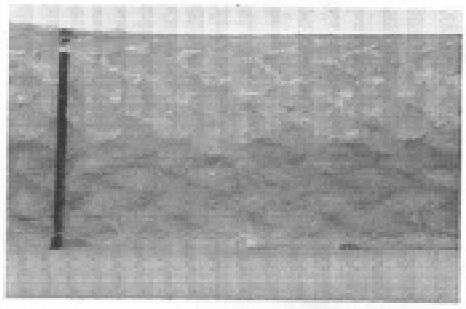

(b)

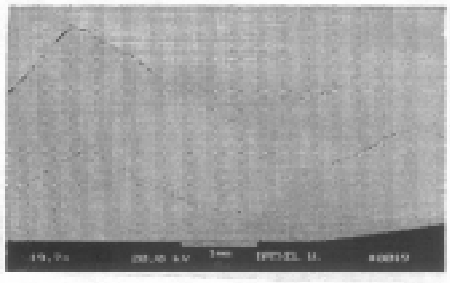

(c)

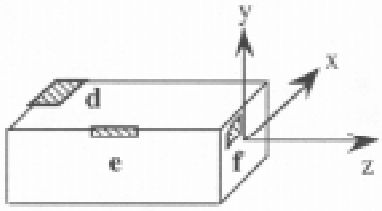

(d)

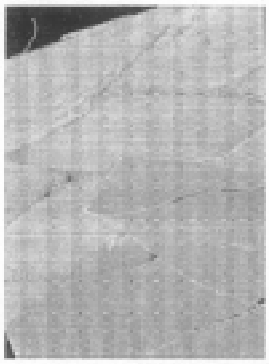

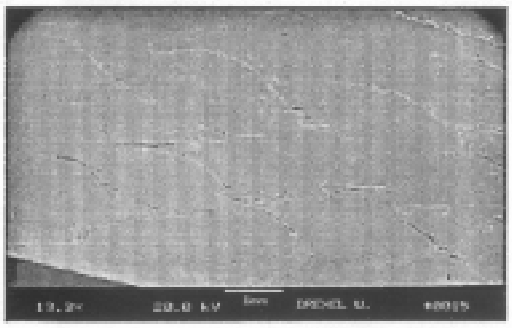

(e)

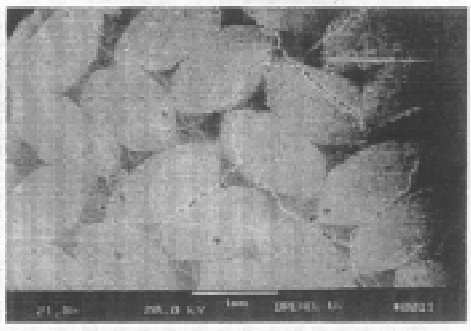

(f)

Fig. 4: Damage modes in tested specimens. (a), (b), (c): top, side and cross-sectional views of an E-glass [11x11] specimen; (d), (e), (f): top, side and cross-sectional views of a graphite [11x11].

Fig.4a is a video frame of the damaged surface taken from an E-glass specimen; note the sur face yarn segments in the pure bending length had all suffered inter-yarn debonding. Fig.4b i a video frame of the frontal surface of the beam; it is seen that the compression zone (top) ha suffered similar inter-yarn debonding while the tension zone (bottom) remained damage-free.

A magnified view (under the SEM) of the beam cross-section is shown in Fig.4c. Note th inter-yarn debonding in the compression zone; the debonding cracks follow the ±α-plates o the interior core. Recall that the ±α-plates intersect each other at ≈90^{o}; the observed debondin lines are zigzagging with ≈90^{o} angle.

Fig.4d, e and f are photographs taken from a graphite [11x11] specimen. Fig.4d shows th damaged compressive surface of the beam where a thin epoxy-grazed layer spalled, thus expos ing the damaged surface cells underneath; Fig.4d shows the damaged side surface in the com pression zone near the top of the beam, revealing the familiar inter-yarn debonding pattern; an Fig.4f shows the damaged beam cross-section with the zigzagging debonding cracks in the ±α plates. These observations indicate that the cells in the core area of the compression zone all fai due to shearing of the interfaces of the ±α-plates.

Inter-yarn Shear Debonding Criterion.

The premise of the criterion is that the ±α-plates, being angle-plied laminates, suffered interfac shear debonding. As illustrated in Fig.5, the α-plate is compressed axially with the strain ε_z; a lateral (tensile) strain $\nu_\alpha \varepsilon_z$ is induced due to Poisson effect. The in-plane shear strain in the α plate is estimated as:

$$\gamma_\alpha \approx (1+\nu_\alpha)\,\varepsilon_z \qquad (11)$$

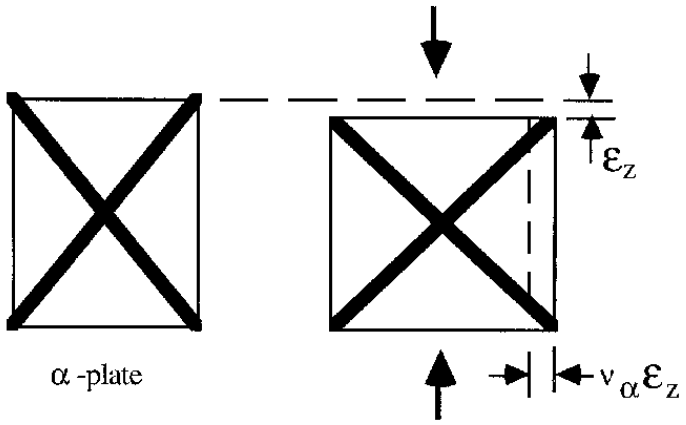

Fig.5: Local deformation of the α-plate under compression

Now, let ε_z be the bending strain of the interior core near the compression surface of the beam and it is computed by:

$$\varepsilon_z = (Md)/(E_{fl}I) \tag{12}$$

where M is the applied bending moment and $d \approx (W_y - \Delta y)/2$, the distance from the bending axis to the interior core near the compression surface.

At the critical load F_{cr} or the critical moment M_{cr}, the shear strain γ_α in the $\pm\alpha$-plates reaches the critical value $(\gamma_\alpha)_{cr}$. The latter is considered a material condition governing the onset of interface debonding of the $\pm\alpha$-plates. Since the moment is uniform in the pure bending length, the α-plates near the compressive surface collapse spontaneously. Calculation of the critical $(\gamma_\alpha)_{cr}$ for the specimens tested yields the following values (average over 2-3 replicates):

Specimen	M_{cr},N-m	$(\gamma_\alpha)_{cr}$ Range (Average)
GR. [11x11]	54.61	0.58-0.83% (0.68%)
GR. [11x7]	18.36	0.46-0.48% (0.47%)
GR. [11x3]	7.65	0.55-0.62% (0.58%)
GL. [11x11]	580.54	1.16-1.21% (1.20%)
GL. [8x8]	315.18	1.48-1.53% (1.51%)
GL. [4x4]	56.41	0.93-1.66% (1.33%)

Note that the $(\gamma_\alpha)_{cr}$ values do exhibit the sort of scatter normally found in fracture and strength properties in composites. If the nominal values of $(\gamma_\alpha)_{cr} = 0.6\%$ for the graphite and 1.35% for the E-glass specimens are used to predict the critical F_{cr} or M_{cr} in conjunction with (11-12), the predicted values would be fairly agreeable with the experimental values. Clearly, independent validations are necessary in order to ascertain the applicability of the proposed criterion in a wide range of loading conditions. Works related to the latter are currently in progress.

Acknowledgments: The results reported in this paper were obtained during the course of research supported by the U. S. Air Force Office of Scientific Research.

REFERENCES

1. Wang, Y. Q. and Wang, A. S. D., "On the Topological Yarn Structure in 3-D Rectangular and Tubular Braided Preforms", *J. Composites Science & Technology* , Vol. 51, 1994. p. 575.

2. Chamis, C. C., "Simplified Composite Micromechanics Equations for Hygral, Thermal and Mechanical Properties," *SAMPE Quart.* April, 1984. p.14.

3. Pagano, N. J., "Exact Moduli of Anisotropic Laminates," in *Mechanics of Composite Materials,* Ed. G. P. Sendeckyj. Academic Press, New York, 1974. p.23.

PREDICTION OF THE COMPRESSION-AFTER-IMPACT STRENGTH OF 2-D BRAIDED COMPOSITES

Paul J. Falzon[1] , Israel Herszberg[2]

[1] Cooperative Research Centre for Advanced Composite Structures Ltd. (CRC-ACS), 506 Lorimer St., Fishermens Bend, Victoria, 3207, Australia.
[2] Sir Lawrence Wackett Centre for Aerospace Design Technology, Royal Melbourne Institute of Technology, GPO Box 2476V, Melbourne, Victoria, 3001, Australia.

SUMMARY: This paper presents an analysis used to predict the compression-after-impact (CAI) strength of 2-D braided carbon/epoxy composites. A closed-form solution, developed to approximate the stress distribution of an orthotropic composite laminate with an elliptical hole loaded in compression, was applied to estimate the stress distribution in the impact damaged braided composite under compression loading. Then, using the semi-empirical point stress failure model, the CAI strength was predicted. Comparisons made between predicted and measured CAI strengths revealed good agreement, with differences less than 10% in most cases. The use of such models to predict failure of composites made from unidirectional prepreg is of little advantage because the characteristic length depends on the ply orientation, hole size and hole aspect ratio. A major finding from this work is that for braided composites, one characteristic length (determined from experiment) was applicable for a range of damage geometries and braid architectures.

KEYWORDS: braided composites, CAI strength, characteristic length, impact

INTRODUCTION

Fibre reinforced composite materials have been successfully employed as structural materials for various applications. These composites have shown superior performance over metals in applications requiring high strength/stiffness, excellent fatigue and corrosion resistance, as well as low weight. However, a major concern with composite materials is their susceptibility to impact damage. Unlike metallic materials, composites can suffer a significant reduction in mechanical performance due to impact damage. Methods which have been used to address this problem include the application of toughened resins and the introduction of through-thickness fibre reinforcement. Well established and highly automated processes developed for the textile industry, such as braiding [1], have the capability to fabricate near net-shape preforms of the desired fibre orientations and necessary through-thickness reinforcement. Combined with a liquid moulding technique, there is the potential to produce reliable low-cost, high-quality components with improved damage tolerance.

To investigate the damage resistance and tolerance of braided composites, a series of low-velocity drop-weight impact tests were performed on 2-D braided carbon/epoxy laminates [2]. Damaged specimens were then loaded in compression to measure their compression-after-impact (CAI) strength [2]. This paper presents an analysis used to predict the CAI strength of 2-D braided carbon/epoxy composites measured from these tests.

Impact damage introduced into a composite laminate results in a significant reduction in stiffness in the damaged area, causing load to be redistributed to the undamaged region. This redistribution of load results in a stress concentration, similar to that expected of a panel with an open hole. In fact, the CAI damage behaviour found in the braided specimens was similar to that observed in composite panels with holes loaded in compression. A closed-form solution, developed to approximate the stress distribution of an orthotropic composite laminate with an elliptical hole loaded in compression, was applied to estimate the stress distribution in the impact damaged braided composite under compression loading. Then, using the semi-empirical point stress and average stress failure models, the CAI strength was predicted.

MATERIALS

A series of four different braid architectures have been considered in this study. Compression specimens were prepared from panels manufactured from 2-D triaxially braided preforms. The specimens tested are summarised in Table 1. The braided preforms were manufactured from 12K AS4 carbon fibre tows using a 72 carrier Wardwell braider at the Center for Composite Materials, University of Delaware. They were manufactured as a tubular preform then cut open to form a flat preform. The specimens were consolidated using Resin Transfer Moulding (RTM) with Ciba Geigy RTM6 epoxy resin system. Note that specimen types BR-45a and BR-45b have identical fibre orientations, although BR-45b was a tighter braid.

Table 1: Summary of composite materials used in this study

Laminate I.D.	Nominal Thick. (mm)	Fibre Volume Fraction (%)	Laminate Construction	No. of plies	Percentage of 0° fibres
BR-45a	2.1	58	0°/±45° braid	5	26.1
BR-45b	2.1	58	0°/±45° braid	4	26.1
BR-60	2.1	58	0°/±60° braid	4	20.0
BR-LA	2.1	58	0°/±45° braid	3	41.4

EXPERIMENT

A series of low-velocity drop-weight impact tests were performed on 2-D braided carbon/epoxy composites followed by compression tests on the damaged specimens. A brief description of the tests methods and findings is given in this section. Detailed results have been published elsewhere by Falzon et al. [2].

Impact Test

Impact testing of low to medium impact energy levels (up to 7 J/mm), were carried out on specimens measuring 92 x 117 mm using an instrumented drop weight test rig [2]. The specimens were clamped using a support frame with a test window measuring 80 x 90 mm. The impactor, which had a hemispherical steel tup 12.5 mm in diameter and variable weights ranging between 200 and 1200 grams, was dropped from heights of up to 2 m to impact the specimens at various energy levels. Only one impact was performed at each energy level.

Impacted specimens were then ultrasonically C-scanned to quantify the extent of damage introduced into the specimens due to the impact event.

Ultrasonic C-scans revealed that post-impact damage zones of all specimens exhibited a quasi-circular, almost elliptical, shape for all energy levels considered (Fig. 1). Visual inspection of the impacted specimens revealed that the sustained damage was due primarily to the delamination of plies. On the impacted surface of the braided specimens, at energy levels exceeding 3 J/mm, there was evidence of compressive cracking which took the form of an indentation. The opposite face of the specimens exhibited fibre break-out or tensile splitting. Crack propagation tended to follow fibre directions and stop at fibre tow cross-over points.

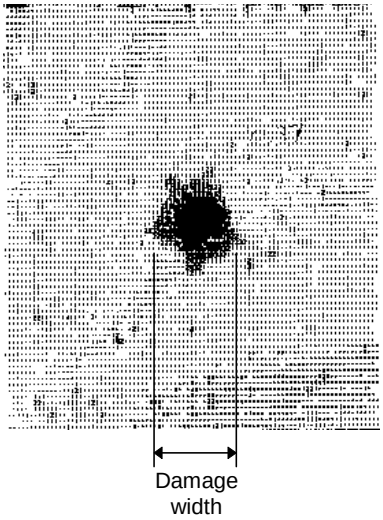

Fig. 1: Typical C-scans of an impacted 2-D braided composite (Impact energy ≈ 4.5 J/mm)

Compression-After-Impact Test

The test rig used to measure the compression strengths of the impacted specimens [2] comprises three separate components - lower and upper clamping blocks between which the specimen is set for testing, a pair of anti-buckling face plates with a 40 mm diameter central window to ensure the impact damage zone is not restricted from propagating during the test, and a die press with a ball-and-cup arrangement to ensure the specimen is loaded axially. The specimens were loaded at a rate of 0.5 mm/min and the tests were terminated at the first onset of failure. Failure was defined as the first sudden drop in load.

In all the specimens tested, failure initiated at the impacted region and progressed in a direction transverse to the loading direction, with little or no damage growth in the load direction. The indentation of the impact site and the area of fibre breakage reduced the stiffness across the damage area causing load to be redistributed into the undamaged region, thus increasing the stresses around the damage site. Global failure of the damaged specimens occurred as a result of the kink band mechanism, and not from sub-laminate buckling as is found in unidirectional prepreg materials. This redistribution of load at the impact site results in a stress concentration, similar to that expected of a panel with an open hole. In fact, the CAI damage behaviour found in the braided specimens was similar to that observed in composite panels with holes loaded in compression. Soutis and Curtis [3] also found the CAI damage pattern in laminated composites to be similar to that observed in laminated plates

with open holes loaded in compression. The variation of CAI strength with damage width for all the specimens tested can be seen in Figures 4 to 7. Damage width is defined in Fig. 1.

MODELLING APPROACH

Impact damage introduced into a composite laminate results in a significant reduction in stiffness in the damaged area, resulting in a complex stress distribution surrounding the damaged zone. The reduction in compression strength is a result of this stress concentration. Attempts at predicting the reduced strength or CAI strength encompasses models of varying degrees of sophistication. Statistical methods have been proposed by Guild et al. [4] and Prichard and Hogg [5] which relate CAI strength with damage width using linear regression. Soutis and Curtis [3] applied their cohesive zone model, developed initially to predict notched compressive strengths, to estimate the CAI strength of some prepreg composites. Others [6] have modelled the damaged area as a soft inclusion. One approach proposed by Xiong and Poon [7] involved modelling the damaged area as a soft elliptical inclusion. Then using a complex variable method outlined by Lekhnitskii [8], the in-plane stresses can be calculated. The CAI strength of the laminates is then predicted using an empirical failure criterion.

To predict the CAI strength of the braided composites, a similar approach was adopted. The difference being rather than modelling the damage as a soft inclusion, it was conservatively assumed that the damage area behaved as an elliptical opening or hole. That is, the material in the damaged area does not provide any load carrying capacity. As mentioned earlier, the CAI damage behaviour found in the braided specimens was similar to that observed in composite panels with holes loaded in compression. The accuracy of this assumption is dependent on the extent of impact damage. The assumption is more accurate in cases where impact damage causes fibre fracture or penetration compared with events where impact loading causes internal delaminations with only barely visible impact damage. The idealisation of an impacted braided composite panel is illustrated in Fig. 2. The dimensions of the elliptical holes (*2a* and *2b*) used in the analysis are measured from ultrasonic C-scan results, like that shown in Fig. 1.

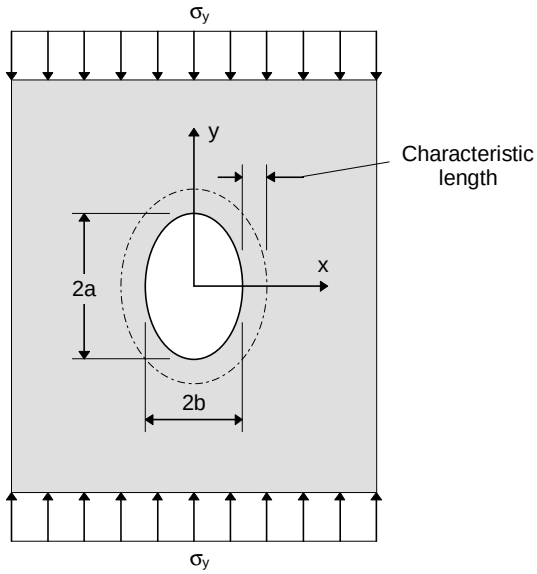

Fig. 2: Idealised impact damage in a composite panel represented as an elliptical hole

The exact solution of the stress distribution of an infinite orthotropic composite laminate with an elliptical hole has been presented by Lekhnitskii [8]. This solution was approximated by Tan [9] to express the stress distribution in a simple closed-form solution. Using this closed-form solution with appropriate failure criteria, the CAI strength can be predicted. Two criteria used in this work include the point stress and average stress failure models, developed by Whitney and Nuismer [10,11].

Point Stress Failure Model

The point stress failure model assumes that failure would occur when the stress at a characteristic length, b_0, ahead of the damage first reaches the undamaged compressive strength of the laminate, σ_0. Using this criterion along with the approximate stress distribution of an infinite orthotropic symmetric laminate containing an elliptical opening [11], then the CAI strength, σ_{CAI}, may be expressed as:

$$\sigma_{CAI} = \sigma_0 \left\{ 1 + \frac{1}{\sqrt{\xi_1^{-2} - 1 + \lambda^2}\left(\xi_1^{-1} + \sqrt{\xi_1^{-2} - 1 + \lambda^2}\right)} + \frac{\lambda^2(1+\lambda)\left(\xi_1^{-1} + 2\sqrt{\xi_1^{-2} - 1 + \lambda^2}\right)}{\left(\xi_1^{-2} - 1 + \lambda^2\right)^{3/2}\left(\xi_1^{-1} + \sqrt{\xi_1^{-2} - 1 + \lambda^2}\right)^2} - \frac{\lambda^7}{2}\left(K_T - 1 - \frac{2}{\lambda}\right) \times \left[\frac{5\xi_1^{-1}}{\left(\xi_1^{-2} - 1 + \lambda^2\right)^{7/2}} - \frac{7\lambda^2\xi_1^{-1}}{\left(\xi_1^{-2} - 1 + \lambda^2\right)^{9/2}} \right] \right\}^{-1} \quad (1)$$

where,

$$\lambda = b/a \quad (2)$$

$$\xi_1 = a/(a + b_0) \quad (3)$$

$$K_T = K_T^{\infty} \Bigg/ \left[\frac{\lambda^2}{(1-\lambda)^2} + \frac{(1-2\lambda)}{(1-\lambda)^2}\sqrt{1 + (\lambda^2 - 1)(2a/W)^2} - \frac{\lambda^2}{(1-\lambda)} \frac{(2a/W)^2}{\sqrt{1 + (\lambda^2 - 1)(2a/W)^2}} \right.$$
$$\left. + \frac{\lambda^7}{2}\left(\frac{2a}{W}\right)^6 \left(K_T^{\infty} - 1 - \frac{2}{\lambda}\right) \left\{ \left[1 + (\lambda^2 - 1)\left(\frac{2a}{W}\right)^2 \right]^{-5/2} - \left(\frac{2a}{W}\right)^2 \left[1 + (\lambda^2 - 1)\left(\frac{2a}{W}\right)^2 \right]^{-7/2} \right\} \right] \quad (4)$$

Where λ denotes the hole aspect ratio of the major and minor diameters, $2a$ and $2b$ respectively; b_0 is a characteristic length to be determined empirically; W is the width of the panel; K_T is the stress concentration factor for a finite width panel; and K_T^{∞} is the stress concentration factor for an infinitely wide panel, which is expressed as follows [11]:

$$K_T^{\infty} = 1 + \frac{1}{\lambda}\sqrt{2\left(\sqrt{\frac{E_y}{E_x}} - \nu_{xy}\right) + \frac{E_y}{G_{xy}}} \quad (5)$$

where E_x and E_y are the laminate in-plane stiffnesses in the respective x and y (loading) directions respectively, ν_{xy} is the in-plane Poisson's ratio and G_{xy} is the in-plane shear modulus.

Average Stress Failure Model

The average stress failure model assumes that failure would occur when the averaged laminate stress over a characteristic length, a_0, away from the edge of the damage first reaches the undamaged compressive strength of the laminate. Using this criterion along with the approximate stress distribution of an infinite orthotropic symmetric laminate containing an elliptical opening [11], then σ_{CAI} may be expressed as:

$$\sigma_{CAI} = \sigma_0 \left\{ \frac{\lambda^2}{(1-\lambda)^2}\xi_2^{-1} + \frac{(1-2\lambda)}{(1-\lambda)^2}\sqrt{\xi_2^{-2}-1+\lambda^2} - \frac{\lambda^2}{(1-\lambda)\sqrt{\xi_2^{-2}-1+\lambda^2}} + \frac{\lambda^7}{2}\left(K_T - 1 - \frac{2}{\lambda}\right) \times \left[\frac{1}{\left(\xi_2^{-2}-1+\lambda^2\right)^{5/2}} - \frac{\lambda^2}{\left(\xi_2^{-2}-1+\lambda^2\right)^{7/2}} \right] \right\}^{-1} \quad (6)$$

where,

$$\xi_2 = a/(a+a_0) \quad (7)$$

λ and K_T have been defined in Eqns 2 and 4, respectively, and a_0 is a characteristic length to be determined empirically.

RESULTS AND DISCUSSION

Theoretical predictions of the CAI strength were made using damage dimensions obtained from C-scans along with the elastic properties for each of the braid architectures tested. The critical parameter in the calculations is the characteristic length, which was determined empirically for the two stress models. Fig. 3 shows the variation of characteristic length with damage width. The characteristic lengths were determined so as to obtain an exact correlation between the predicted and measured CAI strength for each data point. It can be seen that there is a linear relationship between the characteristic length and the damage width for the average stress model, where as the characteristic length is independent of damage width for the point stress model.

The criteria used in selecting the characteristic length included keeping it independent of damage size, damage aspect ratio and braid architecture, while maintaining good correlation between measured and predicted CAI strengths. Although the correlation could be further improved by using different characteristic lengths for different braid architectures, it is the authors opinion that a constant characteristic length value, which may sacrifice some accuracy, is of considerably more use. Establishing a constant characteristic length removes the necessity to perform tests to determine a new characteristic length for a new braid architecture. Using this philosophy, only the point stress model was used to predict the CAI strength of braided composites. Using the values shown in Fig. 3, an average characteristic length of 5.31 mm with a standard deviation of 1.52 mm was calculated.

Comparisons between the measured CAI strengths and those predicted by the point stress model are shown in Figures 4 to 7. Predictions for three characteristic lengths were calculated, based on the average characteristic length (b_0 = 5.31 mm) and the upper and lower deviations (b_0 = 6.83 mm and b_0 = 3.79 mm respectively). As can be seen, the point stress model

adequately predicts the CAI strength using the average characteristic length, where in most cases the differences are less than 10%. There are only a few cases where discrepancies exceed 15%. The upper and lower deviations illustrate that the point stress analysis is not very sensitive to the characteristic length and is a major reason why a constant characteristic length is applicable.

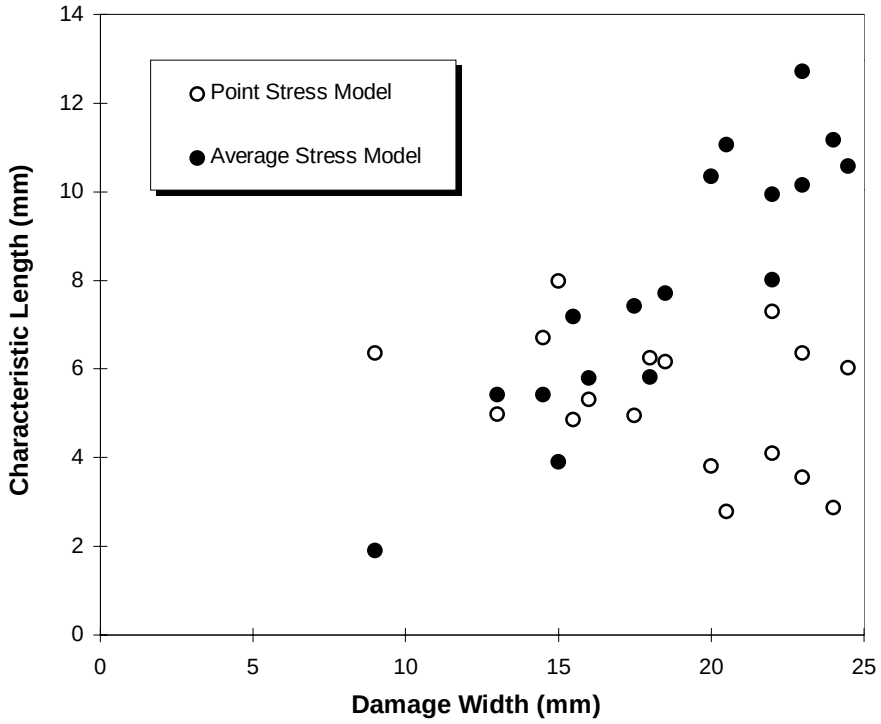

Fig. 3: Variation of characteristic length with damage width for all specimens

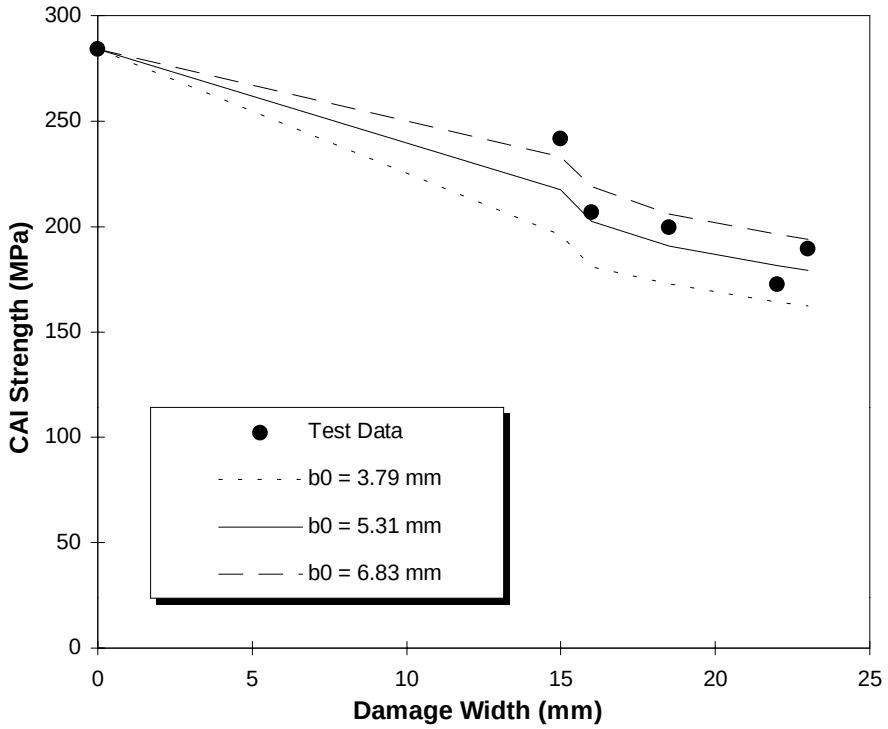

Fig. 4: Comparison of predicted and measured CAI strengths for BR-45a specimens

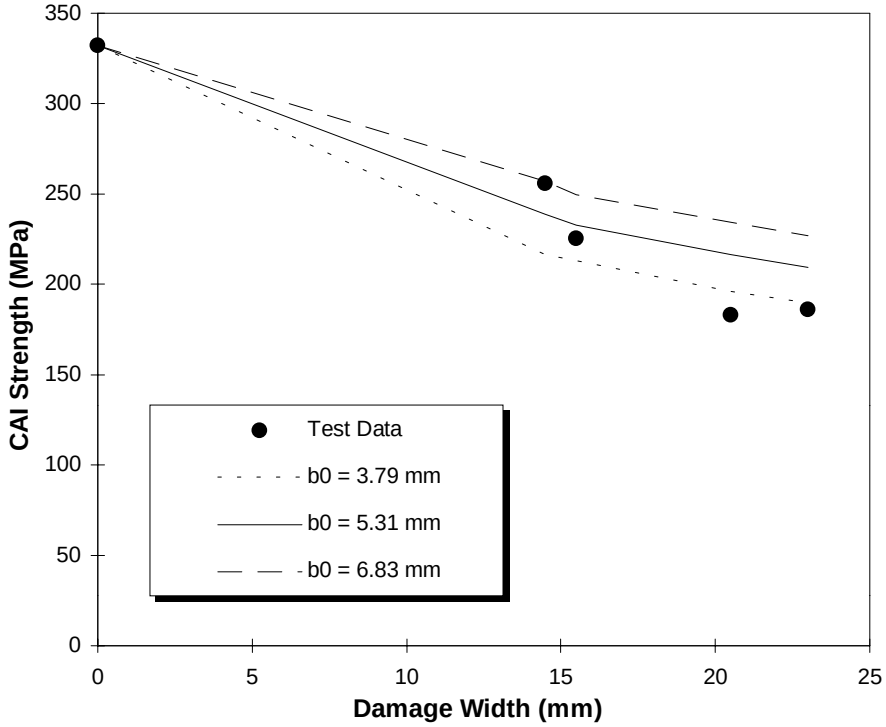

Fig. 5: Comparison of predicted and measured CAI strengths for BR-45b specimens

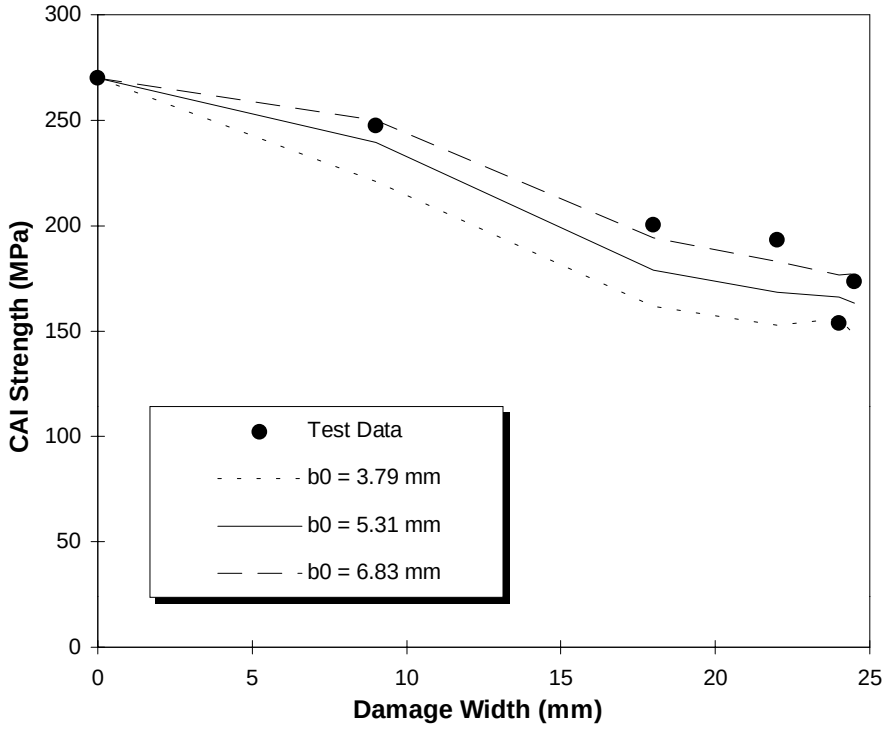

Fig. 6: Comparison of predicted and measured CAI strengths for BR-60 specimens

Although further testing would be required to substantiate the findings, the fact that a common characteristic length could be used to predict the CAI strength of different braid architectures of a limited number of damage geometries, is a major finding. This is not the case with prepreg composites. Naik [12], in his compression strength modelling of prepreg

composite panels with holes, used different characteristic dimensions for a range of stacking sequences and lay-ups. While Tan et al. [13], who performed tension tests on carbon/epoxy prepreg panels with elliptical holes, shows there is a need to change the characteristic length as the size of the hole increases. Tan et al. [13] empirically formulated relationships between characteristic length, hole size, and hole aspect ratio to improve the correlation between predicted and measured notch strengths. One reason for the need to vary the characteristic length for prepreg composites is the change in failure mechanism which occurs for different lay-ups and hole geometries. Fortunately for the braided specimens studied there was no apparent need to vary the characteristic length. This is due to the non-sensitivity of the analysis as explained earlier, and may physically be due to the fact that there was no change in failure mechanism, or that the range of damage sizes modelled was not large enough to reveal any dependencies on damage geometry.

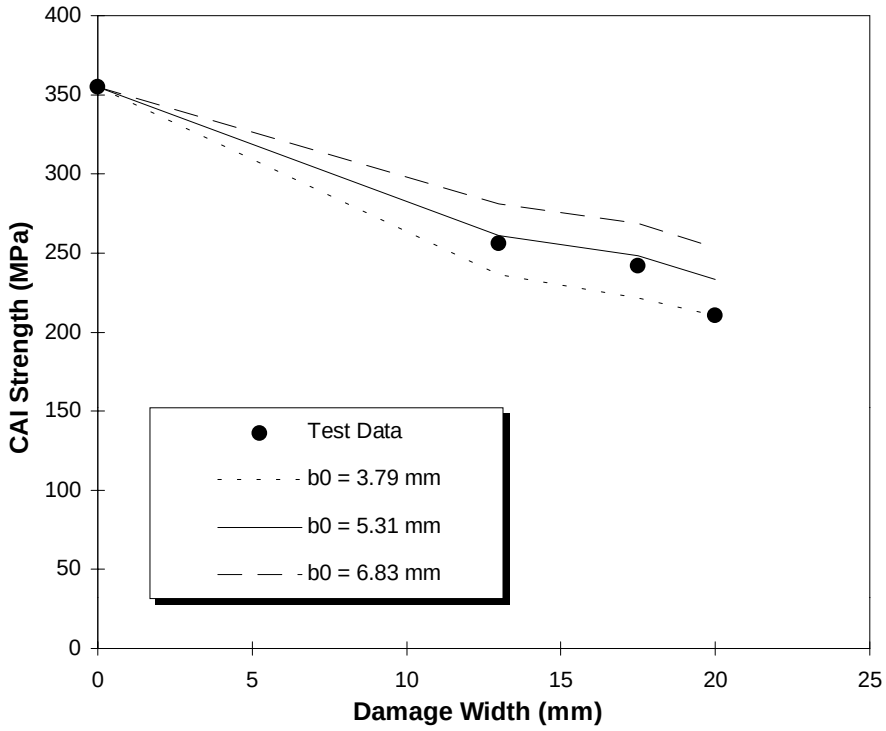

Fig. 7: Comparison of predicted and measured CAI strengths for BR-LA specimens

CONCLUSIONS

A method was proposed to predict the CAI strength of 2-D braided carbon/epoxy composites. The model involves idealising the impact damage in the braided composite as an elliptical hole. Using the semi-empirical point stress failure criterion, which necessitates the use of a characteristic length, the CAI strength was predicted for a range of architectures investigated in this study. Comparisons made between predicted and measured CAI strengths revealed good agreement, with differences less than 10% in most cases.

A major finding from this work, which would need to be substantiated with further testing, is that for braided composites, one characteristic length (determined from experiment) was applicable for the range of damage geometries and braid architectures investigated in this study. This is not the case with composites made from unidirectional prepreg, where the characteristic length depends on the ply orientation, hole size and hole aspect ratio.

REFERENCES

1. Falzon, P.J., Herszberg, I. and Karbhari, V.M., "Design and Manufacture of 2-D Braided Preforms for Aerospace Structural Applications", *Proceedings of PICAST-2/AAC-6*, Melbourne, Australia, March 1995, pp.539-544.

2. Falzon, P.J., Herszberg, I., Bannister, M.K. and Leong, K.H., "Compression and Compression-After-Impact Properties of 2-D Braided Carbon/Epoxy Composites", *Australasian Congress on Applied Mechanics*, Australia, February 21-23, 1996, pp.297-302.

3. Soutis, C. and Curtis, P.T., "Prediction of the Post-Impact Compressive Strength of CFRP Laminated Composites", *Composites Science & Technology*, Vol. 56, 1996, pp.677-684.

4. Guild, F.J., Hogg, P.J. and Prichard, J.C., "A Model for the Reduction in Compression Strength of Continuous Fibre Composites After Impact Damage", *Composites*, Vol. 24, No. 4, 1993, pp.333-339.

5. Prichard, J.C. and Hogg, P.J., "The Role of Impact Damage in Post-Impact Compression Testing", *Composites*, Vol. 21, No. 6, 1990, pp.503-511.

6. Dost, E.F., Ilcewicz, L.B. and Gosse, J.H., "Sublaminate Stability Based Modelling of Impact Damage Composite Laminates", *Proceedings of the American Society for Composites 3rd Conference*, U.S.A., September 25-29, 1988, Seattle, USA, pp.354-363.

7. Xiong, Y. and Poon, C., "Failure Prediction of Composite Laminates Containing Impact Damage", National Research Council Canada, *LTR-ST-1898*, September 1992.

8. Lekhnitskii, S.G., *Anisotropic Plates*, Gordon and Breach Science Publishers, New York, 1968.

9. Tan, S.C., "Laminated Composites Containing and Elliptical Opening. I. Approximate Stress Analysis and Fracture Models", *Journal of Composite Materials*, Vol. 21, 1987, pp.925-948.

10. Whitney, J.M. and Nuismer, R.J., "Stress Fracture Criteria for Laminated Composites Containing Stress Concentrations", *Journal of Composite Materials*, Vol. 8, 1974, pp.253-265.

11. Nuismer, R.J. and Whitney, J.M., "Uniaxial Failure of Composite Laminates Containing Stress Concentrations", *Fracture Mechanics of Composites, ASTM STP 593*, 1975, pp.117-142.

12. Naik, N., *Woven Fabric Composites*, Technomic Publishing Co., Philadelphia, 1996.

13. Tan, S.C., "Laminated Composites Containing and Elliptical Opening. II. Experiment and Model Modification", *Journal of Composite Materials*, Vol. 21, 1987, pp.949-968.

A STUDY ON THE MICROSTRUCTURE OF THREE-DIMENSIONAL BRAIDS

L . Chen, X. M.Tao and C. L.Choy

The Hong Kong Polytechnic University, Hung Hom, Hong Kong

SUMMARY: This paper describes a study of the microstructure of three-dimensional braids produced by a four-step method. An analytical approach is employed in conjunction with experimental investigations to establish the relationship between the braid structure and braiding parameters. Based on microscopic observations of yarn orientation and distortion, we divide a three-dimensional braid structure into three representative regions, i.e., the interior, surface and corner, and establish three types of microstructural unit-cell models for the three regions, respectively. An equivalent cross sectional area has been defined by averaging the effect of yarn localised distortion, based on which, the yarn packing factor has been examined at the jamming conditions. Expressions for the fibre volume fractions in the three regions and the whole braided composite have been derived accordingly. Based on these expressions, the total fibre volume fractions in several braided composites have been calculated and found to be in good agreement with experimental results.

KEYWORDS: three-dimensional braids, microstructure, braided composites

INTRODUCTION

The properties and performance of a three-dimensional braided composite depend primarily on the microstructure of braided preform and the mechanical and physical properties of the constituent materials. In the past, a considerable amount of effort has been placed on the understanding of the microstructure of braids. Ko [1] first identified a unit cell representing the fiber architecture of rectangular braided performs, which was a cuboid containing four diagonally intersecting yarns. Later Du and Ko [2] re-examined the earlier treatment and found that the unit cell was oversimplified and incorrect. Li et al [3] reported an experimental study of the internal structure of braids and identified a unit cell for braided composites, based on the assumptions that yarns were straight rods with a circular cross-section and there were no lateral deformations at the yarn cross-over points. Li et al also observed that the structure on the surface of the braid preforms was different from that in the interior. Subsequent studies conducted by Lei [4] and Kosher [5] revealed that the corners were unique in the preform structure. Recently, Wang [6] presented an analysis of the topological structure in three-dimensional braided preforms and defined three distinctive types of unit cells in the preform interior, surface and corner regions, respectively.

To date, the topological structure of three-dimensional braids, which is determined by the braiding sequence and number of yarns, can generally be understood on the basis of previous models. However, experimental evidence [7] showed that the mechanical performance of 3D braided composites deteriorated greatly by cutting the edge off the preform. Moreover, the mechanical properties of the braided composites were affected by the

yarn bundle size. These phenomena cannot be explained by existing models. Therefore, there is a need to use more realistic geometrical unit cells, which combine the braid topology with the yarn configuration, in order to successfully predict the mechanical properties of the three-dimensional braided composites. This paper presents a study of the microstructure of three-dimensional braids fabricated by a four-step method. An analytical approach is employed in conjunction with experimental investigations to establish the relationship between the braid structure and the braiding parameters.

MICROSCOPIC OBSERVATIONS

Eight samples of three dimensional braid preforms were made by the four-step method. The specifications for the braids are given in Table 1. Carbon fibre T300-12K, an epoxy resin TED-85 and a curing agent, acid annydride-70, were used to fabricate the composite samples. The curing conditions were: 130^{o}C for 2 hours, then 150^{o}C for 1 hour, followed by 160^{o}C for 8 hours and finally 180^{o}C for 3 hours. The final dimensions of the composite samples were 250 x 25 x 6 (mm^{3}). Samples of the braid preforms were embedded in a resin, Nej-o-lac, such that the cutting of the braids became easy and the yarns could be carefully removed from the braids without alternating their original shapes. The rectangular braids were cut at 45^{o} to its sides. Optical and electron scanning microscopes were used to examine the yarn surface and the interior of braid preforms.

Table 1: Specifications of samples

Samples	D_y(mm)	m ×n	α	h(mm)	γ	θ	β
HKT3002-1	0.757	22 ×6	19.0	5.22	26.0	10.8	7.3
HKT3003-1	0.757	22 ×6	21.0	4.70	28.5	12.0	8.1
HKT3004-1	0.757	22 ×6	21.0	4.73	28.5	12.0	8.1
HKT3005-1	0.757	22 ×6	21.5	4.60	29.1	12.3	8.3
HKT3002-2	0.757	19 ×5	40.0	2.57	49.9	25.0	17.3
HKT3003-2	0.757	19 ×5	40.0	2.59	49.9	25.0	17.3
HKT3004-2	0.757	19 ×5	40.0	2.60	49.9	25.0	17.3
HKT3005-2	0.757	19 ×5	39.0	2.64	48.9	24,2	16.7

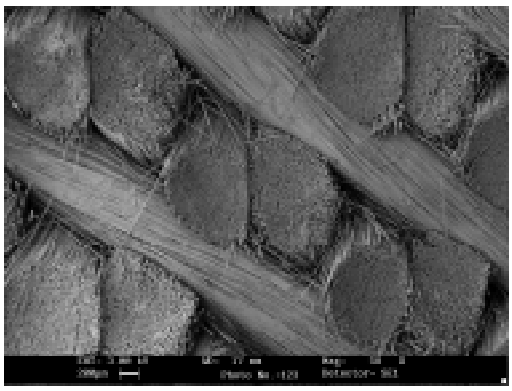

Fig. 1: SEM micrograph of the interior of a four-step braid interior

Figure 1 is a micrograph of the cross-section in the braiding interior cut at a 45^{o} angle with the braid surface. It shows that the axes of the multifilament yarns remain straight in spite of

having lateral deformation at the yarn surface. Moreover, there is an additional yarn tortuosity caused by the braiding process and this tortuosity changes direction according to the braider movement. Microscopic evidence further reveals that large localized distortions of the yarn occur along the yarn, as shown by the configuration of the yarn drawn from the braid interior in Figure 2. This indicates that the helical traces have been formed on the yarn surface and the fibers are no longer parallel to the yarn axes due to the lateral compression of adjacent yarns.

BASIC ASSUMPTIONS

In our analysis of the geometrical structure of a braid, the following assumptions have been made:

1. The cross-section of the multifilament braiding yarns is elliptical with major and minor radii, a and b, respectively;
2. In all the three regions, the braiding yarns have a uniform cross sectional area; thus a uniform packing factor is assumed along the length after jamming;
3. The braiding process is quite stable so that the braid structure is uniform, at least over a certain length;
4. All yarns in the braid structure have the same size and flexibility.

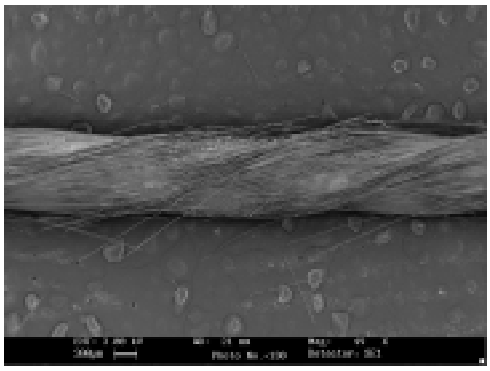

Fig. 2: SEM micrograph of a braiding yarn in braid interior

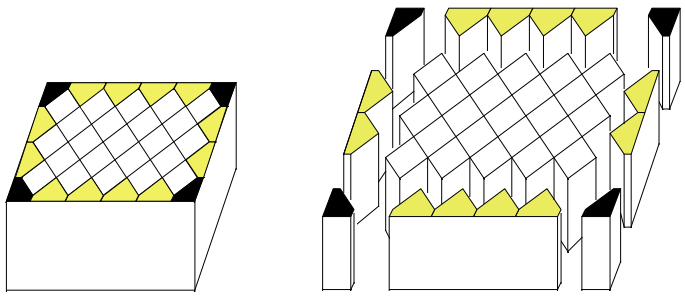

(a) *(b)*

Fig. 3: Schematic illustration of the interior, surface and corner of a braid

In the braid interior, every yarn is subjected to lateral compression of six adjacent yarns with different directions. In our present analysis, an equivalent area of yarn cross section is defined as the average of yarn cross sectional area along the length in a unit cell. Let Ω represents the area of the cross-section of the elliptical yarns, and $s(l)$ the area of the cross-section of the distorted yarn along the yarn length, then, Ω is defined as:

$$\Omega = \frac{1}{L}\int_0^L s(l)dl \tag{1}$$

where L is the length of a yarn in a unit-cell.

THREE TYPES OF UNIT CELLS

Selection of Control Volumes

As shown in Figure 3, a braid has a skin-core structure and can be divided into there regions: interior, surface and corner regions. Each of these three regions is built up by an identical unit cell, respectively, though the exact manner of composition depends on the initial yarn carrier pattern. The traces of yarn carriers in the interior, on the surface and the corner have their unique features, which lead to the different yarn structures in the three regions. These regions must be treated separately.

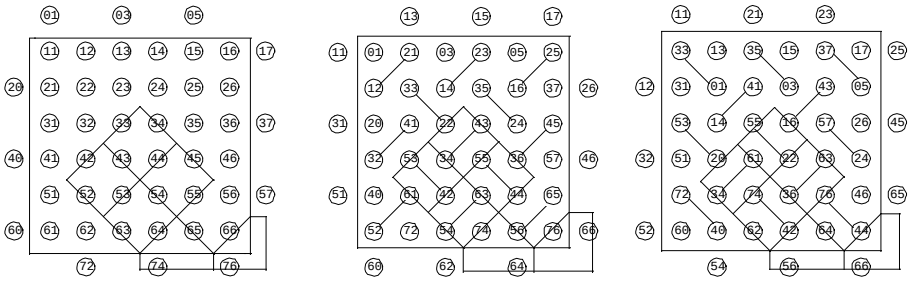

(a) Original *(b) Second step* *(c) Fourth step*

Fig. 4: The movement of carriers during a machine cycle [6×6:(1-1)]

Although the braiding process is achieved by translational permutations of column and row tracks, these permutations can be combined into a rotational operation as indicated by the diagonal lines in Figures 4b and 4c. Considering the carrier positions after every 2 and 4 steps, the carriers connected by these lines exchange their positions by rotation. These continuous rotational exchanges result in the repeatability of the topological structure in the braid interior. In our analysis, a control volume method is employed to describe the topological structure of a three-dimensional braid. The control volume for the interior is defined by the cuboid enclosed by carriers 33, 34, 45, 55, 64, 63, 52 and 42 in the original pattern and two parallel planes separated by the height of four braiding steps. There are twelve yarns in this control volume. The control volume for the surface is represented by a cylinder with the bottom area enclosed by carriers 64, 65 and 74 while the corner one is enclosed by carriers 66 and 76.

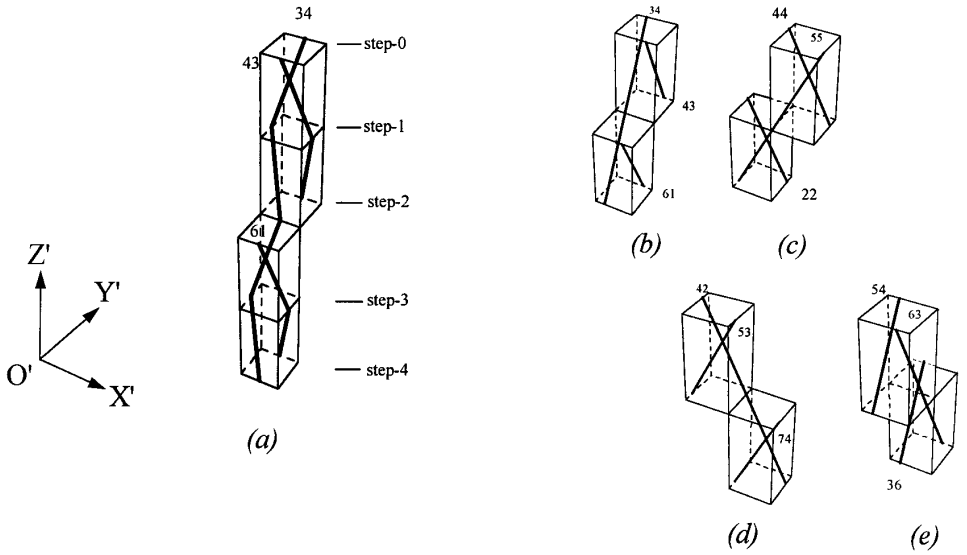

Fig. 5: Yarn paths in braid interior during four braiding steps

Braid Interior Region

In the interior control volume, carriers 34, 55, 63 and 42 remain in the control volume after the 4-step machine cycle while the others move out. The spatial traces of the yarn carried by carriers 34, 43 and 61 during the four braiding steps are shown in Figure 5a , where the lines connecting the yarn carriers represent the yarn axes. Note that carriers 34, 43 exchange their respective positions after step 2 and carriers 34, 61 do so after step 4. Thus the yarn follows a zigzag trace before compacting. However, when a uniform yarn-compacting action is applied by yarn jamming, the yarns will be straightened and repositioned in the space as shown in Figure 5b. Figures 5b-5e illustrate the configuration of the axes of all the twelve yarns in the four sections of the control volume. Assembling the four sections, the unit-cell of the braid interior can be obtained as shown in Figure 6a.

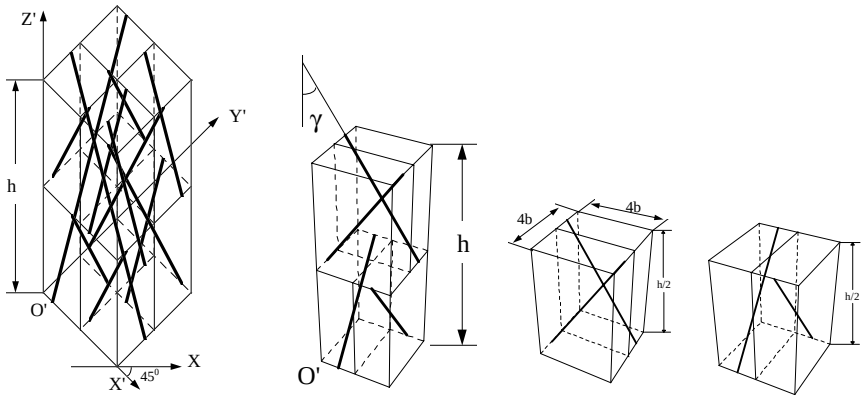

(a) (b) (c) d)

Fig. 6: A unit-cell (a), a quarter unit-cell (b) and two sub-cells (c and d) in the braid interior

According to the orientation angles, the braid interior comprises four groups of yarns, and intersecting two sets of parallel planes of a cuboid. The control volume can be further divided

into eight sub-cuboids as shown in Figure 6. Among the eight sub-cuboids, there are only two non-identical sub-cuboids which can be re-assembled into the control olume in an alternating manner. The axes of the twelve yarns inside the control volume or unit cell are all straight and do not intersect each other in the space. The distance between the two yarn axes in a sub-cell is 2b where b is the minor radius of the yarn.

Braid Surface Region

As shown in Figure 4a, the control volume for the braid surface is defined by the cylinder with a bottom area including carriers 64, 65 and 74 in the original pattern and two parallel planes with a separation equal to the height of four braiding steps. The yarn carrier movements in the control volume are shown in Figure 7a. As an example, let us follow the movement of carrier 64: it enters the surface control volume from the interior at step 0, moves one position along +X- direction at step 1, and then shifts one position along -Y-direction at step 2, holds its position at step 3, moves one position along +Y-direction at step 4, then leaves the control volume and returns to the interior. Similar movements also occur for carriers 74 and 56. After jamming, the yarns will be repositioned, as shown in Figure 7b.

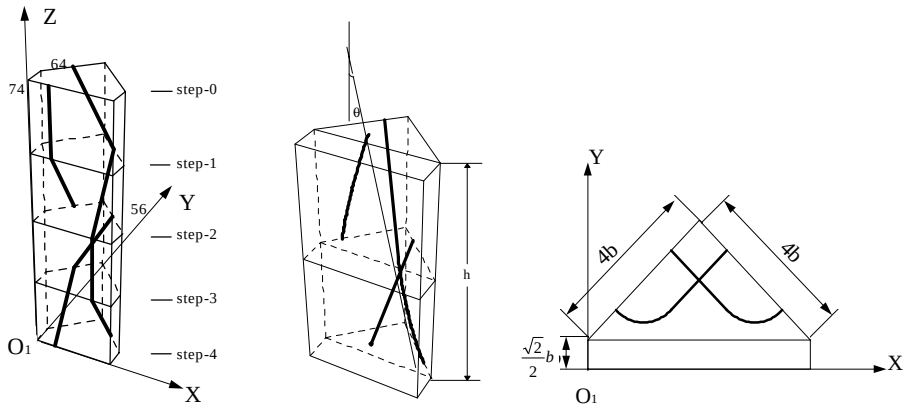

(a) *(b)* *(c)*

Fig. 7: The yarn trace and the unit-cell on the braid surface

The yarn axes are spatial curves comprising a straight line and a segment of a helix, not just straight lines. For these two distinct segments, different orientation angles are required. In a surface unit-cell, there are three yarns divided into two groups.

Braid Corner Region

At the corners of a braid, a control volume is defined by the cylinder with bottom area including carriers 66 and 76 (as shown in Figure 4a) and two parallel planes separated by the length of four braiding steps. For instance, carrier 66 comes into the control volume at step 0 from the interior, shifts its position from step 1 to step 6 according to the braiding process and re-enters the interior at step 7. Upon yarn jamming, the yarns adjust to the positions shown in Figure 8b, where the helical yarn is inclined to the braid axis by the corner braiding angle β. Thus, as shown in Figures 8c and 8d, a unit-cell at the braid corner can be defined, such that it has a height of h and two helical yarns do not intersect each other's axis.

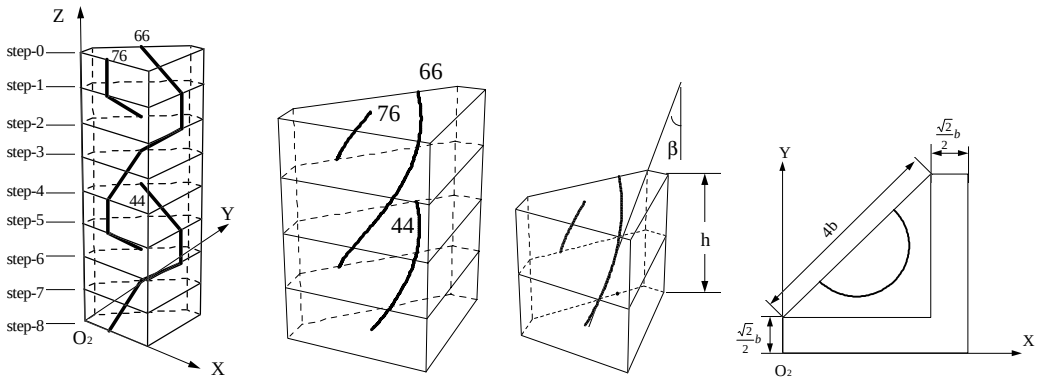

(a) (b) (c) (d)

Fig. 8: Yarn traces at the corner and the corner unit-cell : (a) Yarn traces during 8 steps of braiding; (b) Yarn traces after jamming; (c) and (d) The unit cell for the corner region.

Relationship Between the Three Regions

Suppose one carrier in the interior occupies one unit volume. For a m x n braid, the volumes of the regions in term of the unit volume, as can be seen from Figures 9, are given in Table 2:

Table 2: Volumes occupied by the interior, surface and corner regions

Units	M and N are Even Numbers	M or N is not an Even Number
Surface	3(m + n - 4) / 2	3(m + n -2) / 2
Corner	4	2
Interior	mn - m - n + 2	mn -m -n + 1
Total	mn + (m + n) / 2	mn + (m + n) / 2

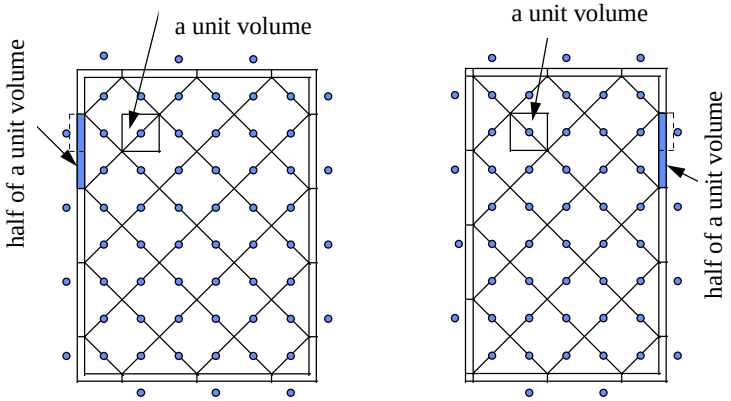

(a) 8×6 pattern (b) 8×5 pattern

Fig. 9: Volume occupied by the interior, surface and corner regions

Thus for the braids with m and n both even, the volume proportions of the regions in the whole structure can be calculated as:

$$V_i = \frac{2(m-1)(n-1)+2}{2mn+m+n}$$
$$V_s = \frac{3(m+n-4)}{2mn+m+n} \qquad (2)$$
$$V_c = \frac{8}{2mn+m+n}$$

Similarly, for the case where either m or n is an odd number , the volume proportions of the regions are given by:

$$V_i = \frac{2(m-1)(n-1)}{2mn+m+n}$$
$$V_s = \frac{3(m+n-2)}{2mn+m+n} \qquad (3)$$
$$V_c = \frac{4}{2mn+m+n}$$

YARN PACKING FACTOR

The yarn packing factor can be defined as:

$$\varepsilon = \frac{\pi D_y^2}{4\Omega} = \frac{D_y^2}{4ab} \qquad (4)$$

where D_y is the equivalent diameter of a solid braiding yarn, which is determined by the yarn tex and fibre density.

From the triangle marked in Figure 11b, we have the following geometric relation:

$$h = 8b / \tan\gamma \qquad (5)$$

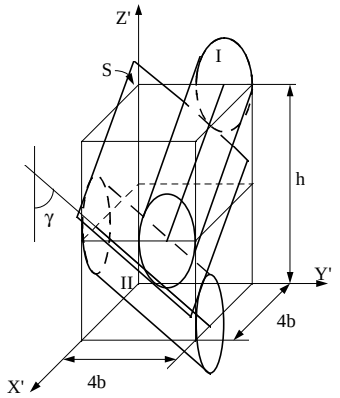

Fig. 10: The geometry of the jamming condition

Upon yarn jamming, the yarns contact each other as shown in Figure 10. The equations for the inclined elliptical-cylinder surface of two braiding yarns, Y1 and Y2, in the given coordinate system are:

$$\text{Y1:}\quad [(x-8b)\cos\gamma + z\sin\gamma]^2 / a^2 + (y-3b)^2 / b^2 = 1 \tag{6}$$

$$\text{Y2:}\quad (x-3b)^2 / b^2 + [(y-4b)\cos\gamma + z\sin\gamma]^2 / a^2 = 1 \tag{7}$$

The plane, S, which is parallel to the elliptical-cylinders, Y1 and Y2, can be described by the following expression:

$$Ax + By + Cz + D = 0 \tag{8}$$

The orientation vector of the axis of the elliptical-cylinder Y1 is {-sinγ, 0, cosγ}. The plane S is parallel to Y1, thus the following condition is satisfied:

$$A = C / \tan\gamma \tag{9}$$

The orientation vector of the axis of the elliptical-cylinder Y2 is {0, -sinγ, cosγ}. The plane S is parallel to Y2; similarly, we have:

$$B = C / \tan\gamma \tag{10}$$

Dividing Equation 8 by C/tanγ yields :

$$x + y + z\tan\gamma + D' = 0 \tag{11}$$

Since the plane S is a tangent plane to Y1 defined by Equation 6, then, by letting x=4b, and solving Equations 6 and 11, there must be one and only one real solution:

$$D' = -11b + \sqrt{a^2 + b^2\cos^2\gamma} / \cos\gamma \tag{12}$$

A similar relation exists for Y2. Plane S is a tangent plane to Y2 described by Equation 7. Letting y=4b and solving Equations 7 and 11 leads to

$$D' = -7b - \sqrt{a^2 + b^2\cos^2\gamma} / \cos\gamma \tag{13}$$

By equating Equations 12 and 13, we obtain:

$$a = b\sqrt{3}\cos\gamma \tag{14}$$

Substituting Equations 5 and 14 into Equation 4, the expression for the yarn-packing factor ε can be rewritten as follows:

$$\varepsilon = 16\sqrt{3}D_y^2 / (3h^2\tan^2\gamma\cos\gamma) = 16\sqrt{3} / (3h_d^2\tan^2\gamma\cos\gamma) \tag{15}$$

where h_d=h/D_y, is a normalized pitch length.

FIBRE VOLUME FRACTION

With reference to Figure 6, the fiber volume fraction in the braid interior can then be obtained by multiplying the yarn volume fraction by the yarn-packing factor.

$$V_{if} = \frac{Y_i}{U_i}\varepsilon = \frac{2\pi}{h_d^2 \tan^2\gamma \cos\gamma} \tag{16}$$

From Figure 7, the fiber volume fraction in a braid surface can be estimated as:

$$V_{sf} = \frac{Y_s}{U_s}\varepsilon = \frac{4\pi}{3h_d^2 \tan^2\gamma}\left(\sqrt{1+\frac{1}{4}\tan^2\gamma}+\frac{1}{\cos\theta}\right) \tag{17}$$

From Figure 8, the fiber volume fraction at a braid corner can be given as:

$$V_{cf} = \frac{Y_c}{U_c}\varepsilon = \frac{3\pi}{h_d^2 \tan^2\gamma \cos\beta} \tag{18}$$

Finally, the total fiber volume fraction in a braid can be written as:

$$V_f = V_i V_{if} + V_s V_{sf} + V_c V_{cf} \tag{19}$$

Table 3 lists the calculated and experimental values of fibre volume fraction of several braid composites. Good agreement between the theoretical predictions (TV_f) and experimental data (EV_f) of the total fibre volume fraction has been obtained. The calculated values also indicate that the fibre volume fractions on the surface (TV_s) and at the corners (TV_c) are higher than that in interior (TV_i) when the braiding angle is small (20^o). However this trend reverses when the braiding angle is larger (40^o).

Table 3: Comparison between the theoretical and experimental values of fibre volume fraction

Samples	EV_f(%)	TV_f(%)	TV_i(%)	TV_s(%)	TV_c(%)	V_i	V_s	V_c	ε(%)
HKT3002-1	65.42	66.06	61.98	76.06	84.27	0.726	0.247	0.027	91.13
HKT3003-1	68.70	66.70	62.93	75.91	83.80	0.726	0.247	0.027	92.52
HKT3004-1	68.33	65.86	62.14	74.95	82.74	0.726	0.247	0.027	91.35
HKT3005-1	69.07	66.43	62.77	75.36	83.12	0.726	0.247	0.027	92.28
HKT3002-2	61.09	59.59	60.07	58.48	60.81	0.673	0.308	0.019	88.32
HKT3003-2	60.35	58.68	59.15	57.58	59.87	0.673	0.308	0.019	86.96
HKT3004-2	59.97	58.23	58.70	57.14	59.41	0.673	0.308	0.019	86.30
HKT3005-2	61.18	59.66	59.89	59.05	61.68	0.673	0.308	0.019	88.05

CONCLUSION

In this paper, an analysis of the microstructure of three-dimensional braids produced by a four- step method has been presented. Three distinct unit cells have been defined for the three regions of a 4-step braid made from multifilament yarns. According to the yarn orientation angles, the braid interior has been represented by a unit cell comprising twelve straight yarns, intersecting two sets of parallel planes of the cuboid unit cell which can be further divided into eight sub-cells. Among the eight sub-cells, there are only two non-identical cells which can be re-assembled into the unit cell in an alternating manner. In the surface unit cell, the braiding yarn axes are spatial curves comprising a straight line and a segment of a helix. For these two distinct segments, different orientation angles have been determined. The unit-cell at the braid corner has been defined, as having two helical yarns which do not intersect each other's axis.

In addition, an equivalent cross sectional area was defined by averaging the effect of yarn localized distortion, based on which, the yarn packing factor has been examined at the jamming conditions. Expressions for the fibre volume fractions in the three regions and the whole braided composite have been derived accordingly. Based on these expressions, the total fiber volume fraction in several braided composites have been calculated and found to be in good agreement with experimental results.

ACKNOWLEDGMENT

One of us (Mr. Chen L.) wishes to acknowledge the financial support received from the Hong Kong Polytechnic University for the work carried out in this project.

REFERENCES

1. Ko,F.K., "Three dimensional fabrics for composites-an introduction to the magnaweave structure", *Proc. ICCM-4, Japan Soc. Composite Material,* Tokyo, Japan, 1982, p.1609.
2. Du,G.W. & Ko,F.K., "Unit cell geometry of 3-D braided structure", *Proc.Am. Soc.Com.*, 1991.
3. W.Li, M.Hammad and A.El-Shiekh, "Structural analysis of 3-D braided preforms for composites", *J. Text. Inst.*, 1990, 81 No 40, p.491-514.
4. Lei,C., Cai,Y.j. & Ko,F.K., "Finite element analysis of 3-D braided composite", *In Adv. in Eng.Software and Workstations*, Elsevier Science, 1992, p.187-194.
5. T.D.Kostar and T-W.Chou, "Design and automated fabrication of 3-D braided preforms for advanced structural composites", *Computer Aided Design in Composite Material Technology III* , Elsevier Science, 1992, p.63-78.
6. Y.Q.Wang & A.S.D.Wang, "On the topological yarn structure of 3-D rectangular and tubular braided preforms", *Composites Science and Technology,* 51(1994), p.575-586.
7. F.K Ko, "Three Dimensional fabrics for composites", in "*Textile Structural Composites*", Elsevier, 1989.

THE EFFECT OF ARCHITECTURE ON THE MECHANICAL PROPERTIES OF KNITTED COMPOSITES

K.O. Anwar [1], P.J. Callus [1], K.H. Leong [2], J. I. Curiskis [3] & I. Herszberg [1]

[1] Sir Lawrence Wackett Centre for Aerospace Design and Technology,
Royal Melbourne Institute of Technology, GPO Box 2476V, Melbourne, VIC 3001, Australia.
[2] Cooperative Research Centre for Advanced Composite Structures Ltd.,
506 Lorimer Street, Fishermens Bend, VIC 3207, Australia.
[3] Department of Textile Technology, University of New South Wales,
Sydney, NSW 2052, Australia.

SUMMARY: The aim of this paper is to investigate the tensile and compression properties, and failure mechanisms, of three different Milano ribs and one 1x1 rib weft-knit architecture. These fabrics were impregnated with vinyl ester resin to make thin, flat panels using the resin transfer moulding technique. The fibre volume fractions of the composites were maintained constant at approximately 53%. Tensile and compression specimens were cut in both the wale and the course directions and then tested to failure. Fractography was performed using a stereo optical microscope to establish the locus of failure. The wale-tested specimens were superior in tensile properties to the course-tested specimens. Tensile properties were greatly affected by the loop structure of the knitted fabrics, whereas compression properties were almost independent of test direction, loop length and loop density. It was observed that tensile fracture occurred in the planes of lowest fibre content for both specimens tested in the wale as well as in the course directions. This coincided with fibre fractures at legs of the loops for the wale-tested specimens and at needle-sinker loops for the couse-tested specimens.

KEYWORDS: knit, rib, milano, wale, course, loop length, loop density, anisotropy.

INTRODUCTION

Considerable research has been directed at understanding the behaviour of composites made using textile manufacturing techniques in an attempt to gain industrial acceptance. One of these textile techniques, knitting, has been used, to produce structural preforms that provide the required fibre orientations and through-the-thickness fibre reinforcement. The near net shape manufacture of knitted preforms and their excellent drapability hold promise to be used in the composite manufacturing industry as cost effective and mechanically efficient structural components. Unfortunately, there is insufficient understanding of the effect of knitted textile reinforcements on the mechanical behaviour of structural composites.

Marvin [1] is believed to be the earliest worker to have studied the tensile properties of knitted glass/phenolic laminates with a view to replacing the metallic nose cones of subsonic and supersonic missiles. Rudd *et al.* [2] investigated plain weft-knit glass/polyester laminates both experimentally and analytically. Attempts were made to improve the stiffness of the laminates by using cross-floated knitted fabric. Verpoest and Dendauw [3] showed

experimentally that plain weft knit glass/epoxy laminates were anisotropic and dependent upon the knit architecture, fibre volume fraction and degree of fabric stretching. Fatigue properties of weft knitted composites were investigated by Chou *et al.* [4]. Wu *et al.* [5] showed that knitted structures greatly affect the in-plane anisotropic nature, tensile strength, and modulus of basic warp-knit fabric-reinforced composites. Ramakrishna and Hull [6] studied experimentally the tensile properties of 1x1 rib weft-knit carbon-fibre-fabric/epoxy laminates with and without inlay fibres. Significant increases in the modulus and tensile strength were achieved by inserting unidirectional tows of carbon fibres in the course direction. More recently, Herszberg and colleagues [7-10] studied experimentally the mechanical performance of weft-knit E glass/epoxy composites using the Milano rib and half-Milano architecture. The tensile properties of the half-Milano were found to be inferior to those of the Milano rib and extremely anisotropic.

For this study, an epoxy-based vinyl ester resin was used. Derakane 411C-50 resin was chosen because it has an exceptionally low resin viscosity and has been specially designed for the resin transfer moulding (RTM) process. Four different weft knit structures were studied. The effects of knit architecture, fibre orientation, loop lengths and loop density (course/cm and wale/cm) on the tensile and compression properties were discussed. Failure mechanisms were examined based on fractographic studies using a stereo optical microscope.

EXPERIMENTAL TECHNIQUES

Three different Milano rib (M1, M3, M9) and one 1x1 rib (R3) weft-knit architectures were produced from E-glass yarns by combining 2x68 tex on an 8-gauge V-bed knitting machine. Components of weft-knit loop structure are shown in Fig. 1. Rib knit fabrics contain loops in alternate groups of wales meshed on one side of the fabric with the loops in the remaining wales meshed on the opposite side. Each wale contains either all plain stitches or all purl or back stitches. In the 1x1 rib structure, every second stitch alternates from front to back. Fig. 2(a) shows a schematic presentation of 1x1 rib structure. In the Milano, shown in Fig. 2(b), each complete repeat of the structure consists of three courses - two rows of plain or back loops, knitted on two separate sets of needles, which are held together by a row of 1x1 rib course. Since the face and the back surface are identical in construction, the resultant fabric is completely balanced.

Thin flat composite panels (405 mm x 540 mm) were fabricated by the resin transfer moulding technique using Derakane 411C-50 vinyl ester resin. Resin injection was performed with 210 KPa at the inlet and 100 KPa vacuum at the outlet. The panels were postcured at 120^{o}C for an hour to optimise resin properties. In order to maintain fairly constant specimen thickness of 3 mm and fibre volume fraction of approximately 53%, the number of layers of each preform were 6, 6, 6 and 10 in types R3, M3, M1, and M9 respectively. Panel details are summarised in Table 1.

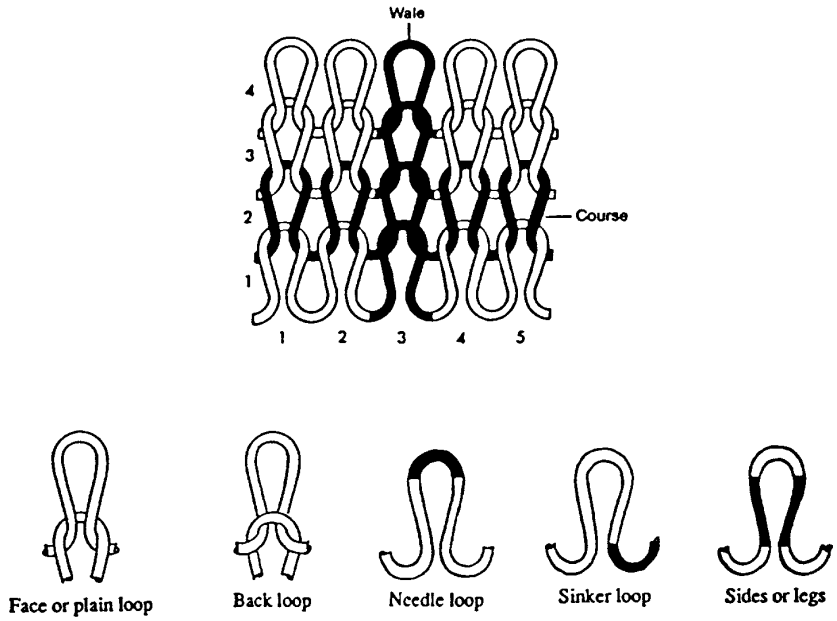

Fig. 1: Components of weft-knitted loop structure

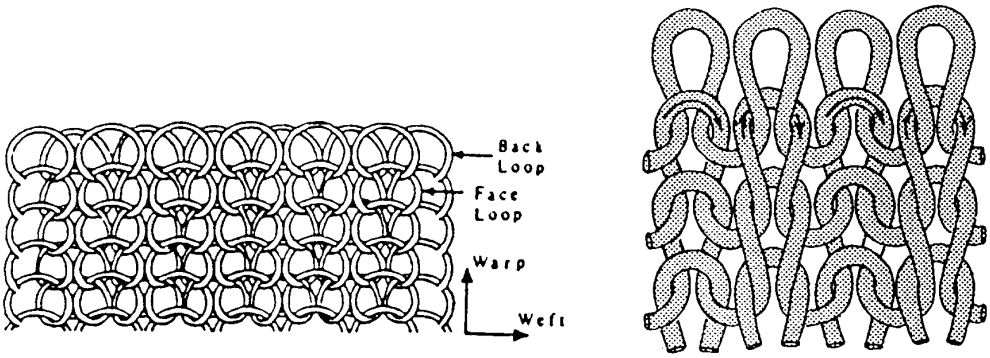

(a)

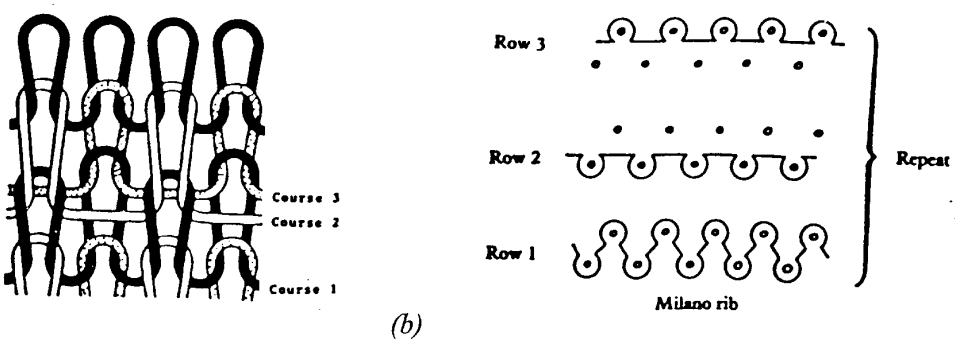

(b)

Fig. 2: Schematic diagrams of weft-knitted fabrics
(a) 1 x 1 rib structure
(b) Full Milano structure

Table 1: Variation of weft-knit architectures and panel details

Type	Loop density		Loop length		Panel details		
	Course density (C/cm)	Wale density (W/cm)	Plain course (mm)	Rib course (mm)	Fabric layers/ test panel	Areal Weight (g/m^2)	Volume Fraction (%)
R3	10.2	3.92	-	6.2	6	675	52.94
M3	9.2	4.70	6.2	6.5	6	680	53.33
M1	8.8	4.50	5.8	6.6	6	664	52.10
M9	6.2	2.80	7.8	9.1	10	415	54.25

Tensile specimens (250 mm x 25 mm) were cut from the panels parallel to the wale (W) and the course (C) direction. Tensile tests were performed on an MTS machine using a 128 mm gauge length extensometer, at room temperature and at a test speed of 0.5 mm/min. 250 series strain gauges were bonded to the surface of the tensile specimens. Compression specimens (56 mm x 25 mm) were also cut in both the wale and the course direction and tested to failure using a modified IITRI (Illinois Institute of Technology Research Institute) test rig on an MTS machine at a speed of 0.5 mm/min. The ultimate strength, strain to failure, elastic modulus and Poisson's ratio were determined for each specimen. Elastic modulus and Poisson's ratio were calculated in the strain range of 0.1 to approximately 0.3%. Fracture paths were recorded by taking photomicrographs of the tested specimens.

RESULTS AND DISCUSSION

Tensile properties

As shown in Table 1, the loop length and loop density for the three Milano rib and 1x1 rib architectures were different. The results of tensile tests are summarised in Table 2. It was observed that the tensile strength, tensile modulus and strain to failure in the wale direction were higher than those in the course direction.

Table 2: Tensile properties of weft knitted fabric-reinforced composites

Type	Strength (MPa)		Strength Ratio	Tensile Modulus (GPa)		Strain to Failure (%)	
	W	C	W/C	W	C	W	C
R3	96.0	75.8	1.27	14.7	14.0	1.40	0.84
M3	122	82.8	1.47	14.9	13.2	2.20	1.40
M1	134	83.0	1.62	14.3	12.3	2.40	1.40
M9	160	113	1.41	15.5	14.1	2.40	2.00

Figure 3 shows the typical tensile stress-strain curves for all four weft-knit composite laminates. On the whole, the response of all laminates was linear up to a 'knee point', which occurred at a strain of approximately 0.3%. Strains at that point were almost independent of the testing direction for all four structures. From the 'knee point', all specimens displayed significant softening, which continued until failure.

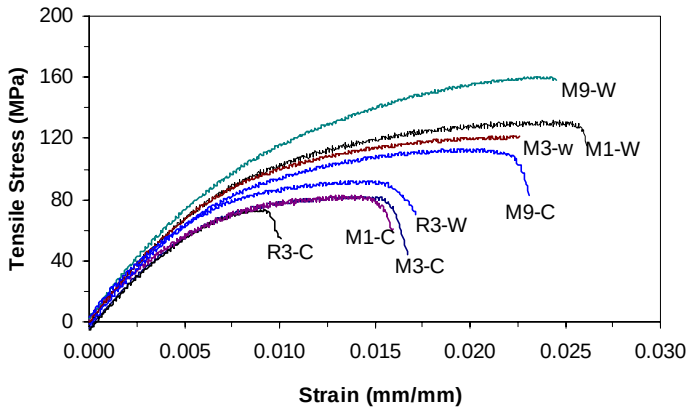

Fig. 3: Tensile stress-strain curves of weft-knit composites.

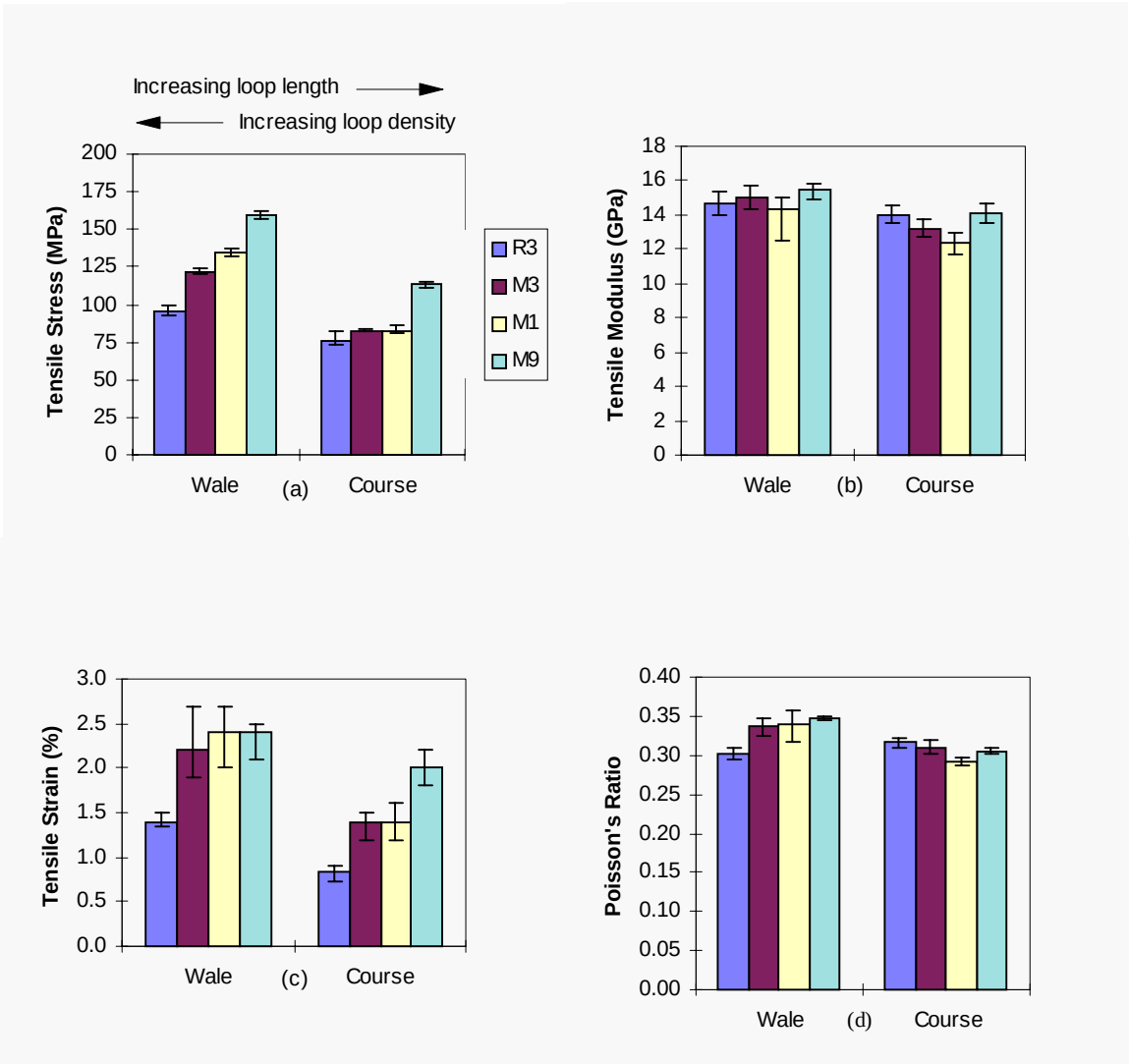

Fig. 4: Tensile properties of weft knitted composites (a) strength, (b) elastic Modulus, (c) strain to failure, and (d) Poisson's ratio

Inspection of Fig. 4(a) revealed that the tensile strength in the wale direction was much higher than that in the course direction for all laminates. It was also observed that the tensile strength

in the wale direction increased with increasing loop length and decreasing loop density. This effect was found to be less significant in the course direction.

Figure 4(b) shows that the tensile modulus was slightly higher in the wale direction than in the course direction for each laminate type. For either test direction, modulus was almost constant, despite changes in loop length and loop density.

As shown in Fig. 4(c), the tensile strain to failure in the wale direction was also observed to be higher than that in the course direction. As loop length increased or loop density decreased, tensile strains increased in both testing directions.

The Poisson's ratio shown in Fig. 4(d) slightly increased in the wale direction as loop length increased and loop density decreased, whereas it was almost independent of loop structure in the course direction.

Figure 5 shows photomicrographs of tensile tested specimens. Fracture appeared to have occurred in the planes of lowest fibre content for both specimens tested in the wale as well as in the course directions. This coincided with fibre fractures at legs of the loops for the wale-tested specimens and at needle-sinker loops for the course-tested specimens.

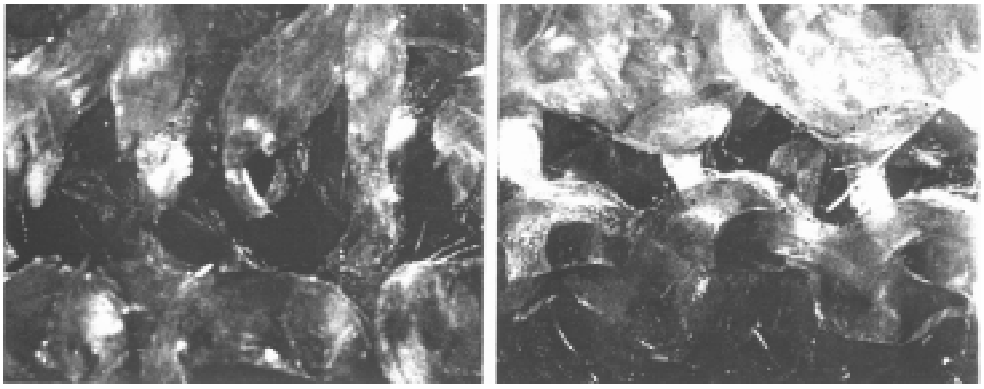

(a) (b)

Fig.5: Micrographs of fracture surface of weft-knit composites tested in the a) wale and (b) course direction

Fibre bundle debonding and resin cracking from the debonded sites were evidenced in Fig. 5. The microcracks generated from the debonded sites propagated through the adjacent resin-rich areas within the knit structure. In the wale direction, the fibre bundles were oriented at a denser proportion compared with the course direction. This was caused by the course density along the wale direction being about 50% higher than the wale density along the course direction. Hence the wale-tested specimens were capable of absorbing significantly more energy before failure compared to the course-tested specimens. Such phenomena are in agreement with the observations reported by Ramakrishna and Hull [6].

Again, it was observed that tensile properties for the knit structure, M9 were higher than the others in both testing directions. It was assumed that the defects in the weft-knit structure which caused the fibre to fail, were the highly curved or looped interlocking regions. Table 1 showed that, type M9 displayed the largest loop length and smallest loop density and thus it contained the least number of such defects in both directions when compared to the others.

Therefore, type M9 proved to be the strongest among all the knit structures considered in this study.

Compression Properties

Figure 6 shows the response of the weft-knit composite structures under compression. The curves were almost overlapping regardless of the test direction and the knee point occurred at a higher strain level of about 1.0%. Compression properties are summarised in Table 3.

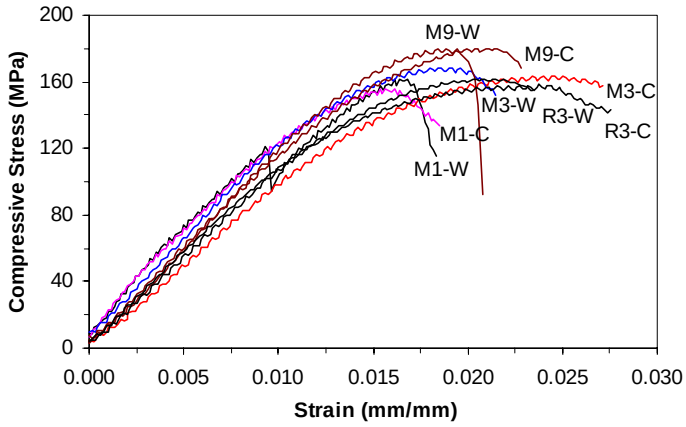

Fig. 6: Compression stress-strain curves of weft-knit composites

Table 3: Compression properties of weft knitted fabric-reinforced composites

Type	Strength (MPa)		Strength ratio	Compresive Modulus (MPa)		Strain to Failure (%)	
	W	C	W/C	W	C	W	C
R3	162	159	1.02	10.5	9.82	2.10	2.50
M3	169	163	1.04	11.9	9.65	2.00	2.50
M1	160	156	1.03	10.0	11.4	1.80	1.70
M9	180	181	0.99	12.0	11.3	1.90	2.20

Compression strengths, moduli and failure strains are shown in Fig. 7. Compression properties of weft-knit composite structures appeared to be almost independent of the knitting direction and loop structure. It is proposed that under compression, knitted composites act as short fibre reinforced composites, where the loop length is analogous to the short fibre length. The elastic-plastic analysis of short fibre composites by Agarwal and Broutman [11] suggests that, for the same applied load on the composite the stress within fibres will remain approximately constant when the short fibre aspect ratio, l/d exceeds 25 (where l=fibre length and d=fibre diameter). In the present study of weft-knit structures under compression, the ratio l/d ranges from 480 to 700. Since $l/d >> 25$, the stress supported by these fibres is dependent only on applied stress to composite, not on loop length. Hence knitted structures with different loop lengths showed no significant variation in their compression properties.

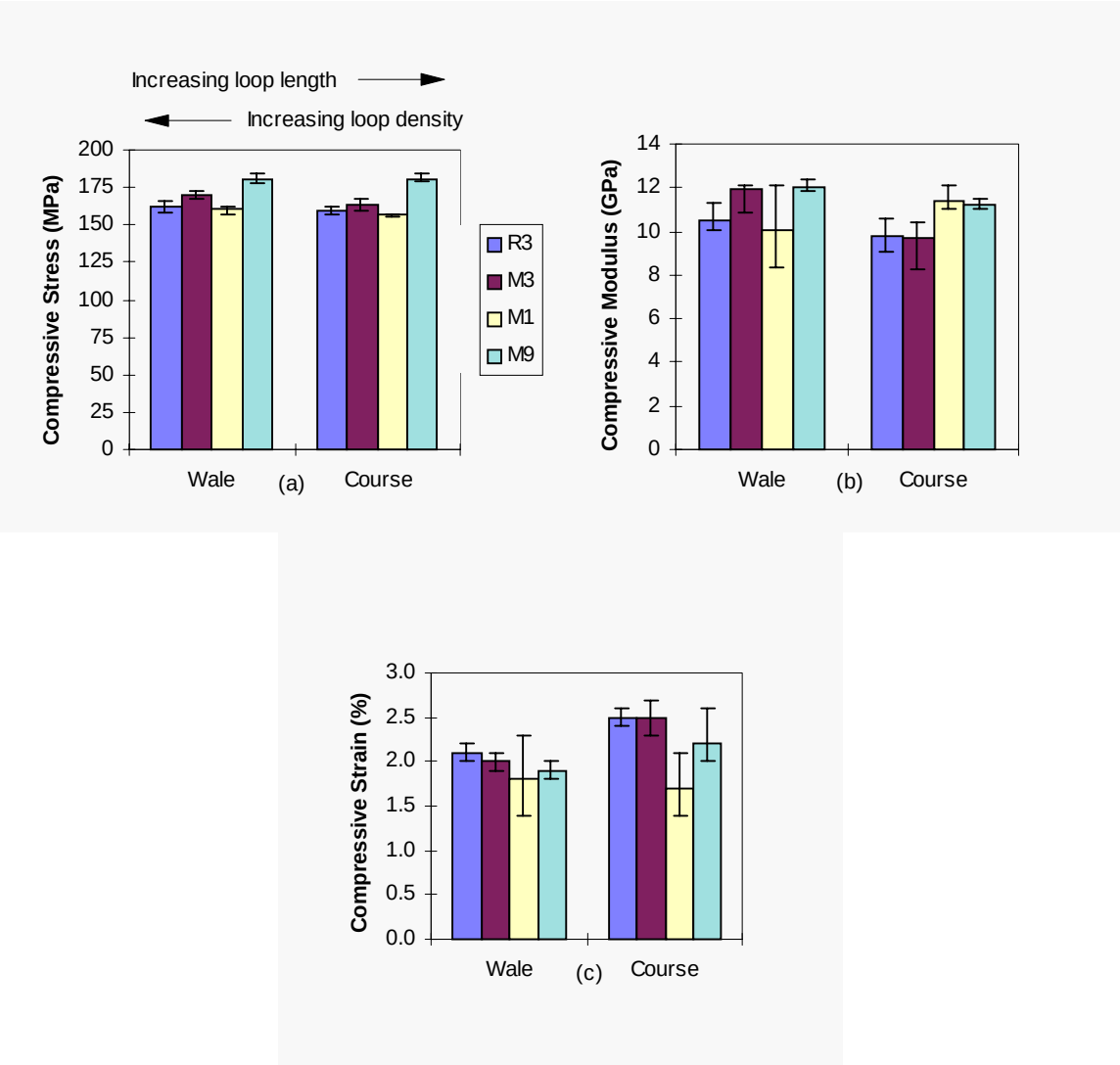

Fig. 7: Compression properties of weft-knit composites (a) strength, (b) elastic modulus, and (c) strain to failure

CONCLUSIONS

The weft-knit composite laminates tested were anisotropic in tensile strength and strain to failure, but the elastic tensile modulus of these composites were similar in both the wale and the course direction. In the wale direction, the fibre bundles were oriented at a denser proportion compared with the course direction. Hence the tensile properties in the wale direction were superior to the course direction.

Tensile strength and strain to failure were greatly affected by the loop length and loop density. With increasing loop length, the tensile strength and strain to failure increased, whereas loop density showed an inverse effect on these properties. The change was more predominant in the wale direction than in the course direction. On the whole, the Milano rib structure seemed to be stronger than 1x1 rib structure.

The tensile Poisson's ratio slightly increased in the wale direction with increasing loop length and decreasing loop density, whereas it was almost independent of loop structure in the course direction.

Despite the influence of test direction, loop length and loop density on tensile properties, the compression properties were seen to be almost unaffected by these parameters.

It was observed that tensile fracture occurred in the planes of lowest fibre content for both specimens tested in the wale as well as in the course directions. This coincided with fibre fractures at legs of the loops for the wale-tested specimens and at needle-sinker loops for the couse-tested specimens.

ACKNOWLEDGEMENTS

The authors are grateful to S. Savçi and T. Sifniotis of the Department of Textile Technology, University of New South Wales for useful discussions and the supply of knitted fabrics and the data outlined in Table 1. Thanks are also due to K. Houghton of CRC-ACS for assistance in test panel manufacture and specimen preparation, and to M. Wilson of Department of Aerospace Engineering, RMIT for assistance in conducting mechanical tests.

REFERENCES

1. Marvin, A. G., “The Development of Knitted Glass Fabrics for Use in Resin Lamination”, *M.Sc. Thesis*, University of Strathclyde, 1969.

2. Rudd, C.D, Owen, M. J. & Middleton, V.,“ Mechanical Properties of Weft Knit Glass Fibre/Polyester Laminates”, *Journal of Composites Science and Technology*, Vol. 39, 1990, pp. 261-277.

3. Verpoest, I.and Dendauw, J., “Mechanical Properties of Knitted Glass Fibre/Epoxy Resin Laminates”, *(Proc. Conf.) 37th International SAMPE Symposium*, March 9-12, 1992, pp. 369-377.

4. Chou, S., Chen, H.C. and Lai, C.C., “The Fatigue Properties of Weft-Knit Fabric Reinforced Epoxy Resin Composites”, *Journal of Composites Science and Technology*, Vol. 45, 1992, pp. 283-291.

5. Wu, W.L., Kotaki, M. and Fujita, A.,“ Mechanical Properties of Warp- Knitted, Fabric-Reinforced Composites”, *Journal of Reinforced Plastics and Composites*, Vol. 12, No. 10, 1993, pp. 1096-1110.

6. Ramakrishna, S. and Hull, D.,“Tensile Behaviour of Knitted Carbon-Fibre-Fabric/Epoxy Laminates-- Part I: Experimental”, *Journal of Composites Science and Technology*, Vol. 50, No. 2, 1994, pp. 237-247.

7. Bannister, M.K and Herszberg, I.,“The Manufacture and Analysis of Composite Structures from Knitted Preforms”, *(Proc. Conf.) Fourth International Conference on Automated Composites*, September 6-7, 1995, Nottingham, U.K., Vol. 2, pp. 397-404.

8. Herszberg, I., Falzon, P.J., Leong, K.H. and Bannister, M.K., "Bearing Strength of Glass/Epoxy Composites Manufactured from Weft-Knitted E-glass Fabric", *(Proc. Conf.) The First Australian Congress on Applied Mechanics*, February 21-23, 1996, Melbourne, Australia, pp. 279-284.

9. Leong, K.H., Falzon, P.J., Bannister, M.K. and Herszberg, I.," An Investigation of the Mechanical Performance of Weft-Knitted Milano Rib Glass/Epoxy Composites", Submitted to *Journal of Composites Science and Technology*, 1996.

10. Leong, K.H., Nyugen, M. and Herszberg, I., "The Effect of Deformation of Glass Fibre Knitted Fabrics on the Resultant Composite Tensile Properties", To be presented at *The Eleventh International Conference on Composite Materials*, *ICCM-11*, Gold coast, Australia, July 14-18, 1997.

11. Agarwal, B.D. and Broutman, L.J., "*Analysis and Performance of Fibre Composites*", Second Edition, Chapter 4, Pages 122-128.

WEFT-KNITTED GLASS-FIBRE PREFORMS FOR COMPOSITE MATERIALS

S. Savci and J.I. Curiskis

Department of Textile Technology, University of New South Wales, Sydney 2052, Australia

This work has been carried out as part of a CRC-ACS research programme.

SUMMARY: Weft knitted preforms have become increasingly popular in recent years for the processing of composite materials due to their low cost and exceptional mechanical properties. The main attributes of weft-knits for composite materials are their fatigue resistant properties and their ability to conform to complex three-dimensional shapes, either by deep drawing/moulding or by integral knitting techniques. The experimental work reported in this paper examines various physical and mechanical properties of the dry preform with respect to knitting machine settings. The investigation of mechanical properties is directed towards the formability (drapability) of the dry preform in terms of KESF testing and a modified CBR plunger test method. The results demonstrate that both methods may provide useful design parameters of formability for subsequent composite processing.

KEYWORDS: weft-knitted preforms, formability, deep drawing, KESF testing.

INTRODUCTION

The use of textile technology, such as weaving and braiding, in the manufacture of preforms for advanced composite materials has and continues to be under intense investigation due to the potential of these processes to produce low-cost high-quality structures with improved mechanical performance. In recent years, weft-knitted structures have become of increasing interest due to their potential as crash/fatigue resistant materials and their ability to conform to complex three-dimensional shapes. The latter may be derived from deep drawing/moulding techniques utilising the formability properties of the flat preform or by integral knitting techniques to manufacture the near net shape. In this paper, the term formability is preferred to drapability because, in the textile sense, the latter refers to the shape adopted by an initially flat fabric under the effects of gravity loading only rather than by drawing/moulding processes. With integral knitting, the essential preform shape is actually manufactured on the knitting machine with added benefits of low material wastage and low labour costs [1], providing an appropriate machine type is available. While it may seem contradictory in view of the three-dimensional nature of the knitted loop, weft-knitted preforms with inlay yarns/tows can also yield higher strength than that of woven fabrics because the inlay yarns are essentially uncrimped [2].

Reports in the literature have generally been with respect to the mechanical properties of composite test specimens and/or demonstrations of the shaping potential. The basic mechanical properties of weft-knitted composites have been extensively studied. The effect of volume fraction on the properties of weft-knitted composites has been of particular interest

[3]. Methods of increasing the fibre content and stiffness of knitted laminates, together with composite fracture mechanisms has also been studied [4]. Various weft-knitted composite structures have been investigated with respect to stiffness and fatigue resistance [5] and, later, other structures were examined with respect to composite strength [6]. The effect of pre-stretch of the dry preform on composite properties has also been examined [7]. However, there have been no studies carried out on the properties of the dry preform and no formability concepts have been developed for shaping. Yet it has been well established that weft knitting is an excellent candidate for forming complex shapes due to its formability properties. The only related area in which work has been undertaken is for woven fabrics [8].

Knowledge of the mechanical properties and formability of the dry preform is important for providing a systematic engineering approach for weft-knitted preform design and manufacture and subsequent composite fabrication. Work to this end is currently being undertaken by the authors, and progress is reported in this paper.

WEFT KNITTING BACKGROUND

In the textile industry, weft knitting is a well-established fabric-forming technology and a large variety of structures can be manufactured depending upon machine type available [9]. Such structures include simple plain knits, ribs, purls, interlocks and double-knit structures, such as full milano and punto-di-roma, as well as more complex designs in which surface effects and/or colour are developed for apparel applications. For composite applications, the simple and double-knit structures, together with the use of inlay, plating and integral knitting techniques, are likely to be of greatest interest. Fundamental terms used to characterise such weft-knitted structures include the following:

loop length,	L (mm)	=	length of yarn to form one complete knitted stitch.
average Lav,	Lav(mm)	=	total length of yarn to form one repeat / no. of stitches in one repeat.
course density,	c/cm	=	number of horizontal rows of loops per cm.
wale density,	w/cm	=	number of vertical columns of loops per cm.
areal density,	g/m^2	=	mass of fabric in grams / area of fabric in sqm.
tightness factor,	K	=	$\sqrt{}$tex / Lav
run-in-ratio,	L_1:L_2	=	ratio of loop lengths in one structural repeat.
Tex,	T	=	linear density in g/km

Available in the textile literature are many studies on the geometry and structural mechanics of weft-knitted fabrics as well as the mechanics of fabric formation. They emphasise the importance of loop length and run-in-ratio in the control of fabric dimensions and of other basic physical properties such as areal density. Such studies were initially carried out on plain fabrics [10] and later on double jersey constructions [11]. Further, these properties are dependent upon the existence of various relaxation states for the fabric due to such factors as the visco-elastic nature of most textile fibres, the effects of inter-fibre friction and the subsequent finishing treatments that may be applied to the fabric. Investigations into the mechanics of weft knitting have shown that the variables of most importance in controlling loop length are the stitch cam setting, the input tension setting, the fabric take-down tension, and the yarn-metal friction [12]. The development of weft-knitted preforms composed of high performance fibres must therefore recognise this pre-existing knowledge. The knittability of high performance yarns has been shown to be dependent upon the frictional

properties, pliability and strength of the yarn [13]. Glass fibres are very brittle in nature, have high stiffness and high coefficient of friction, and consequently require a low input tension, tension control and minimal metal surface contact for knitting.

EXPERIMENTAL PROCEDURE

A range of full milano rib structures together with their plain knit and 1x1 rib components (see Figure 1) were manufactured on an 8-gauge (E8) Stoll ANVH/BLM-es knitting machine - this is a computer-controlled rib-jacquard V-bed machine which uses the Sintral programming language.

Figure 1: a) Full Milano b) 1x1 Rib, c) plain tubular jersey nomenclature

These structures were produced with 68 x 2 tex glass fibre tows with silane size from Silenka Glass Yarns. Yarn input tension and fabric take-down tension were set at minimal values consistent with good knitting performance. In addition, the yarn feed path was linearised and metal contact surfaces polished to reduce the effects of abrasion on the glass fibres. Different values of stitch cam settings were set to produce different loop lengths within the preform structures. All preforms were allowed to relax under standard ambient conditions of 25^{o}C, 65% relative humidity for a minimum of 24 hours prior to testing. Sampling was carried out in accordance with the Australian standard for testing and then quantified in terms of their loop lengths, areal density, wale and course densities, thickness [14] and tightness factor. These physical tests were followed by mechanical testing on the Kawabata Evaluation System for Fabrics (KES-FB) instrumentation, which was initially developed for fabric objective measurement in the textile and clothing industries, and a simple formability test based on the CBR burst test for geotextiles.

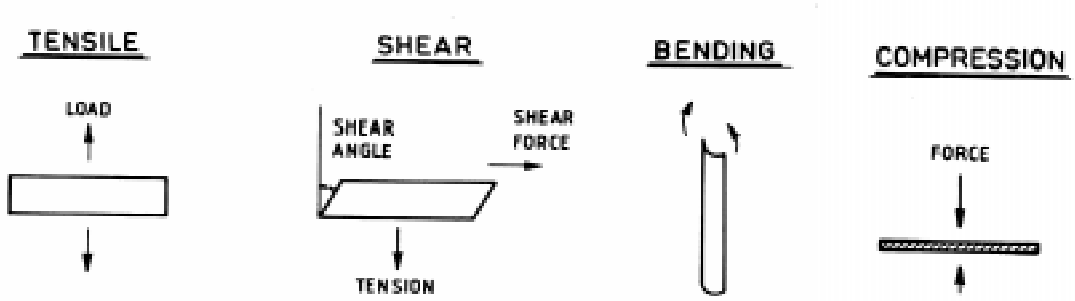

Figure 2: Schematic representation of KES-FB instrumentation

The four fabric mechanical properties assessed using the KES-FB instrumentation are in-plane tension, in-plane shear, transverse compression and out of plane bending as shown in Figure 2. These instruments are designed to take measurements at low stress levels whilst providing data on a wide range of parameters including deformation and recovery for each mechanical property obtained [15]. The operating procedure for the KESF instrumentation is given elsewhere [16]. Figure 3 gives a typical representation of the deformation/recovery

curves for a fabric subjected to extension or lateral compression and bending or shear in KESF testing.

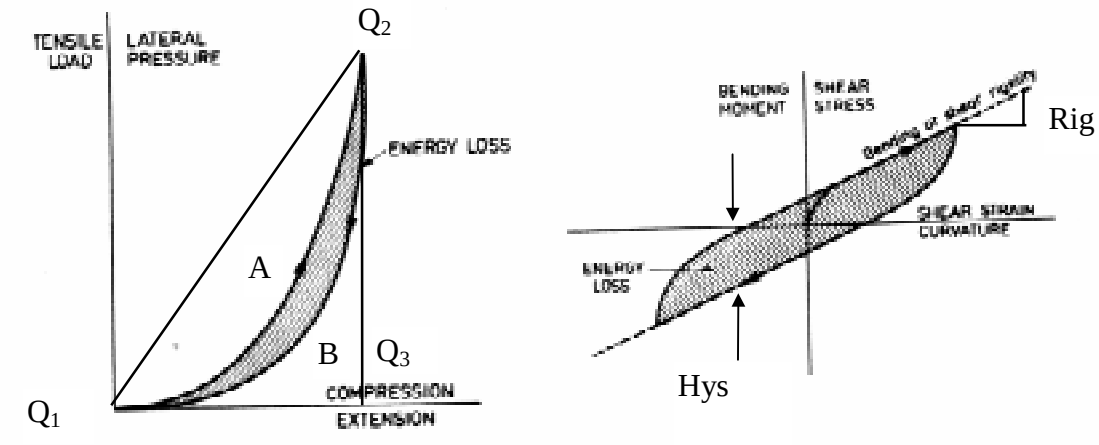

Figure 3: a) in-plane tension and transverse compression, b) in-plane shear and out-of plane bending

The important features of the curves are that they are non-linear and exhibit hysteresis; the latter implies that energy is lost during the deformation cycle. The hysteresis is shown by the shaded areas in the graphs and is due to inter-fibre friction effects and the visco-elastic behaviour of the fibres [15]. In the textile and clothing industries, the following standard parameters have been defined from these curves [16]:

tensile	LT	tensile linearity	WT/area $Q_1Q_2Q_3$	%
	WT	tensile energy	area Q_1 A Q_2Q_3	J/m^2
	RT	tensile resilience	area Q_1 B Q_2Q_3 /WT	%
	EMT	tensile extensibility	Q_3	%
shear	G	shear rigidity	slope Rig	Nm/m^2
	2HG	hysteresis of shear force at 0.5°	width of Hys	N/m
	2HG5	hysteresis of shear force at 5°	width of Hys	N/m
bending	B	bending rigidity	slope Rig	μNm
	2HB	hysteresis of bending moment	width of Hys	μNm
compression	LC	compressional linearity	WC/area $Q_1Q_2Q_3$	%
	WC	compressional energy	area Q_1 A Q_2Q_3	J/m^2
	RC	compressional resilience	area Q_1 B Q_2Q_3 /WC	%
	EMC	compressibility	Q_3	%

The simple formability test was based on the CBR burst strength test for geotextiles [17]. In this test, a cylindrical plunger is forced through the centre of a circular specimen which is gripped around its entire circumference by clamps in a loading frame; Figure 4 illustrates the plunger and clamping arrangements. The plunger displacement and reactive force are recorded. In the present case, the plunger is taken to a maximum displacement of 50 mm rather than to specimen failure (burst); the plunger displacement speed was set to 20 mm/min.

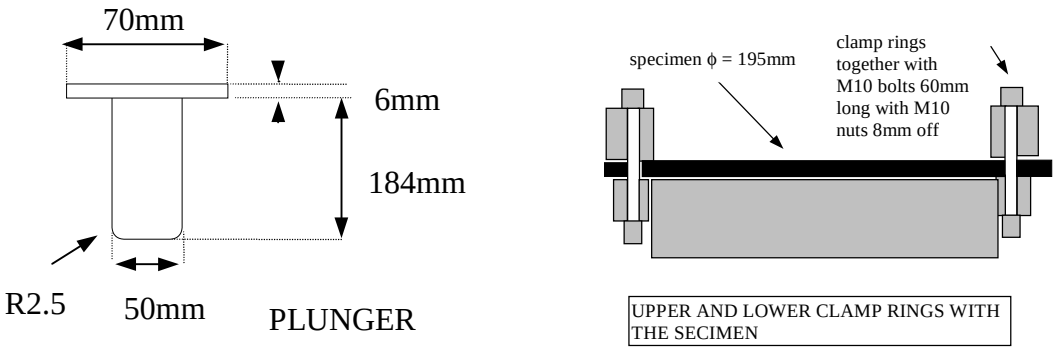

Figure 4. Plunger and clamping arrangement for the CBR test

RESULTS AND DISCUSSION

The results of the physical property tests are given in Table 1where Lr and Lp refer to the stitch cam settings on the knitting machine for the rib courses and the plain knit courses, respectively. From these tables, it is clear that larger loop lengths result from increasing the stitch cam settings for all three knit structure types, although the run-in-ratio decreases for the milano structures. Further, the increase in loop length(s) yields reductions in areal density, tightness factor, and wale and course densities. In the case of thickness, however, the effect is dependent upon knit structure as the loop length is increased, with thickness decreasing for the milano fabrics and increasing for the plain knit and rib fabrics.

Table 1 Preform physical properties

PREFORM	M3	M61	M9	R3	R6	R9	P61	P9
g/sqm	670	601	434	742	607	504	396	290
Lr (mm)	6.6	7.3	8.7	6.6	7.6	9.2	N/A	N/A
Lp (mm)	5.8	6.7	9	N/A	N/A	N/A	6.6	8.9
2Lr:Lp	2.28	2.17	1.93	N/A	N/A	N/A	N/A	N/A
Lav	6.1	6.9	8.9	N/A	N/A	N/A	N/A	N/A
C/cm	8.9	8.2	6.5	9.9	7.8	6.9	8.3	6.6
W/cm	4.45	3.65	2.65	4.25	3.6	2.9	4.8	3.3
Thickness (mm)	2.35	2.19	1.98	2.04	2.30	2.59	1.14	1.35
K	1.92	1.64	1.27	1.77	1.53	1.27	1.77	1.31
Lr (setting)	8.1	9.5	11	8.1	9.5	11	N/A	N/A
Lp (setting)	10.1	11	13	N/A	N/A	N/A	11	13

The results were not only informative of the preforms' physical properties but also provided an insight into the interaction between machine, yarn/tow and the structure being knitted. The milano fabric M3 is at the limits of the knitting capabilities of the machine, ie. milano fabric could not be knitted at smaller stitch cam settings due to excessive yarn/tow breaks, dropped stitches and knitting needle damage. The results for eight additional milano fabrics (not reported here) emphasise this knittability limit in terms of stitch cam settings. Although this limit was not directly explored for the plain knit and rib structures, it is notable that the plain knit structure P3 could not be knitted even though its component in the milano M3 was successfully manufactured at the low stitch cam setting, Lp=10.1. Further, while the results in Table1 indicate a general correlation between the various physical parameters of the milano

structures and their plain knit and rib components, it is notable that the rib loop lengths differ between the rib and milano structures at the higher stitch cam settings. These phenomena can be explained with reference to the "robbing back theory" [12] which states that the loop length achieved is dependent on the maximum tension developed in the knitting zone associated with the stitch cam. This maximum tension is essentially constant (allowing for statistical variabilities) when knitting simple structures such as plain knit and 1x1 rib. In the case of full milano rib, the maximum tension alternates from the value of the plain loop components for two courses to that of the rib loop components for one course. In addition, the unstable nature of the plain knit fabrics required a higher take-up tension to overcome the unbalanced internal forces inherent to these structures. This higher take-up tension would increase the maximum tension within the knitting zone and yield higher loop lengths. In fact, this principle also accounts for the plain loop lengths being slightly smaller in the plain knit and the rib loop lengths being slightly larger in the 1x1 rib as compared to the corresponding component values in the milano fabrics.

The results of the KES-FB tests are summarised in Figs 5-14 for three milano structures. It is to be noted that the hysteresis (energy loss) for all mechanical properties was substantially higher than for most apparel fabrics (approximately 10-fold). It is highly probable that these hysteresis losses are due to inter-fibre friction as the fibres are essentially elastic. Further, the fabrics display some permanent deformation upon removal of load. This is emphasised in Fig. 15 which presents the results of a number of tensile cycles on one specimen.

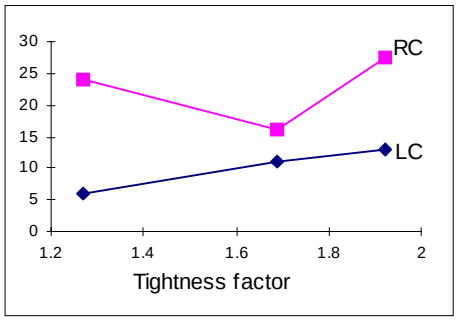

Figure 5: Compression linearity & resilience

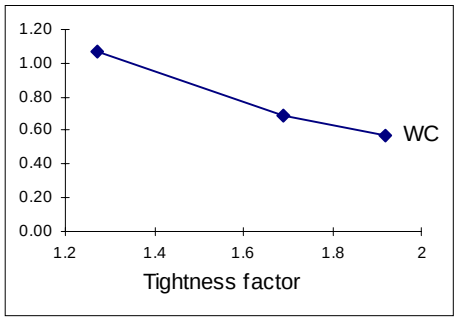

Figure 6: Compressional energy

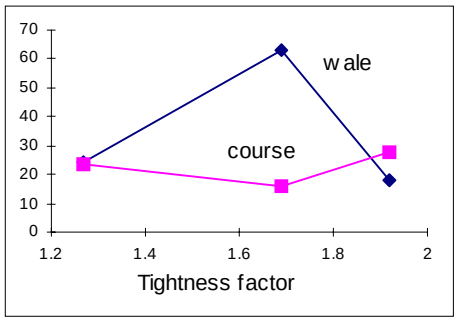

Figure 7: Bending rigidity

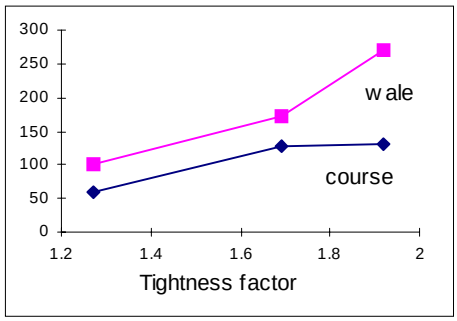

Figure 8: Hysteresis of bending moment

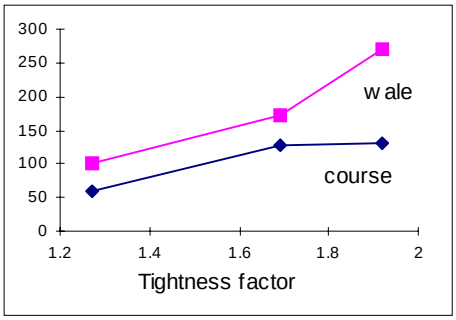

Figure 9: Shear rigidity

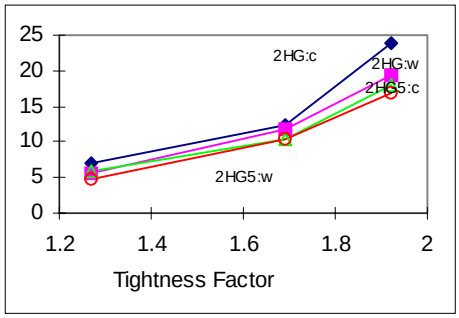

Figure 10: Shear hysteresis

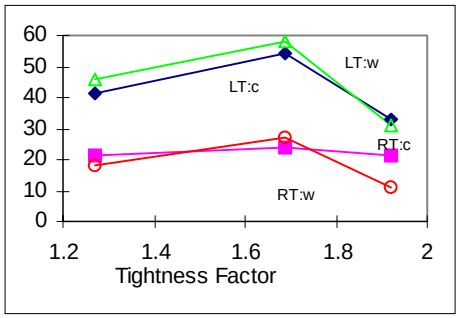

Figure 11: Tensile linearity and resilience

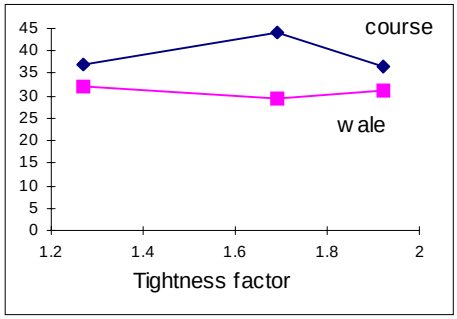

Figure 12: Tensile energy

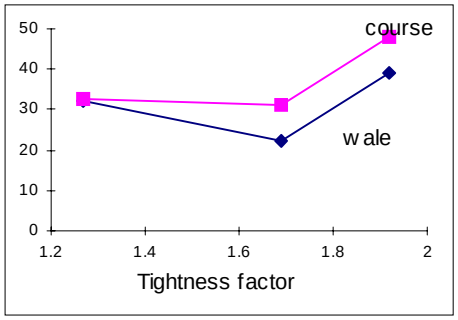

Figure 13: Tensile extensibility

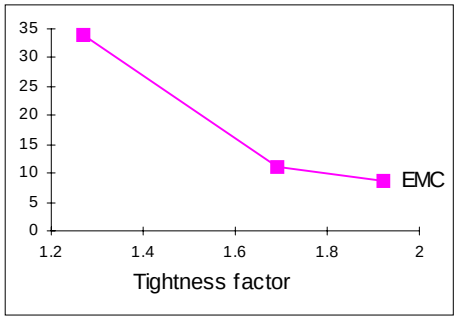

Figure 14: Compressibility

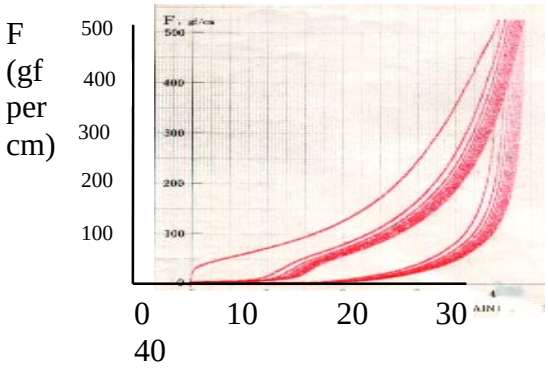

Figure 15: Tension deformation/recovery curve

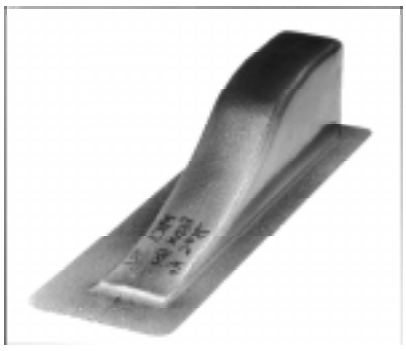

Figure 16: Helicopter door track pocket composite

In general, increasing the tightness of the fabric results in hysteresis and rigidity increases for the shear and bending properties. In the case of tensile and compressional behaviour, the hysteresis energy can be determined from the following relation,

$$\text{hysteresis energy loss} = W_x (1-R_x) \quad \text{where } x = \text{T(tensile), C(compression).}$$

Thus, compressional hysteresis also increases as the fabric tightness is increased and this is accompanied by a decrease in the compressional strain due to the increased quantity of fibre opposing the deformation. In the case of the tensile tests, increasing fabric tightness tends to decrease the load extension curve, with the middle tightness fabric showing a maximum in tensile linearity and resilience, and energy and hysteresis in the course direction, together with a minimum in tensile extensibility, and energy and hysteresis in the wale direction. Further work is currently being undertaken to examine these effects in terms of run-in-ratio as well as fabric tightness.

Fig. 16 illustrates a composite part of complex shape produced by deep-drawing a glass fibre milano preform with subsequent matrix impregnation by resin transfer moulding (RTM). Examination of fabric distortions in the final composite emphasise complex strain fields exhibiting high fabric shear and in-plane extensibility, together with areas of high curvature. Laboratory simulation of the deep-drawing process can be undertaken using formability tests such as that previously described.

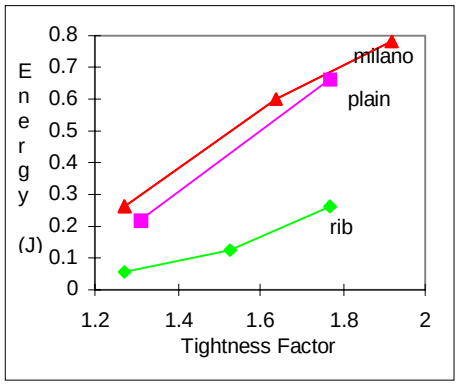

Figure 17: Milano: Formability/energy

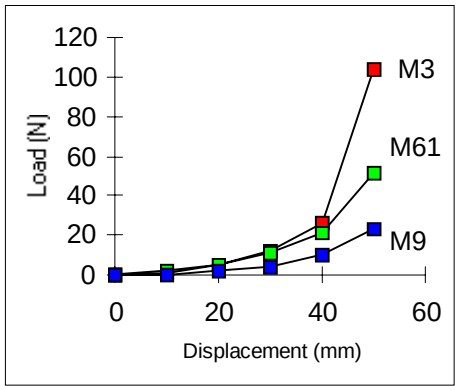

Figure 18 Milano: Formability/displacement

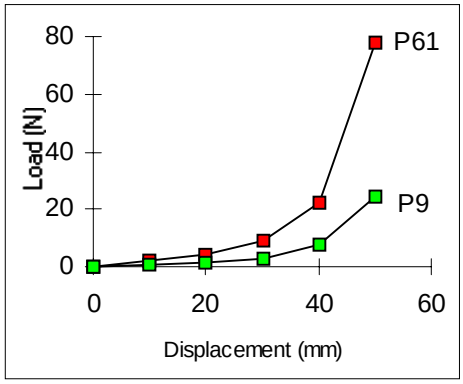

Figure 19: Plain: Formability/displacement

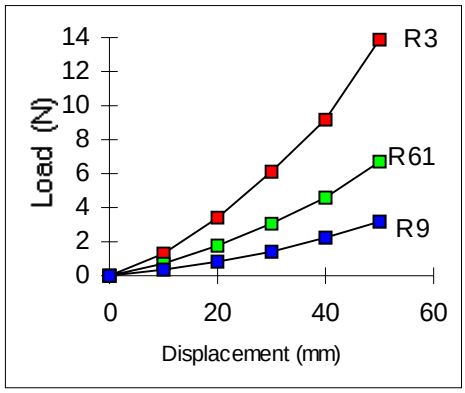

Figure 20: Rib: Formability/displacement

The results of these tests are shown in Figs 17-20 for the three milano structures and their rib and plain knit components. With increasing tightness factor, the total energy yielded increases as does the slope of the load-displacement curves for all fabric structures tested. This is consistent with the above results for physical and mechanical behaviour. Interestingly, the results also suggest that the plain knit components are the dominating factor for determining resistance to load for the milano structures.

CONCLUSION

The results reported in this paper demonstrate that there is a definite interplay between the physical properties of weft-knitted preforms and knitting machine settings through study of the working limits of the loop length dimensions together with replications of these settings in different structures.

The mechanical properties derived from the KESF testing are useful for determining the engineering formability of knit structures for subsequent composite processing. However, all tensile, shear, bending and compressive properties complement one another for this purpose. The simpler design parameters for assessing the formability offered by the modified CBR plunger test method require further investigation. Such work is in progress.

ACKNOWLEDGMENTS

The first author (SS) would like to thank the Corporate Research Centre for Advanced Composite Structures (CRC-ACS) for the provision of a post graduate scholarship and for their financial support of this research. Useful discussions with Drs K.H. Leong and M.K. Bannister of the CRC-ACS and Assoc. Prof. I. Herszberg of RMIT University are also gratefully acknowledged.

REFERENCES

1. Raz S., “Flat Knitting: the New Generation”, Bamberg, Meisenbach, 1991.

2. Marvin A.W., “Combined Weft-Knitted-Woven Fabrics”, Proc. Diamond Jubilee Conf. of the Textile Institute: Studies in Modern Fabrics, London, 1970, pp 40-45.

3. Verpoest I. and Dendauw J., “Mechanical Properties of Knitted Glass Fibre/Epoxy Resin Laminates” 37th International SAMPE Symposium, March 9-12, 1992.

4. Ramakrishna S. and Hull D., “Tensile Behaviour of Knitted Carbon-Fibre-Fabric/Epoxy Laminates: Parts I & II”, Composites Science and Technology, vol 50, 1994, pp 237-258.

5. Chou S., Chen H.C. and Lai C.C. “The Fatigue Properties of Weft-Knit Fabric Reinforced Epoxy Resin Composites”, Composite Science and Technology, vol 45, 1992 pp 283-291.

6. Wu W.L., Inoda M., Kotaki M., Goto A., Fujita A., Hamada H. and Maekawa Z.I., “Mechanical Properties of Weft Knitted Reinforced Composites” Journal of the Japan Society for Composite Materials, vol 19, no 5, 1993, pp 17-26.

7. Ha S.W., Mayer J., Haan D.E., Petitmermet M. and Wintermantel E, “Knitted Carbon Fibres Reinforced Biocompatible Thermoplastics, Mechanical Properties and Structure Modelling”, 6th European Conference on Composite Materials, Sept 20-24, France, 1993, pp 637-642.

8. Cai Z., Yu J.Z. and Ko F.K. “Formability of Textile preforms for Composite Processing: Parts 1 and 2” Composites Manufacturing, vol 5, no.2, Butterworth - Heinmann Ltd., Oxford, 1994.

9. Spencer D., “Knitting Technology”, 2nd edition, Permagon Press, Oxford, 1989.

10. Hearle J.W.S., Grosberg P. and Backer S., “Structural Mechanics of Fibres, Yarns and Fabrics”, vol 1, John Wiley and Sons Inc, New York, 1969.

11. Knapton J.J.F, “Knitting High Quality Double Jersey Cloth: Parts I & II”, Textile Institute and Industry, Feb. & March, 1972.

12. Knapton J.J.F. and Munden D.L., “A Study of the Mechanism of Loop Formation on Weft -Knitting Machinery: Parts I & II”, Textile Research Journal , vol 36, 1966, pp 1072-1091.

13. Lau K.W. and Dias T., “Knittability of High Modulus Yarns”, Journal of the Textile Institute, vol 85, no. 2, 1994, pp 173-91.

14. AS200.1.2.15., “Method 2.15 Physical tests - Determination of Thickness of Textile Fabrics”, Methods of Test for Textiles, Standards Australia, 1989.

15. Harlock S.C., “Fabric Objective Measurement: Principles of Measurement”, Textile Asia, July, 1989, pp 4-8.

16. Kato Tekko Co. Ltd., “KES-FB-1, KES-FB-2, KES-FB-3: Manual for Pure Bending Tester, Tensile and Shear Tester, Compression Tester”, Kyoto, 1991.

17. AS30706.4., “Method 4: Determination of Burst Strength - California Bearing Ratio Plunger Method”, Geotextiles - Methods of Test, Standards Australia, 1990.

FABRICATION OF LARGE SCALE BRAIDED COMPOSITE WITH I-SHAPED STRUCTURE

Asami Nakai, Mikio Masui and Hiroyuki Hamada

Faculty of Textile Science, Kyoto Institute of Technology
Matsugasaki, Sakyo-ku, Kyoto 606, Japan

SUMMARY: In these days, it is expected that textile preforms are applied to large scale composite structure since they have good stability and drapability. In this paper, the method to fabricate large braided composite was proposed. Firstly the width of braided fabric when a type and a number of fiber bundle was changed was measured. As the result, it was evident that the width of braided fabric was narrow and huge braiding machine with large number of spindles is necessary to fabricate large braided fabric. In this study the method which link braided fabric transversely with kited technique was introduced to fabricate a large braided fabric without using a huge braided machine. Using this knitted technique, braided fabrics can be linked without injuring reinforcements. Tensile test of linked braided fabric was carried out and it was evident that fabricating large braided composite without decreasing strength was possible using this link method.

KEYWORDS: CAE, braid, large composite structure, link, knitted technique, loop stitch, tensile test, I-beam

INTRODUCTION

The properties of fiber reinforced plastic (FRP) are decided not only by the combination of matrix and reinforcing materials but also by the unique geometry of the reinforcements. The geometry of the reinforcements has been investigated in addition to development of fiber and resin. Composite materials reinforced with fabric preforms made by either woven, braided or knitted fabrics are currently being considered as alternatives to tape laminates. "Textile" composites can be defined as composite materials reinforced with textile fabrics such as woven, knitted and braided fabrics. Manufacturing process for textile composites could also be automated, so it could potentially lead to lower costs. In textile forming technique not only two-dimensional plate shape but also thick or three-dimensional shape can be fabricated. These textile preforms can be applied in structural composites with complex shapes, since they have good stability and drapability, and can be fabricated directly to their final shapes. Such fabric reinforced textile composites have potential for improved out-of-plane stiffness, strength, delamination resistance and toughness properties. It has been expected that textile composites are used widely as structural parts in various fields from these reasons.

There are many published papers related to textile composites. They are divided into three categories; one is designing a new fabric that includes three dimensional weaving fabric, 2.5 dimensional warp knitted fabric and so on. The second one is developing a new machine that can correspond to the new fabrics. The third one is mechanical properties of textile composites such as static properties and impact properties. In this category numerical

modeling of textile composites is included. According to these classifications we have developed CAE system for braided composites as shown in Fig.1.

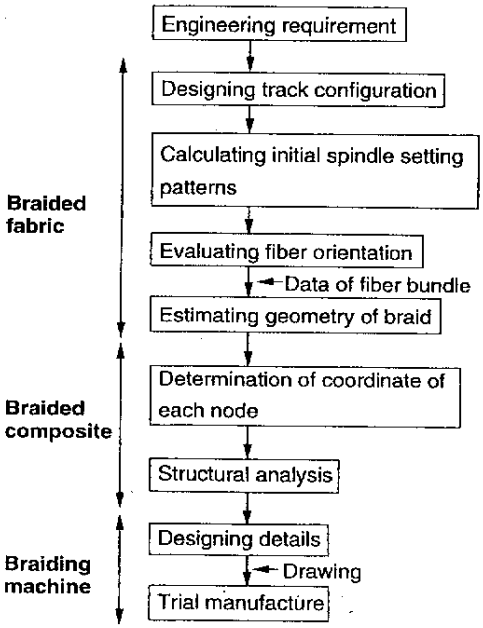

Fig. 1: CAE system for braided composites

In braided composites there are two basic fabrics; cord braiding and flat braiding. Determination of dimension of these fabrics such as width and thickness are very difficult problem because they greatly depend on not only fiber characteristics such as type of fibers, number of filaments, diameter of filaments but also weaving structure as fiber orientation angle, density of weaving structure and so on. Therefore designing the fabrics is needed as shown in flow chart of CAE system, and detail of this problem would be mentioned in the latter section. Another particular problem in the braided composites is that one machine can fabricate a specific braided fabric when materials type is fixed. The machine with large number of spindles can fabricate large braided fabric, however this large machine can not fabricate small braided fabric in proper fiber orientation state. Of course, small machine can not make large fabric. That means applicable ability of braiding is very small in terms of machine. According these circumstances in order to expand application field of braided composites wider an attempt that is fabricating large braided structure by using small machine was made in this study. Concretely, large braided composite with I-shaped structure was fabricated by using existing braiding machine in braiding technique and linking machine in knitting technique. First width of flat braided fabrics was examined by changing fiber types. After our basic concept of fabricating large braided structure was mentioned, some experimental results were described. Here it was clear that proposed linking method was very effective. Finally large I beam was appeared.

Dimension of Braided Fabric

In this section the width of flat braided fabrics using some kinds of fiber bundles was measured. The schematic of flat braided fabric is shown in Fig.2. Flat braided fabric has two

dimensional shape like a belt. The fiber bundles are continuously oriented in this fabric because they reverse themselves at the side edge. Therefore, when tensile load applies to flat braided fabric, all the fibers bare the load, so that it can become a string. The fibers will change their orientation angles smaller and then the width will become narrow. This point is the most important point for braided fabric. Changing orientation angle leads to changing fabric width. Moreover there are many different weaving structures. The surface of braided fabric shows a zig-zag pattern since the fiber bundles alternately pass over and under each other. Fig.3 shows repeating pattern in braided fabric, and (a) is Diamond braid where a fiber bundle continuously passes over one fiber bundle and then under one fiber bundle of the opposing group. Whereas Fig.3(b) shows Regular braid in which one fiber bundle passes two fiber bundles. The width of flat braided fabric depends on these braided patterns greatly.

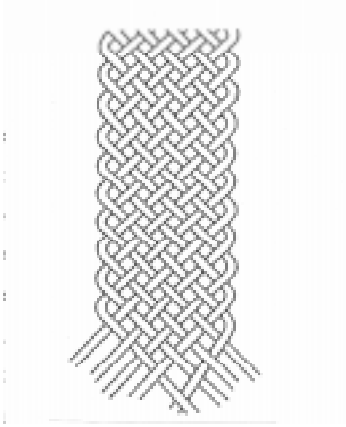

Fig. 2: Schematic of flat braided fabric

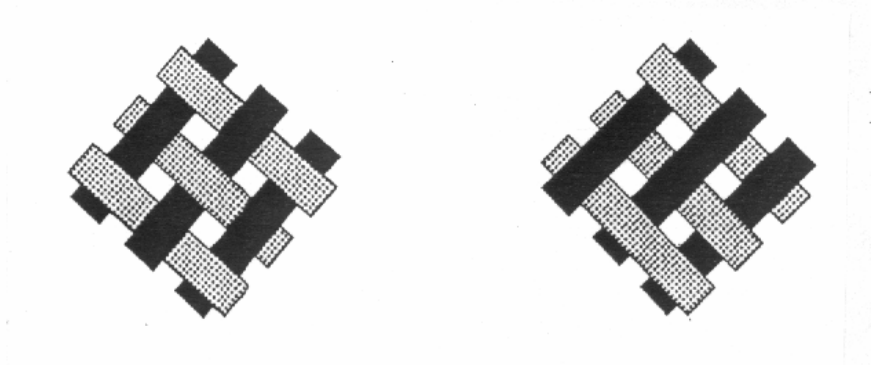

(a) Diamond braid *(b) Regular braid*

Fig. 3: Braided pattern

Fiber bundles used in this experiment were glass fiber bundles with 2000 filaments and 900 filaments. The diameter of a filament 17.0μm. For Diamond braid the machine with 43 spindles was used and for Regular braid the machine with 85 spindles was used. Also, two different loading conditions were selected for changing fiber orientation angle; one was light weight and the other was heavy weight. Table 1 shows measurement results of width in each case. According to these results the widths in the cases of heavy weight are smaller than those in the case of light weight. The maximum value was 82.0mm and this was a limitation by using these material systems and machines.

Table 1: Measurement results of width of flat braided fabric

Type of Fiber Bundle	Weight	Braided Pattern	Braiding Angle	Width (mm)
900 Filaments	Light Weight	Diamond Braid	24°	37.0
		Regular Braid	28°	53.0
	Heavy Weight	Diamond Braid	15°	25.5
		Regular Braid	20°	36.0
2000 Filaments	Light Weight	Diamond Braid	28°	52.3
		Regular Braid	26°	82.0
	Heavy Weight	Diamond Braid	21°	35.0
		Regular Braid	17°	54.5

Basic Concept for Large Braided Structure

One of solutions for fabricating large braided composites was to make wider flat braided fabrics. When we can fabricate wider fabrics, that technique will be applied to various fields. Our basic concept for large braided structure in this paper was to link narrow flat braided fabrics. Accordingly very wider fabrics in any dimension can be produced by narrow one. Of course this system does not need huge machine with large number of spindles.

There are many linking method such as lacing stitch and loop stitch so on.(1) In this paper for linking knitted fabric technique was applied. This technique is similar to looping stitch technique. The schematic drawing of knitted link method is shown in Fig.4. This system has some superior points than other technique for linking fabrics. One is that braided fibers do not have some damages in linking process. This is very important point for mechanical properties of braided composites. In lacing stitch technique reinforced fibers suffer some damages and finally reduce their strength. As shown in Fig.4 knitted fibers go through braided fibers at the reversing point, so that knitted fibers do not make any damage on the braided fibers.

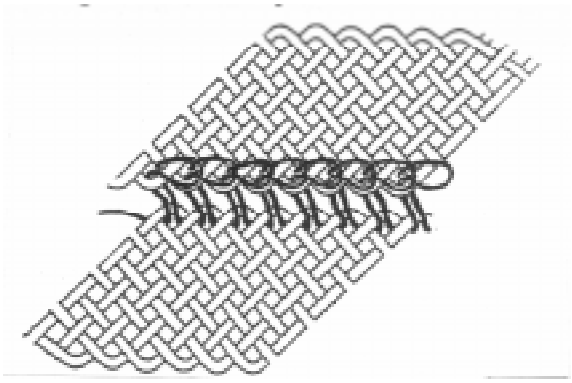

Fig. 4: Schematic drawing of knitted link method

Experiments

Fibers used in the experiments was glass fiber bundles with 2000 filaments and flat braided fabric was fabricated by the machine with 85 spindles. Fiber orientation angle to longitudinal direction was 38 degree. Linking was made by using dial linking machine as shown in Fig.5. This machine is a commercial available machine and is not special machine for linking. In this experiment aramid fiber was used for linking fibers. Three different linking methods were adopted as shown in Fig. 6; one was L shaped linking (L type) and the second one was single lap type link (S type), finally the third method was multi linked method (M type).(2) In these developed linking methods linking fibers do not make any damage on the braided fibers. After linking two flat braided fabrics, resin was impregnated into the fabrics and cured. The linked part was seemed to be the weakest part in the large braided structure. Therefore in order to the effects of linking part on the composite properties tensile tests were performed. For comparison, transverse strength of flat braided composites was also measured. Dimensions of specimens are 30 mm of width , 80 mm of gauge length and 1.6 mm of thickness.

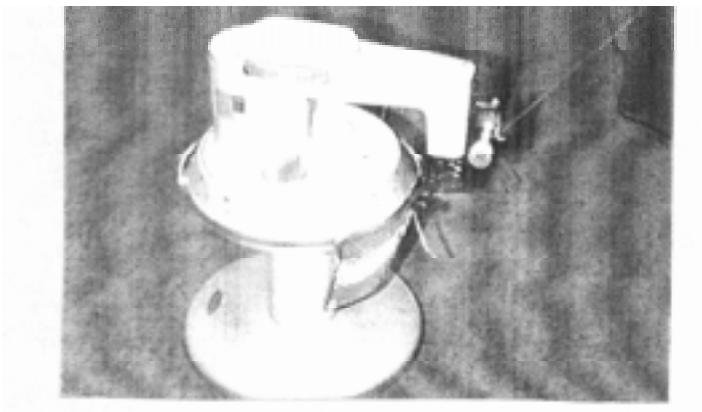

Fig. 5: Dial knitted machine

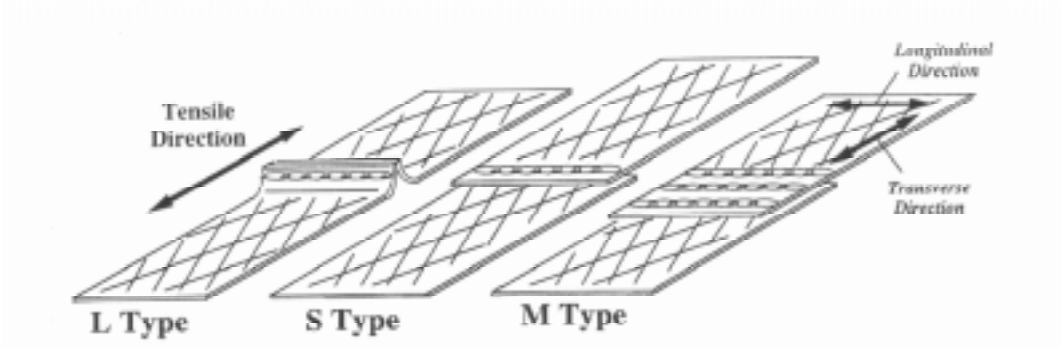

Fig. 6: Linking method

Results

The experimental results are shown in Table 2. Also the fracture aspects of each specimen are shown in Fig.7. The strength of L type was the lowest and the strength increased in order of S type and M type. Surprisingly, the strength of M type was higher than transverse strength (53MPa). The transverse specimen was failed at the middle of the specimen and the crack inclined to the loading direction. In the cases of L type and S type specimens the fracture occurred at the linked part and finally linked fibers were stretched. On the other hand M type specimen did not exhibit fracture at the linked part and the aspect was similar to the transverse specimen.

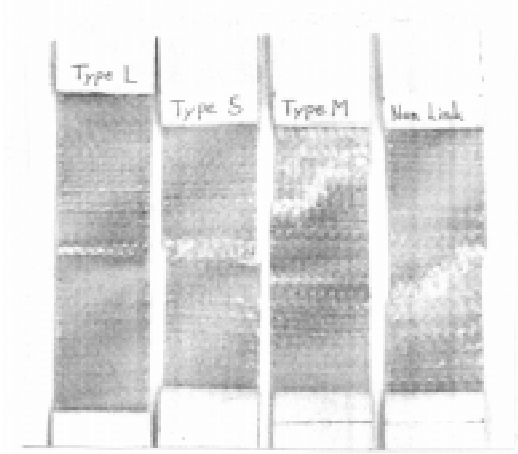

Fig. 7: Fracture aspects of each specimen

Table 2: Tensile strength of each link type

Link Type	Strength (MPa)
L Type	26
S Type	37
M Type	69
Non Link (Transverse Direction)	53

According to detail observation of fiber orientation state in these specimens, there were two possible explanations for the strength differences between transverse specimen and M type specimen. The transverse specimen was cut out from the center on flat braided fabrics, whereas the linked specimens were from the edge of the fabrics. Fig. 8 shows the schematic drawings of fiber orientation state in flat braided fabric. Normally fiber orientation states are divided into three regions; both side edge regions and the center region. Fiber orientation angle in each region is different. At the center both fiber bundles which across each other have same angle and at the side edge one group have low angle and the other has large angle to the loading direction (transverse direction). In the linked specimen there are some fibers oriented at small angle to loading direction, so that there was possibility that the strength of the M type specimen was higher than that of transverse specimens. Also in the transverse specimen the fibers were cut at the edge, whereas in the M type specimen the fibers continuously oriented through linking fibers between tabs. This state was similar to the specimen to longitudinal specimen in which reinforcing fibers orient through out the specimen from one end to the other end. This result was one of possible reason for the strength differences. Consequently, M type linked method was very useful for fabricating large scale braided structure without decrease the strength.

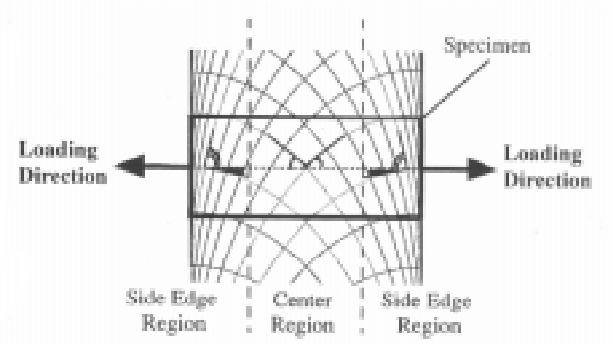

Fig. 8: Fiber orientation state in flat braided fabric

Large Scale I beam Braided Structure

In the I-shaped beam, connecting part between flange part and web part is the weakest point, so that our basic concept for braiding, that fiber continuously oriented throughout the products, is applied to the connecting part in our product. According to our previous paper the I beam posses higher bending strength than aluminum. For fabricating large scale I beam, T-shaped braided fabric and flat braided fabric were linked together. At the connecting part between flange part and web part T-shaped braided fabric was used, so that the fiber bundle oriented continuously from flange part to web part as shown in Fig. 9. Our final product of I beam at the moment was shown in Fig. 10 in which the thickness was 3 mm, the height was 400 mm and width of flange was 400 mm. Further mechanical properties of these large scale products were measured.

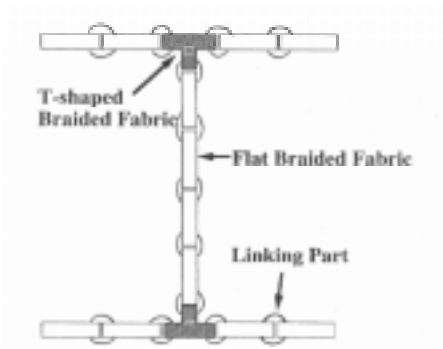

Fig. 9: Structure of large scale I beam

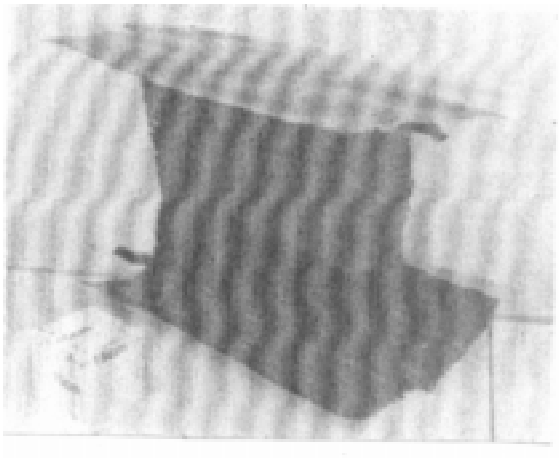

Fig. 10: Final product of large scale I beam

CONCLUSION

In this paper a method which can fabricate large scale braided structure was presented. Knitting technology was applied for linking narrow flat braided fabrics, and three kinds of linking methods were proposed. M type linking provided higher strength than normal braided fabrics. According to proposed method a big lack of braided composites could be solved, so that it was believed that further usage of braided composites would be expanded.

REFERENCES

1. *Handbook of Composite Materials*, Japan Society for Composite Materials Edition, Nikkan Ko-gyo Sinbunsha Ltd., pp.197 (1989)

2. M. Y. Tsai and J. Morton, "The effect of a spew fillet on adhesive stress distributions in laminated composite single-lap joints", *Composite Structures* , 32, (1995), pp.123-131.

MECHANICAL MODEL OF 3-DIMENSIONAL MULTI-STEP BRAIDED COMPOSITES

Joon-Hyung Byun

Composite Materials Lab, Korea Institute of Machinery & Materials
Sangnam-Dong, Changwon, Korea.

SUMMARY: The mechanical model of 8-step braided composites has been proposed for more comprehensive understanding of three-dimensional (3-D) textile composites. The analysis includes the geometric model of unit cells, microstructural characteristics (i.e., yarn orientation and fiber volume fraction), and prediction of elastic constants of the composites. The coordinate transformation and the averaging of stiffness and compliance constants are utilized in the prediction of elastic constants. Since nine types of unit cells are identified in the thickness and width directions of 8-step braided composites, characterization of mechanical properties is based upon the macro-cell, which occupies the entire cross-section and the unit pitch length of the sample. Relatively good correlation has been observed between the model prediction and the test results of the carbon/epoxy composite samples.

KEYWORDS: 8-step braiding, unit cell, coordinate transformation, macro-cell, average stiffness, compliance, elastic constants

INTRODUCTION

Recent development of textile preforming technology has significantly expanded the potential of three-dimensional (3-D) textile composites in various applications. Among several types of 3-D reinforcements the braided preforms have gained considerable attention due to the possibility of near-net shaping [1,2]. However, the application of 3-D rectangular braided composites has some limitations due to the slow fabrication speed and cross-sectional size. There have been a lot of efforts to overcome the limitation of 3-D braiding. An automated 2-step braiding machine has been developed to increase the preforming speed [3], and the concept of multi-step braiding has been proposed to broaden the range of attainable braid architecture [4]. Kostar and Chou [4] has demonstrated that the multi-step braiding can produce 2-step, 4-step and 8-step braids.

By utilizing the concept of the multi-step braiding, the possibility of the microstructural design of 3-D braided composites can be enlarged. The 2-step and 4-step braids have been the subjects of extensive studies [5-8] due to their unique microstructure and performance characteristics. Although axial yarns can be inserted into a 4-step braid, the amount of axial yarn volume is less than that could be achieved in 2-step braids. Thus, the longitudinal elastic stiffness of 4-step braided composites is lower than that of 2-step braided composites but, 4-step braids are more conformable to a curved shape. The geometric pattern of 8-step braids is close to that of 4-step braids, resulting in the similar characteristics for the composites performance. The advantage of 8-step braid is that the structure is more integrated that the 4-

step when the braider yarn angle is very small. This is due to the fact that the machine cycle of the 8-step braiding doubles that of the 4-step braiding, and the braider yarns are intertwined at a longer pitch length. Although Kostar and Chou [4] suggested that the 8-step braids can be applied to hybrid composites where specific fibers can be placed in the desired location, there seems to be size limitation for this effect.

The development of three-dimensionally reinforced materials are associated not only with the manufacturing processes of textile preforms and composites but also with the assessment of structural performance of the composites. Considerable effort has been made by researchers to evaluate the effectiveness of various 3-D textile composites [9]. Most of the previous studies on the analytic characterization of 3-D textile composites have shown that the proposed unit cells do not represent the entire structure of braided composites. Recently, Byun and Chou [5] have proposed a macro-cell model which describes accurate representation of 3-D braided composites. In an attempt to extend the applicability of the analytic methodology into other types of braided composites, the mechanical model is developed in this paper to predict the elastic constants of 8-step braided composites, and the correlation between the model prediction and the experimental results is made. The analysis includes identifying the unit cell structures and macro-cell approach based upon the averaging technique.

8-STEP BRAIDING PROCESS

The 8-step braiding [4], which is an extension of the 4-step braiding, involves shifting distance of column movement is twice as that of rows as depicted schematically in Fig. 1. The yarn arrangement is [8 x 4] in the figure, where the numbers of column and row carriers of the machine bed are 8 and 4, respectively. It is noted that at the end of eight steps (i.e., one machine cycle) the

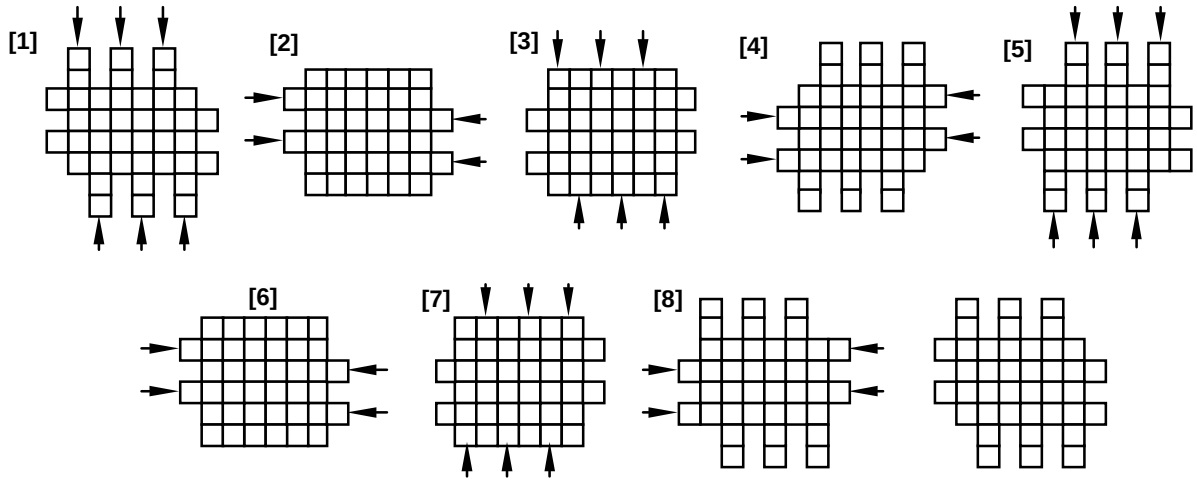

Fig. 1: 8-step braiding process [4]

yarn carrier arrangement is the same as the initial configuration, although the individual carriers have changed their locations. In the 3-D braiding process, the arrangement of braiding yarns determines the number of axial yarns and the cross-sectional shape of the braid. The preform is advanced by the given pitch length after specified steps, and this sequence repeats to produce a desired preform length.

The key geometric parameters are the pitch length and the braider yarn angle. The pitch length is the take-up distance of the preform, and the braider yarn angle is the lower angle between the axial direction of the preform and braiding yarns. The surface of an 8-step braided preform is shown in Fig. 2. The pattern is characterized by the braider yarn angle, θ, and the pitch length, h. Although the braider yarn angle is the most important parameter in designing the preform, it is not easy to control the angle directly. Since the pitch length and the braider yarn angle has a reciprocal relation [5], the pitch length is usually controlled in the braiding process.

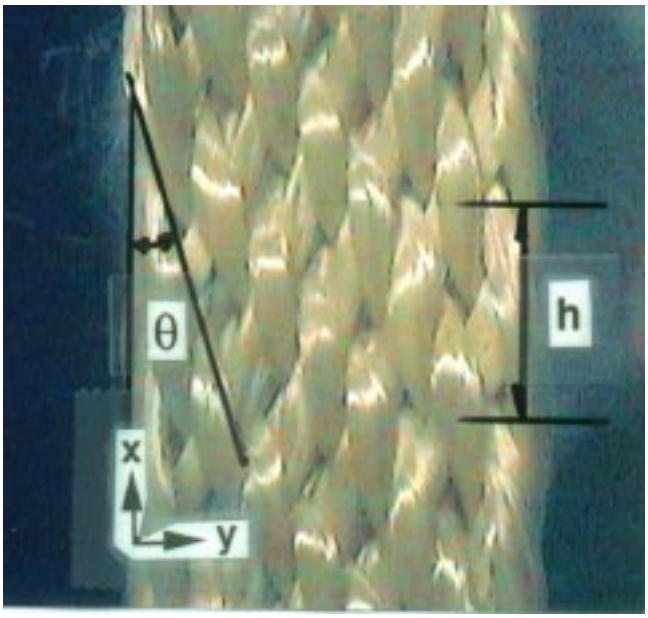

Fig.2: The surface of an 8-step braided preform

GEOMETRIC CHARACTERISTICS

Unit Cells

Identification

The identification of unit cells is to determine the orientation angle of the braider yarn. If the yarn movement is independent of one another and there are no interactions among them, unit cells can be easily identified from the braider yarns on the machine bed. In the real situation, however, yarns shift the locations due to the cross-over pass with each other, and their cross-sectional shapes are deformed. Those changes also occur in accordance with mold size, which determines the dimension of the composite specimen. The accurate description of the microstructure can be achieved by observing the yarn cross-sections cut from the progressive sections of a composite specimen along the longitudinal direction. This procedure has been successfully applied to the unit cell identification of 4-step braided composites [5]. Due to the machine operation in Fig.1, the yarn arrangement in the cross-section of the composite is 180^{o} rotated configuration with respect to the central point of the section. After the cross-section was photographed, the specimen was sanded to remove a thin layer of Δt, and the surface is polished again for observation. By plotting each yarn at every successive cut, the

yarn path was constructed as shown in Fig. 3. It should be noted that only the representative yarn paths were plotted for clarity, and the distance between two neighboring point is Δt in the longitudinal direction (x-axis).

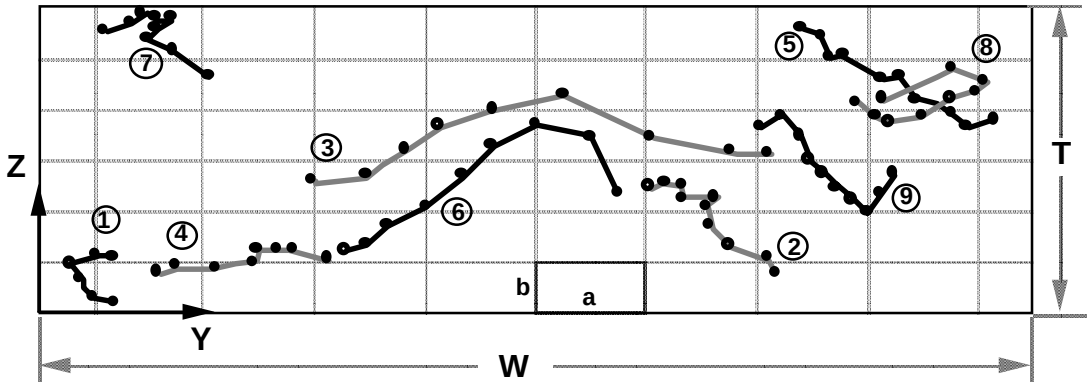

Fig. 3: Yarn path of an 8-step braided composites for [8x4] arrangement

Idealization

Based upon Fig. 3, the unit cells of the composite can be constructed. Nine different types of unit cells can be identified as shown in Fig. 4. Each unit cell is idealized as a parallelepiped containing a single yarn. The unit cell geometry can be described by the yarn orientation angle, and the unit cell size (h, a, and b). Here, h is the pitch length, and a and b are related to the yarn movement on the machine bed and the preform compaction in the mold. Parameters a and b can be obtained from the width and the thickness of the sample. It is noted that the yarn at the sides of the sample occupies half of the yarn width.

$$a = \frac{W}{m+1} \quad ; \quad b = \frac{T}{n+2} \tag{1}$$

Utilizing Eqn 1, the braider yarn orientation angle can be expressed as follows:

$$\theta_1 = \tan^{-1}\left(\frac{1}{h}\sqrt{a^2+b^2}\right) \; ; \; \theta_2 = \tan^{-1}\left(\frac{1}{h}\sqrt{a^2+4b^2}\right) \tag{2}$$

$$\theta_3 = \tan^{-1}\left(\frac{2}{h}\sqrt{(2a)^2+b^2}\right) \; ; \; \theta_4 = \tan^{-1}\left(\frac{2a}{h}\right) \; ; \; \theta_5 = \tan^{-1}\left(\frac{2}{h}\sqrt{a^2+b^2}\right) \tag{3}$$

$$\theta_{6A} = \tan^{-1}\left(\frac{3}{h}\sqrt{a^2+b^2}\right) \; ; \; \theta_{6B} = \tan^{-1}\left(\frac{3}{2h}\sqrt{a^2+4b^2}\right) \tag{4}$$

$$\theta_{7A} = \tan^{-1}\left(\frac{a}{h}\right) \; ; \; \theta_{7B} = \theta_2 \tag{5}$$

$$\theta_{8A} = \tan^{-1}\left(\frac{3}{h}\sqrt{a^2+(b/2)^2}\right) \; ; \; \theta_{8B} = \tan^{-1}\left(\frac{3}{2h}\sqrt{a^2+b^2}\right) \tag{6}$$

$$\theta_9 = \tan^{-1}\left(\frac{3}{h}\sqrt{(2a)^2+(3b)^2}\right) \tag{7}$$

Fiber Volume Fraction and Braider Yarn Angle

In order to analyze the macroscopic characteristics of 3-D textile composites, it is necessary to employ the *macro-cell* approach. This approach is effective in characterizing the complex structure of 3-D textile composites, in which no single unit cell repeats in the thickness and width directions. For the case of 8-step braided composites, the macro-cell encompasses the entire cross-section and the unit pitch length. Since the yarn cross-sectional area and the orientation angle have been obtained in the previous sections, the yarn volume in the macro-cell can be readily determined by multiplying the yarn area with the actual yarn length :

$$V_i = \frac{\lambda h}{\rho \kappa \cos\theta_i} \qquad (i = 1 - 9) \tag{8}$$

where, λ, ρ and κ are the linear density of the yarn (kg/m), fiber density (kg/m^3) and fiber packing fraction. The fiber packing fraction is the local fiber volume fraction of the yarn. Thus, the fiber volume fraction of the 8-step braided composite can be determined by considering the number of each unit cell and the fiber packing fraction.

$$V_f = \frac{\kappa \Sigma N_p V_p}{WTh} \tag{9}$$

where, N_p is the number of unit cell type p in the macro-cell as shown in Fig. 5. Similarly, the braider yarn orientation angle (θ_a) can be obtained by averaging the yarn angle for each unit cell and by taking into account the number of unit cells in the macro-cell.

$$\theta_a = \frac{\Sigma N_p \theta_p}{m(n+2)+n} \tag{10}$$

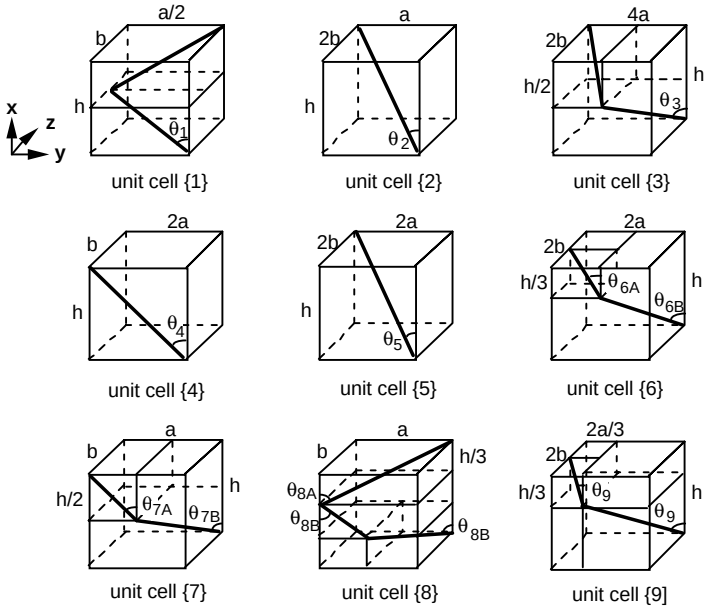

Fig. 4: Unit cells for 8-step braided composites

	1	2	6	2	6	2	6	2	
3	4	3	4	3	4	9	7	9	
	9	8	5	6	5	3	5	3	5
5	3	5	3	5	6	5	8	9	
	9	7	9	4	3	4	3	4	3
	2	6	2	6	2	6	2	1	

Fig. 5: Unit cell distribution in the macro-cell

COMPOSITE ELASTIC PROPERTIES

The elastic properties of 8-step braided composites can be predicted based upon the fiber and matrix properties and the three-dimensional fiber architecture. From the unit cell identification, the macro-cell of the braided composites can be regarded as an assemblage of anisotropic elastic unit cells whose properties are those of spatially oriented yarn and the matrix system. Since the principal material direction of the three-dimensionally located yarn do not coincide with the coordinate directions of our interest, the stress-strain relations are transformed from one coordinate system to another. Then, the effective elastic constants of 3-D textile composites can be obtained in two ways, either by assuming uniform stress or uniform strain throughout the macro-cell. The assumption of uniform stress implies a serial stacking of unit cells and averaging of compliance constants. In a similar manner, the case of uniform strain can be conceived as parallel arrangement of unit cells and averaging of stiffness constants.

Coordinate Transformation

Figure 6 shows the coordinate systems of a spatially oriented yarn segment. The local coordinate system is indicated as 1-2-3, where axis 1 coincides with axial yarn direction. In the global coordinate system, x-axis is along the composite longitudinal direction, and y-z-axes are in the width and thickness directions of the composite. The braider yarn orientation is indicated as θ, and angles, ϕ and ψ are defined as the *off-axis* and *inclination* angles, respectively.

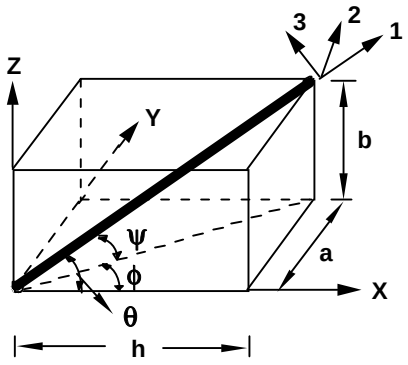

Fig. 6: Coordinate systems of a spatially oriented yarn segment

The compliance matrix of the composite cylinder in the 1-2-3 coordinate system is expressed as follows due to the transverse isotropy,

$$[S] = \begin{pmatrix} 1/E_{11} & -\nu_{21}/E_{22} & -\nu_{21}/E_{22} & 0 & 0 & 0 \\ -\nu_{12}/E_{11} & 1/E_{22} & -\nu_{32}/E_{22} & 0 & 0 & 0 \\ -\nu_{12}/E_{11} & -\nu_{23}/E_{22} & 1/E_{22} & 0 & 0 & 0 \\ 0 & 0 & 0 & 1/G_{23} & 0 & 0 \\ 0 & 0 & 0 & 0 & 1/G_{12} & 0 \\ 0 & 0 & 0 & 0 & 0 & 1/G_{12} \end{pmatrix} \tag{11}$$

where the Young's modulus E_{ij}, shear modulus G_{ij}, and Poisson's ratio ν_{ij} are obtained from the fiber and matrix properties using micro-mechanics analysis. Then, the compliance matrix of the unidirectional composite rod, referring to the 123 coordinate system, is transformed to $[S']$, referring to the xyz coordinate system:

$$[S'] = [T]^t [S] [T] \tag{12}$$

where [T] is the transformation matrix, and $[T]^t$ is a transposed matrix of [T]. The general transformation matrix between the local and the global coordinate systems has the following form [10]:

$$[T] = \begin{pmatrix} \alpha_1^2 & \alpha_2^2 & \alpha_3^2 & 2\alpha_2\alpha_3 & 2\alpha_3\alpha_1 & 2\alpha_1\alpha_2 \\ \beta_1^2 & \beta_2^2 & \beta_3^2 & 2\beta_2\beta_3 & 2\beta_3\beta_1 & 2\beta_1\beta_2 \\ \gamma_1^2 & \gamma_2^2 & \gamma_3^2 & 2\gamma_2\gamma_3 & 2\gamma_3\gamma_1 & 2\gamma_1\gamma_2 \\ \beta_1\gamma_1 & \beta_2\gamma_2 & \beta_3\gamma_3 & \beta_2\gamma_3+\beta_3\gamma_2 & \beta_1\gamma_3+\beta_3\gamma_1 & \beta_1\gamma_2+\beta_2\gamma_1 \\ \gamma_1\alpha_1 & \gamma_2\alpha_2 & \gamma_3\alpha_3 & \gamma_2\alpha_3+\gamma_3\alpha_2 & \gamma_1\alpha_3+\gamma_3\alpha_1 & \gamma_1\alpha_2+\gamma_2\alpha_1 \\ \alpha_1\beta_1 & \alpha_2\beta_2 & \alpha_3\beta_3 & \alpha_2\beta_3+\alpha_3\beta_2 & \alpha_1\beta_3+\alpha_3\beta_1 & \alpha_1\beta_2+\alpha_2\beta_1 \end{pmatrix} \tag{13}$$

where α,β, and γ with subscripts are direction cosines, which can be simplified by setting the 2-axis perpendicular to the z-axis from Fig. 6 :

$$\begin{gathered} \alpha_1 = \cos(1,x) = \cos\phi\cos\psi\ ;\ \alpha_2 = \cos(1,y) = \sin\phi\cos\psi\ ;\ \alpha_3 = \cos(1,z) = \sin\psi \\ \beta_1 = \cos(2,x) = -\sin\phi\ ;\quad \beta_2 = \cos(2,y) = \cos\phi\ ;\quad \beta_3 = \cos(2,z) = 0 \\ \gamma_1 = \cos(3,x) = -\cos\phi\sin\psi\ ;\ \gamma_2 = \cos(3,y) = -\sin\phi\sin\psi\ ;\ \gamma_3 = \cos(3,z) = \cos\psi \end{gathered} \tag{14}$$

The coordinate transformation is conducted for the yarn segment in the unit cells. From Fig. 4, ϕ and ψ for each unit cell can be expressed as follows.

$$\phi_i = \tan^{-1}\left[\frac{\tan\theta_i}{\sqrt{1+R_i^2}}\right]\ ;\quad \psi_i = \tan^{-1}(R_i \sin\phi_i) \qquad (i = 1 - 9) \tag{15}$$

where, R is the length ratio of the yarn segment in the y-direction with respect to that in the z-direction. For example, R_1 = b/a, R_3 = b/2a, R_4 = 0, R_{6a} = b/a, and R_{6b} = 2b/a. By combining Eqns 14 and 15, transformation matrix [T] can be calculated for each type of unit cell, and the transformed compliance constants of braider yarns in the global coordinate system are determined from Eqn 12.

Elastic Constants

Considering the macro-cell (Fig. 5) under external force in the x-direction, the uniform strain can be assumed for each unit cell. For the yarns in the unit cell {8}, however, their various reinforcing directions result different elastic constants. Unit cell {8} consists of three yarn segments which are arranged in series with respect to the x-axis. Thus, the uniform stress assumption is applied for these yarn segments, and the transformed compliance constants of these segments are averaged based upon their projected length in the x-axis. The other types of unit cells do not need this averaging process because the yarn segments are in parallel arrangement in those unit cells. The averaged compliance constants of unit cell {8} is :

$$(S'_{ij})8 = \frac{1}{3}(S'_{ij})\,8a + \frac{2}{3}(S'_{ij})\,8b \tag{16}$$

where, S'_{ij} is the transformed compliance constants of each yarn segment.

In the macro-cell, in which all the unit cells are arranged in parallel under the loading in the x-direction, the deformation properties of the composite is obtained by averaging the stiffness constants of unit cells based upon their volume contribution.

$$C^c_{ij} = \frac{\Sigma N_p V_p (C'_{ij})_p}{WTh} + \left(1 - \frac{\Sigma N_p V_p}{WTh}\right)(C_{ij})_m \qquad (p = 1 - 9) \tag{17}$$

where, V and C'_{ij} with subscript, p, refer to the yarn volume and inverted stiffness matrix from S'_{ij} of each type of unit cell . The subscript m denotes the matrix material. It should be noted that the yarn volume is considered in Eqn 17 because the stiffness and compliance matrices are for the unidirectional composites. Finally, the stiffness matrix of the macro-cell is inverted to the compliance matrix, S^c_{ij} , and the elastic constants are then obtained as follows :

$$\begin{gathered} E_{xx} = 1/S^c_{11} \;\; ; \;\; E_{yy} = 1/S^c_{22} \;\; ; \;\; E_{zz} = 1/S^c_{33} \\ G_{yz} = 1/S^c_{44} \;\; ; \;\; G_{zx} = 1/S^c_{55} \;\; ; \;\; G_{xy} = 1/S^c_{66} \\ \nu_{xy} = -S^c_{12}/S^c_{11} \;\; ; \;\; \nu_{zx} = -S^c_{31}/S^c_{11} \;\; ; \;\; \nu_{yz} = -S^c_{32}/S^c_{22} \end{gathered} \tag{18}$$

CORRELATION

The 8-step braids were fabricated using 12K T300 carbon fiber, and the consolidation of the preforms was accomplished by the resin transfer molding (RTM) technique using the epoxy and curing agent. The samples were cured at 150 ^{o}C for two hours. In order to verify the analytical characterization of 8-step braided composites, experiments on mechanical response have been conducted. Tensile test was performed to measure the longitudinal modulus and Poisson's ratio of the composites. The dimension of specimens was 12.9 mm x 4.3 mm x 229 mm, and they were instrumented with biaxial strain gages of 6.35 mm in gage length. All tests were conducted on a screw-driven Instron machine at a cross-head speed of 1.27 mm/min.

Table 1 summarizes the input data for the calculation, and the results of model prediction and experiments. Relatively good correlation between the model prediction and the test results can be observed. It is also noted that three-dimensional elastic constants can be predicted in the proposed mechanical model. This can provide important data in analyzing and designing the structures consisting of 3-D textile composites.

Table 1: Input data for calculation, the model predictions and experimental results

Input Data		**Model Prediction**	**Test Results**
Mechanical Data T300 Carbon Fiber E_{1f} = 240 GPa E_{2f} = 16.6 GPa G_{12f} = 8.27 GPa G_{23f} = 5.89 GPa ν_{12f} = 0.26 Epoxy E_m = 4 GPa ν_m = 0.38	*Geometric and Physical Data* T = 4.3 mm W = 12.9 mm h = 15.0 mm [m x n] = [8 x 4] κ = 0.8 $\lambda = 8.212 \times 10^{-4}$ (kg/m) $\rho = 1.77 \times 10^{3}$ (kg/m^3)	*Engineering Constants* E_{xx} = 62.7 GPa E_{yy} = 9.97 GPa E_{zz} = 10.38 GPa G_{yz} = 3.77 GPa G_{zx} = 4.70 GPa G_{xy} = 5.06 GPa ν_{yz} = 0.34 ν_{zx} = 0.25 ν_{xy} = 0.35 *Geometric Characteristics* θ = 12^o V_f = 0.46	*Engineering Constants* E_{xx} = 65.1 GPa E_{yy} - E_{zz} - G_{yz} - G_{zx} - G_{xy} - ν_{yz} - ν_{zx} - ν_{xy} = 0.37 *Geometric Characteristics* θ = 14^o V_f = 0.485

CONCLUSION

(1) A mechanical model has been proposed to predict the elastic properties of 8-step braided composites. Nine types of unit cell were identified by observing the sample cross-section in a progressive cut. The analytical approach for characterizing the 8-step braided composite was based upon the macro-cell, which basically occupies the entire cross-section and unit pitch length of the sample.

(2) The coordinate transformation and the averaging of stiffness and compliance constants are utilized in the prediction of elastic constants. The experimental results compared favorably with the model predictions. Although the experimental characterization was not enough to support the model prediction due to the lack of established test methods for 3-D textile composites, the methodology introduced in this paper can be effectively utilized by the materials and structural designers in obtaining the three-dimensional elastic constants of the composites.

REFERENCES

1. Chou, T-W., *Microstructural Design of Fibrous Composites*, Chapter 6 & 7, Cambridge University Press, Cambridge, 1992.

2. Chou, T-W. and Ko, F.K., *Textile Structural Composites*, Pipes, R.B., Editor, Elsevier Science Publisher, 1989.

3. Byun, J-H., "Development of an Automated 2-Step Braiding Machine and the Process Model", *Proceedings of Innovative Processing and Characterization of Composite Materials*, ASME WAM, 1995, pp. 305-315.

4. Kostar, T.D. and Chou, T-W., "Process Simulation and Fabrication of Advanced Multi-Step Three-Dimensional Braided Preforms", *J. Mat. Sci.*, 1994, Vol. 29, p. 2159.

5. Byun, J-H. and Chou, T-W., "Process-microstructure relationship of 2-step and 4-step braided composites", *Composites Science and Technology*, 1996, Vol. 56, pp. 235-251.

6. Pandy, R. and Hahn, H.T., "Designing with 4-Step Braided Fabric Composites", *Composites Science and Technology*, 1996, Vol. 56, pp. 623-634.

7. Du, G-W, Popper, P., and Chou, T-W.1991. "Analysis of 3-D Textile Preforms for Multi-directional Reinforcement of Composites", *J. Mat. Sci.*, Vol. 26, pp.3438-3448.

8. Macander, A.B., Crane, R.M., and Camponeschi, E.T., "Fabrication and Mechanical Properties of Multidimensionally (X-D) Braided Composite Materials", ASTM STP 873, 1986, pp. 422-445.

9. Byun, J-H., and Chou, T-W., "Three-Dimensional Textile Composites: A Review", 112th ASME Winter Annual Meeting, *Symposium on Composites in Transportation Vehicles*, Atlanta,Georgia, Dec.1-6, 1991.

10. Lekhnitskii, S.G., *Theory of Elasticity of an Anisotropic Elastic Body*, San Francisco, Holden-Day, 1963.

TOWARDS AN INTEGRATED PROCESSING MODEL FOR A CO-MINGLED THERMOPLASTIC COMPOSITE

T. A. Cain, M. D. Wakeman, R. Brooks, A. C. Long and C. D. Rudd

Department of Mechanical Engineering, University of Nottingham, UK.

SUMMARY: This paper describes work which has been undertaken in order to model the three major processes which occur during the processing of a co-mingled thermoplastic composite, namely material deformation, consolidation and heat transfer. Material deformation has been modelled using a kinematic fabric draping model which predicts fibre orientation, and which may be used to estimate variations in local component thickness. The consolidation model, which predicts developed moulding pressure, is a 1-D formulation based on fibre bed compaction and matrix flow in fibre bundles. Heat transfer during processing is simulated via a 1-D through-thickness formulation which predicts the temperature distribution within the laminate. This model uses simple convective and conductive boundary terms so that the temperature distribution within the laminate may be determined at any instant from the end of pre-heat, up to the completion of moulding. The paper concludes with a discussion on the integration of these models, and the utility of the resulting processing model in component and process design.

KEYWORDS: modelling, co-mingled, thermoplastic, consolidation, fabric deformation, heat transfer

INTRODUCTION

Co-mingled fabrics allow production of parts containing aligned glass fibres at higher volume fractions using lower moulding pressures than are attainable using flow moulded materials. This makes them particularly attractive to the automotive industry with the potential to permit cost and weight benefits over established material systems. Several manufacturing routes exist for processing of co-mingled materials including press moulding, vacuum bagging and autoclave moulding. In order to produce high quality laminates using any of these processes it is important to have an understanding of the effect of the processing parameters upon the finished laminate. Through the development and integration of models for the deformation, consolidation and cooling of a co-mingled thermoplastic laminate, the component design and process optimisation can be integrated with a reduced need for experimentation and prototyping.

DEFORMATION

Several workers have investigated the application of large deformation shell finite-element theories to the prediction of draped fabric forms [1, 2]. Good results may be obtained via this route, but the method can appear computationally expensive in comparison to the kinematic fabric deformation models which others have used for drape simulation, notably Long [3] and Van West [4].

The fabric deformation simulation in this work is based on kinematic drape model developed at Nottingham. This model assumes that the fabric drapes over a surface via in-plane fabric shearing only.

In order to generate a unique solution for the draped configuration, one fibre path in each of the warp and the weft directions must be constrained. Fig. 1 shows the predicted fibre configuration when a fabric is draped over a thick disc mounted on a flat plate. In this example, symmetry has been used to reduce the scale of the modelling problem, and the constrained fibre paths are co-incident with the planes of symmetry.

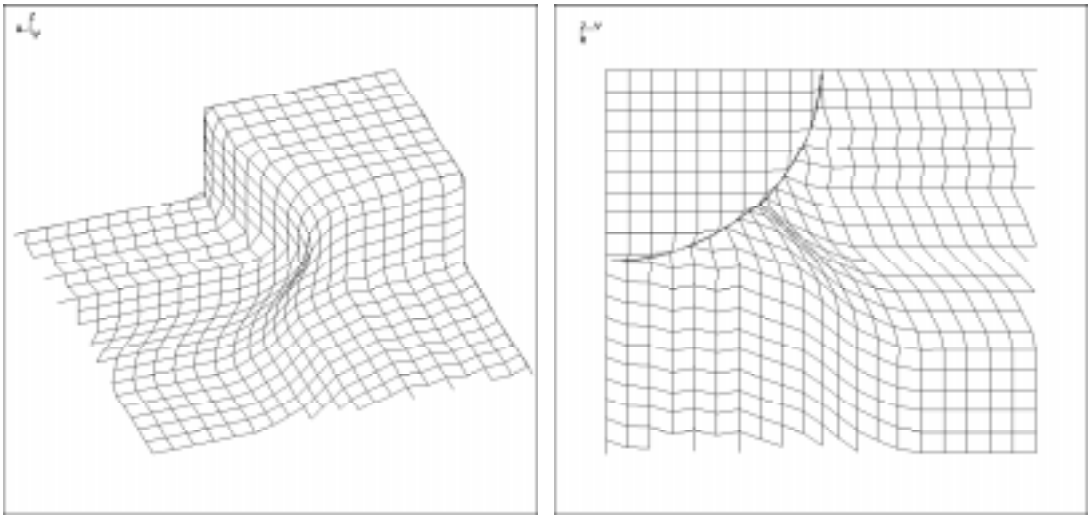

(a) General View *(b) Plan View*

Fig. 1: Draped fabric configuration—2 views

CONSOLIDATION

Previous investigators, notably Klinkmuller [5], Ye [6] and Van West [7], have studied the impregnation and consolidation mechanisms occurring during the isothermal compaction of co-mingled materials. Van West developed a 1-D consolidation model for co-mingled materials based on a worst-state case of fibre interspersion, with the glass and matrix material located in two adjacent, but completely separate regions. Staged compaction of a co-mingled fabric has been used to obtain micrographs of the fibre dispersion and matrix impregnation at states of consolidation ranging from unconsolidated to completely consolidated [8]. Observations from these micrographs suggest a modification to the Van West Model which allows improved simulation of the fibre dispersions for the material under study. In addition,

an investigation into the effect of in-plane shear on fabric compaction has been undertaken in order to allow further modification to the consolidation model.

Experimental Details

Materials

A balanced twill weave fabric of superficial density 650g/m^2 consisting of a yarn of 60% by mass co-mingled E-glass and carbon black pigmented polypropylene supplied by Vetrotex SA International under the trade name "Twintex™" was used throughout the studies. The glass fibres and the polypropylene filaments had nominal diameters of 17 and 20 - 25 microns respectively.

Specimens consisting solely of the glass reinforcement which is incorporated in Twintex were required in order to determine the compressive response of the fibre constituent. Samples of material were treated in a furnace at 400^{o}C for 300 seconds to remove the polypropylene filaments without disturbing the glass fibre architecture.

Isothermal Compaction Trials

An Instron Universal Mechanical Testing Machine model 1195 with a 100 kN load cell and a model 3111 hot air oven was used to compact 100 x 100 mm squares of co-mingled fabric between steel platens. The temperature between the platens was monitored using K-type thermocouples. Four layers of fabric were placed into the platens at 180-185^{o}C with a thermocouple inserted into the centre of the fabric. When the temperature of the material reached 180^{o}C the fabric was compacted at 1mm/min. The laminate was cooled to 100^{o}C, the load removed and the plaque extracted.

To investigate the consolidation mechanism 4 samples were prepared, with compaction to 25%, 50%, 75% and 100% of the cross-head displacement required to produce full consolidation. The theoretical laminate height of 0.46mm/layer was calculated on the basis of the material superficial density, the constituent densities and fibre volume fraction. At 25% consolidation the reinforcement bundles were distinct and separate, with some matrix material interspersed within the bundle. At 50% consolidation the matrix had almost coalesced, but large voids remained within and around the bundles and dispersion of fibres within the matrix was uneven. At 75% consolidation the laminate still contained significant voidage, but matrix and reinforcement were well interspersed, and the longitudinal bundles were increasing in aspect ratio as they were compressed. At 100% consolidation, the fibre distribution had improved still further, and little voidage remained.

Sheared Fabric Compaction

In order to investigate the effect on the compaction response of in-plane fabric shear, 4 layers of Twintex fabric were sheared to the required angle in a parallelogram clamping frame. The fabric was then clamped at the periphery using a two-piece clamping frame, with one frame located below the fabric, and the other located above the fabric, the two halves being joined using captive bolts and wing nuts.

Three groups of sheared samples were compacted:
1. Fabric un-sheared, as a control.

2. Fabric sheared to the maximum shear angle attainable with this fabric, which was found to be approximately 25^o at room temperature.
3. Fabric in a median state of shear, between zero and the determined maximum, which is approximately 13^o.

The samples were sheared as described previously, and then compacted using an Instron model 1195 testing machine equipped with electrically heated platens. The platen temperature was regulated using one PID controller per platen, which was set to 190^{o}C. The sheared fabric stack was placed into the platens with a K-type thermocouple inserted through the fabric into the stack centre. When the thermocouple within the material registered a temperature of 189^{o}C, the material was compacted at 50mm/minute. Compaction was halted when the force at the load cell exceeded 45kN, or when the laminate was compacted to a height of 1.5mm.

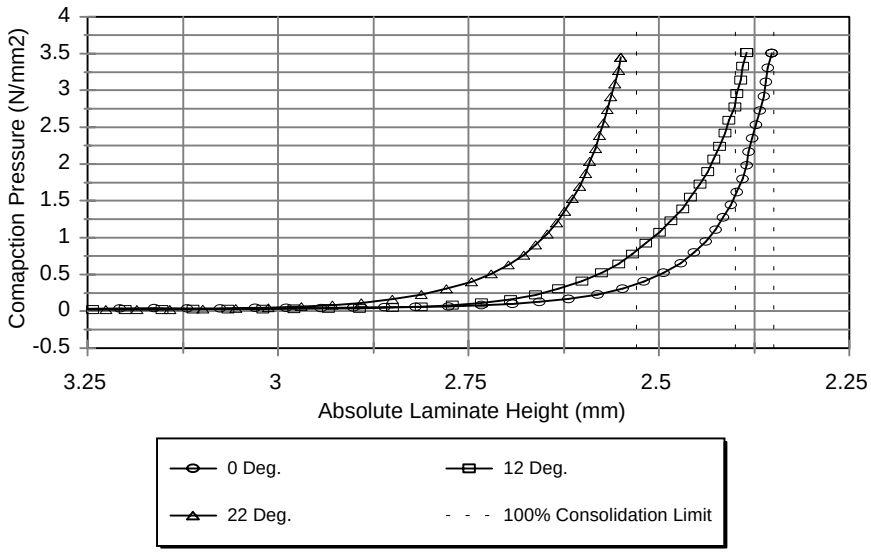

Fig. 2: Pressure vs laminate height for compaction of sheared co-mingled fabric

Fig. 2 shows a plot of pressure *vs* laminate height for compaction of laminates which have been sheared by 0^o, 12^o and 22^o. The theoretical minimum height for each laminate has been calculated on the basis that material is conserved when shear is applied, so that the height of a sheared sample may be calculated by Eqn. 1:

$$h_{fs} = \frac{h_f}{Sin(90 - \theta)} \qquad (1)$$

where h_f is the un-sheared minimum laminate height, θ is the angle of shear and h_{fs} is the minimum sheared laminate height. The theoretical minimum heights are marked on the graph as dashed lines. The curves show that the minimum height attained (all tests terminated at the upper load, rather than displacement, limit of 45kN = 3.4N/mm^2) increases with increasing shear angle.

Figure 3 shows a plot of minimum laminate height *vs*. laminate shear angle. This also shows a trend of increasing laminate height with increasing shear angle, albeit with some scatter in the results. Again, the theoretical minimum height is plotted on this graph, and it should be

noted that all the experimental data lies above this curve. This may be attributed to incomplete consolidation of the test plaques - as soon as the upper load limit was reached during compaction, the testing machine cross-head returned to the upper set-point, removing all load from the plaque.

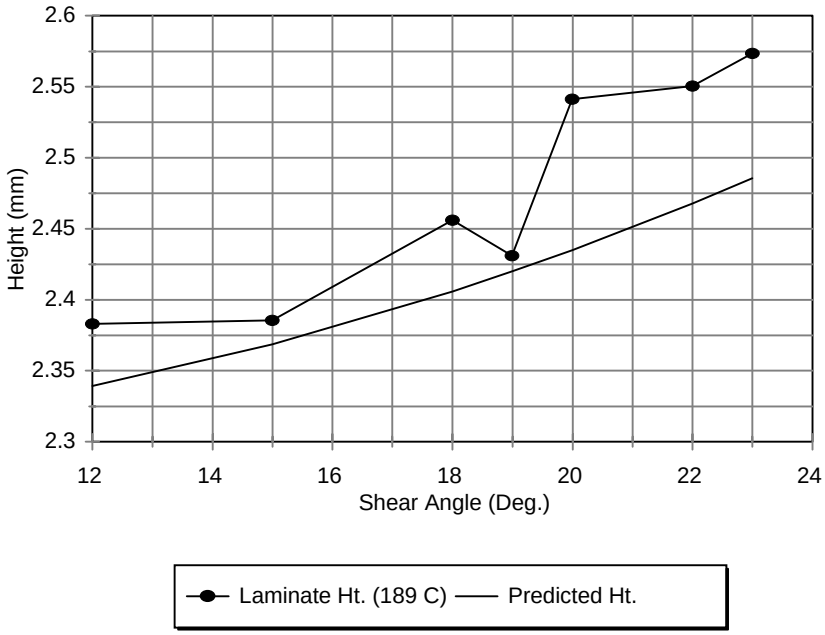

Fig. 3: Minimum Laminate Height Attained vs In-plane shear.

Consolidation Modelling

A 1-D isothermal consolidation model for co-mingled has been developed [8], which is based on the work of Van West [7] and uses the same single fibre bundle unit-cell, but differs from the original in several of the modelling assumptions which are applied. The model assumes a constant rate of compaction is applied to the material, the matrix material may be non-Newtonian, and the viscosity of the matrix material is temperature dependent. The material resistance to compaction is assumed to be the sum of the fibre bed compressive response and the matrix pressure. The impregnation portion of the model uses an 'effective bundle radius' which is determined as the distance the matrix must flow to wet out the fibres, and is based on observations of cross-sectional micrographs of the unconsolidated material. This model is composed of four sub-models:

Fibre Compaction

Modelling of the elastic response of the reinforcement is based on experimental data. Compaction tests were performed upon reinforcement only, which was obtained as described previously. The reinforcement was lubricated with an automotive 20/50 oil ("Century" supplied by Chemac Ltd), and a single layer of reinforcement was compacted at 1mm/minute using an Instron model 1195 testing machine. It was found that the behaviour of the fibre bed could be represented by a power-law relationship, where P_{fb} is the fibre bed pressure, h is the instantaneous fibre bed height, and h_0 is the initial fibre bed height, which was found to be 0.3mm:

$$P_{fb} = A \cdot \left(\frac{h}{h_0} \right)^b \tag{2}$$

The constants *A* and *b* were calculated to be 0.0355 and 10.0 respectively.

Permeability

A modified Kozeny-Carman equation as proposed by Gutowski [9] is used to predict the fibre bundle permeability coefficient:

$$K = \frac{r_i^2}{4k'} \frac{\left(\sqrt{\frac{v_a}{v_f}} - 1 \right)^3}{\left(\frac{v_a}{v_f} + 1 \right)} \tag{3}$$

In Eqn (3), K is the permeability, r_i is the fibre radius and v_f is the instantaneous fibre volume fraction. The value of v_a, fibre volume fraction at zero permeability, was calculated to be 0.91 assuming hexagonal close packing of fibres. The value of k', the modified Kozeny constant is based on Seo's work [10] and uses a value of 0.9.

Impregnation

Impregnation of the fibre bed is governed by Darcy's law, which can be applied to a compacting circular fibre bundle (Eqn 4). In this polar form, V_r is the fluid (matrix) velocity, U_r is the fibre velocity, P is the pressure, K is the permeability, and μ is the fluid viscosity. The subscript 'r' denotes 'at radius r'.

$$V_r - U_r = -\frac{K}{\mu} \cdot \frac{dp_r}{dr} \tag{4}$$

Matrix Shear Thinning

It is proposed that at ultimate compaction the reinforcing fibres will assume a hexagonal close packed structure, and at each intermediate stage of compaction the fibres will lie in a proportionately packed hexagonal array. The mean inter-fibre spacing x, can then be determined from the instantaneous volume fraction v_f by solving Eqn 5.

$$\left(\frac{x}{r_f} \right)^2 + 4\left(\frac{x}{r_f} \right) + 4 = \frac{1}{\left(Cos\frac{\pi}{6} \cdot v_f \right)} \tag{5}$$

If the flow path between the fibres is idealised as a rectangular channel, then the shear-strain rate attributable to flow between the fibres is given by Eqn 6, where V is the matrix flow velocity, n is the matrix power-law index, and γ_a is the shear strain rate.

$$\gamma_a = \frac{2n+1}{n}\left(\frac{2V}{x}\right) \tag{6}$$

The viscosity of the matrix is then determined from the manufacturer's power-law description of the matrix material shear/viscosity relationship at the required temperature using Eqn 7. For example, at 189^o C, B = 3971.9 and n = 0.37 .

$$\mu_a = B \cdot (\gamma_a)^{(n-1)} \tag{7}$$

Incorporation of In-plane Material Shear

The effect of in-plane material shear is incorporated into the consolidation model by modifying several geometrical parameters in order to conserve mass:

1. The initial, instantaneous and final laminate heights are increased using Eqn 1.
2. The *sheared* fabric fibre bundle aspect ratio A_r*, is calculated from the undeformed fabric fibre bundle aspect ratio A_r using Eqn 8, where θ is the total deviation from 90^o at the fibre cross-overs:

$$A_r^* = A_r \cdot \sin(90-\theta) \tag{8}$$

The fibre bed sub-model is not explicitly modified, but the pressures predicted by this model will be increased with increasing material shear angles, because of the increase in fibre volume fraction at a given laminate height with increasing shear.

Fig 4 shows a plot of predicted developed moulding pressures at a laminate height of 2.625mm, and the corresponding experimental results. As expected, the predicted pressures increase with increasing shear angle, although this increase is greater than that displayed in the experimental results.

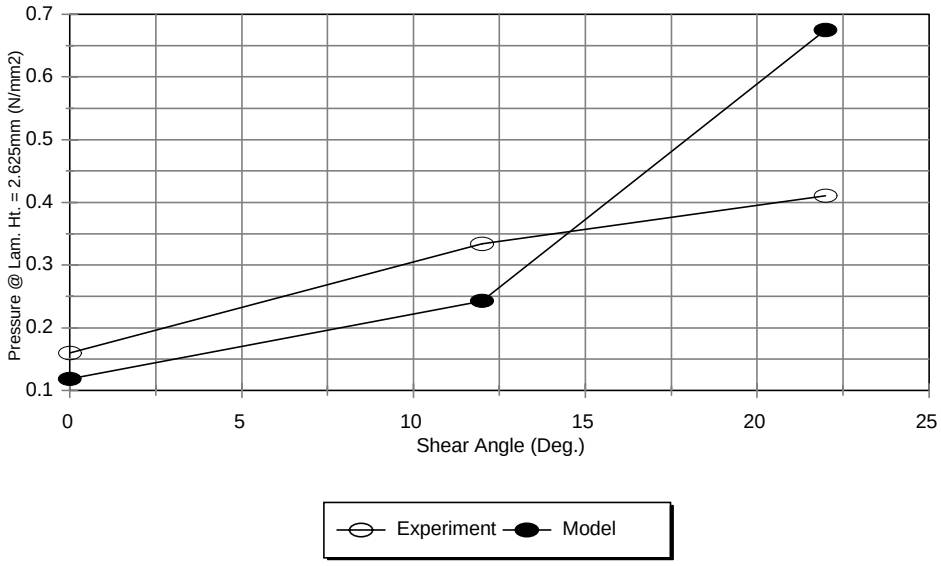

Figure 4: In-plane fabric shear vs developed moulding pressure, predicted and experimental results

HEAT TRANSFER

The cooling of a thin laminate may be idealised as a one-dimensional heat transfer problem. Internal heat conduction through the laminate thickness is governed by Eqn 9, where t is the time, T is the temperature, x is the through-thickness coordinate, and α is the thermal diffusivity of the laminate.

$$\frac{\partial T}{\partial t} = \alpha . \left(\frac{\partial^2 T}{\partial x^2} \right) \tag{9}$$

The laminate, which in the unconsolidated state consists of glass fibre, polypropylene and air, is idealised as a 'rule of mixtures' material [11]. That is, the laminate thermal properties are calculated on a proportionate basis using the thermal properties of the constituents.

Eqn 9 may be discretised using a forward finite difference scheme, giving an expression for the temperature at an interior node in the laminate in terms of the temperatures at the neighbouring nodes at the previous time step.

$$t_{n,t} = F .(t_{(n-1),(t-\Delta t)} + t_{(n+1),(t-\Delta t)}) + t_{(n),(t-\Delta t)} .(1 - 2F) \tag{10}$$

In Eqn 10, the first temperature subscript denotes the nodal position, and the second denotes the time step, while Δt is the time step and F is the fourier number.

This formulation has been used in a heat transfer model for laminate cooling. This model is intended to describe the through-thickness temperature distribution within the laminate from the end of the preheat stage until completion of the moulding cycle. Three distinct cooling regimes are imposed:

1. The material is removed from the preheat facility, and is transported to the press. Heat is lost by convection from the upper and lower laminate surfaces.
2. The material is placed in the mould, and the upper mould half is lowered towards the laminate. Heat is lost by convection from the upper surface, and conduction form the lower surface.
3. The mould is closed, and compression of the laminate begins. Heat is lost by conduction from both upper and lower laminate surfaces until the moulding cycle is completed.

Fig. 6 shows sample output for the process heat transfer model for laminate materials, for a nominal thermoforming process which uses a preheat temperature of 200^o C, with a transit time from preheat to first tool contact of 10 seconds and a tool closure time of 3 seconds. The tools are assumed to be massive in relation to the laminate charge and so maintain a steady-state temperature of 20^{o}C. This figure shows that the heat lost during transport is relatively insignificant when compared to the much more rapid heat loss via conduction, which occurs once the material is placed in the mould.

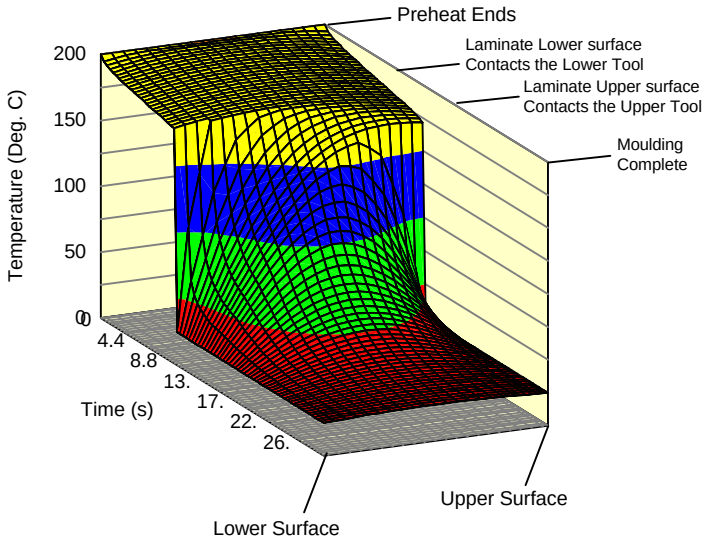

Fig: 6: Laminate process heat transfer model, sample output

PROCESS MODEL INTEGRATION

The simplest basis for integration of the three process models is based on the assumption that during the moulding of a component comprised from a co-mingled thermoplastic composite, deformation and consolidation of the fabric occur consecutively: The material is introduced into the mould cavity and is formed during mould closure. Consolidation commences once forming is complete. Laminate cooling may be modelled from the end of the preheat cycle until all points within the laminate fall below the crystallisation temperature of the matrix material.

This idealisation allows the moulding process to be modelled by using the fabric deformation model to determine the local fibre orientations within the mould. If in-plane matrix flow is prohibited, then simulation of the compaction of the draped form is reduced to a serial application for the consolidation model to each area of the deformed fabric on a facet-by-facet basis.

Fig. 6 shows the predicted fibre orientations when a fabric is formed over a 100mm diameter hemisphere. The main captions denote the fibre crossover angles, which have been used in conjunction with the consolidation model for sheared co-mingled materials to estimate the developed moulding pressures for in-mould compaction of this part at 50mm/minute. The pressure estimates are given as the bracketed values directly below the relevant material shear angle.

The heat transfer from the fabric can be considered during both deformation and consolidation by dividing the fabric thickness into a number of sub-layers. Using the through-thickness temperature distribution which is given by the heat transfer model, the material state may be determined within each sub-layer. The known temperatures can be used to determine the state of the matrix within each sub-layer, and if molten, the viscosity of the matrix can be ascertained. This updated viscosity data can be supplied to the consolidation model, allowing the effect of local cooling as well as local fibre-architecture deformation to be accounted for.

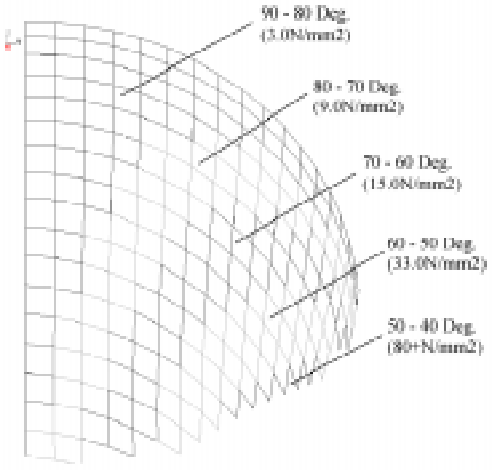

Fig. 6: Draped hemisphere, showing fibre orientations and consolidation pressure estimates

CONCLUSIONS

The three principal processes which control the moulding of a co-mingled thermoplastic composite have been identified, and a process model for each has been developed. Partial integration of the deformation and consolidation models has been achieved, and a strategy for complete integration of the process models has been proposed.

ACKNOWLEDGEMENTS

The authors thank the EPSRC, DTI and the following companies for their support in this work: AMM Ltd, Automold Ltd, Ford Motor Co. Ltd, Jaguar Cars Ltd, MIRA, Park Hill Textiles / Carr Reinforcement, Symalit AG, Vetrotex International.

REFERENCES

1. J. R. Collier, B. J. Collier, G. O'Toole, S. M. Sargand, "Drape Prediction by Means of Finite Element Analysis",*Journal of the Textile Institute* 82, 96-107 (1991).

2. B. Chen, M. Govindaraj, "A Physically Based Model of Fabric Drape Using Flexible Shell Theory",*Textile Research Journal* 65, 324-330 (1995).

3. C. D. Rudd, E. V. Rice, L. J. Bulmer, A. C. Long, "Process Modelling and Design For Resin Transfer Moulding",*Plastics, Rubber and Composites Processing and Applications* 20, 67-76 (1993).

4. B. P. Van West, R. B. Pipes, M. Keefe, S. G. Advani, "The Draping and Consolidation of Commingled Fabrics",*Composites Manufacturing* 2, 10-22 (1991).

5. V. Klinkmuller, M.-K. Um, M. Steffens, K. Friedrich, B.-S. Kim, "A New Model for Impregnation mechanisms in Different GF / PP Commingled Yarns",*Applied Composite Materials* 1, 351-371 (1995).

6. L. Ye, K. Friedrich, "Manufacturing of CF/PEEK Thermoplastic Composites From Flexible Preforms", *ICCM-10*, Whistler, B.C., Canada (1995).

7. B. P. Van West, R. B. Pipes, S. G. Advani, "The Consolidation of Commingled Thermoplastic Fabrics",*Polymer Composites* 12, 417-427 (1991).

8. T. A. Cain, M. D. Wakeman, R. Brooks, A. C. Long, C. D. Rudd, "Isothermal Consolidation of a Co-mingled Thermoplastic Composite", *The Seventh European Conference on Composite Materials*, London, UK (Woodhead Publishing Ltd., 1996).

9. T. G. Gutowski, et al., "Consolidation Experiments for Laminate Composites",*Journal of Composite Materials* 21, 1987 (1987).

10. J. W. Seo, W. I. Lee, "A Model of the Resin Impregnation in Thermoplastic Composites",*Journal of Composite Materials* 25, 1127-1142 (1991).

A THEORETICAL FRAMEWORK FOR THE CONSIDERATION OF DAMAGE ENTITIES IN 3D WOVEN COMPOSITE STRUCTURES

S. John[1] , F. Coman[1], I. Herszberg[2], M. Bannister[3]

[1]Royal Melbourne Institute of Technology, Department of Manufacturing Systems Engineering, Bundoora East Campus, Vic. 3083, Australia.
[2]Royal Melbourne Institute of Technology, Department of Aerospace Engineering, The Sir Lawrence Wackett Centre for Aerospace Design Technology, GPO Box 2476V, Melbourne, 3001, Australia.
[3]Cooperative Research Centre for Aerospace Structures, 506 Lorimer St. Fishermens Bend, Vic.3207, Australia

SUMMARY: This paper addresses the microstructural features of multilayer woven composite materials and how they collectively contribute to the overall deformation response. Due to the complexity of perceived interplay amongst damage parameters within the composite material, an energy framework is used as a basis to rationalise the manifestation of these parameters within a deformation response scenario. These parameters are quantified in general terms of damage tensors and are shown to resemble energy-type functions. The discussion in this paper is centred around geometrical features of fibre configurations in multilayer woven glass fibre composite panels with a lattice of uncrimped warp and weft yarns supported by through-thickness weft binders.

KEYWORDS: damage entities, energy, representative volume element (RVE), thermodynamics, continuum mechanics, woven composites, deformation response

INTRODUCTION

The study of damage in composite structures has attracted some interest of late due to emerging technologies used in experimental and computational techniques. This increased sophistication in obtaining credible experimental and computational data has allowed the development of analytical techniques that, for the first time, can incorporate these new physical and computational data. The trend in recent years has been to gain an insight into the progressive mechanics of failure rather than coming up with some universal failure criterion in the study of the mechanical properties of composite structures.

This paper attempts to describe the damage progression, in the warp and weft directions, of 3-D woven polymer matrix composites when statically loaded in the tensile mode. The main design feature-based variables are the binder configurations and comparison in strength between the warp and the weft directions; the binders are only present in the weft direction. A typical binder-architecture design used in the study reported in [1] is shown in Fig. 1:

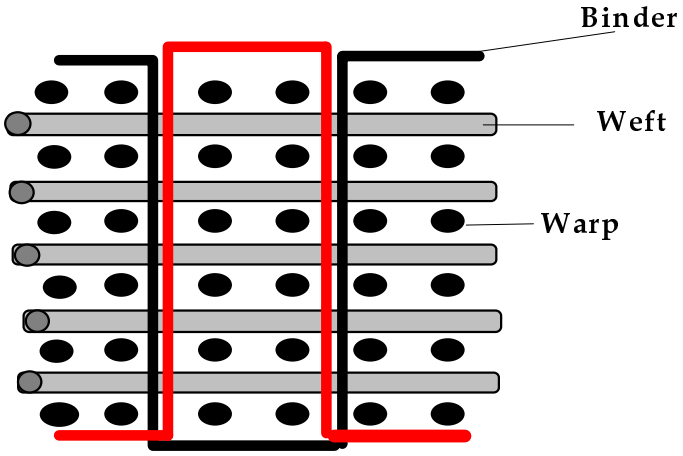

Fig. 1 Orthogonal through-thickness binder (idealised schematic)

This is paper is an extension of Talreja's work [3] on damage mechanics in composite materials to 3-dimensional woven composite structures. A theoretical energy framework is introduced to utilise energy-related damage entities as observed from micrographs of damage zones in these structures. The intent here is to attempt to initiate novel experimental techniques that can be based on sound theoretical and computational developments in the field of damage mechanics.

THEORETICAL CONSIDERATIONS

General

The view taken in this paper is that trying to predict observed macromechanical behaviour from essentially micromechanical features is extremely difficult and that the results are predicated on assumptions that are in many instances, very hard to justify. What will be attempted here however, is to build up an argument by identifying and quantifying parameters thought to be players in the overall process of composite failures. As a stance taken by several others [3, 4, 5], and that adopted in this paper, it is essential not to pursue absolute agreement between theory and experiment but rather to emphasise general trends and identify consistencies. The reasons of taking this route of analysis evolved out of the realisation that the ever changing physical and geometric entities involved in the failure process of polymer matrix composite components **cannot** be modelled and measured accurately in its entirety. The challenge is however, to identify and model significant parameters thought to be responsible for macromechanical behaviour, particularly that of static deformation and failure modes. The discussion [6, 7, 8, 10] currently evolves around whether a continuum mechanics, thermodynamic or a combination of both models is appropriate for providing a sound theoretical basis for understanding the deformation process in 3D woven composite structures. A discussion on this subject is given below.

The concept of a unit cell or Representative Volume Element (RVE) is introduced here and a typical element is essentially a 3-dimensional version of Fig. 1. This is used to represent yarn and binder configurations as well as a cell that would have polymer matrix composite microstructural entities such as voids, interfaces and cracks is not unlike the RVE in the work of Nemat-Nasser and Hori [5] and Talreja [3, 4]. Using the concept of a damage entity as

defined by Talreja in [3], it is an individually identifiable change in the microstructural constitution of a solid which is brought about by an internal energy dissipative mechanism. Examples in the context of the present study include voids, cracks, debonds and interfacial slip. A vectorial representation of damage is chosen so that both magnitude and orientation of the damage is defined. A conceptual damage entity modified by Talreja [3], defines a damage entity d_{ij} as:

$$d_{ij} = \int_S a_i n_j dS \tag{1}$$

where S is the surface area of the damage entity; a_i and n_j are 'damage-influencing' and normal vectors associated with the damage entity as shown in Fig. 2. If a_i is taken as some function of displacement, then if a_i is zero, d_{ij} fails to qualify as a damage entity. Another definition, a damage mode, [2] is a collective reference to a subset of damage entities which, on account of their geometrical features and the local driving forces, evolve in a similar fashion. Therefore, as shown in Fig. 2, assuming there are n distinct damage modes in the RVE of volume V, denoted by α = 1,2,.....n, a damage tensor is defined for each mode as:

$$D_{ij}^{\alpha} = \frac{1}{V} \sum_{k_\alpha} (d_{ij})_{k_\alpha} \tag{2}$$

where k_α is the number of damage entities in the αth mode.

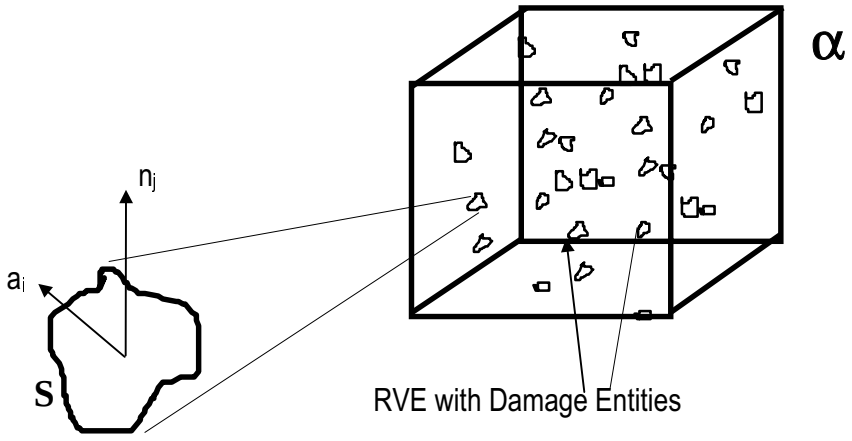

Fig. 2: A Damage entity: yet to be physically quantified

Equation (2) is then used as a field variable using the Coleman-Gurtin [6] theory of thermomechanical response, to get stiffness-damage relationships as shown by Talreja *et al* [3, 7]. This essentially showed a form of virgin or undamaged property degradation as shown in Equation (3) below for the case of cross-ply laminates with intralaminar cracks:

$$E_1 = E_1^0 - f(C, \nu)$$
$$E_2 = E_2^0 - f(C, \nu)$$
$$\nu_{12} = \nu_{12}^0 - f(C, E_2) \quad (3)$$

Where E^0 and ν^0 is the Young's modulus and the Poisson's ratio respectively in the undamaged state and C is a combined representation of material constants and geometrical entities.

3-Dimensional Woven Composites

As the damage entity as defined in Equation (2) above is not feature or mechanism-specific, it can be applied to any RVE and all suspected damage entities can be incorporated in it. As the RVE for the 3-D composite structure considered here involves both geometric and inherent damage entities, the actual RVE for deformation analysis should strictly be the superpositioning of Fig. 1 (3D version [1]) and Fig. 2. Also, as mentioned above, the theoretical thrust here is **not** to identify **all** the damage and geometrical entities responsible for deformation but to highlight prominent players in this process such as voids, fibre breaks, debond areas and fibre-matrix interface slip.

Consider the damage entity in Equation (1), d_{ij} , to be a form of dissipative (unrecoverable) work done by a damage entity such as a growing crack, then,

$$d_{ij} = \int_S a_i n_j dS \Rightarrow \frac{\partial w}{\partial a}\Big|_{Microcrack} \quad (4)$$

where $\partial w / \partial a$ is the local elastic energy release rate; w is the energy and a is the crack length.

Similarly, if d_{ij} represents some sort of work done by the damage entity such as a debond, then,

$$d_{ij} = \int_S a_i n_j dS \Rightarrow \int_0^{e_{ij}} \sigma_{ij} de_{ij} \quad (5)$$

where $\int_0^{e_{ij}} \sigma_{ij} de_{ij}$ is the strain energy density , dW/dV [2].

John *et al* [1] showed that the damage tensor for a 3-D woven composite structure should incorporate not only the inherent damage entities such as that represented by Equations (4) and (5), but also that from the woven yarn and binder configurations. Therefore, Equation (2) would decompose to:

$$D_{ij} = \frac{1}{V}\left(\sum_{k_\alpha} (d_{ij})_{k_\alpha} \Big|_{Inherent\ Damage} + \sum_{k_\alpha} (d_{ij})_{k_\alpha} \Big|_{Woven\ Geometry} \right) \quad (6)$$

Evidence of damage from the 'Woven Geometry' Component of Equation (6) is reported by John *et al* in [1].

DISCUSSION ON AN ENERGY-BASED CONSTITUTIVE FRAMEWORK

The need to quantify the damage variables above emanates from the desire to place these evolving entities into a framework around which physical arguments can be made. The intent here is to predict a material response to external forces rather than emerge with some sort of failure criterion for 3D woven composite components. Gurney [10] argues that continuum mechanics cannot cater for stress-induced phase changes. Thermodynamic considerations by Gurney [10], Talreja [3] and Colman *et. al* [5], have all resulted in considerations of entities other than damage such as entropy, heat flux vectors and 'Helmholz' free energies; all of which are phenomenonistically difficult to measure and adapt to 3D composite structures. As a result, the following analysis is undertaken.

Assuming a RVE, α, shown in Fig. 2, is an isothermal, quasi-static and macro-elastic system, the energy transformations within it are both reversible and irreversible, albeit on a microscale. Ignoring any phase change due to an evolving damage entity such as a disbond or an initiating crack, the external work, at time t = 0 (pre-damage evolution), W can be expressed as:

$$dW_o = d\Lambda_o + RdA \tag{7}$$

where Λ is reversible work, R is the fracture toughness, A is the 'new crack area' (in this case, meant to collectively represent voids, potential disbonds sites, friction and other irreversible energy phenomena) and subscript o refers to a the pre-mechanical induced damage state. Equation (7) is that used by Gurney [10] to describe elastic cracking and using this as a simplistic model to incorporate damage entities as described in Equations (4) to (6). Elucidating further, $d\Lambda$, will represent the reversible elastic within the RVE (such as locked in strain energy during the component manufacture), which is expected to dominate the minor irreversible energy changes represented by R dA.

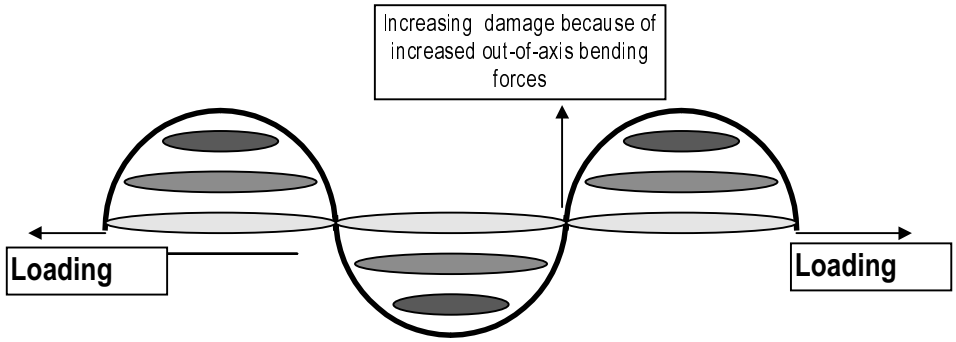

Fig. 3: Schematic of suspected mechanics responsible for binder-inflicted damage

At time t > 0 (after the onset of damage induced by mechanical deformation), $d\Lambda$ begins to transform to irreversible energy dissipation such as the damage from the binder causing

microcracks in the yarn tows as reported in [1] and illustrated in Fig. 3. Therefore Equation (7) becomes:

$$dW_i = d\Lambda_r + \sum_{t=0}^{t=t_i} RdA\Big|_{Int} + \sum_{t=0}^{t=t_i} RdA\Big|_{Ext} \tag{8}$$

where,

$$d\Lambda_r = d\Lambda_o - \sum_{t=0}^{t=t_i} RdA\Big|_{Int} \tag{9}$$

and the total summation of irreversible energies within the RVE is,

$$\sum_{t=0}^{t=t_i} RdA\Big|_{Total} = \sum_{t=0}^{t=t_i} RdA\Big|_{Int} + \sum_{t=0}^{t=t_i} RdA\Big|_{Ext} \tag{10}$$

where t_i is the time during which irreversible new energy dissipations have occurred as a direct result of a diminished $d\Lambda_r$ due to internal strain energy conversions from reversible ($d\Lambda$) energy to irreversible ($\sum_{t=0}^{t=t_i} RdA$) energy. The $\sum_{t=0}^{t=t_i} RdA\Big|_{Ext}$ component is the irreversible energy transformations from disbonds, matrix cracking and so on, directly attributable to the external load. From the results displayed in [1], it is postulated that if the damage entities are identified and suitably quantified as energy terms similar to the strain energy definition [1] in Equation (5), it can be equated to $\sum_{t=0}^{t=t_i} RdA\Big|_{Total}$, i.e,

$$\sum_{t=0}^{t=t_i} RdA\Big|_{Total} \Rightarrow D_{ij} = \frac{1}{V}\left(\sum_{k_\alpha} (d_{ij})_{k_\alpha} \Big|_{Inherent\ Damage} + \sum_{k_\alpha} (d_{ij})_{k_\alpha} \Big|_{Woven\ Geometry} \right) \tag{11}$$

CONCLUSION

From the analysis proposed above, it is clear that the challenge is how to quantify the damage entities in Equations (4) - (6) and how these manifest themselves in an energy framework described in Equation (8) - (11). It needs to be recognised that while binders can have a deleterious effect on the composite structure as proposed in Equation (6) and as suggested by John *et. al* in [1], it might have benefits in other ways. It must be stated here that while a thermodynamically-based constituitive framework is probably a more rigorous and thorough approach to understanding micro and meso-phenomena in composite materials, parameters within it remain very difficult to measure. On the other hand, the continuum mechanics approach is also, inherently flawed for quantifying entities with constantly evolving geometrical and physical parameters. The energy approach is suggested as a model to relate phenomena (physical and otherwise) in a deforming body. The challenge remains the proper definition of damage and other entities involved in the deformation response of

3D composite structures and how they can correctly be transformed to energy functions as indicated in Equation (11) .

REFERENCES

1. John S, Coman F, Herszberg I, Bannister M, *Correlation of Weave Parameter-Micromodels of 3D Woven Composite Structures with its Macromechanical Properties,* Proceedings of the 4th Int. Conference on Deformation & Fracture of Composites, Manchester, UK, 1997.

2. Sih G C, *Dynamics of Composites with Cracks* - contribution in *Failure Mechanics of Composites,* Vol. 3, Editors Sih G C and Skudra A M, North-Holland Publishers, 1985.

3. Talreja R, *Damage Mechanics of Composite Materials,* Vol. 9, Composite Materials Series, Elsevier publishers , 1994.

4. Talreja R, *Damage Mechanics Concepts for Durability Analysis of Composite Materials,* Keynote address and Proceedings of the 3rd Int. Conference on Deformation & Fracture of Composites, Guildford, UK, pp. 15-25, 1995.

5. Nemat-Nasser S and Hori M, *Micromechanics: Overall Properties of Heterogeneous Materials,* North-Holland, Amsterdam, 1993.

6. Coleman B D and Gurtin M E, J. Chem. Phys., **47,** pp 597-613, 1967.

7. Talreja R, Yalvac S, Yats L D and Wetters D G, *Transverse Cracking and Stiffness Reduction in Cross Ply laminates of Different Matrix Toughness,* Journal of Composite Materials, Vol. 26, No. 11, 1992.

8. Backhouse R, Blakeman C and Irving P E, *Mechanisms of Toughness Enhancement in Carbon Fibre Non-crimp Fabrics,* Proceedings of the 3rd Int. Conference on Deformation & Fracture of Composites, Guildford, UK, pp. 307-316, 1995.

9. Dransfield K A, Bader M G, Baillie C A and Mai Y-W, *The Effect of Cross-stitching with an Aramid Yarn on the Delamination Fracture Toughness of CFRPs,* Proceedings of the 3rd Int. Conference on Deformation & Fracture of Composites, Guildford, UK, pp. 414-423, 1995.

10. Gurney C, *Continuum Mechanics and Thermodynamics in the Theory of Cracking,* Philosophical Magazine A, Vol. 69, No. 1, pp. 33-43, 1994.

EFFECT OF MATRIX RIVETTING IN WOVEN FABRIC HOLES TO INTERLAMINAR FRACTURE TOUGHNESS OF COMPOSITE LAMINATES

F. Gao [1] and M. Yao [2]

[1] *Department of Textile Engineering,* [2] *Department of Textile Materials, Northwest Institute of Textile Science and Technology, Postbox135, Xi'an 710048, P.R. China.*

SUMMARY: Matrix rivetting formed in woven fabric holes of woven fabric-reinforced composite laminates is proposed. The geometry of fabric holes is analysed and a method for calculating the matrix rivetting area is established. In order to know the effect of interlaminar matrix rivetting to delamination resistibility, the relation between matrix rivetting area and interlaminar fracture (G_{1c} and G_{2c}) is studied. Glass-fiber plain woven fabrics with eight different warp and filling densities are adopted to reinforce epoxy resin. The experimental results indicate that interlaminar fracture toughness will evidently increase with the increasement of matrix rivetting area. It is suggested that weaves with relative low warp or filling densities should be used to improve delamination growth resistibility of woven fabric-reinforced composite laminates when adhesion strength between fibers and matrices is low and delamination occurred easily.

KEYWORDS: matrix rivetting, woven fabric hole, interlaminar fracture toughness

INTRODUCTION

Nowadays, woven fabric composite laminates are widely used in technical practice, especially in the field of aerospace, marine and sports technology. This is because of their favorable mechanical properties and low fabrication cost. Then, interplyer delamination is considered the most critical failure mode limiting the long-term fatigue life of certain composite laminates [1]. Previous studies in this area have been largely concerned in improving fiber-matrix adhesion strength and using three-dimensional woven fabric and great effects had been obtained in improving delamination growth resistance. But, for example, cost and fabrication, to a certain extent, their application have been limited. By a great amount observation of delamination surface of fabric composite laminates we find that one part of matrix is peeled from the fiber surface and the other part in fabric holes is matrix fracture. Therefore, we propose that interlayers are combined by bonding between fibers and matrices and matrix rivettings formed in fabric holes. Vandeurzen and Naik analysed the effect of the yarn undulation to performance of woven fabric composites [2-4]. However, the influence of woven fabric holes is neglected. In order to know the effect of interlaminar matrix rivetting to interlaminar fracture energy, two commonly used tests DCB (Double-Cantilever Bean) and ENF (End-Notched Flexure) are adopted. Glass-fiber plain weaves with eight different warp and filling densities are adopted to reinforce epoxy resin. A three-dimensional analytical

model is presented to analyse the geometric characteristics of fabric holes to obtain matrix rivetting area.

RIVETTING AREA OF WOVEN FABRIC HOLES

The shape of matrix rivetting in woven fabric hole is determined by hole's space shape. Therefore, it is necessary to analyse the hole's geometric characteristics before we calculate the rivetting area. The space shape of woven-fabric hole is not a sample cuboid as imagination. In fact, it is very complicated. Generally, the hole's cross section is similar to rectangle with relatively small acute angle as Figure.1(b) shows. The shape and size of cross section will change with different position. The area of cross section is smallest in hole's center and it will expand with the increasement of the distance between section position and center. Considering fracture principle, we define the smallest cross section area as rivetting area. To facilitate the analytical model of fabric hole we assume: 1) the cross section shape of warp and filling is track-round, as Fig.1(a) shows; 2) the spatial curve of warp and filling in interlacing points circuncircle; 3) woven fabric structure phase is 5.0 [5].

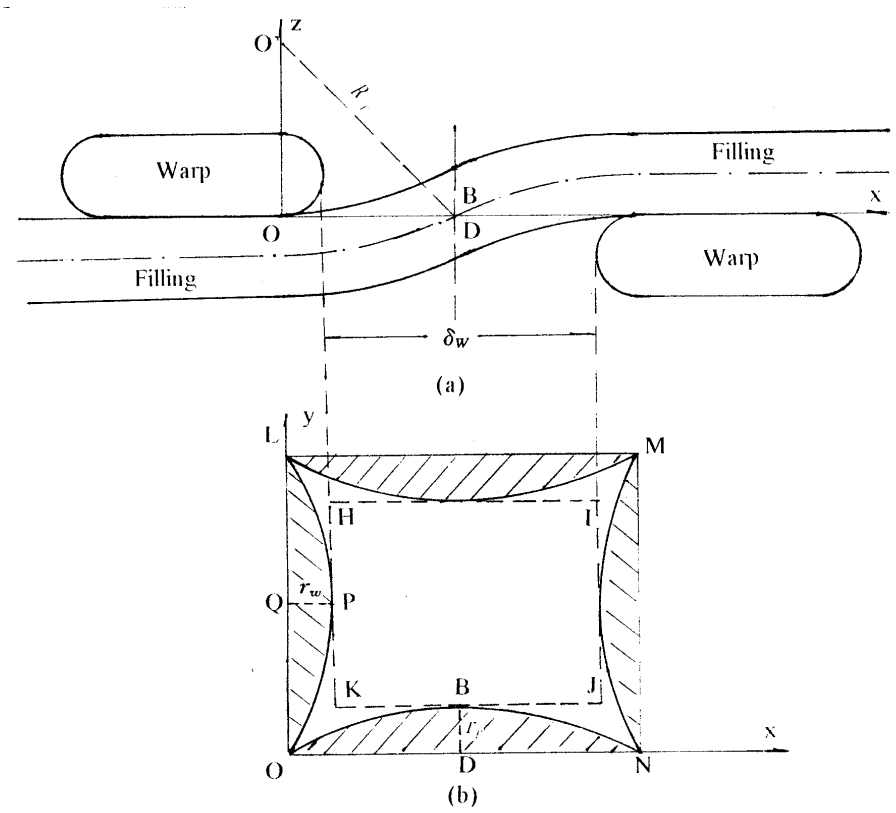

Figure 1: Analytical mode of woven fabric hole

According to geometric symmetry of woven fabric hole, based on above assumption, matrix rivetting area A_r can be obtained by:

$$A_r = A_{LONM} - 4(A_{OBD} + A_{OPQ}) \quad (1)$$

where A_{LONM} is the rectangle area of LONM, A_{OBD} and A_{OPQ} represent the area of curve-side triangle OBD and OPQ. A_{LONM} can be calculated by warp and filling densities and yarns' width and thickness. However, the calculation of A_{OBD} and A_{OPQ} is relatively complicated. So, a three-dimensional analytical model is established. By projective geometrical analysis of cross section, the curve equation of curve OB can be expressed by:

$$Y(x) = r_f \sqrt{1 - [\frac{\sqrt{{R_f}^2 - x^2} - (R_f - r_f)}{\sqrt{{R_f}^2 - x^2} - \sqrt{(R_f - r_f)^2 - x^2}}]^2} \tag{2}$$

where R_f is the curve-radius of filling in interlacing point, $2r_f$ is the thickness of filling. Therefore, A_{OBD} can be calculated by:

$$A_{OBD} = \int_0^{\delta_w/2+\gamma_w} Y(x)\,dx \tag{3}$$

where δ_W is the distance among warps, $2r_W$ is the thickness of warp. In the same way, A_{OPQ} can be obtained. Now, we introduce a rivetting area corrected coefficient K_r:

$$K_r = \frac{A_r}{A_{HIJK}} \tag{4}$$

where A_{HIJK} is the projective area of woven fabric hole. So, the percentage of rivetting area of unit woven fabric area P_r (%) can be calculated by:

$$P_r(\%) = K_r[1 - E(\%)] \tag{5}$$

where E(%) is the percentage of yarn projective area of unit woven fabric area. Figure.2 shows a SEM micrograph of glass-fiber plain woven fabric for reinforcement. The relevant parameters of glass-fiber plain woven fabrics with different warp and filling densities are listed in Table 1.

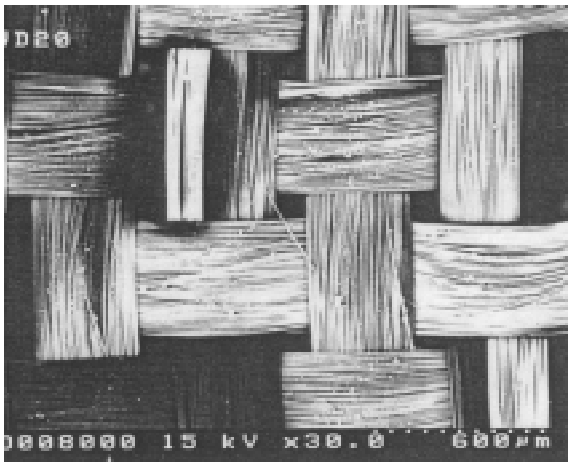

Figure 2: A SEM micrograph of plain woven fabric

Table 1: Relevant parameters of glass-fiber plain woven fabric

Number of Glass-Fiber Plain Woven Fabric	Densities of Warp and Filling (Ends and Picks/cm)		Kr (%)	E (%)	Pr (%)
1	20	22	1.279	93.75	7.99
2	20	20	1.257	92.51	9.34
3	20	16	1.236	90.23	12.07
4	20	12	1.219	87.89	15.13
5	14	14	1.328	95.68	5.74
6	14	12	1.292	93.79	8.02
7	14	10	1.273	91.91	10.30
8	14	8	1.259	89.86	12.77

EXPERIMENTAL

Material

Glass-fiber plain woven fabrics with different structure parameters (different rivetting area) are used to reinforce epoxy. Consolidation agent is triethlene amine.

Interlaminar Fracture Toughness Testing

In gerenal, interlaminar fracture toughness of composite laminates are determined by interlaminar fracture energy. A number of test methods have been developed to measure the interlaminar fracture energy of composite laminates [6]. The interlaminar fracture energy, measured in term of the strain energy release rate, is defined as the amount of strain energy released in propagating delamination by a unit length. In this experimental, two commonly used interlaminar fracture toughness test methods of the double-cantilever beam (DCB) `test and the end-notched flexure (ENF) test are adopted to measure the strain energy release rate G_{1c} and G_{2c} under mode I loading and mode II loading. The specimens for both DOC test and ENF test are rectangular beams 300x12x3mm^3 cut from laminates $(0^0/0^0/45^0/-45^0/90^0)_s$. Initial delamination are formed by PBTP film (thickness 50 μm) embedded in the mid-place of the laminates. The unit crack length of propagating delaminaton is 10mm. The test are carried out on an Instron 1185 universal testing machine at a cross-head speed of 2mm/min [7]. In DCB test, optical microscope is used to observe crack initiation.

RESULTS AND DISCUSSION

Figure 3 shows the variation of interlaminar fracture toughness with percentage of matrix rivetting area Pr(%). With the increasement of Pr(%), the values of both G_{1c} and G_{2c} will increase evidently. Under the condition of a certain warp density, the reduction of fiber volume fraction 5~10% (by reducing filling density 10~20%) will obtain the improvement of

interlaminar fracture toughness 50~100%. We consider the main reason is that the woven fabrics with relative low warp or filling densities have more rivetting area and more matrix rivetting will formed in interlayers, so more fracture energy is needed in propagating delamination. Generally, tensile or shear fracture energy of per unit matrix area is larger than the energy of interface peeling between matrix and fiber. The delamination surface of both DCB and ENF specimens were analysed with scanning electron microscope. Figure 4 shows four SEM micrographs of the gold coated delamination fracture surfaces. At lower magnification (a) and (b), shows the existence of matrix rivetting in woven fabric holes and the fracture cross section shape of matrix rivetting. At higher magnification (c) and (d), shows that matrices are peeled from the yarn surface. Observations indicate that delamination fracture associates with the fracture of matrix rivetting and the failure of fiber/matrix interface.

CONCLUSIONS

The test results indicated that matrices will form matrix rivetting in woven fabric holes of woven fabric-reinforced composite laminates and their influences upon interlaminar fracture toughness of composite laminates are very evident. This research provided a convenient and effective method to improve the interlaminar fracture toughness of woven fabric-reinforced composite laminates by structure design of woven fabric. It is suggested that woven fabrics with relative low warp or filling densities should be adopted to improve delamination resistibility of composite laminates when adhesion strength between fibers and matrices is low and delamination failure often occurs.

ACKNOWLEDGMENTS

Thanks are due to faculty of Textile Material Lab of Northwest Institute of Textile Science and Technology. Further thanks are addressed to Yiou KeXun who kindly supplied the testing materials.

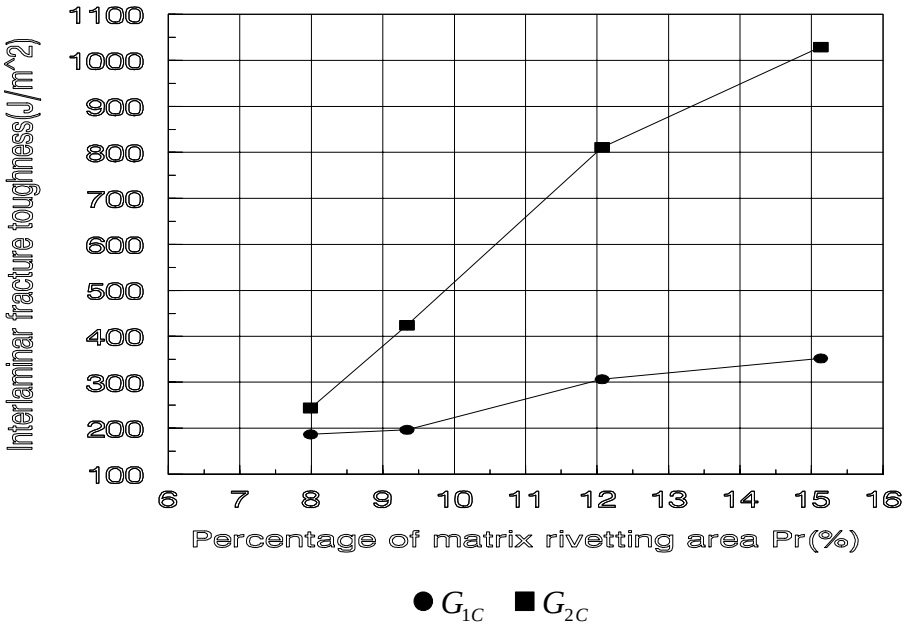

(a) Warp densities: 20 Ends/cm

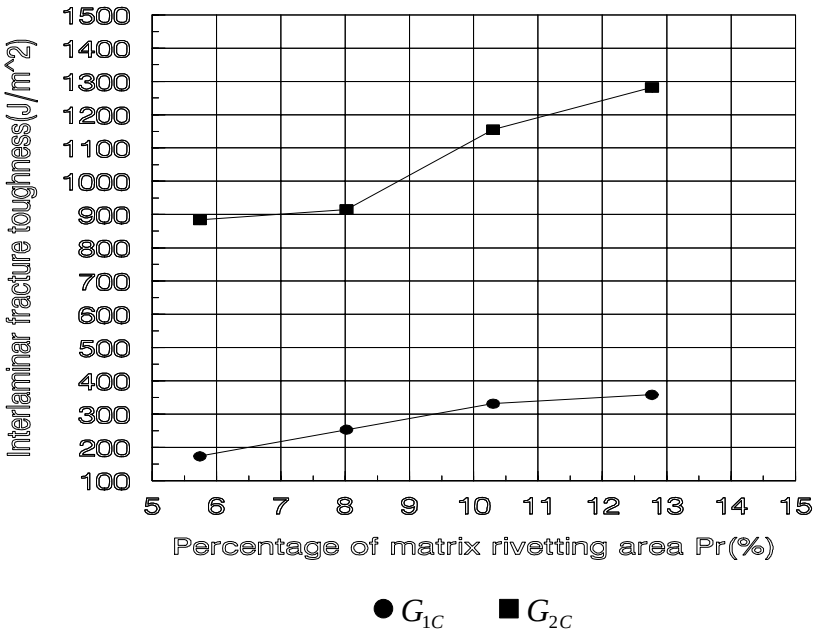

(a) Warp densities: 14 Ends/s

Figure 3: Variation of interlaminar fracture toughness with percentage of matrix rivetting area P_r (%)

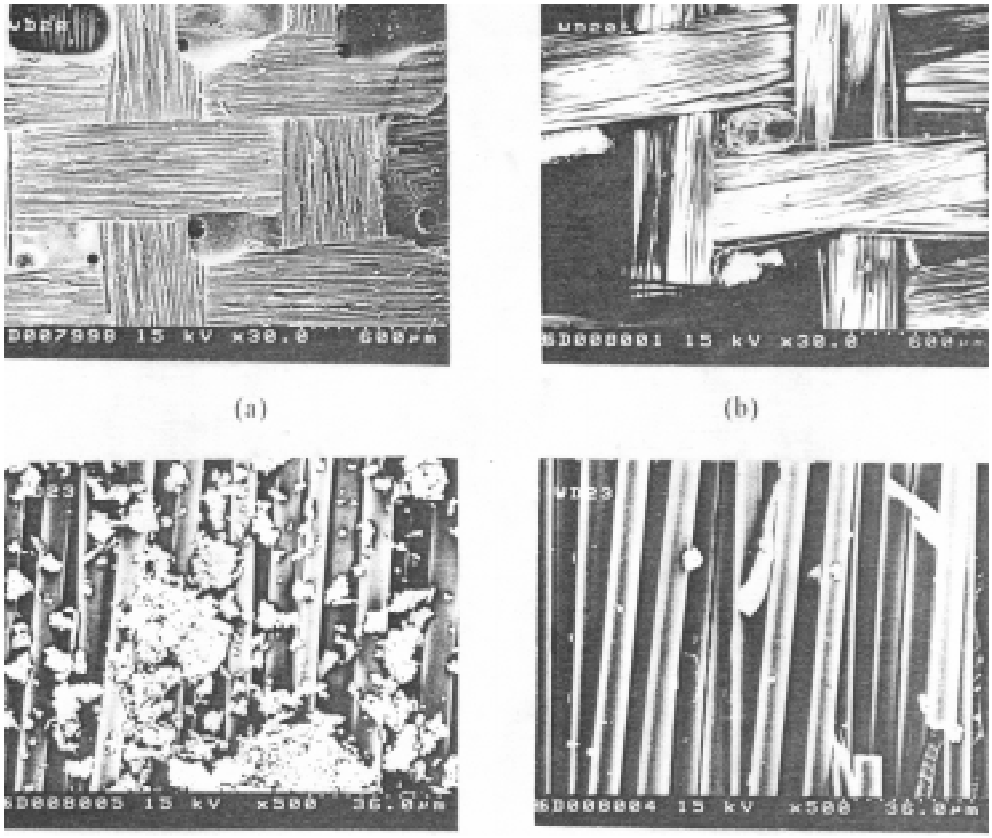

Figure 4: Micrograph of delamination surface of woven fabric reinforced composite laminates. SEM magnifications:(a),(b) 30 x; (c),(d) 500 x.

REFERENCES

1. D.J. Wilkins, J.R.Eisenmann, R.A. Camin, W.S.Margolis and R.A.Benson, characterizing delamination growth in graphite-epoxy, Damage in Composite Materials, ASTM STP *775* 168 (1980).
2. P.Vandeurzn, J.Ivens and I.Verpoest, Structure-Performance Analysis of Two-Dimensional Woven Fabric Composites, *Proceedings of the Tenth International Conference on composite materials* (ICCM/10), Whistler, B.C., Canada, Vol.4, pp. 261-268 (1995).
3. N.K.Naik, P.S.Shembekar, Elastic Behavior of Woven Fabric Composites, *Journal of composite Materials* **26**, No.15, pp. 2196-2246, (1992).
4. N.K.Naik, V.K.Ganesh, An analytical method for plain weave fabric composites, *Composites*, **26,** pp.281-289, (1995).
5. M.Yao, Textile Materials, China Textile Industry Press, Beijing, 1988.
6. L.A.Carlson and R.B.Pipes, Experimental Characterization of Advanced Composite Materials, Prentice-Hall, Englewood Cliffs, New Jersey (1987).
7. J.M.Whitney, I.M.Daniel and R.B.Pipes, Experimental Mechanics of Fiber Reinforced composite Materials, Science Press, Beijing, 1990.

STRUCTURAL INTEGRITY OF DISCONTINUOUS BLADE STIFFENED BRAIDED AND WOVEN COMPOSITE PANELS

Kunigal Shivakumar[1], Mannur Sundaresan[1], Peter Shyprykevich[2], Vishnu S. Avva[1], and Vivek Ramanujapuram[1]

[1]Center for Composite Materials Research, Department of Mechanical Engineering
North Carolina A&T State University, Greensboro, NC 27411
[2]FAA Tech Center, Atlantic City Int. Airport, NJ

SUMMARY: The objective of this study was to evaluate the structural integrity of discontinuous blade stiffened panels made of textile preform composites and compare the failure stresses and modes with that of conventional laminated stiffened panels. Three-dimensional braided and 3-D orthogonal woven composite panels were evaluated. Panels were made of BASF G30-500 graphite fiber yarns and Dow Chemicals Tactix-123 matrix. Panels were consolidated by resin transfer molding. The panel configuration was similar to that used in a previous FAA contract. Three-dimensional finite-element analysis was used to establish the geometrical configuration and identify the regions of high stresses. Test results showed that fracture in both braided and woven panels was by net section tensile failure. Notch root stress (strain) concentration causes failure initiation but its influence on the ultimate strength was minimal. Failure initiation in braided panel was by peeling and in woven panel it was by shear.

KEYWORDS: blade stiffened panel, braided composites, woven composites, tension load, structural integrity, resin transfer molding, 3-D finite-element analysis, stress concentration

INTRODUCTION

Advances made in laminated polymeric composites have proved that they are stronger, stiffer, and lighter than conventional metallic materials for number of applications, including aerospace structures, sports equipment and transport structures. The current emphasis on affordability of composite structures is driving material scientists and manufacturing technologists to focus on the use of low cost materials and manufacturing techniques. Textile fabric preforms and resin transfer molding (RTM) lend themselves to manufacture near net shape components. The RTM process uses cheaper dry preform and matrix instead of expensive prepregs. Hence, it is found to be a viable low cost manufacturing technique for structural components.

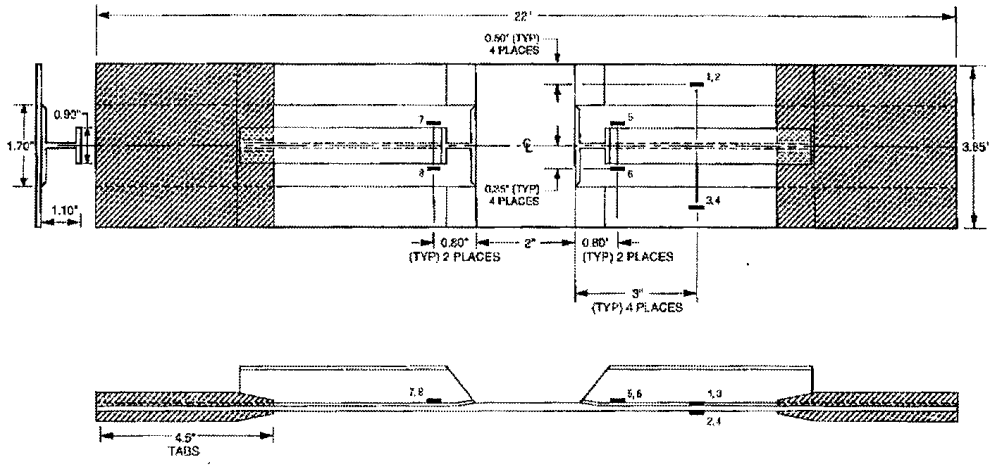

Figure 1.- Northrop-Grumman test specimen

A number of studies are being made in government agencies, industries, and universities to evaluate the engineering properties and structural integrity of textile composites. The objective of this paper is to evaluate the structural integrity of discontinuous blade stiffened 3-D braided and woven composite panels. Both analytical as well as experimental techniques were used for this purpose. Northrop-Grumman Corp. under a FAA contract investigated the structural integrity of discontinuous blade stiffener in laminated composite panel (see Fig. 1) [1]. The present study is focused on integrally braided and woven composite panels. In such panels, problems associated with laminated composites no longer exists, but there may be other problems related to the fiber architecture. Both 3-D finite-element analysis and experiments are conducted and the results are compared with each other and with the results of Northrop-Grumman test data.

TEST PANEL AND MATERIAL SYSTEM

In an earlier study Northrop-Grumman Corporation examined the structural integrity of discontinuous blade stiffened laminated composite panel (see Fig. 1), fabricated from unidirectional composite laminae. The purpose of that study was to establish a certification procedure for terminating stiffeners used in selected sections in transport aircraft wings. In the present study the focus is on the evaluation of the structural integrity of integrally constructed textile preform composite panels. These panels were made of BASFís G30-500 graphite fibers and Dow Chemicals Tactix 123 matrix. Integral braiding and weaving technology was used in manufacturing the panels with stiffeners. Fabric architecture of the braid is designated by $(0/\pm 17^{o})$ with 46% axials, whereas the 3-D orthogonal woven fabric architecture is (0/90/90) with 50% axials. The average fiber volume fractions of braided and woven composites were 0.38 and 0.44 [2], respectively. Originally, the preform fabrics were manufactured to have two-blade stiffeners and were resin transfer molded into two blade stiffened panels.

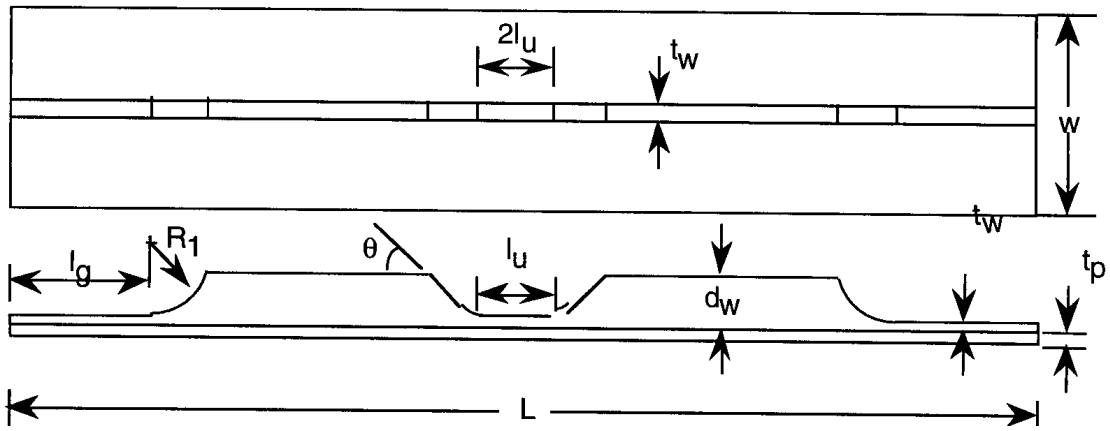

Figure 2: NCA&TSU test specimen

Table 1: In-situ Properties of stiffened Panels

Property	Braided Panel B3a GPa (Msi)	Woven Panel W3b GPa (Msi)
Ex	67.8 (9.8)	77.9 (10.9)
Ey*	33.9 (4.9)	37.4 (5.4)
Ez*	33.9 (4.9)	37.4 (5.4)
Gxy	5.5 (0.8)	2.8 (0.4)
Gyz*	2.1 (0.3)	2.1 (0.3)
Gxz*	5.5 (0.8)	2.8 (0.4)
ν_{xy}	0.77	0.06
ν_{yz}*	0.05	0.05
ν_{xz}*	0.77	0.05

* Assumed Properties

The nominal dimensions of the panel were: length = 457 mm, width = 165 mm, thickness = 6.1 mm, blade depth = 19 mm, and spacing between blades = 89 mm. From each of these resin transfer molded panels, two single blade stiffened panel specimens as well as other specimens required for in-situ mechanical property evaluation were obtained. Figure 2 shows the geometric configuration of the panel in terms of geometric parameters. A detailed finite element study [3] was conducted to establish these geometric parameters. The criteria used were: Constant strain should be present over a minimum length of 50 mm in both unnotched and notched sections of the panel, and the highest strain concentration should occur at the notch root. The grip length was designed based on the load required to fracture the panel using friction grips. The geometry of the test specimens finally chosen for the discontinuous blade stiffened panel specimen is shown in Fig. 2.

In-situ Properties

The ends of the panel were tabbed using 8 mm (5/16") thick cross-ply glass/epoxy tabs. This tab thickness was chosen based on the stiffener height at the grip end. In-situ properties of braided and woven panels were measured for simulating the panel test response by finite element analysis. Tension, compression, and Iosipescu shear specimens were extracted from the stiffened panels. These specimens were tested using procedures similar to the ASTM test procedures [4, 5] to obtain E_z, ν_{xy}, and G_{xy}. At least 3 specimens were tested for each of the above properties. Table 1 lists the average values of the different properties measured along with some of the assumed properties which are indicated by the superscript '*' in the table.

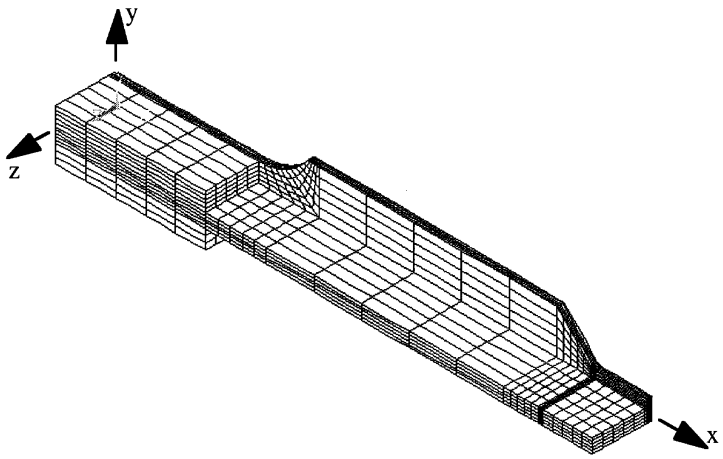

Fig. 3: Finite-element model of one-quarter of the specimen.

Fig. 4: Deformed shape of the finite-element model.

FINITE ELEMENT ANALYSIS OF TEST PANELS

Finite Element Model

A finite element model of one-quarter of the test panel is shown in Fig. 3. This model had 2575, 20-node isoparametric solid element and 12,740 nodes. Symmetric boundary conditions were imposed on z = 0 and x = l/2 planes. A uniform displacement u_x was imposed on the specimen at x = 0. The displacement corresponding to an average axial strain of 1% was imposed. To simulate gripping conditions, additional rigid body displacement in y-direction was imposed at x = y = z = 0. Because the friction grips does not allow the tabbed length of the specimen to rotate, an equivalent condition was simulated by restraining y-direction displacement of the tabs.

A preliminary calculation showed that the tab deformation due to friction induced load in y-direction was about 0.05 mm (0.002 in.). Therefore one-half of this displacement was imposed on top and bottom tab surfaces. The material properties given in Table 1 were used for both flange and stiffener of the panel. A linear elastic analysis [6] was conducted and the displacements, strains, and stresses were calculated at the nodes.

Finite-Element Results

Figure 4 shows a typical deformed shape of the finite-element model. Note that the deformation of the 2nd half of the model is added to get a total view of the panel deformation. The deformed shape indicate that: (1) Maximum strain occurs at top surface in the mid section of the panel and (2) Concentration of stiffener peeling (σ_y) and shear (τ_{xy}) stresses is present at the notch root of the stiffener. Figures 5 and 6 show the distribution of σ_y and τ_{xy} ahead (towards the unnotched section) of the notch for both braided and woven panels. All stresses are normalized by the average applied stress at the gripped ends. High stresses are limited to a distance of 25 mm from the notch root. Although the notch stress concentration varies from 30% to 40% of the average σ_x stress, they are high enough to cause peeling and/or shearing of the stiffener. Orthogonal weaves are weak in shear, therefore, the failure can initiate as shearing failure. Braided composites are strong in shear but not in peeling (a matrix dominant direction). Because of interlocking of fiber yarns, failure initiation by peeling would be suppressed. More details of the stress analysis are given in Ref. 3.

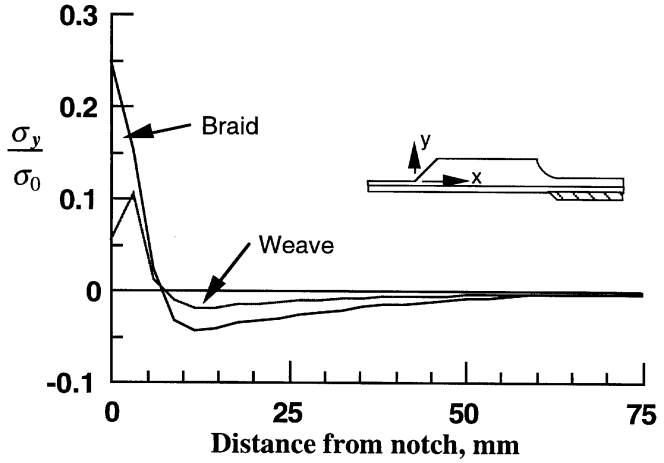

Fig. 5: σ_y distribution away from the notch.

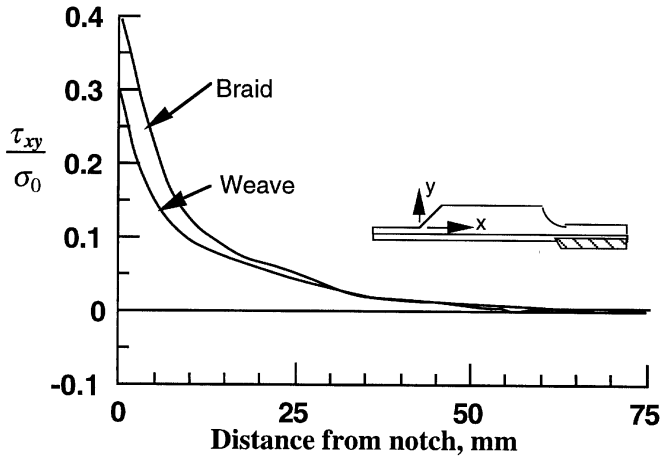

Fig. 6: τ_{xy} distribution away from the notch.

STIFFENED PANEL TESTS

Instrumentation and test procedure

The panel specimens were instrumented with strain gages at selected locations as shown in Fig. 7. Strain gages with 12.3 mm x 4.6 mm active grid were used. The strain gage readings as well as load levels and displacements from the test machine were recorded using a 20 channel strain gage data acquisition system. In addition, the corners between the stiffener and flange, where high peel and shear strains are expected, were coated with a thin uniform layer of typewriter correction fluid. This layer served in a manner similar to brittle coating, indicating regions of severe strains. Failure initiation in these regions were monitored during the tests. Panels were tested in an MTS 810 test machine, under load control, at the rate of 22.24 KN/min. until failure.

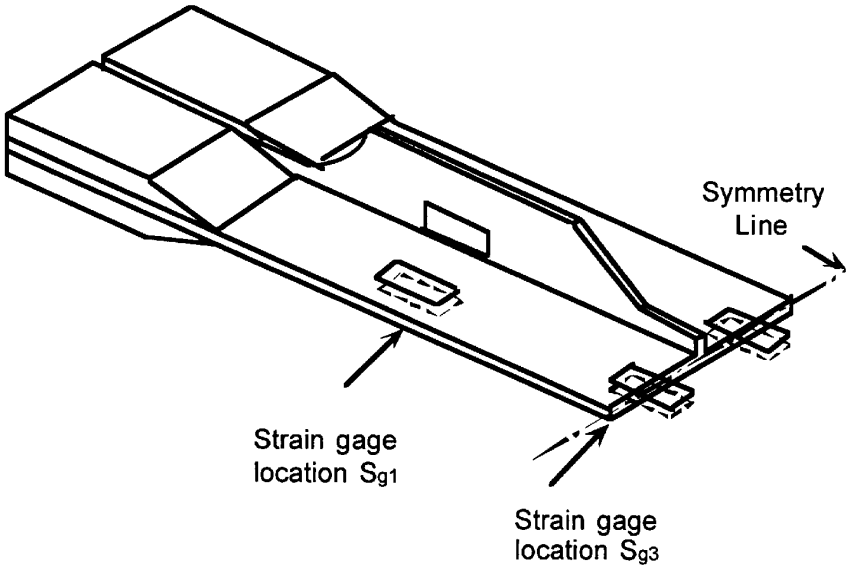

Fig. 7: Strain gage locations.

Test Results

The load displacement curves for the braided and woven panels are shown in Figs. 8 and 9. The load-displacement response is initially linear and then it becomes nonlinear (softening). The softening was due to a number of microscopic failures initiating and progressing in the specimens.

Most of the braided specimens showed first failure around the notch root of the stiffener. As the load increased, the number of cracks increased both at the notch root and all along the notch section. Finally specimens failed as net section tensile failure.

In the woven panels the failure initiated as shear failure at the notch root and then leading to shearing of the stiffener. The final fracture was by the net section tensile failure of the panel. Three of the five panels fractured and the strength of remaining two exceeded the machine capacity. Table 2 lists the fracture load and the fracture stress (based on the cross-sectional area at the notch section) of all the tested panels. The average fracture stress of the barided and woven panels were 433.7 and 501.9 MPa, respectively. Data scatter was less than 2% for

woven panels and it was +17%/-15% for braided panels. In conclusion, fracture in both braided and woven panels was by net section tensile failure. Notch root stress (strain) concentration causes failure initiation but its influence on the ultimate strength is minimal. Failure initiation in braided panel is by peeling and in woven panel it is by shear.

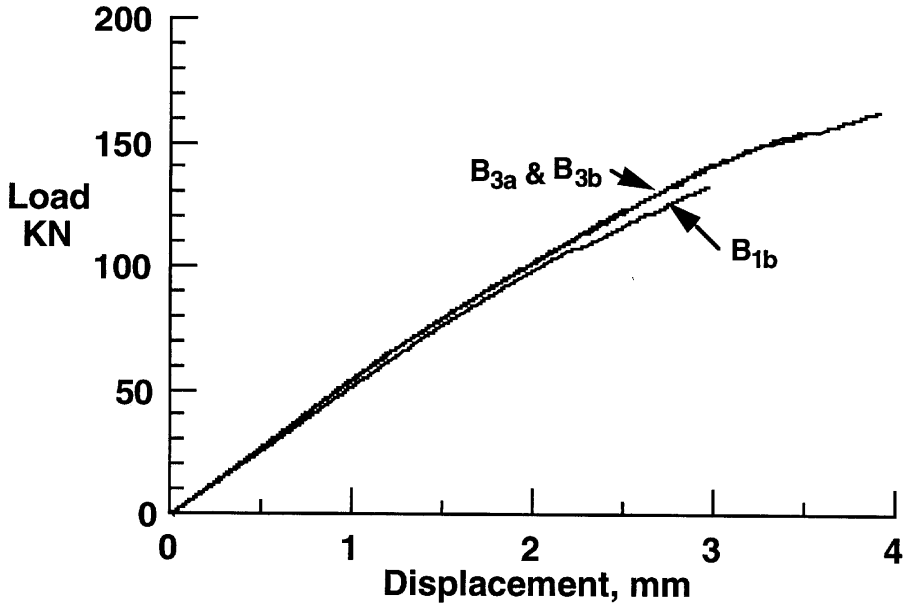

Fig 8: Load-elongation response of braided composite panels.

Table 2: Panel test results

Specimen No	Area of cross-section @ mm^2	Failure load KN	Fracture Strength MPa
Braided composite panels:			
B1B	362.1	133.4	368.5
B3A	322.2	163.7	508.1
B3B	319.3	154.8	484.8
BT0	359.7	133.4	370.8
BT1	411.5	179.6	436.5
Woven composite panels			
W2A*	333.4	-	-
W3B	320.5	160.1	499.6
W2B*	328.8	-	-
WT0	324.9	165.7	510.1
WT1	354.5	175.8	496.1

* Load exceeded test machine's capacity

Figure 10 shows load versus strain response at selected locations in the braided panel. The locations at the mid-section of the stiffener (S_{g3} and S_{g11}, the strain gages at the top and bottom surfaces), mid-section of the notch which was also the mid-section of the panel (S_{g5} and S_{g9}, the strain gages at the top and bottom surfaces), and the strain gage S_{g2}, on the stiffener. Refer to Fig. 7 for the description of the strain gage locations. The top and bottom strain gage pair indicate that the panel is subjected to both bending and membrane strains. The bending strain at the mid-ssection of the panel is large (difference between S_{g5} and S_{g9} is larger than the difference between S_{g3} and S_{g11}). Furthermore, stiffener does carry some load (non-zero strain). But the stiffener strain values are less than 50% of the membrane strains. Note that the horizontal steps in the strain gage response are indicative of major failures in the specimen. Membrane and bending components of the strain at mid-section of the stiffener and the notch are shown in Figs. 11 and 12 respectively.

Membrane strains at these locations are almost identical for braided panel and the difference for the woven panels is less than 10%. Bending strains., as it can be inferred from the finite-element results (see Fig. 4) is larger at the mid-section of the panel (location 3) than at the mid-section of the stiffener (location 1). The bending strain at location 1 is almost half the bending strain at location 3 for braided composites. However, bending strain is much smaller (stabilized around 250 με) for woven composite panel. The difference in the two composites results may be due to difference in the material properties.

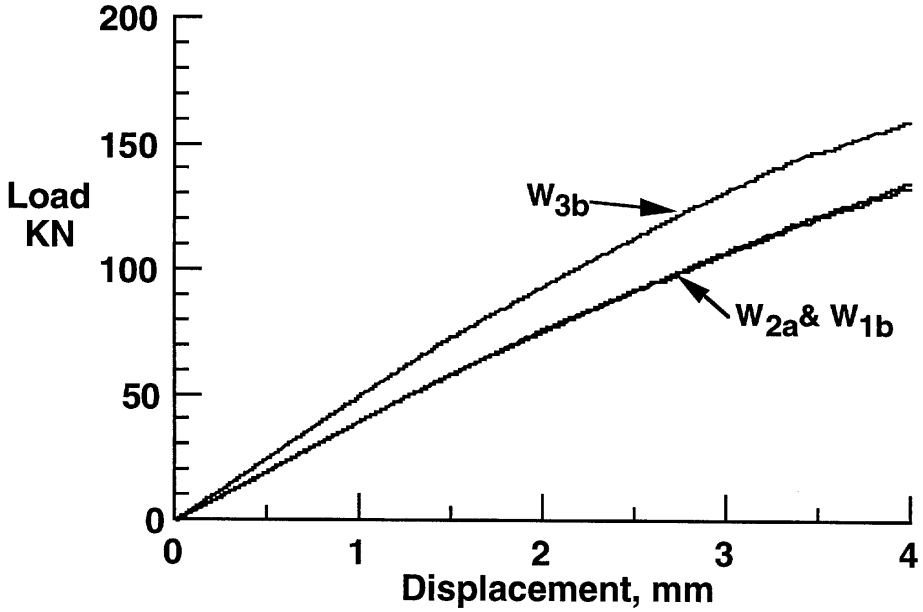

Fig 9: Load-elongation response of woven composite panels.

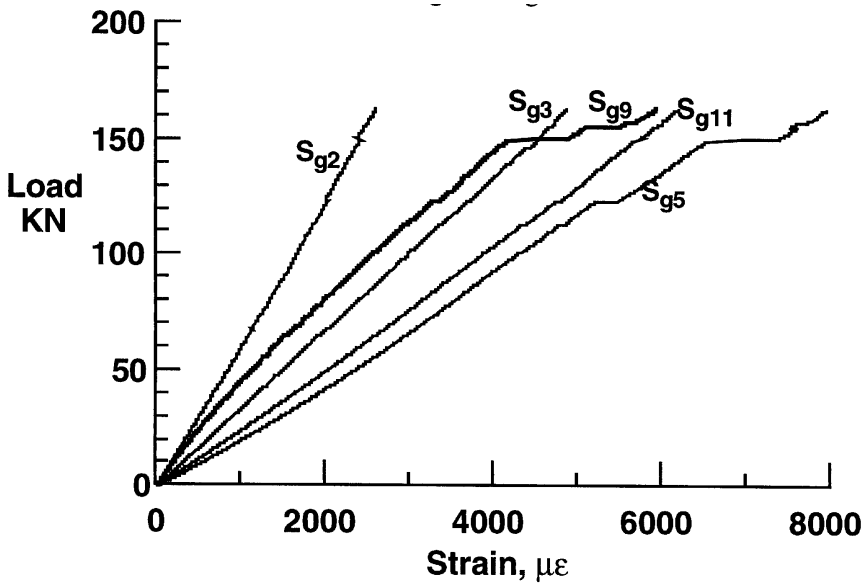

Fig. 10: Load-strain plot at selected strain gage locations for braided composite panel ($B_{3\alpha}$).

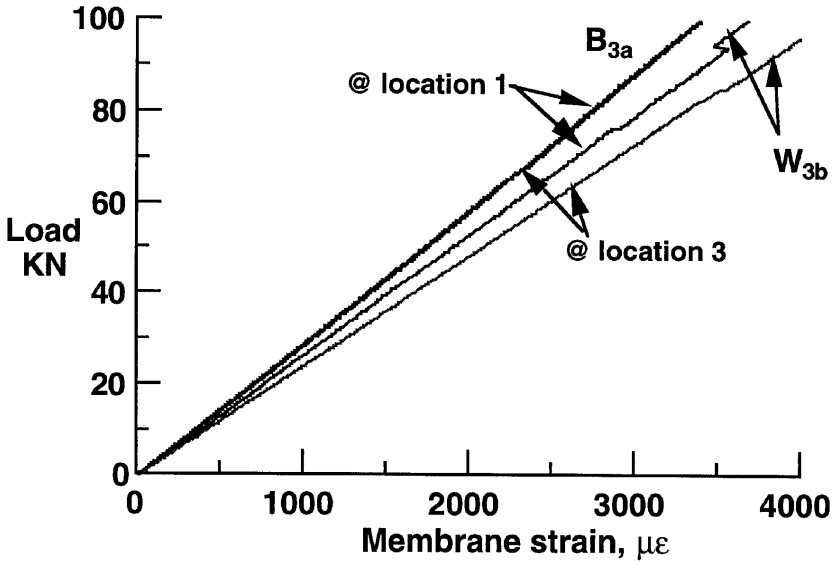

Fig. 11: The membrane component of the strains at strain gage locations 1 and 3.

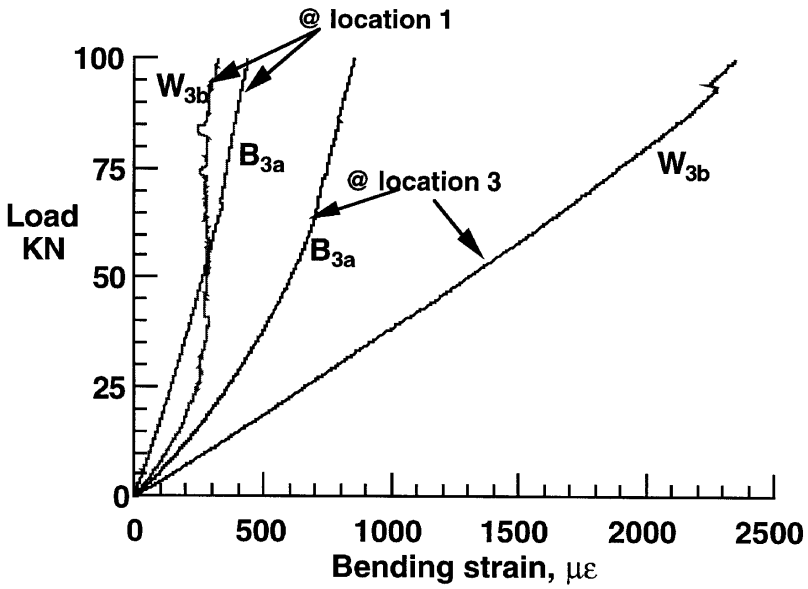

Fig. 12: The bending component of the strains at strain gage locations 1 and 3.

Fig. 13 shows comparison of strains S_{g1} and S_{g3} obtained from the finite-element analysis with the test data for the woven specimen. Broken lines through symbols represent the analysis and solid lines represent the test. Finite-element strains at S_{g1} agreed very well with test data, whereas the F-E strains at S_{g3} were larger than the test data; but the difference is less than 10% and may be due to local variations in the material properties.

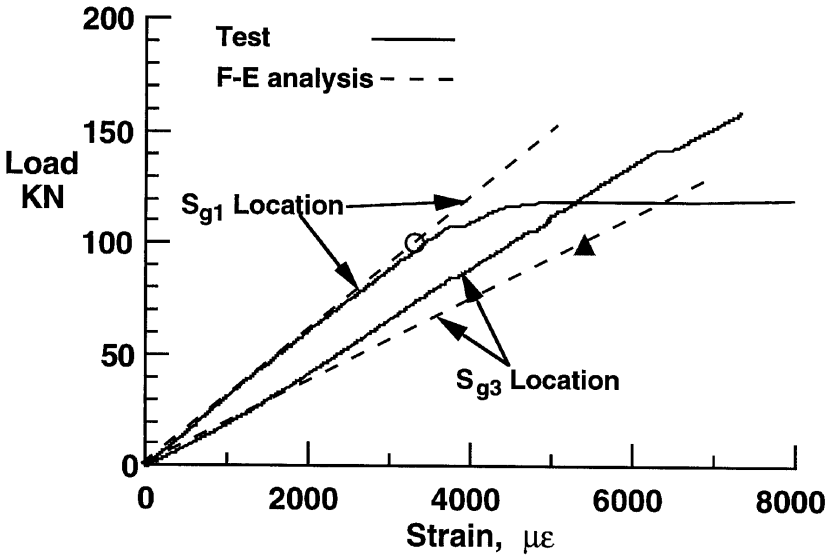

Fig. 13: Comparison of F-E strain data with test for woven composite panel(W_{3b}).

CONCLUDING REMARKS

The objective of this study was to evaluate the structural integrity of discontinuous blade stiffened panels made of textile preform composites and compare the failure stresses and modes with that of conventional laminated stiffened panels. Three-dimensional braided and 3-D orthogonal woven composite panels were evaluated. Panels were made of BASF G30-500 graphite fiber yarns and Dow Chemicals Tactix-123 matrix. Panels were consolidated by resin transfer molding. The panel configuration was similar to that was used in a previous FAA contract. Three-dimensional finite-element analysis was used to establish the geometrical configuration and identify the regions of high stresses. Peel and shear stress concentrations were found to be at the notch root and it was the site for failure initiation. Furthermore, the bending stress at the mid-section of the panel was larger than that at the stiffener section. Test results showed that fracture in both braided and woven panels was by net section tensile failure. Notch root stress (strain) concentration causes failure initiation but its influence on the ultimate strength was minimal. Failure initiation in braided panel was by peeling and in woven panel it was by shear. The average fracture stress of the barided and woven panels were 433.7 and 501.9 MPa, respectively. Strains calculated from the finite-element analysis generally agreed with the test data.

ACKNOWLEDGMENTS

The CCMR authors acknowledge the financial support of the FAA Technical Center (Grant No. 95-G-013), Atlantic City Airport, NJ.

REFERENCES

1. Shah, C.H., Kan, H.P., and Mahler, M., “Certification Methodology for Stiffener Terminations,” Northrop Grumman Final Report NASI-19347, January 1995.

2. Emehel, T. C. and Shivakumar, K. N., "Tow Collapse Model for Compression Strength of Textile Composites", Proc. of ASC 10th Technical Conference, Santa Monica, Ca. October 18-20, 1995.

3. Vivek Ramanujapuram, Kunigal Shivakumar, Vishnu Avva, and Mannur Sundaresan, “Design of Discontinuous Blade Stiffened Textile Composite Test Panel”, 38th SDM Conference, AIAA/ASME/ASCE/AHS/ASC, Kissimmee, Florida, April 8-10, 1997.

4. ASTM Standards 1993 Annual Book, Section 15, Vol. 15.03, American Society for Testing and Materials, Philadelphia, Pa.

5. Minguet, P. J., Fedro, M. J., and Gunther, C. K., “Test Methods for Textile Composites”, *NASA CR-4609*, July 1994.

6 DeSalvo, G. J., and Gorman, R. W., *ANSYS Engineering Analysis System user's manual*, Version 4.4, Swanson Analysis Systems, Inc., Houston, PA , May 1989.

INFLUENCE OF MOISTURE ABSORPTION ON HOT/WET COMPRESSIVE STRENGTH OF T800H/PMR-15 CARBON/POLYIMIDE COMPOSITE

Yasumasa Hamaguchi, Toshiyuki Shimokawa, and Hisaya Katoh

Airframe Division, National Aerospace Laboratory
6-13-1 Ohsawa, Mitaka, Tokyo 181, Japan

SUMMARY: Statistical compression tests for moisture absorbed specimens of a T800H/PMR-15 carbon/polyimide composite with a quasi-isotropic stacking sequence were conducted at 260°C. These tests clarified the compression fracture mode, the influence of moisture absorption on hot/wet compressive strength, statistical properties of hot/wet compressive strength, the effectiveness of a traveler coupon to monitor moisture absorption, and the relationship between specimen thickness and hot/wet compressive strength.

KEYWORDS: carbon/polyimide composite material, moisture absorption, hot/wet compressive strength, fracture mode, statistical features, traveler coupon, specimen thickness.

INTRODUCTION

The authors are conducting a series of reliability evaluation tests for the static strength of T800H/PMR-15 carbon/polyimide composite material. This material is a high temperature polymer composite to be applied to the tip fin and other secondary structures of the HOPE-X (H-II Orbiting PlanE), which is an experimental, unmanned, small space shuttle being jointly developed by the National Aerospace Laboratory (NAL), and National Space Development Agency (NASDA).

One of the most important mechanical properties in applying polymer composites to the space vehicle structures is hot/wet strength, especially hot/wet compressive strength. Many fundamental studies on carbon/polyimide composites and their applications were conducted and reported in Refs. 1 and 2. However, not much design data [1-4] has been published for these kinds of materials. The hot/wet tensile strength of polyimide composite materials is known to be fairly lower than that at room temperature, as reported in Ref. 3. However, no data of hot/wet compressive strength were found in Refs. 1 to 4. Moreover, statistical features of this property are not clarified for any carbon/polyimide materials, though this property is very important and expected to have a relatively large scatter.

This study investigated the influence of moisture absorption on hot/wet compressive strength and the distribution of hot/wet compressive strength of a T800H/PMR-15 carbon/polyimide composite. Static compression tests conducted at 260°C clarified the compressive failure mode, the influence of moisture absorption on hot/wet compressive strength, the statistical properties of hot/wet compressive strength, the effectiveness of a traveler coupon to monitor

the moisture content of a specimen tested, and the relationship between hot/wet compressive strength and specimen thickness.

MATERIAL AND SPECIMEN

The prepreg tape of T800H/PMR-15 carbon/polyimide was supplied by Yokohama Rubber Co. Laminate panels with a quasi-isotropic stacking sequence, 32 plies $(45/0/-45/90)_{4S}$, and coupon type specimens cut from these panels were made by Fuji Heavy Industries, Ltd. A specimen and a traveler coupon, i.e., an accompanied specimen, have the same configuration as illustrated in Fig. 1 and were not distinguished before a static test.

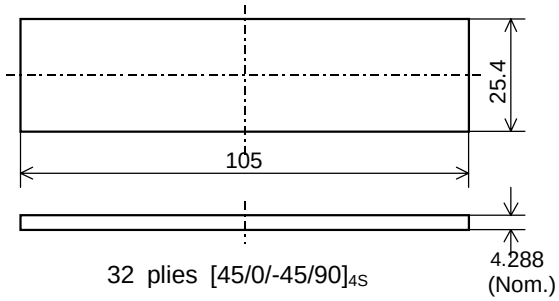

Fig. 1: Geometry of specimens and traveler coupons; dimensions in mm

MOISTURE ABSORPTION PROCESSING

Specimens were one by one sealed in a polyethylene bag and supplied to NAL. These specimens were moisturized by the following process. The moisture content of a specimen in this study was defined by that calculated from the weight change measured by a chemical balance.

Moisture Disorption Processing

At first specimens and traveler coupons were dried in a vacuum oven. Figure 2 presents the relationship between moisture disorption in weight percent and drying time in hours at 120°C. All specimens and traveler coupons were kept in the oven for 288 hours at 120°C. After this processing, the moisture contents of specimens and traveler coupons were defined to be zero percent.

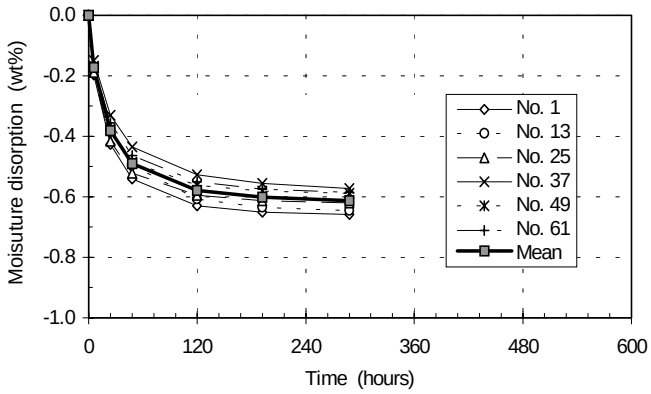

Fig. 2: Moisture disorption in weight percent and drying time in hours at 120°C

Moisture Absorption Processing

Specimens and traveler coupons were soaked in a hot water bath for moisture absorption. The temperature of water was kept at 75°C. Figure 3 illustrates the relationship moisture absorption in weight percent and soaking time in hours. Since after 576 hours moisture absorption was considered to be saturated, the electric heater of the water bath was switched off. Specimens and traveler coupons were kept in this water bath in order to keep their moisture contents. However, this figure indicates the increase in the moisture content to about 1.8% after the stop of electricity. This phenomena seems to be generated because of the lower saturated vapor pressure inside of the specimen at room temperature than that at 75°C.

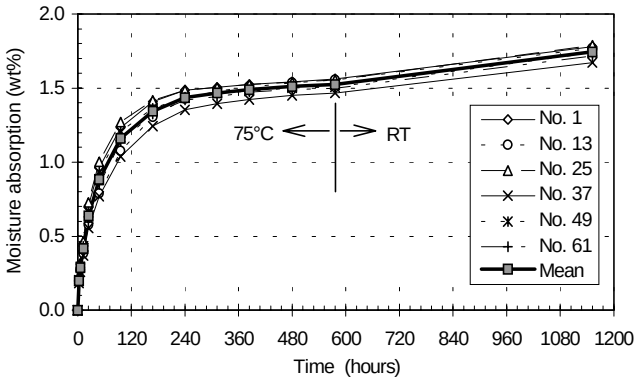

Fig. 3: Moisture absorption in weight percent versus soaking time in hours

The specimens in which the moisture content exceeds the required value were dried in the vacuum oven again. Then the moisture content was adjusted close to the required value by wrapping a specimen in wet tissue or drying it by an electric dryer. To investigate the statistical properties of hot/wet compressive strength, the water contents of 30 specimens and 30 traveler coupons before tests were controlled to be 1.2 weight percent as a target value. This target is 70% of the saturated moisture content, 1.7%, estimated in the planning stage of this study. The actually controlled values were from 1.19% to 1.24%. In addition, to know the effect for the large change of moisture content on the hot/wet compressive strength, three specimens and traveler coupons each were adjusted to about 1.78%, and the same number of specimens and traveler coupons were also adjusted to 1.35%.

COMPRESSION TEST PROCEDURE

Figure 4 shows the external appearance of the compression test fixture clamping a specimen and a traveler coupon placed beside the specimen. Compression tests were conducted at 260°C in an environmental chamber. This temperature is tentatively fixed as the upper limit of this material under mechanical loading for the structures of the HOPE-X. The temperatures of the specimen and the traveler coupon during a test were measured by thermocouples of a foil gage type installed to both surfaces of the specimen and to one surface of the traveler coupon. The temperature near the opening of the chamber from which hot air blew in was controlled at 295°C. When the lower temperature of those measured on the specimen reached 259°C, the compression test was started and finished under 261°C.

Heating a specimen up to 260°C and conducting the test were tried to be completed within 25 to 35 minutes. All the tests were finished within this time range after placing the compression

test fixture clamping a specimen on a test platen in the chamber. The average time was approximately 32 minutes. No preheating was given to the test fixture before clamping a specimen. Figure 5 indicates an example of temperature records of the specimen and traveler coupon. Since the traveler coupon was placed beside the specimen, the temperature of the traveler coupon rose faster than that of the specimen.

Specimens were evenly sampled from the location of the original laminate panels. A coupon adjacent to each specimen was selected as the traveler coupon in each test.

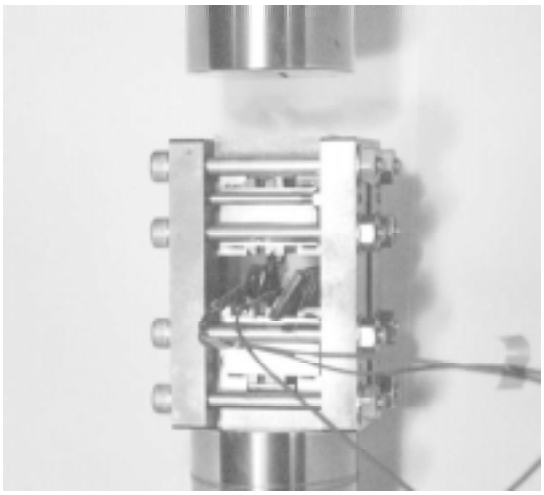

Fig. 4: External appearance of the compression test fixture clamping a specimen

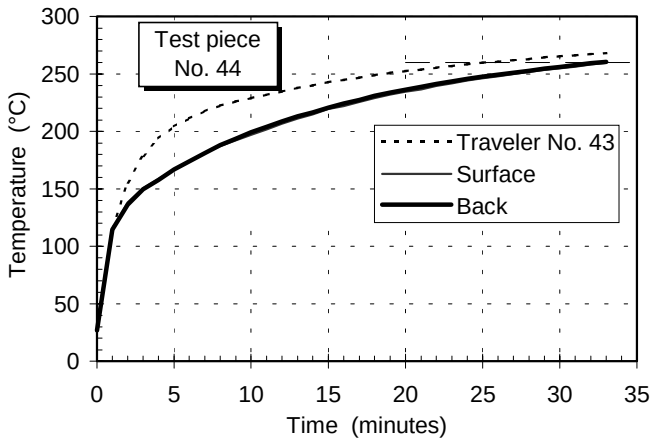

Fig. 5: An example of temperature records of the specimen and traveler coupon during a hot/wet compression test

Compressive strength is represented by the nominal strength based on the nominal thickness. A digital servo-hydraulic testing machine was used for static tests. The speed of the actuator moving in a test was controlled at 1.3 mm/min.

Moisture content of the specimen and traveler coupon before and after a static test was obtained by measuring their weights. Their moisture content was not necessarily equal but very close. Not to disperse specimen debris, the testing machine was stopped by its limit function right after the specimen failed. This enabled an accurate measurement of the moisture content after the test.

TEST RESULTS

Relationship Between Compressive Strength and Temperature

Figure 6 illustrates the relationship between compressive strength and temperature. In these test results, the data of dry compressive strength obtained by the authors before this study were included.

This figure shows that the hot/wet compressive strength at 260°C is significantly lower than the dry compressive strength at 260°C; furthermore, on average, it is even lower than the dry compressive strength at 300°C.

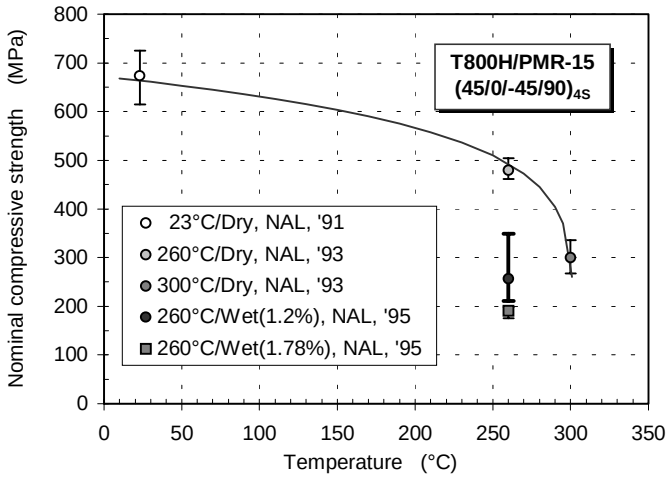

Fig. 6: Compressive strength versus test temperature

Relationship Between Compressive Strength and Moisture Content

Figure 7 indicates the influence of moisture content on hot/wet compressive strength at 260°C. The compressive strength may have a weak correlation with the moisture content before the tests. However, a fairly clear correlation is recognized between the compressive strength and the moisture content after the tests, i.e., the residual moisture content. Therefore, it should be considered that the compressive strength has a strong and negative correlation with the residual moisture content. Moreover, this figure indicates that, if measurable, the moisture content of the specimen during static loading must be used. The specimen which showed the highest strength, about 350MPa, away from the group had an especially small residual moisture content. In this case the traveler coupon also had a very small moisture content after the test. Roughly a linear or semi-log linear line seems to be applicable to represent their relationship.

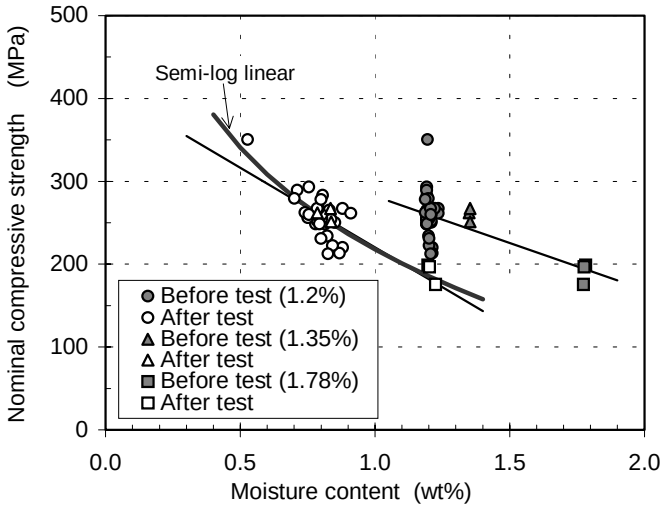

Fig. 7: Influence of moisture content on hot/wet compressive strength at 260°C

Most specimens indicated a shear fracture mode, that is, the specimen was obliquely broken on the side face. However, the specimen broken at the maximum strength showed a fracture mode of a rhombus shape as a side view dominantly caused by delamination. This fracture mode generally appears in a compression test at room temperature. This fact means that the fracture mode generally seen at room temperature appears when the residual moisture content is low enough and in such case the hot/wet compressive strength is restored. Therefore, the large reduction in hot/wet compressive strength can be prevented, if the residual moisture content is kept low enough to show the general fracture mode at room temperature. Figure 7 indicates that the fracture mode will change at around 0.6% of the residual moisture content.

Statistical Distribution of Hot/Wet Compressive Strength

Figure 8 illustrates the 30 observations of hot/wet compressive strength plotted on normal probability paper. These data were obtained by the specimens of which moisture content before the tests were adjusted to within 1.19 to 1.24%. Except for the value of the maximum strength, these data fit a normal distribution very well. As described above, the maximum strength is obtained by a different fracture mode. Therefore, this value should be removed from the data evaluated for structural design.

The mean hot/wet compressive strength is estimated to be 256 MPa from the censored data of a sample size of 29 on this probability paper. This value is approximately 53% of the mean dry compressive strength at 260°C in Fig. 6. The coefficient of variation as an index of data scatter is 8.9% and twice as large as that of the dry/room temperature compressive strength, obtained from a sample size of 30 [5]. This value is 2.5 times larger than that of dry compressive strength at 260°C, obtained from a sample size of 6.

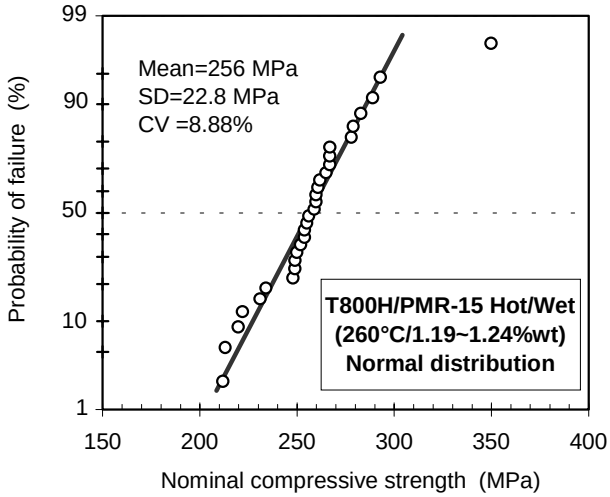

Fig. 8: Hot/wet compressive strength distribution obtained by the specimens of which moisture contents were adjusted to within 1.19% to 1.24% before tests

Moisture Contents Before and After Test

Figure 9 illustrates the relationship between the moisture content before the test and that after the test separately for specimens and traveler coupons. It seems possible to control the residual moisture content, if only a small number of observations of large moisture contents before the tests were noticed. However, the residual moisture contents have a wide scatter of the moisture content controlled at about 1.2% in both cases of specimens and traveler coupons. For these data, no relation was recognized between the residual moisture content and the retention time from placing a specimen clamped by the test fixture on the test platen in the environmental chamber until the end of the test. This fact means that control of the residual moisture content is very difficult, though this content is deeply related with the hot/wet compressive strength as described above.

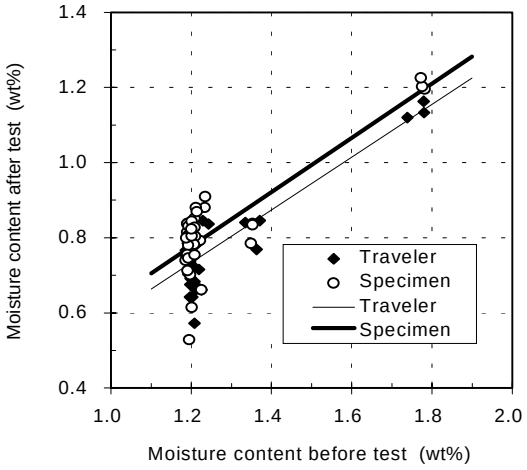

Fig. 9: Moisture contents before and after test for specimens and traveler coupons

Moisture Content Reductions of the Specimen and Traveler Coupon Used in the Same Test

The moisture content of a specimen or a product is generally estimated by that of a traveler coupon placed in the same environment in a practical process control. This method is

discussed here. Figure 10 presents the relationship between the moisture reduction of the specimen and that of the traveler coupon in the same test. Though the data points were expected to converge in a straight line, they are distributed in a wide band as shown in this figure. Therefore, to precisely estimate the moisture content by this method is impossible, but effective enough for a rough estimation.

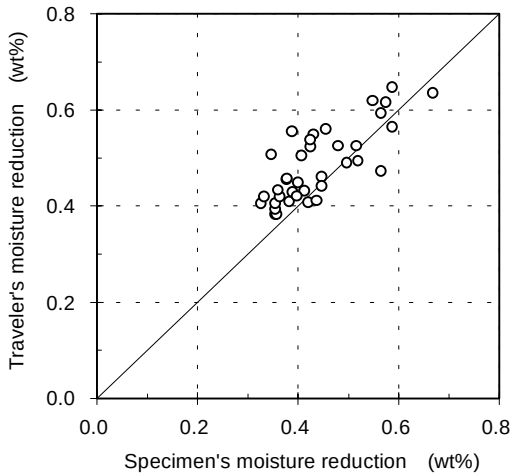

Fig. 10: The relationship between the moisture reduction of the specimen and that of the traveler coupon in the same test

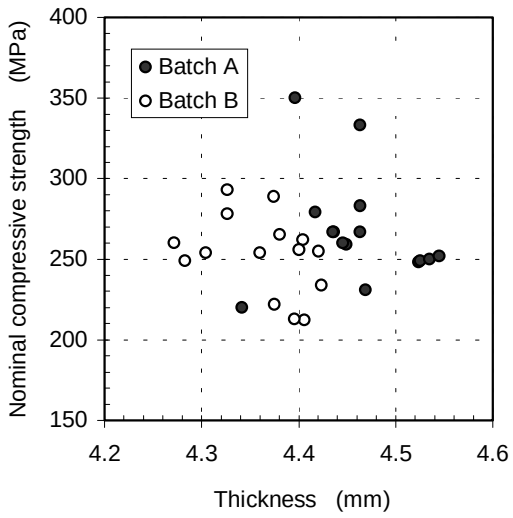

Fig. 11: Nominal hot/wet compressive strength versus measured specimen thickness

Relationship Between Hot/Wet Compressive Strength and Specimen Thickness

Specimens were machined from two panels cured at different times using the same cure condition. These specimens were separated from the original panels into two groups, called Batch A and Batch B. Figure 11 presents the relationship between nominal hot/wet compressive strength and measured specimen thickness, separated by each batch using different symbols. This figure shows that no correlation is recognized between hot/wet compressive strength and specimen thickness within this study.

CONCLUSIONS

The hot/wet compressive strength of the T800H/PMR-15 carbon/polyimide composite material was statistically investigated by static tests at 260°C. Major conclusions are as follows:

(1) The fracture mode in most specimens is of shear fracture obliquely broken on the side face. However, at the maximum strength, a fracture mode of a rhombus shape as a side view, dominantly caused by delamination appeared, which is generally observed in a test at room temperature.
(2) Hot/wet compressive strength was deeply related with the residual moisture content measured right after the test. When decreasing this content, the hot/wet compressive strength became higher.
(3) The distribution form of the hot/wet compressive strength is approximated well with a normal distribution except for the maximum strength. The mean and coefficient of variation should be estimated from this censored distribution.
(4) The mean hot/wet compressive strength of specimens absorbing moisture of 1.19 to 1.24 weight % before tests decreased to 53% of that of dry specimens at 260°C.
(5) The coefficient of variation of hot/wet compressive strength was approximately twice as large as that of room temperature/dry compressive strength.
(6) Control of the residual moisture content was considered difficult.
(7) The traveler coupon used to monitor the moisture content of the specimen in the same test is effective only for a rough estimation, but is difficult for an accurate estimation.
(8) No strong correlation was found between hot/wet compressive strength and specimen thickness.

ACKNOWLEDGMENT

The authors wish to thank Mr. Hirofumi Tamura, Fuji Heavy Industries, Ltd., for his valuable suggestions to this study.

REFERENCES

1. Dexter, H.B., and Davis, J.G., Jr., eds., *Graphite/Polyimide Composites*, NASA CP-2079, 1979.
2. *High Temperature Polymer Matrix Composites*, NASA CP-2385, 1985.
3. McCleskey, S.F., Cushman, J.B., and Skoumal, D.E., “High Temperature Composites for Advanced Missile and Space Transportation Systems,” AIAA Paper 82-0707, Proc. SDM Conf., American Institute of Aeronautics and Astronautics, 1982, pp. 212-222.
4. Wilson, D.W., Pipes, R.B., Riegner, D., and Webster, J., “Mechanical Characterization of PMR-15 Graphite/Polyimide Bolted Joints,” *Test Methods and Design Allowables for Fibrous Composites*, ASTM STP 734, 1981, pp. 195-207.
5. Shimokawa, T., Hamaguchi, Y., and Kakuta, Y., “Statistical Evaluation of Compressive Mechanical Properties of a T800H/PMR-15 Carbon/Polyimide Composite,” Journal of the Japan Society for Composite Materials, Vol. 22, No. 5, 1996, pp. 184-192. (in Japanese)

STRENGTH REDUCTION OF GRP COMPOSITES EXPOSED TO HIGH TEMPERATURE MARINE ENVIRONMENTS

J M Hale and A G Gibson

Department of Mechanical, Materials and Manufacturing Engineering
University of Newcastle Upon Tyne, NE1 7RU, U.K.

SUMMARY: A programme of tests has been conducted to characterise the strength reduction of three GRP composites as a function of temperature and testing environment. The materials were two E-glass reinforced epoxies and E-glass reinforced phenolic. The testing environments were sea water and crude oil condensate at temperatures from ambient to 150°C. Results are presented for the strength of the three materials as a function of temperature in fibre and resin dominated failure modes when tested dry and saturated in water and oil respectively.

- Fibre dominated strength is insensitive to high temparatures.
- Resin dominated strength of epoxy based materials is greatly reduced at high temperatures.
- Resin dominated strength of the phenolic based material is reduced only slightly at high temperatures, but its low temperature strength is poor.
- Sea water saturation greatly exacerbates the strength reduction of all the materials tested. Oil has little effect.

KEYWORDS: GRP, FRP, tensile strength, tensile testing, environmental testing, sea water, marine environment, offshore environment

INTRODUCTION

Composite materials are progressively gaining acceptance for use in offshore applications where their perceived virtues of low weight and good corrosion resistance are much sought after by designers and operators. Glass fibre reinforced plastics (GRP) in particular have won widespread acceptance in nonstructural applications, including fire water piping, decking and cable trays. There is however considerable interest in the use of GRP of various types in more demanding applications offshore. Such new applications involve using the material in contact with aggressive process fluids at elevated temperatures. Examples of applications under consideration include separator vessels (where various hydrocarbons and water are present at 70-80°C, with possible excursions above 100°C), subsea flowlines and, perhaps the most demanding application, down hole tubing and drill stream parts. Although the temperatures involved in the most demanding down hole applications are too high to permit the use of organic matrix composites, there is a range of applications where the temperatures are somewhat lower and GRP offers significant potential advantages.

To help assess the suitability of GRP in these demanding offshore applications, a programme of tests has been carried out to measure the strength of three candidate materials as a function of temperature in typical operating environments. This is the work described in this paper.

The effects of environment on GRP

Most tests carried out to date to determine the response of composite materials to environmental degradation have been carried out at ambient temperature. However, it is known that elevated temperature softens most resins, particularly above the glass transition temperature (T_G) [1]. This reduces the interlaminar shear strength and so the strength of the composite when it is loaded such that the fibres are not in pure tension. The glass fibres are not susceptable to corrosion unless the absorbed water is acidic, in which case the effect can be dramatic [2].

The flexural strength of glass/polyester laminates and glass/epoxy pipes aged in sea water at ambient temperature have been shown to reduce by up to 20% within a year [3]. Absorbed water is known to act as a plasticiser [4], reducing T_G, and has been shown to reduce the strength and modulus of amine cured epoxies [1]. It can thus be expected to exacerbate this loss of properties at high temperatures.

The presence of oil is believed to have little effect on fibre composites. Polyester/glass laminates exposed to dehydrated oil at temperatures up to 90°C for 90 days have been shown to behave in the same way as unexposed laminates [5].

EXPERIMENTAL DETAILS

Test Programme

The programme of tensile tests was undertaken on coupon specimens of three different GRP materials at elevated temperatures in two marine environments: natural sea water and oil condensate. For comparison, the materials were also tested in the normal laboratory environment (air at ambient humidity) and at ambient temperature in the test environments.

The tensile tests were carried out on specimens that had previously been saturated in the test environment. To ensure that the specimens were truly saturated, a series of absorption tests was first carried out on each material in each environment to determine the time required to reach saturation.

Tensile tests were carried out on coupon specimens with the fibre reinforcement laid in two different directions: 0/90° and ±45° with respect to the direction of loading. With the fibres oriented at 0/90° approximately half of the fibres were loaded axially and so the failure was controlled by the strength of the fibres (fibre dominated failure mode). With the ±45° oriented fibres, the failure was largely controlled by the strength of the resin matrix (resin dominated failure mode).

Tensile tests were carried out under quasi-static axial loading conditions with the specimen at constant temperature and immersed in the test environment.

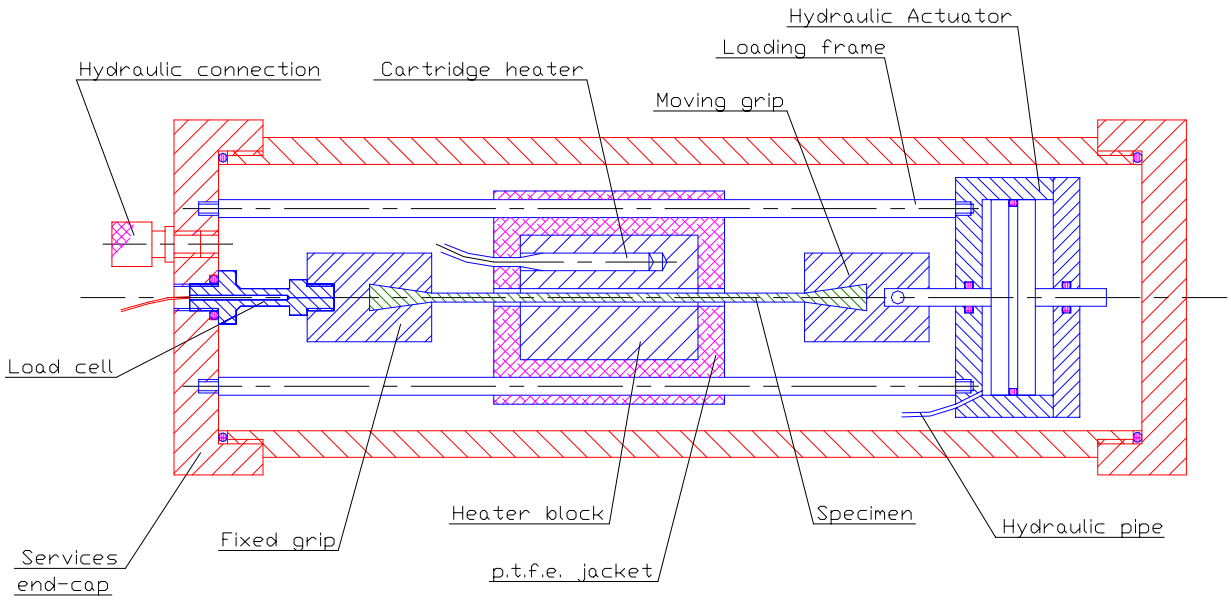

Figure 1: Schematic representation of the environmental tensile testing chamber

The tensile tests were carried out in the specially developed environmental tensile testing chamber shown schematically in Figure 1, described fully in [6]. Briefly, it consists of a tensile testing machine (loading frame, hydraulic actuator, load cell and specimen grips) contained within a pressure vessel. This facility made possible the testing of specimens whilst immersed in liquids at high temperatures above the normal boiling point. Boiling was inhibited by allowing the pressure to rise as the temperature increased.

A particular feature of the testing chamber is the thermally defined gauge length. The specimen is heated to the test temperature only in a short region near its mid-length. The ends of the specimen remain relatively cool. Since the material is weakened at elevated temperatures, this differential heating ensures that the specimens always fail in the gauge length and not at the entrance to the grips. This arrangement eliminates the need for special specimen geometry.

Test Environments

Natural Sea Water. Sea water was taken directly from the North Sea at the coast near Newcastle upon Tyne.

Oil Condensate. Samples of crude oil, modified only by flashing off the light fractions, were supplied by Philips Petroleum. The samples supplied were typical of light crudes.

MATERIALS

Resin Matrix Materials. Three generic resin types were chosen for this work, representing the materials of greatest interest to the offshore community. These were:

- aromatic amine (MDA) cured epoxy,

- cycloaliphatic amine (IPD) cured epoxy, and
- acid-cured phenolic.

These resins are all capable of being processed into GRP components by liquid fabrication methods such as contact moulding and filament winding.

The epoxy resins were of the type widely employed in the fabrication of GRP pipework. The aromatic amine curing agent, MDA, is known to give resins with the higher T_G and generally good high temperature properties. Unfortunately there are some health and safety concerns about the carcinogenicity of this material. This has led to its replacement in Europe, for some applications, by the cycloaliphatic amine curing agent IPD which is less toxic. IPD is known to give resins with a somewhat lower T_G and hence inferior high temperature properties. Clarification of the relative thermal performance of composites based on these two key thermosetting resins in liquid environments was the main reason for their inclusion in the test programme.

The epoxy resins used for the fabrication of coupon samples were of the same composition used for the commercial manufacture of GRP pipes. The epoxy component was supplied by Shell Chemicals (Epikote 827). The IPD curing agent was Vestamin IPD, supplied by Hülls and the MDA curing agent was Ancamine 1692, supplied by Anchor Chemicals (Air Products). Both agents were used in the proportion recommended by the manufacturer of the epoxy resin.

The phenolic resin samples were fabricated from the acid-cured liquid phenolic resin, Cellobond J2042L, supplied by BP. They were cured by the addition of the manufacturers' recommended quantity of strong acid catalyst, Phencat 382.

Glass Reinforcement Material. The reinforcement used throughout was epoxy and phenolic compatible E-glass woven rovings (600gm/m^2), supplied by Owens Corning Fibreglass.

COUPON SPECIMEN MANUFACTURE

The specimens were made in-house by contact moulding, with dove-tail ends for mounting in purpose-designed matching grips of the tensile testing machine. This technique ensured a consistent fibre volume fraction from sample to sample and from sheet to sheet. The mould included chamfered ends in which the dove-tails were built up by placing extra strips of glass between the normal fibre layers. The mould was used to make flat sheet laminate of 500 × 500mm, two sides of which had a 50mm wide dove-tail with an included angle of 10°. This sheet was then cut into strips approximately 23mm wide using a fine tooth band saw. These strips were then milled down to 21mm in order to minimise damage to the edges.
The final specimen dimensions were 600mm long × 21mm wide × ≈3.5mm thick.

ABSORPTION TEST PROCEDURE

Samples 60mm and 100mm long were cut from the coupon specimens. The samples were weighed initially and then immersed in the test liquids (sea water and oil condensate) at 100°C. They were removed from the environment at intervals and reweighed. This procedure was repeated until the rate of increase in mass had reduced to a level that indicated that effective saturation had been achieved.

TENSILE TEST PROCEDURE

Dry Tests. Specimens of the three material systems investigated were tested to failure at various temperatures in air (i.e. in the absence of any aggressive environment). The results of these tests were used as a baseline against which the subsequent tests on specimens subjected to conditioning in the test environments could be compared.

Saturated Water Tests. Prior to testing, specimens were conditioned in the test environment for a period sufficient to ensure saturation (as determined in the absorption tests described above). Each specimen was loaded into the test rig and immersed in the environment as quickly as possible after removal from the conditioning chamber. The heater was switched on and, as soon as the gauge length had settled at the test temperature, the specimen was loaded quasi-statically to failure. Load and temperature were monitored and recorded for subsequent analysis.

Saturated Condensate Tests. The testing procedure was the same as that for saturated water testing, using the appropriate conditioning time to ensure saturation of the specimens prior to testing.

RESULTS

Absorption Tests

Sea Water Absorption. The water absorption data for coupon tests of the three materials are given in Table 1. The water uptake was in all cases quite low. The epoxies show a 1-2% increase in mass due to water absorption at saturation and the phenolic, though slightly higher, was still only 2.2%.

Table 1: Saturation of materials in sea water at 100°C

Resin system	Time to saturation	Added mass at saturation
MDA Epoxy	6 days	1.8%
IPD epoxy	3 days	1.1%
Phenolic	5 days	2.3%

It was found that the expected high initial rates of absorption varied between materials, but that in all cases the rate of absorption quickly fell. In the case of the IPD epoxy and phenolic systems there was little further uptake after two days immersion. With the MDA cured epoxy the time to effective saturation was five days.

Oil Condensate Absorption. As shown in Table 2, there was very little absorption of oil into the epoxy materials. In the case of the phenolic resin composite, which is known to form voids in the matrix, it is believed that the increased mass is due to these voids being filled rather than any interaction with the fibre or matrix materials.

Table 2: Saturation of materials in crude oil condensate at 100°C

Resin system	Time to saturation	Added mass at saturation
MDA Epoxy	5 days	<0.1
IPD epoxy	2 days	<0.1
Phenolic	2 days	1.4

TENSILE TESTS

Dry Tests. The results for the matrix dominated ±45° coupon tests (Figure 2) show that in all cases the matrix material is strongly dependent on temperature. At ambient temperature, the aromatic amine (MDA) cured epoxy was the strongest of the three materials tested with a tensile strength of 90MPa. This strength is only slightly reduced at temperatures up to 60°C, but is reduced by 50% to 45MPa at about 110°C and to only 12MPa at 120°C. The aliphatic amine (IPD) cured epoxy system was weaker than the aromatic at all temperatures and followed a similar curve. The tensile strength at ambient temperature was around 80 MPa, began to drop at only 40°C and was reduced to 50% of its initial strength (40 MPa) at 80°C.

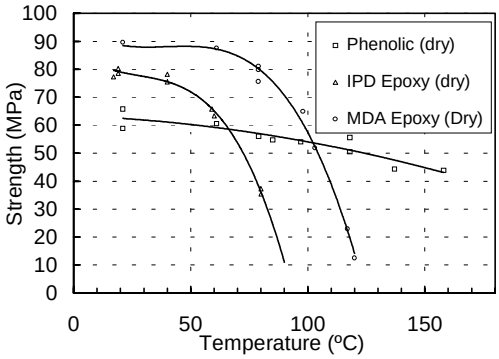

Figure 2: ±45°specimens tested dry

At low temperatures the phenolic based material is weaker in the matrix dominated mode than either of the epoxy materials, but it is less affected by temperature than the epoxies due to its high T_G. Even at a temperature of 160°C the strength of the phenolic material was reduced by only 30% to 42MPa. Its tensile strength becomes greater than that of the MDA cured epoxy material (the stronger of the two epoxies) at about 100°C.

The results of the 0/90° dry tests (Figure 3) show that the specimens were only marginally affected by an increase in temperature. This is to be expected in this fibre dominated mode since the E-glass is not greatly affected by moderate temperatures. All three materials show a reduction in strength of approximately of 8% over the range from ambient to 160°C.

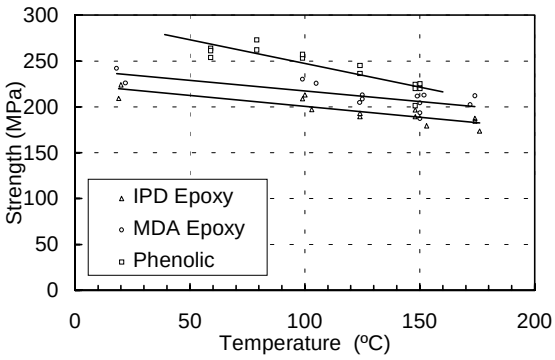

Figure 3: 0/90° specimens tested dry

Sea Water Tests. Figures 4-6 show the results of tensile tests carried out at various temperatures on coupon specimens using the three resin systems in the matrix dominated ±45° mode. In all cases the specimens were saturated in sea water prior to testing and the tests were conducted with the specimens in contact with the water. As may be seen, all three materials showed a reduction in strength due to the environment, but this effect was most pronounced in the two epoxy materials.

The results for the aromatic amine (MDA) cured epoxy material in Figure 4 show that this material is only moderately affected by sea water at elevated temperatures. At ambient temperature, the strength of the saturated material is reduced by about 15% relative to the dry material. The strength reduces as a function of temperature similarly to the material in the dry state, being reduced by 50% to 40MPa at 100°C.

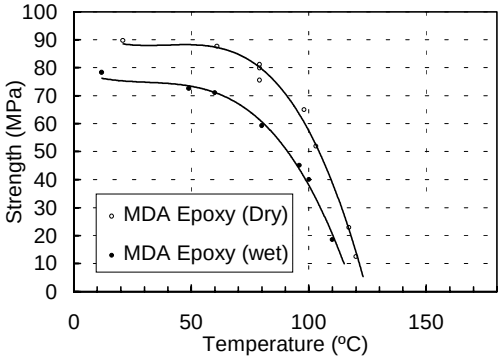

Figure 4: strength reduction in ±45° MDA cured epoxy specimens due to sea water saturation

The results for the aliphatic amine (IPD) cured epoxy material shown in Figure 5 are more dramatic. Of the two epoxy systems tested, this is the more sensitive to even moderate temperatures in the dry state. When saturated with sea water, the material is slightly weakened even at ambient temperature. At 40°C its tensile strength is reduced significantly, at 50°C it is reduced to 50% of its ambient temperature value and at 60°C its strength is negligible.

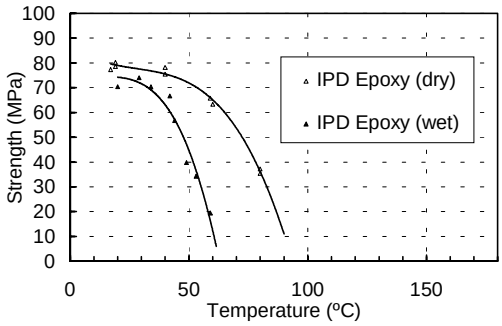

Figure 5: strength reduction in ±45° IPD epoxy cured specimens due to sea water saturation

As shown in Figure 6, the phenolic system was only marginally affected by the salt water ingress at moderate temperatures up to 80°C. Above this temperature the effect is more marked, with strength falling rapidly above 100°C.

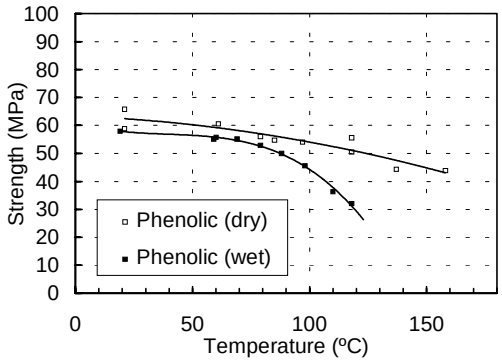

Figure 6: strength reduction in ±45° phenolic specimens due to sea water saturation

Oil Tests. As shown in Figure 7, oil immersion has no significant effect on the strength of any of the composite systems tested. In each case the strength of the material as a function of temperature follows the curve obtained in the baseline "dry" tests. This is to be expected as the absorption tests described above indicate very little penetration of the oil into the material.

DISCUSSION OF RESULTS

The effect of temperature and environment has been tested on coupon specimens of three composite materials. These comprise E-glass woven mat in a matrix of MDA cured epoxy, IPD cured epoxy and phenolic respectively.

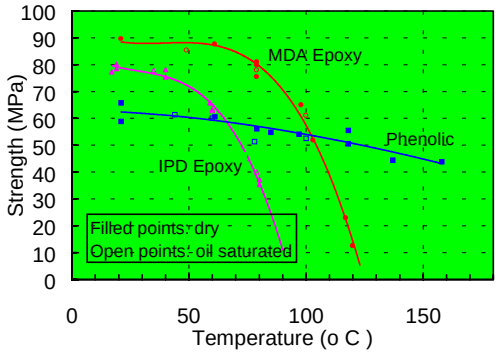

Figure 7: strength reduction in ±45° phenolic specimens due to sea water saturation

The time required to saturate coupon specimens of the three material types with sea water was established in a series of absorption tests at 100°C. In the same way, saturation times were established for oil penetration into the coupon specimens. It was found that in all cases the materials became saturated in five days or less. This information was used to establish the conditioning times for the specimens used subsequently in the environmental degradation tests.

Loading modes of the specimens were selected to test the materials subject to both resin and fibre dominated failure modes. This was done by preparing coupon specimens with the fibres oriented at ±45° and 0/90° to the loading axis respectively.

In all cases, the strength of the coupon specimens was found to reduce as testing temperature increased. However, there was considerable variation between materials, both in terms of the rate of fall off of strength with temperature and in the absolute value of the strength at any given temperature.

When not subjected to a hostile environment, the 0/90° (fibre dominated) materials were all only slightly affected by increased temperature. However, the ±45° (resin dominated) epoxy based materials were strongly effected by increased temperature with strength greatly reduced. This is due to the softening of the resin, particularly close to and above the glass transition temperature (T_G).

When tested in the dry state, the ±45° IPD cured epoxy, which was the weaker of the two epoxy materials at room temperature, was also the more sensitive to temperature. By 80°C the strength had dropped from 80MPa to 35MPa, which might be considered the limit of integrity in the resin dominated failure mode. The ±45° MDA cured epoxy was also severely weakened at high temperatures, dropping from 90MPa to 35MPa at 110°C, which might also be considered the limit of integrity in the matrix dominated mode. The ±45° phenolic based material was considerably weaker than either of the epoxy systems at low temperature, but was shown to be much less sensitive to temperature. This is undoubtedly due to the high T_G of the material which prevents softening in the temperature range tested. The phenolic material was found to be the strongest of the three materials in this mode at temperatures above 100°C, retaining a strength greater than 40MPa at 160°C. On the same basis it can be considered to have easily retained its integrity up to this high temperature.

As an alternative to an absolute residual strength, rate of strength loss migtht be a useful criterion for upper temperature limit of integrity since this reflects the sensitivity to small temperature excursions. On the basis of an integrity limit of 1MPa/degree, the resin dominated integrity limits for dry MDA and IPD cured epoxy GRPs are 90°C and 60°C respectively. On the same basis dry phenolic GRP retains its integrity to above 160°C.

All three materials tested showed a marked reduction in strength at all temperatures due to salt water absorption. This effect is particularly marked in ±45° IPD cured epoxy coupon specimens, in which the strength is reduced to 35MPa at 50°C and becomes negligible above 60°C. The effect is rather less significant in ±45° MDA in which the temperature for 35MPa strength is reduced from 110°C to just over 100°C. However, for the ±45° phenolic coupon specimens, which are particularly good when tested dry, the strength starts to fall away rapidly at temperatures above 80°C and drops to 35MPa at 110°C, though the rate of strength reduction of 0.8MPa/degree at that temperature.

IPD cured epoxy GRP loses its strength very quickly at elevated temperatures under these conditions, reducing to 35MPa at only 50°C and reaching the 1MPa/degree integrity limit below 40°C. Clearly it is unsuited for use in contact with sea water at elevated temperatures. The MDA cured material is much better, retaining its integrity to 100°C and 90°C according to the 35MPa and 1MPa/degree criteria respectively.

Phenolic based GRP has excellent stability at moderate temperatures, with very little loss of strength below 80°C. Even at higher temperatures it retains good stability and reaches the 35MPa integrity limit at 115°C, before the 1MPa/degree limit. However, its poor strength at

ambient temperature means that it is still weaker than the MDA cured epoxy material below 90°C. Only above this temperature does it emerge as the best material of the three tested.

The integrity of phenolic based GRP at high temperatures when saturated in sea water is thus seen to be only slightly superior to that of a MDA epoxy material in terms of residual strength. However, the phenolic material does have the advantage of much better stability in that its strength is much less dependent on temperature changes at high temperatures. If the operating temperature is not well defined at the design stage this could well be significant.

It is evident that immersion in oil, at least in the form of condensate, has very little effect on the strength of GRP in any of the forms tested. For each material tested the data points for strength at a given temperature lie squarely on the curve for the equivalent dry tests. This is to be expected since the absorption tests indicated very little ingress of the oil into any of the composite materials investigated in this work.

CONCLUSIONS

1. A cost effective methodology has been developed for preparing and testing the strength of both coupon and pipe specimens of fibre reinforced composite materials at elevated temperatures in liquid environments.

2. Three materials have been tested: E-glass reinforcement in cycloaliphatic amine (IPD) cured epoxy, aromatic amine (MDA) cured epoxy and acid-cured phenolic.

3. The time required for effective sea water saturation at a temperature of 100°C has been established for each material. In all cases this is five days or less.

4. The effects of sea water saturation on strength have been quantified as a function of temperature for the three material systems.

5. In all the materials tested, strength is reduced only slightly at elevated temperatures in fibre dominated failure mode.

6. In matrix dominated failure mode, the strength of both epoxy based materials falls off rapidly at elevated temperatures. This effect occurs at lower temperature in IPD cured epoxy than MDA cured epoxy.

7. In matrix dominated failure mode, the strength of phenolic based GRP is less affected by high temperature. However, its strength is lower than epoxy materials at ambient temperature. It was found to be stronger than IPD/epoxy GRP above 60°C and stronger than MDA/epoxy GRP above 100°C. At all temperatures the phenolic based GRP was found to be less sensitive to temperature change than either of the epoxy based systems.

8. Sea water was found to be the most aggressive of the environments tested, reducing the strength of all the materials at all temperatures. The strength reduction due to sea water absorption was approximately independent of temperature in MDA/epoxy GRP, but increased with temperature in IPD/epoxy and phenolic GRPs.

ACKNOWLEDGEMENTS

Thanks are due to the following sponsors of the Marinetech Research managed programme on *The Cost Effective Use of Fibre Reinforced Composites Offshore* for their support and for permission to publish this paper:

Admiralty Research Establishment, AGIP, Amerada Hess, Ameron bv, Amoco Research, Balmoral Group, BP Exploration, BP Research, Brasoil, British Gas, Bow Valley Petroleum, Ciba-Giegy, Conoco, Cray Valley Products, Dow Deutschland Inc, Elf (Aquitaine), Elf (UK), Enlchem spa, Exxon, Fibreforce Composites, Hunting Engineering plc, Kerr McGee Oil (UK) Ltd, MaTSU, Marine Technology Directorate Ltd, Mobil Research and Development, Mobil North Sea Ltd, Norsk Hydro, PetroBras, Phillips Petroleum, Shell Expro, Statoil, Total Oil Marine, UK Department of Energy, UK Ministry of Defence (Navy), UK Offshore Supplies Office, VSEL and Vosper Thornycroft. The programme involves the Universities of Newcastle upon Tyne, Glasgow, Liverpool, Salford and UMIST.

REFERENCES

1. Hull D., An Introduction to Composite Materials, Cambridge University Press 1981
2. Morgan R.J., Structure-Property Relationships and the Environmental Sensitivity of Epoxies, in: Developments in Reinforced Plastics - 1 (G. Pritchard - ed) Applied Science Publishers, London, p211, (1980).
3. Ishida H., and Koenig J.L., Reinforcement Mechanism of Fiber-Glass Reinforced Plastics under Wet Conditions: a Review Polymer Engineering and Science, 18, (2), p128, (1978).
4. Carter H.G., and Kibler K.G., Langmuir-Type Model for Anomalous Moisture Diffusion in Composite Resins, Journal of Composite Materials, 12, p188, (1978).
5. Vinson J.R.(ed), Advanced Composite Materials - Environmental Effects, ASTM Special Technical Publication 658, (1978).
6. Bunsell A.R., Hydrothermal Ageing of Composite Materials, Revue de L`Institut Francais du Petrole, 50, no1, (1995).

THE EFFECT OF THERMOPLASTIC ADDITIVES AND CARBON FIBRES ON THE THERMALLY ENHANCED MOISTURE ABSORPTION BY EPOXY RESINS

James A. Hough, Frank R. Jones

Department of Engineering Materials, University of Sheffield, Mappin St, S1 3JD, UK

SUMMARY: The moisture absorption of the base resin, polyether sulphone (PES) modified blend and carbon fibre composite under isothermal and thermal spiking conditions has been examined. The addition of PES reduced proportionally the moisture in the isothermally conditioned coupons but not for those thermally spiked. The maximum enhancement temperature of 140°C, was a function of the base epoxy resin. A secondary relaxation peak (Tg_2) developed at a significantly lower temperature than the main relaxation. For the PES modified epoxy resin, thermal spiking did not reduce Tg_2 below that for the isothermally conditioned sample. However, in the presence of carbon fibres, Tg_2 was sensitive to thermal spiking, indicating an interphasal component to the moisture mechanisms.

KEYWORDS: thermal spiking, moisture absorption, polyether sulphone, epoxy resin, carbon fibre composites

INTRODUCTION

Epoxy resins are the most common matrices for high performance carbon-fibre composites because of the ease with which the curing process can be controlled. However they readily absorb moisture usually resulting in lower strength and softening temperature. Certain aircraft components can be exposed to temperatures in excess of 100°C for only a few minutes [1]. Under conditions of rapid heating and cooling, the moisture absorption of epoxy/carbon laminates can be increased significantly [2-4], over that for hygrothermal conditions. The mechanisms of enhanced moisture absorption as a result of a thermal spike are unclear.

In this paper, the effect of the polyether sulphone (PES) thermoplastic modifier on the thermally enhanced moisture absorption of an epoxy resin system has been studied..

EXPERIMENTAL

Materials

The system chosen was the Fibredux 924 laminate system from Ciba Geigy. This is a diaminodiphenylsulphone cured TGDDM epoxy resin with added polyethersulphone (PES) thermoplastic. The manufacturer provided the base epoxy resin without added PES (924E),

and cast tape of resin containing the commercial concentration of PES (924T), which is used for fibre impregnation. The finished prepreg tape was also supplied. To obtain resin samples of varying PES concentration, the base 924E resin was blended with different weight fractions of the modified 924T resin at 100°C. The actual concentration of PES is unknown for commercial reasons, (Table 1).

Table 1: Resin Blends with relative PES concentration

Resin System Under Study	PES concentration as a percentage of the commercial content)
924E	0
924/¼T	25%
924/½T	50%
924/¾T	75%
924T	100%
924C (composite)	100%

The base resin, commercial resin and blends, were degassed at 110°C for 1.5 hours, poured into a mould and degassed for a further 0.5 hours. The resins were then cured in a press-clave under a nitrogen atmosphere at a pressure of 700 KN/m^2. The recommended cure cycle was as follows; heat from room temperature at 2°C/min to 130°C, dwell for 2.5 hours, heat at 1°C/min to 180°C, dwell for 2 hours, then cool to room temperature at less than 3°C/min. For the 924C system, the prepreg tape was cut to the required dimensions and stacked to form an 8-ply laminate which was cured in a press-clave for 2 hours at 180°C, using recommended vacuum bagging procedures and cure cycles.

Conditioning

For conditioning, the 924 resin samples were cut to dimensions of 60 by 30 mm using a water cooled diamond saw, whilst 924C composite samples were cut to dimensions of 20 by 140 mm. The resin coupons were then milled to a thickness of 1mm. The edges of all samples were polished to a 1200 grit finish prior to post-curing at 180°C for 2 hours. The coupons were dried to constant weight in a vacuum oven at 50°C, and placed on racks above a saturated salt solution of potassium sulphate (K_2SO_4) in distilled water, in a sealed humidity chamber held at 50°C in an air-circulating oven to provide a relative humidity of 96%. The coupons were removed intermittently, weighed and returned to the humidity chamber (control samples) or subjected to a thermal spike (spiked specimens). After spiking, they were reweighed and replaced in the environment. Sorption curves were plotted as moisture content, M_t in weight percent, against $\sqrt{time}$. The weight changes were determined using an electro-balance accurate to 10^{-5}g.

Thermal Spike Program

Coupons were placed in metal racks, to ensure both major surfaces were heated evenly, and placed in an air-circulating oven pre-heated to the spike temperature. Time spent at the spike

temperature was calculated so that the specimen was maintained at this temperature for 1 minute. Table 2 lists the spiking times for 924 8-ply laminates.

For consistency, the same spike times were used for the 1mm thick un-reinforced resin specimens. The samples were and allowed to cool before replacement in the conditioning chambers.

Table 2: The time spent in the spike oven for samples spiked to between 100 and 200°C.

Thermal Spike Temperature (°C)	Spike Time for O_8 924 laminates and resin coupons (min.)
100	3.5
120	4
140	4.5
160	5
180	5.5
200	6

Thermomechanical Analysis

Dynamic Mechanical Thermal Analysis (DMTA) was performed in dual cantilever bending mode using a Polymer Laboratories Mk II analyser. This allowed the effect of thermal spiking and enhanced moisture absorption on the viscoelastic properties, such as the glass transition temperature to be measured. Samples of dimensions 10 by 40 mm were cut from the conditioned specimens. For 924C samples, the fibres were at 90°C to the DMTA clamp faces. A frequency of 1Hz was used over a temperature of 50°C to 300°C.

RESULTS

Fig. 1 shows the moisture absorption curves for the 140°C spiked and control 0_8-924C coupons. For the 140°C spike curve, the peaks correspond to the moisture content prior to a thermal spike , and the troughs correspond to the moisture content after a thermal spike. Moisture is lost during the thermal spike. For simplicity the moisture content after a thermal spike is omitted from subsequent plots of moisture absorption.

Figs. 2-4 show the moisture absorption curves for coupons of 924E resin, 924T epoxy/PES resin, and 924C composite respectively. These were subjected to 22 spikes to between 100°C and 200°C, and 5000 hours conditioning.. The first 4 points on the curves are of the same value since the samples have not been spiked. Thus the fourth point on the curves represents the moisture content prior to the first spike. It can be seen that spikes as low as 100°C result in an increased moisture concentration, in all three systems.

The moisture concentration of the spiked samples exceeds that of the control samples after the first spike (i.e. the fifth point on the curves). Maximum moisture enhancement occurs in samples spiked to 140°C. Spiking above this temperature results in lower moisture absorption. After 5000 hours and 22 spikes, an equilibrium moisture content has not been reached for the resin systems, since moisture concentration is still increasing. This is also true of the unspiked control resin specimens. The sorption curves for the 924C laminates show lower rates of absorption than their resin counterparts, however equilibrium is still not reached after 5000 hours and 22 spikes. The highest rate of absorption was observed between the first and seventh spike for resin and composite coupons spiked to 160°C. After 12 spikes, the 140°C spiked coupons absorb moisture at the highest rate.

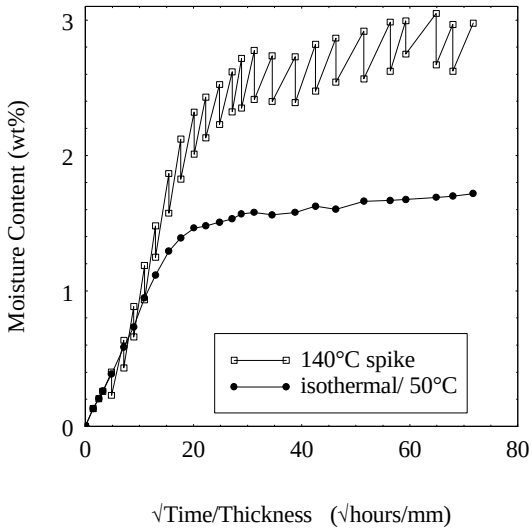

Fig.1: The effect of thermal spikes to 140°C on the moisture absorption of 924C-0_8 laminates conditioned at 50°C/96% R.H

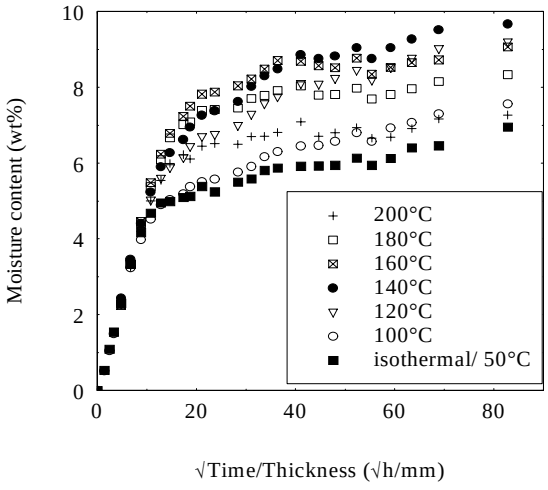

Fig.2: Moisture absorption curves for 924E epoxy resin after 5000 hours conditioning & 22 thermal spikes

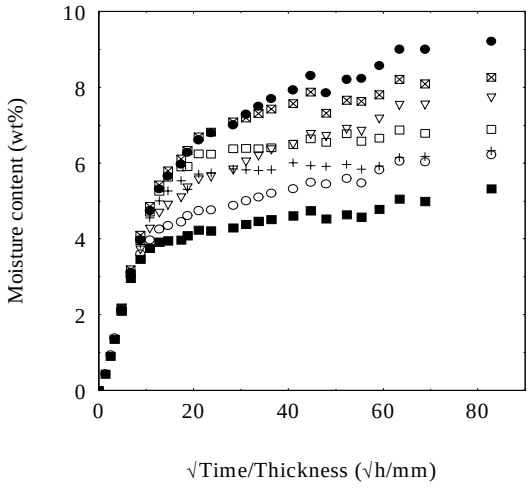

Fig.3: Moisture absorption curves for 924T epoxy/PES resin after 5000 hours conditioning & 22 thermal spikes. [See Fig 2 for key]

Table 3 lists the final moisture contents of 924E, 924T resins, and 924C composite samples after 22 thermal spikes and over 5000 hours conditioning. Since moisture absorption is a matrix dominated property and the matrix volume fraction is approximately 35% of the composite, normalised values for the matrix moisture absorption in the 924C composite are also presented. That is moisture contents are multiplied by 2.86, to calculate the moisture concentration in the matrix alone. The normalised 924C value for moisture concentration in matrix alone was 4.92 wt.%. The moisture concentration increases in the order 924C<924T<924E, for each spike temperature. However, the normalised values for 924C samples approximately equal those of the 924T resin alone. Thermal spikes to 140°C, the maximum moisture enhancement temperature, result in moisture concentrations of 9.66, 9.20, 2.98 wt.% in the 924E, 924T and 924C systems respectively.

Table 3: Final moisture concentrations in 924E, 924T resins and 924C laminates

	Moisture Content after 22 spikes & 5000 hours conditioning wt.%			
Spike Temp (°C)	924E (no PES)	924T (with PES)	924C	924C (normalised)
isothermal/50	6.95	5.32	1.72	4.92
100	7.57	6.22	2.37	6.78
120	9.20	7.75	2.84	8.12
140	9.66	9.20	2.98	8.52
160	9.06	8.26	2.88	8.24
180	8.33	6.88	2.43	6.95
200	7.27	6.32	2.08	5.95

This represents an increase relative to the isothermal moisture concentrations, of 39% for the 924E resin, and an increase of 73% for the 924T resin and 924C composite containing PES. Fig. 5 shows the moisture concentrations plotted as a function of spike temperature of all 3 systems and the normalised matrix moisture concentration in the 924C laminates. It is seen that a maximum moisture enhancement temperature exists at 140°C for all systems.

Under isothermal conditions the 924E base resin absorbed 6.95 wt.% moisture, while 924T toughened resin absorbed 5.32 wt.% moisture, and the 924C laminates absorbed 1.72 wt.%, which was the lowest moisture concentration.

Resin samples of differing PES content, as listed in Table 1, were conditioned for over 4000 hours, and subjected to 18 thermal spikes to 140°C or 160°C. The absorption curves for these samples were similar in appearance to those for the isothermal 140°C and 160°C spiked 924E and 924T resin specimens shown in Figs. 2 & 3. Table 4 lists the moisture concentrations

after 4000 hours conditioning at 96% R.H., and 18 thermal spikes for 924 resin specimens containing ¼,½,¾ of the commercial amount of PES.

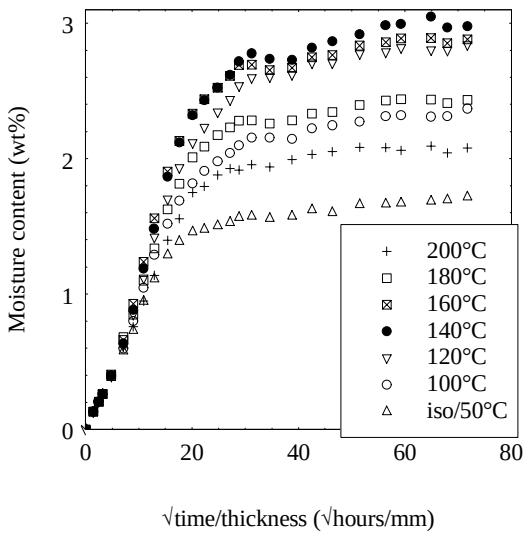

Fig.4: Moisture absorption curves for 924C-O_8 composite after 5000 hours conditioning & 22 thermal spikes

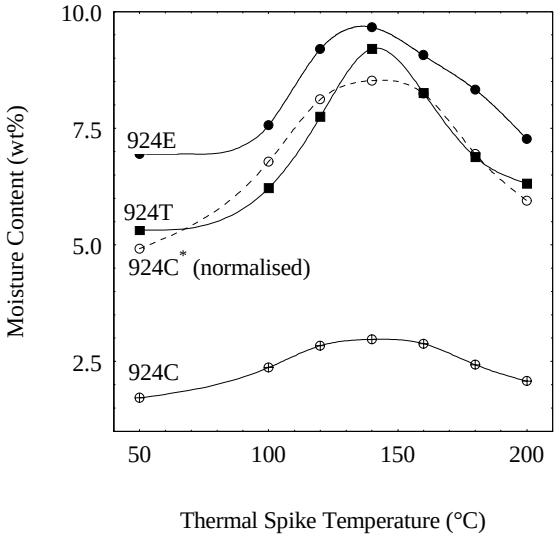

Fig.5: Moisture concentration against spike temperature, for 924E, 924T & 924C samples after 5000 hours conditioning & 22 spikes

Table 4: Final moisture concentrations for 924 resin samples of varying PES content

Spike temperature (°C)	Moisture Content after 4000 hours conditioning and 18 thermal spikes (wt.%)				
	924E	924/¼T	924/½T	924/¾T	924T
isothermal/50	6.40	6.13	6.68	6.77	5.05
140	9.27	8.98	9.13	8.76	9.00
160	8.67	8.39	8.18	7.99	8.20

The enhanced moisture absorption phenomenon is unaffected by PES content, and occurs in all samples when thermally spiked to 140°C or 160°C. The maximum moisture enhancement temperature of 140°C, is in agreement with that for the 924C composite. A Thermal spike temperature of 160°C results in the fastest initial moisture uptake, for all levels of PES. This data is plotted against the relative PES content in Fig. 6. As already shown in Fig. 5, under isothermal conditions the moisture concentration in 924T samples is approximately 20% less than in the 924E base epoxy resin. However moisture concentrations in resin formulations of intermediate PES content do not follow any clear trend. Under isothermal conditions, the 924/¾T samples containing 75% of the commercial amount of PES contain the highest moisture concentration at 6.77 wt.%.

Figure 7, illustrates schematically the effect of thermal spiking and moisture absorption on the DMTA tanδ and storage modulus, log E', curves for the resins and laminates. The traces shown are for a dry as-cured sample, an isothermally conditioned sample, and a thermally spiked sample. The primary tan δ peak, Tg_1, which was observed for the as-cured/dry samples, fell slightly on isothermal moisture absorption. A secondary peak, Tg_2, emerged in all wet specimens. This peak was least prominent for the 924E samples, compared to 924T epoxy/PES samples. The intensity of the Tg_2 peak was greatest and shifted to lower temperatures in 924C laminates samples after moisture absorption and thermal spiking, relative to the two resin systems. It can be seen that the temperature at which the slope of the storage modulus, log E', curve begins to decrease rapidly, termed the glass transition onset, $Tg_{E'}$, is reduced on isothermal moisture absorption. This is further reduced when the laminates are thermally spiked.

Fig. 8a) & b) plots of Tg_1 and Tg_2 for samples conditioned for over 5000 hours against thermal spike temperature. It is seen that Tg_1 for 924C laminates, is approximately 15° to 20°C lower than for the 924E and 924T resin systems. Isothermal moisture absorption reduces Tg_1 by approximately 10°C for each system. Thermal spikes to 100°C further reduce Tg_1 only slightly in the 924C and 924T samples to 239°C and 217°C respectively, but do not effect Tg_1 in 924 samples which remains at approximately 240°C. Thermal spikes to 120°C and above do not significantly reduce Tg_1 any further. For the dry systems, one relaxation peak was observed. However on isothermal moisture absorption a secondary relaxation peak, Tg_2, emerges for all three systems, at a temperature between 174°C and 189°C. Thermal spiking to 100°C reduces Tg_2 further by 22°C in 924 laminates, but is unaffected in the 924E and 924T resin samples. Thermal spikes to 120°C and above does not reduce Tg_2 further.

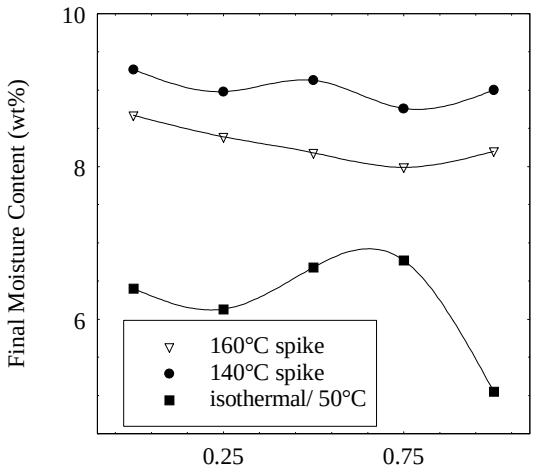

Fig.6: Moisture content in 924 resin samples of differing PES content after 4000 hours conditioning at 96% R.H., and 18 spikes

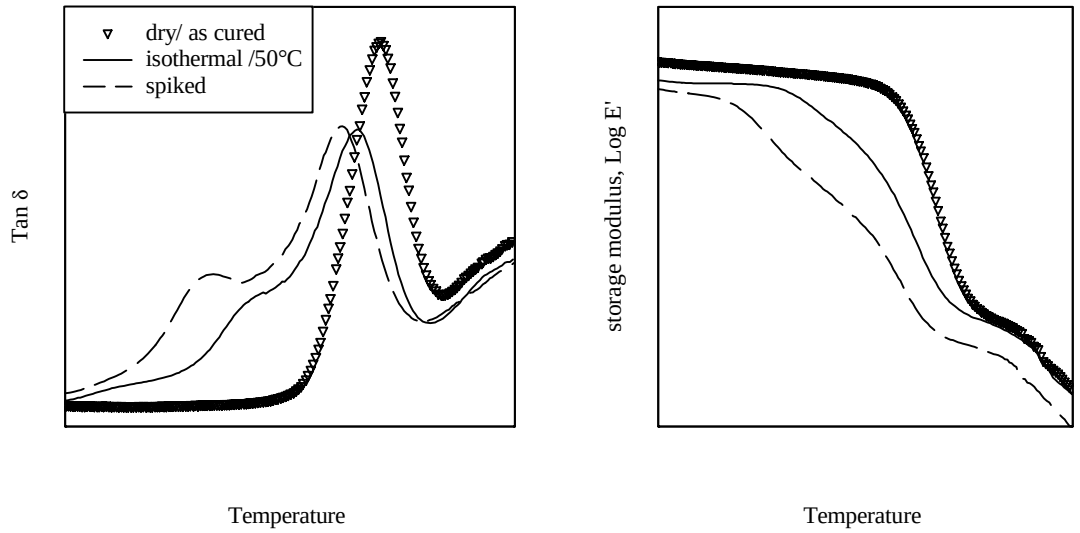

Fig.7: Schematic illustration of the effect of moisture absorption and thermal spiking on the DMTA relaxation spectra, tan δ, and the storage modulus, log E', in 924 systems

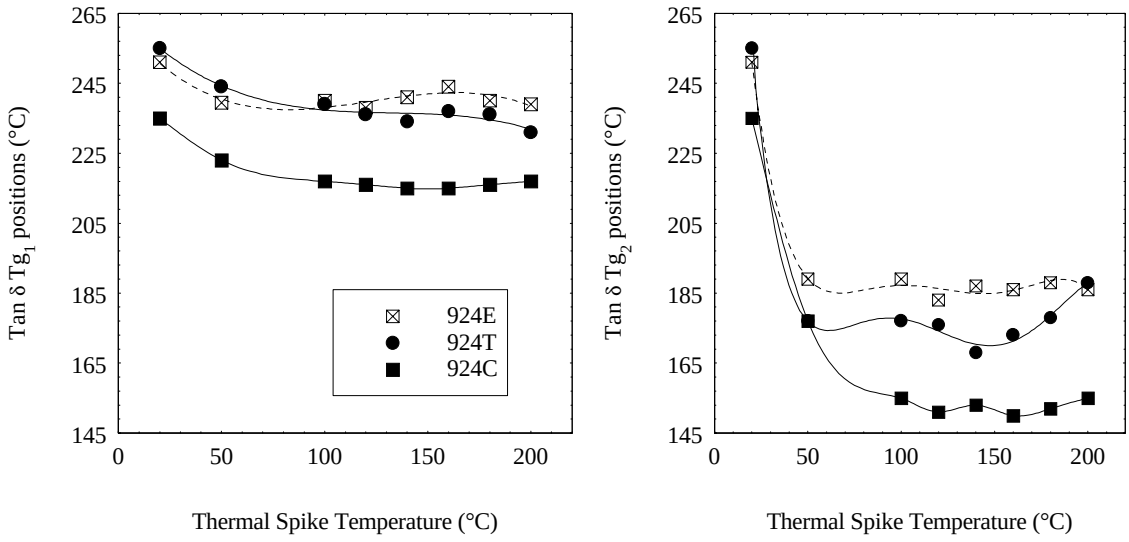

Fig.8: Changes in DMTA a) primary and b) secondary tan δ peaks with thermal spike temperature for 924E, 924T resin and 924C laminate systems

Fig. 9 shows how the glass transition onset temperature, $Tg_{E'}$, changes with thermal spike temperature, for the three systems. It is seen that the dry/ as-cured $Tg_{E'}$ is 225°C for the 924E resin, 201°C for the 924T resin, and 207°C for the 924C laminate. Isothermal absorption of moisture results in a $Tg_{E'}$ of 160°, 168° and 152°C for the 924E, 924T and 924C systems respectively. Thermal spikes to 100°C reduce $Tg_{E'}$ further in the 924T and 924C systems to 153°C and 135°C respectively, whereas $Tg_{E'}$ for the 924E base epoxy is relatively unaffected. Thermal spikes to 120°C and above reduce $Tg_{E'}$ of 924C to a minimum of 129°C, 20°C lower than the $Tg_{E'}$ of both resin systems which are unaffected.

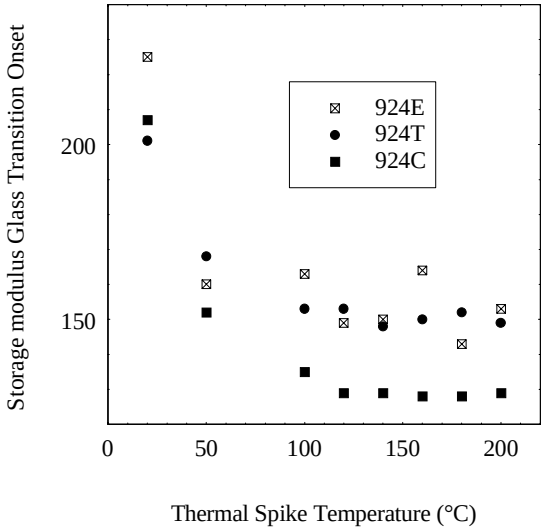

Fig.9: Changes in glass transition onset temperature, $Tg_{E'}$, with thermal spike temperature in 924E, 924T resin and 924C composite systems

DISCUSSION

The absorption curves shown in Figs. 2-4, are non-Fickian for all 3 systems. That is an equilibrium moisture content is not reached, and the initial linear region does not account for 60% of the total moisture absorbed. The addition of PES to the base epoxy resin, reduces the concentration of moisture absorbed under isothermal conditions by approximately 20%. The weight fraction of PES in the 924T commercial resin is considered to be approximately 18 wt.%, hence this can be explained simply by the lower moisture absorption of the PES component. The addition of carbon fibres, reduces the moisture concentration by a further 65%. As shown in Fig. 5 the moisture concentration in 924C laminates when normalised to the volume fraction of matrix, are close to that of the 924T resin-only samples. Thermal spiking results in an increased moisture concentration for all three systems. The 924E base epoxy samples absorbed the most moisture, where the 924T resin and normalised 924C composite values were approximately equal. Suggesting that the addition of carbon fibres has a minimal effect on the enhanced moisture absorption phenomena. At the maximum moisture enhancement temperature of 140°C, the moisture concentration is increased by approximately 40% in the 924E samples. In the 924T samples, the increase was 73%, to a concentration close to that of the 924E base epoxy system. Normalised data for the 924C composite showed a 73% increase to similar values. This implies that the addition of PES to the base epoxy reduces the amount of moisture absorbed under isothermal conditions, but when thermally spiked to 140°C, the difference is less prominent..

Fig. 5 shows that the enhanced moisture absorption is greatest for the base epoxy resin, and that the addition of PES and reinforcing carbon fibres does not affect this significantly. Microscopic examination of the spiked samples did not show any significant damage such as microcracks, voids or delaminations in the composite, confirming that the additional moisture must reside in the polymer network on a molecular level [5]. Analysis of absorption curves for the resin samples with intermediate PES content, show that changing the weight fraction of PES does not alter the enhanced moisture absorption phenomena, and that the maximum

moisture enhancement spike temperature remains at 140°C (Fig.6). Specimens spiked to this temperature contained between 30 to 45% more moisture than the isothermally conditioned specimens. However the moisture concentration did not decrease significantly with increasing PES content. Since this is an assumption behind the blending technology it is clear that the maximum moisture content after thermal spiking is not a simple dilution of the most moisture sensitive component. However the mixing procedure employed in the laboratory may differ from that used commercially so that the homogeneity of the cured resin-blends may differ from the commercial systems. Thus the re-distribution of unoccupied volume into free volume of molecular size and microvoids of larger dimensions could be affected.

In Fig. 7 it is seen that the secondary relaxation peak Tg_2 is most sensitive to thermally enhanced moisture absorption. This suggests that the water may plasticise one component in the polymer network more efficiently. Water present in a polymer network is often considered to be present in the free volume where it interrupts the attractive forces acting between polar structures in the network [6], leading to plasticisation. Thus at high moisture concentrations a greater depression of Tg is predicted. This is true for isothermal absorption. However moisture absorbed through thermal spiking does not appear to plasticise the polymer further. It is evident from Fig.8b that the addition of PES to the base epoxy results in a larger reduction in Tg_2 on moisture absorption. The implication of this result is that the PES phase modifies the susceptibility of the epoxy resin network to plasticisation by water. However, an alternative explanation could revolve around the dimensions of the unoccupied volume. It is also evident that the addition of carbon fibres reduces Tg_1 and Tg_2 even further. The reasons for this are not clear, but one possible cause may be the presence of a sizing resin on the fibres which is usually epoxy based, and may combine with the matrix resin to form a cured region of lower glass transition temperature (i.e. an interphase).

CONCLUSIONS

The enhanced moisture absorption which results from thermal spiking is shown to be a function of the epoxy resin. Thermal spiking of 924E epoxy-only resin, epoxy/PES resin and 924C laminates conditioned in humid environments, increased the rates and concentrations of moisture absorbed. Maximum moisture enhancement occurs at a spike temperature of 140°C. The addition of the thermoplastic PES and carbon fibres to the epoxy matrix reduced the total moisture absorbed under isothermal conditions. However, the enhanced moisture absorption was unaffected under thermal spiking. A secondary relaxation peak appears in the Tan δ curves for the wet resin and composites. Tg_2 appears at the lowest temperature and with greatest intensity for the composite. The non-modified base epoxy resin was the least susceptible. Thus the addition of PES and carbon fibres appears to increase the susceptibility of the bulk resin to plasticisation under isothermal conditions. The extra moisture absorbed as a result of thermal spiking does not shift this secondary peak to lower temperatures. The moisture is resident in the polymer network, rather than in thermally induced voids or microcracks. Moisture can be accommodated in the free volume of a polymer network, where the interactions between polar groups are displaced. This results in a reduction in glass transition temperature. However this study indicates that the extra moisture as a result of thermal spiking does not plasticise the polymer material in this manner. The enhanced moisture absorption in thermally spiked epoxy resins is unaffected by the addition of the PES modifier. Only the total moisture absorbed is affected. The softening point of 924C laminates is reduced by thermal spikes of 100°C and above to well within the ‘Hot/Wet’ maximum service temperature stated by the manufacturers.

ACKNOWLEDGEMENTS

We are indebted to DRA, Farnborough for financial support, Ciba Geigy plc, Duxford for the resins.

REFERENCES

1. Whiteside, J.B., DeIasi, R.J., Schulte, R.L., "Distribution of Absorbed Moisture in Graphite/Epoxy laminates After Real-time Environmental Cycling", *Long-term Behaviour* of *Composites, ASTM STP 813, K. O'Brien, Ed., American Society for Testing Materials, Philadelphia*, 1983, pp. 192-205.
2. Clark, G., Saunders, D.S., van Blaricum, T.J., Richmond, M., "Moisture Absorption in Graphite/Epoxy Laminates", *Composites Science and Technology*, vol. 39,1990, pp.355-375.
3. Adamson, M.J., "A Conceptual Model of the Thermal-Spike Mechanism in Graphite/Epoxy Laminates", *Long-term Behaviour of Composites, ASTM STP 813, K. O'Brien, Ed.*, American *Society for Testing Materials, Philadelphia*, 1983, pp. 192-205.
4. Xiang, Z.D., Jones, F.R., "Thermal Spike Induced Enhanced Moisture Absorption by Polymer Matrix Carbon Fibre Composites", submitted to *Composites Science and Technology.*
5. Hough, J.A., Xiang, Z.D., Jones F.R., "The effect of thermal spiking and resultant enhanced moisture absorption on the mechanical and viscoelastic properties of carbon fibre reinforced epoxy laminates", *Conference Proceedings of Experimental Techniques and Design in Composite Materials/3, Cagliari, Italy, October 1996. in press.*
6. Lee, M.C., Peppas, N.A., "Water Transport in Graphite/Epoxy Composites", *Journal of Applied Polymer Science*, vol.47, 1993, pp. 1349-1359.

MODELLING OF ENVIRONMENTALLY INDUCED DAMAGE IN POLYMER MATRIX COMPOSITES

Bethany J. Foch and Hugh L. McManus

Department of Aeronautics and Astronautics, Massachusetts Institute of Technology
77 Massachusetts Ave, Cambridge, MA 02139

SUMMARY: An investigation has been performed into the behavior of composite laminates exposed to severe environmental conditions. Given material properties, laminate geometry and specified cyclical thermal and moisture environments, a model predicts absorbed moisture, chemical degradation, and stresses in the laminate as functions of position and time. A simplified solution allows very efficient calculations for large numbers of complex thermal and moisture cycles. Cases relevant to the proposed High Speed Civil Transport show two types of moisture absorption behavior: rapid fluctuation of levels near the surface, and gradual settling to an easily computed equilibrium value in the interior. Chemical degradation is (based on preliminary, parametric calculations) shown to be a concern for surface plies. Stress levels due to these effects will enhance damage in surface plies. Stress effects do not fully account for observed moisture induced damage, suggesting material property changes or enhanced cracking mechanisms.

KEYWORDS: moisture, degradation, analysis, cyclic exposure, environmental effects, hygral stresses, thermal stresses, damage

INTRODUCTION

Aircraft systems such as the proposed High Speed Civil Transport (HSCT) experience severe cyclic environments during normal operations. Aircraft skins reach extreme temperatures due to high vehicle speeds; diffusion of moisture and oxygen into the material is accelerated by these temperatures; these in turn can cause property changes and/or permanent material degradation. An example exposure cycle with time-dependent temperature and moisture levels is shown below. This is a test cycle; similar cycles may be repeated over 20,000 times in an aircraft lifetime. Under such conditions, thermal, hygral, and chemical degradation effects result in a complex and time-varying stress profile over the course of many experimental or use cycles.

A set of models and computer codes has been developed to aid in the calculation of severe environmental effects. Using as inputs ambient temperature, relative humidity (RH), oxidative environment, material properties and laminate geometry, the codes predict the material state, degraded properties, and resulting stress state as functions of position and time.

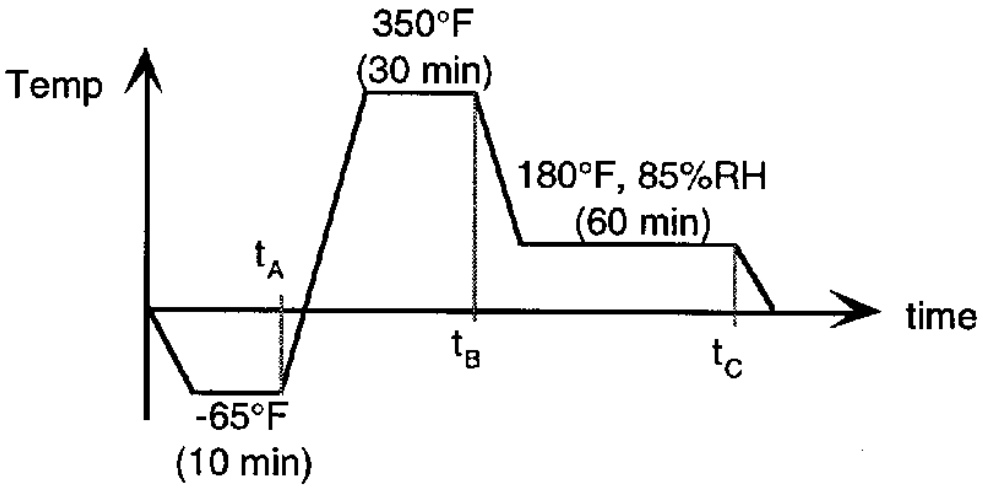

Fig. 1: Sample environmental test profile

BACKGROUND

The influence of environmental effects on composite structures has received a great deal of attention in the literature. Investigators have attempted to decouple temperature, moisture and chemical effects [1-5] as well as analyze the interactions during combined exposure [6-11].

A good development of the behavior of a substance diffusing into another is given by Crank [12] and expanded by Springer [2] and Tsai and Hahn [3]. For a limited range of environmental conditions, moisture sorption follows Fickian behavior. Moisture sorption in to a laminate has a much slower diffusion rate than does temperature (~10^6 times slower). For this reason the laminate response to temperature change is often considered instantaneous and constant across a laminate's thickness. Theories have been developed to account for the coupled distributions of moisture and temperature [13]. Several mathematical formulations have been developed in order to simplify the calculations required for predicting moisture sorption. Springer's "W8GAIN" model was developed in 1981 in order to predict the distribution of moisture and temperature in a laminate exposed to wet conditions [14], and Weitsman developed a code (also in 1981) that searched for the most efficient calculation for moisture sorption in a laminate over time periods with fluctuating ambient conditions [7].

Chemical changes in composite materials attributed to environmental exposure are less well understood than moisture effects. Several distinguishing characteristics mark chemical degradation: discoloration and embrittlement of the surface; weight loss; decrease of material strength; and microcracking. Recently, much work has been done to characterize the reactions occurring in the polymer in an attempt to understand these changes [4,5,15].

Calculations of stresses resulting from temperature, moisture, and degradation states in the material is common in the literature via micromechanics and composite laminated plate theory (CLPT). Tensile residual stresses that are inherent in general composite laminates after cool-down from cure temperature (due to ply coefficient of thermal expansion mismatch) may be at least partially relieved by moisture-induced stresses (resulting from swelling of the laminate) [16]. Chemical degradation adds complexity, altering the material properties at the exposed surface. The potential for microcracking damage is high during

cyclic environmental exposure [17-19,9]. Microcracking has been seen to increase the diffusion rate of moisture [20,21,6] resulting in non-Fickian sorption behavior.

MODEL DEVELOPMENT

A code was developed in order to characterize the state of a material exposed cyclically in air to an environmental profile in which temperature and moisture vary with time. User defined inputs include this profile, relevant material properties, laminate geometry and number of cycles.

It is assumed that an infinite plate is exposed to uniform environmental conditioning on its top and bottom surfaces ($z=0$ and $z=h$). Diffusion is assumed to be one-dimensional through the thickness (the z direction). Temperature is constant through the thickness, and instantaneously equal to the time-varying ambient temperature.

Moisture Sorption

It is assumed that moisture and oxygen diffuse into the material following a one-dimensional Fickian law. Outlined below is the development for moisture; the reasoning for oxygen diffusion is similar. Fick's Law is given by:

$$\frac{\partial C}{\partial t} = D\frac{\partial^2 C}{\partial z^2} \tag{1}$$

where C is the concentration of moisture in the laminate, z is the through thickness direction, and D is the diffusion rate. The diffusion rate is dependent on the diffusion constant, D_0, activation energy, E_A, gas constant, R, and absolute temperature, T [12]:

$$D = D_0 \exp\left[\frac{-E_A}{RT}\right] \tag{2}$$

Initial and boundary are required to solve Eqn 1. These are given below:

$$\text{for } t < 0 \qquad C(z) = C_0(z) \tag{3}$$

$$\text{for } t > 0 \qquad C(0) = C_\infty(t) \ , \ C(h) = C_\infty(t) \tag{4}$$

The value $C_0(z)$ is simply the initial state of moisture through the laminate. The quantity $C_\infty(t)$ represents the concentration at the surface. At every instant of exposure, the surface of the laminate is assumed to be saturated at the level corresponding to the current atmospheric relative humidity. Saturation level is a function of relative humidity, Φ, and material constants a and B, which must be determined empirically [2].

$$C_\infty = a(\Phi)^B \tag{5}$$

An efficient solution to the above problem is needed to compute moisture and oxygen levels in structures undergoing large numbers of complex thermal and environmental profiles. Here, profiles including relative humidities that remain constant over specified lengths of time (Fig. 2a) and temperatures that remain constant or change at a constant rate (Fig. 2b) are considered. Such profiles can be repeated an arbitrary number of times.

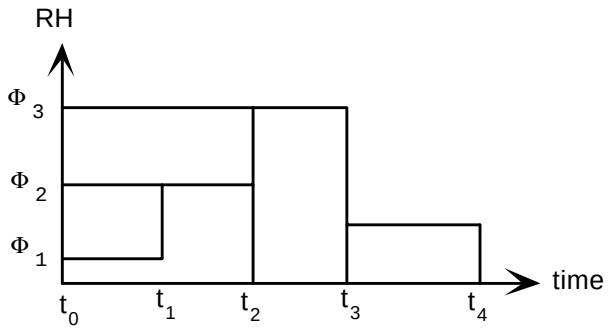

Fig. 2a: Possible moisture profile

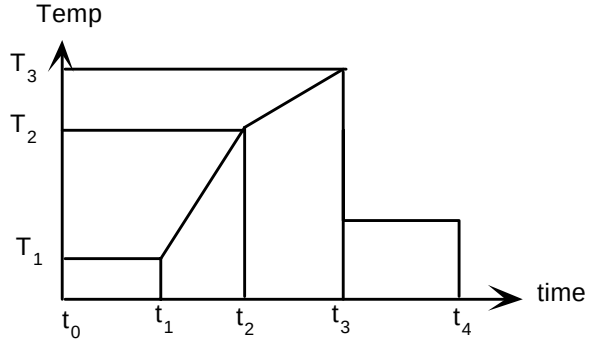

Fig. 2b: Possible temperature profile

A modal solution of Eqn 1 in the time interval starting at t_{i-1} is:

$$C(z,t) = C_{\infty i} - \sum_{n=0}^{\infty} A_{ni} \sin\left(\frac{n\pi\ z}{h}\right) \exp\left[\frac{-n^2\pi^2 D\Delta t}{h^2}\right] \qquad (6)$$

where the change in time $\Delta t = t - t_{i-1}$, and $C_{\_i}$ is calculated from Φ_i using Eqn 5. In Eqn 6, A_{ni} represents the amplitude of each mode calculated from the concentration at time t_{i-1}, and n is the index of each mode. In order to find the first set of modal amplitudes from the initial conditions, we make use of a Fourier series expansion [22].

$$A_{n1} = \frac{2}{h}\int_0^h \left(C_{\infty 1} - C_0(z)\right) \sin\left(\frac{n\pi\ z}{h}\right) dz \qquad (7)$$

where the subscript 1 represents values at the first time step (i =1). We can therefore perform the first set of calculations for A_{ni}, and use these values in Eqn 6 to find the concentration levels, $C(z,t)$. In order to calculate subsequent modal amplitudes, $A_{n(i+1)}$, and thus new concentrations, we substitute $C(z,t_i)$ (from Eqn 6) for $C_0(z)$, and $C_{\_(i+1)}$ for $C_{\_1}$, in Eqn 7, simplify, integrate, and exploit the orthogonality of the sine function to get the general form:

$$A_{n(i+1)} = \frac{4}{n\pi}\left(C_{\infty(i+1)} - C_{\infty i}\right) + A_{ni} \exp\left(\frac{-n^2\pi^2 D\Delta t_i}{h^2}\right) \qquad (8)$$

where $\Delta t_i = t_i - t_{i-1}$. For the geometry of interest only odd values of n need to be calculated. This form is useful in that it does not require the evaluation of integrals of the form of Eqn 7 except at the initial time step.

The previous development is appropriate for periods of constant temperature, as the moisture diffusivity, *D*, is constant, and can be calculated via Eqn 2. For the segments with changing temperatures, however, this calculation is complicated by the time dependence of temperature. The resulting variation in *D* invalidates the solutions above. This problem is solved by substituting Eqn 2 into Eqn 6 and defining a modified time step, Δt^*. This yields an equation for the calculation of the current moisture concentration during a temperature ramp:

$$C(z,t) = C_{\infty i} - \sum_{n=0}^{\infty} A_{ni} \sin\left(\frac{n\pi\ z}{h}\right) \exp\left[\frac{-n^2\pi^2 D_o \Delta t^*}{h^2}\right] \tag{9}$$

where

$$\Delta t^* = \int_{t_{i-1}}^{t} \exp\left[\frac{-E_A}{RT(t)}\right] dt \tag{10}$$

If the moisture and temperature profiles are repeated (cycled), we can calculate the values of Δt_i^* for each segment prior to doing the cyclical calculations

$$\Delta t_i^* = \int_{t_{i-1}}^{t_i} \exp\left[\frac{-E_A}{RT(t)}\right] dt \tag{11}$$

and Eqn 8 becomes

$$A_{n(i+1)} = \frac{4}{n\pi}\left(C_{\infty(i+1)} - C_{\infty i}\right) + A_{ni} \exp\left(\frac{-n^2\pi^2 D_0 \Delta t_i^*}{h^2}\right) \tag{12}$$

This allows easy calculation of moisture concentrations for each segment. The coefficients A_{ni} are found by progressive application of Eqn 12, and then the concentration at any time can be found from Eqn. 9. The calculations are repeated for as many cycles as needed.

Oxidative Degradation

The same scheme outlined above is used to calculate the diffusion of oxygen into the laminate. Once the local oxygen concentration is calculated, both thermal and oxidative reactions altering the polymer structure in the laminate are calculated via the method outlined by Cunningham and McManus [15]. The resulting output is in the form of a dimensionless metric, *b*, of the reaction process that is related to material mass loss. This metric is referred to below as the level of completeness of the reaction, reaching a value of one when all of the available material has been chemically degraded.

Stress Predictions

Varying thermal conditions, absorbed moisture, and chemical degradation of the material all affect the stress state in the structure. The resulting stress state in the laminate can be computed by including the environmental effects in a constitutive equation [24]:

$$\sigma_{ij} = E_{ijkl}(T,C,b)[\varepsilon_{kl} - \alpha_{kl}\Delta T - \beta_{kl}\Delta C - \chi_{kl} b] \tag{13}$$

In Eqn 13, Young's modulus, *E*, is dependent on the current temperature, *T*, the moisture concentration, *C*, and the chemical state, *b*. The coefficients of thermal and moisture expansion (α and β respectively) determine material expansion due to changes in temperature, ΔT, from the stress free temperature, T_0 , and changes in moisture level from the

dry condition. The degradative effects are treated in much the same way, with χ representing the coefficients of degradation induced expansion or shrinkage. This equation can be used in conjunction with composite laminate plate theory (CLPT) to determine stresses in each ply. An available code capable of handling all of the above effects, a modification of the Integrated Composites Analyzer (ICAN) [24], was used to do these calculations.

ANALYSIS

Material properties for IM7/PETI-5 were supplied by the Boeing Company and McDonnell Douglas Aircraft [23]. Properties relating to moisture and oxygen diffusivity were approximated from values of similar materials (primarily C6000/PMR-15). Calculations were done using values from Table 1, along with oxygen diffusion and reaction values from [15].

Table 1: Properties used

E_{11} GPa (ksi)	E_{22} GPa (ksi)	G_{12} GPa (ksi)	ν_{12}	G_{IC} J/m² (Btu/in²)	ρ kg/m³ (lb/in³)	X_t MPa (ksi)	X_c MPa (ksi)	Y_t MPa (ksi)	Y_c MPa (ksi)	S MPa (ksi)
157.3 (22.8)	9.7 (1.4)	4.20 (0.6)	0.33	1000 (6×10^{-4})	1600 (0.06)	2160 (310)	1560 (230)	70 (10)	150 (22)	80 (12)

α_{11} με/K	α_{22} με/K	k_1 W/m²K	k_2 W/m²K	D_o mm²/s	E_A kJ/mol	a	B	T_o (°F)
-0.7	36.9	8.65	0.35	0.8	42	0.018	1	600

Results of some sample runs of the codes, using the material described above, in sixteen ply laminates of unidirectional ($[0]_{16}$) or quasi-isotropic ($[0/\pm45/90]_{2s}$) lay-up, exposed to up to 5000 of the cycles shown in Fig. 1, are depicted in the following figures. Moisture levels are given as fractions of dry weights, which reach a maximum at 0.0153 (1.53%) for a RH level of 85% (see Eqn 5). The initial moisture condition is specified as either dry (C_0 = 0) or saturated at 85% RH (C_0 = 0.0153).

RESULTS

Results are presented in terms of time histories at specific locations, or profiles at specific times. Times are specified by cycles elapsed, and select times within a cycle are noted by the designations t_A, t_B, and t_C from Fig. 1.

Cyclic moisture exposure causes two types of response under the conditions studied. The first is vacillation of the moisture at the surface (shown in both Figures 3a and 3b). The first time, t_A, designates the time just after cold, dry exposure. Due to the dry atmosphere, the very edge of the laminate dries out. However, little moisture diffuses out at this low temperature in the given amount of time. The hot, dry exposure just before t_B allows moisture near the surface to dry almost completely. The t_C marker designates the period just after the warm, wet exposure, when the surface is saturated. Comparison of Figures 3a and 3b shows that moisture level fluctuation near the surface continues relatively unchanged with each cycle. The second type of response is the slow soak of moisture in towards the center of the

laminate. This internal behavior does not respond to the cycling; instead, we can observe a gradual change from cycle 2 (Fig. 3a) to cycle 100 (Fig. 3b).

Figure 4 shows a different perspective on these effects. Full time histories at different points in the material are shown. At the edge of the laminate, oscillations of the moisture is evident. The sharp rises and falls in moisture levels at the edges are a result of the boundary condition defined earlier: the surface is always saturated at the current ambient humidity. At one ply thickness into the laminate, there are significant fluctuations in moisture level throughout each cycle. At the center of the laminate, the slow change of moisture level can be seen.

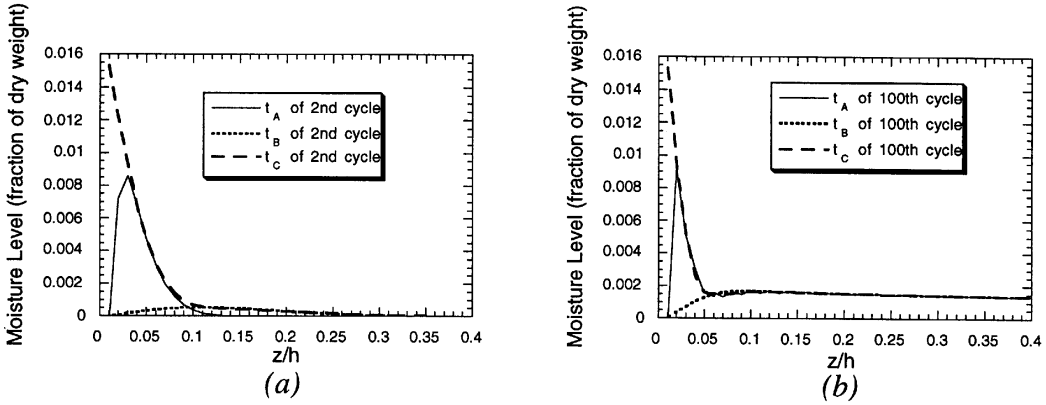

Fig. 3: Snapshot of moisture levels at points in cycle 2 (a) and cycle 100 (b)

In Fig. 5, the slow change in the center of the laminate over many cycles is shown more clearly. Experimental values based on weight change measurements during hygrothermal cycles are from reference [23]. The moisture content equilibrates at some non-zero level. Plots of the through-thickness moisture levels at distinct points in many cycles show this same trend. Figure 6 shows concentration profiles at time t_B in a 16 ply laminate over the course of 100 cycles for two different initial conditions.

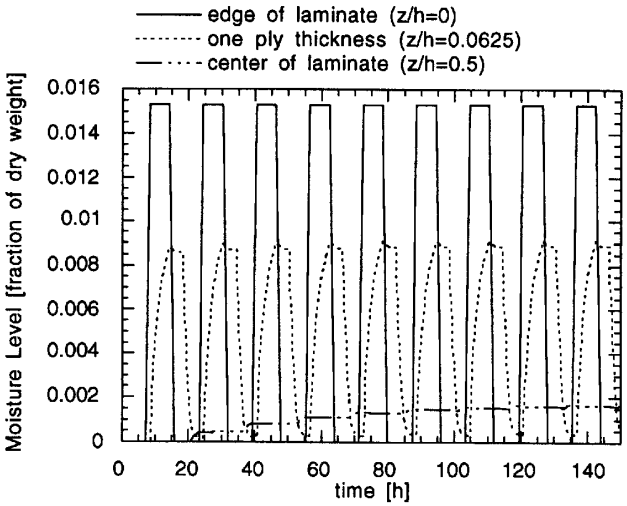

Fig. 4: Moisture fluctuations at various points in laminate

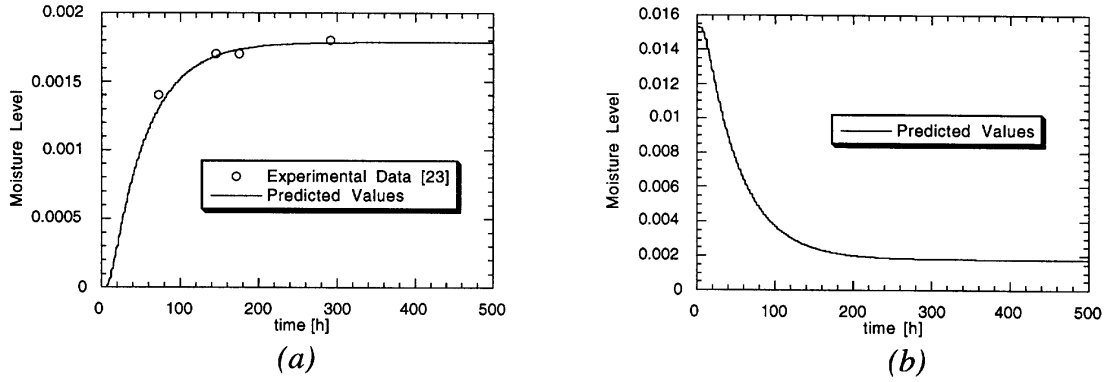

Fig. 5: Predicted and experimental moisture levels at center of a 16 ply laminate exposed to 200 cycles (a) dry initially, and (b) saturated, then exposed

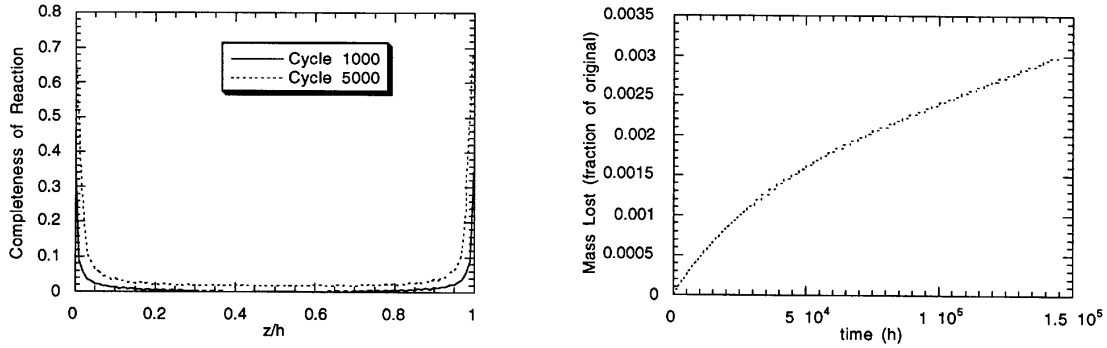

Fig. 6: Moisture level through thickness of 16 ply laminate at t_B in multi-cycle run (a) dry initially, and (b) saturated, then exposed

Output from different conditions (varying laminate thicknesses and initial conditions) show similar equilibrium values in the center of the laminate. This value may be calculated using the Eqn 14. It is simply a diffusion rate weighted average of the environmental conditions, and agrees with both values predicted by the full analyses and experimental data. The value predicted for the cycle shown in Fig. 1 and the material described in Table 1 is 0.18%.

$$C_{eq} = \frac{\int_{cycle} C_\infty \exp\left[\frac{-E_A}{RT}\right] dt}{\int_{cycle} \exp\left[\frac{-E_A}{RT}\right] dt} \qquad (14)$$

Chemical Degradation

The conditions of the cycle in Fig. 1 result in minimal chemical changes, using the values of oxygen diffusion and reaction chemistry given in [15]. As these are for PMR-15 material, the possibility that the PETI-5 material may be more susceptible to degradation was explored. Calculations were done with the same material values, but the original profile accelerated in terms of temperature and time of exposure. The maximum temperature was 475° F (replacing

the 350° F segment in the cycle in Fig. 1), which was held for 2.5 hours (compared with 30 minutes in the original). When the model was run simulating a 5000 cycle exposure, the degradation shown in Figures 7 and 8 resulted. After one thousand cycles, there is non-trivial degradation occurring at the surface. Such degradation is observed as a visible surface layer. This layer has been seen to correspond with altered material properties [4,5]. After as many as five thousand cycles, the degradation has begun to grow toward the interior of the laminate.

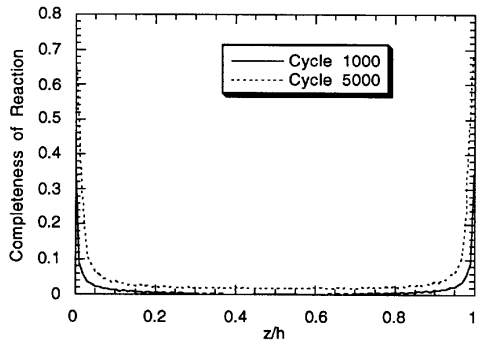

Fig. 7: Completeness of reactions in 8 ply laminate exposed to an extreme cycle

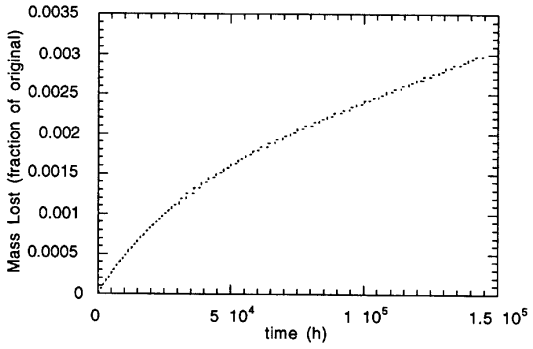

Fig. 8: Total mass lost in laminate over 5000 cycles

Stress States

Calculated stresses are shown as functions of position through the laminate under various conditions. Only the stresses locally perpendicular to the fibers are shown as these are the stresses primarily responsible for microcracking. The matrix materials proposed for this project have very high cure temperatures, resulting in large thermal stresses in the quasi-isotropic ($[0/\pm45/90]_{2s}$) laminates. Thermal stresses resulting from the profile depicted in Fig. 1 range from approximately 3 ksi to 10 ksi.

In Fig. 9, stresses due solely to moisture sorption are shown. This laminate has been left in a wet environment long enough to reach saturation, and subsequently cycled. As it begins the cycle, the external plies dry out first. The notable result of the hygral stresses in this example is the large gradient between the outer plies (loaded in tension) and the internal plies (loaded in compression). Figure 10 shows the stress field due to degradation at five thousand of the higher temperature, extended time cycles. Stresses reach large tensile values near the surface.

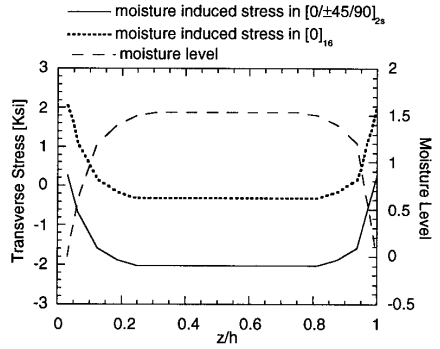

Fig: 9. Stress due to moisture only in 16 ply laminates

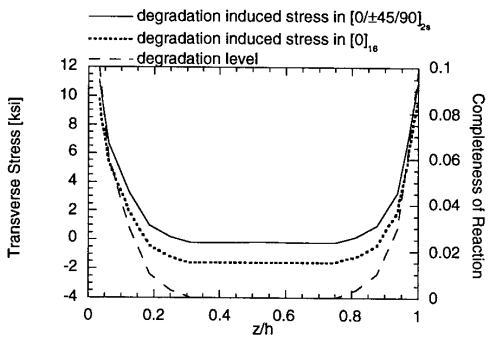

Fig. 10: Stress due to degradation only in 16 ply laminates

CONCLUSIONS

A computationally efficient model has been developed for computing the response of composite laminates to hygro-thermal cycling. This model predicts two significant effects of cyclic moisture absorption: large fluctuations in absorbed moisture level at the material surface due to changing ambient conditions; and a slow increase in the interior of the laminate to an equilibrium level. This equilibrium level can be calculated easily using a simple temperature-weighted average of the environmental conditions. The moisture absorption results agree with experimentally measured moisture gains.

Sample problems suggest that the environmentally-induced stress state is determined primarily by thermal stresses. If degradation takes place, it will result in significantly enhanced stresses near the surface. This could explain the surface microcracking observed in numerous studies [4,5,11,13,15,18,19]. The moisture stresses, though smaller in magnitude, are non-trivial and can induce stress gradients through the thickness. The worst case hygral stresses are on the same order of magnitude as the thermal stresses. In particular, moisture stresses can be severe in unidirectional laminates undergoing dry-out from a saturated condition. The computed stresses do not fully explain the increased cracking observed under exposure to moisture [6,8,10,17,18,20], suggesting that there are mechanisms for moisture-induced cracking beyond moisture-induced stresses. The presence of moisture in the laminate could cause temporary or permanent changes in material properties, in particular the transverse fracture toughness, or it could enhance the cracking mechanisms in ways not yet understood.

ACKNOWLEDGMENTS

This work was supported by the Boeing Company, under Contract FO 563289 07LLN.

REFERENCES

1. Shen, C.H. and G.S. Springer, "Moisture Absorption and Desorption of Composite Materials," *J. Composite Materials*, Vol. 10, No. 1, 1976, pp. 2-20.

2. Springer, G.S., "Environmental Effects," *Composites Design*, 4th Ed., S. Tsai, ed., Think Composites, Dayton, Ohio, 1988, pp. 16-1 to 16-18.

3. Tsai, S.W, and H.T. Hahn, *Introduction to Composite Materials*, Technomic Publishing, Lancaster PA, 1980.

4. Bowles, K.J., "A Thermally Modified Polymer Matrix Composite Material with Structural Integrity to 371°C," *Proceedings Twentieth SAMPE Technical Conference*, Minneapolis, MN, Sept, 1988.

5. Roberts, G.D. and R.D. Vannucci, "Effect of Solution Concentration and Aging Conditions on PMR-15 Resins," *SAMPE Journal*, Mar/Apr 1986, pp. 24-28.

6. Burcham, L.J., M.R. VanLandingham, R.F. Eduljee, and J.W. Gillespie, "Moisture Effects on the Material Behavior of Graphite Polyimide Composites," *Proceedings Ninth International conference on Composite Materials*, Newark, DE, Sept, 1994.

7. Weitsman, Y. "A Rapidly Convergent Scheme to Compute Moisture Profiles in Composite Materials under Fluctuating Ambient Conditions," *J. Composite Materials*, Vol. 15, No. 7, 1981, pp. 349-358.

8. Beckwith, S.W. and B.D. Wallace, "Effects of Aging and Environmental Conditions on Kevlar/Epoxy Composites," *SAMPE Quarterly*, Vol. 14, No.6, July, 1983.

9. Upadhyay, P.C. and J. Prucz, "Parametric Damage Modeling of Composites due to Moisture Absorption," *J. of Reinforced Plastics and Composites*, Vol. 11, 1992, pp. 198-210.

10. Whiteside, J.B., R.J. DeIasi, and R.L. Schulte, "Distribution of Absorbed Moisture in Graphite/Epoxy Laminates After Real-Time Environmental Cycling," *Long Term Behavior of Composites, ASTM STP 813*, O'Brien, T.K., Ed., American Society for Testing and Materials, Philadelphia, 1983, pp. 192-205.

11. Ming, L, "The Environmental Effects of Carbon Fiber Reinforced Polyethersulphone Composites," *Proceedings Tenth International Conference on Composite Materials*, Whistler, B.C., Canada, August, 1995, pp. 297-303.

12. Crank, J., *The Mathematics of Diffusion*, 2nd Ed., Clarendon Press, Oxford, England, 1975.

13. Chang, W-J., T-C. Chen, and C.-I. Weng, "Transient Hygrothermal Stresses in an Infinitely Long Annular Cylinder," *J. of Thermal Stresses*, Vol. 14, 1991, pp. 439-454.

14. Springer, G.S. *Environmental Effects on Composite Materials*, Technomic Publishing, Lancaster, PA, Vols.1 and 2, 1981.

15. Cunningham, R. and McManus, H., "Coupled Diffusion-Reaction Models for Predicting the Distribution of Degradation in Polymer Matrix Composites," Presented at the 1996 ASME International Mechanical Engineering Congress and Exposition Atlanta, GA, Nov. 1996.

16. Chamis, C.C., "Simplified Composite Micromechanics Equations for Hygral, Thermal and Mechanical Properties," *SAMPE Quarterly*, April, 1984, pp. 14-23.

17. Mandell, J.F., "Origin of Moisture Effects on Crack Propagation in Composites," Dept. of Materials Science and Engineering Research Report R77-4, Massachusetts Institute of Technology, Dec. 1977.

18. Martin, R.H., E.J. Siochi and T.S. Gates, "Isothermal Aging of IM7/8320 and IM7/5260," Presented at the 7th Technical Conference on Composite Materials, The Pennsylvania State University, University Park, PA, October, 1992.

19. Chester, R.J, and A.A. Baker, "Environmental Durability of F/A-18 Gr/Ep Composites," *Proceedings Tenth International Conference on Composite Materials*, Whistler, B.C., Canada, August, 1995, pp. 239-246.

20. Lucas, J.P. and J. Zhou, "Moisture Interaction Characteristics and Fracture in Polymer Composites," *Proceedings Tenth International Conference on Composite Materials*, Whistler, B.C., Canada, August, 1995, pp. 247-256.

21. Cai, L.-W. and Y. Weitsman, "Non-Fickian Moisture Diffusion in Polymeric Composites," *J. Composite Materials*, Vol. 28, No.2, 1994, pp. 130-154.

22. Hildebrand, F.B. *Advanced Calculus for Applications*, Englewood Cliffs, N.J.: Prentice-Hall, 1976.

23. Zabora, R. Personal correspondence, July and September, 1996.

24. McManus, H.L. and C. Chamis, "Stress and Damage in Polymer Matrix Composite Materials Due to Material Degradation at High Temperatures," *NASA TM 4682*, January, 1996.

EXPERIMENTAL STUDIES ON COMPOSITE BONDED JOINTS

Steven L. Donaldson [1] and Ajit K. Roy [2]

[1] WL/MLBM, Bldg. 654, 2941 P St. Ste. 1, Wright-Patterson AFB, OH 45433-7750 USA
[2] University of Dayton Research Institute, 300 College Park Ave., Dayton, OH 45469 USA

SUMMARY: The double lap shear specimen is examined in detail to serve as a baseline for further research on the behavior of composite to composite adhesive bonded joints. Four laminate surface preparation techniques were examined in detail. The four are a simple acetone wash, hand sanding, surface grinding, and grit blasting. A comparison is made between the 3D stress analysis and the experiments using small strain gages placed in regions of high strain gradients. The results match well except in the region precisely at the corner of the adherends where stress singularities occur. The damage propagation modes were observed and characterized. Failure within the composite was the general mode of failure, resulting in final ultimate strengths which did not appear to be sensitive to the surface preparation method.

KEYWORDS: adhesive, bonding, failure modes, surface preparation, double lap joint, 3501-6, FM-300

INTRODUCTION

An understanding of the behavior of bonded joints has become increasingly important to the U. S. Air Force. This is primarily for two reasons: first, the use of composite materials in Air Force aircraft has been increasing dramatically over the past decade, and with the future introduction of aircraft with higher percentages of highly loaded primary composite structures, the need to repair these structures is critical. It is envisioned that many of the repairs will require adhesively bonded scarf joints. The second primary reason for the renewed interest in bonded structure is that many of the future concepts for low cost composite structures entail large, highly unitized structures, for which adhesively bonded joints may play a large role. For both of these applications, an understanding of the long-term performance of the joints under repeat mechanical and environmental (primarily moisture and temperature) loading is required.

The long range objective of the overall program, then, is to develop analysis methods for the accurate prediction of failure in composite bonded joints. It is envisioned that this effort will entail many components, including fully three dimensional stress analysis, testing and characterization of failure, the extension or development of 3D failure criteria necessary for the correlation between analysis and experiments, the understanding of cyclic moisture, temperature, and mechanical loading effects on failure in adhesively bonded composite joints, and, finally, the effects of 'real world' issues on bond failure, to include poor surface preparation, uneven curing of the bondline adhesive, and uneven bondline thickness. The

objective of the current study, however, is far more modest. It is to establish a baseline understanding of the failure modes of composite to composite adhesive bonds in the double lap shear specimen (the description of and rationale for selection will be given in the next section). Further studies will continue to explore the areas described above.

MATERIALS, SPECIMEN CONFIGURATION AND PREPARATION

The material chosen for the adherents was Hercules AS4/3501-6, considered a well characterized, commonly used carbon fiber reinforced brittle epoxy system. The adherent lay-ups were $[0]_{16T}$. The bonding adhesive chosen was Cytec FM300-2U (neat film) and FM300-2K (film with 3% woven glass scrim).

The specimen geometry is shown in Fig. 1. The specimens were fabricated in several steps: first, the adherent plates, measuring 30.5 cm x 30.5 cm (12" x 12") were cured following the manufacturer's instructions. Next, the bonding surfaces underwent one of four surface treatments: 1. acetone wash only, 2. moderate hand sanding with 240 grit sandpaper, followed by an acetone wash, 3. surface grinding with a 56 grit silicon carbide wheel to remove 0.05 mm (0.002") of the panel surface, followed by an acetone wash, and 4. grit blasting with 30 grit particles at 0.62 MPa (90 psi), also followed by an acetone wash. The film adhesive was then applied to the full sized plates; shim plates were added to prevent the adherents from bending during the application of external pressure, and the plates were placed in a hot press at 0.69 MPa (100 psi) to cure the adhesive. The adhesive cured according to the manufactures recommend cure cycle (Fig. 2) resulted in an unacceptable level of porosity and uneven bond quality, as shown by the C-scan results in Fig. 3. To remedy this, several steps were taken. The first was the addition of a temperature hold step, at the point of minimum resin viscosity, at a temperature slightly below the final cure temperature, as depicted in Fig. 4. It was believed the additional resin flow time would assist in allowing volatiles to escape from the adhesive. In addition, the plates were placed in an autoclave to apply the external pressure, also 0.69 MPa (100 psi). The results are shown in Fig. 5, and indicate significantly improved bondline quality. Once cured, the panels were cut into 2.54 cm (1") width specimens, after which strain gages (in locations to be discussed) and tabs were applied.

The results of the various surface preparation techniques are shown in Figures 6-9, which are low magnification views of the surfaces prior to bonding. In Fig. 6, the imprints of the woven peel ply texture in the surface of the laminate are apparent (recall that this laminate is unidirectional). Fig. 7 shows the effects of moderate hand sanding, where the peaks in the surface resin have been removed, however the low regions are unaffected. Fig. 8 illustrates the intermediate roughness created by the surface grinding, and Fig. 9 shows the highly roughened surface from the grit blasting. It should be noted that, also in this same sequence of surface preparation techniques, the surface roughness increases, as does the amount of fiber breakage and microcrack formation in the laminate. The extreme case is depicted in Fig. 10, which is a high resolution magnification of the damage caused by the grit blasting. The high surface roughness, broken fibers, resin splitting, and surface debris are apparent.

TEST RESULTS

Many of the specimens were instrumented with strain gages to monitor the surface strains at select locations. Back-to-back gages on both the single adherent section of the specimen, as

well as in the region of bond overlap, indicate by their nearly identical output that a high level of symmetry exists in the specimen. In addition, very small gages, 0.38 mm (0.015") in length, were located in regions on the specimen edges near the bond line. A sample output from a single set of such gages is given in Fig. 11. It is worth noting that gages 4 and 5 measure transverse strains, whereas gages 6 and 7 measure axial strains. Also, gages 4 and 6 are located just in the corner region of the adherent, whereas gages 5 and 7 are also located on the laminate, directly adjacent to the adhesive bond, but at a distance of 0.63 mm (0.25") from the end of the bondline. In this example, the specimen was loaded to a peak load approximately 30% of the load required to cause crack initiation, and approximately one fifth of the ultimate load. Even at this low load level, hysteresis can clearly be seen in the gage outputs at the crack tip.

Two dimensional [1] and a three dimensional [2] analytical solutions for stress and strain were developed for this configuration. The stress results for the 2D solution are presented in Fig. 12. The results clearly show the non-uniformity in shear stress along the length of the specimen, as well as the significant singular peel stress that develop at the ends of the bondline. In reality, the specimen has double free edges: the edges along the sides of the specimen, as well as the edges perpendicular to the longitudinal axis of the specimen. The strain gage output was compared with the 3D results, and the comparison is given in Table 1. It is clear that the corner strains vary significantly between specimens, as well as between specimens and the analytical solution. However, the strains 6.3 mm (0.25"), still fairly close to the crack tip, match the analytical solution fairly well. It should be noted that the results for the analytical solution were averaged over the gage area to provide a fair comparison.

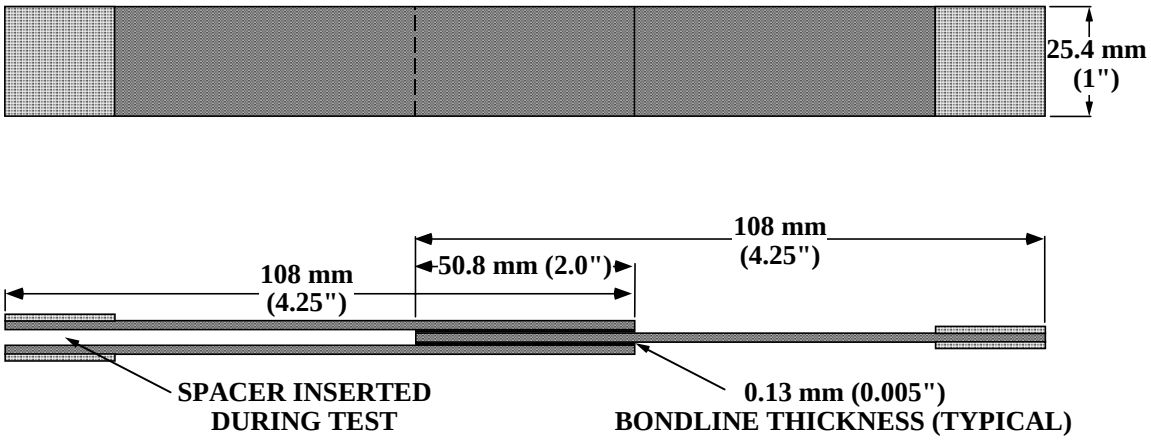

Fig. 1: Configuration of the double lap shear shear specimen

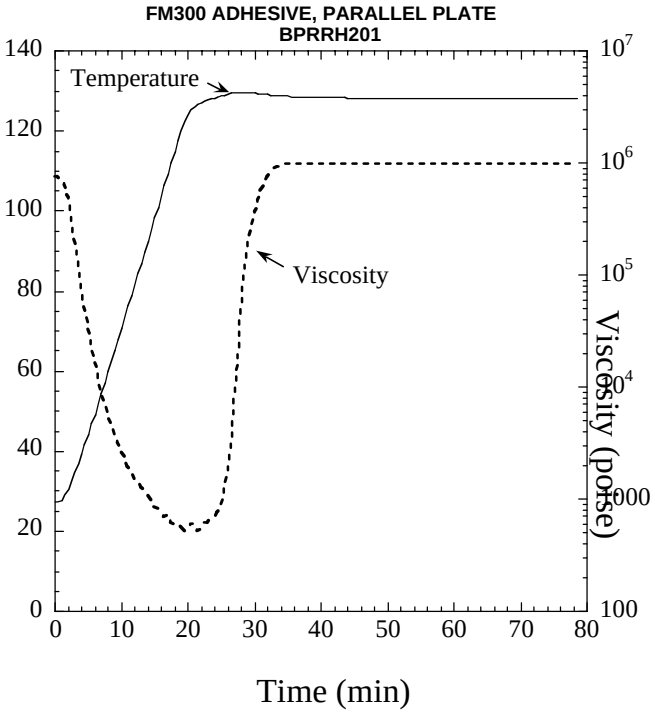

Fig. 2: Temperature and viscosity profiles cycle of the Cytec FM-300 adhesive subjected to the standard processing cycle

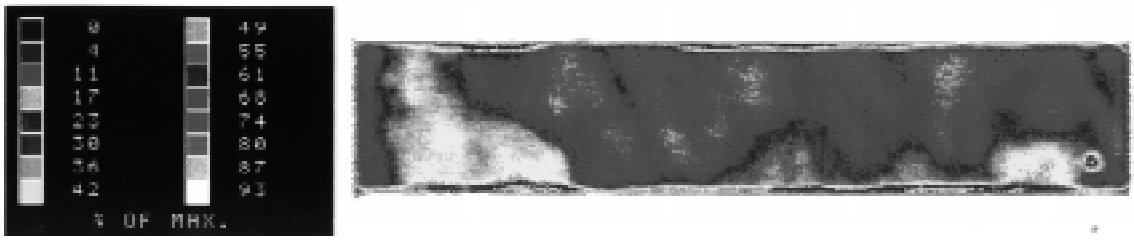

Fig. 3: Ultrasonic C-scan of the FM-300 bonded plates cured in a hot press at 0.69 MPa using the standard cure cycle

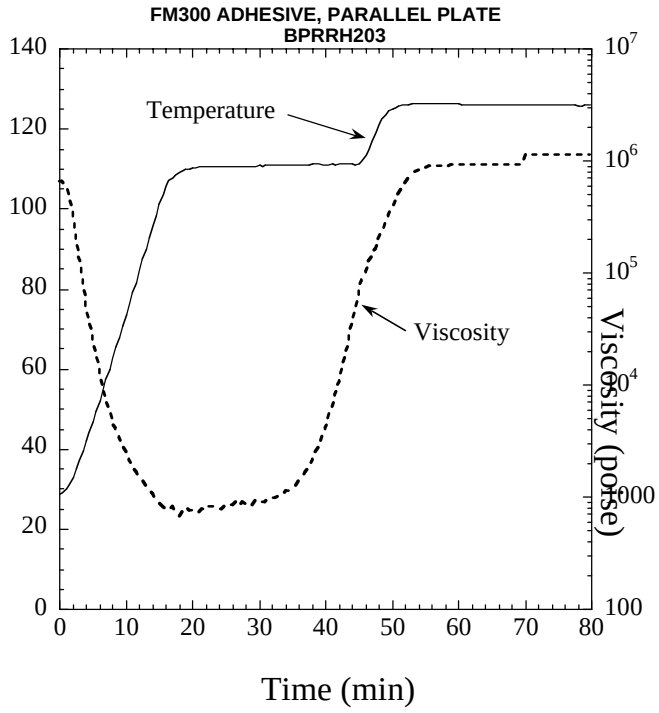

Fig. 4: Temperature viscosity profiles cycle of the Cytec FM-300 adhesive subjected to the modified processing cycle

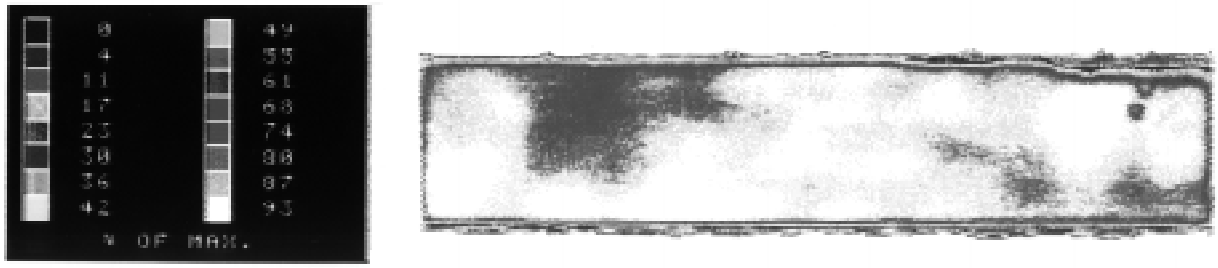

Fig. 5: Ultrasonic C-Scan of the FM-300 bonded plates cured in an autoclave at 0.69 MPa using the modified cure cycle

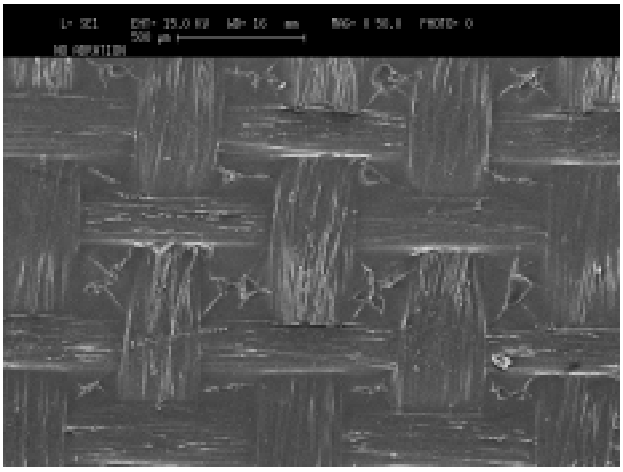

Fig. 6: Surface of the laminate with acetone wash only. Note the textile texture imprint from the peel ply

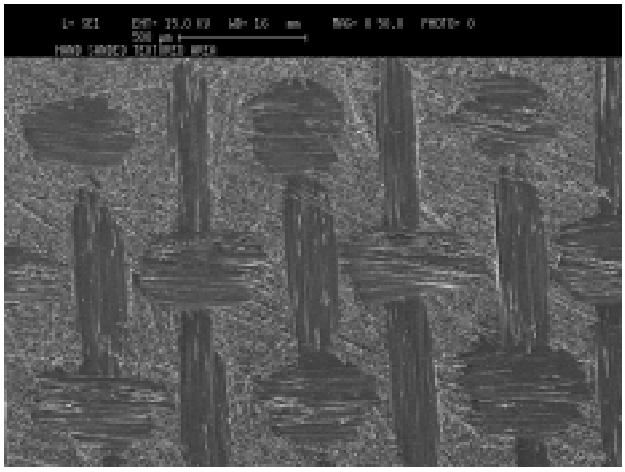

Fig. 7: Surface of the laminate with moderate hand sanding

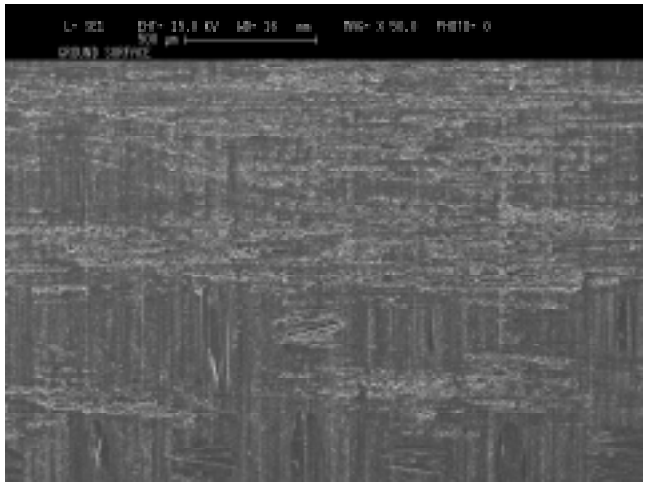

Fig. 8: Surface of the ground laminate before bonding

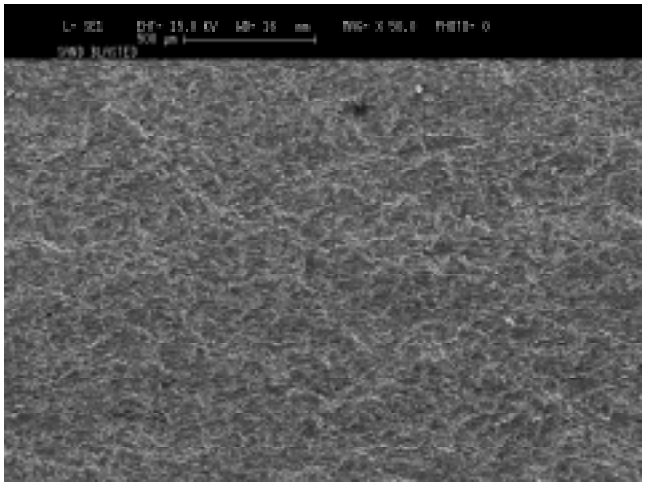

Fig. 9: Surface of the grit blasted laminate before bonding

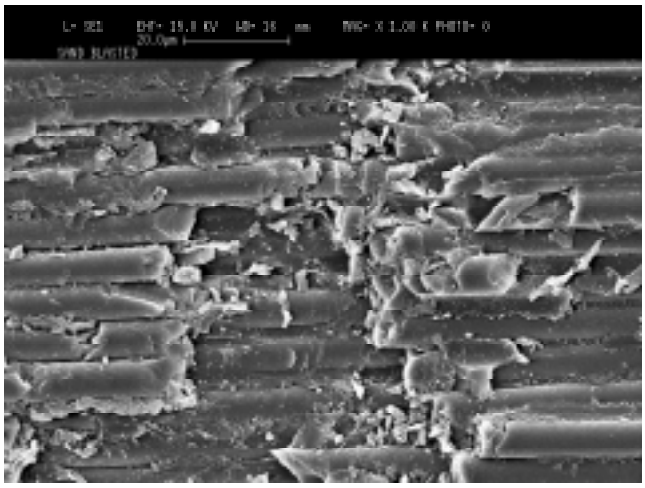

Fig. 10: Close-up of the surface of the grit blasted laminate before bonding

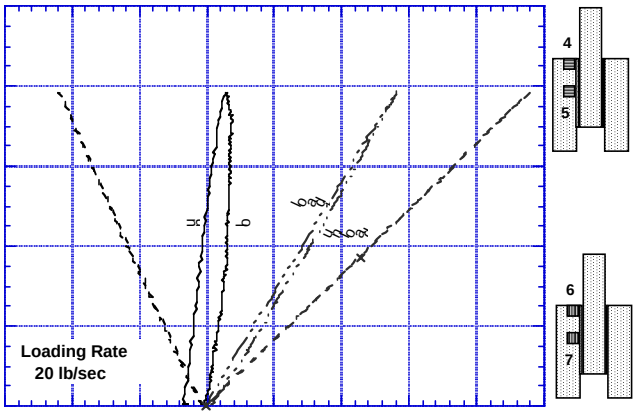

Fig. 11: Output from the 0.38 mm (0.015") size strain gages located on the specimen adherent edges adjacent to the adhesive bondline

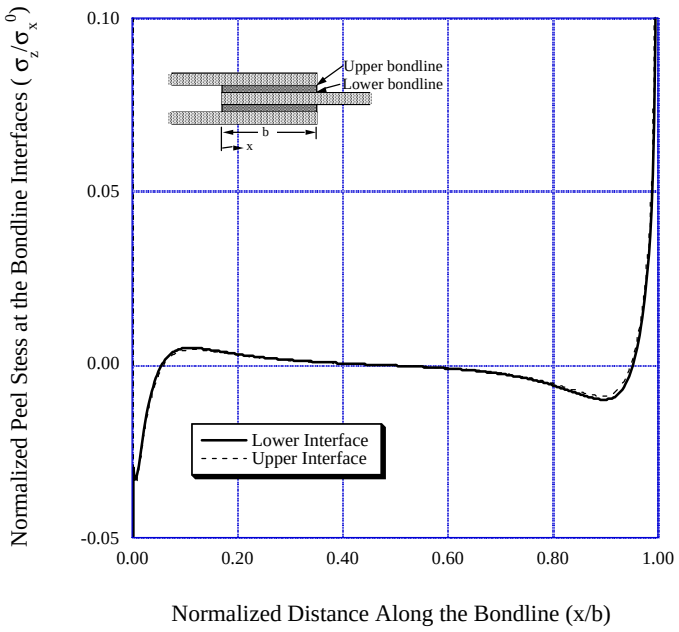

Fig. 12(a): Normalized (by the axial stress in the single adherend) shear stress at the bondline interface as a function of bondline position

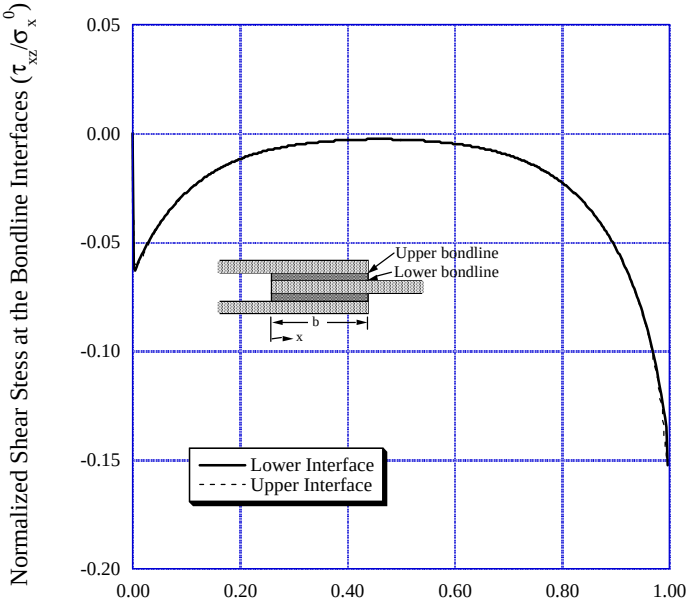

Fig. 12(b): Normalized (by the axial stress in the single adherend) shear stress at the bondline interface as a function of bondline position

Table 1: Comparison of Experimental Strains and Analytical Predictions

CORNER STRAINS

	EXP: DL2-2	EXP: DL3-1	ANALYTICAL
$\varepsilon_x/\varepsilon_{x0}$	0.2458	0.1915	0.1070
$\varepsilon_y/\varepsilon_{x0}$	0.0500	0.2010	0.7740

NEAR CORNER STRAINS
0.25" INSET

	EXP: DL2-2	EXP: DL3-1	ANALYTICAL
$\varepsilon_x/\varepsilon_{x0}$	0.3933	0.3103	0.3529
$\varepsilon_y/\varepsilon_{x0}$	-0.1930	-0.1929	-0.1744

In order to observe the failure sequence, the edges of the specimens were polished prior to testing. Next, the specimens were loaded incrementally until crack initiation and propagation was observed. Fluorescent die was applied to the polished edge while the specimens were still under load. The loading was then removed, and the specimens edges were observed under an optical microscope, illuminated by a flourescent light source. The onset of crack initiation was also indicated by acoustic emission output. Failure in nearly all of the specimens followed a regular pattern, as depicted in Fig. 13. The cracks generally initiated in the region of maximum peel stress at 70% of the ultimate failure load. The cracks then propagated to approximately the midpoint of the specimen. A second crack, at the opposite side of the bondline, then forms within the specimen. These cracks then link via a third crack which traverses the bondline.

The cracks, when observed under the optical microscope, appeared to be located at the interface between the composite and the adherent. Upon careful examination under the scanning electron microscope, however, it was clearly observed that for all four surface preparation techniques, the failure was within the laminates themselves, just several fiber diameters from the laminate surface. This is illustrated in Fig. 14, which shows clearly the presence of fibers (as does the mating surface), indicating primary crack propagation within the laminate. In addition, as observed in the laminates before bonding, the number of broken fibers increased when examining the acetone washed only, the hand sanded, the ground, and the grit blasted specimens, respectively.

The ultimate failure loads are given in Table 2. It is felt that the variation in strength of the specimens is not significantly effected by the surface preparation method (the high failure value in the acetone wash specimen is based on only one test).

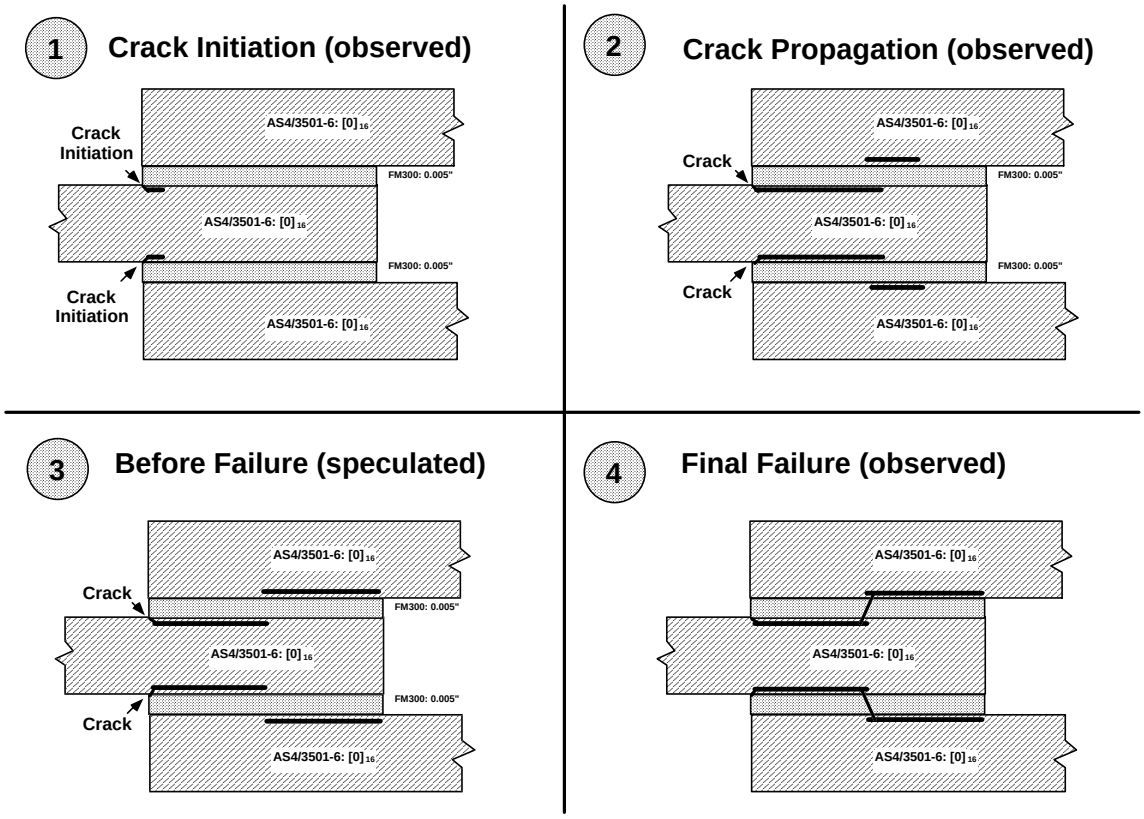

Fig. 13: Depiction of the damage initiation and growth as seen by flourescent enhanced edge microscopy

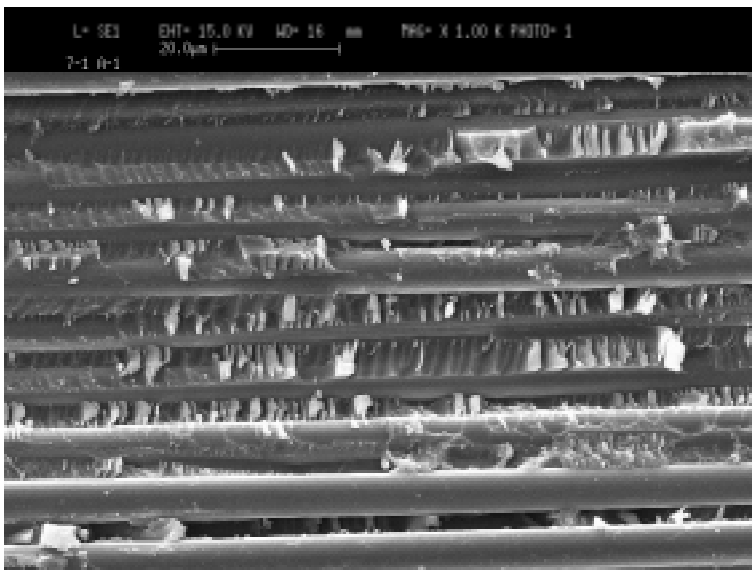

Fig. 14: Typical image of the fracture surface showing intra-ply failure

Table 2. Ultimate failure load for four surface preparation techniques

	Failure Stress (Far Field in the Single Adherent) MPa (ksi)	Number of Specimens
Acetone wash	501 (72.7)	1
Hand sanding	439 (63.7)	3
Grinding	469 (68.0)	2
Grit blasting	453 (65.7)	3

DISCUSSION AND CONCLUSIONS

Several significant issues become apparent when examining the results. First, in the corner region of the specimen, potential viscoelastic effects may be present and must be accounted for in the stress analysis. In addition, the shape of the adhesive fillet was generally uncontrolled and may effect the stress state in that region.

The effect of surface preparation did not appear to have a significant effect on the specimen strength. This may not be surprising, as all failures were observed to occur within the composite, and hence the intra-ply strengths dictate the failure level. However, as future tests are conducted under more extreme moisture and temperature conditions, the failure modes may change.

Immediate future plans for this project include the use of full field moiré instead of strain gages to monitor strains in the regions of high strain gradients, the use of multi-directional laminates as adherents, and the testing of moisture conditioned specimens at cold, room, and elevated temperatures. An additional laminate and adhesive will also be added to the test matrix. Longer term plans include the addition of alternate test geometries to alter the stress state in the bond region.

In summary, the double lap shear specimen has been examined in detail to serve as a baseline for further research on the behavior of composite to composite adhesive bonded joints. Four laminate surface preparation techniques were examined in detail. A comparison was made between the 3D stress analysis and the experiments using small strain gages placed in regions of high strain gradients. The damage propagation modes were observed and characterized, and the final ultimate strengths reported and discussed with respect to them.

REFERENCES

1. Schoeppner, G. A. and Pagano, N. J., “Stress Fields and Energy Release Rates in Cross-ply Laminates”, submitted to *International Journal of Solids and Structures*, 1996.

2. Bogdanovich, A. E. and Rastogi, N., "3-D Variational Analysis of Bonded Composite Plates", 1996 International Mechanical Engineering Congress and Exposition, Atlanta, GA, November 17-22, 1996. *Proceedings of the ASME Aerospace Division*, AD-Vol. 52, 1996, pp. 123-143.

3. Chin, J. W. and Wightman, J. P., "Surface Characterization and Adhesive Bonding of Toughened Bismaleimide Composites", *Composites: Part A*, Vol. 27A, 1996, pp. 419-428.

THE EFFECT OF ENVIRONMENT ON THE DAMAGE TOLERANCE OF GLASS AND CARBON FIBRE REINFORCED EPOXY LAMINATES

G. A. Bibo[1], P. J. Hogg[1] and M. L. Kay[2]

[1]Department of Materials, Queen Mary and Westfield College, London, UK
[2]National Physical Laboratory, Teddington, Middlesex, UK

SUMMARY: An examination of the damage tolerance of two distinctly different performance (carbon and glass fibre reinforced epoxy prepreg) composites, each targeted at separate ends of the engineering market were put into context by subjecting them to environmental extremes. The conditioning was chosen such that it reflected likely scenarios in industry and facilitated an accelerated programme of testing. The observed response of each material to its particular environmental conditioning is discussed and the immediate implications of these findings commentated upon, within the realms of their potential application. Subsequently, the interpretation and relevancy of the damage tolerance test for these extreme conditions was put into perspective.

KEYWORDS: accelerated testing, environmental cconditioning, compression after impact

INTRODUCTION

Compression after impact test data obtained under elevated temperature or moisture conditions requires careful interpretation compared with room temperature tests. This is due to reduced fundamental strengths at high temperature and moisture and/or changes in failure mechanism induced by impact or subsequent compression testing. This paper examines the behaviour of two well characterised materials, under extreme conditions of temperature and environmental exposure and compares the results to room temperature tests.

MATERIALS

Two principal reinforcement fibre types, carbon and glass, were used in this study and subjected to extreme (accelerated) environmental conditions commensurate with their industrial applications e.g. carbon - aerospace and glass - chemical and marine.

The material tested under a range of high temperature impact and compression after impact conditions, was an Hexcel (formally Ciba Composites) 924C (a toughened epoxy with the Torayca T800H carbon fibre).

For the hygrothermal investigation, Hexcel's (formally Ciba Composites) 913 resin system was reinforced by E-glass.

The carbon and glass fibre laminates' lay up consisted of a 16 ply quasi-isotropic construction as follows: $[-45,0,45,90]_{2S}$. Both unidirectional prepreg tape stacks were cured in accordance with their respective recommended resin cure cycles - 913 @ 120 ^{o}C and 924 @ 180 ^{o}C. All the material was non-destructively inspected prior to testing using ultra-sonic C-scan and any defective material rejected.

The fibre volume fraction is the carbon laminates was estimated to be 60% based on the cured thickness (nominally 2 mm).

The fibre content in the glass laminates was determined by resin burn off to be approximately 55%.

TEST METHODS

The thermal conditioning, Table 1, of the carbon fibre composite was representative of trans and supersonic temperatures generated in aircraft skins arising from kinetic heating.

The impact specimens were preheated in an oven to an over temperature and removed for testing. An instrumented specimen was manufactured to calibrate the temperature time behaviour to ensure impact occurred in the desired temperature range.

Table 1: Impact and compression after impact test matrix for 924C

Impact Temperature (°C)	Compression after Impact Temperature (°C)	
20	20	150
80	20	80
150	20	150

Laminates for the hygrothermal element of the investigation resulted in one set of three being immersed in a temperature controlled bath of water at 70°C for six months before being tested. A second set was impacted over an energy range prior to conditioning for six months, while the third set was used as a control and not subjected to any environmental extremes.

All the laminates were cut into specimens, 89 mm long and 55 mm wide, using a liquid cooled diamond saw.

The impact and compression after impact tests were performed using inhouse equipment. The specimens, supported on a 40 mm ring were struck by a 20 mm diameter hemisphere weighing 3.96 kg. Complete details regarding the post impact compression jig, and its derivative for elevated temperature testing, may be found else where [1]. Elevated temperature undamaged plate compression testing was also conducted using the modified compression after impact jig for insitu heating. All mechanical testing was carried out on a screw driven Instron 1195 at a controlled constant displacement rate of 0.5 mm/min.

The impact induced delamination extents in the carbon and glass fibre laminates were determined using ultra-sonic C-scan. In the case of the carbon fibre laminates these

specimens were also re-scanned after the residual compression phase to qualitatively measure delamination propagation.

RESULTS

Elevated Temperature Testing

Impact

To facilitate ease of comparison, the 924C room temperature results are incorporated to define a baseline against which performance changes may be measured.

The impact induced delamination damage extent increases not only with incident energy, but also with increasing temperature, Figure 1. This is particularly evident for the data generated at 150 ^{o}C. At the highest impact energy level (6 J) used for this material, the room temperature delamination spread has been observed to approach the support dimensions, thus the measured damage extent for the high temperature impact may be in error as they may be constrained by the boundary conditions.

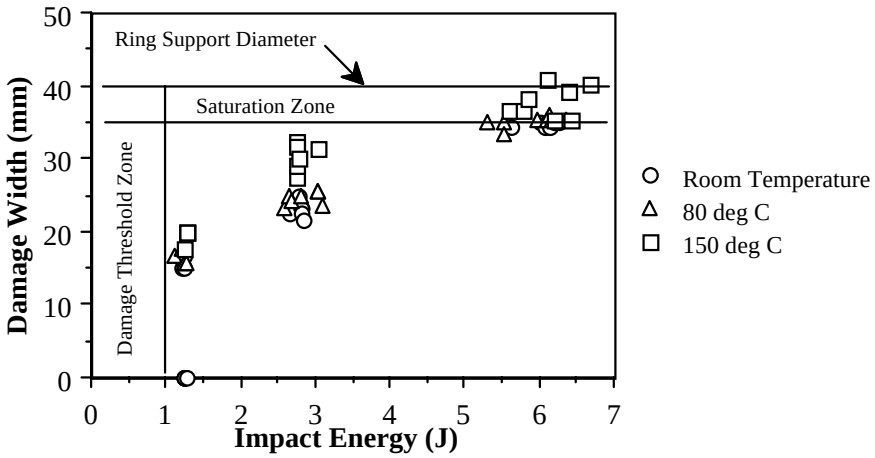

Figure 1: Damage extent versus impact energy over a range temperatures

Undamaged Plate Compression Strength

The 'undamaged plate compression strength' decreases monotonically with increasing temperature, Figure 2.

The plate compression tests conducted at 80 ^{o}C, unlike the room temperature tests failed at the base support and not the unsupported region, in a splaying or brooming mode. At 150 ^{o}C similar fracture characteristics occur, however, the failure region is less extensive, the high temperature having softened the matrix sufficiently to allow the composite to yield.

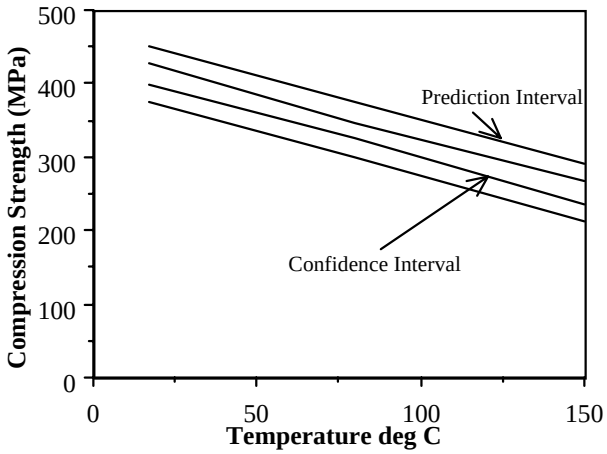

Figure 2: Undamaged plate compression strength as a function of temperature

Compression After Impact

Figure's 3a and 3b present the compression after strength versus impact energy and damage extent respectively for all the temperature combinations used, normalised with respect to the 'undamaged plate compression strength' at that temperature.

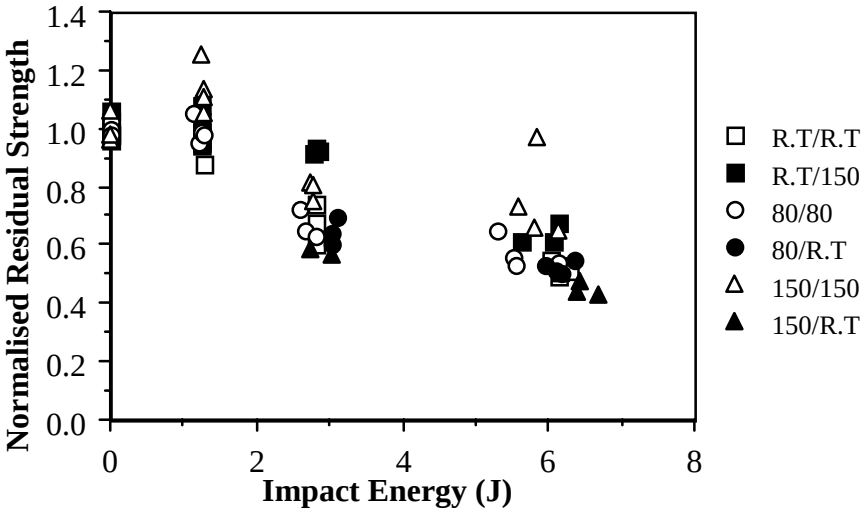

Figure 3a: Normalised residual compression strength versus impact energy over a temperature range (impact temperature/compression after impact temperature)

The trends indicate, Figure 3a, that there is a slight improvement in the normalised residual strength retention when the compression phase is performed at 150 ^{o}C, although there is little or no apparent difference between room temperature and 80 ^{o}C strengths. However, when the normalised residual strength is plotted against damage width, Figure 3b, the samples compression tested at 150 ^{o}C now clearly show a higher relative strength retention compared to those tested at room temperature and 80 ^{o}C.

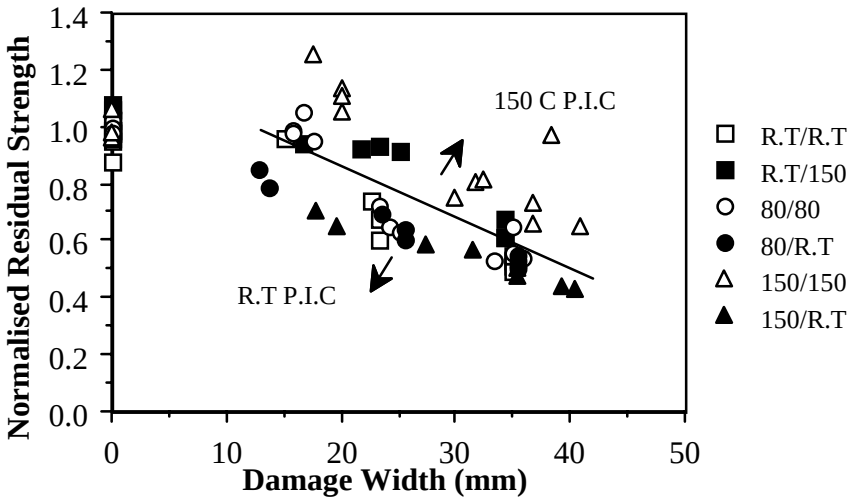

Figure 3b: Normalised residual compression strength versus damage extent over a temperature range (impact temperature/compression after impact temperature)

Hygrothermal Testing

Moisture Diffusion

Gravimetric analysis indicated that the glass/epoxy laminates resembled Fickean diffusion, although continued moisture uptake may occur through other mechanisms [2]. Visual observation revealed that the specimens developed an opacity, with blisters occurring on the outer plies after approximately two months exposure.

Impact

To facilitate ease of comparison, unconditioned data are incorporated to define a datum against which changes may be determined. The impact induced delamination damage extents in the unconditioned and six month environmentally (70 ^{o}C water) exposed glass/epoxy are plotted as a function of impact energy, Figure 4. The data demonstrate that samples conditioned actually contained delamination damage better than the benchmark specimens.

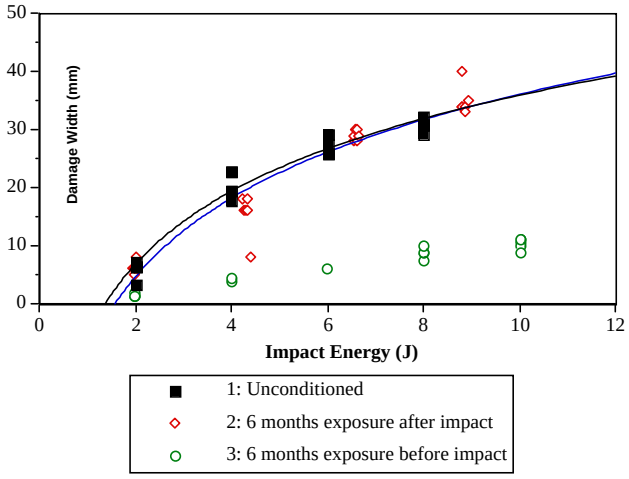

Figure 4: Damage extent versus impact energy with and without conditioning

Compression After Impact

The compression after impact data are presented in the classical fashion, that is, against incident energy, Figure 5a.

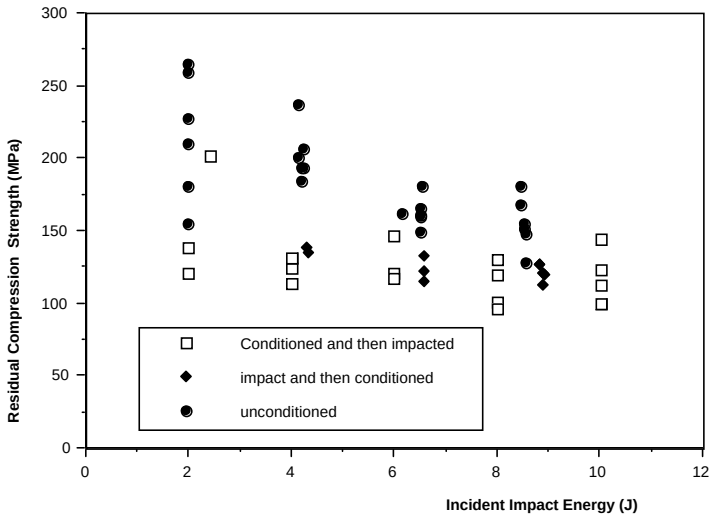

Figure 5a: Compression after impact strength versus impact energy for all conditions

The absolute trends indicate that the detrimental effect of delamination damage is exacerbated by the addition of environmental exposure. The subtle difference being between those samples that were conditioned then impacted and those that were impacted then conditioned.

This affect is magnified when considering the residual strength on the basis of the delamination damage extent, Figure 5b, and infact the presence of any impact induced damage may be disregarded inview of the almost non-existent rate of strength loss with increasing impact energy or damage extent, provided, a measure of the undamaged strength of an exposed laminate is known.

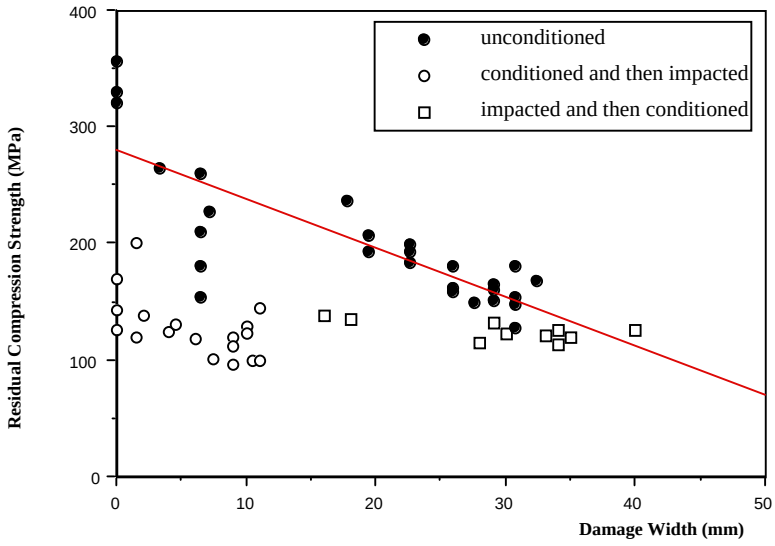

Figure 5b: Compression after impact strength versus damage extent for all conditions

DISCUSSION

Carbon/Epoxy

While the 924C may not be the ideal candidate material choice for a second generation Concorde due to its instability at prolonged high temperature exposure, it may be indicative of the behaviour of the better suited resin systems, e.g. Bismaleimides (BMI) or polyimides.

The reduction in plate compression strength may only be representative of a trend, however, there is sufficient experimental evidence available clearly stating this link, much of it attributing this behaviour to fibre instability through a reduced matrix shear modulus [3-5].

Examination of the 924C's compression after impact results, Figures 3a and 3b, demonstrate some interesting characteristics - the elevated temperature residual (normalised) compression strengths are higher for a given impact energy than the room temperature results, and especially so if the impact themselves were generated at the high temperatures. This effect is accentuated if the data are analysed on the basis of damage extent. On this Figure (3b), a line has been drawn which divides all the data generated by compression testing at 150^{o}C and room temperature, such that the elevated temperature data lie above this line and the room temperature below.

This behaviour may be partly explained by the post failure ultra-sonic C-scan of the specimens, Figure 6. The interpretation may be that as the temperature in the compression phase increases so the corresponding delamination propagation band decreases, suggesting that the effective delamination extent is reduced [1].

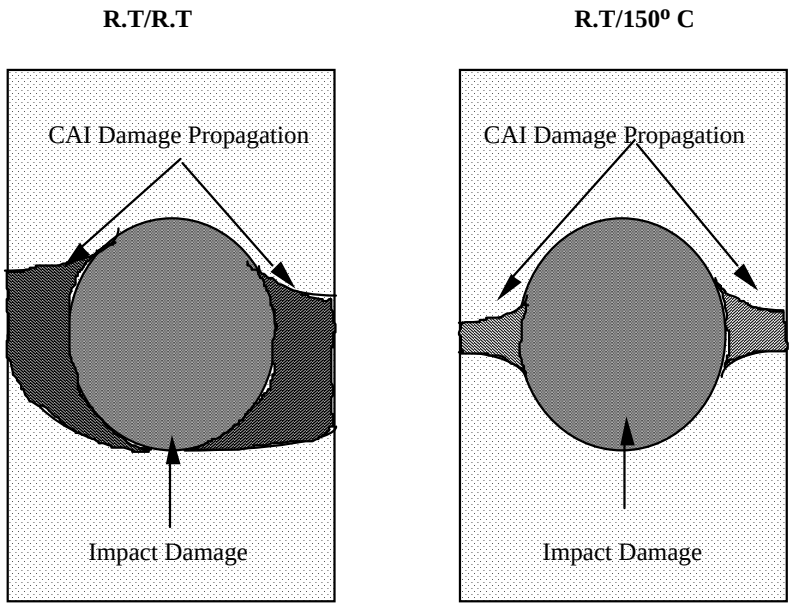

Figure 6: Schematic representations of room temperature impact and the subsequent propagation of delaminations at: i) room temperature and ii) 150 ^{o}C

Glass/Epoxy

The trends observed in the carbon/epoxy composite in terms of undamaged strength may also be achieved through an increased presence of moisture in the composite. This, acting concert with the hydrophilic nature of glass fibres (attack of the interface leading to irreversible degradation) may further reduce fundamental properties [6].

The reduction in damage extent in the conditioned samples may be due to plasticisation of the matrix and reduction of the interfacial bond. This concentration of damage was linked to an increase in crack density through the thickness of the laminate beneath the point of contact [7]. This mechanism may be more severe than wide spread delamination and might responsible, in conjunction with general matrix and fibre/matrix degradation, for the poor compression after impact strength. However, the presence of damage prior to exposure may be expected to further encourage fracture through extension of existing matrix and delamination cracks leading to further reductions in residual strength, but this was not the observed behaviour and may be due more to the changes in basic strength through exposure.

An Interpretation of the CAI Relevancy to Extreme Condition Testing

The combinations of test conditions for the carbon/epoxy specimens listed in the matrix (Table 1) reflect a range of potential temperatures when impact may occur, however, it must be emphasised that these specimens were mechanically unstressed, which, particularly at high temperatures, may not be the case as the aircraft may be in flight. Consequently, the damage may be greater, resulting in possible catastrophic failure by either penetration or immediate delamination propagation induced by the pre-stressed state of the structure. Similar concerns may be raised in regard the data generated by the hygrothermal testing.

Conventional wisdom has had the compression after impact strength analysed solely on the basis of impact energy. The behaviour of the materials investigated in this programme clearly showed that this may lead to erroneous interpretations of the data.

It is a recipe for disaster if the essential elements of composite durability are not incorporated in damage tolerance tests as room temperature data may not be extrapolated. The performance of the 924C is surprisingly good when compared on the basis of its undamaged strength at temperature, exceeding that of the room temperature data. This result may not have been expected given the increase in damage extent with temperature.

In contrast, the mechanisms associated with hygrothermal testing may at first glance appear insignificant, in terms of undamaged strength for these conditions, however, the near penetration of the laminate may have more serious consequences.

It has been argued in previous papers that the accepted approach to compression after impact test analysis, whereby the residual strength is assessed as a function of impact energy is misleading [8,9]. This is because the separate phenomena of damage creation and damage propagation are not distinguished. The environmental influence of either temperature or exposure to moisture clearly exacerbates this problem. In some instances damage size is largely irrelevant, in others strength is linked to initial damage size. In some cases all damage propagates (sideways), in others only partial propagation occurs. Consequently, simple trends observed between materials at room temperature and without long term environmental exposure can not be assumed to continue under more aggressive test conditions. Materials

that appear relatively good (compared to others) at room temperature and low humidity can not be relied upon to hold the same relative position in any table of performance with hot or wet test conditions.

CONCLUSIONS

The link between impact damage size and the residual compression strength varies according to the temperature at testing and the environmental history of the specimen.

Now that composites are readily achieving more extensive acceptance among engineering sectors it is now critical that stock is taken of where these materials have reached new applications and examine their suitability, before a catastrophic failure results in confidence being undermined and their usage set back a number of years.

Misadventure and a lack of understanding of what the damage tolerance test provides may require more infrastructure around the basic test to facilitate better judgement and interpretation of the materials suitability to the chosen application.

ACKNOWLEDGEMENTS

The authors are grateful to the Engineering and Physical Sciences Research Council (EPSRC), the Defence Research Agency (DRA) and the National Physical Laboratory (NPL) for supporting this programme of work.

REFERENCES

1. Bibo, G. A., Hogg, P. J. and Kemp, M., “High-temperature damage tolerance of carbon fibre-reinforced plastics: 2. Post-impact compression characteristics”, *Composites*, Vol. 26, No. 2, 1995, pp 91-102.

2. Mensitieri, G., Apicella, A., Nicolais, L., and Del Nobile, M. A., “Progress in durability analysis of composite systems”, A. Cardon et al Eds , A A Balkema Publishers, Rotterdam, 1996, pp 249-258.

3. Bishop, S. M., “The mechanical performance and impact behaviour of carbon-fibre reinforced PEEK”, *Composite Structures*, 3, 1985, pp 295-318.

4. Fisher, J. M., Palazotto, A. N. and Sandhu, R. S., “A study of failure characteristics in thermoplastic composite material at (250 ^{o}C) 121 ^{o}C, *Composites Technology and Research*, Vol. 13, No. 3, 1991, pp 152-160.

5. Lifshitz, J. M., “Strain rate, temperature and humidity influences on strength and moduli of a graphite/epoxy composite”, *Composites Technology Review*, Vol. 4, No. 1, 1982, pp 14-19.

6. Wyatt, R. C. and Ashbee, K. H. G., Fibre Science and Technology, Vol. 2, 1969, pp 29-40.

7. Hogg, P. J. and Kay, M. L., "The effect of environment on the damage tolerance of glass and carbon fibre reinforced epoxy laminates", *Deformation and Fracture of Composites*, Manchester, UK, 1997, Institute of Materials.

8. Prichard, J. C. and Hogg, P. J., "The role of impact damage in post-impact compression testing", *Composites*, Vol. 21, No. 6, 1990, pp 503-511.

9. Bibo, G. A., Hogg, P. J. and Kemp, M., "Damage tolerance of UD tape and textile glass reinforced epoxy", *3rd International Conference on Deformation and Fracture of Composites*, Surrey, UK, 1995, pp 374-383.

MECHANICAL BEHAVIOUR OF CARBON/MODIFIED BISMALEIMIDE COMPOSITES AT ELEVATED TEMPERATURES

X.J. Xian, F.G. Shin, C.L. Choy

Department of Applied Physics and Materials Research Center
The Hong Kong Polytechnic University, Hong Kong

SUMMARY: The fracture toughness K_{1c} , interlaminar shear strength τ_{ILSS} and tensile strength σ_t of composites of carbon fiber T300 reinforced modified bismaleimide QY8911 (T300/MBMI) have been investigated in the temperature range 20-200^{o}C. These are compared with the corresponding results for carbon fiber composites with epoxy matrix (T300/EP). In-situ observation of the above experiments in the scanning electron microscope has provided indications of important characteristics of dynamic crack propagation and delamination development. T300/MBMI composites are found to have higher K_{1c}, τ_{ILSS}, and σ_t than the epoxy based composites. In general, the MBMI composites show a higher temperature resistance and lower crack and delamination propagation rates, and are thus superior to the epoxy based composites. This is so because of the greater thermal stability and toughness and better interfacial adhesion in the modified BMI matrix material. The failure mechanisms of the composites are investigated by analyses of SEM fractographs. Of the three mechanical properties studied, interlaminar shear strength is most affected by temperature.

KEYWORDS: carbon fiber reinforced modified bismaleimide composites, mechanical behaviour, fracture toughness, interlaminar shear, microstructure, elevated temperature

INTRODUCTION

Advanced fiber reinforced polymer matrix composites, as a class of high performance materials, finds major use in structural applications. Very often, a judicious choice of the matrix material can enable special requirements to be met in particular applications. Epoxy resins are most popularly used in high performance fiber composites. Disadvantages of epoxy-based composites, however, include low fracture toughness, low delamination resistance and poor performance in a hot/wet environment. These reflect the inherent brittleness and low thermal resistance of the epoxies. Compared to the epoxies, bismaleimide (BMI) resins exhibit better thermal as well as humidity resistance, and are thus more suited to be used in demanding environments. BMIs are, however, brittle and difficult to process [1], and various chemical and physical modifications are the subject of active investigation.

This work makes use of a modified bismaleimide resin, QY8911 (MBMI-1), reported in [2]. This MBMI-1 resin has good processability and possesses better toughness than BMI while retaining the original advantages in thermal stability. We have previously investigated the impact resistance [3] and the fracture fatigue [4] as well as the interlaminar fracture [5] behaviour of carbon fiber reinforced MBMI-1 composites (CF/MBMI-1) under room temperature conditions.

In the present work, the fracture toughness, interlaminar shear strength and tensile strength of CF/MBMI-1 composites are evaluated at elevated temperatures and comparison of performance with epoxy-based CF composites is made. To gain an understanding of the thermal fracture and delamination processes, experiments have also been performed in a scanning electron microscope with in-suit heating and loading capabilities. We aim to provide an evaluation of the thermal resistance as well as to elucidate the high temperature failure mechanisms in CF/MBMI-1 composites.

SPECIMENS AND EXPERIMENTAL METHODS

The specimens were made from T300 carbon fiber with modified bismaleimide QY8911 (T300/MBMI-1) and epoxy EP618 (T300/EP) matrices. The MBMI-1 resin was prepared by incorporating a dispersion of thermoplastic PES particles in BMI resin [2]. The elongation at break of MBMI-1 (2.2%) matches that of T300 carbon fiber. The tensile strength and modulus of MBMI-1 are 66 MPa and 3.5 GPa, respectively, and are higher than the corresponding epoxy values. The fiber volume fraction in the composites was approximately 65%; [0] and [±45] lay-ups were prepared from unidirectional prepregs of thickness 0.11 mm. The quality of the laminates was examined by the ultrasonic C-scan technique before test. Specimen dimensions conformed with ASTM D3039-76 for test of tensile strength, ASTM D2234-84 for interlaminar shear strength and ASTM E399 for fracture toughness. Testing was performed on an Instron 1175 machine with an auxiliary high temperature oven. Fracture and short beam shear tests were also carried out on a Cambridge S-250 scanning electron microscope (SEM) with in-situ heating and loading capabilities. For SEM study, specimen dimensions were reduced in proportion to the ASTM size. The damage process and dynamic crack propagation could be observed and photographed in the SEM loading stage. Experiments in this study were performed at room temperature 20^{o}C as well as at elevated temperatures (150 and 200^{o}C).

COMPARISION OF CARBON FIBER REINFORCED MODIFIED BISMALEIMIDE AND EPOXY COMPOSITES

The fracture toughness K_{1c}, interlaminar shear strength τ_{ILSS} and tensile strength σ_t of T300/MBMI-1 [0] (U-B), T300/MBMI-1 [±45] (M-B), T300/Epoxy [0] (U-E) and T300/EP [±45] (M-E) specimens at various temperatures are shown in Table 1.

Table 1: Comparison of mechanical properties of carbon fiber T300 reinforced MBMI-1 and EP618 composites at elevated temperatures

Specimen Type	Symbol	T ^oC	Tensile Strength σ_t(MPa)	R(%)	Interlaminar Shear τ_{ILSS} (MPa)	R(%)	Fracture Toughness K_{1C} (MPa$\sqrt{m}$)	R(%)
T300/MBMI-1 [0]	U-B	20	1327	100	90.1	100	46.4	100
		150	1163	88	54.7	61	41.6	90
		200	617	47	26.1	29	27.8	60
T300/EP618 [0]	U-E	20	1275	100	72.8	100	30.6	100
		150	1049	71	12.4	17	18.0	59
		200	470	37	7.3	10	15.3	50
T300/MBMI-1 [±45]	M-B	20	102	100	28.6	100	26.4	100
		150	72	71	4.9	17	5.1	19
		200	35	34	2.6	9	2.8	11
T300/EP618 [±45]	M-E	20	94	100	26.3	100	19.7	100
		150	52	56	2.3	9	2.4	12
		200	20	21	1.5	6	1.8	9

R-Retention Rate, MBMI-1 - Modified BMI Resin, EP618 - Epoxy Resin

Fracture Toughness

The room temperature fracture toughness K_{1c} value of U-B (resp. M-B) is 46.4 MPa$\sqrt{m}$ (26.4 MPa$\sqrt{m}$), and is 52% (34%) higher than that of U-E (resp. M-E). At 150^{o}C, the retention rate R of K_{1c} in U-B (resp. M-B) is 90% (19%) and is 31% (7%) better than in U-E (resp. M-E). At 200^{o}C, although the R values of the MBMI-1 and EP composites are comparable, the K_{1c} value of U-B (resp. M-B) is 82% (56%) larger than that of U-E (resp. M-E). The [0] composites are seen to be much less affected by temperature than the [±45] composites. MBMI-1 composites in either lay-up have greater fracture toughness than in the corresponding EP composites at all temperatures investigated. This is attributed to the greater toughness of MBMI-1 at room temperature and at elevated temperatures.

Interlaminar Shear Strength

The room temperature τ_{ILSS} value of U-B (resp. M-B) is 90.1 MPa (28.6 MPa) and is 24% (9%) higher than that of U-E (resp. M-E). At 150^{o}C, the R value in U-B (M-B) is 61% (17%) and is 44% (8%) better than that in U-E (resp. M-E). At 200^{o}C, the τ_{ILSS} value of U-B (resp. M-B) is 258% (73%) larger than that of U-E (resp. M-E). Again, the [0] composites are less affected by temperature than the [±45] composites. MBMI-1 composites in either lay-up have greater τ_{ILSS} than in the corresponding EP composites at all temperatures investigated because MBMI-1 has better interfacial adhesion properties. Deterioration in τ_{ILSS} in the [0] composites at elevated temperatures is much more marked than in the case of fracture toughness or tensile strength, and is therefore a sensitive performance indicator for the evaluation of a new matrix material.

Tensile Strength

The room temperature σ_t value of U-B (resp. M-B) is 1327 MPa (102 MPa) and is a little higher than that of U-E (resp. M-E). At 150°C, the R value in U-B (resp. M-B) is 88% (71%) and is 17% (15%) better than that in U-E (resp. M-E). At 200°C, the σ_t value of U-B (resp. M-B) is 31% (75%) larger than that of U-E (resp. M-E). In the [0] composites, σ_t is mainly determined by the fiber performance, thus σ_t differences between MBMI-1 and EP composites are minimal; the matrix contribution is seen to become more apparent in [±45] composites, with those based on MBMI-1 giving higher retention rates.

From the above experimental results, it is clear that the fracture toughness, interlaminar shear strength and tensile strength of T300/MBMI-1 composites are uniformly better than those of T300/EP, at room temperature as well as at elevated temperatures.

IN-SITU SEM OBSERVATION OF FRACTURE TOUGHNESS TEST

Single edge notched specimens with notch length to specimen width of 0.3 were subjected to three point bending fracture test in the SEM. Micrographs of the damage zone at the notch tip were taken during test. The fracture process followed the three stages : (1) initial cracking at notch tip, (2) crack propagation and development of damage, (3) failure and fracture.

For M-B (resp. M-E) at 150°C, cracks started to occur at the notch tip when the load level reached 60% (29%) of fracture load P_f, and propagated along the 45° interface direction with further load increase (Fig. 1) (resp. Fig. 2). Sudden failure occurred at 98% P_f (73% P_f) level. At this point, M-E failed by brittle fracture while with M-B more 45° cracks began to develop and complete fracture (Fig. 3) came at a slightly higher load. Comparing initial cracks, M-E also showed brittle cracking (Fig. 4), reflecting a break down of epoxy at the notch tip at 150°C. Overall, damage in M-B is much less extensive than in M-E, indicating MBMI-1 has a better thermal resistance than EP, and hence a higher fracture toughness for M-B.

For U-E at 200°C (150°C), the notch tip opened (Fig. 5) at 25% P_f (32% P_f) and started to propagate along the 0° interface direction at 30% P_f (49% P_f), resulting in more than one slip line (Fig. 6). The phenomenon of multiple slip lines does not normally occur in room temperature testing, and hence its occurrence suggests the thermal cracking of the epoxy matrix. For U-B, notch opening occurred at higher load levels, but U-B and U-E failed in similar ways.

IN-SITU SEM OBSERVATION OF INTERLAMINAR SHEAR STRENGTH TEST

Short beam shear tests were performed in the SEM. For U-B (resp. U-E) at 200°C, noticeable deformation occurred at 67% (27%) of the maximum load P_{max} , then shear delamination at 89% P_{max} (63% P_{max}). Beyond P_{max} , the load recovered after a slight decrease, followed by a succession of drops as interlaminar layers gave way. Fig. 7a (resp. Fig. 7b) shows the delamination failure of U-B (resp. U-E). Shear delamination in U-B is less serious than in U-E. Interface debonding as observed in between the outermost plies and matrix damage in U-B (Fig. 8) are not as severe as in U-E (Fig. 9) where the epoxy is smashed with broken fibers visible. The latter phenomenon does not occur in room temperature testing. For [±45] composites, failure also occurred via shear cracking at roughly 45° through the thickness of a

ply connecting adjacent delaminated interlaminar layers (Fig. 10). This is a result of the interface debonding of 45° plies which will not appear in [0] composites, manifesting in more noticeable thermal degradation of [±45] composites compared to [0] composites.

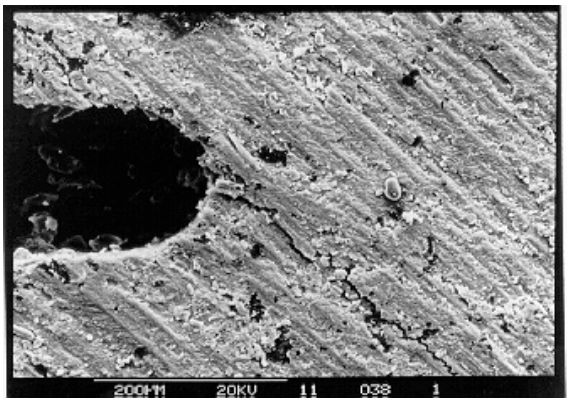

Fig. 1: Cracks propagate along interface direction in T300/MBMI [±45] specimen (150°C)

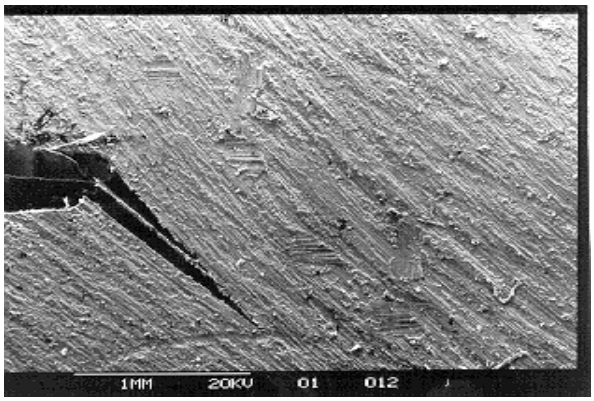

Fig. 2: Brittle cracking along 45° interface direction in T300/EP[±45] specimen (150° C)

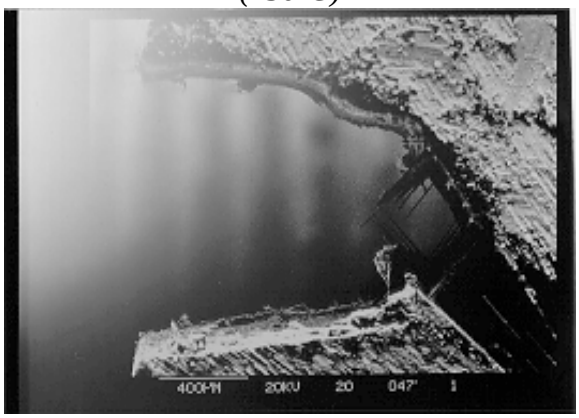

Fig. 3: Brittle fracture of T300/EP [±45] specimen (150°C)

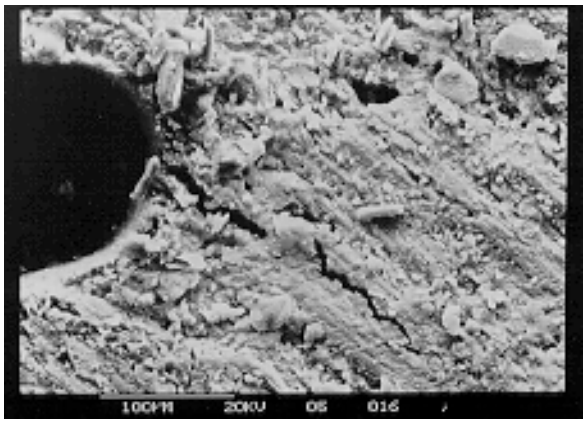

Fig. 4: Enhanced thermal resistance in T300/MBMI [±45] specimen (150°C)

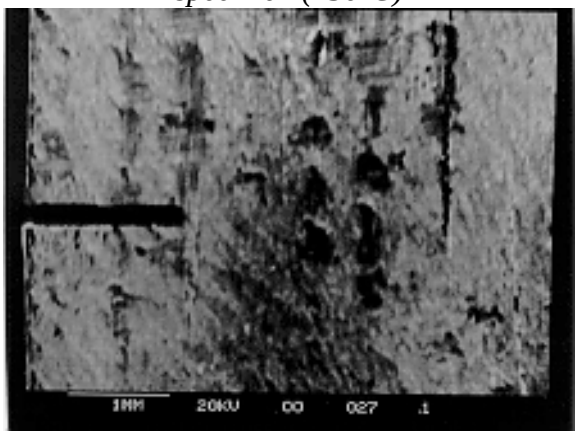

Fig. 5: Notch opening and cracking in T300/EP [0] specimen (200°C)

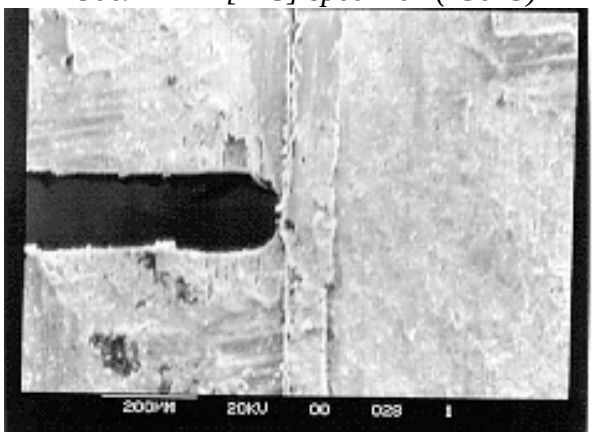

Fig. 6: Cracks propagate along 0° interface direction in T300/EP [0] specimen (200°C); more than one slip line is visible


(a) T300/MBMI [0] (b) T300/EP [0]
Fig. 7: Interlaminar shear failure at 200°C

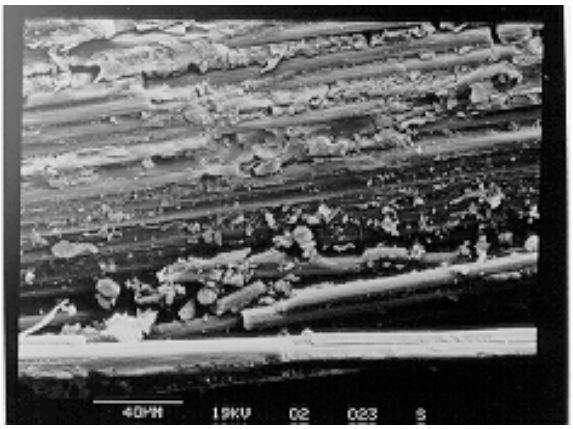

Fig. 8: Debonding in T300/MBMI [0] specimen (200°C)

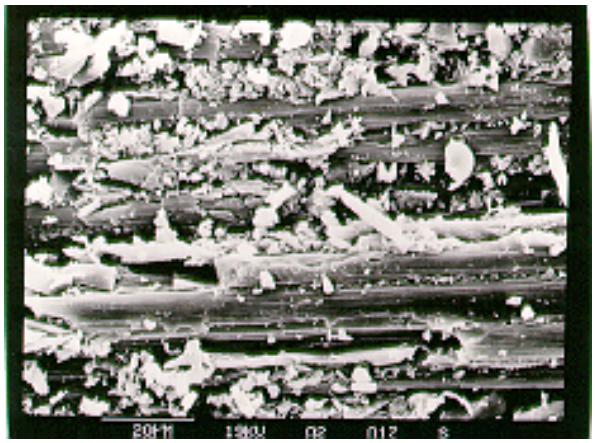

Fig. 9: Debonded matrix and broken fiber in T300/EP [0] specimen

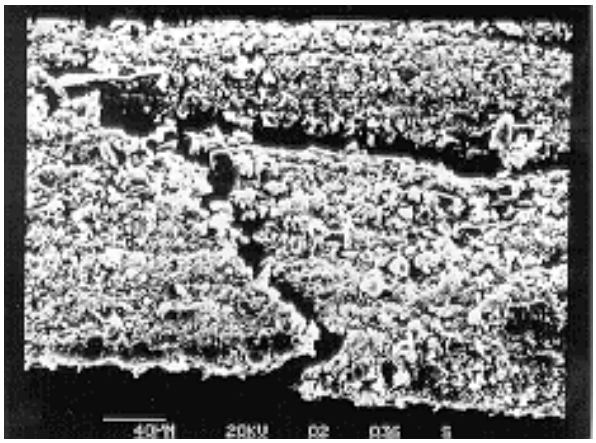

Fig. 10: 45° shear cracking through ply thickness in T300/MBMI [±45] specimen (150°C)

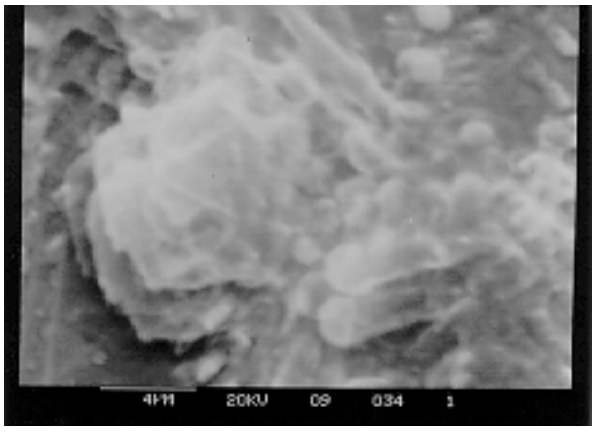

Fig. 11: Shear yielding in MBMI matrix at 200°C

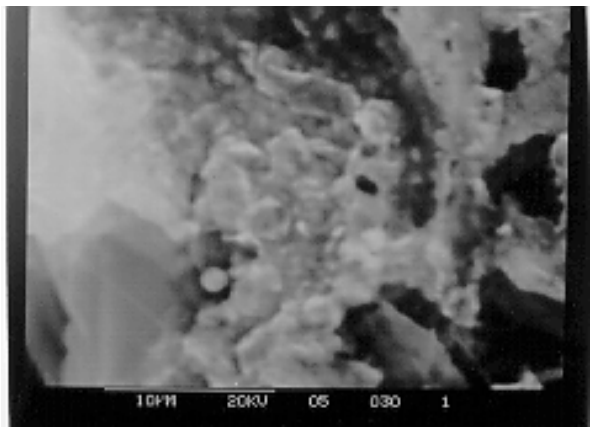

Fig. 12: Thermal cracking and decomposition of epoxy matrix (200°C)

RESIN DEGRADATION AT ELEVATED TEMPERATURES

Higher crosslink density and stiffer molecular chains contribute to the stronger interfacial adhesion in MBMI-1. At 200°C, the epoxy resin will experience thermal cracking as well as chemical decomposition, while MBMI-1 can still maintain good thermo-oxidative stability. Major decomposition of MBMI-1 resin occurs at approximately 390°C with glass transition at 257°C, which are higher than epoxy's 200°C and 150°C, respectively. Moreover, MBMI-1 is toughened by PES particles, with a high fracture work of 2381 N-m. Its elongation at break is 2.2%, which is 46% higher than epoxy's 1.5%, matching that of T300. All these contribute to an adequate fiber-matrix adhesion and to the occurrence of shear yielding in MBMI-1 composites even at elevated temperatures (Fig. 11). In epoxy composites at high temperatures, however, interface debonding as well as matrix cracking and decomposition often occur (Fig. 12).

CONCLUSION

(1) As a result of the good thermal resistance and thermal stability of MBMI-1, there is a high retention rate of mechanical properties, especially fracture toughness, in T300/MBMI-1 composites at elevated temperatures. In particular, the unidirectional MBMI-1 composites seem to be capable of working in 150°C service environments under all loading conditions investigated here, and perhaps also in 200°C environments to a limited extent. In all cases tested, MBMI-1 composites have a notable advantage over EP composites at 150°C.

(2) The PES-toughened MBMI-1 resin gives MBMI-1 [0] and MBMI-1 [±45] composites 52% and 34% more fracture toughness than that found in EP [0] and EP [±45] composites, respectively. The good room-temperature toughness of MBMI-1 composites also offers potential for practical applications.

(3) The thermal fracture mechanisms and failure processes of the carbon fiber MBMI-1 and EP composites have been characterized by in-situ observation of tests performed in the SEM. In MBMI-1 composites, delamination as well as notch tip blunting and cracking are delayed by the toughened matrix, especially at elevated temperatures. Interfacial adhesion and bonding tend to be less affected by temperature. However, in EP composites, the brittle nature and the lower thermal resistance of epoxy lead to earlier occurrence of initial cracking, faster crack propagation rates and more serious delamination. At elevated temperatures, cracks propagate along the fiber direction as is the case at room temperature. There are, however, more slip lines in the thermal environment. In both MBMI-1 and EP composites, interlaminar cracking through the ply thickness also occur in [±45] composites, resulting in more serious thermal degradation than in [0] composites. The thermal degradation in interlaminar shear strength is more marked than in fracture toughness or tensile strength; this is because the effect of debonding has less influence on tension and fracture. Important thermal degradation mechanisms for the carbon fiber composites studied include matrix cracking, interface debonding and matrix decomposition, the latter being a limiting factor for the performance of EP composites at 200°C.

(4) Our results indicate that MBMI-1 has high temperature resistance and good toughness and MBMI-1 based carbon fiber composites can retain a useful fraction of room

temperature mechanical performance when tested at elevated temperatures. It appears that these composites are suitable for use at service temperatures of up to 150^{o}C. Together with the good processability of the MBMI-1 resin, there is a substantial potential for MBMI-1 composites to find a variety of applications.

ACKNOWLEDGMENTS

This work is supported by the Croucher Foundation of Hong Kong and The Hong Kong Polytechnic University. We are grateful to Mr. D.Y. Li for carrying out some of the measurements.

REFERENCES

1. Byung, H., Lee, M., Ashraf, C. and Yefin, B., "Recent Development of High Performance Bismaleimide Resins", *Polymer News*, Vol. 13, 1988, pp. 297-301.

2. Zhao, Q.S., Li, Y.H., Cao, Z.H. and Sun, D.S., "New Modified Bismaleimide Resin for Graphite Composites", *Proc. of SAMPE* 34th, 1989, pp. 27-32.

3. Xian, X.J. and Choy, C.L., "Impact Resistance and Damage Evaluation of Carbon Reinforced Modified Bismaleimide Composites", *Journal of Reinforced Plastics and Composites*, Vol. 13, December 1994, pp. 1135-1153.

4. Xian, X.J. and Choy, C.L., "Fatigue Fracture Behaviour of Carbon Fiber Reinforced Modified Bismaleimide Composites", *Composite Science and Technology*, Vol. 52, 1995, pp. 93-98.

5. Xian, X.J. and Choy, C.L., "The Interlaminar Fracture Behaviour and Toughening Mechanism of New Carbon Fiber Reinforced Bismaleimide Composites", *Composites*, Vol. 26, No. 1, 1995, pp. 33-39.

EVALUATION OF ULTIMATE STRENGTH OF HIGH TEMPERATURE COMPOSITE MATERIALS FOR SST STRUCTURES AT ELEVATED TEMPERATURES AND AFTER THERMAL AGING

Toshiyuki Shimokawa[1], Yasumasa Hamaguchi[1], Yoshiaki Kakuta[1], Hisaya Katoh[1], Tomio Sanda[2], Hiroshi Mizuno[3], and Yasuhiro Toi[4]

[1]Airframe Division, National Aerospace Laboratory,
6-13-1 Ohsawa, Mitaka, Tokyo 181, Japan
[2]Airframe Technology Research Department, Gifu Technical Institute,
Kawasaki Heavy Industries, LTD., 1 Kawasaki, Kakamigahara 504, Japan
[3]Engineering Research Department, Nagoya Aerospace Systems,
Mitsubishi Heavy Industries, LTD., 10 Oye, Minato, Nagoya 455, Japan
[4]Aerospace Division, Utsunomiya Plant, Fuji Heavy Industries, LTD.
1-1-11 Yonan, Utsunomiya 320, Japan

SUMMARY: The objective of this experimental study was to evaluate the effect of thermal aging on the ultimate strength of three kinds of carbon/high-temperature polymer composite materials, which are current candidate structural materials for a super sonic transport of the next generation. The notched and unnotched panels, before being machined to specimens, were aged at 120°C and 180°C for up to 15,000 hours. Static tests at room and elevated temperatures before and after thermal aging provided the notched tensile, notched compressive, and short beam shear strengths. Moreover, the effects of five oxidation resistant treatments on notched compressive strength at 180°C were investigated after thermal aging of 5,000 hours at 180°C. The obtained results were presented and a possibility to develop an accelerated environment test methodology is examined.

KEYWORDS: bismaleimide composites, thermoplastic polyimide composite, super sonic transport, notched strengths, short beam shear strength, thermal aging, oxidation resistant treatments, accelerated test methodology

INTRODUCTION

The structures of super sonic transports (SST) of the next generation require long term durability of structural materials in environments that include temperature, loads, and fluids, not only in constant states, but also during cyclic fluctuations. Moreover, the structural weights must be drastically reduced to achieve commercial success. This requirement demands a wide application of high temperature polymer composite materials.

Many fundamental studies have been conducted for investigating oxidation, micro-cracking, and weight loss by thermal aging, creep, etc. on high temperature polymer composites.

However, only a few results [1,2] are found suitable to directly evaluate their practicality for the SST structures.

As a part of structural material evaluation for a SST of the next generation, this study investigated the strength degradation of high temperature composites by thermal aging, the effects of oxidation resistant treatments, and a possibility to establish accelerated test methodology to simulate environmental conditions encountered by SSTs in their lives. Namely, the tensile and compressive strengths of notched specimens, and the short beam shear (SBS) strength were investigated for three kinds of carbon/high-temperature polymer composites at room and elevated temperatures, before and after thermal aging of up to 15,000 hours. In addition, composite panels were given five kinds of oxidation resistant treatments and thermally aged. The effects of these treatments on notched compressive strength were examined. The obtained test results are evaluated and the possibility of developing an accelerated test method is discussed using a modified Larson-Miller type equation.

MATERIALS, SPECIMENS, AND TEST PROCEDURE

The three kinds of carbon/high temperature polymer composite laminates tested were made of two kinds of carbon/bismaleimide prepreg systems, G40-800/5260 (NARMCO) and MR50K/ MR2000N (Mitsubishi Rayon Co.), and a carbon/amorphous thermoplastic polyimide prepreg system, T800H/PI-SP (Mitsui Toatsu Co.), which are current candidate composites for the SST structures.

The two kinds of panels with quasi isotropic stacking sequences, 24 plies $(45/0/-45/90)_{3S}$ for tensile notched specimens, and 32plies $(45/0/-45/90)_{4S}$ for compressive notched specimens, were circular-hole notched before thermal aging. The panels for SBS specimens were a unidirectional laminate, 20 plies (0_{20}). These panels were isothermally aged for 5,000, 10,000, and 15,000 hours at 120°C or 180°C in air circulating ovens. Specimens were machined from virgin and thermally aged panels. Figure 1 shows the geometry of panels for thermal aging and specimens tested.

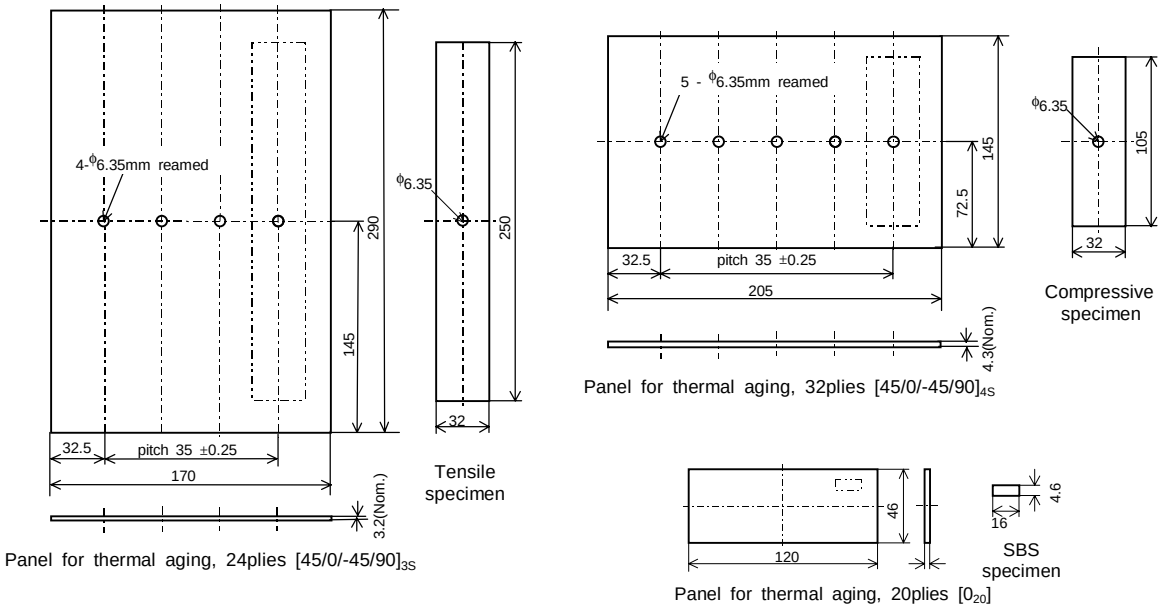

Fig. 1: Geometry of panels for thermal aging and specimens tested; dimensions in mm

Prior to static tests, specimens were dried in a vacuum oven for 6 hours at 70°C and then for 144 hours at 110°C. Static tests were conducted at room and thermal aging temperatures. Moreover, the surfaces of the MR50K/MR2000N panels were given five kinds of oxidation resistant treatments. The effects of these treatments on notched compressive strength at 180°C were investigated after thermal aging of 5,000 hours at 180°C.

The notched tensile and notched compressive strengths are represented by nominal strength calculated using the nominal thickness based on the nominal prepreg thickness and the net width. The SBS strength is represented by net strength calculated using the measured thickness.

TEST RESULTS

Notched Tensile Strength of G40-800/5260 Composite After Thermal Aging

Two batches of G40-800/5260 laminates were produced, and four specimens were used for each test. Figure 2 presents the relationship between notched tensile strength and thermal aging time separated by the batches A and B. The presence of the strength degradation by thermal aging at 120°C is not clear. It is a future problem to elucidate that the obtained results are within a scatter band, or that the strength slightly decreases with thermal aging time. In the case of thermal aging at 180°C, fairly large strength degradation appeared. Thermal aging time over 15,000 hours is necessary to know if the strength degradation will saturate like in metallic materials [3]. The strengths at room and thermal aging temperatures, at the same aging time, are close for either thermal aging at 120°C or 180°C. A small difference between the two batches of specimens appeared in the strength and degradation with thermal aging time, as shown in Fig. 2.

There is no example to show the large scatter in notched tensile strengths observed for each experimental condition, i.e., a combination of test temperature, aging temperature, and thermal aging time.

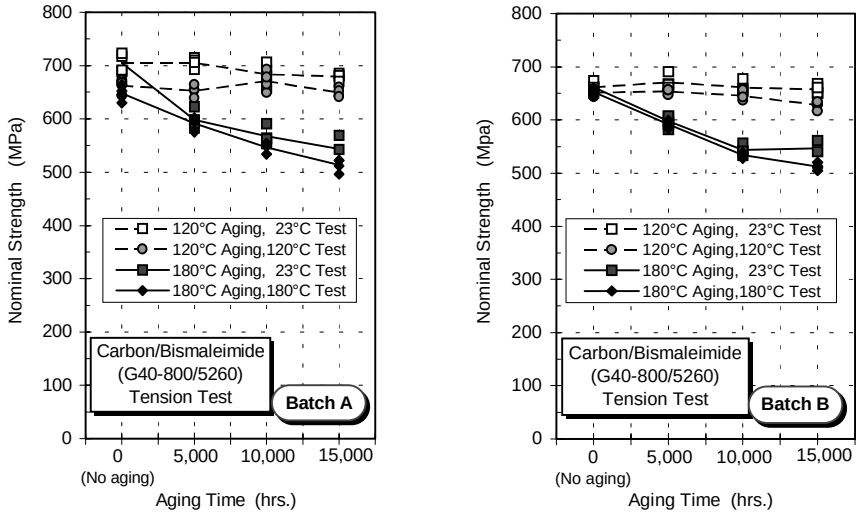

Fig. 2: Notched tensile strength of G40-800/5260 carbon/bismaleimide composite versus thermal aging time for two batches A and B

Notched Compressive Strength After Thermal Aging

Figure 3 shows the relationships between notched compressive strength and thermal aging time for the three kinds of high temperature polymer composites. Five specimens were used for each test in Fig. 3, except for a special case.

In the case of the G40-800/5260 bismaleimide composite and thermal aging at 120°C, the strength at room temperature does not reduce with thermal aging time, but that at 120°C slightly reduces. In the case of 180°C aging, the strength remarkably decreases with thermal aging time, and after 5,000 hours, this drop is almost proportional to thermal aging time. A similar trend of the notched compressive strength of a IM7/5260 composite at room temperature was reported by Rogalski [1]. The difference of the strengths at room and thermal aging temperatures at the same aging time are fairly large for thermal aging at both 120°C and 180°C. This is different from the notched tensile strength in Fig. 2.

In the case of the MR50K/MR2000N bismaleimide composite and thermal aging at 120°C, the strength at 120°C shows a slight drop after thermal aging of 15,000 hours. In the case of thermal aging at 180°C, the strength significantly decreases with thermal aging time. The strength degradation is especially great from 5,000 to 10,000 hours, and dulls after 10,000 hours.

In the case of the T800H/PI-SP polyimide composite, non-aged strengths at room temperature and 180°C are slightly lower in comparison with those of the other two materials. However, the strength degradation by thermal aging at 120°C and 180°C, up to 15,000 hours, was not found.

There is no example to show the large scatter in notched compressive strengths observed for each experimental condition and the three materials.

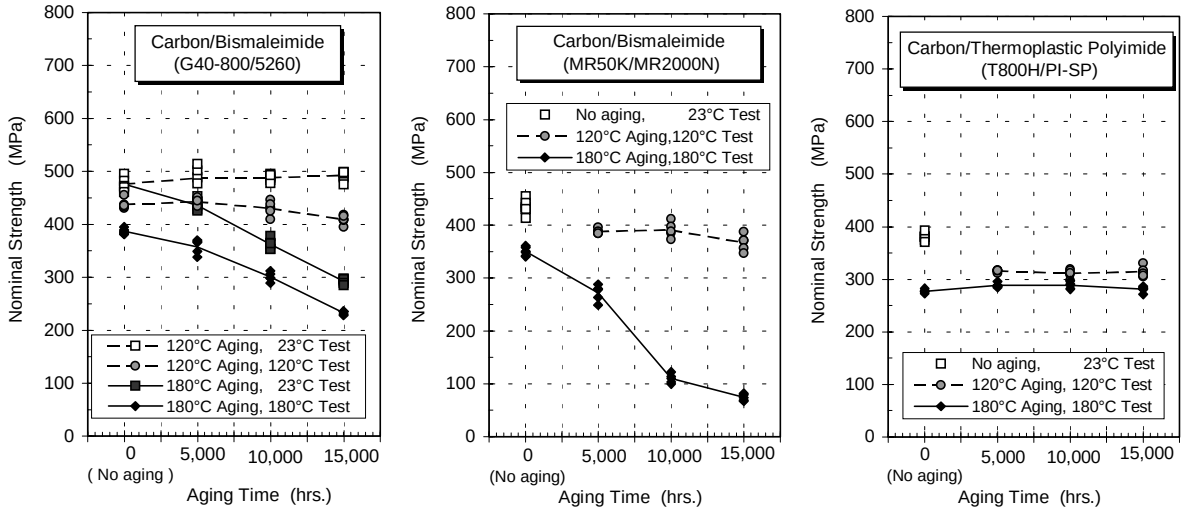

Fig. 3: Notched compressive strength versus thermal aging time for three kinds of high temperature composites

Short Beam Shear Strength After Thermal Aging

In SBS tests, various behaviors appeared in the relationship between the central displacement of a SBS specimen and load, according to the combination of material, test temperature, thermal aging temperature, and thermal aging time. Therefore, it was difficult to physically define the SBS strength in a way common to all cases. The SBS strength in this study is represented by the maximum stress which can be commonly determined for all test cases, though this definition is questionable as a SBS strength.

Figure 4 depicts the obtained results of SBS strength versus thermal aging time for three kinds of high temperature composites. The test number is fundamentally five for each case.

In these cases, for both carbon/bismaleimide composites, the SBS strengths at room temperature and at 120°C, did not drop after thermal aging at 120°C. The SBS strengths of the G40-800/5260 composite at room temperature and 180°C, after thermal aging at 180°C, reduced with fluctuations. In this material, the difference of strengths at room and thermal aging temperatures, at the same aging time, are large for thermal aging at bothe 120°C and 180°C. This difference is largest among the notched tensile, notched compressive, and SBS strengths, as presented in Figs. 2, 3, and 4.

The SBS strength of the MR50K/MR2000N composite at 180°C indicated a fairly large drop with thermal aging time. The scatter of the SBS strength was high after the thermal aging at 180°C.

In the case of the T800H/PI-SP composite, there was no reduction of the SBS strength after thermal aging at 120°C and 180°C.

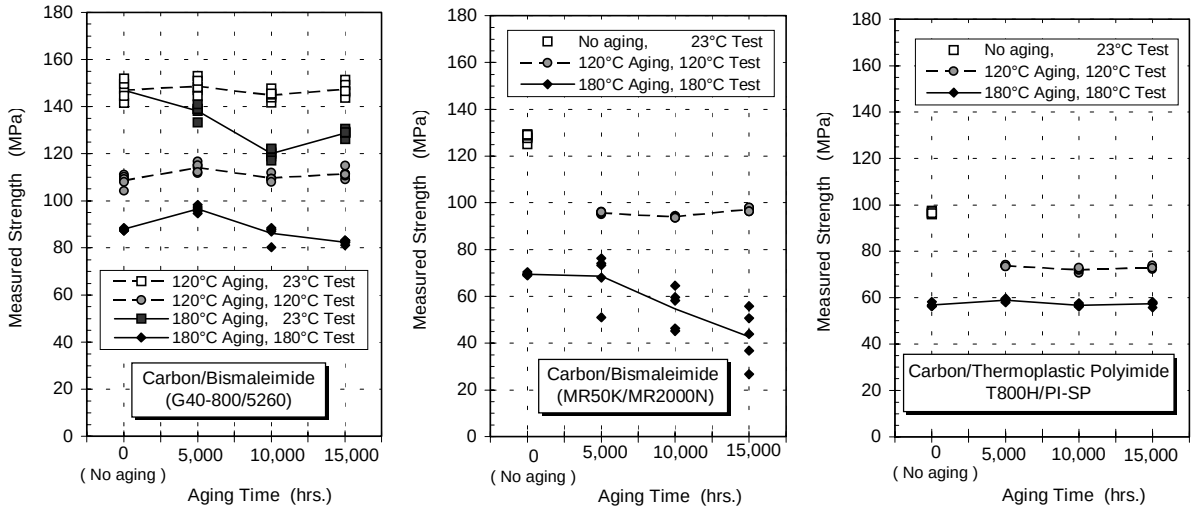

Fig. 4: Short beam shear (SBS) strength versus thermal aging time for three kinds of high temperature composites

Effect of Oxidation Resistant Treatment on Notched Compressive Strength

The notched compressive strength of the MR50K/MR2000N composite was heavily reduced by thermal aging at 180°C, as shown in Fig. 3. With respect to this material, the following oxidation resistant treatments against circulating hot air were given to the panels to be

thermally aged, and the effects of these treatments on notched compressive strength were investigated. Six panels of a new batch were made. They were of the same size indicated in Fig. 1, and their surfaces and sections were given the following oxidation resistant treatments. **A**: no treatment given to get base data, **B**: holes were bolted, **C**: holes and sections were sealed by a bismaleimide resin, **D**: full surfaces and sections were painted by a thermal protection paint, **E**: only holes and sections were painted by the same paint, **F**: covered by a glass fiber cloth. The main element of the thermal protection paint used was silicon.

Notched compressive specimens were machined from each panel after thermal aging of 5,000 hours at 180°C. Compression tests were conducted at 180°C. Each case was tested four times and the results obtained are presented in Fig. 5. In order to compare these results with the strengths obtained at room temperature with no thermal aging, and those at 180°C after thermal aging of 5,000 hours at 180°C in Fig. 3, the data of Fig. 3 were also plotted in Fig. 5.

The strengths at 180°C of the unprotected panels from different batches after the thermal aging are slightly different. This is considered to originate from the difference of the two batches. The strength of the unprotected panel **A** and those of the protected panels **B**, **D**, **E**, and **F** are almost equal. Therefore, the protections **B**, **D**, **E**, and **F** had no effect on notched compressive strength. The protection **C** improved the average strength to only approximately 10% higher than those of the other cases. This indicates a very important fact that if an appropriate protection method is selected, the strength degradation can be improved.

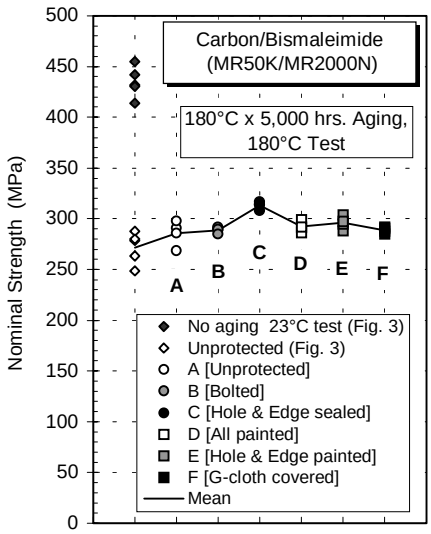

Fig. 5: Effect of oxidation resistant treatment on the notched compressive strength of MR50K/MR2000N carbon/bismaleimide composite

DISCUSSION

Characteristics of High Temperature Composite Materials

In the case of two kinds of bismaleimide composites, microscopic observation of the surfaces and sections indicated that the degradation by thermal aging at 180°C was produced mainly by the matrix oxidation and micro-cracking in and inter the layers. No significant degradation caused by thermal aging at 120°C was found on the panels of both bismaleimide composites.

The upper limit of applicable temperature for both bismaleimide composites is considered to be higher than 120°C, but lower than 180°C. It is necessary to find the upper limit between the two temperatures. Moreover, the notched compressive strength of these materials at 120°C, after thermal aging at 120°C, indicated a trend of slight degradation. Meanwhile, Rogalski presented no degradation of the notched compressive strength of the IM7/5260 bismaleimide composite at room temperature after thermal aging of 16,000 hours at 149°C [1]. In order to discern this problem, it is necessary to conduct static tests at elevated temperatures after thermal aging longer than 15,000 hours.

In the G40-800/5260 composite, the ascending order of the strength differences at room and aging temperatures, at the same aging time, is notched tensile strength, notched compressive strength, and SBS strength.

Figures 3 and 4 present promising results for the T800H/PI-SP thermoplastic polyimide composite; however, micro-cracks were observed after thermal aging at 120°C and 180°C in both outer and inner layers. To prevent micro-cracking is an issue of vital importance for this material.

In comparison of the test results in Fig. 4 with those in Fig. 3, the degradation tendency in notched compressive strength and SBS strength is a bit different for both bismaleimide composites after thermal aging at 180°C. However, the notched compressive strength did not drop when no degradation appeared in the SBS strength, such as the SBS strength at room temperature and 120°C, after thermal aging at 120°C, and those of T800H/PI-SP composite at 120°C and 180°C, after thermal aging at 120°C and 180°C respectively. These results provide a rough suggestion that no degradation of SBS strength means no degradation in notched compressive strength.

A large scatter in the data points was observed in the SBS strength of the MR50K/MR2000N composite after thermal aging at 180°C. Except for these cases, the scatter of test results is considerably small.

Application of a Modified Larson-Miller Equation in Analyzing the Strength After Thermal Aging

Shimokawa and Katoh modified Larson-Miller's equation, which is generally applied in analyzing the creep strength of metals, as

$$\ln S = (a + b \cdot T) + (c + d \cdot T) \ln L \,, \tag{1}$$

and used to analyze the strength of light metallic materials after thermal aging [3]. Strength is denoted by S, temperature by T, aging time by L. a, b, c, and d are parameters. Original Larson-Miller's equation is given by c=0.

Equation (1) indicates that if T is constant, ln$S$ and ln$L$ have a linear relationship. If at least the test results satisfy this relationship, an accelerated thermal aging test can be performed. The test results given in Figs. 2, 3, and 4 are separately plotted on double logarithmic graph paper, though they are not presented here. Equation (1) is considered to be not applicable for the test results except for the notched compressive and SBS strengths of the T800H/PI-SP composite. They were unchanged with thermal aging time. Meanwhile, Eq. (1) can be applied

for only the data within a limited range of aging time. This problem is left for future investigation.

CONCLUSIONS

The notched tensile, notched compressive, and short beam shear strengths of two kinds of bismaleimide composites and a kind of thermoplastic polyimide composite were investigated at room and thermal aging temperatures, before and after thermal aging, up to 15,000 hours. Major conclusions obtained are as follows:

(1) In the case of the G40-800/5260 bismaleimide composite, the degradation of notched tensile strength by thermal aging at 120°C was not clear. Although the notched compressive strength at room temperature was not reduced by thermal aging at 120°C, this strength at 120°C slightly decreased after thermal aging of 15,000 hours. The latter fact was also identical for the MR50K/ MR2000N bismaleimide composite.
(2) Significant reduction was observed in the notched tensile, notched compressive, and SBS strengths of both G40-800/5260 and MR50K/MR2000N composites after thermal aging at 180°C.
(3) In the case of the G40-800/5260 composite, a small difference between the specimens of two batches appeared in the notched tensile strength and its reduction with thermal aging time.
(4) The upper limit of practically applicable temperatures for both G40-800/5260 and MR50K/ MR2000N composites is considered to be between 120°C and 180°C, though the notched compressive strength of both materials at 120°C should be investigated, even after thermal aging at 120°C for longer than 15,000 hours.
(5) In the case of the G40-800/5260 composite, the ascending order of the strength differences at room and aging temperatures, at the same aging time, is notched tensile strength, notched compressive strength, and SBS strength.
(6) No degradation of notched compressive and SBS strengths was observed for the T800H/PI-SP thermoplastic polyimide composite after thermal aging at 120°C and 180°C up to 15,000 hours.
(7) Only one kind of oxidation resistant treatment provided a slight improvement of the notched compressive strength of the MR50K/MR2000N composite after thermal aging of 5,000 hours at 180°C.
(8) Large scatter was observed only in the SBS strength of the MR50K/MR2000N composite after thermal aging at 180°C.
(9) At least the relationship between strength and thermal aging time, under a constant aging temperature, must be linear on double logarithmic graph paper for an accelerated thermal aging test using a modified Larson-Miller's equation. In the case of thermal aging at 180°C, this kind of relationship was not observed for both bismaleimide composites.

REFERENCES

1. Rogalski, M.E., "Aging of Polymeric Materials for Use on HSCT," SAE Technical Paper Series 942162, SAE International, 1994.

2. Poole, E.L. and Lin, K.Y., “Effects of Aging on Compressive Strength of Composites After Impact,” AIAA-94-1532-CP, Proc. 35th SDM Conf., American Institute of Aeronautics and Astronautics, 1994, pp. 1683-1690.

3. Shimokawa, T. and Katoh, H., “Application of the Larson-Miller Equation to Strength Estimation of Light Metallic Materials After Thermal Aging,” Proc. 34th Aircraft Symposium, Japan Society for Aeronautical and Space Sciences, 1996, pp. 241-244. (in Japanese)

THE EFFECT OF MOISTURE ON THE INTERFACIAL STRENGTH OF GRAPHITE-EPOXY AND E-GLASS-EPOXY COMPOSITES

W. L. Bradley, C. A. Wood, B.A. Pratt, and C. S. Chatawanich

Department of Mechanical Engineering and Offshore Technology Research Center
Texas A&M University, College Station, TX 77843-3123, USA

SUMMARY: The effect of absorbed moisture on the fiber/matrix interfacial strength and 90^0 ply strength have been studied for E-glass and carbon fiber reinforced epoxy. Single fiber fragmentation tests have indicated a 19% reduction in the interfacial strength in carbon/epoxy composites which absorbed 1.4% of their matrix weight in seawater. Micro indentation measurement on E-glass/epoxy composites indicated a 25% reduction in the interfacial shear strength when the absorbed seawater increased from 1.2 to 2.2% of the matrix weight. In-situ observations of fracture in an environmental scanning electron microscope with associated calculations indicated reductions in interfacial strength ranging from 0 to 30%, with 2/3rds attributed to reductions in interfacial strength and the balance due to changes in the residual thermal stresses.

KEYWORDS: polymeric composites, carbon, E-glass, epoxy, seawater, interfacial strength, microindention, single fiber fragmentation test

INTRODUCTION

The prospect of large oil reserves at 2000m of ocean depth has created a significant interest in the possibility of using polymeric composite tubulars for both drilling risers and production risers. The higher specific strength of polymeric composite material systems can potentially allow conventional equipment designed for drilling and oil production using floating ships and platforms for depths of <1000m to be used at these greater depths by reducing the hanging weight of the tubulars. The potential use of polymeric matrix composites for offshore applications has been recently reviewed [1] and the economic feasibility of using polymeric composite tubulars for production risers has already been demonstrated [2].

Polymeric matrix composites are known to have excellent fatigue resistance, do not corrode, and can be tailored to give optimal combinations of stiffness, strength, and thermal expansion by proper ply sequencing. The two technical obstacles to the use of polymeric composite materials for offshore risers are joining and long-term durability. While polymeric composite materials do not corrode like metals, they do absorb moisture, generally 1-3% of the weight of the matrix. This absorbed moisture can potentially soften the matrix, reduce the strength of the glass fibers (carbon fibers appear to be unaffected by moisture), and/or degrade the strength of the fiber matrix interface. Since production risers will be immersed continuously for 10-20 years, they will certainly reach saturation levels of moisture absorption eventually. Thus, the effect of the absorbed moisture on long term durability needs to be determined.

The purpose of this study has been to investigate effect of the absorbed moisture on the interfacial strength of several polymeric composite material systems. Direct observations of the initiation of damage in the systems investigated in this study indicate that the failure scenario begins with interfacial failure by debonding leading to transverse cracking, and subsequently, delamination. Absorbed moisture can perturb this failure scenario by reducing the chemical adhesion at the fiber/matrix interface, relaxing the residual compressive stresses at the fiber/matrix interface, reducing the ply level residual tensile stresses in the 90^o plies, and toughening the polymeric matrix. Since these various effects of absorbed moisture can potentially postpone interfacial failure or cause it to occur prematurely, a more careful study has been undertaken to determine the effect of absorbed moisture on the interfacial strength and on the ply level mechanical stress at which interfacial failure leading to transverse cracking occurs.

To determine the effect of absorbed moisture on the initiation of ply level damage in a multi axial laminate, micro indentation tests [3] and tensile tests in-situ in an environmental scanning electron microscope have been performed on specimens as received and specimens aged in seawater until a saturation level of moisture absorption has occurred. Single fiber fragmentation tests [4] have also been used to investigate the effect of absorbed moisture on the interfacial shear strength.

EXPERIMENTAL AND ANALYTICAL PROCEDURES

Two polymeric composite material systems have been studied in this investigation: (a) a Shell 828 epoxy (DGEBA), cured at 398K with meta-phenylene diamine (mPDA), reinforced with E-glass type 30 Owens Corning fibers and (b) a proprietary diglycidyl ether bisphenal-A (DGEBA) with 5% rubber added for toughening, with a cure temperature of 422K, reinforced with E-glass fibers and graphite fibers (a hybrid composite). Two different sizings were used on the E-glass fibers in the 828 epoxy, one properly coated for compatibility with an epoxy matrix and the other coated for use with a vinyl ester. Hereafter, the 828 epoxy will be referred to as Epoxy 1 and the proprietary epoxy with 5% rubber additions will be referred to as Epoxy 2.

Single-fiber fragmentation test specimens were prepared by casting AS4 carbon fibers from Hercules in a dog bone shaped tensile specimen of Epoxy 2. Load and displacement measurements were made during testing using a load cell and an LVDT, with fiber breaks recorded using acoustic emission. Aging of specimens was done by emersion for 110 days in simulated seawater prepared from *Instant Ocean Mix* (purchased from a pet store). Other specimens were dried by heating in a vacuum furnace until the specimen weight stabilized. The moisture content for the three specimens tested were 0, 0.65 and 1.40% of the weight of the epoxy. The number of breaks as a function of strain was recorded and analyzed using the Kelly-Tyson approach [5]. Fiber strength was calculated using Weibull statistics applied to the single fiber fragmentation test itself, as suggested by Wagner [6]. The strain used to determine the stresses which were then used in the Weibull distribution was calculated from the mechanical strain applied to the specimen, the thermal cool down strain, and the swelling strain which occurs with moisture absorption. Additional information about the experimental details and analysis are presented in Reference 7.

Micro indentation tests were performed on Epoxy 1 reinforced with E-glass fibers in a laminate made from prepreg with a stacking sequence of $(\pm 45/90)s$. Fiber volume fraction was 0.65 and curing was at 398K for 2 hours. One laminate was made using E-glass with a proper sizing for vinyl ester to see how sensitive to sizing is the moisture sensitivity of the interfacial strength. Some specimens were aged by soaking to saturation in simulated seawater prepared from *Instant Ocean Mix*. Weight gain was 1% of the matrix weight, for a total moisture content of 2.2%, since drying experiments indicated an initial moisture content as fabricated of 1.2% of the matrix weight. Testing was performed on a carefully polished surface using an Interfacial Testing System (ITS) manufactured by Dow Chemical. Since the debonding of glass fibers is gradual rather than at a single load, the debonding load was taken when debonding was $>90^o$ of the circumference of the fiber. The interfacial shear strength was determined using software which utilizes a linear elastic analysis [8]. During the testing of the aged specimens, it was necessary to keep the surface covered with seawater during the testing to avoid changes in the measurement due to dehydration of the specimens. Approximately 10 interfacial shear strength measurements were made on each specimen. Additional experimental details are summarized on Reference 8.

Tensile tests were performed in an environmental scanning electron microscope (ESEM) to allow direct observations of the failure scenario of 90^o plies. Special tensile specimens were prepared by grinding and polishing the edges of rectangular specimens 38mm long by 6mm wide, as seen in Figure 1. The reduced specimen width at the midpoint of the specimen length gives a maximum stress at this same location, causing the damage initiation to be sufficiently localized to allow it to be captured in the early stages. Getting a good metallographic polish on a curved surface required the development of some new polishing techniques. The aged specimens were tested in the ESEM with a 100% relative humidity to avoid dehydration during testing. Unaged specimens were tested at a much lower pressure and humidity in the ESEM. The specimens were loaded in displacement control, with both load and displacement monitored. The displacements were applied in step wise fashion, with careful surveying of the polished edge and photographic documentation of damage accumulation being done at each displacement step.

The laminate load measured at a given displacement was used to calculate the ply level stresses in the 90^o plies at the initiation of debonding and at the first occurrence of transverse cracking using software based on classical laminate theory [9]. The ply level residual stresses on cool down to room temperature were also calculated using the same laminate analysis [9]. The residual stresses at the fiber/matrix interface were calculated using a micromechanics analysis based on linear elasticity called MICSTRAN [10,11]. MICSTRAN was also used to calculate the local stress concentration as a function of location around the circumference of the fiber/matrix interface as seen in Fig. 1c. Thus, the local redial stresses at the fiber matrix interface due to ply level mechanical and residual thermal stresses can be calculated. Alternatively, the residual thermal stresses at the fiber/matrix interface or the interfacial strength for debonding due to normal stressing could be converted into an equivalent ply level residual or critical stress.

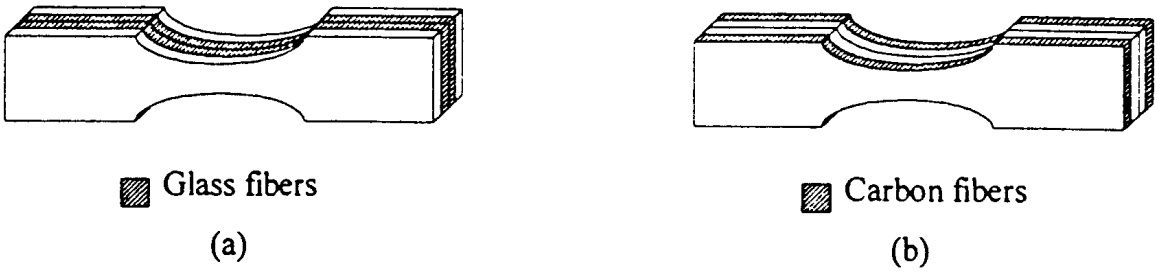

Figure 1 a & b: The test geometry for specimens loaded to fracture in the ESEM, indicating the stacking sequence for the hybrid composites (E-glass and carbon/epoxy-2), (a) $[O_c\ 190_g]_s$

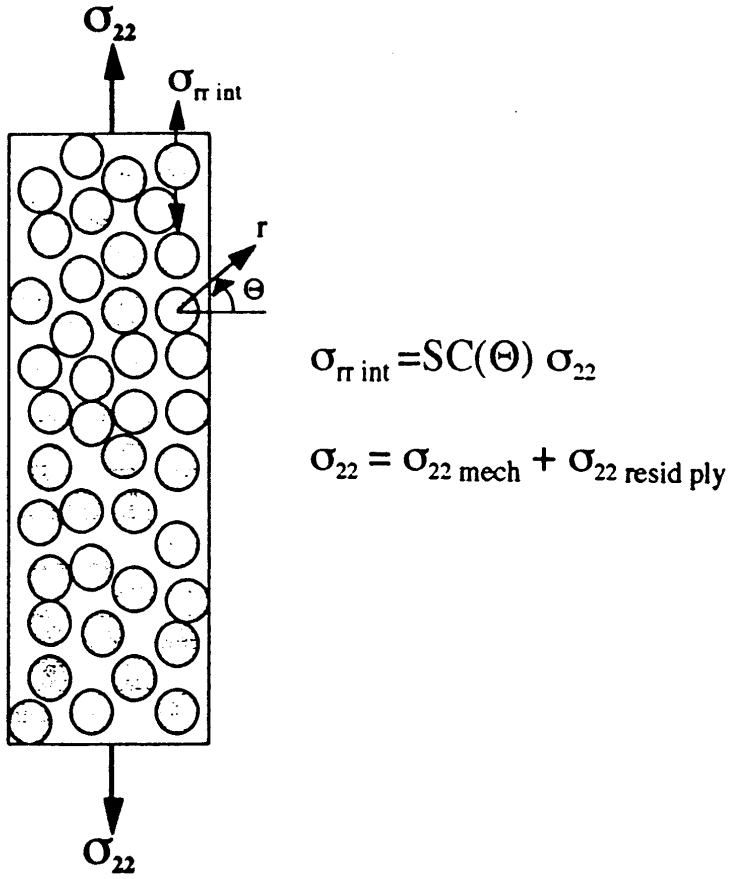

Figure 1c. Schematic showing the calculation of local radial stress at the fiber/matrix interface as a function of the ply level thermal and mechanical stresses

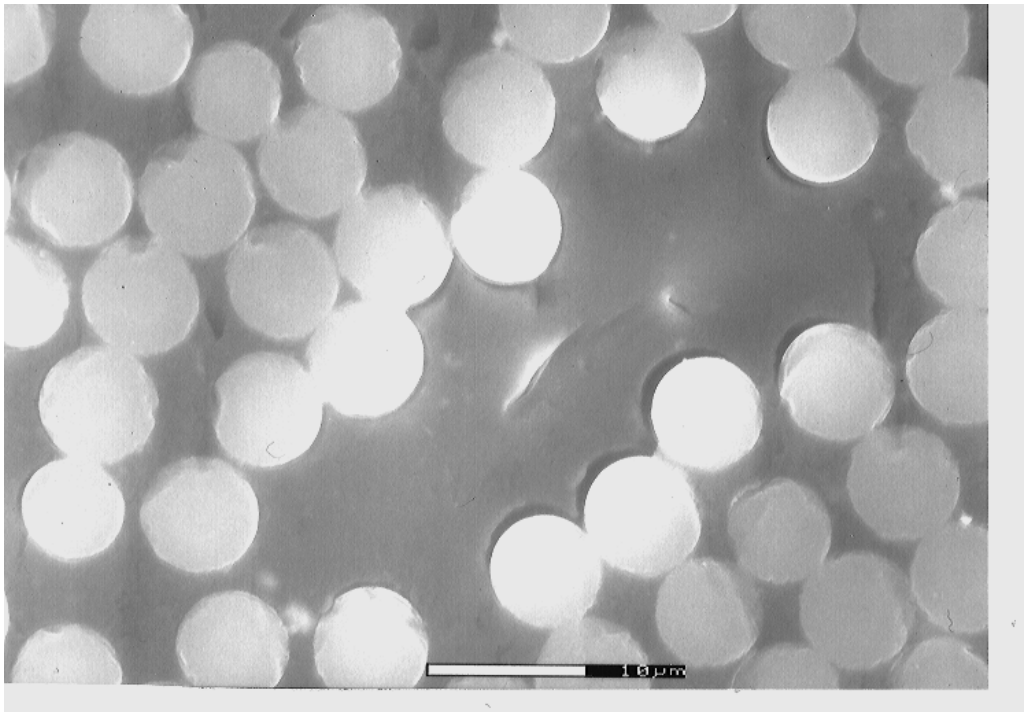

Figure 2a: Coalesced debonds adjacent to a resin rich region in an aged hybrid composite with carbon fibers in the 90^0 ply

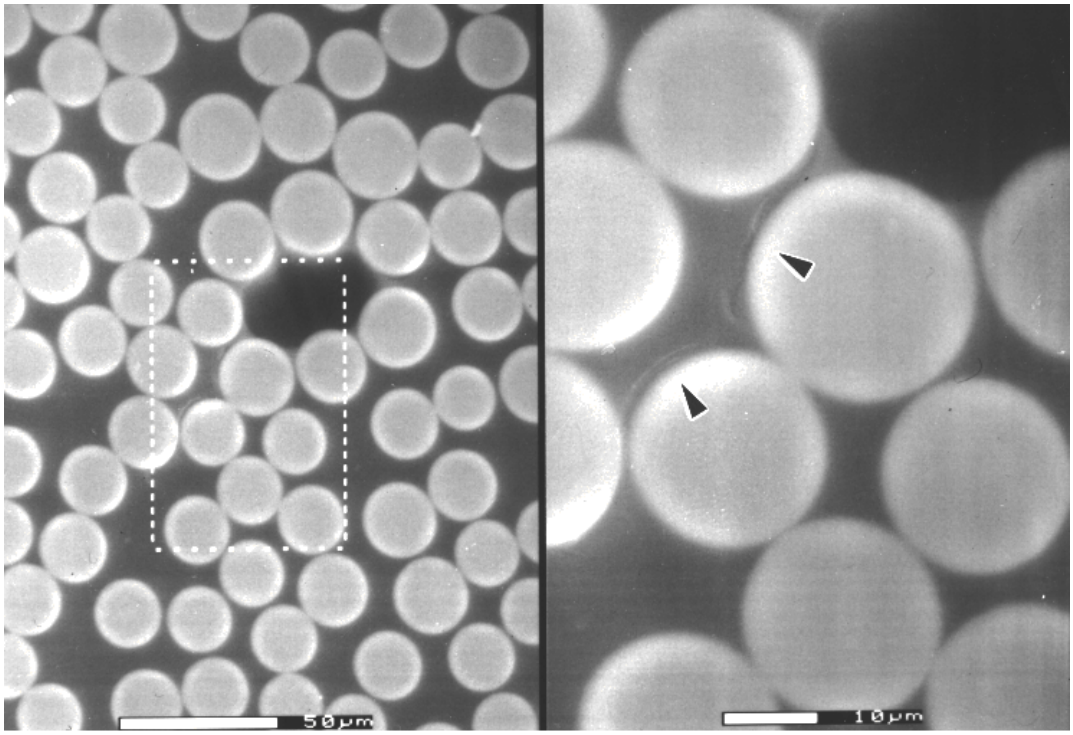

Figure 2b: Debonds adjacent to a void in E-glass/epxoy 1 composite

RESULTS AND DISCUSSION

Direct observations of fracture in the ESEM is seen in Figure 3. In the E-glass/epoxy 1 system, interfacial failures usually occurred first adjacent to local heterogeneities such as voids whereas in the carbon and E-glass/epoxy 2 system it occurred adjacent to local resin rich regions. In neither case was debonding found to be in a homogeneous region of the composite microstructure. Once debonding initiated in a local region, new debonds were found to take place adjacent to the original ones as the load is locally redistributed.

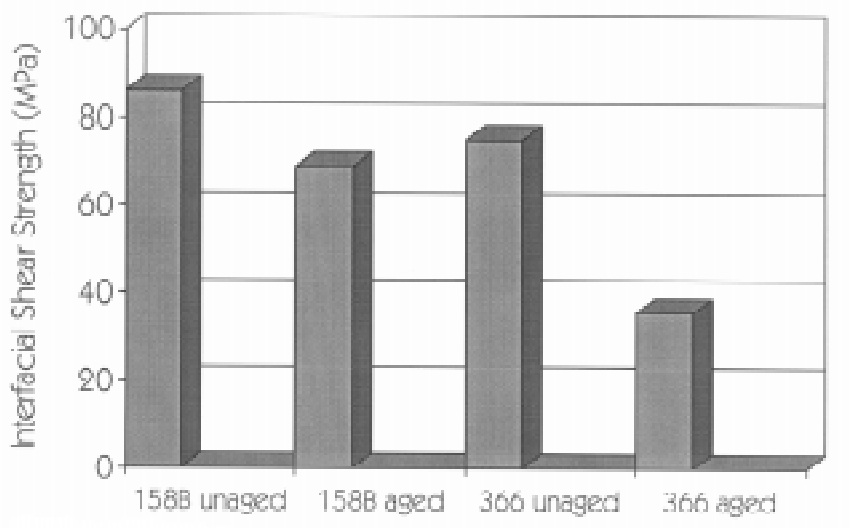

Figure 3: Interfacial shear strength determined from microindentation tests for E-glass/epoxy-1 system with an appropriate sizing for epoxy (158B) and a sizing for vinylesters (366), unaged (1.2% moisture), and aged (2.2% moisture)

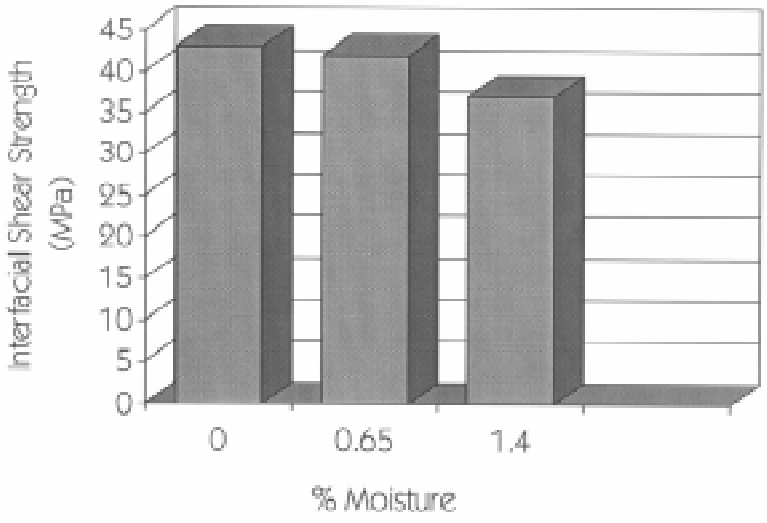

Figure 4: Interfacial shear strength for carbon/epoxy-2 system with different levels of absorbed seawater, determined using single fiber fragmentation tests

A general observations of randomly arranged debonds which ultimately begin to coalesce when the local density reaches some critical level (like fiber failures) was never observed in any of the more than 50 tests run on a variety of specimens. It seems clear that debonding leading to transverse cracking is controlled by local heterogeneities and once initiated tends to

remain quite localized. Absorbed moisture was not found to affect the failure scenario, but only the load levels at which debonding began and transverse cracking ultimately was consummated.

The results of the Micro indentation tests to measure interfacial strength are presented in Figure 3 for the carbon/epoxy-2 system. The effect of moisture level as manufactured compared to artificially dried is seen to be insignificant. The absorbed moisture at a saturation of 1.4%, however, gives a reduction of 19%.

The interfacial shear strength in the E-glass/epoxy-1 system as measured by the micro indentation test is seen in Figure 4. Note that the E-glass with the proper 158B sizing had a better unaged interfacial strength and was less moisture sensitive, losing only 25% of its interfacial strength. On the other hand, the E-glass with the 366 sizing for vinyl esters lost more than 50% of its interfacial strength when saturated with seawater, indicating the importance of the use of a proper sizing for seawater immersion applications.

To analyze the interfacial stress at the fiber/matrix interface at which interfacial debonding occurs, the local stress at the fiber matrix interface was calculated beginning with the local stress due to ply level stress, as shown in Figure 1c, with the value of the stress concentration factor used being determined from MICSTRAN. Since almost all debonds were observed at the top or bottom of the fibers (theta = 90^o), the local stress due to ply level mechanical and residual thermal stresses was evaluated at this position. The local interfacial residual thermal stress in the radial direction was also determined using MICSTRAN. Finally, the interfacial strength was calculated as follows:

$$\sigma_{22\ int} = (\sigma_{22\ mech\ ply}+\sigma_{22\ resid\ ply}) \times SC(\theta=90^o) + \sigma_{rr\ int\ th} \quad (1)$$

where $\sigma_{22\ mech\ ply}$ and $\sigma_{22\ resid\ ply}$ are the mechanical stress due to external loading and the residual thermal stress due to differntial thermal contraction during cool down (modified by moisture induced swelling) in the 90^o ply, SC is the stress concentration factor relating local stress in the radial direction to ply level stress, and $\sigma_{rr\ int\ th}$ is the local residual thermal stresses due to differential thermal contraction between the fiber and the matrix. It is worth noting that the ply level residual thermal stress is tensile in the 90^0 plies whereas the local residual thermal stress is compressive. Thus, one is helpful in postponing debonding whereas the other makes debonding easier. Both the local level residual thermal stress and the interfacial strength can be converted to equivalent ply level stresses using the stress concentration factor (SC), which is 1.45 for carbon fiber/epoxy and 1.82 for E-glass/epoxy. When the debonding occurs next to a spherical void, an additional stress concentration factor of 2.18 [13] needs to be multiplied times the 1.82 to calculate the local interfacial stress from ply level stresses or to calculate equivalent ply level stresses from the local thermal residual stresses or interfacial strength. Equation 1 can be rearranged to express the ply level mechanical stress at which debonding and subsequent transverse cracking occur, as follows:

$$\sigma_{22\ mech\ ply} = (\sigma_{rr}\ int - \sigma_{rr\ int\ th})/SC - \sigma_{22\ resid\ ply} \quad (2)$$

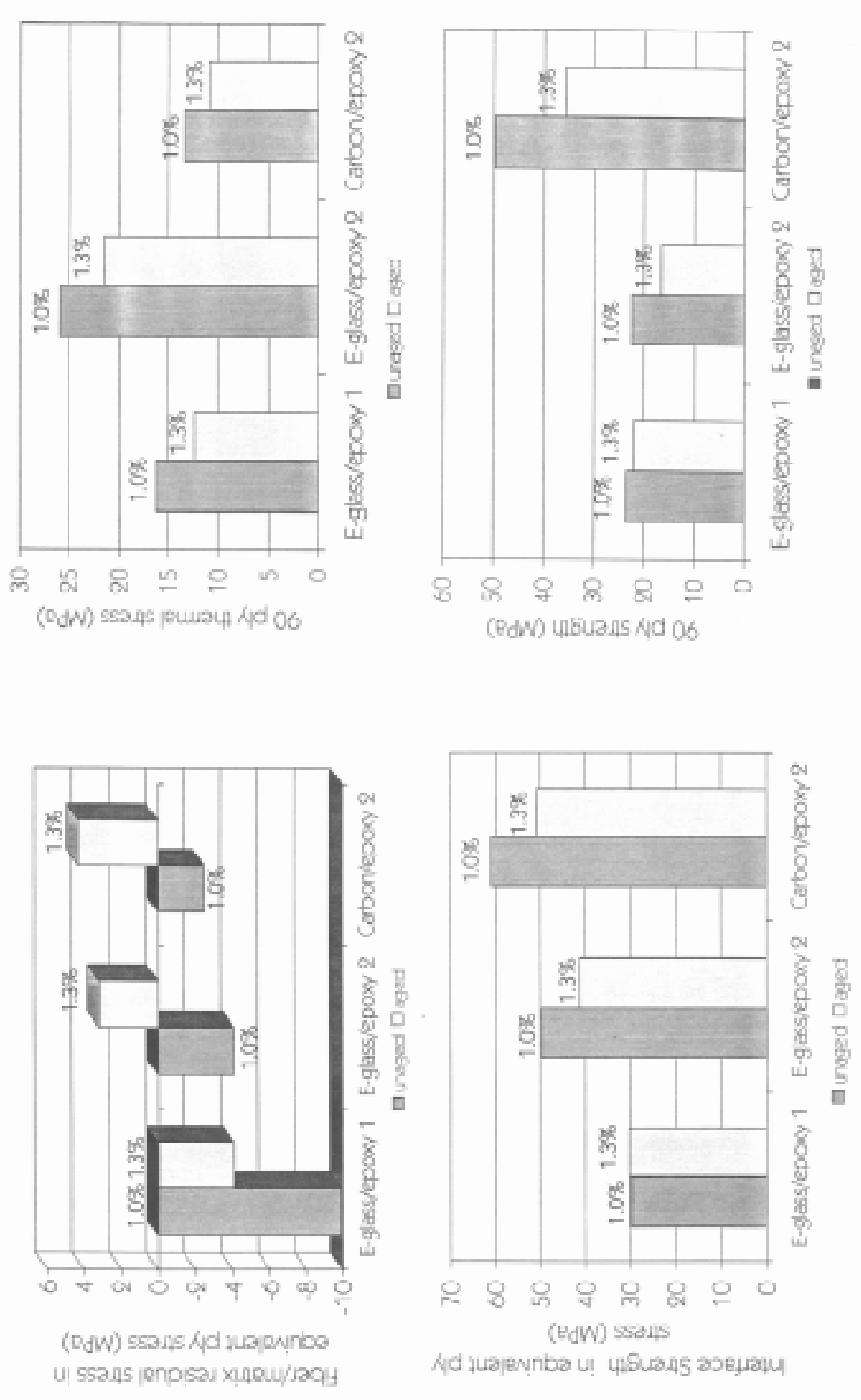

Figure 5: The effect of absorbed seawater on the ply strength (lower, right) and on the interfacial strength, local residual thermal stress normal to the fiber/matrix interface and ply level thermal residual stress. Note the interfacial strength and local residual thermal stress are expressed in equivalent ply level stresses which are calculated by dividing the local values by an appropriate stress concentration factor, as described in the text

At transverse cracking, σ_{22} mech ply is the 90^0 ply strength and σ_{rr} int is the interfacial strength for stresses applied normal to the fiber matrix interface. The results of this analysis are presented in Figure 5 for all three systems. From an engineering point of view, the effect of the absorbed moisture on the mechanical stress level at which debonding and subsequent transverse cracking initiates is most important, and is presented in Fig. 5, lower right. The remaining three graphs allow one to infer the reasons for the observed changes in the allowable mechanical stress level in a seawater saturated polymeric composite. The absorbed moisture decreases the residual thermal stresses in the radial direction at the fiber/matrix interfacial, causing then to go net positive in two of the systems. However, the ply level residual thermal stresses which are tensile are relaxed by the absorbed seawater, which would give a greater ply level mechanical strength. In each of the systems studied, the combined effects of the residual thermal stresses at the ply level and the local interfacial level was to give a net decrease in the ply level mechanical strength of between 1.4 and 4.2 MPA in the three systems studied, or 6-8% of the respective unaged ply strength of the systems studied.

The reduction in interfacial strength resulted in a decrease in the ply strength ranging from essentially zero in the system with only 1.0% increase in seawater to 10.1 MPa, or 20% in the carbon/epoxy-2 system, which absorbed 1.3% seawater. It should be noted that the same system in the single fiber fragmentation test absorbed 1.4% seawater and gave a 19% reduction in the interfacial shear strength, which is surprisingly consistent, since one is measuring changes in interfacial strength for shear stressing and the other is measuring interfacial strength for stresses applied perpendicular to the fiber/matrix interface; however, the absolute values of the unaged and aged interfacial strengths are different, as one might expect. These results suggest that 2/3rds of the overall decrease in the critical strain (or stress) at which damage begins in 90^o plies is due to moisture reduced changes in interfacial strength with the remaining 1/3rd due to changes in residual thermal stresses (at the ply and local level, combined).

The very low values of ply strength in the E-glass/epoxy-1 system were due to damage initiation always occurring at small, spherical voids in the microstructure which were introduced during processing. While the overall void content was less than 1%, these voids still dominated the failure process in the 90^0 plies. The low ply strength in the E-glass/epoxy-2 was due to the very high ply thermal stresses due to the very stiff adjacent 0^o plies of carbon fiber. In the E-glass/epoxy-1 system, the plies adjacent to the 90s were $\pm$45s of glass. In the graphite/epoxy-2 system, adjacent 0^0 plies were E-glass.

Finally, the values presented in Figure 5 should be consider illustrative, but only semi-quantitative since the residual thermal stresses were not calculated with a viscoelastic analysis but just used the room temperature modulus of the matrix. The stress concentration and thermal residual stresses calculated with MICSTRAN are dependent on the local fiber arrangement, with only diamond and square arrangement permitted. The actual fiber arrangements in the microstructure were more complicated and were generally neither square or diamond arrays.

REFERENCES

1. Gibson, A.G., "Composite Structures in Offshore Applications", *Composite Materials in Marine Structures*, Chapter 3, 1993, R.A. Shenoi, Ed. Cambridge Ocean Technology Series.

2. Tamarelle, P.J. C. and Sparks, C.P., *Proceedings of Nineteenth Annual Offshore Technology Conference*, Houston, TX, May 1987 (Richardson, TX: Offshore Technology Conference), p. 255.

3. Chen, E.J.H., and R.B. croman. 1993. "Microdebonding Investigation of the Effects of Thermal Residual Stress on the Bond Strength of a Graphite/Polyimide Composite", *Composites Science and Technology*, 48: 173-179.

4. Drzal, L.T., Rich, M.J. and Lloyd, P.E., "Adhesion of Graphite Fibers to Epoxy Matrices: I. The Role of Fiber Surface Treatment", *Journal of Adhesion*, Vol. 16, 1982, pp. 1-30.

5. Kelly, A. and Tyson, W.R., *Journal Mech. Phys. Solids*, 1965, Vol. 13, p.329.

6. Yavin, B., Gallis, H.E., Scherf, J., Eitan, A. and Wagner, H.D., "Continuous Monitoring of the Fragmentation Phenomenon in Single Fiber Composite Materials", *Polymer Composites*, Vol. 12, No. 6, 1991, pp. 436-446.

7. Pratt, B, *"Determining the Effect of Seawater on the Interfacial Shear Strength of Fiber Reinforced Eopoxies using the Single Fiber Fragmentation Test"*, M.S. Thesis, Texas A&M University, December, 1996.

8. Chatawanich, Candy, *"The Effect of Moisture on a Glass/Epoxy Composite"*, M.S. Thesis, Texas A&M University, May 1996.

9. Wood, Catherine, *"Determining The Effect of Seawater on the Interfacial Strength of an Interlayer E-Glass-Graphite/Epoxy Composite Using Observations of Transverse Cracking Made in-Situation"*, M.S. Thesis, Texas A&M University, September, 1996.

10 Chen, E.J.H., and R.B. Croman. 1993, "Microdebonding Investigation of the Effects of Thermal Residual Stress on the Bond Strength of a Graphite/Polyimide Composite", *Composites Science and Technology*, 48: 173-179.

11. Naik, R.A. 1992. "Micromechanical Combined Stress Analysis - MICSTRAN, A User Manual", *NASA Contractor Report 189694*, National Aeronautics and Space Administration, Langley Research Center, Hampton, VA.

12. Crews, J.H., R.A. Naik, and S.J. Lubowinski. 1993. "An Analysis of Fiber-Matrix Interface Failure Stresses for a Range of Ply Stress States", *NASA Technical Memorandum 108999*, National Aeronautics and Space Administration, Langley Research Center, Hampton, VA.

13. Timoshenko, S.P. and Goodier, J.N., *Theory of Elasticity*, New York: McGraw-Hill Book Company, 1934.

DURABILITY OF FIBRE REINFORCED COMPOSITE MATERIALS AFTER TWENTY YEARS OF EXPOSURE TO WEATHERING

A. Yoosefinejad and P. J. Hogg

Queen Mary and Westfield College,
Department of Materials,
Mile End Road, London E1 4NS, UK

SUMMARY: Two GRP panels (a bus shelter and a building panel) of 12 and 20 years old respectively were obtained and their service histories were established. Test specimens were prepared to mechanically characterise the weathered panels. Fresh GRP panels were obtained from the manufacturers and the test data from them were used to establish the effect of 20 years of weathering on the GRP panels. No significant deterioration in the moduli of the weathered panels was observed. The tensile and flexural strengths of the bus shelter has shown a 40% decrease in comparison with the fresh panels.

KEYWORDS: durability, GRP, weathering, mechanical properties of GRP

INTRODUCTION

Although the use of fibre reinforced composite (FRC) materials is becoming wide spread in construction, their use dates back to the late sixties and early seventies as facia panels mostly for aesthetic purposes. One such panel has come to our possession at QMW. The panel was installed in a council housing estate (Elgin Towers, London) which was subsequently demolished in 1993 and this particular panel (Panel A) was saved from destruction and finally found its way to QMW. The panel was estimated to be 20 years old and its primary purpose was as a cladding panel. It had no structural role but was subjected to environmental attack. The panel was exposed to open air on one side and the inner face was insulated with polyurethane foam.

The panel, Fig. 1, was divided into two and one half was used to determine its mechanical properties and the fibre volume fraction.

At the same time as the panel arriving at QMW, London Transport (LT) was in the process of upgrading London bus shelters with a new design and one of the bus shelters was situated outside the Engineering building of QMW. After it was dismantled the roof of the shelter was donated to us. The shelter consisted of a metal frame and chopped strand mat composite panel (Panel B), Fig. 2. LT were able to provide us with the date of manufacture and the name of the manufacturers. The shelter was in service from 1983-1995. The manufacturer gave us the details of the material and two further plates were sent to us (Panel C and D) which represented the same lay up as the old bus shelter. All panels were mechanically characterised.

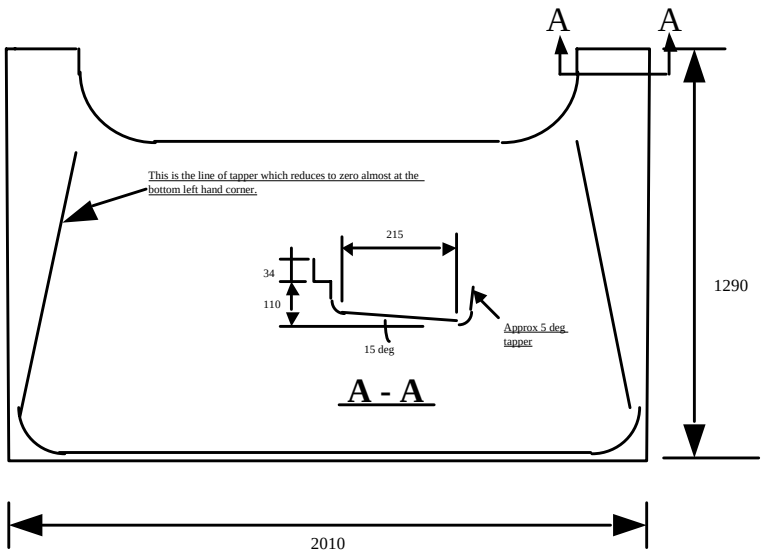

Fig. 1: Schematic representation of panel A

THE AIMS

- to establish mechanical properties of the panels
- to determine their constituents
- to manufacture similar panels using more or less the same type of materials used in the construction of the old panels
- to provide a better understanding of the degree of degradation due to exposure to twenty and twelve years of weathering by comparing the properties of the old and new panels

MECHANICAL CHARACTERISATION

The specimens were prepared according to ASTM standards. The samples were cut from the panels and no additional cleaning was under-taken, unless strain gauges were necessary to carry out testing. The panels showed typical matrix cracking on the exposed surfaces, particularly so on the bus shelter. Closer inspection of the bus shelter gel coat showed voids filled with dust and airborne particles such as vehicle emission which were consolidated in the voids, perhaps by rain water. In some areas of the panel signs of rust spots were observed which were perhaps caused by metallic particles thrown about in the air by vehicles. There was no evidence that damage caused by the environment had penetrated the gel coat to the fibre and resin layer.

Mechanical test data revealed that panel A had superior mechanical properties in comparison to panel B, as shown in Tables 1 and 2. The reason for this became apparent by further burn-off test on the two panels; the fibre content of the panel A was twice the amount obtained from panel B. The average thickness of the both panels is the same, but the bus shelter was gel coated on the both sides and average thickness of the gel coat was measured to be 0.6 mm The data generated for panels C and D provided a base line to determine the degradation of the panel B. The stiffness values were very close compared with the weathered materials but there was a marked difference in the strength values. Panels C and D yielded strength values of almost twice the values obtained from panel B.

Table 1: Tensile test data for panels A and B

Tensile test ASTM D3039	Fibre volume fraction %	Young's Modulus (GPa)	Tensile strength (MPa)
Panel A	25 - 30	9.0±1	76.2±10.3
Panel B	14 - 15	4.5±0.6	47.3±9.3

Table 2: Flexure test data for panels A and B

Flexure test ASTM D790M	Fibre volume fraction %	Flexural Modulus (GPa)	Flexural strength (MPa)
Panel A	25 - 30	11.9±0.6	135.3±2.8
Panel B	14 - 15	5.50±0.3	60.1±4.4

Table 3: Tensile data for panels C and D

Tensile test ASTM D3039	Plate thickness (mm)	Young's Modulus (GPa) Resin : glass ratio = 2.4	Tensile strength (MPa)
Panel C	1.74	4.5±0.4	75.2±4.1
Panel D	3.0	4.70±0.3	84.9±10.7

The tensile and flexure data reported in Ref. 1 and 2 do correspond with the data generated here at a given volume fraction.

Table 4: Flexure test data for panels C and D

Flexure test ASTM D790M	Plate thickness (mm)	Flexural Modulus (GPa)	Flexural strength(MPa)
Panel C	1.74	6.3±0.4	119.6±5.6
Panel D	3.0	7.1±0.7	94.4±4.1

The impact properties of panels A and B are shown in Table 5. The variation in the impact data between panels A and B follow the same trend as tensile and flexure data. All the impact specimens were fractured and the total energy absorption and maximum force were noted, Fig. 3. The total energy absorption of both plates was slightly below that expected for this general class of materials as shown in Fig. 4, Ref. 2. The impact data illustrated in Fig. 4 is a master curve of energy absorption versus volume fraction drawn through data for SMCs and wet lay-up GRPs in general. The below average response of panel B could also be linked to the surface degradation of the gel coat on the panel.

Table 5: Impact properties of panels A and B

	Thickness (mm)	Fibre volume fraction %	Force (N)	Energy absorption (Joules)
Panel A	2.9	28-30	4500	13.7
Panel B	2.9	14 - 15	1500	30

LONG TERM DATA

There is limited long term weathering data on chopped strand mat composite materials and one of such study was published by Norris et al. [3]. They reported an average increase of 15% in tensile modulus during a two year study. The increase was due to the effect of radiation which in turn increased the post curing. The flexural modulus was reported to decrease by 15 - 20% for the same duration, since flexural modulus depends on the surface properties and since weathering degrades surfaces (as was observed on panels A and B) causing a reduction in flexural modulus.

CONCLUSION

The panels A and B were not exposed to any structural load for any significant period of time and the only major attack had been due to the natural environment of the panels. The bus shelter perhaps was more exposed to such conditions than the building panel since the bus shelter was situated on a busy main road. The gel coat contained cracks and as a result of which rain water and other effluents could have reached the fibres and the matrix. Mechanical test data had shown no significant deterioration in the stiffness of the panel B, but a significant decrease in the strengths of the panel in comparison with the fresh samples was observed. This deterioration in strength has been primarily due to weathering. There were no direct comparisons made with panel A since none of the panels tested were of the same volume fraction. Thus only mechanical test data is reported and relative comparison can be made with panels B, C and D.

ACKNOWLEDGEMENT

The authors would like to acknowledge Mr Trevor Starr of composite processing association for the supply of the panel A, Mr Clive Barton of London Transport (Adshel) for information regarding the history of the bus shelter and also Mr David Barclay of Quality Mouldings for the supply of panels and information regarding the lay up of the bus shelter materials.

REFERENCE

1. Johnson, A. F, Engineering design properties of GRP, British Plastics Federation.

2. Hogg, P. J and Woolstencroft, D. H. Non crimp thermoplastic composite fabrics: Aerospace solution to automotive problem. Advanced composite materials: *New developments and applications conference proceedings*, Detroit, Michigan USA, Sept. 1991.

3. Norris J. F, Crowder, J. R and Probert, C. The weathering of glass reinforced polyesters under stress-short term behaviour. *Composites*, Vol. 7, No. 3, 1976, pp 16-171.

Fig. 2: Photograph of the bus shelter prior to its removal

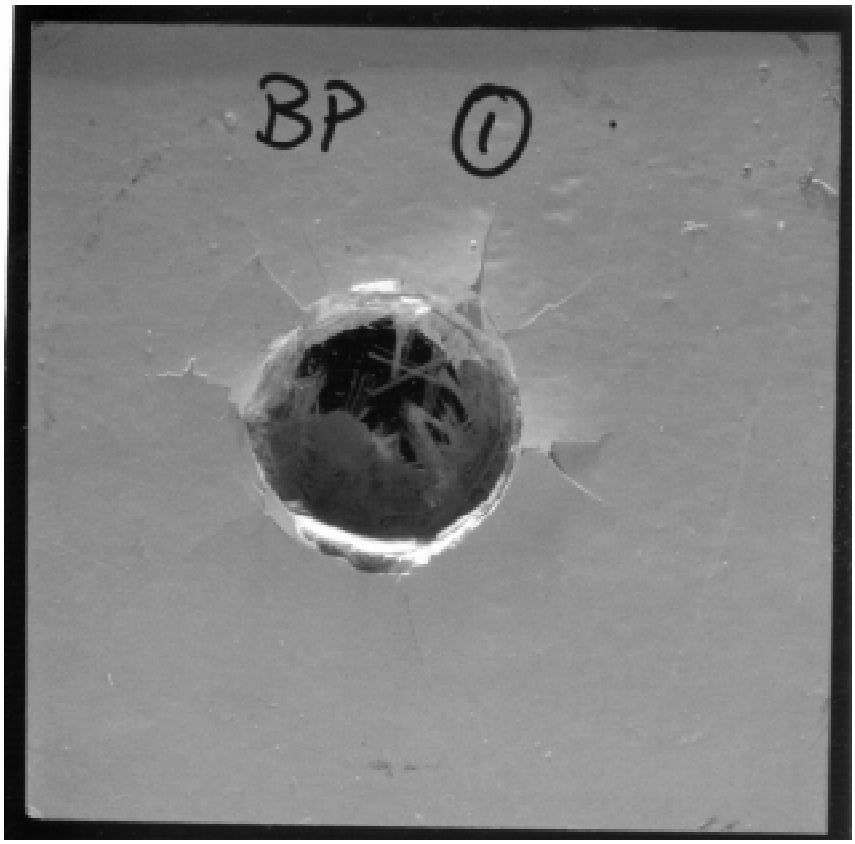

Fig. 3: Building panel specimen after impact

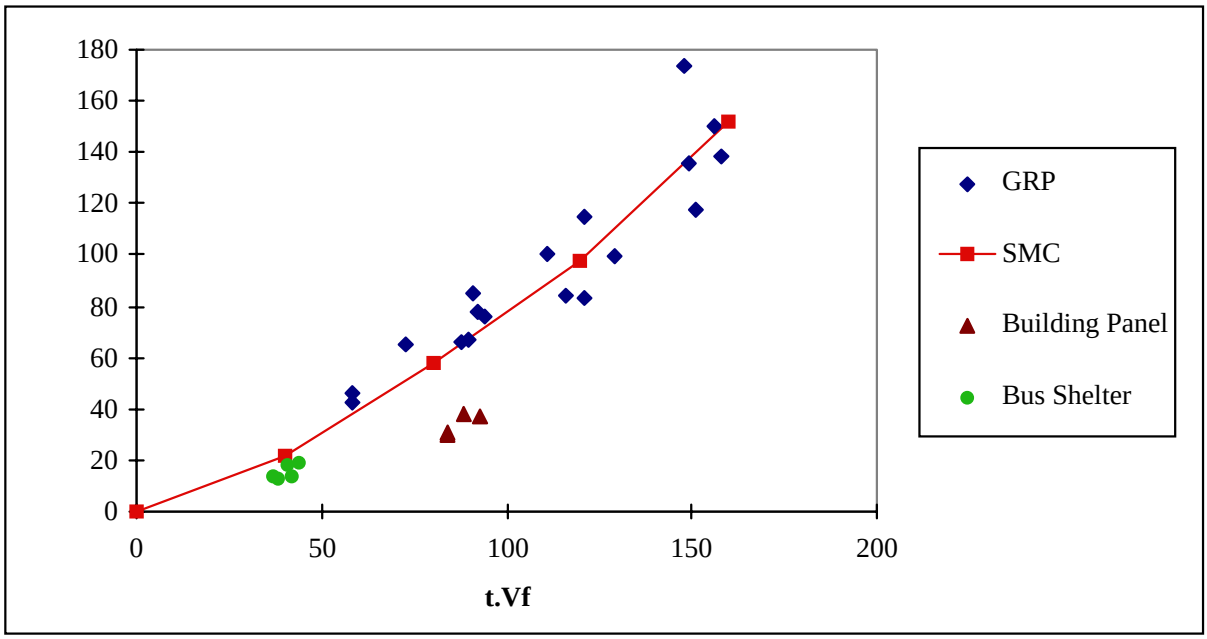

Fig. 4: Energy absorption as function of plate thickness and fibre volume fraction

STATISTICAL ANALYSIS OF WATER ABSORPTION IN COMPOSITE MATERIALS

B.Hu X.J.Gong J.C.Kneip G.Verchery

Institut Supérieur de l'Automobile et des Transports (ISAT) - Université de Bourgogne
49, Rue Mademoiselle - Bourgeois - B.P. 31 - 58027 - NEVERS CEDEX - FRANCE

SUMMARY: The objective of the present work is to study the statistical characteristics of data obtained on the moisture absorption process of composite materials. For this purpose, the glass/epoxy composite specimens were immersed in distilled water at a temperature of 46°C and the moisture content of specimen was measured in function of time. The analytical results indicated that the statistical distributions of the moisture content closely approximated the normal distribution on the nearly whole absorption process. Based on this, the statistical law of the moisture content was described and a reliability curve of water absorption was given which may be practically employed for the moisture absorption process of glass/epoxy laminated composites.

KEYWORDS: water absorption, moisture content, statistical analysis, normal distribution

INTRODUCTION

Hygrothermal environments have evident effects on the mechanical properties of composite materials. For this reason, moisture absorption has received much attention since the beginning of use of composites in structural applications. However, there is often a considerable spread in the reported results obtained on the moisture absorption process. Twenty or thirty percent variations in the data are quite common. In some cases, the results obtained by different laboratories even differ by forty percent or more[1, 2]. This fact leads to great loss of confidence of potential users in published data.

In this paper, a statistical technique was used to study the statistical characteristics of these measured moisture parameters and the conclusions obtained here should be useful to the researchers and engineers in the field.

EXPERIMENT

All tests were performed on 8 ply glass/epoxy specimens having the following laminated types a) $[0°]_8$, b) $[90°]_8$, c) $[\pm 45°]_{2S}$ and d) $[0°/\pm 45°/90°]_S$. The nominal dimensions were: thickness h = 2.00 mm, width b = 15.00 mm and length l = 150.00 mm. The fiber volume fraction was about 60 percent for all specimens.

The specimens were primarily dried in a dry environment chamber until no more weight losses were observed. The dry specimens were then immersed in distilled water at a constant temperature about 46°C. The weight changes of specimens were measured by weighing them periodically on a mettler analytical balance with an accuracy of 0.001g.

CLASSICAL LAW AND EXPERIMENTAL RESULTS

Fick's Law

It has been demonstrated that under most conditions the moisture content of composites such as glass/epoxy may be calculated using the equivalent unidirectional Fick's law[1], namely:

$$\frac{\partial c}{\partial t} = D\frac{\partial^2 c}{\partial x^2} \tag{1}$$

where c is the moisture concentration at time t at a point a distance x from the surface and D is the moisture diffusivity.

Using the Equation (1), we obtain the moisture content of the specimens studied :

$$M = M_m\left(1 - \frac{8}{\pi^2}\sum_{j=0}^{\infty}\frac{\exp\left[-(2j+1)^2\pi^2(\frac{Dt}{h^2})\right]}{(2j+1)^2}\right) \tag{2}$$

According to Shen and Springer[1], Equation (2) may be approximated by :

$$M = M_m\left(1 - \exp\left[-7.3\,(\frac{D\,t}{h^2})^{0.75}\right]\right) \tag{3}$$

where M_m is the maximum moisture content and t is the immersion time.

In fact, the water also enters the specimen through the "edges"(surfaces hl and hb), so D in Equation (2) and (3) should be considered as a equivalent diffusivity , it can be expressed as[1]:

$$D = D_x(1 + \frac{h}{l}\sqrt{\frac{D_y}{D_x}} + \frac{h}{b}\sqrt{\frac{D_z}{D_x}})^2 \tag{4}$$

where D_X, Dy, Dz are the diffusivity respectively along the direction of thickness h, length l, and width b of the specimens.

According to Equation (4), the process of water absorption will vary with the laminated types of composites due to "Edge Effects"[1]. But, the real cases have showed that the errors of measured data were much more important than this kind of "Edge Effects", so that, the calculated results by Equation (4) nearly lost their practical significances [3]. Analysing the causes, we think the Equation (4) is only a mathematical diffusion model, some more important parameters were not taken into account [3], such as the factors of manufacturing process, the inherent variation of different laminates and so on.

However, considering the considerable dispersion of data, these factors, including the variation of different laminates, may be treated as random variables in the statistical analysis.

The Moisture Content

The weight change of specimen is defined as:

$$M = \frac{weight\ of\ specimen \quad - \quad weight\ of\ dry\ specimen}{weight\ of\ dry\ specimen} \times 100\ percent \tag{5}$$

It should be noted that the change of weight is complex because this parameter includes weight gain due to water absorption and weight loss due to material dissolution[4,5]. However, in the early stage of the process, the weight loss is relatively small and could be neglected. Here, in order to simplify the analysis we approximately regard the total weight change M as the moisture content of material during whole absorption process studied.

So, using equation (5), we can measure M as a function of immersion time for the four different laminates ($[0°]_8$, $[90°]_8$, $[\pm 45°]_{2s}$ and $[0°/\pm 45°/90°]_s$). The Figure 1 presents experimental results of M obtained in function of the root of the immersion time. It is interesting to note that the data dispersion is remarkable during the whole water absorption process and face to this dispersion, it is not so significant the effect of the laminate type on the values of M. If we fit the experimental results with the Fick's law curve (Eq.3) in Figure 1, the classical Fick' law seems giving a good tendency, but it can't give any assessment of dispersion of the measured moisture parameter. Therefore we will use statistical technique to study the dispersion characteristics of M and try to give a statistical law for describing the water absorption process, where each M measured for any laminate type whatever will be considered as one event .

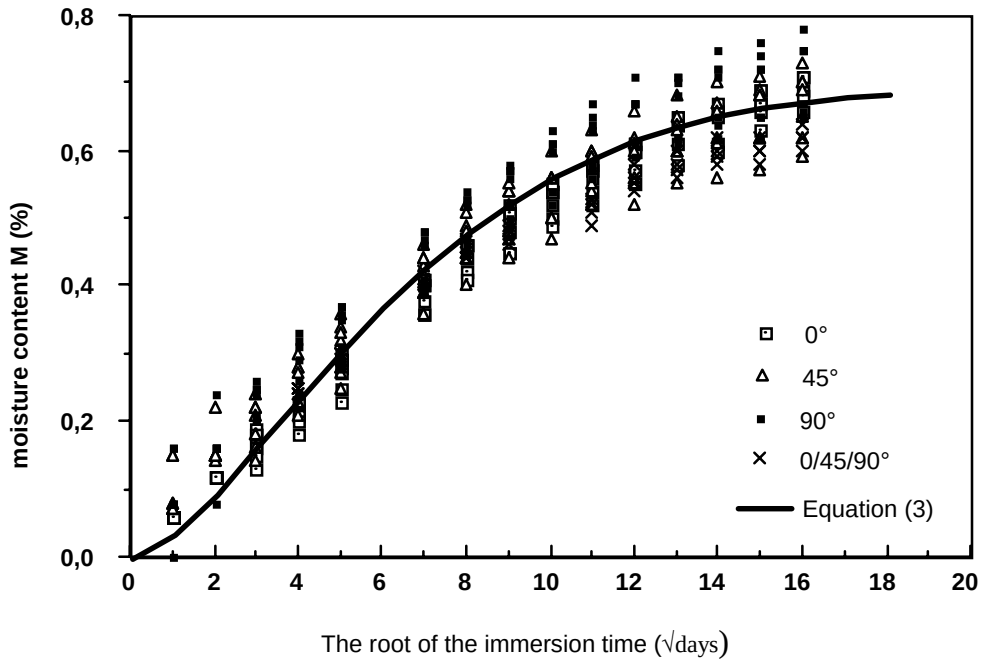

Figure 1: Moisture content in function of the root of the immersion time for the four laminates of glass/epoxy

STATISTICAL LAW OF WATER ABSORPTION

Test Method for Normal Distribution

As well known, the statistical advantages of the normal distribution are quite considerable and many physical measurements has been found following approximately the normal curve. The normal distribution corresponds to the following equation:

$$F(x) = \int_{-\infty}^{x} \frac{1}{\sqrt{2\pi}\sigma} \exp\left[-\frac{(t-\mu)^2}{2\sigma^2}\right] dt \tag{6}$$

where F(x) is the cumulative probability from -∞ to an assigned value x, μ is the mean of the population and σ is the standard deviation of the population.

In order to determine whether the frequency distribution of the M values for a given immersion time approximates a normal distribusion, the following steps have be performed:

1. range the data of M from smallest to largest value and divide them into a series of equal-valued "class intervals", and calculate, for the class interval number i, the mean of M: M_i;
2. determine the frequency of the data falling within class interval number i and the corresponding cumulative frequency, the last was transformed then as the standard normal variable μ_{pi} with the help of the statistical table of normal distribution;
3. The M_i values so obtained are plotted against the μ_{pi} values. If these points can be fitted well with a straight line, the normal distribution of the measured M is verified.

This method will be used for determining the statistical distribution of the moisture parameter.

Statistical Distributions of the Moisture Content

In our statistical analysis, under the same immersion time, the M measurement has been carried out on at least 21 specimens, which are grouped as a sample of population. The population, in this case, is the collection of all laminated types of composite studied which possessed the same volume fraction of the fiber and were tested under the same condition. Certainly, this treatment will provide us a statistical law in a more broad sense.

Using the method mentioned above, we have tested 15 groups of data corresponding respectively to different immersion times. The relations between M and μ_p are illustrated in Figure 2 . It is indicated that the points for each immersion time correspond well to a straight line and so we can conclude that the statistical distributions of the moisture content well approximate the Normal Distribution on the nearly whole absorption process.

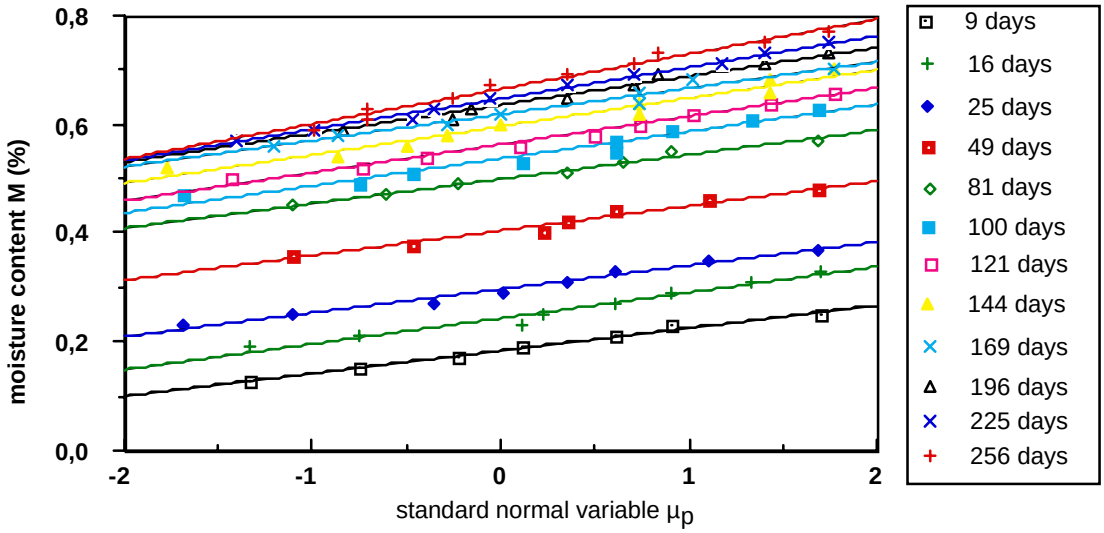

Figure 2: The relations between M and μ_p

This resultant can be described as:

$$M(t) = \overline{M}(t) + \sigma(t)\,\mu_p \qquad (7)$$

where $\overline{M}$ (t) is the mean of the population, σ(t) is the standard deviation of the population for a given immersion time t and μ_p is the standard normal variable.

Table 1 presents the results obtained for the normal parameters $\overline{M}$ (t) and σ(t) at each immersion time studied.

Table 1: Estimated parameters $\overline{M}$ (t) and s(t) in function of the immersion time

Immersion time t (days)	Mean of the population μ (%)	Standard deviation σ (%)	Linear correlation coeffient r
4	0.184	0.0417	0.994
16	0.243	0.0472	0.984
25	0.297	0.0435	0.990
49	0.404	0.0455	0.984
64	0.462	0.0447	0.990
81	0.499	0.0449	0.993
100	0.537	0.0498	0.978
121	0.563	0.0519	0.991
144	0.596	0.0520	0.983
169	0.619	0.0480	0.987
196	0.636	0.0527	0.992
225	0.648	0.0574	0.997
256	0.665	0.0641	0.990

Correlation to Fick's Law

Based on the results of $\overline{M}$ (t) presented in Table 1, we can estimate the maximum moisture content: M^{μ}_{m} = 0.68%, and the moisture diffusivity D^{μ} = 6.251×10^{-8} mm^2/sec. They are necessary to establish the Fick's law (Eq. 3). The figure 3 makes a comparison between the points of $\overline{M}$ (t) presented in Table 1 and the equation 3, a good correlation has been observed.

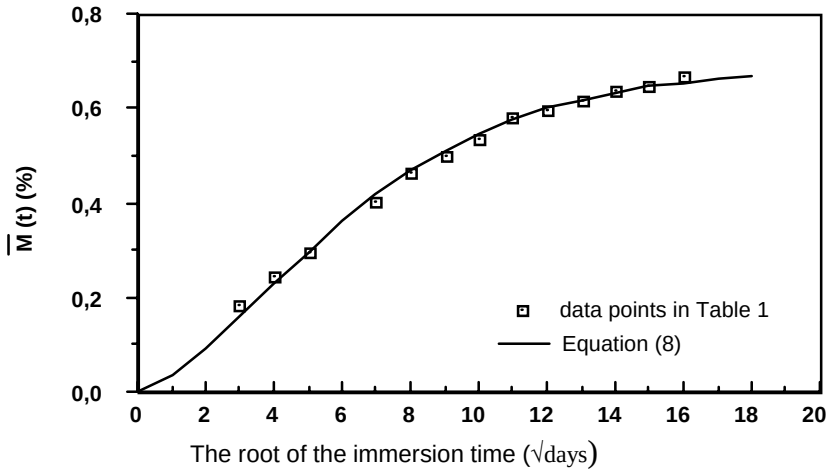

Figure 3: $\overline{M}$ (t) as a function of the root of the immersion time

Similarly, analysing the standard deviation σ(t) obtained (Tab.1), it seems that the results of σ(t) can be well described by an empirical model as (to see Figure 4):

$$\sigma(t) = A\exp(B\sqrt{t}) \tag{9}$$

where A = 0,037%, B = 0,0127$days^{-1/2}$.

So, the statitical law of the moisture content M(t) can be written as :

$$M(t) = M^{\mu}{}_{m}\left(1-\exp\left[-7.3\left(\frac{D^{\mu}\,t}{h^2}\right)^{0.75}\right]\right) + A\exp(B\sqrt{t})\,\mu_p \tag{10}$$

where μ_p is the standard normal variable and the second term of the equation may be regarded as the statistical modification of classical Fick' law.

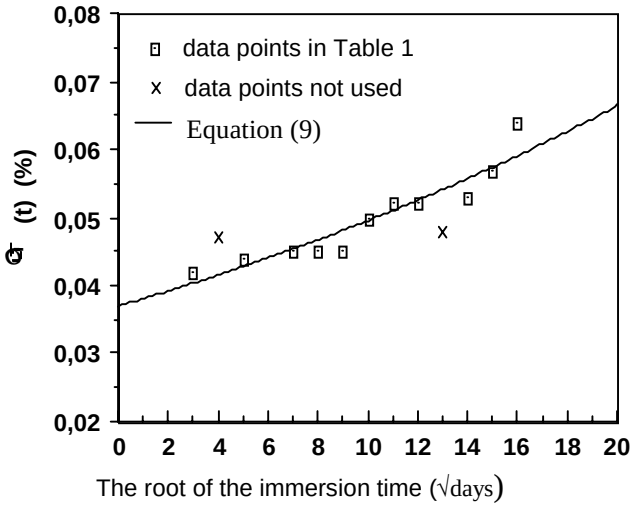

Figure 4: σ(t) as a function of the root of the immersion time

Application — Reliability Curve of M(t)

Based on the above results, we can deal quantitatively with the dispersion of water absorption process. The reliability curve of M(t) is a valuable example.

If we define the reliability degree R=0.90, the values of M(t) under the cumulative probability 5% (correspond to μ_p = -1.645) and 95% (correspond to μ_p = 1.645) can be determined by using equation (10). Plotting the results on the figure 5, a reliability curve of M(t) is obtained. It means that for the 8 ply glass/epoxy specimens with a 65% volume fraction of the fiber under a test condition of this paper, it has 90% reliability for the M(t) to fall within the interval of 5% and 95% cumulative probability curves presented in figure 5.

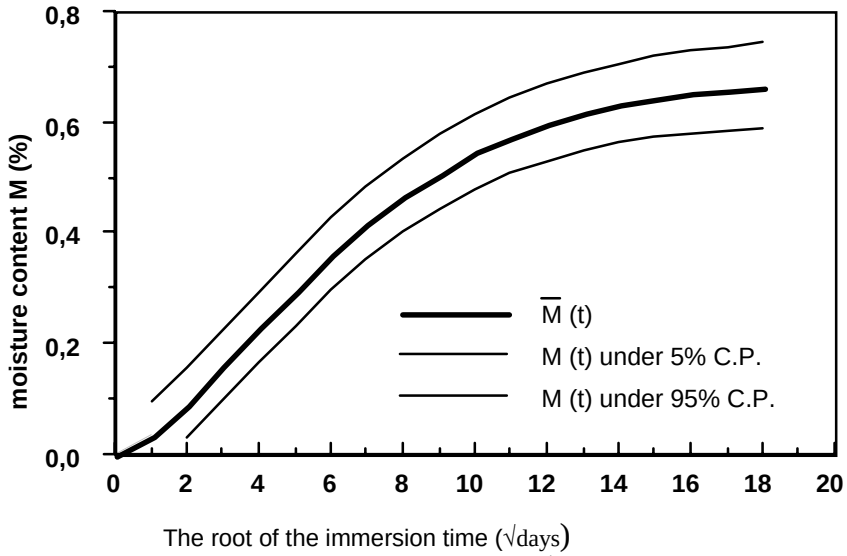

Figure 5: Reliability curve of M versus √t (C.P. — cumulative probability)

In the same way, we can obtain the reliability curve of M(t) for any reliability degree R (0.95, 0.99 or others).

These curves provide a statistical estimate of the water absorption process; moreover, they provide an analytical base for us to study the dispersion on degradation of mechanical properties of composite materials due to water absorption.

CONCLUSIONS

On the basis of the results obtained, the following conclusions can be made regarding the statistical analysis on the water absorption process of the glass/epoxy composites:

1. The statistical analysis of this paper is established on the specimens which possess the same volume fraction of the fiber but different laminated types. This kind of treatment will result in a statistical law in a more broad sense.
2. The statistical distributions of the moisture content well approximate the Normal Distribution on the nearly whole absorption process.
3. The statistical law of water absorption can be described as the classical Fick' law with addition to a statistical modification.
4. A reliability curve of the moisture content M(t) is given which may be practically employed for the water absorption process of the glass/epoxy composites.

ACKNOWLEDGMENT

The authors would like to express appreciation to Mr. Sh.AIVAZZADEH for supporting the work presented here.

REFERENCE

1. Springer, G.S., Environment Effects on Composites Materials, Vol. 1, Technomic Publishing Co. Inc., 1981.

2. Springer, G.S., Environment Effects on Composites Materials, Vol. 2, Technomic Publishing Co. Inc., 1981.

3. Hu B., Gong X.J., "Modélisation de l'absorption de l'eau dans les composite stratifiés verre/époxyde", MECAMAT, Journée scientifique et Technique, Chatillon, France, 29 mai 1997

4. Morii T., "Weight Changes of Randomly Oriented GRP Panel in Hot Water", Composites Science and Technology, Vol. 49, 1993, pp. 209-216.

5. Morii T., "Weight Changes of the Fiber/Matrix Interface in GRP Panels Immersed in Hot Water", Composites Science and Technology, Vol. 50, 1993, pp. 373-379.

6. Baillargeon G., Méthodes Statistiques de L'ingenieur, Les Editions SMG, 1990.

7. Dieter Engineering Design - a Materials and Processing Approach, McGraw-Hill Inc., 1991.

DURABILITY OF ISOTHERMALLY AGED POLYMER MATRIX COMPOSITES

David Harmon

McDonnell Douglas Aerospace, P. O. Box 516, MC S102-1322, St. Louis, MO 63166, USA

SUMMARY: Several composite material systems representing different classes of polymer materials have been selected for an isothermal aging program designed to assess the durability of these systems when exposed to temperatures up to 232°C/450°F. Data discussed will include results up to 10,000 hours of aging. Properties that are monitored include weight loss, glass transition temperature, and various mechanical properties. The results of these studies have identified systems which have better temperature stability and have helped identify some of the dominant degradation processes that effect residual physical and mechanical properties. This data is being used to develop strength and life prediction analyses which in turn will be used for screening potential accelerated aging methodologies.

KEYWORDS: composite durability, long term aging, accelerated aging, residual strength, prediction methodology, oxidation/diffusion

INTRODUCTION

An understanding of advanced polymeric matrix composite (PMC) material durability behavior in the extreme flight regimes associated with the High Speed Civil Transport (HSCT) is necessary before these materials can be implemented. PMC materials under development for advanced military aircraft may meet these durability requirements, but are costly and not optimized for the long-term elevated temperature HSCT environment. Long-term and accelerated test procedures and methods are required to shorten the development and verification time of new PMC materials for the HSCT.

Under the High Speed Research program, NASA and an industry team, composed of The Boeing Company, McDonnell Douglas Aerospace, Lockheed-Martin Aeronautical Systems, and Northrop-Grumman Corporation, are working together to assess the long term durability of candidate polymer matrix composite material systems. This work is divided into three tasks: Database Generation, Prediction Methodology, and Accelerated Aging Test Methodology. Efforts conducted under this program in each of these areas has provided the foundation for the current NASA/Industry Materials and Structures Program for the HSCT.

The database generation task is designed to provide test data for material systems which have been exposed to real time, long term exposure conditions. This is being accomplished in a building block fashion which allows for an understanding of the individual factors which control the mechanisms which dominate the material performance. Aging conditions include isothermal aging, isothermal aging with an applied constant axial load, thermal cycling, and thermomechanical fatigue. It is also in this task in which real time, long term flight profile testing is being conducted. Large composite panels have been placed in test frames with ovens and are being subject to a simulated flight profile. These tests will be conducted for up

to 60,000 hours and will provide the necessary real time data to which the accelerated test methods will be compared for purposes of verification.

In the accelerated test methodology task, additional testing is being performed to examine how it may be possible to accelerate the aging process in the composite materials without changing the degradation mechanism as compared to the real time test results. Changing the damage mechanism would invalidate the accelerated test technique. To accomplish this goal, additional testing is performed to specifically examine those factors and their magnitudes which have the most effect on material behavior, both physically and mechanically. Examples of the types of aging conditions are: isothermal aging at temperatures slightly below the glass transition temperature, changing the exposure environment (i.e. argon, air, oxygen), examining the effects of moisture and ultraviolet radiation, etc.. Essentially, the concept is to make use of those environmental factors that the aircraft will be exposed to naturally and increase their magnitude to determine if the aging process can be accelerated. And if so, how fast can it be accelerated. This task also allows for the examination of synergistic effects associated with exposing the composite material system to two or more environmental conditions at the same time.

Once an understanding of how the material behaves under different exposure conditions is obtained, then analysis methods may be developed and used to predict the material performance. This is being accomplished under the prediction methodology task. These methods will be used to help define the exact accelerated test conditions needed to accelerate the aging process for a material system. It is important to note that the accelerated test methods will be material dependent. It is presumptuous to believe that all material age the same way and therefore will degrade identically. In this program, we have selected candidate and model materials for evaluation. The candidate material is one which is hoped will show little or no degradation over 1 lifetime of aging. While that means the material is good for the aircraft, it tells us little of how to accelerate the aging process in the material. Therefore, model materials are also chosen which are known to degrade over 1 lifetime of exposure. Ideally, the chosen model material is of the same family as the candidate material such that any accelerated methods that are proven to work for the model system may also work for the candidate system over a longer period of time.

DATABASE GENERATION

In the Database Generation task, efforts are focused on the selection and screening of candidate polymeric composite materials that showed potential to operate for long duration (>60,000 hours) at temperatures between 121°C/250°F and 177°C/350°F. Eight (8) material systems were initially selected for a series of mechanical and physical screening tests after isothermal aging as shown in Figure 1. The objective of these screening tests was to select three (3) material systems for extensive long-term thermal aging studies and to select two (2) material systems for accelerated test methodology development. Results discussed will include test data of material systems aged up to 10,000 hours [1]. Aging of these systems will continue past 60,000 hours.

A series of physical/chemical tests were performed on each of the eight screening materials to: l) characterize the material systems for comparison with each other, 2) establish baseline values for each of the material systems for later comparison with aged data; and 3) develop possible screening tools. Each of these physical/chemical tests provided information about

the material system on the molecular or microscopic level as compared to the mechanical testing that provided data on a macroscopic scale. It is critical that data from both the microscopic and macroscopic scales be gathered on these materials systems for comparison and correlation. At the temperatures of the HSCT flight environment, the long-term durability of a material system depends ultimately on the molecular properties of the polymer chain and on the interface of the resin with the carbon fibers as well as their microscopic order or morphology. In addition, it is crucial to establish and understand the nature of the molecular-structure/macroscopic property relationships that exist in these high performance polymer systems if meaningful accelerated aging studies are to be conducted.

Weight change and microcracking measurements shown in Figures 2 and 3 were made periodically to determine the effect of aging at the various temperatures on the different material properties. It is obvious from these measurements that the thermoplastic IM7/ITX and the thermoplastic/polyimide IM7/K3B appear to have been the least affected by the aging conditions. Based on these results, these two materials and a third, G40-800/XU71787.09L cyanate ester, were chosen for more extensive mechanical testing and evaluation. Both IM7/ITX and IM7/K3B were considered candidate HSCT material systems at 149°C/300°F and 177°C/350°F, respectively. The cyanate ester system, G40-800/XU71787.09L, was chosen as a model material system at 177°C/350°F.

Mechanical tests conducted on IM7/ITX, IM7/K3B, and G40-800/XU71787.09L included open-hole tension, open hole compression , and compression strength after impact on quasi-isotropic laminates. Data from these tests are shown in Figures 4 and 5. Glass transition temperature measurements also shown in Figure 5 were also made on the unaged and aged material. The data is consistent in that the IM7/K3B and IM7/ITX material systems show no statistical degradation in mechanical properties, while the G40-800/XU71787.09L material system does. Glass transition temperature increased with aging time for IM7/ITX, was constant for IM7/K3B, and decreased for G40-800/XU71787.09L.

ACCELERATED TEST METHODOLOGY

The goal in this effort was to establish a method for obtaining end-of-life thermomechanical properties of advanced polymer matrix composites through accelerated aging. Considering that future aircraft require two lifetimes of testing to meet reliability requirements as currently outlined by the Federal Aviation Administration, a means of obtaining certification in an accelerated fashion is required. This accelerated certification testing must simulate flight and produce the failure modes and property degradation expected during the aircraft lifetime.

An environment screening program was performed to identify test parameters and magnitudes required to accelerate the aging process. The test program included exposure temperatures of 177°C/350°F, 193°C/380°F, 204°C/400°F, and 232°C/450°F, and pressure levels of 0.14 atm, 1.0 atm, and 6.8 atm. Exposure times ranged from 250 hours to 2000 hours. Panel lay-up was a 16 ply quasi-isotropic panel $[45/0/-45/90]_{2s}$. Studies for this effort concentrated on two polymeric composite material systems; IM7/K3B and G40-800/XU71787.09L. Chemical, physical and mechanical studies were conducted on specimens after exposure to the various accelerated aging environments. Weight loss was large for the G40-800/XU71787.09L material system relative to IM7/K3B. This data is plotted in Figure 6.

An empirical model was developed to predict weight loss response of the G40-800/XU71787.09L system to temperature and pressure. Data correlation with this model is provided Figure 7. This model assumed a diffusion controlled process through the thickness of the laminate. Diffusivity data was calculated for each weight loss curve and plotted to provide relationships with exposure temperature, pressure, and time. Edge effects were also accounted for by dividing the diffusivity by a geometry dependent factor.

The model was used to define accelerated aging environments based on the premise that equivalent laminate weight loss results in equivalent damage. Three accelerated aging conditions were defined to provide identical weight loss measurements to real time aging conditions for the G40-800/XU71787.09L material system:

Real Time Aging Condition	Accelerated Test Condition (ATC)
177°C/350°F, 1.0 atm, 5000 hours	204°C/400°F , 1.0 atm, 960 hours (ATC #1)
177°C/350°F, 1.0 atm, 5000 hours	182°C/360°F , 6.8 atm, 990 hours (ATC #2)
177°C/350°F, 1.0 atm, 10000 hours	204°C/400°F , 1.0 atm, 2000 hours (ATC #3)

A second set of G40-800/XU71787.09L panels with different length to width ratios as compared to the original screening tests were aged under the real time and the accelerated aged conditions described above. Weight loss measurements compared very well with the model predictions. Weight loss for the 5000 hour real time condition and the two accelerated aging conditions (ATC #1 and ATC #2) was 0.57%. It should be noted that the model was derived with data which had accumulated at most 5000 hour of exposure time. Therefore, the 10000 hour weight loss prediction was an extrapolation of the available data and as a result was the case with the worst agreement with the data. In fact, it took 2900 hours of exposure at 204°C/400°F and 1.0 atm in order to match the 10000 hour weight loss measurement under real time conditions.

Mechanical property testing was also performed to determine if weight loss could be a tracking parameter to which mechanical property changes in the material system could be linked. Open hole tension and compression tests were conducted at room and elevated temperatures and compared to data from all aging conditions as shown in Figure 8. The data was plotted against the simulated time for the accelerated aging conditions. For all conditions except one the data from all aged conditions fell within the scatter band. Statistically, the accelerated aged conditions provided the same residual properties as the real time conditions. The one case in which that was not true was for the elevated temperature open hole compression test performed after 10000 hours of aging. The residual strength of the accelerated aged panel fell well below the residual strength of the real time aged panel.

The poor correlation after 10,000 hours at 204°C/400°F can be traced to the glass transition temperature of the material. Dynamic mechanical analysis of specimens from aged panels shows that the glass transition temperature changes significantly as the material ages as can be observed in Figure 9. For less than 5,000 hours, the glass transition temperature (Tg) does not change significantly at the two lower aging temperature; and little change is observed in the mechanical properties. After 10,000 hours at 177°C/350°F, the Tg is reduced to 242°C/468°F which is still well above the elevated test temperature of 177°C/350°F. For the ATC #3 (2,900 hours at 204°C/400°F) condition, however, the Tg has dropped to 182°C/360°F which is below the aging temperature and only 10°C above the test temperature. It is not surprising that the compression strength was severely degraded.

PREDICTION METHODOLOGY

Under the Prediction Methodology task, efforts are directed toward developing both a physical degradation (aging) model and a structural mechanics model to account for long term aging effects on the residual mechanical properties of polymer matrix composites. The long term goal of this work is to combine these models into one analysis package that would allow an engineer to predict residual properties of candidate polymer matrix composite materials after exposure to a typical HSCT environment. This will be particularly useful in defining accelerated aging theromechanical spectra.

The overall predictive methodology for polymer composites has three parts. First, develop a model capable of predicting the change in a physical parameter, such as weight change or glass transition temperature, due to the exposure environment. Second, establish an empirical, material dependent relationship between the physical parameter and specific mechanical properties (i.e. stiffness, strength, etc.). Third, the "aged" lamina properties are fed into a laminate strength code to predict the residual properties of the laminate. The entire analysis package is called ISAAC (Integrated Strength Analysis for Aged Composites). Work is currently on-going in each of these three areas. The overall prediction methodology is being validated by predicting the results of the many aged laminate tests.

The physical aging model concentrated on an oxygen diffusion/oxidation model to analytically simulate the diffusion of oxygen into the composite and the subsequent oxidation of the polymer material [2-5]. Diffusion and reaction rate data was measured from controlled experiments on G40-800/XU71787.09L and IM7/K3B material systems. This data was used in a finite element model to measure the concentration of oxygen through the thickness of the laminate. The results are plotted in Figure 10. Based on photomicrographs of the surface layers, a two-phase model was develop which allowed a surface "ash" layer to form with different diffusion and reaction rate constants than the center core laminate. The model was correlated with "ash" layer thickness measurements as shown in Figure 11 for G40-800/XU71787.09L laminates aged at 149°C/300°F and 177°C/350°F [6].

The strength analysis portion of the ISAAC code allows prediction of laminate modulus [7] and strength based on constituent and ply properties. The analysis can be used for predicting unnotched and center notched laminates subject to axial and/or bending running loads [8, 9]. The analysis is done on a ply-by-ply basis and provides output every time a ply is predicted to fail. Failure modes are determined and specified based on ply failures. Multiple failure criteria are provided including maximum stress, maximum strain, modified maximum shear strain (based on work done by Hart-Smith [10]), Tsai-Hill, and Tsai-Wu. The effects of thermal residual stresses may also be included in the analysis.

This portion of the ISAAC code was designed to accept constituent and ply properties after being degraded due to long term exposure to harsh environments. Currently, the analysis can be used to predict the strength and stiffness of aged composite coupons when provided degraded constituent and lamina data. ISAAC predictions and test data for the G40-800/XU71787.09L material system are shown in Figure 12. The ply-by-ply nature of the input allows different levels of deterioration for layers closer to the surface of the laminate. The ISAAC code, in its current form, is well suited for performing trade studies to evaluate the effects of degradation on laminate mechanical performance. These trade studies have correlated laminate mechanical properties with ply degradation as a function of ply location in the laminate. These studies have been useful in defining the number of surface plies which

must be degraded in order to match aged material response. Although not completed, the long term goal for the ISAAC strength analysis code is to tie it to physical aging model which would determine the amount of degradation as a function of ply location and environment.

CONCLUSIONS

Key to the development of a High Speed Civil Transport is ensuring that the materials selected are capable of withstanding the exposure conditions for an estimated lifetime of 60,000 hours. However, without adequate test data, reliable prediction capability, and verifiable accelerated test methodology this cannot be accomplished. Each of these tasks are very important and rely on each other.

In this paper, a brief review is provided which demonstrates the type of data being developed under each of the three main tasks: Database Generation, Accelerated Test Methodology, and Prediction Methodology. Data is provided for several systems with particular attention focused on the cyanate ester material system, G40-800/XU71787.09L. This material system is a good example of one which shows significant degradation within the operating envelope of the HSCT. As a result this material is not considered a candidate material system. Testing on this system continued however, because it was originally considered a model material system. Further testing discovered its key degradation mechanism to be a drop in glass transition temperature as aging exposure time increased. This drop was accelerated at higher aging temperatures. In order to develop reliable and accurate prediction methods for G40-800/XU71787.09L, it would be necessary to map the glass transition temperature as a function of each exposure condition and then to model the effect of a change in Tg with changes in mechanical properties. However, since the degradation mechanism of G40-800/XU71787.09L is not the same as the candidate materials further work on this system is not required. Instead new model materials are now being defined and similar exploratory testing is underway.

It is prudent to point out that the risk associated with the development of accurate and reliable accelerated test techniques is high. In fact, it may be too lofty a goal. A more likely outcome of this work could be a series of screening tests to which a material would be subject. Further testing of the material system would be dependent on passing each preceding test series. If a material passes each test series, than it would be a candidate for long term exposure testing and eventual use on the aircraft. The testing and analytical efforts discussed are required to define these screening tests. Ideally, this work will provide a template which will define the types of tests that should be conducted on new materials as they become available.

REFERENCES

1. Renieri, M. P., Hipp, R. C., Harmon, D. M., Grayson, M. A., Wanthal, S. P., Finefield, M. A., and Saff. C. R., “High Speed Research: Composite Materials and Structures Development”, NASA Contractor Report 198346, Part 1, September 1996.

2. Emanuel, N. M. and Buchachenko, A. L., Chemical Physics of Polymer Degradation and Stabilization, translated from Russian by E. N. Ilyina, VNU Science Press, Utrecht, the Netherlands, 1987.

3. Crank J., The Mathematics of Diffusion, 2nd Ed., Oxford University Press, New York, 1975.

4. Carslaw, H. S. and Jaeger, J. C., Conduction of Heat in Solids, 2nd Ed., 1959.

5. Zienkiewicz, O. C. and Parekh, C. J., "Transient Field Problems: Two-Dimensional and Three-Dimensional Analysis by Isoparametric Finite Elements," International Journal for Numerical Methods in Engineering, Vol. 2, pp. 61-71, 1970.

6. Nam, J. D. and Seferis, J. C., “Anisotropic Thermo-Oxidative Stability of Carbon Fiber Reinforced Polymeric Composites,” SAMPE Quarterly, June 1992.

7. Jones, R. M., Mechanics of Composite Materials, McGraw-Hill Company, St. Louis, 1975.

8. Harmon, D. M. and Finefield, M. A., "Thermomechanical Load History Effects in Metal Matrix Composites - 3rd Interim Report", MDA 93B0050, February 1993.

9. Lehknitskii, S. G., Anisotropic Plates, Gordon and Breach Science Publishers, 1968.

10. Hart-Smith, L. J., "A Scientific Approach to Composite Laminate Strength Prediction," DAC 8467, April 1990.

Material ID	Material Name	Polymer Family	Aging Temperatures		
			121°C/250°F	149°C/300°F	177°C/350°F
A	IM7/ITX	Thermoplastic	X	X	
B	IM7/SP500-2	Epoxy	X	X	
C	IM7/5250-4	Bismaleimide	X	X	
D	G60-600/5250-4	Bismaleimide	X	X	
E	IM7/3135	Bismaleimide		X	X
F	IM7/K3B	Polyimide		X	X
G	G40-800/XU71787.09L	Cyanate Ester		X	X
H	IM7/AB-BCB-MI	Benzocyclobutene		X	X

Figure 1: Polymer composites in durability program

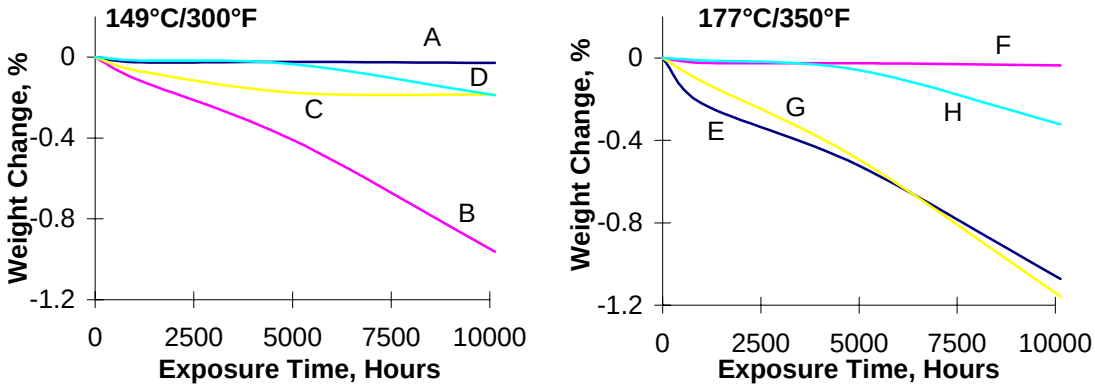

Figure 2: Thermal aging screening

Material	Aging Temp °C/°F	5000 Hours aging		10000 Hours Aging	
		Center	Surface	Center	Surface
IM7/ITX	149/300	None	None	Several	Minor
IM7/SP500-2	149/300	Several	Several	Extensive	Extensive
IM7/5250-4	149/300	None	None	None	Minor
G60-600/5250-4	149/300	Several	Several	Several	Several
IM7/3135	177/350	None	Several	None	Several
IM7/K3B	177/350	None	None	None	Minor
G40-800/XU71787.09L	177/350	None	Major	None	Major

Figure 3: Microcracking studies after aging

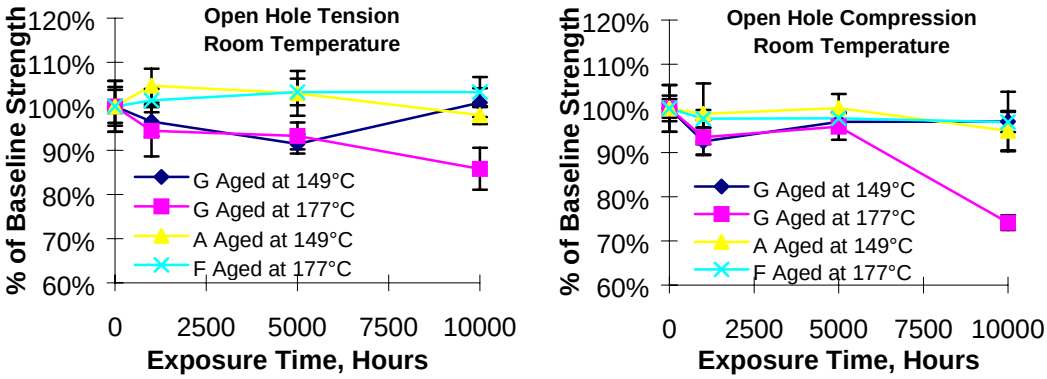

Figure 4: Open hole tension and compression data

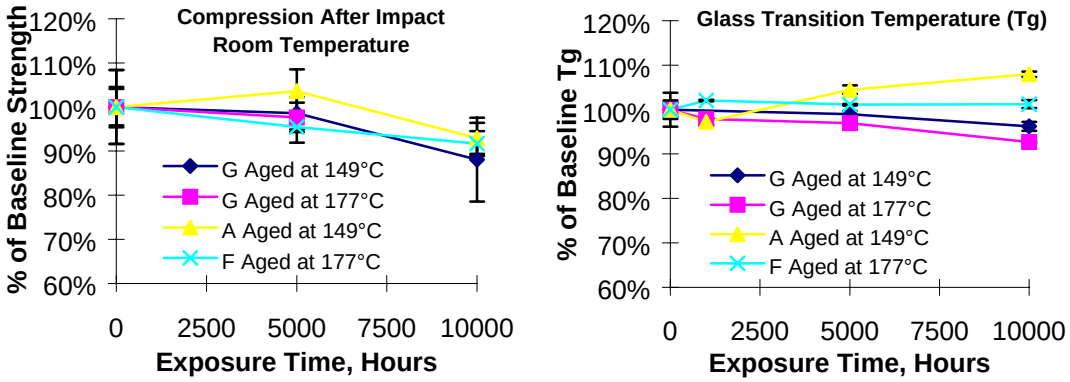

Figure 5: Compression after impact and glass transition temperature data

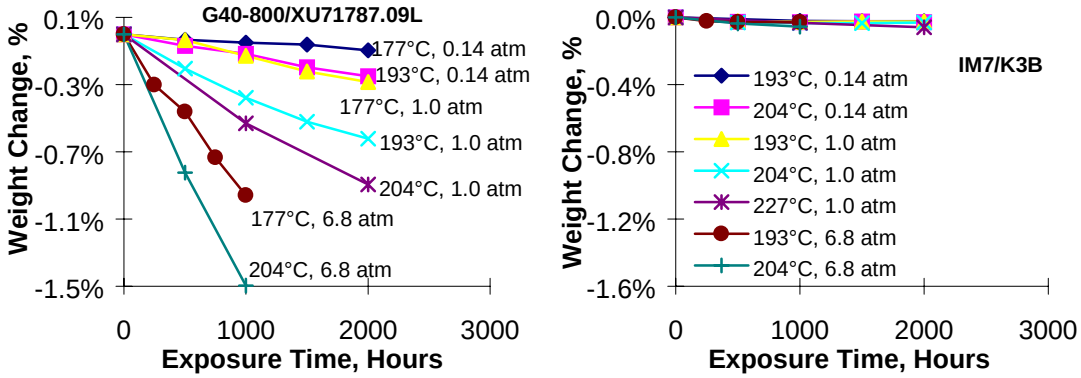

Figure 6: Accelerated weight loss data

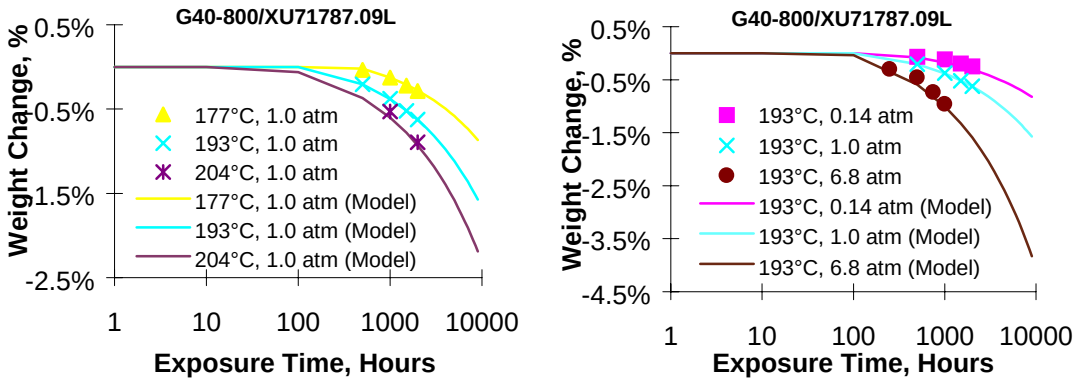

Figure 7: Model weight loss predictions for G40-800/XU71787.09L

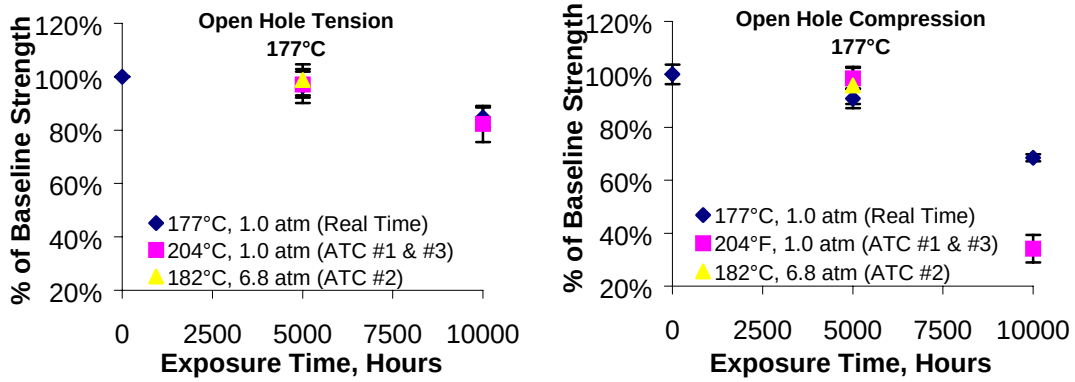

Figure 8: Accelerated and real time open hole tension and compression data

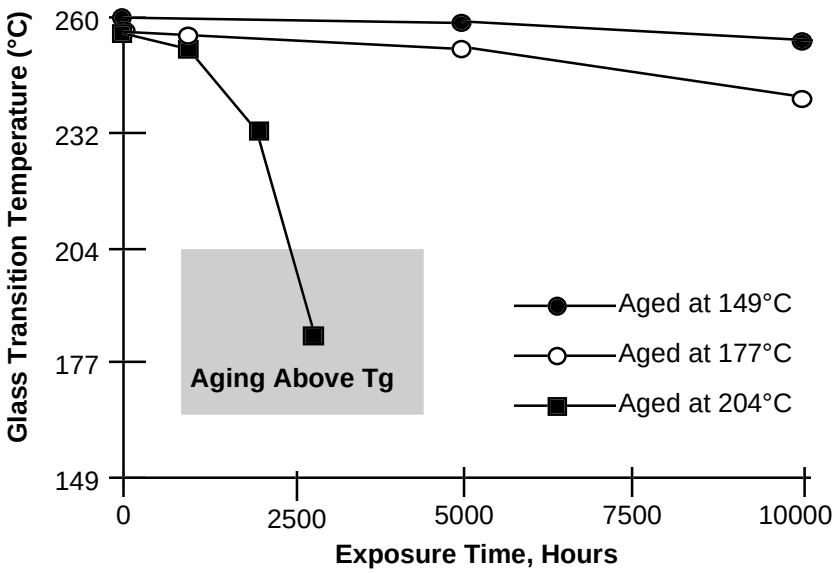

Figure 9: DMA data for G40-800/XU71787.09L

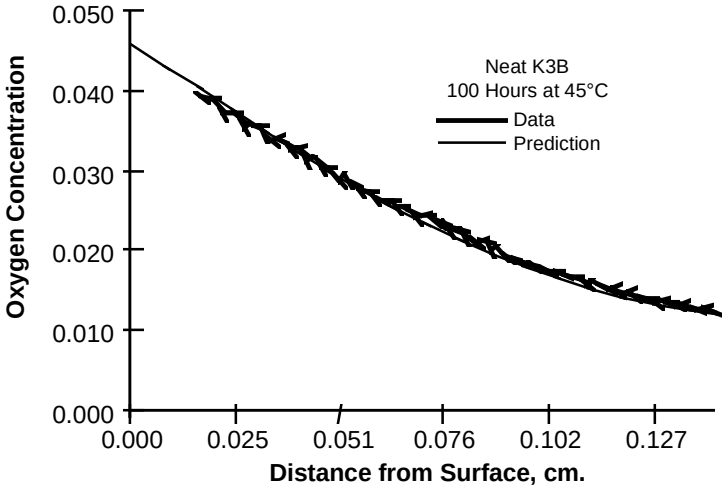

Figure 10: Oxygen diffusion model correlation

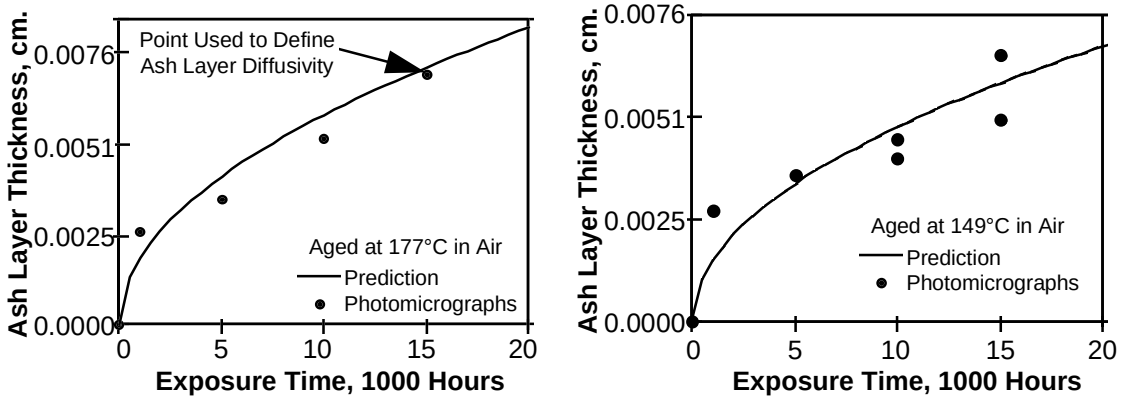

Figure 11: Ash layer model correlation

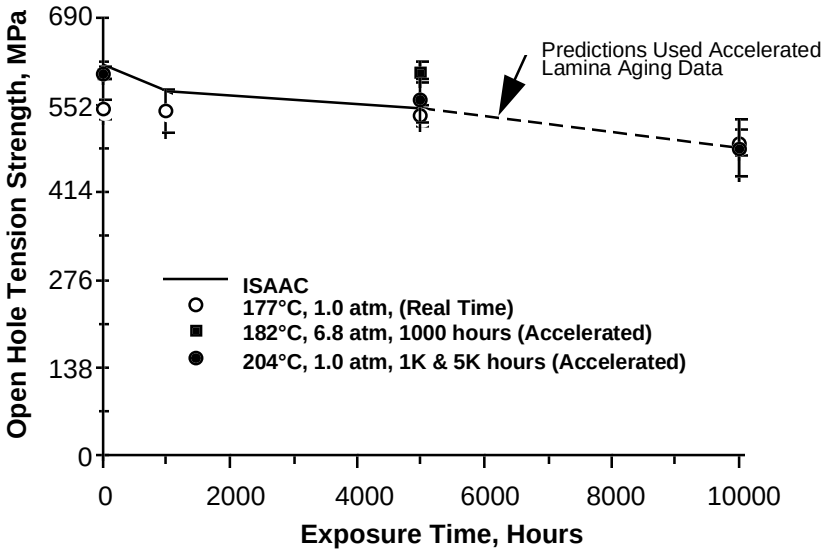

Figure 12: ISAAC strength predictions

THE MECHANICAL TESTING OF CONTINUOUS FIBRE REINFORCED THERMOPLASTIC PIPES

B.J. Chapman[1], J.T. Evans[1], S.R. Frost[2] and A.G. Gibson[1]

[1] Centre for Composite Materials Engineering,
University of Newcastle upon Tyne, Newcastle upon Tyne NE1 7RU, U.K.
[2] Shell Research and Technology Centre, P.O. Box 38000,
1030 BN Amsterdam, The Netherlands.

SUMMARY: The results of tests on reinforced thermoplastic pipes, internally pressurised with closed end conditions, are reported. Because the fibres used for reinforcement are not infiltrated, a feature of the deformation at low pressures is a high degree of non-linearity. The behaviour can be understood if it is assumed that non-linear visco-elastic and plastic deformation of the polyethylene occurs without fibre loading over a range of strain required to straighten the fibre yarn. At higher strains load is increasingly borne by the fibres up to the point of rupture. The strain pressure relations are interpreted in terms of netting analysis and laminate theory.

KEYWORDS: reinforced thermoplastics, pressurised pipes, reinforcing tape, non-infiltrated fibres, non-linear deformation.

INTRODUCTION

Reinforced thermoplastic pipes (RTPs) possess an attractive combination of properties. They have good strength under internal pressure, flexibility in installation and good corrosion resistance. These features make RTPs attractive for replacing steel and glass fibre-reinforced thermosets. Possible applications include offshore flexible risers and umbilicals and onshore flow lines. The materials costs of RTPs greatly outweigh those of steel and glass reinforced epoxy but owing to the particular combination of properties of RTPs, resulting in ease of handling during installation, the total capital expenditure costs are comparable with other pipeline options. In addition, because of its good corrosion resistance, the life of an RTP may be up to four times longer than the equivalent steel pipeline in many operations. Consequently, there is much current interest in the development of RTP systems. The introduction of RTPs can be viewed as a development leading on from the polyethylene pipes that have replaced cast iron in low pressure gas and water distribution systems. The advantage of RTPs is that they have much higher pressure capacity, whilst retaining much of the bending flexibility of polyethylene.

MATERIALS AND METHOD

The RTPs were manufactured using a special composite tape (Fig. 1). This consists of non-infiltrated aramid yarn encapsulated in medium density polyethylene (MDPE) to form tape, 105 mm wide and 0.85 mm thick. The tape contains 0.32 volume fraction of fibres and has a

Young's modulus of 27.8 GPa in the fibre direction and 0.5 GPa in the transverse direction. The in-plane shear modulus is 0.4 GPa and the Poisson's ratio is 0.315 for transverse contraction in reaction to a strain applied parallel to the fibres. The tubes were manufactured using a pull-winding process in which the tape was wrapped around either a MDPE or a high density polyethylene (HDPE) liner to provide a reinforcement inclined at ±55° to the tube axis. An outer skin of MDPE was then added by an extrusion process. Tubes supplied by two manufacturers were tested. Specimens supplied by Wavin (MDPE liner) contained two tape layers (internal diameter 100 mm, total wall thickness of 25 mm). The tubes supplied by Tubes d'Aquitaine contained four tape layers over a HDPE liner with a MDPE skin (internal diameter 141 mm, total wall thickness 31.2 mm).

A particular problem in testing RTPs is attachment of the end fittings. Because of the difficulty in forming a strong adhesive bond with thermoplastics, mechanical methods of fitting are preferred. The Wavin RTPs were press fitted into PECAT fittings (supplied by WASK-RFM). These are steel-flanged end fittings with a steel core fitted with O-rings. The end closure for the Tubes d'Aquitaine RTP was made by cutting an external thread in the outer MDPE layer. A threaded aluminium fitting was screwed on over the tube end. The tubes were tested in 1.5 m lengths by hydraulically pressurising at a mean rate of 10 bar per minute in the region of linear behaviour.

Hoop strain was deduced from the mean change in the tube diameter measured at the centre of the specimen and at two other points 100 mm on either side. The changes in diameter were measured with linear displacement transducers held in special fittings. With the Wavin specimens, the axial strain was deduced from change in length of the tube measured with three linear displacement transducers spaced 120° apart around the circumference and connected to the end fittings. This measurement is liable to error if there is any slippage in the end fittings. The axial strain for the Tubes d'Aquitaine specimens were measured over a shorter gauge length using transducers attached to the tube surface with special fittings.

RESULTS

Examples of the strain-pressure relations are shown in Figs. 2. It is possible that the hoop strain increases linearly with pressure at very low pressures but on the pressure scale adopted for the tests the hoop strain is decidedly non-linear up to a strain of between 1.5 and 2%. Thus, a substantial hoop strain accumulates with relatively little pressure increase. At hoop strains larger than a critical value the pressure rises more rapidly for a given strain increment to give an approximately linear strain-pressure relation up to the burst point. These results can be rationalised if it is assumed that the aramid fibres do not begin to support the hoop stress until after the critical strain has accumulated. This is possible if the fibres within the yarn are initially slack and have to straighten to begin to support the load. The critical strain is required to take up the slack in the fibres and is here termed the "take up" strain. On this interpretation, the deformation observed in the non-linear region simply reflects the deformation of the polyethylene, without any effect of the fibres. An analytical model has been developed to

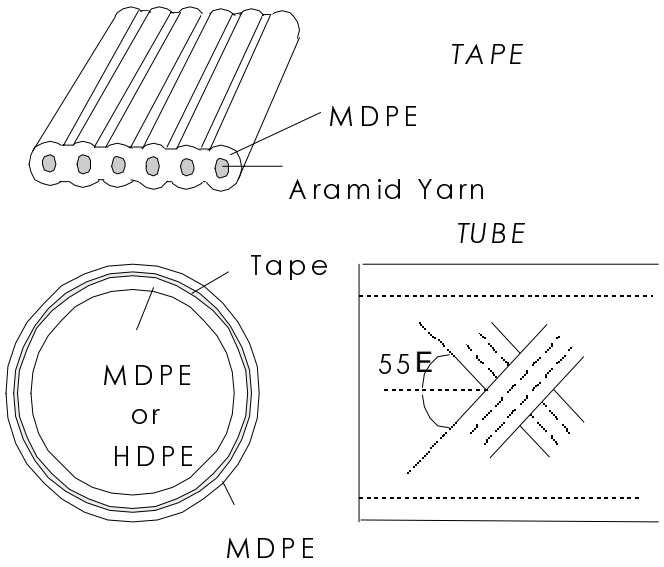

Fig. 1: Structure of reinforced thermoplastic pipes (RTPs)

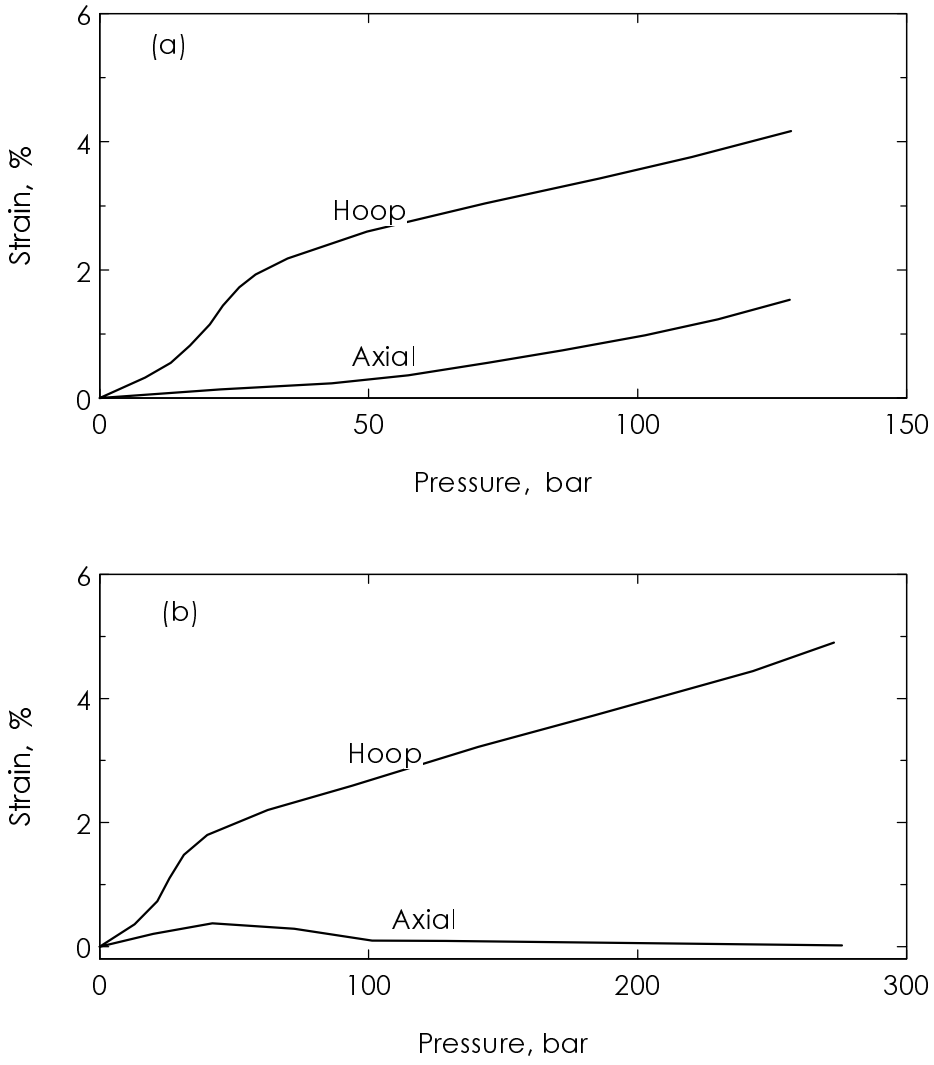

Fig. 2: Strain-pressure curves. (a) Wavin specimen (b) Tubes d' Aquitain specimen

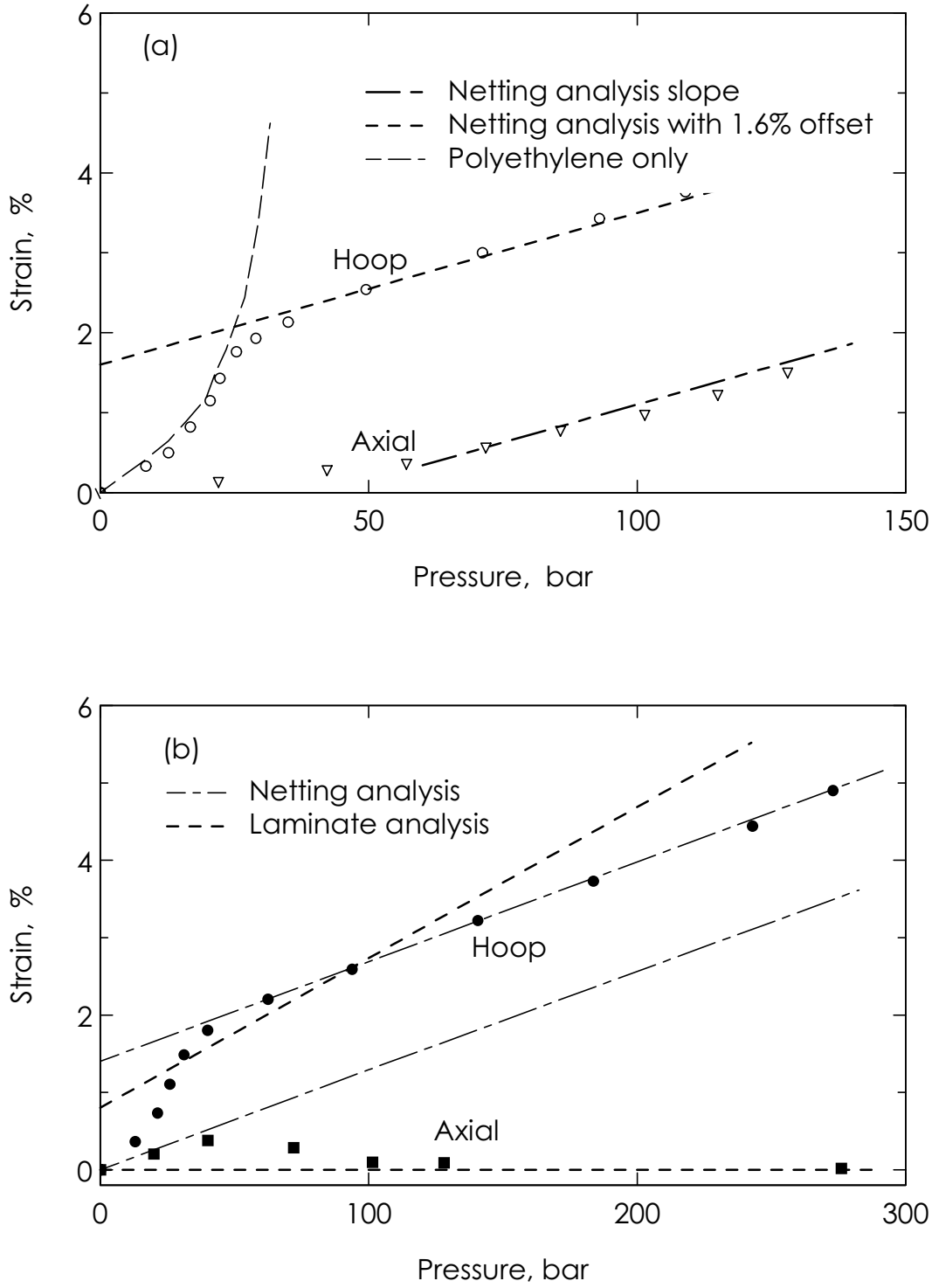

Fig. 3: Experimental data (points) fitted with composite curves (a) Wavin specimen (b) Tubes d'Aquitaine specimen

account for the size of the take up strain in terms of fibre characteristics [1] but this is not presented here.

In contrast to the hoop strain, the axial strain does not exhibit pronounced non-linearity in the pressure range from zero to 40 bar. In other words, as the tube inflates, with an increasing hoop deformation of the polyethylene, the axial strain increases by a much smaller amount. It will be argued below that the difference is due to the influence of the deviatoric stress components on plastic or non-linear visco-elastic deformation.

The axial strain-pressure relation in the Wavin specimen showed a degree of non-linearity at pressures greater than about 60 bar with a reduced slope at the higher pressures (Fig. 2 (a)). The axial strain in the Tubes d'Aquitaine specimen showed a small increase with pressure up to about 25 bar but reduced towards zero at higher pressures (Fig. 2 (b)).

The burst pressure was 128 bar for the Wavin specimen and 273 bar for the Tubes d'Aquitaine specimens. The form of the rupture was similar in all cases. It is probable that rupture begins when a critical fraction of the fibres in any location have fractured. Rupture then proceeds by necking of the polyethylene wall in the through-thickness direction. This is followed by extension of the rupture along one of the fibre directions accompanied by extrusion of fibres through the gap in the wall and depressurisation. The Wavin tubes exhibited a 150 mm long rupture after depressurisation. The length of rupture was slightly larger (200 mm) in the Tubes d'Aquitaine specimens and was found to zig-zag following both fibre directions alternately in the course of its development. The location of the rupture sites was found to vary. In some specimens the sites were located near the end fittings. In other specimens the rupture occurred closer to the central portion of the tube.

Analysis Of Deformation

For simplicity we assume the thin wall approximation for the stresses so that the effect of radial pressure is ignored. We also consider membrane stresses only and ignore bending stresses that might arise, for example, from the constraints exerted by the end fittings [2]. The reference coordinates are θ for the circumferential direction, r for the radial direction and z for the axial direction. The system is statically determinate, so with the thin wall approximation for a closed end cylinder, diameter D and wall thickness t the applied stress components are: $\sigma_{\theta\theta} = \sigma_h$, $\sigma_{rr} = 0$, and $\sigma_{zz} = \frac{1}{2}\sigma_h$, where $\sigma_h = pD/2t$.

Plastic or Non-linear Visco-elastic Deformation

In the pressure and strain range before the take up strain has accumulated the deformation is believed to reflect only the deformation of the polyethylene, with no influence exerted by the fibres. This idea is supported by the curve shown in Fig 3(a) of stress-strain data for MDPE tubes [3] fitted to the non-linear deformation observed in the RTP. However, no large scale, non-linear deformation is indicated by the axial strain at low pressures. The difference between the hoop and axial strain behaviour is believed to arise from the response of the material to the deviatoric stress components, as discussed below.

Pressure cycling tests and creep tests [1] have revealed that the non-linear deformation is composed of both plastic and non-linear visco-elastic components. Approximately, one half of the hoop strain observed in the take up region is plastic and irreversible. The other half of the

non-linear strain is reversible and rate and time dependent. The axial strain in the take up region was also found to be visco-elastic, but on a much smaller scale than the hoop strain.

It is well known that plastic deformation responds only to the deviatoric components of stress (e.g. ref. 4). We assume here that the same is true for non-linear, visco-elastic deformation. Since the hydrostatic stress component is equal to $\frac{1}{2}\sigma_h$, the deviatoric components are: $s_{\theta\theta} = \frac{1}{2}\sigma_h$, $s_{rr} = -\frac{1}{2}\sigma_h$ and $s_{zz} = 0$. The Prandtl-Reuss equations [4] give the total elastic-plastic strain rates in terms of the stress rates and the deviatoric stress components, i.e.

$$\begin{aligned} \dot{e}_{\theta\theta} &= \frac{1}{E}[\dot{\sigma}_{\theta\theta} - \nu(\dot{\sigma}_{rr} + \dot{\sigma}_{zz})] + \lambda s_{\theta\theta} , \\ \dot{e}_{rr} &= \frac{1}{E}[\dot{\sigma}_{rr} - \nu(\dot{\sigma}_{\theta\theta} + \dot{\sigma}_{zz})] + \lambda s_{rr} , \\ \dot{e}_{zz} &= \frac{1}{E}[\dot{\sigma}_{zz} - \nu(\dot{\sigma}_{\theta\theta} + \dot{\sigma}_{rr})] + \lambda s_{zz} , \end{aligned} \qquad (1)$$

where E is Young's modulus and ν is Poisson's ratio. The parameter λ can be considered to control the rate of plastic strain and has to be determined from a flow criterion for a full description of plasticity. However, in the present case we need only note that, by inspection of eqns. (1), plastic deformation cannot contribute a component to the axial strain e_{zz} because $s_{zz} = 0$. Thus plastic or visco-elastic deformation causes the tube to inflate with no change in axial length from these modes of deformation. The increase in the hoop strain from plasticity is entirely accommodated by a plastic contraction in the through-thickness direction.

Elastic Deformation at Strains Above the Take Up Strain

When the take up strain has been exceeded, the overall deformation becomes elastic again. The aramid fibres now support an increasing proportion of the hoop force and constrain further deformation of the yielded polyethylene. Since the polyethylene is in the plastic state it can support only a portion of the total load to an extent determined by its yield or flow stress. The elastic deformation can thus be approximated by ignoring the polyethylene and considering only the fibres. In this case it is appropriate to use netting analysis [5,6]. Treating the reinforcing tape as an entity, the netting analysis prediction for both the hoop and axial strain is

$$e_{\theta\theta} = e_{zz} = \frac{3}{2}\frac{\sigma_h}{E_t V_t} , \qquad (2)$$

where E_t is the longitudinal Young's modulus of the reinforcing tape and V_t is the volume fraction of the tape. This gives a reasonable fit for the slope of the hoop strain-pressure curve for the Wavin specimen if an offset strain of 1.6% is added to allow for the take up strain (Fig. 3(a)). Netting analysis also predicts that the axial strain is equal to the hoop strain. This is not the case at lower pressures, but at pressures greater than about 70 bar, netting analysis gives a reasonable approximation to the *slope* of the axial strain-pressure relation (Fig. 3(a)).

The results for the Tubes d'Aquitaine specimen are more difficult to explain. The constitution of the Wavin and Tubes d'Aquitaine specimens are similar, and although there may be small

differences owing to the different manufacturing routes, it is difficult to explain why there should be such a large difference in the hoop to axial strain ratios.

An alternative method of predicting the pressure-strain relation is to use laminate analysis. This is based on the assumption of linear elasticity, which is obviously not the case here. However, laminate analysis can be applied in a loose way, if representative rather than actual elastic constants are adopted for the matrix-related elastic constants.

The orthotropic elastic constants for a laminae are denoted by the q symbols where $q_{11} = E_L/(1-\nu_{LT}\nu_{TL})$, $q_{22} = E_T/(1-\nu_{LT}\nu_{TL})$, $q_{12} = \nu_{LT}E_L/(1-\nu_{LT}\nu_{TL})$ and $q_{66} = G_{LT}$. Here, E_L is Young's modulus in a direction parallel to the fibres, E_T is Young's modulus transverse to the fibres and G_{LT} is the in-plane shear modulus, where ν_{LT} and ν_{TL} are the in-plane Poisson's ratios.

The elastic constants for the laminate referred to the hoop and axial reference axes are given by the rotation formulae [6,7]

$$\begin{aligned} Q_{11} &= q_{11}\cos^4\phi + 2(q_{12} + 2q_{66})\sin^2\phi\cos^2\phi + q_{22}\sin^4\phi \ , \\ Q_{22} &= q_{11}\sin^4\phi + 2(q_{12} + 2q_{66})\sin^2\phi\cos^2\phi + q_{22}\cos^4\phi \ , \\ Q_{12} &= q_{12}(\sin^4\phi + \cos^4\phi) + (q_{11} + q_{22} - 4q_{66})\sin^{22}\phi\cos^2\phi \ , \\ Q_{66} &= (q_{11} + q_{22} - 2q_{12} - 2q_{66})\sin^2\phi\cos^2\phi + q_{66}(\sin^4\phi + \cos^4\phi) \ , \end{aligned} \tag{3}$$

where ϕ is the magnitude of the angle between the z-axis and the fibre directions. The constants in (3) allow the stress to be calculated in terms of a given strain. To obtain the strain in terms of a given applied stress requires the matrix associated with the Q values in (3) to be inverted. For the present case of a biaxial stress with $\sigma_h = \sigma_{\theta\theta} = 2\sigma_{zz}$ we have

$$\begin{aligned} e_{zz} &= \sigma_h \frac{\frac{1}{2}Q_{22} - Q_{12}}{Q_{11}Q_{22} - Q_{12}^2} \ , \\ e_{\theta\theta} &= \sigma_h \frac{Q_{11} - \frac{1}{2}Q_{12}}{Q_{11}Q_{22} - Q_{12}^2} \ . \end{aligned} \tag{4}$$

Numerical evaluation using eqns. (3) and (4) for various test cases shows that the strain ratios are inordinately sensitive to the values of the matrix-related constants when ϕ is close to the special angle $\phi = \arctan(\sqrt{2}) = 54.74°$ (the ideal netting angle). However, numerical examples do not highlight the interaction of different factors in producing this sensitivity. This interaction is more clearly seen using analytical expressions that result from a consideration of some limiting cases.

Imagine that those elastic constants that are controlled mainly by the properties of the matrix material (q_{12}, q_{22} and q_{66}) become very small, to the extent that second order terms (e.g. q_{22}^2, q_{12} q_{22}, q_{12} q_{66} or any similar products where the subscripts 2 or 6 appear twice or in combination) can be ignored. With this approximation, and with ϕ taken to be equal to $\arctan(\sqrt{2})$, eqns. (3)

and (4) can be used to obtain simpler analytical expressions. After some algebraic manipulation, the details of which are not shown here, we obtain:

$$e_{zz} = \frac{3}{2}\frac{\sigma_h}{E_L}\frac{[8-(1+2\nu_{LT})E_T/G_{LT}]}{[8+E_T/G_{LT}]}\ ,$$
$$e_{\theta\theta} = \frac{3}{2}\frac{\sigma_h}{E_L}\frac{[8+(2+\nu_{LT})E_T/G_{LT}]}{[8+E_T/G_{LT}]}\ . \qquad (5)$$

The effect of taking various limits can now be obtained by inspection of eqn. (5). The key parameter is the ratio E_T/G_{LT}.

(i) If E_T goes to zero whilst G_{LT} remains finite, both e_{zz} and e_θ go to the limiting value 3/2 σ_h/E_L, i.e. the strain ratio is unity. If the term E_L is identified with E_tV_t the result is identical to that of netting analysis.

(ii) If G_{LT} goes to zero whilst E_T remains finite, the limiting strain values are

$$e_{zz} = -\frac{3}{2}(1+2\nu_{LT})\sigma_h/E_L\ ,$$
$$e_{\theta\theta} = \frac{3}{2}(2+\nu_{LT})\sigma_h/E_L\ . \qquad (6)$$

In this case, the hoop strain is more than twice the value predicted by netting analysis and the axial strain is negative.

(iii) Another special case worth investigating is when the axial strain is zero. The ratio of E_T to G_{LT} where this occurs can be obtained from eqn. (5). The following particular result for the hoop strain then obtains when $e_{zz} = 0$:

$$e_{\theta\theta} = \frac{9}{4}\frac{\sigma_h}{E_L}\ . \qquad (7)$$

In this case, in addition to the fact that the axial strain has been set to zero, the predicted hoop strain is about 50% larger than the netting analysis result.

Equation (7) was fitted to the results for the Tubes d'Aquitaine specimen (Fig. 3(b)). Although the axial strain corresponds approximately with the experimental data, as is imposed by adopting eqn. (7), the predicted hoop strain is larger than is observed experimentally. On the other hand, although the netting analysis prediction (with 1.4% offset) fits the observed hoop strain well, the predicted axial strain does not correspond with the experimental observations.

DISCUSSION

The take up strain observed in the present work is a consequence of the reinforcing fibres not being infiltrated. In contrast with the present results, thermoplastic tubes reinforced with glass

fibres that *are* infiltrated do not exhibit the non-linear behaviour shown in Fig. 2 [8]. In the present case, the polyethylene components have to yield in order load the fibres. Although yielding of the polyethylene produces a larger hoop strain than would otherwise occur with fully infiltrated fibres, the associated properties confer useful, additional advantages on RTPs. For example, the flexural resistance of the tubes is low as a consequence of the non-infiltration. Thus, the tubes are easily coiled, giving considerable flexibility in installation. In addition, if an RTP is collapsed by external pressure or concentrated loads, its subsequent ability to contain high pressure is very little affected [1].

At strains greater than the take up strain, the hoop strain behaves as predicted by netting analysis. However, the axial strain as a function of pressure is observed to be less predictable. This is not entirely unexpected, since in netting analysis the fibres can only support the load when they are inclined at exactly the ideal angle, i.e. some shear resistance is required to compensate for any slight deviation from the ideal angle. Laminate analysis is preferred in this case although there is uncertainty about its application to fibres in a non-linear matrix. When the matrix-related elastic constants become very small, as might be considered an approximation when the matrix is plastic, the predicted strain ratio is rather sensitive to the ratio of the notional transverse and shear moduli. Thus, a full analysis of elastic fibres in a non-linear, yielding matrix is required to resolve this point.

CONCLUSIONS

Pressure tests have been carried out on closed end reinforced thermoplastic pipes.

(ii) The hoop strain-pressure relation shows a high degree of non-linearity in the early stages of deformation. Because the fibres are not infiltrated, the polyethylene has to yield by plastic and non-linear visco-elastic deformation to load the fibres.

(iii) The axial strain does not exhibit non-linearity in the low pressure region because the deviatoric component of stress in the axial direction is zero.

(iv) Netting analysis can account for the hoop strain at strains greater than the take up strain.

(v) The axial strain is less predictable than the hoop strain. Some approximations derived from laminate analysis have been used to investigate this point.

ACKNOWLEDGEMENTS

One of the authors (BJC) gratefully acknowledges the support of an Engineering and Science Research Council CASE award (with Shell Research) in the period when this work was done.

REFERENCES

1. B.J. Chapman, University of Newcastle upon Tyne, unpublished results 1996.

2. S.R. Frost, Shell Research and Technology Centre, Amsterdam, private communication.

3. L.M. dos Reis Henrique, R.B. Goldman, "Thin-walled Laminated Composite Cylindrical Tubes: Part I- Boundary Value Problems", *Journal of Composites*, Vol. 9, 1987, pp. 47-52.

4. R. Hill, `Theory of Plasticity', Oxford University Press ,1950.

5. T.G. Rogers, `Problems for Helically Wound Cylinders' in *Continuum Theory of the Mechanics of Fibre-Reinforced Composites* (ed. A.J.M. Spencer), pp.147-178, Springer-Verlag, 1984.

6. D. Hull, `An Introduction to Composite Materials', Cambridge University Press, 1981.

7. S.G. Lekhnitskii, `Theory of Elasticity of an Anisoptopic Body', Holden-Day (San Francisco), 1963.

8. A. Fahrer, University of Newcastle upon Tyne, private communication 1996.

QUALITY CONTROL OF GLASS FIBRE REINFORCED PLASTIC LONG TUBULAR MEMBERS

Carlo A. Castiglioni, Andrea Spessa

Structural Engineering Dept. (DIS), Politecnico di Milano
P.zza Leonardo da Vinci 32, 20100 Milano, Italy

SUMMARY: This paper presents the results of an experimental analysis on the mechanical properties of glass-fibre reinforced plastic (GRP) tubular conical columns widely used as cable supports by telephone and electric companies.

The aim of the study is mainly a quality control for the assessment of the characteristic values of the Young's modulus and the tensile strength of the material to be performed on specimens manufactured by different firms. Tensile tests have been carried out on specimens cut from the columns accordingly UNIPLAST EN-61 and ASTM D638-72. Usually, recommendations for bending tests (UNIPLAST EN-63 and ASTM D790-71) consider the possibility of evaluating the Young modulus of the material by testing small size specimens (of the same kind of the tensile specimens). Due to the large curvature of the tubes considered in this study, whose diameter is variable between 150 mm and 250 mm, the "slices" cut from the tubes for obtaining the specimens are not plane. A testing procedure was then identified, to perform four points bending tests on large size specimens (2 meters long) cut from the central portion of the tubes. Furthermore, compression tests have been performed on stubs.

The experimental data obtained from the 3 different types of testing and their statistics are compared and discussed.

KEYWORDS: long tubular members, mechanical behaviour, tensile Young’s modulus of elasticity, tensile strength, bending modulus of elasticity

INTRODUCTION

Glass-fibre reinforced plastic columns are being extensively used for supporting light weights such as cables, lamps or antennas. They have many advantages over conventional materials (like wood, steel or concrete) such as light weight and high corrosion resistance and the mass production (as well as the technical improvements achieved in the last two decades) make composite materials convenient with respect to conventional ones from an economical point of view. Since 1984 GRP poles have been used in Italy to support overhead lines; many shapes and geometries are available, depending on the producer and on the application; usually, however, these poles were no more than 8 meters long. In 1990 a longer pile, 9 meters long, was adopted by a Company for sustaining overhead lines in street crossing. This occasion originated a co-operation between the Company and the Structural Engineering Department of Politecnico di Milano, with the aim of performing:

1) a quality control of the mechanical properties of the poles, manufactured by various firms all over the national territory;

2) a reliability analysis of the products delivered by the various manufacturers.

In the study, attention was concentrated on poles having an hollow truncated conical shape, 9 meters long; the maximum external diameter is equal to 250 mm and the minimum external diameter at the top section is equal to 115 mm. The nominal wall thickness is equal to 7.0 mm. All poles possess a perfectly smooth external surface and thus qualify at the 1st level of ASTM 2563-70 rules. Furthermore, the external surface is overlaid with a special not woven fabric, which guarantees protection against UV rays and environmental chemical attacks.

As the production procedures of these poles, which are centrifuged, are such that the glass fibre content (and consequently the mechanical properties of the material) vary along the longitudinal axis of the member, for each pole 5 portions were identified along the longitudinal axis (Fig. 1). From 4 portions compression and tensile specimens were obtained while from the intermediate portion a 2 m long specimen was obtained to be submitted to bending tests.

Usually, recommendations for bending tests - e.g. EN-63, ASTM D790-71 - consider the possibility of evaluating the Young modulus of the material by testing small size specimens (of the same kind of the tensile specimens) “sliced” from the member. Due to the large curvature of the tubes under evaluation, whose diameter is variable between 150 mm and 250 mm, the "slices" cut from the tubes, for obtaining the specimens are not plane. A testing procedure was then identified, to perform four points bending tests on 2 meters long specimens cut from the central portion of the columns.

Specimens cut from the 9 meters long pole were collected from six different producers; each firm provided 5 poles; for each pole provided one 2.0 m long specimen for bending test, 4 stubs for compression test and a total of 100 specimens for tensile test. A second phase of this study dealt with the axial load carrying capacity of these members. Full scale tests were carried out on 9 m long poles to analyse the behaviour of these members under working conditions. Experimental buckling tests were carried out on full scale tubes to analyse the working behaviour of the pole (Ref. /1/). The results of the first phase are herein presented and discussed. Concluding remarks complete the paper.

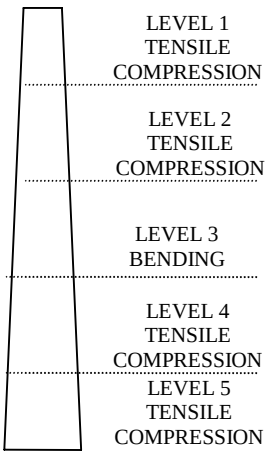

Fig. 1: Specimen outcoming zones

WORKING CONDITIONS OF THE MEMBERS AND MATERIAL CHARACTERISTICS

Working conditions and Material

A particular application of tubular conical columns is their use as cable support by telephone and electric companies. With regard to this application the buckling problem is mainly connected to the corner poles of the lines which are guyed in order to reduce lateral deflections due to the transversal component of the cable tension. Hence, these members are subjected to compression and bending; the amplitude of the axial load depends on the transversal force and the guy inclination. The poles are usually driven into the ground for a length of 1.3 ± 0.2 m, and can be considered as cantilevered, with a 7.7 ± 0.2 m free length. Concerning to these working conditions, the companies adopting GRP poles defined technical recommendations about mechanical and geometrical properties, that should be provided by the different manufacturers. The leading requirements were related to the mean thickness (equal to 7 mm), the tensile strength (greater than 160 MPa) and the modulus of elasticity (greater than 20000 MPa).

Furthermore, all poles must guarantee protection against UV and chemical attacks.

All the poles were made by centrifugal casting, a production technique for fabricating cylindrical and conical shapes in which glass-fibre mats and roving are positioned inside a hollow mandrel designed to be heated and rotated as resin is cured. The internal side of the mandrel reproduces the external shape of the product. By controlling step by step the angular velocity - slow rotational velocity during the resin filling and a faster velocity during the curing - and the resin viscosity - mainly operating on the mandrel temperature -, it is possible to get a well impregnated fabric with an almost constant thickness; the poles tested, had a thickness included between 6.4 and 7.1 millimetres.

The poles were all produced with unsatured (thermosetting) polyester resins, with E-glass fibres and fabrics.

EXPERIMENTAL PROCEDURE

Defining the mechanical properties of the material in the case of truncated conical tubes is not a conventional problem since:

- the specimens cut from the manufact do not result plane but they have concavity, which could produce difficulties during the test; as a matter of fact, in tensile tests, the clamps can carve the specimen that can break. Furthermore, in conventional bending test the specimen convexity makes hard the correct load application and the specimen arc behaviour in transversal direction causes bias in the results.

- glass-fibre reinforced plastic, as all the fibre-reinforced materials, towers for its anisotropic behaviour, and it is strongly influenced from profile working like the preparation of the specimen.

Since the aim was to get a reliable value of mechanical properties of the material, it was decided to consider specimens with dimension not influenced from tool working by deriving them from longitudinal and transversal cutting, at different levels of the pole axis.

The specimens were manufactured in six batches from six different producers. Each manufacturer provided 5 poles. Each pole was cut in 5 sections. From the intermediate section, 2 meter long, a 4 point bending test specimen was obtained. From each of the two upper and the two lower sections one compression test specimen having a slenderness ratio $\lambda = 6$ according to the UNIPLAST 4279 specifications (ASTM D695-69 prescribes $\lambda = 11 \div 15$) and five 400 mm long tensile test specimens were obtained.

In total each manufacturer provided:
- five 2 meter long flexural specimens
- one hundred 400 mm long tensile specimens
- twenty $\lambda = 6$ compression stubs.

Furthermore, since the aim of the study was to get information about the product quality from a mechanical performance point of view, an evaluation of physical specimen parameters was carried out to determinate glassfibre volumetric content and specimen thickness. By tensile strength and Young's modulus, the effective rigidity was calculated and correlated to the glass percentage and specimen thickness.

Tensile Tests

Tensile tests were carried out on specimens 25 mm wide and 400 mm long, to get a mid-part length equal to 200 mm where the stress is not influenced by the external clamps and by the tool working of the ends; in fact, to prepare the specimen, both ends were worked by some resin cured and levelled to make the surfaces complanate with the clamps of the testing machine (EN-61). Furthermore, to improve the adherence between the specimen and the clamps, some carborundum dust was applied on the resin reinforcements at the ends.

The specimen is qualitatively illustrated in Fig. 2.

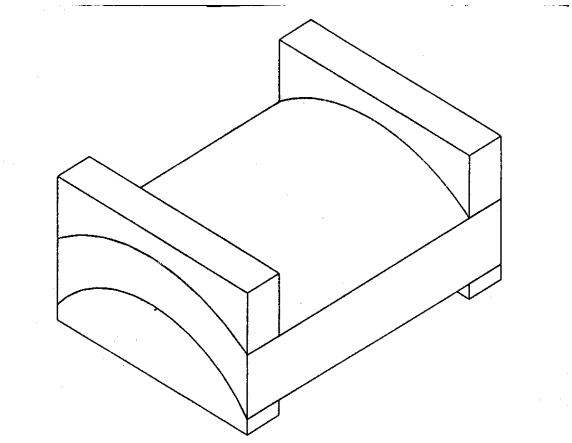

Fig. 2: Tensile specimen (qualitative)

Test were carried out by means of a Schenk universal testing machine having a 2000 kN total capacity.

The load applied on the specimen was measured by a dynamometer while the elongation was got by LVDT, with reference length equal to 100 mm, directly applied on the specimen.

By this way it was possible to measure the exact strain of the specimen and to keep out any spurious component due to the axial strain of the testing machine and to the sliding of the specimen between the clamps.

Compression Tests

The measured compression strength of composites is sensitive to the specimen configuration and the fixture used for loading. Compression tests have been performed on 4 stubs per column. The slenderness λ for stubs has been evaluated as the ratio between specimen length and midspan radius of inertia. All stubs have the same slenderness equal to 6, according to the Italian rule UNIPLAST 4279. The slenderness has been adopted to define the specimen length, as a function of its transversal dimensions. The experimental analysis was carried out on stubs obtained from cutting the poles at different levels as it is illustrated in Fig. 1. The test stubs were cut to size with a high degree of accuracy using a diamond tip saw, and, later on, levelled with a precision within 0.1 mm. The analysis was performed by displacement controlled centred compression tests using a numeric control testing machine MTS with maximum load equal to 2300 kN. This machine is adequately stiff and rigid enough to reduce any possible secondary effect such as the machine/test-rig interaction. The stub displacements were measured by four LVDTs installed between the testing machine plates in opposite diametral positions. Before leading the specimens to collapse, compression loading cycles were applied to each specimen to evaluate its behaviour and testing repeatability under different load levels.

Bending Tests

As the aim of the investigation was to get information about the in service behaviour of the poles and in order to avoid the procedural problems involved with the large curvature of the members, resulting in a concavity of the specimens usually prescribed by recommendations for bending tests, it was decided to disregard recommended testing procedures such as those proposed in UNIPLAST EN-63 and, in the case of bending tests, to identify an ad hoc testing procedure, operating on large size specimens (2.0 meters long) cut from the central portion of the pole. The cutting position along the pole axis was decided according to the following items:

- the mats are usually positioned not uniformly along the pole axis and, because of the truncated cone shape, the most of them are concentrated in the lower part of the pole where the diameter is maximum. Only few mats go up to the end of the pole while all the others stop at different elevations; similar distributions are adopted by various manufacturers although the length of each mat is different for every producer. As a matter of fact, in order to get information about the average behaviour, it was decided to analyse a part of the pole were mats are distributed on average; the mechanical properties, in fact, are related to the glass fibre content and higher values could be obtained by testing the pole lower part which usually represents the most stressed section if the member is a cantilever.

- the poles are produced by different firms and consequently their dimensions are different for the various manufactures.

In order to maintain the same testing configuration for all specimens, it was asked to the manufacturers to provide - from the intermediate part of the pole - a 2.0 m long specimen, having a given diameter at two cross section spaced 1800 mm. In fact, the specimens were supported at the end by two wooden saddles of 100 mm-width. The saddles were shaped to keep the longitudinal axis of the specimen horizontal and to surround a semicircular half of

the tube. This support shape reduces deformability and section ovalization under the applied loads and prevents out-of-plane displacements of the specimen.

Furthermore, rubber pads (Teflon) were placed on both supports in order to reduce friction between the saddle and the specimen and to avoid local failures; of course, this testing configuration caused the specimen to have well defined transversal dimensions.

An hydraulic jack was used to apply the load that was distributed to two loading points located at the third points of the stub using a steel beam and two additional wooden saddles. The magnitude of the total applied load (i.e., two times the load at each load point on the log) was monitored by a load cell placed in series with the hydraulic jack.

Vertical displacements were measured using 5 linear LVDT. The deflections were measured at the specimen midspan, at the two load points and at 5/12 and 7/12 of the span.

Each specimen was loaded in a series of short term loading/unloading cycles to verify the mechanical behaviour and its reproducibility under different load levels.

The target load was fixed equal to 100 kN although some stubs collapsed before the target load was reached.

RESULTS

The normal model was used to calculate the characteristic values *B*. They have been calculated in terms of the sample mean $\overline{X}$ and standard deviation *S* using the formula:

$$B = \overline{X} - kS \tag{1}$$

where *k* is a coefficient connected to the risk formulation 1-α and to the confidence level. A 95% probability of survival was assumed, connected to 95% confidence level, in order to define the characteristic values of the various properties.

To get information about production quality by mechanical material properties, all the data obtained were computed following the described procedure.

The computing was mainly aimed to identify the elastic modulus mean value E_m, the root-mean-square deviation *S* and the Young's modulus characteristic value E_b by the application of :

$$E_b = E_m - kS \tag{2}$$

Tensile Young's Modulus

Because of the small specimen width equal to 25 mm, the area *A* was measured by concavity neglecting.

The initial tangent Young's modulus E_T was computed by the following formula:

$$E_T = \frac{l_0 \cdot R \cdot \Delta F_1}{A \cdot \Delta Z_1} \tag{3}$$

where l_0 = 100 mm is the LVDT reference length, R is the magnification typical transformer coefficient, ΔF_1 is the load variation and ΔZ_1 is the apparent elongation variation connected to ΔF_1.

The test results showed an increasing of the Young's modulus with strain. The tensile secant modulus of elasticity E_S was evaluated according to UNI-EN61, basing on Eqn. 3 with ΔZ_1 corresponding to a 0.5% apparent elongation percentage.

Considering the target values, testing phase was carried out as shown in Table 1 where are illustrated the values got for the poles manufactured by the six different firms herein called A, B, C, D, E and F.

Table 1: Tensile Young's modulus statistics

FIRM	E_{mT} (MPa)	E_{bT} (MPa)	S (MPa)
A	26495	21175	2700
B	23384	20383	1436
C	25230	22640	1282
D	22586	20241	782
E	22616	16817	2416
F	22944	19669	1621

A global analysis of results has been carried out as shown in Fig. 3 where the Young's modulus distribution is illustrated; it was derived considering the whole batch. The figure shows that the specimens that don't touch the target value are less than 3.5% of the total. Despite this fact, because of the standard deviation high value - S = 2598 MPa - the resulting characteristic value of the tensile Young modulus is 19733 MPa, a little lower than the target required. Then, a statistical analysis has been performed considering the zone where the specimen was got from; all the specimens were cut from 4 different pole levels as shown in Fig. 1. Table 2 illustrates the results got for each level; it shows how the Young's modulus increases moving from the top of the pole - level 1 - to its lower part - level 5 -. Level 5 shows lower values than level 4 ; it is due to a great result dispersion with 20 results above 26000 MPa. Neglecting them, the target values are got.

Table 2: Tensile Young's modulus statistics per level

	Level 1	Level 2	Level 4	Level 5
E_{mT} (MPa)	24064	24308	24456	23885
E_{bT} (MPa)	17569	19302	20581	20246
S (MPa)	3168	2515	1947	1793

The mean values are always greater than the target required; the characteristic values are greater than the target only for the fourth and the fifth levels. The values progress is mainly due to the high concentration of glass-fibre in the lowest part of the pole where there is the most stressed section in operative conditions. By this reason, it seemed acceptable to re-calculate the distribution of tensile elastic modulus values of Fig. 3 by ignoring specimens which belong to level 1.

The result is shown in Fig. 4: by re-analysing the new sample, a value of E_{bT} = 21372 MPa is obtained, satisfying the minimum required.

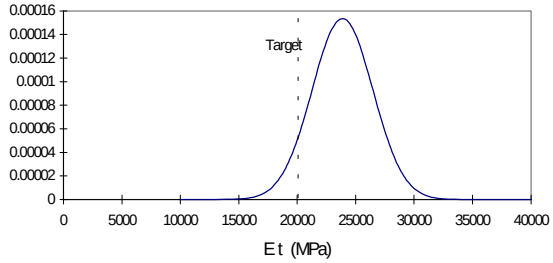

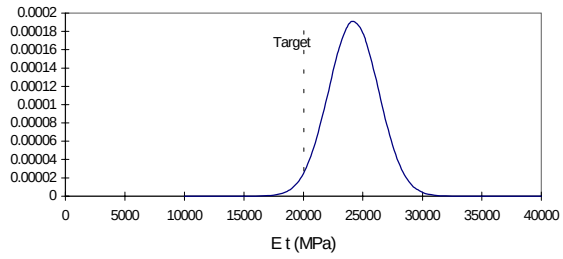

Fig. 3:Young's modulus distribution (all levels) *Fig. 4:Young's modulus distribution (levels 2,4 & 5)*

Tensile Strength

The ultimate tensile strength was evaluated for the four levels with the same procedure used for Young's Modulus computing; main results are shortly resumed in Table 3.

Table 3: Ultimate tensile strength statistics for each pile level

	Level 1	Level 2	Level 4	Level 5
f_{mT} (MPa)	281.8	292.6	301.3	311.1
f_{bT} (MPa)	183.5	199.7	183.6	193.6
S (MPa)	47.9	46.7	59.2	59.0

where f_{mT} and f_{bT} are respectively the mean value and the characteristic value for the ultimate tensile strength. The distribution is shown in Fig. 5. The correlation between tensile strength and glassfibre volumetric content is discussed in § 5.

Thickness

A statistical analysis of specimen thickness was performed during tensile tests.

About half of the total specimen sample has a thickness lower then the 7 mm required. The mean value is 7.15 mm but, being S = 1.17 mm, the characteristic value is 5.03 mm; in Fig. 6 the Young's modulus is correlated to the specimen thickness; a large scattering is evident. According to the "mixing rule" (Voigt model), the figure also shows that at increasing thickness corresponds a decreasing tensile modulus.

If E_{gf} and E_m are respectively the glassfibre and the matrix Young's modulus and α is the glassfibre volumetric content, the composite Young's modulus can be derived from the following formula:

$$E_t = \alpha E_{gf} + (1-\alpha)E_m + E_{int} \tag{4}$$

where E_{int} means the effect of the different lateral strain due to the different Poisson's ratios of the two materials. In elastic field E_{int} is negligible. Being $E_{gf} >> E_m$, if during manufacturing α value decreases - i.e. the resin volumetric content increases more then the glassfibre volumetric content - also the value of E_t decreases.

Furthermore, the ultimate tensile strength appeared to decrease with the increasing thickness; this fact confirms the need for caution in applying design allowables derived from small scale tests to large GRP structures.

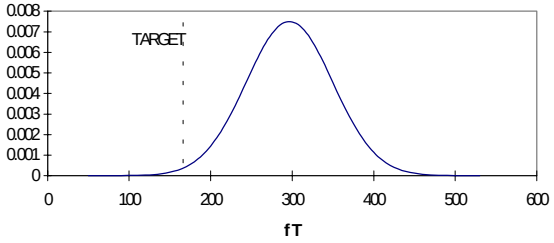

Fig. 5: Tensile strength distribution

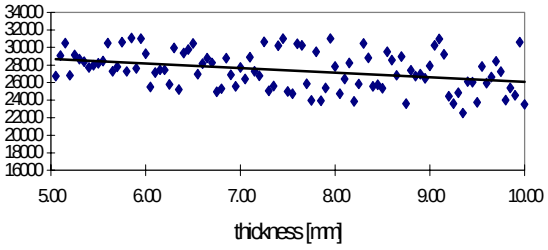

Fig. 6: E_T predicted by thickness

Compressive Modulus of Elasticity

The experimental analysis was carried out by MTS testing machine. This is able to provide a maximum load of 2300 kN. The high magnification drum recorder integral to the MTS machine was used to plot the load/end-shortening curves.

Cyclic loads were applied to each specimen to evaluate its behaviour and the repeatability under different load levels. After the checking and several loading and unloading tests, the specimen was then tested to failure.

Since the testing machine had a displacement controlled process, collapse of the panel was denoted as a sudden reduction in load.

The theoretical specimen shortening was estimated by numerical integration of the virtual work equation. The shortening was calculated as the mean of the two values measured by LVDT placed between the testing machine plates on opposite sides.

The secant modulus of elasticity was evaluated by numerical computing of the slope of the lines connecting in the stress and strain plane points corresponding to load increments equal to 10 kN.

By a statistical interpretation of the results, the mean value computed for different load levels was obtained. Furthermore, the standard deviation allowed interesting information about the linearity of the diagram to be obtained. The characteristic value of the modulus of elasticity measured by compression tests resulted far from the minimum required. Mainly, the Young's modulus showed a decreasing behaviour with strain increasing. These values are illustrated in Table 4, where E_{mC} is the mean value while E_{bC} is the characteristic value.

Table 4: Compressive modulus of elesticity statistics

FIRM	E_{mC} **(MPa)**	E_{bC} **(MPa)**	S **(MPa)**
A	17011	12975	1345
B	20716	13532	2395
C	20093	12956	2379
D	20691	12389	2768
E	21333	16423	1637
F	20552	13865	2229

Bending Modulus of Elasticity

The load was applied within the elastic range and removed to allow the specimen to further settle.

After the checking and several loading and unloading tests, the specimen was then tested to failure. For all tests fibre breaking could be heard well before final failure. There was quite a significant variation in the way the failures occurred. In few cases it initiated on the supports due to the shear force. In bending there are displacement gradients also in the circumferential direction in addition to those gradients in the axial direction. The intralayers stresses associated with these displacement gradients, coupled with the brittle nature of the material, can be severe enough to cause material failure within these boundary regions. In most cases failure started at the loading seddles or in the mid span zone. The values computed are illustrated in Table 5, where E_{mB} is the mean value while E_{bB} is the basis value.

Table 5: Bending modulus of elasticity statistics

FIRM	E_{mB} (MPa)	E_{bB} (MPa)	S (MPa)
A	22762	19451	1850
B	20486	19550	529
C	20500	19406	618
D	21588	20318	572
E	22923	21572	764
F	19765	18825	531

With bending, in addition to the possibility of material failure on the compression and tension sides of the structure there is also the stability issues associated with the compression side of the truncated cone.

Chemical and Physical Parameters

Some other important parameters, such as glass percentage and specific weight, have been investigated during testing phase.

A polymer analysis was accomplished with x-ray photoelectron spectroscopy (XPS). This technique provides a total element analysis and the chemical bonding information.

By XPS, the matrix composition was determined for the whole batch as a mixture of polystyrene with unsatured polyester. Mainly, specific weight SW and glassfibre volumetric content α were measured providing a mean specific weight equal to 1.49 and the following values for α: α_m = 72.9%, α_b = 61.1% and S = 3.9%. The glassfibre volumetric content distribution computed for a single batch is illustrated in Fig. 7; Fig. 8 shows for the same batch the correlation between E_t and the specimen glass percentage. By this analysis it was possible to get the correct α values and to verify once more the “mixing rule” accuracy.

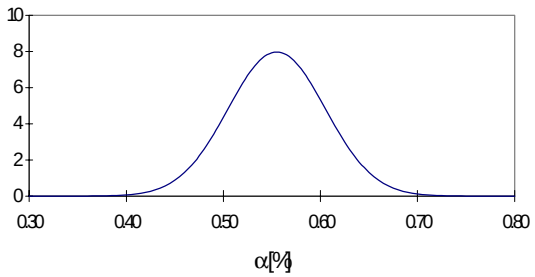

Fig. 7: Glassfibre vol. content distribution

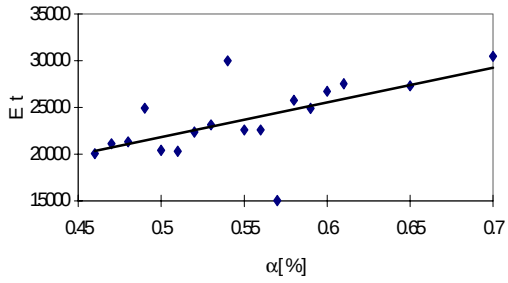

Fig. 8: E_T predicted by glassfibre vol. content

DISCUSSION AND CONCLUSIONS

Composite cylindrical and quasi-cylindrical structures, such as the examined ones, are known for their efficiency. The curvature effectively increases the stiffness of the structure, resulting in a more economical use of material.

From experimental analysis it is found that the compressive modulus of GRP decreases with strain whilst the tensile modulus increases. This can results in much lower stresses on the compression side of the specimen then on the tension side; although in bending tests failure often begins on the compression side because of geometric non-linear response.

The experimental investigation has shown a good agreement with the theoretical mixing rule, by which it is possible to predict the Young's tensile modulus vs. glassfibre volumetric content α (Fig. 8).

Furthermore, the correlation between tensile strength f_T and glassfibre volumetric content, illustrated in Fig. 9, confirms theoretical predictions; when α is lower than α_{min}, material behaviour is governed by matrix deformation and is lower than matrix resistance; for $\alpha_{min} < \alpha < \alpha_{cr}$ the GRP material resistance is controlled by fibre deformation but is lower than matrix resistance. Only for α greater than α_{cr} there is an effective matrix reinforce by glassfibre so that α_{cr} is a minimum target that must be exceeded.

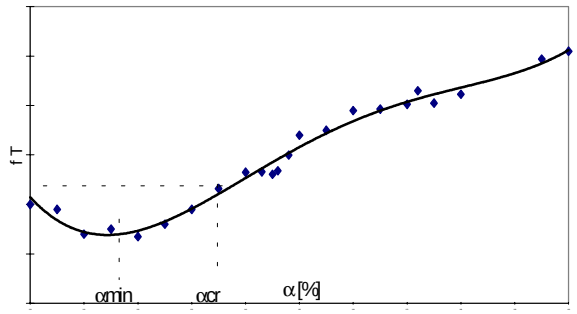

Fig. 9: f_T predicted by glassfibre volumetric content

Testing analyses showed that a wide experimental investigation is needed in order to design GRP structures; as a matter of fact, all testing phases confirm the need for caution in applying design allowables derived from small scale tests to large GRP structures.

ACKNOWLEDGEMENT

This research was carried out with the financial support of the Italian CNR, Consiglio Nazionale delle Ricerche.

REFERENCES

1. Castiglioni C.A., Spessa A., "Axial load carrying capacity of glassfibre reinforced plastic long tubolar members", *Proceedings of the Tenth International Conference on Composite Materials*, Whistler, British Columbia, Canada, August 14-18, 1995.

2. UNIPLAST En 61 "*Materie plastiche rinforzate con fibra di vetro. Determinazione delle caratteristiche a trazione*", UNI 1978.

3. Agarwal B. D., Broutman L. J., *Analysis and Performance of Fiber Composite*, John Wiley & Sons, 1980.

4. Calcote L. R., *The Analysis of Laminated Composite Materials*", Van Nostrand Reinhold Company, 1969.

5. Castiglioni C. A., "*Controllo di qualità su campioni di tubi rastremati in vetroresina*", Internal Report, Structural Engineering Dept., Politecnico di Milano, 1993.

6. Chawla K. K., *Composite Materials*, Springer-Verlag, 1987

MICROMECHANICAL MODELLING OF THE DAMAGE INITIATION AND THE COMPETITION BETWEEN DIFFERENT MECHANISMS OF ± 55° FILAMENT-WOUND GLASS-FIBRE/EPOXY-RESIN TUBES

Jinbo Bai, Gengkai Hu* and Philippe Bompard

Lab. MSS/MAT, CNRS URA 850,
Ecole Centrale de Paris, 92295 Châtenay Malabry CEDEX, France
** Applied Mechanics Department, Beijing Institute of Technology, P.R.China*

SUMMARY: The objective of this paper is to investigate the damage initiation mechanisms and the competition between different mechanisms of ± 55° filament-wound glass-fibre/epoxy-resin tubes under biaxial loading. First, the microstructure, mechanical behaviour and damage initiation mechanisms were determined. Then, micromechanical modelling of the damage initiation was conducted in order to determine the mechanical conditions under which different microcracking mechanisms occur and the critical s_{zz}/s_{qq} ratios which correspond to the change from interfacial failure to microcracking at porosity. The porosity volume fraction should be kept below 5% to avoid any detrimental effect. Failure envelopes of our composite tube were predicted based on the different criteria at meso- and microscopic scales. The predicted results in an internal pressure dominated region are conservative compared with experimental ones. The possible improvement may reside in introducing a variation of the shear modulus due to the matrix viscous effect and the interfacial sliding effect.

KEYWORDS: composite filament-wound tube, interply and intraply porosity, axial tensile, internal pressure and combined loading, damage, transversal cracking, delamination, micromechanical modelling

INTRODUCTION

Filament-wound glass fibre reinforced epoxy (GRE) tubes are increasingly being used for high pressure containment in chemical plant and aerospace applications, and also in the oil and nuclear industry [1-5]. The design of this kind of tube was optimised essentially for the fabrication of internal pressure containers which are frequently thin-walled and possess characterisations like low cost and weight effective utilisation of materials. Their fabrication route consists of impregnating the fibre strands with resin and then winding them on to a rotating mandrel of a predetermined fibre path under controlled tension. The wound part is cured in an oven to form the final product which has continuous fibres of the same orientation and axisymmetrical configuration. The most frequently observed microstructural defects of this kind of composite structure are inter and intra-ply porosity in the matrix, non-uniform fibre distribution (local fibre volume fraction fluctuation and interlayer fibre free resin layer)

and fibre deviation off the ± 55° alignment. A series of mechanical tests have been carried out with various combinations of hoop and axial stresses. The investigation of mechanisms of failure has shown that there are fibre/interface/matrix interactions and interactions between layers which have a dominant effect on the early stages of mechanical failure and damage (microcracking and delamination) initiation [1-10]. To account for these micromechanical effects, it is necessary to perform analyses of the stress states especially the interply stress components and their sensitivity to the microstructural defects [11].

This paper begins with a description of our numerical models, the material properties and the structure analysed. In the results and discussion section, we will focus on the stress states and their sensitivity to microstructural defects and damage. After a micromechanical analysis, the competition between different mechanisms and the effect of a few important factors will be discussed. Failure envelopes of the composite tube will also be presented.

NUMERICAL MODELLING DESCRIPTION

Material Characteristics of Tubing Structure

The internal and external diameters of the tubes are 60 mm and 65 mm respectively. The average thickness of each ply is 0.417 mm. The lay-up sequence is $[55°/-55°]_3$. The epoxy resin used is CIBA - GEIGY LY 556. The fibres are roving 2400 TEX (Vetrotex). In Table 1 the Young's moduli E and the Poisson's ratios n of the resin and the fibres are shown. The basic constituents of the composite ply (fibres and resin) are assumed as isotropic materials with linear elastic behaviour. Mechanical characteristics of unidirectional ply are needed as input data for the 3D finite element calculations. Many approximate averaging and asymptotic homogenisation techniques have been proposed to obtain the overall characteristics of a heterogeneous material containing periodically or randomly distributed inhomogeneities. In this paper we used the Mori-Tanaka theory [10]. The nominal average fibre volume fraction is 56%. Moreover, each unidirectional reinforced ply is considered as an orthotropic material with two privileged directions: longitudinal (fibre direction) and transversal (perpendicular to the previous) directions. Six independent coefficients are required for its complete mechanical behaviour characterisation. In Table 1 the six homogenised elastic moduli are given expressed in a local orthotropic system (1, 2, 3) as defined in Fig. 1, where E_1 and E_2 are transverse and longitudinal Young's moduli, n_{ij} the Poisson ratios and G_{ij} the shear moduli.

Table 1. Mechanical properties of fibres, resin and a unidirectional ply. Engineering constants

	E (MPa)	**n**	**s_r (MPa)**	**e_r (%)**
Epoxy resin	3400	0.35	40	1.7
Glass fibre	73800	0.23	2400	-

E_1 (Gpa)	**E_2 (GPa)**	**n_{12}**	**n_{23}**	**G_{13} (GPa)**	**G_{23} (GPa)**
10.26	42.89	0.067	0.28	3.58	4.03

Numerical Models and Results of Numerical Calculation

A whole tube is shown in Fig. 2. The total height of the structure equals 2H = 330 mm. In the following calculations, it is supposed that the internal pressure p = 10 MPa and the tensile force T=10 kN imposed on the tube extremity, are uniformly distributed on the corresponding faces. The 3D finite element calculations were first conducted on a long whole tube [11]. The choice of modelling a whole tube was made in order to avoid any hoop boundary condition effect. The stress distribution through the thickness presented in Fig.3 represents typical results for composite shells. The results were obtained for the cases of pure internal p=10 MPa (s_{qq}=120MPa) and pure tensile T=10 kN (s_{zz}=20.37 MPa), respectively. In the case of pure internal pressure the stress S22 which is higher in the internal ply slowly drops by 8% on moving towards the external ply.

EXPERIMENTAL PROCEDURE

Test Procedure and Data Acquisition Systems

Tubular specimens from three different manufacture lots (Lot A, B and C) were tested on a MTS hydraulic tensile machine. Constant crosshead speed of 0.03 mm/s was maintained

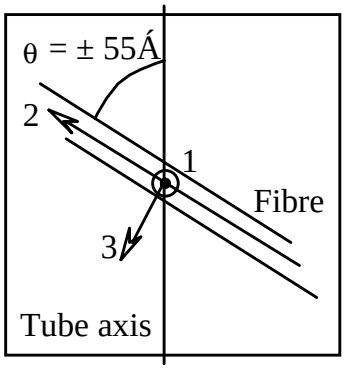

Fig. 1. Local orthotropic system

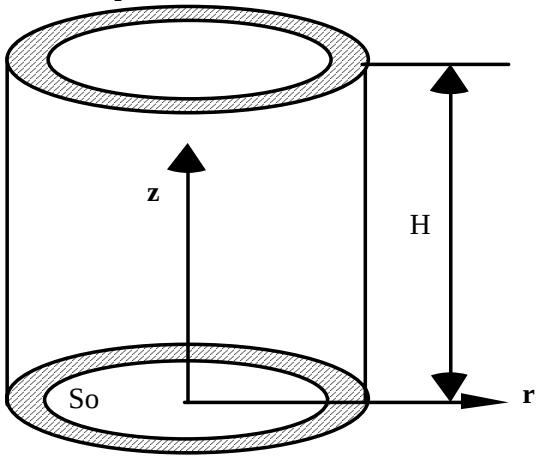

Fig. 2. Geometry features of the numerical models

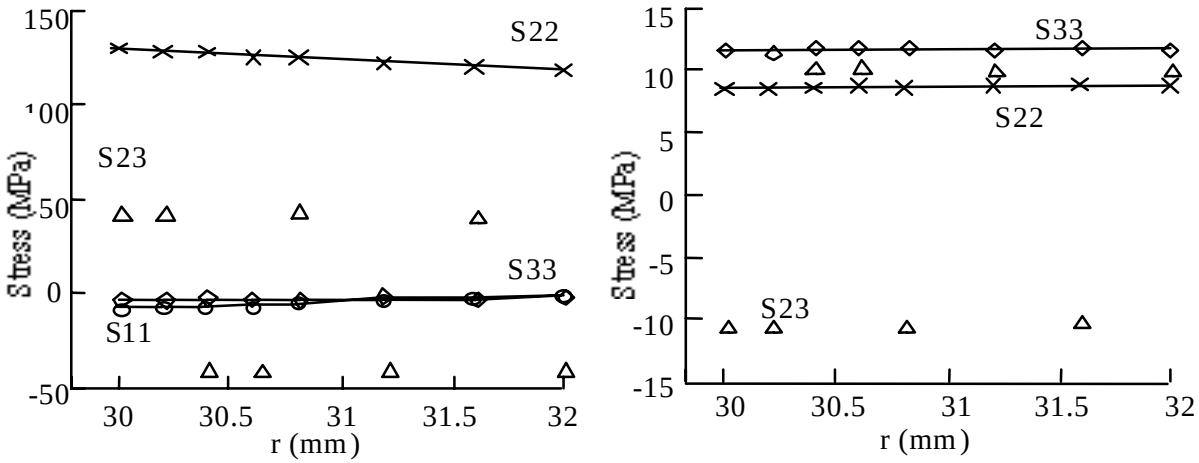

Fig.3(a,b). Stress distributions for the pure internal pressure (left) and tensile loading (right) expressed in local co-ordinates.

during the pure tensile test. For pure internal pressure and combined loading, the loading rate is 0.16 $MPas^{-1}$. Several specimens under the same loading conditions were tested. A biaxial testing apparatus and a special gripping system designed by LMARC (Besançon, France), was developed to test the tubular specimens under various loading conditions [6]. This testing facility is capable of applying up to 100 kN axial load in tension or compression, and 80 MPa internal pressure. The reason to choose displacement controlled loading pattern for pure tensile tests is to obtain a well developed delamination process, which should produce same damage mechanisms before the peak force as force controlled loading pattern.

The system recorded axial load and position from the servohydraulic machine; axial and hoop strains from the extensometers; the pressure and piston displacement from the pressure intensifier. Real time data acquisition, storage and test pilotage were achieved by the program Labview. The specimens were also carefully observed during the progress of the test in order to detect the eventual whitening, cracking and delamination which could be then correlated with the load-displacement and AE traces. Some tests were stopped at selected load levels so that further micro-examination could be performed using optical or electron microscopy.

Mechanical Behaviour of Composite Tube Specimens

Pure tensile test results and mechanisms of damage initiation

A typical stress-strain curve up to failure is shown in Fig. 4. There is a pronounced peak at a strain of about 1.2%. The curves are essentially linear and elastic for strains lower than 0.5%. The applied fracture force is 30 kN (corresponding fracture stress 61 MPa) for Lot A tubes and 36 kN (corresponding fracture stress 73 MPa) for Lot B tubes. A significant difference in AE signal intensity was noticed for the three types of tubes. Compared to Lot A tubes, there was a delay (thus moving to higher stress levels) in AE for Lot B and Lot C tubes. The first but very few signals were recorded at 6 MPa for Lot A tubes, at 10 MPa for Lot B tubes and at 24 MPa for Lot C tubes.

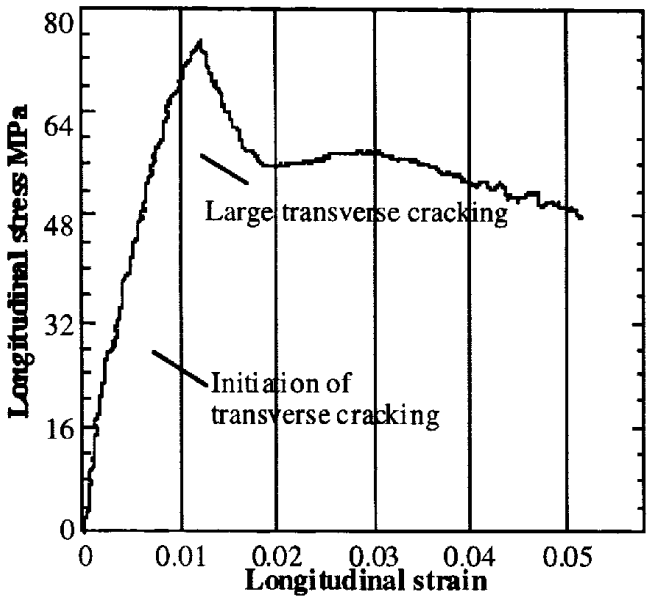

Fig. 4. Typical pure tensile stress-strain curve for a Lot B tube.

The first damage mechanism is the matrix cracking, the cracks initiating in the zones free of fibres or in the outer resin skin. The cracks are of mode I nature and often perpendicular to the

macroscopical loading direction. In increasing the stress level, the second damage mechanism is observed and is the transverse cracking. The average value of this stress is about 30 MPa for the tubes tested in this study. Observations of the specimens loaded to a lower stress level showed that the cracks were mainly located at the vicinity of the porosity, indicating the strong effect of porosity on the damage initiation mechanism. Furthermore, these cracks are more numerous in the internal ply where there is more porosity and which is highly stressed. They progress and appear in all plies with increasing stress level. In the case of Lot A and Lot B tubes, localised deformation occurred around one main crack along the filament direction. Delamination then initiates and propagates from the main cracks at the interface between plies, which corresponds to the post-peak plateau on the stress-strain curve in Fig. 4. The cracking was, however, more dispersed in Lot C tubes resulting in some kind of necking as in metals. In this zone, there is no longer adhesion between the fibres and the matrix. The real gauge length of the specimen is much reduced.

Pure internal test results and mechanisms of damage initiation

The pure internal pressure tests were performed at a loading rate of 1.6 bar/s. Pressure was gradually increased to the final values. Typical stress-strain (longitudinal and circumferential) curves for a Lot B tube specimen are shown in Fig. 5. The curves were essentially linear and elastic for strains lower than 1%. The tubes, being much stronger when loaded in this direction, were not tested up to failure in order to examine the damage initiation mechanisms. Lower density of AE was recorded for the three types of tubes in comparison to pure tensile testing.

For Lot B tubes, a few matrix microcracks were observed in the external resin layer at s_{qq} = 210 MPa. These cracks did not cause the initiation of transverse cracking. For a higher stress level (s_{qq} = 320 MPa), delamination was initiated either due to the intraply matrix cracking or to the interply porosity, being located between the two external plies. Whitening was observed on the outer skin of the tubes though few damage traces were found on a large examination surface. The whitening phenomenon has been investigated by several authors [5] and has been attributed mainly to local interface debonding and matrix cracking. A thorough study is being conducted in order to correlate the local stress state to this phenomenon. A significant difference was noticed between these cracks and the transverse cracks under pure tensile loading. In the case of pure internal pressure, a damaged or microcracked band propagates around the fibres without attacking their interface.

Observation of a Lot A tube specimen loaded to s_{qq} = 240 MPa revealed delamination, indicating the possible influence of numerous voids contained in this kind of tube.

Combined loading test results and mechanisms of damage initiation

Tests with various s_{zz}/s_{qq} ratios were also performed at a loading rate of 1.6 bar/s regarding internal pressure. The load was gradually increased to the final values. In general, as far as the mechanical response was considered, the tubes appeared stronger than in pure internal pressure tests. The tubes were not tested up to failure in order to examine the damage initiation mechanisms. The results are presented in two groups regarding the s_{zz}/s_{qq} ratio value.

Tests with s_{zz}/s_{qq} equal to 0.5: A typical stress-strain curve for a Lot A tube specimen is shown in Fig. 6. for s_{zz}/s_{qq} equal to 0.5, i.e. internal pressure testing with an end effect. Very similar

damage initiation mechanisms to axial tensile tests were observed, meaning matrix cracking first (s_{qq} = 75 MPa) followed by transverse cracking (s_{qq} = 110 MPa). However, the difference between the loading conditions in question and pure internal pressure is that the matrix cracking is more effective in provoking transverse cracking initiation. Transverse cracking was the main damage mechanism which initiated from pre-existing defects, matrix cracking or porosity. For lower stress levels, transverse cracking remained inside one ply. For higher stress levels, however, it crossed several plies. This could be due either to the change of crack direction inside the interply resin layer when the former crosses it, or to just a few cracks having joint traces on the observation plane. It should be noted that there seems to be a correlation between the transverse cracking and the delamination in this kind of loading. A possible process is the transversal cracking giving rise to the delamination at the interface when it propagates through the interply resin layer. For a Lot B tube specimen, delamination was not observed at s_{qq} = 365 MPa. Only transverse cracking was initiated at the intraply porosity.

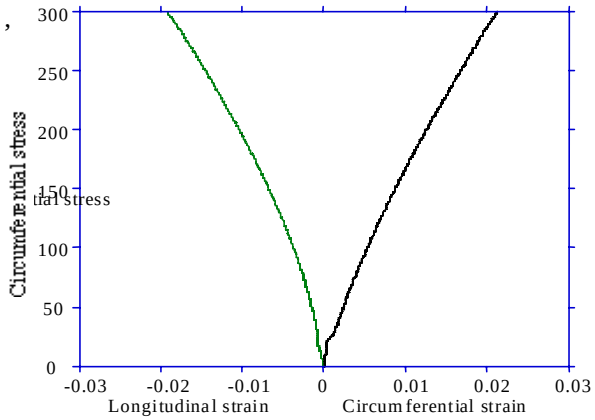

Fig. 5. Typical pure internal pressure stress-strain curves for a Lot B tube.

Tests with s_{zz}/s_{qq} equal to 0.1, 0.2 and 0.3: The purpose of this series of tests was to determine the critical ratio of shift of the main damage mechanism from transverse cracking to delamination. According to the microscopical observations, it seems that the shift occurred for s_{zz}/s_{qq} between 0.2 and 0.3. No transverse cracking was observed for s_{zz}/s_{qq} equal to 0.1 and 0.2. No delamination was observed for s_{zz}/s_{qq} equal to 0.3. A cautionary phenomenon is a heavily damaged band observed at the interface between the two external plies for a test ratio of s_{zz}/s_{qq} equal to 0.1, in which some kind of crazing was produced probably by shear stresses.

Finally, Figure 7a summarises the behaviour of the tubes by relating the damage mechanisms to the applied stresses obtained by microscopical observation and experimental tests.

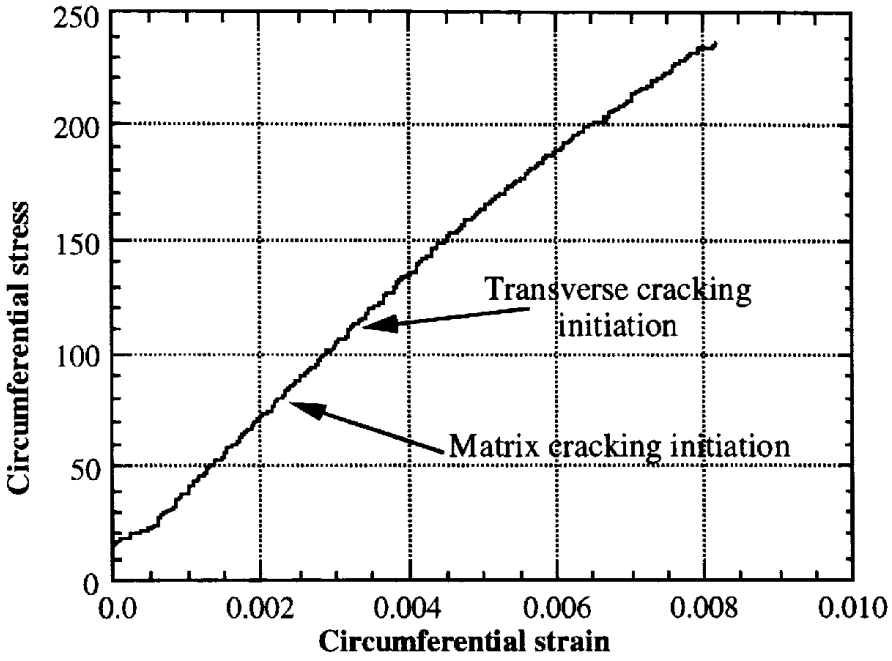

Fig. 6. Typical stress-strain curve *for a Lot A tube tested with* $s_{zz}/s_{qq} = 0.5$.

FAILURE PREDICTION OF A PLY BY MICROMECHANICAL MODELLING

Three local failure modes are investigated, which enable to study the competition between different damage mechanisms and to determine the corresponding critical macroscopic loads. The three failure criteria employed here are based on the experimental observations, corresponding to three damage mechanisms: (a) micro-crack initiation from the cavities (porosity), (b) crack initiation at the interface of matrix and fibre by interfacial shear stress, and (c) transverse ply crack initiated at the interface by interfacial normal stress. Using these three local damage criteria, it is possible to determine the corresponding macroscopic applied loads. The method can be explained as following: under a given combined macroscopic loading, the stress fields in each ply can be determined; then both the stresses near the voids, and normal and shear stresses along the interface in each ply can be evaluated by means of micromechanical methods. Subsequently we compare these local stresses with corresponding critical values and determine in this manner the strength of composite tube. The following local values are chosen: σ_{nc} = 80 MPa, τ_c = 53.3 MPa: when the principle maximum stress near a void reaches 80 MPa, a crack will be initiated at this void; when the interfacial shear stress reaches 53.3 MPa, a crack will be initiated or sliding will take place at the interface; when the interfacial normal stress reaches 80 MPa, a crack will be initiated at the interface by debonding. The choice of 80 MPa for s_{nc} was made after a uniaxial tensile test on pure resin specimens. The maximum value is considered as the fracture strength of the resin. There are no credible values for t_c. Most probably, a ratio smaller than 2 should be used for s_{nc}/t_c, a value of 1.5 was used in this investigation.

Figure 7b shows the predicted results together with the experimental ones. It can be seen that in an internal pressure dominated region the predicted results by micromechanical approach are again conservative. Explanation for such a difference is not evident, since from a mesoscopic point of view, the predicted results have the same tendency (conservative prediction for internal pressure dominated region). It should be mentioned that the

delamination observed in this study is always of interply nature. It is not controlled directly by the stresses inside plies, but depends on the different deformation patterns inside two adjacent plies. The incompatible shear strains between two plies may be the origin of delamination. They change sign when crossing the interface between two plies. The thin resin layer between plies may be the preferred site for delamination initiation.

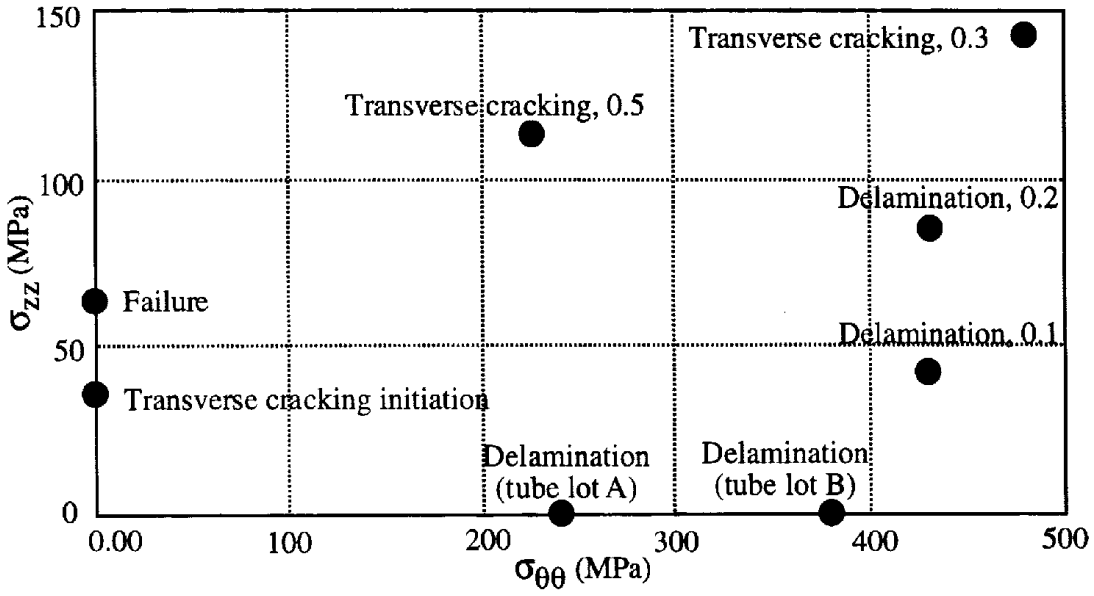

Fig. 7a. Stress envelope with damage mechanisms and failure modes for different s_{zz}/s_{qq} ratios

DISCUSSION

Comparison with Microscopical Observations

The general tendency predicted by the micromechanical modelling agrees well with micromechanism observation. The threshold stresses increase with an increasing s_{zz}/s_{qq} ratio. In the case of tensile loading, the first damage mechanism was matrix cracking, the cracks initiating at the zones free of fibres or at the outer resin skin. The second damage mechanism observed was transverse cracking, being mainly located at the vicinity of the porosity, indicating the strong effect of porosity on the damage initiation. In the case of internal pressure loading, besides a few matrix microcracks being observed in the external resin layer, for a higher stress level, delamination initiated either from the intraply matrix cracking or from the interply porosity. Whitening was also observed on the outer skin of the tubes though few damage traces were found on a large examination surface.

According to the micromechanical modelling prediction, one should be able to observe, for a tensile test, the cracks initiating at the porosity first for s_{zz} = 62 MPa. Some kind of interfacial failure due to interfacial shear stresses should also be visible for a higher stress level. In the case of internal pressure loading, interfacial sliding due to interfacial shear stresses would occur for s_{qq} = 120 MPa. The explanation of the absence of this phenomenon in microscopical observations on long tube specimens may reside in the constraint effect of symmetric filament-wound tubes. The sliding along the continuous fibres is or not possible or without any noticeable traces. This sliding might be also partially reversible due to the viscous effect

of the matrix or the elastic nature of it. A special study is under progress at the moment which will help to understand this phenomenon. It can be concluded that this interfacial sliding occurred at a pre-polished free surface at about s_{qq} = - 90 MPa in compression and s_{qq} = 140 MPa in hoop tensile tests. This observation indicates that the choice of t_c = 53 MPa for the local interfacial fracture criteria is relatively correct.

On the contrary, for combined loading with s_{zz}/s_{qq} > 1.9, another mechanism related to the interface failure, is very detrimental on the composite tube behaviour: debonding by interfacial normal stress. The threshold stress is quite high and increases with the s_{zz}/s_{qq} ratios. The average effect results in very numerous microcracks (one crack for one fibre). A continuous path can be created easily by these cracks which leads to weeping. Stress transfer capacity of the fibres and the tube integrity can be/or not much deteriorated. The macroscopical loading level should be kept below a certain value above which there is still margin before the local stress fields to reach this fracture criterion. A possible way to take into account the effect of both of these two mechanisms is to reduce the corresponding modulus for each of them, namely reducing G_l for interfacial shear stress damage and E_3 for interfacial normal stress damage.

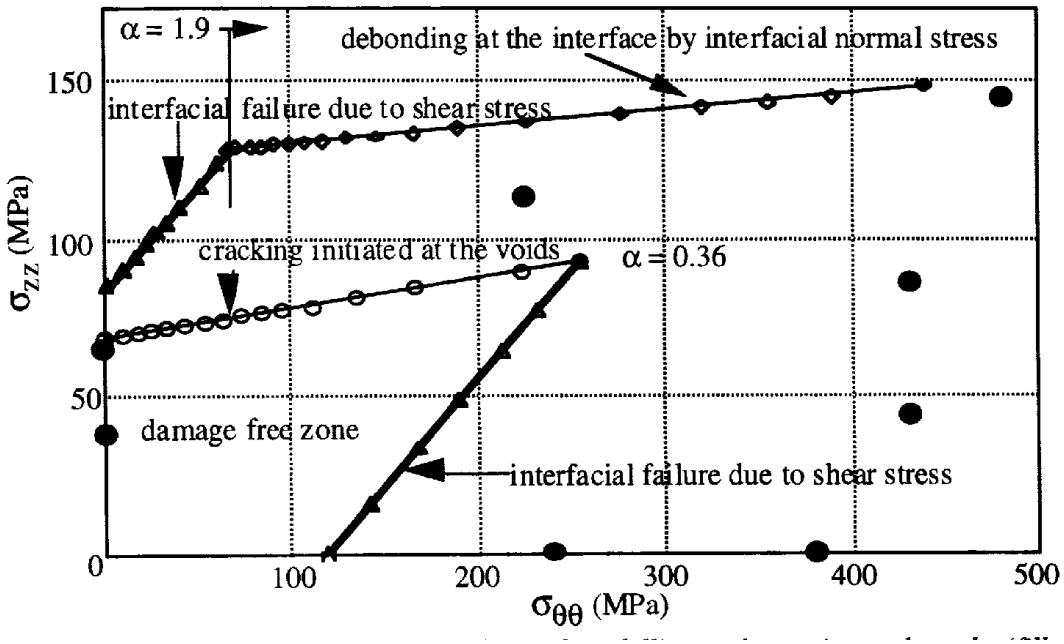

Fig. 7b. Comparison between micromechanical modelling and experimental results (filled cycle)

Effect of the Choice of Local Criteria

In this study, values of σ_{nc} = 80 MPa, τ_c = 53.3 MPa were used as the local critical strengths and the absence of coupling of t_c and s_{nc} for the local fracture criteria. Physically, there would be some interaction effect between these two components, as in most cases. However, the experimental data is insufficient to qualify this. Differences in the state of stress and the geometry of the problem will result in vastly different failure mechanisms. The poker-chip strains to failure in the primary loading direction were 0.5-0.8%, so the uniaxial stress state in composite matrices may therefore by itself be a sufficient explanation for low values of transverse composite strains to failure. Furthermore an investigation of pressurised glass-fibre/polyester pipes provides an example of how transverse cracks form early in the

deformation process of a composite structure. Onset of weepage due to transverse cracks occurred at transverse strains of about 0.2% whereas final failure occurred much later. On the other hand, it was recently proposed that with polymers, which have extended covalently bonded structures, molecular disruption in shear is as difficult as it is in tension, and may well be activated by tension instead of shear. Subsequently the failure process in shear tests is almost certainly tension rather than shear.

From a quantitative point of view, the micromechanical prediction gave higher threshold stresses for first damage initiation (transverse cracking) than observations in principally tensile loading regions. Two explanations could be given, one is that the value of s_{nc} was not correctly chosen. The second may be that the stress state effect was not correctly represented by the micromechanical modelling - average theory. To improve this prediction, tests under a similar stress state should be performed in order to determine the critical values for s_{nc} and t_c. Under internal pressure loading, only delamination was observed as a main damage mode at a stress level much higher than that for interfacial shear failure predicted by micromechanical modelling. The plies are subjected to 3D loading with a very large in-plane shear stress, meaning shear along the fibre axis. This situation does not correspond to any known tests in literature.

Effect of the Number and Volume Fraction of Voids (Porosity)

Micromechanical modelling indicates that the average effect of an increase in the void volume fraction on the local stress field, proportionally increased, is small. A local mechanical effect of the porosity is the increase in the stress concentration at the interface. A complementary coefficient of stress concentration Ktc should be introduced to take into account this effect, because the micromechanical modelling gives only an average effect. By 2D Finite Element calculation, it was found that for $f_v = 0.05$ and a cubical distribution of fibres and porosity, K_{tc} equals 1.2. This coefficient, larger than one, will still reduce the strength of the interface. The technical importance of this effect is that a void can affect the interface of the fibres in its environment, showing again the detrimental effect in increasing the number of voids.

In practice, a detrimental effect of porosity is to provide more nucleation sites for microcracks and then to reduce the length of the propagation path before their coalescence. To get a quantitative description, the concept of the representative defect is used. The value of $f_v = 0.05$ (volume fraction of porosity) means having one void in the ply thickness direction within a circumferential distance of about 625 mm in the case of ideal distribution. The propagation distance is reduced to 210 mm (half thickness). If f_v increases to 0.1, there may be two voids in the thickness direction (in the worst case), the propagation distance becoming 105 mm. From this point of view, a small size porosity of is more detrimental than a larger size one, for the same volume fraction. The present authors suggest a limit of f_v below 5% in order to avoid any possible detrimental effect.

In this study an aspect ratio of 15 was used for the porosity in the micromechanical modelling. The choice of this value is a result from an average over the microstructural analysis information. According to the microstructural analysis in [1], some of the voids have an aspect ratio larger than 15. The porosity is less stressed with a smaller aspect ratio. This enhancing effect, however, is stabilised for an aspect ratio larger than 14.

CONCLUSIONS

A micromechanical model based on the Mori-Tanaka Theory is used which enables the determination of the local stress fields at the interface and at the porosity in a critically loaded ply of the studied composite tube. The general tendency of the threshold stresses predicted by the micromechanical modelling agrees well with the micromechanism observation. The modelling also provided useful information in order to correlate the microscale damage to the macroscopical behaviour of the tubes under combined loading. The porosity volume fraction should be kept below 5% to avoid any detrimental effect. There still remains some work to be done in order to improve the local criteria and the choice of critical stress values used in them.

ACKNOWLEDGEMENTS

The present research is supported by EDF-DER (Electricité de France). The authors are grateful to Drs. F. Nagot, J. Le Bras and M. Lasne (EDF-MTC) and Professor D. François for their discussions. The work was carried out in the laboratory MSS/MAT of Ecole Centrale Paris (CNRS URA 850). We would like to acknowledge the assistance rendered by our colleagues.

REFERENCES

1. Bai, J.B., Seeleuthner, Ph. & Bompard, Ph., Mechanical behaviour of ± 55° filament-wound glass-fibre/epoxy-resin tubes: Part I - Microstructure analyses and mechanical behaviour and damage mechanisms of composite tubes under pure tensile, pure internal pressure and combined loading, *Composite Science and Technology*, Vol. 56, 1996 (in press).

2. Karayaka, M., Srinivasan, S., Miyase, A. & Wang, S.S., Leakage damage and failure of glass-fibre reinforced composite tubular vessels under combined internal pressure and axial loading, *Proceedings of 10th Int. Conf. on Composite Materials (ICCM-10)*, Vol. I, 1995, pp. I-747 - 54.

3. Anderssen, R., Gradin, P.A., Gustafson, C-G. & Nygard, P., Prediction of crack development and stiffness degradation in angle-ply filament wound pipes, *ibid.*, pp. I-407 - 14.

4. Frost, S.R., Predicting the long term fatigue behaviour of filament wound glass fibre/epoxy matrix pipes, *ibid.*, pp. I-649 - 56.

5. Bader, M.G., Bailey, J.E., Curtis, P.T. & Parvizi, A., The mechanisms of initiation and development of damage in multi-axial fibre-reinforced plastics laminates, *Proc. of 3rd Int. Conf. on materials (ICM-3)*, Cambridge, England, August 1979, pp. 227-39.

6. Pérreux, D., Maire, J.F., Siqueria, C., Varchon, D. & Oytana, C., Multiaxial testing of composite materials, *Matériaux et Techniques*, vol. 6-7, 1993, pp. 37-40.

7. Mok-Yeo, B. L. & Bader, M.G., Sub-critical damage in glass-fibre/epoxy-resin laminates: use of laser diffraction and CLSM technique, *Proc. of 10th Int. Conf. on Composite materials*, Whistler, August 1995, Vol. V, pp. V-357-64.

8. Carroll, M., Ellyin, F., Kujawski, D. & Chiu, A.S., The rate-dependent behaviour of ± 55° filament-wound glass-fibre/epoxy tubes under biaxial loading, *Composite Science and Technology*, Vol. 55, 1995, pp. 391-403.

9. Mok-Yeo, B. L. & Bader, M.G., Influence of winding angle on the strength and deformation of filament-wound composite tubes subjected to uniaxial and biaxial loads, *ibid.*, Vol. 46, 1993, pp. 363-78.

10. Bai, J.B., Hu, G.K. & Bompard, Ph., Mechanical behaviour of ± 55° filament-wound glass-fibre/epoxy-resin tubes: Part II - Micromechanical modelling of the damage initiation - competition of the different mechanisms, Vol. 56, 1996 (in press).

11. Demyanushko, K. & Bai, J.B., Local and global stress state analyses of a ± 55° filament winding tube with damage effect, submitted to Composite Structures, 1996.

EFFECT OF STACKING SEQUENCE ON STRENGTH AND FAILURE PROCESS IN QUASI-ISOTROPIC CFRP LAMINATES WITH TOUGHENED INTERLAMINAR LAYERS

Shinji Ogihara[1], Nobuo Takeda[2], Satoshi Kobayashi[1] and Akira Kobayashi[1]

[1]Department of Mechanical Engineering, Science University of Tokyo, 2641 Yamasaki, Noda, Chiba 278, Japan

[2]Center for Collaborative Research (CCR), The University of Tokyo, 4-6-1 Komaba, Meguro-ku, Tokyo 153, Japan

SUMMARY: Effects of stacking sequences on the strength and microscopic failure processes in quasi-isotropic CFRP laminates under static tensile loading are investigated. Observation of microscopic failure process is conducted by using an optical microscope and a X-ray radiography. The material system used is a CFRP with a toughened interlaminar layer at every ply interface. The stacking sequences are $(0/45/90/-45)_S$ and $(45/0/-45/90)_S$. By the edge observation of the plain specimens, transverse crack density is measured as a function of laminate stress. By the X-ray radiography observation, delamination onset and growth is detected. To discuss the transverse cracking, a modeling based on damage mechanics analysis is conducted. To explain delamination behavior, a simple energy release rate analysis is conducted.

KEYWORDS: delamination, energy release rate, interlaminar layer, microscopic failure process, quasi-isotropic laminates, strength, transverse crack, X-ray radiography

INTRODUCTION

Carbon fiber reinforced plastics (CFRP) are used in the form of multidirectional laminates. Failure process in CFRP laminates involves unique damages, such as, transverse cracks and delamination. It is very important to understand the behavior of these microscopic damages.

O'Brien [1] conducted static and fatigue tensile tests on quasi-isotropic CFRP laminates. Delamination onset and growth were observed by X-ray radiography. He derived the energy release rate associated with free-edge delamination by using the classical lamination theory.

Masters and Reifsnider [2] observed multiplication of transverse cracks in quasi-isotropic CFRP laminates under tensile loading by using the replica technique. It was found that the transverse crack density saturates before the final fracture of the laminates. They explained the saturated crack density by using the shear-lag analysis.

As listed above, the experimental observations of damage progress in quasi-isotropic CFRP laminates have been conducted, but the modeling of damage progress is not well established.

On the other hand, it is pointed out that CFRP has low interlaminar fracture toughness. To overcome this problem, some methods to toughen laminates are suggested. One of them is to utilize good processability of thermoset resin and high fracture toughness of thermoplastic resin. This hybridization of thermoset and thermoplastic resins is achieved by dispersing particulate thermoplastic resin into thermoset base resin. One example of these material systems is T800H/3900-2 which is used in the present study [3, 4].

The effectiveness of employment of the interlaminar layers to enhance the interlaminar fracture toughness is proved [3, 4], but the mechanical behavior of their laminates is not well understood including microscopic failure process. In the present study, effects of stacking sequences on the strength and microscopic failure processes in quasi-isotropic CFRP laminates with toughened interlaminar layers under tensile loading are investigated.

EXPERIMENTAL PROCEDURE

Materials

A material system used is interlaminar toughened carbon/epoxy T800H/3900-2 laminates in which polyamide particle-dispersed epoxy matrix layers are placed between each layer. The T800H/3900-2 prepreg system has tough and fine polyamide particles on its surfaces, which results in formation of the interlaminar-toughened layers at every ply interface in the laminates. The thickness of the interlaminar-toughened layers is about 30μm. The laminate configurations are quasi-isotropic $(0/45/90/-45)_S$ and $(45/0/-45/90)_S$. The fiber volume fraction is about 55 %. The specimen size is 150 mm long and 25 mm wide. GFRP tabs are glued on the specimens which results in specimen gage length of 90 mm.

Damage Observation

Quasi-static tensile tests are performed at room temperature. The crosshead speed is 0.5mm/min. By the observation of polished specimen edge, damage progress is measured as a function of laminate strain. During the tests, the testing machine is periodically stopped, and the specimen edge is observed by an optical microscope. Observed area is 50 mm long at the center of the specimen. The number of transverse cracks in each ply is counted to obtain the transverse crack density, which is defined as the number of transverse cracks per unit length.

The specimens are also observed by a X-ray radiography. By the X-ray radiography, delamination onset and growth are detected. Iodozinc (ZnI), a dye penetrant opaque to X-rays, is applied along the specimen edge. Specimens are exposed to X-rays for 150 s at 20 kV and 2 mA. A X-ray point-source unit positioned 570 mm away from the specimen is used.

RESULTS

Table 1 shows the mechanical properties of T800H/3900-2 quasi-isotropic laminates. Figure 1 shows typical stress-strain curves and damage progress in the laminates. Large effect of stacking sequence is seen in tensile strength, that is, tensile strength of $(0/45/90/-45)_S$ laminate is higher than that of $(45/0/-45/90)_S$ laminate. It should be noticed that Young's modulus and failure strain are very similar. In stress-strain curves of $(45/0/-45/90)_S$ laminate, more knee points or discontinuous points are observed than in those of $(0/45/90/-45)_S$ laminates, which may be due to occurrences of severe damages.

Figure 2 shows edge damage state observed by an optical microscope in (a) $(0/45/90/-45)_S$ at σ = 785MPa where σ is laminate stress, (b) $(45/0/-45/90)_S$ at σ =550MPa and (c) $(45/0/-45/90)_S$ at σ = 733MPa. Figure 3 shows transverse crack density as a function of laminate strain in (a) $(0/45/90/-45)_S$ and (b) $(45/0/-45/90)_S$ laminates.

In $(0/45/90/-45)_S$ laminates, the first microscopic damage observed is a transverse crack in 90° ply. At higher strain levels, transverse cracks in 45° and -45° plies are observed. As the laminate strain increases, the number of transverse cracks in each ply increases. The transverse cracks in 45° ply run through the thickness of two adjacent -45° plies at the center of the laminate. The transverse crack density in 90° ply is much higher than those in 45° and -45° plies. The transverse crack density in -45° ply is slightly higher than that in 45° ply. In this laminate configuration, delamination is not observed in the failure process.

In $(45/0/-45/90)_S$ laminates, the transverse cracks in 90° ply and free-edge delamination at -45/90 interface are observed at similar strain level. At higher strain levels, transverse cracks in -45° ply are observed, but not in 45° ply. In 45° ply, surface damage as shown in Fig.2 (b) is observed. Delamination in 90° ply is also observed.

Figure 4 shows X-radiographs of T800H/3900-2 $(45/0/-45/90)_S$ ((a) σ=452MPa, (b) σ=517MPa, (c) σ=581MPa, (d) σ=646MPa, (e) σ=711MPa). Delamination growth in the laminate width direction and transverse crack multiplication is clearly observed.

DISCUSSION

Transverse Cracking

To explain the difference in transverse cracking due to the difference in stacking sequence, micromechanical modeling is conducted. In the present study, the energy release rate associated transverse crack formation is considered.

Gudmundson and Zang [5] developed an analytical model for the prediction of the thermoelastic properties of composite laminates containing transverse cracks. The in-plane compliance matrix of laminates with transverse cracks , $\boldsymbol{S}_{\mathrm{II}(c)}$,can be expressed using in-plane compliance matrix without transverse cracks, $\boldsymbol{S}_{\mathrm{II}}$, as

$$\boldsymbol{S}_{\mathrm{II(c)}} = \left((\boldsymbol{S}_{\mathrm{II}})^{-1} - \sum_{k=1}^{N} v^k \rho^k \left(\boldsymbol{A}^k\right)^T \sum_{i=1}^{N} \boldsymbol{\beta}^{ki} \boldsymbol{A}^i \right)^{-1} \tag{1}$$

where v: volume fraction of ply k, ρ: normalized crack density in ply k, $\boldsymbol{A}$: matrix defined by compliance matrix of each ply and unit normal vector on the crack surface, $\boldsymbol{\beta}$: matrix associated with average crack opening displacement. In the present study, the energy release rate associated with transverse crack formation is derived.

Assuming that transverse cracks occur at a constant load and that they occur at the midway between the existing transverse cracks, the energy release rate when the transverse crack density becomes 2ρ from ρ, $G_t(2\rho)$ at laminate stress σ is expressed as

$$G(2\rho) = \frac{\sigma^2}{2} \left(\frac{1}{E(2\rho)} - \frac{1}{E(\rho)} \right) \frac{h}{\rho t} \tag{2}$$

where $E(2\rho)$ and $E(\rho)$: Young's modulus of the laminate in which the transverse crack density is 2ρ and ρ, respectively, h: the laminate thickness and t: the cracking ply thickness. Young's modulus of the laminate is obtained by using eq.(1) as a function of the transverse crack density. In the present study, normalized energy release rate associated with transverse cracking, G_{tn}, when $\rho \rightarrow 0$ defined as

$$G_{tn} = \lim_{\rho \rightarrow 0} \frac{G(2\rho)}{\sigma^2} \tag{3}$$

is calculated. Material properties used in the analysis are listed in Table 2.

Table 3 shows the normalized energy release rate associated with transverse cracking in each ply. In $(0/45/90/-45)_S$ laminate, the energy release rate in -45° ply is higher than in 45° ply, which corresponds to the results that transverse crack density is higher in -45° ply than in 45° ply. In $(45/0/-45/90)_S$ laminate, the energy release rate in 45° ply is very small which is consistent with the experimental result that transverse crack is not observed. In 45° ply, the surface damage is observed instead of transverse cracks as shown in Fig.2 (b). In both laminates, the energy release rate in 90° ply is relatively small though many transverse cracks are observed. This implies that the critical energy release rate in 90° ply is smaller than that in 45° (or -45°) ply. The analysis will be a basis for a quantitative estimation of transverse crack density.

Delamination

O'Brien [1] derived an equation for the energy release rate associated with straight-edge delamination growth, G_d, as

$$G_d = \frac{\varepsilon^2 h}{2m} \left(E_{LAM} - E^* \right) \tag{4}$$

where ε: the nominal strain, m: the number of delaminations formed and E_{LAM} and E^*: the laminate modulus before and after delamination. In the present study, normalized energy release rate associated with delamination growth, G_{dn}, defined as

$$G_{dn} = \frac{G_d}{\varepsilon^2 h} \tag{5}$$

is calculated. Material properties used in the analysis are lised in Table 2. Table 4 shows the normalized energy release rate associated with delamination growth at each ply interface. It is found that the energy release rate at -45/90 interface at which delamination was observed is much higher than that at other interfaces. This implies that this analysis is useful to predict delamination location.

CONCLUSION

Tensile tests are conducted on quasi-isotropic CFRP laminates with toughened interlaminar layers. Effects of stacking sequences on the strength and microscopic failure processes are investigated. Observation of microscopic failure process is conducted by using an optical microscope and a X-ray radiography. To explain the difference in microscopic failure process due to the difference in stacking sequence, micromechanical modeling of damage onset and growth is conducted. Micromechanical modeling based on the precise observation of microscopic failure process will be a basis for damage tolerance design.

REFERENCE

1. O'Brien, T.K., "Characterization of Delamination Onset and Growth in a Composite Laminates", ASTM STP 775, 1982, pp. 140-167
2. Masters, J.E. and Reifsnider, K.L., "An Investigation of Cumulative Damage Development in Quasi-Isotropic Graphite/Epoxy Laminates", ASTM STP 775, 1982, pp. 40-61
3. Odagiri, N., Murai, T. and Tobukuro, K., "Toughness Improved High Performance TORAYCA Prepreg T800H/3900 Series", Proceedings of 33rd International SAMPE Symposium, 1988, pp. 272-283
4. Odagiri, N., Kishi, H. and Nakane, T., T800H/3900-2 Toughened Epoxy Prepreg System : Toughening Concept and Mechanism", Proceedings of American Society for Composites, 6th Technical Conference, 1991, pp. 46-52
5. Gudmundson, P. and Zang, W., "An Analytic Model for Thermoelastic Properties of Composite Laminates Containing Transverse Matrix Cracks", Int. J. Solids Structures, 30, 1993, pp. 3211-3231

Table 1. Mechanical properties of T800H/3900-2 quasi-isotropic laminates.

Laminates	Young's Modulus (GPa)	Tensile Strength (MPa)	Failure Strain (%)
$(0/45/90/-45)_S$	52.8	799	1.48
$(45/0/-45/90)_S$	53.4	744	1.49

Table 2. Material properties used in the analyses.

Material System T800H/3900-2	
Longitudinal Young's modulus, E_1 (GPa)	143
Transverse Young's modulus, E_2 (GPa)	7.99
In-plane shear modulus, G_{12} (GPa)	3.96
Longitudinal Poisson's ratio, ν_{12}	0.345
Transverse Poisson's ratio, ν_{23}	0.490

Table 3. Normalized energy release rate associated with transverse cracking.

Laminates	**Cracking ply**	**Normalized energy release rate [$\times 10^{-17}$ $N^{-1}m^3$]**
$(0/45/90/-45)_S$	45° ply	22.7
	90° ply	3.28
	-45° ply	45.4
$(45/0/-45/90)_S$	45° ply	11.2
	-45° ply	22.7
	90° ply	6.54

Table 4. Normalized energy release rate associated with delamination growth.

Laminates	**Delamination Interface**	**Normalized energy release rate [GPa]**
$(0/45/90/-45)_S$	0/45	0.000323
	45/90	0.733
	90/-45	0.818
$(45/0/-45/90)_S$	45/0	0.818
	0/-45	0.733
	-45/90	2.05*

* Delamination is observed.

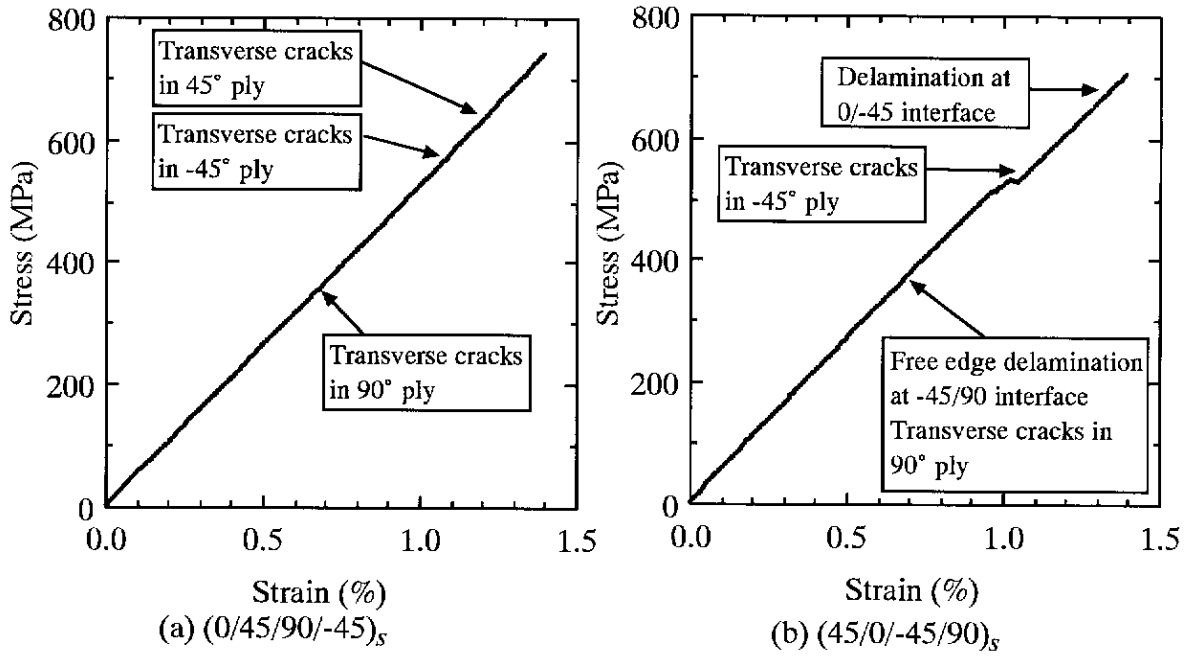

Figure 1: Typical stress-strain curves and damage progress in T800H/3900-2 quasi-isotropic laminates. (a) $(0/45/90/-45)_s$ (b) $(45/0/-45/90)_s$

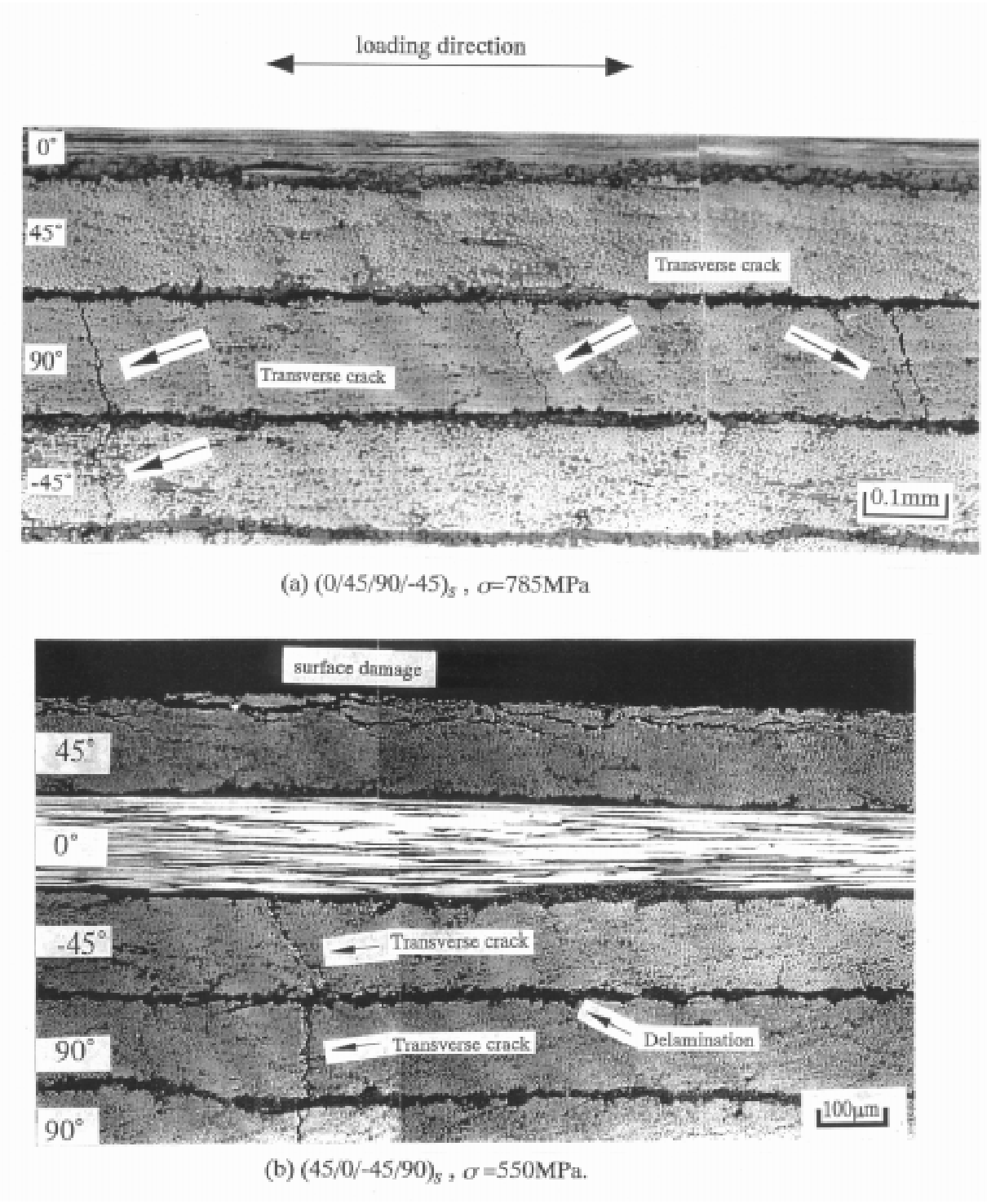

Figure 2: Edge damage state observed by an optical microscope in (a) $(0/45/90\text{-}45)_s$ at σ = 785 MPa, (b) $(45/0/\text{-}45/90)_s$ at σ = 550MPa and (c) $(45/0/\text{-}45/90)_s$, σ = 733 MPa.

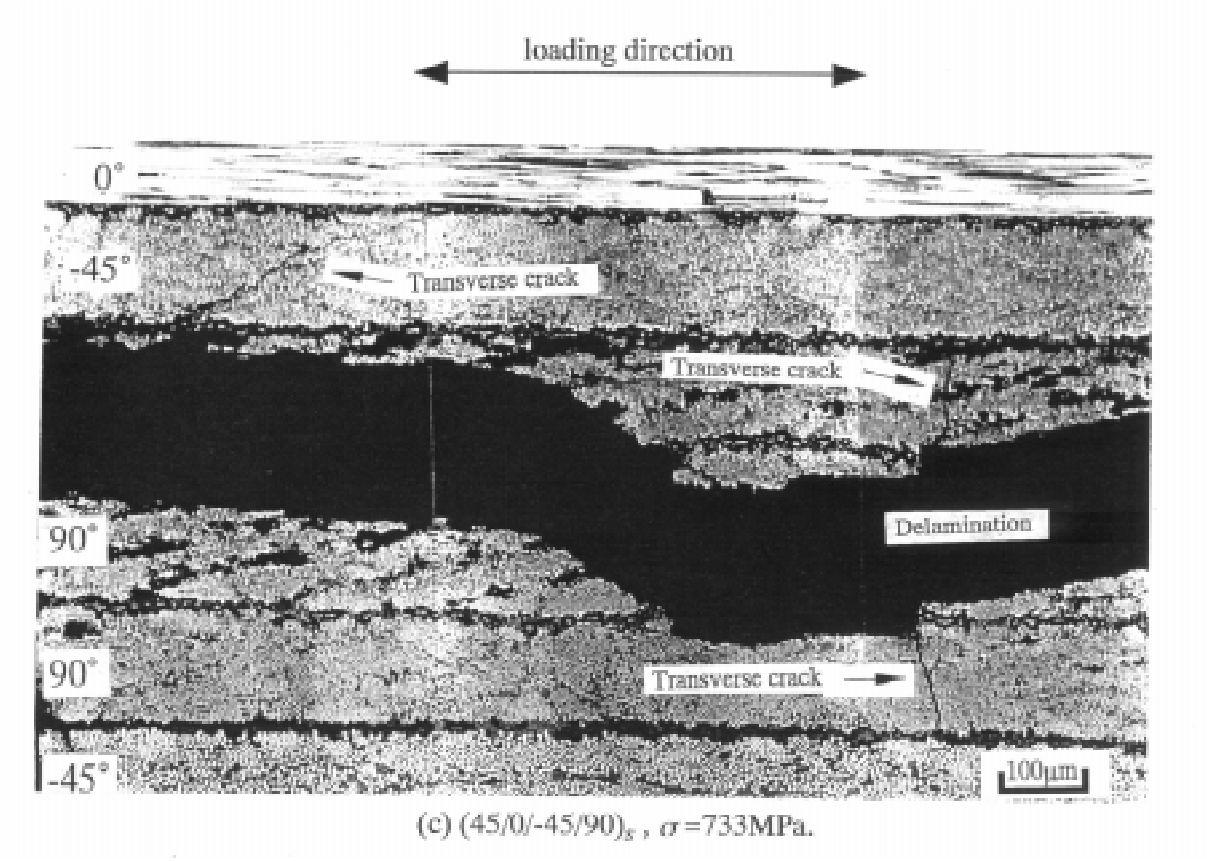

Figure 2: (Continued) Edge damage state observed by an optical microscope in (a) (0/45/90-45)$_s$ at σ = 785 MPa, (b) (45/0/-45/90)$_s$ at σ = 550MPa and (c) (45/0/-45/90)$_s$, σ = 733 MPa.

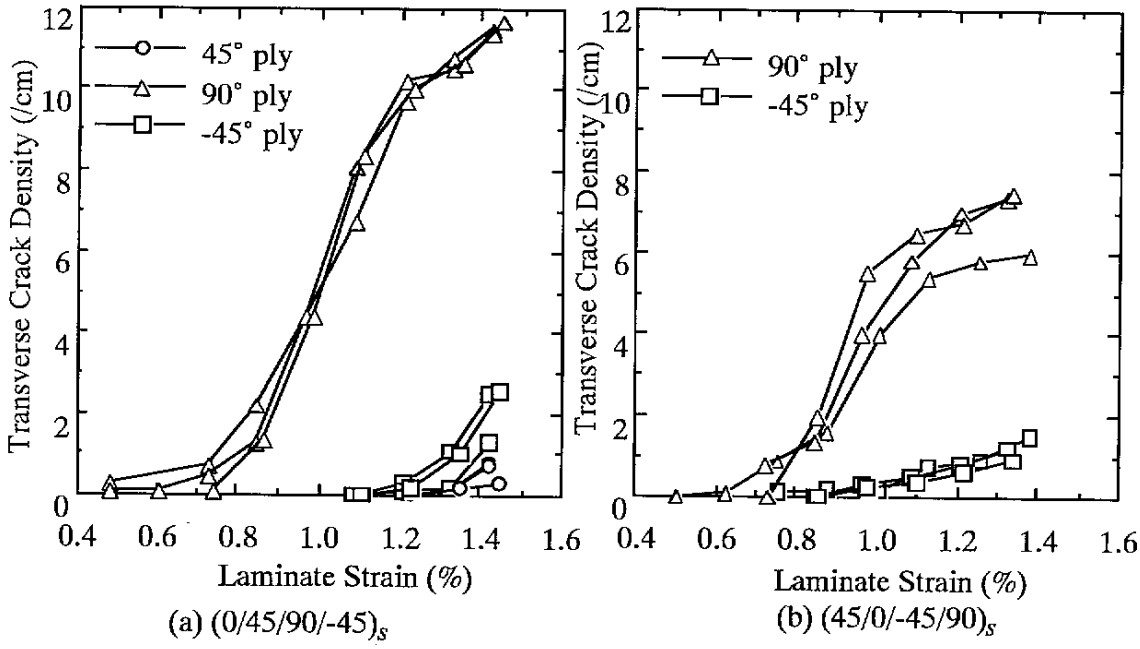

Figure 3: Transverse crack density as a function of laminate strain in T800H/3900-2 quasi-isotropic laminates. (a) (0/45/90-45)$_s$, (b) (45/0/-45/90)$_s$

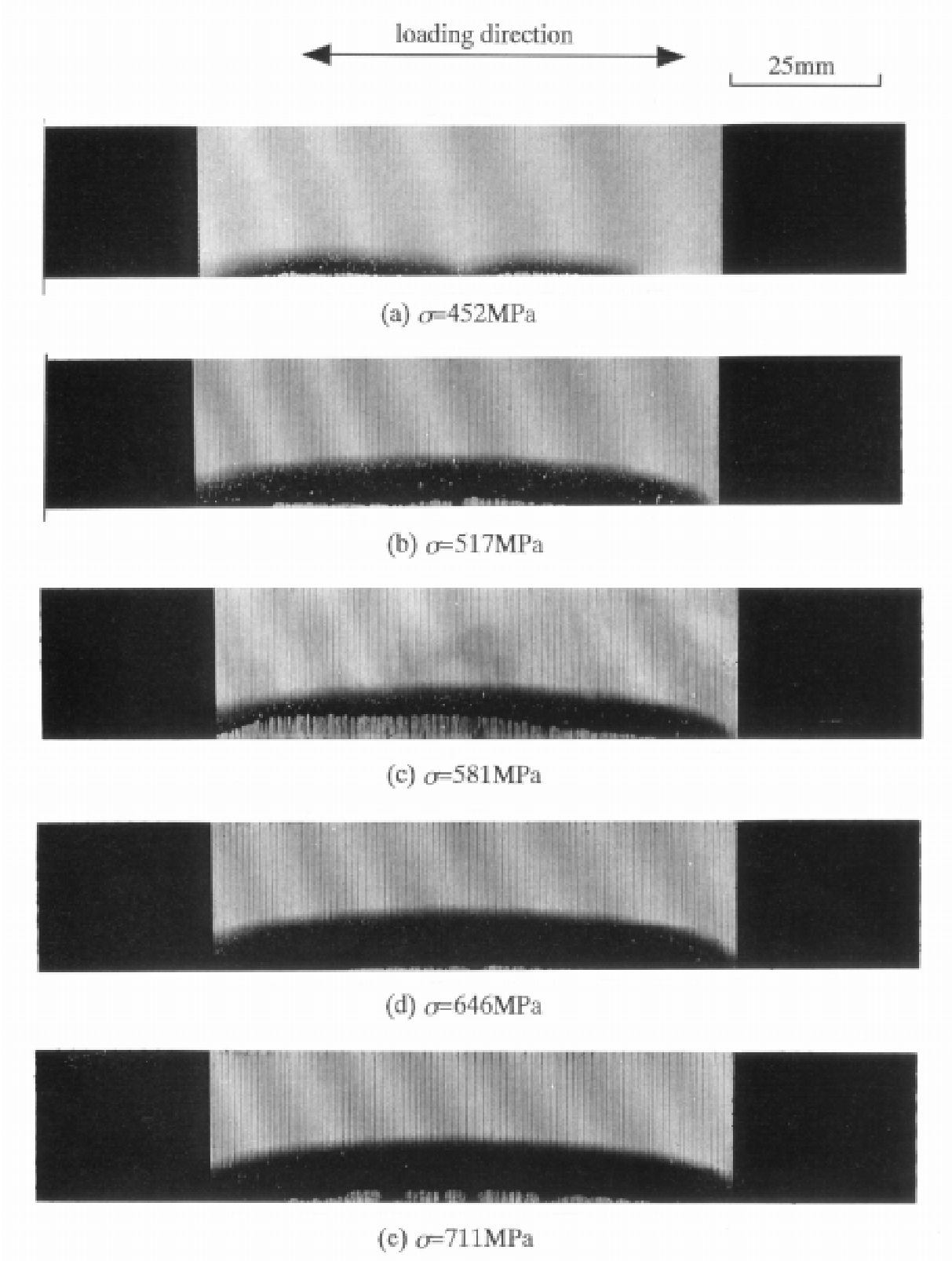

Figure 4: X-radiographs of T800H/3900-2 (45/0/-45/90)s, (a) σ = 452 MPa (b) σ = 517 MPa, (c) σ = 581 MPA, (d) σ = 646 MPa (e) σ = 711Mpa.

EXPERIMENTAL MICRO-MECHANICAL CHARACTERIZATION OF INTERLAMINAR SHEAR DEFORMATION IN INTERLAMINAR-TOUGHENED CFRP LAMINATES

Nobuo Takeda[1] and Shinji Ogihara[2]

[1]Composites Science and Mechanics Laboratory, Center for Collaborative Research (CCR), The University of Tokyo, 4-6-1 Komaba, Meguro-ku, Tokyo 153, Japan

[2]Dept. Mech. Eng., Science University of Tokyo, 2641 Yamasaki, Noda, Chiba 278, Japan

SUMMARY: Tensile tests of CFRP cross-ply laminates with interlaminar resin layers were carried out in a SEM (scanning electron microscope), and microscopic interlaminar deformation and damage near the transverse crack tip was visualized by micro-lines or micro-grids on the specimen edge surface. The local deformation around the transverse crack tip was observed at 20°C, 80°C, 120°C, and 160°C to evaluate the effect of thermal residual stress on the microscopic deformation and damage in the interlaminar region near transverse crack tips. Temperature dependence of interlaminar shear deformation in the resin-rich interlaminar region was clearly demonstrated microscopically. Temperature dependence of the axial COD (crack opening displacement) was also measured. The displacement field of the specimen edge surface obtained from these experimental results were compared with the two dimensional approximate elastic analysis.

KEYWORDS: crack opening displacement, cross-ply laminate, interlaminar shear deformation, micro-line/grid methods, temperature effect, transverse crack, thermal residual stress, Young's modulus reduction

INTRODUCTION

In many applications of fiber-reinforced plastics, they are mainly used in the form of multidirectional laminates. Among these composites, cross-ply laminates have been extensively investigated [1-7] through both theoretical and experimental studies because this is a basic laminate configuration. The failure process of cross-ply laminates is known to invlove an accumulation of transverse cracks and delamination.

Most previous studies of the failure process of cross-ply laminates have been focused on the experimental measurement of transverse crack density as a function of applied load or the theoretical prediction of the onset of transverse cracking and its multiplication. In conjunction with the theoretical prediction of mechanical behavior and damage progress of cracked laminates, micromechanical stress analyses of damaged cross-ply laminates have been conducted.

Takeda and Ogihara [2, 3] conducted *in-situ* observation of microscopic failure process in CFRP cross-ply laminates at R.T. and at 80°C. Progressive damage parameters, the

transverse crack density and delamination ratio, were presented. They pointed out that the thermal residual stress had significant effect on the failure process and that quantitative estimation of thermal residual stress was important.

Hashin [4] conducted variational stress analysis for cracked cross-ply laminates under tension and shear, and predicted stiffness reduction. In the analysis, an admissible stress state was assumed and the principle of minimum complementary energy was applied. Nairn [5] extended Hashin's analysis to consider the thermal residual stresses and derived the energy release rate associated with transverse crack formation. The energy release rate was used to predict transverse crack density as a function of laminate stress.

Lee et al. [6] proposed a mathematical model for predicting the stiffness reduction of cracked cross-ply laminates. In their analysis, the principle of minimum potential energy was utilized with assumed displacement fields. McCartney [7] analyzed stress transfer between 0° and 90° plies in cracked cross-ply laminates. The solutions were determined to satisfy the stress-strain-temperature relations either exactly or in an average sense.

In recent years, interleaved laminates have been developed in which resin rich layers are placed in interlaminar regions to enhance the interlaminar fracture toughness of CFRP laminates and to restrict delamination onset. In this paper, micro-lines or micro-grids were printed on edge surface of interleaved CFRP cross-ply laminate specimens to measure the local displacement fields near the transverse crack. Observations are carried out in a scanning electron microscope (SEM) at different temperatures to evaluate the effect of thermal residual stress on the local deformation. Quantitative measurement of microscopic deformation was conducted and the experimental results were compared with the predictions based on two dimensional approximate elastic analysis. Loading-unloading testes were also conducted to obtain the Young's modulus reduction as a function of the transverse crack density. A reasonable agreement between the experimental results and analytical predictions were obtained.

EXPERIMENT

Materials

Two material systems were used. One was interleaved CFRP, T800H/3631-FM300, with epoxy resin (FM300) layers about 100μm thick between 0° and 90° plies. Another was toughness-improved CFRP, T800H/3900-2, with selectively toughened interlaminar layers about 30μm thick at all the ply interfaces. The interlaminar layers have tough and fine thermoplastic resin particles dispersed in the base epoxy resin.

T800H is a high strength carbon fiber. The 3631 is a modified epoxy system with improved toughness compared with a conventional TGDDM/DDS epoxy system. The average thickness of each ply was 0.135mm for T800H/3631-FM300 and 0.190mm for T800H/3900-2. The fiber volume fraction was about 45% for T800H/3631-FM300 and about 55% for T800H/3900-2. The low fiber volume fraction for T800H/3631-FM300 is due to the insert of the FM300 resin film. The laminate configuration was cross-ply $(0/90_4/0)$.

Preparation of Micro-lines and Micro-grids

The micro-lines or micro-grids were made using the photo-lithography technique on specimen edge surfaces. First, the surface of the specimen was polished, then coated by the photo-resist, or photo-chemical reactive resin. The specimen was heated to cure the resist, and the surface was exposed to the light through the photo-mask, or the glass plate with micro-lines or grids. Then the exposed part of the resist was removed in the developer, and vacuum-evaporated metal was deposited on the surface. Finally, the remaining resist was removed in the solvent to prepare the micro-lines or grids on the specimen surface.

Measurement of Microscopic Deformation and Young's Modulus Reduction

Tensile tests of CFRP symmetric cross-ply laminates were carried out in a SEM (scanning electron microscope) with a servo-hydraulic loading machine and a specimen heating unit. The specimen was loaded at 20°C until the transverse crack intervals became uniform, and the images of local area near the crack tip and a whole view of the crack were photographed. Then the temperature was raised to 80°C and the crack was photographed again. This procedure was repeated at 120°C and 160°C. The COD of the transverse cracks and the interlaminar shear strain, γ_{xy} ($=\partial v/\partial x+\partial u/\partial y$) near the transverse crack tip were measured from these photos, where u and v are displacements in x and y directions, respectively (Fig.1). Since the $\partial u/\partial y$ component is considered small, the shear strain was replaced by $\partial v/\partial x$ in the following. Both the average shear strain in interleaf and the shear strain at 90°/interleaf interface were measured.

Loading-unloading tests were also conducted to obtain Young's modulus reduction as a function of the transverse crack density. The loading-unloading procedure cycles were repeated several times with continuous recording of the stress-strain curves. The laminate configurations used in the loading-unloading tests were cross-ply $(0/90_m/0)$ where m = 4, 8 and 12 for both material systems.

ANALYSIS

In the present study, stress and displacement fields in an interleaved CFRP cross-ply laminates with transverse cracks are analyzed [8]. The analysis is based on the two dimensional model developed by McCartney [7] which assumes that generalized plane strain conditions prevail. Account is taken of thermal residual stresses arising from a mismatch in thermal expansion coefficients of 0°, 90° plies and the interleaf layer.

Consider a cross-ply laminate subjected to mechanical and thermal loading as shown in Fig.1 in which interleaf layers are of thickness t. In the present study, two cases are considered; (a) the transverse crack tip stops at 90°/interleaf interface, and (b) transverse crack penetrates into the interleaf and stops at 0°/interleaf interface. The displacement in y-direction in interleaf, v_i, and that in 90° ply, v_m, are expressed as

$$v_i = \left(\frac{1}{\mu^i} - \frac{\nu'^m_T}{E'^m_T}\right) b(x-a)C'(y) - C'''(y)\left[\frac{b}{E'^i}\left\{-\frac{1}{6}\left(x^3 - a^3\right) + \frac{1}{2}a^2(x-a) + \left(a + t + \frac{b}{2}\right)\left\{\frac{1}{2}\left(x^2 - a^2\right) - a(x-a)\right\}\right\} - \frac{ab}{6E'^m_T}\{a - 3(h+t)\}(x-a)\right] + A_2(y) \tag{1}$$

$$v_m = \frac{b}{2a}\left(\frac{1}{\mu^m_T} - \frac{\nu'^m_T}{E'^m_T}\right)\left(x^2 - a^2\right)C'(y) + \frac{b}{6aE'^m_T}C'''(y)\left\{\frac{1}{4}\left(x^4 - a^4\right) - \frac{3}{2}a(h+t)\left(x^2 - a^2\right)\right\} + A_2(y) \tag{2}$$

where a and b are thicknesses of 90° and 0° plies, respectively, $C(y)$ is a function found for each case, and $A_2(y)$ is an arbitrary function arising from integration. E, μ, and ν are constants determined from the mechanical properties of the plies and the interleaf material. The shear strain and crack opening displacement are compared with experimental results.

By using the displacement fields obtained above, Young's modulus reduction as a function of the transverse crack density can be derived for each case [8]. The experimental results were compared with the analytical predictions.

RESULTS AND DISCUSSION

Figure 2 shows a transverse crack in a T800H/3631-FM300 cross-ply laminate (σ=216MPa, 20°C, where σ is laminate stress). By printing micro-lines, we can clearly observe shear deformation in FM300 layer and damage (fiber/matrix interfacial debonding) near transverse crack tip. By inserting the FM300 layer, delamination from the tips of the transverse cracks were not observed which is due to the enhancement of interlaminar fracture toughness. The transverse crack tip propagates into the FM300 layer at some depth and crack tip blunting can be observed.

Figure 3 shows the temperature dependence of the shear strain for T800H/3631-FM300 as a function of distance from the crack tip. The shear strain at 160°C is much larger than that at other temperatures, which is considered due to the drastic reduction in the shear modulus of FM300 at 160°C. The average shear strain in the interleaf layer is larger than that at 90°/interleaf interface. In Fig.3, the analytical predictions are also shown for Case (b), because it seems more realistic than Case (a). The thermo-mechanical properties used in the analysis are shown in Table 1. The most values in Table 1 are taken from Ref.(9).

Figure 4 shows the temperature dependence of COD as a function of the position in the thickness direction. The experimental results shows that temperature dependence of COD is small. This is due to the combined effect of the decrease in the thermal residual stress and the decrease in shear modulus of the interleaf and 90° ply at higher temperature. In Fig.4, the analytical predictions are also shown for both Cases (a) and (b). Cases (a) and (b) are considered lower and upper bounds for COD. For more quantitative estimation of COD, a model in which a transverse crack penetrates into the interleaf at arbitrary depth is necessary.

Figure 5 shows a transverse crack in a T800H/3900-2 cross-ply laminate (σ = 160MPa, (a) 20°C, (b) 160°C). As the temperature rises, the COD in the interlaminar layer increases, while that at the center of the 90° layer changes little.

Figure 6 shows the local highly-deformed area near a transverse crack tip in a T800H/3900-2 cross-ply laminate. It is observed that at 160°C the shear strain in the interlaminar layer becomes rather large. The shear strain in 90° ply, on the contrary, slightly decreases.

Figure 7 shows the temperature dependence of the shear strain for T800H/3900-2 as a function of distance from the crack tip. Larger shear strain is observed in the interlaminar layer at higher temperature, which is considered due to the softening of the interlaminar layer. This corresponds well with the experimental results where the COD in the interlaminar layer magnifies at higher temperature. In Fig.7, the analytical predictions are also shown for Case (b). A reasonable agreement is obtained between the experimental and analytical results except for 160°C. With more proper selection of mechanical properties of interleaf material as a function of temperature, the deformation will be predicted more precisely.

Figure 8 shows the temperature dependence of COD as a function of the position in the thickness direction for T800H/3900-2. Similar to T800H/3631-FM300, temperature dependence of COD is small. This is considered to be due to the reduction in the thermal residual stress and the decrease in the load transmission capability of the softened interlaminar layer. In Fig.8, the analytical predictions are also shown for both Cases (a) and (b). The difference in lower and upper bounds for COD is smaller than for T800H/3631-FM300, because the interleaf thickness is small. Case (b) seems to be a good approximation to this material system.

Figures 9 and 10 show the comparison of experimental results and analytical predictions for the Young's modulus reduction at room temperature in T800H/3631-FM300 and T800H/3900-2 cross-ply laminates, respectively. The analytical results are shown only for Case (a) because the difference between the cases are very small. A reasonable agreement is obtained between the experimental and analytical results. Similar results were obtained at higher temperatures.

CONCLUSIONS

Tensile tests of interleaved CFRP cross-ply laminates were carried out in a SEM, and microscopic interlaminar deformation and damage around the transverse crack was observed at different temperatures by means of micro-lines or grids printed on the specimen edge surface. Temperature dependence of the experimentally-obtained interlaminar shear strain and crack opening displacement were compared with the two-dimensional approximate elastic analysis.

Loading-unloading testes were also conducted to obtain the Young's modulus reduction as a function of the transverse crack density. A reasonable agreement between the experimental and analytical results were obtained.

REFERENCES

1. Bailey, J.E., Curtis, P.T., and Parvizi, A., "On the Transverse Cracking and Longitudinal Splitting Behavior of Glass and Carbon Fiber Reinforced Epoxy Cross Ply Laminates and the Effect of Poisson and Thermally Generated Strain", Proc. R. Soc. Lond., A., 366, 1979, PP. 599-623.

2. Takeda, N. and Ogihara, S., "*In-Situ* Observation and Probabilistic Prediction of Microscopic Failure Processes in CFRP Cross-Ply Laminates", Comp. Sci. Tech., 52, 1994, pp. 183-195.

3. Takeda, N. and Ogihara, S., "Initiation and Growth of Delamination from the Tips of Transverse Cracks in CFRP Cross-Ply Laminates", Comp. Sci. Tech., 52, 1994, pp. 309-318.

4. Hashin, Z., "Analysis of Cracked Laminates: A Variational Approach", Mechanics of Materials, 4, 1985, pp. 121-136.

5. Nairn, J.A., "The Strain Energy Release Rate of Composite Microcracking: A Variational Approach", J. Comp. Mat., 23, 1989, pp. 1106-1129.

6. Lee, J.W., Allen, D.H. and Harris, C.E., "Internal State Variable Approach for Predicting Stiffness Reductions in Fibrous Laminated Composites with Matrix Cracks", J. Comp. Mater., 23, 1989, pp. 1273-1291.

7. McCartney, L.N., "Theory of Stress Transfer in a 0°-90°-0° Cross-Ply Laminate Containing a Parallel Array of Transverse Cracks", J. Mech. Phys. Solids, 40, 1992, pp. 27-68.

8. Ogihara, S., Takeda, N. and Kobayashi A., Submitted for publication.

9. Takeda, N., Niizuma, H., Ogihara, S. and Kobayashi, A., "Experimental Evaluation of Thermal Residual Stress in CFRP Cross-Ply Laminates", Materials System, 14, 1995, pp. 73-78 (in Japanese).

Table 1. Material Properties Used in the Analysis.

T800H/3631-FM300

T800H/3631		FM300	
E_A (GPa)	169-0.111xT	E^i (GPa)	2.65-0.010xT
E_T (GPa)	9.62-0.010xT	ν^i	0.38
G_A (GPa)	4.50	α^i (/°C)	60.6 x 10^{-6}
ν_A	0.349		
ν_T	0.490		
α_A (/°C)	0.10x10^{-6}		
α_T (/°C)	35.5x10^{-6}		

T800H/3900-2

Base Composite		Polyamide Particle-Dispersed Layer	
E_A (GPa)	132-0.090xT	E^i (GPa)	2.71-0.0105xT
E_T (GPa)	8.17-0.007xT	ν^i	0.38
G_A (GPa)	4.50	α^i (/°C)	60.6x 10^{-6}
ν_A	0.349		
ν_T	0.490		
α_A (/°C)	-1.73x10^{-6}		
α_T (/°C)	34.7x10^{-6}		

T: degrees centigrade (°C)

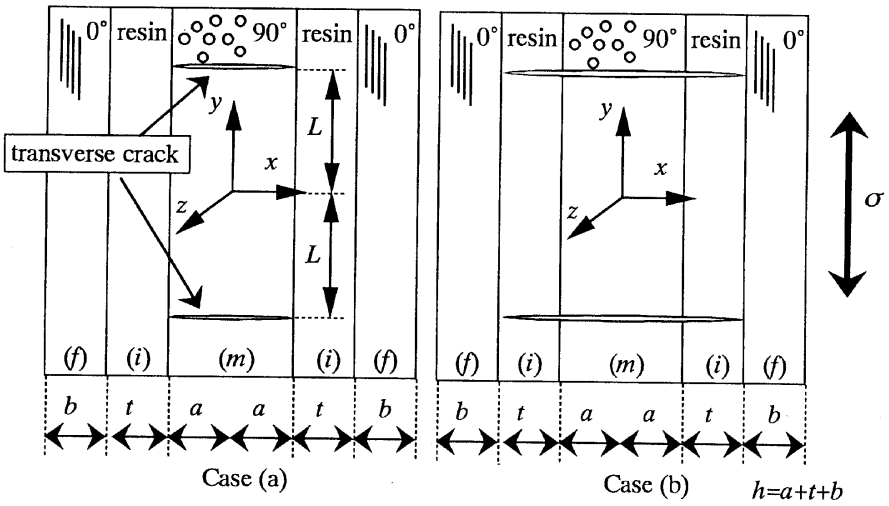

Figure 1. A model of interleaved cross-ply laminate containing transverse cracks in 90° ply. Case (a); Transverse crack tips stop at 90°/interleaf interface. Case (b); Transverse cracks penetrate into interleaf and stop at interleaf/0° interface.

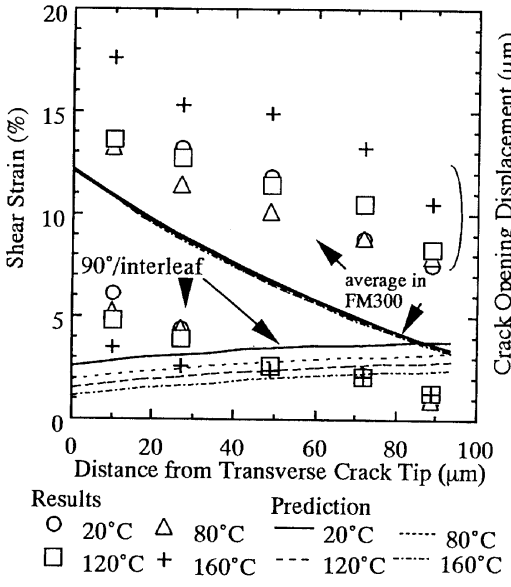

Fig.3 Shear Strain as a Function of Distance from the Transverse Crack Tip in T800H/3631-FM300.

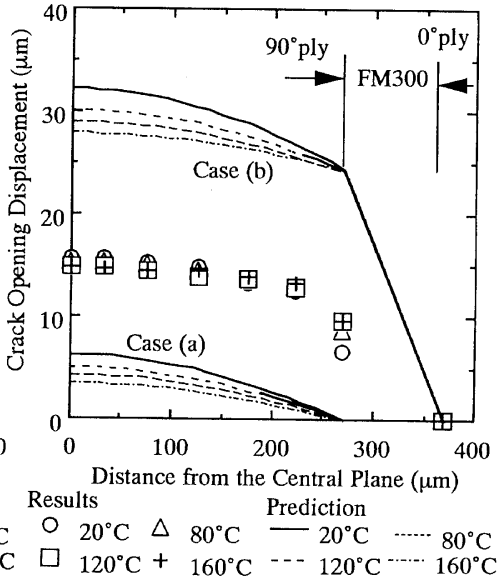

Fig.4 COD as a Function of Distance from the Central Plane in T800H/3631-FM300.

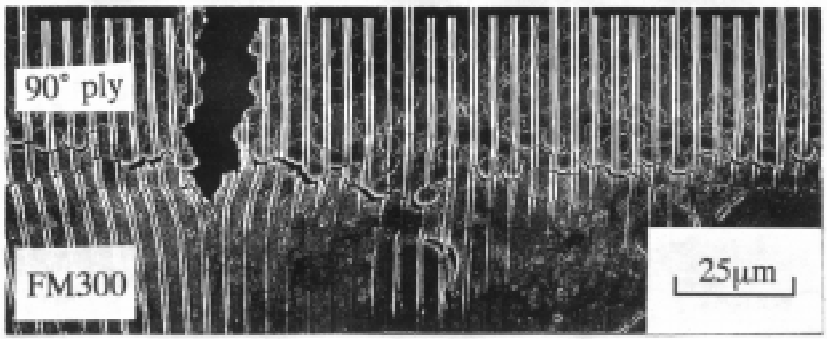

Fig.2 Transverse Crack Tip in T800H/ 3631-FM300 (Laminate Stress=216MPa, 20°C).

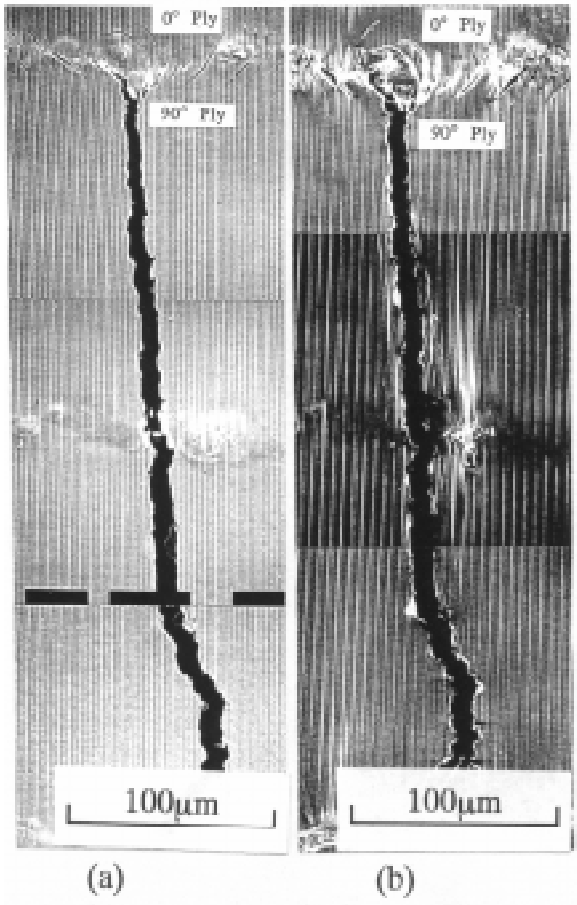

Fig. 5 Transverse Crack Tip in T800H/3900-2 (Laminate Stress=160MPa, (a) 20°C, (b) 160°C).

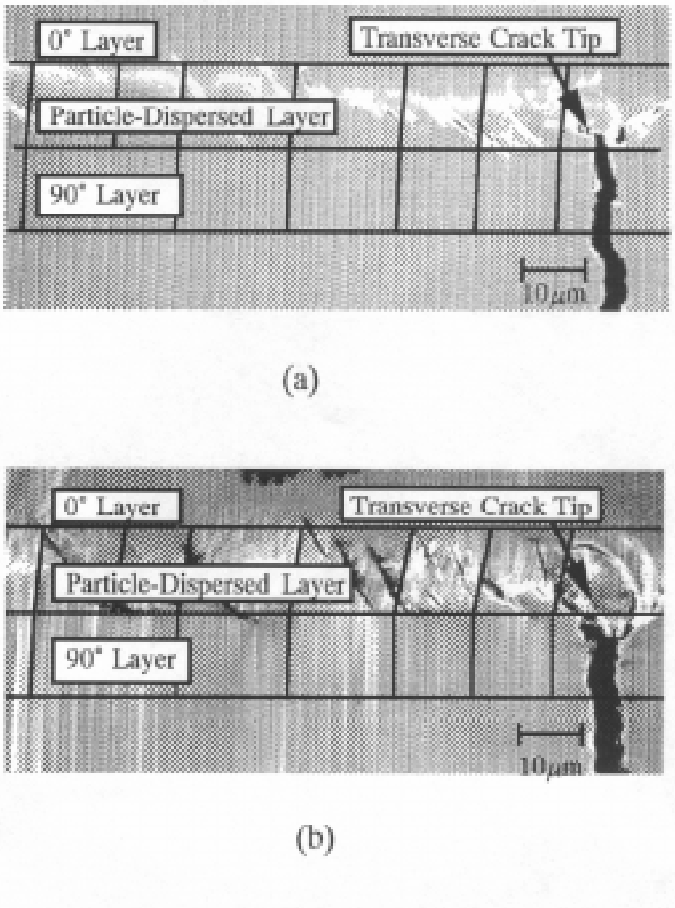

Fig.6 Interlaminar Shear Deformation near Transverse Crack Tip in T800H/3900-2 (Laminate Stress=160MPa, (a) 20°C, (b) 160°C).

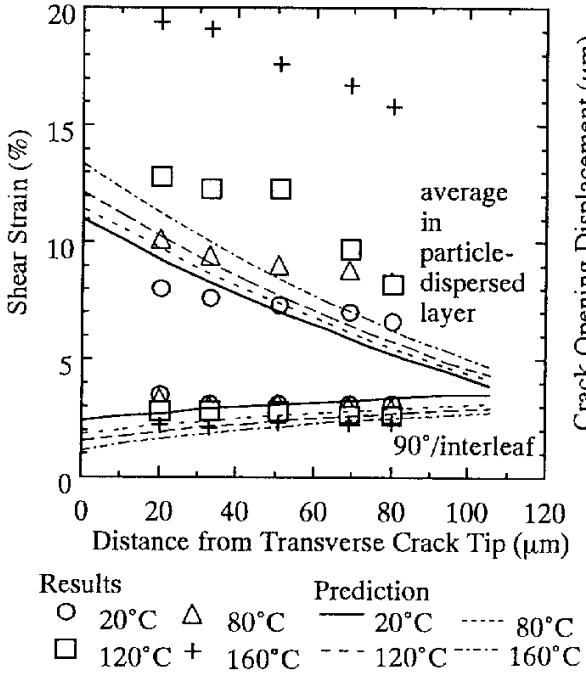

Fig.7 Shear Strain as a Function of Distance from the Transverse Crack Tip in T800H/3900-2.

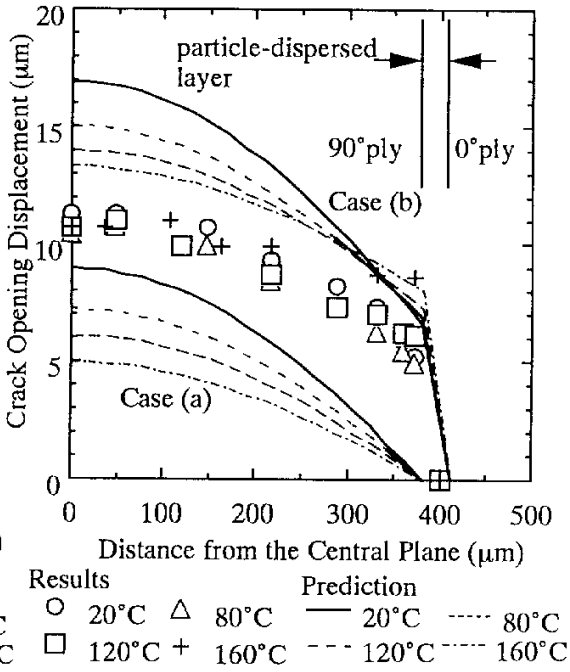

Fig.8 COD as a Function of Distance from the Central Plane in T800H/3900-2.

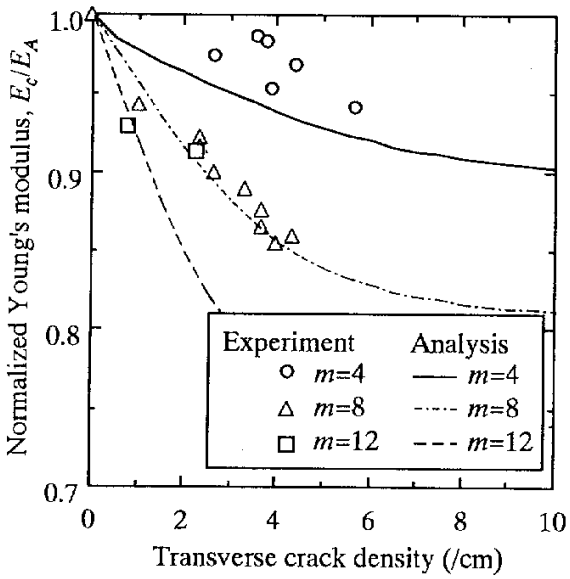

Fig.9 Normalized Young's modulus as a function of transverse crack density in T800H/3631-FM300 cross-ply laminates ($0/90_m/0$) at room temperature.

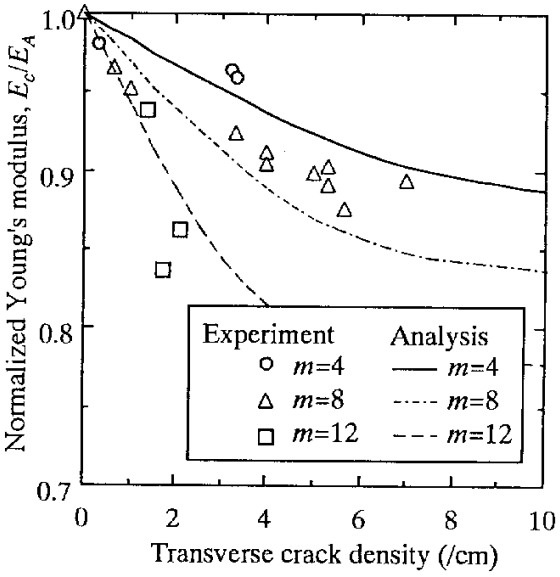

Fig.10 Normalized Young's modulus as a function of transverse crack density in T800H/3900-2 cross-ply laminates ($0/90_m/0$) at room temperature.

ACCURATE ESTIMATION OF THE ELASTIC PROPERTIES OF POROUS FIBERS

Richards Thissell,[1] Anna K. Zurek,[1] and Frank Addessio[2]

Materials Research and Processing Science, MS: G755
[2.] Fluid Dynamics, MS: B21 Los Alamos National Laboratory
Los Alamos NM 87545

SUMMARY: A procedure is described to calculate polycrystalline anisotropic fiber elastic properties with cylindrical symmetry and porosity. It uses a preferred orientation model (tomé ellipsoidal self-consistent model) for the determination of anisotropic elastic properties for the case of highly oriented carbon fibers. The model predictions, corrected for porosity, are compared to back-calculated fiber elastic properties of an IM6/3501-6 unidirectional composite whose elastic properties have been determined via resonant ultrasound spectroscopy. The Halpin-Tsai equations used to back-calculated fiber elastic properties are found to be inappropriate for anisotropic composite constituents. Modifications are proposed to the Halpin-Tsai equations to expand their applicability to anisotropic reinforcement materials.

KEYWORDS: anisotropy, elastic properties, preferred orientation, porosity correction, resonant ultrasound spectroscopy, self-consistent methods.

INTRODUCTION

Many reinforcement materials commonly used in composites are anisotropic and polycrystalline with a strong preferred orientation. A long standing and difficult problem is the estimation of the anisotropic constituent elastic properties because experimental measurements of non-axial reinforcement properties are often difficult. Numerical methods for simulating bulk composite material performance require composite constituent elastic properties and would benefit from accurate estimates of constituent anisotropic elastic properties.

The Halpin-Tsai equations accurately describe composite elastic properties when the constituent materials are isotropic [1]. Application of the Halpin-Tsai equations to composites consisting of anisotropic constituent materials, such as carbon and graphite fibers, require accurate determination of the constituent elastic properties. The longitudinal fiber properties are relatively easy to measure, but measurement of the transverse and shear properties are very difficult.

Graphite is one of the most anisotropic single crystals currently known. The single crystal anisotropy arises due to the bonding types within the lattice. Figure 1 shows the lattice of graphite and its two different bond types. Sp^2 bonds are strong planar bonds, while π^* bonds are weak. Table 1 lists unirradiated and irradiated graphite single crystal elastic constants.

Blakslee et. al. [2] values were measured from highly oriented compression annealed pyrolytic polycrystalline graphite which can be made in dimensions large enough for accurate determination of elastic properties via standard testing techniques. Naturally occurring graphite single crystals are often only a few millimeters in size which limits the testing methods applicable for determining elastic constants [2]. Measurements of naturally occurring single crystals can indicate elastic stiffnesses that can differ by 1/3 for c_{33} up to a factor of eight for the off-diagonal terms [3] from the values listed in Table 1. Although, some of the values in Table 1 differ significantly from measurements of naturally occurring single crystals, they are assumed to be the best representation of single crystal graphite elastic properties.

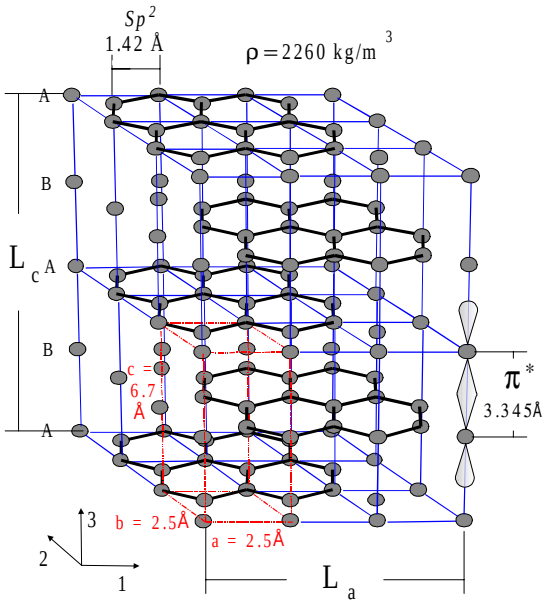

Fig. 1: Graphite lattice and bonding. The space group is P1, the stacking sequence is ABAB. The extreme anisotropy is due to the large difference in bonding type between the ab plane and the bc and ac planes. The ab plane contains strongly covalent sp^2 bonds of ~1020 kJ/mole bond energy, while the bc and ac planes contain weak π^* bonds of ~10 kJ/mole bond energy. Also note that each carbon not at a vertex of the P1 unit cell does not have a π^* bond.

Table 1: Elastic Constants of Single Crystal Graphite in GPa

Elastic Stiffness	Unirradiated	Irradiated	Ref.
c_{11}	1060	1060	[2]
c_{33}	36.5	36.5	[2]
c_{12}	180	180	[2]
c_{13}	15	15	[2]
c_{44}	0.246 (average of 20)	3.965 (average of four at neutron dose of 7.1×10^{18} nvt)	[5]

The shear term between basal planes, c_{44}, has the lowest stiffness and is worth particular mention because it is the most difficult to determine and it is the most sensitive to the

presence of dislocations and defects in the lattice. For example, neutron irradiation induced imperfections that pin dislocations [4] and increase c_{44} from 0.250±0.033 GPa to 3.965±0.212 GPa [5]. The bonding between basal sheets is so weak that shear between them has little resistance unless defects are present. Neutron induced point defects, grain boundaries, and nanometer-sized porosity (called Hohlstellen) can all act to impede dislocation motion [4]. This is important for carbon fibers that contain significant nanometer sized grains and porosity. An analysis of polycrystalline graphite elastic constants [6] concluded that the crystallite shear term c_{44} is the controlling factor to explain the effect of neutron irradiation on the polycrystalline elastic moduli. It is important to note that the graphites in the latter study had an average crystallite size of 1000-5000 Å, far larger than the crystallite size in carbon fibers. Fourdeux's [7] neutron irradiation of carbon fibers experiments resulted in the longitudinal modulus to increase by about 10 %, implying that dislocations in carbon fibers are not completely pinned by the porosity and small crystallite size. Therefore, the question remains as to which bound of c_{44} is more suitable to represent carbon fiber's elastic properties.

This paper first discusses preferred orientation descriptors in carbon, and follows with a discussion of three elastic constant models applied to sp^2 bonded anisotropic carbon fibers. We use the Tomé ellipsoidal self-consistent model [8] to predict the polycrystalline elastic properties. We apply this model into a procedure to determine polycrystalline porous fiber elastic properties starting with three measured properties; the longitudinal fiber modulus, fiber density, and single crystal elastic properties of graphite from Table 1. We fit the Tomé model prediction for longitudinal elastic modulus, corrected for porosity, to known fiber longitudinal modulus by adjusting the effective preferred orientation. Finally, a comparison is made between the elastic model predictions of fiber elastic constants and those back calculated from a composite laminate.

Description of Preferred Orientation in Carbon Fibers

Experimental determination of x-ray (002) diffraction intensity, $I(\varphi)$, for slender carbon and graphite fibers is complicated and error prone. Orienting bundles of fibers along a single axis is difficult for the extreme preferred orientation usually encountered with the fibers. Therefore, the effective $I(\varphi)$ that is measured of a fiber bundle in an x-ray machine is a convolution of the actual $I(\varphi)$ with spreading due to angular dispersion of fibers within the fiber tow. Bacon and Schalamon [9] have shown that fiber types with identical experimentally measured orientation half-widths can have measured axial Young's moduli differing by over a factor of three. Reynolds [10] described a focused x-ray technique that can measure the (002) diffraction arc from single fibers in a few hours of exposure. This technique eliminates the spreading of the true $I(\varphi)$ due to slight misorientations of fibers in a tow. The (002) distributions shown in Fig. 2 were measured using this technique. This figure shows a graph of an experimentally measured $I(\varphi)$ for a Type I (~2500 °C heat treatment temperature) carbon fiber under no load and under 0.79 GPa tension. This graph also compares intensity expressed in one parameter with a similar two-parameter approximation:

$$I(\varphi) = \sin^m \varphi \quad \text{and} \quad I(\varphi) = \sin^m \varphi^{\,q}. \tag{1a,b}$$

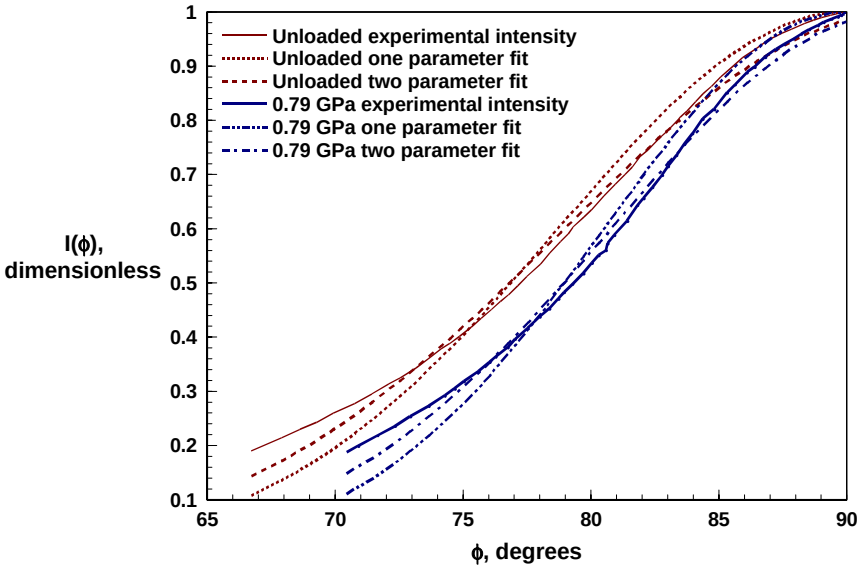

Fig. 2: Comparison of (1a) and (1b) with experimental (002) x-ray diffraction intensities for a single Type 1 (~2500 °C heat treatment temperature) carbon fiber. The experimental data is from [10]. Loading the fiber to 0.79 GPa increases the preferred orientation significantly. The results of the fits are listed in Table 3.

Table 2: (002) Diffraction Arc Approximation Fits

Unloaded Fiber (002) I(φ) Approximation Fit Results			Loaded Fiber (002) I(φ) Approximation Fit Results	
	One Parameter	Two Parameter	One Parameter	Two Parameter
q		0.99463		0.99503
m	26.1551	20.10889	37.01956	27.71807
χ^2	0.00127	0.00036	0.00142	0.00035

The effect of loading is to increase the degree of preferred orientation. The one-parameter fit has three times the error in χ^2 (sum of the squares of the deviations) compared to the two-parameter fit for both of the experimental measurements. Isotropy is achieved by setting m = 0. Increasing m is indicative of increasing preferred orientation and hence anisotropy.

Polycrystalline Elastic Constant Models

Three models are discussed to predict the elastic constants of polycrystalline materials based upon preferred orientation of the crystallites. These models are: the Voigt uniform stress, Reuss uniform strain, and Tomé ellipsoidal self-consistent models.

An inherent limitation of two of these models, the Voigt uniform strain model and the Reuss uniform stress model, is that they ignore the complex interactions at the crystallite boundaries necessary to accommodate the strain and stress jump conditions [3]. The uniform stress model assumes that the stress is constant among the crystallites and provides the upper limit of polycrystalline elastic constants. The uniform strain model assumes that the strain is constant among the crystallites, and is therefore provides the lower bound of polycrystalline elastic constants. The differences between these two models increase with increasing crystallite anisotropy and decreasing preferred orientation for most crystals.

The self-consistent model considers the case of an elastic inclusion embedded in a homogeneous equivalent medium (HEM) with the same elastic properties as those of the polycrystal [11, 12]. This model assumes that the bulk strain is the average of the individual crystallite strains. The advantage of the self-consistent model over the constant stress and constant strain models is that it considers the interactions of a grain with the surrounding HEM. The self-consistent model can also take into account non-equiaxed grain shapes. Graphites and carbons have crystallite grain shapes that depend strongly on deposition conditions, heat treatment temperatures, and meso-phase (intermediate phase(es) between initial hydrocarbon and final carbon phase) deformation conditions.

The ellipsoidal self-consistent model [8] solves the problem of an ellipsoidal elastic inclusion (ellipsoidal Eshelby inclusion [13]) embedded in a HEM. The self-consistency arises from numerically adjusting the elastic properties of the HEM to coincide with the average of the inclusions. This model accurately represents intergranular interactions only in very oriented polycrystalline highly anisotropic materials. The ability of this model to accurately predict elastic constants in highly oriented carbon fibers will be evaluated in the following section.

We applied the ellipsoidal self-consistent model to calculate carbon fiber elastic constants. A computer program, written by Tomé, takes an input file which describes the preferred orientation as weighting factors at a given angular window in a coordinate system as described in the Bunge notation [14]. The file orientation weights were calculated using:

$$w_{\bar{\theta},\bar{\varphi}} = \int_{\varphi_j}^{\varphi_{j+1}} \int_{\theta_i}^{\theta_{i+1}} I(\theta) \sin\theta \; d\theta \; d\varphi \quad , \tag{2}$$

where

$$\theta_i = i\delta\theta \, , \quad \varphi_j = j\delta\varphi \, , \quad \omega = 0 \, , \tag{3}$$

$I(\theta)$ is given by equation (1b), θ, φ, ω are the Bunge angles, δ is angular window width, and i, j are the angular window steps. Typical analyses were performed using 1368 equivalent grains to represent the distribution of preferred orientation. The Tomé program also calculates elastic constants using the uniform stress and uniform strain models, hence the two-parameter approximation, (1b), can be conveniently employed. Model predictions differed by about 10 % when the two parameter approximation (1b) for $I(\theta)$ was used instead of the one parameter approximation (1a) for the cases shown in Fig. 2.

Carbons consisting of sp^2 bonding can exhibit extremely anisotropic elastic and thermal expansion properties, and are hence excellent example materials to develop a practical analytical procedure to predict their elastic constants. Furthermore, significant porosity exists in these materials due to packing effects caused by the small crystallite size of carbons and graphites combined with the typically large crystallite aspect ratios. The porosity consists of nanometer-sized voids. These voids can also become highly ellipsoidal in carbon fibers exhibiting a large degree of preferred orientation.

APPLICATION OF ELASTIC CONSTANT MODELS TO ORIENTED SP^2 BONDED CARBON FIBERS

Carbon fibers have significant porosity on the order of 20 %. This porosity has a very large aspect ratio along the fiber axis [7]. The effect of porosity is accounted for by the application of the Halpin-Tsai equations [1]. Based on an analysis of x-ray circular intensity measurements [7], the porosity aspect ratio is 100,000. The rule of mixtures is applied to correct the Poisson's ratios for the effect of porosity.

Table 3: Elastic Model Calculations of Carbon Fibers

	Case:	Type I Fiber, No stress, Irradiated Properties	Type I Fiber, No stress, Irradiated Properties	Type I Fiber, No stress, Non-Irradiated Properties	Type II Fiber, IM-6, Irradiated Properties	Type II Fiber, IM-6, Non-Irradiated Properties	Type II Fiber, IM-6, Non-Irradiated Properties
	M	20.10889 (see Table 2)	4.5 (fitted)	7.15 (fitted)	3.35 (fitted)	4.85 (fitted)	3.6 (fitted)
Crystallite Lengths	1	0.14	0.14	0.14	0.25	0.25	0.14
	2	0.14	0.14	0.14	0.25	0.25	0.14
	3	0.86	0.86	0.86	0.75	0.75	0.86
Upper Bound (Voigt):	E_{11},	700.65	601.96	646.14	542.87	607.60	577.84
	E_{33},	292.09	308.70	292.57	317.46	302.50	311.24
	$G_{12}=G_{13}$, Gpa	171.72	178.16	175.65	178.09	176.68	176.83
	G_{23},	105.82	120.92	112.63	125.48	117.85	122.40
	$\upsilon_{12}=\upsilon_{13}$	0.15	0.17	0.17	0.17	0.17	0.17
	υ_{31}	0.06	0.09	0.08	0.10	0.09	0.10
	υ_{32}	0.24	0.21	0.22	0.20	0.21	0.20
Experiment:	**E_{11}, $G_{12}= G_{13}$, GPa**	**355,** [10] **24.8,** [10]	**355,** [10] **24.8,** [10]	**355,** [10] **24.8,** [10]	**276**	**276**	**276**
Self-Consisten	**E_{11}, GPa**	**531.16**	**354.27**	**354.74**	**276.83**	**275.47**	**277.41**
	$E_{22}=E_{33}$, GPa	**37.50**	**48.46**	**25.13**	**55.93**	**32.33**	**30.93**
	$G_{12}= G_{13}$, GPa	**56.77**	**55.80**	**40.11**	**54.26**	**39.81**	**38.12**
	G_{23},	**12.08**	**17.58**	**8.19**	**20.68**	**11.03**	**10.55**
	$\upsilon_{12}=\upsilon_{13}$	**0.34**	**0.38**	**0.46**	**0.35**	**0.42**	**0.44**
	υ_{31}	**0.02**	**0.05**	**0.03**	**0.07**	**0.05**	**0.05**
	υ_{32}	**0.37**	**0.28**	**0.41**	**0.26**	**0.35**	**0.35**
Lower Bound (Reuss):	E_{11},	75.23	31.86	2.64	27.00	2.19	1.95
	E_{33},	17.91	16.87	1.29	16.94	1.27	1.26
	$G_{12}=G_{13}$, GPa	6.36	7.15	0.45	7.25	0.47	0.48
	G_{23},	5.32	5.58	0.37	5.68	0.37	0.38
	$\upsilon_{12}=\upsilon_{13}$	0.33	0.33	0.38	0.32	0.38	0.38
	υ_{31}	0.08	0.18	0.19	0.20	0.23	0.26
	υ_{32}	0.47	0.39	0.56	0.37	0.53	0.50

Comparison of the calculated elastic constants with literature reported and measured experimental data requires conversion of the elastic constants to engineering Young's moduli and Poisson's ratios. The models calculate elastic constants with the 3 axis along the fiber

axis, and the 2 and 1 axes normal to the fiber axis, thereby maintaining hexagonal symmetry. Common engineering design practice is to consider the fiber axis to be along the 1 axis, called *specially orthotropic symmetry*. Therefore a coordinate transformation is performed on the calculated elastic constants notation via the fourth order tensor transformation rule [15].

Table 3 compares the three models for two different carbon fibers, a Type I fiber (~2500 °C HTT) whose experimental (002) diffraction arc is shown in Fig 2, and a Type II fiber (Hercules IM-6 ~1600 °C HTT). The reported moduli and Poisson's ratios are corrected for porosity as described above and are listed using specially orthotropic symmetry. The ellipsoidal crystallite lengths are reported using hexagonal symmetry notation with the 3 axis along the fiber axis. The lengths are dimensionless and only the ratios of the lengths are important. The values used are qualitatively obtained from high-resolution transmission micrographs [7, 16]. The value of q used in (1b) is held constant at 0.99463 for all of the cases. The density used for the Type I fiber is that reported for the Type II fiber (ρ = 1.76 g/cm^3) and should be considered conservatively low; the actual density may be 5-8 % higher. Note that none of the models accurately predict the experimentally measured axial modulus for the Type I fiber when the experimental (002) diffraction arc is used. m from (1b) is adjusted in the second and third columns such that the self-consistent model Young's modulus along the fiber, E_{11}, fits the experimental measurement. However, the shear modulus, G_{12}, predicted by the self-consistent model does not closely correspond to Reynolds's experimental measurement, even for the non-irradiated single crystal property case. Columns four through six compare the results when m is fitted so that the self-consistent model prediction for E_{11} matches the experimental fiber axial moduli for Hercules IM6 fiber. Column four uses the irradiated single crystal higher value for c_{44}, while column five shows the results when the non-irradiated lower value is used. The non-fitted parameters differ by up to 50 % between the two cases of c_{44}. Column six uses the same single crystal properties as five, but with a larger crystallite aspect ratio. The lower bound and upper bound cases are listed to illustrate the difference between their predictions and experimental measurements of carbon fiber elastic constants. This is attributed to the high, but far from perfect, degree of preferred orientation common in carbon fibers. The magnitude of the difference between the upper and lower bound model values also illustrate the severity of the problem of estimating elastic constants of polycrystals consisting of highly anisotropic crystallites. There is also a tremendous difference between the upper and lower bound model values and the experimentally measured moduli. This second difference is in contrast to what has been previously determined for less anisotropic bulk carbons where the porosity corrected, lower bond model (constant stress) predicted moduli were very close to experimental measurements [3].

Effect of c-Axis Spacing on the Elastic Models Predictions

Polycrystalline graphite and carbon fibers have an interlayer c axis spacing as determined from the x-ray analysis that is greater than the single crystal value shown in Table 1. The c-axis spacing in polycrystalline graphite is a strong function of maximum heat treatment temperature and a weak function of maximum heat treatment time [17]. For example, Type 1 carbon fibers have a c axis spacing of about 3.39 Å [18]. The increase in c-axis spacing effects the crystallite density and elastic stiffnesses c_{33}, and possibly c_{13} and c_{44}. This results in a unit cell volume expansion of about 1.3 % and hence a theoretical density of 2230 kg/m^3. Since actual fiber densities are considerably smaller, due to the presence of nano-porosity, small changes in the c-axis spacing have a negligible effect on the macroscopic density. Decreasing c_{33} by 25 % of the value in Table 1 had no significant effect on the three elastic

models' results for the case of a sine approximation with m = 10, q = 0.994. This and the results shown in Table 3 indicate that the models' predicted elastic constants are mostly dependent upon the graphite single crystal c_{11}, c_{44}, and the polycrystalline preferred orientation.

RESONANT ULTRASOUND SPECTROSCOPY OF A LAMINATED COMPOSITE

We have used Resonant Ultrasound Spectroscopy (RUS) to determine the elastic constants of a unidirectional laminated composite of IM6 fibers in a 3501/6 epoxy matrix (v_f = 0.62). RUS can determine all of the elastic constants at once to a deterministic level of accuracy, the level of which depends upon the material, quality of machining of the sample, appropriateness of the symmetry model, and identification of the fitting peaks [19]. It is especially accurate in determining the shear elastic constants and this is facilitated by the first few resonances that are usually strong and are almost entirely due to shear modes. This also has the advantage of increasing the accuracy of determining the c_{11} and c_{12}.

The application of RUS to fibrous composite systems is relatively new and poses special difficulties. RUS has recently been applied to determine the elastic constants of a ceramic-fiber laminated-ceramic matrix composite and many similarities exist in the application to polymer matrix composites [20]. There are significant differences that are important in RUS between laminated ceramic fiber ceramic matrix composites and carbon fiber laminated polymer matrix composites. These include the much lower Q (resonant gain factor) typical in polymers, a far greater anisotropy and greater differences in stiffness constants between the fiber and matrix. The lower Q factor in the polymer composite leads to broader peaks of lower intensity. The typically lower values for the shear and transverse elastic constants in the polymer composite results in many more predicted peaks. The combination of low Q and low shear and transverse elastic constants results in many lost peaks that must be correctly accounted for in the fitting process. Hence, reasonably accurate starting values of the elastic constants must be provided.

The sample dimensions were 5.70 (5.691), 5.44 (5.437), and 6.20 (6.207) mm, along the 1, 2, and 3 (fiber) axes, using the hexagonal symmetry orientation. The values in parentheses are the best-fit sample dimensions. The composite spectrum was scanned from 100 kHz to 1 MHz and 31 peaks were identified and are listed in Table 4. Fig. 3 shows an example scan. Several scans were performed with repositioning the sample between the transducers from one scan to the next in order to improve the distinction between real and false resonances due to contact artifacts. Each scan was an average of 5 or 8 individual scans to improve the signal to noise ratio. 293 peaks were estimated from the fitting program between the lowest and highest observed resonance; and the best fit assuming hexagonal (transversely isotropic) symmetry resulted in a RMS error of 0.23%. This is approximately the same overall error to what has been reported for the other laminated composite [20]. This level of error may be the lowest that can be expected from laminated fibrous composite materials, although it is typically about an order of magnitude higher than what can be achieved in polycrystalline metals. The error that could be obtained by starting with the manufacturer supplied elastic constant data shown in Table is ~2.35% RMS. Iterating around that data results in the axial c_{11} dropping to ~150 GPa, an unrealistically low value considering the ease of traditional measurement and rule of mixture prediction of that property. The lowest RMS error obtained after iterating around the manufacturer supplied data is about ~0.50% RMS.

Table 4: RUS Peaks

Spectra Peaks, kHz	Fitting Weights	Best Fit Results
136.030	30	135.846
152.086	2	152.691
217.710	20	217.535
252.950	6	254.497
293.790	10	293.356
301.001	1	301.402
309.409	1	311.942
323.023	3	323.875
336.236	2	340.088
351.452	1	350.514
363.464	1	365.025
371.472	4	368.875
395.890	3	396.287
402.300	12	403.629
426.727	2	428.055
449.149	3	450.979
483.580	4	482.347
493.990	6	492.003
536.436	2	536.182
546.246	1	546.816
558.350	1	558.335
579.170	3	578.869
660.960	1	658.940
675.670	3	674.291
761.568	2	759.548
785.280	2	780.870
804.500	3	804.060
827.020	2	828.473
853.450	5	853.184
895.790	2	895.771
945.340	6	945.118

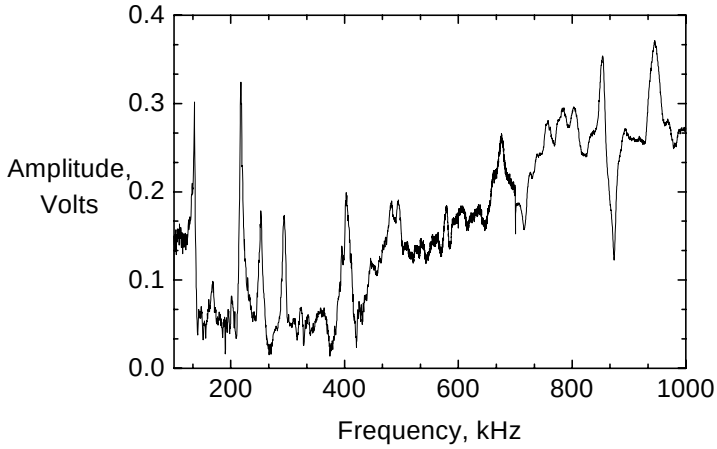

Fig. 1: RUS spectra of a unidirectional IM6-3501/6 composite. This is a composite plot of scans performed from 100-500 kHz, 500-600 kHz, 600-700 kHz, and 700-1000 kHz. Transition artifacts occur at the boundaries between scans.

Table 5: IM6-3501/6 Unidirectional Laminate Elastic Properties

E_{11}, GPa	$E_{22}=E_{33}$, GPa	G_{23}, GPa	$G_{13}=G_{12}$, GPa	$\upsilon_{12}=\upsilon_{13}$	υ_{21}	$\upsilon_{23}=\upsilon_{32}$
170[a]	9.5[a]	3.45[a]	5.75[a]	0.31[a]	0.04[a]	0.34[a]
172.4[b]	6.41[b]	5.44[b]	5.69[b]	0.324[b]	0.011[b]	0.381[b]
[a] Supplied by Hercules, Inc.			[b] Resonant Ultrasound Spectroscopy (RUS)			

Table 6: RUS Best Fit Elastic Constants, GPa In Specially Orthotropic Symmetry

c_{11}	$c_{22}=c_{33}$	$c_{12}=c_{13}$	c_{23}	c_{44}	$c_{66}=c_{55}$
174±0.16	7.57±0.079	3.62±0.01579	2.93±0.0026	2.32±0.0007	5.65±0.0045

Table 6 lists the best-fit elastic constants of the unidirectional composite in specially orthotropic orientation. The listed errors are the variation in estimated values necessary to change the value of χ^2 by 2 %. Table 5 compares the unidirectional laminate elastic properties in engineering Young's moduli and Poisson's ratios in specially orthotropic symmetry, as supplied by the manufacturer and measured by RUS.

EXPANSION OF THE HALPIN-TSAI EQUATIONS TO HANDLE ANISOTROPIC CONSTITUENTS

A most interesting comparison can be made between the elastic model predictions of fiber elastic properties and those properties predicted by the Halpin-Tsai equations. The Halpin-Tsai equations were developed using isotropic reinforcement materials, and their application to anisotropic reinforcements is questionable. Table 8 lists the 3501/6 epoxy resin and IM6 fiber engineering elastic properties. The elastic properties of the fiber in Table 7 are listed for comparison with calculated respective properties listed in Table 7. The elastic properties for the resin are used in the Halpin-Tsai equations. Only the fiber axial modulus can be directly

determined, the other listed elastic properties were back-calculated from laminate data. Table 7 lists fiber properties predicted from the Halpin-Tsai equations in column two. A comparison of these properties to the self-consistent model predictions of the IM6 fiber listed in Table 3, which are repeated in column one of Table 7, is not close. However, the following modifications can be made to the Halpin-Tsai equations that will greatly increase the correspondence between the laminate measured Halpin-Tsai back-calculated fiber properties and those predicted by the ellipsoidal self-consistent elastic model of preferred orientation, when corrected for porosity. υ_{21} of the composite and the fiber can be calculated by:

$$\upsilon_{21} = \upsilon_{12} \frac{E_{22}}{E_{11}}. \tag{4}$$

The fiber Poisson's ratios listed in column two and three of Table 7 are calculated using the rule of mixtures, as suggested by Halpin [1]. υ_{21} in columns two and three of Table 7 are calculated using (4).

The modification for the calculation of E_{22} utilizes the Sih, Paris, and Irwin effective modulus for orthotropic materials [21], which has been previously employed to correlate mode I fracture toughness with fracture energy in orthotropic materials. The effective modulus is given by:

$$E_{22}^{\,eff} = 2\left[\frac{(c_{23}+c_{33})\left(c_{12}^{\,2}-c_{11}c_{33}\right)}{(c_{23}-c_{33})\left(-2c_{12}^{\,2}+c_{11}(c_{23}+c_{33})\right)^{2}}\right]^{-1/2}\left[\frac{-2c_{12}^{\,2}-2c_{12}c_{66}+(c_{23}+c_{33})\left(c_{11}+2c_{66}\sqrt{\frac{c_{12}^{\,2}-c_{11}c_{33}}{c_{23}^{\,2}-c_{33}^{\,2}}}\right)}{c_{66}(c_{23}+c_{33})}\right]^{-1/2}. \tag{5}$$

when expressed in elastic stiffness constants for specially orthotropic orientation. The c_{ij} in

(5) are corrected for fiber porosity using the Halpin-Tsai equations for the diagonal terms and the rule-of-mixtures for the off-diagonal terms. Thus, for determining E_{22} using the Halpin-Tsai equations, the engineering elastic property of the reinforcement, p_r, becomes:

$$p_r^{\,E_{22}} = E_{22}^{\,eff}\left(\frac{E_{22}}{E_{11}}\right). \tag{6}$$

The correction factors when calculating the shear terms involve non-integer powers. p_r becomes:

$$p_r^{\,G_{12}} = \sqrt{G_{12}G_{23}} \quad , \quad p_r^{\,G_{23}} = G_{12}^{\,1/3}G_{23}^{\,2/3} \tag{7a, b}$$

for determining G_{12} and G_{23}, respectively.

A comparison between column one and column three of Table 7 reveals a close correspondence among all of the engineering elastic constants, with the exception of E_{22}, where the difference is 13.7%. These corrections are admittedly rather arbitrary due to the limited number of experimental cases (present and isotropic), but
(6)-(7a, b) have the advantage that in the limit of isotropy they simplify back to E and G, respectively.

Table 7: Comparison of Elastic Model Predicted Fiber Properties and Halpin-Tsai Predicted Fiber Properties

Property	Self-Consistent (Table 3, case 4)	Halpin-Tsai Back Calculated From RUS data	Modified Halpin-Tsai Back Calculated From RUS data
E_{11}, GPa	275.47	276	276
$E_{22}=E_{33}$, GPa	32.33	8.15	37.45
$G_{13}=G_{12}$, GPa	39.81	20.97	39.88
G_{23}, GPa	11.03	17.11	11.25
$\upsilon_{12}=\upsilon_{13}$	0.423	0.299	0.410
υ_{21}	0.052	0.00754	0.058
$\upsilon_{23}=\upsilon_{32}$	0.352	0.391	0.350

Table 8: Composite Constituent Properties

Property	**IM6 Fiber**	**3501/6 Epoxy**
E_{11}, GPa	276[(a)]	4.24[(a)], 4.275[(b)]
E_{22}, GPa	13.8[(a)]	
G_{12}, GPa	108[(a)]	1.793[(b)]
υ_{12}	0.28[(a)]	0.365[(a)], 0.34[(b)]
υ_{23}	0.30[(a)]	
ρ, g/cm^3	1.76[(a)]	1.265

[(a)] Supplied by Hercules, Inc.
[(b)] Courtesy of Don Adams, University of Wyoming.

SUMMARY

The ellipsoidal self-consistent model provides much more accurate predictions of elastic constants of highly oriented carbon fibers than either the constant stress or constant strain models. However, model predictions when experimental (002) diffraction arcs are used significantly overestimate the axial fiber moduli. The correspondence improves considerably when corrections are made for porosity and *m* is adjusted such that the ellipsoidal self-consistent model prediction for E_{11} matches the experimentally measured axial modulus. The essential effect of adjusting *m* in such a fashion is to provide a correction for the complex stress and strain accommodations occurring at the graphite crystallite grain boundaries that differ from the mathematically ideal accommodations implicit in the ellipsoidal self-consistent model. The porosity correction is made using the Halpin-Tsai equations to account

for the long axial aspect ratios of fiber porosity reported by TEM investigations [7, 9]. An advantage of choosing the fiber density and axial modulus as inputs is that they are easily measured accurately and are usually supplied by the fiber manufacturer.

Significant differences occur in model predictions, which depend upon the chosen single crystal value of c_{44}. The ellipsoidal self-consistent model predictions based upon the irradiated (pinned glissile dislocations) single crystal c_{44} value overestimates the fiber transverse and shear elastic properties by a significant factor. Use of the non-irradiated single crystal c_{44} value yields much more realistic fiber elastic properties. This result addresses the question of the role of the small crystallite size and porosity in Type II fibers. Grain boundaries and spherical porosity (Hohlstellen) have been observed in the TEM to impede the motion of glissile dislocations in graphite [4]. The elastic model predictions indicate that grain boundaries and porosity in carbon fibers do not significantly impede the motion of glissile dislocations.

Significant differences exist between the Halpin-Tsai equations back calculated fiber properties from RUS measured unidirectional composite laminate properties and the predicted properties based upon the Tomé ellipsoidal self-consistent model. These differences are attributed to the fact that the Halpin-Tsai equations were developed using isotropic reinforcement materials and hence are not directly applicable to cases of anisotropic reinforcement materials. Simple correction factors are proposed that greatly improve the correspondence between the self-consistent model predictions and the RUS back calculated fiber properties. These correction factors simplify back to the original Halpin-Tsai equations in the limit of isotropic reinforcement materials.

ACKNOWLEDGEMENTS

The authors wish to thank Carlos Tomé for helpful discussions and access to his ellipsoidal self-consistent model source code. Al Migliori and Timothy Darling are greatly appreciated for tutelage in RUS. Roland deWit is thanked for giving a fascinating lecture at the 1996 Mechanics-Materials Linkage summer course that provided the motivation for this work. Carl Cady is thanked for his meticulous review and numerous suggestions for this manuscript. This work was funded by the DoD/DOE Joint Munitions Program.

REFERENCES

1. Halpin, J. C., *Primer on Composite Materials Analysis*, Technomic Publishing Company, Inc., Lancaster, 1992.

2. Blakslee, O. L., D. G. Proctor, E. J. Seldin, G. B. Spence, and T. Weng, "Elastic Constants of Compression -Annealed Pyrolytic Graphite," *Journal of Applied Physics*, Vol. 41, No. 8, July 1970, pp. 3373-3382.

3. Price, R. J., "Young's Modulus of Pyrolytic Carbon in Relation to Preferred Orientation," *Philosophical Magazine*, Vol. Series 8, No. 12, 1965, pp. 561-571.

4. Bacon, R., and Richard Sprague, "Direct Observation of Imperfections In Graphite Single Crystals", *Fifth Conference on Carbon*, Pennsylvania State University, 1961, Vol. 1, pp. 466-472.

5. Seldin, E. J., and C. W. Nezbeda, "Elastic Constants and Electron-Microscopy Observations of Neutron-Irradiated Compression-Annealed Pyrolytic and Single-Crystal Graphite," *Journal of Applied Physics*, Vol. 41, No. 8, July 1970, pp. 3389-3400.

6. Kelly, B. T., "The Elastic Constants of Polycrystalline Carbons and Graphites," *Philosophical Magazine*, Vol. 9, No. 1964, pp. 721-737.

7. Fourdeux, A., R. Perret, and W. Ruland, "General Structural Features of Carbon Fibres", *Ist International Conference on Carbon Fibres*, 1971, Vol. pp. 57-67.

8. Tomé, C., "Chapter 7: Tensor Properties of Textured Polycrystals," in *Textures & Anisotropy*, edited by F. Kocks, C. Tomé, and R. Wenk (Cambridge University Press, Cambridge, 1996).

9. Bacon, R., and W. A. Schalamon, "Physical Properties of High Modulus Graphite Fibers Made From A Rayon Precursor," *Applied Polymer Symposia*, Vol. 9, No. 1969, pp. 285-292.

10. Reynolds, W. N., "Structure and Mechanical Properties of Carbon Fibres", *3rd International Conference on Industrial Carbons and Graphites*, London, 1970, Vol. pp. 427-430.

11. Humbert, M., and J. Diz, "Some Practical Features for Calculating The Polycrystalline Elastic Properties From Texture," *Journal of Applied Crystallography*, Vol. 24, No. 1991, pp. 978-981.

12. Diz, J., and M. Humbert, "Practical Aspects of Calculating the Elastic Properties of Polycrystals from the Texture According to Different Models," *Journal of Applied Crystallography*, Vol. 25, No. 1992, pp. 756-760.

13. Eshelby, J. D., "The Determination of The Elastic Field Of An Ellipsoidal Inclusion, and Related Problems," *Proceedings of the Royal Society of London*, Vol. A241, No. 1957, pp. 376-396.

14. Wenk, H. R., and U. F. Kocks, "The Representation of Orientation Distributions," *Metallurgical Transactions A*, Vol. 18A, No. June 1987, pp. 1083-1092.

15. Nye, J. F., Physical Properties of Crystals: Their Representation by Tensors and Matrices, Clarendon Press, Oxford, 1959.

16. Johnson, W., "The Structure of PAN Based Carbon Fibres and Relationship to Physical Properties," in *Strong Fibres*, edited by W. W. a. B. V. Perov (North Holland, Amsterdam, 1985), Vol. 1, p. 389-443.

17. Fair, F. V., and F. M. Collins, "Effect of Residence Time on Graphitization At Several Temperatures", *Fifth Conference on Carbon*, Pennsylvania State University, 1961, Vol. 1, pp. 503-508.

18. Brydges, W. T., D. V. Badami, and J. C. Joiner, "The Structure and Elastic Properties of Carbon Fibres," *Applied Polymer Symposia*, Vol. 9, No. 1969, pp. 255-261.

19. Migliori, A., J. L. Sarrao, William M. Visscher, T. M. Bell, Ming Lei, Z. Fisk, and R. J. Leisure, "Resonant Ultrasound Spectroscopic Techniques for Measurement of the Elastic Moduli of Solids," *Physica B*, Vol. 183, No. 1993, pp. 1-24.

20. Yongmei Liu, Y. H., Fuming Chu, and Terrance E. Mitchell, "Elastic Properties of Laminated Calcium Aluminosilicate/Silicon Carbide Composites Determined By Resonant Ultrasound Spectroscopy," *Journal of the American Ceramic Society*, Vol. 80, No. 1, 1997, pp. 142-148.

21. Sih, G. C., P. C. Paris, and G. R. Irwin, "On Cracks In Rectilinearly Anisotropic Bodies," *International Journal of Fracture*, Vol. 1, No. 1, 1965, pp. 189-203.

PREDICTION OF THE LARGE STRAIN MECHANICAL BEHAVIOUR OF HETEROGENEOUS POLYMER SYSTEMS BY A MULTI-LEVEL APPROACH

R.J.M Smit, W.A.M.. Brekelmans and H.E.H.Meijer

Faculty of MechanicalEngineering, Eindhoven University ofTechnology, P.O. Box 513, 5600 MB Eindhoven, The Netherlands

SUMMARY: Shear band formation in heterogeneous tensile bars is investigated by using an accurate homogenisation method that allows for a numerical coupling between the microscopic and macroscopic stress-strain behaviour. The procedure is based on a classical homogenisation theory, assuming local spatial periodicity of the microstructure, and supplies a consistent objective relationship between the local macroscopic deformation and the microstructural deformation of a spatially periodic representative volume element (RVE), representing the local microstructure. The method was used to predict the influence of the microstructure on localisation phenomena in plane strain hour-glass-shaped polycarbonate specimen with different volume fractions non-adhering low-modulus rubbery particles. One important result is that an irregular particle distribution seems to promote the widespread of deformation over the sample. This is believed to have an important contribution to the toughness enhancement of heterogeneous polymer systems by the addition of easily cavitating rubbery particles.

KEYWORDS: homogenisation, global-local analysis, multi-level finite elements, heterogeneous polymers

INTRODUCTION

Although heterogenous polymer materials form a large part of the commercially important commodity plastics, a reliable constitutive model that describes their typical time-dependent mechanical behaviour accurately is still lacking. Recently, we proposed a new homogenisation technique that provides an unambiguous objective relationship between macroscopic and microscopic properties, which can be used to predict the overall mechanical behaviour of heterogeneous polymeric solids from their microstructure [1].

The homogenisation method is based on the classical concept of a local spatially periodic representative volume element (RVE) representing the local microstructure [2, 3]. The RVE enables the (numerical) decoupling of the macrostructure and microstructure. In a finite element context a unique representative volume element is assigned to each integration point of the discretised homogenised macrostructure. The macro-micro relationship

is obtained by the assumption that the local macroscopic (integration point) deformations and stresses equal the (discretised) RVE averaged deformations and stresses.

In the presented research the homogenisation method was applied to predict the shear band formation in plane strain hour-glass-shaped polycarbonate specimen with a fine dispersion of different volume fractions non-adhering low-modulus rubbery particles. A recently developed constitutive model [4, 5] was used to predict the large-strain time-dependent behaviour of the glassy polycarbonate. Finite element models of plane strain RVEs with an irregular stack of voids, representing debonded or cavitated rubbery particles, are introduced to model the microstructure. Results of the multi-level finite element simulations on the voided hour-glass-shaped polycarbonate specimen are discussed. The paper ends with some conclusions and recommendations for further research.

HOMOGENISATION STRATEGY

Consider a heterogeneous body consisting of a composite of two materials, e.g. a glassy polymer matrix with rubbery inclusions, and assume that the size of a heterogeneity is very small compared to the body dimensions. When the body is subjected to external loads, the real deformation and stress fields show large local gradients because of the inclusions. Since the heterogeneities are orders of magnitude smaller than the total body, the deformation field in the vicinity of one inclusion will be approximately the same as the deformation field near neighbouring inclusions. Such repetitive deformations strongly suggest that the macroscopic stress-strain relation at point $\mathcal{P}$ can be determined by (i) applying the local macroscopic strain to a microstructural spatially periodic representative volume element belonging to $\mathcal{P}$ in such a way that the RVE averaged strains equal the local macroscopic strains, and by (ii) averaging the non-uniform RVE stress field. This homogenisation strategy implies that a heterogeneous macroscopic body can be replaced by an equivalent homogeneous body with an effective macroscopic constitutive description.

Spatially periodic representative volume element

According to the aforementioned arguments, it is assumed that the representative cell deforms in a repetitive way identical to its neighbours. In an RVE, the spatial periodicity conditions follow from compatibility demands with respect to the opposite edges. The demands enforce two adjacent RVEs to show identical deformations, while neither overlapping nor separation may occur [6]. For the two-dimensional RVE depicted in Fig. 1 the compatibility of two opposite boundaries can be summarised as follows:

(1) The shape of both boundaries is and remains identical. This can be enforced by (i) tying point positions on the left boundary Γ_{14} to their associated opposite points on the right boundary Γ_{23} and to the vertex points 1 and 2, and (ii) tying points on the upper boundary Γ_{43} to the opposite points on the lower boundary Γ_{23} and to the vertex points 1 and 4, according to

$$\mathbf{y}_{\Gamma_{14}} = \mathbf{y}_{\Gamma_{23}} - \mathbf{y}_2 + \mathbf{y}_1 \tag{1}$$

$$\mathbf{y}_{\Gamma_{43}} = \mathbf{y}_{\Gamma_{12}} - \mathbf{y}_1 + \mathbf{y}_4 \tag{2}$$

where $\mathbf{y}_{\Gamma_{ij}}$ indicates the position vector of points on edge Γ_{ij}.

(2) The stress vectors acting on two opposite boundaries are opposite in sign. If the stress vector acting on a boundary with outward normal $\mathbf{n}$ is given by $\boldsymbol{\sigma} \cdot \mathbf{n}$, this

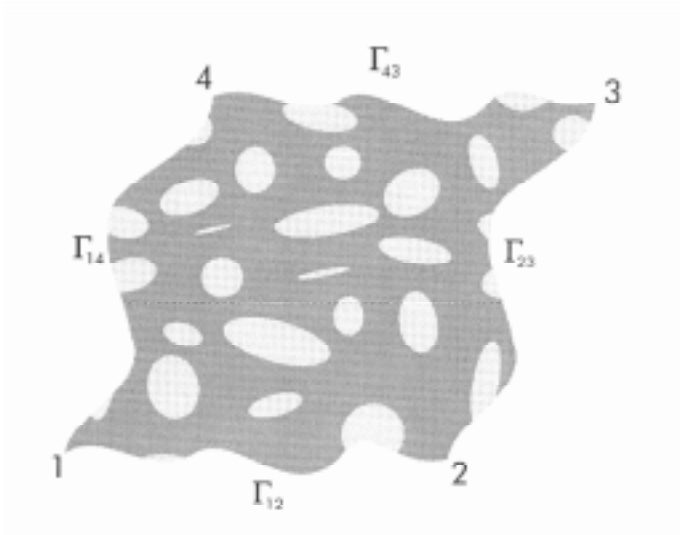

Figure 1: Plot of a typical two-dimensional (deformed) representative volume element (RVE), composed of a matrix with inclusions.

condition can be written as

$$\begin{aligned} \boldsymbol{\sigma} \cdot \mathbf{n}_{\Gamma_{14}} &= -\boldsymbol{\sigma} \cdot \mathbf{n}_{\Gamma_{23}} \\ \boldsymbol{\sigma} \cdot \mathbf{n}_{\Gamma_{12}} &= -\boldsymbol{\sigma} \cdot \mathbf{n}_{\Gamma_{43}} \end{aligned} \tag{3}$$

where s_{ij} represents a local material coordinate along boundary Γ_{ij} with point i as its origin.

The above combination of kinematical and natural boundary conditions enforces the edge shapes to deform such that the spatial periodicity conditions are preserved. The distance between the edges is prescribed by the positions of the retained vertices 1, 2, and 4. A change of retained vertex positions results in a change of edge positions and, consequently, in a change of RVE dimensions and/or orientation. Hence, only the positions of the retained vertices determine the average deformation of the RVE.

Macro-micro relationship

Macroscopic and microscopic levels are related by the assumption that the local macroscopic deformation and stress tensors at point $\mathcal{P}$ equal the average deformation and stress tensors in the RVE assigned to $\mathcal{P}$. If possible cavities in the RVE are considered as relatively very soft inclusions with finite strains and negligible stresses, the deformation tensor at an arbitrary point $\mathcal{P}$ with reference position $\mathbf{y}_0(\mathcal{P})$ is defined by

$$\boldsymbol{F}(\mathbf{y}_0) = (\nabla_0 \mathbf{y})^c \tag{4}$$

where the label $\mathcal{P}$ is omitted and where $\mathbf{y}$ denotes the actual position of $\mathcal{P}$ in the deformed RVE, $\mathbf{y}_0$ is the reference position of $\mathcal{P}$ in the undeformed RVE, and ∇_0 is the gradient operator in $\mathcal{P}$ with respect to the reference configuration. Since the deformation tensor refers to the initially undeformed configuration at reference position $\mathbf{y}_0$, the volume averaging is performed over the initial volume of the unit cell $V_{0_{\mathrm{RVE}}}$:

$$\bar{\boldsymbol{F}}_{\mathrm{RVE}} = \frac{1}{V_{0_{\mathrm{RVE}}}} \int_{\mathbf{y}_0 \in V_{0_{\mathrm{RVE}}}} \boldsymbol{F}(\mathbf{y}_0)\, \mathrm{d}V_0 \tag{5}$$

A straightforward definition of the average stress in the RVE is the volume averaged Cauchy stress tensor according to

$$\bar{\boldsymbol{\sigma}}_{\mathrm{RVE}} = \frac{1}{V_{\mathrm{RVE}}} \int_{\mathbf{y} \in V_{\mathrm{RVE}}} \boldsymbol{\sigma}(\mathbf{y}) \, \mathrm{d}V \tag{6}$$

where $\boldsymbol{\sigma}(\mathbf{y})$ represents the stress tensor at position $\mathbf{y}$. Notice that this averaging occurs over the current volume of the RVE because the Cauchy stress is defined in the current deformed configuration. It can be proved that the RVE averaged deformation gradient tensor can be prescribed by imposing the displacements at the angular points of the unit cell according to:

$$[\mathbf{u}_1 \ \mathbf{u}_2 \ \mathbf{u}_4] = \left[\bar{\boldsymbol{F}}_{\mathrm{RVE}} - \boldsymbol{I}\right] \cdot [\mathbf{y}_{0_1} \ \mathbf{y}_{0_2} \ \mathbf{y}_{0_4}] \tag{7}$$

where $\mathbf{u}_i$ is defined as the displacement of angular point i.

Based on these considerations, the relationship between stresses and strains on macroscopic and microscopic levels can be obtained by the following procedure:

(1) Replace the macroscopic heterogeneous structure by a (mesh of a) homogeneous one with an identical geometry.
(2) Assign to each relevant macroscopic point $\mathcal{P}$ (in fact the integration points in the macroscopic finite element mesh) a unique periodic RVE($\mathcal{P}$).
(3) Compute the local macroscopic deformation gradient tensor $\boldsymbol{F}_{\mathrm{macro}}(\mathcal{P})$ from an estimate of the macroscopic nodal displacements, and impose appropriate displacements at the angular points of the unit cell according to relation (7) with $\bar{\boldsymbol{F}}_{\mathrm{RVE}} = \boldsymbol{F}_{\mathrm{macro}}(\mathcal{P})$, so that the RVE averaged deformation tensor equals the macroscopic deformation tensor.
(4) Compute the resulting non-uniform stress and deformation fields in the RVE($\mathcal{P}$) and compute the average stress in the RVE with relation (6). The RVE averaged stress is returned to $\mathcal{P}$ as the local macroscopic stress.

This procedure is repeated for each macroscopic (integration) point in order to compute an estimation of the macroscopic stress field. Finite element procedures are applied to converge to a deformed macroscopic equilibrium state.

CONSTITUTIVE MODELLING OF HOMOGENEOUS GLASSY POLYMERS

For the constitutive modelling of the large-strain time-dependent mechanical behaviour of the individual polymeric components, a constitutive model was applied that was recently developed by Tervoort [4] and Timmermans [5]. It concerns a so-called "Leonov model with hardening", a Maxwell model with an Eyring viscosity describing the typical visco-elastic polymeric behaviour combined with a neo-Hookean model describing strain hardening behaviour due to molecular orientation. The resulting elasto-viscoplastic constitutive model is assumed to predict the strain rate, temperature and history dependent yield, intrinsic strain softening and subsequent strain hardening of glassy polymers. In the following the Leonov model with hardening is summarised.

In the Leonov model with hardening, the Cauchy stress $\boldsymbol{\sigma}$ is additively decomposed in an effective stress $\boldsymbol{s}$ and a hardening stress $\boldsymbol{r}$, according to:

$$\boldsymbol{\sigma} = \boldsymbol{s} + \boldsymbol{r} \tag{8}$$

The hardening stress is described by a simple neo-Hookean model:

$$\boldsymbol{r} = H\tilde{\boldsymbol{B}}^{d} \tag{9}$$

where H is the strain hardening modulus, and $\tilde{\boldsymbol{B}}$ represents the isochoric left Cauchy-Green strain tensor, defined as $\tilde{\boldsymbol{B}} = J^{-\frac{2}{3}}\boldsymbol{F}\cdot\boldsymbol{F}^{c}$, where $\boldsymbol{F}$ is the actual deformation gradient tensor and $J = \det(\boldsymbol{F})$ represents the relative volume change of the material.

The effective stress, determining the visco-elastic behaviour of the material, is defined by the Leonov model, originally proposed by Leonov [7] as an incompressible model to describe the rheological behaviour of polymer melts, later extended by Baaijens [8] to its current compressible form. The model is based on the multiplicative decomposition of the actual deformation gradient tensor $\boldsymbol{F}$ in an isochoric elastic part $\tilde{\boldsymbol{F}}_e$, an isochoric plastic part $\boldsymbol{F}_p$ and a volumetric part $J = \det(\boldsymbol{F})$, according to

$$\boldsymbol{F} = J^{\frac{1}{3}}\tilde{\boldsymbol{F}}_e \cdot \boldsymbol{F}_p \tag{10}$$

Here, $\boldsymbol{F}_p$ defines the state that would instantaneously be recovered if all loads were removed from the sample. If it is assumed that the total spin tensor equals the elastic spin tensor, it can be proved that the elastic shape deformation, defined by the isochoric elastic left Cauchy-Green deformation tensor $\boldsymbol{B}_e = \tilde{\boldsymbol{F}}_e \cdot \tilde{\boldsymbol{F}}_e^{c}$, is given by the following rate equation

$$\overset{\triangledown}{\boldsymbol{B}}_e = \boldsymbol{D}_p \cdot \boldsymbol{B}_e + \boldsymbol{B}_e \cdot \boldsymbol{D}_p - \frac{2}{3}\mathrm{tr}(\boldsymbol{B}_e)\boldsymbol{I} \tag{11}$$

Here, $\boldsymbol{D}_p$ and $\boldsymbol{I}$ represent the plastic strain rate tensor and the unit tensor, respectively, and the upper triangle defines the Truesdell objective rate as

$$\overset{\triangledown}{\boldsymbol{B}}_e = \dot{\boldsymbol{B}}_e - \boldsymbol{L}\cdot\boldsymbol{B}_e - \boldsymbol{B}_e\cdot\boldsymbol{L} \tag{12}$$

where $\boldsymbol{L}$ denotes the velocity gradient tensor. Assuming only small volumetric deformations, the deviatoric part of the effective stress $\boldsymbol{s}^{d}$ is related to $\boldsymbol{B}_e^{d}$ through the generalised Hookean relation $\boldsymbol{s}^{d} = G\boldsymbol{B}_e^{d}$, with G representing the shear modulus, while the hydrostatic part of the effective stress is coupled to the volume deformations by $\boldsymbol{s}^{h} = \kappa(J-1)\boldsymbol{I}$, with κ the bulk modulus.

With this system of equations, defining the compressible Leonov model, the effective stress $\boldsymbol{s}$ is determined once the dissipative plastic strain rate $\boldsymbol{D}_p$ is known. Tervoort *et al.* [4] proposed to apply the Leonov model with hardening to predict the large-strain deformation behaviour of glassy polymers. They introduced a generalised Newtonian flow rule with a stress dependent Eyring viscosity η to relate the deviatoric effective stress to the plastic deformation rate as $\boldsymbol{D}_p = \boldsymbol{s}^{d}/(2\eta)$. Timmermans [5] added pressure dependence (p) and intrinsic softening effects (D) to the viscosity equation, using a softening evolution equation originally proposed by Hasan *et al.* [9]:

$$\eta = \frac{A_0\, s}{\mathrm{e}^{D}\sinh((s-\mu p)/\tau_0)} \quad , \quad s = \sqrt{(\mathrm{tr}(\boldsymbol{s}^{d}\cdot\boldsymbol{s}^{d})/2)} \quad , \quad p = -\frac{1}{3}\mathrm{tr}(\boldsymbol{\sigma}) \tag{13}$$

$$\dot{D} = (1 - D/D_{\mathrm{inf}})\frac{hs}{\eta\sqrt{2}} \tag{14}$$

with the material parameters A_0 as a time constant, τ_0 as a characteristic stress, μ as a pressure coefficient, h as the softening rate and D_{inf} as the softening limit.

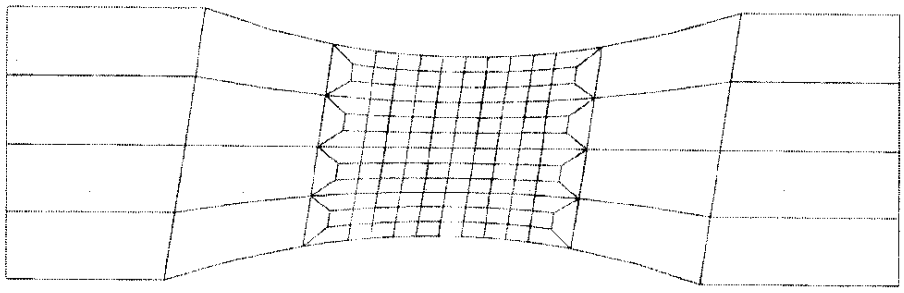

Figure 2: Geometry and mesh of undeformed plane strain hour-glass-shaped tensile specimen.

RESULTS

Numerical simulations of shear band formation in heterogeneous plane strain hour-glass-shaped tensile specimen have been performed, using the homogenisation method and Leonov model introduced in the previous sections. The heterogeneous systems considered are polycarbonate with 0, 10 and 30 vol.% dispersed non-adhering low-modulus rubbery particles.

The initial geometry and mesh of the macroscopic plane-strain tensile specimen is shown in Fig. 2. The specimen is chosen to be asymmetrical in order to obtain a preferred and thus controlled shear direction (the curved edges, with identical radii, are shifted with respect to each other). The geometries and meshes of the plane strain periodic RVEs, representing the voided microstructures near the macroscopic integration points, are visualised in Fig. 3. The rubbery particles are considered as being voids, since the properties of the non-adhering low-modulus particles are expected not to influence the mechanical behaviour of the unit cells under the expected positive hydrostatic stress states. The time-dependent mechanical behaviour of the glassy polycarbonate is modelled by the Leonov model with hardening, using the following set of material parameters adopted from Timmermans [5]: $G = 884$ MPa, $\kappa = 1916$ MPa, $A_0 = 8.172 \cdot 10^{25}$ s^{-1}, $\tau_0 = 0.707$ MPa, $\mu = 0.098$, $h = 120\, s^{-2}$, $D_{\text{inf}} = 43$ and $H = 27$ MPa.

The averaged stress-strain and volume-strain responses of the RVEs under isothermal uniaxial plane strain extension (strain rate 0.01 s^{-1}) are depicted in Fig. 4. The homogeneous

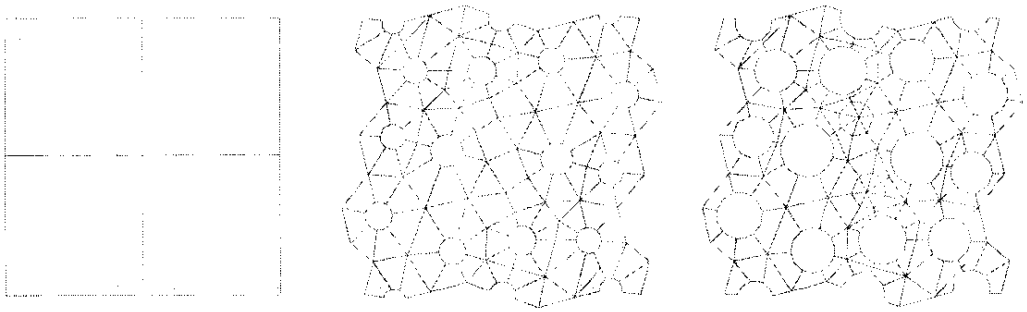

a b c

Figure 3: Geometry and mesh of the spatially periodic RVEs that represent the local microstructure in the macroscopic hour-glass-shaped sample: (a) solid polycarbonate; (b) polycarbonate with 10 vol.% voids; (c) polycarbonate with 30 vol.% voids.

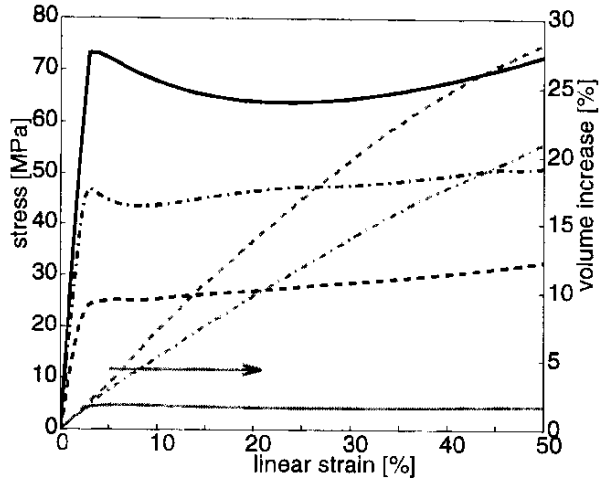

Figure 4: RVE averaged tensile stress (black) (defined with respect to the deformed cross sectional area of the RVE) and volume increase (grey) vs. natural strain for isothermal plane strain uniaxial tensile tests on the RVEs shown in Fig. 3: (solid) no voids; (dash-dot) 10 vol.% voids; (dashed) 30 vol.% voids.

polycarbonate shows the typical mechanical behaviour that is representative for a range of glassy polymers: a small-strain elastic response, followed by intrinsic strain softening and subsequent strain hardening. The maximum volume increase is approximately 3% and thus almost negligible.

The introduction of voids has a pronounced influence on the deformation behaviour: stiffness and yield stress are reduced considerably, the stress drop by intrinsic strain softening is diminished and the volume increase becomes relatively large. The reduction of stiffness and yield stress is evidently caused by the decrease of load-bearing material by the presence of voids. The strong volume response is also caused by the presence of (zero-bulk-modulus) voids. The reduction of strain softening originates from the irregular distribution of the voids. Due to this irregular distribution, the shear bands are formed between the holes in an arbitrary order and subsequently stabilised by the strain hardening, before they coalesce into large shear bands that dominate the RVE deformation behaviour. This is in contrast with the predictions of the heterogeneous material behaviour by computations on RVEs with regularly stacked inclusions. Then the overall material behaviour shows a considerable softening behaviour because all the shear bands in the material are formed at the same moment and join each other simultaneously. This is illustrated in Fig. 5 where the overall stress-strain response of a voided RVE with an irregular stack is compared with the response of an RVE with a cubic stack. Since intrinsic strain softening is known to be the main cause of unstable material behaviour, often resulting in a concentration of deformation in a relatively small volume of the specimen (e.g. shear bands), the decrease of softening will probably evolve in a more stable overall material behaviour.

The macroscopic specimen is stretched with a constant strain rate of 0.01 s^{-1} to a total nominal strain of 10%. The predicted macroscopic nominal stress responses (defined with respect to the undeformed cross sectional area of the specimen) are shown in Fig. 6. The equivalent strain and volume increase in the macroscopic samples at 4 and 10% strain are plotted in Fig. 7 and 8, respectively.

Pure polycarbonate shows a characteristic deformation behaviour: at a nominal strain

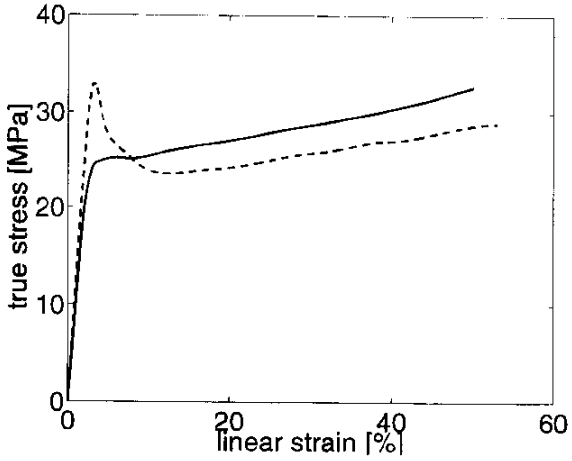

Figure 5: True Stress vs. natural strain for RVEs with voids in an irregular stack (solid) and in a cubic stack (dashed). The void volume fraction of both RVEs is 30%.

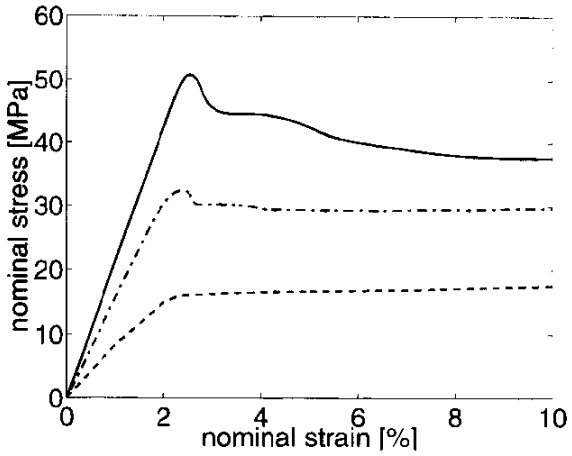

Figure 6: Nominal stress vs. nominal strain of the macroscopic polycarbonate specimen, predicted with no voids (solid), 10 vol.% voids (dash-dot) and 30 vol.% voids (dashed).

of 0-2%, initial stiff overall elastic response; 2-3%, load fall by the shear band formation (45^o with load direction); 3-4.5%, some stabilisation and growth of the first shear band; 4.5-5.5%, load fall by the second shear band formation (-45^o with the load direction); 5.5-10%, formation and growth of the neck. Hence, the behaviour of the pure polycarbonate is characterised by a strong concentration of deformation in the shear bands (up to 75% local strain), neck formation and a large unstable post-yield stress drop (much apparent softening). The volume plots show a small, almost negligible volume increase of approximately 3%.

The addition of voids results in a broader shear band under an angle of 22^o (10% voids) or -5^o (30% voids). As a result, the maximum equivalent strain at 10% nominal strain decreases with a factor 2-4. A decrease in stiffness and yield stress results, and the post-yield stress drop diminishes. The contour plot of the volume strain shows that the addition of 10 % voids leads to concentration of volume deformation at small macroscopic strains. A higher volume fraction results to a broader dilatation zone. This is probably caused by decreasing intrinsic strain softening in the voided specimen, as shown in Fig.

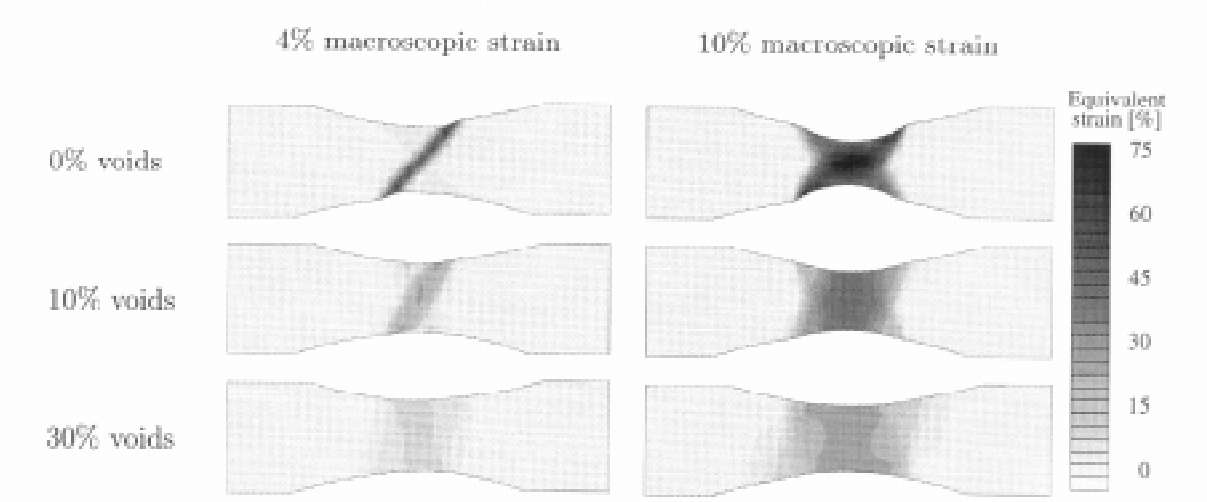

Figure 7: Contours of equivalent strain of the deformed polycarbonate sample with 0, 5 and 10 vol.% voids, at a nominal macroscopic strain of 4 and 10%.

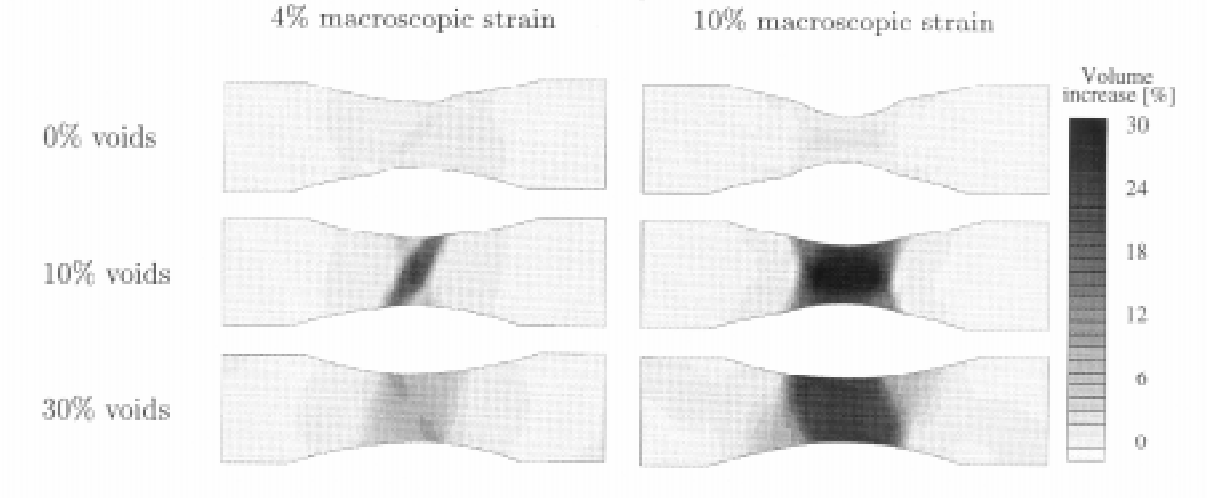

Figure 8: Contours of the volume increase of the deformed polycarbonate samples with 0, 5 and 10 vol.% voids, at a nominal macroscopic strain of 4 and 10%.

4: at 10% voids the decreased but still significant intrinsic softening results in relatively unstable post-yield deformation behaviour and thus into the formation of narrow shear bands; at 30% voids the heterogeneous specimen shows no intrinsic softening at all and the deformation spreads out over the whole specimen. It should be noted that the inhomogeneous microstructure implies that a low macroscopic strain could correspond to high local microscopic strains (e.g. stretching of the ligaments between the inclusions).

Many experimental evidence is available indicating that toughness is enhanced by the addition of easily cavitating and/or non-adhering rubbery particles [10, 11]. However, the basic mechanism of this toughness enhancement was not really understood yet. The results of these multi-scale analyses are believed to indicate that the random stack of easily cavitating rubbery particles has a pronounced influence on the toughness enhancement of heterogeneous polymeric systems by the removal of the intrinsic softening behaviour.

CONCLUSIONS AND RECOMMENDATIONS

A new homogenisation method has been used to predict the shear band formation in plane strain hour-glass-shaped heterogeneous polycarbonate specimen. The homogenisation method results in an unambiguous objective relationship between micro- and macroscopic properties. It has been demonstrated that the deformation behaviour changes dramatically by the addition of a high volume fraction of a fine dispersion of low-modulus non-adhering particles: the irregularly distributed heterogeneities result in a decreased intrinsic softening, a more stable deformation and a widespread of strains. This is thought to be a strong indication that the interaction between randomly distributed cavitating or non-adhering particles increases the toughness of polymeric systems.

Future research will focus on the influence of well-adhering cavitating rubbery particles on the overall deformation behaviour of heterogeneous polymers. Furthermore, the effect of local failure on the macrostructural behaviour will be investigated.

REFERENCES

1. Smit, R.J.M., Brekelmans, W.A.M. and Meijer, H.E.H., "Prediction of the mechanical behavior of non-linear heterogeneous systems by multi-level finite element modeling", *Comp. Meth. Appl. Mech. Engng*, 1997, submitted.
2. Hill, R., "Elastic properties of reinforced solids: some theoretical principles", *J. Mech. Phys. Solids* 11, 1963, pp. 357–372.
3. Bensoussan, A., Lions, J.L. and Papanicolaou, G., *Asymptotic Analysis for Periodic Structures*, North-Holland, Amsterdam, 1978.
4. Tervoort, T.A., Klompen, E.T.J. and Govaert, L.E., "A multi-mode approach to finite, three-dimensional, nonlinear viscoelastic behavior of polymer glasses", *J. Rheol.* Vol. 40, No. 5, 1996, pp. 779–797.
5. Timmermans, P.H.M., *Evaluation of a constitutive model for solid polymeric materials: model selection and parameter quantification*, Ph.D. thesis, Eindhoven University of Technology, Eindhoven, The Netherlands, 1997.
6. Suquet, P.M., "Local and global aspects in the mathematical theory of plasticity", In *Plasticity Today: Modelling, Methods and Applications*, edited by A. Sawczuk and G. Bianchi, AMD-Vol. 212/MD-Vol. 62, pp. *279–310*, Elsevier Science Publishers, London, 1985.
7. Leonov, A.I., "Non-equilibrium thermodynamics and rheology of viscoelastic polymer media", *Rheol. Acta*, Vol. 15, 1976, pp. 85–98.
8. Baaijens, F.P.T., "Calculation of residual stresses in injection molded products", *Rheol. Acta*, Vol. 30, No. 3, 1991, pp. 284–299.
9. Hasan, O.A., Boyce, M.C., Li, X.S. and Berko, S., "An investigation of the yield and postyield behavior and corresponding structure of poly (methyl methacrylate)", *J. Polymer Sci.: Part B: Polymer Phys.*, Vol. 31, 1993, pp. 185–197.
10. van der Sanden, M.C.M., de Kok, J.M.M. and Meijer, H.E.H., "Deformation and toughness of polymeric systems: 7. Influence of dispersed rubbery phase", *Polymer*, Vol. 35, No. 14, 1994, 2995–3004.
11. Magalhães, A.M.L. and Borggreve, R.J.M., "Contribution of the Crazing Process to the Toughness of Rubber-Modified Polystyrene", *Macromolecules*, Vol. 28, 1995, pp. 5841–5851.

CALCULATION OF EFFECTIVE MODULI OF VISCOELASTIC COMPOSITES WITH PERIODIC MICROSTRUCTURES USING A HOMOGENIZATION METHOD

Yeong-Moo Yi, Sang-Hoon Park and Sung-Kie Youn

Department of Mechanical Engineering, Korea Advanced Institute of Science and Technology, 373-1,Gusung-dong, Yusung-gu, Taejon, 305-701, Korea

SUMMARY: For composites with viscoelastic material phases, a systematic way of calculating the effective viscoelastic moduli in time domain is developed. With the effective moduli in time domain, effective complex moduli in frequency domain are obtained by using the Fourier transformation. The problem of calculating the effective moduli of general vicoelastic composites is formulated using the asymptotic homogenization method. The memory effects due to the homogenization are presented in general form and a sufficient condition for the effects to disappear is discussed. The effective relaxation moduli are calculated in Laplace transformed domain and are numerically inverse-transformed into time domain. Numerical examples are presented to illustrate and verify present approach and to discuss the memory effects. Results show that due to the presence of memory effects, additional terms are required for the accurate inverse Laplace transformation in the Prony series approximation of the homogenized relaxation moduli.

KEY WORDS: effective moduli, viscoelastic, homogenization, memory effects.

INTRODUCTION

The behavior of the composite materials is highly complex and the characterization of the constitutive behavior is important for accurate analysis of composite structures. But it is almost impossible to analyze the composite structures on the microscopic level by considering the heterogeneity of composite materials. There are several different approaches to obtain the macroscopic properties of such composites. Among many other methods of obtaining the effective moduli, the asymptotic homogenization method[1,2] has several attractive features mainly due to its systematic mathematical approach. Hollister and Kikuchi [3,4] showed that the homogenization method gave better estimations of the effective elastic moduli of composites than standard mechanics approaches.

Although Sanchez-Palencia [1] and Suquet [5] have dealt with the problems for the simple cases of the Voigt model and the Maxwell model, respectively, in viscoelastic composites, the discussions on the estimation of the effective relaxation moduli or the effective creep compliances of general viscoelastic composites in time domain are rarely found.

EFFECTIVE VISCOELASTIC MODULI BY A HOMOGENIZATION METHOD

A heterogeneous medium with a periodic structure may be replaced by an effective homogeneous one when the period is very small compared to the global length scale. In the homogenization method, the field variables are assumed to vary in the multiple scales, i.e., in the local and global scales and they are represented by asymptotic expansions in each spatial scale. Due to the periodicity of the microstructure, field variables such as displacement, strain, and stress are assumed to be periodic with respect to the local scale. The effective moduli are then obtained by investigating the asymptotic behavior of the medium as the period of the microstructure goes to zero.

Derivation of the Homogenized Moduli

To deal with two different length scales associated with the microscopic and the macroscopic behaviors, the global coordinate is designated by $\boldsymbol{x}$ and the local coordinate by $\boldsymbol{y}$. The global coordinate and the local coordinate are related with each other by a positive real parameter ε as follows.

$$\boldsymbol{y} = \boldsymbol{x} / \varepsilon \tag{1}$$

For the averaging process of the homogenization, the mean operator, ~, on Y is defined as follows . $|Y|$ is the measure of Y.

$$\tilde{\bullet} = \frac{1}{|Y|}\int_Y \bullet \, dy \tag{2}$$

The following problem of viscoelastic composites with a periodic microstructure is considered, where the inertia effects and the body forces are not present.

$$\frac{\partial \sigma_{ij}^{\varepsilon}(\boldsymbol{x},t)}{\partial x_j} = 0 \qquad in \qquad \Omega \tag{3}$$

$$u_i^{\varepsilon} = 0 \qquad on \qquad \partial_1\Omega \ , \quad \sigma_{ij}^{\varepsilon} n_j = F_i \qquad on \qquad \partial_2\Omega \tag{4}$$

$$\sigma_{ij}^{\varepsilon}(\boldsymbol{x},t) = \int_0^t G_{ijkl}^{\varepsilon}(\boldsymbol{x},t-\tau)\frac{\partial e_{kl}(\boldsymbol{u}^{\varepsilon}(\boldsymbol{x},\tau))}{\partial \tau} d\tau \tag{5}$$

where Ω is an open connected domain, $\partial_1\Omega$ the displacement-prescribed boundary, $\partial_2\Omega$ the traction-prescribed boundary, and F_i the traction force on $\partial_2\Omega$. $G_{ijkl}^{\varepsilon}(\boldsymbol{x},t)$ is relaxation tensor.

Since $G_{ijkl}^{\varepsilon}(\boldsymbol{x},t)$ is dependent on ε, $u_i^{\varepsilon}(\boldsymbol{x})$ is also dependent on ε. The asymptotic behavior is to be observed as ε goes to zero. $u_i^{\varepsilon}(\boldsymbol{x},t)$ has an asymptotic expansion as follows.

$$u_i^{\varepsilon}(\boldsymbol{x},t) = u_i^0(\boldsymbol{x},t) + \varepsilon u_i^1(\boldsymbol{x},\boldsymbol{y},t) + \varepsilon^2 u_i^2(\boldsymbol{x},\boldsymbol{y},t) + \cdots \ ; \ \boldsymbol{y} = \boldsymbol{x} / \varepsilon \tag{6}$$

where $u_i^m(\boldsymbol{x},\boldsymbol{y})$ is *Y*-periodic in $\boldsymbol{y}$ and is independent of ε. The asymptotic expansions for e_{ij}^{ε} and $\sigma_{ij}^{\varepsilon}$ are obtained as follows.

$$e_{ij}^{\varepsilon}(\boldsymbol{x},t) = e_{ij}(\boldsymbol{u}^{\varepsilon}(\boldsymbol{x},t)) = e_{ij}^0(\boldsymbol{x},\boldsymbol{y},t) + \varepsilon e_{ij}^1(\boldsymbol{x},\boldsymbol{y},t) + \cdots \quad ; \boldsymbol{y} = \boldsymbol{x}/\varepsilon \tag{7}$$

$$\sigma_{ij}^{\varepsilon}(\boldsymbol{x},t) = \sigma_{ij}^0(\boldsymbol{x},\boldsymbol{y},t) + \varepsilon \sigma_{ij}^1(\boldsymbol{x},\boldsymbol{y},t) + \cdots \quad ; \boldsymbol{y} = \boldsymbol{x}/\varepsilon \tag{8}$$

$$e_{ij}^0(\boldsymbol{x},\boldsymbol{y},t) = e_{ijx}(\boldsymbol{u}^0) + e_{ijy}(\boldsymbol{u}^1) \tag{9a}$$

$$\sigma_{ij}^0(\boldsymbol{x},\boldsymbol{y},t) = \int_0^t G_{ijkl}(\boldsymbol{y},t-\tau)\frac{\partial e_{kl}^0(\boldsymbol{x},\boldsymbol{y},\tau)}{\partial \tau} d\tau \tag{9b}$$

In (9) the subscripts *x* and *y* mean the differentiation with respect to x_i and y_i, respectively.

By introducing (8) into (3), arranging it against ε^{-1} and ε^0, applying the mean operator, we obtain following two equations.

$$\frac{\partial \sigma_{ij}^0(\boldsymbol{x},\boldsymbol{y},t)}{\partial y_j} = 0 \tag{10}$$

$$\frac{\partial \tilde{\sigma}_{ij}^0(\boldsymbol{x},t)}{\partial x_j} = 0 \tag{11}$$

Equations (10) and (11) represent the local and the global problems, respectively. By solving the local problem (10), the homogenized viscoelastic moduli can be obtained. Applying Laplace transformation to (10), the local problem becomes

$$-\frac{\partial}{\partial y_j}\left[s\hat{G}_{ijkl}(\boldsymbol{y},s)e_{kly}(\hat{\boldsymbol{u}}^1(\boldsymbol{x},\boldsymbol{y},s))\right] = e_{klx}(\hat{\boldsymbol{u}}^0(\boldsymbol{x},s))\frac{\partial(s\hat{G}_{ijkl}(\boldsymbol{y},s))}{\partial y_j} \tag{12}$$

where variables with ^ indicate that they are Laplace transformed. Then the following variational formulation of the local problem is obtained in Laplace transformed domain.

$$\begin{aligned} &\textit{Find}\ \ \hat{\boldsymbol{u}}^1(\boldsymbol{x},\boldsymbol{y},s)\ \textit{such that} \\ &\int_Y s\hat{G}_{ijkl}(\boldsymbol{y},s)e_{kly}(\hat{\boldsymbol{u}}^1(\boldsymbol{x},\boldsymbol{y},s))e_{ijy}(\boldsymbol{v})dy = -e_{klx}(\hat{\boldsymbol{u}}^0(\boldsymbol{x},\boldsymbol{y},s))\int_Y s\hat{G}_{ijkl}(\boldsymbol{y},s)e_{ijy}(\boldsymbol{v})dy \end{aligned} \tag{13}$$

In (13), when $\hat{\boldsymbol{u}}^0$ is given, $\hat{\boldsymbol{u}}^1$ can be obtained in terms of $\hat{\boldsymbol{u}}^0$. To treat this problem, we define a space with the associated inner product as follows.

$$\tilde{V}_Y = \left\{\boldsymbol{u} \in V_Y \mid \tilde{\boldsymbol{u}} = \boldsymbol{0}\right\} \tag{14}$$

$$(\boldsymbol{u},\boldsymbol{v})_{\tilde{V}_Y} = \int_Y s\hat{G}_{ijkl}(\boldsymbol{y})e_{kly}(\boldsymbol{u})e_{ijy}(\boldsymbol{v})dy \tag{15}$$

$$(\hat{\boldsymbol{w}}_{kl}(s)\ ,\boldsymbol{v})_{\tilde{V}_Y} = \int_Y s\hat{G}_{ijkl}(\boldsymbol{y},s)e_{ijy}(\boldsymbol{v})dy, \quad \forall \boldsymbol{v} \in \tilde{V}_Y \tag{16}$$

Then (13) becomes

$$(e_{klx}(\hat{\boldsymbol{u}}^0(\boldsymbol{x},s))\hat{\boldsymbol{w}}_{kl}(\boldsymbol{y},s) + \hat{\boldsymbol{u}}^1(\boldsymbol{x},\boldsymbol{y},s),\boldsymbol{v})_{\tilde{V}_Y} = 0, \quad \forall \boldsymbol{v} \in \tilde{V}_Y \tag{17}$$

Therefore, $\hat{\boldsymbol{u}}^1$ is given in terms of $\hat{\boldsymbol{u}}^0$ and $\hat{\boldsymbol{w}}_{kl}$ as follows.

$$\hat{\boldsymbol{u}}^1(\boldsymbol{x},\boldsymbol{y},s) = -e_{klx}(\hat{\boldsymbol{u}}^0(\boldsymbol{x},s))\hat{\boldsymbol{w}}_{kl}(\boldsymbol{y},s) + \boldsymbol{C}(\boldsymbol{x},s) \tag{18}$$

By applying inverse Laplace transform to (18), we obtain

$$\begin{aligned}\sigma_{ij}^0(\boldsymbol{x},\boldsymbol{y},t) = \int_0^t G_{ijkl}(y,t-\tau)\frac{\partial}{\partial\tau}\Big[\; & e_{klx}(\boldsymbol{u}^0(\boldsymbol{x},\tau)) \\ & - \int_0^\tau e_{mnx}(\boldsymbol{u}^0(\boldsymbol{x},\tau)(\tau-p))e_{kly}(\boldsymbol{w}_{mn}(\boldsymbol{y},\tau)(p))\; dp\Big]d\tau\end{aligned} \tag{19}$$

By using the Leibnitz rule, by changing the order of the double integration, and by applying the mean operator, the homogenized stress-strain relations are obtained as follows.

$$\tilde{\sigma}_{ij}^0(t) = \int_0^t G_{ijkl}^h(t-\tau)\,\frac{\partial}{\partial\tau}e_{klx}(\boldsymbol{u}^0(\boldsymbol{x},\tau))\,d\tau \tag{20}$$

where the homogenized viscoelastic relaxation modulus, G_{ijkl}^h, is given as follows.

$$G_{ijkl}^h(t) = \left[G_{ijkl}(\boldsymbol{y},t) \; - \int_0^t G_{ijmn}(\boldsymbol{y},\, t-p)\, e_{mny}(\boldsymbol{w_{kl}}\,(\boldsymbol{y},p))\, dp\right]^{\sim} \tag{21}$$

Consequently, when the original moduli are replaced by the corresponding homogenized ones, the homogenized problem has exactly the same form as the original problem defined by equations (3),(4) and (5).

Calculation of the Effective Relaxation Moduli

By taking Laplace transformation of (21), we obtain

$$s\hat{G}_{ijkl}^h(s) = \left\{s\hat{G}_{ijmn}(\boldsymbol{y},s)\left[\delta_{mk}\delta_{nl} - e_{mny}(\hat{\boldsymbol{w}}_{kl}\,(\boldsymbol{y},s))\right]\right\}^{\sim} \tag{22}$$

where $\hat{\boldsymbol{w}}_{kl}(\boldsymbol{y},s)$ is the solution of the following local problem in Laplace transformed domain.

$$\int_Y s\hat{G}_{ijmn}(\boldsymbol{y},s)e_{mny}(\hat{\boldsymbol{w}}_{kl}\,(\boldsymbol{y},s))e_{ijy}(\boldsymbol{v})dy = \int_Y s\hat{G}_{ijkl}(\boldsymbol{y},s)e_{ijy}(\boldsymbol{v})dy,\; \forall\boldsymbol{v}\in\tilde{V}_Y \tag{23}$$

$G_{ijkl}^h(t)$ can be obtained from inverse Laplace transformation of $\hat{G}_{ijkl}^h(s)$ which is obtained from (22). Note that (23) has nearly the same form as the typical elastostatic problems. The right-hand side of (23) acts like body forces. The boundary conditions are specified in the form of periodic boundary conditions on $\hat{\boldsymbol{w}}_{kl}$. The homogenized elastic moduli can be calculated by the finite element codes with slight modifications.

MEMORY EFFECTS

In addition to the original memories of the constituent materials of viscoelastic composites, the homogenization process induces the additional long-term memories. This behavior is termed as the memory effects. Sanchez-Palencia[1] and Suquet[5] showed that the long-term memory appeared as a result of homogenization for composites in which the viscoelastic phase is treated with a Voigt model or a Maxwell model. In the following, the memory effects are discussed in the general form.

Memory Effects

The integral term in (21) represents the memory effects. It can be seen that the homogenized relaxation moduli depend on the history of the relaxation moduli of the constituent materials as well as on the current value of the moduli. If the relaxation moduli $G_{ijkl}(\boldsymbol{y},t)$ is separable with respect to space and time , the memory effects do not appear. If $G_{ijkl}(\boldsymbol{y},t)$ is separable in $\boldsymbol{y}$ and t, Laplace transform of $G_{ijkl}(\boldsymbol{y},t)$ is given by

$$s\hat{G}_{ijkl}(\boldsymbol{y},s) = sF_{ijkl}(\boldsymbol{y})\hat{T}(s) \tag{24}$$

Plugging (24) into (23), the following local problem is obtained.

$$s\hat{T}(s)\int_Y F_{ijmn}(\boldsymbol{y})e_{mny}(\hat{\boldsymbol{w}}_{kl})e_{ijy}(\boldsymbol{v})d\boldsymbol{y} = s\hat{T}(s)\int_Y F_{ijkl}(\boldsymbol{y})e_{ijy}(\boldsymbol{v})d\boldsymbol{y}, \quad \forall \boldsymbol{v} \in \tilde{V}_Y \tag{25}$$

From (25), it is evident that $\hat{\boldsymbol{w}}_{kl}$ is not a function of s. Thus from (22), we obtain

$$s\hat{G}^h_{ijkl}(s) = \left\{ s\hat{T}(s)F_{ijmn}(\boldsymbol{y})\left[\delta_{mk}\delta_{nl} - e_{mny}(\hat{\boldsymbol{w}}_{kl}(\boldsymbol{y}))\right]\right\}^{\sim} = s\hat{T}(s)F^h_{ijkl} \tag{26-a}$$

$$G^h_{ijkl}(t) = F^h_{ijkl}T(t) \tag{26-b}$$

From the above results, it can be seen that the memory effects come from the coupling effects of the spatial and the temporal variations of the viscoelastic moduli. The memory effects make the homogenization problem complicated. It is required to solve the local problem for every s if the relaxation moduli are not separable with respect to space and time variables, while it is sufficient to solve the local problem only once when the relaxation moduli are separable as can be seen in [25].

Inverse Laplace Transformation

Since the homogenized relaxation moduli are calculated in Laplace transformed domain, inverse Laplace transformation is required if the memory effects appear. In the present work, the least-square fitting in Laplace transformed domain is employed based on the Prony series representations of the relaxation moduli. Since it is difficult to optimize the relaxation times of the fitting function because of its nonlinear behavior, the relaxation times should be properly chosen in the region where the relaxation curve changes rapidly [6]. Because of memory effects, more terms in the Prony series are required in the fitting function than the number of terms in the Prony series representations. Once the approximations are made in the

Laplace transformed domain, the relaxation moduli in time domain and the complex moduli as well as the loss tangent in frequency domain are readily obtained using the known relations [7].

NUMERICAL EXAMPLES AND DISCUSSIONS

Numerical examples are presented to discuss the memory effects and their applications. In the following examples, two dimensional plane stress states is considered and the constituent materials are assumed isotropic.

As a first example, in order to observe the memory effects, a viscoelastic composite with the elastic circular inclusions in the viscoelastic matrix in which the stiffness of the elastic inclusions is comparable to that of the viscoelastic matrix is treated. The moduli and Poisson's ratio of the elastic inclusions are

$$E = 20, \qquad \nu = 0.21 \tag{27}$$

The moduli of the viscoelastic matrix, which are represented by using the standard linear solid model [7] , are given by

$$E(t) = 3 + 17e^{-t}, \qquad \nu = 0.38 \tag{28}$$

The volume fraction of the inclusions is 40%. Due to the presence of the long term memory effects, the homogenized relaxation moduli cannot be represented exactly with the standard linear solid model. It is, therefore, required to introduce additional terms in the Prony series representation. To see the effect of the number of the terms in the Prony series approximations, the number of relaxation terms (N_f) is varied by 1, 3, 5, and 7. Figure 1 shows the results. They show that small errors introduced in the Prony series approximations of the homogenized relaxation moduli in Laplace transformed domain may cause large errors in converting the data into those of time and frequency domains.
As a second example, composites with the microstructure composed of two isotropic viscoelastic materials with different relaxation times are used. The relaxation moduli are given as follows.

$$E(t) = 3 + 17e^{-t/10}, \nu = 0.38 \quad \textit{for material 1} \tag{29}$$

$$E(t) = 3 + 17e^{-t}, \quad \nu = 0.38 \quad \textit{for material 2} \tag{30}$$

The effective moduli of the two composites are calculated. In the first composite, material 1 is used as the circular inclusion and material 2 as the matrix, and in the second one, the roles of material 1 and 2 are interchanged. The volume fractions of material 1 and 2 are the same in both composites, i.e., 50%, respectively. Figure 2 shows the calculated results. The results show that the loss tangents and thus the damping effects of the homogenized materials as a function of frequency can be significantly affected by the configurations of the microstructure as well as the relaxation moduli of the constituent materials. Also figure 2 (c) shows that we may be able to get the increased damping effect in a certain desired frequency interval by fabricating the composites, which has a special microstructural configuration, of two or more viscoelastic materials even if each of the constituent material has low damping effect in that frequency interval.

CONCLUSIONS

A systematic way of calculating the effective or homogenized relaxation moduli of the general linear viscoelastic composite materials in time domain is developed by using a homogenization method. The memory effects due to homogenization have been presented in general form and it has been shown that the memory effects disappear if the relaxation moduli are separable in space and time. The memory effects make the numerical inverse Laplace transformation very complicated.

The memory effects and inverse Laplace transformation are discussed in detail. Due to the presence of the memory effects, in the Prony series approximation of the homogenized relaxation moduli, the additional terms are required for the accurate inverse Laplace transformation. It is also shown in the numerical example that maximum damping can be achieved by choosing specific configuration of the microstructures of the composites.

REFERENCES

1. Sanchez-Palencia E., *Non-Homogeneous Media and Vibration Theory*, Lecture Notes in Physics 127., Springer-Verlag, Berlin, 1980.
2. Bensoussan A., Lions J. -L., and Papanicolaou G., *Asymptotic analysis for Periodic Structures*, Studies in Mathematics and Its Applications 5, Amsterdam, North-Holland, 1978.
3. Hollister S. J. and Kikuchi N., “A comparison of homogenization and standard mechanics analyses for periodic porous composites”, *Comp. Mech.*, Vol. 10, 1992, pp. 73-95.
4. Guedes J. M. and Kikuchi N., “Preprocessing and postprocessing for materials based on the homogenization method with adaptive finite element methods”, *Comp. Meth. Appl. Mech. Engng.*, Vol. 83, 1990, pp. 143-198.
5. Suquet P.M., *Elements of homogenization for inelastic solid mechanics*, Homogenization Techniques for Composite Media (Eds. E. Sanchez-Palencia and A. Zaoui), Lecture Notes in Physics 272: pp. 193-278, Springer-Verlag, Berlin, 1987.
6. Cost T. L. and Becker E. B., “A multidata method of approximate Laplace tranform inversion” , *Int. J. Numer. Meth. Engng.*, Vol. 2, 1970, pp. 207-219.
7. Christensen R. M., *Theory of Viscoelasticity: An Introduction*, 2nd Ed., Academic Press., New York, 1982.

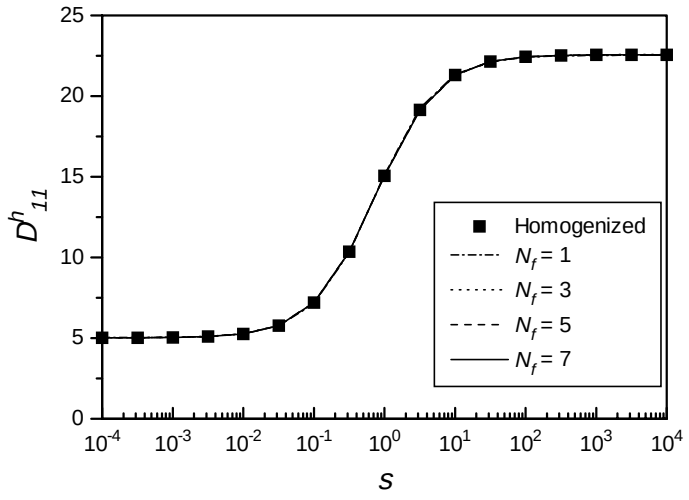

(a)

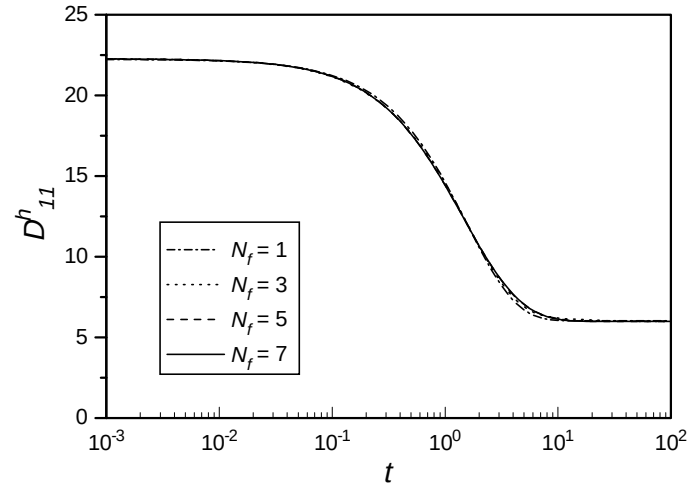

(b)

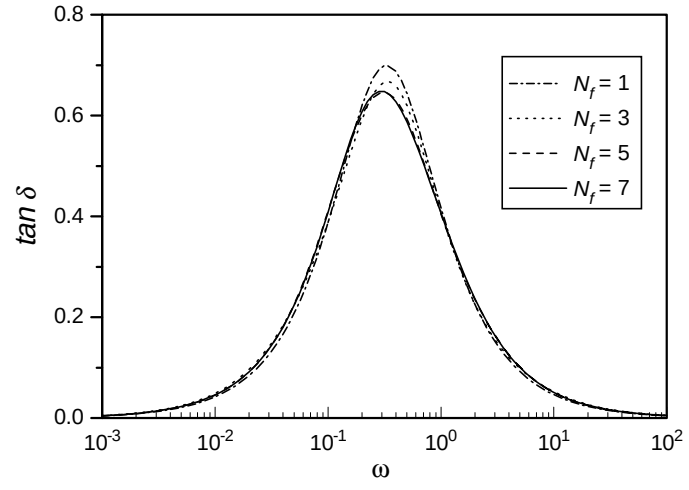

(c)

Fig. 1: Effect of number of fitting terms; a) effective modulus in Laplace transformed domain, b) effective modulus in time domain and c) effective loss tangent in frequency domain.

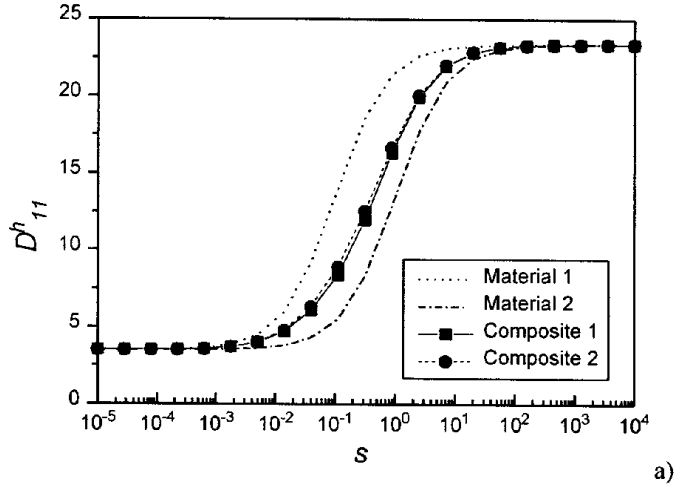

a)

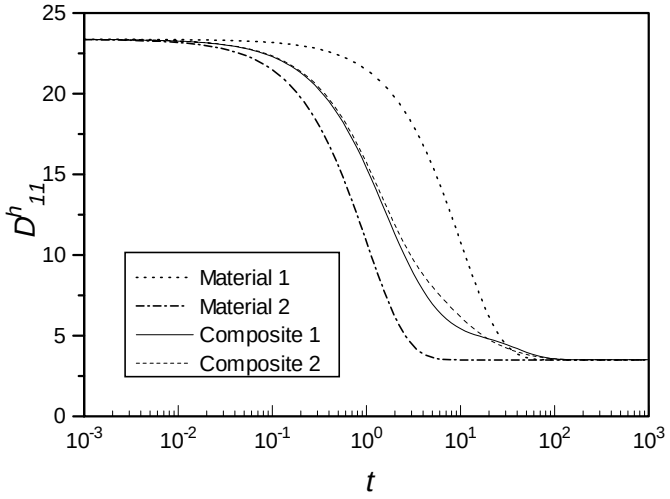

(b)

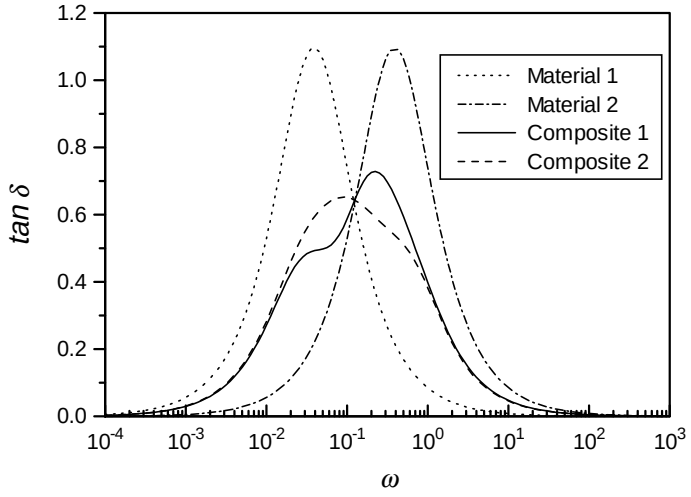

(c)

Fig. 2: Composite of two viscoelastic materials; a) effective modulus in Laplace transformed domain, b) effective modulus in time domain and c) effective loss tangent in frequency domain.

BEHAVIOUR OF DELAMINATED BEAM-PLATES UNDER COMBINED THERMAL AND MECHANICAL LOADS

Kosuke Hayakawa and Takahira Aoki

Department of Aeronautics and Astronautics, University of Tokyo,
7-3-1 Hongo, Bunkyo-ku, Tokyo, Japan 113

SUMMARY: A one-dimensional model has been developed to analyse the post-buckling behaviour of a homogeneous, isotropic, delaminated beam-plate with rotationally fixed ends, under a combined thermal and mechanical (compressive) load. Analysis indicates that a thermal load alone can cause the beam-plate to buckle out of plane. Moreover, when a mechanical load is applied together with a thermal load, the initial deformation due to thermal effects, causes the beam-plate to deflect further indicating the significance of thermal loads. Under a combined load the beam-plate deflects two to three orders of magnitude more than the case when a thermal load is not applied. Energy release rates for various load conditions have also been calculated, the results of which confirm the significance of thermal loads.

KEYWORDS: composite laminate, delamination, buckling, combined load, thermal load

INTRODUCTION

Fibre-reinforced composite laminates have been studied in detail in the past and many papers have been presented dealing with buckling of a delaminated beam-plate under a mechanical load. However, in practice, structures have to withstand mechanical loads under various heat conditions (thermal loads). Therefore, it is to our interest to study the post-buckling behaviour of a delaminated beam-plate under a combined thermal and mechanical load, and to make comparisons with that of one under a mechanical load alone.

There is bound to be a difference in heat conductivity between the delaminated region and the intact region. Therefore, when heat is applied to a delaminated beam-plate, it is expected to suffer a non-uniform temperature increase arising in thermally induced stresses which will cause it to buckle, predominantly in the delaminated region. Thus, the overall buckling resistance of a beam-plate under a thermal load is suspected to be inferior to one not experiencing a thermal load at all.

The paper deals primarily with the post-buckling deformation of a beam-plate due to a combined thermal and mechanical load. Energy release rates for various load conditions have also been calculated to confirm the significance of thermal loads.

ANALYSIS

A homogeneous, isotropic beam-plate of length $2l$ and thickness t, with an across-the-width delamination of length $2a$ is considered [1] (Fig. 1). The delamination is located symmetrically with respect to the two rotationally fixed edges and at an arbitrary depth h from the top surface. Thermal load is applied from the top surface and compressive axial load is applied from the two ends $x = \pm l$. Young's modulus $E = 59$ GPa, Poisson's ratio $\nu = 0.31$, and thermal expansion coefficient $\alpha = 1.1\times10^{-5}/^{\circ}\mathrm{C}$. In order to simplify the analysis further, the following assumptions have been made.

1. Thermal load is applied only to the upper delaminated region and the delaminated area does not conduct any heat.
2. The beam-plate undergoes cylindrical bending deformation and a state of plane strain exists in the width direction.
3. Kirchhoff hypothesis is applicable. That is, the delamination divides the beam plate into four regions, as shown in Fig. 1, such that each region has dimensions for Kirchhoff hypothesis to be viable.

Using the Kirchhoff hypothesis, the deformations are assumed as

$$\begin{aligned} u_i(x,z_i) &= u_i^o(x) - z_i w_i(x)_{,x} \\ w_i(x,z_i) &= w_i^o(x) = w_i(x) \end{aligned} \tag{1}$$

where x is the global co-ordinate as shown in Fig. 1 and z_i is measured from the mid surface of each region i. The comma denotes differentiation with respect to the index that follows. Moreover, u_i and w_i (i = 1, 2, 3, 4) are the axial and the transverse displacements, respectively, of region i and the superscript o denotes the values for the midplane of each region. Strain-displacement relation in the axial direction can be written as,

$$\varepsilon_{xi}(x,z_i) = u_{i,x} + \frac{1}{2}\left(w_{i,x}\right)^2 \tag{2}$$

into which Eqn 1 is substituted to yield

$$\begin{aligned} \varepsilon_{xi}(x,z_i) &= \varepsilon_{xi}^o(x) - z_i w_{i,xx} \\ \varepsilon_{xi}^o(x) &= u_{i,x}^o + \frac{1}{2}\left(w_{i,x}\right)^2 \end{aligned} \tag{3}$$

For a plane stress state in the z-direction the strain-stress relations can be written as

$$\begin{aligned} \varepsilon_{xi} - \alpha T_i(z_i) &= \frac{1}{E}\left(\sigma_{xi} - \nu\sigma_{yi}\right) \\ \varepsilon_{yi} - \alpha T_i(z_i) &= \frac{1}{E}\left(\sigma_{yi} - \nu\sigma_{xi}\right) \\ \gamma_{xyi} &= \frac{1}{G}\tau_{xyi} \end{aligned} \tag{4}$$

from which the inverse relation

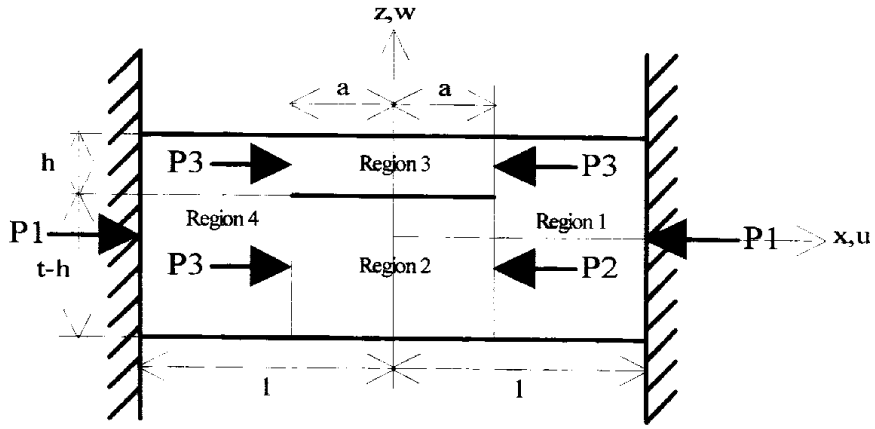

Fig. 1: Geometry of the model

$$\sigma_{xi} = \frac{E}{1-\nu^2}\left(\varepsilon_{xi} + \nu\varepsilon_{yi} - \alpha(1+\nu)T_i(z_i)\right) \tag{5}$$

is obtained, where E is the Young's modulus, ν is the Poisson's ratio and α is the thermal expansion coefficient of the beam-plate. Further, $T_i(z_i)$ is the temperature distribution of region i in the thickness direction. Substituting Eqn 3 and ε_{yi} = 0 into Eqn 5 gives the constitutive relation

$$\sigma_{xi} = \frac{E}{1-\nu^2}\left(u^o_{i,x} + \frac{1}{2}\left(w_{i,x}\right)^2 - z_i w_{i,xx} - \alpha(1+\nu)T_i(z_i)\right) \tag{6}$$

The force resultant P_i and the moment resultant M_i can be obtained by integrations of the stress given by Eqn 6 through the thickness of each region t_i.

$$P_i = \frac{12D_i}{t_i^2}\left(u^o_{i,x} + \frac{1}{2}\left(w_{i,x}\right)^2 - T_{pi}\right)$$
$$T_{pi} = \frac{\alpha(1+\nu)}{t_i}\int_{-\frac{t_i}{2}}^{\frac{t_i}{2}} T_i(z_i)dz_i \tag{7}$$

$$M_i = D_i\left(w_{i,xx} + T_{mi}\right)$$
$$T_{mi} = \frac{12\alpha(1+\nu)}{t_i^3}\int_{-\frac{t_i}{2}}^{\frac{t_i}{2}} T_i(z_i)z_i dz_i \tag{8}$$

where D_i is the bending stiffness of each region and is given by

$$D_i = \frac{Et_i^3}{12\left(1-\nu^2\right)} \tag{9}$$

The equilibrium equations in the axial and transverse directions are as follows.

$$P_{i,x} = 0 \tag{10}$$

$$D_i w_{i,xxxx} + P_i w_{i,xx} = 0 \tag{11}$$

Since there is symmetry about $x = 0$, only the regions in the interval $0 \le x \le l$ will be considered. Each region is governed by Eqns 7, 10 and 11. The exact solution for the whole system can be derived by using the symmetry condition with respect to the midpoint, the boundary conditions at the two ends $x = \pm l$ and the continuity of deflection and slope at the junction of the regions at $x = a$. The expressions for the postbuckling deflection of the intact region and of the lower and upper delaminated regions, respectively, regardless of whether a thermal load is applied or not are

$$w_1 = A_1\left(1-\cos\beta_1(l-x)\right) \qquad \{x: a \le x \le l\} \tag{12}$$

$$w_2 = A_1\left(\frac{\beta_1 \sin\beta_1(l-a)}{\beta_2 \sin\beta_2 a}\left(\cos\beta_2 x - \cos\beta_2 a\right) + 1 - \cos\beta_1(l-a)\right) \qquad \{x: 0 \le x \le a\} \tag{13}$$

$$w_3 = A_1\left(\frac{\beta_1 \sin\beta_1(l-a)}{\beta_3 \sin\beta_3 a}\left(\cos\beta_3 x - \cos\beta_3 a\right) + 1 - \cos\beta_1(l-a)\right) \qquad \{x: 0 \le x \le a\} \tag{14}$$

where

$$\beta_i^2 = \frac{P_i}{D_i} \qquad (i = 1,2,3) \tag{15}$$

Here, β_1 is a known value whereas β_2 and β_3 are unknown values. Note that Eqns 12~14 are valid only when the delamination remains completely open. The two unknowns β_2 and β_3 can be obtained by solving Eqn 7 and taking into account the continuity in forces and the kinematic continuity conditions at $x = a$. The amplitude A_1 can be obtained by considering the continuity in moments at $x = a$.

$$A_1 = \frac{-(t-h)^3 h\beta_2^2 + h^3(t-h)\beta_3^2 + 2h^3 T_{m3}}{2\beta_1 \sin\beta_1(l-a)\left\{t^3\beta_1 \cot\beta_1(l-a) + (t-h)^3\beta_2 \cot\beta_2 a + h^3\beta_3 \cot\beta_3 a\right\}} \tag{16}$$

To confirm the significance of thermal loads, energy release rate G will also be calculated using the expression given by [3]

$$G = \frac{1}{24D_1}\left(\frac{\left(P^* t\right)^2}{\bar{h}\left(1-\bar{h}\right)} + \frac{12M^{*2}}{\bar{h}^3} + \frac{12\left(P^* t/2 - M^*\right)^2}{\left(1-\bar{h}\right)^3}\right) \tag{17}$$

where

$$
\begin{aligned}
P^* &= \bar{h}\left(P_1 + \frac{6\left(1-\bar{h}\right)}{t} M_1 - \frac{2D_1\bar{h}^3 T_{m3}}{h} \right) - P_3 \\
M^* &= M_3 - \bar{h}^3\left(M_1 + D_1 T_{m3}\right) \\
\bar{h} &= \frac{h}{t}
\end{aligned}
\tag{18}
$$

This expression is also applicable in the current analysis, since thermal load is substituted by its mechanical load equivalence. In the next section, the relations between the nondimensionalised energy release rate $\bar{G}$ and the nondimensionalised axial load $\bar{\beta}_1$ will be discussed. The expressions for $\bar{G}$ and $\bar{\beta}_1$ are given by

$$
\bar{G} = \frac{1}{24}\left(\frac{\left(\bar{P}\bar{t}\right)^2}{\bar{h}\left(1-\bar{h}\right)} + \frac{12\bar{M}^2}{\bar{h}^3} + \frac{12\left(\bar{P}\bar{t}/2 - \bar{M}\right)^2}{\left(1-\bar{h}\right)^3} \right) \tag{19}
$$

where

$$
\begin{aligned}
\bar{P} &= \bar{h}\left(\bar{\beta}_1^2 + \frac{6\left(1-\bar{h}\right)}{\bar{t}} \overline{A_1\beta_1}^2 \cos\bar{\beta}_1\left(1-\bar{a}\right) - \frac{2\bar{h}^2\overline{T_{m3}}}{\bar{t}} \right) - \bar{h}^3\bar{\beta}_3^2 \\
\bar{M} &= -\bar{h}^3\overline{A_1\beta_1}\sin\bar{\beta}_1\left(1-\bar{a}\right)\left[\bar{\beta}_3\cot\bar{\beta}_3\bar{a} + \bar{\beta}_1\cot\bar{\beta}_1\left(1-\bar{a}\right)\right] \\
\overline{T_{m3}} &= T_{m3}l \\
\bar{t} &= \frac{a}{l} \\
\bar{a} &= \frac{a}{l}
\end{aligned}
\tag{20}
$$

and

$$
\bar{\beta}_j^2 = \frac{P_j l^2}{D_j} \qquad (j = 1,3) \tag{21}
$$

RESULTS AND DISCUSSION

The post-buckling deflections of the right half of a beam-plate with dimensions of $2l$ = 200 mm, t = 1 mm, $2a$ = 20 mm and h = 0.1 mm are shown in Figs. 2~5. In Fig. 2, the beam-plate is under a mechanical load alone and in Fig. 3, it suffers only a thermal load. In Figs. 4 and 5, the beam-plates are under combined thermal and mechanical loads. The upper delaminated region experiences an uniform temperature increase of 40℃ in Figs. 3 and 4 and in Fig. 5, a temperature gradient in the thickness direction is taken into account. Note that in Fig. 2 the mechanical load β_1 is higher than those used in Figs. 4 and 5. This is due to the fact that under a mechanical load alone, a beam-plate with the dimensions given above does not buckle until

$\beta_1 = 0.0311$.

From Figs. 2~5, it can be observed that the existence of a thermal load causes the beam-plate to deflect two to three orders of magnitude more than when there is no thermal load, indicating that the overall buckling resistance is reduced by thermal loads. The effect of a combined load is made evident by comparing Figs. 3 and 4. By studying Figs. 4 and 5, the effect of the temperature gradient may be noted. Moreover, it will be seen when energy release rates are calculated that the existence of a temperature gradient makes a beam-plate more vulnerable to delamination growth.

Beam-plates of dimensions different to those in Figs. 2~5 are considered in Figs. 6 and 7. In Fig. 6, $2l$ = 200 mm, t = 1 mm, $2a$ = 100 mm and h = 0.1 mm and in Fig.7, $2l$ = 200 mm, t = 1 mm, $2a$ = 20 mm and h = 0.7 mm. Both figures consider combined thermal and mechanical loads. Comparison of Figs. 4 and 6 indicate that for a relatively long delamination, significant transverse deflection occurs mainly in the thin layer of the delamination. It can be noted from Fig. 7 that when a delamination is located relatively deep down from the top surface, the delamination is practically closed.

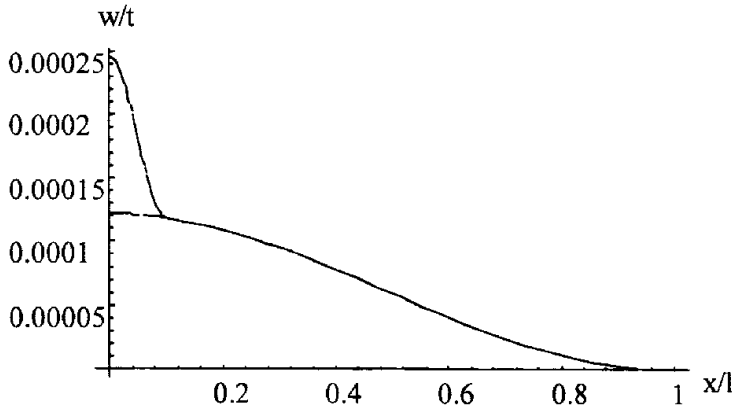

Fig. 2: Buckling deflection of a delaminated beam-plate #1 ($a/l = 0.1$, $h/t = 0.1$, $T_3(z_3) = 0$, $\beta_1 = 0.0311$)

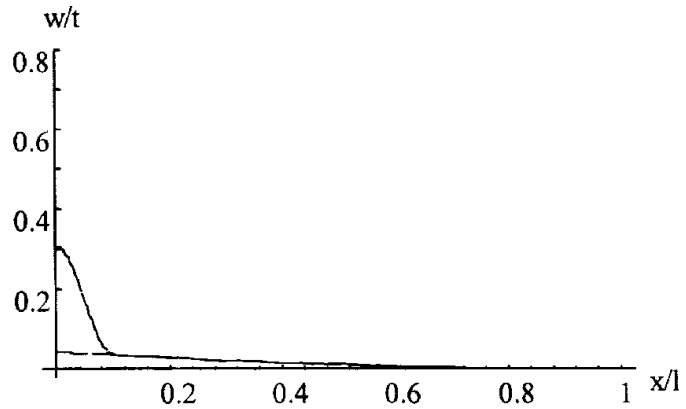

Fig. 3: Buckling deflection of a delaminated beam-plate #2 ($a/l = 0.1$, $h/t = 0.1$, $T_3(z_3) = 40$, $\beta_1 = 0$)

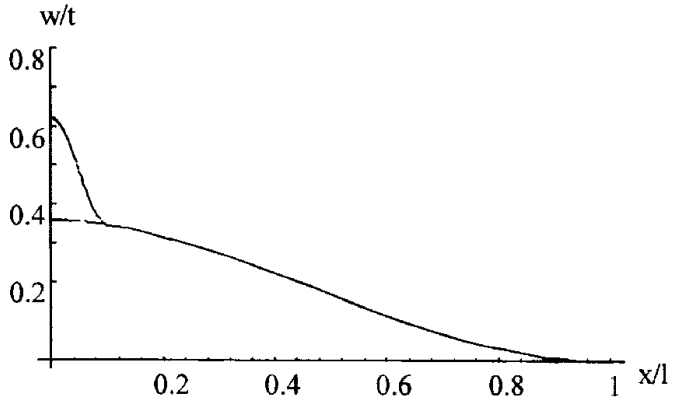

Fig. 4: Buckling deflection of a delaminated beam-plate #3 ($a/l = 0.1$, $h/t = 0.1$, $T_3(z_3) = 40$, $\beta_1 = 0.03$)

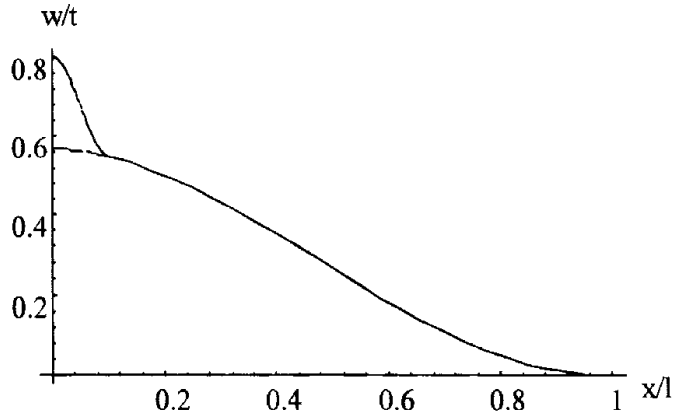

Fig. 5: Buckling deflection of a delaminated beam-plate #4 ($a/l = 0.1$, $h/t = 0.1$, $T_3(z_3) = 80z_3/h+40$, $\beta_1 = 0.03$)

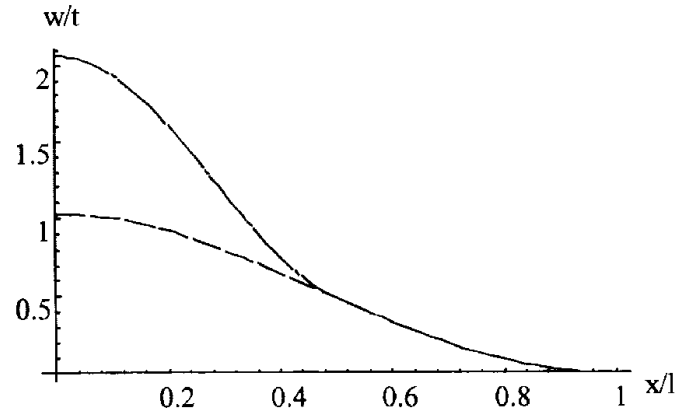

Fig. 6: Buckling deflection of a delaminated beam-plate #5 ($a/l = 0.5$, $h/t = 0.1$, $T_3(z_3) = 40$, $\beta_1 = 0.03$)

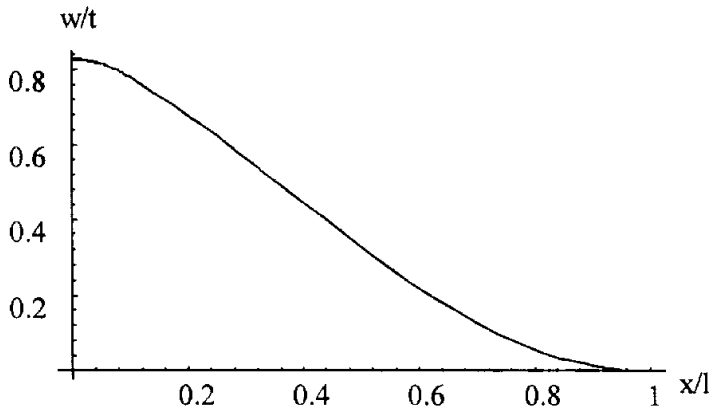

Fig. 7: Buckling deflection of a delaminated beam-plate #6 ($a/l = 0.1$, $h/t = 0.7$, $T_3(z_3) = 40$, $\beta_1 = 0.025$)

To confirm the significance of thermal loads (T.L.), energy release rate G has been calculated for several cases. The relations between the nondimensionalised energy release rate $\overline{G}$ and the nondimensionalised axial load $\overline{\beta_1}$ for beam-plates under various thermal loads are shown in Figs. 8~12. In Figs. 8~11, the beam-plates are under uniform thermal loads. In Figs. 8, 9 and 10, $2l = 200$ mm, $t = 1$ mm and $2a = 20$ mm, with $h = 0.1$ mm, 0.5 mm and 0.9 mm, respectively. Figure 11 considers beam-plates of dimensions $2l = 200$ mm, $t = 1$ mm, $h = 0.3$ mm under a thermal load of $T_3(z_3) = 40$ for various delamination length. The case in which $2l = 200$ mm, $t = 1$ mm, $2a = 20$ mm and $h = 0.3$ mm, under a thermal load with a temperature gradient, is considered in Fig. 12.

The significance of thermal loads is apparent from Figs. 8~12. It can be seen from these figures that the existence of a thermal load increases the likelihood of delamination growth. The large effect that the temperature gradient has on the energy release rate should be noted (see Fig. 12). It can also be learnt from these figures that the energy release rate is affected by various parameters in a complex way (note especially Fig. 11). From Figs. 8~10 and also from Fig. 11, it can be seen that the energy release rate is greatly affected by the volume of the heated region.

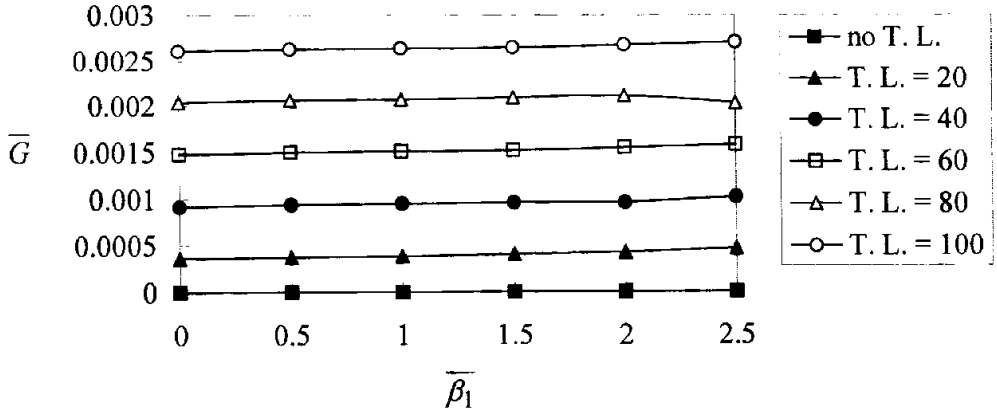

Fig. 8: $\overline{G}$-$\overline{\beta_1}$ for various thermal loads ($\overline{a} = 0.1$, $\overline{h} = 0.1$) [T.L. in ℃]

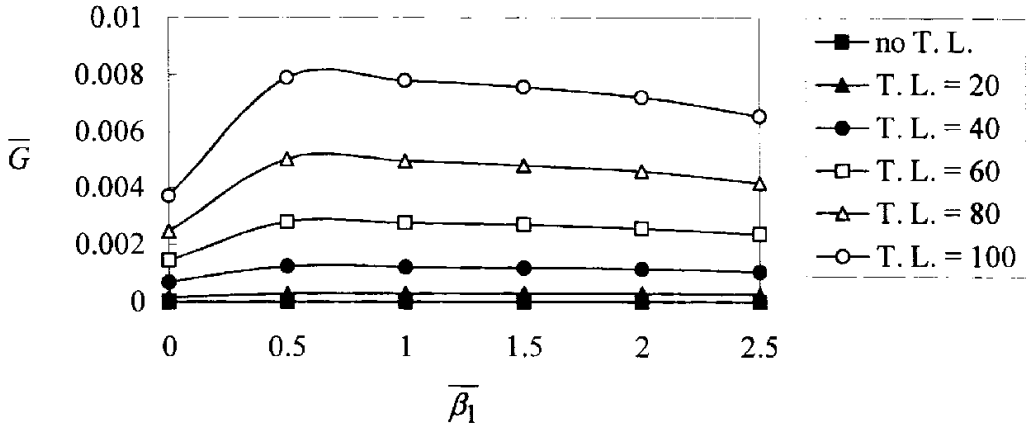

Fig. 9: $\overline{G}$ - $\overline{\beta_1}$ for various thermal loads ($\bar{a}$ = 0.1, $\bar{h}$ = 0.5) [T.L. in °C]

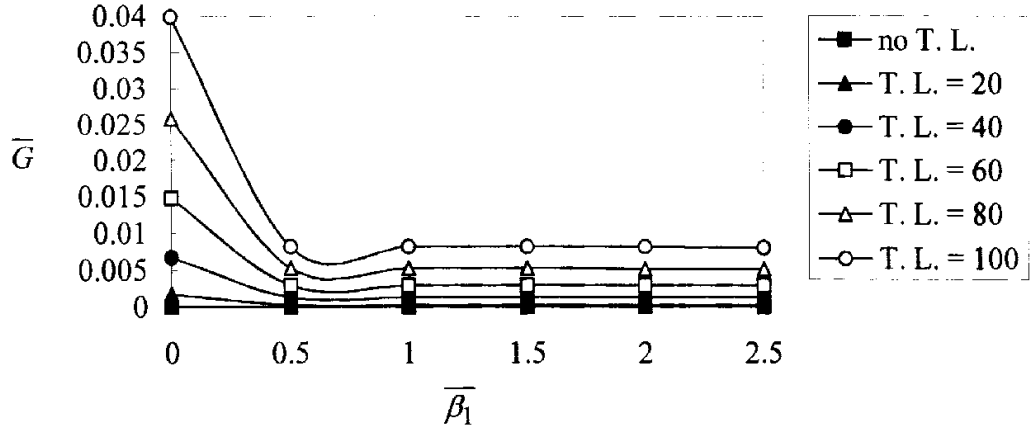

Fig. 10: $\overline{G}$ - $\overline{\beta_1}$ for various thermal loads ($\bar{a}$ = 0.1, $\bar{h}$ = 0.9) [T.L. in °C]

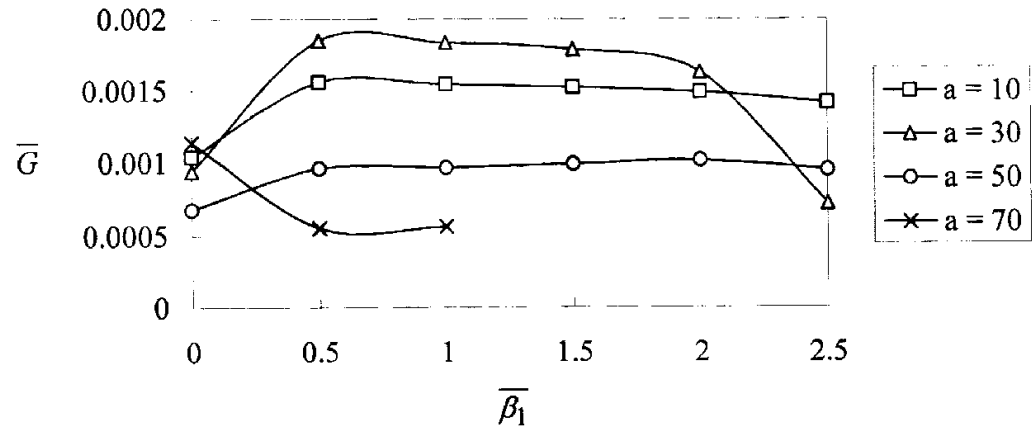

Fig. 11: $\overline{G}$ - $\overline{\beta_1}$ for various delamination lengths (T.L. = 40, $\bar{h}$ = 0.3) [T.L. in °C]

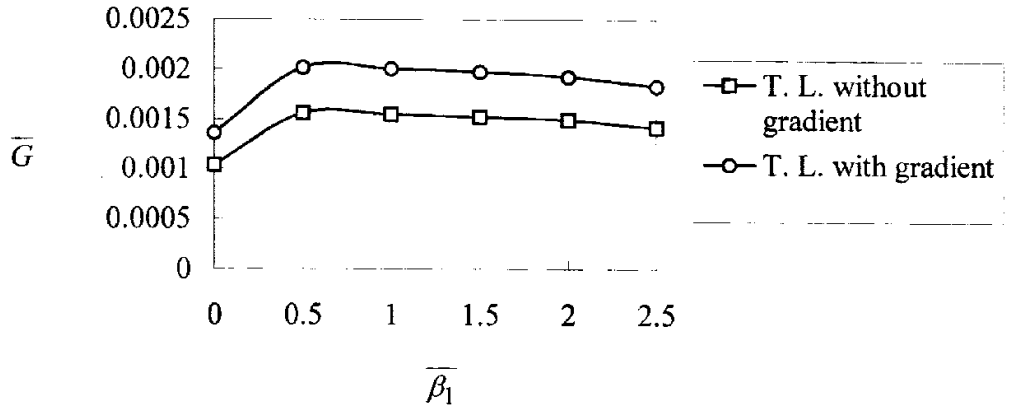

Fig. 12: $\bar{G}$ - $\bar{\beta}_1$ for a thermal load with and without gradient ($\bar{a}$ = 0.1, $\bar{h}$ = 0.3)
(T.L. with gradient: $T_3(z_3) = 40$, T.L. without gradient: $T_3(z_3) = 80z_3/h + 40$) [T.L. in °C]

CONCLUSION

A one dimensional beam-plate model has been employed to study the effect of a combined thermal and mechanical load. It serves to give a good indication of the significance of thermal loads. A study of the post-buckling deflections indicates a reduction in the buckling resistance. Calculation of the energy release rates reveals an increase in the likelihood of delamination growth, especially with the existence of a temperature gradient in the thickness direction. The simplicity of the model in the current analysis limits the applicability to homogeneous, isotropic materials. However, the analysis presented in this paper can be easily extended to orthotropic laminates.

REFERENCES

1. Yin, W.-L., Sallam, S.N. and Simitses, G.J., "Ultimate Axial Load Capacity of a Delaminated Beam-Plate", *AIAA Journal*, Vol. 24, January 1986, pp.123-128.

2. Simitses, G.J., Sallam, S. and Yin, W.-L., "Effect of Delamination of Axially Loaded Homogeneous Laminated Plates", *AIAA Journal*, Vol. 23, September 1985, pp.1437-1444.

3. Yin, W.-L. and Wang, J.T.S., "The Energy-Release Rate in the Growth of a One-Dimensional Delamination", *Journal of Applied Mechanics*, Vol. 51, December 1984, pp. 939-941.

4. Brush, D.O. and Almroth, Bo.O., *Buckling of Bars, Plates, and Shells*, McGraw-Hill, 1975.

MECHANICAL PROPERTIES OF 3-D CARBON/BISMALEIMIDE HEAT-RESISTANT COMPOSITES

Ippei Susuki[1], Masahiro Shinya[2], and Yosiharu Yasui[3]

[1]Head of Damage Mechanism Section, Airframe Division, National Aerospace Laboratory, 7-44-1Jindaiji Higashi-machi, Chofu, Tokyo 182, Japan
[2]Material and Process Engineer, Chemical Research Section,Engineering Research Department, Mitsubishi Heavy Industries, Ltd., 10 Oye-cho, Minato-ku, Nagoya 455, Japan
[3]Assistant General Manager, Mechanical Research Group, R&D Center, Toyoda Automatic Loom Works, Ltd., 8 Chaya, Kyowa-cho, Obu-shi, Aichi-ken 474, Japan

SUMMARY: Mechanical properties of three-dimensional (3-D) carbon/bismaleimide woven composite were investigated and compared to two dimensional textile laminates of the same material system under static tension, compression, and compression-after-impact tests. Bismaleimide (BMI) 5250-4 resin from Cytek, Inc. was chosen as the matrix in this study due to it being a candidate resin for use in high-temperature composite airframe structures for next generation supersonic transport. A near net-shape dry 3-D preform comprising pi-by-four orientation carbon fibers reinforced with orthogonal z-direction fibers was prepared after which molding took place utilizing the resin film infusion (RFI) process. A high volume fraction of about 56% was attained by this 3-D processing due to the use of straight in-plane fibers. Experimental results showed the longitudinal modulus of both materials to be fairly similar, though the transverse modulus of the 3-D composite was slightly higher. Both the longitudinal tensile and compressive strength of the 3-D composite were approximately 6% lower than those of the 2-D laminate, while the compression-after-impact strength of the 3-D was significantly higher than that of the 2-D composite. The impact damage were also examined by the ultrasonic scanning method.

KEYWORDS: 3-D composite, carbon/bismaleimide composite, heat resistant materials, textile, resin film infusion, compression test, tension test, CAI strength

INTRODUCTION

The application fields of polymeric composite structures have been increasingly expanded in the past few decades especially for the structures where weight are at a premium. A typical example of this kind of structures is composite airframes. After twenty years of scheduled flights of Concorde, the next generation supersonic transports are expected to be developed and manufactured in the near future for replying to the estimated air travel growth [1]. In order to produce an economically viable supersonic transport, it is required to develop and apply high performance polymeric composite materials which will be durable for long term high temperature adverse environments and more tolerable against impact damages [2,3]. Laminated plates of fiber reinforced plastics have been widely adopted to the composite structures as load bearing components. However, increased use of advanced composite materials has required that processes other than traditional prepreg layups and autoclave cure be developed to meet design properties and damage tolerance requirements of structures [4-6].

Three-dimensional (3-D) textile composites offer potential improvements in the ability of a composite structure to survive a high energy impact with minimal decrease of strength [7-9].

In this work, fundamental mechanical properties of 3-D carbon/bismaleimide composite plates were investigated experimentally including in-plane tensile/compressive elastic constants, static tensile and compressive strength, and compression strength after impact. A near net-shape dry fiber preform was formed by pi-by-four fiber orientation in a x-y plain with orthogonal z-direction fiber reinforcement. Firstly, our research work was concentrated on attaining a higher volume fraction of a 3-D dry fiber preform. Secondly, resin film infusion (RFI) processes were studied for making thin plates of carbon/bismaleimide 3-D composites. All specimens were cut out from the plates. In this study, Cytec 5250-4 resin was used for RFI processes, and our estimated volume fraction was about 54 to 57%. In-plane tension and compression tests were carried out and stiffness and strength were measured and compared to two-dimensional (2-D) quasi-isotropic materials which have been laminated of dry cloth plies, and about the same volume fraction values. Our experimental results show that the longitudinal modulus of both materials is quite similar, but that the transverse modulus of the 3-D is slightly higher. In terms of strength, the longitudinal tensile and also compressive strength of the 3-D composite was approximately 6% lower than those of the 2-D laminate. The CAI test was carried out based on the SACMA method. The thickness of our specimens were all about 5 mm. The 3-D composites showed a much higher compressive strength after impact damage than that of 2-D ones. The 3-D composites maintained about 68% values after the impact damage energy of 1500 in-lb/in, and 60% for 2000 in-lb/in. The damage area was examined by the ultrasonic scanning method, and we found both composites have about the same projected damaged areas for these impact energy levels. However, smaller and more distributed cracks seemed to be formed during the impact for the 3-D composites, and this characteristics contributed the compressive strength of the 3-D materials to keep higher levels.

WEAVING PROCESSES FOR THREE-DIMENSIONAL (3-D) FABRICS

The dry fabric preforms were produced by our thrusting apparatus which is schematically shown in Fig.2.1. All 3-D fabrics were formed in two steps. The first step is arranging of in-plane fibers to make a lamina. In this work, these were arranged along 0^0, 45^0 or 90^0 line by engaging with many restriction members such as pins, located with a predetermined pitch on a frame[9]. The second step is insertion of z-direction fibers. The thrusting apparatus for z-direction fiber is consisted mainly of (1) a movable support table which supports the frame and is movable by a predetermined pitch , (2) a press plate which presses the laminated fiber layers , and guides the needles, (3) the perforating needles which make pre-holes in the fiber layers to prevent from damage caused by the insertion of the z-direction fibers, (4) the inserting needles which thrust z-direction fibers, and (5) a lock yarn needle which inserts a lock yarn into loop of z-direction fibers. These z-fibers are thrusted by many inserting needles, which are arranged in a series, into the laminated fiber layers.

Details of the weaving processes are:

(1) pushing the laminated fiber layers by press plate ,
(2) making pre-holes to the laminated fiber layers by perforating needles ,
(3) thrusting the inserting needles to the laminated fiber layers with z-direction fibers,
(4) making loops of z-direction fibers by a little going back of inserting needles, and inserting a lock yarn into the loops,

(5) pulling back the inserting needles and tightening the z-direction fibers.

A sample of our dry fabric preforms and a schematic drawing are shown in Fig.2.2 and Fig.2.3. The advantages of this production method are;

(1) high quality and high volume fraction of 3-D fabric, because the lamination is supported by pins until the insertion of z-direction fibers are completed, and fiber straightness is maintained, and because we use perforated needles, press plate and special tension device ,
(2) capability of high productivity, because z-direction fibers are inserted in a series together ,
(3) capability for production of complex shape fabric by developing of frame and table.

FABRICATION PROCESSES OF BMI-RESIN COMPOSITES

To fabricate a composite part, it is necessary, as in the case of 3-dimensional fabrics, to have molding process performed including impregnation and curing of resin for the preforms which are made of only the "dry" base reinforcement fiber materials. In this study, we have used the resin film infusion (RFI) process as molding method. The principle of this concept is shown in Fig.3.1. The resin has been prepared in the form of a film or a panel beforehand. The resin film/panel was applied to both sides of the preform. Then, they were heated in a vacuum environment to have resin melted and impregnated into the preform by capillary action. Further heating of the assembly was accomplished to cure the impregnated resin. This method used much simpler equipment and operations compared to the general resin transfer molding where resin was impregnated into the preform by applying pressure. Therefore, this method can be considered advantageous for applications to aircraft skins, etc. where relative simpler shapes of preforms are used, because the satisfactory quality level of formed parts can be assured as well as a shorter molding time [10]. Figure 3.2 shows the equipment used for RFI process. The center of the equipment is a vacuum chamber. It can be used to fabricate a part of maximum 200mmW x 300mmL using the metal mold die placed in the vacuum chamber. Figure 3-3 shows the molding cycle. The resin was melted and impregnated at temperature of 100^0C in a vacuum environment of 540mmHg minimum. The specimens were cured at 191^0C. After that, they were applied to post-cure process at temperature of 227^0C. Figure 3-4 shows the section of specimen. The satisfactory quality parts which have almost free from voids, interlaminar cracks, etc. can be fabricated up to maximum thickness of 6mm by the above process.

Table 3-1 shows the specification of the specimens used in this work. The 5 axes 3 dimensional (with 4 in-plane axes directions in 0°, -45°, +45°, 90° and additional one axis in thickness direction) composite (3-D) and 2 dimensional composite (2-D) was prepared. 2-D specimen aims at giving the reference. 3-D's preform is the mentioned 3D-fabric and 2-D's preform is lamination of dry cloths that is pre-impregnated textile. Both 3-D and 2-D specimens were fabricated by the same molding process. Two types of carbon fiber, MR50K of Mitsubishi Rayon and T900 of Toray, were used. MR50K was used for in-plane direction fiber as a plenty of data were available for this material. It was used as a yarn for 3-D specimen, and satin woven fabric for 2-D specimen. T900 twist yarn was used for 3-D through-the-thickness direction fiber. The used resin was bismaleimide resin #5250-4-RTM of Cytec. This resin was chosen from several different types of bismaleimide resins by

comparing the previous test results of their characteristics on better workability, and less possibilities of having voids and/or interlaminar cracks.

TESTING

Specimen Configurations and Testing Methods

Various test methods have been investigated to evaluate the stiffness and strength of textile composites properly, as these materials tend to be less homogeneous than conventional tape laminates, and are known their failure processes are significantly different [11,12]. There seems to be little data base, especially for the 3-D composites, to build up a standard test method. In this study, we focused on the mechanical properties of those compared to the 2-D laminates which we have already had some experiences and test results. Specimen configurations of in-plane tension, compression, and CAI test are shown Fig. 4.1. The SACMA(Suppliers of Advanced Composite Materials Association) method was adopted for the CAI test method [13]. Specimens were impacted at room temperature with a spherical tip impactor at 1500 or 2000 inch-pounds/inch thickness of the energy level. Tensile tests were conducted on the MTS machine under load controlled mode. The compressive tests and CAI test were conducted on the Instron machine under displacement controlled mode at a crosshead speed of 0.4 mm/min and 0.5 mm/min respectively.

Tensile Properties

The 5mm long strain gages were bonded at both surfaces in the longitudinal and transverse directions. Four strain data with loading one were recorded to a developed digital data acquisition system using personal computer. Fig.4.2 and Fig 4.3 are the sample stress-strain curves of 2-D and 3-D specimens. As seen in these figures, the longitudinal modulus of both materials is quite similar, but that the transverse modulus of the 3-D is slightly higher. In terms of strength, the longitudinal tensile strength of the 3-D's are about 6% lower than that of the 2-D laminates.

Compressive Properties

Similar to tensile test specimens, 3mm long strain gages were bonded at both surfaces and measured and recorded by the data acquisition system. The stress-strain curves of 2-D and 3-D specimen under static compressive loads are shown at Fig.4.4 and Fig.4.5, respectively. Again, the longitudinal modulus of both materials is quite similar, but that the transverse modulus of the 3-D is slightly higher. The compressive strength of the 3-D's are about 6% lower than that of the 2-D laminates.

Compression-after-impact Properties

Out-of-plane impact damages were investigated by a ultrasonic imaging system prior to compressive failure tests of CAI specimens. The damage area was measured and examined by the ultrasonic C-scanning method, and our data showed both of 2-D and 3-D composites have about the same projected damaged areas for 1500 and 2000in-lb-in impact energy levels. However, as seen in Fig. 4.6 and Fig. 4.7, smaller and more distributed cracks seemed to be formed during the impact for the 3-D composites. The growth of interlaminar failures was observed to be arrested by the through-thickness reinforcement fibers. Load vs. strain curves

of compression tests after 1500 or 2000in-lb-in impact damages were shown in Fig.4.8 to Fig. 4.11. Strains were measured at the locations of the both sides, S1,S2,S3,S4, as indicated in the SACMA recommendations. Our experiments showed that the 3-D composites maintained about 68% values after the impact damage energy of 1500 in-lb/in, and 60% for 2000 in-lb/in.

Properties of 3-D Composites

The longitudinal modulus of both materials is quite similar, but that the transverse modulus of the 3-D is slightly higher. Both the tensile and compressive strength of the 3-D composite were approximately 6% lower than those of the 2-D laminate, while the 3-D composites showed a much higher compressive strength after impact damage than that of the 2-D composite. The 3-D composites maintained about 68% values after the impact damage energy of 1500 in-lb/in, and 60% for 2000 in-lb/in. Preliminary ultrasonic C-scan data indicated the z-fiber in the 3-D composite contributed to arrest the propagations of distributed cracks generated by out-of-plane impacts. Experimental results are summarized in Table 5.1

CONCLUSIONS

A high volume fraction of about 56% was attained in this work for the 3D carbon/bismaleimide composite which was molded by resin film infusion process. Although the data are limited, the compression-after-impact strength of the 3-D composites were significantly higher than that of the 2-D composites.

REFERENCES

1. Condit, P.M.,"Performance, Process, and Value: Commercial Aircraft Design in the 21st Century", Proc. of World Aviation Congress and Exposition, 1996.
2. Rogalski, M.E.,"Aging of polymeric materials for use on HSCT", SAE 942162, 1994.
3. Shin, E.E. et al.,"Durability and critical fundamental aging mechanisms of high temperature polymer matrix carbon fiber composites: Part I", IMECE, Proc. ASME Matl. Div. MD-Vol.69-1, 1995, pp183-189.
4. Shim,S.B., Ahn K., and Seferis,J.C.,"Cracks and microcracks in stitched structural composites manufactured with resin film infusion process", J. of Advanced Materials, July, 1995, pp48-62.
5. NASA CP- 3178,"Third NASA Advanced Composites Technology Conference", 1994.
6. NASA CP-3311, "Mechanics of Textile Composites Conference", 1995.
7. Chou,S.C.,Chen H.-C. and Wu,C.-C.,"BMI resin composites reinforced with 3D carbon-fibre fabrics", Comp. Sci. & Tech. 43, 1992, pp 117-128.
8. Burgess,K.and Paradis,S.,"Application of 3-D woven preforms to laminated composites", AIAA Aircraft Engr.Tech., and Oper. Congr., Sept., 1995, AIAA 95-3890.
9. Pending U.S. patent application ,Yasui, Hori, Amano and Takeuchi , Method and apparatus for production of a three-dimensional fabric, Feb.5, 1996.
10. Yamamoto, et al. "Three Dimensional Fabric Composite Forming Method", Next Gen. Comp. Tech. Handbook, Japan Industrial Standard Assoc., p.254 - 265.

11. Minguet,P.J., Fedro,M.J., and Gunther,C.K.,"Test Methods for Textile Composites", NASA CR-4609, 1994.

12. Masters,J.E., and Portanova,M.A.,"Standard Test Methods for Textile Composites", NASA CR-4751, 1996.

13. SACMA Recommended Test Method: SRM 2-88.

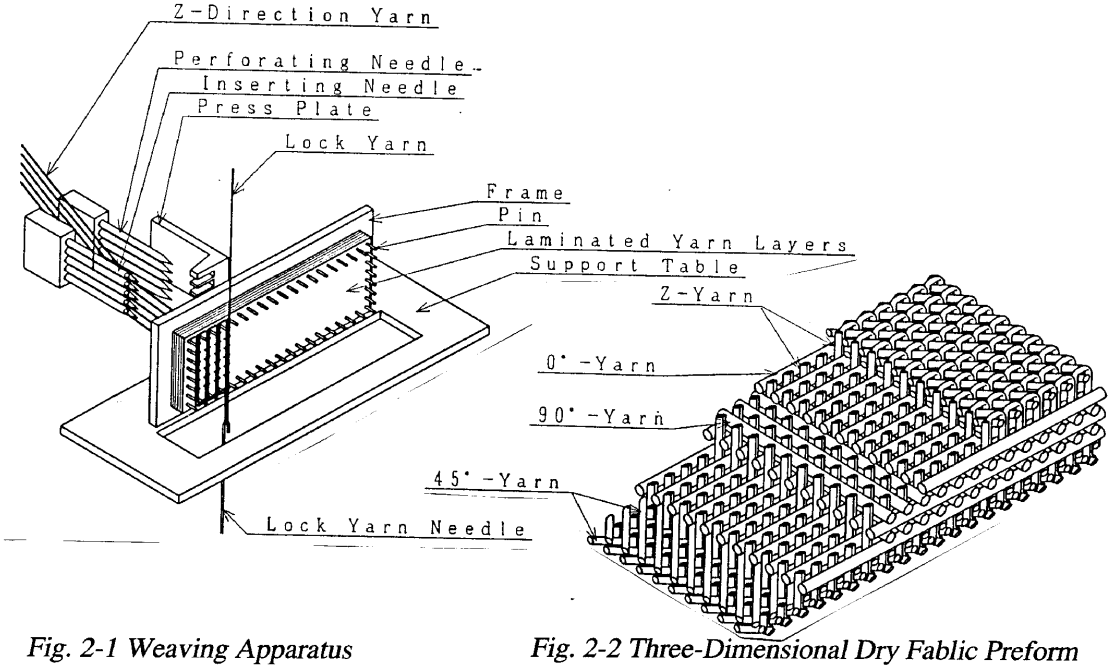

Fig. 2-1 Weaving Apparatus

Fig. 2-2 Three-Dimensional Dry Fablic Preform

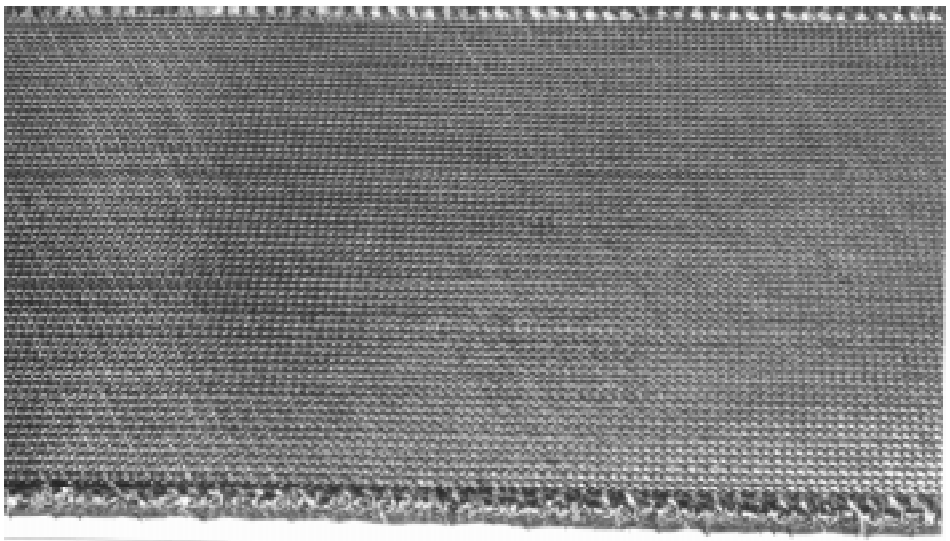

Fig. 2-3 Photograph of Three-Dimensional Dry Fablic Preform

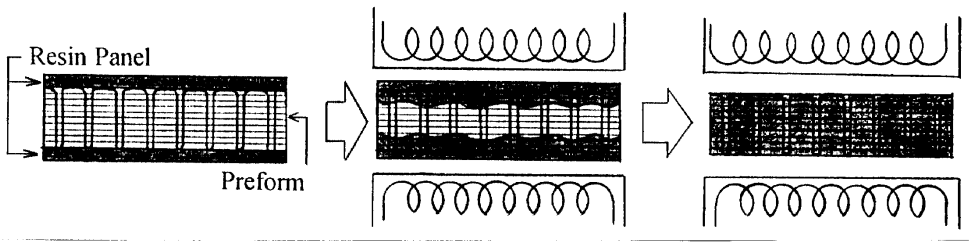

Fig. 3-1 Resin Film Infusion (RFI) Process

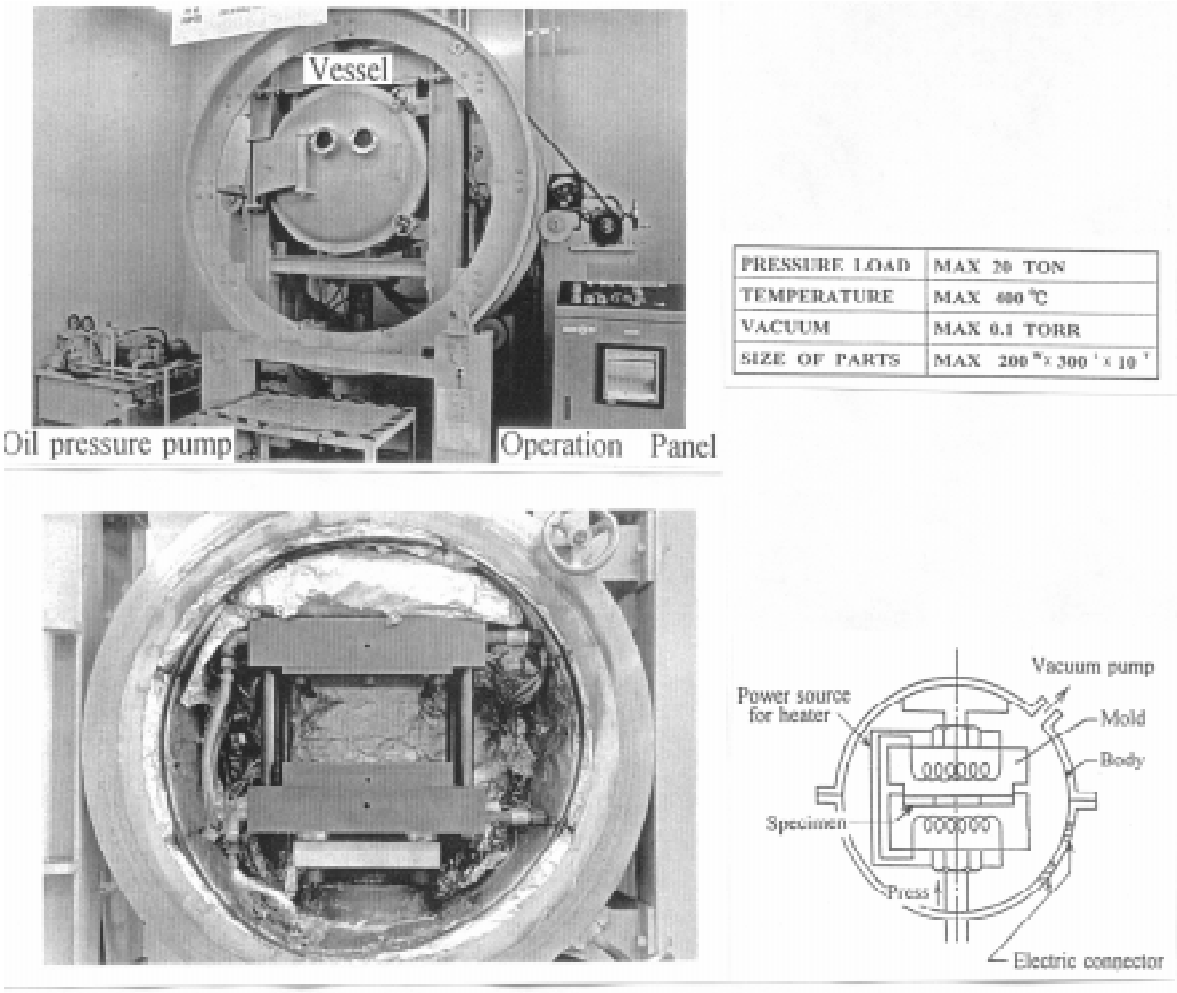

Fig. 3-2 Resin Film Infusion (RFI) Process Equipment

Table 3-1 Specification of Specimens

Sample	3D	2D
Reinforcement	5-axis 3-D Fabric	Laminated 2D-Textile
Fiber		
In the Plain Direction	MR50K	MR50K
In the Thickness Direction	T900	—
Matrix	#5250-4-RTM	#5250-4-RTM
Fiber Arrangement		
in the Plain Direction	Quasi-isotropic	Quasi-isotropic
in the Thickness	Pitch:3 ^{L} X 3 ^{W} (㎜)	—

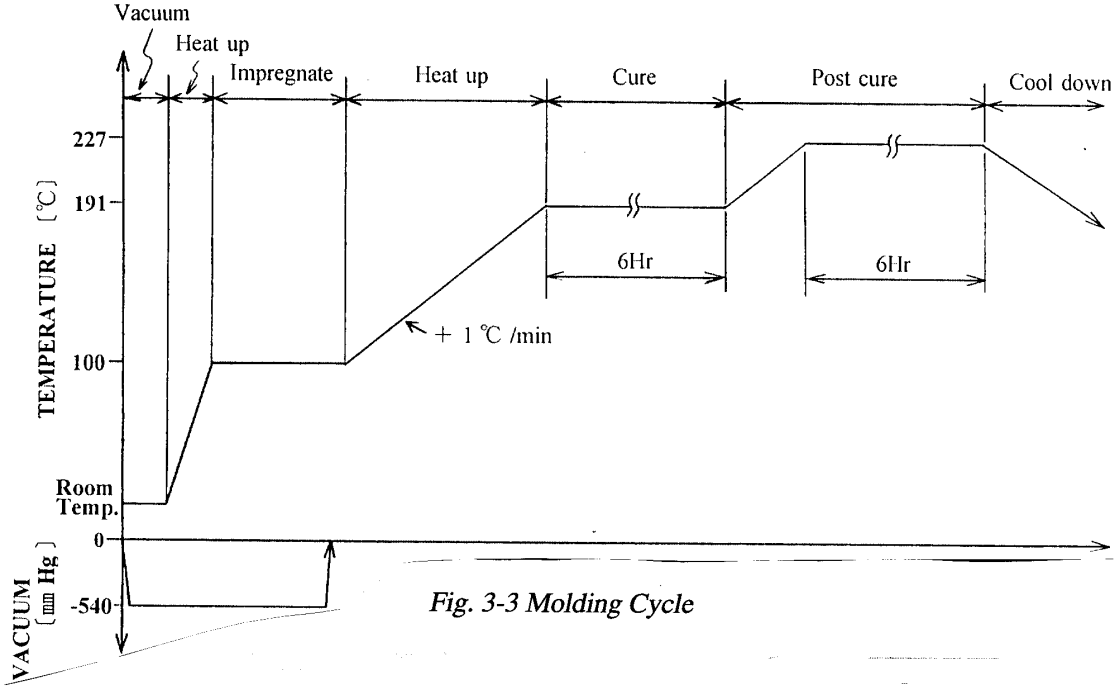

Fig. 3-3 Molding Cycle

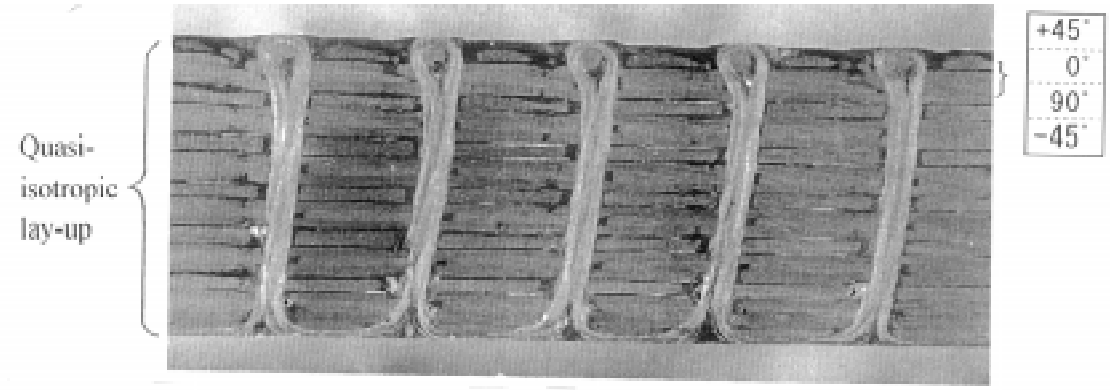

Fig. 3-4 Section of the 3-D Composite Specimen

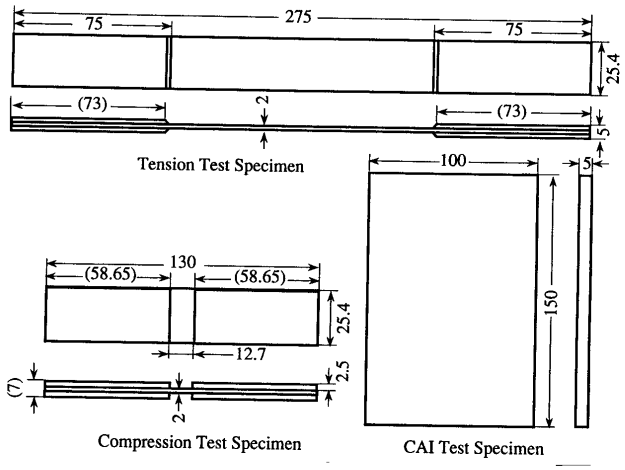

Fig. 4-1 Specimen Configurations

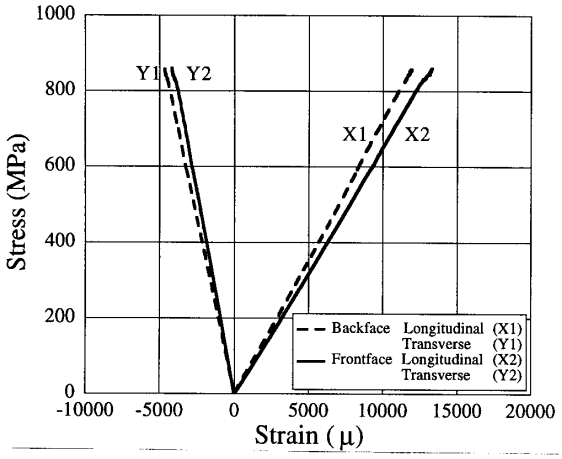

Fig. 4-2 Stress-Strain curves in Tension Test (2-D Specimen)

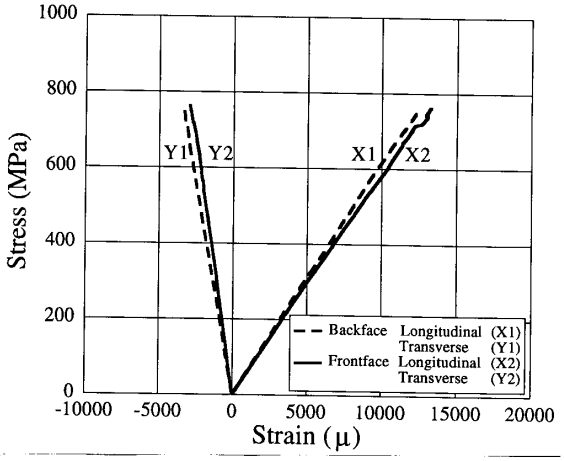

Fig. 4-3 Stress-Strain curves in Tension Test (3-D Specimen)

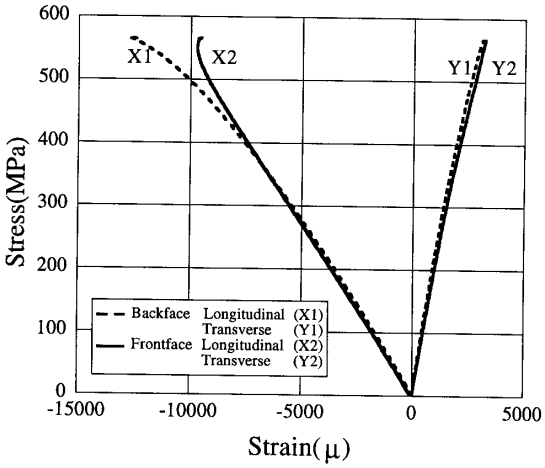

Fig. 4-4 Stress-Strain curves in Compression Test (2-D Specimen)

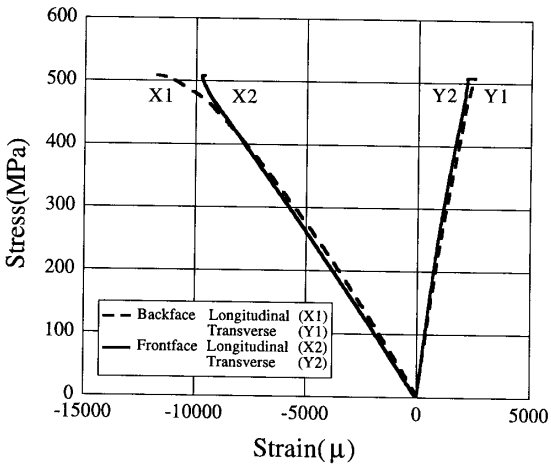

Fig. 4-5 Stress-Strain curves in Compression Test (3-D Specimen)

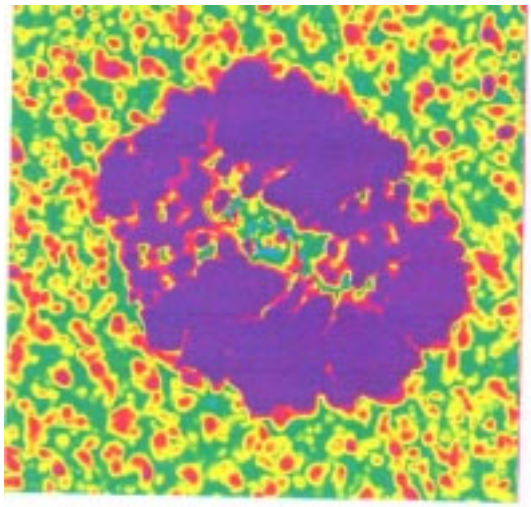

Fig. 4-7 Impact Damage Area (2-D CAI Specimen , 1500in-lb-in)

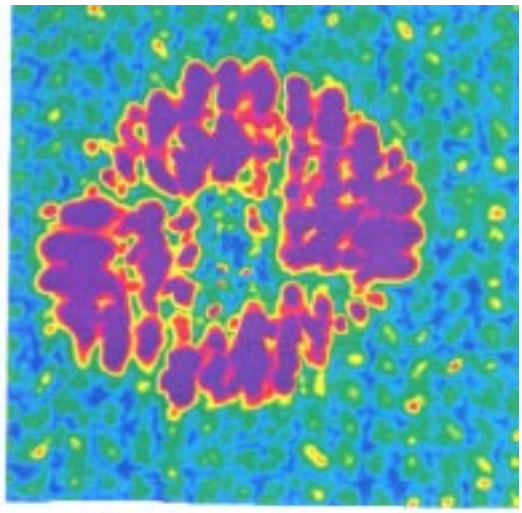

Fig. 4-8 Impact Damage Area (3-D CAI Specimen , 1500in-lb-in))

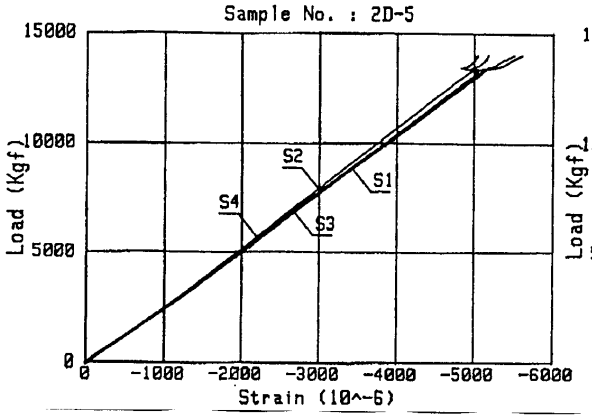

Fig. 4-9 Stress-Strain Curves in CAI Test (2-D Specimen, 1500in-lb-in)

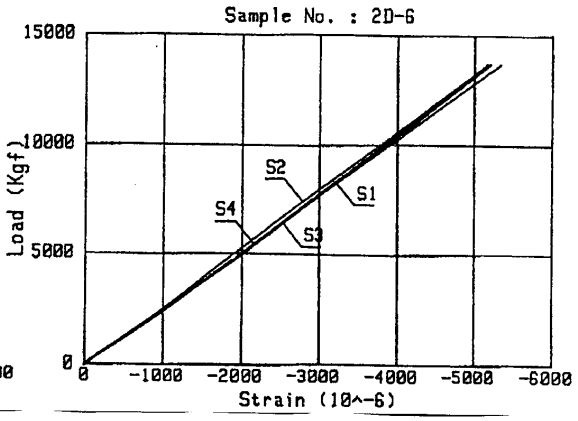

Fig. 4-10 Stress-Strain Curves in CAI Test (2-D Specimen, 2000in-lb-in)

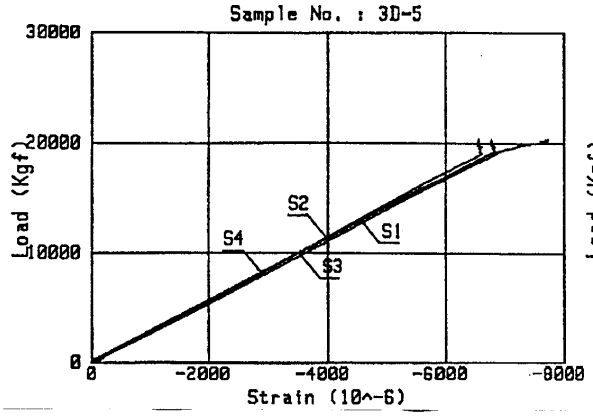

Fig. 4-11 Stress-Strain Curves in CAI Test (3-D Specimen, 1500in-lb-in)

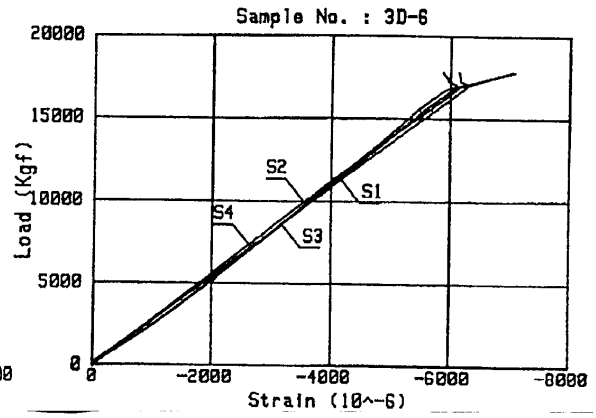

Fig. 4-12 Stress-Strain Curves in CAI Test (3-D Specimen, 2000in-lb-in)

Table 5-1 Test Results of the 3-D and 2-D Composites

Specimen Type		Thickness [mm]	Vf [%]	Modulus [GPa] mean : s.d.		Poisson's Ratio mean : s.d.		Strength [MPa] mean : s.d.	
Tension Test	2-D	2.30	64.0	61.26	0.50	0.340	0.01	876.0	24.0
	3-D	2.10	54.5	57.63	3.10	0.246	0.01	823.1	23.0
Compression Test	2-D	2.30	63.6	50.55	3.20	0.266	0.06	665.1	38.0
	3-D	2.10	54.5	50.67	5.00	0.196	0.02	574.9	32.0
CAI Test (1500in-lb-in)	2-D	5.04	56.9	51.21	—	—	—	266.8	—
	3-D	5.04	56.5	54.54	1.60	—	—	393.4	26.0
CAI Test (2000in-lb-in)	2-D	5.04	56.9	50.71	—	—	—	260.0	—
	3-D	5.04	56.5	54.20	1.60	—	—	344.3	26.0

EVALUATION OF THE ELASTIC PROPERTIES OF FIBER REINFORCED COMPOSITES BY THE VARYING-SPAN METHOD

S. Javad Jalali and Farid Taheri

Department of Civil Engineering, Technical University of Nova Scotia
Halifax, Nova Scotia, Canada B3J 2X4

SUMMARY: Fiber reinforced plastic composites suffer from low shear modulus. Therefore, when such materials are subjected to three- or four-point bending tests, the predicted longitudinal modulus will include the effect of shear deformation, except when the specimen has a large span to depth ratio (*L/h*). This characteristic was used by the authors to introduce the potential of a new methodology for the simultaneous evaluation of the longitudinal and shear moduli (*E* and *G*) of composite materials [1]. In the present work, the proposed testing method is used to evaluate the properties of graphite/epoxy and Kevlar/epoxy composites. The effect of variable strain rates which is inherent in the method is also studied, and the results are presented. The results agree very well with those obtained by the other methods thereby confirming the integrity, efficiency and the reliability of the proposed method. The reliability of the method is also investigated and confirmed by the statistical means.

KEYWORDS: composite materials, fiber reinforced plastics, testing methods, tensile modulus, through-the-thickness shear modulus, shear modulus, varying-span method.

INTRODUCTION

Fiber reinforced plastic composites (FRPC) can be classified as orthotropic materials with 9 independent elastic constants. Referring to Fig. 1, these constants are the elastic Moduli (E_{11}, E_{22}, E_{33}), the Poisson's ratios (ν_{12}, ν_{13}, ν_{23}), and the shear moduli (G_{12}, G_{13}, G_{23}) in orthogonal directions. To evaluate these properties several methods have been developed and used. However, only a few methods have gained popularity in practice. For instance, the standard procedure for evaluating tensile modulus and strength and the Poisson's ratio of FRPC is to subject a flat and rectangular specimen to direct tensile loading (ASTM D3039-93). One must, however, ensure that any bending due to misalignment of the specimen and/or the system itself is minimized. The specimens must be tabbed at the grip regions to ensure that they will not fail prematurely due to stress concentration. Moreover, hydraulic grips (very costly) are often required when testing moderately thick laminates.

Due to the above stringent requirements, and the simplicity and ease offered by a flexural test, ASTM flexural test method D790M-93 has gained a special popularity in industry. However, due to the shear coupling effect, the flexural modulus obtained by this method for specimens with small span to depth ratios (*L/h*) is not reliable . To eliminate this problem, Zweben et al. [2] suggested the use of specimens with *L/h*>60 . The flexural modulus obtained for specimens with the aspect ratios greater than 60 agrees well with the result of the tensile test [3], however the flexural strength are usually more than the tensile strength obtained by the

tensile test. The latter difference should not be construed as a shortfall of the method. Indeed, most structures are subjected to flexural loading in service. Therefore, the response of the material in flexural test is actually very close to its condition in service.

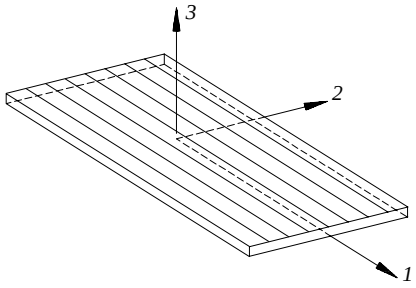

Fig.2: Definition of material principal axes for a lamina.

The most accurate results for the shear properties are believed to be obtained by applying a torsion load to a thin wall tube specimen [4]. Nevertheless, because of the difficulty involved in the preparation of the tubular specimen, other methods are usually employed in industry. The most common methods for the evaluation of shear properties are rail shear test [5] (ASTM D4255M-83), 10^o off-axis [6], $\pm 45^o$ tensile test [7] (ASTM3518-94), Iosipescu [8] (ASTM D5379-93), and the short-beam [9] (ASTM D2344-84) shear test. Among these methods, with the exception to the short-beam and the Iosipescu shear tests, non of the others can be used to evaluate the out-of-plane properties of FRPC. Moreover, the short-beam shear test can provide only an apparent through-the-thickness shear strength of a material, while the Iosipescu shear test requires a specimen with minimum thickness of 20 mm (hence, difficult to prepare). The shortfalls identified above indicate a distinct requirement for a more practical test method capable of evaluating the through-the-thickness shear modulus of FRPC. An in depth overview of the advantages and disadvantages of the above test methods was presented in Ref. 1 and 10.

In summary, common to most of the available test methods, the specimens are not subjected to a combined state of stresses that they often experience during their service. Therefore, the evaluated properties from these methods may not represent the true in service behavior of the materials. The ideal test method would have the following additional capabilities and attributes.

1- would use specimens extracted directly from as-received materials.
2- would use specimens with simple geometry.
3- would not require additional alteration and machining of the specimen.
4- would use a simple fixture, without elaborate mounting requirement.
5- would not require strain gages and/or other expensive instrumentation.
6- would produce reliable results.
7- would be capable of providing several properties from the same set of tests.

The proposed method in this work is believed to have most of the desired attributes of the above list. The method is based on subjecting rectangular specimens with different span to depth ratio (L/h) to three-point bending. Therefore, the proposed test method is referred to as "the Varying-Span Method" (VSM), hereafter. Both longitudinal modulus and the through-the-thickness shear modulus of the specimens along with the flexural and interlaminar shear

strengths can be obtained from the recorded data. A detailed discussion of the parameters influencing the accuracy and the efficiency of this method presented is presented in Ref. 1. Here, after a short review of the relevant theories, we will examine the influence of different strain rate (for different *L/h*) imposed by the proposed method on the properties of graphite/epoxy and a Kevlar/epoxy FRPC. The properties evaluated under this situation are reported and are compared with those obtained by other methods.

THEORY

In our previous work [1] two different approaches for evaluating the properties of FRCP were examined. In one of the approaches the application of the through-the-thickness inextensibility was discussed. This approach is believed to provide more accurate results in comparison to the other approach. However, it is associated with elaborated mathematics, and it has lengthier procedure. The second approach is based on the application of Timoshenko beam theory [11]. This approach, though not as accurate as the first approach, is however, more straight forward. A review of the second procedure and its theory is presented.

Consider a simply supported specimen carrying a concentrated load at mid-span that is subjected to three-point bending (Fig. 2a). Since the localized deformation under the concentrated load and also at the supports cannot be predicted by the Timoshenko beam theory, we define the net mid-span deflection as follows

$$\Delta = \Delta_A - \Delta_B \tag{1}$$

where Δ_A and Δ_B are the displacements of points A and B in the *z* direction, respectively. To compensate for the effect of the concentrated load and the reaction forces on the net mid-span deflection, we assume the load and the reactions are applied over a finite length (for a comprehensive discussion on this matter see Ref. 12).

In Timoshenko beam theory the total deflection is composed of the portion that results from flexure of the beam and the other portion resulting from its shear deformation. They can be calculated separately, and the net deflection at mid-span can be written as:

$$\Delta = \Delta_{Flexural} + \Delta_{shear} \tag{2}$$

Referring to Fig. (2b), one can represent the components of the deflections by

$$\Delta_{flexural} = \frac{F}{48EI}\left(L^3 - 2\bar{b}^2 + \bar{b}^3\right) \tag{3}$$

$$\Delta_{shear} = \frac{3F}{10AG}\left(L - 1.5\bar{b}\right) \tag{4}$$

Substituting these equations into Eqn 2 gives

$$\Delta = \frac{F}{48EI}\left(L^3 - 2\bar{b}^2 + \bar{b}^3\right) + \frac{3F}{10AG}\left(L - 1.5\bar{b}\right) \tag{5}$$

where I and A are the moment of inertia and the area of the beam section, respectively. The value of $\bar{b}$ plays an important role in the accuracy of the results, and it is more convenient to set it as a fraction of the beam depth.

$$\bar{b} = \alpha\ h \tag{6}$$

The value of α is not constant and depends to the geometry of the specimen and the properties of the material. The exact value of α can be obtained from the graphs presented in Ref. 1. However, pre requisite to use of the graphs is the knowledge of the material properties. If no data exists, admissible values can be obtained by the rule of mixture. Nevertheless as it was shown in Ref. 1, for practical purposes the use of an approximate value α=0.7 can produce reliable results. When the width to depth ratio of the specimens are approximately 5, the expected errors with this assumption will be lower than 0.5% for E and lower than 4.5% for G. With some manipulations one can write Eqn 5 in the following form.

$$\frac{1}{E'} = \frac{1}{E} + \frac{1}{G} J\left(\frac{h}{L}\right)^2 \tag{7}$$

where

$$E' = \frac{F}{4\Delta b}\left[\left(\frac{L}{h}\right)^3 - 2\alpha^2 \frac{L}{h} + \alpha^3\right] \tag{8}$$

$$J = 1.2\frac{\frac{L}{h} - 1.5\alpha}{\frac{L}{h} - 2\alpha^2 \frac{h}{L} + \alpha^3\left(\frac{h}{L}\right)^2} \tag{9}$$

and b is the width of the beam. In the above, E' is the apparent modulus of elasticity that includes the shear effect. Therefore, E' is not a constant value and changes as a function of the span. E' value, however, approaches E when L/h ratio becomes reasonably large. J is always smaller than 1.2 and approaches to this value for large L/h.

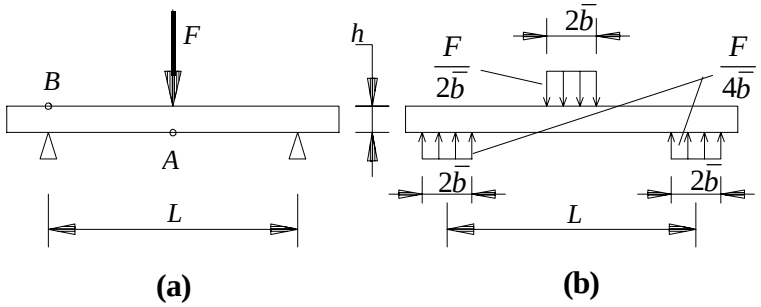

Fig. 2: Equivalence of the concentrated and the reactions forces with uniformly distributed loads.

Equation 7 as outlined in Fig. 3 is the equation of a line that will be referred to as the "characteristic line" of the material hereafter. The intercept and the slope of this line represent $1 / E$ and $1 / G$ of the material, respectively. Therefore, for establishing the characteristic line of a material one needs to perform at least two flexural tests (Fig. 2a), on specimens with

different spans. The slope of the load-deflection curve of each test provides a F/Δ value for Eqn 8, from which one can calculate the E' value that corresponds to a specific value of $J(h/L)^2$. Since each test produces a point in the coordinate system of Fig. 3, having the results of two tests, theoretically, enables one to define the properties of the characteristic line. However, to improve the accuracy and the reliability of the results, it is necessary to do more than two tests and therefore, one needs to employ a linear regression analysis to obtain the best fitted line.

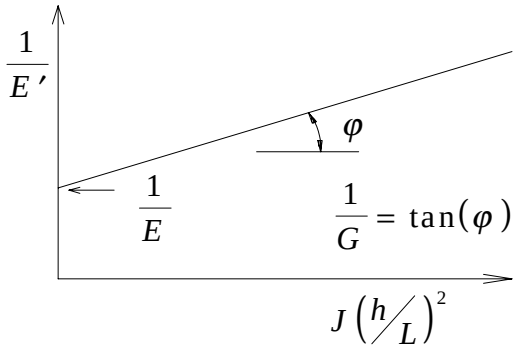

Fig. 3: The characteristic line of the material

EXPERIMENTAL WORK

The proposed method was examined by conducting a series of tests on 0^o unidirectional graphite/epoxy and Kevlar/epoxy specimens. The specimens of graphite/epoxy were cut from 300×300 mm hand lay-up panels composed of 24 layers of Fiberite graphite/epoxy prepreg. The panels were vacuum bagged and were cured in an autoclave with the curing cycle specified by the supplier of the prepreg. The panels were then cut into strips of approximately 12.5 mm width from which the specimens with different lengths were obtained. To eliminate the excess resin rich surface layers of the specimens and also insuring uniform and smooth thickness, the specimens were sanded with No. 400 silicon carbide powder. The thickness of the specimens for the VSM varied between 2.51 and 2.72 mm. The same procedure was followed to prepare the specimens for tensile tests. Three specimens with 25 mm width were also cut from a cross ply laminate panel at angle 45^o for the ASTM $\pm 45^o$ shear tests. The thickness of the specimens for the tensile test was between 2.33 and 2.51 mm and for the $\pm 45^o$ shear test it varied between 2.41 and 2.51 m. The specimens of Kevlar/epoxy were cut from a 150 mm pultruded panel with an average thickness of 1.9 mm. The width of the specimens was about 12.5 mm. No sanding or polishing was applied.

The specimens were tested by the use of a special apparatus designed and fabricated for the VSM at Technical University of Nova Scotia (TUNS). The apparatus enabled us to accurately measure the net mid-span deflection as a function of the applied load. The loading was applied by an universal MTS testing machine.

As it was mentioned in our earlier work [1], it is not possible to maintain a constant strain rate (for different L/h) for both the longitudinal and the shear deformations, simultaneously, in the VSM. To ensure a constant strain rate for the longitudinal strain, the net mid-span deflection rate must vary according to the following equation

$$\dot{\Delta} = \dot{\varepsilon}_{\max} L \left[0.2 \frac{E}{G} \frac{h}{L} + \frac{1}{6} \frac{L}{h} \right] \tag{10}$$

where $\dot{\varepsilon}_{\max}$ is the strain rate at the outermost layer of the specimen. To produce a constant shear strain rate the following relation must hold

$$\dot{\Delta} = \dot{\gamma}_{avr} L \left[0.6 + 0.5 \frac{G}{E} \left(\frac{L}{h} \right)^2 \right] \tag{11}$$

where $\dot{\gamma}_{avr}$ is the average shear strain rate of the section. It should be noted that a constant net mid-span deflection could not be maintained by our loading machine; consequently, the deflection rates from Eqns 10 and 11 were directly used to establish the speed of the actuator for each test. Eqns 10 and 11 indicate that in order to produce a constant longitudinal or shear stain rates a knowledge of the approximate value of *E/G* is necessary. It should be noted that the results are not very sensitive to this parameter. In fact, our analysis indicated that for *L/h* ≅30, under a constant longitudinal strain rate, a large variation in the assumed value of *E/G* did not appreciably change the resulting speed of the actuator. However, for *L/h*≅5.5 the speed for *E/G*=30 is only 1.5 times of what is required for *E/G*=10. This difference in the speed of the actuator cannot have a considerable effect on the results of common composite materials which, in general, are not very strain rate sensitive. Furthermore, it is instructive to note that the pre-assumption of *E/G* value is not a difficult task. Such a value can be obtained with a reasonable accuracy from relevant literature and/or by the use of the rule of mixture. Nevertheless, several tests were conducted to establish the validity of the claims made on the effect *E/G* and also the influence of the strain rate as obtained by Eqns 10 and 11. The variables for all tests are tabulated in Table 1.

Table 1: Test variables for different sets of specimens

Designation	Material	Equation	E/G	$\dot{\varepsilon}_{\max}$	$\dot{\gamma}_{avr}$
GR-1	Graphite/epoxy	10	30	0.01	var.
GR-2	Graphite/epoxy	10	30	0.01	var.
GR-3	Graphite/epoxy	10	10	0.01	var.
GR-4	Graphite/epoxy	11	30	var.	0.01
K-1	Kevlar/epoxy	10	30	0.01	var.
K-2	Kevlar/epoxy	10	30	0.01	var.
K-3	Kevlar/epoxy	10	10	0.01	var.
K-4	Kevlar/epoxy	10	10	0.01	var.
K-5	Kevlar/epoxy	11	30	var.	0.01
K-6	Kevlar/epoxy	11	30	var.	0.01

Each sets of specimens were tested with 5 different spans. At least three specimens were tested for each span. Each specimen was tested twice. In the first test, depending to the linearity limit, the specimen was loaded to about 50% to 80% of its failure load. The test was stopped before the specimen showed significant nonlinearity. In the second test, the specimen was loaded to failure. The initial slope of the load-deflection curve of each test was evaluated. This value was used to represent F / Δ in Eqn 10 and its corresponding E' was calculated. A plot of $1/E'$ versus $J(h/L)^2$ for the results obtained from the first time loading is presented

in Fig. 4. A similar plot was obtained for the results of the second time loading, however for the sake of brevity the plot is not presented in here. The *E* and *G* value obtained from different sets of specimen are presented in Table 2 and 3. As stated earlier, an approximate value of α=0.7 was used for all cases.

The overall distributions of the data points in Fig. 4, for both materials, present a linear trend, therefore, confirming the applicability of the proposed method for the selected materials. Furthermore, the results do not indicate an obvious dependency to the different situations tabulated in Table 1. Consequently, it can be concluded that the varying strain rate imposed by the proposed test method did not influence the results. The selected speeds of the actuator used for testing three different sets of beams having L/h<15 were comparable. For L/h≅30, the required speed of the actuator to produce a constant shear strain rate for E/G=30 was about 3 times higher than that required for maintaining a constant longitudinal strain rate. This ratio approaches to 9 for E/G=10. However, since in specimens with large L/h only a very small portion of the deflection is due to the shear deformation, thus, the significance of maintaining a constant shear strain rate vanishes. On the other hand, the importance of constant longitudinal strain rate increases as L/h becomes large. It should be noted that based on the application of the proposed method, there is no apparent relation between the properties obtained for the selected materials and the various strain rates that was imposed during testing. However, it is recommended that Eqn 10 (along with an appropriate value of E/G) be used for general purposes.

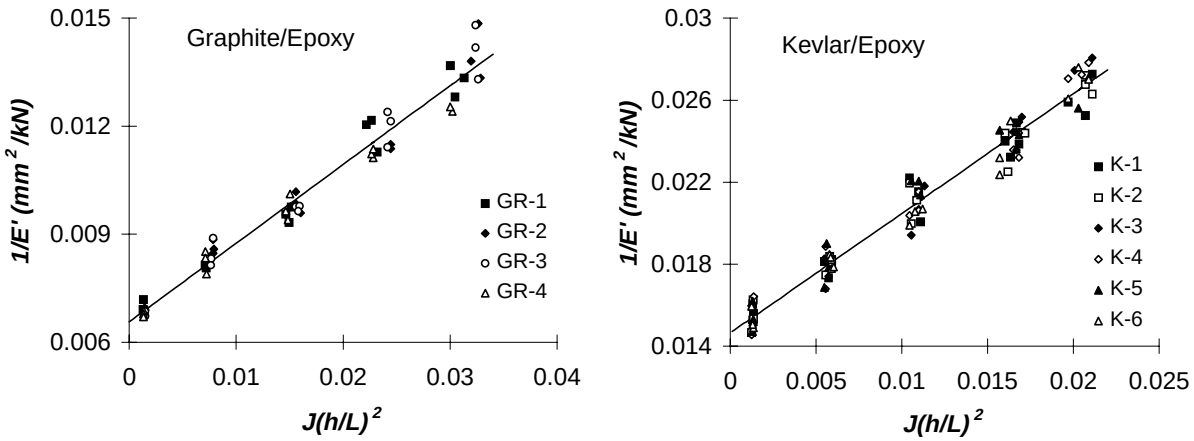

Figure 4: Plot of $1/E'$ *versus* $J(h/L)^2$

Table 2: G_{13} and E_{11} of Graphite/epoxy (GPa)

	First loading				Second loading			
Designation	GR-1	GR-2	GR-3	GR-4	GR-1	GR-2	GR-3	GR-4
E_{11}	151.9	150.8	155.8	149.4	151.0	153.1	156.4	151.0
G_{13}	4.55	4.59	4.32	5.07	4.87	4.7	4.44	4.88

Table 3: G_{13} and E_{11} of Kevlar/Epoxy (GPa)

	First loading						Second loading					
Group	K-1	K-2	K-3	K-4	K-5	K-6	K-1	K-2	K-3	K-4	K-5	K-6
E_{11}	66.9	67.9	69.7	68.3	67.6	69.4	66.0	68.4	68.9	67.6	67.4	68.3
G_{13}	1.82	1.75	1.59	1.71	1.73	1.68	1.76	1.62	1.58	1.69	1.68	1.73

For comparison and validation of the results of the longitudinal and shear moduli obtained by the proposed method, other standard test methods were also used. The longitudinal modulus of the materials were obtained according to ASTM D3039-93 Tensile Test. The in-plane shear modulus (G_{12}) of graphite/epoxy and Kevlar/epoxy were evaluated by the ASTM $\pm 45^o$ and 10^o off-axis shear tests, respectively. As it was mentioned earlier, there exists no simple and practical method for evaluating the out-of-plane shear modulus (G_{13}) of the materials to be used for comparing the results of the proposed method. Theoretically, if the distribution of fibers through the thickness and through the width of the laminate follows the same pattern, G_{13} and G_{12} should be equal. However, in practice the situation may not be as ideal. Moreover, in hand lay-up laminates, the layer interfaces are more susceptible to defects and therefore, a smaller out-of-plane shear modulus (G_{13}) can be expected. A summary of the results of these tests and the results obtained by the VSM are reported in Table 4. The E_{11} and the G_{13} of the VSM in this table were evaluated from the results of all the specimens. The 95% confidence bands are also reported for the results of this method. The small confidence bands confirm the reliability of the proposed method. Furthermore, as the values reported in the table show, the results obtained by the proposed method are in good agreement with those obtained by the other methods. Although the small discrepancy is quite acceptable for practical purposes, one may expect the difference to be the result of the followings:

- In tensile test, the results can be influenced by the effect of the possible bending due to specimen and/or system misalignment.
- The shear modulus obtained by the proposed method is G_{13}, however the results of the other methods are G_{12}. As explained, these values differ from one another, slightly.
- None of the shear test methods used in here is considered to be an exact method.
- 10^o off-axis shear test generally gives higher value, except for specimens with very large aspect ratios [13,14].
- The fabricated fixture for the varying-span method is in its preliminary stage. Further modification and enhancements are necessary.

Table 4: Summary of the results obtained from different testing methods and 95% confidence bands (GPa)

	Graphite/epoxy			Kevlar/epoxy		
	1st loading VSM	2nd loading VSM	other methods	1st loading VSM	2nd loading VSM	other methods
E_{11}	152.4±4.5	153.1±2.9	150.8	68.3±1.3	67.8±1.3	66.6
G_{13}	4.57±0.22	4.69±0.15	—	1.72±0.06	1.68±0.07	—
G_{12}	—	—	4.87	—	—	1.90

SUMMARY AND CONCLUSIONS

Among several test methods developed and used for the evaluation of elastic constants and the corresponding strength of fiber reinforced plastic composites (FRPC), three- and four-point bending tests are unique due to several inherent properties. These methods use a simple fixture to host specimens with simple rectangular geometry, and they do not require additional machining or tabbing. No strain gauge or other expensive instrumentation and/or grips are required either. However, since FRPC suffer from low shear modulus, therefore, the evaluated longitudinal modulus by these methods depends on the span to depth ratio (L/h) of the specimen used in testing. This characteristic of FRPC was used to develop a new method for

simultaneous evaluation of their longitudinal and shear moduli. The proposed method uses specimens with simple rectangular geometry and different spans, and therefore, the method is referred to as "the varying span method" (VSM). This method was used to evaluate the longitudinal and shear moduli of unidirectional 0^o graphite/epoxy and 0^o Kevlar/epoxy. The effect of different strain rate (for different *L/h*) that is inhered in this method was investigated by performing tests under three different situations, with the results presented in Table 1. No obvious dependency was observed between the obtained moduli, and the different situations. However, in general, the use of Eqn 10 which ensures a reasonable constant strain rate is recommended. The 95% confidence band of the evaluated values along with the close agreement of the results with those obtained by the other methods validate the integrity and the reliability of the proposed method.

ACKNOWLEDGMENT

The work presented was supported by a scholarship of the Ministry of Culture and Higher Education of Islamic Republic of Iran to the first author, and NSERC operating grant No. OGP0090736, awarded to the second author. The authors are grateful to these agencies. Acknowledgment is also due to Advanced Material Engineering Center (AMEC) for providing us with the use of their facilities and raw materials. Special thanks goes to Mr. Mike Pineo for his assistance. TW Pultrusion Ltd. is also acknowledged for providing us with material.

REFERENCES

1. Jalali, S.J. and Taheri, F., "A New Test Method for Measuring The Longitudinal and Shear Moduli of Fiber Reinforced Composites," Submitted for publication to J. Composite materials, 1997.

2. Zweben, C., Smith, W.S., and Wardle, M.W., "Test Methods for Fiber Tensile Strength, Composite Flexural Modulus and Properties of Fabric-Reinforced Laminates," Composite Materials: Testing and Design (Fifth Conference), ASTM STP 674, S.W. Tsai, Ed., American Society for Testing and Materials, 1979, pp. 228-262.

3. Whitney, J.M., Browning, C.E. and Mair, A., "Analysis of The Flexural Test for Laminated Composite Materials," Composite Materials: Testing and Design (Third Conference), ASTM STP 546, American Society for Testing and Materials, 1974, pp. 30-45.

4. Pagano, N.J. and Whitney, J.M., "Geometric Design of Composite Cylindrical Characterization Specimens," J. Composite Materials, Vol. 4, 1970, pp. 360-378.

5. Garcia, R., Weisshaar, T.A. and McWithey, R.R., "An Experimental and Analytical Investigation of the Rail Shear-test Method as Applied to Composite Materials," Experimental Mechanics, Vol. 20, 1980, pp. 273-279.

6. Chamis, C.C. and Sinclair, J.H. "Ten-deg Off-Axis Test for Shear Properties in Fiber Composites," Experimental Mechanics, Vol. 17, 1977, pp. 339-346.

7. Rosen, B.W., “A Simple procedure for Experimental Determination of the Longitudinal Shear Modulus of Unidirectional Composites,” J. Composite Materials, Vol. 6, 1972, pp. 552-554.

8. Adams, D.F. and Walrath, D.E., “Current Status of the Iosipescu Shear Test Method,” J. Composite Materials, Vol. 21, 1987 pp. 494-507.

9. Xie, M. and Adams, D.F., “Study of Three- and Four-Point Shear Testing of Unidirectional Composite Materials,” Composites, Vol. 26, No. 9, 1995, pp. 653-659.

10. Lee, S. and Munro, M., “Evaluation of In-Plane Shear Test Methods for Advanced Composite Materials by the Decision Analysis Technique,” Composites, Vol. 17, No. 1, 1986, pp. 13-22.

11. Timoshenko, S.P. and Gere, J.M., Mechanics of Materials, 1972, Van Nostrand Reinhold Company, New York.

12. Jalali, S.J. and Taheri, F., “An Analytical Solution for Cross-Ply Laminated Plates Under Cylindrical Bending Based on Through-the-Thickness Inextensibility, Part I- Static loading,” to be published, Int. J. Solids and Structures, 1997.

13. Pindera, M.-J. and Herakovich, C.T., “Shear Characterization of Unidirectional Composites with the Off-Axis Tension Test,” Experimental Mechanics, Vol. 26, 1986, pp. 103-112.

14. Pindera, M., Choksi, G., Hidde J.S. and Herakovich, C.T., “A Methodology for Accurate Shear Characterization of Unidirectional Composites,” J. Composite Materials, Vol. 21, 1987, pp. 1164-1184.

EXPERIMENTAL BEHAVIOR OF GRAPHITE-EPOXY PANELS WITH HOLES UNDER BIAXIAL COMPRESSION AND SHEAR LOADS

Giulio Romeo and Giacomo Frulla

Department of Aerospace Engineering,
Politecnico di Torino, Corso Duca degli Abruzzi 24, 10129 Torino, Italy

SUMMARY: The buckling and postbuckling behaviour of rectangular panels with cutouts loaded in compression and shear is investigated. With respect to most of the analytical and experimental results found in the open literature, which consider panels loaded in uniaxial compression or shear, several tests were carried out on graphite/epoxy panels with cutouts subjected to uniaxial compression, biaxial compression and biaxial compression with shear. From the comparison of the results between the panel tested with and without cutouts, it has been noted that uniaxial and biaxial tests showed a little reduction in the buckling load with increasing diameter-to-width ratio; biaxial compression and shear loading test showed a wider reduction in the critical load. Furthermore, the out of plane deflection is higher in the biaxial compression and shear loading tests than in the biaxial compression test only. The buckling mode doesn't seem to be modified by the presence of the cutouts; indeed, in one case of uniaxial compression, the mode deflection changed from one to two half-waves at high postbuckling load level, in presence of the hole. Longitudinal membrane strains are reduced in proximity of the cutout edge in the postbuckling regime for all loading cases; indeed, a very high surface strain was measured.

KEYWORDS: buckling, postbuckling, cutouts, plates, biaxial compression and shear

INTRODUCTION

Rectangular panels with holes have wide application in aerospace structural components, making access doors to systems or reducing weight of components loaded moderately.
Several papers are available in the literature on the buckling and postbuckling behavior of unstiffened and stiffened composite panels with circular holes or rectangular cutouts [1-11]. In a very exhaustive overview of past research, carried out by M.P. Nemeth [1], it has been found as cutout size, shape, ply orientation, plate aspect ratio and anisotropy can affect the buckling load; the buckling load results, for high diameter-to-width ratio, higher than the buckling load of corresponding plate without a cutout; furthermore, a noticeable postbuckling behavior of the plates, before failure occurs, was found to be dependant on the width-to-thickness ratio. A reduction in the prebuckling stiffness with increasing diameter-to-width ratio (d/W) was observed for various kind of panels, while the critical load has a different behaviour in dependence of lay-up and diameter. A continuous reduction in the buckling load was observed in unidirectional panels with an increase in d/W. A continuous reduction in the buckling load was observed in angle-ply panels up to d/W=0.33; while it increases for larger d/W ratio. This enables to the conclusion that hole diameter increments

do not always coincide with a reduction in strength of the panels and, in contrast, panels with wider holes have superior buckling performances with respect to panels without holes. Most of the experimental results found in the open literature consider panels, with ends clamped or simply-supported, under uniaxial compression or shear. Little theoretical analysis is available in literature on panels subjected to combined biaxial compression and shear loading; hovewer, no analytical and experimental results were found on such load combination. Several tests have been carried out in our University on graphite/epoxy panels applying simultaneously biaxial compression and shear loads with several combined ratios [12-16]. A nonlinear analysis was also developed for symmetric panels, without holes, under combined biaxial compession and shear loads in order to obtain the out-of-plane panel deflection in the postbuckling range. The nonlinear differential equations are expressed in terms of the out-of-plane displacement and the Airy function. They are solved with the Galerkin method for various boundary conditions, both in load or displacement control.

EXPERIMENTAL RESULTS

A new testing machine has been conceived in order to apply combined biaxial compression and shear loads [12, 16] simultaneously, built by the Italian company "AIP Studio". A maximum longitudinal load of 520 kN in compression and 400 kN in tension, a transverse compression or tension load of 200 kN and a positive or negative shear load of 200 kN can be applied to panels with dimensions lower than 1000 by 700 mm (Fig. 2f). Longitudinal load is applied by two independently controlled servo-actuators; the transverse load application system, which is made up of two independently controlled servo-actuators, floats in order not to interfere with the longitudinal and shear loads. Shear load is applied to thc bottom end of the panel by a servo-actuator. The test rig is completely loop-controlled via electronic modules which are closed by 9 transducers. Hovewer, since the five servo-actuators may be controlled separately, the test rig can apply different load configurations than those reported above; it also may be possible to apply longitudinal or transverse loadings having a triangular or trapezoidal shape along the panel ends and sides. The machine can operate both in load or displacement control.

The panel boundary conditions assumed ends to be clamped and sides simply-supported. The effective panel length and width are 880mm and 580mm; the width between the bolt lateral line is 620mm; the panel lay-up is: $(45/0_4/-45/90)_{3s}$ with a thickness of 8.726mm (Specimen BS1).

Furthermore, a classical test has been carried out on smaller panels (452mm long and 301mm wide) loaded in uniaxial compression with a 200 kN capacity testing machine. The panel boundary conditions assumed ends and sides simply-supported. The effective panel length and width are 418mm and 264mm; the panel lay-up is: $(0_4/45_3/-45_3)_s$ with a thickness of 2.547mm (Specimen no. 11).

Panels were manufactured using graphite/epoxy material and were vacuum bagged and autoclave cured. The pre-pregs T300/5208 Narmco and T300/985 Cycom were used for manufacturing panels no. 11 and BS1, respectively.

Material properties used in the analysis were experimentally determined to be:

T300/5208: $E_1 = 147.2GPa$; $E_2 = 9.6GPa$; $G_{12} = 3.80GPa$; $\nu_{12} = 0.298$

T300/985: $E_1 = 124.0GPa$; $E_2 = 8.3GPa$; $G_{12} = 5.60GPa$; $\nu_{12} = 0.30$

Central circular cutout, 100 mm of diameter, was machined into panels n. 11 corresponding to d/W = 0.33. Rectangular cutouts were machined into panel BS1 having a radius at corner of 25 mm; in a first attempt cutout dimensions were 152 mm long and 100 mm wide (corresponding to a fictitius d/W = 0.16); after several tests had been carried out on this panel, a wider cutout was machined up to 304 mm long and 200 mm wide (corresponding to a fictitius d/W = 0.33) in order to investigate the effect of the cutouts dimensions.

Several results are presented for the two panels. 50 back-to-back strain gauges (sg) were bonded to panel BS1 and 10 to panel 11; 10 inductive transducers (TR) were used for recording the out-of-plane panel deflection, 5 for panel 11. Buckling loads are obtained by the end-shortening curves and by the behaviour of the back-to-back strain gauges bonded in the middle of the panel, relative to the case without hole, and bonded near the hole edge in the other cases. It is known that the slope of the end-shortening curve reduces after buckling occours. Regarding the strain-gauges behaviour, it can be seen that the membrane strain ceases to be linear and tends to remain constant. Furthermore, the load versus the out-of-plane deflection curve gives, also, a good value of critical load.

Uniaxial test of panel 11

Fig. 1a shows the out-of-plane center deflection of the panel without hole, recorded by transducer TR2 placed at B/2 and L/2. A slight difference between the analytical (9.5 kN) and experimental (10.6 kN) buckling loads shows that the boundary conditions experimentally obtained along the ends are restrained slightly more than simply supported. This effect has also been observed in the experimental end-shortening curve. The longitudinal panel strain in the center (gauges n.5-6 at L/2, B/2), reported in Fig. 1e, shows the typical strain reversal behaviour of a buckled panel. Membrane strain is not more linear after buckling occurs and maintains quite a constant value in the postbuckling regime. In Fig. 1f are reported strains measured at L/2, B/4 (gauges n.3-4) very near to the edge of the hole after it has been done; buckling load (8.8 kN) is 17% lower than the load without hole. Although the membrane strain is no higher than that of the panel without hole, a very high surface strain (more than twice) has been measured. The test showed the presence of a snap change in shape from one to two half-waves at approximately five times the buckling load. Strains measured at L/4, B/2 (gauges n.9-10) are reported in Fig. 1c; it is very interesting to compare the strain behaviour without and with the hole: in the presence of the hole (Fig. 1d) the membrane strain is not quite zero until the second buckling-mode occurs. After buckling the graph reveals only a slight increase of bending strain. Fig. 1b shows the out-of-plane deflection of the panel with hole measured near the hole edge (TR0 and TR3 at L/2; TR8 and TR9 at B/2); the presence of a snap change in shape from one to two half-waves is very clear also from this figure as well as from Fig. 1g, showing the out-of-plane deflection along the panel length. Failure (Fig. 1h) happened at 6.5 times the buckling load.

Results of Panel BS1

A summary of the theoretical (no hole) and experimental buckling loads (both without and with cutouts) for panel BS1 is reported in Table I for various loading ratios. The theoretical analysis has been carried out for the panel without cutout only.

Uniaxial Test

Fig. 2a shows the out-of-plane panel deflection, recorded by transducer TR8 placed at L/2 and 102 mm side from the center, for the three panel configurations (d/W=0, 0.16 and 0.33). The presence of cutouts did not alter the buckling load; panel buckled shape corresponds to one half-wave; the presence of the cutouts have modified the out-of-plane deflection (38% higher) only at high load values in the postbuckling field. A reduction in the pre and postbuckling stiffness has also been observed from the experimental end-shortening curves (Fig. 2b), up to 33% in the worst case.
The panel longitudinal strain (gauges n.21-22 placed at L/2 and 102 mm side from the center), reported in Fig. 2e, shows the typical strain reversal behaviour of buckled panels.

Membrane strains increased with the d/W ratio, in the worst case, up to 87%; hovewer, the surface strain resulted 141% higher than the corresponding plate without a cutout. The longitudinal and transverse strains measured below the cutouts (gauges n.29-30 and 27-28 placed at B/2 and 158 mm below the center) show different effects of cutouts: while longitudinal membrane strains (Fig. 2c) reduce with the dimension of the cutout up to 72%, transverse strains (Fig. 2d) grow tremendously up to 372%, not only because of the Poisson's effect, but also because of the load flow around the cutout.

TABLE I - Buckling results for panel BS1

Applied Load Ratio			Longitudinal Buckling Load $P_x(kN)$			
N_x/N_x	N_y/N_x	N_{xy}/N_x	Analytical	Experimental		
				d/W=0	d/W=0.16	d/W=0.33
-1	0	0	-267	-275	-275	-275
-1	-.15	0	-219	-235	-235	-235
-1	-.3	0	-184	-177	-196	-177
-1	-.4	0	-166	-157	-157	-137
-1	-.15	+.5	-154	-167	-147	-127
-1	-.15	-.5	-168	-177	-167	-157
-1	-.4	+.5	-123	-117	-108	-98
-1	-.4	-.5	-132	-137	-127	-123

Biaxial test

Nine biaxial tests have been done on the panel without and with cutouts for several load ratios between the transverse and longitudinal loads (Table I). The presence of cutouts did not altere significantly the buckling load.

Experimental results for a transverse compression load of 40% of the longitudinal load are reported in Fig. 3. The presence of the large cutout (d/W=0.33) produced a 13% reduction of the buckling load with respect to the plate without a cutout. Fig. 3a shows the out-of-plane panel deflection, recorded by transducer TR8 placed at L/2 and 102 mm side from the center, for the three panel configurations; panel buckled shape corresponds to one half-wave and the presence of the cutouts did not modify significantly the out-of-plane deflection. A reduction in the pre and postbuckling stiffness has also been observed from the experimental end-shortening curves, up to 14% in the worst case. The panel longitudinal strain (gauges n.21-22 placed at L/2 and 102 mm side from the center), reported in Fig. 3d, shows the typical strain reversal behaviour of buckled panels. The longitudinal and transverse strains measured below the cutouts (gauges n.29-30 and 27-28 placed at B/2 and 158 mm below the center) show different effects of cutouts: while longitudinal membrane strains (Fig. 3b) reduced with the dimension of cutout up to 115%, transverse membrane strains (Fig. 3c) increased slightly in the pre-buckling load after, became almost zero.

The longitudinal membrane strain distribution over the cross panel mid-width is shown in Fig. 3e and 3f for two values of the applied longitudinal load; the Y coordinate across the panel is normalized by the panel width B. It can be noted that, as an effect of the buckled shape, a reduced strain was measured near the cutout edge, since the applied load is more redistribuited towards the unloaded edge, thus avoiding the very high typical strain concentration near the cutout edge.

Biaxial and shear tests

Twelve tests have been carried on the panel without and with cutouts under biaxial and shear loadings, both with positive and negative shear, for several load ratio between the transverse and longitudinal loads (Table I). The presence of cutouts altered significantly the buckling load only when a positive shear was applied to the panel (maximum reduction of 24%), while only a sligth reduction (11%) was recorded when a negative shear was applied. This effect is due to the panel lay-up. Experimental results for a transverse compression load of 40% and negative shear load of 50% of the longitudinal load are reported in Fig. 4. Regarding the out-of-plane deflection there are significant differences in the presence of the cutout; in Fig. 4a deflections, recorded by transducer TR8 placed at L/2 and 102 mm side from the center, are plotted for the three panel configurations. The deflection is more pronunced and increases with the dimension of the hole; the out-of-plane deflection, at the maximum load reached for d/W=0.33, is 98% higher than the corresponding load without cutouts. Moiré fringes shows a typical one half-wave diagonal buckled shape that seems not to be affected by the hole (Fig. 4e). Longitudinal and transverse strains measured below the cutouts (gauges n.29-30 and 27-28 placed at B/2 and 158 mm below the center) are plotted in Fig. 4b and 4c, respectively; a similar behaviour to the biaxial test was noted. High differences were recorded in strains of gauges 15-16 positioned close to the hole corner in the 45 degree direction (Fig. 4d). Membrane strains increased with the d/W ratio, in the worst case, up to 24%; hovewer, the surface strain resulted 100% higher than corresponding plate without a cutout.

CONCLUSION

The critical ratio K (ratio between critical longitudinal load with cutouts and the critical longitudinal load without cutouts) as a function of the hole ratio d/W (ratio between the cutout width and the panel width) is plotted in Fig. 4f. It can be seen for the biaxial tests, that the presence of the cutout gives, in a case, a little increment in the critical load at maximum of 11%, when the transverse load is 30% of the longitudinal load; in the most of the cases it seems to be ininfluent; in one case, when the transverse load is 40% of the longitudinal load, the cutout produces a reduction of the critical load of 13% . The biaxial and shear tests show a general reduction of the critical load with a maximum of 24% in the case of $d/W = 0.33$. It is interesting to note that the difference between positive and negative shear loading is reproduced also in the presence of the holes. More sensitivity on the buckling behaviour is observed in the biaxial and shear tests with respect to the biaxial tests only . This difference should be due to the hole shape effect that for the biaxial case is in simmetry with the load, while for the biaxial and shear case it is not. Furthermore, in the biaxial test only, it is possible that the applied load is redistribuited towards the lateral sides restrained by the fittings.

Acknowledgments: The authors aknowledge the efficacius cooperation of MSc students M. Calvetto and F. Marena.

REFERENCES

1. Nemeth,M.P., "Buckling and Postbuckling Behavior of Laminated Composite Plates with a Cutout", NASA TP 3587, NASA La.R.C., Hampton, 1996.

2. Nemeth,M.P., "Buckling and Postbuckling Behavior of Square Compression -Loaded Graphite-Epoxy Plates with Circular Cutouts", NASA TP 3007, NASA La.R.C., Hampton, 1990.

3. Nemeth,M.P., Stein,M. and Johnson,E.R., "An Approximate Buckling Analysis for Rectangular Orthotropic Plates with Centrally Located Cutouts", NASA TP 2528, NASA La.R.C., Hampton, 1986.

4. Nemeth,M.P., "Buckling Behavior of Compression-Loaded Symmetrically Laminated Angle-Ply Plates with Holes", *AIAA Journal*, Vol.26, No.3, 1988, pp.330-336.

5. Lee,H.H. and Hyer,M.W., "Postbuckling Failure of Composite Plates with Holes", *AIAA Journal*, Vol.31, No.7, 1993, pp.1293-1298.

6. Falzon,B.G. and Steven,G.P., "An experimental Investigation into the Effects of Flanged Holes in Hat-Stiffened Panels Loaded in Uniaxial Compression". *2nd Pacific Int. Conf. on Aerospace Science and Technology*, Melbourne, Australia, March 20-23, 1995.

7. Falzon,B.G., "An Investigation into the Buckling and Postbuckling Behaviour of Hat-Stiffened Composite Panels". Ph.D. Thesis, Dept. of Aeronautical Eng., The University of Sydney, 1996.

8. Yasui,Y., "The Buckling of Rectangular Composite Plates with Cutout under Uniaxial and Biaxial Compression". *Proc. Eightth Int. Conf. on Composite Materials*, Honolulu, July 15-19, 1991, Vol.I, Tsai, S.W. and Springer, G.S., Eds, pp. 4B1-4B8.

9. Ritchie,D. and Rhodes,J., "Buckling and Post-buckling Behaviour of Plates with Holes", *Aeronautical Q.*, Vol.26, No.4, 1975, pp.281-296.

10. Lin,C.C. and Kuo,C.S., "Buckling of Laminated Plates with Holes", *J. of Composite Materials*, Vol.23, 1989, pp.536-553.

11. Srivatsa,K.S. and Krisna Murty,A.V., "Stability of Laminated Composite Plates with Cut-outs", *Computers & Structures*, Vol.43, No.2, 1992, pp.273-279.

12. Romeo,G. and Frulla.G., "Buckling of Simply Supported and Clamped Anisotropic Plates under Combined Loads". *Proc. Int. Conf. on Spacecraft Structures and Mechanical Testing.* ESA-ESTEC, Noordwijk, NL, April 1991. ESA SP-321, 1991, pp. 161-166.

13. Romeo,G. and Frulla,G., "Analytical and Experimental Results of Composite Panels under Combined Biaxial Compression and Shear Loads", *Journal L'AEROTECNICA MISSILI E SPAZIO*, Vol.70, No.3-4, July-Dec. 1991, pp. 107-116.

14. Romeo,G. and Frulla,G., "Postbuckling Behaviour of Anisotropic Plates under Biaxial Compression and Shear Loads", *Proc. 18th Congress of the Int. Council of the Aeronautical Sciences (ICAS)*, Beijing, P.R. China, Sept. 1992, Vol.2, AIAA Ed., pp.1936-1944.

15. Romeo,G. and Frulla,G., "Nonlinear Analysis of Anisotropic Plates with Initial Imperfections and Various Boundary Conditions Subjected to Combined Biaxial Compression and Shear Loads", *INT. JOURNAL OF SOLIDS AND STRUCTURES*, Vol.31, No.6, 1994, pp.763-783.

16. Romeo,G. and Frulla,G., "Postbuckling Behaviour of Graphite/Epoxy Stiffened Panels with Initial Imperfections Subjected to Eccentric Biaxial Compression Loading", To be pubbl. on: *INT. JOURNAL OF NON-LINEAR MECHANICS*, 1997.

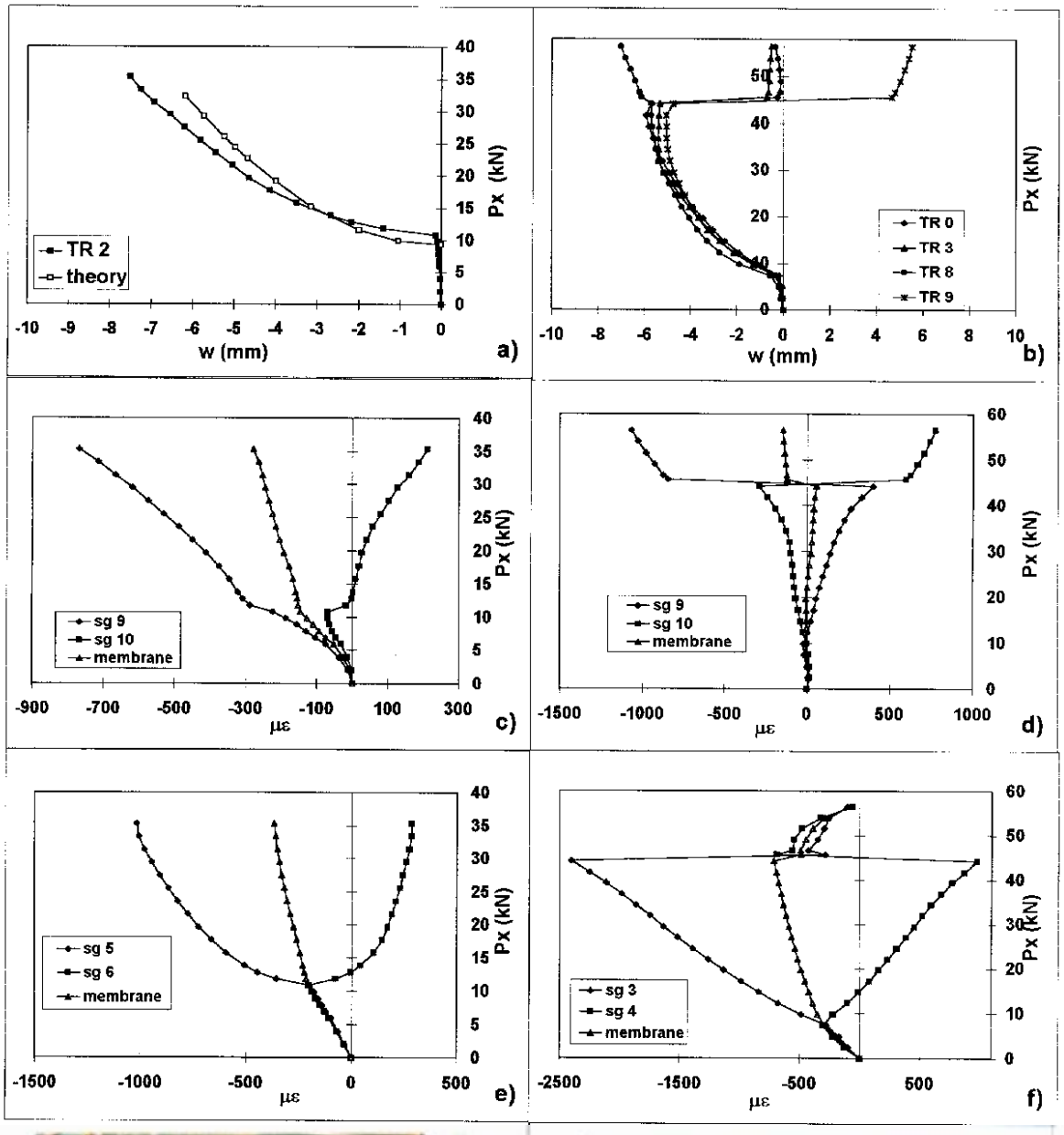

Fig. 1 : Uniaxial test results of panel n.11

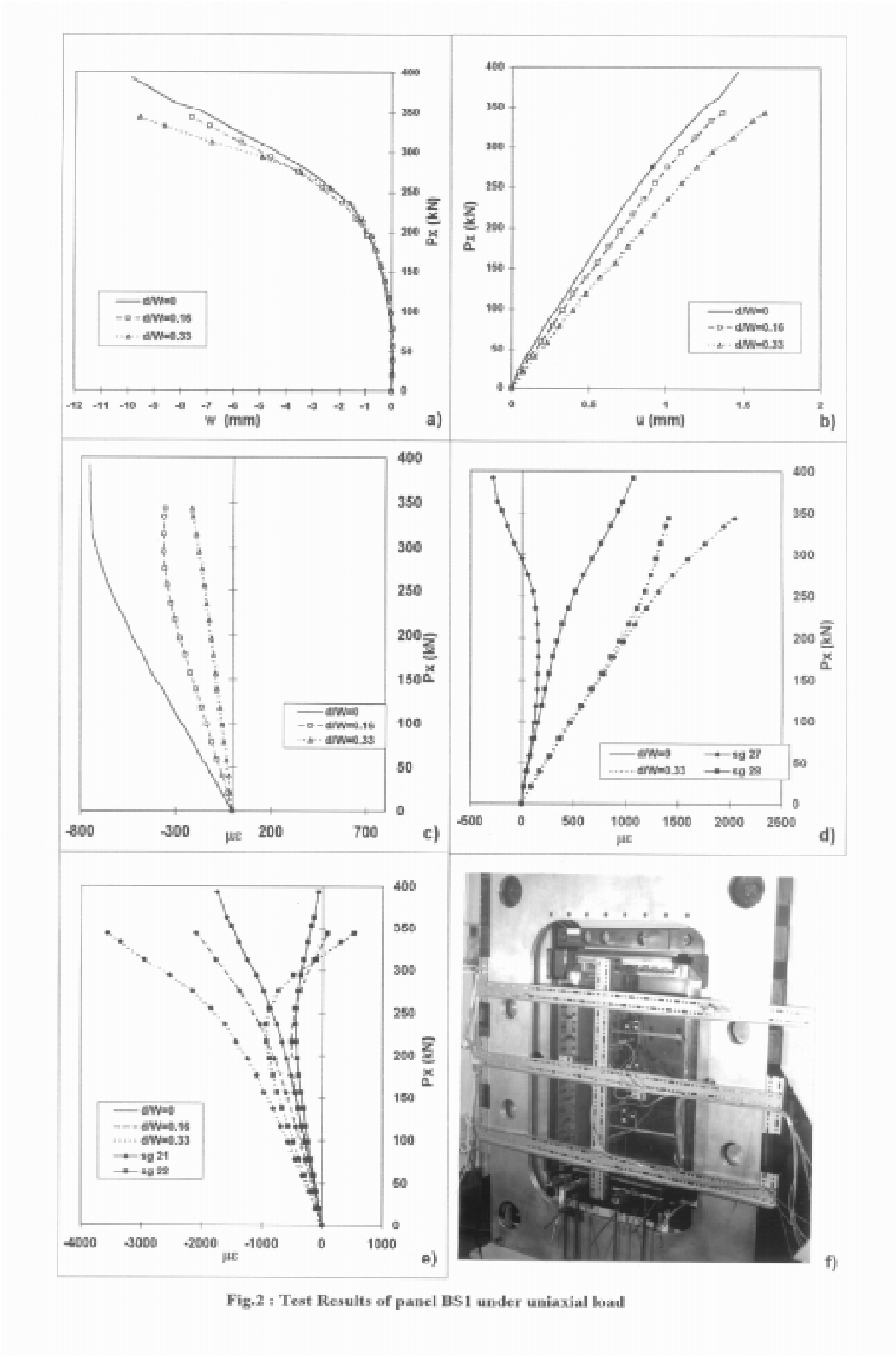

Fig.2 : Test Results of panel BS1 under uniaxial load

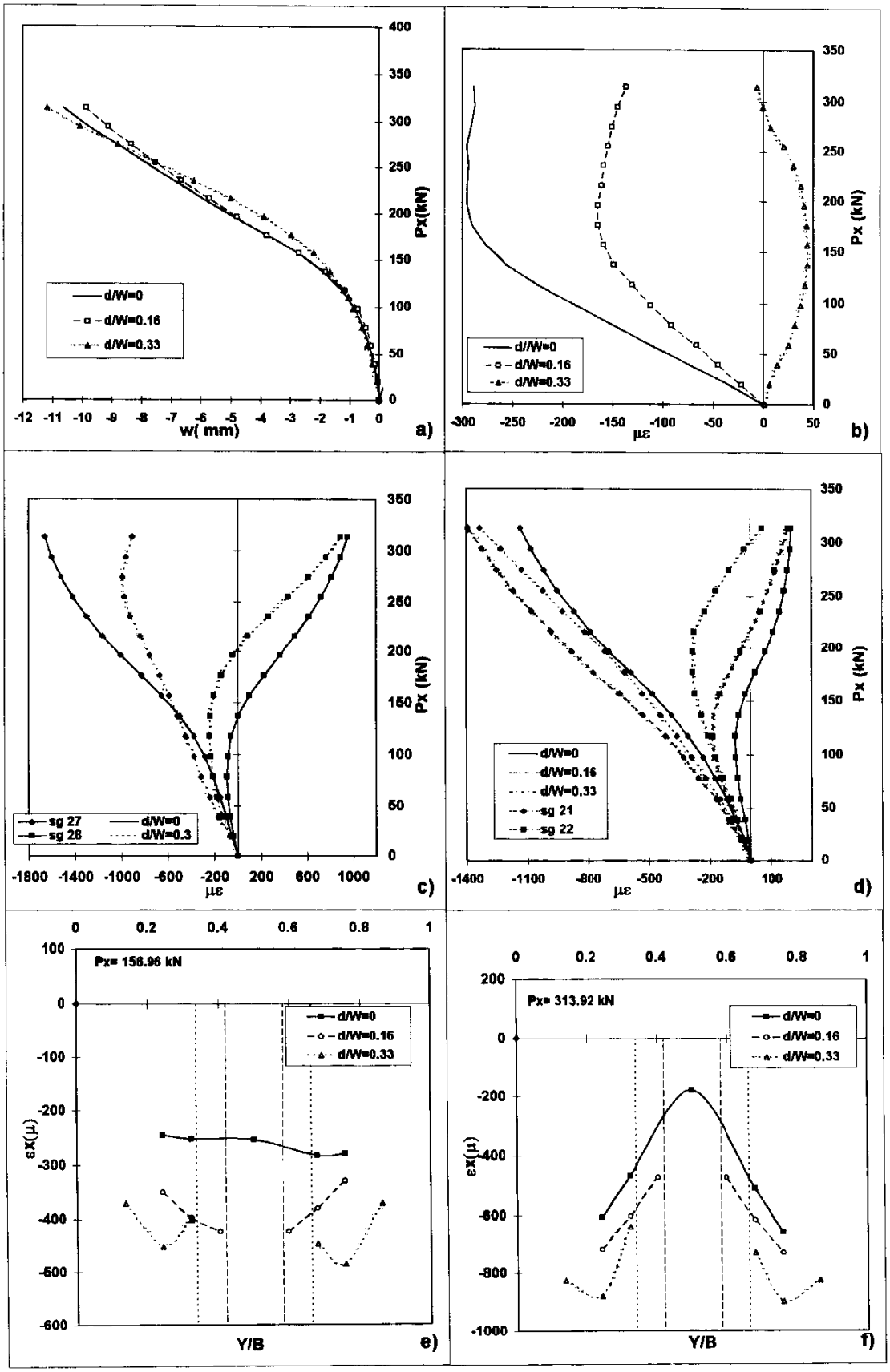

Fig.3 : Test Results of panel BS1 under biaxial load

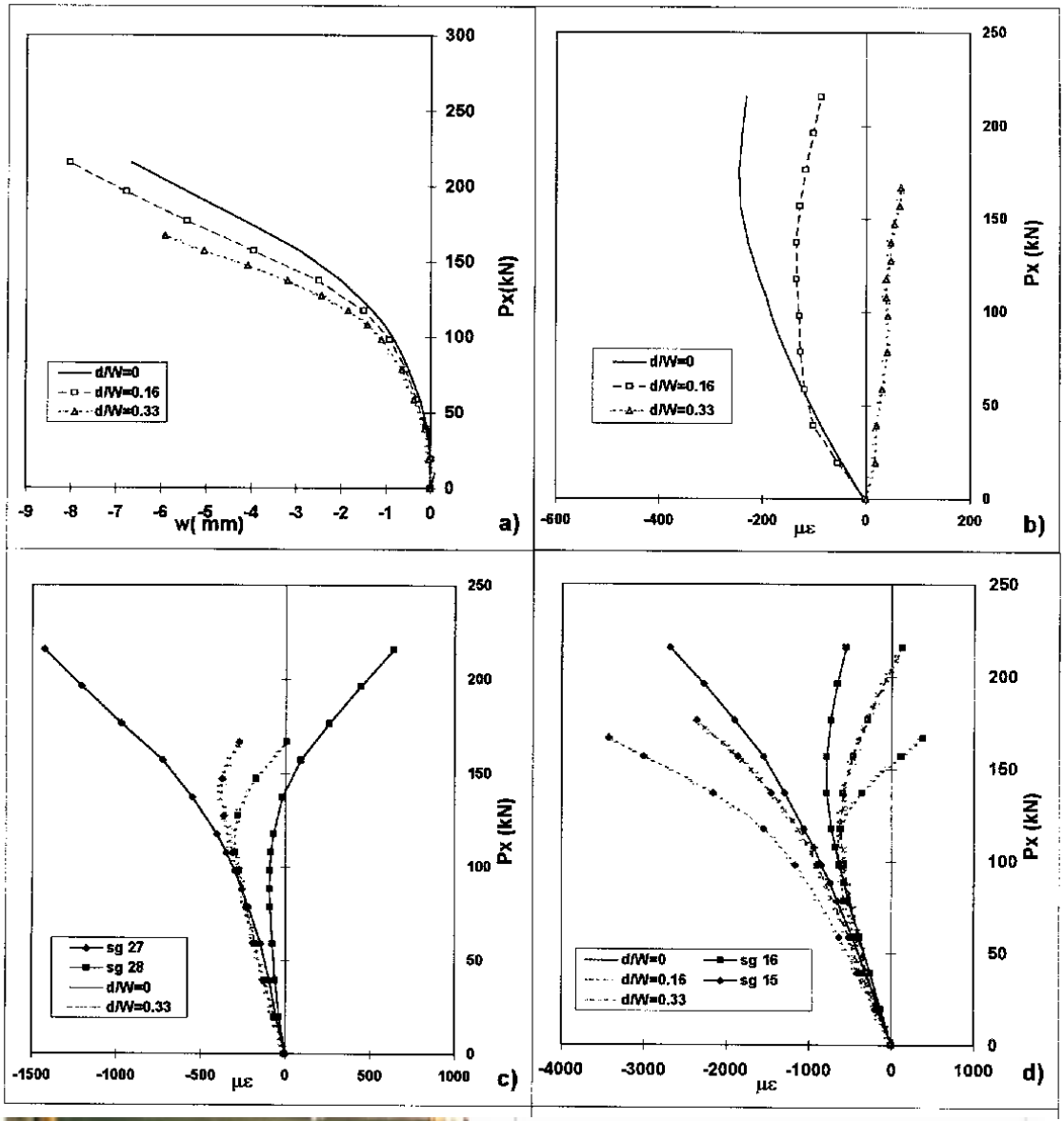

Fig.4 : Test Results of panel BS1 under biaxial compression and shear load

INFLUENCE OF COOLING RATE ON MORPHOLOGICAL AND MECHANICAL PROPERTIES OF THERMOPLASTIC COMPOSITES

Helen C. Y. Cartledge[1], Caroline A. Baillie [2] and Yiu Wing Mai [1]

[1] Centre for Advanced Materials Technology, Department of Mechanical and Mechatronic Engineering University of Sydney NSW 2006 Australia
[2] Department of Materials, Imperial College of Science, Technology and Medicine Prince Consort Road, London SW7 2BP, UK

SUMMARY: The influence of cooling rate on the Morphology (crystallinity, phases, transcrystallization) and mechanical properties (transverse flexural tensile, shear strength and modulus, Iosipescu shear strength) has been investigated for both thin films and bulk unidirectional commingled yarn GF/PA6 composites. Cooling condition from fast to slow, -60°C/min, -3°C/min and -1°C/min, were achieved at 1.5 MPa pressure. XRD and DSC techniques were used to analyse the matrix morphology. SEM observation was used to examine the fracture surfaces of the tested samples. The results indicate that a different morphology was found at each different cooling condition. When the cooling rate was shifted from fast to slow, crystallinity and the ratio of α/γ phases were increased in the PA6 matrix associated with enhanced transcrystallinity and interfacial bond. Consequently, the mechanical properties such as tensile and shear strength and elastic modulus, were improved.

KEYWORDS: GF/PA6, cooling rate, crystallinity, α and γ phases, transcrystallinity, interfacial strength, tensile and shear strength, modulus

INTRODUCTION

The mechanical properties of semi-crystalline polymer composites depend on many morphological factors including crystallinity and phases of the matrix and transcrystallinity of the interface, etc, which are determined by thermal processing. However, it is still unclear how phases of the polymers effect the mechanical behaviour of the polymer composites and how to control the morphologies during manufacturing.

The purpose of this study is to find optimum thermal processing condition for thermoplastic composites to enhance the mechanical properties of these composites. GF/PA6 is commonly used in industrial applications and was selected for this study.

EXPERIMENTAL TECHNIQUE

Materials and Manufacture

Unidirectional GF/PA6 commingled yarn with an E-glass fibre weight fraction of 60% (V_f=40%) was supplied by Toyobo Co., Japan. The consolidating process of the composites

was carried out at 245°C and 1.5 MPa pressure for 10 minutes by using a hydraulic loading hot-press machine. To obtain the different microstructures in the composites, three different cooling processes were conducted, cooled in cold water: -60°C/min, air: -3°C/min and cooled with hot press: -1°C/min with 1.5 MPa pressure. The final dimension of the samples were 200 mm X 200 mm X 4 mm.

Morphological Study

X-Ray Diffraction (XRD) and Differential Scanning Calorimetry (DSC) techniques were used to examine the effect of cooling rate on the morphology of the PA6 matrix. The influence of cooling rate on transcrystallization and microstructure of the GF/PA6 composite thin films was investigated using Polarised Optical Microscopy (POM).

Mechanical Testing

90° three point bending tests were performed according to ASTM 790M-92 to study the influence of cooling rate on the interfacial tensile strength and elastic modulus of the composites. The geometry of the specimens are 80 mm x 10 mm x 4 mm with the fibres perpendicular to the specimen length.

0° double V-notch specimens were used for Iosipescu tests according to ASTM D5379M-93 to measure the interfacial shear strength of GF/PA6 subjected in the different cooling rates. The specimens were cut with fibres parallel to the longitudinal axis-0 degree from the GF/PA6 composite. The geometry of the specimens are 80 mm long, 20 mm wide and 4 mm thick. Two 90° angle notches were cut at the specimen midlength with faces oriented at +45° and -45° to the longitudinal axis. The notches were introduced using a vertical milling machine Pacific FTV-2S with a specially designed parallel fixture. Special care was taken to use optimum cutting rates. A freshly-sharpened cutting tool was used to minimise pre-test damage and produce a sharp notch. The notch tip radius were about 120 μm.

To achieve a pure shear failure in the mid-length of the beam, the width between the two notches tips was reduced to 3 mm instead of the 12 mm which is specified by the ASTM D5379M-93 standard. Both tests were carried out on an Instron 4302 machine at room temperature. SEM observation was used to examine the fracture surfaces of the tested samples.

RESULTS AND DISCUSSION

Morphology

The results from XRD and DSC analysis indicated that crystallinity of the GF/PA6 composites strongly depend on the cooling rates. Figure 1 shows the clear different intensities between the three different cooled GF/PA6 bulk samples in the XRD tests. The area under the sharp peaks represents the crystalline volume in the composites [5]. As it can be seen from the XRD chart, figure 1, that there are two peaks appearing in all of the three cooling rates samples, α and γ phases.

In general, an orderly packed crystalline polymer has higher density than that of a loosely and random packed amorphous polymer. The more crystalline structure formed in the polymers, the more energy should be needed to damage the high density polymers.

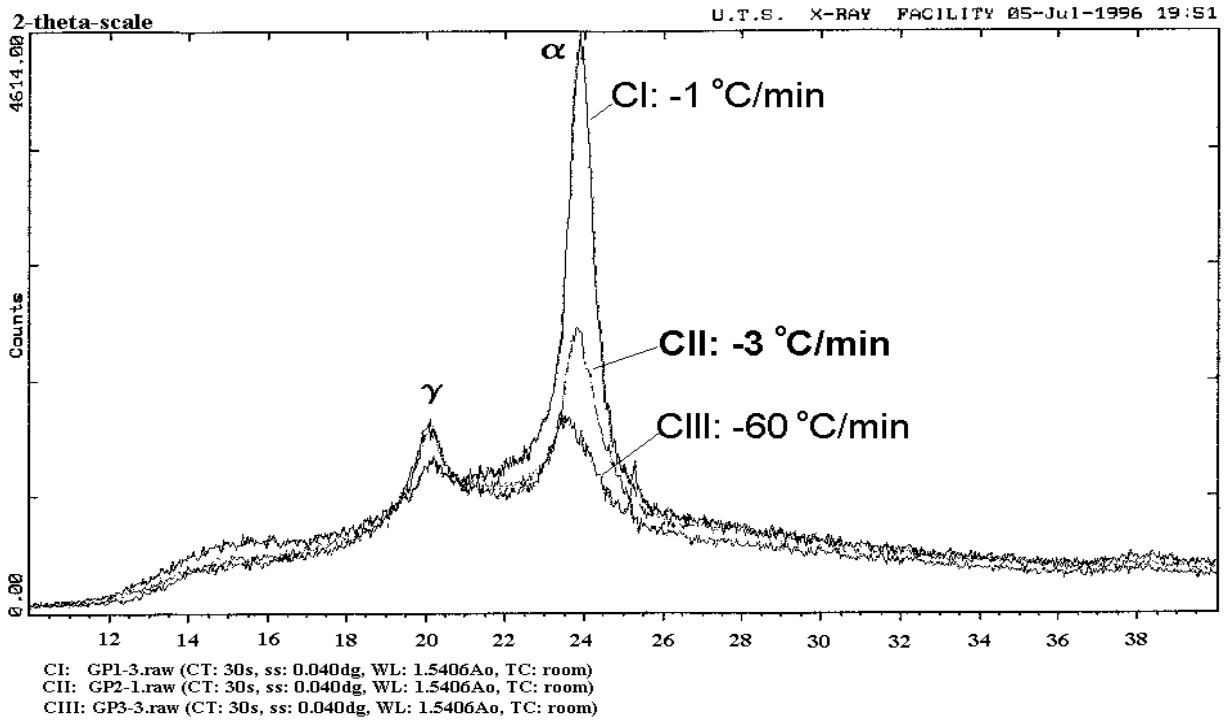

Fig. 1: X-ray chart of GF/PA6 composites subjected in three different cooling conditions

The physical properties of polymers are dominated by intermolecular hydrogen bonding and chain packing. The hydrogen bonding angle in the α crystal is bigger than that of the γ crystal so that the α chain is straighter and longer than that of γ chain. α chains are packed tighter than that of γ. Thus, the density of the α phase is higher than that of the γ phase. Therefore, when damaging an equal volume of the α and γ crystalline matrix, α phase should need more energy than that of γ phase. Table 1 shows the crystallinity and ratio of α/γ phases versus cooling rate.

Table 1: Ratio of α and γ phases and crystallinity of GF/PA6 verse cooling rate

Samples Cooling Rate	Ratio of α/γ Phases	Crystallinity of α+γ Phases
-1^{o}C/min	27	37%
-3^{o}C/min	2.6	20%
-60^{o}C/min	1.2	17%

The Polarised Optical Microscopy (POM) study of the GF/PA6 thin films shows that there are columnar spherulites growing along the glass fibre in the slowest cooled samples. It may be a transcrystalline region between the matrix and fibre. The columnar spherulite structures disappeared with increased cooling rate in the samples.

Mechanical Properties

Returning now to the mechanical tests. It can be seen that the tensile and shear strengths of the GF/PA6 composites are dramatically affected by the cooling rate. The flexural elastic modulus are effected as well. In table 2 it is shown that reducing the cooling rate lead to enhancing the strengths and modulus.

Table 2: The flexural maximum tensile strength and modulus versus cooling rate in 90 ° three point bending test, ultimate failure shear strength versus cooling rate in 0 ° Iosipescu tests.

Samples cooling rate	Flexural Test σ_{max} (MPa)	Iosipescu Test τ_{ult} (MPa)	Flexural Test E (GPa)
-1°C/min	42.89	120	4.3
-3°C/min	33.79	91	3.5
-60°C/min	25.58	79	2.4

The maximum tensile stress, σ_{max}, obtained from 90° flexural test reflects the tensile strength of the interfacial bonding. The ultimate shear stress, τ_{ult} which was obtained from 0° Iosipescu test, occurs at the midlength of the specimen and between the two notch tips. It reflects the shear strength of the GF/PA6 composite interfacial bonding. The modulus reflects the stiffness of PA6 matrix. Therefore, with increasing cooling rate interfacial bond in tension and shear is reduced.

Effect of Morphology on Fracture Mechanisms

The SEM observations show that the rupture surfaces of the flexural and Iosipescu specimens occur between the fibre and the matrix (see figs 2 and 3). Figure 2a and 2b show the fracture surfaces of the GF/PA6 samples subjected in -1°C/min and -60°C/min, respectively, at the lowest point of the midspan in flexural test. Figure 3a and 3b show the fracture surfaces of the GF/PA6 samples subjected in -1°C/min and -60°C/min, respectively, in the midplane of the midspan in Iosipescu test.

It can be seen that there is matrix tears and interfacial debonding in the fracture surfaces. There is more resin adhering to the fibres for the slower cooling rate than that of fast cooling. Thus, it can be inferred that the interfacial strength is stronger for the slowest cooling samples, verifying the previous results. It was also found in the SEM photos, figure 2a and figure 3a, that there is a large amount of fibre breakage appearing in slowest cooled samples. It should be attributed to the strong interfacial bond transferring the force to the fibres.

A high crystallinity and large amount of α phase formed in the slow cooling samples, it gives the matrix higher density and strength which contributes to the maximum tensile stress, σ_{max}, and modulus in flexural tests. The slow cooling leads to the formation of a transcrystalline layer which gives the composite strong interfacial bond and contributes to the ultimate shear stress, τ_{ult}, in Iosipescu tests and maximum tensile stress, σ_{max}, in flexural tests.

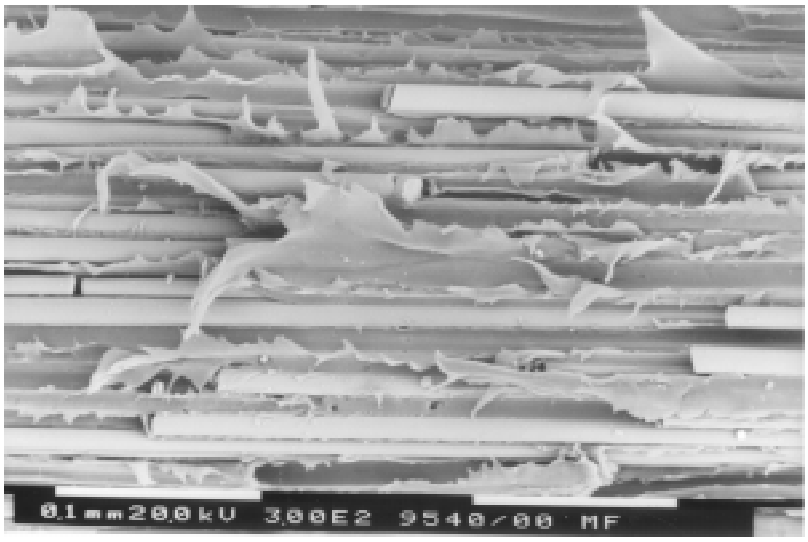

Fig. 2a: SEM photo of midspan lowest point fracture surface from flexural test, -1 ℃/min cooling rate sample

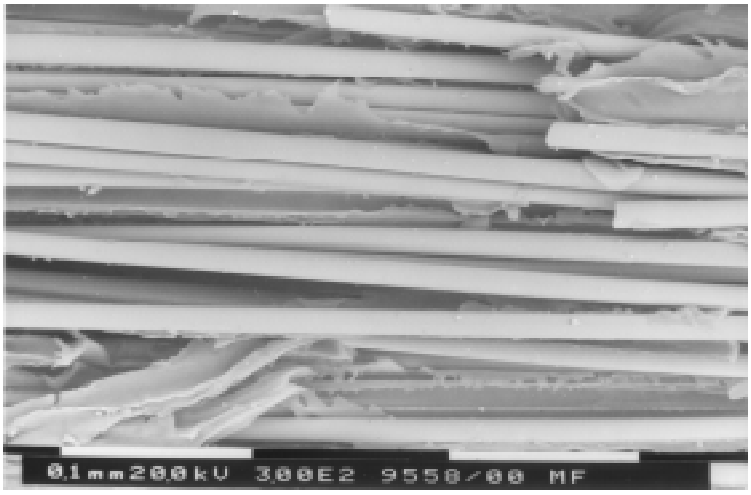

Fig. 2b: SEM photo of midspan lowest point fracture surface from flexural test, -60 ℃/min cooling rate sample

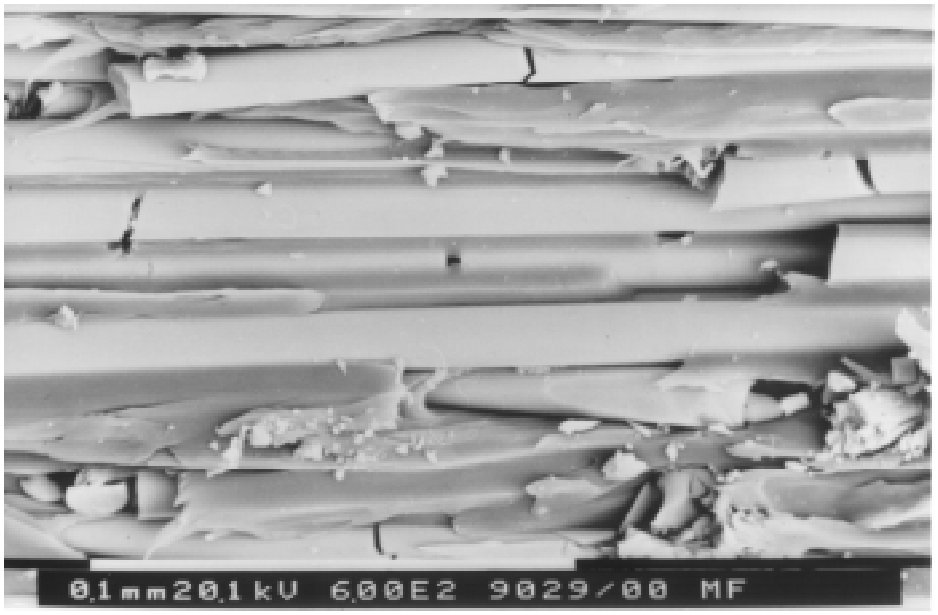

Fig. 3a: SEM photo of midplane fracture surface from Iosipescu test, -1 °C/min cooling rate sample

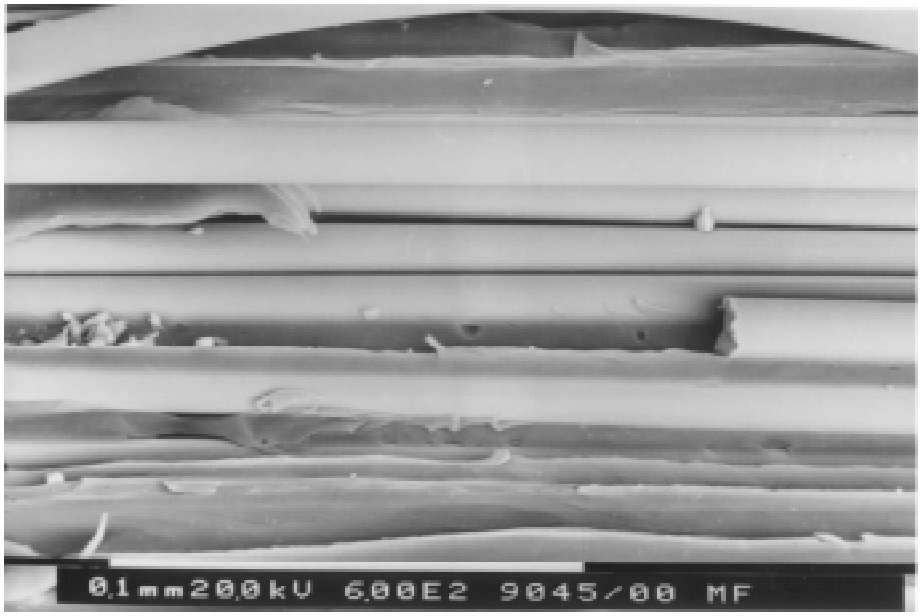

Fig. 3b: SEM photo of midplane fracture surface from Iosipescu test, -60 °C/min cooling rate sample

CONCLUSIONS

The results obtained in this research lead to the following conclusions.

1) The crystallinity of PA6 strongly depends on cooling rate during thermal processing. Slow cooling leads to higher crystallinity and more α crystals formed than fast cooling. The increased α phase leads to higher density of PA6 matrix.
2) The transcrystallinity of GF/PA6 strongly depends on the cooling rate too. Slow cooling leads to the formation of a transcrystalline layer.
3) It is assumed that the high density matrix and strong interfacial bonding between fibre and matrix indicated by Iosipescu, flexural tests and SEM observation result in better mechanical properties in the slow cooled GF/PA6 composite samples than that of fast cooled samples.
4) This is considered to be due to the slow cooling leads to 37% crystallinity and large amount α phase formed in the PA6 matrix which give the composite a harder matrix and higher tensile strength than that of fast cooling. It also improves the interfacial bonding condition and gives the composite higher interfacial strength than that of fast cooling.

REFERENCES

1. D. S. Delkar and N. V. Bhat, "Investigation of structural and mechanical properties of copper-chloride-doped nylon-6 films", *Journal of Applied Polymer Science*, 1991, v43, p191-200.

2. T. J. Bessell, D. Hull and J. B. Shortall, "The effect of polymerization conditions and crystallinity on the mechanical properties and fracture of spherulitic nylon 6", *Journal of Materials Science*, 1975, v10, p1127-1136.

3. M. L. Shiao, S. V. Nair, P.D. Garrett and R. E. Pollard, "Effect of glass-fibre reinforcement and annealing on microstructure and mechanical behaviour of nylon 6.6", *Journal of Materials Science*, 1994, v29, part I: p1973-1981, part II: p1739-1752.

4. I. Arvanitoyannis and E. Psomiadou, "Composites of anionic (Co)polyamides (nylon 6/nylon 12) with short glass E-fibres. Preparation and Properties", *Journal of Applied Polymer Science*, 1994, v51, p1883-1899.

5. F. W. Billmeyer, JR., *Textbook of Polymer Science*, New York, A Wiley-Interscience Publication, 1984.

ANALYSIS OF INTERLAMINAR STRESSES IN AN INTERNALLY-DROPPED PLY REGION

Jaewook Rhim and Anthony J. Vizzini

Composites Research Laboratory
Department of Aerospace Engineering, University of Maryland,
College Park, Maryland 20742

SUMMARY: A high-order polynomial interpolation element is formulated to determine the interlaminar stresses in an internally dropped-ply region. Additional polynomial terms are added to the displacements beyond those generated from a bilinear interpolation. The principle of virtual work is applied to determine the coefficients of the polynomial terms and thus determine the displacements within individual elements. The response of a larger tapered structure under tip extension and tip bending is used to generate the boundary conditions for this local problem. Specifically, three cases are studied: pure extension, pure bending, and an unsymmetric tapered beam under extension which results in extension-bending coupling. The interlaminar stresses determined by the present approach using deflections from a finite element model agree with the finite element model.

KEYWORDS: taper, ply drop, discontinuity, interlaminar stresses, polynomial interpolation, finite elements

INTRODUCTION

Tapered laminates are essential wherever a gradient in the mechanical properties is desired. Typically, plies are terminated at discrete points within the laminate resulting in a severe internal material discontinuity. During the manufacturing process, resin flows in the region near the ply drop resulting in a resin-rich pocket. The discontinuity coupled with the resin-rich region often results in a critical stress-state leading to delamination initiation. The damage can quickly grow through the tapered region and can reduce the stiffness and strength of the structure.

The effect of ply drops on the integrity of the composite structure has received much attention by researchers. Failure mechanisms have been described under static [1–5] and cyclic loadings [6–8]. Structural tailoring techniques have been developed to delay the occurrence of delamination [9–11]. Throughout these efforts one objective has been to understand the load transfer mechanism and to be able to describe it in a simple analytical form. For example, Armanios and Parnas proposed a model composed of extensional and shear springs to predict the interlaminar stresses based on the tendency of the plies to align themselves to the applied load [12]. Their model resulted in a reasonable comparison with a finite element model in

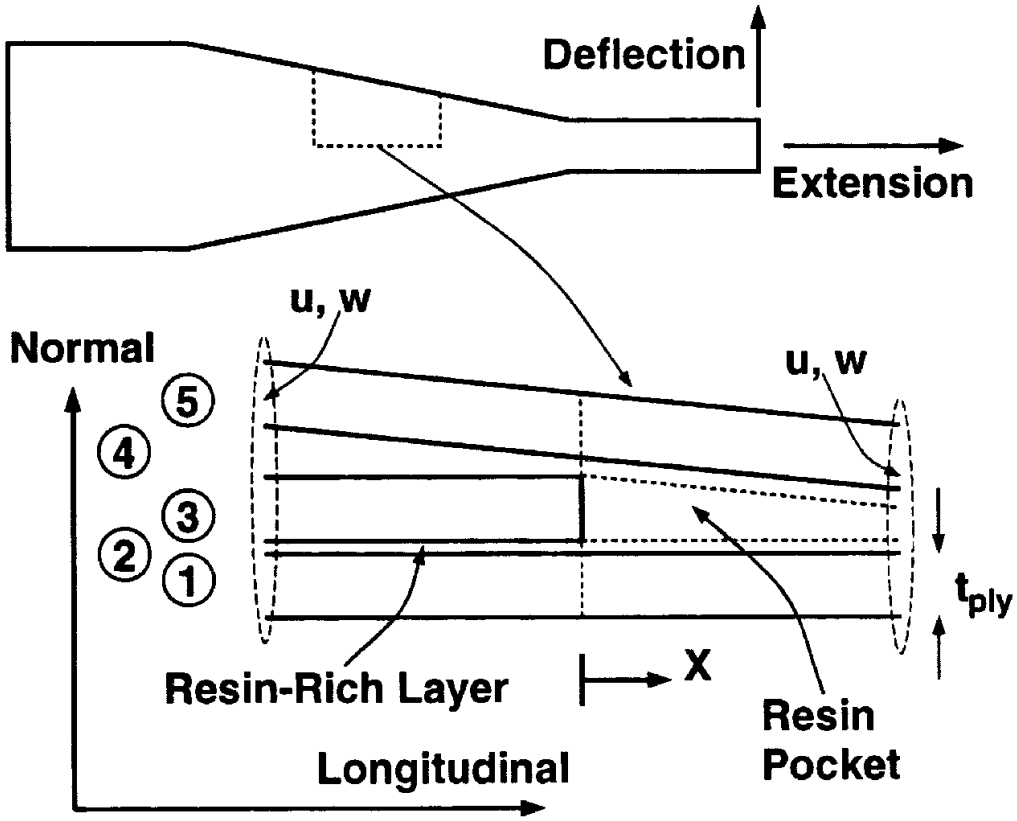

Figure 1 Model of ply-drop region

terms of interlaminar shear stresses; however, they were unable to capture the interlaminar normal stresses. The interlaminar stress state cannot rise from such a realignment of plies [13] and thus a model based on shear lag was introduced [14]. The shear-lag model made use of a finite polynomial series to represent the displacements in the solution method. This model compared very well with a finite element model for the case of a symmetric tapered laminate under uniaxial tension; however, it does not properly account for the occurrence of bending. Harrison and Johnson developed a mixed formulation that correlates well with their finite element model of the section [15].

The approach of the present model is to incorporate a polynomial form for the assumed displacements into an element. By imposing the principle of virtual work, equilibrium is satisfied within the element. The resulting formulation forms the basis of a local analysis that can be coupled with a global finite-element model.

HIGHER-ORDER POLYNOMIAL ELEMENT

The general problem to be solved is shown in Figure 1. It consists of a single ply drop in a longer tapered structure. The larger tapered structure undergoes deformation by tip extension in the longitudinal direction or tip deflection in the normal direction. The interlaminar normal and shear stresses that develop at the ply drop can cause delamination and are of great interest. From previous finite element models, these stresses appear to be smooth functions up to the ply drop itself [13]. At the ply drop abrupt changes of the stresses can occur.

Because the interlaminar stresses vary with respect to the longitudinal coordinate and because the structure to be modeled is of relatively simple geometry, a single element can be formulated to solve the problem. Begin by assuming a four-node element as in Figure

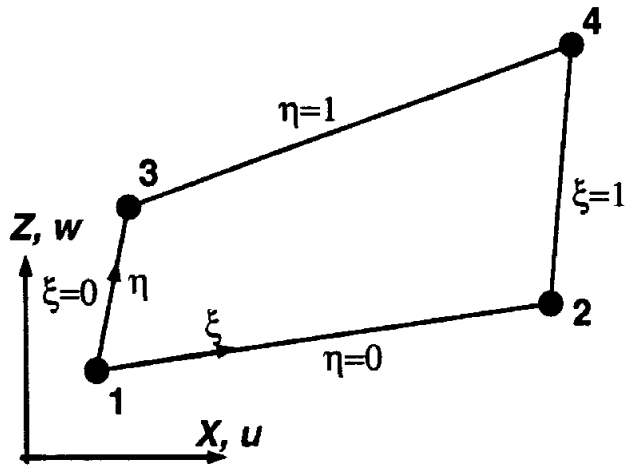

Figure 2 Four-node element

2. There are two degrees of freedom at each node, the u- and w- displacements. The nondimensional coordinates ξ and η are defined ranging from 0 to 1. Thus for this element the mapping between the nondimensional coordinates and the global coordinates (x, z) is given by:

$$\begin{aligned} x &= (1-\eta)[(1-\xi)x_1 + \xi x_2] + \eta[(1-\xi)x_3 + \xi x_4] \\ z &= (1-\eta)[(1-\xi)z_1 + \xi z_2] + \eta[(1-\xi)z_3 + \xi z_4] \end{aligned} \tag{1}$$

where x_i and z_i are the global coordinates of the four nodes. In general, the displacements, u and w can also be interpolated using the mapping functions as the shape functions for the displacements. To capture the higher-order nature of the stresses within the element, a higher-order polynomial interpolation is assumed in the ξ-direction. Thus the displacements are assumed to be of the form

$$\begin{aligned} u &= (1-\eta)\left[(1-\xi)u_1 + \xi u_2 + \sum_{i=2}^{N} a_i(\xi^i - \xi)\right] + \eta\left[(1-\xi)u_3 + \xi u_4 + \sum_{i=2}^{N} c_i(\xi^i - \xi)\right] \\ w &= (1-\eta)\left[(1-\xi)w_1 + \xi w_2 + \sum_{i=2}^{N} b_i(\xi^i - \xi)\right] + \eta\left[(1-\xi)w_3 + \xi w_4 + \sum_{i=2}^{N} d_i(\xi^i - \xi)\right] \end{aligned} \tag{2}$$

where a_i, b_i, c_i, and d_i are nodeless degrees of freedom. The higher-order interpolation contributes nothing along the ξ=0 and ξ=1 sides of the element; however, it does contribute along the η=0 and η=1 edges.

The assumed displacements in Equation 2 can be written symbolically as:

$$\{u\} = \begin{Bmatrix} u \\ w \end{Bmatrix} = [N]\{q\} \tag{3}$$

where the element displacement vector is defined as

$$\{q\} = \lfloor u_1 \;\; w_1 \;\; a_2 \;\; \cdots \;\; a_N \;\; b_2 \;\; \cdots \;\; b_N \;\; u_2 \;\; w_2 \;\; u_3 \;\; w_3 \;\; c_2 \;\; \cdots \;\; c_N \;\; d_2 \;\; \cdots \;\; d_N \;\; u_4 \;\; w_4 \rfloor^T \tag{4}$$

To determine the derivatives of the displacements in the global coordinates, the chain rule is used. Specifically

$$\begin{Bmatrix} \frac{\partial}{\partial x} \\ \frac{\partial}{\partial z} \end{Bmatrix} \{u\}^T = \begin{bmatrix} \frac{\partial x}{\partial \xi} & \frac{\partial z}{\partial \xi} \\ \frac{\partial x}{\partial \eta} & \frac{\partial z}{\partial \eta} \end{bmatrix}^{-1} \begin{Bmatrix} \frac{\partial}{\partial \xi} \\ \frac{\partial}{\partial \eta} \end{Bmatrix} \{u\}^T = [J]^{-1} \begin{Bmatrix} \frac{\partial}{\partial \xi} \\ \frac{\partial}{\partial \eta} \end{Bmatrix} \{u\}^T \tag{5}$$

where *[J]* is the Jacobian matrix. Thus the strains in the global system are known as a function of the degrees of freedom of the element.

$$\{\epsilon\} = \begin{Bmatrix} \epsilon_{xx} \\ \epsilon_{zz} \\ \epsilon_{xz} \end{Bmatrix} = \begin{Bmatrix} \frac{\partial u}{\partial x} \\ \frac{\partial w}{\partial z} \\ \frac{\partial u}{\partial z} + \frac{\partial w}{\partial x} \end{Bmatrix} = [B]\{q\} \tag{6}$$

The variation of the internal strain energy for the element is given as

$$\delta U = \int_V \delta \epsilon^T C \epsilon dV \tag{7}$$

where C is the stiffness matrix of the element. Substituting Equation 6 into Equation 7 results in

$$\begin{aligned} \delta U &= \int_V \{\delta q\}^T [B]^T C [B] \{q\} dx dz \\ \delta U &= \{\delta q\} \left[\int_V [B]^T C [B] |J| d\xi d\eta \right] \{q\} \\ \delta U &= \{\delta q\}[k]\{q\} \end{aligned} \tag{8}$$

where the stiffness matrix of the element is defined as:

$$[k] = \int_V [B]^T [C][B]|J| d\xi d\eta \tag{9}$$

and $|J|$ is the determinant of the Jacobian matrix in Equation 5. The element stiffness matrix is numerically integrated using Gausian quadrature.

EXAMPLE PROBLEMS

Presently, there are three options to implement this formulation in comparison with other finite element solutions. The first option is to reformulate the entire tapered beam using the higher-order polynomial element. This would result in having higher-order interpolations in regions that are not of interest. The second option is to formulate a hybrid model using the higher-order polynomial element in the area of greatest interest. This would probably be the most efficient modeling method but would prevent side-by-side comparison of the present model with previous finite element models. The third option is to post process the results of a finite element model. That is, the displacements from the finite element model far away from

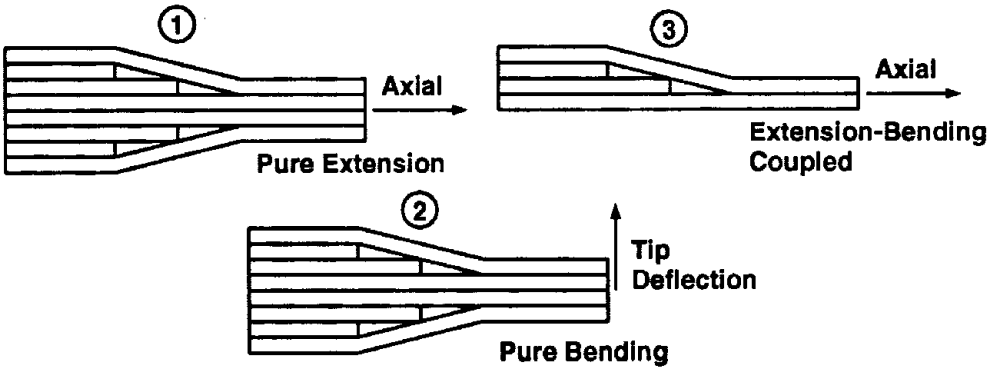

Figure 3 Schematic drawings of tapered laminates and their applied displacements

the point of interest are used as the input boundary conditions of the present formulation. The ability of the present formulation to reconstruct the interlaminar stresses from the farfield boundary conditions can then be assessed directly.

To demonstrate the capability of the model, three different problems will be solved via the higher-order polynomial element (HOP) and a previously-developed finite element model using 8–node, 24 degrees of freedom assumed-stress hybrid brick elements (FEM) [5]. In the first problem, an eight-ply laminate is tapered to four plies in a symmetric fashion. The laminate is 50.8 mm long in the thick section, 50.8 mm long in thin section, 25.4 mm wide and has a taper ratio of 10:1. Uniaxial tension is applied by fixing one end and applying an axial displacement (0.0254 mm) at the other. The second problem takes the geometry of the first and applies a tip deflection (0.0254 mm) bending the tapered laminate. In the third problem, a four-ply laminate is tapered to two plies. The laminate represents only the top half of the first laminate. Again an axial deflection (0.0254 mm) is applied. Because of the lack of geometric symmetry, coupling results in bending. The finite element model and the higher-order polynomial model are linear and thus the comparison of the two solution schemes is independent of the magnitude of the applied displacement. These three laminates and their loadings are shown schematically in Figure 3. All plies in these models are 0° unidirectional glass/epoxy with material characteristics given in Table 1. Also, thin (0.1-t_{ply} thick) resin-rich layers as shown in Figure 1 are included in the models to allow for the direct calculation of interlaminar stresses.

As indicated in Figure 1, the region of interest is divided into ten elements, five layers on either side of the ply drop. Each element represents a portion of a layer in the model, either a composite ply or a resin-rich layer. Note that only the third layer has a discontinuity in material constants across the ply-drop. Elements are assembled in the traditional manner and boundary conditions (u- and w-displacements at the nodes of both ends) are prescribed.

Table 1 Material Properties

Glass/Epoxy Unidirectional Tape	Resin
Extensional Moduli, msi $E_L = 6.4$ $E_T = 1.8$ $E_N = 1.8$	Young's Modulus, msi E = 0.57 msi
Shear Moduli, msi $G_{LT} = 0.65$ $G_{TN} = 0.65$ $G_{NL} = 0.60$	
Poisson's Ratios $\nu_{LT} = 0.29$ $\nu_{LN} = 0.29$ $\nu_{TN} = 0.50$	Poisson's Ratio $\nu = 0.37$

In addition, a plane of symmetry exists for the symmetric tapered beam under longitudinal tension or tip deflection. This results in additional boundary constraints of $u=0$ along the bottom for pure bending and $w=0$ along the bottom for pure extension.

Convergence

The solution from the finite element model has been shown to be converged. Refinement of the mesh results in additional points and thus a smoother curve with values in closer proximity of the actual ply-drop. The order of the polynomial used in Equation 2 in the interpolation of the displacements can be increased until the desired convergence is achieved. Convergence of the shear-lag model is controlled by the number of terms in the polynomial interpolation. Figure 4 indicates the interlaminar shear in the top resin layer using 3, 5, 7, 10 polynomial terms. The loading is pure bending due to a tip deflection. The difference in the solutions is the magnitude of the peak interlaminar shear stress on the right side of the ply drop. As the order of the polynomial increases, the discontinuity in the interlaminar shear becomes more pronounced. Increasing the order of the polynomial beyond 10 has no discernible effect on the interlaminar shear stress. Another area to check the effect of the order of the polynomial is away from the ply drop. Although the stresses are of less concern away from the ply drop, inaccurate representation will result in substantial gradients in the interlaminar stress states and spurious high values especially in the interlaminar normal stress. This area is shown in Figure 5. Note that only the $N=3$ curves tend not to agree with the other curves.

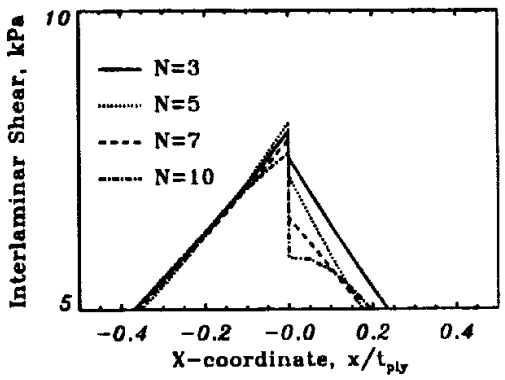

Figure 4 High-order polynomial interpolation solution in top layer about the ply drop for bending

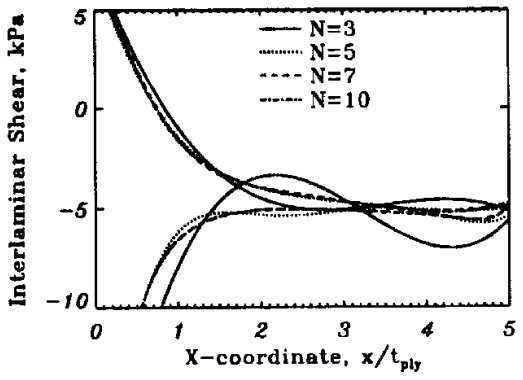

Figure 5 High-order polynomial interpolation solution in top and bottom layers away from the ply drop for bending

Convergence in the interlaminar normal stress is not as straight forward. In particular, the bending case presents a significant challenge. In Figure 6, the peak interlaminar normal stress in the bottom layer increases as the number of terms in the polynomial is increased. Between N=10 and N=20, this peak value only changes by 5%. The disturbance in the stress field caused by the discontinuity in bending is significant as is evidenced in Figure 7. At the ply drop, the interlaminar normal stress is negative, and higher-order polynomials are excited. Beyond $x=1.0t_{ply}$, the solutions follow the same trend represented by the curve generated from N=3.

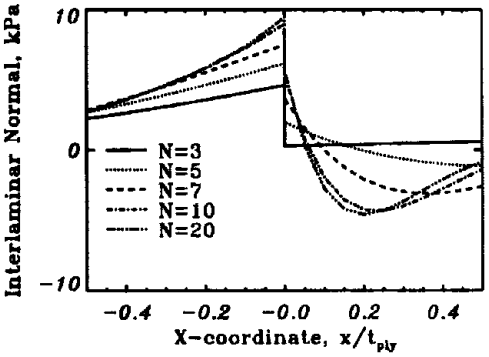

Figure 6 High-order polynomial interpolation solution in bottom layer about the ply drop for bending

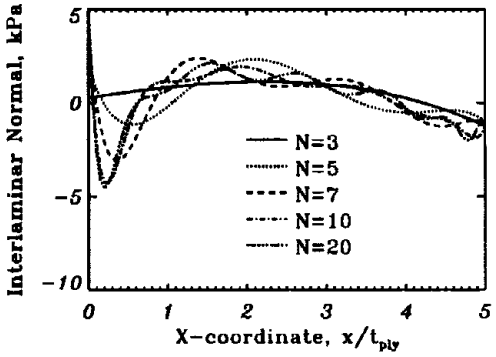

Figure 7 High-order polynomial interpolation solution in bottom layer away from the ply drop for bending

Solutions

The solutions to the three problems shown in Figure 3 are presented in Figures 8 through 13. In these figures the solid and dotted lines indicate the solution for the interlaminar stresses in the upper and lower resin layer, respectively, for the higher-order polynomial model with N=5. The squares and triangles indicate the finite-element solution in the upper and lower resin layers, respectively. All stresses are reported at the center of the interply resin layers in the local x-z coordinate, i.e. the stresses in the top layer are rotated through the taper angle. In general, the agreement for the interlaminar shear stresses is excellent. The higher-order polynomial model indicates an equivalent stress state. Moreover, the higher-order polynomial model provides the value of the interlaminar shear stress in the interply resin layers immediately above and below the ply drop.

The interlaminar normal stress is determined directly from the displacement field. The results indicate reasonable agreement at the ply drop; however, there the higher-order polynomial model does not agree with the finite element at the boundaries where the w-displacements are prescribed. Because no additional terms are included in the interpolation in the z-direction, the contribution to the interlaminar normal stress by ϵ_{zz} is constant through the thickness of the layer. This results in the discontinuity of σ_{zz} at interfaces of elements through the thickness.

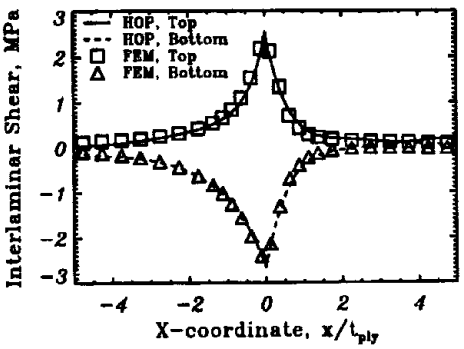

Figure 8 Interlaminar shear stress for symmetric tapered laminate under uniaxial tension

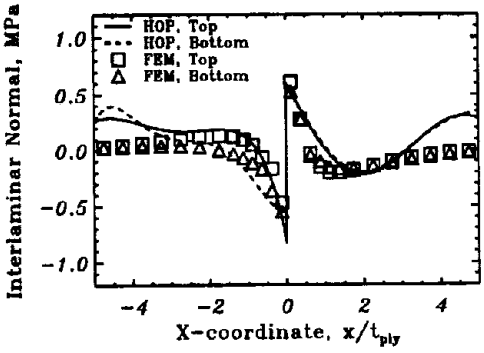

Figure 9 Interlaminar normal stress for symmetric tapered laminate under uniaxial tension

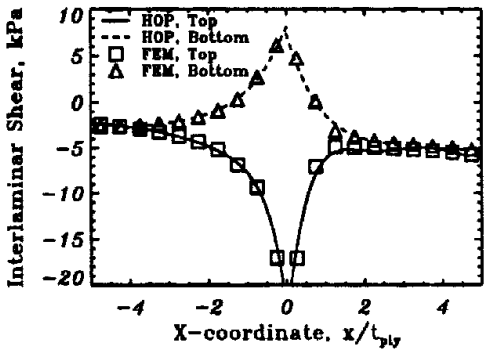

Figure 10 Interlaminar shear stress for symmetric tapered laminate under bending deflection

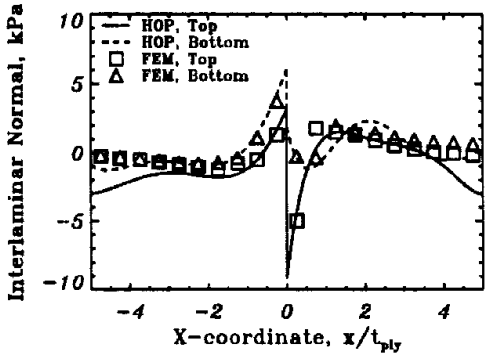

Figure 11 Interlaminar normal stress for symmetric tapered laminate under bending deflection

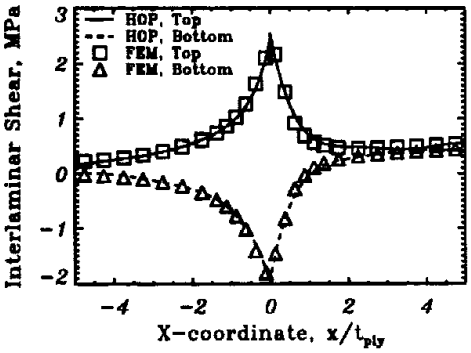

Figure 12 Interlaminar shear stress for unsymmetric tapered laminate under uniaxial tension

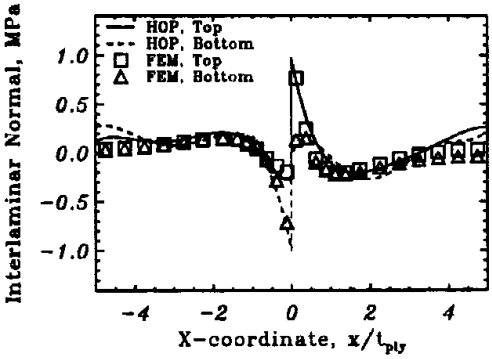

Figure 13 Interlaminar normal stress for unsymmetric tapered laminate under uniaxial tension

CONCLUSIONS

An element was formulated to solve for the interlaminar stresses in the region of a ply drop in a tapered laminate. The element includes a higher-order polynomial interpolation of the deflections in the longitudinal direction. Interlaminar stress states determined by a model constructed with this element were compared to previous results obtained with a finite element model, and the correlation was excellent for interlaminar shear stress throughout the region and very good for interlaminar normal stress near the ply drop.

The nature of the stresses about a ply drop is well known due to previous efforts with robust finite element solutions. Thus the robustness of a solution method can be reduced, as in the present formulation, to provided an equivalent stress state with substantially fewer degrees of freedom. The present formulation represents the use of polynomial terms to increase the accuracy of an element.

ACKNOWLEDGMENTS

The authors wish to thank Prof. Sung W. Lee for lending his expertise in this work.

REFERENCES

1. Curry, J. M., Johnson, E. R., and Starnes, J. H., Jr., "Effect of Dropped Plies on the Strength of Graphite-Epoxy Laminates," *Proceedings of the AIAA/ASME/ASCE/AHS/ASC 28th Structures, Structural Dynamics, and Materials Conference*, Monterey, CA
2. Fish, J. C. and Lee, S. W., "Delamination in Tapered Composite Structures," *Engineering Fracture Mechanics*, Vol. 34, (1), 1989, pp. 43-54.
3. Salpekar, S. A., Raju, T. S., and O'Brien, T. K., "Strain Energy Release Rate Analysis of Delamination in a Tapered Laminate Subjected to Tension Load," *Proceedings of the American Society for Composites Third Technical Conference*, Seattle, WA, September 1988, pp. 642–654.
4. Vizzini, A. J., "Influence of Realistic Ply-Drop Geometries on Interlaminar Stresses in Tapered Laminates," Composite Materials: Fatigue and Fracture—Fifth Volume, ASTM STP 1230, R. H. Martin, ed., American Society for Testing and Materials, Philadelphia, PA, 1995, pp. 467-485.
5. Vizzini, A. J. and Lee, S. W., "Damage Analysis of Composite Tapered Beams," *Journal of the American Helicopter Society*, Vol. 40, No. 2, April 1995, pp. 43-49.
6. Murri, G. B., Salpekar, S. A., and O'Brien, T. K., "Fatigue Delamination Onset Prediction in Unidirectional Laminates," Composite Materials: Fatigue and Fracture, ASTM STP 1110, American Society for Testing and Materials, Philadelphia, 1991, pp. 312–339.
7. Murri, G. B., O'Brien, T. K., and Salpekar, S. A., "Tension Fatigue of Glass/Epoxy and Graphite/Epoxy Tapered Laminates," *American Helicopter Society Journal*, Vol. 38, (1), Jan. 1993, pp. 29–37.
8. Fish, J. C. and Vizzini, A. J., "Delamination of Ply-Drop Configurations," Composite Materials: Testing and Design, 11th Symposium, ASTM STP 1206, American Society for Testing and Materials, Philadelphia, PA, 1995, pp. 323-332.
9. Llanos, A. S. and Vizzini, A. J., "The Effect of Film Adhesive on the Delamination Strength of Tapered Composites," *Journal of Composite Materials*, Vol. 26, No. 13, 1992, pp. 1968-1983.
10. Botting, A. D., Vizzini, A. J., and Lee, S. W., "The Effect of Ply-Drop Configuration on the Delamination Strength of Tapered Composite Structures," *Proceedings of the AIAA/ASME/ASCE/AHS/ASC 33rd Structures, Structural Dynamics, and Materials Conference*, Dallas, Texas, April 1992, pp. 40-47.
11. Fish, J. C. and Vizzini, A. J., "Tailoring Concepts for Improved Structural Performance of Rotorcraft Flexbeams," *Composites Engineering*, Vol. 2, (5–7), 1992, pp. 303–312.
12. Aramanios, E. A. and Parnas, L., "Delamination Analysis of Tapered Laminated Composites Under Tensile Loading," *Composite Materials: Fatigue and Fracture, ASTM STP 1110*, American Society for Testing and Materials, Philadelphia, 1991, pp. 340–358.
13. Vizzini, A. J. and Lee, S. W., "Damage Analysis of Composite Tapered Beams," *Journal of the American Helicopter Society*, Vol. 40, No. 2, April 1995, pp. 43-49.
14. Vizzini, A. J., "Shear-Lag Analysis about an Internally-Dropped Ply," *Proceedings of the American Society for Composites Tenth Technical Conference on Composite Materials*, Santa Monica, CA, October 1995, pp. 473-482.
15. Harrison, P. N., and Johnson, E. R., "A Mixed Formulation for Interlaminar Stresses

in Dropped-Ply Laminates," *Proceedings of the AIAA/ASME/ASCE/AHS/ASC 34th Structures, Structural Dynamics, and Materials Conference*, La Jolla, CA, April 1993, pp. 1740-1752.

STRESS TRANSFER MECHANICS FOR MULTIPLE PLY LAMINATES FOR AXIAL LOADING AND BENDING

L. N. McCartney and C. Pierse

Centre for Materials Measurement & Technology,
National Physical Laboratory, Teddington, Middx. UK,TW11 OLW

SUMMARY : A description is given of a methodology based on a new model that has been developed for predicting stress transfer due to ply cracking in a cross-ply laminate subject to out-of-plane bending. The model is valid for multiple ply laminates which can be unbalanced (i.e. non-symmetrical). Full account is taken of the combined effects of in-plane tension loading (giving rise to out-of-plane bending when the laminate is non-symmetrical) and out-of-plane bending. Thermal residual stresses and bending arising from a temperature gradient are taken into account. The representations for the stress and displacement fields satisfy exactly the equilibrium equations and both traction and displacement continuity conditions at the interfaces between plies. The stress-strain equations are satisfied either exactly or in an average sense for each ply or ply layer. Stress transfer is governed by sets of fourth order ordinary differential equations that are solved by standard methods. Solutions of the differential equations are used to determine the stress and displacement distributions at all points in a laminate subject to bending when equally spaced cracks are present in any of the 90 degree plies subject to tensile loading. The results of these calculations are used to predict the dependence of the flexural modulus of a cracked laminate on crack density.

KEYWORDS: laminates, stress transfer, bending, ply cracking, flexural modulus

INTRODUCTION

Predicting ply crack formation in laminated composites subject to the complex loading that is expected in composite components is an important technological objective. This goal has recently been achieved [1, 2] for general symmetric laminates subject to general in-plane loading. The remaining important deformation mode, that has to date been neglected in the literature, concerns the prediction of ply crack formation in laminates that are subject to out-of-plane bending. The objective of this paper is to describe a new model of stress transfer for unbalanced multiple-ply cross-ply laminates subject to out-of-plane bending for which plane strain conditions prevail. Account is taken of the combined effects of axial loading and bending, and of the effects of uniform temperature changes that also lead to out-of-plane bending when laminates are unbalanced and/or asymmetrically cracked. Full details of the stress transfer model are described elsewhere [3].

GEOMETRY AND STRESS-STRAIN EQUATIONS

While a composite laminate is normally considered to comprise a set of plies perfectly bonded together, it is useful to introduce the concept of perfectly bonded composite layers where more than one layer may represent each ply of the laminate. The refinement of plies into such layers enables through-thickness stress and displacement variations in each ply to be investigated, leading to more

accurate modelling of the stress and displacement fields. A laminate consisting of N+1 perfectly bonded layers of 0° and 90° plies is considered within a Cartesian coordinate system such that the x-axis is in the through-thickness direction pointing in a downward direction, the y-axis is in the horizontal axial direction while the z-axis is in the in-plane transverse direction for which the strain is zero. The origin is selected to lie on the upper surface of the laminate, i.e. it lies in the first of the laminate layers which are labelled i = 1...N+1 from top to bottom. The layer interfaces are located at points $x = x_i$, i = 1...N where $x_0 = 0$ and $x_{N+1} = h$, the total thickness of the laminate. The thickness of the i^{th} layer is denoted by $h_i = x_i - x_{i-1}$.

For the assumed plane strain conditions the stress strain relations for the i^{th} layer are of the form

$$\varepsilon_{xx}^i = \frac{\partial u_i}{\partial x} = \frac{\sigma_{xx}^i}{\tilde{E}_t^i} - \frac{\tilde{\nu}_a^i}{\tilde{E}_A^i}\sigma_{yy}^i + \tilde{\alpha}_t^i \Delta T^i , \tag{1}$$

$$\varepsilon_{yy}^i = \frac{\partial v_i}{\partial y} = -\frac{\tilde{\nu}_a^i}{\tilde{E}_A^i}\sigma_{xx}^i + \frac{\sigma_{yy}^i}{\tilde{E}_A^i} + \tilde{\alpha}_A^i \Delta T^i , \tag{2}$$

$$\varepsilon_{xy}^i = \frac{1}{2}\left(\frac{\partial u_i}{\partial y} + \frac{\partial v_i}{\partial x}\right) = \frac{\sigma_{xy}^i}{2\mu_a^i} , \tag{3}$$

where for the i^{th} layer of the laminate, $\tilde{E}_A^i$, $\tilde{E}_t^i$, $\tilde{\nu}_a^i$, $\tilde{\alpha}_A^i$ and $\tilde{\alpha}_t^i$ denote the Young's moduli, Poisson's ratio, and thermal expansion coefficients that arise for the special case of plane strain conditions where the transverse strain is assumed to be zero everywhere in the laminate. The axial shear modulus is denoted by μ_a^i. The subscripts A and a refer respectively to axial thermoelastic constants involving in-plane and out-of-plane stresses and deformations. The subscripts T and t refer respectively to transverse constants for in-plane and out-of-plane stresses and deformations. The parameter ΔT^i is the difference between the current temperature of the i^{th} layer and the stress-free temperature of the laminate. The temperature is assumed uniform in each layer so that non-uniform through-thickness temperature distributions, independent of y and z, can be dealt with by ply refinement techniques.

REPRESENTATION FOR STRESS AND DISPLACEMENT FIELDS

In [3] the following stress field has been derived that is based on the initial assumption that the shear stress in any layer is a quadratic function of x

$$\sigma_{xy}^i(x, y) = P_{i-1}'(y) + \left[P_i'(y) - P_{i-1}'(y)\right]\xi_i + Q_i'(y)\left[\xi_i^2 - \xi_i\right], \quad i = 1...N+1 , \tag{4}$$

$$\sigma_{xx}^{i}(x, y) = \left[-P_{i-1}''(y)\,\xi_i + \left(P_{i-1}''(y) - P_i''(y)\right)\frac{1}{2}\xi_i^2 - Q_i''(y)\left(\frac{1}{3}\xi_i^3 - \frac{1}{2}\xi_i^2\right)\right] h_i + S_{i-1}(y), \quad i = 1...N+1, \tag{5}$$

$$\sigma_{yy}^{i}(x, y) = \frac{1}{h_i}\left[P_{i-1}(y) - P_i(y)\right] - \frac{Q_i(y)}{h_i}\left[2\xi_i - 1\right] + \sigma_i(x), \quad i = 1...N+1, \tag{6}$$

$$\text{where} \quad \xi_i = \frac{x - x_{i-1}}{x_i - x_{i-1}}, \quad \sigma_i(x) = \tilde{E}_A^i\left[\varepsilon + \hat{\varepsilon}x - \alpha_A^i \Delta T^i\right], \tag{7}$$

where $P_i(y)$, $i = 0...N+1$, $Q_i(y)$, $i = 1...N+1$, and where $S_i(y)$ the normal stress on $x = x_i$ for $i = 0...N$, are functions to be determined. It is understood that $P_0(y)$ and $P_{N+1}(y)$ are identically zero. The quantity $\sigma_i(x)$ is the axial stress experienced by the i^{th} layer of an undamaged laminate when $P_i(y)$ and $Q_i(y)$ are equal to zero for all i. It has been shown [3] that the displacement field corresponding to the stress field specified by (4-7) has the form

$$u_i(x, y) = \frac{(x - x_{i-1})^2}{12\tilde{E}_t^i}\left[2\left(P_{i-1}''(y) - P_i''(y)\right)\xi_i - 6P_{i-1}''(y) - Q_i''(y)(\xi_i^2 - 2\xi_i)\right] - \frac{\tilde{\nu}_a^i}{\tilde{E}_A^i}\left[\left(P_{i-1}(y) - P_i(y)\right)\xi_i - Q_i(y)(\xi_i^2 - \xi_i) + \sigma_i^*(x)\right] + (x - x_{i-1})\left(\alpha_t^i \Delta T^i + \frac{S_{i-1}(y)}{\tilde{E}_t^i}\right) + U_{i-1}(y), \quad i = 1...N+1, \tag{8}$$

$$v_i(x, y) = -\frac{(x - x_{i-1})^3}{120\tilde{E}_t^i}\left[5\left(P_{i-1}'''(y) - P_i'''(y)\right)\xi_i - 20P_{i-1}'''(y) - Q_i'''(y)\left(2\xi_i^2 - 5\xi_i\right)\right] + (x - x_{i-1})\left[\frac{P_{i-1}'(y)}{\mu_a^i} + \left(\frac{1}{\mu_a^i} - \frac{\tilde{\nu}_a^i}{\tilde{E}_A^i}\right)\left\{\left(P_i'(y) - P_{i-1}'(y)\right)\frac{1}{2}\xi_i + Q_i'(y)\left(\frac{1}{3}\xi_i^2 - \frac{1}{2}\xi_i\right)\right\}\right] - \frac{S_{i-1}'(y)}{2\tilde{E}_t^i}(x - x_{i-1})^2 - U_{i-1}'(y)(x - x_{i-1}) + V_{i-1}(y), \quad i = 1...N+1, \tag{9}$$

where $U_{i-1}(y)$ is the through-thickness displacement and $V_{i-1}(y)$ is the axial displacement on $x = x_{i-1}$ and where

$$\sigma_i^*(x) = \int_{x_{i-1}}^{x} \sigma_i(\eta)\, d\eta \ , \qquad i = 1...N+1 \ . \tag{10}$$

INTERFACIAL AND BOUNDARY CONDITIONS

The origin for coordinates is selected to be midway between two neighbouring planes containing one or more transverse cracks in the 90° plies having the same separation 2L. As the layers are assumed to be perfectly bonded the interfacial tractions and displacements must be continuous through the laminate leading to recurrence relations defining the function S_i, U_i and V_i (see [3] for details). Symmetry about the plane $y = 0$ implies that

$$\sigma_{xy}(x, 0) = 0 \ , \qquad v(x, 0) = 0 \ , \qquad \text{for} \quad 0 \le x \le h \ , \tag{11}$$

and the outer surfaces of the laminate are assumed to be stress free so that for $|y| \le L$

$$\sigma_{xx}^{1}(0, y) = 0 \ , \quad \sigma_{xx}^{N+1}(x_{N+1}, y) = 0 \ , \quad \sigma_{xy}^{1}(0, y) = 0 \ , \quad \sigma_{xy}^{N+1}(x_{N+1}, y) = 0 \ . \tag{12}$$

Because the surfaces of the transverse cracks are stress-free

$$\sigma_{yy}^{i}(x, \pm L) = 0 \ , \quad \sigma_{xy}^{i}(x, \pm L) = 0 \quad \text{for } x_{i-1} \le x \le x_i \ , \tag{13}$$

for *cracked* layers only. For a uniform distribution of transverse cracks symmetry requires that for *uncracked* layers

$$\sigma_{xy}^{i}(x, \pm L) = 0 \ , \quad \text{for } x_{i-1} \le x \le x_i \ . \tag{14}$$

The axial displacement for all of the *uncracked* layers is assumed to have the linear form

$$v_i(x, \pm L) = \pm \left[\varepsilon_c + \hat{\varepsilon}_c x \right] L \ , \tag{15}$$

where ε_c and $\hat{\varepsilon}_c$ are parameters whose values characterise the effective axial and bending strains of the cracked laminate. The corresponding values for an uncracked laminate are denoted by ε and $\hat{\varepsilon}$.

The representation defined by (4-10) when used in conjunction with associated recurrence relations for S_i, U_i and V_i automatically satisfies the equilibrium equations, the interfacial continuity conditions, and the stress-strain equations (1) and (3) for ANY values of the functions $P_i(y)$ and $Q_i(y)$.

GOVERNING DIFFERENTIAL EQUATIONS

By demanding that the stress-strain equation (2) is satisfied on averaging and on taking moments it has been shown [3] that the unknown functions $P_i(y)$ and $Q_i(y)$ must satisfy the following system of fourth order ordinary differential equations

$$\sum_{i=1}^{N} F_{ij} P_i''''(y) + \sum_{i=1}^{N} G_{ij} P_i''(y) + \sum_{i=1}^{N} H_{ij} P_i(y) + \sum_{i=1}^{N} F_{i+N,j} Q_i''''(y) + \sum_{i=1}^{N} G_{i+N,j} Q_i''(y) + \sum_{i=1}^{N} H_{i+N,j} Q_i(y) = 0 , \quad j = 1...N , \tag{16}$$

$$\sum_{i=1}^{N} F_{i,j+N} P_i''''(y) + \sum_{i=1}^{N} G_{i,j+N} P_i''(y) + \sum_{i=1}^{N} H_{i,j+N} P_i(y) + \sum_{i=1}^{N} F_{i+N,j+N} Q_i''''(y) + \sum_{i=1}^{N} G_{i+N,j+N} Q_i''(y) + \sum_{i=1}^{N} H_{i+N,j+N} Q_i(y) = 0 , \quad j = 1...N . \tag{17}$$

The differential equations are solved using standard methods (see for example [4]).

APPLICATION OF THE BOUNDARY CONDITIONS

The functions $P_i(y)$ and $Q_i(y)$, for i=1...N, that are required to specify the stress and displacement fields of a cracked laminate are determined from the solution of the 2N differential equations (16) and (17). To ensure a unique solution, 8N boundary conditions must be imposed. By imposing $(13)_2$ and (14), it follows from (4) that 4N boundary conditions are given by

$$P_i'(\pm L) = 0 , \quad Q_i'(\pm L) = 0 , \quad i = 1...N . \tag{18}$$

Suppose there are m *cracked* 90° layers for which $(13)_1$ is to be satisfied for all x. The application of these conditions leads to the following 4m boundary conditions, derived from (6),

$$Q_i(\pm L) = \frac{1}{2} h_i^2 \tilde{E}_A^i \hat{\varepsilon} , \tag{19}$$

$$\frac{1}{h_i \tilde{E}_A^i} \left[P_i(\pm L) - P_{i-1}(\pm L) \right] = \varepsilon - \alpha_A^i \Delta T^i + \left(x_i - \frac{h_i}{2} \right) \hat{\varepsilon} . \tag{20}$$

The remaining required boundary conditions are found by demanding that the averaged and integrated moment of (15) are satisfied for the N + 1 - m *uncracked* layers. On defining

$$P_i^*(y) = \int_0^y P_i(s)\, ds , \quad Q_i^*(y) = \int_0^y Q_i(s)\, ds , \quad i = 1...N+1 , \tag{21}$$

the boundary conditions for *uncracked* layers are of the form (see [3])

$$\frac{2 Q_i^*(\pm L)}{h_i^2 \tilde{E}_A^i L} = \mp (\hat{\varepsilon}_c - \hat{\varepsilon}) , \tag{22}$$

$$\frac{1}{h_i \tilde{E}_A^i}\left[P_{i-1}^*(\pm L) - P_i^*(\pm L)\right] + \frac{2Q_i^*(\pm L)}{h_i^2 \tilde{E}_A^i}\left(x_i - \frac{h_i}{2}\right) = \pm L(\varepsilon_c - \varepsilon) . \tag{23}$$

The parameters ε_c and $\hat{\varepsilon}_c$ are not known in advance and need to be eliminated. This is achieved by subtraction yielding the following 4(N - m) conditions for *uncracked* layers

$$\begin{aligned}\frac{1}{h_i \tilde{E}_A^i}\left[P_{i-1}^*(\pm L) - P_i^*(\pm L)\right] - \frac{1}{h_j \tilde{E}_A^j}\left[P_{j-1}^*(\pm L) - P_j^*(\pm L)\right] \\ + \frac{Q_i^*(\pm L)}{h_i^2 \tilde{E}_A^i}(2x_i - h_i) - \frac{Q_j^*(\pm L)}{h_j^2 \tilde{E}_A^j}(2x_j - h_j) = 0 ,\end{aligned} \tag{24}$$

$$\frac{Q_i^*(\pm L)}{h_i^2 \tilde{E}_A^i} = \frac{Q_j^*(\pm L)}{h_j^2 \tilde{E}_A^j} , \tag{25}$$

where the j^{th} layer is selected to be any one of the uncracked layers. The relations (18-20) and (24) and (25) thus provide the necessary 8N boundary conditions for a unique solution of the differential equations (16) and (17). The methodology enables the accuracy of the satisfaction of both interface and boundary conditions to be checked.

RESULTS OF PREDICTIONS

The new model of stress transfer that can account for the effects of bending and thermal residual stresses needs to be tested by considering a problem for which an accurate solution is already known. The methodology has, therefore, been applied to the tensile deformation (without bending) of a simple symmetric $[0/90_2/0]$ laminate which has been solved using the generalised plane strain stress transfer model described in references [5, 6] and using ply refinement techniques to obtain accurate solutions. The materials properties selected for all calculations are for a laminate whose ply properties correspond to a filament wound composite where Silenka E-glass 1200tex fibre reinforces MY750/HY917/DY063 epoxy [7]

$E_A = 45.6$ GPa	$E_T = 16.2$ GPa	$\nu_A = 0.278$
$\nu_T = 0.4$	$\mu_A = 5.83$ GPa	
$\alpha_A = 8.6 \times 10^{-6}$/°C	$\alpha_T = 26.4 \times 10^{-6}$/°C	

An axial stress of 1 GPa was applied to the laminate and the temperature change was selected so that $\Delta T = -100$°C. The thicknesses of the outer 0° plies was selected to be 0.25 mm while the single inner 90° ply had a total thickness of 0.5 mm. A system of equally spaced ply cracks in the 90° ply was selected so that the crack separation was 5 mm, corresponding to a crack density of 0.2 cracks/mm. When carrying out the generalised plane strain (G.P.S.) analysis for the special case of plane strain conditions using the methods of [5, 6], the 0° plies were each divided into 20 layers having the same properties, while the inner 90° ply was divided into 40 plies. The layers nearest to the interfaces between the 0° and 90° plies were then subdivided successively three times in order to achieve layer refinement near the crack tip singularities. When applying the new model described here, the 0° plies were each divided into 5 layers while the inner 90° ply was divided into 10 layers. Again the layers

at the ply interfaces were successively subdivided three times. The results of predictions using the two methods for this special case are shown in Figs. 1-3.

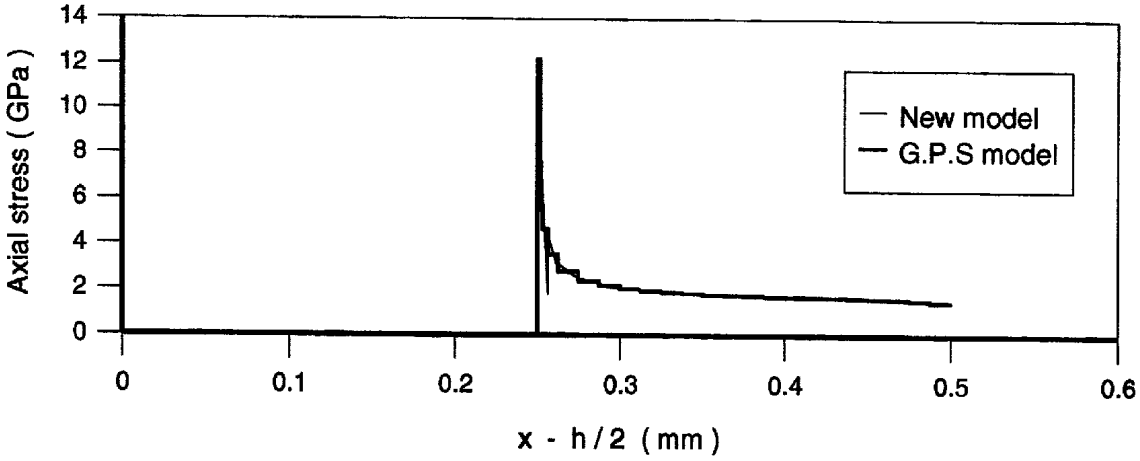

Fig.1 Comparison of axial stresses in the plane of the ply crack for a [0/90$_2$/0] GRP laminate.

Fig.1 shows the axial stress in the plane of a ply crack between the centre of the ply at x = h/2 and the outer surface at x = h. In the region $0 \leq x - h/2 \leq 0.25$ where the 90° ply is cracked, the axial stress is zero as required. For the region $0.25 \leq x - h/2 \leq 0.5$ of the 0° ply, the axial stress is non-uniform exhibiting a singularity at the crack tip $x - h/2 = 0.25$. The step function (thick line) is the prediction based on the generalised plane strain model [5, 6] while the thin line corresponds to predictions based upon the new model described here. The axial stress must be discontinuous at ply interfaces but it is seen also to be discontinuous at all layer interfaces especially as the singularity is approached. In spite of this the two models exhibit very good agreement leading to confidence in the methodology.

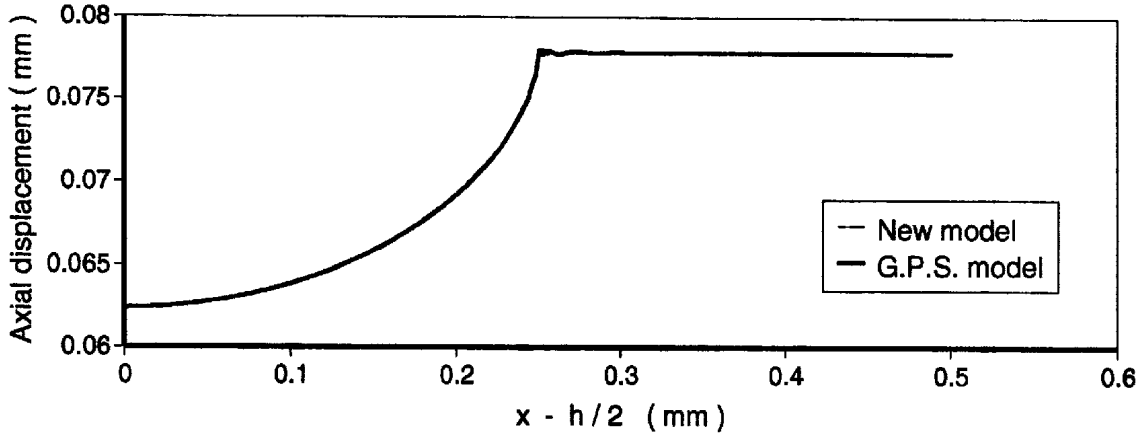

Fig.2 Comparison of axial displacements in the plane of the ply crack for a [0/90$_2$/0] GRP laminate.

Fig.2 compares predictions for the axial displacement in the plane of the crack where the crack opening is clearly seen. The crack opening profile predicted by the two methods is almost coincident, but in the uncracked region $x - h/2 \geq 0.25$ where the axial displacement should be uniform, very slight perturbations of the axial displacement are observed.

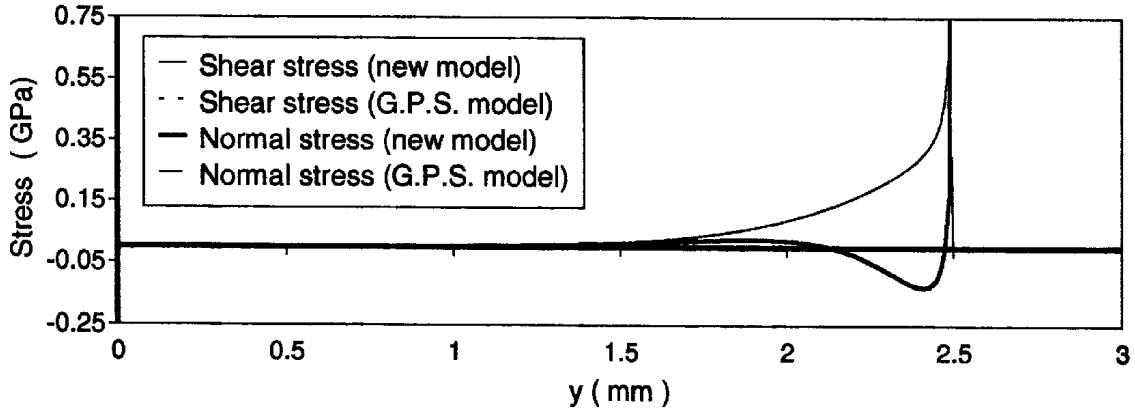

Fig.3 Comparison of the interfacial shear and normal stresses for a [0/90$_2$/0] GRP laminate.

Fig.3 compares the predictions of the distributions of the normal and shear interfacial stresses along the length of the interface between the 0° and 90° plies. It is not possible to distinguish between the predictions of the new model and those obtained using the generalised plane strain model.

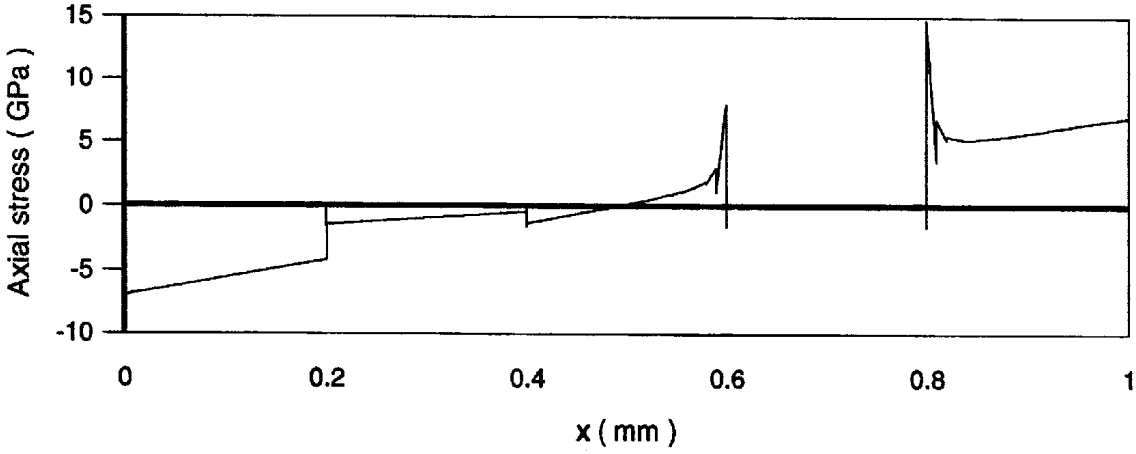

Fig.4 Axial stress in the ply crack plane in the lower 90° ply of a [0/90/0/90/0] GRP laminate.

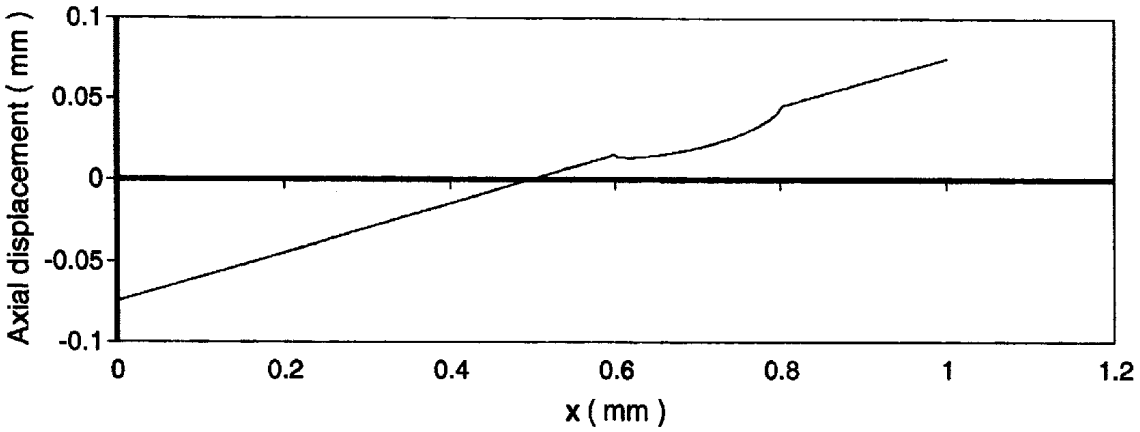

Fig.5 Axial displacement in the ply crack plane for lower 90° ply of a [0/90/0/90/0] GRP laminate.

The new model has also been applied to a symmetric [0/90/0/90/0] laminate where each ply has the same thickness 0.2 mm. A bending moment per unit width of 1 kN was applied together with a temperature difference $\Delta T = -100°C$. Each ply was subdivided into 5 layers of equal thickness and each layer next to the interfaces between plies was successively subdivided twice. An array of equally spaced ply cracks having separation 1 mm was considered only in the lower 90° ply. Fig. 4 shows the resulting predictions of the axial stress and displacement on any plane containing one of the ply cracks. It is seen that in the upper uncracked part of the laminate $0 \le x \le 0.5$ there appears to be little effect of the crack in the lower of the 90° plies. This, however, is not the case as the presence of the crack leads to additional bending. This additional bending is such that the axial stress and displacement remain linear in x for the uncracked plies.

THE FLEXURAL MODULUS

The well known Bernoulli-Euler law for the bending of homogeneous beams states that

$$\frac{1}{R} = \frac{M}{EI}, \tag{26}$$

where R is the radius of curvature of the neutral axis of the beam, M is the applied bending moment per unit width, E is the Young's modulus and I is the second moment of cross sectional area.

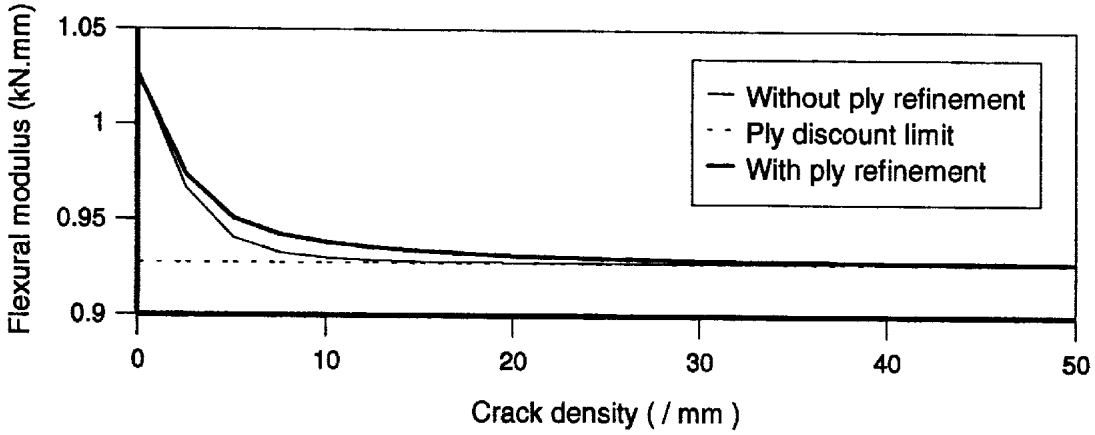

Fig.6 Dependence of flexural modulus on crack density for a GRP [0/90$_2$/0/90$_2$/0] laminate.

The product EI provides a measure of the flexural rigidity of the beam, and is called the modulus of flexural rigidity or the flexural modulus which can be expressed, for the case of the bending of a cracked laminate, as

$$EI = \frac{M}{\hat{\varepsilon}_c}, \tag{27}$$

where, from (22) assuming symmetry about y = 0

$$\hat{\varepsilon}_c = \hat{\varepsilon} - \frac{2Q_j^*(L)}{h_j^2 \hat{E}_A^j L}, \tag{28}$$

where j is the label of the previously selected uncracked layer. The relations (27) and (28) have been used to predict the flexural modulus EI for a cracked laminate as a function of crack density (1/2L) for a $[0/90_2/0/90_2/0]$ laminate having ply thickness 0.1 mm and cracks only in the lower 90° ply. The results are shown in Fig.6 for two cases. The dotted line shows the prediction when each ply is represented by just one layer, i.e. there is no ply refinement. The continuous line shows the more accurate result when the 0° plies are divided into 3 layers and the double thickness 90° plies are divided into 6 layers without any refinement at the interfaces. The predictions tend slowly to the ply discount asymptote as the crack density increases.

CONCLUSIONS

1. The new model of stress transfer, when applied to the axial loading (under plane strain conditions) of a symmetric laminate leads to stress and displacement distributions that are very close to the predictions obtained using a generalised plane strain model, thus demonstrating the accuracy and consistency of both types of model.

2. The application of the model to the bending of a [0/90/0/90/0] laminate where cracks are present in the lower 90° ply leads to accurate solutions for stress and displacement.

3. The methodology has been applied to the prediction of the dependence of flexural modulus on crack density where it has been shown that the flexural modulus tends slowly to the ply discount limit as the crack density increases.

ACKNOWLEDGEMENT

The research described formed part of the 'Materials Measurement Programme', a programme of underpinning research financed by the UK Department of Trade and Industry and the associated collaboration with AEA Technology Harwell (Dr G C Eckold).

REFERENCES

1. McCartney, L.N., 'Stress transfer mechanics for ply cracks in general symmetric laminates', NPL Report CMMT(A)50, December 1996.
2. McCartney, L.N.,'Generalised framework for the prediction of ply cracking in any general symmetric laminate subject to general in-plane loading', NPL Report CMMT(A)51, December 1996.
3. McCartney, L.N.,'Stress transfer mechanics for multiple ply laminates subject to bending', NPL Report CMMT(A)55, February 1997.
4. Hannaby, S.A., 'The solution of ordinary differential equations arising from stress transfer mechanics' NPL Report DITC 223/93, November 1993.
5. McCartney, L.N., 'A recursive method of calculating stress transfer in multiple-ply cross-ply laminates subject to biaxial loading', NPL Report DMM(A)150, January 1995.
6. McCartney, L.N., 'Predicting transverse crack formation in cross-ply laminates resulting from micro-cracking', to appear in Comp. Sci & Tech..
7. Soden M. and Hinton, M., Data being used in an international intercomparison exercise, the results of which will be published in Comp. Sci. & Tech..

COMPARISON OF FAILURE PREDICTION METHODS FOR GLASS/EPOXY AND CARBON/ EPOXY LAMINATES UNDER BIAXIAL STRESS

M. J. Hinton[1], P. D. Soden[2] and A. S. Kaddour[2]

[1] Structural Materials Centre, DRA, Fort Halstead, Sevenoaks, Kent, TN14 7BP, UK.
[2] Applied Mechanics Division, UMIST, Sackville Street, Manchester, M60 1QD, UK.

SUMMARY: A world wide exercise is currently underway to determine the current status of methods for predicting the strength of fibre composite laminates. The exercise is believed to be unique in that it employs an identical set of test cases, input data and output parameters for each theory evaluated, thus facilitating a direct comparison. Additionally, and most importantly, the predictions are being made by the originators of the theories. As part of the exercise, the originators were asked to predict the failure stresses and complete biaxial failure envelopes for two specific laminate configurations, namely (±30/90) glass/epoxy and (0/±45/90) carbon/epoxy materials. This paper contains a comparison of the predicted failure envelopes along with the input data provided to the contributors. The biaxial failure envelopes are superimposed on top of each other and grouped in a convenient manner. Bar charts are also provided, at selected stress ratios, to simplify the comparison of strength predictions for each theory.

KEYWORDS: biaxial envelopes, failure theories, international exercise, glass, carbon/epoxy, comparative study

INTRODUCTION

The origin of the world wide ‘failure exercise’ can be traced to an ‘experts meeting’ held at St Albans, England in 1991 on the subject of ‘Failure of Polymeric Composites and Structures: Mechanisms and Criteria for the Prediction of Performance’. The meeting was organised by the UK Institution of Mechanical Engineers together with the UK Engineering and Physical Sciences Research Council, who invited expert delegates from many countries to attend. The meeting took the form of a series of formal presentations interspersed with informal discussion groups. One of the principal findings which emerged was the lack of faith in the failure criteria, in current use. Attendees concluded that there was a lack of evidence to show whether any of the criteria could provide accurate and meaningful predictions of failure in composite components.

As a result of that meeting, an exercise was launched by Hinton and Soden in 1992 [1] to determine the quality of the current methods for predicting failure in composite laminates. In the exercise, selected workers in the field, including leading academics and developers of software/numerical codes, were invited to submit papers to a strictly controlled format. A series of laminate configurations, load cases and input data were defined by the organisers. Test cases were selected to challenge the theories to the full, embodying a wide range of parameters. These included fibre type (carbon and glass), matrix type (different epoxies) and the type of lay-up (unidirectional lamina and angle ply laminates, cross ply laminate, quasi-isotropic laminate and a

generally oriented laminate) and loading conditions which included uniaxial and biaxial tension, compression and shear and various combinations.

The exercise is being run in two phases:

Part A consists of papers submitted by the contributors who were asked to predict the stress/strain/strength response for each test case, having first provided a description of the theory employed and commented on any strengths or weaknesses of the method. This is a 'blind' test, as the authors have had no sight of any experimental data prior to making the predictions. At the end of this phase, predictions from the authors can be compared and contrasted against each other to identify where (or if) there is convergence or divergence.

Part B will be initiated by providing the contributors with the experimental data for each test case defined in Part A. Authors will then be in a position to compare their predictions with experimental evidence. They are then invited to provide a second paper, containing improvements to their theories or other appropriate clarifications as to the applicability of the theory or admissibility of the experimental evidence.

At the time of writing, Part A is nearing completion and Part B is about to start. In due course, Parts A and B will be published, in full, in the journal 'Composites Science and Technology'. This paper contains an overview of Part A and a slice of the results.

BACKGROUND TO THE SELECTION OF THE PARTICIPANTS

Any attempt to represent the views of all of the groups working on failure theories, worldwide, would be an impossible task. Instead, theories containing distinctly differing analytical approaches were sought, to represent as wide a spectrum as possible. Following a comprehensive publicity campaign in international journals, 38 leading exponents of certain theories were approached to participate in the exercise. For a variety of reasons, (lack of time being a common one !) a number declined to take part. In the final outcome 11 groups agreed to take part, giving the breadth and gravity required to ensure that a genuinely authentic exercise would result. A summary of the participating groups is provided in Table 1. Selected works published by these contributors and/or their groups are listed in Refs [2-13].

INPUT DATA SUPPLIED TO THE PARTICIPANTS

For all the predictions, the authors were asked to use identical input data, so that the theories could be compared on a 'level playing field'. This would also allow independent bodies to be able to attribute any differences between the outcomes of all predictions to inherent features in the formulation of the contributors' theories. Therefore, all the contributors were supplied with identical sets of properties (elastic constants, strengths, stress strain curves etc) for the laminates analyzed. Data was provided at the constituent fibre / matrix level and at the lamina level (Tables 2 to 4).

Table 1: A summary of participants and approaches represented in the exercise.

Contributor	Organisation	Approach Represented
Chamis C C, Gotsis P K and Minnetyan L	NASA Lewis, Cleveland, USA	ICAN and CODSTRAN micromechanics based software.
Hart-Smith L J	McDonnell Douglas, Longbeach, USA	Generalised Tresca.
Hart-Smith L J	McDonnell Douglas, Longbeach, USA	Max Strain theory.
Eckold G C	AEA Technology, UK	Applying British Standard pressure vessel design codes.
Edge E C	British Aerospace, Warton, UK	British Aerospace (BAe) In-house design method.
McCartney L	National Physical Laboratory, London, UK	Physically based 'Damage Mechanics'.
Puck A and Schurmann H	Technische Hochchule, Darmstadt, Germany	Physically based 3-D phenomenological models.
Wolfe W E and Butalia T S	Department of Civil Engineering, Ohio State University, Columbus, Ohio.	Maximum strain energy method, due to Sandhu (Wright Patterson Labs, Dayton, Ohio)
Sun C T and Tao J X	Purdue University School of Aeronautics & Astronautics, West Lafayette, Indiana, USA.	Linear and non-linear analysis (non-linear is FE based plus a plasticity model).
Zinoviev P, Grigoriev S V, Labedeva O V and Tairova L R	Institute of Composite Technologies, Orevo, Moskovkaya, Russia.	General application and methods.
Tsai S W and Liu K-S	Aeronautics and Astronautics Department, Stanford University, California, USA.	Interactive progressive quadratic failure criterion .
Rotem A	Faculty of Mechanical Engineering, Technion-Israel Institute of Technology, Haifa, Israel.	Interactive stress theory.

Table 2: Type of unidirectional laminae, fibres and matrices used in the analysis.

Matl Type	Fibre Type	Matrix Type (all Epoxies)
1	E-Glass fibres, 1200tex, Silenka	MY750/ HY917/ DY063, Ciba Geigy
2	E-Glass fibres, 21xK43, Gevetex	LY556/HT907/DY063, Ciba Geigy
3	T300 carbon fibres, Toray	BSL914C, Ciba Geigy
4	AS4 carbon fibres, Hercules	3501-6, Hercules

Table 3: Mechanical properties of various unidirectional laminae.

Material	**4**	**3**	**2**	**1**
V_f %	60	60	62	60
E_1 GPa	126*	138	53.48	45.6
E_2 GPa	11	11	17.7	16.2
G_{12} GPa	6.6*	5.5*	5.83*	5.83*
υ_{12}	0.28	0.28	0.278	0.278
υ_{23}	0.4	0.4	0.4	0.4
X_T MPa	1950**	1500	1140	1280
X_C MPa	1480	900	570	800
Y_T MPa	48	27	35	40
Y_C MPa	200**	200	114	145**
S_{12} MPa	79**	80**	72**	73**
ε_{1T} %	1.38	1.087	2.132	2.807
ε_{1C} %	1.175	0.652	1.065	1.754
ε_{2T} %	0.436	0.245	0.197	0.246
ε_{2C} %	2.0	1.818	0.644	1.2
γ_{12u} %	2	4	3.8	4
G_{IC} J/m^2	220	220	165	165
α_1 10^{-6}/°C	-1	-1	8.6	8.6
α_2 10^{-6}/°C	26	26	26.4	26.4
Curing temperature °C	177	120	120	120

** Initial modulus, ** Nonlinear stress strain curves are provided.*

Table 4: Mechanical properties of fibres.

Fibre type	**4**	**3**	**2**	**1**
E_{f1} GPa	225	230	80	74
E_{f2} GPa	15	15	80	74
G_{f12} GPa	15	15	33.33	30.8
υ_{f12}	0.2	0.2	0.2	0.2
G_{f23}	7	7	33.33	30.8
X_{fT} MPa	3350	2500	2150	2150
X_{fC} MPa	2500	2000	1450	1450
ε_{f1T} %	1.488	1.086	2.687	2.905
ε_{f1C} %	1.111	0.869	1.813	1.959
α_{f1} 10^{-6}/°C	-0.5	-0.7	4.9	4.9
α_{f2} 10^{-6}/°C	15	12	4.9	4.9

The composite systems used in the test cases are listed in Table 5. It should be noted that the E-glass fibres were treated as being isotropic whereas the carbon fibres were treated as being anisotropic.

Table 5: Mechanical properties of various matrices.

Matrix type	**4**	**3**	**2**	**1**
E_m GPa	4.2	4.0	3.35	3.35
G_m GPa	1.567	1.481	1.24	1.24
υ_m	0.34	0.35	0.35	0.35
Y_{mT} MPa	69	75	80	80
Y_{mC} MPa	250	150	120	120
S_m MPa	50	70	-	-
ε_{mT} %	1.7	4	5	5
α_m $10^{-6}/°C$	45	55	58	58

In order to exercise the theories thoroughly, several laminate configurations and load combinations were chosen. These are referred to as the 'test cases' and are outlined in Table 6.

Table 6: Details of the laminates and loading conditions used by the participants.

Laminate Configuration	**Material Type**	**Loading (a wide range of biaxial stress ratios unless other wise indicated)**
(0) unidirectional lamina	2 (GRP)	σ_y-τ_{xy} failure envelope
(0) unidirectional lamina	3 (CFRP)	σ_x-τ_{xy} failure envelope
(0) unidirectional lamina	3 (CFRP)	σ_x-σ_y failure envelope
$(0/90)_s$ cross ply laminate	1 (GRP)	Uniaxial tension, SR=1/0
$(\pm45)_s$ angle ply laminate	1 (GRP)	SR=1/1 and 1/-1
$(\pm55)_s$ angle ply laminate	1 (GRP)	σ_x-σ_y failure envelope and SR=1/0 and 2/1
$(90/\pm30)_s$ laminate	2 (GRP)	σ_x-σ_y failure envelope
$(90/\pm30)_s$ laminate	2 (GRP)	σ_x-τ_{xy} failure envelope
$(0/\pm45/90)_s$ quasi-isotropic laminate	4 (CFRP)	σ_x-σ_y failure envelope and SR=1/0 and 2/1

THEORETICAL RESULTS

Having described the overall scope of the failure exercise in the preceding paragraphs, a slice of the data, emerging from Part A, is presented below. In order to avoid prejudicing the ethos of the overall exercise, for the purposes of this 'advanced' paper the data is presented without specific reference to the originating author (readers will need to wait until Part A is published, in full, for this information). Though this reduces the impact somewhat, a number of very useful lessons can be drawn from the information. The theories used by their originators are referred to as A , B, C, D, E,.... and M. (It is worth mentioning that two contributors have used more than one theory in

their analysis). Predictions of the final failure envelopes from two of the laminate configurations, $(90/\pm30)_s$ GRP and $(0/\pm45/90)_s$ CFRP laminates, have been selected and are discussed more fully below. Also, a comparison has been made with the aid of bar charts between the predictions of all the theories at key stress ratios $SR=\sigma_y/\sigma_x=1/1$, -1/-1 and 1/0, selected from the failure envelopes.

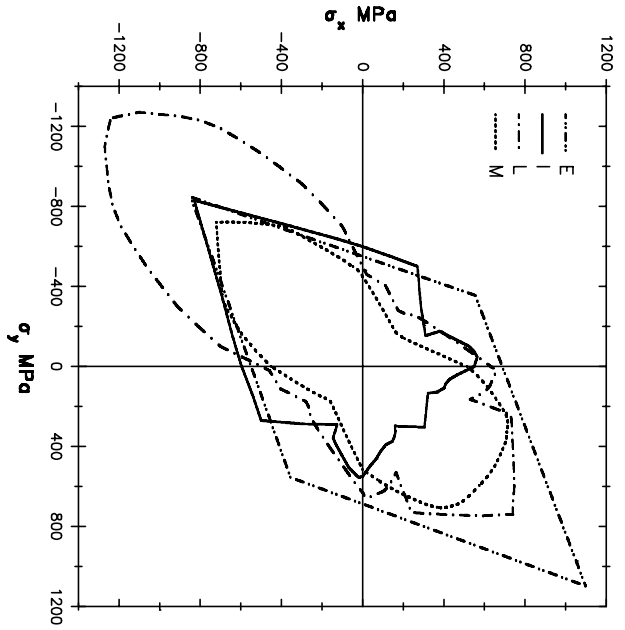

Fig. 1: Comparison between final failure envelopes for the (0/±45/90)s carbon/epoxy laminate predicted by theories E, I, L and M.

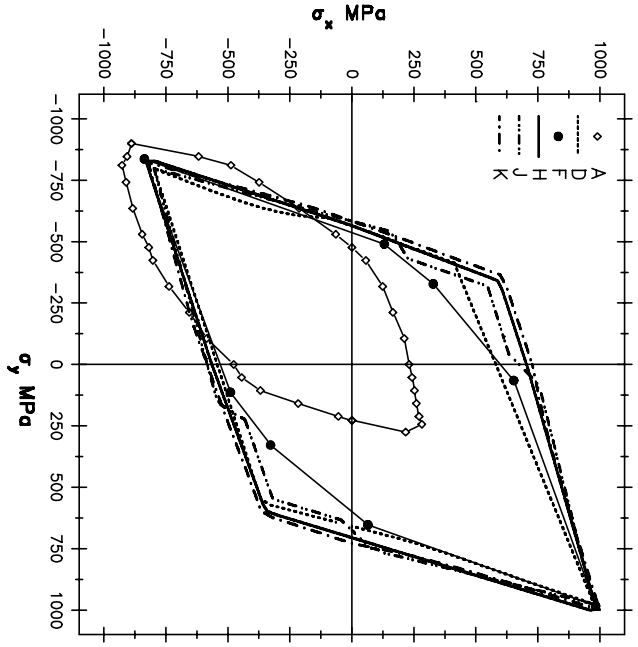

Fig. 2: Comparison between final failure envelopes for the (0/±45/90)s carbon/epoxy laminate predicted by theories A, D, F, H, J and K.

AS4/3501-6, $(0/\pm45/90)_s$ Quasi-Isotropic Carbon/Epoxy

Figs 1 to 2 show the final failure envelopes predicted by different contributors for this configuration. The envelopes are superimposed in order to observe the general differences between the various predictions. Figs 3-5 concentrate on comparing the predicted strengths at specified stress ratios. For this purpose, bar-charts are presented showing 'initial' and 'final' strengths (where appropriate) at biaxial stress ratios of $SR=\sigma_y/\sigma_x=1/1$, -1/-1 and 1/0, selected from the failure envelopes.

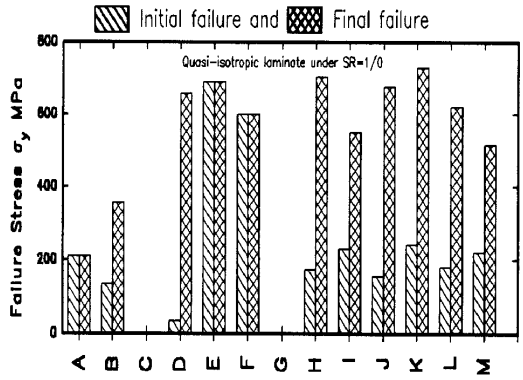

Fig. 3: Initial and final failure stresses predicted by various theories (A-M) for $(0/\pm45/90)_s$ laminate at SR=1/0.

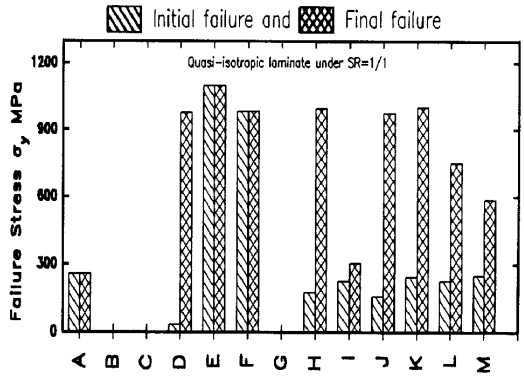

Fig. 4: Initial and final failure stresses predicted by various theories (A-M) for $(0/\pm45/90)_s$ laminate at SR=1/1.

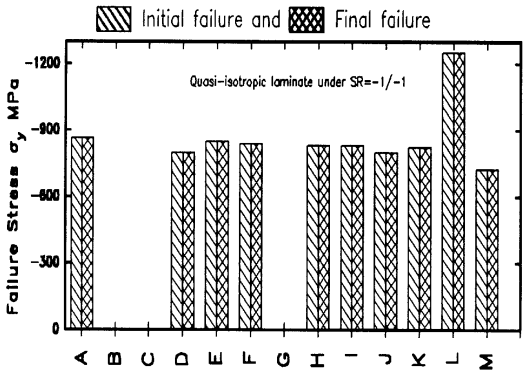

Fig. 5: Initial and final failure stresses predicted by various theories for $(0/\pm45/90)_s$ laminate at SR=-1/-1.

The most immediate impression one gets from Figs 1 and 2 is that the predictions fall broadly into two camps. In the first, one can see that theories (D, E, F, H, J and K) predict failure envelopes which are nearly identical in shape and in magnitude. However, in the second, each theory predicts an envelope which is unique in shape and in magnitude (A, I, L, M). Indeed there are no common features at all. A more detailed insight can be gained through examination of Figs 3-5. At the extremes of prediction (ie lowest prediction compared with highest prediction), the differences between the theories are more than 400% at a stress ratio of 1/1 (Fig 4, between I and E), more than 300% at 1/0 (Fig 3, between A and K) and more than 50% at -1/-1 (Fig 5, between L and M) for the final failure stresses. For the initial failure, the differences between the theories are more than 30 fold at SR=1/1 (Fig 4, between E and D), 20 fold at SR=1/0 (Fig 3, between E and D) and just over 70% at SR=-1/-1 (Fig 5, between L and M).

It is noted that all the theories predicted the initial failure load to be the same as the final failure under SR=-1/-1.

E-glass/LY556, (90 /±30)$_s$ glass/epoxy

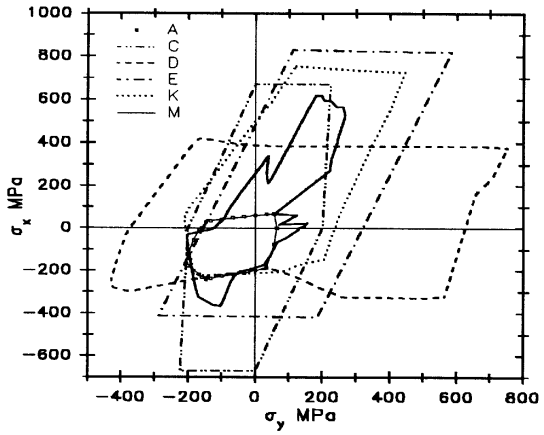

Fig. 6: Biaxial final failure envelopes for (90/±30) laminate predicted by theories A,C, D, E, K and M.

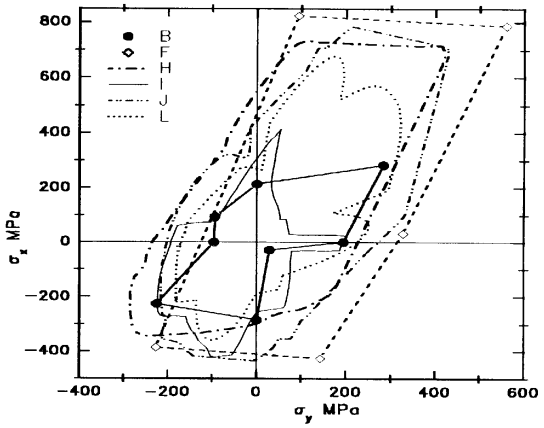

Fig. 7: Biaxial final failure envelopes for (90/±30) laminate predicted by theories B, F, H, I, J and L.

Figs 6 to 7 show the final failure envelopes predicted by different contributors for this configuration. As above, the envelopes are superimposed in order to observe the general differences between the various predictions. Figs 8-10 concentrate on comparing the predicted strengths at specified stress ratios. For this purpose, bar-charts are presented showing 'initial' and 'final' strengths (where appropriate) at biaxial ratios of SR=1/1, -1/-1 and 1/0.

The final failure envelopes of theories C, D, E and K (Fig 6) and F, H and J (Fig 7) are similar in shape in most parts of the stress space while theories A and M (Fig 6) and B, I and L (Fig 7) do not have many common features.

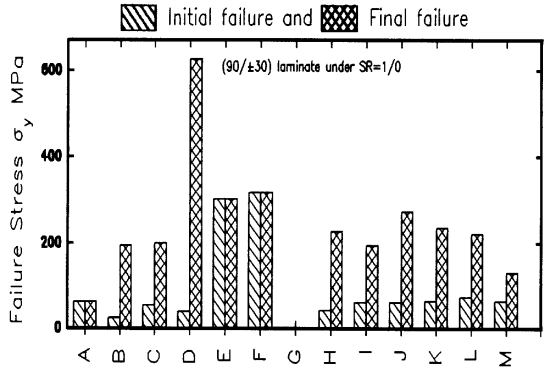

Fig. 8: Predicted initial and failure stresses versus theory label for (90/±30) Glass/epoxy laminate under SR=1/0.

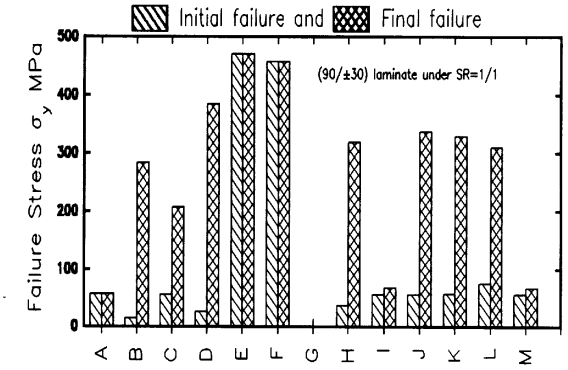

Fig. 9: Predicted initial and failure stresses versus theory label for (90/±30) Glass/epoxy laminate under SR=1/1.

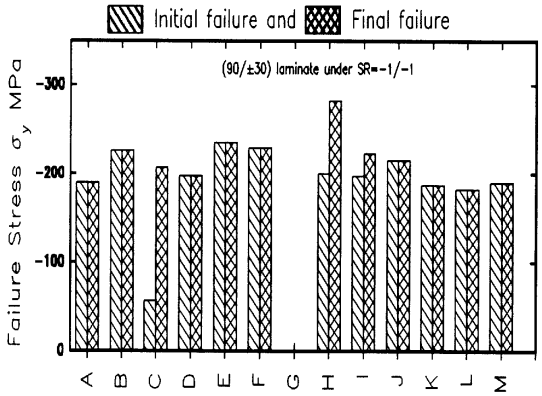

Fig. 10: Predicted initial and failure stresses versus theory label for (90/±30) glass/epoxy laminate under SR=-1/-1.

Comparisons between the final failure stresses show that at the extremes of prediction (i.e. the lowest prediction compared with the highest prediction), the differences between the theories are 10 fold at SR=1/0 (Fig 8, between A and D), more than 8 fold at SR=1/1 (Fig 9, between A and E) and just above 50% at SR=-1/-1 (Fig 10, between H and L). Larger differences were noticed in the prediction of the initial failure strengths where the differences reached 33 fold for SR=1/1 (Fig 9, between E and B), 12 fold at SR=1/0 (Fig 8, between F and B) and about 4 fold at SR=-1/-1 (Fig 10, between E and C).

CONCLUSIONS

1. Leading failure theories, currently available, have been identified as part of a world wide exercise to determine the current status of methods for predicting the strength of fibre composite laminates.
2. The comparison between various theories is highlighting, on one hand, the richness of the theoretical understanding of the mechanics of composite materials and, on the other hand, the large diversity in the predictive accuracy of the existing theories.
3. In this paper, the leading theories have been employed, by their originators, to predict the response of two laminate configurations ($(90/\pm 30)_s$ glass/epoxy, and $(0/\pm 45/90)$ quasi-isotropic carbon/epoxy laminates) when subjected to in-plane biaxial loading. The results show dramatic differences in predicted strengths, depending on the theory used. Differences (lowest to highest) in the final strengths as great as 400% have been demonstrated, even for what is often assumed to be a well understood situation, a quasi-isotropic laminate.
4. The widely diverging predictions are a clear indication that this theoretical area is far from mature and is in need of a concerted action to set it on a firmer footing. The alternative for designers will be to continue to rely on a ‘make and test’ philosophy, which is rapidly beginning to price composite materials / structures out of certain markets.
5. This paper contains a slice of that data from a world wide failure exercise. It is hoped that, once completed, the exercise will help contribute to an improved understanding within the composites community.

REFERENCES

1. Hinton M J and Soden P D,“Failure criteria for composite laminates”, *Composite Science and Technology*, V22, pp 121-122, 1991.
2. Sun C T and Chen J L, “A simple flow rule for characterising non linear behaviour of fibre composites”, *Journal of Composite Materials*, V23, pp1009-1020, 1989.
3. Rotem A and Nelson H G, “Fatigue behaviour of graphite epoxy laminate at elevated temperatures”, *ASTM, STP 723*, pp152-173, 1981.
4. Tsai S W , *Theory of Composite Design*, Think Composites, Palo Alto, 1992
5. Puck A, “Failure criteria for highly stresses fibre plastics composites which met requirements of design practice”, *Kunststoffe*, V82, pp34-38, 1992.
6. Edge E C, Final report, *BAe report SOR (177)* October 1987, with addendum 1, Feb 1989.

7. Sandhu R S, “Nonlinear analysis of unidirectional and angle ply laminates”, *Journal of Aircraft*, V13, pp104-111, 1976.
8. Alfutov N A and Zinoviev P A, “Deformation and failure of fibrous composites with brittle polymeric matrix under plane stress”, in *Mechanics of Composites*, (I.F. Obraztsov and V V Vasiliev, eds.), Moscow MIR publishers, 1982.
9. Murthy D L N and Chamis C C, “ICAN, Integrated Composite analyzer users and programmers manual”, NASA-TP-2515, 1985.
10. McCartney L N, “Theory of stress transfer in 0-90-0 cross ply laminate containing a parallel array of transverse cracks”, *Journal of Mechanics and Physics of Solids*, V40, P27-68, 1992.
11. Hart-Smith L J,“The truncated maximum strain composite failure model”, *Composites*, V24, P587-591, 1993.
12. Hart-Smith L J, “Predicting the strength of fibrous composites by an orthotropic generalisation of the maximum-shear-stress (Tresca) condition”, Proc. I Mech Eng, Part G, *Journal Of Aerospace Engineering*, V208, pp9-18, 1994.
13. Eckold G C, “ A design method for filament wound GRP vessels and pipework”, *Composites*, V16, pp 41-47, 1985

COMPRESSIVE FAILURE UNDER FLEXURAL LOADING: EFFECTS OF SPECIMEN SIZE, STRAIN GRADIENT AND FIBRE WAVINESS

Michael R. Wisnom

University of Bristol, Department of Aerospace Engineering,
University Walk, Bristol B28 ITR, U.K.,

SUMMARY: Recent experimental and finite element results are presented on factors affecting compressive failure of carbon fibre composites. Scaled flexural tests in a pin-ended buckling rig showed a 32% decrease in strain at failure for a factor of 8 increase in specimen dimensions. Tests on specimens with different lengths and widths but the same thickness suggested that the size effect was mainly due to the different strain gradients through the thickness. This was supported by constrained buckling tests where the ratio between compressive and flexural loading was varied. Fibre waviness was investigated with a surface profiling technique, and artificial waviness induced by laying up material on a curved panel which was straightened prior to curing. Finite element modelling of the effects of out-of-plane fibre waviness reproduced very well the trends observed experimentally.

KEYWORDS: compressive failure, flexural loading, strain gradient, size effects, shear instability, microbuckling, fibre waviness

INTRODUCTION

Compressive strength is an important factor in the design of composite structures, and consequently a great deal of research has been undertaken on failure under compressive loading. Despite this, there is still a lack of understanding of many aspects of compressive failure and the factors controlling it. This paper summarises experimental and analysis work carried out to try to develop a better understanding of some of these issues.

One question is the effect of specimen size. Reductions in strength with increasing stressed volume have been reported for a number of different failure modes [e.g. 1-4]. There have been suggestions of size effects in compressive failure [2,5], although the difficulties of obtaining reliable test results make this harder to establish. Results are presented here of a series of scaled buckling tests on unidirectional carbon fibre-epoxy which show an unequivocal reduction in compressive strain at failure with increasing specimen size [6].

This size effect could be due to differences in stressed volume, or it could be due to differences in the stress or strain gradient through the thickness, which a number of modelling studies have shown to have a significant effect on compressive strength [7-9]. This has been investigated with a new constrained buckling rig which enables the ratio of compressive to

flexural loading to be varied independently of the specimen size [10]. Results presented show a definite effect of strain gradient on compressive strain at failure.

Fibre waviness has received much more attention, and a number of studies of natural and artificially induced waviness have been published [e.g. 11-14]. Results are reported here of measurements of fibre waviness in the same material as that used for the other experiments [15]. Artificial waviness has also been generated, and its effects on compressive failure under flexural loading studied [15].

Compressive failure in many composites is believed to be caused by shear instability, sometimes referred to as microbuckling. Finite element analysis of this failure mechanism has been undertaken, and comparisons made with the experimental results.

EFFECT OF SPECIMEN SIZE

Tests were performed on unidirectional T800/924 carbon fibre-epoxy specimens in the pin-ended buckling rig shown in Fig. 1 [6]. This produces flexural failure in the gauge length, avoiding any stress concentration effects. Three sets of tests were carried out with all specimen and test rig dimensions geometrically scaled. Specimens were 1, 2 and 8 mm thick, machined out of the same 66-ply panel of material. Strain gauges at the centre of the specimens on each surface were used to measure the strain at failure.

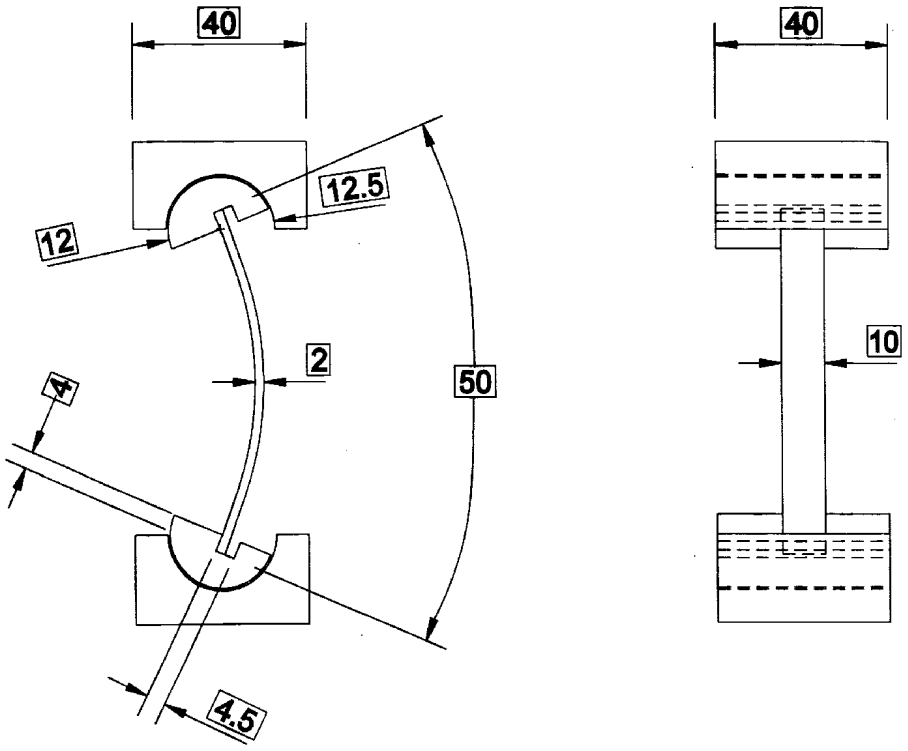

Fig. 1: Medium sized pin-ended buckling rig and specimen (dimensions in mm)

Specimen size (mm)	Failure strain (cv), % compressive	tensile	Number of specimens
200 x 40 x 8	-1.47 (1.9)	1.13 (6.1)	4
50 x 10 x 2	-1.77 (5.6)	1.35 (3.2)	9
25 x 5 x 1	-2.16 (5.7)	1.67 (2.7)	7
150 x 40 x 2	-1.82 (8.2)	1.54 (7.7)	15
150 x 10 x 2	-1.89 (5.2)	1.57 (5.6)	15
30 x 10 x 2	-1.89 (9.6)	1.06 (11.3)	15

Table 1: Results of pin-ended buckling tests

All specimens behaved similarly, with catastrophic failure, and consistent compressive failures in the gauge length. The results are presented in the top half of Table 1. There is a 32% decrease in strain at failure with the factor of 8 increase in all specimen dimensions.

Three further sets of tests were conducted where the thickness was kept constant and the length and width of the specimens varied. These specimens were cut from a 2 mm thick plate of the same material. Strains at failure were all very similar, as shown in the lower half of Table 1. This suggests that the size effect observed with the scaled specimens is most likely to be due to the reduction in strain gradient with increasing specimen thickness rather than a statistical effect due to differences in stressed volume.

The results for all six sets of tests are plotted in Fig. 2 as a function of the strain gradient, defined as the difference in surface strains at the centre of the specimen at failure divided by

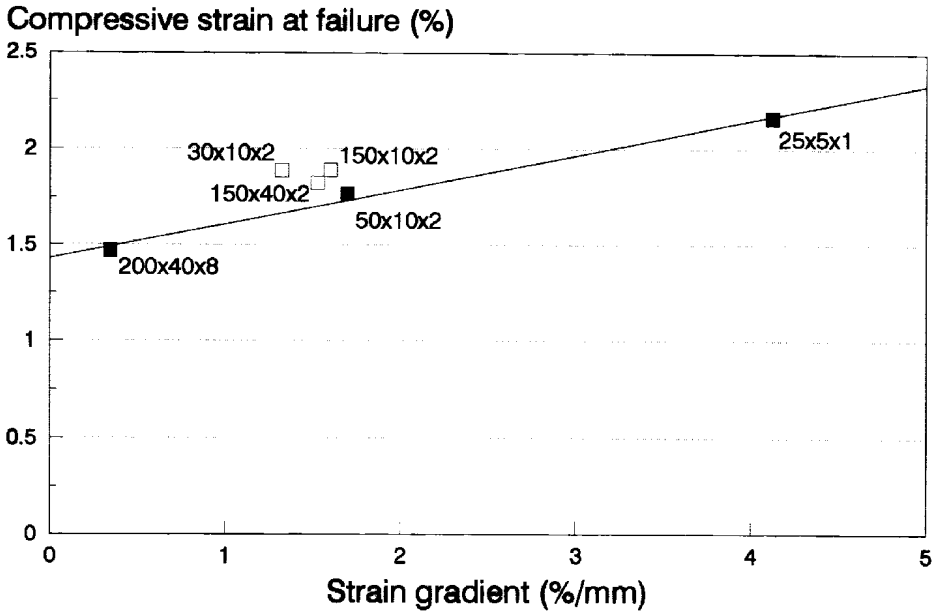

Fig. 2: Strain gradient effect with different sized specimens

the thickness. A least squares straight line has been put through the scaled results, and gives a good fit. The results for the second set of tests are slightly above the line, which could be because the specimens were cut from a thinner plate where the fibre alignment may have been better.

EFFECT OF STRAIN GRADIENT

A new buckling rig was developed which allowed the ends of the specimen to rotate initially, and then lock up [10]. By changing the amount of rotation permitted, the ratio between compression and bending could be varied.

Fig. 3 shows the rig. The specimen (12) is clamped to end fittings (10) which can rotate on pins (3). Adjustable tie rods (5) lock the rig after a certain amount of rotation, effectively changing the end conditions from pinned to clamped.

Two different sized specimens were tested, both 2 mm thick and 10 mm wide, with gauge lengths of 20 mm and 40 mm. Initial tests were carried out to determine the range of rotation angles which gave consistent gauge length failures. Two sets of tests were then undertaken for each length with the minimum and maximum rotation angles.

All specimens failed in the gauge length, with similar compressive failures to those obtained in the pinned ended buckling tests. The strains at failure were measured with strain gauges at the centre of the specimens. For the 20 mm gauge length case with the minimum rotation angle there was some asymmetry in the response which meant that the maximum strain did not necessarily occur at the centre of the specimen. In this case the maximum strains were estimated from the readings of three strain gauge at different positions along the length.

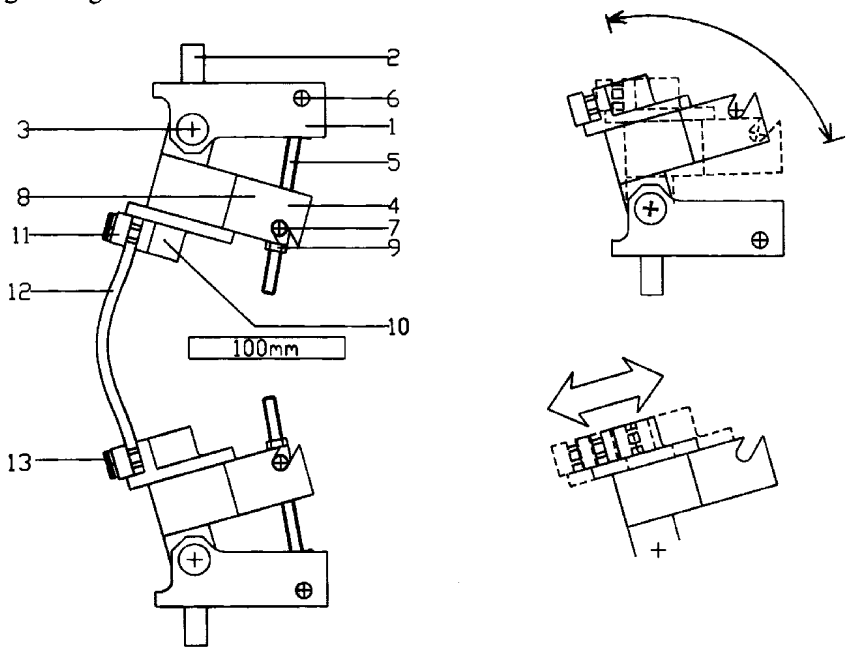

Fig. 3: Constrained buckling rig

Specimen size (mm)	Rotation Angle (deg)	Failure strain (cv), % compressive	tensile	Number of specimens
40 x 10 x 2	20	-1.94 (7.5)	1.53 (6.0)	5
40 x 10 x 2	5	-1.77 (4.8)	1.11 (8.7)	6
20 x 10 x 2	13	-1.80 (3.7)	1.24 (7.2)	5
20 x 10 x 2	1	-1.61 (5.2)	0.25 (60.9)	6

Table 2: Results of constrained buckling tests

Fig. 4 shows the results for all four sets of tests plotted against the strain gradient through the thickness, and the values are given in Table 2. There is a consistent trend, with a 20% increase in strain at failure for a 85% increase in strain gradient through the thickness. The results cannot be explained in terms of statistical effects due to differences in stressed volume. The trend is similar to that obtained with the pin-ended buckling tests, and provides further support for the conclusion that the strain gradient through the thickness is critical in determining the compressive strain at failure.

EFFECT OF FIBRE WAVINESS

A technique was developed for measuring out-of-plane waviness using a surface displacement transducer mounted on a traversing table [15]. Measurements within the laminate were made by splitting it open along ply interfaces treated with release agent prior to curing.

Fig. 5 shows typical results in terms of the out-of-plane misalignment angles at the centre of a 2 mm thick T800/924 plate, measured along a 120 mm length in the fibre direction. The

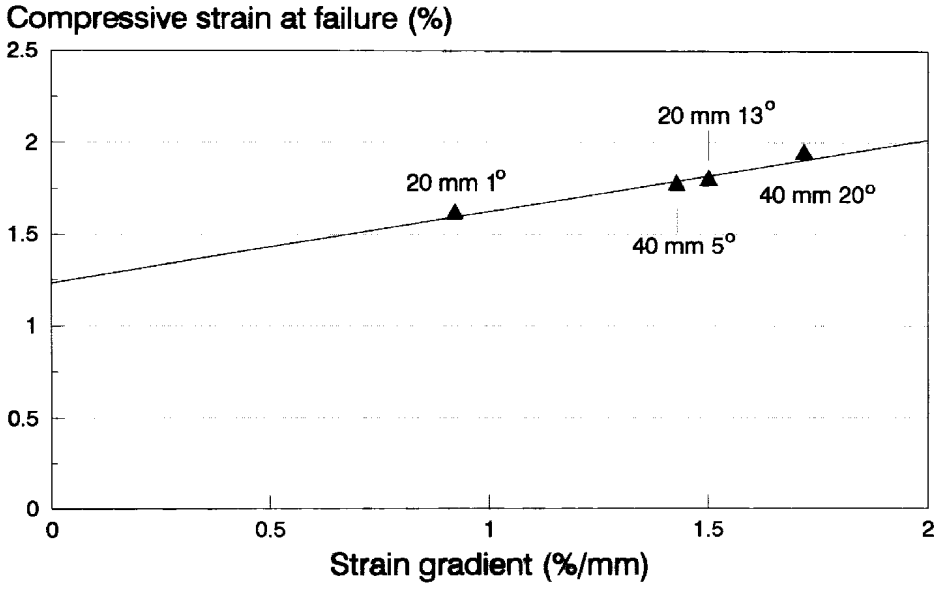

Fig. 4: Strain gradient effect with different ratios of compression to bending

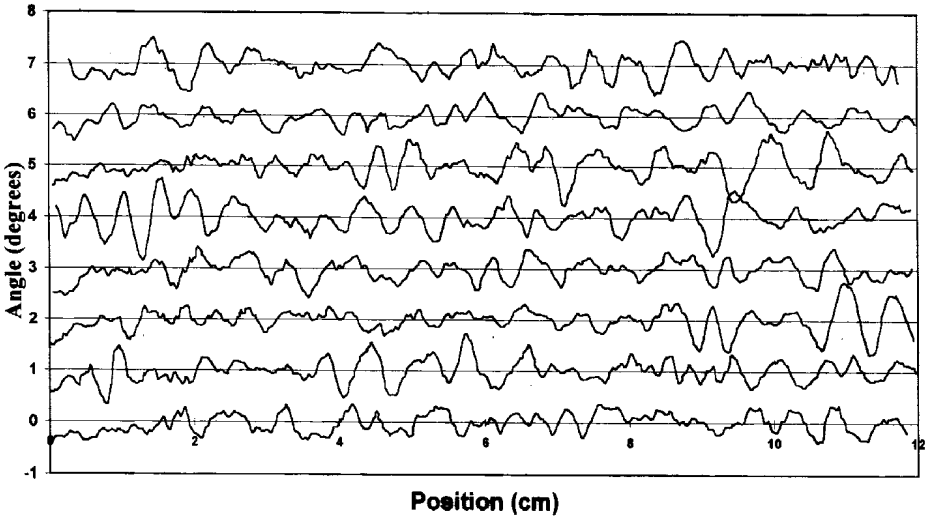

Fig. 5: Out-of -plane misalignment angles, runs at 1 mm pitch across width offset by 1 degree

successive traces are at 1 mm increments across the width, offset by 1 degree for clarity. Most of the angles lie within a range of ±0.5 degrees, with maximum misalignments of about 1 degree. There is little correlation between the different traces, showing that the waviness is localised to relatively small areas. These angles are relatively small, and it is possible that the technique underestimates the true misalignments of the fibres. It has been assumed that the surface profile of the split open panels represents the geometry of the fibres, but resin on the surface could tend to smooth out undulations in the plies.

Similar measurements at other ply interfaces showed that the misalignment angles were highest near the centre of the panel, reducing in magnitude towards the surfaces.

Artificial waviness was produced by laying up unidirectional prepreg on a curved plate, and then straightening it before curing [15]. This gave severe in-plane waviness in the centre of the upper surface, but no signs of waviness on the lower surface. Two panels were made, one of which included release agent in the lay-up to enable it to be split open to measure the waviness.

Out-of-plane misalignment angles were similar to those from the flat panel with no artificially induced waviness, with peak values of about 1 degree near the centre of the panel. After splitting the panel through the thickness along the release treated interfaces, the resulting two ply thick layers were split along their length. The splits followed the fibres, allowing the in-plane waviness to be measured by examining the geometry of the splits under the microscope. Severe misalignment angles of up to 24 deg. were found at the surface, reducing to up to about 6 deg. in plies 3 and 4. No significant in-plane waviness was observed deeper than ply 4.

Specimens 50 x 10 mm were cut from the non release treated panel with their centres in the middle of the worst kinks. They were tested to failure in the pin-ended buckling rig with the side of the specimen with waviness on the compression surface. The behaviour was very similar to that of the previously tested ones with nominally straight material. The mean compressive strain at failure was 1.46%, a reduction of 17%. The scatter was also considerably increased, with a coefficient of variation of 16.4%.

The relatively small reduction in strain at failure is rather surprising considering the severity of the waviness. However, the waviness was largely in-plane, and limited to the surface. Modelling studies have shown that where waviness changes over short distances, the strength is determined more by the average misalignment angle, and so small areas of poor alignment would not be expected to have such a great effect [16]. This is also consistent with previous results where localised areas of naturally occurring waviness on the surface were found to have negligible effect on compressive strains at failure [6].

FINITE ELEMENT MODELLING

An approach developed previously [8,14,16] was used to analyse the effect of the strain gradient on compressive failure due to shear instability. A 2-D finite element model was prepared of a section of material subject to pure bending. The representation of fibre waviness was greatly simplified. All waviness was assumed to be out-of-plane, with a sinusoidal waveform and constant amplitude through the thickness. Beam elements were used to model the fibre direction properties, and continuum elements to represent the transverse and shear properties of the composite. This hybrid approach allows the fibre bending stiffness to be included, and models correctly the change in material axes which occurs under shear deformation.

A short section of 0.25 mm was modelled, corresponding to one half wavelength. The amplitude was such as to give a maximum misalignment angle of 2 degrees. These values were chosen arbitrarily as the basis of a parametric study before any measurements had been made. In fact, the observed wavelengths were greater than this and the maximum misalignments measured were somewhat less. Boundary conditions and loading were applied to model a continuous beam with constant waviness subject to bending with no axial load. The model is shown in Fig. 6. Further details can be found elsewhere of the modelling approach [16] and its application to flexural loading [8].

Measured non-linear fibre direction and shear properties for T800/924 were used [14]. The transverse response was assumed to be linear. Three different models were analysed, 1, 2 and 8 mm thick, corresponding to the three thicknesses of beams investigated in the pin-

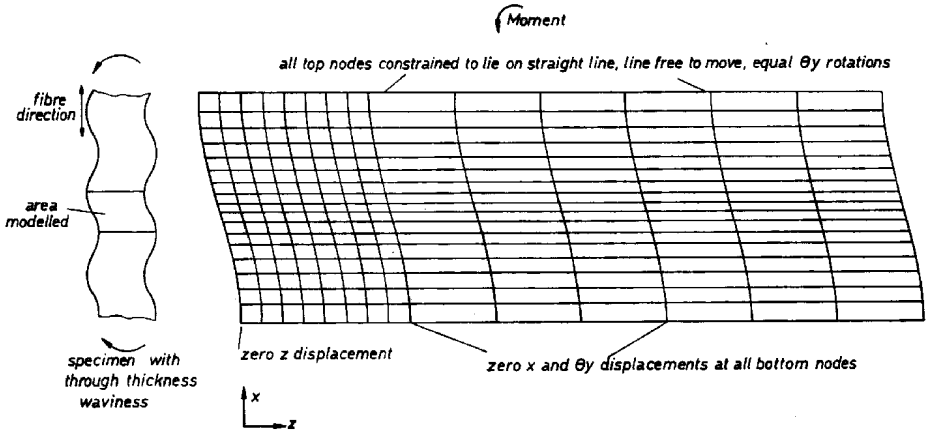

Fig. 6: Typical finite element mesh and boundary conditions (waviness exaggerated)

ended buckling tests. In all cases a maximum moment was obtained at which the response became unstable. The surface strains at this point were taken as the failure strains.

Results are presented in Fig. 7 in terms of the compressive strains at failure as a function of the strain gradient through the thickness. There is a strong trend of increasing strain at failure with decreasing thickness, as shown previously [8]. The misalignment caused by the waviness produces shear stresses in the highly loaded surface region. This in turn produces increased misalignment, and at a certain point the process becomes unstable leading to catastrophic collapse. As the strain gradient increases, the less highly loaded fibres away from the surface are able to provide more support, increasing the stress at which instability occurs.

The 2 mm thick model was rerun with a combination of direct compressive and bending loading instead of pure bending. The surface compressive strains at onset of instability as a function of strain gradient fitted very closely with the results for pure bending on the different thickness specimens. This shows that the strain gradient is the critical parameter, irrespective of whether it varies due to changes in thickness or changes in the ratio of compressive to flexural loading. The same conclusion was drawn from the two series of tests presented earlier.

The experimental results from the scaled pin-ended buckling and constrained buckling tests are also shown on Fig. 7. The trends shown in the analysis and test results are very similar. The actual strains at failure are higher than predicted for a number of reasons. Firstly the analysis was based on arbitrarily assumed waviness parameters. The measured maximum misalignment angles were up to about 1 degree compared with the 2 degrees assumed in the model. The wavelength used was also shorter than typical measured values. The amplitude was assumed to be constant, whereas in fact it tends to decrease towards the surface of the

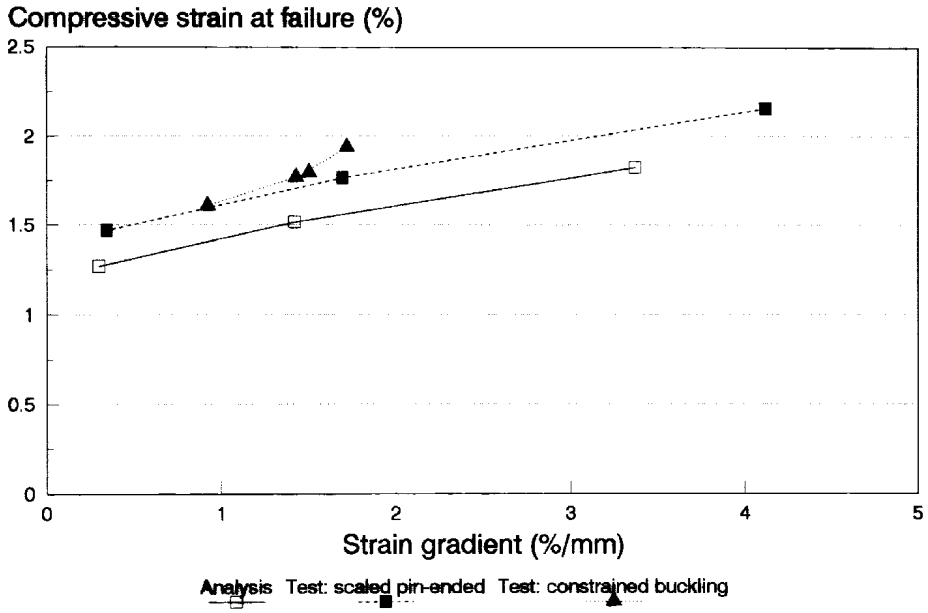

Fig. 7: Predicted strain gradient effect and comparison with test results

panel. All three factors would tend to increase the strain at failure [8,16], and if they were all accounted for in the model, the predicted strains would be greater than the measured ones.

On the other hand the model also makes a number of simplifying assumptions that would tend to overestimate the strain to failure. It is a 2-D model, and neglects the effect of in-plane waviness, which may combine with that out of the plane to produce higher effective waviness. The model assumes that the shear response is independent of the fibre direction strain, neglecting any interaction which may occur in practice. It also neglects the effects of overall shear stresses which are present in the pin-ended buckling tests due to the end load and the angle that develops during the test as a result of the bending. Any tendency for creep to occur due to the high shear stresses in the areas of waviness is ignored.

Clearly compressive failure is a very complex problem. Excellent qualitative agreement has been obtained between the model and the experimental trends, and the analysis has provided a better understanding of the effects of the different parameters. However, quantitative comparisons are made difficult by the assumptions required in the analysis, and uncertainties with regard to the appropriate parameters to represent fibre waviness realistically.

CONCLUSIONS

The strain gradient through the thickness is a critical parameter affecting the compressive strain at failure under flexural loading. This has been demonstrated by scaled tests in a pin-ended buckling rig, by constrained buckling tests varying the ratio between compressive and flexural loading, and by finite element modelling accounting for the effect of out-of-plane fibre waviness. Size effects observed in the scaled tests are predominantly due to the changes in the strain gradient with different thicknesses, rather than due to the different stressed volumes.

Out-of-plane ply level misalignment angles of up to about 1 degree have been measured. Highest values were near the centre, decreasing towards the surface, and with significant variations across the width.

Specimens with severe fibre waviness induced on the surface showed only a 17% reduction in compressive strain at failure when tested in the pin-ended buckling rig. This is thought to be because the waviness was mainly in-plane, and limited to the region close to the surface.

Finite element modelling of the shear instability failure mechanism was able to reproduce very well the trends observed experimentally, and can give valuable insight into the factors affecting failure.

ACKNOWLEDGEMENT

This work was funded by the U.K. EPSRC/MOD under contract number GR/H75017 in collaboration with Westland Helicopters and DRA Farnborough.

REFERENCES

1. Hitchon, J.W. and Phillips, D.C., The effect of specimen size on the strength of CFRP, Composites 9:119-124, 1978.

2. Wisnom, M.R., The effect of specimen size on flexural strength of unidirectional carbon fibre-epoxy, Composite Structures 18:47-63, 1991.

3. O'Brien, T.K. and Salpekar, S.A., Scale effects on the transverse tensile strength of graphite epoxy composites, Composite Materials: Testing and Design Vol. 11, pp 23-52, ASTM STP 1206, 1993.

4. Wisnom, M.R. and Jones, M.I., Size effects in interlaminar tensile and shear strength of unidirectional glass fibre-epoxy, Journal of Reinforced Plastics and Composites 15:2-15, 1996.

5. Reeder, J. R., Stitching vs a toughened matrix - compression strength effects, Journal of Composite Materials 29:2464-2487, 1995.

6. Wisnom, M.R., Atkinson, J.W. and Jones, M.I., Reduction in compressive strain to failure with increasing specimen size in pin-ended buckling tests, Composites Science and Technology, in press.

7. Gardin, C., Grandidier, J.C. and Potier-Ferry, M., Compressive behaviour of composite materials: a theoretical and experimental study, Proc. ICCM9, Vol. III pp 301-307, Madrid, July 1993.

8. Wisnom, M.R., The effect of fibre waviness on the relationship between compressive and flexural strengths of unidirectional composites, Journal of Composite Materials 28:66-76, 1994

9. Swanson, S.R., Constraint effects in compression failure of fiber composites, Proc. ICCM10, Vol. I pp 739-746, Whistler, Canada, August 1995.

10. Wisnom, M.R. and Atkinson, J.A., Constrained buckling tests show increasing compressive strain to failure with increasing strain gradient, submitted to Composites.

11. Camponeschi, E.T., Lamina waviness levels in thick composites and its effect on their compressive strength, Proc. ICCM8, Honolulu, July 1991.

12 .Adams, D.O. and Hyer, M.W., Effects of layer waviness on the compression strength of thermoplastic composite laminates, Journal of Reinforced Plastics and Composites 12:414-429, 1993.

13. Mrse, A. M. and Piggott, M. R., Compressive properties of unidirectional carbon fibre laminates: II. The effects of unintentional and intentional fibre misalignments, Composites Science and Technology 46:219-227, 1993.

14. Wisnom, M.R. and Atkinson, J.A., Compressive failure due to shear instability: experimental investigation of waviness and correlation with analysis, Journal of Reinforced Plastics and Composites, 15:420-439, 1996.

15. Wisnom, M.R. and Atkinson, J.A., Fibre waviness generation and measurement, and its effect on compressive strength, to be published.

16. Wisnom, M.R., Analysis of shear instability under compression due to fibre waviness, Journal of Reinforced Plastics and Composites 12:1171-1189, 1993.

HIGH STRAIN RATE MECHANICAL PROPERTIES OF A TOROSPHERICAL SHELL COMPOSED OF IM7/E7T1-2 GRAPHITE EPOXY COMPOSITE

Alexander T. Dee[1], Jack R. Vinson[1] and George Leon[2]

[1] *Department of Mechanical Engineering, University of Delaware.*
[2] *Electric Boat Division, General Dynamics, Groton, Connecticut.*

SUMMARY: Polymer matrix composites offer excellent mechanical properties such as high specific strength and stiffness, making them attractive for applications in several naval, aerospace, automotive, and recreational-sports structural components. Although many composite materials are selected for applications where high strain rate loading is probable, little is known of their responses to shock loading. Mechanical properties can vary significantly with strain rate. Therefore, the use of static properties in the analysis and design of structures which undergo dynamic loading may unfortunately lead to very conservative, overweight designs or lead to designs which fail prematurely and unexpectedly. The use of dynamic material properties ensures that designs are optimized for structural integrity and weight efficiency when subjected to dynamic loading.

In this study, a Split Hopkinson Pressure Bar is used to obtain high-strain-rate, compressive mechanical properties of a 48 inch diameter, quasi-isotropic, torospherical shell composed of IM7/E7T1-2 graphite epoxy composite. The shell is part of an external, pressure-proof storage module which is attached to a submersible vehicle and designed to support equipment internally at atmospheric pressure. In combat situations, this structure may be exposed to underwater explosions, therefore warranting the need for dynamic material properties. For in-plane and out-of-plane directions, the yield strength, yield strain, ultimate strength, ultimate strain, and modulus of elasticity are presented for strain rates varying from 381 sec^{-1} to 1154 sec^{-1}. The data from the 49 dynamic tests are statistically analyzed, represented by equations, compared to quasi-static material properties, and discussed in some detail.

KEYWORDS: high-strain-rate, IM7/E7T1-2, Split Hopkinson Pressure Bar.

INTRODUCTION

The Split Hopkinson Pressure Bar facility at the University of Delaware is described Ref. 1. Impact is initiated by releasing nitrogen gas from a pressurized chamber which causes the specimen to be compressed between the two bars. The striker bar is displaced on Teflon rings through the barrel where it strikes the incident bar (bar 1). The velocity of the striker bar, V_{sb}, just prior to impact is measured using two infrared beams set four inches apart.

Upon impact with the striker bar, the incident bar receives an elastic compressive strain wave with a wave velocity C_B and a wave shape $\varepsilon_I(t)$ and is displaced along its length axis. This bar is guided by Teflon bearings which are bolted to a steel I-beam and secured on a reinforced concrete base to minimize any vibration. When the wave reaches the bar 1-specimen interface, a portion of the incident wave is reflected back into bar 1 as a tensile wave with a

wave shape $\varepsilon_R(t)$. The remaining portion is transmitted into the specimen as a compressive wave. The wave transmitted into the specimen travels through the specimen and reaches the specimen-bar 2 interface, where a portion of the wave is reflected back into the specimen. The remaining portion is transmitted into bar 2 as a compressive wave with a wave shape $\varepsilon_T(t)$. Bar 2 is displaced similarly to bar 1, but is arrested after the test by a simple dash pot.

Because the specimen length is short compared to the bar lengths, the initial stress wave in the specimen undergoes numerous internal reflections during the test. It is calculated that the initial wave duration in a typical specimen is approximately two microseconds. Within a composite material specimen, there may be differences in the wave speed in the fiber and matrix materials. However, if a minimum of four wave reflections within the specimen is achieved prior to specimen failure, the stress distribution along the specimen length is smoothed out and the specimen is assumed to be in a uniform state of stress at any instant [2,3]. At the University of Delaware SHPB, the wave pulse time window (defined as the time it takes a wave to travel the length of the striker bar and back) is approximately 290 microseconds. Thus, to record information accurately at specimen failure, the specimen must fail within 290 microseconds after the start of the test and also after a time such that four internal reflections in the specimen has been achieved.

Strain gages are mounted on bars 1 and 2 equidistant from the specimen interfaces and are connected to an oscilloscope. The oscilloscope records and stores the output from the strain gages. Using this data, the stress and strain versus time of the specimen during the test can be calculated for the strain rate of that particular test.

MATERIAL DESCRIPTION

The shell is made of IM7/E7T1-2 (rubber toughened) with the following quasi-isotropic lay-up: $[45/135/90_2/45/135/0_2/45/135/90_5[45/135/0_8/45/135/90_8]_5 45/135/0_5/45/135]s$. A section of the torospherical shell was provided by the Electric Boat Division of General Dynamics.

SPECIMEN PREPARATION

Compression specimens in the shape of right circular cylinders (1/4 inches in diameter and 3/8 inches in length) were machined from the shell and prepared for testing by the senior author. Care was taken to machine samples which displayed minimal visible effects of the inherent shell curvature. However, the effects of the curvature are expected to give some variation in the results. Another source of error is due to the stacking sequence coupled with the small diameter of each test sample. Since core drilling was done at random locations in the through-thickness, specimens are expected to have slightly different stacking sequences.

TEST RESULTS

Since the laminate lay-up is such that the shell is quasi-isotropic, the 1-direction refers to any in-plane direction, while the 3-direction denotes the through-thickness direction perpendicular to the fibers. For completeness, all the data from the 24 tests in the 1-direction and the 25 tests in the 3-direction are presented in Tables 1 and 2. Quasi-static tests were performed on an Instron universal machine at a strain rate of 0.05 inches/second. Quasi-static strength data for the shell material is provided in Table 5. These data will allow other researchers to study and analyze the tests independently. These data are then presented statistically in Tables 3, 4, and 6 which provide mean values and standard deviations.

STATISTICAL ANALYSIS, RESULTS, AND DISCUSSION

It is interesting to see that with the complexities of these high strain rate tests, and the small sample sizes, how small the coefficient of variance (COV), (i.e. the ratio of standard deviation to mean value, given as a percentage), is for the various mechanical properties as shown in Table 7. The highest COV value is 35.8% (on a modulus of elasticity) while the lowest COV is 2.1% (on a yield strength).

To analyze the trends from Tables 3, 4, and 6, it is important to define significant differences. For the present purpose, a quantity P is said to be significantly different from Q if the mean value of P falls outside the region of the mean ± 3 standard deviations of Q. The ± 3 standard deviations are plotted as error bars for each relevant dynamic material property in Figures 1-5 as a visual means of determining significant differences.

From Table 3, it is seen that there is little significant difference in the range of strain rates for the 1-direction. Only the strain rates of groups D and E are significantly different from the group A strain rate. Failure of the specimens was achieved at each strain rate. Yielding was not found in the 1-direction except at the low strain rate. Therefore, in the strain rate range between 381.1 sec^{-1} and 457.1 sec^{-1}, a transition from ductile to brittle behavior must occur. This trend from ductile behavior to brittle behavior has been noticed in other polymer matrix composite materials. Concerning ultimate strength, Figure 1 shows that these values do not differ significantly with strain rate. Ultimate strain values show that group D is significantly different to group C, and that group E is significantly different to groups B and C (Figure 2). Modulus of elasticity values show little dependence on strain rate. Only the group A modulus of elasticity is significantly different from the other groups (Figure 5).

From Table 4, strain rates in the 3-direction are generally significantly different except that groups F, G, H, and J are not significantly different from group I, and Group I is not significantly different from group J. Yielding was found in the 3-direction for all strain rates, and yield strength values show an increasing trend with strain rate. Yield strength values of groups F and G are significantly different from the other groups with the exception of group H, and groups H and J are only significantly different from group F. Group I is only significantly different from groups F and J (Figure 3b). Yield strain values show an increasing trend with strain rate but have little significant difference among the groups. Only the yield strain of group F is significantly different from the other groups (Figure 4). Ultimate strength, ultimate strain, and modulus of elasticity all show no strain rate dependence (Figures 3a, 4, and 5, respectively).

It is seen that significant differences are prevalent when comparing dynamic material properties to the quasi-static material properties in Table 6. The quasi-static ultimate strength value in the 1-direction is significantly different only from groups C and E. However, the ultimate strength value of groups A-E are all significantly different from the quasi-static value. For the 3-direction, the ultimate strength quasi-static value shows a significant difference only to group F. However, the ultimate strength value of groups F-J are all significantly different from the quasi-static value. Yielding was not present in quasi-static tests for either the 1 nor the 3-direction.

FRACTOGRAPHY

Figure 6 shows a scanning electron microscope (SEM) photo of a 1-direction fracture surface tested at 527 sec^{-1}. The photo shows interfacial debonding, resin cusps associated with brittle fracture in resin rich areas [4], and resin cracks. Figure 7 shows an SEM photo of a 3-direction fracture surface tested at 245 sec^{-1}. The photo shows interfacial debonding and fiber fracture near a large crack.

CONCLUSIONS

The data from these 49 experiments for the IM7/E7T1-2 torospherical shell in the in-plane and through-thickness directions provides a data bank for this material at room temperature for strain rates between 381 sec^{-1} to 1154 sec^{-1}. Yielding in the 1-direction occurs only at the low strain rate. Thus, there is a transition from a ductile to a brittle behavior between strain rates of 381 sec^{-1} and 457 sec^{-1}. Yielding is present in the 3-direction for all strain rates, with yield strength increasing 2.13 times and yield strain increasing 4.97 times between strain rates of 382 sec^{-1} and 1154 sec^{-1}.

The ultimate strength in the 1-direction is strain rate insensitive. Ultimate strain and modulus of elasticity are nearly strain rate insensitive, with only the group A ultimate strain and modulus of elasticity being significantly different from the other groups. In the 3-direction, the ultimate strength, ultimate strain, and modulus of elasticity are strain rate insensitive.

There are significant differences between dynamic and quasi-static compressive material properties. In the 1-direction, the quasi-static ultimate strength is lower than all dynamic ultimate strengths. The quasi-static ultimate strength in the 1-direction is 29.4% lower than the highest, dynamic ultimate strength reported. In the 3-direction, the quasi-static ultimate strength is higher than its dynamic counterpart, being 28.3% higher than the lowest dynamic ultimate strength.

Yielding was not observed in quasi-static compression tests. Since yielding is seen in the 1-direction only at the lowest strain rate of 381 sec^{-1}, the 1-direction appears to display a second transitional behavior: the first being the transition from ductile to brittle behavior discussed earlier, and the second being a transition from brittle to ductile behavior between quasi-static loading and the 381 sec^{-1} strain rate. Since yielding is seen in all the 3-direction dynamic tests, a transition from brittle to ductile behavior must exist between quasi-static loading and the 382 sec^{-1} strain rate. More experiments may provide greater detail for all of the above conclusions.

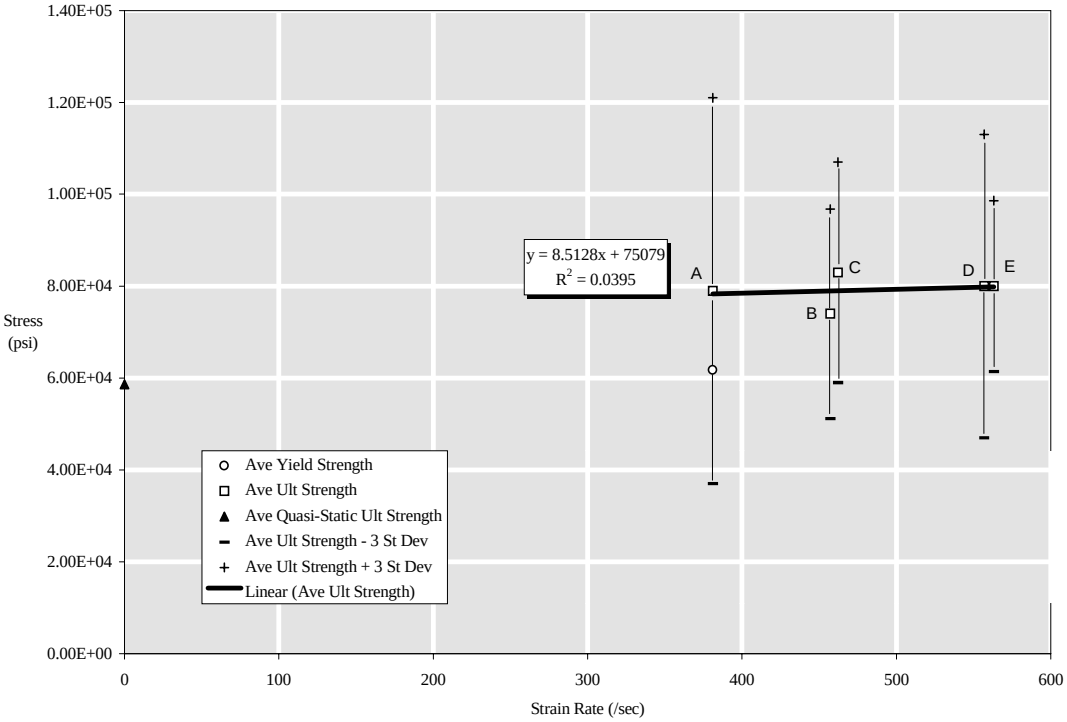

Fig. 1: Ultimate and Yield Strength as a Function of Strain Rate: Torospherical Shell Composed of IM7/E7T1-2, 1-direction

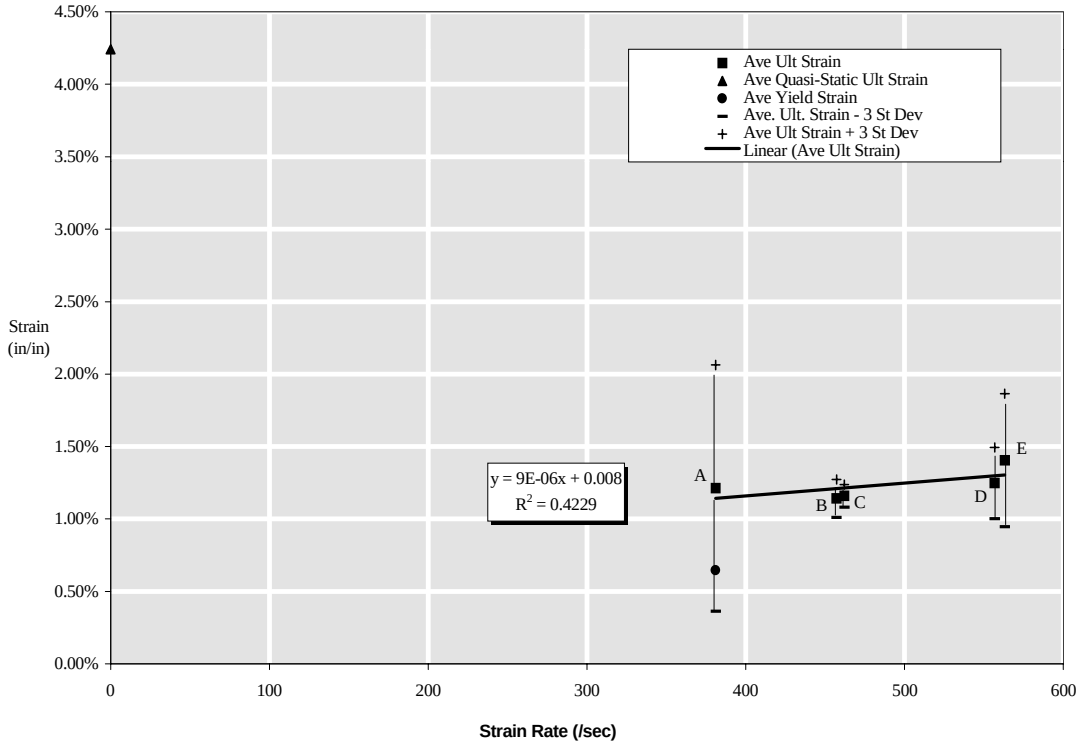

Fig. 2: Ultimate and Yield Strain as a Function of Strain Rate: Torospherical Shell Composed of IM7/E7T1-2, 1-Direction

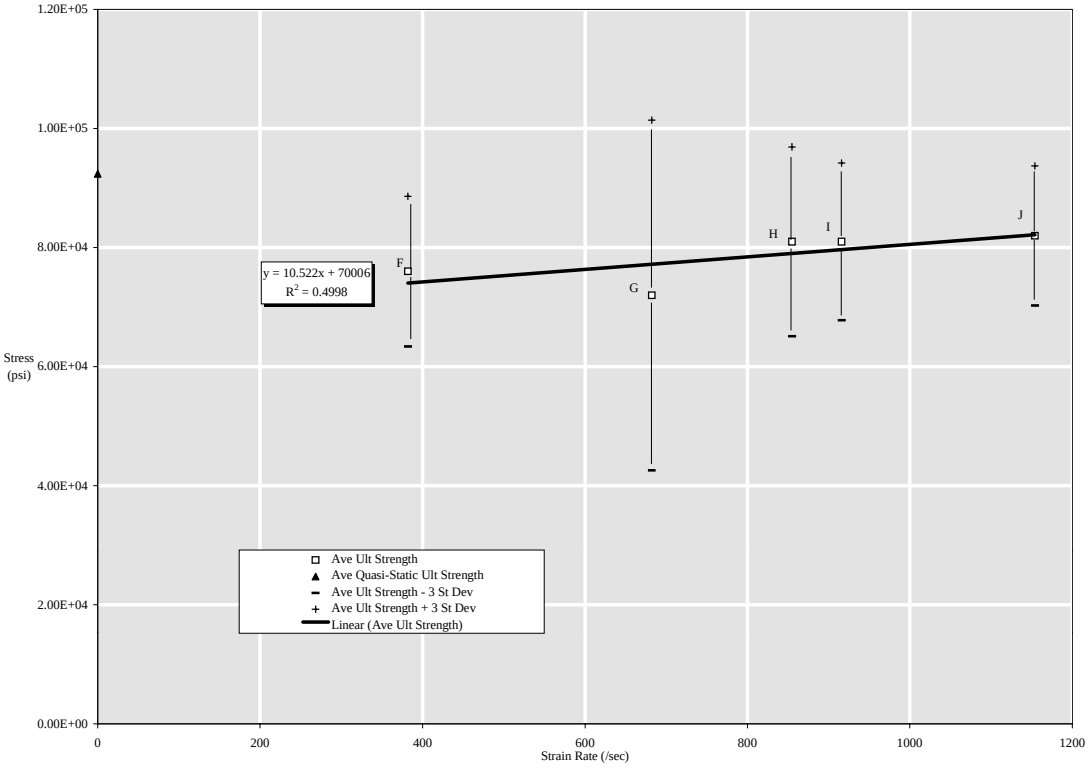

Fig. 3a: Ultimate Strength as a Function of Strain Rate: Torospherical Shell Composed of IM7/E7T1-2, 3-Direction

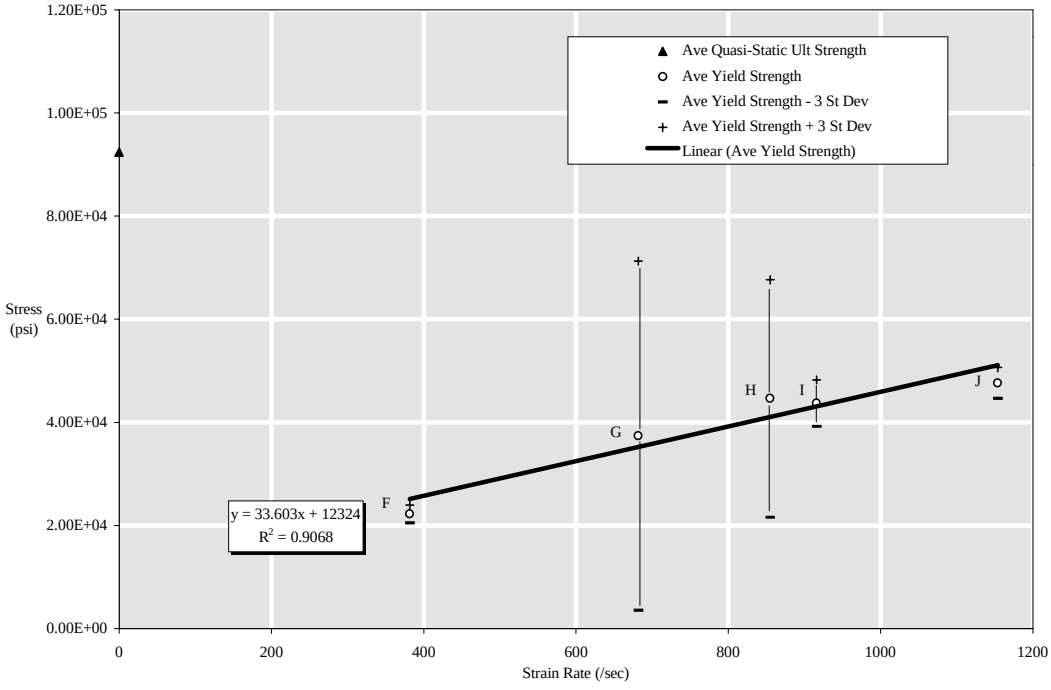

Fig. 3b: Yield Strength as a Function of Strain Rate: Torospherical Shell Composed of IM7/E7T1-2, 3-Direction

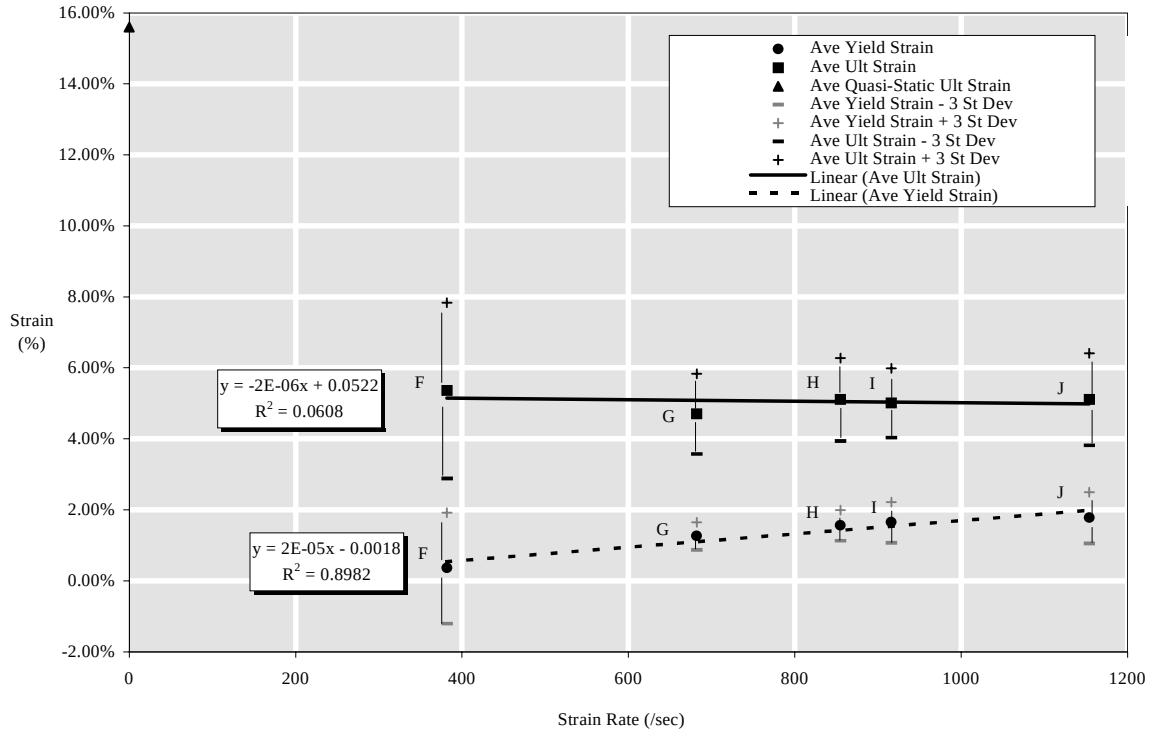

Fig. 4: Ultimate and Yield Strain as a Function of Strain Rate: Torospherical Shell Composed of IM7/E7T1-2, 3-Direction

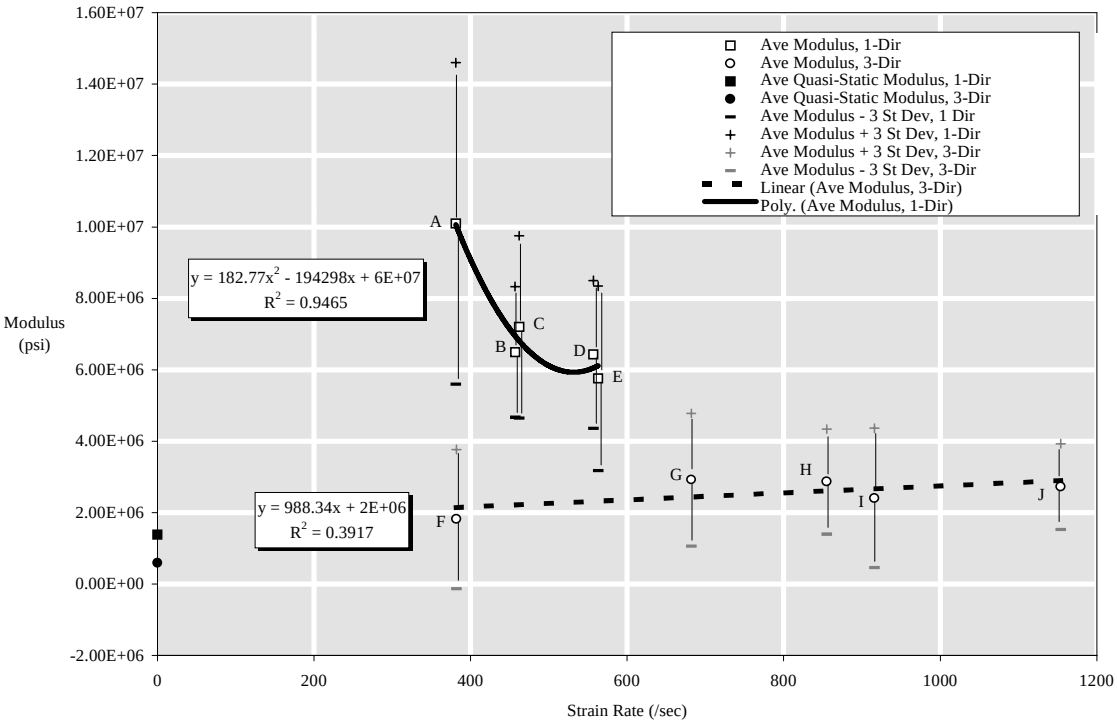

Fig. 5: Modulus of Elasticity as a Function of Strain Rate: Torospherical Shell Composed of IM7/E7T1-2

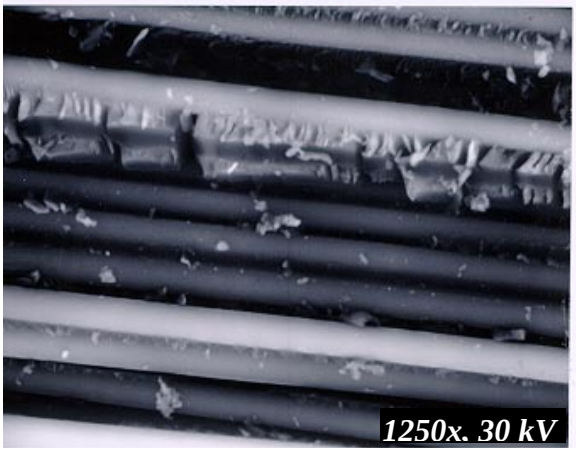

Fig. 6: SEM photo of a 1-direction specimen failure surface tested at 527 sec^{-1}, showing interfacial debonding, resin cracks, and cusps

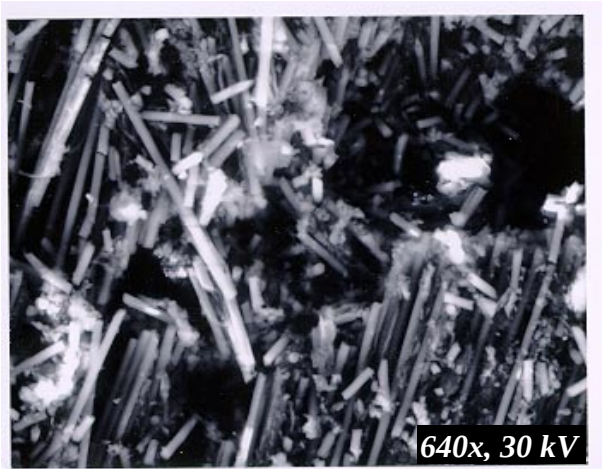

Fig. 7: SEM Photo of a 3-Direction Specimen Failure Surface Tested at 245 sec^{-1}, showing fiber failure and interfacial debonding near a crack

Table 1: Torospherical Shell Composed of IM7/E7T1-2: 1-Direction Tests

Group	Pressure (psi)	Strain Rate (/sec)	Yield Strength (psi)	Ult Strength (psi)	Yield Strain (%)	Ult Strain (%)	Modulus (psi)	Notes
A1	20	349	6.52E+04	8.50E+04	0.63%	1.26%	1.04E+07	Fracture predominately
A2	20	387	6.30E+04	7.11E+04	0.60%	1.20%	1.06E+07	in the fiber direction.
A3	20	434	5.70E+04	5.97E+04	0.71%	1.61%	8.06E+06	Fracture between plies
A4	20	351	6.18E+04	8.06E+04	0.65%	1.19%	9.49E+06	adjacent to the
A5	20	384	-	9.68E+04	-	0.81%	1.20E+07	woven ply visible.
B1	40	527	-	7.62E+04	-	1.10%	6.93E+06	Fracture predominately
B2	40	514	-	6.46E+04	-	1.10%	5.88E+06	in the fiber direction.
B3	40	370	-	8.54E+04	-	1.17%	7.30E+06	Fracture between plies
B4	40	481	-	7.16E+04	-	1.20%	5.97E+06	adjacent to the
B5	40	393	-	7.35E+04	-	1.14%	6.45E+06	woven ply visible.
C1	60	433	-	9.35E+04	-	1.13%	8.27E+06	Fracture predominately
C2	60	520	-	7.78E+04	-	1.17%	6.65E+06	in the fiber direction.
C3	60	490	-	7.62E+04	-	1.19%	6.41E+06	Fracture between plies
C4	60	406	-	8.59E+04	-	1.15%	7.47E+06	adjacent to the woven ply visible. Many splinters.
D1	80	468	-	9.41E+04	-	1.24%	7.59E+06	Fracture mostly in the
D2	80	666	-	7.57E+04	-	1.28%	5.90E+06	fiber direction. Fracture
D3	80	420	-	6.56E+04	-	1.11%	5.91E+06	between plies adjacent to
D4	80	619	-	8.32E+04	-	1.31%	6.35E+06	woven ply visible. Many
D5	80	611	-	8.27E+04	-	1.30%	6.36E+06	splintered fragments.
E1	100	465	-	7.41E+04	-	1.27%	6.00E+06	Fracture mostly in the
E2	100	712	-	7.35E+04	-	1.65%	4.46E+06	fiber direction. Fracture
E3	100	573	-	8.32E+04	-	1.42%	5.86E+06	between plies adjacent to
E4	100	552	-	8.16E+04	-	1.41%	5.79E+06	woven ply visible. Many
E5	100	515	-	8.79E+04	-	1.28%	6.87E+06	splintered fragments.

Table 2: Torospherical Shell Composed of IM7/E7T1-2: 3-Direction Tests

Group	Pressure (psi)	Strain Rate (/sec)	Yield Strength (psi)	Ult Strength (psi)	Yield Strain (%)	Ult Strain (%)	Modulus (psi)	Notes
F1	20	320	-	7.41E+04	-	4.95%	1.50E+06	Fracture predominately at one end of specimen. 50-75% of specimen intact.
F2	20	339	-	7.73E+04	-	6.54%	1.18E+06	
F3	20	398	2.27E+04	8.19E+04	0.83%	5.33%	2.72E+06	
F4	20	477	2.18E+04	7.34E+04	0.96%	4.96%	2.28E+06	
F5	20	376	-	7.11E+04	-	5.03%	1.41E+06	
G1	40	693	4.98E+04	7.78E+04	1.38%	4.57%	3.62E+06	Fracture predominately in the fiber direction.
G2	40	698	2.95E+04	6.50E+04	1.11%	4.54%	2.66E+06	
G3	40	640	3.16E+04	8.01E+04	1.17%	5.37%	2.69E+06	
G4	40	666	4.94E+04	7.71E+04	1.41%	4.47%	3.50E+06	
G5	40	713	2.67E+04	5.75E+04	1.25%	4.56%	2.15E+06	
H1	60	860	4.35E+04	8.43E+04	1.55%	5.33%	2.81E+06	Fracture predominately in the fiber direction. Many splinters.
H2	60	873	3.82E+04	8.47E+04	1.37%	4.98%	2.78E+06	
H3	60	839	4.75E+04	8.45E+04	1.51%	5.12%	3.15E+06	
H4	60	857	5.63E+04	7.58E+04	1.62%	4.55%	3.46E+06	
H5	60	846	3.77E+04	7.42E+04	1.76%	5.58%	2.15E+06	
I1	80	583	-	7.46E+04	-	5.58%	1.34E+06	Fracture predominately in the fiber direction. Many splinters.
I2	80	990	4.32E+04	8.60E+04	1.51%	4.85%	2.85E+06	
I3	80	1016	4.31E+04	8.14E+04	1.45%	4.78%	2.97E+06	
I4	80	997	4.60E+04	8.40E+04	1.80%	4.88%	2.55E+06	
I5	80	993	4.27E+04	7.97E+04	1.81%	4.97%	2.35E+06	
J1	100	1020	4.80E+04	8.55E+04	1.52%	4.49%	3.17E+06	Some fracture visible in the fiber direction. Many splinters.
J2	100	1126	4.85E+04	8.63E+04	1.63%	5.29%	2.97E+06	
J3	100	1139	4.82E+04	8.32E+04	1.68%	4.90%	2.88E+06	
J4	100	1151	4.59E+04	7.96E+04	2.08%	5.29%	2.21E+06	
J5	100	1334	4.76E+04	7.73E+04	1.98%	5.60%	2.41E+06	

Table 3: Torospherical Shell Composed of IM7/E7T1-2: 1-Direction Statistics

Group		Strain Rate (/sec)	Yield Strength (psi)	Ult Strength (psi)	Yield Strain (%)	Ult Strain (%)	Modulus (psi)
A	Average	381	6.18E+04*	7.90E+04	0.65% *	1.21%	1.01E+07
	St Dev	34	3.45E+03*	1.40E+04	0.05% *	0.28%	1.50E+06
B	Average	457	-	7.40E+04	-	1.14%	6.50E+06
	St Dev	71	-	7.60E+03	-	0.04%	6.10E+05
C	Average	462	-	8.30E+04	-	1.16%	7.20E+06
	St Dev	52	-	8.00E+03	-	0.03%	8.50E+05
D	Average	557	-	8.00E+04	-	1.25%	6.43E+06
	St Dev	107	-	1.10E+04	-	0.08%	5.76E+06
E	Average	563	-	8.00E+04	-	1.41%	5.76E+06
	St Dev	93	-	6.20E+03	-	0.15%	8.60E+05

Table 4: Torospherical Shell Composed of IM7/E7T1-2: 3-Direction Statistics

Group		Strain Rate (/sec)	Yield Strength (psi)	Ult Strength (psi)	Yield Strain (%)	Ult Strain (%)	Modulus (psi)
F	Average	382	2.23E+04*	7.60E+04	0.36% *	5.36%	1.82E+06
	St Dev	61	5.82E+02*	4.20E+03	0.52% *	0.83%	6.50E+05
G	Average	682	3.74E+04	7.20E+04	1.26%	4.70%	2.92E+06
	St Dev	29	1.13E+04	9.80E+03	0.13%	0.38%	6.20E+05
H	Average	916	4.46E+04	8.10E+04	1.56%	5.01%	2.87E+06
	St Dev	13	7.67E+03	5.30E+03	0.14%	0.39%	4.90E+05
I	Average	650	4.37E+04**	8.10E+04	1.65% **	5.01%	2.41E+06
	St Dev	186	1.503E+03**	4.40E+03	0.19% **	0.33%	6.50E+05
J	Average	1154	4.76E+04	8.20E+04	1.78%	5.12%	2.73E+06
	St Dev	113	1.00E+03	3.90E+03	0.24%	0.43%	4.00E+05

*F3-4 used for average and standard deviation

**I2-5 used for average and standard deviation

Table 5: Torospherical Shell Composed of IM7/E7T1-2: Quasi-Static Tests

Direction	Number	Yield Strength (psi)	Ult Strength (psi)
1	1	-	6.33E+04
1	2	-	4.78E+04
1	3	-	6.47E+04
3	1	-	9.38E+04
3	2	-	9.10E+04

Table 6: Torospherical Shell Composed of IM7/E7T1-2: Quasi-Static Statistics

Direction		Ult Strength (psi)
1	average	5.86E+04
	st dev	9.37E+03
3	average	9.24E+04
	st dev	1.99E+03

Table 7: Variance of the Dynamic Mechanical Properties

Property	1-Direction	3-Direction
Strain Rate	9.0 - 19.1%	1.5 - 16%
Yield Strength	5.60%	2.1 - 30.2%
Ultimate Strength	7.7 - 17.8%	1.7 - 13.7%
Yield Strain	7.30%	9.1 - 13.6%
Ultimate Strain	2.2 - 23.4%	6.5 - 15.4%
Modulus	9.4 - 14.4%	14.7 - 35.8%

REFERENCES

1. Powers, B.M., J.R. Vinson and I.W. Hall, “High Strain Rate Mechanical Properties IM7/8551-7 Graphite Epoxy Composite,” Proceedings of the 10th Technical Conference of the American Society for Composites, October 1995.

2. Sierakowski, R.L., “Dynamic Measurements of the Mechanical Properties of Filamentary Composites,” In Dynamic Response of Composite Materials, SEM, 1985.

3. Ravichandran, G. and G. Subhash, “Critical Appraisal of Limiting Strain Rates for Compression Testing of Ceramics in a Split Hopkinson Pressure Bar,” In Journal of the American Ceramic Society, Volume 77, Number 1, January 1994, pp. 263-267.

4. Gilchrist, M.D., N Svensson, “A Fractographic Analysis of Delamination within Multidirectional Carbon/Epoxy Laminates,” Composites Science and Technology, Volume 55, 1995, pp 195-207.

5. Yoon, H.S., “Dynamic Void Growth in a Non-Linear Viscous Solid,” Ph.D. Thesis, Department of Mechanical Engineering, University of Delaware, 1987.

6. Zukas, J. (ed.), Impact Dynamics, John Wiley and Sons, New York, N.J., 1982.

7. Choe, G.H., “Impact Testing of Composite Materials at High Strain Rates,” Master’s Thesis, Department of Mechanical Engineering, University of Delaware, 1989.

8. Powers, B.M., “High Strain Rate Effects on the Properties of Composite Materials,” Master’s Thesis, Department of Mechanical Engineering, University of Delaware, 1995.

9. Powers, B.M., J.R. Vinson, I.W. Hall and R.F. Hubbard, "High Strain Rate Mechanical Properties of Cycom 5920/1583," Proceedings of the 36th AIAA/ASME/ASCE/AHS/ASC Structures, Structural Dynamics and Materials Conference, April 1995, pp. 2386-2392.

10. Powers, B.M., J.R. Vinson, I.W. Hall and V. Nardone, "High Strain Rate Mechanical Properties of Silicon Carbide Reinforced 2080 Aluminum Metal Matrix Composites," Proceedings of the 10th International Conference on Composite Materials, 1995, pp. 317-322.

11. Powers, B.M. and J.R. Vinson, "High Strain Rate Effects on Materials in Sandwich Construction," Proceedings of the Third International Conference on Sandwich Constructions, 1995, pp. 769-778.

MICROMECHANICAL APPROACH TO THE STRENGTH OF UNDIRECTIONAL COMPOSITES

Atsushi Wada and Hiroshi Fukuda

Department of Materials Science and Technology
Science University of Tokyo, Yamazaki, Noda, Chiba 278, Japan

SUMMARY: This paper deals with a probabilistic strength of unidirectional composites. Using a shear-lag analysis originated by Hedgepeth and Van Dyke, we first calculated the stress concentration factors around broken fibers in a three-dimensional, hexagonal-array model. Next, we carried out a Monte Carlo simulation to evaluate the strength of unidirectional composites. Parametric studies were first done and a comparison with experiments and other existing theories were next conducted. Our simulation was pretty close to the experimental results.

KEYWORDS: unidirectional composites, stress concentration factor, Monte Carlo simulation, Rosen model, Zweben model, parametric study, comparison with experiment

INTRODUCTION

Composite materials are composed of reinforcements and matrices and therefore, it becomes necessary to deal with these materials from a micromechanical view point. Since the original report of Rosen[1], many works have been done on the micromechanical and statistical evaluation of the strength of unidirectional composites.

The characteristics of individual fibers, matrix, and fiber/matrix interface are the most important factors for evaluating FRPs from a micromechanical view point. Since some synergistic effects at the fiber/matrix interface exist in advanced composite materials, the strength of advanced composite materials cannot be predicted by simple averaging the strength of its constituents. Prediction of the strength of advanced composite materials requires the factor of stress concentrations around broken fibers and the effect of the fiber/matrix interface the latter of which can be derived from the test of one fiber buried in a matrix.

Among various existing models for the strength of unidirectional composites, a Rosen model [1]

and a Zweben model [2] would be fundamental and most important.

The Rosen model does not take into consideration the stress concentration factors (SCFs). Phoenix [3] called this idea an Equal Load Sharing (ELS) rule. The Rosen model predicts higher strength than that of actual composite.

Zweben [2], on the other hand, introduced the SCFs calculated by Hedgepeth [4] which was based on a shear-lag analysis. However, Hedgepeth's original work was for a unidirectional sheet rather than three-dimensional composites. Two-dimensional calculation ends up with larger SCFs and therefore, the Zweben model leads lower composite strength. The Rosen and the Zweben models are somewhat upper and lower bounds of the strength althongh this classification is not done in a precise manner.

The objective of the present paper is to predict the strength more accurately than the Rosen or the Zweben model. To this end, we need more accurate SCFs. After calculating the SCFs in a three-dimensional, hexagonal-array model, we try a Monte carlo simulation for the strength of composites.

STRESS CONCENTRATION FACTORS

Hedgepeth and Van Dyke [5] already derived the SCFs in a hexagonal-array model, Fig.1, although their numerical results are for limited cases and there may include somewhat minor error. The work of Suemasu [6] seems more sophisticated and we adopt his formulation. What we need to do is to calculate the SCFs at various combination of broken fibers.

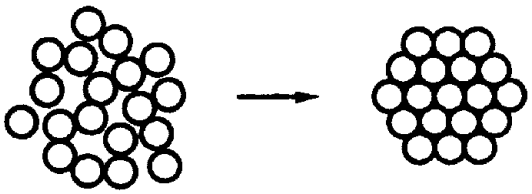

Fig.1 Hexagonal array

Figure 2 demonstrates the SCFs around irregulary broken fibers. Calculations were done for all necessary combinations of broken fibers. One point to be noted is that the number of fibers is infinite.

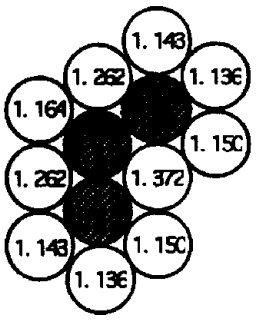

Fig.2 Stress Concentration Factors (SCFs) around 3 broken fibers

MONTE CARLO SIMULATION

Weibull distribution

The strength of many high performance fibers can be well represented by the Weibull distribu-

tion, which, in one functional form, may be written as

$$F(x)=1-\exp\left\{-\left(\frac{x}{\alpha}\right)^m\right\} \qquad (1)$$

where F(x) is the cumulative distribution function of the strength, x is the strength, and m and α are, respectively, the shape and scale parameters. Large m corresponds to a small scatter and large α indicates large strength. Equation (1) is known as a two-parameter Weibull distribution.

If the shape and scale parameters are known, and if we specify a probability of failure F(x), then we can solve Eq.(1) for the strength associated with that probability by

$$x=\alpha\{-\ln(1-F(x))\}^{1/m} \qquad (2)$$

For a Monte Carlo analysis, in order to simulate fiber strengths that follow the Weibull distribution, uniform random numbers between 0 and 1 are first generated. These random numbers are substituted into Eq.(2) producing a composite whose fiber strengths follow a Weibull distribution.

Simulation program

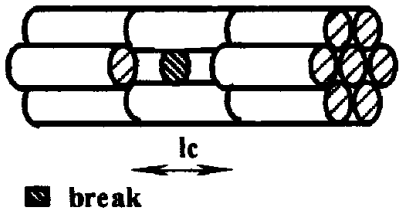

Fig.3 Critical length

In the simulation, it is assumed that the influence of broken fiber is limited to a critical length lc of Fig.3 [1], and that the stress concentration occurs to only neighboring fibers. The basic idea of the failure process is the same as Rosen[1] or Zweben[2] model. That is, when all fibers within a critical length are broken, the specimen is considered to break.

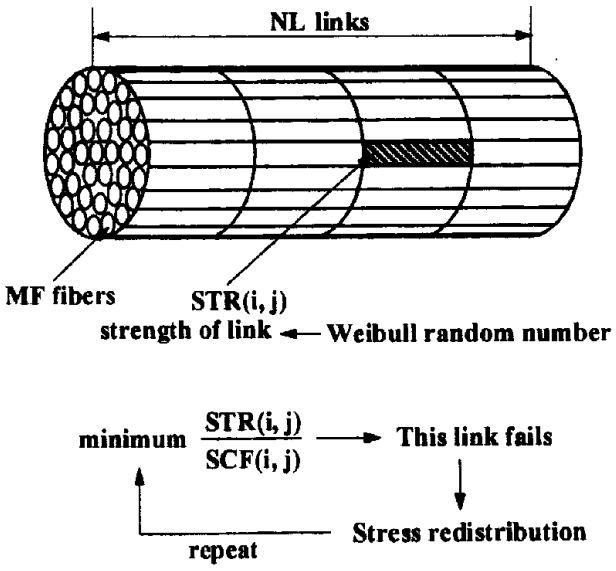

Fig.4 Monte Carlo simulation of 3-dimensional model

The formulation of the computer program is close to Oh's work [7] which may be described as follows. First, a

model of MF fibers with NL links is settled. The total number of links is MF × NL. Then each Weibull random number is allocated to each link. This Weibull random number represents the strength of the link, denoted by STR(i,j), where i=1,...., MF indicates each fiber and j=1,...., NL shows the link number. The stress concentration factors of links, SCF(i,j), were originally settled to unity. In the actual simulation, MF=7,19,37,61,91 were chosen.

A link (i,j) which has the smallest STR(i,j)/SCF(i,j) is searched. This link is considered to break at the normalized stress of STR(i,j)/SCF(i,j). If the link breaks, the stress redistribution will take place, and hence, the SCF(i,j) should be changed. Again the link of the smallest STR(i,j)/SCF(i,j) is looked for among the surviving fibers; this link should break next. The flow chart of this simulation is shown in Fig.4.

This process should be continued until all links in the same critical length are broken. However, in the present simulation, the following procedure was adopted to reduce the computational time. Figure 5 is an example of the load versus the number of broken links in a 91-fiber model. In this case, the maximum load appears when the 12th link breaks. After that, the load decreases and therefore, it is not necessary to continue the computation. The present computer program was made so that it stops when the load reduces to 70 persent of the maximum load. The simulations was carried out on a WorkStation.

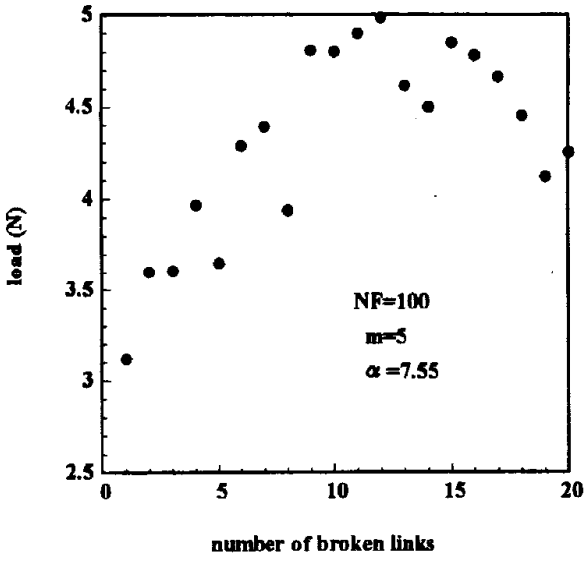

Fig.5 Faiure sequence of fiber bundle

RESULTS AND DISCUSSION

One hundred iterations were conducted for each case and in most cases, the number of links(NL) of each fiber was 50.

Figure 6 shows an example of the successive failure of individial fibers in the same case as Fig.5 where numerals are the order of breakage. In this case, the maximum load takes place when 12 fibers breaks as was pointed out before. Before 12th fiber breaks, we can find a group of

34 00 02 00 01 05
33 00 00 00 00 04 00
03 28 37 38 00 00 07 00
31 30 29 36 39 40 08 00 00
32 26 25 16 15 41 00 00 00 00
00 21 18 17 10 42 43 00 00 00 00
35 22 19 06 09 00 00 00 00 00
23 20 24 12 14 11 00 00 00
27 00 00 13 00 00 00 00
00 00 00 00 00 00 00
00 00 00 00 00 00

Fig.6 Location and order of broken links (shape parameter=5)

broken fibers 1,4,5,7,8 at the top-right corner of Fig.6 and another group 6,9,10 in the middle. This may correspond to a cluster [8] although details are not clear.

Figure 7 shows the dependence of the bundle scale parameter for strength upon the fiber shape parameter for strength at various number of fibers. The bundle strength increases when the fiber shape parameter for strength increases. Also, the bundle strength decreases when the number of fibers increases. This figure should be compared with the work of Lienkamp et. al. [8] where only seven fiber models were discussed. Our present simulation is a step forward to Ref. [8] from a view point of number of fibers. As was pointed out before, the SCFs were calculated in an infinite model. In that sense, our simulation is close to an upper bound because fibers other than MF fibers of our present concern are not broken.

Figure 8 is a rearrangement of Fig.7 and it clearly shows that the bundle for strength decreases when the number of fibers increases.

Figure 9, on the other hand, shows the effect of number of links. The scale parameter with incerasing the number of links, decreases monotonically, which is a so-called size effect.

So far we have done a parametric study. Now, let's try to predict the strength of actual unidirectional composites. In our previous study [9], the scale and shape parameters for the strength of monofilaments

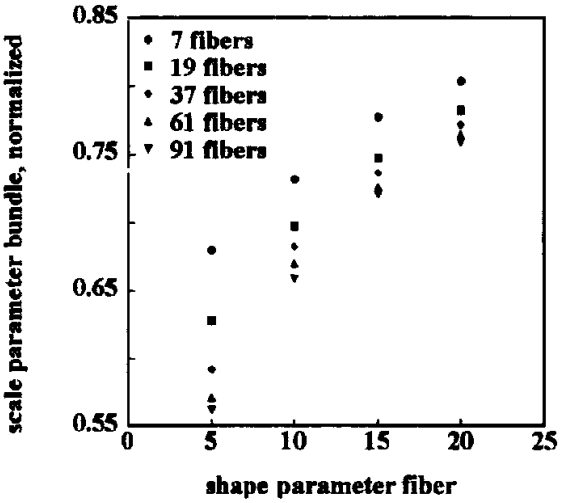

Fig.7 Scale parameter of the bundle versus fiber shape parameter

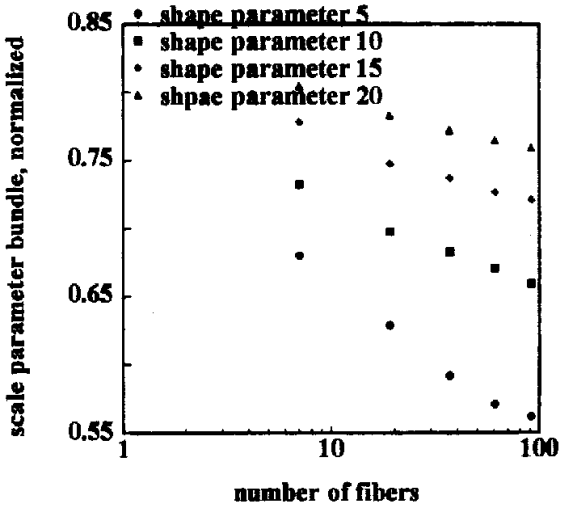

Fig.8 Scale parameter of the bundle versus number of fibers

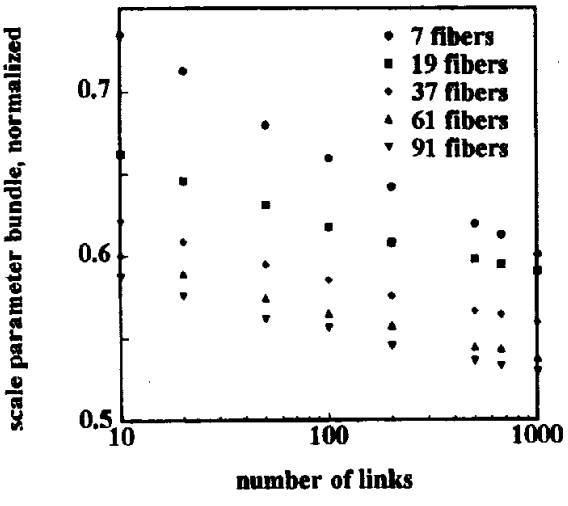

Fig.9 Effect of size, increasing bundle length

(T300) of 25mm length were α =3.17GPa and m=5.1. The average strength of the CFRP unidirectional composite with 3000 filaments of 200mm length was 2.88GPa. By another experiment [10], the critical length, lc, was determined to be 0.3mm in which length the Weibull scale parameter is 7.55 GPa.

Substituting α =7.55, m=5.1 and NL=667 (200mm/0.3mm) in our simulation, we got Fig.10. The present simulation predicts the strength lower than the Rosen's upper bound. In addition, our previous work[11] deals with the modification of the Zweben's lower bound, although it was not directly mentioned there. This increase of the lower bound is also shown in Fig.10. Through the present simulation, the bound has got narrow, and the value of the present estimation is close to the experimental value.

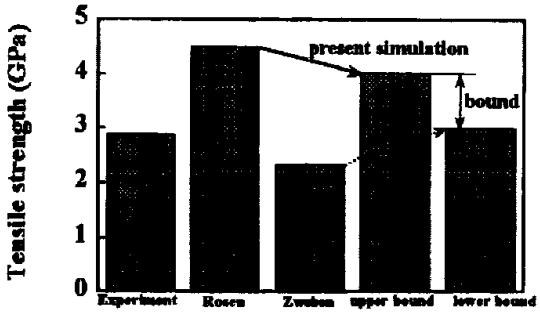

Fig.10 Comparison of experimental data and various model for the strength of unidirectional composites

CONCLUSIONS

The SCFs at various combination of broken fibers in a hexagonal array were calculated applying a shear-lag analysis. Using these SCFs, a parametric study on the strength of unidirectional composites was conducted by means of Monte Carlo simulation. Effects of monofilament scale and shape parameter, number of fibers and number of links on the bundle strength were made clear. The present estimation of the bundle strength was close to the experimental value. Also the bound of the bundle strength got narrow.

REFERENCES

1. Rosen, B.W., "Tensile Failure of Fibrous Composites, " AIAA J., Vol.2,1964, pp.1985-1991.
2. Zweben, C., "Tensile Failure of Fiber Composites, " AIAA J., Vol.6, 1968, pp.2325-2331.
3. Harlow, D. G. and Phoenix,S. L., "The Chain-of-bundles Probability Model for the Strength of Fibrous Materials I: Analysis and Conjectures, " J. Composite. Mater., Vol.12, 1978, pp.195-214.
4. Hedgepeth, J. M and Van Dyke, P., "Local Stress Concentrations in Imperfect Filamentary Composite Materials, " J. Composite Mater., Vol.1, 1967, pp.294-309.
5. Hedgepeth, J. M, "Stress Concentrations in Filamentary Structures, " NASA Technical Note, TN D-882, 1961.
6. Suemasu, H., " An Analytical Study of Probabilistic Aspects of Strength of Unidirectional Fiber Reinforced Composites Under Tensile Loads, " Trans. Japan Soc. Composite Mater.,

Vol.8, 1982, pp.29-36.

7. Oh, K. P.,"A Monte Carlo Study of the Strength of Unidirectional Fiber-Reinforced Composites," J. Composite Mater., Vol.13, 1979, pp.311-327.
8. Lienkamp, M.. and Schwartz, P. , "A Monte Carlo Simulation of the Failure of a Seven Fiber Microcomposite, " Composite Sci. Tech., Vol.46, 1993, pp.139-146.
9. Fukuda, H. and Miyazawa, T., "Micromechanical Approach to the Tensile Strength of Unidi rectional Composites, II, " Advanced Composite Mater., Vol.4, 1995, pp.287-295.
10. Fukuda, H. and Yasuda, J., "Monte Carlo Simulation of the Strength of Unidirectional Composites," Proc. Amer. Soc. Composites, Delaware, 1994, pp.195-202.
11. Fukuda, H., and Wada, A., "Monte Carlo Simulation for the Strength of Unidirectional Composites," Proc. International Conference on Advanced Materials, (ICAM'96), Beijing, 1996, pp.499-504.

A PHENOMENOLOGICAL-MECHANISTIC MODEL FOR RANDOM FIBER COMPOSITE STIFFNESS AND STRENGTH PREDICTION

Yi Zhang and D.L. Sikarskie

Department of Mechanical Engineering and Engineering Mechanics Michigan Technological University, Houghton, MI 49931

SUMMARY: A phenomenological-mechanistic model, or a lamini model, for stiffness and strength prediction of random fiber composite materials has been developed in this paper. The model assumes a series of unidirectional layers (lamini) in such a manner that it achieves a global transversely isotropic nature. The lamini model accurately predicts the Young's modulus and shear modulus of a random fiber composite. A bound analysis was developed to predict random fiber composite in-plane strengths, namely uniaxial tensile, compressive and shear strengths. The lower bound was the lamini model with zero residual strength in the failed layers, while the upper bound was the same model with perfectly plastic residual strength in the failed layers. It was found that the experimental in-plane failure stresses lie between the upper and lower bound predictions, however, are, in general, closer to the lower bound prediction than to the upper bound, although the lower bound analysis does not achieve as reasonable a stress-strain relation after initial failure as the upper bound analysis does. Failure envelopes for the in-plane stress states were also calculated both for upper and lower bounds. The application of the lamini model for random fiber composite beam strength prediction, one of its major advantages, will be reported in a separate paper.

KEYWORDS: random fiber composite, failure, stiffness, strength

INTRODUCTION

Increasing structural applications of random fiber composite materials demand a better understanding of the stiffness and strength properties of this category of materials. Due to the microstructural complexity of random fiber composites, relatively little has been done in modelling stiffness and strength predictions [1]. A purely mechanistic approach (when possible) has the advantage of providing behavioral detail as well as numerical prediction, but, unfortunately in this case again, because of complexity, it does not appear to be possible. Instead an approach is formulated which is mechanistic in the sense of dividing the composite into a series of layers through thickness and phenomenological in the sense of the failure criterion applied to each layer. This has the advantage of being able to track damage growth both through the thickness and in the plane of structure (plate) while still being numerically efficient. The model does a reasonable job of predicting failure both qualitatively and quantitatively. In the present paper the theory is presented for initially homogeneous stress fields only, i.e. uniaxial tension, compression, and shear. A follow on paper will develop the theory for initially non-homogeneous stress fields, i.e. bending. It should be noted that even initially homogeneous fields quickly become non-homogeneous as damage progresses. A review of the available literature is given below.

Following a purely mechanistic approach, Stowell and Liu (1961) developed a discontinuous tensile failure criterion for unidirectional short fiber composites, based on three observed failure mechanisms [11]. Lees (1968) averaged the Stowell-Liu equations over all

angles (0~180°) and obtained a tensile strength prediction equation for random short fiber composites [7]. The Lees' averaging operation is questionable for strength prediction because material failure is a local phenomenon. Lavengood (1972) tested Lees' equation experimentally and found that tensile strength was underestimated [6].

Recognizing the difficulty of the mechanistic approach for random fiber composite stiffness and strength prediction on the single fiber level, Halpin and Pagano (1969, 1978) proposed a so-called "laminate analogy" method, a purely phenomenological approach, to predict the engineering constants and tensile strength of random fiber composites. They used a laminate composed of 0°, 90°, ±45° unidirectionally oriented short fiber laminas to simulate the random fiber composite [4,5]. The maximum strain criterion was employed to predict the failure of each lamina and the damage growth was traced lamina by lamina following the procedure proposed by Petit and Waddoups (1969) [10].

Due to the obvious drawbacks of the mechanistic and phenomenological approaches, a phenomenological-mechanistic model which can capture partially the microscopic failure mechanisms, but in a phenomenological manner becomes an appealing approach for random fiber composite strength prediction. Hahn (1975) extended the laminate simulation model and used unidirectional short fiber layers with the fiber directions oriented continuously from 0° to 360° to simulate random fiber composite materials [3]. These unidirectional short fiber layers now physically represent all the fibers oriented in the same direction in the random fiber composite. Hahn achieved the same tensile strength equation as Lees' [7] and also an additional new equation by applying the Stowell-Liu tensile failure criterion [11] and the rule of mixtures into the model. Manera (1977) followed same idea and achieved an accurate stiffness properties prediction [9].

The Hahn model may be a legitimate approach for stiffness or strength prediction for the plane stress state. However, it is not a viable model for beam or plate structures, since the bending stiffness is then a function of the spatial position of the unidirectional fiber layers, i.e. different spatial arrangements for the unidirectional fiber laminis would result in different beam deformation and strength predictions. To achieve the goal of predicting the stiffness and strength properties of a general random fiber composite structure such as a beam or plate, a new phenomenological-mechanistic model, or lamini model, is therefore developed. In this paper, the lamini model is developed and its uniaxial tension, uniaxial compression, and shea strength prediction are compared with experiment. The complete theoretical failure envelopes are also included. It will be proved in the later paper that the [A], [D] matrices converge as the number of laminas and laminis tend to infinity.

MODEL DESCRIPTION

The lamini model is schematically illustrated in Figure 1. A random fiber composite panel of thickness h is viewed as a stack (n layers) of transversely isotropic laminas of equal thickness h/n. Each lamina, however, is composed of $2m$ layers of unidirectional short fiber laminis, having the same material constituents and processing conditions as the random fiber composite panel itself. The laminis have their fiber directions uniformly oriented from 0° to 180° and are symmetrically arranged to achieve the transversely isotropic nature of each lamina. Each lamini represents all fibers oriented in same direction within a lamina and with the same fiber volume fraction as the lamina. In the case where a random fiber composite panel has a fiber direction preference, i.e. the composite has more fibers in a certain direction, the lamini thickness can vary in different directions to give a representative behavior.

Composite failure is defined on the lamini level, i.e. only the laminis reaching the stress states defined by a failure criterion fail whereas the other laminis remain intact. With increasing load, laminis fail one after another until all of them are damaged. This defines ultimate failure of the composite panel. To a first order, the lamini is approximated as a linearly elastic orthotropic material. Lamini failure can be determined by any suitable failure criterion. In this study, we use the Tsai-Wu failure criterion, where for a two dimensional stress state,

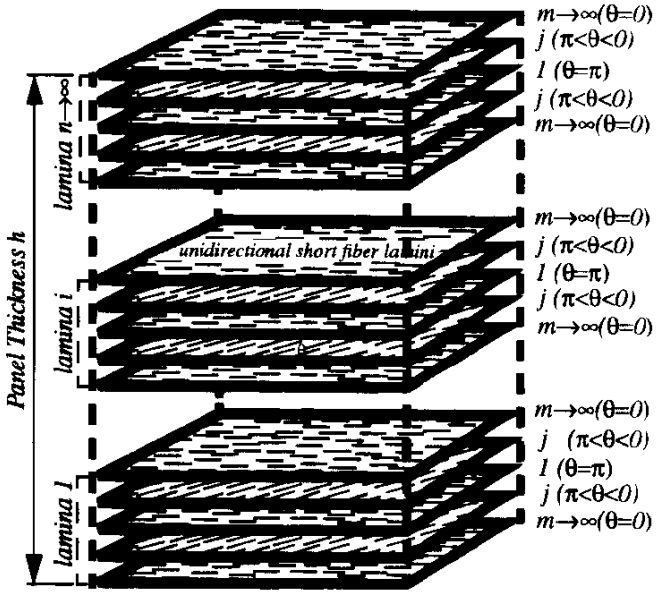

Figure 1 Schematic illustration of lamini model.

$$F_1\sigma_1 + F_2\sigma_2 + F_{11}\sigma_1^2 + F_{22}\sigma_2^2 + 2F_{12}\sigma_1\sigma_2 + F_{66}\sigma_6^2 = 1 \qquad (1)$$

where $F_1 = \frac{1}{\sigma_x^t} + \frac{1}{\sigma_x^c}$, $F_2 = \frac{1}{\sigma_y^t} + \frac{1}{\sigma_y^c}$, $F_{11} = -\frac{1}{\sigma_x^t\sigma_x^c}$, $F_{22} = -\frac{1}{\sigma_y^t\sigma_y^c}$, $F_{66} = \frac{1}{\tau_f^2}$, σ_x^t, σ_x^c, σ_y^t, and σ_y^c are tensile and compressive strengths of the unidirectional short fiber lamini in the two principal material directions respectively. Note that the compression strength σ^c is negative. τ_f is the composite shear strength. The stress tensor σ_i is also defined in the material coordinate system. The term F_{12} can be approximated as $-\frac{1}{2}\sqrt{F_{11}F_{22}}$ instead of running an additional biaxial test for determining it [2].

A very important issue now arises, how does a unidirectional short fiber lamini behave after failure is initiated? The stress-strain behavior of the post-failure laminis is very complicated, and is also very difficult to establish experimentally. Both Petit and Waddoups [10] and Hahn [3] assumed a perfectly plastic behavior, while Craddock (1985) implemented three different residual strength models: elastic-perfectly plastic, negative tangent modulus, and reduced modulus models [2]. Unfortunately, non of these models simulate the exact material behavior. In this study, a similar approach is utilized, i.e. a bound analysis is performed instead of modelling the real lamini post-failure behavior. The perfectly plastic behavior and no residual strength behavior are logically treated as upper and lower bounds respectively. The actual lamini post-failure stress-strain behavior is reasonably expected to fall between these two bounds, see Figure 2.

As mentioned in the introduction, applying classical lamination theory to the lamini model produces the well known $[A]$, $[D]$ matrices, and $[B] = 0$ for the model. It is shown in Zhang [12] that as $m, n \to \infty$, the $[A]$ and $[D]$ matrices satisfy the required transversely isotropic relationship $[D] = \frac{h^2}{12}[A]$. Thus, the lamini model achieves transverse isotropy even for the bending problem as opposed to the Hahn model [3]. The lamini model also reflects, to certain extent, the anisotropic nature of the random fiber composites at microscopic scale, which

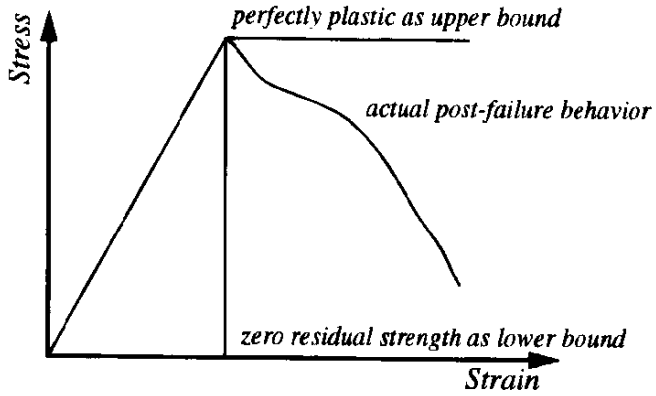

Figure 2 Schematic illustration of lamini post-failure behavior.

allows a phenomenological-mechanistic description of the failure initiation and growth process in composite structures, i.e. non-homogeneous stress fields. This will be discussed in a separate paper in detail.

ESTIMATE OF LAMINI STIFFNESS AND STRENGTH PROPERTIES

To do numerical calculations on the lamini model both elastic and failure characterization data for a unidirectional short fiber composite panel having the same fiber and matrix material, and the same volume fraction as the material tested is needed. The random fiber composite panel (0.125 inch nominal thickness) used in this study was Structural Injection Reaction Molding (SRIM) panel provided by the Technical Center of the General Motors Corp. The matrix polymer is a DOW MM364 isocyanate thermoset resin having a 5% elongation and the reinforcing fibers are 2 inch long chopped Owens Corning glass fibers. A mat preform was made in house by G.M. staff by chopping a glass roving and spraying it onto a screen. An epoxy binder was sprayed with the glass to give some stability to the preform. The preform was then placed in a mold, the resin injected and resultant plaque formed/ molded. Its tensile, compressive, and shear stress-strain behavior was tested by following appropriate testing protocols [12].

Ideally, the required characterization data should be established from the unidirectional short fiber composite coupons of the same matrix, processing condition, and fiber volume fractions as the SRIM panel. This proved to be extremely difficult to accomplish and in the final analysis the required characterization data for the unidirectional lamini was estimated using techniques available in the literatures.

Following Manera's paper [9], the stiffness properties, namely E_1, E_2, G_{12} and ν_{12}, of the unidirectional chopped fiber lamini can be estimated by following equations,

$$E_1 = V_f E_f + (1 - V_f) E_m \tag{2}$$

$$E_2 \sim E_m (3.92 V_f + 0.89) \tag{3}$$

$$G_{12} \sim 0.36 E_2 \tag{4}$$

$$\nu_{12} = V_f \nu_f + (1 - V_f) \nu_m \tag{5}$$

where V_f is the fiber volume fraction, E_f and E_m are respectively fiber and matrix Young's modulus, ν_f and ν_m are respectively fiber and matrix Poisson's ratio. Young's modulus of the glass fiber used in the G.M. manufactured composites is 72.4 GPa and Poisson's ratio is 0.25. The initial elastic modulus of the matrix material (DOW MM364) is 2.83 GPa. Poisson's ratio, not provided by the supplier, is assumed to be 0.4 [9]. The fiber volume fraction of the random fiber composite panel was found using a burn test to be 0.33 [12]. Substituting these

data into equations (6), (7), (8) and (9), the stiffness properties of the unidirectional chopped fiber laminis were calculated as follows; $E_1 = 25.8\,\text{GPa}$, $E_2 = 6.1\,\text{GPa}$, $G_{12} = 2.2\,\text{GPa}$, and $\nu_{12} = 0.35$.

As the unidirectional chopped fiber composite stiffness asymptotically approaches the stiffness of the continuous fiber composite at large aspect ratio, the strength of the unidirectionally oriented chopped fiber composites also asymptotically approaches a plateau value. This is only a fraction of the continuous fiber composite strength, however, due to the existence of the stress concentrations caused by the fiber ends. Halpin and Kardos (1978) developed an equation for the estimation of the strength reduction factors $[SRF]$ for a unidirectionally oriented discontinuous fiber composites as a function of the fiber aspect ratio, fiber stiffness, matrix stiffness, and the fiber volume fraction [5]. The equations are collectively denoted as the Halpin-Kardos equations,

$$\frac{[SRF]-[SRF]_0}{[SRF]_\infty-[SRF]_0} = 1-\exp\{-15\beta^{0.95}\} \tag{6}$$

in which

$$[SRF] = \frac{\sigma^t}{\sigma_f V_f} \tag{7}$$

$$\beta = \frac{l}{d}\frac{\tau_m}{\sigma_f} \tag{8}$$

where σ^t is the tensile strength of unidirectional chopped fiber composite, l and d are fiber length and diameter, σ_f is the fiber strength, V_f is the fiber volume fraction, and τ_m is the interfacial shear strength or matrix shear strength, whichever is the lowest. In the limit of very short fiber aspect ratio ($\frac{l}{d} \to 1.0$) the $[SRF]$ approaches its lower limit $[SRF] \approx [SRF]_0$. When the fiber aspect ratio is larger than the critical value, the $[SRF]$ approaches its upper limit $[SRF] \approx [SRF]_\infty$. If the fiber stiffness is larger than five times of the matrix stiffness, i.e. $\frac{E_f}{E_m} > 5$, the $[SRF]_\infty$ can be estimated as

$$[SRF]_\infty \approx \left[\frac{E_f}{E_m}\right]^{-0.87} + 0.50 \tag{9}$$

For both glass fiber/epoxy and boron/epoxy composites, the $[SRF]_0$ are both reported to be 0.08. Therefore, for a glass fiber strength of 3.45 GPa, the tensile strength in the fiber direction σ_1^t for unidirectional chopped fiber composite, estimated by using equation (7) and (9), is equal to 636.7 MPa. The tensile strength in the transverse direction σ_2^t of the unidirectional chopped fiber composite is estimated by using $[SRF]_0 = 0.08$. Although the matrix material in this study is polyurethane rather than epoxy, similar behavior is expected. Thus, σ_2^t was estimated as 91.0 MPa, slightly higher than the matrix strength of 71.7 MPa.

Methods for estimating the compression and shear strengths of unidirectional chopped fiber composites has not been found from the available publications. In their paper [5], Halpin and Kardos cited a set of ultimate strain allowables and the correspondent stiffness properties for a glass fiber/epoxy unidirectional fiber composite with a 0.5 fiber volume fraction. It can be easily calculated that the compression strength in the fiber direction is 57.5% of the tensile

strength in the same direction. The compression strength in the transverse direction is 3.74 times the tensile strength in the same direction, and the shear strength is 10.9% of the tensile strength in the fiber direction or 3.7 times the tensile strength in the transverse direction. These four factors were used to estimate the compression and shear strengths of the unidirectional fiber composite in this study. The compression strength in the fiber direction σ_1^c was estimated as 365.4 MPa, the compression strength in the transverse direction σ_2^c was 340.6 MPa. The shear strength τ_{12} estimated based on 10.9% of the tensile strength in the fiber direction is 68.9 MPa. The shear strength τ_{12} based on 3.7 times the tensile strength in the transverse direction is 336.5 MPa. The difference between these two estimates is significant. Since no test data is available, an average value, 202.7 MPa, is used for further calculation in this study. The strength properties for the unidirectional composite for strength prediction of random fiber composites can be summarized as σ_1^t = 636.7 MPa, σ_1^c = 365.4 MPa, σ_2^t = 91.0 MPa, σ_2^c = 340.6 MPa, τ_{12} = 202.7 MPa.

UNIAXIAL TENSILE, COMPRESSION AND SHEAR STRENGTH PREDICTION

The non-linear stress-strain curves of the random fiber composite under uniaxial tensile, compressive, and shear loads predicted with the lamini model with perfectly plastic lamini post-failure residual strength and zero residual strength, superimposed by the experimental results [12] are illustrated in Figures 3, 4, and 5, respectively. For all the calculations,

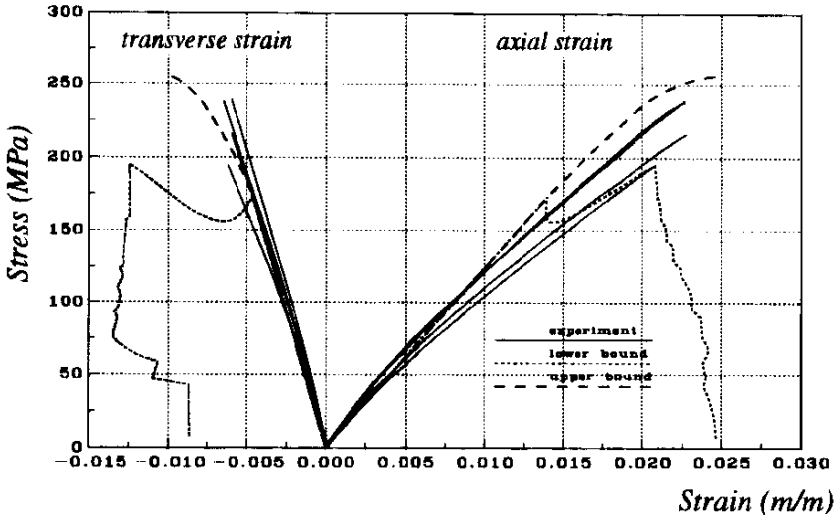

Figure 3. Predicted tensile stress-strain curves (dash) by lamini model, superimposed by experimental results (solid).

100 layers of laminis were used for achieving smooth stress-strain curves, although 10 layers of laminis have already achieved good convergence for the strength prediction. Note that for the in-plane stress state only one layer of lamina is necessary, i.e. n = 1 since all laminis with same fiber orientation in different laminas behave identically due to the uniform strain field through the panel thickness. Figure 3 indicates that the lamini model prediction of the tensile non-linear stress strain curves match well with the experimental results in both the load and transverse directions, while Figure 4 and 5 indicate that the upper bound analysis results in an extreme overestimation in the compression and shear strength predictions, although the predicted initial stress-strain behavior matches well with the experimental results. Note that for the pure shear stress-strain curve prediction, its equivalent biaxial, equal tension and compres-

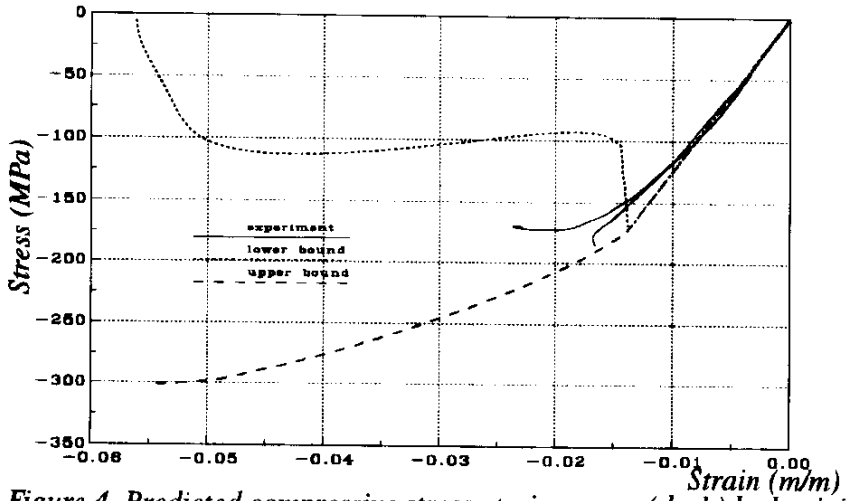

Figure 4. Predicted compressive stress-strain curves (dash) by lamini model, superimposed by experimental results (solid).

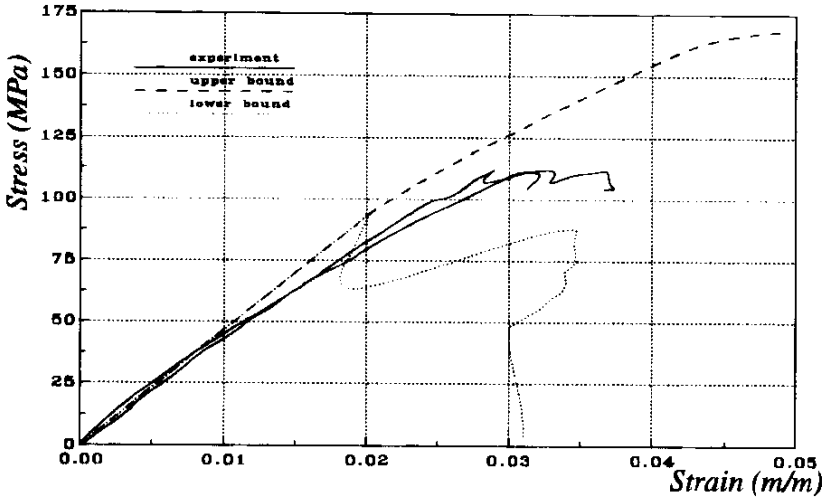

Figure 5. Predicted shear stress-strain curves (dash) from lamini model, superimposed by experimental results (solid).

sion stress state, i.e. $\sigma_1 = \tau_f$ and $\sigma_1 = -\tau_f$, was used for the lamini progressive failure calculation. The shear stress-strain curves predicted by these two stress states deviate from each other after the first lamini failure is predicted, with the biaxial stress state producing a more conservative estimate on the composite strength. The global inhomogeneity and anisotropy induced by the lamini failure is believed to be the direct cause for this result.

The predicted stress-strain curves from zero residual strength for tensile, compressive and shear tests do not represent the experimental results well after a first lamini failure is predicted (Figure 3, 4 and 5). In all three predicted stress-strain curves, there is a common feature, i.e. as the strain increases, the stress falls at certain points, then increases again with a softer modulus to another point, and then falls down again. This phenomenon is attributed to the damage growth mechanisms involved in the lamini model and the nominal nature of the plotted stress values. As the load is increased to a certain level, the lamini which reaches the failure criterion first starts to fail. Because the failed lamini completely loses its load carrying capability, its load share is transferred to the rest of the laminis, resulting in a actual stress increase in those undamaged laminis. Since the plotted stress values in those figures were calculated by averaging the load over an entire thickness, the actual stress shifting due to the lamini failure is not reflected. This failure induced stress increase can therefore cause a

sequential failure of other laminis. To stop the chain reaction, the average stress applied to the composite panel has to be reduced as the fall in the stress-strain curves in the figures suggest. The chain failure will also be arrested by the laminis whose fibers are oriented in such a direction that allows them to have a higher load carrying capability in certain direction. Then, the stress and strain curves will gradually pick up again. As the average stress further increases, so does the number of failed lamini layers. Until a certain point, the lamini chain failure reaction following the same mechanism will occur once again and this time will lead to a dynamic ultimate failure process as the final stages of the dashed lines suggest in Figures 3, 4 and 5. It is worthwhile to note here that although the rapid fall off phenomenon was not observed for the current composite tests, it was observed by Leung and Li for a ceramic matrix short fiber composite tensile test [8]. It is speculated that the matrix material may play a critical role here in determining the actual residual strength of the failed composite laminis, i.e. very brittle matrices have very little residual strength after failure.

The predicted and experimental maximum failure stresses for tensile, compressive, and shear tests are summarized in Table 1. Table 1 shows that the experimental strengths are

Table 1. Summary of predicted and experimental composite failure stresses and strains

Methods	Tension		Compression		Shear	
	Stress (MPa)	Strain (%)	Stress (MPa)	Strain (%)	Stress (MPa)	Strain (%)
Upper Bound	256.5	2.51	301.3	5.44	168.2	4.90
Lower Bound	195.8	2.08	171.7	1.38	94.2	2.02
Experimental	222.0	2.22	178.6	1.86	111.7	3.10

bounded by the predicted strengths from the lamini model with the perfectly plastic residual lamini strength (upper bound) and the zero residual lamini strength (lower bound). The zero residual strength model results in a fairly accurate prediction of the uniaxial tension, compression, and shear strengths, although not the stress-strain curves after the initial failure.

It can also be noticed from Figure 3, 4,and 5 that the lamini model predicts the initial tensile, compressive and shear moduli of the random fiber composite very accurately. The model predicts the tensile and compressive moduli to be 12.8 GPa and the shear modulus to be 4.8 GPa, while the experiments achieved 13.7 GPa for the tensile modulus, 13.1 GPa for the compressive modulus, and 5.0 GPa for the shear modulus.

IN-PLANE FAILURE ENVELOP PREDICTION

The in-plane failure envelopes in the principle stress coordinate system predicted by using the lamini model both with perfectly plastic post-failure stress-strain behavior and zero residual strength are illustrated in Figures 6 and 7. The failure envelopes in both figures are composed of two envelops. The dashed one represents the failure initiation envelope, i.e. failure of the first lamini, while the solid one represents the ultimate failure envelope, i.e. failure of the last lamini. The failure initiation envelopes for both zero and perfectly plastic residual strengths models are identical, since their difference only starts after the first lamini failure is predicted.

The uniaxial tensile, compression, and shear test data are also included in the figures as the triangles indicate. It is noted that all the test results lie beyond the failure initiation envelop. In anther words, the failure initiation envelope is a conservative failure estimate for random fiber composites. The ultimate failure envelope predicted from the lamini model with perfectly plastic residual strength encompasses all the test results, implying that it overestimates the composite strength. For the lamini model with zero residual strengths, the failure initiation envelope is the same as the ultimate failure strength for most stress states, i.e. the failure initiation stress state is the maximum stress state, see Figure 7. For stress states close to uniaxial tension, a slight difference between the failure initiation and ultimate failure enve-

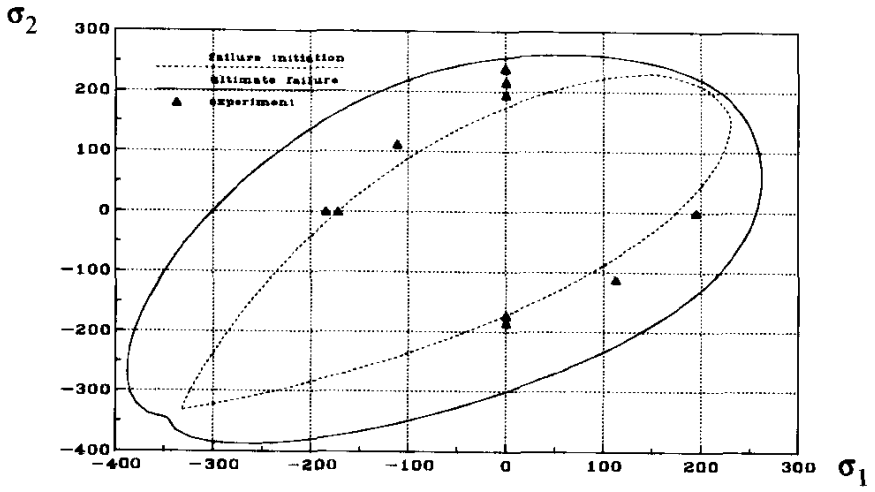

Figure 6. Failure envelope predicted in principle stress field by lamini model with perfectly plastic residual strength.

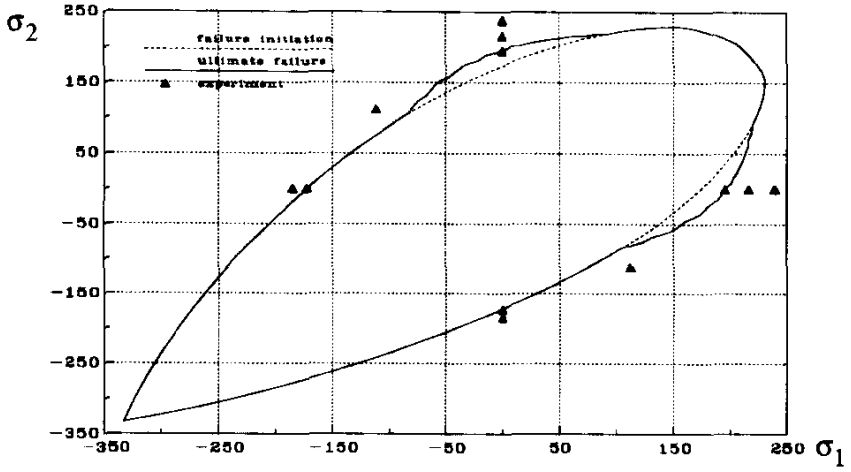

Figure 7. Failure envelope predicted in principle stress field by lamini model with zero residual strength.

lopes exists. Again, the test results are upper-bounded by the lamini model with perfectly plastic residual strength and lower-bounded by the lamini model with zero residual strength, and are much closer to the lower bound.

CONCLUSIONS

A phenomenological-mechanistic model, or lamini model, for stiffness and strength prediction of random fiber composites has been developed in this paper. This model bridges the gap between random fiber composite materials and classical composite laminates by constructing a transversely isotropic structure from a series of unidirectional layers (lamini). Classical lamination plate theory can then be employed for the prediction of random fiber composite stiffness and strength properties. The merits of this model are that it is not expensive for engineering applications and is also capable of reflecting part of the microscopic failure mechanisms involved in random fiber composite structural failure.

The bound analysis was performed for predicting random fiber composite in-plane strengths, namely uniaxial tensile, compression and shear strengths. The lower bound was the lamini model with zero residual strength, while the upper bound was the same model with perfectly plastic residual strength. It was found that the experimental in-plane failure stresses are

bounded by the upper and lower bound predictions. The experimental results, however, are closer to the lower bound prediction than to the upper bound. The lower bound analysis did not predict the stress-strain behavior after initial failure developed as well as the upper bound analysis did. Failure envelopes for the in-plane stress state were also calculated both for zero residual and fully plastic residual strengths.

ACKNOWLEDGEMENT

Authors would like to sincerely acknowledge the financial and technical support of the General Motors Corp. and the financial support of the State of Michigan through the Michigan Material and Processing Institute.

REFERENCES

1. Bert, C.W. and Kline, R.A., 1990. Handbook of Ceramics and Composites, Vol. 1 Synthesis and Properties: Chapter 7, Planar-Random Fiber Composites, Marcal Dekker, Inc.
2. Craddock, J.N., 1985. Composite Structures, Vol. 3: 187-200.
3. Hahn, H.T., 1975. Journal of Composite Materials, Vol. 9: 316-326.
4. Halpin, J.C. and Pagano, N.J., 1969. Journal of Composite Materials, Vol. 3: 720-724.
5. Halpin, J.C. and Kardos, J.L., 1978. Polymer Engineering and Science, Vol. 18: 496-504.
6. Lavengood, R.E., 1972. Polymer Engineering and Science, Vol. 12: 48-52.
7. Lees, J.K., 1968. Polymer Engineering and Science, Vol. 8: 195-201.
8. Leung, C.K.Y. and Li, V.C., 1990. Composites, Vol. 21: 305-317.
9. Manera, M., 1977. Journal of Composite Materials, Vol. 11: 235-247.
10. Petit, P.H. and Waddoups, M.E., 1969. Journal of Composite Materials, Vol. 3: 2-19.
11. Stowell, E.Z. and Liu, T.S., 1961. Journal of Mechanics and Physics for Solids, Vol. 9: 242-260.
12. Zhang Y., 1996. Ph.D. Dissertation, Michigan Technological University.

DETERMINING THE INTER-PLY AND INTRA-PLY VISCOSITIES OF UNI-AXIAL THERMOPLASTIC COMPOSITES BY THE ROLLER BEND METHOD

T.A. Martin[1] and I.F. Collins[2]

[1]Department of Mechanical Engineering, The University of Auckland, Private Bag 92019, Auckland, New Zealand
[2]Department of Engineering Science, The University of Auckland, Private Bag 92019, Auckland, New Zealand

SUMMARY: As high-speed manufacturing technology for forming continuous fibre reinforced thermoplastics (CFRTs) has developed, the need to reliably characterise the thermo-rheological material properties of CFRTs has increased. This paper investigates the primary deformation mechanism of viscous shear and considers the development of an experimental method to determine the inter-ply and the intra-ply shear properties of uni-directional laminates. By simply melting the strips and pulling them through a series of rollers, the steady state drawing forces are measured and related to the material's longitudinal viscosity. The advantage of using this method lies in its ease of execution. The results show that, while the inter-ply shear viscosity of PLYTRON is slightly lower than the intra-ply shear viscosity, it is much higher than that reported elsewhere. The polymer also displays a typical shear thinning behaviour. The *roller bend technique* can be used to characterise the shear properties of many other thermoplastic composites.

KEYWORDS: inter-ply shear viscosity, thermoplastic composite sheets, continuous fibres

INTRODUCTION

Continuous fibre reinforced thermoplastic (CFRT) materials have become increasingly popular in recent years due to the relative ease with which they can be molded into components. By simply melting the matrix polymer and applying moderate forces, complex geometries can be formed. In this molten state the matrix behaves like a viscous liquid and the fibres, which retain their elasticity, introduce a high degree of anisotropy into the material. To predict the physical response of these materials in a real forming situation, it is necessary to firstly understand the way in which they deform and secondly to determine their relevant material properties. Thus it is important to consider the heirarchy of flow mechanisms described by Cogswell and Leach [1]; resin percolation, transverse squeeze flow, inter-ply shear and intra-ply shear. These four flow mechanisms pertain to CFRT sheets with uni-directional plies and they are commonly present in combination, depending on the forming operation. Resin percolation and transverse squeeze flow, are typically associated with consolidation and welding processes, so they are not the main focus of this paper. However, inter-ply and intra-ply shear, are absolutely essential for shaping processes which induce

single and double curvature in a sheet. To form parts with single curvature the plies must shear through their thicknesses or slide over one another in the resin rich layers between the plies. When double curvature is required, intra-ply shear also takes place, that is, shear along the fibres within the plane of the sheet. In order to progress towards analytical/numerical forming solutions, which accurately reflect real moulding processes, both these mechanisms require investigation.

To quantify the viscous material properties of CFRTs, a number or authors have suggested various types of experimental methods; the ply pull-out test [2], the torsional rheometry test [3], the picture frame test [4] and the vee-bend test [5]. These techniques have various problems associated with them. The ply pull-out test often leads to gross fibre bundle movement during testing which alters the material behaviour and the transverse movement of the plies cannot be easily constrained. The torsional rheometry test is really only suited to infinitesimal deformations and the longitudinal shear response cannot be separated from the transverse shear response, without making prior assumptions about the material's constitutive behaviour. The picture frame test suffers from a similar problem. Furthermore, the flow mechanism is complicated by inducing squeeze flow within the plane of the sheet. A vee-bend test provides a much better method for determining the inter-ply shear properties of CFRT laminates, but it is not suitable for measuring the intra-ply shear properties and much data reduction is required to calculate the viscosity of the material from the non-linear load response curves.

This paper examines a new method for measuring the shear properties of CFRTs. *The roller bend technique* is experimentally simpler than any previously suggested methods, induces finite strains at realistic strain rates and specifically isolates the shear response of the material. Consider the schematic diagram of the experimental set-up shown in Figure 1. An initially straight laminate, with its fibres aligned along its length, is forced to shear through its thickness by bending around three rollers. In this case, a plane strain forming condition is enforced by circular side plates, indicated by dotted circles in Figure 1. The deformation is therefore entirely kinematically specified in the bend region. As the strip is pulled upwards it experiences a positive-negative-positive shear sequence, so that it exits the final roll as a flat sheet. The strip is pulled through the rollers until a steady state is reached, and for each forming speed the measured drawing force can be directly related to the steady state viscosity of the material. In addition, by turning the specimen 90° in the test apparatus, either the intra-ply or inter-ply material properties can be readily measured. This approach could be adopted as a standard technique to measure and compare the viscous properties of various thermoplastic composite laminates in their molten states. While this paper investigates PLYTRON test specimens, the objective is not to provide an exhaustive study of the shear properties of PLYTRON, but rather to demonstrate the principle of the *roller bend technique*.

THEORY

The analytical model presented in this section yields a mathematical description of the effects of the forming speed and the roller/strip geometry on the steady state drawing forces. The theory pertains to an idealised material model, which accounts for the fluid nature of the molten polymer and the high elongational stiffness of the fibres, by treating the composite like an incompressible viscous continuum containing thin homogeneously distributed inextensible cords [6].

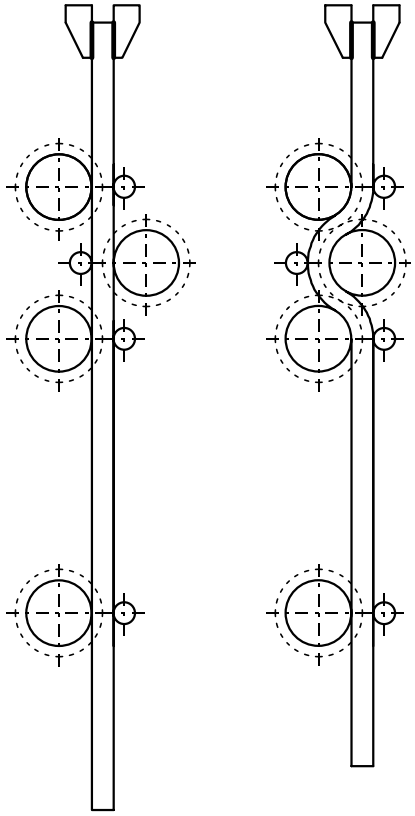

Fig. 1: A diagram of the roller bend test concept

Constraints and Kinematics

In the continuum considered here the fibres all lie in parallel surfaces in the plane of deformation and each fibre path is characterised by a field of unit tangent vectors, **a**, as shown in Figure 2. The components of **a** are denoted a_i. During the deformation the fibres are convected with the continuum, so that the same material particles lie on the same fibre at any given time. The orthogonal trajectories to the **a**-lines are characterised by a field of unit normal vectors, **n**. The components of **n** are denoted n_i. The **n**-lines are not material curves in general, because the particles lying on an **n**-line before deformation will not necessarily lie on the same **n**-line after deformation. We now consider the kinematic constraints imposed on this idealised material. The incompressibilty and fibre inextensibility conditions are respectively expressed by

$$\frac{\partial \mathrm{v}_i}{\partial x_i} = d_{ii} = 0 \qquad \text{and} \qquad a_i a_j \frac{\partial \mathrm{v}_\mathrm{i}}{\partial x_\mathrm{j}} = a_i a_j d_{ij} = 0 \tag{1}$$

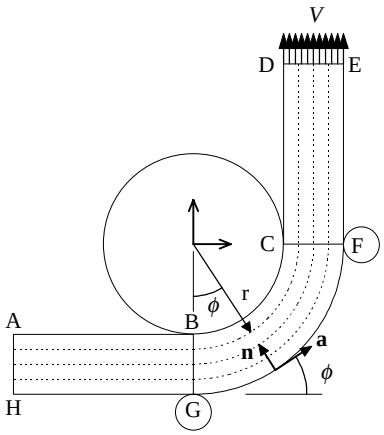

Fig. 2: An idealised sheet wrapped around a roller.

where x refers to the spatial coordinates of the velocity vector, **v**, and d_{ij} is the rate of deformation tensor defined by

$$d_{ij} = \frac{1}{2}\left(\frac{\partial \mathrm{v}_i}{\partial x_j} + \frac{\partial \mathrm{v}_j}{\partial x_i} \right) \tag{2}$$

The rate of change of **a** is given by

$$\dot{a}_i = a_k \frac{\partial \mathrm{v}_i}{\partial x_k} \tag{3}$$

For a detailed derivation of these equations the reader is refered to Rogers and O'Neill [7]. Consider the deformation of a flat sheet wrapped around a single roller in Figure 2. Two side plates, not illustrated in the diagram, are positioned on either side of the large central roller to prevent the laminate from spreading normal to the plane.

Pipkin and Rogers [8] have derived the governing equations for plane strain deformations of incompressible, inextensible materials and two significant results follow from their work: (a) the initially straight fibres remain in parallel surfaces, so the normal lines main straight and (b) the thickness of the sheet does not change during forming. These two requirements permit only simple shear deformations along the fibres. The amount of shear in the continuum is measured by the change in angle between two adjacent fibres. As there is no deformation up to the normal line BG in Figure 2, the shear strain along any normal line in the fan region BCFG is equal to the fibre angle, ϕ, and the shear rate is equal to the rate of rotation of a normal line, $\dot{\phi}$.

Stress in a Constrained Material

The total stress in a constrained material can be thought of as the sum of a reaction stress, r_{ij}, and an extra stress, S_{ij}.

$$\sigma_{ij} = r_{ij} + S_{ij} = -p(\delta_{ij} - a_i a_j) + T a_i a_j + S_{ij} \tag{4}$$

where S_{ij} satisfies the constraints $a_i a_j S_{ij} = 0$ and $n_i n_j S_{ij} = 0$. In other words, S_{ij} has no normal stress component on surface elements normal to the **a** direction or the **n** direction. The reaction stress does no work in a deformation and the reactions p and T arise as a result of the incompressibility and fibre inextensibility constraints respectively. T is the total tension on elements normal to the fibre direction and p represents the total pressure on elements normal to the **n** direction. These scalar terms must be determined by solving the equilibrium equations, whereas the deviatoric stress tensor, S_{ij}, needs to be specified by an appropriate constitutive relationship. If the material has reflectional symmetry in the x_3 plane and the deformation is homogeneous, under plane strain conditions the only non-zero components of σ_{ij} are

$$\sigma_{ij} = -\mathrm{p}(\delta_{ij} - a_i a_j) + \mathrm{T}\, a_i a_j + \mathrm{S}(a_i n_j + a_j n_i) + S_{33} k_i k_j \tag{5}$$

where **k** is the vector normal to the plane of deformation.

Constitutive Equation

In the present analysis, the deformation of an incompressible fluid reinforced with a single family of inextensible fibres in the (x_1,x_2) plane is considered. According to Rogers [9], the constitutive relationship for a viscous fluid subjected to these two constraints is given by

$$S_{ij} = 2\mu_T d_{ij} + 2(\mu_L - \mu_T)(a_i a_k d_{kj} + a_j a_k d_{ki}) \tag{6}$$

where μ_L and μ_T are the respective viscosities of the continuum along and transverse to the fibres. In a plane strain deformation, $v_3=d_{33}=0$, so that, σ_{33}=-p. Hence, a stress must be applied normal to the plane of deformation to maintain the plane strain condition. Using equations (5) and (6) it is readily shown that

$$\mathrm{S} = a_i n_j \sigma_{ij} = a_i n_j S_{ij} = 2\mu_L a_i n_j d_{ij} = \mu_L \dot{\phi} \tag{7}$$

where S is the shear stress associated with simple shear along the fibre direction. For a viscous fluid model, S depends only on the shear rate. In this particular example the only material property which can be determined in the constitutive equation is the longitudinal shear viscosity, μ_L. If a shear thinning fluid material model is chosen, instead of a linear viscous fluid model, then a power law expression for the apparent viscosity, μ_L, as a function of the shear rate can be introduced, so that

$$\mu_L = \frac{\mathrm{S}}{\dot{\phi}} = m_L \dot{\phi}^{n-1} \tag{8}$$

where m_L is the pseudo longitudinal shear thinning viscosity and n is the consistency index. By including fibre layers in the laminate which are not aligned with the longitudinal direction, the transverse shear viscosity may also be determined [5]. So a similar expression could be written for μ_T in terms of m_T and n. It is likely that n depends only on the shear thinning behaviour of the matrix polymer and is unaffected by the anisotropy in the composite, although it could be a function of the fibre volume fraction. When n=1 the fluid becomes Newtonian.

Stress Equilibrium

Consider the equilibrium of the force resultants acting on an elementary cross section of the deformed plate shown in Figure 3. When the only boundary traction is the pressure exerted on the inner surface, it is a simple matter to deduce that

$$\frac{\partial T^*}{\partial \phi} - S^* = 0 \qquad \text{and} \qquad T^* + \frac{\partial S^*}{\partial \phi} = r_0 p_0 \tag{9}$$

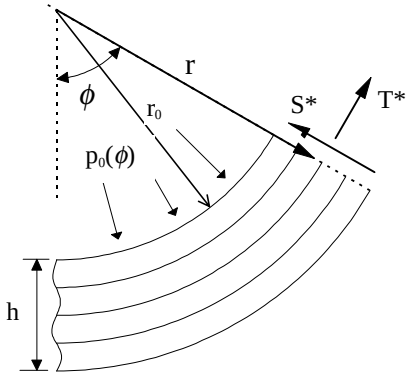

Fig. 3: Stress Equilibrium in a Polar Coordinate System

The force resultants, S* and T*, are the resultant shear and tensile forces per unit length in the **k** direction acting across a normal line ϕ=constant.

$$S^* = \int_{r_0}^{r_0+h} S\, dr \qquad \text{and} \qquad T^* = \int_{r_0}^{r_0+h} T\, dr \tag{10}$$

Velocity Field Kinematics

If we now consider the velocity field equations for plane strain deformations and resolve the 2-D velocity vectors along the **a** and **n** directions, two important equations may be obtained. In a polar coordinate system, the incompressibilty and inextensibility equations (1) become

$$\frac{\partial v_n}{\partial r} + v_a \frac{\partial \phi}{\partial r} = 0 \qquad \text{and} \qquad \frac{\partial v_a}{\partial \phi} - v_n = 0 \tag{11}$$

These two equations (Geiringer's equations) have been presented in their more general form by Spencer[6], along with the following equation for the shear rate, which is derived from (3)

$$\dot{\phi} = \frac{1}{r}\left(\frac{\partial v_n}{\partial \phi} + v_a\right) \tag{12}$$

Using equations (7)-(12), the shear stress, the fibre tension and the surface pressure can be determined for the entire sheet, when the kinematics of the deformation are prescribed as a continuous function of time. In this theoretical model the requirement that the normal lines remain straight during forming means that $\partial\phi/\partial r = 0$; so equation (11) yields $v_n=f(\phi)$.

An Admissible Stress Solution

In the following stress analysis, the boundary conditions are fixed in time and space and the kinematic model leads to a statically admissible stress solution. In order to determine the stress state in the sheet, we again refer to the geometry in Figure 2. In regions ABGH and CDEF the strip is straight and the shear rate is zero. Therefore S*=0 in these two regions. In the fan region BCFG, $v_n=0$ and $v_a=\text{const}=V$, by the second equation (11), so the resultant shear force is derived from equations (7), (8), (10) and (12).

$$S^* = \int_{r_0}^{r_0+h} \mu_L \dot{\phi}\, dr = \int_{r_0}^{r_0+h} m_L \dot{\phi}^n\, dr = \int_{r_0}^{r_0+h} m_L \left(\frac{V}{r}\right)^n dr = \frac{m_L V^n}{1-n}\left[\frac{1}{(r_0+h)^{n-1}} - \frac{1}{r_0^{\,n-1}}\right] \tag{13}$$

Consequently S* is positive in the bend region and tends to zero as r_0 approaches infinity. However, equation (12) indicates that the shear rate is not constant across the thickness of the sheet. The maximum shear rate occurs at the inside radius of the bend and the minimum shear

rate occurs at the outside radius. As the roller radius increases and the sheet thickness decreases these rates tend towards the same value. The average shear rate is defined by

$$\dot{\phi}_{avg} = \frac{1}{h}\int_{r_0}^{r_0+h}\dot{\phi}dr = \frac{1}{h}\int_{r_0}^{r_0+h}\frac{V}{r}dr = \frac{V}{h}ln\left(1+\frac{h}{r_0}\right) \tag{14}$$

Using the equilibrium equation (9) it is a straightforward matter to determine the fibre tension

$$T^* = \int_0^{\phi} S^* d\phi = \frac{m_L V^n}{1-n}\left[\frac{1}{(r_0+h)^{n-1}} - \frac{1}{r_0^{n-1}}\right]\phi + T_0^* \tag{15}$$

As there is no back tension in region ABGH in Figure 2, $T_0^*=0$ and the tension in the fibres increases linearly with ϕ. The fibre tension reaches its maximum value, T_{max}^*, when $\phi=\phi_0$. Lastly we consider the pressure on the large roller as a result of the shearing action. Within the fan region BCFG the shear stress is independent of ϕ, so the second equation in (9) yields

$$p_0 = \frac{T^*}{r_0} = \frac{m_L V^n}{r_0(1-n)}\left[\frac{1}{(r_0+h)^{n-1}} - \frac{1}{r_0^{n-1}}\right]\phi \tag{16}$$

Thus the hydrostatic pressure within the sheet is a maximum at the inside radius and decreases to zero at the outside radius of the bend. In addition to the distributed load on the inside radius of the sheet, two reaction forces must be applied to the strip to keep it in contact with the large roller in Figure 2. Because statically admissible solutions for incompressible inextensible materials admit stress discontinuities, a positive radial force must be applied at point B and a negative radial force must be applied at point F equal to the jump in shear stress across the **n**-lines BG and CF respectively. These finite point loads and the distributed pressure, p_0, cause the strip to spread normal to the plane, when there are no side constraints in the bend region. From the foregoing analysis it is clear that additional bends generate extra tension in the fibres in a commutative manner. In this particular study the roller bend apparatus causes the strip to deform into four fan regions of equal angle, ϕ_0. Hence, the total load, P, to pull the laminate through the four bends is

$$P = 4wT_{max}^* = 4w\frac{m_L V^n}{r_0(1-n)}\left[\frac{1}{(r_0+h)^{n-1}} - \frac{1}{r_0^{n-1}}\right]\phi_0 \tag{17}$$

where w is the width of the sheet. As the fibre tension increases, the hydrostatic pressure in the sheet also increases. In the special case when n=1, equations (13) and (15)-(17) become invalid. The fibre tension, the hydrostatic pressure and the drawing loads become linear functions of the forming speed and the hyperbolic term with respect to the radius is replaced by the natural log term in equation (14).

EXPERIMENTAL PROCEDURE

The test specimens were prepared using PLYTRON pre-preg uni-directional plies. PLYTRON is a PP/GF material supplied by Borealis Ltd. with a 35% fibre volume fraction

and a melting temperature of 168°C. The pre-preg plies were consolidated between heated platens in a Satim press at a pressure of 1MPa to produce a 9.3mm thick laminate. This laminate was subsequently cut up into test strips 340mm long and 9.3mm wide. The experimental apparatus consisted of four sets of rolls supported between two parallel plates as shown in Figure 4. The parallel plates were attached to a base plate which was screwed onto a cylindrical Aluminium tube. An additional carbon/epoxy tube was subsequently attached to this tube. Each set of rolls consisted of a large roll and a small roll. These were designed so that the test specimens could fit into a 10mm square gap, as shown in Figure 5. This gap was slightly larger than the dimensions of the test specimens to allow for thermal expansion in the polymer upon melting. By inserting the strips in the roller bend apparatus at 0° or 90°, the inter-ply and the intra-ply shear properties could be measured respectively. The upper three sets of rolls could be located in three different positions to test bend angles of 41.4°, 60° and 90°. After some initial tests the 41.4° bend angle was selected to minimise the hydrostatic pressure in the strip during forming. The roller bearing system consisted of tapered stainless steel pins, which were spring loaded to apply a constant side force to the rollers. This arrangement was cost effective and eliminated the need for high temperature ball bearings. The bulk of the test equipment, including the rolls, was manufactured from Aluminium to minimise the thermal capacity of the device. The test equipment was mounted in an enviromental chamber and attached to the cross-head of a Zwick tensile testing machine. The oven and the apparatus were pre-heated to the melting temperature of the specimen. To eliminate any thermal gradients in the chamber, the carbon/epoxy cylindrical tube was used to insulate the apparatus from the ambient temperature outside the oven. Each test strip was gripped by a set of spring loaded jaws inside the oven and allowed to hang in the environmental chamber between the rolls. The forming rolls were initially aligned with the specimen to avoid bending it until it had reached its melting temperature. A thermocouple was put into each sheet at a point 50mm below the grips, to ensure an accurate measurement of the strip temperature. As soon as the matrix polymer had completely melted, the forming rolls were translated in the horizontal direction and fixed in place. A further 15 minutes was then allowed to let the strip temperature stabilise. The Zwick cross-head was moved downwards, so that the strip was pulled through the roller bend apparatus at speeds of 100-1000 mm/min. While the strips were being formed, a 1kN load cell was used to measure the drawing loads. The load data was stored on disk and the results are illustrated in the next section.

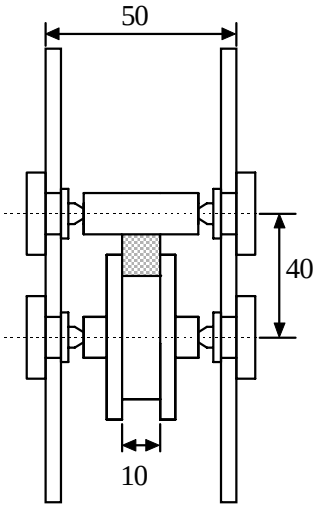

Fig. 4: A plan view of the rolls

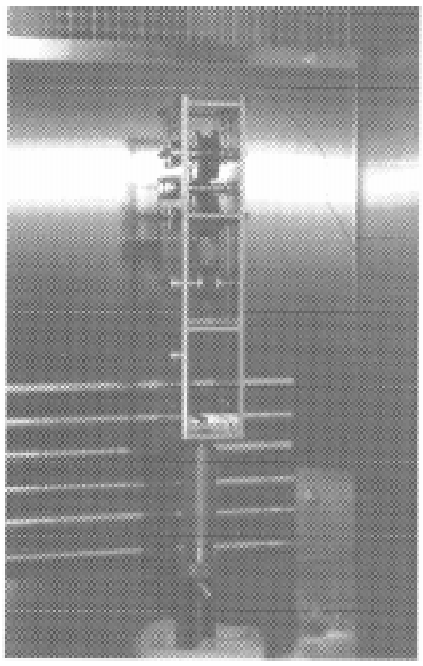

Fig. 5: Experimental apparatus

RESULTS AND DISCUSSION

The first set of experimental results, shown in Figure 6, illustrates the effect of forming speed on the inter-ply shear response of PLYTRON at 180°C. The first thing which is immediately evident from these results is the small forces needed to draw the thermoplastic composite specimens through the bending rolls. Secondly, the curves follow a consistent pattern and demonstrate some fluctuations in the steady state region. These fluctuations become more irregular with increasing forming speed. For a viscous fluid material it is not surprising that the drawing loads increase with the forming speed; however, the drawing speed has increased by an order of magnitude, while the steady state drawing forces have only increased by a factor of three. This result demonstrates the non-Newtonian shear thinning behaviour of PLYTRON. To eliminate the transient start up phase and the unsteady tail end results, the average steady state forming load was calculated for displacements from 30mm to 80mm. These average values are indicated by dotted lines in Figure 6. The effect of forming speed on the intra-ply drawing forces is demonstrated in Figure 7. Again the forming loads increase non-linearly with the forming speed. In this case the shape of the load curves is similar to those shown in Figure 6 except at higher forming speeds, where the curves tend to rise to a peak and then drop down to a much lower value for the remainder of the process. This feature may be explained in terms of the transverse spreading phenomenon, which was caused by the hydrostatic pressure in the bend region. Unfortunately the experimental side plates could not extend to the outside thickness of the bend because of physical interference from the other rolls. So instead of deforming in a plane strain mode, the edges of the strip tended to widen in the regions between the rolls and then get squashed at the points where the rolls came into contact with each other. This was particularly a problem for the intra-ply specimens at higher forming speeds and is evident by the increasing irregularity in the load results of Figure 7. This problem could be solved by introducing fixed side plates over the entire lengths of the

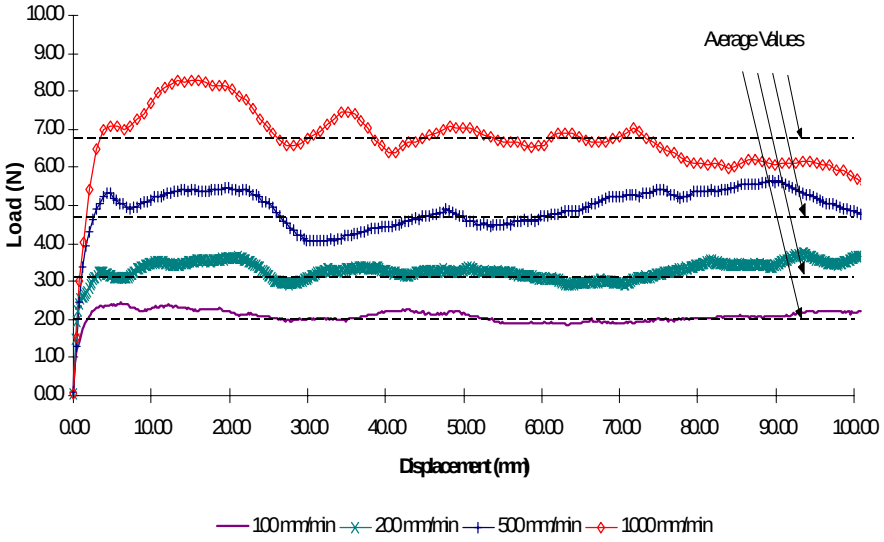

Figure 6: Drawing load versus displacement for inter-ply shear tests at various forming speeds. Forming temperature=180°C

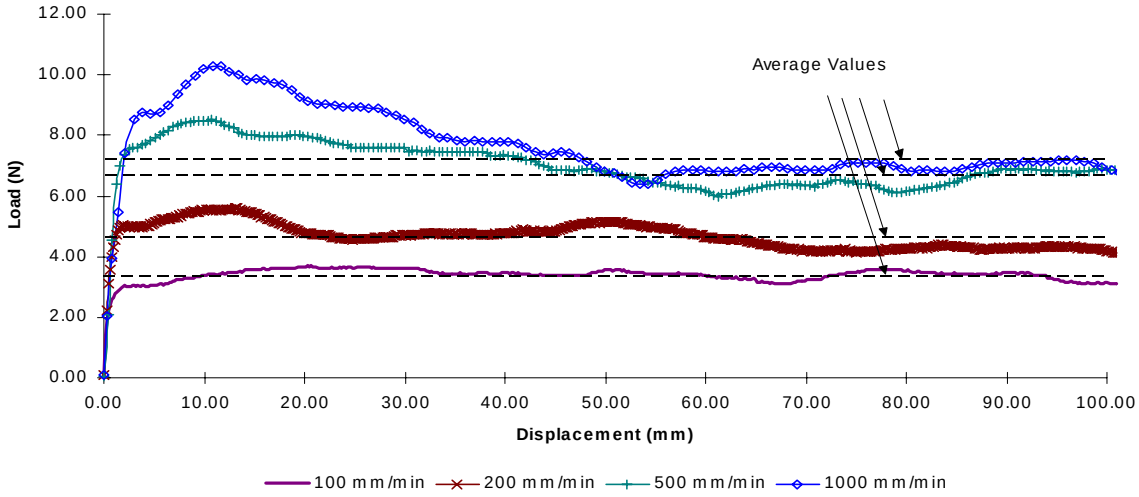

Figure 7: Drawing load versus displacement for Intra-ply shear tests at various forming speeds. Forming temperature=180°C

strips. Such a physical constraint would add a friction load to the side of the specimens, but this could be measured and subtracted from the total load to determine the fibre tension due to shearing. Alternatively, interlocking sprockets could be used instead of solid circular side plates.

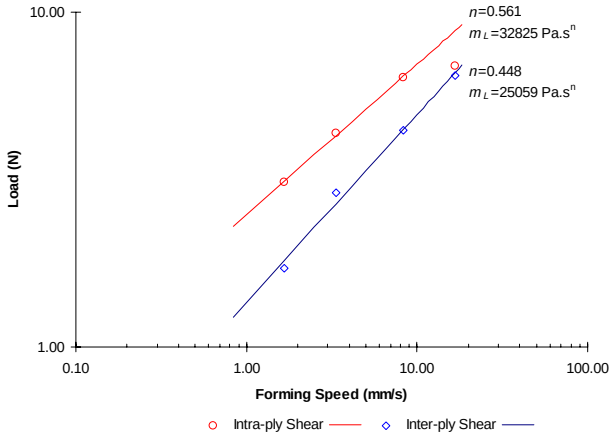

Figure 8: A log-log plot of the steady state loads versus forming speed

At each forming speed a dead load test was performed to determine the friction load associated with the roller bearings and polymer adhesion. By pulling a straight strip through the aligned rolls, the steady state dead load was found to be 0.3N regardless of the forming speed. This dead load was subtracted from the average gross forming loads shown in Figure 6 and Figure 7. Using this data, the drawing forces were plotted against the forming speed on a log-log scale and a linear regression was used to determine the pseudo longitudinal shear viscosity and the consistency index of the material from equation (17). The linear regression curves and the experimental steady state forming loads are shown in Figure 8. For the intra-ply tests the 1000mm/min data point was ignored in the regression analysis due to the unreliability caused by the transverse spreading effects.

The results indicate that the intra-ply shear viscosity of PLYTRON is about 25% higher than the inter-ply shear viscosity. Given the possible error in the intra-ply drawing loads at higher forming speeds, it is likely that the consistency indices could be much closer to each other in reality. A typical *n* value for Polyproylene is 0.3-0.4. Thus the shear thinning effect is most likely attributed to the behaviour of the polymer and is only mildly affected by the presence of the fibres. In comparison with the vee-bend test results [10] for the inter-ply shear viscosity of PLYTRON, the roller bend inter-ply shear viscosity appears to be about 75 times greater. This massive increase in the shear viscosity may be due to the present use of a thin pre-preg material. This unexpected outcome might be explained by considering the micro-structure in the experimental specimens. Micrographs of the specimens used in the roller bend tests, with an average ply thickness of 0.2125mm, showed a much more uniform fibre distribution in comparison with the specimens used for the vee-bend tests. In particular, the vee bend test specimens were made from 0.5mm thick plies and showed resin rich regions between the plies and bundled fibre spacing within the laminate. The vee-bend specimens would probably show a significant difference between their inter-ply and intra-ply shear properties. For a homogeneous micro-structure the inter-ply and intra-ply shear viscosities converge. Thus the composite tends towards a transversely isotropic material behaviour. The increased shear viscosity in the current results has implications regarding the formability of the material. A

CFRT material which resists shear deformation will naturally require higher forming stresses and is more likely to exhibit fibre wrinkling and gross buckling. In the current experimental setup the elastic loads are applied directly to the rollers, while the load cell only measures the viscous energy dissipated by the movement of the strip. If the material exhibits visco-elastic effects, these can only be considered by measuring the loads on the rolls. This feature could be incorporated into future tests.

CONCLUSIONS

The *roller bend technique* is in principle ideally suited to isolating and measuring the inter-ply and intra-ply shear properties of molten continuous fibre thermoplastic composites. The experimental method can be easily executed and the steady state drawing forces can be quickly converted into steady shear viscosity data. The theory also correctly predicts the transverse spreading of the uni-directional laminates due to shearing. Unfortunately, the multi-bend apparatus did not enforce a plane strain condition across the entire strip thickness, so the test specimens attempted to spread rather than shear during forming. More reliable experimental data might be obtained with fixed side plates or interlocking sprocket side plates. A comparison between the inter-ply and intra-ply shear properties of PLYTRON was made possible using the *roller bend technique*. This has never been done before. The results indicate that for a homogeneously distributed fibre micro-structure, the intra-ply viscosity is not much greater than the inter-ply viscosity. Consequently, the material behaves in a nearly transversely isotropic manner. The reduction in viscosity of the composite with increasing forming speed appears to be independent of the in-plane or out-of-plane shear mode and can be attibuted to the power-law shear thinning behaviour of the polymer matrix. The calculated inter-ply pseudo longitudinal viscosity of PLYTRON was found to be significantly higher than that reported elsewhere. This could be due to the use of a thinner pre-preg material and a uniform distribution of fibres across the laminate. Further experimental investigation is required to verify this finding.

ACKNOWLEDGEMENTS

Dr. Todd Martin would like to thank the Institut für Verbundwerkstoffe (IVW) GmbH, Germany, for hosting him as a guest scientist in 1996, and the Deutscher Akademischer Austauschdienst (DAAD) for providing a short term research scholarship. The authors also gratefully acknowledge the support received from the Foundation for Research, Science and Technology, N.Z., for conducting this research.

REFERENCES

1. Cogswell, F.N., Leach, D.C., “Processing Science of Continuous Fibre Reinforced Thermoplastic Composites,” *SAMPE Journal*, Vol. 24, No. 3, 1988, pp. 11-14.
2. Goshawk, J.A., Jones, R.S., “The Flow of Continuous Fibre Reinforced Composites in Steady Shear,” *Composites Science and Technology*, Vol. 56, 1996 , pp. 63-74.
3. Groves, D.J., Bellamy, A.M., Stocks, D.M., “Anisotropic Rheology of Continuous Fibre Thermoplastic Composites,” *Composites*, Vol. 23, No. 2, 1992, pp. 75-80.

4. McGuinness, G.B., Canavan, R.A., Nestor, T.A., O Bradaigh, C.M., "A Picture Frame Intra-ply Shearing Test for Unidirectional and Fabric Reinforced Composite Melts," *ASME Winter Annual Meeting*, San Francisco, Nov 1995.
5. Dykes, R., Martin, T.A., Bhattacharyya, D., "Determination of Longitudinal and Transverse Behaviour of Continuous Fibre-Reinforced Composites from Vee-Bending," *Fourth Int. Conference on Flow Processes in Composite Materials, FPCM '96*, Aberystwyth, Wales, Sept. 9-11. 1996.
6. Spencer, A.J.M., "Deformations of Fibre Reinforced Materials," *Clarendon Press*, Oxford, 1972.
7. Rogers, T.G., O'Neill, J.M., "Theoretical Analysis of Forming Flows of Fibre-Reinforced Composites," *Composites Manufacturing*, Vol. 2, No. 3, 1991, pp. 153-159.
8. Pipkin, A.C., Rogers, T.G., "Plane Deformations of Incompressible Fibre Reinforced Materials," *Journal of Applied Mechanics, Transactions of the ASME*, Sept 1971, pp. 634-640.
9. Rogers, T.G., "Rheological Characterization of Anisotropic Materials," *Composites*, Vol. 20, No. 1, Jan 1989, pp. 21-27.
10. Martin, T.A., Mander, S.J., Dykes, R.J., Bhattacharyya, D., "Bending of Continuous Fibre Reinforced Thermoplastic Sheets," *Composite Sheet Forming*, ed. D. Bhattacharyya, Composite Materials Science Publishers, Amsterdam, Netherlands, 1997.

THERMAL SHOCK RESISTANCE OF HYBRID PARTICULATE-FILLED EPOXY COMPOSITES

Masatoshi Kubouchi[1], Tetsuya Handa[2], Ken Tsuda[1], Toshio Shimizu[3] and Mitsuhiko Koyama[4]

[1] Tokyo Institute of Technology, 2-12-1, O-okayama, Meguro-ku, Tokyo 152 JAPAN.
[2] Graduate School, Tokyo Institute of Technology, 2-12-1, O-okayama, Meguro-ku, Tokyo 152 JAPAN.
[3] Heavy Apparatus Engineering Lab., Toshiba Co., 1, Toshiba-cho, Fuchu-shi, Tokyo 183 JAPAN.
[4] Generator Dept., Toshiba Co., 2-4, Suehiro-cho, Tsurumi-ku, Yokohama 230 JAPAN.

SUMMARY: For improvement in toughness of epoxy casting materials, hybrid particle-filled composites have been reported. Since toughening mechanisms of hard and soft particles are effective at the same time, large improvement can be expected. In this study, an effect of hybrid filler on thermal shock resistance using silica particulate as hard filler and MBS rubber as soft filler is examined. The thermal shock test which we have been proposed was conducted on mono-filler and hybrid-filler composites. The results were concluded that, hard and soft hybrid filler effect on thermal shock was smaller than that on fracture toughness. This tendency is due to the debonding of silica filler and matrix interface.

KEYWORDS: thermal shock, epoxy resin, hybrid filler, fracture toughness, particulate-filled resin, thermal shock test, silica filler, MBS rubber.

INTRODUCTION

The epoxy resin has many good properties as insulating materials, such as high insulation resistance, adhesive property, moldability, *etc.*. Unfortunately, the epoxy casting materials usually show low cracking resistance. Therefore, the second phase materials are added to the resin for improvement in toughness. The second phase materials often consist of either a hard inorganic filler [1] or a soft rubbery material [2]. The hard particulate branches off the crack propagation and makes it zigzag way, that is crack pinning effect which improves fracture toughness. On the other hand, soft particulate locally deforms matrix resin and by this energy consumption the fracture toughness also increases. Since these toughening mechanisms are effective at the same time, recently new composites *i.e.*, hybrid particulate-filled epoxy resins have been reported as highly toughened insulating materials [3, 4]. For these composites, in which both hard and soft particles are filled, large improvement in toughness can be expected.

In application of these epoxy resins or epoxy based composites in electric and electronic fields, high resistance to thermal shock is required to guarantee the high reliability. Failure by thermal shock is a complex phenomena because it is greatly affected by many factors, such as the geometry of the testing sample, the thermal and mechanical properties, and so forth.

We had already proposed a new test method to evaluate the thermal shock resistance of the epoxy resins and particulate filled resins [5~8]. The thermal shock test is easily conducted in laboratory, and the thermal shock resistance is evaluated analytically based on linear fracture mechanics. In our previous studies, the thermal shock resistance of hard particulate filled resin and soft second phase filled resin are reported. Both types of toughened resins showed improvement in thermal shock resistance.

In this study, effect of hybrid filler on thermal shock resistance using silica particulate as a hard filler and MBS rubber particulate as a soft filler was examined.

EXPERIMENTAL

Materials

The thermal shock test was conducted for neat resin, silica filled composite, rubber filled composite and silica & rubber hybrid type composite. The neat resin or the matrix resin of the other composites was bisphenol-type epoxy (epoxy equivalent weight = 5.1 - 5.6 equiv./kg) cured with acid anhydride hardener. The silica filler was angular-shaped particulate without surface treatment and the average diameter of the filler was about 13 μm. The Metacryl-Butadiene-Styrene (MBS) rubber was used as rubber filler material. This filler consisted of under micron particle, which made about 100 μm size cluster.

Two series of mono-filler composites and two series of hybrid-filler composites were used. The silica filler content was varied from neat resin to 300 phr (per hundred resin), and the MBS filler content was varied from neat resin to 15 phr respectively. Hybrid filler composites content of hard filler and soft filler were also changed as shown in Table 1. The MBS content was fixed 10 phr for one of the hybrid composites series, and the silica content was fixed 200 phr for the other series.

Table 1 Composition of tested materials.

	silica filler (phr)	**MBS rubber filler (phr)**
hard particulate filled composites	100, 200, 300	0
soft particulate filled composites	0	5, 10, 15
hybrid particulate filled composites	100, 200, 250, 300, 320	10
	200	5, 10, 15

Thermal Shock Test Method

In this test, pre-notched disk shaped specimen was checked whether crack was propagated or not from the tip of notch after thermal shock. The test specimen of 60 mm diameter and 10 mm thickness disk has a radial direction pre-notch as shown in Fig.1. The notch length (*c* in Fig.1) was kept 6 mm. The specimen held between two heat insulators was put into the cooling bath which consisted of dry ice / pentane coolant system. Then, since the disk was cooled from the cylindrical surface to the center along the radius, thermal stress for mode-I fracture was created at the tip of the pre-notch. The temperature difference was controlled by changing the initial temperature of the specimen. The thermal shock resistance was evaluated quantitatively as the minimum temperature difference at which initial notch propagated.

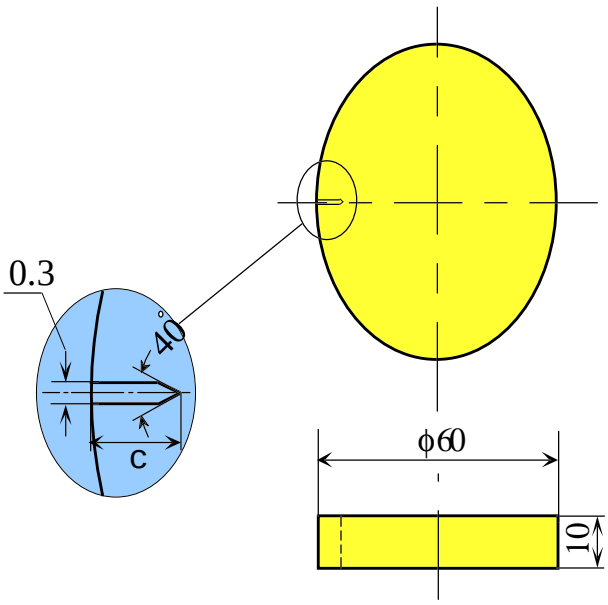

Fig. 1 The size and shape of thermal shock test specimen [5,7].

Morphological Study

Fracture toughness was measured by 3 point bending with single edge notched specimen. The fracture surfaces near crack starting portion after the thermal shock test and the fracture toughness test were compared. The surface was observed by SEM equipped with back scattering image (BEI) detector, which could easily distinguish inorganic filler from matrix resin.

RESULTS AND DISCUSSION

Mono-filler Composites

The silica filled composite and rubber filled composite increased fracture toughness and thermal shock resistance in comparison with neat resin. Fig.2 shows thermal shock test result on (a) silica and (b) MBS filled resin. The open circle denotes that crack initiated and propagated and the solid circle shows that crack did not propagate. The critical temperature difference which corresponds to the minimum temperature difference to initiate the crack from the notch clearly increases with silica filler content, as shown in Fig.2 (a). In the case of the MBS filled resin, thermal shock resistance also improves well. In this figure, solid triangle means that the crack propagation did not occurred but the notch deformed obviously. These tendencies are agree with the other epoxy composites toughened with silica filler [6,8] or CTBN [5].

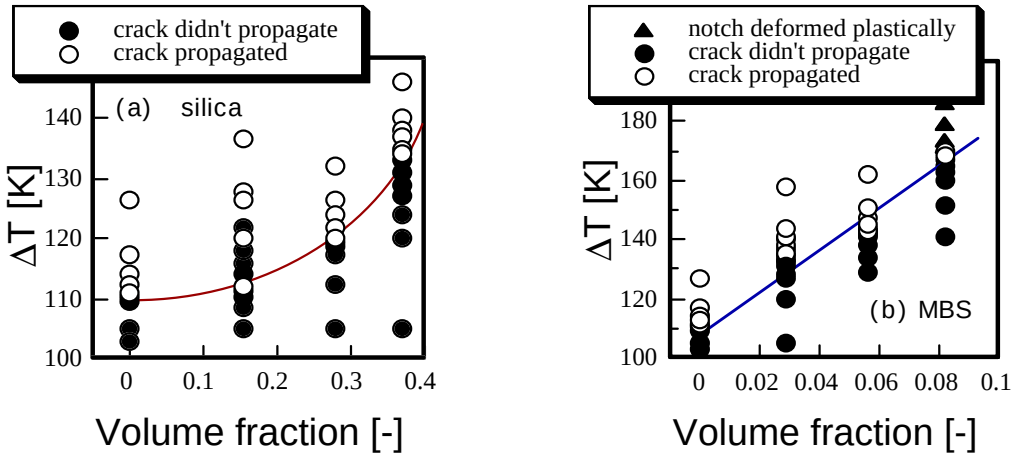

Fig.2 Effect of filler content on thermal shock resistance.

Hybrid-filler Composites

The hybrid type composite also showed large improvement in fracture toughness [3], but showed constant or slightly decreasing tendency of thermal shock resistance at highly filler content as shown in Fig.3 and Fig.4.

Fig.3 shows the experimental results of the fracture toughness and the thermal shock resistance of hybrid filler composite, in which rubber content was 10 phr constant and silica filler content was varied. The fracture toughness increase linearly. On the other hand, the thermal shock resistance gradually decreases with silica filler content.

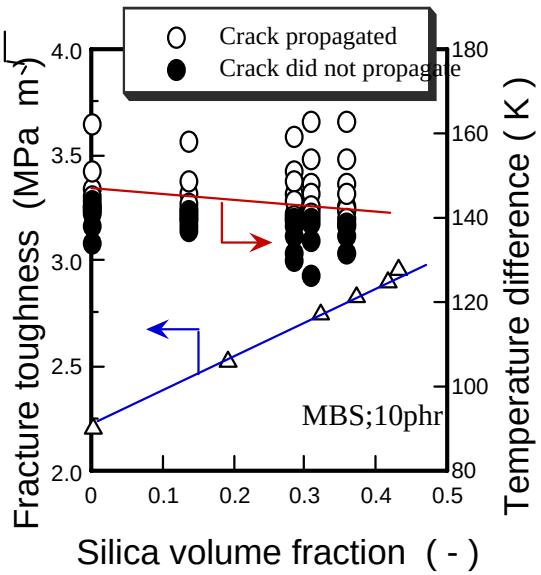

Fig.3 Effect of silica filler content on fracture toughness and thermal shock resistance of hybrid composite (rubber ; 10 phr).

The test result of hybrid filler composite in which silica filler content was kept at 200 phr and rubber content was varied is also shown in Fig.4. Same as Fig.3, the fracture toughness increases linearly. On the other hand, in the contrast with the effect of silica filler on the thermal shock resistance shown in Fig.3, the rubber content effect is positive. However, at high rubber content the effect is very small, so that a tendency that the thermal shock resistance of the mono MBS filler composite surpass the hybrid MBS / silica composite over 0.06 volume fraction (*cf.* Fig.2) is recognized.

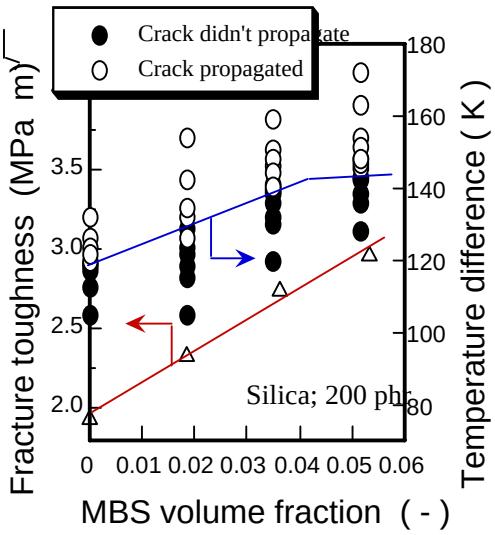

Fig.4 Effect of rubber filler content on fracture toughness and thermal shock resistance of hybrid composite (silica ; 200 phr).

Thermal Shock Resistance Evaluation Based on Fracture Mechanics and Fractography

To discuss the effect of filler content on thermal shock resistance, thermal stress intensity factor was evaluated with some thermal and mechanical properties. Based on our previous study, the thermal shock resistance ΔT_c is expressed as;

$$\Delta T_c = \frac{(1-\nu)\cdot K_{Ic}}{\alpha \cdot E}\cdot\frac{C_1}{\sqrt{R}} + \frac{k\cdot(1-\nu)\cdot K_{Ic}}{\alpha \cdot E}\cdot\frac{C_2}{h\cdot\sqrt{R^3}}$$

where α is coefficient of thermal expansion, E is elastic modulus, K_{Ic} is fracture toughness, ν is Poisson's ratio, k is thermal conductivity, h is heat transfer coefficient, R is the radius of the disk specimen and C_1, C_2 are constants determined by the condition of thermal shock test, respectively. The coefficients of thermal shock resistance *i.e.*, the fraction $(1-\nu)K_{Ic}/\alpha E$ in the first term and the fraction $k(1-\nu)K_{Ic}/\alpha E$ in the second term are measured experimentally and they are shown in Fig.5. Because h and R are constant, the evaluated values showed the tendency of increasing thermal shock resistance. These tendencies differed form that of Fig.3. Then, some factors should be considered to evaluate the thermal shock resistance of hybrid filler composites.

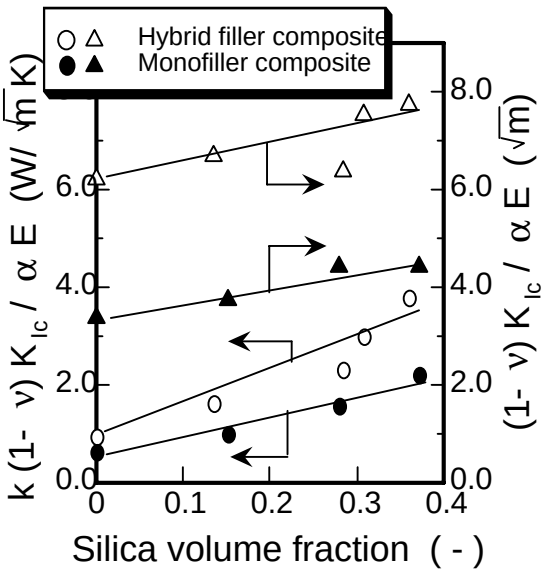

Fig.5 Silica filled effect on coefficients of thermal shock resistance.

This difference between experimental and theoretical evaluation was also obtained in the alumina filled resin, because of the poor adhesion, as we had already shown in previous study [7,8]. Then, the fracture surface after thermal shock test and fracture toughness test are observed by SEM and compared each other. Generally silica filler has good adhesion with epoxy matrix resin. For mono filler composite, both fracture surfaces showed good interface bond between silica particle and matrix, but for hybrid filler composite, especially at high silica content, the thermal shock test sample showed debonding at the interface. SEM photographs of fracture surfaces of silica 250 phr and MBS 10 phr hybrid system are shown in Fig.6, where (a) is that after fracture toughness test and (b) is thermal shock test. Obviously Fig.6 (a) shows flat silica fractured surface, that means crack propagate with breaking silica particles. On the other hand, Fig.6 (b) shows filler original surface is recognized between some particles and the matrix.

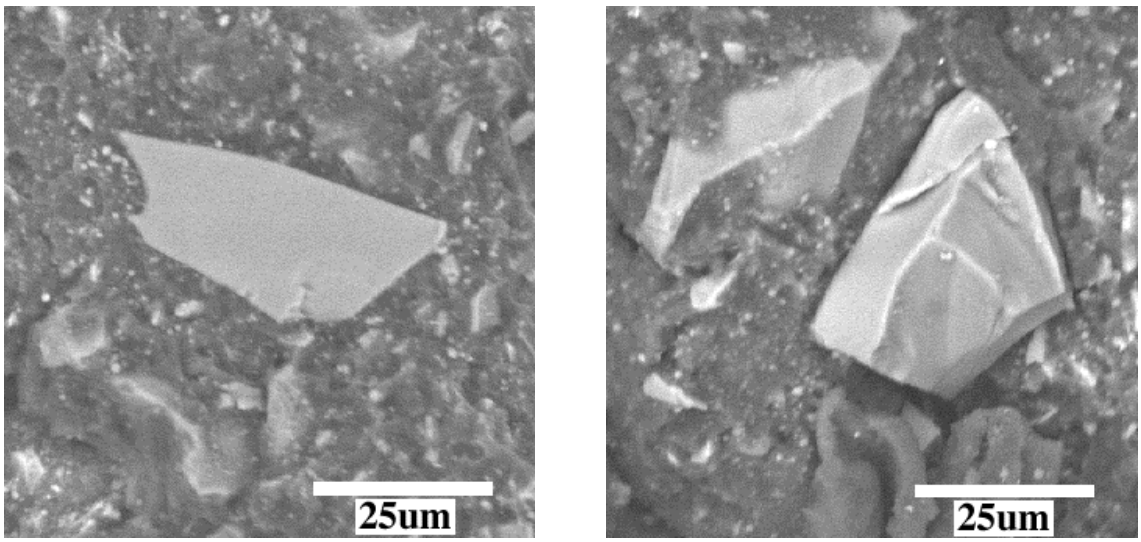

(a) Fracture toughness test *(b) Thermal shock test*

Fig.6 SEM photographs of fracture surfaces of hybrid composite (silica 250 phr & MBS 10 phr).

Then the difference of fracture mechanisms in fracture toughness test and thermal shock test is expected. This weakened interface caused low thermal shock resistance of hybrid filler composites.

CONCLUSION

In this study, thermal shock resistance of hybrid particulate filled composites were examined. The fracture toughness and the thermal shock resistance evaluated is summarized in Fig.7. As shown in Fig.7, hard and soft hybrid filler effect on thermal shock is smaller than that on fracture toughness. This tendency is due to the debonding of silica filler / matrix interface. For this reason, hybrid filler composite should be taken care not to crack if the material used under thermal shock condition.

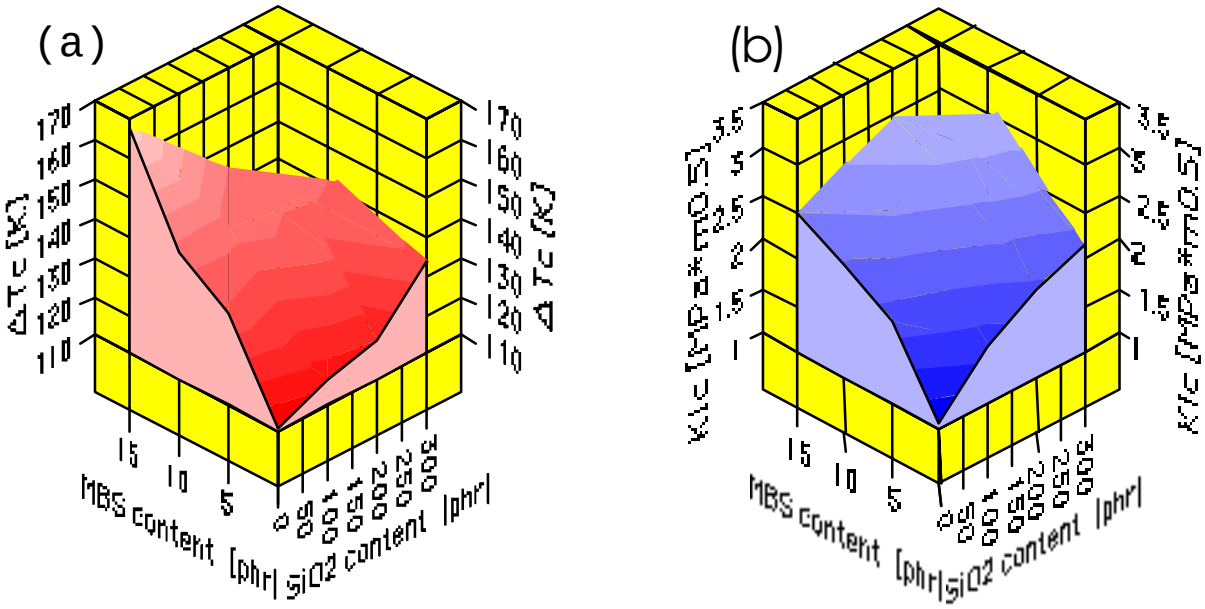

Fig.7 Silica & MBS hybrid filler effect on
(a) thermal shock resistance and (b) fracture toughness.

REFERENCES

1. Y.Nakamura, M.Yamaguchi, A.Kitayama, M.Okubo & T.Matsumoto, "Effect of Particle Size on Fracture Toughness of Epoxy Resin Filled with Angular-shaped Silica", *Polymer*, Vol. 32, No. 12 (1991) pp.2221-2229.

2. A.C.Moloney, H.H.Kausch, T.Kaiser & H.R.Beer, "Review: Parameters Determining the Strength and Toughness of Particulate Filled Epoxide Resins", *Journal of Material Science*, Vol. 22, No. 2 (1987) pp.381-393

3. T.Shimizu, Y.Hirano, M.Kamino & A.J.Kinloch, "Improvement in Toughness of Epoxy Casting Materials by Filling Secondary Particles", *Journal of Thermosetting Plastics, Japan*, Vol. 15, No. 4 (1994) pp.175-184.

4. F.Martinatti & T.Ricco, “High-rate Fracture Toughness of Polypropylene-based, Hybrid, Particulate Composites”, *Journal of Material Science*, Vol. 29, No. 2 (1994) pp.442-448.

5. M.Kubouchi & H.Hojo, “Thermal Shock Resistance of Toughened Epoxy Resins”, *Toughened Plastics I; Science and Engineering, ACS Advanced in Chemistry Series, Vol. 233*, C.Keith Riew & Anthony J.Kinloch Eds, (1992) pp.365-379.

6. M.Kubouchi, K.Tsuda, T.Nakagaki, K.Arai & H.Hojo, “Evaluation of Thermal Shock Fracture Toughness of Ceramic Particulate-filled Epoxy Resin”, *Proceedings Tenth International Conference on Composite Materials*, Whistler, British Columbia, Canada, August 14-18, Vol. I: Fatigue and Fracture, Anoush Poursartip & Ken Street Eds, (1995) pp.479-486.

7. M.Kubouchi, “Thermal Shock Test and Evaluation Method of Epoxy Resin for Electrical Insulation”, *Journal of Network Polymer, Japan*, Vol. 17, No. 2 (1996) pp.89-97.

8. M.Kubouchi, K.Tsuda & H.Hojo, “Thermal Shock Behavior and Evaluation of Epoxy Resins Toughened with Ceramic Particulate”, *Toughened Plastics II; Novel Approaches in Science and Engineering, ACS Advanced in Chemistry Series, Vol. 252*, C.Keith Riew & Anthony J.Kinloch Eds, (1996) pp.119-132.

STIFFNESS PROPERTIES OF THREE DIMENSIONALLY (3-D) REINFORCED GLASS FABRICS PRODUCED BY NEEDLE-FELTING

M. Veidt

Department of Mechanical Engineering, The University of Queensland, Brisbane, Australia

SUMMARY: This paper describes the influence of a needle-felting textile process on the in-plane and through thickness stiffness properties of glass fibre-reinforced fabrics. It was shown in [1] that the 3-D reinforcement considerably improves the fracture and delamination resistance of the material. In the current investigation the changes in the tensile stiffness in the plane of the laminate and the tensile and shear properties in the thickness direction are quantified in-situ by applying non-destructive evaluation techniques. The results show that the fast and cost effective needle-felting process which results in toughness-optimised, glass fibre-reinforced fabrics does not noticeably affect the in-plane stiffness properties of the laminate.

KEYWORDS: glass fibre-reinforced laminated composite, three dimensional, needle-felting, elastic properties, non-destructive evaluation, ultrasonics

INTRODUCTION

The number of applications of advanced composite materials being employed in manufacturing constantly increases. But there still remain several obstacles which must be overcome before fibre-reinforced composites will be used exclusively in highly loaded primary structures. Foremost amongst these are: damage tolerance, delamination resistance and labor intensive manufacturing procedures. Many investigations have shown that the most effective way to improve the toughness and delamination characteristics of traditional two dimensional (2-D) laminates is through thickness reinforcement, eg. [1-5]. Applying cost effective textile processing technologies such as conventional stitching or needle-felting, the damage tolerance, delamination resistance and compression strength can be significantly improved. In general, the textile technologies used in the additional production step needed are very cost effective and do not dramatically increase the total manufacturing costs. Compared to the extensive data available describing the influence of these reinforcement techniques on the strength, fracture and fatigue behaviour of a large variety of materials, only limited data can be found in the open literature describing their influence on the stiffness properties of the final product, although they are equally essential for a material to find optimum application in design and production.

In this paper the influence of needle-felting on the in-plane and through thickness stiffness properties of fibre-reinforced laminates comprised of plain weave glass fabrics is studied. It was shown in [1] that the extremely fast and cost effective textile process significantly

improves the fracture and delamination characteristics of the material. The tensile stiffnesses in the plane of the laminate and the tensile and shear properties in the thickness direction of the material are determined in-situ by applying non-destructive evaluation techniques which were introduced earlier, eg. [6-8].

SPECIMENS

3-D Reinforcement by Needle-Felting

Needle-felting is a fast and cost effective process that can convert stacks of unidirectional prepreg laminates or woven fabrics into 3-D reinforced preforms in a single operation. The technique is considerably more economical than other methods of three dimensional reinforcement such as transverse stitching, weaving or braiding. In the needle-felting process a large number of individual, shaped needles are penetrating an aligned lay-up. The punching density in a one step operation may exceed 80 stitches/cm^2. The punching process forces fibres to bend out of the laminate plane which results in a 3-D fibre network. The manufacturing process is finished by infiltration of the preforms with matrix material and subsequent curing.

In the current investigation two square plates were tested. Both plates were comprised of four layers of glass fabric. The individual plies were woven from 3 mm thick fibre bundles in a plain weave pattern (Eifatex 19). The preform of plate B2 was punched with 80 stitches/cm^2 using a conventional needle-felting textile machine. Hot press curing using vacuum infiltration of the matrix material (Ciba Geigy LY556 Epoxy raisin, HY917 hardener, DY070 accelerator) was used to manufacture the final laminates. The characteristic properties of the two sample plates are summarised in Table 1.

Improved Delamination Resistance

The influences of the needle-punching process on the mechanical properties of the materials and their microstructures have been reported earlier, [1]. The major results of these investigations are included in Table 1 and briefly summarised below.

Table 1: Characteristic properties of the glass fibre-reinforced square plates.

Specimen Notation		**B1**	**B2**
Material		four layers of roving fabric, unpunched	four layers of roving fabric, punched (80 stitches/cm^2)
Lateral Length L	[mm]	190	190
Mean Thickness 2H	[mm]	1.88	2.15
Fibre Volume Fraction	[%]	62	51
Density ρ	[g/cm^3]	2.10	1.92
In-plane Tensile Strength R_m	[N/mm^2]	480	370
Delamination Resistance G_{Ic}	[kN/m]	1.0	5.0
Delamination Resistance G_{IIc}	[kN/m]	0.8	3.9

Obviously, the needle-felting process changes the microstructure of the material. The 3-D reinforcement increases the volume of the preform. As a result, the thickness of the punched laminate is approximately 15% larger than the one of the unprocessed laminate, and the fibre volume fraction and the density of the punched material are smaller. An additional effect which contributes to these reductions is that air or gas is likely been trapped in the 3-D fibre network. Microscopical investigations have shown that the unpunched stacks of specimen B1 mainly feature individual, longitudinal gas inclusions which are located primarily between the laminate layers. In specimen B2 the total volume of the trapped gas is approximately twice as high. The inclusions are mainly round, their average diameter is approximately (0.5 ± 0.1) mm, and they are evenly distributed over the entire thickness of the laminate.

The results show that the mode I and mode II crack resistance of the 3-D reinforced laminates are approximately 5 times the ones of the unpunched material. As expected, the in-plane strength is slightly reduced due to the needle-felting process but an ultimate strength of 370 N/mm^2 is still sufficient for most technical applications using glass fibre-reinforced composites. The results for the needle-felting processed preforms are in good agreement with results for other, more expensive through thickness reinforcement techniques such as stitching, weaving or braiding.

EXPERIMENTAL TECHNIQUES

Owing to the symmetry of the individual layers with respect to the laminate plane, six independent stiffness values are needed to describe the linear-elastic behaviour of the specimens. In the Cartesian coordinate system introduced in Fig. 1, these are: $E = E_{11}$, $E' = E_{22} = E_{33}$, $G' = G_{12} = G_{13}$, $G = G_{23}$, $\nu' = \nu_{21} = \nu_{31}$ and $\nu = \nu_{23}$.

There exist many static and dynamic measurement techniques to determine the elastic moduli of fibre-reinforced materials. In the current investigation the emphasis was on finding the tensile stiffness E in the laminate plane and the tensile and shear stiffnesses E' and G' in the direction of the thickness of the laminate. Therefore, two non-destructive, dynamic measuring techniques which have proven to allow for the accurate, in-situ determination of these stiffness components are used to quantify the influence of the needle-felting process, eg. [6 - 8]. The two techniques are briefly recapitulated below.

Flexural Waves

The tensile stiffness E in the plane of the laminate and the shear modulus G' in the thickness direction are determined by analysing the propagation behaviour of centrally excited flexural waves. The detailed derivation of the second order solution describing the propagation of flexural waves in an orthotropic material which is needed to analyse the experimental data, an extensive description of the measuring setup as well as an error propagation analysis can be found in [6]. Fig. 1 schematically outlines the measuring concept.

A piezoceramic transducer is used to excite a narrow band, ultrasonic pulse. From the displacement signals captured at distinct points along rays using a heterodyne Doppler laser interferometer, the phase velocity c as a function of frequency f or wavenumber k, ie. the dispersion curve, can be determined. Fig. 2 shows a measured dispersion curve for specimen B1 and B2, respectively.

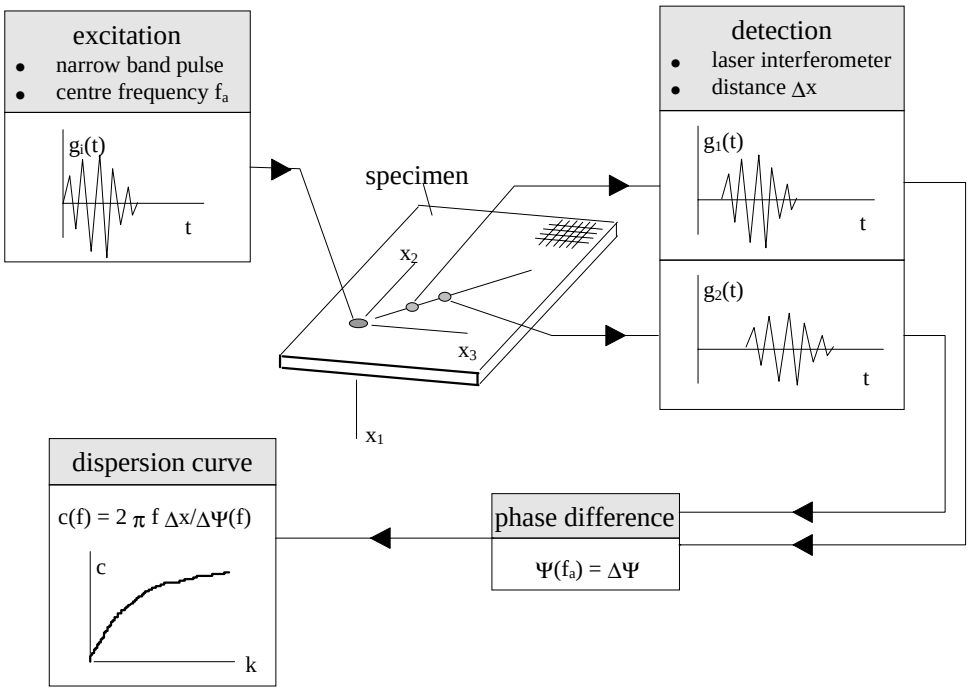

Fig. 1: Measuring principle of the flexural wave experiments.

The locations of the piezoceramic transducer used as excitation source and the measuring points along the main axes of orthotropy were selected according to Fig. 3. With this setup, the measurement and model-related requirements may be met. Firstly, the narrow band excitation pulse can be separated from the reflections at the edges of the laminate. Secondly, the wavelength of the flexural waves are much larger than the characteristic lengths of the laminates. The resulting lower and upper limits for the centre frequency f_a of the excitation pulse are 40 kHz and 150 kHz, respectively.

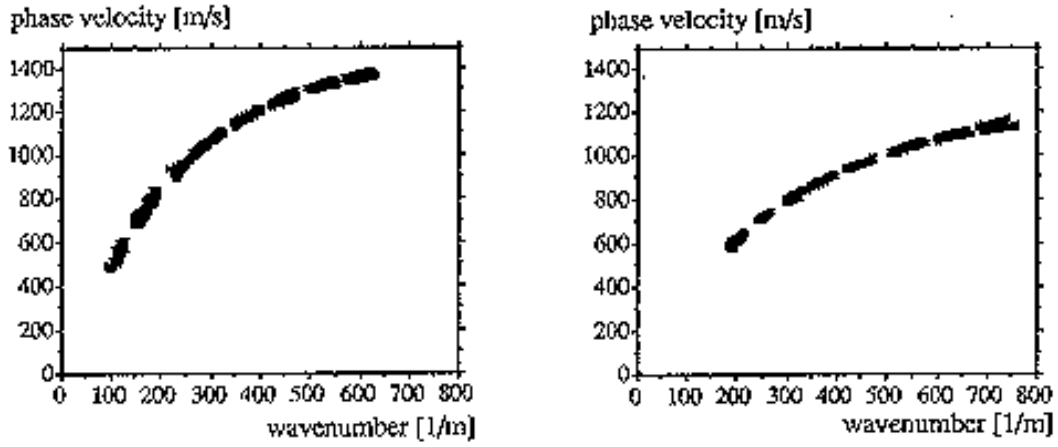

Fig. 2: Measured dispersion curves for propagation along the principal axis x_2, a) specimen B1, 587 data points, b) specimen B2, 533 data points.

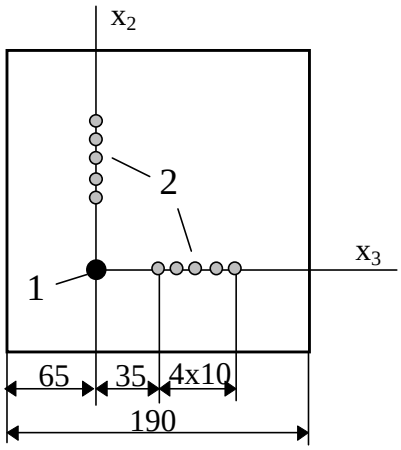

Fig. 3: Selection of excitation location and measuring points (dimensions in [mm]), 1: excitation point, 2: measuring points, Δx = 10 mm.

Evaluation of the measured dispersion curves is based on the theoretical analysis of the propagation behaviour of flexural waves in an orthotropic plate, [6]. A perturbation method was used to derive the general, second order dispersion relation. For propagation along the principal directions x_2 and x_3, we may write:

$$c \cong Hk\sqrt{\frac{E}{3\rho}}\left[1+(Hk)^2\frac{2E}{5G'}\right]^{-1/2} \tag{1}$$

Point Source/Point Receiver Technique

The stiffness E' in the thickness direction was determined using a point source/point receiver (PS/PR) ultrasonic measurement technique, eg. [7, 8]. The setup is schematically outlined in Fig. 4.

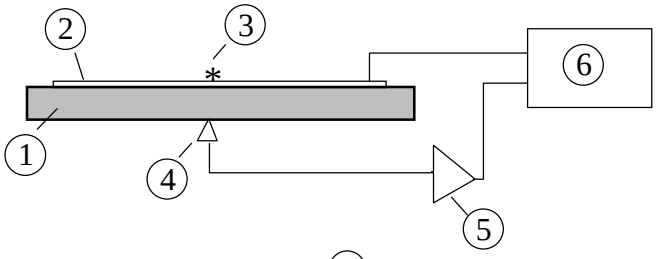

1 specimen

2 trigger generator
PVDF piezofilm (Keynar), thickness 9 μm

3 broadband excitation
fracture of glass capillary

4 piezoceramic point detector
pinducer (Valpey Fisher), aperature 1.3 mm

5 ultrasonic preamplifier
(Panametrics, 5660C)

6 transient recorder
(Tektronix, AD390)

Fig. 4: Schematic of the setup used in the PS/PR experiments.

Calculation of the stiffness is based on measuring the arrival time of a broad band excitation pulse. The group velocity c_p of the primary wave is calculated from the measured time of flight Δt and the distance between the excitation point and the receiver location. If the spring-

loaded receiver is mounted at the so-called epicentral location, ie. directly below the excitation point, the stiffness E' in the thickness direction can be determined using:

$$E' \cong \rho c_p^2 = \rho \left(\frac{2H}{\Delta t} \right)^2 \qquad (2)$$

RESULTS AND DISCUSSION

In the case of the flexural waves the dispersion curves were determined using eight different centre frequencies f_a between 40 kHz and 140 kHz. Owing to the possibility of determining the phase velocity by analysing the signals captured at randomly selected measuring points along the principal directions x_2 and x_3, twelve dispersion curves with respectively about 100 data points were determined for each laminate. The characteristic stiffness values E and G' are determined from these data points by non-linear regression using equation (1). Evaluation of the twelve dispersion curves for the specimens B1 and B2 affords the following values for the desired stiffness components.

Specimen B1	E = (36 ± 3) GPa	G' = (6.0 ± 0.5) GPa
Specimen B2	E = (31 ± 3) GPa	G' = (5.7 ± 0.5) GPa

The standard deviations greatly exceed the inherent accuracy of the measuring technique itself which was determined from an error propagation analysis, [6]. The reason is that the microstructure of the specimens produced by hot press curing using vacuum infiltration, considerably varies from point to point and consequently, the standard deviation of the determined stiffness values is large. Nevertheless, the mean values represent reliable quantities describing the global stiffness behaviour of the structures.

The needle-felting process has only a slight effect on the two stiffness components. Although the delamination resistance of the needle-punched laminate is a multiple of the conventional material, the stiffness values in the plane of the laminate are of the same order of magnitude. The considerable improvements in terms of crack resistance do not have an noticeable adverse effect on the in-plane tensile properties.

The test setup for the PS/PR experiments outlined in Fig. 4 makes it possible to easily collect data at various locations. Finding the average of all measurements thus affords values for the tensile stiffness E'.

Specimen B1	E' = (8.5 ± 2) GPa
Specimen B2	E' = (15 ± 3) GPa

As expected, the above mentioned inhomogenities turn out to have a considerable influence which results in large standard deviations. The mean values, however, definitely show that due to the additional reinforcement in the thickness direction, the tensile stiffness E' increases by about 70%.

CONCLUSIONS

Needle-felting of stacks of conventional glass textiles considerably improves the interlaminar properties of the laminates without having an appreciable adverse effect on the elastic properties. The tensile stiffness in the plane of the plate decreases by less than 10% while the tensile stiffness in the thickness direction increases by about 70%. The shear modulus G' in the direction of the thickness of the plate remains approximately constant. The needle-felting process seems to be an extremely cost effective method to produce toughness-optimised, glass fibre-reinforced fabrics whose in-plane elastic properties are not noticeably affected.

It remains to be elucidated whether this promising manufacturing process affords the same favourable results for aramide and also for carbon fibre-reinforced materials.

ACKNOWLEDGMENTS

This investigation was initiated by Dr C. Wuethrich (ABB, Switzerland) and the company Micafil AG (Zuerich). The author acknowledges the support of Prof. M.B. Sayir, Institute of Mechanics, ETHZ and Prof. W. Sachse, Theoretical and Applied Mechanics, Cornell. Dr K.Y. Kim is thanked for valuable help in setting up the point source/point receiver measuring system and Mr A. Hochuli for collecting some of the flexural wave propagation data.

REFERENCES

1. Wuethrich, C. and Keser, G., "Better mechanical properties of composites through needling", *Kunststoffe/German Plastics*, Vol. 82, 1992, pp. 127 - 131.
2. Dransfield, K., Baillie, C. and Mai, Y.W., "Improving the delamination resistance of CFRP by stitching - a review", *Composites Science and Technology*, Vol. 50, 1994, pp. 305 - 317.
3. Evans, D.A. and Boyce, J.S., "Transverse reinforcement methods for improved delamination resistance", *34th International SAMPE Symposium and Exhibition - Tomorrow's Materials*, Book 1, SAMPE, Covina, USA, 1989, pp. 271 - 282.
4. Bannister, M.K. and Herszberg, I., "Textile preforms for composite structures", *5th Australian Aeronautical Conference*, Part 2, IE Aust, Crows Nest, AU, 1993, pp. 357 - 362.
5. Burnett, E.J. and Harris, J.A., "High performance needled structures in composites", *35th International SAMPE Symposium and Exhibition - Advanced Materials*, Part 2, SAMPE, Covina, USA, 1990, pp. 1533 - 1543.
6. Veidt, M. and Sayir, M.B., "Experimental evaluation of global composite laminate stiffnesses using flexural waves", *Journal of Composite Materials*, Vol. 24, 1990, pp. 688 - 706.
7. Sachse, W. and Kim, K.Y., "Point source/point receiver materials testing", *Ultrasonic Materials Characterization*, Vol. 2, J. Boussiere, Ed., Plenum Press, New York, USA, 1987, pp. 707 - 715.
8. Every, A.G., Sachse, W., Kim, K.Y. and Niu, L., "Determination of elastic constants of anisotropic solids from group velocity data", *Review of Progress in Quantitative Non-Destructive Evaluation*, Vol. 10B, D.O. Thompson and D.E. Chimenti, Eds, Plenum Press, New York, 1991, pp. 1663 - 1668.

MECHANICAL RESPONSE OF PARTICLE-FILLED POLYETHYLENE ON ELECTRICALLY GENERATED THERMAL SHOCK PULSE

Joachim Glatz-Reichenbach, Jørgen Skindhøj and Ralf Strümpler

ABB Corporate Research, CH-5405 Baden-Dättwil, Switzerland

SUMMARY: Highly conducting metal-filled polyethylene with positive temperature coefficient (PTC) of resistivity have been prepared and exposed to strong transient current pulses. Caused by the strong non-linear change of resistivity with temperature, a narrow hot-zone is formed in the center part of the test samples. The resistivity switches by eight orders of magnitude and interrupts the current flow. The thermally stimulated mechanical shock pulse is monitored with a laser distance sensor system and the surface temperature development by an infrared camera. The combined results of electrical, mechanical and temperature measurement are used to determine extension and Young's Modulus of the hot-zone.

KEYWORDS: positive temperature coefficient of resistivity, electrical conductivity, thermal expansion, thermal imaging, mechanical response, polymer composite

INTRODUCTION

In order to meet the needs of industry for materials with new and suitable electrical, mechanical and thermal properties, the interest in composites is more and more increasing. One class of functional composites are polymers which are filled with particles having tailored properties. Such kind of materials can combine flexibility, lightweight, low cost and simple processability of polymeric materials with an additionally desired functionality of the filler material as, e.g., high electrical [1] or thermal conductivity [2], polarizability [3], magnetic [4] or non-linear dielectric properties [5,6].

Carbon black or metal filled polymers show, for example, a positive temperature coefficient (PTC) of the electrical resistivity. Therefore, they are widely used as self-regulating heating tapes [7] or circuit protecting devices [8,9]. Such polymer based composites with PTC behavior are also interesting systems in order to study the correlation between thermal, mechanical and electrical properties of composites in general. The thermal energy is generated mainly close to the contact points of the conducting filler particles. Due to the high thermal conductivity of the filler particles, they heat up first. Then the surrounding polymer is heated too and expands due to its relatively large thermal expansion coefficient. The thermal expansion works against internal mechanical stresses, which have been built up during the preparation of the sample, until a certain expansion has been achieved. Then a strong change in resistivity is observed caused by changes in gap distance of the particle-particle contacts in the expanded matrix. This view is supported by measurements on metal particles in epoxy [10] and holds for a thermoplastic matrix as well. A similar explanation has been given by Carmona et al. for carbon fibers in epoxy [11].

For applications under severe conditions (i.e. high current or electrical field, elevated temperature and mechanical shock), it is important to understand the dynamic correlation between electrical, thermal and mechanical properties of such composites in order to find their physical limits. It has been shown recently, that the filler particle size has a strong influence on the tripping dynamic under high current load. The PTC material trips faster, the smaller the particles are [12].

In the present paper, the strong nonlinearity of the resistivity with temperature is utilized to generate a thermo-mechanical shock wave. When a strong current is applied to the PTC material, it is heated very fast by Joule's losses. Due to the nonlinearity of the resistivity, it becomes even faster and concentrates on hot-spots. The temperature increase gives rise to a rapid thermal expansion of the polymer and results in a thermo-mechanical shock wave. This is accompanied by a resistance increases of several orders of magnitude, which interrupts the current flow. The motion of the sample, detected by a laser interferometer system, and the current are measured simultaneously. The amplitude of the expansion is related to the extension of the hot-zone and the thermal expansion coefficient of the composite. The frequency of the oscillation can be correlated to the Young‘s Modulus of the hot composite and the total accelerated mass of the test samples.

MATERIAL PREPARATION AND CHARACTERIZATION

The active body of the PTC-samples is a polymer-metal composite consisting of 50 vol.-% of highly conducting TiB_2 particles in different polyethylene matrixes (see Table 1). In order to achieve a homogeneous dispersion, filler and matrix material were compounded for several minutes by using a Brabender Plasticorder at temperatures around 180°C. After compounding the composites were hot-pressed at 145°C and 11 MPa to form several mm thick plates. The dependence of the electrical resistivity of the composite material on the temperature was determined by using an HP 4247 A Impedance Analyzer. The small test samples had sizes of 20mm·10mm·2mm and were measured in four-probe geometry.

Fig. 1 shows the behavior of the resistivity ρ as a function of temperature for a heating and a succeeding cooling run of the composite with high-density polyethylene (HDPE5261Z) as matrix material. The resistivity increases by eight orders of magnitude from about $10^{-2}\Omega$cm at ambient room temperature to more than $10^{6}\Omega$cm at 140°C. After cooling, the resistivity comes back to almost the same value as before heating, i.e. the PTC effect is repetitive.

The temperature dependence of ρ between 30 and 120°C is weak. Around 135°C, however, a strong increase of seven orders of magnitude in ρ occurs within a narrow temperature range of only 15°C. The strong step in resistivity is observed close to the melting temperature T_m = 134°C, as expected [1], and can be associated with the strong non-linear temperature dependent thermal expansion of the polyethylene matrix near its melting temperature [13]. The strong nonlinearity of ρ(T) can be expected as the driving force for the creation of only one localized hot-zone in one composite PTC element. The thermal expansion of e.g. high-density polyethylene HDPE5231, filled with 50 vol.-% TiB_2, was measured by dilatometry as shown in Fig. 2. The thermal expansion coefficient α is defined by the slope of the curve and exhibits a strong increase when approaching the melting temperature of the matrix material. The composite material looses mechanical strength at elevated temperatures which restricts the measurement of α(T) by dilatometry to temperatures below the melting temperature.

Table 1: Important material parameters at T = 25°C are listed for two high density polyethylene materials; Melting temperature (T_{melt}), specific heat (c), specific melting enthalpy (c_{melt}), thermal conductivity (λ), mass density (ρ), Young's Modulus (E), tensile strength ($E_{tensile}$) and thermal expansion coefficient (α) between 20 and 80°C.

⇓ property ; material ⇒	HDPE5231	HDPE5261Z
T_{melt} (°C)	133	134
c (J/gK)	1.9	1.7
c_{melt} (J/g)	165	200
λ (W/Km)	0.37	0.41
ρ (g/cm^3)	0.952	0.954
E (GPa)	1.1	1.3
$E_{tensile}$ (MPa)	25	27
α (20-80°C) (10^{-6}/K)	150-180	130-160

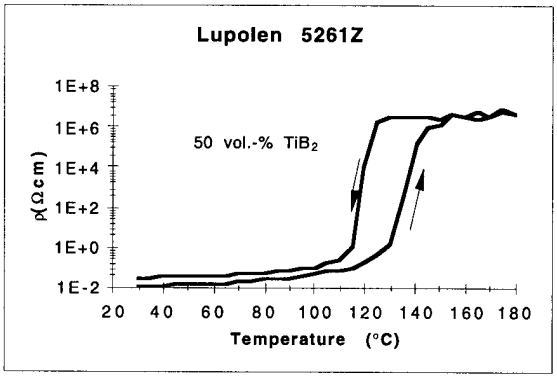

Fig. 1. The specific resistivity ρ of 50 vol.-% TiB_2 filled high density polyethylene HDPE5261Z as a function of temperature for one heating/cooling cycle, which was done within three hours.

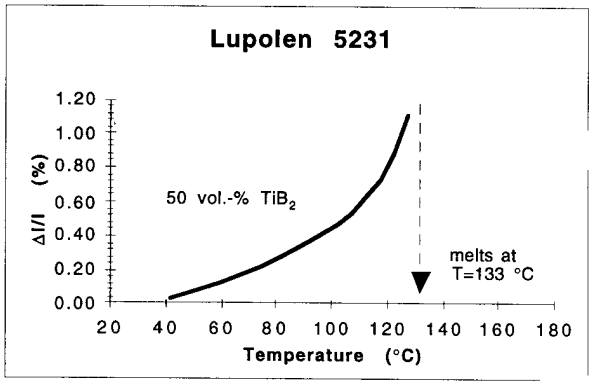

Fig. 2: The relative thermal expansion • l/l of 50 vol.-% TiB_2 filled high density polyethylene of type HDPE5231 as a function of temperature.

TEST SAMPLES

A side-view sketch of the used sample arrangement is shown in Fig. 3a. The sample consists of an about 2 mm thick plate of the composite material with aluminum contacts, which are pressed onto the composite. The press contacts are mounted by flexible brass plates. A ceramic varistor disc is fixed and pressed between the two brass plates together to form a good electrical connection to the PTC element.

In order to make sure that the sample trips in the center part of the PTC element, the cross-section of the PTC-body is simply reduced by holes. This technique to define a tripping zone by reduced cross-section, is well known and already industrially used [14,15]. A top view of the composite body with the aluminum contacts is seen in Fig. 3b.

The total resistance R^{cold}_{PTC} of the sample comprises the resistance of the composite plate between the contacts R_{cold}, plus the contact resistance $R_{contact}$ between the composite material and the metal contacts but without the negligible resistance of the brass terminals themselves.

$$R^{cold}{}_{PTC} = R_{cold} + R_{contact} = 1.0832 \cdot \frac{\rho \cdot l}{A} + R_{contact} \qquad (1)$$

where A is the cross-section of the PTC plate, l is the length of the PTC plate between the electrodes, $R_{contact}$ is the contact resistance between the PTC-body and the press contacts, and ρ is the specific resistivity of the PTC composite well below T_c. The factor 1.0832 results from the particular sample geometry.

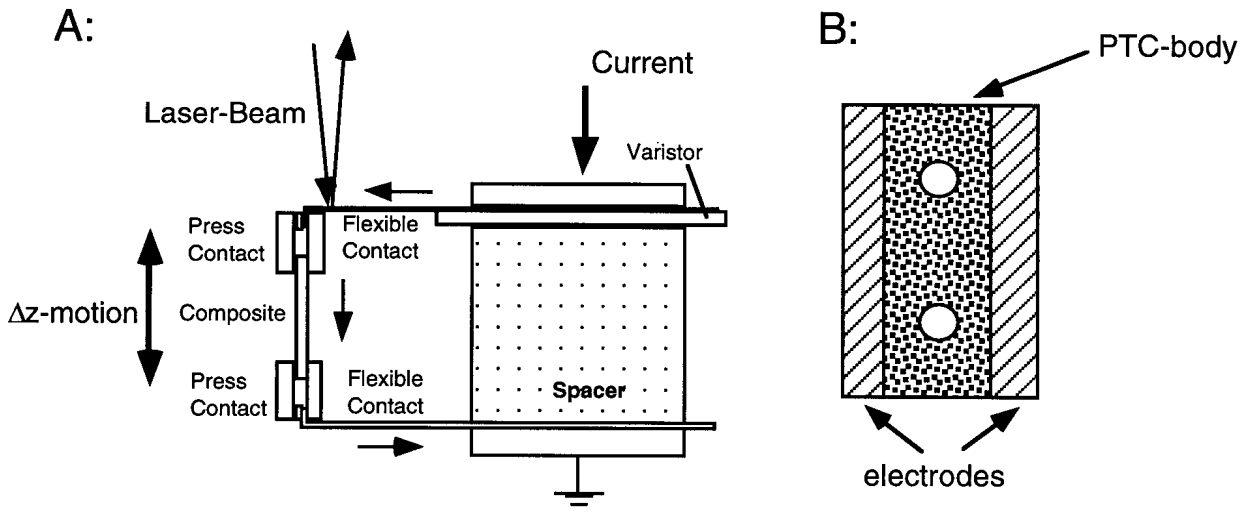

Fig. 3: (a) The sample set-up of the PTC composite resistor (very left), connected in parallel to a spacer, which provides mechanical stability and a ceramic varistor disc (top right in (a)). The incident and reflection direction of the laser beam and the direction of the motion of the expansion (Δz) are also indicated. (b) Sketch of PTC-body and the contacts as seen from top.

ELECTRICAL MEASUREMENTS

The electrical arrangement to generate the high and fast increasing current through the PTC composite sample is realized with a low impedance capacitor bank. The circuit lay-out is given in Fig. 4. The varistor limits over-voltages in the circuit which are generated during the resistance change of the PTC composite. The relevant circuit parameters are: C = 14.6mF, L = 54μH, which give rise to I_{max} = 4.9kA at a frequency of 179 Hz for a loading voltage U = 300V.

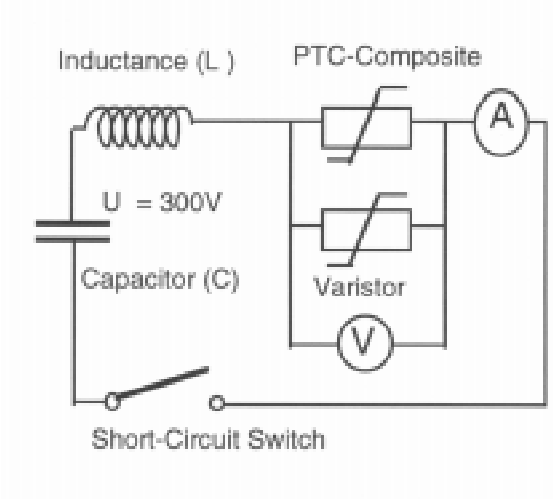

Fig. 4: Sketch of the used electrical circuit for generating the high current pulse through the composite material. The circuit parameters are: Capacitor C = 14.6mF, Inductance L = 54µH.

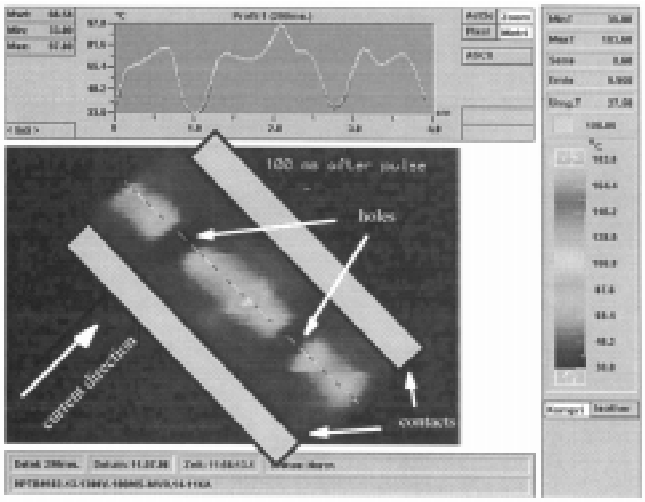

Fig. 5: Thermal image of 50 vol.-% TiB_2 filled HDPE5261Z material 100ms after tripping. The insert in the upper part shows the temperature distribution along the line perpendicular to the current flow direction.

EXPANSION MEASUREMENT

A commercially available laser distance sensor, Type: Keyence LC-2400A, is used for the detection of the dynamic expansion of the PTC resistor during the high current flow and its limitation. The principle of measurement bases on optical triangulation and is described elsewhere [16,17]. The distance signal is calibrated and directly available as an analogue output signal (for example: 1V for 10µm). For the described experiments a resolution of 0.5 µm and a sampling rate of 50 kHz is obtained with the optical sensor. In order to avoid disturbing mechanical resonance oscillations, the expansion is measured in some cases with one fixed contact. The expansion of the entire composite plate is detected at the polished surface of one flexible contact about 3 mm apart from the sample's axis. Therefore a multiple correction factor of 1.12 has to be taken into account to get the right Δz-amplitude.

With the simultaneous measurement of dynamic expansion and current flow through the PTC composite it is possible to demonstrate on a µs-timescale how the current limitation is correlated to the thermal expansion.

THERMAL IMAGING

During the experiments thermal images of the sample surface are recorded at video frequency (i.e. 30 pictures/s) by an infrared detection system (Nippon Avionics Co. Ltd., TVS-2200ST). With this method the surface temperature of the PTC sample can be monitored and provides additional information to estimate approximately the size and the shape of the region where the PTC trips. In Fig. 5 a typical image of an infrared picture is shown, which was taken 90 to 120 ms after the current flow through the PTC element was started.

RESULTS AND DISCUSSION

In Fig. 6 measurements of the current and voltage response (top part) and the energy input into the PTC element and the parallel varistor (bottom part) are given. Current flow starts at t_0 = 1.45ms and heats up the PTC sample. The PTC sample warms up, increases its resistance which is accompanied by a voltage drop across the sample. At t = 2.1ms the maximum resistance is reached, the current is commuted to the parallel varistor according to its voltage-current characteristic, and the current through the PTC element is suppressed nearly to zero. At t_{end} = 2.8ms, i.e. approximately 1.35ms after the start of experiment, no current can be detected anymore.

The energy input into the PTC element (E_{PTC}) and the varistor (E_{VAR}), as plotted in Fig. 6, are calculated by Eqn 2

$$E = E_{PTC} + E_{VAR} = \int_{t_0}^{t_{end}} I_{PTC} \cdot U \cdot dt + \int_{t_0}^{t_{end}} I_{VAR} \cdot U \cdot dt \qquad (2)$$

where I_{PTC} and I_{VAR} are the currents through PTC element and varistor, U is the voltage across them, and t_0 and t_{end} are the times when current flow starts and ends, respectively. The input energies are typically 150J for the PTC element and 250J for the parallel varistor.

The particular sample geometry with reduced cross-section in the center part of the PTC-body gives rise to a well defined tripping region. The temperature distribution at the PTC sample surface, as recorded just 100 ms after current flow start, is displayed in Fig. 5. Only a narrow zone of the PTC-body with an extension of few mm in current flow direction seems to be heated up sufficiently high for the PTC effect to take place. Therefore, three different regions of energy input during current flow can be localized. The contact region close at and also under the aluminum contacts, the PTC-body with constant cross-section, and the center part of the PTC-body with reduced cross-section. When a current is applied to the PTC sample, it is heated by Joule's losses with the power

$$P(t) = U(t) \cdot I_{PTC} = R_{PTC}(t) \cdot (I_{PTC}(t))^2 \qquad (3)$$

and the total energy input into the PTC sample can be calculated with Eqn 4

$$E_{PTC} = \int_{t_0}^{t_{end}} R(t)_{PTC} \cdot (I(t)_{PTC})^2 \cdot dt \qquad (4)$$

where $R_{PTC}(t)$ and $I_{PTC}(t)$ are the time dependent total resistance and current of the composite sample. With respect to the sample geometry, Eqn 4 can be split into three single contributions, i.e. the contribution of the contact ($E_{contact}$), of constant cross-section (E_{side}) and of reduced cross-section (E_{center}) as formulated in Eqns 5 and 6

$$E_{PTC} = E_{contact} + E_{side} + E_{center} \qquad (5)$$

$$E_{PTC} = \int_{t_0}^{t_{end}} [(R_{contact} + R_{cold} + \sum_{n=1}^{k} (\rho_n(T(t)) - \rho) \cdot \frac{l_n}{A_n}) \cdot (I_{PTC})^2] \cdot dt \qquad (6)$$

where $R_{contact}$ is the contact resistance, R_{cold} is the resistance of the entire PTC-body at room temperature (25°C), ρ is the specific resistance at room temperature, $\rho_n(T(t))$ is the time and temperature dependent specific resistivity of a volume element ($l_n \cdot A_n$) inside the hot-zone, A_n is the cross-section of a n^{th} volume element of the length l_n in current flow direction and finally I_{PTC} is the current through the PTC element.

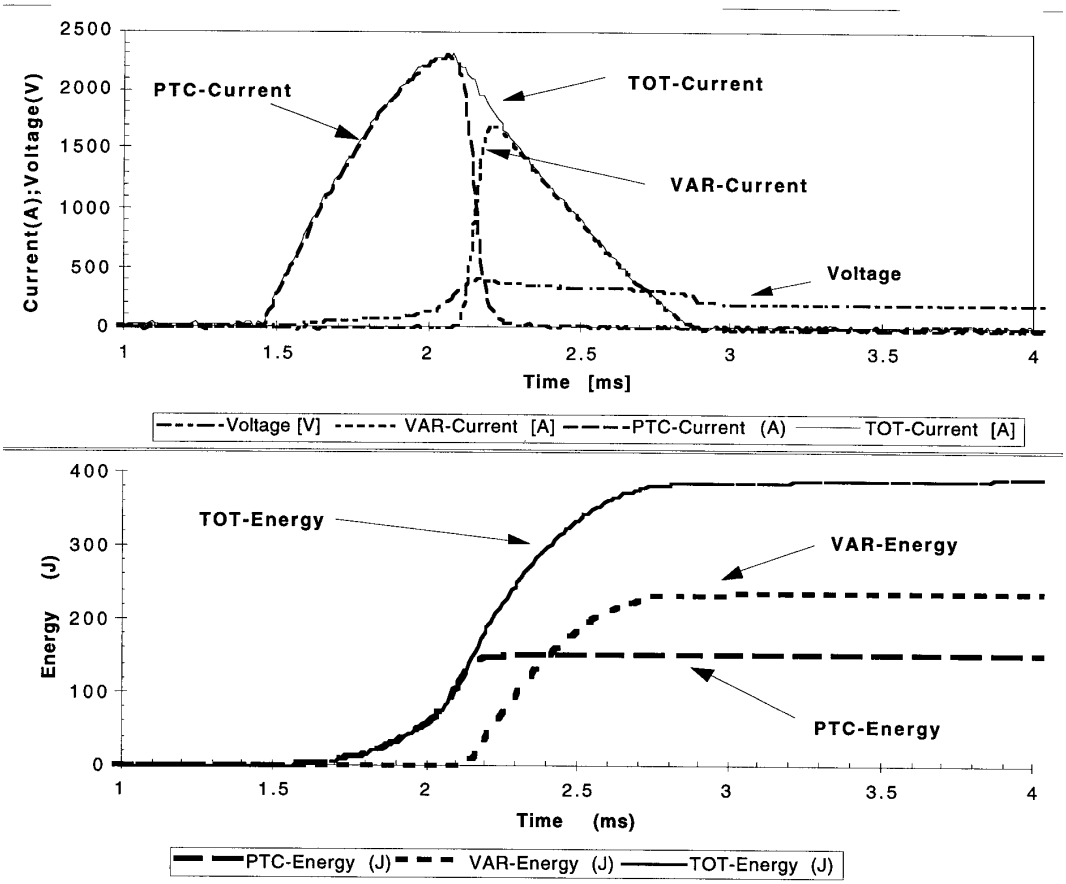

Fig. 6: Upper part: Voltage across PTC element (Voltage), varistor current (VAR-Current), current through the PTC element (PTC-Current) and total current (TOT-Current), as mentioned in the foot line, are displayed in the relevant time window. The current flow starts at t_o = 1.45ms. Bottom part: The energy input into the PTC element (PTC-Energy), the varistor (VAR-Energy) and the total input energy (TOT-Energy) as calculated from the measured voltage and currents of the upper part.

Eqns 5 and 6 determine the energy input into the three regions separately. The result for a PTC element with HDPE5261Z matrix is seen in Table 2, with k = 20 and all l_n of same length, $R_{contact}$ = 11.1 mΩ and R_{cold} = 27 mΩ, with the $\rho(T)$-characteristic from Fig. 1 and a current response as seen in Fig. 6 (top part). It is observed that a major part of the energy is deposited in the region of constant cross-section. A rough estimation of the temperature development of the parts of constant and reduced cross-section can be done by assuming adiabatic conditions during heating up within few ms, i.e. there is no energy exchange with the surrounding. The entire electrical energy (E_{input}) is used to heat the parts of the PTC from a starting temperature T_{start} to an end temperature T_{end} homogeneously. Eqn 7 is applied for both regions separately with different m and T_{end} and a specific heat $c(T)$ of weak temperature dependence.

$$E_{input} = \int_{T_{start}}^{T_{end}} m \cdot c(T) \cdot dT \qquad with \qquad \Delta T_{\max} = T_{end} - T_{start} \tag{7}$$

The PTC part of reduced cross-section is heated above melting temperature, thus an additional melting enthalpy of about 200J/g for the polyethylene has to be taken into account. The resulting average temperature increase is listed in Table 2. Although the temperature increase of the part of constant cross-section is only 45°C, the major part of the energy is deposited in this region. A smaller energy input of 41J into the middle part is sufficient to bring the PTC element into the high-resistive state.

The results are in good agreement with the measured input energy into the PTC element as seen in Fig. 6 and the surface temperature development as seen from Fig. 5.

Table 2: For the three different regions of the PTC sample the resulting input energies and the maximum average temperature increase ΔT_{max} are listed.

part of the PTC sample	Input-Energy (J)	ΔT_{max} (°C)
contact region	26	-
constant cross-section	73	45
reduced cross-section	41	125
entire PTC sample	140	> 45

In Fig. 7 the dynamic expansion of a test sample (full line) and the current through it (dashed line) are shown within a time window of 10ms. The current starts to increase with a slope of about 5kA/ms at t_o = 1.45ms, reaches the maximum value of 2.3kA about 0.6ms later and is suppressed nearly to zero at t_{end} = 2.3ms. Of course, even after this time, there is still a residual current in the mA-range, which is high enough to keep the sample in the high-resistive state. This current is mainly determined by the external cooling conditions and the $\rho(T)$-characteristic.

It is interesting to note that the short-circuit current is limited long before the element reaches its final expansion. The expansion starts at t = 1.75ms and reaches at t = 2.9ms a maximum elongation of 65µm. After reaching the maximum expansion, mechanical oscillations are observed around the new stable position of the sample at about 50µm elongation.

The thermal energy is supposed to be generated mainly close to the contact points of the conducting filler particles. Due to the low thermal conductivity of the polymer, a time delay of about one ms between the maximum of the current and the thermal expansion of the composite is observed. The resistivity increase by the mechanical separation of the conducting filler particles is obviously high enough to suppress the current to about zero long before the full expansion is achieved.

The thermal images, which were taken 100ms later, show a hot-zone which expands over the entire sample cross-section perpendicular to current flow direction. In current flow direction, the hot-zone is strongly localized to a narrow region of only a few mm. Thus, as already confirmed in the previous section, the tripped PTC-body can be divided into a cold part with $T_{low} << T_c$ and a hot part with $T_{high} \approx T_c$.

The extension of the hot-zone can be determined by analyzing the thermal images and the thermal expansion into the new stabile Δz-position of the PTC sample. The linear one dimensional thermal expansion in current flow direction can be approximated by Eqns 8 and 9

$$\Delta z = \Delta z_{hotzone} + \Delta z_{cold} = \int_{T_{start}}^{T_{high}} \alpha(T) \cdot z_{hotzzone} \cdot dT + \int_{T_{start}}^{T_{low}} \alpha(T) \cdot (l - z_{hotzone}) \cdot dT \tag{8}$$

$$\Delta z = \int_{T_{low}}^{T_{high}} \alpha(T) \cdot z_{hotzone} \cdot dT + \int_{T_{start}}^{T_{low}} \alpha(T) \cdot l \cdot dT \tag{9}$$

The extension of the hot-zone can be estimated by integrating Eqn 9, using a measured $\Delta z = 60\mu m$, $T_0 = 25°C$, $T_{low} = 55°C$, $T_{high} = 120°C$, $l = 15mm$, and $\alpha(T)$ from Fig.2. This results in an extension of the hot-zone $z_{hotzone} \approx 1.5mm$, which is about 10% of the total length of the PTC element.

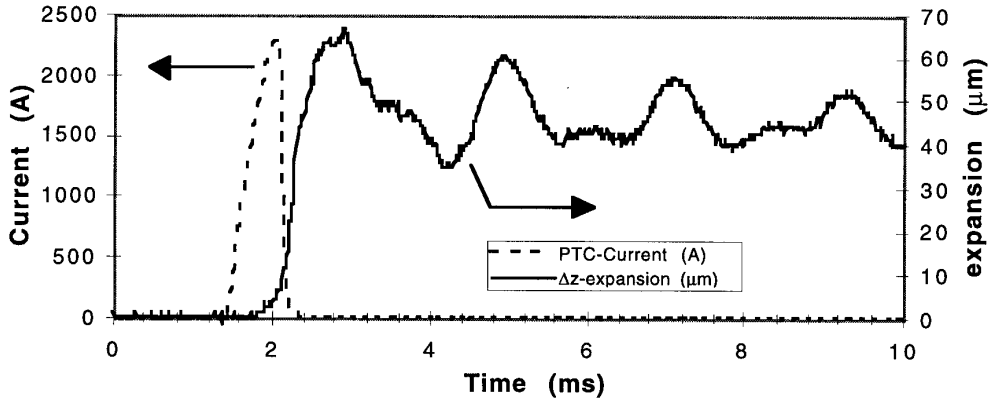

Fig. 7: The current (dashed line) and the expansion of a test sample (full line) of HDPE5261Z composite material, are shown within a time window of 10ms. After reaching the maximum expansion of 65μm, mechanical oscillations are observed around the new stable position of the sample at about 50μm elongation.

The temperature induced expansion reaches a maximum elongation and oscillates little later with a small amplitude around a stable extended position. The center part of the PTC-body develops the highest temperature. Due to the strong decrease of Young's Modulus of polyethylene when approaching the melting point, the center part of the PTC (the hot-zone) may be the region of largest mechanical deformations during the oscillations.

From the mechanical oscillations around the stable Δz-position of the expanded PTC sample the calculation of the Young's Modulus of the hot-zone is possible. The oscillation around the new stabile position can be approximated by a harmonic oscillator with frequency f and amplitude Δx. In Eqn 10, m denotes the total accelerated mass, a is the acceleration, D the spring constant of the used brass terminal and $Y_{hotzone}$ is the mean Young's Modulus of the composite material inside the hot-zone. The cross-section of the hot-zone is assumed to be constant $A_{hotzone} \approx 0.5\ cm^2$ for simplification.

$$F = m \cdot a = m \cdot 4\pi^2 \cdot f^2 \cdot \Delta x = \left(\frac{Y_{hotzone} \cdot A_{hotzone}}{z_{hotzone}} - D \right) \cdot \Delta x \tag{10}$$

A mean Young's Modulus of the hot-zone can be determined by using the measured frequency f = 460Hz, m = 0.014kg, D = 11kN/m and $z_{hotzone}$ = 1.5mm. Eqn 10 yields $E_{hotzone}$ = 3.84MPa, which is less than 0.5 % of the value of the pure polyethylene at room temperature.

CONCLUSION

The combined on-line measurement of electrical current and mechanical motion, combined with the monitoring of the surface temperature by an infrared detecting system is a powerful tool to investigate the impact of locally generated thermal shock waves in structured composite materials. The technique correlates the thermally stimulated mechanical expansion of the composite to the heat generation and transport in the electrically conducting composite material. The combined measurement gives an interesting insight to the interaction of the electrical, mechanical and thermal properties of electro-composites.

The calculations yield a length of about 1.5mm for the hot-zone with an average Young's Modulus of about 4MPa.

REFERENCES

1. Strümpler, R., *J. Appl. Phys.* Vol. 80, 1996, pp. 6091-6096 .
2. Bujard, P. and Ansermet, J.P., *Proc. SEMI-THERM*, San Diego Feb. 7-9, 1989, pp. 126-130.
3. Dougherty, J.P. and Chen, Y., *Proc. 2nd Int. Conf. on Intelligent Mater. (ICIM'94),* Colonial Williamsbug, Virginia, June 5-8, 1994, eds.: C. Rogers, G. Wallace, Technomic Publ. Co. (Lancaster, Basel) pp. 462 - 473.
4. Ponomarenko, A.T., Buts, A.V. and Shevchenko V.G., *SPIE Proc.* Vol. 2191, 1994, pp. 399-406.
5. Strümpler, R., Rhyner, J., Greuter, F. and Kluge-Weiss, P., *J. Smart Mater. and Struct.* Vol. 4, 1995, pp. 215-222.
6. Glatz-Reichenbach, J., Meyer, B., Strümpler, R., Kluge-Weiss, P. and Greuter, F., *J. Mat. Sci.,* Vol. 31, 1996, pp. 5941-5944.
7. Smith-Johannsen, R. and McLean Walker, J., US Patent 3,861,029, 1975.
8. Doljack F.A., *IEEE Trans. on Comp., Hybrids and Manufact. Techn.* Vol. CHMT-4, No.4, 1981 pp. 372.
9. Hansson, T., *ABB Review* No. 4/92, 1992, pp. 35-38.
10. Strümpler, R., Glatz-Reichenbach, J. and Greuter, F., *Mat. Res. Soc. Symp. Proc.,* Vol. 411, 1996, pp. 393-398.
11. Carmona, F., Valot, E., Servant, L. and Ricci, M., *J. Phys. I France* Vol. 2, 1992, pp. 503-510 .
12. Strümpler, R., *ICCE/3, Third Int. Conf. on Comp. Eng.*, D. Hui (ed.), New Orleans, July 21 - 26, 1996, pp. 801-802.
13. Moffatt, D., Runt, J.P., Halliyal, A. and Newnham, R.E., *J. Mat. Sci.,* Vol. 24, 1989, pp. 609-614.
14. Middleman, L.M., Evans, J.H., Blake, A.E. and Scheff, V.A., US Patent 4,352,083, 1982.
15. Datasheet ABB Distribusjon N-H 4174 GB Edition 4-June-1992, 1992.
16. Manual for Laser displacement meter LC-2400A Series, Keyence Corporation, 1-3-14 Higashinakajima Higashiyodogawa -ku, Osaka, 533 Japan.
17. Skindhøj, J., Glatz-Reichenbach, J. and Strümpler, R., Repetitive Current Limiter based on Polymer PTC Resistor, submitted to *IEEE PES, 1996.*

MICROMECHANICS FOR CONTINUOUS FIBER REINFORCED COMPOSITES VIA FIBER SUB - STRUCTURING

Subodh K. Mital[1], Theo G. Keith, Jr.[1] and Pappu L. N. Murthy[2]

[1]Department of Mechanical, Industrial and Manufacturing Engineering
The University of Toledo, Toledo, Ohio 43606, U.S.A.
[2]Structures Division, Lewis Research Center,
National Aeronautics and Space Administration, Cleveland, Ohio 44135, U.S.A.

SUMMARY: A methodology combining composite micromechanics with a unique fiber substructuring concept is described. In this new concept, the conventional unit cell (the smallest representative volume element) of the composite is modified by substructuring it into several slices and developing the micromechanics-based equations at the slice level. This methodology has several advantages and allows for a more accurate micromechanical representation of the various constituents of the composite. Although, applicable to different types of composite materials, it is particularly well-suited to simulate the ceramic matrix composites (CMC's) behavior. Important features of this approach and its effectiveness are described by using select examples for a SiC/RBSN composite system. Comparison of predictions and limited experimental data are also provided.

KEYWORDS: micromechanics, unit cell, interphase, interface, progressive fracture, progressive debonding, partial interphase bond, stress redistribution

INTRODUCTION

Recently, there has been growing interest in the use of fiber reinforced composite materials in widely varying applications such as aerospace, civil infrastructure, sporting goods, marine applications, automobiles etc. Fiber reinforced composites offer many advantages over traditional materials in higher stiffness/weight ratio, flexibility in design capabilities, excellent corrosion/wear/impact resistance and fatigue strength. The characterization of these materials is fundamental to their reliable use. The analysis of fiber reinforced composites presents many modeling challenges due to heterogeneity of these materials. Unlike their homogeneous isotropic counterparts, the anisotropic construction of laminated composites results in many unique phenomena that occur at different geometrical scales - at the global (laminate) level, the lamina (ply) level as well as at the fiber-matrix (constituent) level. To account for these phenomenon in a more accurate manner, a unique micromechanics based fiber sub-structuring technique has been developed. Although, the technique is applicable to any kind of composite material behavior simulation, it is particularly well suited for simulating aspects unique to ceramic matrix composite behavior. The design of interphase/coating plays a key role in ceramic matrix composites to enhance their fracture toughness. It is well known that ceramic matrix composites are reinforced primarily to enhance their fracture toughness. A weak fiber/matrix interface allows the toughening mechanisms such as fiber bridging, crack

deflection, matrix microcracking, fiber debonding, and fiber pullout to be combined to reduce residual stresses and eliminate catastrophic failures. The methodology is based on micromechanics models in which customarily a representative volume element or unit cell is arranged in a square array pattern. However, the present approach employs a unique multilevel substructuring : from laminate to ply, to subply and then to fiber (figs. 1 and 2). The fiber is substructured into several slices and the micromechanics equations are applied at the slice level. The laminate theory is used recursively to obtain the laminate level properties. This technique has several advantages - it can model partial interphase bond, provides more accurate damage tracking and shows greater detail in stress distribution at a high computational efficiency.

The objective of this report is to describe the methodology and shows its capabilities and versatility by demonstrating several example cases for a select composite material system. The computationally predicted results are compared with experimental data, where such data is available.

FIBER-SUBSTRUCTURING AND MICROMECHANICS

The primary objective of the composite micromechanics is to determine equivalent elastic properties of a composite material in terms of the elastic properties of the constituent materials. The fiber sub-structuring technique divides the customary unit cell or the representative volume element (RVE) into several slices. The micromechanics equations are developed at the slice level, i.e. the slice equivalent properties are computed based on the properties of the fiber, matrix and the interphase. The micromechanics equations are based on mechanics of materials approach and use certain simplifying assumptions. They are not mathematically rigorous in that, although they do ensure the force equilibrium in all directions, but they do not impose the continuity of displacements, strains and stresses across various constituents. Such a rigorous solution can only be obtained through the use of three-dimensional theory of elasticity. However, such a solution is quite tedious for composite materials. The micromechanics predictions are routinely compared with those of detailed three-dimensional finite element analyses and with measured data to ensure adequacy of mechanics formulation and inclusion of all physical phenomena. The micromechanics equations are not shown here because of page limitations, but are available elsewhere (ref. 1). The laminate theory equations are available in any standard textbook on composite mechanics such as ref. 2.

The fiber substructuring approach is general , versatile and applicable to any kind of composite material. By controlling the number of slices in a unit cell, one can easily incorporate various degrees of bond around the fiber circumference. The fiber breaks, matrix microcracking etc. can be easily modeled and their effects on the ply thermal and mechanical properties/response can be easily evaluated.

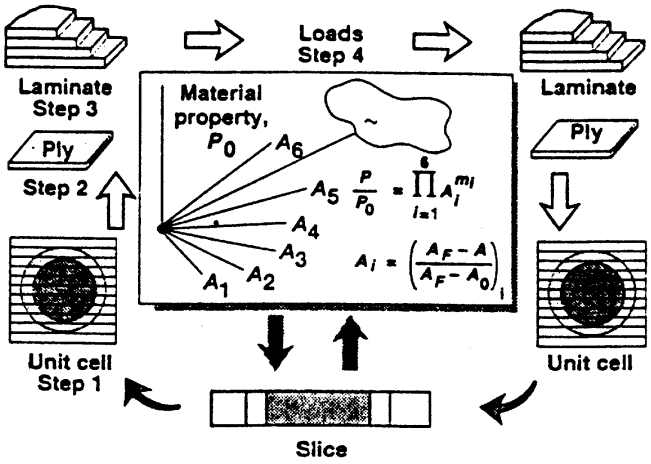

Figure 1.—Integrated analysis approach embedded in CEMCAN computer code.

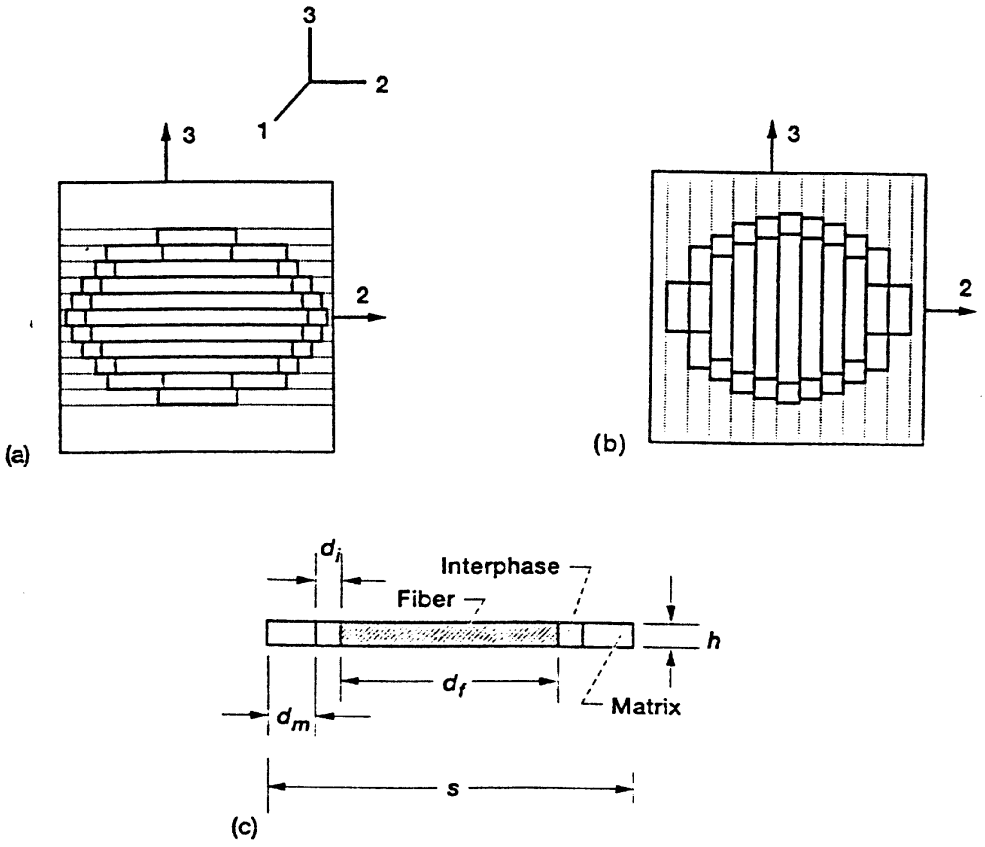

Figure 2.—Ply/fiber substructuring concepts for ceramic matrix composites micromechanics. (a) Horizontal slicing (along 2-2 direction). (b) Vertical slicing (along 3-3 direction; note: 1-1 is along fiber direction). (c) Individual slice showing fiber, matrix, and interphase regions.

MATERIAL NON-LINEAR BEHAVIOR

The authors during their past research have developed a unified law to describe the material degradation behavior applicable to composite materials. The law referred to as multi-factor interaction relationship (MFIR) accounts for the degradation effects of environment, fabrication, and loads on the constituent material behavior. However, in the present work dealing with the ceramic matrix composites, the constituent properties, namely the modulus and the coefficient of thermal expansion, are considered a function of temperature only. As an example, the modulus is assumed to have the following functional relationship with the temperature:

$$\frac{E}{E_0} = \left(\frac{T_f - T}{T_f - T_0} \right)^n \tag{1}$$

where E is the modulus at temperature T, E_0 is the reference modulus at temperature T_0, and the T_f is the final temperature where the modulus is zero. Based on the available experimental data, the exponent n and the final temperature T_f must be calibrated separately for fiber and matrix materials.

MICROSTRESSES AND STRESS REDISTRIBUTION DUE TO PROGRESSIVE FRACTURE

The thermal and mechanical loads are specified or obtained at the laminate level. Through the successive use of lamination theory, the stresses and strains at the mid-plane of the slices are obtained. The constituent microstresses are then computed from microstress equations that relate the equivalent slice stress to the constituent stresses. These equations are also based on the principles of micromechanics.

Non-linearities in the stress-strain behavior occur due to the dependence of constituent properties on temperature etc. (material non-linearity) as well as due to matrix microcracking that leads to stress redistribution. Both of these are accounted for in the present work. In the present work, the failure is based on maximum stress criterion. Once, the stress in a constituent exceeds the allowable value, that constituent is assumed to have failed and the corresponding modulus of that constituent is assigned an almost negligible value. A slice is assumed to have failed in the normal direction if the fiber portion of the slice indicated a stress value higher than the fiber fracture strength in the longitudinal direction. Similarly, a slice is assumed to have failed in the transverse direction if the matrix region stresses indicate failure in the transverse normal or shear direction. Once, a slice fails, all the stresses that are carried by that slice up to that point are redistributed to the regions that have not failed. The load that was carried by that slice is added to the laminate load and a laminate analysis is carried out again (fig. 3). This process is continued for a given load step until an equilibrium (convergence) is reached between the applied load and a damage state. Presently, the convergence is checked for laminate mid-plane strains, ply and slice strains. When all the strains are within 5 percent of the values from the previous iteration, convergence is assumed to have been reached. This mechanism is mainly responsible for the overall non-linear behavior in the laminate stress-strain curve at the room temperature.

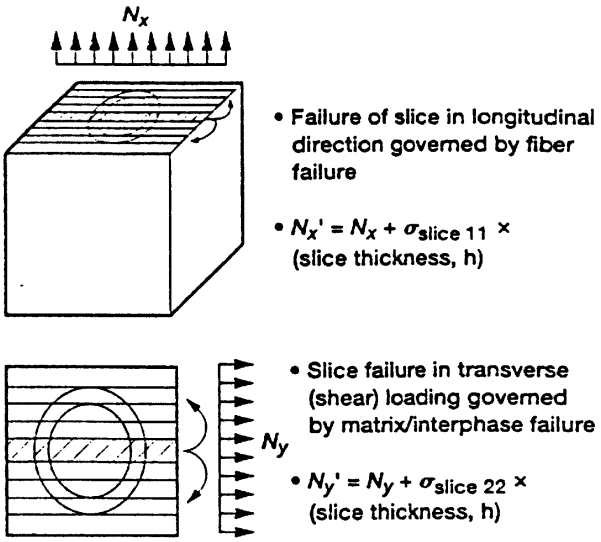

Figure 3.—Local stress redistribution due to progressive fracture. Failure based on maximum stress criterion.

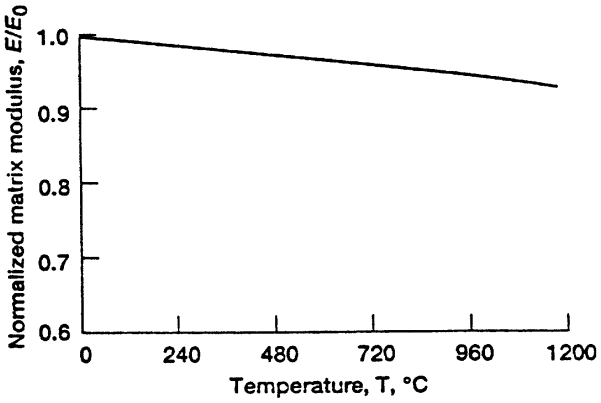

Figure 4.—Effect of temperature on constituent (fiber and matrix) moduli according to equation (1), $(E/E_0) = [(T_f - T)/(T_f - T_0)]^n$. Final fiber temperature, T_f, 2500 °C for n = 0.25; final matrix temperature, T_f, 2200 °C for n = 0.1.

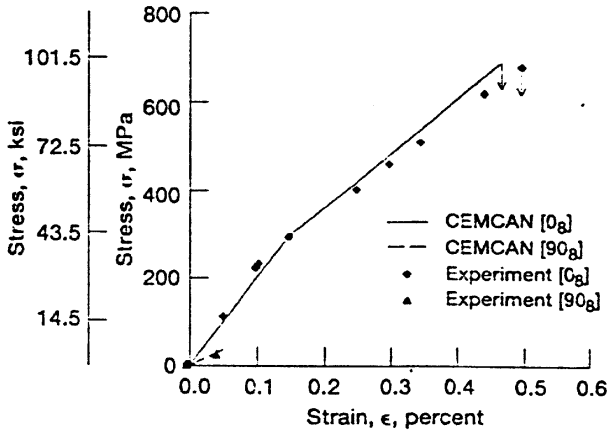

Figure 5.—Room-temperature stress-strain curves to failure of $[0]_8$ and $[90]_8$ SiC/RBSN composite.

The associated micromechanics equations, fiber sub-structuring technique and macromechanics/laminate theory equations are programmed into a computer code - CEMCAN (Ceramic Matrix Composites Analyzer, ref. 3). A resident databank of constituent properties of commonly available materials is also included in the computer program.

RESULTS AND DISCUSSION

To demonstrate the methodology and its capabilities, a SiC/RBSN composite system (SCS-6 fibers in a reaction bonded silicon nitride matrix) was chosen because of vast amount of readily available experimental data. These data are documented in ref. 4, which forms the basis for the computed properties that are used in the present work. The use of such a calibration procedure is mandatory for any new material system in order to arrive at a set of constituent properties.

Prediction of Mechanical Properties

The interphase (usually a combination of outer carbon layer and the "reaction zone") is treated as a separate constituent, the properties of which are not explicitly and readily available. Since the interphase modulus has little effect on longitudinal modulus of the unidirectional composite, fiber volume ratio (fvr) of the composite is calibrated from the measured longitudinal modulus of the unidirectional SiC/RBSN composite. Once, the nominal fvr is known, the interphase modulus is computed by comparing the measured and predicted values of the in-plane transverse modulus of the unidirectional composite. These values are shown in Table I. Once calibrated, these values are used to predict certain mechanical properties of a cross-ply and an angle-ply laminate and compared with measured values as shown in Tables II and III. The comparison is very good within the scatter of the measured values. To account for this scatter, one has to systematically account for the variabilities in various material and fabrication properties and perform a probabilistic micro- and macromechanics analysis. Such a analysis, predicts the mean value and a scatter bound on predicted values. Such an effort is well underway by the authors.

Prediction of Tensile Stress/Strain Behavior Under Uniaxial Loading

This section presents comparisons of experimental data and the predictions of composite stress/strain behavior under uniaxial tensile loading at room-temperature for various layups. The fabrication induced thermal residual stresses are accounted for in these simulations, i.e. composites are cooled down to room-temperature from an assumed stress-free temperature (little less than the actual fabrication temperature), prior to application of any mechanical loading. The material non-linearity as a function of temperature is accounted for in a form shown by equation 1 (fig. 4). The stress-strain curves for $[0]_8$ and $[90]_8$ composites are shown in figure 5. Based on the observed tensile strengths of these composites, the matrix in-situ tensile strength was calibrated to be 100 MPa (14.5 ksi) by comparing the knee in the stress-strain curve for $[0]_8$ composite and the average fiber bundle strength to be 2 GPa (285 ksi) by comparing the ultimate tensile strength of the same composite. The knee represents the initiation and subsequent saturation of matrix microcracking. These value agree well with the fiber and matrix tensile strengths reported in ref. 4. Once calibrated, the same strength values were used in subsequent simulations. The stress strain behavior of $[0]_8$ composite is a bi-

linear behavior, the knee of which represents matrix microcracking to saturation. During the second part of that curve, the load is entirely carried by the fibers only until fibers fracture. The behavior of $[90]_8$ laminate is linear until failure, at which point the matrix failed in transverse tension at a relatively low stress level of 45 MPa (6.5 ksi).

In contrast, the off-axis laminates $[10]_8$ and $[45]_8$ stress-strain behavior is largely linear up to failure as shown in figure 6. Such behavior is characteristic of a brittle failure. The final fracture in these laminates is controlled by a combination of matrix and interphase normal and shear failure modes. The room-temperature stress-strain curve to failure for a $[\pm 45_2]_s$ laminate is shown in figure 7. The shear strength of the matrix is estimated to be half the matrix tensile strength to match the ultimate tensile strength of these laminates. This laminate also fails in a combination of matrix normal and shear failure modes and shows a graceful failure. Although, the optical micrographs in ref. 4 confirmed the aforementioned failure modes, the unloading portion of the stress-strain curve for the laminate was not predicted. The experimental data shown in these figures was also taken from ref. 4.

TABLE I.—FIBER, MATRIX, AND CALIBRATED INTERPHASE PROPERTIES OF SiC/RBSN COMPOSITE SYSTEM

Constituent	Property								
	Poisson's ratio, ν	Modulus, E		Shear modulus, G		Coefficient of thermal expansion, α		Thermal conductivity, K	
		GPa	Mpsi	GPa	Mpsi	10^{-6}/°C	10^{-6}/°F	W/m-K	Btu/ft-hr-°F
SiC (SCS-6) Fiber	0.17	390	56.6	117	17	4.1	2.3	22	12.7
RBSN Matrix	.22	110	15.95	45	6.5	2.2	1.2	5	2.9
Interphase	.22	3.5	.5	1.4	.2	2.0	1.1	2.0	1.2

TABLE II.—PREDICTED (CEMCAN) AND MEASURED ELASTIC PROPERTIES OF SiC/RBSN $[O_8]$ LAMINATE

[Unidirectional SiC/RBSN $[O_8]$ composite fiber volume ratio, 0.36[a].]

Value	Property						
	Young's modulus (longitudinal), E_{11}		Young's modulus (transverse), E_{22}		In-plane shear modulus, G_{12}		Poisson's ratio, ν_{12}
	GPa	Mpsi	GPa	Mpsi	GPa	Mpsi	
Predicted	189	27.4	68.3	9.9	27	3.9	0.21
Measured[b]	193±7	28±1	69±3	10±0.4	31±3	4.5±0.4	.2

[a]The measured value of longitudinal modulus E_{11} for a unidirectional composite was used to compute fiber volume ratio (fvr) whereas the transverse modulus E_{22} was used to compute the interphase modulus.

[b]Reference 4

TABLE III.—PREDICTED (CEMCAN) AND MEASURED ELASTIC PROPERTIES OF SiC/RBSN $[0_2/90_2]_s$ and $[\pm 45_2]_s$ LAMINATES

Laminate	Property						
	Poisson's ratio, ν_{12}	Young's modulus (longitudinal), E_{11}		Young's modulus (transverse), E_{22}		In-plane shear modulus, G_{12}	
		GPa	Mpsi	GPa	Mpsi	GPa	Mpsi
$[0_2/90_2]_s$ Predicted	0.112	129	18.7	129	18.7	27	3.9
Measured[a]	.12	124±6	18±0.9	124±6	18±0.9	31±2	4.5±0.3
$[\pm 45_2]_s$ Predicted	0.46	78.6	11.4	78.6	11.4	58	8.4
Measured[a]	.36	78±3	11.3±0.4	78±3	11.3±0.4	---	---

[a]Reference 4

Influence of Partial Interphase Bond

The concept of fiber substructuring allows one to specify a partial bond around the fiber circumference and integrate its effect up to the composite properties and response. The variation of some composite mechanical and thermal properties as a function of fiber circumference debonded is shown in figure 8. Longitudinal or fiber-controlled properties show little degradation whereas the transverse properties reveal greater degradation as a function of debonding. The properties plotted have been normalized with respect to the property for a composite with no debonding.

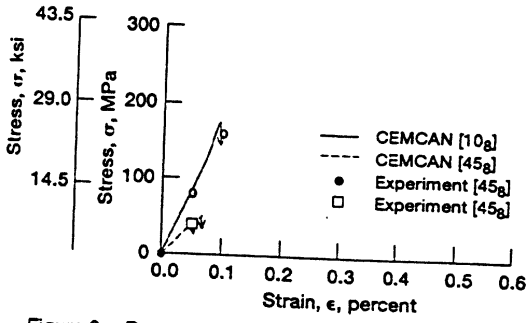

Figure 6.—Room-temperature stress-strain curves to failure of $[10]_8$ and $[45]_8$ laminates of SiC/RBSN.

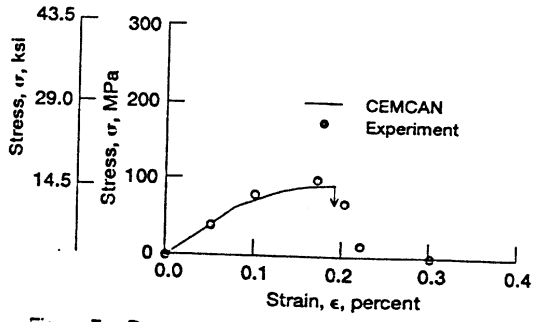

Figure 7.—Room-temperature stress-strain curves to failure of $[\pm 45_2]_s$ SiC/RBSN laminate.

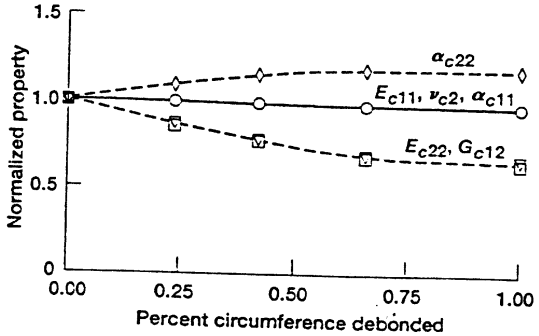

Figure 8.—Variation of thermal and mechanical properties (normalized with respect to property with strong interphase) due to partial bonding.

CONCLUSIONS

A unique and novel fiber sub-structuring technique has been presented here. Although, general in nature, the technique is especially well-suited for the simulation of ceramic matrix composites behavior. Its features are illustrated with select examples. Experimental validation is provided where such data is available. This concept enables one to study in greater local detail ceramic matrix composites behavior pertaining to varying degree of interfacial bond. The matrix microcracking at relatively low stress levels and the resulting redistribution of stress is also taken into account. Based on the results shown for the SiC/RBSN composite system, the following specific conclusions can be drawn:

1. Fiber substructuring captures and represents greater local detail than other unit-cell based micromechanics theories.

2. The predictions from the simulations have been successfully verified for this particular composite system for available data.

3. The material non-linear behavior model and stress redistribution with progressive damage have enabled the prediction of stress-strain behavior up to failure. The agreement with experimentally observed behavior is excellent for this particular composite system.

REFERENCES

1. Murthy, P.L.N. and Chamis, C.C. : Towards the Development of Micromechanics Equations for Ceramic Matrix Composites via Fiber Substructuring. NASA TM-105246, 1992.

2. Agarwal, B.D. and Broutman, L.J.: Analysis and Performance of Fiber Composites. Second Ed., Wiley and Sons, New York, 1990.

3. Mital, S.K. and Murthy, P.L.N. : CEMCAN - Ceramic Matrix Composites Analyzer User's Guide - Version 2.0 NASA TM-107187, 1996.

4. Bhatt R.T. and Phillips, R.E. : Laminate Behavior of SiC Fiber-Reinforced Reaction-Bonded Silicon Nitride Matrix Composites. NASA TM-101350, 1988.

THE EFFECT OF FIBRE-BUNDLING ON THE MECHANICAL PROPERTIES OF A SHORT-FIBRE COMPOSITE

David R. Mulligan[1], Stephen L. Ogin[1], Paul A. Smith[1], Garry M. Wells[2] and Christopher M. Worrall[2]

[1]Department of Materials Science and Engineering, University of Surrey, Guildford, Surrey, GU2 5XH, UK
[2] Kobe Steel Europe Ltd. Research Laboratory, 10 Nugent Rd., Surrey Research Park, Guildford, Surrey GU2 5AF, UK.

SUMMARY : The effect of fibre-bundling on the tensile modulus and tensile strength of short carbon fibre reinforced polypropylene composite materials has been investigated. The fibre was either filamentised or in bundles of 6000 fibres. Materials containing 0 %, 25 %, 50 %, 75 % and 100 % of the fibres in bundles were produced. It was found that fibre-bundling leads to a significant reduction in both the tensile modulus and tensile strength compared with the fully filamentised composite. The reduced reinforcing efficiency of fibre bundles compared to individual fibres has been estimated using the Cox model. This approach gives reasonable agreement with the experimental modulus of laminates containing only filamentised fibres or only fibre bundles, but overestimates the modulus of laminates containing a mixture of fibres and bundles.

KEYWORDS : fibre-bundling, mesostructure, short-fibre composite

INTRODUCTION

The longitudinal Young's modulus of a continuous aligned composite material can be predicted satisfactorily from the constituent moduli and the fibre volume fraction using a simple rule-of-mixtures expression. Such an expression may be modified for a short-fibre composite by introducing factors which account for the reduced reinforcing efficiency of short-fibres [1] and the orientation of the fibres [2]. In calculating the reduced reinforcing efficiency, it is usually assumed that individual fibres are the basic unit of reinforcement and that they are straight, aligned and regularly spaced. However it is generally the case that at least some of the fibres are in clusters, or even bundles, reflecting the tow structure from which they were cut originally. The behaviour of fibres contained in bundles will differ from that of an equivalent number of fibres dispersed more uniformly. This type of structure, on a scale between that of the individual fibre and that of the material as a whole, has been described as mesostructure [3], and is not usually a feature of models for composite materials.

A number of workers have studied the effect of fibre-bundling, with the objective of improving the toughness of composite materials. The most frequently used method to manufacture a composite with the fibres in bundles is to impregnate a fibre tow with a resin, which is then cured, and the resulting rod is subsequently manufactured into a laminate. The first study to use this technique was by Fila, Bredin and Piggott [4] who constructed continuous, aligned laminates of glass or carbon fibre in a copolymer of styrene and polyester. A similar approach was taken

by Kim and Mai [5] who manufactured random and aligned discontinuous fibre composites of carbon fibre bundles impregnated with epoxy resin or polycarbonate, in an epoxy resin matrix. Both of these studies recommended this as a method to achieve tougher composite materials. While this approach has yielded some valuable results there are obvious difficulties if the aim is to examine the mechanisms associated with fibre bundling, the most significant being the extra interface that is created between the polymer used to impregnate the bundle and the polymer matrix.

Ericson and Berglund [6] compared two types of glass-mat-reinforced polypropylene; these contained either short individual fibres or looped (continuous) fibre bundles. They found that the material containing individual short-fibres had a higher modulus and a slightly higher strength. They accounted for the reduced modulus of the bundled material in terms of the reduced reinforcing efficiency of the bundles, which was estimated using the Cox model applied to the bundles. This work is important since it considers commercially manufactured materials and ultimately the findings of this area of work should be used to produce composite materials which achieve the required properties in the most efficient manner.

There is a limited amount of theoretical work on fibre-bundling. The most relevant treatment is by Kataoka, Taya and Saito [7], who analysed the case of a composite material containing fibres and fibre clusters, using the Eshelby method. They found that with regard to the Young's modulus the most significant variable was the volume fraction of bundles in the material. The fibre volume fraction in the bundle, the fibre aspect ratio and bundle aspect ratio all had relatively minor effects on the Young's modulus. Trapeznikov, Toropov, and Loskutov[8] modelled the effect of fibre-bundling on the strength of a carbon-carbon composite and found that the strength of the material decreased when the number of fibres in the tow forming the bundle was increased.

Methods for quantifying the degree of fibre-bundling in a random short-fibre composite are currently under development. For example Worrall and Wells [9] have described a "fractal-variance characterisation method", which they used successfully to analyse the size of bundles in a material. However it is not possible, at present, to find the volume fraction of bundles of a given size using this technique.

The present work is aimed at characterising the effect of fibre-bundling on the mechanical properties of a carefully controlled range of short-fibre composite materials in which the volume fraction of the fibre in bundles has been varied. The mass of the individual fibre mats used to produce the composites varied, resulting in differences in the overall volume fraction and a normalisation procedure has been carried out to enable the results to be compared. Data are presented for the moduli and strength of the materials.

EXPERIMENTAL

The carbon fibre tow (Torayca T300), consisting of 6000 fibres, was coated with molten wax, which solidified before the tow was chopped into 5 mm lengths by a chopping machine. The fibre could be incorporated in the mats in this form, resulting in bundles in the mat, or the wax could be burnt off, resulting in filamentised fibres in the mat. The appropriate proportions of wax-coated and uncoated fibre were dispersed in a glycerine solution and the mixture was poured over a stainless steel mesh to produce a random mat. The mats were washed and then dried at 100 °C, and the wax was burnt off the wax-coated bundles in the mat to produce mats which had varying proportions of bundled and filamentised fibres. Mats with the following compositions

were produced; 0 % bundles (i.e completely filamentised), 25 % bundles, 50 % bundles, 75 % bundles and 100 % bundles

The mats were impregnated with the polypropylene matrix using a film stacking technique. Layers of carbon fibre were interleaved with polypropylene film to give a laminate approximately 1 mm thick and an overall volume fraction of about 0.15. This stack was heated to 250 °C for three minutes with contact pressure, then full pressure was applied for one minute. During this time the pressure was released three times to "pump" the stack, which allowed entrapped air to escape and aided the infiltration of the fibre bundles by the polymer melt. To verify that infiltration was satisfactory, samples from the laminates were mounted in epoxy resin and sectioned using a Jung microtome with a glass knife. Sections 20 μm thick were viewed in transmission on an Axiophot microscope and showed no evidence of porosity.

Tensile test coupons, 150 mm long by 20 mm wide, were cut from the composite plates using a water-lubricated diamond saw. The coupons were tensile tested on an Instron 1175 with 30 mm long friction tabs made from emery cloth. A crosshead speed of 0.5 mm / min was used and the strain on the sample was measured using a 50 mm gauge length extensometer, which was attached to the specimen surface with rubber bands. Five specimens were tested for each laminate type.

The volume fraction of the laminates was found using a burn-off method. From each laminate four samples of about 0.5 g were accurately weighed and then heated to 420 °C in a crucible for five hours. After cooling, the mass of the residue was determined. The volume fractions were calculated based on density values of 1.76 g/cm^3 for the carbon fibre and 0.90 g/cm^3 for the polypropylene.

RESULTS & DISCUSSION

Tensile Modulus

The tensile modulus was calculated by applying a linear regression fit to the stress-strain curve between 0 % and 0.5 % strain. The results are shown in Fig. 1 and the values for the overall fibre volume fractions are indicated. The results show a large reduction in the modulus of the laminates with an increase in the percentage of fibres in bundles. Previous work by Ericson and Berglund [6] accounted for a lower than expected modulus for a bundled material by considering the bundle as a large fibre and calculating the length efficiency factor accordingly. In the present study such an approach is developed to allow for the presence of filamentised fibres in the matrix surrounding the bundle.

The usual expression for a randomly oriented short fibre composite is :

$$E_c = \eta_o \eta_l E_f V_f + E_m V_m \qquad (1)$$

where E_c, E_f and E_m are the modulus of the composite, fibre and matrix respectively; η_o is the Krenchel orientation factor [2], which is taken as 0.375 for a planar random fibre architecture; η_l is the length efficiency factor; V_f and V_m are the volume fractions of fibre and matrix respectively.

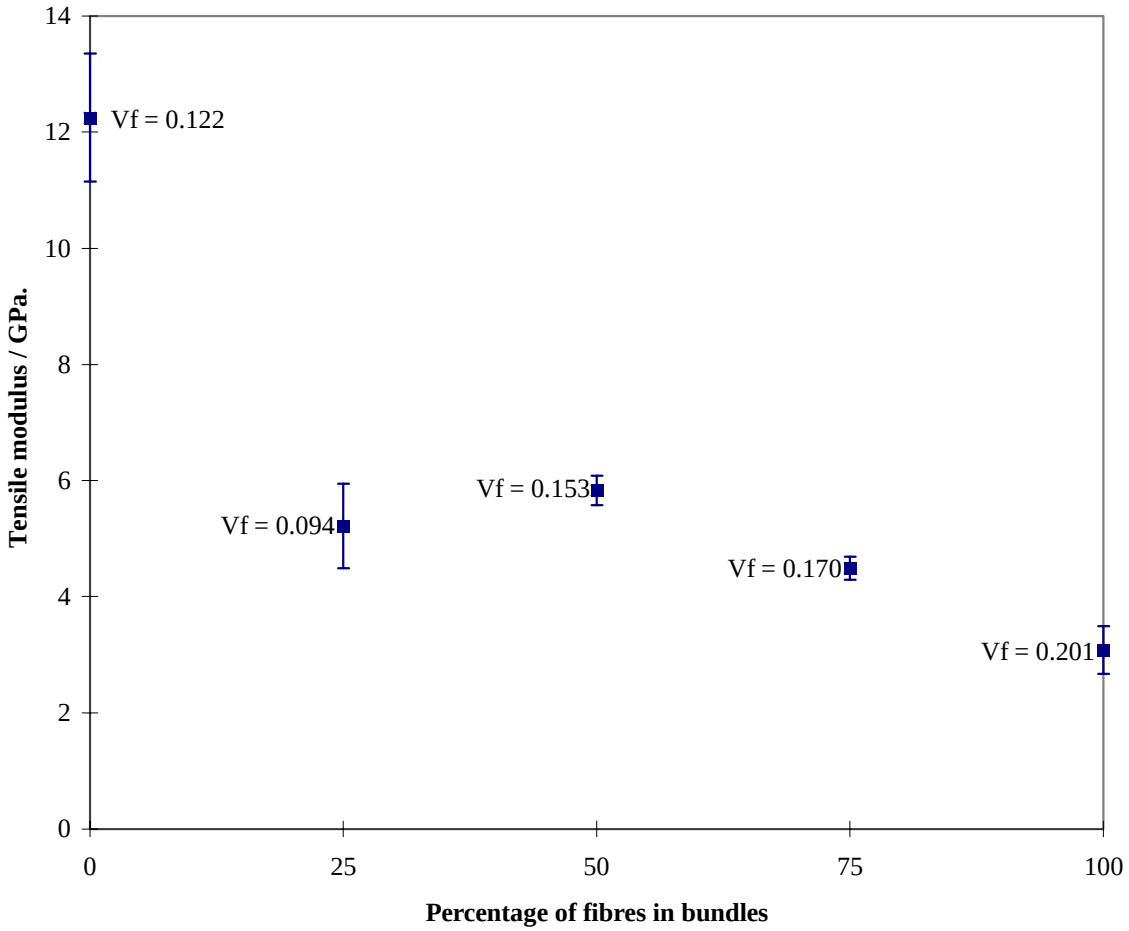

Fig. 1: Graph showing the variation of tensile modulus with percentage of fibres in bundles (the data points are labelled with the volume fraction of the laminate)

Eqn 1 may be modified to include a third term that represents the contribution of the fibre bundles i.e.

$$E_c = \eta_o \eta_{lo} E_f V_{fo} + \eta_o \eta_{lb} E_b (V_{fb} + V_{mb}) + E_m V_{mo} \qquad (2)$$

In this modified expression V_{fo}, V_{fb}, V_{mo} and V_{mb} are volume fractions, where the first subscript, "f" or "m", describes whether the volume fraction is of fibre or matrix, while the second subscript, "b" or "o", indicates whether a component is inside a fibre bundle, "b", or outside a fibre bundle, "o". These definitions result in :

$$V_f = V_{fo} + V_{fb} \qquad (3)$$

$$V_m = V_{mo} + V_{mb} \qquad (4)$$

Table 1 shows the value of these quantities for composites with an overall fibre volume fraction (V_f) of 0.15 and a volume fraction of fibres in the bundled region of 0.6 i.e.

$$V_{fb} / (V_{fb} + V_{mb}) = 0.6 \qquad (5)$$

Table 1 : The values of the four volume fraction terms for the laminates

laminate/ % bundles	V_f	V_{fo}	V_{fb}	V_m	V_{mo}	V_{mb}
0	0.150	0.150	0.000	0.850	0.850	0.000
25	0.150	0.113	0.038	0.850	0.825	0.025
50	0.150	0.075	0.750	0.850	0.800	0.050
75	0.150	0.038	0.113	0.850	0.775	0.075
100	0.150	0.000	0.150	0.850	0.750	0.100

E_b, the modulus of the bundle, is calculated using the Voigt model for a continuous aligned composite applied to the fibre bundle:

$$E_b = E_f V_{fb} + E_m V_{mb} \tag{6}$$

Table 2 shows the values of the three moduli, together with other values used in the calculation.

Table 2 : Values used in the modulus calculation

Tensile modulus of fibre	E_f	230 GPa
Tensile modulus of bundle	E_b	139 GPa
Tensile modulus of matrix	E_m	1.40 GPa
Shear modulus of matrix	G_m	0.54 GPa
Radius of fibre	r (for η_{lo})	3.95×10^{-6} m
Radius of bundle	r (for η_{lb})	3.95×10^{-4} m

The length efficiency factors in Eqn 2 account for the reduced reinforcing efficiency of a discontinuous reinforcement compared to continuous reinforcement and were calculated using the expressions from Cox[1] i.e.

$$\eta_l = 1 - \frac{\tanh(\beta l/2)}{(\beta l/2)} \tag{7}$$

where

$$\beta = \sqrt{\frac{2G_m}{E_f r^2 \ln(R/r)}} \tag{8}$$

The length efficiency factor for the filamentised fibres (η_{lo}) is derived by considering only the material outside the fibre bundles. The length efficiency factor for the filamentised fibres (η_{lb}) is calculated by considering the bundles as reinforcing fibres within a "matrix" that consists of polypropylene and filamentised fibres. The resulting values of the efficiency factors are shown in table 3.

Table 3 : The resulting values of η_{lo} and η_{lb}.

Laminate	η_{lo}	η_{lb}
0% bundles	0.978	-
25% bundles	0.976	0.352
50% bundles	0.974	0.351
75% bundles	0.971	0.297
100% bundles	-	0.127

Based on the steps outlined above the moduli of the composites can be calculated from Eqn 2. Further, it is possible to normalise the experimental results for the fibre volume fraction, using the relation shown in Eqn 9.

$$Normalised\ experimental\ modulus = \frac{Prediction\ for\ V_f = \ 0.15}{Prediction\ for\ actual\ V_f} \times experimental\ value \qquad (9)$$

The normalised experimental results and the predictions from the model are shown in Fig. 2, based on a fibre volume fraction of 0.15. A comparison of the two curves in Fig. 2 shows that while there is good agreement for the 0 % and 100 % materials, the model overestimates significantly the modulus of the laminates when there is a mixture of fibres and bundles present. It seems that this is because the presence of fibre bundles reduces the efficiency of the filamentised fibres; it is unlikely that the filamentised fibres are distributed evenly in the presence of bundles. In particular it seems likely that there will be matrix-rich regions in the vicinity of the bundles and these may contribute to the observed moduli.

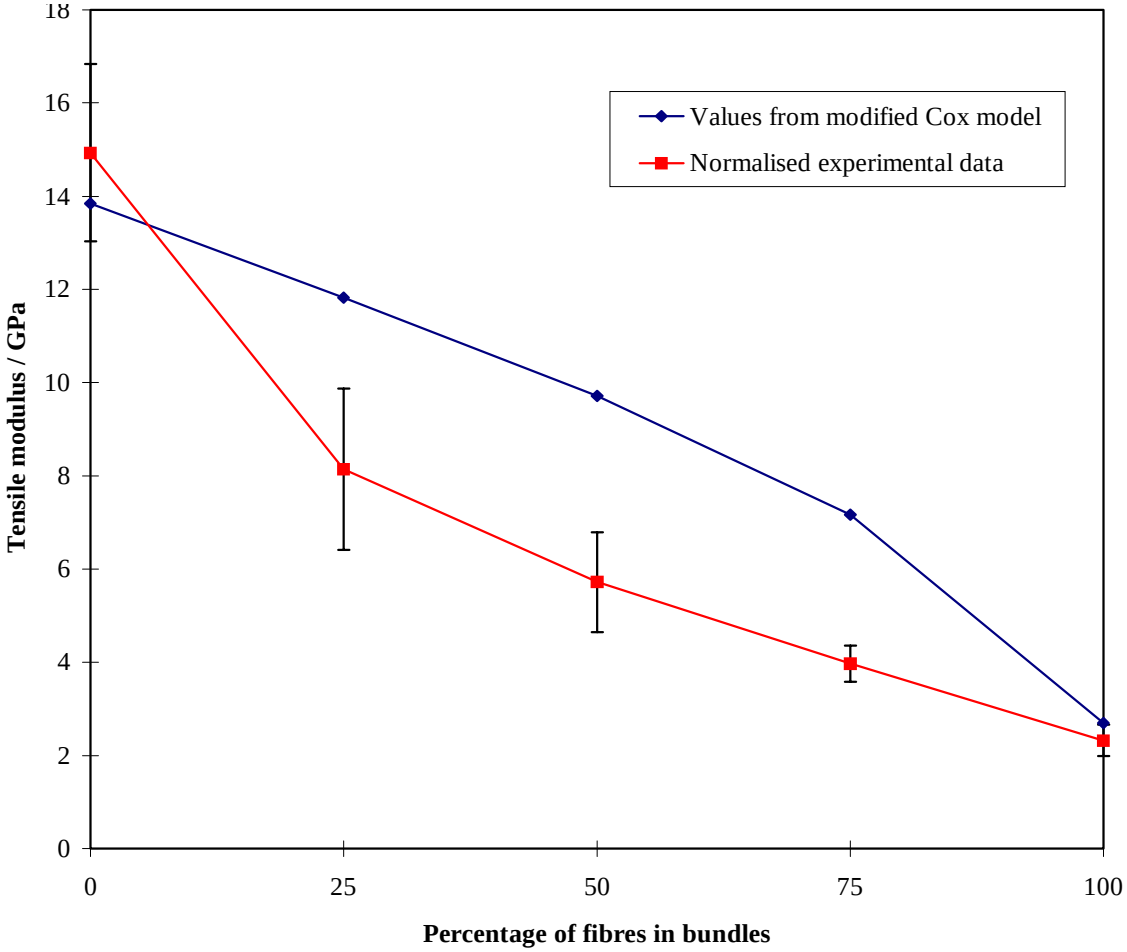

Fig. 2 : Graph showing the tensile modulus predictions from the modified Cox model and the normalised experimental data.

Tensile Strength

The values for the tensile strength were taken from the maximum stress on the stress-strain curve. The results are shown in Fig. 3. The results show that the strength for the 25% to 100% materials is reasonably constant and about a quarter of the strength of the filamentised material.

This suggests that the reduction in strength is due to the presence of bundles, rather than the volume fraction of bundles. It seems reasonable to suggest that the failure is initiated either at bundles oriented transverse to the applied stress, or at bundle ends when they are aligned with the tensile load. The same sites are likely to be preferred for the propagation of the crack, although in this case the transversely oriented bundles are likely to be more significant. This interpretation supports the shape of the graph in Fig. 3, since even in the 25% bundle material there will be regions where there are a number of bundles spaced closely together.

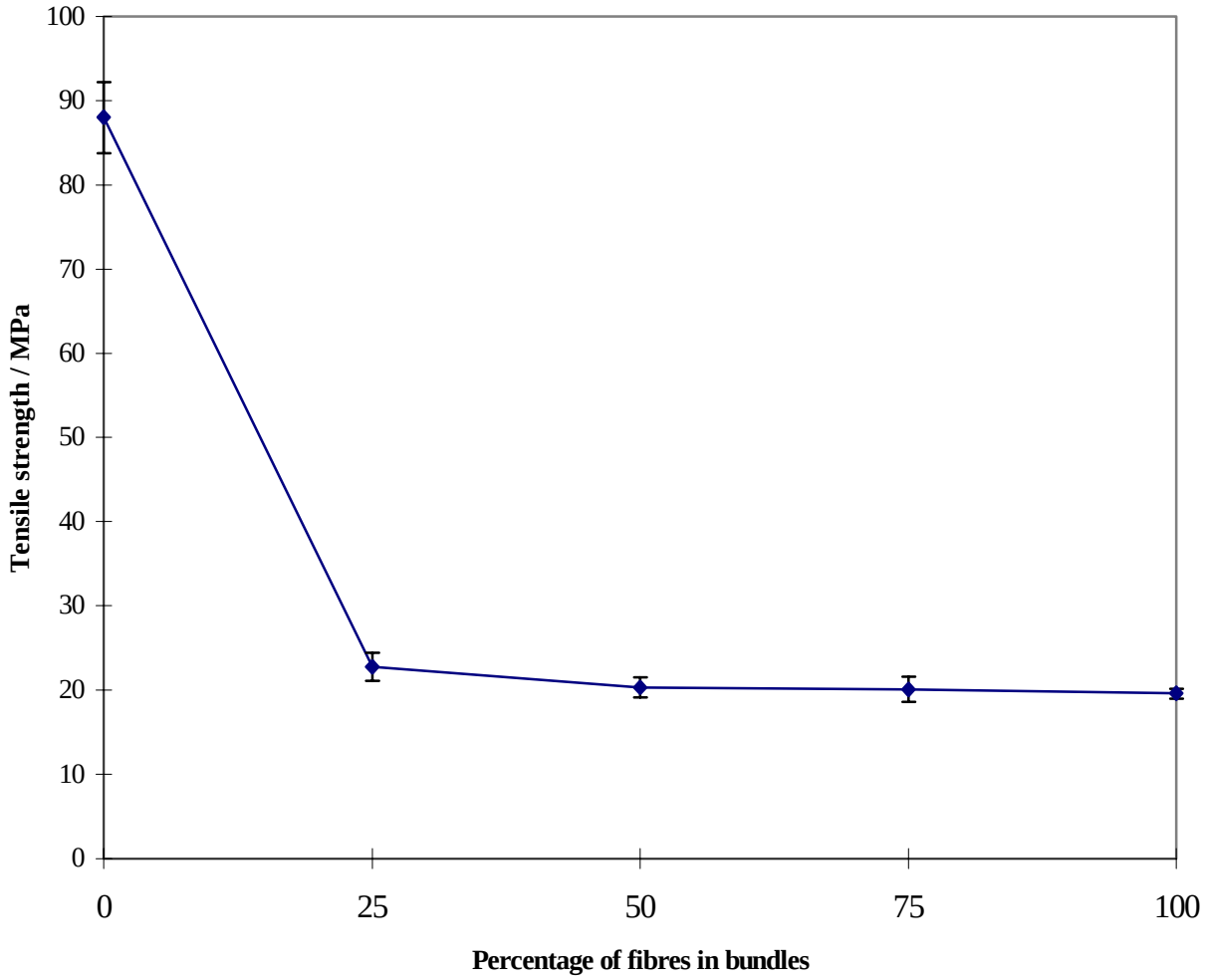

Fig. 3 : Graph showing the variation of tensile strength with percentage of fibres in bundles

CONCLUSIONS

Fibre-bundling was found to have a substantial effect on both the tensile modulus and tensile strength of a short-fibre composite. An analysis using the Cox model gives reasonable agreement for both the filamentised and the completely bundled material, but overestimates the moduli of the materials containing a mixture of fibres and bundles. The tensile strength data show that the strength of laminates containing 25% to 100% of the fibres within bundles is about one quarter of the strength of a filamentised material.

ACKNOWLEDGEMENTS

The authors would like to thank Mr. R. Whattingham of the University of Surrey for his help with the manufacture of fibre mats, Mr. P. Ives of Kobe Steel Europe Ltd. for his invaluable assistance with the film-stacking technique and Kobe Steel Europe Ltd. and the EPSRC for funding a CASE studentship for D. Mulligan

REFERENCES

1. Cox, H. L., "The elasticity and strength of paper and other fibrous materials", *British Journal of Applied Physics*, Vol. 3, 1952, pp. 72-75.

2. Krenchel, H., "Fibre Reinforcement", Akademisk Forlag, Copenhagen, 1964.

3. Piggott, M. R., "Preface: Realistic models for fibre composites", *Composites Science & Technology*, Vol. 53, 1995, pp. 121-122.

4. Fila, M., Bredin, C. and Piggott, M., "Work of fracture of fibre-reinforced polymers", *Journal of Materials Science*, Vol. 7, 1972, pp. 983-988.

5. Kim, J. K. and Mai, Y. W., "Fracture of CFRP containing impregnated fibre bundles", *Composites Science and Technology*, Vol. 49, 1993, pp. 51-60.

6. Ericson, M. and Berglund, L., "Deformation and fracture of glass-mat-reinforced polypropylene", *Composites Science & Technology*, Vol. 43, 1992, pp. 269-281.

7. Kataoka, Y., Taya, M. and Saito, M., "Effect of fibre clustering on the stiffness and strength of a short fibre composite", *Proceedings of the seventh Japan/U.S. Conference on Composite Materials*, Kyoto, Japan, June 19-22 1995, Ch. 93, pp. 505-514.

8. Trapeznikov, D. A., Toropov, A. I., and Loskutov, O. D., "Modelling approach to optimization of mechanical properties of discontinuous fibre-reinforced C/C composites", *Composites*, Vol. 23, No. 3, 1992, pp. 174-182.

9. Worrall, C. M. and Wells, G. M., "Fibre distribution in discontinuous fibre reinforced plastics: Characterisation and effect on material performance", *Proceedings of the seventh European Conference on Composite Materials*, London, U. K., May 14-16 1996, Vol. 1. pp. 247-252.

COMPRESSIVE BEHAVIORS OF MULTIPLY DELAMINATED RECTANGULAR COMPOSITE PLATES

Hiroshi Suemasu and Tatsuya Kumagai

Department of Mechanical Engineering, Sophia University
7-1 Kioicho Chiyoda-ky Tokyo 102 Japan

SUMMARY: Compressive behaviors of rectangular composite plates with multiple circular delaminations are studied numerically and experimentally. In the experiment, two types of laminates with a conventional and toughened epoxy resins are prepared. Embedded delaminations are introduced at a regular interval in the thickness direction at the center of the plate. The loading edges are fixed and the side edges simply-supported. Postbuckling behavior is numerically calculated by a finite element method. Three dimensional block element is adopted to accurately obtain energy release rates G_I, G_{II}, G_{III} along the delamination fronts based on Virtual Crack Closure method. The contact problem of the delaminated surface is considered by introducing a spring element between the nodes on the upper and lower surfaces of the delaminations, which resists only compression force. The buckling loads obtained from finite element analysis agree well with those from the experiment and a classical Rayleigh-Ritz analysis. The distribution of the energy release rates can well explain the failure load and failure mode obtained by the experiment.

KEYWORDS: composite plate, buckling, postbuckling, multiple delaminations, energy release rate, finite element analysis

INTRODUCTION

Significant loss of compressive strength of composite laminates subjected to low velocity impact of a foreign object, known as CAI (Compression After Impact), is one of the most important issues for composite materials, because the decreased compressive strength often becomes critical in the design of composite structures.

Since the delaminations below the impact point are thought to be major cause of the significant reduction of the compressive strength of laminated plates, the effects of delamination(s) on buckling and post-buckling properties of composite plates are analytically and experimentally studied by many researchers. The analytical studies are performed particularly on one dimensional beam type model with delamination(s) by quite many workers for its relative simplicity of the modeling[for example, 1-4]. They have shown possibility of significant loss of compressive buckling and post-buckling properties.

But it is said that the model cannot well explain the real CAI problem and the research on two dimensional plate type modeling is necessary. Analytical works on the effect of delamination(s) on the compressive behavior of two dimensional plates are limited only to special cases. Chai and Babcock [5] have analytically studied compressive buckling behavior of surface elliptical delamination by Rayleigh-Ritz method. Whitcomb and Shivakumar [6] have studied the problem numerically through finite element method. Shahwan and Waas[7] have also studied postbuckling behavior of surface delamination considering the contact problem. Suemasu[8-10] has studied buckling and postbuckling behavior of square plates with a through-width delamination by Rayleigh-Ritz method and shown that the coupling of the local and global deformation plays very important roll for the buckling and postbuckling behavior. Impact tests [11-13] have shown that multiple delaminations, which are relatively small compared to the size of the plate, were left at the impact point of CF/epoxy plates and the compressive strength of the impacted CF/epoxy plates reduces to less than half of that of virgin plates. The major cause of the compressive strength reduction is thought to be the existence of the multiple delaminations. So, Suemasu [14,15] has analytically studied the effects of multiple delaminations on the buckling behavior of rectangular plates by using Rayleigh-Ritz method and compared with a experiment.

A model of the delaminated plate shown in Fig. 1 is numerically analyzed by a finite element method to study post-buckling and failure mechanism. The failure mechanism is discussed fracture mechanically by using energy release rates.

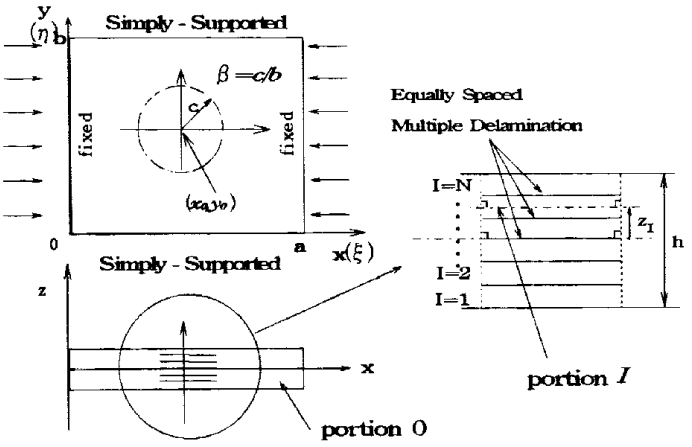

Fig. 1: A rectangular laminate with circular multiple delaminations

EXPERIMENT

Plain woven fabric reinforced composite quasi-isotropic laminates (Toray T400 carbon epoxy, 12 plies, $V_f \approx 50\%$, $[0,90^{\circ}/\pm 45^{\circ}]_{3S}$) with five equally spaced multiple circular delaminations were prepared for the experiment. Two types of epoxy resin were used for

the laminates; the one is conventional and the other toughened epoxy. The elastic constants of the both plates measured were almost equal to each other (E_L=E_T=41.9GPa, ν_{LT}=0.31 for A-specimens and E_L=E_T=41.8GPa, ν_{LT}=0.32 for B-specimens). The suffices L and T denote the loading and the transverse directions. The delaminations were introduced by placing two thin Teflon sheets (about 0.03 *mm* thick). Specimens shown in Fig. 2 were cut out from 300 *mm* × 300*mm* plates so that the delaminations locate at their centers. The delamination sizes and plate thicknesses are listed in Table 1. The test region was 150 *mm* × 100*mm* and the plates were clamped at the end portions (20*mm* wide) with steel blocks and supported along the lines 3*mm* from the sides by two round edges, considering the widely used experiment for measuring CAI strength of laminated plates[16]. Along the supported line on the specimen, solid lubricant MoS_2 was spread in order to make the surface friction as small as possible. The specimen, set in a test machine (Shimadzu, autograph 10TB) as shown schematically in Fig. 3, was pushed very slowly with a cross head speed of 0.1*mm/min*. The transverse deflections were measured at the centers of front and back surfaces of the specimen by using non-contact displacement-meters (Emic, NPA-100). Steel dishes supported by ball bearings had little resistance in horizontal movement. The test data were stored by a personal computer and analyzed after the experiment.

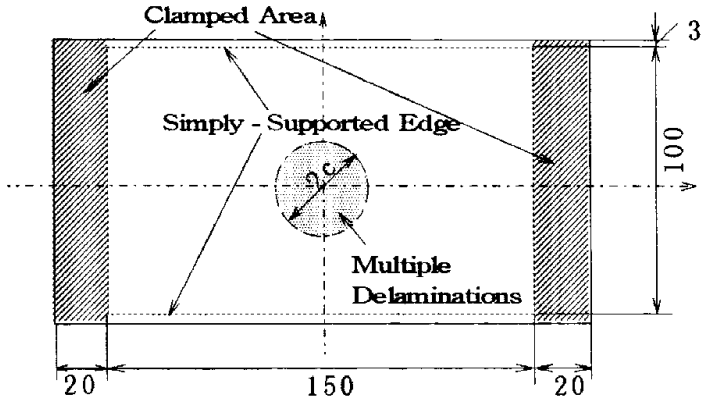

Fig. 2: Specimen

Table 1: Delamination diameters and thickness of the specimens

specimen	pre-preg name	delamination diameter	plate thickness
A0	F7373-30K	------	2.51mm
A10		10mm	2.48mm
A20		20mm	2.50mm
A30		30mm	2.51mm
B0	F7373-06M	-------	2.63mm
B10		10mm	2.63mm
B20		20mm	2.64mm
B30		30mm	2.65mm

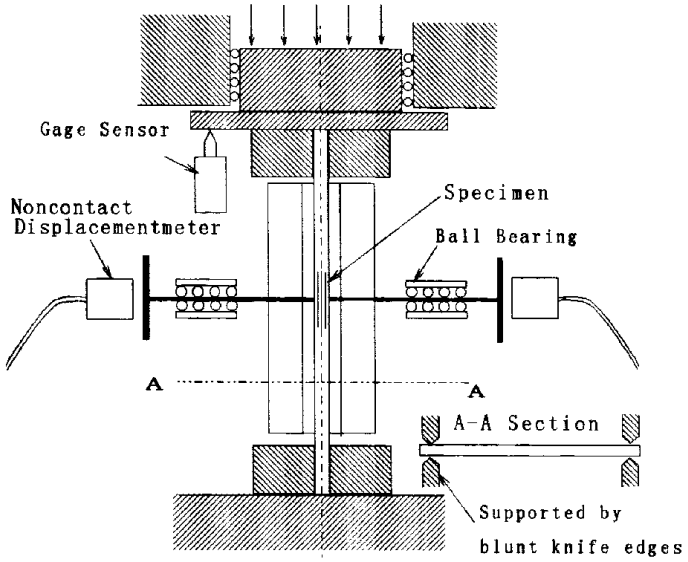

Fig. 3: Experimental apparatus

The specimens without a delamination and with small delaminations (A0, A10, A20, B0, B10) failed at a position about 1/3 of the plate length from fixed edge probably due to the bending stress. When the delaminations are large (A30, B20, B30), instability of multiple delaminations was probably a trigger of the final failure. The delaminations spread in the transverse direction.

The buckling and failure loads are plotted against the diameter of the multiple delaminations in Fig. 4. The buckling load reduction with respect to the size of the delaminations is similar for A and B specimens. However, the failure loads of B-specimens made of conventional epoxy resin are substantially lower than those of A-specimens made of tougher resin, when the size of the delaminations is large. The failure load of A-specimen decreases only 10% even when c=30mm, though the reduction reaches about 30% for B-specimen. The buckling load reduction becomes significant when the diameter of the delaminations exceeds a certain value which does not depend on the interlaminar toughness of the specimen. The strength

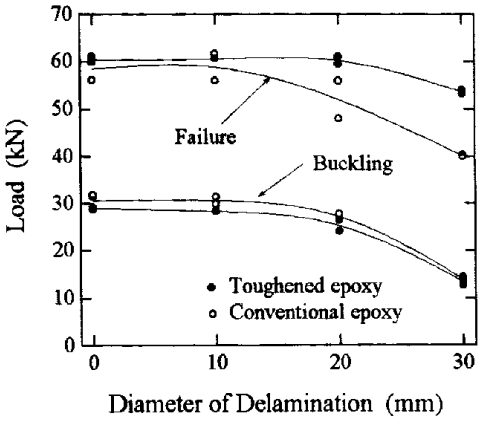

Fig. 5: Buckling and failure load

of the delaminated plate, however, depends on the interlaminar toughness.

FINITE ELEMENT ANALYSIS

The compressive behavior of the rectangular plate with multiple delaminations as shown in Fig. 1 is numerically studied by a finite element method (ABAQUS 5.5). We studied cases of the plates without a delamination and with the multiple delaminations of diameters 10mm, 20mm and 30mm.Number of the delaminations is five considering the specimens used in the experiment. Since the effect of the elastic properties in the thickness direction on the compressive buckling behavior is not important, the material properties is assumed to be isotropic(E=41.9GPa, ν =0.31). In order to obtain energy release rates G_I, G_{II}, G_{III} along the delamination edges, three dimensional iso-parametric 20-node block element is chosen for the present analysis. Fig. 5 is a typical finite element mesh. Since the deformation is symmetric about the center line parallel to the loading direction, a half of the plate is analyzed. Instead of giving the initial imperfection, small concentrated loads are applied at two points on the centerline as shown in Fig. 5, which deflect the plates about 1/20 of the plate thickness due to the loads. The calculation is quite difficult and needs large numerical efforts, because not only a geometrical nonlinearity but also contact problem on the delaminated surface must be considered.

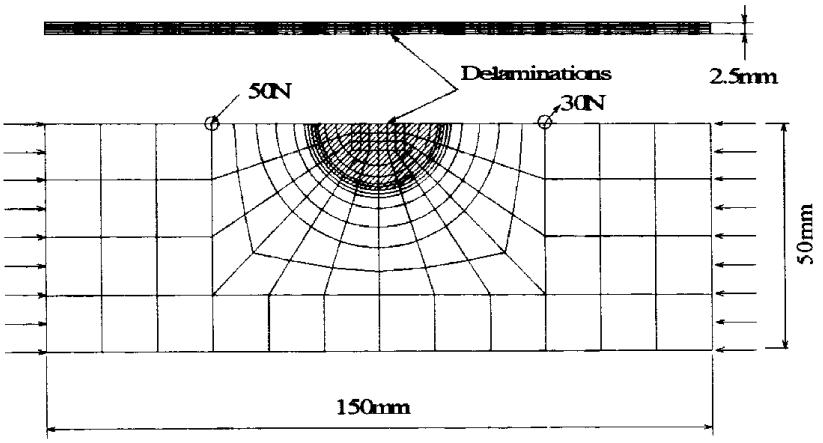

Fig.5: A typical finite element mesh (c=20mm)

In order to consider the contact problem on the delaminated surface, a spring element is used between the nodes on the upper and lower delaminated surfaces, which has very large reaction force when the relative displacement in the thickness direction δw is negative and no force when the relative displacement is positive.

The energy release rates are obtained through the virtual crack closure technique[16]. Nodal forces are easily obtained by setting very stiff spring elements of no length between the nodes of the elements along the delamination edges in three directions.

RESULTS AND DISCUSSIONS

Since the effect of the low transverse stiffness of the composite laminate is not very important for the bending problem of thin plate, only the isotropic material is considered here. The center deflection and the loading edge displacements obtained from the experiment and the finite element analysis are compared in Figs. 6 and 7. The postbuckling path above 43kN for the plate without a delamination could not be obtained by the present finite element code probably due to the unstable snap-through secondary buckling. The plates with multiple delaminations gradually changed their deformed shapes from symmetric to anti-symmetric. The low buckling loads of the delaminated plates are thought to be caused by thickness reduction of the delaminated portion due to the insertion of the teflon sheets. Though the plate with $2c$=30mm buckles by about 18kN for the finite element analysis and 14kN for the experiment, the stiffness reductions are barely visible just after the buckling. It means that the buckling is only a local buckling of the delaminated portion and the rest of the plate can hold load-carrying capacity. The stiffness reduction becomes appreciable with the increase of the load and eminent when the center deflection stops to increase due to the secondary buckling. The delamination closes during the symmetric postbuckling and a little opens when the plate is in the secondary postbuckling path. The opening of the delaminations is a little larger in the case of the experiment than the finite element analysis. Initial opening of the delaminations of the specimens, the order of the thickness of the teflon sheets, are thought to be larger than that of the finite element analysis. The analytical results explain well the experimental ones, considering the complex influences of the boundary conditions and initial imperfections. All the specimens failed in the anti-symmetric shape.

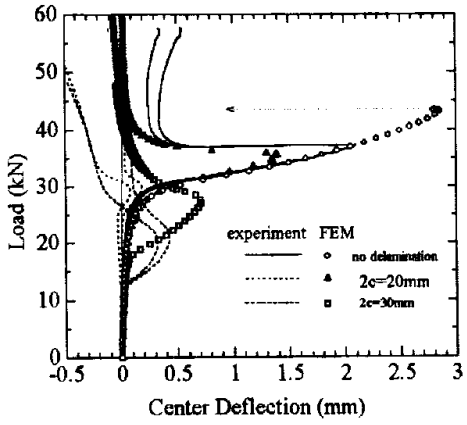

Fig. 6: Center deflection and applied load

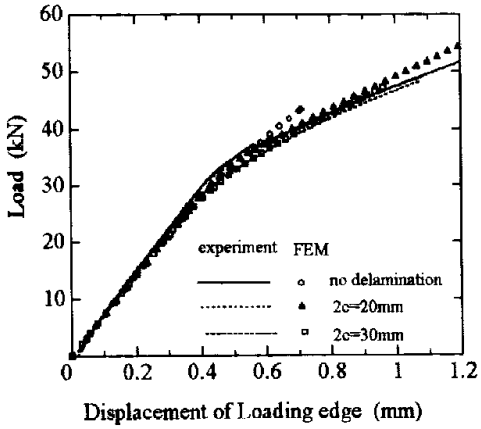

Fig. 7: Loading edge displacement and applied load

Dimensionless buckling loads are plotted against a normalized delamination diameter in Fig. 8. The buckling loads obtained from the finite element analysis are about 3% smaller than the Rayleigh-Ritz analysis[15] based on the Kirchhoff hypothesis and 10-20% higher than the experiment. The low buckling load of experiment is caused by the reasons

mentioned above. The finite element results may agree well with the experiment when initial imperfection, boundary conditions and thickness of the delaminated layers are precisely given.

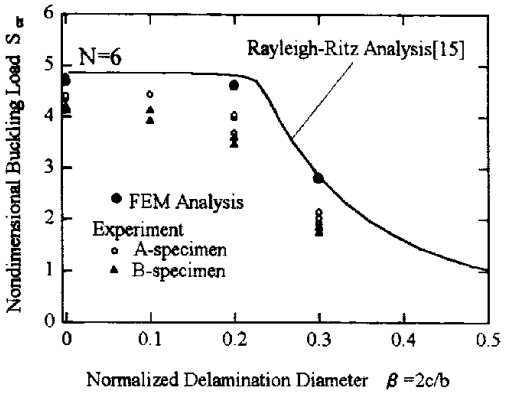

Fig. 8: Nondimensional buckling load $S_{cr}=P_{cr}b/(Eh^3)$ and Normalized Delamination Diameter $\beta=2c/b$

The position of the maximum deflection comes away from the center of the plate with the increase of the anti-symmetric component, whose magnitude depends on initial imperfection, even when the plate is on the symmetric postbuckling path. When the delaminated portion locates at the inclined portion, the component of G_{III} increases compared to G_{II} as shown in Figs. 9 (A) and (B). Fig. 9(A) is the results of the plate of larger anti-symmetric initial imperfection than that of the plate of Fig. 9(B).

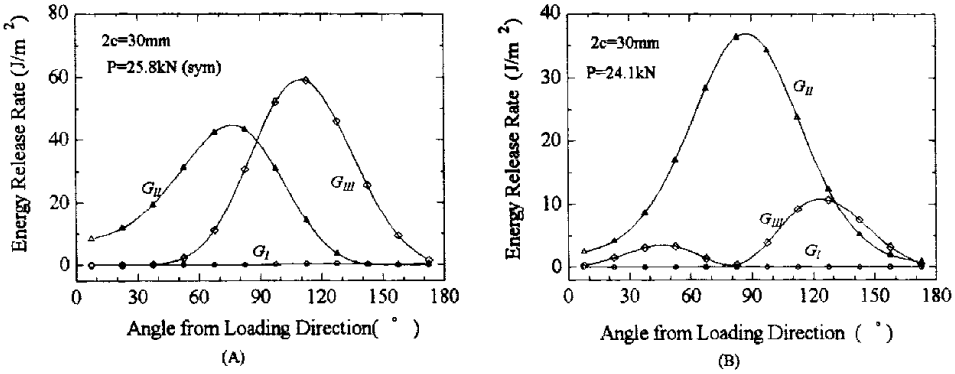

Fig. 9: Effect of initial imperfection on the energy release rate components. (A)$P_1=50N$, $P_2=30N$, (B) $P_1=40N$, $P_2=0$

Distributions of the energy release rates G_I, G_{II} and G_{III} along the delamination edges are plotted in Figs. 10, 11 and 12, respectively. The value of G_I is almost zero at P=25.8kN, because the delamination closes. When the load increase and the component of antisymmetric deformation becomes dominant, G_I increases a little in the transverse direction to the load. However, the value is negligible compared with G_{III}. Along the symmetric postbuckling path, G_{II} increases linearly with the load and almost symmetric about the center line. In this case, the value is same order as G_{III}. This is because the anti-symmetric component is not very small. Along the antisymmetric path, G_{II} reduces with

the load particularly at the edge of the transverse direction, because the deflection along the center line becomes almost zero. The value is even smaller than G_I and also negligible, when the load becomes large and the plate deformed into antisymmetric shape. The value of G_{III} is most important. The increase of G_{III} is little in the symmetric postbuckling path. However, it grows rapidly with the increase of the antisymmetric deformation. The value exceeds 1000J/m^2 when P=47.7kN. The energy release rate always tends to be maximum at the position of 90° from the loading direction. The results intend that the delaminations tend to propagate into the transverse direction. This coincides with the experimental results, that the delaminations spread in the transverse direction. The value of 1000 J/m^2 is a possible G_{III} toughness of the woven CF/epoxy. The failure loads obtained in the experiment, about 40kN for B-specimen and 53kN for A-specimen, are good values, considering the energy release rate obtained from finite element analysis. We may predict the failure load if we know the toughness of G_{IIIc} of the laminated composite.

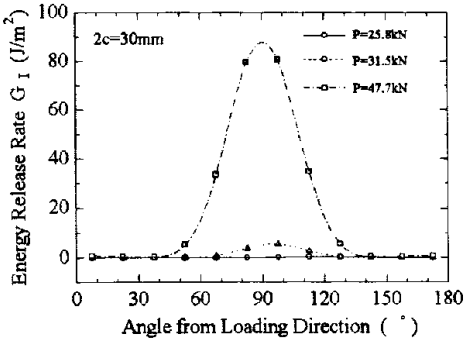

Fig. 10: distribution of G_I and the load

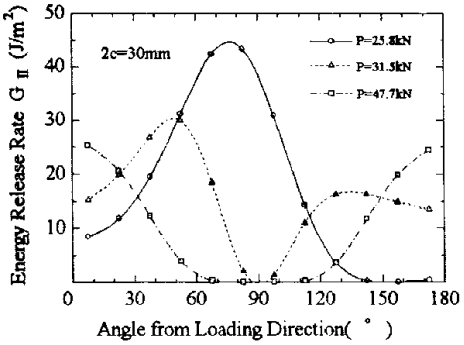

Fig. 11: Distribution of G_{II} and load

CONCLUSIONS

The results of the present finite element analysis agree well with the experimental ones.So, we have the following conclusions.

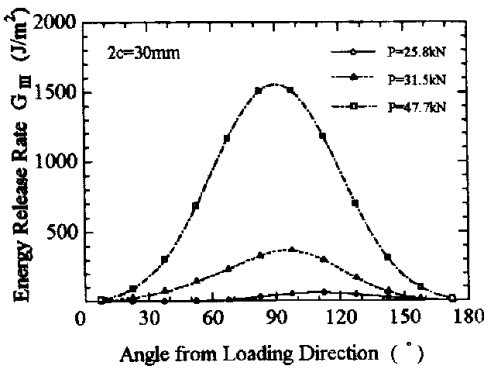

Fig. 12: Distribution of G_{III} and load

1. Plates with multiple delaminations buckles in a symmetric shape. However, their shape changes gradually with the load increase from symmetric to anti-symmetric.
2. The compressive strength of the composite plate with multiple delaminations, whose failure is initiated by the delamination propagation to transverse direction, can be predicted well

by obtaining the energy release rate.

3. When the postbuckling deformation is large, G_{III} becomes dominant among three energy release rate components.

Acknowledgments

The present research is supported by Ministry of Education, Science and Culture, Japan (Grant Aid for Scientific Research(C) No.06650765) and Iketani Science and Technology Foundation (061014-BA).

References

1. Wang S.S., Zahlan N.M. and Suemasu H., "Compressive Stability of Delaminated Random Short-Fiber Composite, Part I-Modeling and Methods of Analysis", Journal of Composite Materials, Vol.19, July 1985, pp.296-316.

2. Vizzini A.J. and Lagace P.A., "The Buckling of Sublaminate on an Elastic Foundation", Journal of Composite Materials, Vol.21, December 1987, pp.1106-1117.

3. Chai H. and Babcock C.D., " One Dimensional Modeling of Failure in Laminated Plates by Delamination Buckling", International Journal of Solids and Structures, Vol.17, No.11, 1981, pp.1069-1083.

4. Suemasu H., "Postbuckling Behavior of Composite Panels with Multiple Delaminations", Journal of Composite Materials, Vol.27, No.11, 1993, pp.1077-1096.

5. Chai H. and Babcock, C.D., "Two Dimensional Modeling of Compressive Failure in Delaminated Laminates", Journal of Composite Materials, Vol.19, January 1985, pp.67-98.

6. Yin W.-L. and Jane K.C., "Refined Buckling and Postbuckling Analysis of Two-dimensional Delaminations I. Analysis and Validation", International Journal of Solids and Structures, Vol.29, No.5, 1992, pp.591-610.

7. Whitcomb, J. D. and Shivakumar, K.N., "Strain-Energy Release Rate Analysis of Plates with Postbuckled Delaminations", Journal of Composite Materials, Vol.23, July 1989, pp.714-734.

8. Shahwan K.W. and Waas A.A., "A Mechanical Model for the buckling of unilaterally Constrained Rectangular Plates", International Journal of Solids and Structures, Vol.31, No.1, 1994, pp.23-37.

9. Suemasu H., "Compressive Behavior of Fiber Reinforced Composite Plates with a center Delamination", Advanced Composite Materials, Vol.1,No.1, 1991, pp.23-37.

10.Suemasu, H., "Compressive Behavior of Composite Panels with a Delamination", Proceedings of Fifth Japan-U.S. Conference on Composite Materials, June 24-27, 1990, Tama-City Tokyo.

11.Suemasu H., Gozu K., Hayashi K. and Ishikawa T., "Compressive Buckling Property Reduction of Composite Plates with Three Simply-Supported and One Free Edges Due to a Delamination", AIAA J., Vol.33, No.2, 1995, pp.312-319.

12.Lee S.M., "Compression-After-Impact of Composites with Toughened Matrices" SAMPE Journal, 1986, pp.64-68

13.Prichard J.C. and Hogg P.J., "The Role of Impact Damage in Post-Impact Compression Testing", Composites, Vol.21, No.6, 1990, pp.503-511.

14.Dost E.F., Ilcewicz W.B., Avery W.B. and Coxon B. R., "Effects of Stacking Sequence on Impact Damage Resistance and Strength for Quasi-Isotropic Laminates", Composite Materials: Fatigue and Fracture, ASTM STP 1110, 1991, pp.476-500.

15.Suemasu H., "Compressive Behavior of Rectangular Composite Laminates with Multiple Elliptical Delaminations, Proceedings of Japan-U.S. Conference on Composite Materials, Kyoto, Japan, 1995, pp.239-246.

16.Suemasu H. and Kumagai T. and Gozu K., Compressive Behavior of Rectangular Composite Laminates with multiple Circular Delaminations, Proceedings of AIAA/ASME/ASCE/AHS/ASC 37th Structures, Structural Dynamics, and Materials Conference, April 15-17, Salt Lake City, UT, USA, 1996, pp.2252-2559.

17.SACMA(Suppliers of Advanced Composite Materials Association) : Recommended Test Method, SRM 2-88 .

18.Shivakumar, K.N.,Tan P.W. and Newman J.C., "A Virtual Crack-Closure Technique for Calculating Stress Intensity Factors for Cracked Three Dimensional Bodies", International Journal of Fracture, 36, 1988, pp.R43-R50.

BEHAVIOUR OF +55/-55° ANGLE PLY LAMINATES UNDER EXTERNAL PRESSURE AND AXIAL COMPRESSION

A. S. Kaddour[1], P. D. Soden[1] and M. J. Hinton[2]

[1]Applied Mechanics Division, UMIST, Sackville street, Manchester, M60 1QD, UK.
[2] Structural Materials Centre, DRA, Fort Halstead, Sevenoaks, Kent, TN14 7BP, UK.

SUMMARY: This paper is concerned with the strength of ±55° filament wound E-Glass/epoxy tubes subjected to external pressure with and without axial compression. A few tests are reported on buckling behaviour of thin tubes. Thicker walled tubes were tested to determine crushing strength. Finite element analysis was carried out to determine the form of end reinforcement and end closures in order to avoid end failure and minimise stress concentration at the edges of the tubes. Tubes with radius to thickness ratio R_i/h down to 2.5 were tested to fracture under a large range combination of external pressure and axial compression. The biaxial crushing strength is compared with theoretical predictions obtained using simple two dimensional laminate and failure theory.

KEYWORDS: crushing strength, biaxial failure, buckling, ±55° angle ply tubes, compression, external pressure

INTRODUCTION

Tests on tubular specimens are often used to investigate the strength of fibre reinforced composites under biaxial loads, see for example Refs [1-3]. The behaviour and strength of ±55° angle ply laminates is of particular interest. Tubes of such construction are frequently employed as pipes and pressure vessels because 55 degrees is considered to be the optimal angle for closed ended cylindrical vessels which are subjected to internal pressure where the ratio of circumferential to axial stress (SR) is 2:1 or to external pressure where SR is -2:-1. Furthermore, in practice, pipes and vessels may encounter a variety of biaxial loads. Thin walled tubes of low stiffness, glass fibre reinforced composite materials are liable to buckle when subjected to compressive loads and buckling rather than crushing has tended to dominate in some experimental studies [3-7] of the compressive strength of composite tubes. The objective of this paper is to present experimental results on the response of ±55 laminates to external pressure with and without axial compression and to compare the results with theoretical predictions. The experimental results describe both crushing and some buckling strengths of ±55° filament wound tubes. The experimental methods are first outlined and numerical results are presented from the finite element analysis that was used to design a suitable test specimen and end attachments to avoid end failures.

EXPERIMENTAL DETAILS

Specimens

The specimens tested were filament wound glass/epoxy tubes produced by the Structural Materials Centre, Defence Research Agency (DRA), Fort Halstead. The E-glass fibre reinforcement was Silenka 051L, 1200 tex and the epoxy resin system was Ciba-Geigy MY750/HY917/DY063. A simple ±55 helical winding pattern was employed. (The winding angle is measured between the fibre direction and axial direction of the tube). Tubes of 100mm and 51mm inner diameter were employed, in a variety of wall thicknesses (h). In most of the tests, specimens with inner radius to thickness ratios R_i/h of 5 were used but to investigate the effects of buckling some tests were conducted on thicker specimens with (R_i/h) ranging from 5 to 2.5 . The results of a few tests on thinner tubes with R/h of 25 and 15 are also reported. The mean thicknesses were determined from measurements taken at 40 positions around the surface of each specimen. The fibre volume fraction was approximately 68%, measured using burn-off tests. The basic form and dimensions of the 100mm and 51mm diameter specimens used for biaxial crushing tests are shown in Fig 1. The R_i/h ratio of 5 for the gauge length portion, was selected on the basis of simple shell buckling calculations.

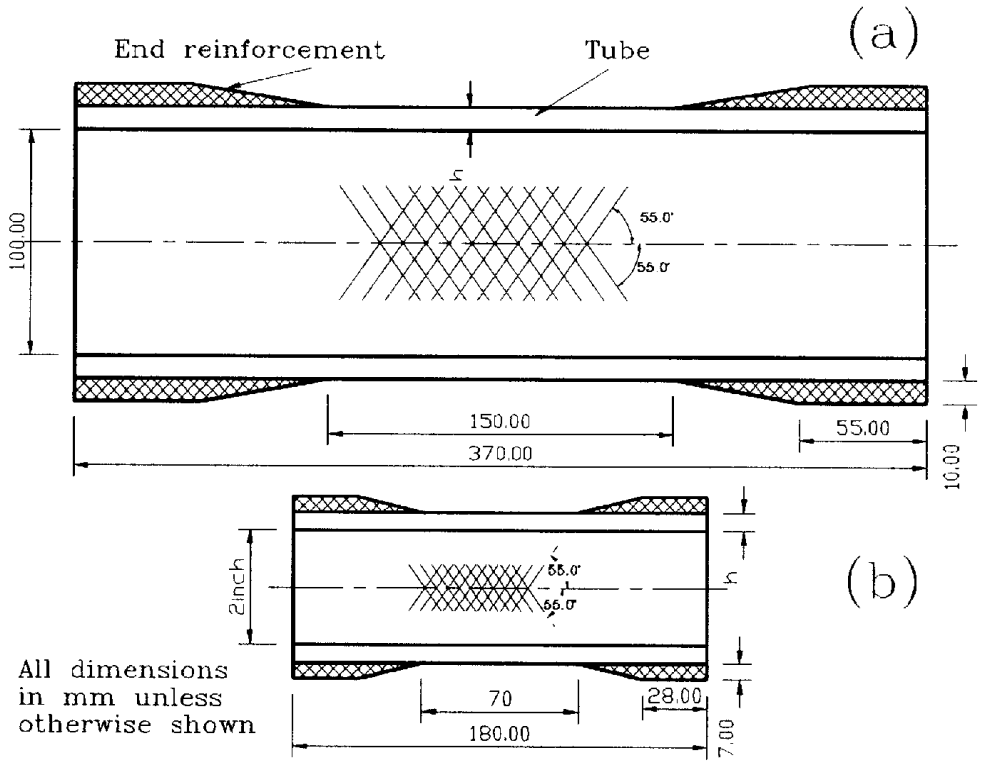

Figure 1: Schematic diagrams of test specimens used in the biaxial compression. (a) 100mm ID and (b) 2 inch ID.

The ends of the thicker specimens had additional reinforcement which was designed to introduce the load smoothly into the gauge length whilst avoiding premature end failure and excessive stress concentrations. End fittings were carefully designed in order to minimise stress concentration near the tube ends. The end reinforcement and attachments were designed with the aid of finite element analysis, see below.

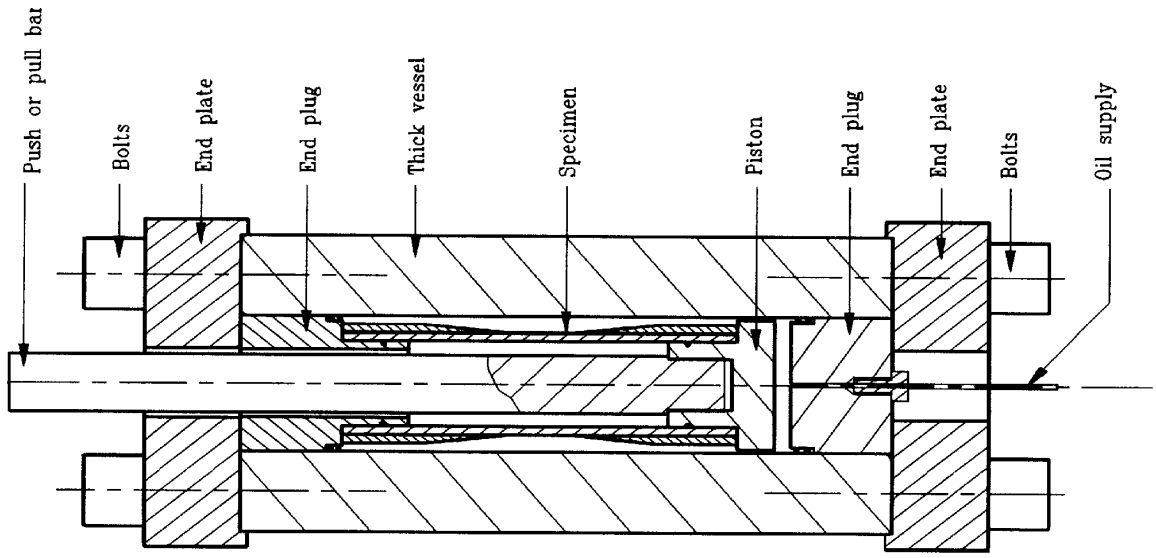

Figure 2: Test rig used for biaxial compression of composite tubes.

Material Properties

The end reinforcement was made of circumferentially wound unidirectional Eglass/epoxy material having the 3-D elastic constants shown in Table(1). The elastic constant of ± 55 laminates were computed on the basis of that the filament wound cylinder was treated as orthotropic monolithic material whose axes of symmetry coincide with the hoop (θ), axial (x) and radial (r) directions. The 3-D elastic properties of the cylinder material are listed in Table 2.

Table 1: Mechanical properties of E-glass/epoxy unidirectional lamina

a) Elastic constants:
E_1 (GPa)=50.74, E_2=E_3 (GPa)=19.39, G_{12} =G_{13} (GPa)=7.06, υ_{12}= 0.268, υ_{23}= 0.4,
α_1 ($\mu\varepsilon/°C$)=20.4, α_2=α_3 ($\mu\varepsilon/°C$)= 7.0.

(b) Strength values:
X_{1T} =1280MPa, X_{1C} =-950 MPa, Y_{2T} =40 MPa, Y_{2C} =-145 MPa, Z_{3T} =40 MPa,
Z_{3C} = -153 MPa, S_{12} = 73 MPa.

Table 2: Mechanical properties of $\pm 55°$ angle ply E-glass/epoxy tube calculated using 3-D analysis, Ref[10]

E_θ=27.325 (GPa), E_x=18.53 (GPa), E_r= 20.312 (GPa), $G_{\theta x}$=14.382 (GPa), G_{xr}=6.969(GPa), $G_{\theta r}$= 7.015(GPa), $\upsilon_{x\theta}$= 0.37, $\upsilon_{\theta r}$=0.128, $\upsilon_{\theta x}$= 0.298

Test Rigs and Methods

The high pressure (200MPa) test rig is shown in Fig 2. Pressure was applied directly to the outer surface of the specimens and axial load was applied via the tension/compression bar. The test techniques have been described in detail in Ref[11]. Fig 3 shows a low pressure test rig (20MPa) together with a buckling wave measuring device, Ref[5]. External pressure was applied via ports (3) and (8) to give SR = -2:-1 and via port (8) only with port (3) closed and with axial clearance between the tube and the end fitting (5) to allow the tube to move freely and obtain SR = -1:0. Deformations of the specimens were measured using electrical strain gauges (Techni Measurement type YFLA-5 and FLA-3-23) bonded to the inner and outer surfaces of the working section of the specimen. Failure was detected by an abrupt drop of pressure (or load) accompanied frequently by a loud bang.

FINITE ELEMENT ANALYSIS OF END REINFORCEMENT AND FITTINGS

Details of the Structure

The basic form of the specimen analyzed was as shown in Fig 1. The $\mp 55°$ angle ply filament wound Eglass/epoxy tubes were 100mm inner diameter, 10mm thick and 370mm long. Solid plugs of different forms are used as end closures. These include (1) cylindrical plugs and (2) plugs with constant nose radius of 2000mm. The reinforcement was made of circumferentially wound E-glass/ epoxy material and consisted of (a) a portion of a constant thickness of 10mm and (b) another portion of a varying thickness, see Fig 1. Various plug and reinforcement geometries were analyzed [12].

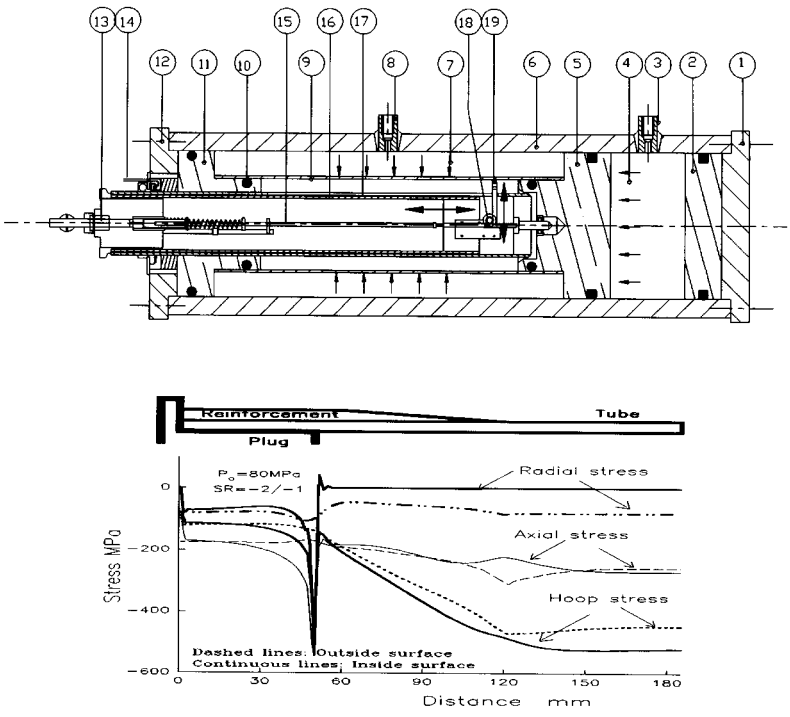

Figure 3: (top) Test vessel used for buckling of thin tubes under external pressure, Ref[5]
Figure 4: (bottom) Stress distribution along a ±55° GRP tube with end reinforcement using cylindrical plug

Finite Element Model

The material of the cylinder and the reinforcement was assumed to behave in a linear elastic orthotropic manner. The ABAQUS general purpose finite element code [8] was used. An axisymmetric model was employed and thus only a quarter of the structure is analyzed. The elements used were axisymmetric, quadrilateral eight node elements CAX8. The number of elements was 500. Contact elements were used between the solid plug and the cylinder. Geometric non linearity was considered..

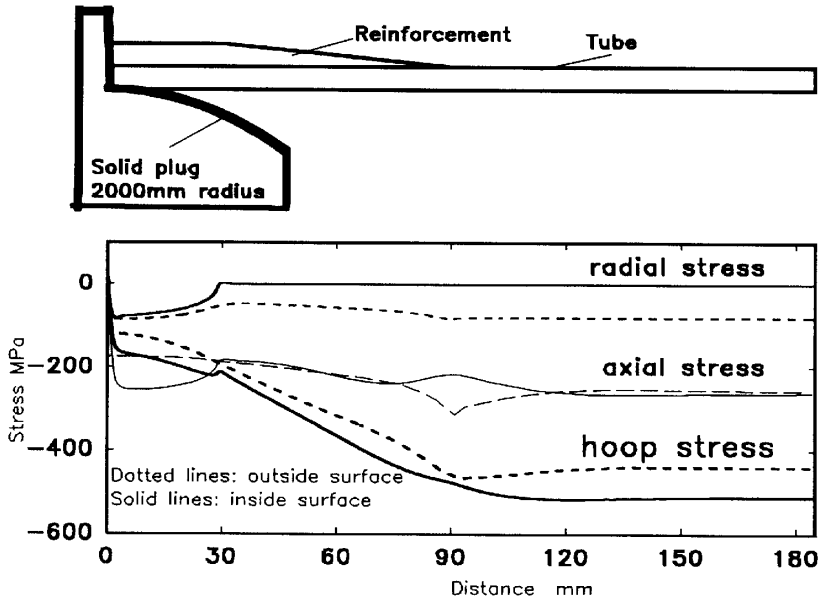

Figure 5: Stress distribution along a ±55^o GRP tube with end reinforcement using end plug of radius of 2000mm.

Finite Element Results

The ABAQUS results are shown in Figs 4 and 5 for a plain cylindrical plug and a shaped plug with a nose radius of 2000mm. The distributions of hoop, axial and radial stresses along the specimen length are shown for an external pressure load of 80MPa with SR=-2/-1. It can seen that the usage of shaped plugs minimises the stress concentration near the end of the plug. The end reinforcement results in lowered stresses in that region, the gradual thickness transition avoids excessive stress concentrations at the end of the reinforcement and the stresses away from end reinforcement are uniform.

THEORETICAL CONSIDERATIONS

Thick Cylinder Theory

Due to the anisotropic nature of the composites considered here, the variation in stresses throughout the thickness of the tubes is greater than predicted by the classical thick cylinder theory used for metals and isotropic cylinders. Equations describing the variation of stresses and strains through the thickness, derived by treating the tube wall as consisting of a single monolithic, orthotropic material, are given in Ref [10]

Failure Theory

A simple, two dimensional, progressive, maximum stress failure theory was employed. An element of the tube wall was treated as a flat angle-ply, laminated plate under in-plane loading. A lamina by lamina stress analysis was carried out as described in Ref [2]. The load was increased incrementally. Allowance was made for non-linear lamina shear-stress strain behaviour and for laminate residual thermal stresses arising from cooling after curing. When one of the lamina stresses exceeded the failure level, the lamina stiffness (and Poisson's ratio) corresponding to that mode of failure was set to zero and loading was continued until a second and final mode of failure occurred. The Maximum stress failure criterion was used in its two dimensional form. Some effects of the through-thickness radial stress on the strength of thick walled orthotropic E-glass/epoxy cylinders have been considered elsewhere [9,10].

Buckling

Buckling pressures were estimated using the following equation taken from Ref [6]

$$P_{buckling} = \frac{0.807\ E_\theta}{\sqrt[3/4]{(1 - \upsilon_{x\theta}\upsilon_{\theta x})}} \left(\frac{R_i}{L}\right) \left(\frac{h}{R_i}\right)^{2.5} \quad (1)$$

This equation was based on the buckling of thin cylindrical shells of isotropic material and was used by Mistry et al [6] for predicting the behaviour of composites by replacing the Young's modulus by the hoop modulus and the squared Poisson's ratio term by the product of the major and minor Poisson's ratio of laminates.

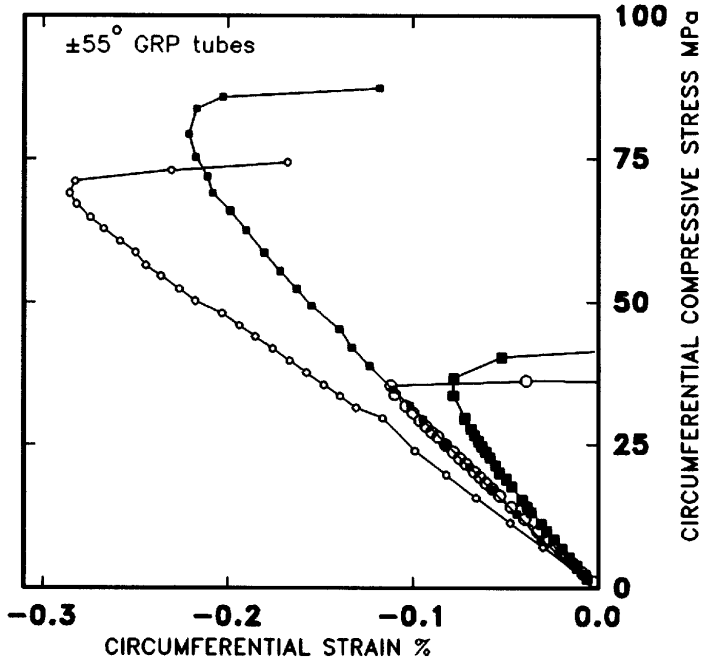

Figure 6: Hoop stress versus strain for ±55 °E-glass/epoxy tubes tested under SR=-2/-1 (squares) and SR=-1/0 (Circles). D=100mm, L~250mm and h=1.9mm (large symbols) or 3.2mm (small symbols), Ref [5]

EXPERIMENTAL RESULTS

Pressure-Strain and Stress-Strain Curves

Fig 6 shows experimental hoop stress versus strain curves for two 100mm inner diameter $\pm 55^\circ$ GRP tubes of thickness of 1.94mm and 3.2mm, each subjected to two types of loading; hydrostatic pressure (SR=-2/-1) and radial pressure (S=-1/0). The length between end fittings of tubes tested under SR=-2/-1 (240mm) was marginally smaller than the length of specimens tested under radial pressure only (265mm). As expected the tinner tube buckles at much lower stress. For each thickness, the final buckling pressures are almost identical for both loading cases.

Fig 7 shows the results of a thicker (h~9.5mm) and shorter tube(parallel test section length 150mm, length between end fittings 250mm) tested under SR=-2/-1. This tube started buckling at a pressure of 67MPa and finally fractured at 80MPa. The compressive strains measured at the inside surface were greater than those at the outside surface and are of similar magnitude to those calculated using the linear elastic thick orthotropic cylinder theory [10].

Fig 8 shows the pressure- strain curves for an even thicker specimen (h=14.5mm, diameter=100 mm). This specimen failed by crushing and there is no pronounced deviation of the pressure-strain curves as failure is approached, Ref [11]

Effect of Thickness on Strength

It is well known that thinner walled tubes fail by shell buckling at relatively lower stresses, as demonstrated in Figs 6-8. The strength of the tubes is plotted against wall thickness (h/R_i) in Fig 9. Included in this Figure are the results taken form Fig 6 and also results from Mistry et al[6]. It should be pointed out the mechanical properties and lengths of the tubes of Ref [6] are slightly lower than those from Fig.6. Nevertheless, both sets of results seem to indicate the same trend.

In order to obtain a true value of crushing strength, tests were carried out on thicker specimens ranging from h/R_i=0.19 to h/R_i=0.4, at a fixed stress ratio of -2/-1 [10]. The results (see Fig. 9) show that, at this stress ratio, as the ratio of h/R_i increases the hoop strength increases and approaches a limiting average value of approximately -820MPa at h/R_i >0.30.

Fig 6 showed that thin tubes tested in uniaxial circumferential compression (SR=-1:0) buckled at almost the same pressure as tubes of the same thickness and similar length tested at SR=-2:-1 but thick walled tubes tested at SR=-1:0 failed at lower pressures than in SR=-2:-1 tests so the transition from buckling to crushing occurred at a lower value of h/R_i. As will be shown in Figs 9 and 10, the hoop strength for tests carried out at SR=-1/0 is much lower than that for tests carried out at -2/-1, using tubes of identical geometry.

For the case of axial compression (i.e. for SR=0:-1), the transition from buckling to crushing again occurred at a lower thickness that for the SR= -2;-1 loading case. The strength reaches a limiting value of approximately 152MPa at h/R_i>0.07 above which there is no increase in the failure stress [10].

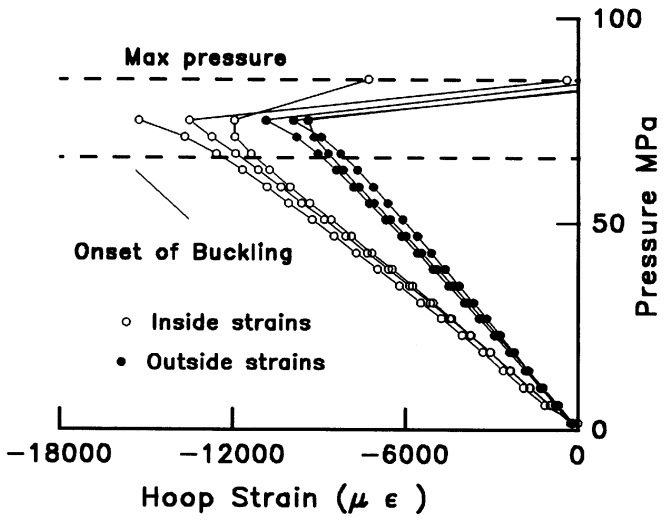

Figure 7: Pressure versus hoop strains for a ±55 E-glass/epoxy tube tested under SR=-2/-1. (D=100mm, L=150mm, h=9.5mm)

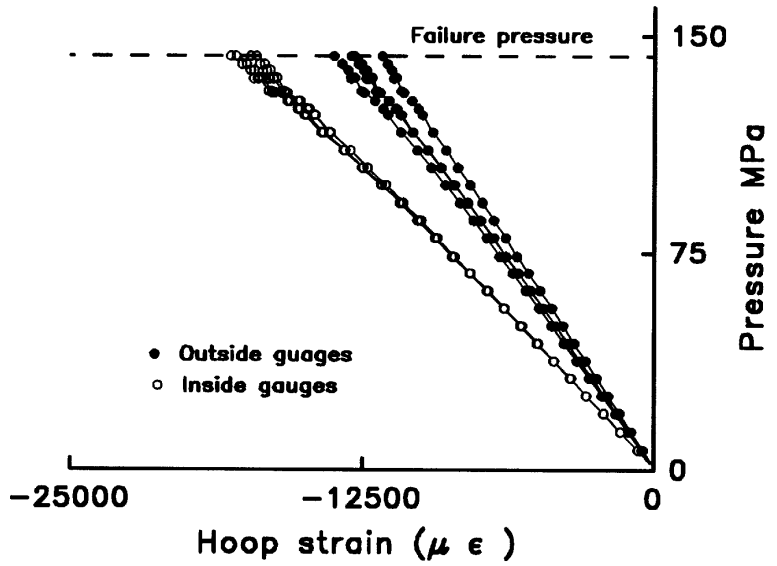

Figure 8: Pressure versus hoop strains for a ±55 GRP tube tested under SR=-2/-1. (D=100mm, h=14.5mm)

Biaxial Compression Strength

The results from the biaxial compression tests on ±55° filament wound tubes are plotted in Fig 10. The data cover almost all of the compression-compression quadrant. Since the test specimens are thick walled, the quoted 'experimental failure stress' values are actually derived from the measured failure pressure and load using thick orthotropic cylinder theory. They represent the failure stresses at the inner surface of the cylinder (the position of maximum stress) . The corresponding hoop stresses at the outside of the tubes are expected, according to thick orthotropic cylinder theory, to be lower than those at the outside surface while the outside surface axial stresses are close to the inside surface ones. All the specimens for which the results are

presented in Fig 10 failed by crushing rather than buckling and none of them leaked before final failure.

The highest failure stresses were recorded for the thickest specimens at the SR= -2/-1 loading condition. The strength at this loading ratio was significantly greater than the uniaxial compressive strengths in the circumferential or axial directions.

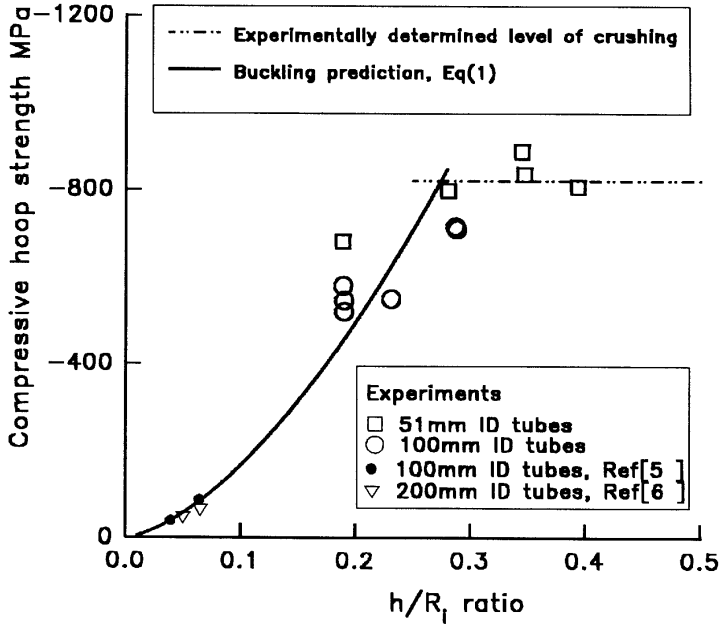

Figure 9: Hoop stress versus h/R_i ratio for ±55 GRP tubes tested under SR= -2/-1.

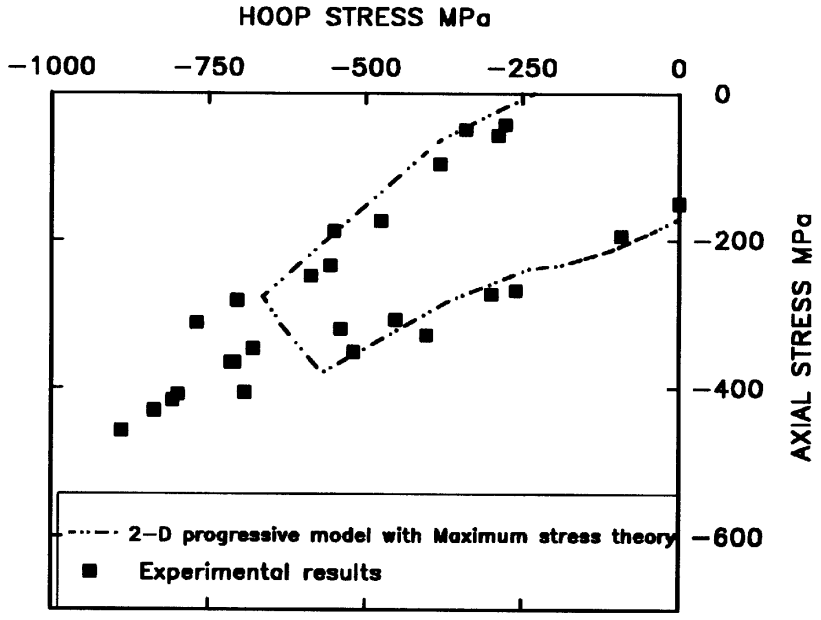

Figure 10: Biaxial compression-compression failure envelope for ±55° GRP tubes.

COMPARISON OF THEORETICAL AND EXPERIMENTAL RESULTS

Buckling

A few test results are presented in Fig 9 showing the buckling pressure versus diameter to thickness ratio of ±55 GRP tubes. The lines drawn in Fig 9 were obtained from Eq(1) with $L/R_i=4.8$ and the hoop stress was calculated from the buckling pressure using thin shell equation ($\sigma=P_{buckling} * R_m/h$) . They agree reasonably well with the experimental results.

Biaxial Compression

The experimental results for the ±55° tubes are shown in Fig 10, along with the predicted final failure envelopes using the simple 2-D laminate analysis with the progressive Maximum Stress criterion. According to the 2-D progressive model, the predicted biaxial strength values for stress ratios between -2.7:-1 and -3:-2 depend strongly on the lamina longitudinal compressive strength. The experimental results tend to be higher than the theoretical results in that region of the failure envelope. Otherwise, the agreement between the experimental and theoretical results is reasonably good.

CONCLUSIONS

- Only a few experimental buckling pressure results were obtained for thin walled ±55° E-glass/epoxy tubes subjected to external pressure with and without pressure end load but those pressures were in reasonable agreement with classical buckling theory.
- In experiments on thicker walled tubes the failures were by crushing rather than buckling.
- The end reinforcement and fittings designed with the aid of finite element analysis were successful in avoiding end failures and minimising stress concentrations at the end of the test section.
- Tests were conducted over a wide range of combinations of external pressure and axial compressive load. The strength of ±55° GRP tubes under the application of biaxial compressive loading was shown to be substantially greater than either the axial or circumferential uniaxial compressive strengths.
- The simple progressive Maximum Stress laminate failure theory was reasonably successful in predicting the strength of the tubes under a range of biaxial compressive loads. It underestimated the final failure strength at some stress ratios where the predictions are sensitive to the assumed strength of the composite in compression parallel to the fibres.

ACKNOWLEDGEMENTS

The work reported here was sponsored by the Defence Research Agency (DRA) in Great Britain under a contract No MoD/DRA 2044/191. The authors would like to thank the sponsors for their support.

REFERENCES

1 Soden P D, Kitching R, Tse P C, Tsavalas Y and Hinton M J, "Influence of winding angle on the strength and deformation of filament wound composite tubes subjected to uniaxial and biaxial loads", *Composites Science and Technology*, V46, 1993, pp 363-378.

2 Hinton M J, Soden P D and A S Kaddour,"Biaxial failure of composite laminates under combined loads", *Applied Composite Materials*, V3, 1996, pp151-162.

3 Swanson S R and Colvin G E,"Compressive strength of carbon/epoxy laminates under multiaxial stress", Final Annual Report to the Lawrence Livemore National Laboratory, UCRL-21235, 1989.

4 Garala H J," Experimental evaluation of graphite/epoxy composite cylinders subjected to external hydrostatic compressive loading", Proc 1987 SEM Spring Conf on Experimental Mechanics, Houston, Texas, 14-19 June, 1987. pp 948-951.

5 Al-Khalil M F S, Soden P D and Kaddour A S," Buckling of thin angle ply GRP tubes under external pressure loading", submitted to *International Journal of Solids and Structures, 1997*

6 Mistry J, Gibson A G and Wu Y S, "Failure of composite cylinders under combined external pressure and axial loading", *Composite Structures*, V22, 1992, pp 193-200.

7 Graham D, "Composite pressure hulls for deep ocean submersibles", *Composite Structures*, V32, 1995, pp331-343.

8 Hibbit, Karlsson and Sorensen Inc., *ABAQUS User Manual*, VERSION 5.5, 1995, Providence, RI, 1996.

9 Al-Khalil M F S, Soden P D, Kitching R, and Hinton M J," The effects of radial stresses on the strength of thin walled filament wound GRP composite pressure cylinders", *Intenational Journal of Mechanical Sciences*, V38, 1995, pp 97-120.

10 Kaddour A S, Soden P D and Hinton M J (1997),"Failure of $\pm 55^\circ$ filament wound glass/epoxy tubes under biaxial compression", sent to *Journal of Composite Materials.*

11 Kaddour A S and Soden P D, "Design of high pressure rig for biaxial and triaxial compression testing of composite tubes", *Science and Engineering of Composite Materials*, V5, 1996, pp 27-38.

12 Liu W, Soden P D and Kaddour A S," Design of end plugs for biaxial compression loading of thick composite tubes", in preparation.

OFF-AXIS FIBER ORIENTATION HIGH-STRAIN RATE COMPRESSION TESTING OF K-49/3501-6 KEVLAR®/EPOXY COMPOSITES

Eric Preissner, Eyassu Woldesenbet, Jack R. Vinson

Department of Mechanical Engineering, University of Delaware, Newark, DE 19716, USA

SUMMARY: The Split-Hopkinson Pressure Bar (SHPB) was used to study the dynamic compressive properties of K-49/3501-6 KEVLAR®/Epoxy laminates. Both a unidirectional (UD) and a cross-ply (XP) laminate were examined. Each laminate was a 30.5 cm (12 in) square flat panel composed of 75 plies; the test specimens were approximately 0.95 cm (3/8 in) cubes. The tested fiber orientation angles were 0, 15, 30, 45, 60, 75, and 90 degrees. Quasi-static tests were also conducted for comparison purposes. The strain rate values varied from 200 - 1100 /s. The data for the KEVLAR®/Epoxy composites were obtained from 120 tests for the UD laminate and 90 tests for the XP laminate. The ultimate stress of both materials shows some strain rate sensitivity in the 1-direction, with significant reductions in stress, but no rate sensitivity for other angles. The ultimate strains for both materials increase with increasing angle, but show no rate sensitivity.

KEYWORDS: dynamic material properties, high-strain-rate, Split-Hopkinson Pressure Bar, KEVLAR® 49, 3501-6 Epoxy, off-axis, unidirectional, cross-ply

INTRODUCTION

At present, a program is underway at the University of Delaware under the Office of Naval Research sponsorship (Dr. Y.D.S. Rajapakse) that involves three tasks:

1. The high-strain-rate testing in compression and tension of various polymer matrix composite (and other) materials using the existing SHPB facility, and correlation and statistical analysis of the dynamic material properties obtained.

2. Examination of the samples tested, using optical and scanning electron microscopy to characterize the deformation and fracture processes.

3. The evaluation of the suitability of current models, such as Johnson-Cook, Ferilli-Armstrong, Steinberg-Guinan-Lund, and Bodner-Partom, to describe the strength, deformation, and failure of these materials at high-strain-rates and the modification of these models, or whenever necessary, the development of new models.

The present paper concentrates on Task 1.

The SHPB facility at the University of Delaware has been described previously in [1-6]. Kolsky [7] introduced a method for determining mechanical properties of materials at high-strain-rates using the SHPB in 1949. The method was developed based on wave propagation

theory in elastic bars and the interaction between a stress wave and a short specimen. To begin a test, a specimen is placed between two long, 1.9 cm (3/4 in) diameter Inconel bars, the "incident bar" and the "transmitted bar", which are supported by Teflon® bearings. Impact is initiated by releasing nitrogen gas from a pressurized chamber. The gas propels a striker bar (supported by and riding on Teflon® rings) through a guiding barrel, at the end of which it strikes the incident bar. The velocity of the striker bar just prior to impact is measured using two infrared beams at the end of the barrel. At impact, the incident bar receives an elastic compressive stress wave with a specific wave velocity and a wave shape that is a function of time. When the wave reaches the incident bar/specimen interface, a portion of the incident wave is reflected back into the incident bar as a tensile wave. The remaining portion of the wave is transmitted into the specimen as a compressive wave. The wave transmitted into the specimen travels through the specimen and reaches the specimen/transmitted bar interface, where a portion of the wave is reflected back into the specimen. The rest is transmitted into the transmitted bar as a compressive wave.

Because the specimen length is short, the initial stress wave in the specimen undergoes numerous internal reflections during the test. The stress distribution in the specimen is assumed to be uniform due to these numerous reflections. In addition it is assumed that the stress waves undergo minimal dispersion, that the bars remain elastic, and that the ends of both the incident and transmitted bars in contact with the specimen remain flat. Based on the length of the striker bar, there is a characteristic time window corresponding to the duration of the stress wave. The wave pulse time window of the University of Delaware SHPB is approximately 290 microseconds. This means that the specimen must fail within 290 microseconds after the start of the tests for failure to be accurately characterized. This has not been a problem with the relatively brittle composites tested to date.

Strain gages, connected to a Fluke PM3394A recording oscilloscope, are mounted on the incident and transmitted bars, equidistant from the specimen interfaces. The oscilloscope records the strain gage's output as a voltage versus time graph. Using this data, along with the speed of the striker bar and the physical dimensions of the bars and specimens, stress versus strain curves can be generated for different strain rates. Zukas [8] has shown that for many metals, mechanical properties vary significantly with strain rate. This new data will add to what is now available for other materials. At the University of Delaware, material systems tested to date include glass/epoxy, glass/polyester, graphite/epoxy, carbon/metal matrix, and carbon/ceramic matrix, and the most recent papers regarding these materials are given in [1-6].

SAMPLE PREPARATION

The KEVLAR®/Epoxy composite discussed herein is a DuPont KEVLAR® 49 fiber with a Hercules 3501-6 epoxy matrix. The basic UD 30.5 cm (12 in) wide prepreg tape was originally manufactured by the "hi-E" Company, and stored in the freezer at the Center for Composite Materials (CCM) at the University of Delaware. Two 30.5 cm (12 in) square flat panels, each made up of 75 plies were fabricated. The nominal thickness of each panel after curing was approximately 0.95 cm (3/8 in). One panel was laid up as a UD laminate, while the other was a mid-plane symmetric, XP laminate. All specimens were then fabricated out of these panels by using a water-cooled surface grinder equipped with a thin-kerf diamond grit saw blade. All UD and XP specimens were produced from the same respective panel by orienting the primary fiber direction at the proper angle to the saw travel. Two sets of perpendicular cuts resulted in cubic samples with approximately 0.95 cm (3/8 in) sides. The

wet diamond saw produced very little delamination and smooth cut surfaces. Further improvement of the cut surfaces was accomplished by wet polishing with 600 grit SiC paper.

Previous research, [1-6], performed using the University of Delaware SHPB facility involved right circular cylinders with a length-to-diameter (L/D) ratio of approximately 1.5. Recently, a study using a graphite/epoxy composite was conducted [9] that examined both various L/D ratios from 0.5 to 2.0 as well as a comparison between square/rectangular and cylindrical specimen geometries. Within the range of variables examined in [9], no statistically significant differences could be found in the material properties determined by the testing. These results are fortuitous, as the properties of KEVLAR® which make it a desirable material also make it difficult to machine, particularly smooth, cylindrical, core-drilled specimens. Consequently, square/rectangular specimens were produced and used for the tests discussed herein. The decision to use a cubic geometry also made preparation of the off-angle specimens considerably easier than if they had been core drilled.

RESULTS AND DISCUSSION

In this paper, the typical notation convention for fibrous composite materials is followed. The 1-, 2-, and 3-directions are three mutually orthogonal axes, with the 1-direction parallel to the primary fiber direction, the 2-direction perpendicular to the primary fiber direction in the transverse dimension, and the 3-direction also perpendicular to the primary fiber direction but in the thickness dimension. Theoretically, the 2- and the 3-directions are identical in a UD material, while the 1- and the 2- directions are identical in a XP material. This theoretical orthotropic symmetry has been demonstrated for the panels in this paper in [9, 10]. The off-axis angle, Θ, for this paper is defined as the angle between the axis of the SHPB and the 1-direction of the samples; therefore $\Theta = 0$ is equivalent to the 1-direction, and $\Theta = 90$ is equivalent to the 2-direction. Because of the symmetry of the XP material it was tested only at $\Theta = 0$, 15, 30, and 45 degrees.

The fiber volume fraction (V_f) of the KEVLAR® used for this testing was estimated to be 41%. This calculation was based on the measured weight and volume of a selected number of samples (average density 1.324 g/cm^3), the published density of KEVLAR® 49 (1.44 g/cm^3, [11]), and an unconfirmed density for the 3501-6 epoxy (1.26 g/cm^3). The V_f of the composite that was used in [11] to provide the published ultimate stress and strain data was 60% and used an unidentified epoxy matrix.

The dynamic results from the SHPB are also compared with quasi-static compression tests performed at the CCM. The quasi-static tests were performed on an Instron 1125 screw-type machine in the constant speed mode for all Θ angles. These tests used specimens with geometry identical to that for the SHPB tests, with the samples simply placed between two flat platens and compressed to failure, and the results recorded on a strip chart. The results for the UD quasi-static tests are shown in Table 1, while those for the XP are shown in Table 2. These results are the averages of three tests for each Θ. The published quasi-static ultimate stresses in [11] for a KEVLAR® 49/Epoxy laminate (unspecified epoxy) with $V_f = 0.60$ are 276 MPa for the 1-direction and 137.9 MPa for the 2-direction. The published quasi-static ultimate strains in [11] for the same material are approximately 1.33% for the 1-direction and 3.11% for the 2-direction. Additionally, quasi-static compression data for the 3501-6 epoxy using an IITRI fixture has been given in [12]. The values given in [12] for ultimate stress and strain are approximately 81 MPa and 2.05% respectively. The stress-strain relation for the

3501-6 epoxy was found to be non-linear. The published comparison data from [11] and [12] are also included in Figs. 2 and 3.

Table 1: UD Quasi-Static Test Results

Θ (deg. from 1-dir)		Strain Rate at Failure (/sec)	Ultimate Strain (%)	Ultimate Stress (MPa)
	Average		0.0496	240.29
0	Std. Dev.	Quasi-static	0.0009	10.35
	Coeff. of Var.		1.90%	4.31%
	Average		0.0530	224.23
15	Std. Dev.	Quasi-static	0.0027	3.79
	Coeff. of Var.		5.04%	1.69%
	Average		0.0563	157.02
30	Std. Dev.	Quasi-static	0.0004	1.97
	Coeff. of Var.		0.66%	1.25%
	Average		0.0627	130.25
45	Std. Dev.	Quasi-static	0.0023	1.24
	Coeff. of Var.		3.61%	0.95%
	Average		0.0604	109.58
60	Std. Dev.	Quasi-static	0.0026	3.22
	Coeff. of Var.		4.29%	2.94%
	Average		0.0521	100.94
75	Std. Dev.	Quasi-static	0.0003	1.35
	Coeff. of Var.		0.65%	1.34%
	Average		0.0493	90.55
90	Std. Dev.	Quasi-static	0.0000	2.59
	Coeff. of Var.		0.05%	2.86%

Table 2: XP Quasi-Static Test Results

Θ (deg. from 1-dir)		Strain Rate at Failure (/sec)	Ultimate Strain (%)	Ultimate Stress (MPa)
	Average		0.0985	191.05
0	Std. Dev.	Quasi-static	0.0017	0.49
	Coeff. of Var.		1.74%	0.26%
	Average		0.0884	167.53
15	Std. Dev.	Quasi-static	0.0049	9.47
	Coeff. of Var.		5.56%	5.66%
	Average		0.1014	150.85
30	Std. Dev.	Quasi-static	0.0156	2.33
	Coeff. of Var.		15.35%	1.55%
	Average		0.1521	142.00
45	Std. Dev.	Quasi-static	0.0036	3.25
	Coeff. of Var.		2.39%	2.29%

The averaged dynamic test results are given in Tables 3-13. Each average value represents from three to five repeated tests at each test condition. A single test condition consisted of a specific combination of: UD or XP lay-up; fiber orientation angle, Θ (0 - 90 in 15 deg increments); and applied SHPB pressure. The applied pressure was held approximately constant for each test series (denoted by each average value) in an attempt to control the strain rate achieved in the specimen to a specific level. Within each test series, fluctuations did occur for various reasons in the applied pressure and/or the achieved strain rate. Because of this, standard deviations and coefficients of variation are given in these tables for each test series. An example of a typical stress-strain plot, developed from the recorded strain gage data, for the UD material at Θ = 15 degrees and an average strain rate of 436 /sec is given in Fig. 1.

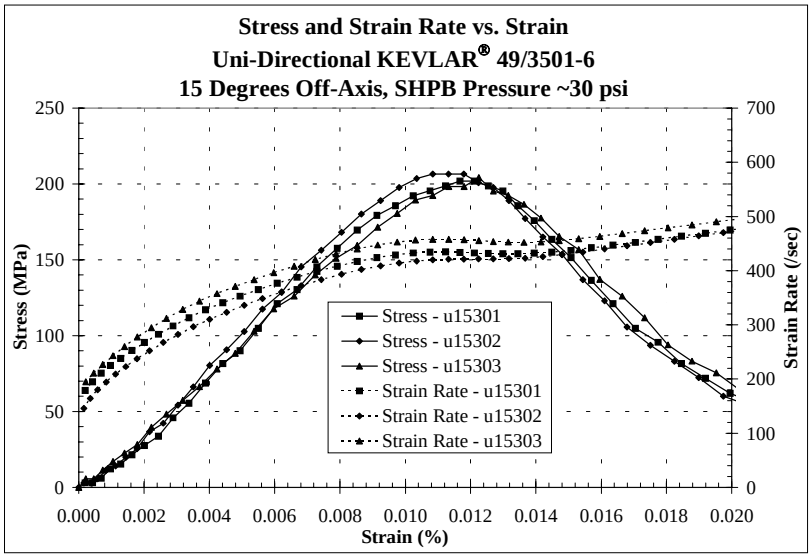

Figure 2: Example Stress-Strain Plot for the UD Material

Table 3: UD SHPB Results for Θ = 0

Θ = 0 deg. (from 1-dir)	Strain Rate at Failure (/sec)	Ultimate Strain (%)	Ultimate Stress (MPa)
Average	187.82	0.01633	294.23
Std. Dev.	28.05	0.00179	15.31
Coeff. of Var.	14.93%	10.98%	5.20%
Average	379.74	0.0071	238.48
Std. Dev.	17.05	0.0005	29.69
Coeff. of Var.	4.49%	7.05%	12.45%
Average	433.36	0.01199	315.12
Std. Dev.	15.00	0.00023	8.01
Coeff. of Var.	3.46%	1.92%	2.54%
Average	489.25	0.0128	306.97
Std. Dev.	21.63	0.0003	3.82
Coeff. of Var.	4.42%	2.15%	1.25%
Average	553.02	0.0137	314.68
Std. Dev.	43.29	0.0012	3.97
Coeff. of Var.	7.83%	8.41%	1.26%
Average	549.02	0.0142	294.34
Std. Dev.	24.00	0.0013	10.52
Coeff. of Var.	4.37%	9.13%	3.57%

Table 4: UD SHPB Results for Θ = 15

Θ = 15 deg. (from 1-dir)	Strain Rate at Failure (/sec)	Ultimate Strain (%)	Ultimate Stress (MPa)
Average	318.06	0.0121	186.72
Std. Dev.	23.84	0.0007	11.04
Coeff. of Var.	7.50%	5.46%	5.91%
Average	436.40	0.0120	204.22
Std. Dev.	14.13	0.0002	1.93
Coeff. of Var.	3.24%	1.61%	0.95%
Average	517.83	0.0124	190.60
Std. Dev.	10.83	0.0004	10.50
Coeff. of Var.	2.09%	3.53%	5.51%
Average	550.15	0.0129	189.05
Std. Dev.	64.26	0.0002	7.85
Coeff. of Var.	11.68%	1.73%	4.15%
Average	578.25	0.0133	163.01
Std. Dev.	19.25	0.0004	31.46
Coeff. of Var.	3.33%	2.85%	19.30%

Table 5: UD SHPB Results for Θ = 30

Θ = 30 deg. (from 1-dir)	Strain Rate at Failure (/sec)	Ultimate Strain (%)	Ultimate Stress (MPa)
Average	392.50	0.0191	121.39
Std. Dev.	13.75	0.0009	6.60
Coeff. of Var.	3.50%	4.72%	5.44%
Average	592.10	0.0181	108.00
Std. Dev.	72.92	0.0009	39.14
Coeff. of Var.	12.32%	4.92%	36.24%
Average	674.95	0.0181	118.90
Std. Dev.	33.91	0.0004	10.52
Coeff. of Var.	5.02%	2.13%	8.85%
Average	716.33	0.0182	124.58
Std. Dev.	38.61	0.0007	7.33
Coeff. of Var.	5.39%	3.68%	5.88%
Average	769.60	0.0189	133.30
Std. Dev.	81.10	0.0005	5.61
Coeff. of Var.	10.54%	2.42%	4.21%

Table 6: UD SHPB Results for Θ = 45

Θ = 45 deg. (from 1-dir)	Strain Rate at Failure (/sec)	Ultimate Strain (%)	Ultimate Stress (MPa)
Average	424.8618	0.0260	109.60
Std. Dev.	42.9467	0.0007	24.14
Coeff. of Var.	10.11%	2.75%	22.02%
Average	622.87	0.0249	116.57
Std. Dev.	40.36	0.0004	11.30
Coeff. of Var.	6.48%	1.50%	9.69%
Average	646.56	0.0266	123.73
Std. Dev.	65.85	0.0018	2.86
Coeff. of Var.	10.18%	6.88%	2.31%
Average	791.64	0.0253	126.37
Std. Dev.	51.23	0.0014	7.21
Coeff. of Var.	6.47%	5.43%	5.70%
Average	907.52	0.0250	121.31
Std. Dev.	63.54	0.0013	5.51
Coeff. of Var.	7.00%	5.20%	4.54%

Table 7: UD SHPB Results for Θ = 60

Θ = 60 deg. (from 1-dir)	Strain Rate at Failure (/sec)	Ultimate Strain (%)	Ultimate Stress (MPa)
Average	425.47	0.0263	109.88
Std. Dev.	17.80	0.0020	15.66
Coeff. of Var.	4.18%	7.72%	14.25%
Average	635.93	0.0276	117.06
Std. Dev.	8.36	0.0011	3.71
Coeff. of Var.	1.31%	4.15%	3.17%
Average	720.63	0.0279	114.72
Std. Dev.	30.86	0.0011	3.00
Coeff. of Var.	4.28%	4.07%	2.61%
Average	876.58	0.0286	119.20
Std. Dev.	12.22	0.0011	5.48
Coeff. of Var.	1.39%	4.00%	4.59%
Average	929.67	0.0273	119.49
Std. Dev.	43.46	0.0010	2.23
Coeff. of Var.	4.68%	3.78%	1.87%

Table 8: UD SHPB Results for Θ = 75

Θ = 75 deg. (from 1-dir)	Strain Rate at Failure (/sec)	Ultimate Strain (%)	Ultimate Stress (MPa)
Average	460.34	0.0258	90.64
Std. Dev.	8.26	0.0012	5.16
Coeff. of Var.	1.79%	4.57%	5.70%
Average	652.28	0.0274	113.86
Std. Dev.	6.70	0.0003	5.37
Coeff. of Var.	1.03%	1.07%	4.71%
Average	769.33	0.0262	100.11
Std. Dev.	23.98	0.0006	7.18
Coeff. of Var.	3.12%	2.33%	7.17%
Average	821.08	0.0277	117.52
Std. Dev.	10.56	0.0006	0.11
Coeff. of Var.	1.29%	2.08%	0.09%
Average	930.68	0.0264	114.18
Std. Dev.	21.09	0.0005	4.94
Coeff. of Var.	2.27%	1.91%	4.33%

Table 9: UD SHPB Results for Θ = 90

Θ = 90 deg. (from 1-dir)	Strain Rate at Failure (/sec)	Ultimate Strain (%)	Ultimate Stress (MPa)
Average	468.13	0.0282	105.75
Std. Dev.	17.00	0.0022	13.29
Coeff. of Var.	3.63%	7.69%	12.56%
Average	683.25	0.0275	103.51
Std. Dev.	38.99	0.0003	1.17
Coeff. of Var.	5.71%	1.26%	1.13%
Average	848.49	0.0263	101.59
Std. Dev.	9.69	0.0013	2.03
Coeff. of Var.	1.14%	4.78%	2.00%
Average	876.62	0.0262	109.79
Std. Dev.	34.22	0.0012	5.75
Coeff. of Var.	3.90%	4.45%	5.23%
Average	993.78	0.0249	110.75
Std. Dev.	30.95	0.0007	5.42
Coeff. of Var.	3.11%	2.79%	4.89%
Average	1058.05	0.0259	98.21
Std. Dev.	18.14	0.0004	2.70
Coeff. of Var.	1.71%	1.71%	2.75%

Table 10: XP SHPB Results for Θ = 0

Θ = 0 deg. (from 1-dir)	Strain Rate at Failure (/sec)	Ultimate Strain (%)	Ultimate Stress (MPa)
Average	209.10	0.0254	222.06
Std. Dev.	15.48	0.0013	2.78
Coeff. of Var.	7.40%	4.97%	1.25%
Average	412.20	0.0282	237.30
Std. Dev.	23.54	0.0022	5.57
Coeff. of Var.	5.71%	7.64%	2.35%
Average	582.40	0.0299	233.42
Std. Dev.	36.20	0.0008	6.09
Coeff. of Var.	6.22%	2.51%	2.61%
Average	729.20	0.0176	216.06
Std. Dev.	38.45	0.0061	12.62
Coeff. of Var.	5.27%	34.68%	5.84%
Average	878.60	0.0275	219.48
Std. Dev.	87.13	0.0048	13.06
Coeff. of Var.	9.92%	17.27%	5.95%

Table 11: XP SHPB Results for Θ = 15

Θ = 15 deg. (from 1-dir)	Strain Rate at Failure (/sec)	Ultimate Strain (%)	Ultimate Stress (MPa)
Average	385.40	0.0239	173.40
Std. Dev.	41.26	0.0038	12.97
Coeff. of Var.	10.71%	15.84%	7.48%
Average	641.20	0.0265	176.20
Std. Dev.	44.49	0.0045	12.11
Coeff. of Var.	6.94%	16.95%	6.87%
Average	846.80	0.0246	186.60
Std. Dev.	36.36	0.0063	8.79
Coeff. of Var.	4.29%	25.50%	4.71%
Average	1053.80	0.0215	226.20
Std. Dev.	74.74	0.0002	49.73
Coeff. of Var.	7.09%	0.78%	21.99%

Table 12: XP SHPB Results for Θ = 30

Θ = 30 deg. (from 1-dir)	Strain Rate at Failure (/sec)	Ultimate Strain (%)	Ultimate Stress (MPa)
Average	378.40	0.0373	154.40
Std. Dev.	28.18	0.0018	21.94
Coeff. of Var.	7.45%	4.95%	14.21%
Average	687.20	0.0340	156.40
Std. Dev.	41.47	0.0056	9.32
Coeff. of Var.	6.03%	16.42%	5.96%
Average	969.40	0.0330	155.60
Std. Dev.	39.42	0.0050	36.99
Coeff. of Var.	4.07%	15.11%	23.77%
Average	1140.20	0.0272	156.00
Std. Dev.	54.98	0.0023	12.21
Coeff. of Var.	4.82%	8.38%	7.82%

Table 13: XP SHPB Results for Θ = 45

Θ = 45 deg. (from 1-dir)	Strain Rate at Failure (/sec)	Ultimate Strain (%)	Ultimate Stress (MPa)
Average	407.20	0.0366	136.00
Std. Dev.	24.84	0.0020	7.97
Coeff. of Var.	6.10%	5.37%	5.86%
Average	731.00	0.0421	132.80
Std. Dev.	27.18	0.0012	12.38
Coeff. of Var.	3.72%	2.77%	9.32%
Average	961.00	0.0293	141.00
Std. Dev.	58.56	0.0106	14.75
Coeff. of Var.	6.09%	36.17%	10.46%
Average	1139.40	0.0266	139.40
Std. Dev.	72.90	0.0024	9.18
Coeff. of Var.	6.40%	9.02%	6.59%

For the UD material, the above data are plotted in Figs. 2 and 3. Fig. 2 plots the average ultimate stress versus Θ for several groupings of strain rates. It is seen that the quasi-static results for this paper are significantly lower (14% and 35% lower for the 1- and 2-directions respectively) than the published values. All of the data does show the typical and expected reduction in ultimate stress with increasing off-axis angle. The dynamic data also shows an increase in ultimate stress with increasing strain rate for the 1-direction (except for the group

at approximately 550 /sec), but with a larger fall-off in stress with increasing off-axis angle. For $\Theta > 45$ degrees, all data tends to similar values.

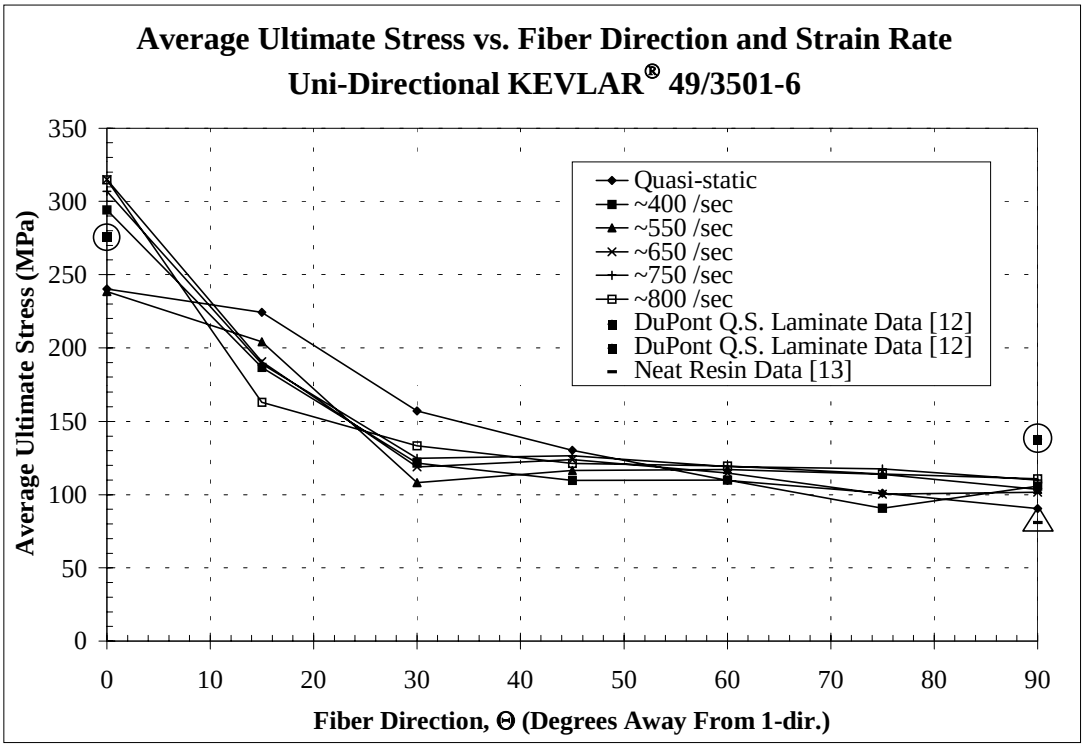

Figure 2: UD Average Ultimate Stress vs. Fiber Direction and Strain Rate

Fig. 3 plots the average ultimate strain versus Θ for several groupings of strain rates for the UD material. Except for the 1-direction results for the 400 /sec and 550 /sec groups, there does not seem to be a significant influence of strain rate on ultimate strain. Due to the relatively small number of samples at each test condition, it is difficult to determine whether the differences shown in the 400 /sec and 550 /sec groups are real effects or just statistical variances. Overall, this format for presentation of both the stress and strain results is not completely satisfactory as, within each of the strain rate "groups", there is a significant variation in strain rate with Θ. However, due to limitations in the plotting program, plotting the stress and strain versus both off-axis angle and the distinct strain rate for each point was not possible.

For the XP material, Figs. 4 and 5 show that the ultimate stresses and strains of this composite are also sensitive to Θ. The ultimate stress is shown to decrease as the off-axis angle is increased to $\Theta = 45$. Fig. 4 also shows that the ultimate stress of the material becomes strain rate insensitive as the off-axis testing angle is increased. Fig. 5 shows that the ultimate strain values tend to increase for $15 < \Theta < 45$ for all strain rates. The ultimate strain of the material in the XP composite tends to be more strain sensitive at the larger off-axis testing angles, but no clear trend is evident. In both Figs. 4 and 5, the data plotted for $\Theta > 45$ is just a reflection of that for $\Theta < 45$ due to the symmetry of the material.

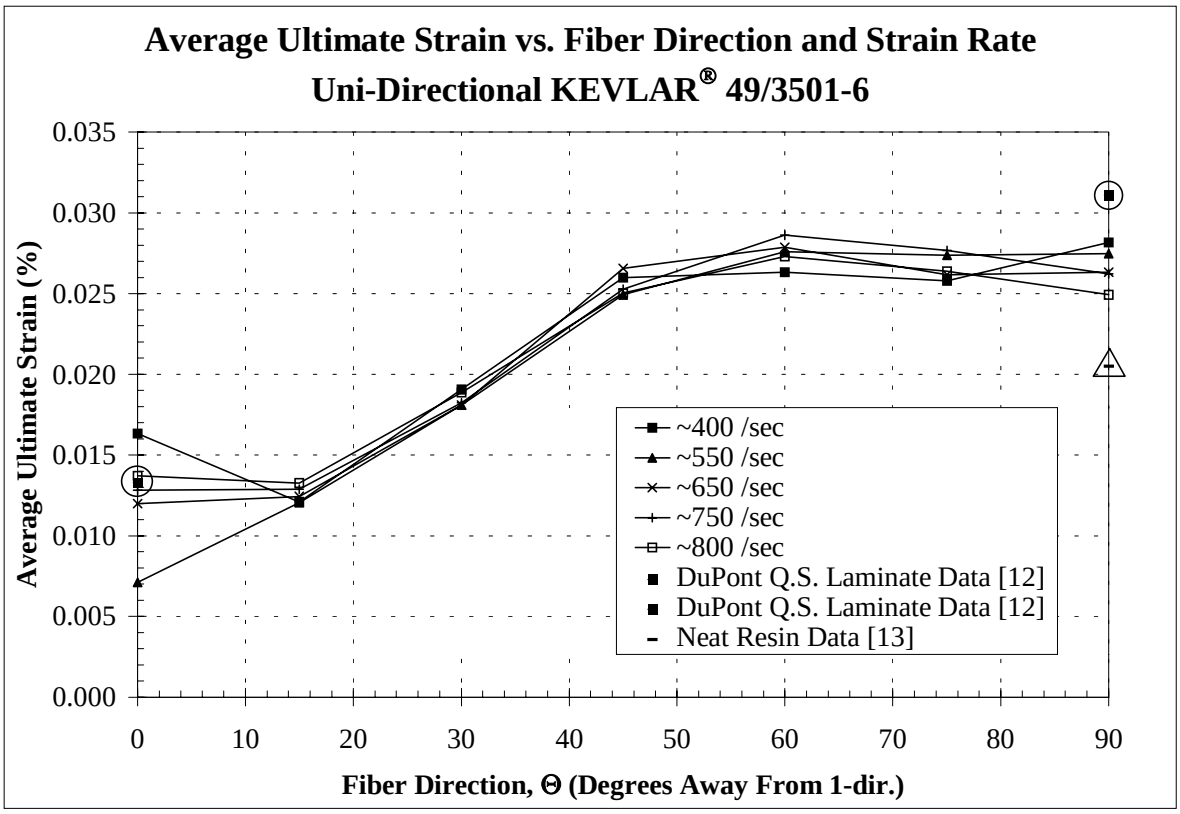

Figure 3: UD Average Ultimate Strain vs. Fiber Direction and Strain Rate

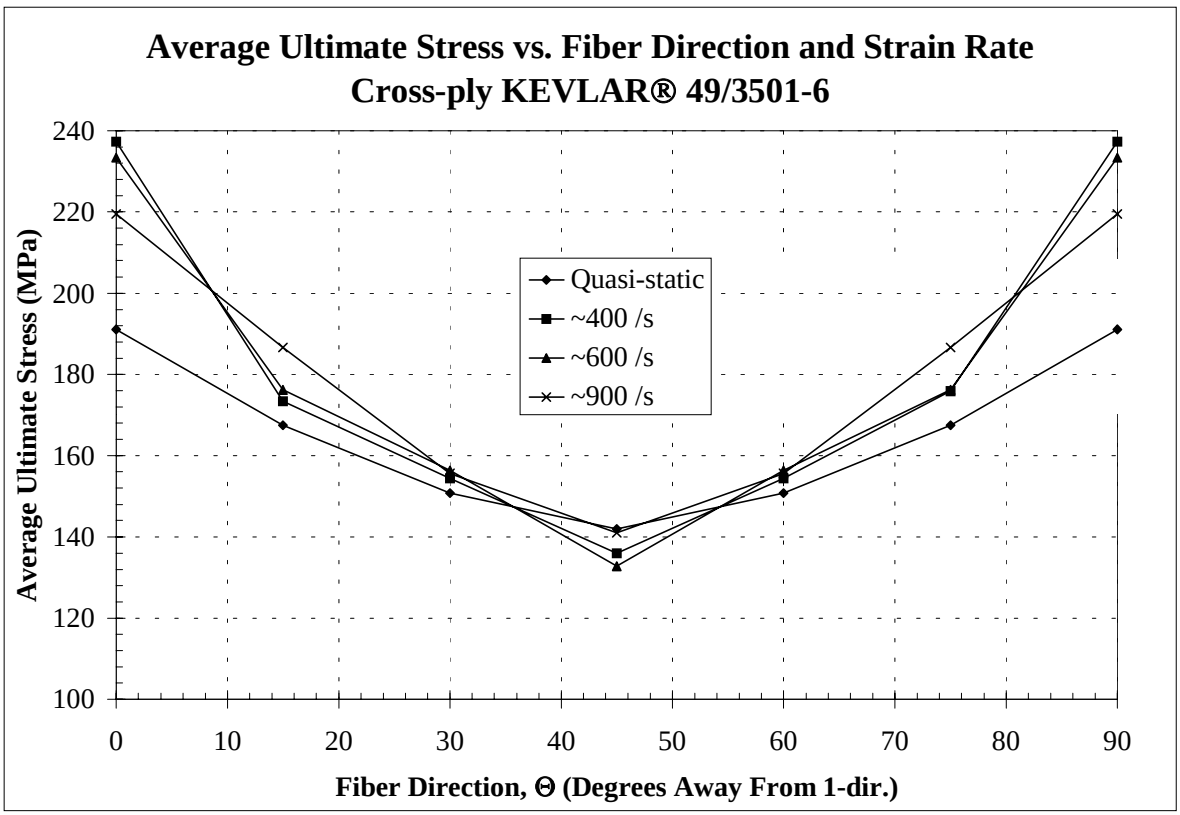

Figure 4: XP Average Ultimate Stress vs. Fiber Direction and Strain Rate

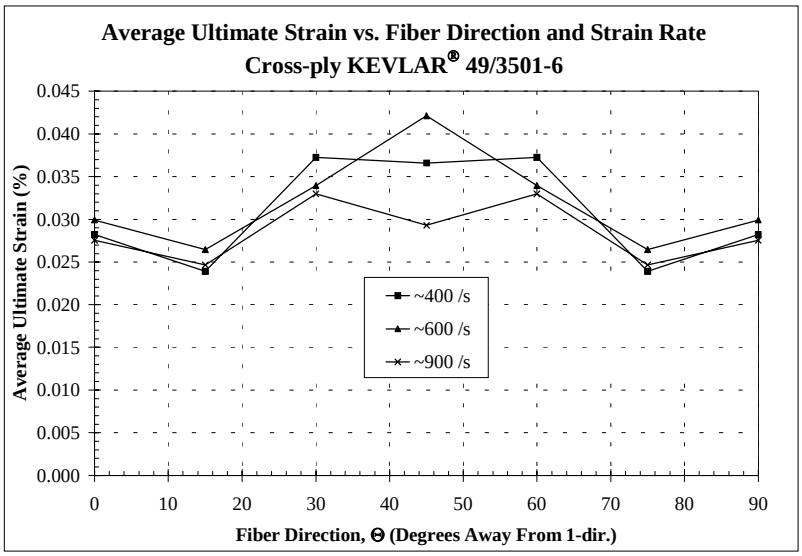

Figure 5: XP Average Ultimate Strain vs. Fiber Direction and Strain Rate

CONCLUSIONS

As expected, changing the fiber orientation angle with respect to the test direction changes the values of the ultimate stress and strain of the K-49/3501-6 KEVLAR®/Epoxy composites. Increasing the off-axis angle reduces the reinforcing effectiveness of the fiber, decreasing the composite's ultimate stress and increasing the failure strain. This effect is mitigated somewhat in the XP laminate due to more isotropic nature inherent in an XP lay-up.

The lay-up of the material influences the resulting material properties. While the UD material is stronger in the 1-direction than the XP material (~300 MPa compared to ~220 MPa), the XP material's ultimate stress suffers less of a reduction as the off-axis angle is increased. The UD material decreases from a stress of ~300 MPa at $\Theta = 0$ degrees to a stress of ~120 MPa at $\Theta = 45$ degrees, a reduction of 60%. The XP material decreases from a stress of ~220 MPa at $\Theta = 0$ degrees to a stress of ~135 MPa at $\Theta = 45$ degrees, a reduction of only 40%. Additionally, while the UD ultimate stress remains essentially constant for $\Theta > 45$ degrees, the XP ultimate stress returns to the higher values for $\Theta > 45$ degrees.

The results seem to indicate that, in compression, the KEVLAR® fiber is possibly strain rate sensitive, but that the 3501-6 epoxy matrix is not. This is supported by the result that, for both the UD and XP material, tests for the 1-direction show a noticeable increase in ultimate stress with increasing strain rate, but with a rapid return to the nominal quasi-static values for $\Theta \geq 15$ degrees.

The ultimate failure strain for both the UD and the XP material seem to be strain rate insensitive. At $\Theta = 45$ degrees, the XP material does show a significant amount of variation in the data, but the small statistical database makes it difficult to determine whether this is just data scatter or a material effect.

The statistical correlation of the data is very good, despite the small number of individual tests within each test series. This is shown by the fact that for ultimate stress, in a total of 65 test series performed for this research, 34 have coefficients of variation under 5%, 24 have

coefficients of variation between 5% and 10%, three have coefficients of variation between 10% and 20%, and only four have coefficients of variation greater than 20%

REFERENCES

1. Powers, B.M. and J.R. Vinson, “High-strain-rate Effects in Materials in Sandwich Construction”, *Sandwich Construction, 3rd Ed.*, Allen, H.G., Ed., Engineering Materials Advisory Services, Ltd., England, 1996, pp. 769-778.
2. Powers, B.M., J.R. Vinson, I.W. Hall, and V. Nardone, "High-strain-rate Mechanical Properties of Silicon Carbide Reinforced 2080 Aluminum Metal Matrix Composites", *Proceedings of the 10th International Conference on Composite Materials*, 1995, pp. 317-322.
3. Powers, B.M. and J.R. Vinson, "High-strain-rate Mechanical Properties of IM7/8551-7 Graphite Epoxy", *Proceedings of the 10th Technical Conference of the American Society for Composites*, 1995, pp. 227-238.
4. Powers, B.M., J.R. Vinson, M. Wardle, and B. Scott, "High-strain-rate Effects on Two AS4 Graphite Fiber Polymer Matrix Composites", *ASME Aerospace Division Bound Volume AD-48, High-strain-rate Effects on Polymer, Metal, and Ceramic Matrix Composites and Other Advanced Materials*, 1995, pp. 179-189.
5. Powers, B.M., J.R. Vinson, I.W. Hall and R.F. Hubbard, "High-strain-rate Mechanical Properties of Cycom 5920/1583", *36th AIAA/ASME/ASCE/AHS/ASC Structures, Structural Dynamics, and Materials Conference Collection of Technical Papers, v4*, 1995, AIAA, New York, NY, pp. 2386-2392.
6. Powers, B.M., J.R. Vinson, M. Wardle, and B. Scott, "High-strain-rate Effects on Two Graphite Fiber K3B Polyimide Matrix Composites", *Proceedings of the 37th AIAA/ASME/ASCE/AHS/ASC Structures, Structural Dynamics, and Materials Conference*, 1996, pp. 30-38.
7. Kolsky, H., "An investigation of the Mechanical Properties of Materials at Very High Rates of Loading", *Proc. Phys. Soc. B.*, No. 62, 1949, pp. 676-701.
8. Zukas, J. (ed.), *Impact Dynamics*, John Wiley and Sons, New York, N.Y., 1982.
9. Woldesenbet, E. and J.R. Vinson, "Effect of Specimen Geometry in High-strain-rate Testing of Graphite/Epoxy Composites", to be presented at the *38th AIAA/ASME/ASCE/AHS/ASC Structures, Structural Dynamics, and Materials Conference*, 1997.
10. Preissner, E., Woldesenbet, E., and Vinson, J.R., “High-strain-rate Compression Testing of K-49/3501-6 KEVLAR®/Epoxy Composites”, to be presented at the *38th AIAA/ASME/ASCE/AHS/ASC Structures, Structural Dynamics, and Materials Conference*, 1997.
11. Anonymous, *Data Manual for KEVLAR® 49 Aramid*, DuPont Technical Information, 1986, pp. 29-32.
12. Crasto, A.S., Kim, R.Y., and Whitney, J.M., “Advanced Laminate Compression Strengths From a Novel Sandwich Test Specimen”, *Proceedings of the 32nd AIAA/ASME/ASCE/AHS/ASC Structures, Structural Dynamics, and Materials Conference*, 1991, pg. 14.

ANALYTICAL MODEL FOR PREDICTION OF MICROBUCKLING INITIATION IN COMPOSITE LAMINATES

Pierre J. Berbinau and Ernest G. Wolff

Department of Mechanical Engineering, Oregon State University, Corvallis, OR 97331, USA

SUMMARY: In order to model the initiation of failure modes arising from static compression loading of multidirectional composites, namely kinking and free-edge delamination, we have developed a theory that predicts analytically the interlaminar shear stresses τ_{zx} and τ_{zy}. We then incorporate these shear stresses into a model of the influence of adjacent angled plies on the microbuckling and kinking of fibers in 0° plies. This leads to a general prediction of the compressive failure strains of multidirectional composite laminates. Experimental verification is described, which uses an AS4/PPS thermoplastic composite with the generic layup $[\theta/-\theta/0_2/\theta/-\theta/0]_s$ with θ varying between 10° and 90°. The theory is in good qualitative and quantitative agreement with experimental results, and explains the order of occurrence of the various failure modes.

KEYWORDS: microbuckling, kinking, interlaminar stresses, free-edge stresses, compression, laminates, modeling

INTRODUCTION

It is well-known that in-plane kinking, starting at the sample edges, is the primary failure mode of unidirectional high fiber volume fraction composites, and the initial failure mode of multidirectional composites [1-10]. To our knowledge, only five attempts have been made to model the compression behavior of non-unidirectional composites: cross-ply [11], angle-ply [12], and multidirectional composites [13-15]. None of these consider free-edge stresses. We contend that these stresses play a major role in the in-plane kinking of 0° fibers since experiments show that in-plane kinking starts at the edges [8], [16-18]. (Out-of-plane microbuckling can also occur depending on lateral constrains [19] and in cross-ply laminates [20]). We assume that for unnotched laminates, the failure of a 0° ply triggers failure in the remaining plies, especially for laminates containing significant percentages of 0° plies (note 43% of 0° plies in our experiments). Previous work [17] suggested an influence of the angle θ if plies adjacent to the 0° plies on the microbuckling strain of the latter. Among the interlaminar stresses σ_z, τ_{zx} and τ_{zy}, only the shear stresses could have an influence on the in-plane movement of the 0° fibers. This is a reasonable assumption because σ_z is normal to the movement of the 0° fibers when they buckle in-plane and should not affect their in-plane motion. FEA studies on composites show that interlaminar stresses are zero in the central portion of the specimen and become significant only in a thin boundary layer near the edges where they display exponential behavior [21-24]. Calculation of these interlaminar stresses for any layup is required. We shall then incorporate these stresses into a general microbuckling equation for a 0° fiber located at the edge of a 0° ply. A criterion governing

fiber failure is described and compared to other possible failure mechanisms, such as matrix or interlaminar failures. This enables the observed failure strains to be related to the predicted failure modes.

THEORY

Interlaminar Edge Stresses

It is seen that we need to calculate analytically the interlaminar stresses, especially their magnitude at the free edges. This is not readily done with FEA due to mesh sensitivity [24]. The work of Puppo and Evensen [25] suggests a useful approach, although their original theory applied only to a 4-layer symmetrical laminate in tension. Extension to an arbitrary number of layers requires modification of the equilibrium equations. We adopt the equivalent ply construction of [25]. A ply is replaced by a central anisotropic layer surrounded by layers of the matrix material. The thickness e of the latter is estimated from microscopy to be on the order of a fiber diameter. These matrix layers carry the interlaminar stresses. We consider a symmetrical laminate of 2N plies. A given ply k ($1 <= k < N$) has a thickness h_k and its fibers make an angle θ_k with the loading direction x. The width direction is y and the thickness direction is z. The plate has a width Wi and a length L. Modification of the equilibrium equations of [25] is described in detail in [27]. The initial solution is made for the case of an infinitely wide laminate under uniform compression. We then superimpose the solution for a laminate under no compression but subjected to normal (p_k) and shear stresses (t_k) at the edges (based on stresses at $y = \pm Wi/2$ and the new boundary conditions). Displacement solutions of the form $u_k(y) = A \cdot e^{ry}$ are chosen since the solution is independent of x. The final expressions for the interlaminar shear stresses have the form [27]:

$$\begin{cases} \tau_{zx}^{(k)}(y, u_a) = \dfrac{G_m}{2e} \displaystyle\sum_{i=1}^{2N-2} A_i^{(1)} \cdot \left(FacA_i^{(k)} - FacA_i^{(k+1)} \right) sinh\left(\sqrt{\rho_i}\, y \right) \\ \tau_{zy}^{(k)}(y, u_a) = \dfrac{G_m}{2e} \displaystyle\sum_{i=1}^{2N-2} A_i^{(1)} \cdot \left(FacB_i^{(k)} - FacA_i^{(k+1)} \right) sinh\left(\sqrt{\rho_i}\, y \right) \end{cases} \quad \text{for } 1 \le k \le N\text{-}1 \quad (1)$$

where G_m is the matrix shear modulus, at an interface (k) between plies (k) and (k+1). The coefficients $\left\{ A_i^{(1)} \right\}_{1 \le i \le 2N-2}$ are a linear function of the applied displacement u_a. Laminates that contain only 0° and 90° plies have to be treated separately due to the decoupling of the equilibrium equations. In this case [27]:

$$\begin{cases} \tau_{zx}^{(k)}(y, u_a) \equiv 0 \\ \tau_{zy}^{(k)}(y, u_a) = \dfrac{G_m}{2e} \displaystyle\sum_{i=1}^{N-1} B_i^{(1)} \cdot \left(FacB_i^{(k)} - FacB_i^{(k+1)} \right) sinh\left(\sqrt{\rho_{i+N-1}}\, y \right) \end{cases} \quad \text{for } 1 \le k \le N\text{-}1 \quad (2)$$

The coefficients $\left\{ B_i^{(1)} \right\}_{1 \le i \le N-1}$ are a linear function of the applied displacement u_a.

Microbuckling of 0° Fibers

The next step is to incorporate the action of the adjacent angled plies (by means of interlaminar shear stresses) on the 0° plies and derive a general microbuckling equation for the 0° fibers. We consider general buckling for a beam on foundation. Both the fiber and the foundation are modeled as linear elastic isotropic materials. The medium surrounding the fiber may act on it in three ways: ① through a distributed couple m, ② through a distributed axial force p in the fiber direction, ③ through a distributed transverse force q normal to the fiber. It is assumed that the fiber has (before loading) the shape of a sine function $v_0(x)$ of amplitude V_0 and wavelength λ_0. Assuming small deflections v(x), we obtain the fiber equilibrium equation:

$$E_f I \frac{d^4(v - v_0)}{dx^4} + q + \frac{dm}{dx} + P\frac{d^2 v}{dx^2} = 0 \qquad (3)$$

where P is the loading force, E_f the fiber stiffness and I its moment of inertia. The next step consists in assessing the quantities m and q. Since fibers deform in the shear mode, we have:

$$m = -A_f G \frac{d(v - v_0)}{dx} = -A_f \frac{G_m}{1 - V_f} \frac{d(v - v_0)}{dx} \qquad (4)$$

where A_f is the fiber cross-section area and V_f the fiber volume fraction. Now interlaminar shear stresses τ_{zy} will develop at the interface between a 0° ply and an adjacent angled-ply, in the interlaminar matrix region of thickness 2e. They will tend to push the fiber along the y direction. Because τ_{zy} varies with y, the half of the fibers closest to the edge will be submitted to a distributed force different from the one experienced by the half of the fiber further away from the edge. The normal force q on the fiber has therefore a magnitude:

$$2r_f\left\{\tau_{zy}\left(y = \frac{Wi}{2}\right) - \tau_{zy}\left(y = \frac{Wi}{2} - 2v\right)\right\} \approx 2r_f\left\{\left[\frac{d\tau_{zy}}{dy}\right]_{\frac{Wi}{2}}\right\} \cdot 2v \qquad (5)$$

The microbuckling equation (3) becomes therefore:

$$E_f I \frac{d^4(v - v_0)}{dx^4} - 2(2r_f)\left[\frac{d\tau_{zy}}{dy}\right]_{\frac{Wi}{2}} v - A_f \frac{G_m}{1 - V_f} \frac{d^2(v - v_0)}{dx^2} + \frac{A_f}{V_f}\left|\sigma_{0°ply}\right| \frac{d^2 v}{dx^2} = 0 \qquad (6)$$

As a first approximation, we may consider that the shear stress τ_{zx} has no significant effect on the microbuckling of 0° fibers. Indeed, this stress is uniformly distributed on the fiber but in the loading direction, so its effect cancels out globally.

The solution to the homogeneous differential equation (6) is sinusoidal. Solving for the amplitude V and taking into account the edge position of the fibers, we obtain:

$$V(u_a,\theta_k)=\frac{V_0}{1-\dfrac{\dfrac{A_f}{V_f}\left|\sigma_{0^\circ ply}(u_a)\right|+2(2r_f)\cdot\left[\dfrac{d\tau_{zy}(u_a,\theta_k)}{dy}\right]_{\frac{Wi}{2}}\left(\dfrac{\lambda_0}{\pi}\right)^2}{E_f I\left(\dfrac{\pi}{\lambda_0}\right)^2+(0.6)\,A_f\dfrac{G_m}{1-V_f}}} \tag{7}$$

Fiber failure

Failure will occur when the tensile strain in the fiber ε_f reaches the fiber failure strain in tension ε_{tf}. The maximum tensile strain in the fiber occurs at the fiber surface. The criterion for fiber failure is:

$$\varepsilon_f=-\frac{\left|\sigma_{0^\circ ply}\right|}{V_f E_f}+r_f\left(\frac{\pi}{\lambda_0}\right)^2(V)=\varepsilon_{tf} \tag{8}$$

where V is given by (7). Eqn 8 will yield a value for the critical applied displacement u_a. Dividing u_a by L will then give us the failure strain $\varepsilon_{failure}$.

Matrix Failure

Failure of the matrix may occur in two modes: interlaminar failure due to the interlaminar stresses, and failure within a 0° ply due to shear stresses that develop in-between 0° fibers as a result of their in-phase buckling. For interlaminar shear failure, we choose a quadratic criterion:

$$\sqrt{\left(\tau_{zy}\left(\frac{Wi}{2},u_a\right)\right)^2+\left(\tau_{zx}\left(\frac{Wi}{2},u_a\right)\right)^2}=\tau_f \tag{9}$$

where τ_f is the shear failure strain of the matrix. Eqn 9 will yield a value for the critical applied displacement u_a. Dividing u_a by L will then give us the failure strain $\varepsilon_{failure}$. This failure criterion is not conservative because it does not include the interlaminar normal stress σ_z which could play a role if the layup sequence is such that σ_z is positive, that is, if it tends to peel off 0° plies from their neighboring plies. For in-ply shear failure, the acting stress is τ_{xy}, given by the relation:

$$max\left\{\tau_{xy}\right\}=G_m\cdot max\left\{\gamma_{xy}\right\}=G_m\cdot max\left\{\left[\frac{d(v-v_0)}{dx}\right]\right\} \tag{10}$$

The failure criterion will

$$G_m\left(\frac{\pi}{\lambda_0}\right)(V-V_0)=\tau_f \tag{11}$$

Eqn 11 will yield a value for the critical applied displacement u_a. Dividing u_a by L will then give us the failure strain $\varepsilon_{failure}$. We are now able to investigate analytically the failure in compression of a laminate $[\theta/-\theta/0_2/\theta/-\theta/0]_s$ as a function of the angle θ.

EXPERIMENTAL RESULTS

Composite plates with generic layups $[\theta/-\theta/0_2/\theta/-\theta/0]_s$ were compression molded at 320 °C at 0.85 MPa for 15 min from a roll of AS4 fiber/polyphenylene sulfide (PPS) prepregs. Untabbed samples (80 mm x 12.7 mm x 1.7 mm) were diamond machined from these plates for uniaxial compression testing in a Boeing modified ASTM D695 compression fixture. Specially manufactured jigs (similar to [20]) were used to clamp the top and bottom of the specimens to prevent crushing and brooming of the ends. Bolt torque of the compression fixture was close to zero and maintained at a uniform level to allow accurate comparisons between samples (see [28]). Strain gages were mounted on both sides of each specimen in the central gage region. The chosen gage length was calculated to prevent gross Euler buckling of the specimens and allow for positioning of the strain gages. An Instron 4505 compression tester was used to obtain load/deflection curves. Tests were performed at a loading speed of 0.05 mm/min. Specimens final failure was considered to coincide with the fibers microbuckling failure strain. This was justified by the fact that fully straight samples failed catastrophically.

The failure strains for all samples as a function of the angle θ are plotted in Figure 1 together with a fourth degree polynomial fitting curve as shown. The coefficient of determination R^2 is 0.88, thus confirming the existence of a minimum strain around $\theta = 20°$ and a maximum strain around $\theta = 60°$.

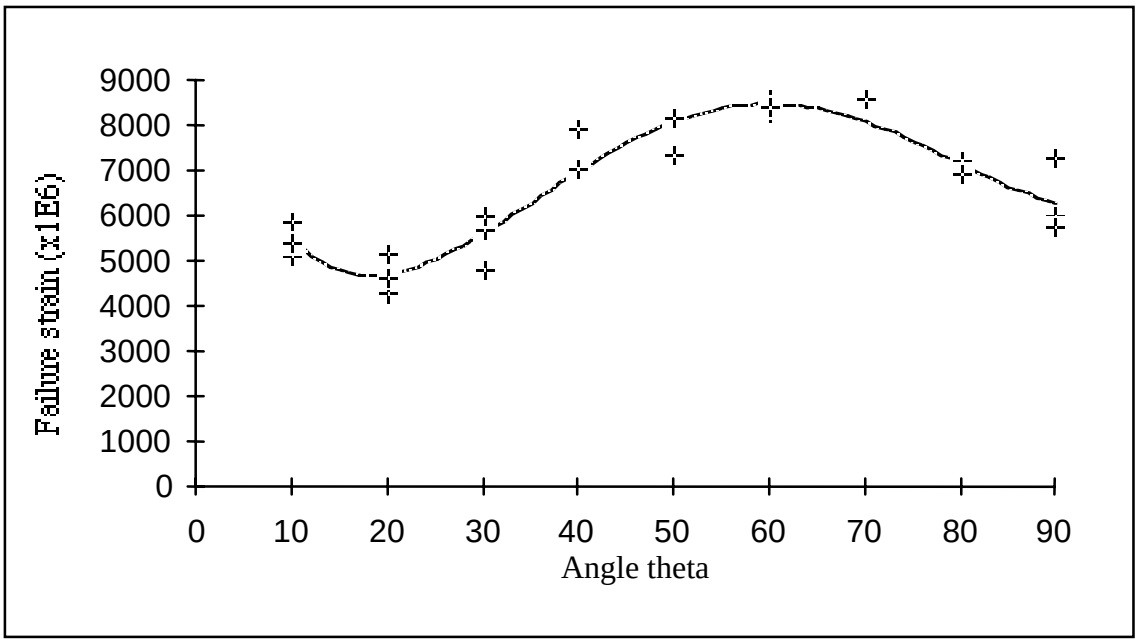

Fig. 1: Curve fit of experimental data

ANALYSIS

Parameter values used for analysis are summarized in Table 1.

Table 1: Parameter values

E_f (GPa)	E_m (GPa)	G_m (GPa)	τ_f (GPa)	ν_{12}	ε_{tf} (m/m)	r_f (μm)	e (μm)	V_f
214	3.4	1.3	80	0.3	0.014	3.5	12.3	0.6

The interlaminar stresses were calculated using the symbolic software package "Maple V" (Release 3). The shear stresses τ_{zx} and τ_{zy} were maximum at the edges. Figure 2 shows the variation of the amplitude of these stresses at the edge at the three (θ/0) interfaces. These are interfaces (2), (3) and (5), numbered from the top surface ply downward. The numbers in parentheses on Fig. 2 refer to the interface. Eqn 7 indicates that τ_{zy} promotes the microbuckling of all 0° fibers for all θ below 60°, while above 60° τ_{zy} hinders microbuckling. Figure 3 superimposes theoretical predictions on the data. Predictions are made for interface 2 in the $[\theta/-\theta/0_2/\theta/-\theta/0]_s$ layup, since interlaminar stresses are maximum there. The separate curves, numbered 1 to 5, refer to the following failure mechanisms: ① In-plane kinking (Eqn. 7), ② Out-of-plane kinking with full matrix support (Eqn. 15), ③ Out-of-plane kinking with reduced matrix support (Eqn. 16), ④ Interlaminar shear (Eqn. 9), and ⑤ In-ply matrix shear (Eqn. 11). Experimental results are indicated by cross-hairs. The predicted curve for in-plane kinking shows good agreement with experiment up to θ = 60°, while the out-of-plane kinking with reduced matrix support predicts the failure strains at θ greater than 60° (see paragraph below on out-of-plane microbuckling). The minimum strain at θ around 25° is a strong indication that shear stresses are the central mechanisms involved in the in-plane kinking of the edge fibers below 60°. The study of the curves showing matrix failure give some additional insight into the failure mechanisms taking place. We note that the curve predicting interlaminar failure is well above both the curve predicting fiber microbuckling and the test results. This implies that the microbuckling of the 0° fibers located at the edge, and consequently of the other 0° fibers, precedes interlaminar failure. We recall that interlaminar normal stresses σ_z were not taken into account in the failure criterion (Eqn 9), and consequently the strain for interlaminar failure predicted by our theory would in general be conservative. However the interlaminar failure strain must still be higher than the microbuckling failure strain because curves on Fig. 3 are in agreement with experiments with a similar layup [17] which showed that microbuckling was the initial failure mode.

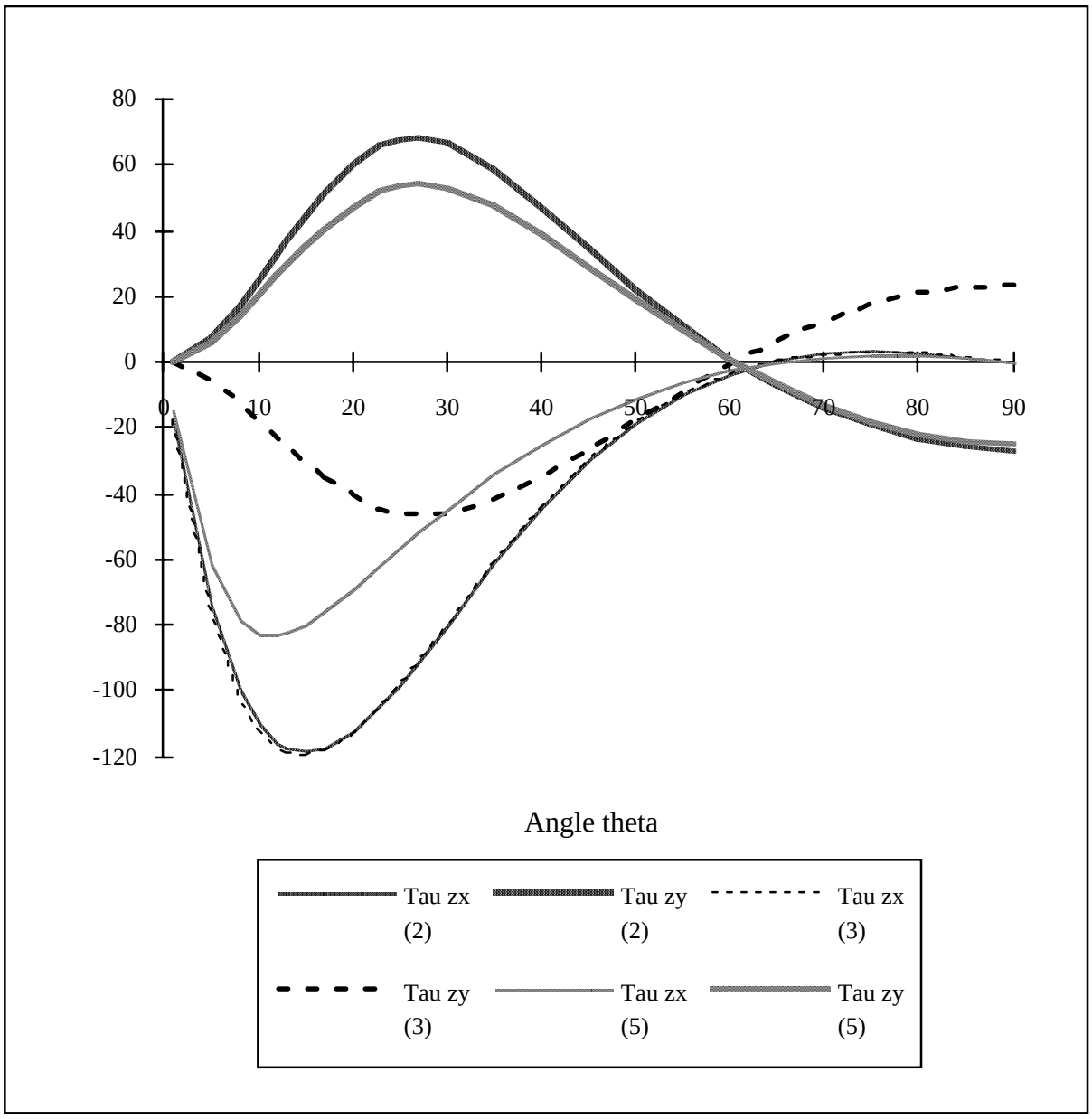

Fig. 2: Amplitude of interlaminar shear stresses at (θ/0) interfaces (2), (3) and (5)

The curve predicting shear failure of the matrix between fibers inside a 0° ply is, on the contrary, below the curve predicting fiber microbuckling and the tests results (except possibly above $\theta = 80°$ for the tests). This indicates that the matrix fails in shear in between the 0° fibers before these fail in bending. This is in agreement with previous experimental results which showed matrix cracking in between 0° fibers [19]. In fact, the fiber rotation that occurs in the

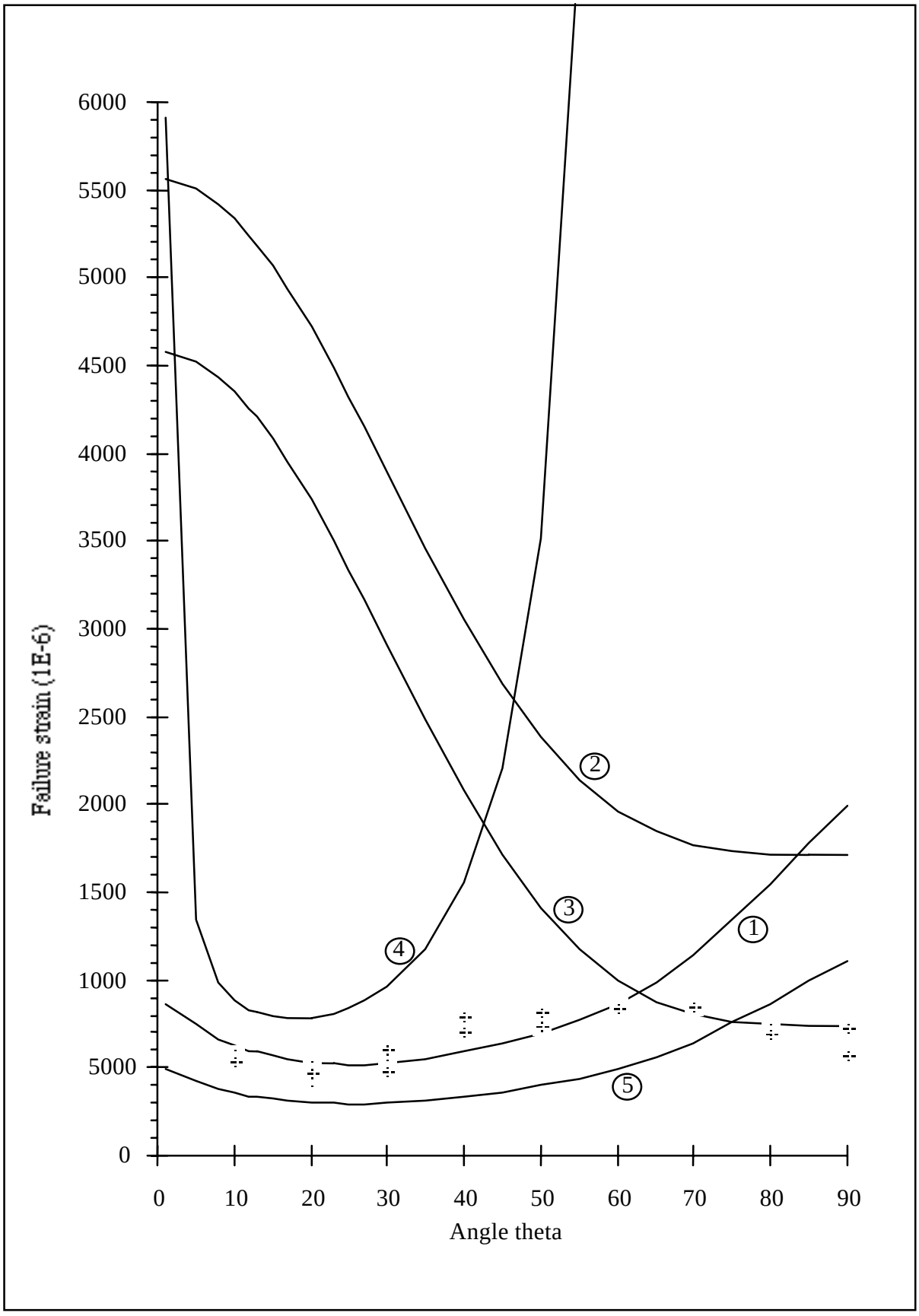

Fig. 3: Theoretical curves for failure strain vs. θ in $[\theta/-\theta/0_2/\theta/-\theta/0]_s$

later stage of microbuckling and during kinking [7] will cause plastic yielding of the matrix. Plasticity and non-linear shear behavior were not considered in this work because the matrix was modeled as linear elastic.

Out-of-Plane Buckling

There remains a discrepancy between the in-plane kinking prediction curves and experimental results at high angles, $\theta > 60°$. While the theory predicts a failure strain that keeps on increasing with θ, tests show a decrease in failure strain beyond $\theta = 60°$. Study of the sign of the interlaminar stress τ_{zy} [27] shows that above $\theta = 60°$ τ_{zy} and its derivative with respect to y are negative. The stress τ_{zy} thus tends to push the fibers toward the center of the specimen, and consequently to hinder the microbuckling of 0° fibers over the whole specimen width, the effect being more severe at the edges. We may therefore assume that the 0° fibers will then buckle out-of-plane, that is through the thickness (z direction). The intuitive argument behind this assumption is the following: the out-of-plane movement of the 0° fibers will cause bending of the surface (θ/-θ) plies. The resistance to the movement of the 0° fibers will thus be proportional to the bending stiffness of the surface (θ/-θ) plies. Because the bending stiffness of (θ/-θ) plies is minimum at θ=90° and increases as θ decreases to 0°, the out-of-plane buckling amplitude of a 0° fiber should decrease with θ and consequently the strain to failure $\varepsilon_{failure}$ should increase as θ decreases from 90°. Physically, we will also recall that out-of-plane kinking of 0° fibers had been observed in cross-ply composites [20], which is a clue that out-of-plane buckling could occur at angles θ close to 90°. In order to give a quantitative aspect to this analysis and prove that out-of-plane buckling is the favored failure mode at high angles θ, an estimation of the strain to failure due to out-of-plane buckling of the 0° fibers may be done as detailed below.

We model the surface plies (θ/-θ) as a cantilever beam of thickness (2·h), width Wi, and moment of inertia I_b that is subjected to a distributed lateral load q'. From the geometry of the loading and the top and bottom clamps, we consider that this beam has a length equal to g, where g is the distance between the clamps. The force q' is then [26]:

$$q'(\theta) = \frac{384\,\overline{Q}_{11}(\theta)\,I_b}{g^4}\cdot w \qquad (12)$$

Using Eqn 6 but substituting the out-of-plane amplitudes w and w_0 for v and v_0, and replacing q by q' as given by Eqn 12, we obtain the following out-of-plane microbuckling equation:

$$E_f I\frac{d^4(w-w_0)}{dx^4} + \frac{384\,\overline{Q}_{11}(\theta)\,I_b}{g^4}\cdot w - A_f\frac{G_m}{1-V_f}\frac{d^2(w-w_0)}{dx^2} + \frac{A_f}{V_f}\left|\sigma_{0°ply}\right|\frac{d^2w}{dx^2} = 0 \qquad (13)$$

We then derive the following relation between W, u_a, and θ, in the same way Eqn 7 for $V(u_a,\theta)$ had been obtained:

$$W(u_a,\theta)=\frac{W_0}{1-\dfrac{\dfrac{A_f}{V_f}\left|\sigma_{0°ply}(u_a)\right|-\dfrac{384\,\bar{Q}_{11}(\theta)\,I_b}{g^4}\left(\dfrac{\lambda_0}{\pi}\right)^2}{E_f I\left(\dfrac{\pi}{\lambda_0}\right)^2+A_f\dfrac{G_m}{1-V_f}}} \qquad (14)$$

Now the actual distributed force q' on one 0° fiber is actually less than q' given by Eqn 12. Indeed, we may expect that several and possibly all fibers along the width will buckle out-of-plane. The distributed force q' should therefore be divided by the number of rows of fibers buckling out-of-plane. On the other hand, we have not taken into account the additional resistance to buckling that arises from the fact that the (θ/-θ) surface plies are not isolated, but bound to the remaining plies by the matrix interlayers. This would contribute to an increase in the value of q'. We therefore introduce a correction coefficient C_{corr} in the expression for q', with $0 < C_{corr} < 1$. Eqn 14 becomes then:

$$W(u_a,\theta)=\frac{W_0}{1-\dfrac{\dfrac{A_f}{V_f}\left|\sigma_{0°ply}(u_a)\right|-C_{corr}\left(\dfrac{384\,\bar{Q}_{11}(\theta)\,I_b}{g^4}\right)\cdot\left(\dfrac{\lambda_0}{\pi}\right)^2}{E_f I\left(\dfrac{\pi}{\lambda_0}\right)^2+A_f\dfrac{G_m}{1-V_f}}} \qquad (15)$$

For a correction coefficient equal to 0.25, Eqn 15 yields predictions for the buckling strain which are well above experimental values in the angle range $\theta > 60°$, as shown on Fig. 3. This indicates that the matrix offers actually a less than ideal support to the buckling fibers. In any case the actual support from the matrix depends on the three dimensional stress field around the fibers, which cannot reasonably be computed, as well as on possible matrix yielding and cracking. We may therefore model the reduced matrix support by introducing a coefficient of reduction C_{red} and modifying Eqn 15 as follows:

$$W(u_a,\theta)=\frac{W_0}{1-\dfrac{\dfrac{A_f}{V_f}\left|\sigma_{0°ply}(u_a)\right|-C_{corr}\left(\dfrac{384\,\bar{Q}_{11}(\theta)\,I_b}{g^4}\right)\cdot\left(\dfrac{\lambda_0}{\pi}\right)^2}{E_f I\left(\dfrac{\pi}{\lambda_0}\right)^2+A_f\dfrac{G_m}{1-V_f}C_{red}}} \qquad (16)$$

Choosing C_{red} equal to 1/3 yields results in agreement with experimental values, as shown on Fig. 3.

CONCLUSIONS

The present work proposes a new theory for the prediction of compressive failure strains for multidirectional GFRP laminates. The theory (and its associated failure criterion) hinges on the in-plane microbuckling of the 0° fibers, but unlike previous attempts, it incorporates the influence of interlaminar shear stresses upon 0° fibers microbuckling. Such a modeling

approach is physically more sound as it takes into account experimental observation of critical microbuckling initiation at specimens edges. Good agreement between theoretical predictions and experimental results is obtained at low and intermediate angles (below 60°), and consequently it establishes the critical role played by interlaminar edge shear stresses in the failure process of multidirectional laminates. Modification of the theory to cover out-of-plane microbuckling of the 0° fibers reveals that out-of-plane microbuckling becomes the preferred failure mode at high angles (above 70°). The theory also predicts correctly that kinking occurs before interlaminar shear failure, and that the matrix in between the 0° fibers within a 0° ply would yield or crack before fiber failure in bending.

REFERENCES

[1] Soutis C., Composites Science & Technology 42, p.373 (1991)

[2] Bazhenov S., Kozey V., J. Materials Science 26 p.2677 (1991)

[3] Fleck N., Budiansky B., *Proceedings of the IUTAM Symposium on Inelastic Deformation of Composite Materials* , p.235 (1990).

[4] Evans A., Adler W., Acta Metallurgica 26, p.725 (1978)

[5] Hahn T., Williams J., ASTM STP 893, p.115 (1986)

[6] Weaver C., Williams J., J. Materials Science 10, p.1323 (1975)

[7] Moran P., Shih C., Soc. Engineering Science 32nd Meeting, p.383 (1995)

[8] Waas A.*et al.*, Int. J. Solids & Structures 26, n°9, p.1071 (1990)

[9] Effendi R., Barrau J., Guedra D., Composite Structures 31, n°2, p.87 (1995)

[10] Curtis P., Gates J., Molyneux C., Composites 22, n°5, p.363 (1991)

[11] Tadjbakhsh I., Wang Y., Int. J. Solids & Structures 29, n°24, p.3169 (1992)

[12] Shuart M., AIAA J. 27, n°9, p.1274 (1989)

[13] Swanson S., J. Engineering Materials & Technology 114, p.8 (1992)

[14] Shuart M., NASA Technical Memorandum 87640 (1985)

[15] Drapier S. *et al.*, J. Composites Science & Technology 56, p.861 (1996)

[16] Sohi M., Hahn H., Williams J., ASTM STP 937, p.37 (1987)

[17] Guynn E., Bradley W., Ochoa O., J. Composite Materials 26, p.1617 (1992)

[18] Wung E., Chaterjee S., J. Composite Materials 26, n°13, p.1885 (1992)

[19] Sutcliffe M., Fleck L., Acta Metallurgica et Materialia 42, n°7, p.2219 (1994)

[20] Kominar V. *et al.*, J. Materials Science 30, p.2620 (1995)

[21] Jones R., *Mechanics of Composite Materials*, p.210, Ed.Taylor & Francis (1975)

[22] Gu Q., Reddy J., Int. J. Non-linear Mechanics 27, n°1, p.27 (1992)

[23] Schellekens J., De Borst R., Composite Structures 28, p.357 (1994)

[24] Lessard L. *et al*, Int. J. Solids & Structures 33, n°15, p.2243 (1996)

[25] Puppo A., Evensen H., J. Composite Materials 4, p.204 (1970)

[26] Timoshenko S., Gere J., *Theory of Elastic Stability*, p.9-16, Ed. McGraw-Hill (1961)

[27] Berbinau P.J., Wolff E.G., submitted to J. Composite Materials (1997)

[28] Welsh J., Adams O., SAMPE J. 33, n°1, p.35 (1997)

FINITE ELEMENT MODELING OF THE HIGH STRAIN RATE BEHAVIOR OF S-2 GLASS/VINYL ESTER COMPOSITES UNDER COMPRESSIVE LOADING

Hassan Mahfuz, Bazle A. Gama, Roshan P. Raines and Shaik Jeelani

Tuskegee University's Center for Advanced Materials (T-CAM), Tuskegee University, Tuskegee, Alabama 36088, USA

SUMMARY: Transient dynamic Finite Element Analysis (FEA) of the high strain rate behavior of S-2 Glass/Vinyl Ester composites under compressive loading is performed at a maximum strain rate of 1700 s^{-1}. The stress propagation and distribution through the specimen with respect to time are presented. The stress contours show the distribution of stress through the specimen and also identify the location of maximum stresses. In the initial stage of loading, in the thickness direction, the FEA prediction of the stress-strain behavior correlates well with the experiment. However, for the fill direction loading the correlation is not as good. For both cases, the normal stresses in the thickness direction are found to be alternately compressive and tensile with respect to time. The interlaminer shear stresses also change their sign with time. This alternating nature of stresses with respect to time occurs much earlier in the case of fill direction loading. Experimental observation and FEA in the case of thickness direction loading show that compressive failure initiates at the transmission face of the specimen in the initial stage, which is followed by delamination in the later stage. During fill direction loading, however, fiber buckling, edge cracks and disintegration of the specimen have been observed to be the dominant failure modes.

KEYWORDS: finite element, high strain rate, S-2 glass, vinyl ester, compressive loading

INTRODUCTION

In recent years, composite structures subjected to high strain rate dynamic loading have become a subject of great interest to various defense and commercial industries. High strain loading may arise in different ways. High speed automotive crash, a flying bird's impact to an airplane wing, ballistic penetration and explosive shock impact to static and moving structures are a few examples. Due to the higher strength to weight ratio over metals, composite materials are being used more as structural materials, both in aerospace and defense industries. One such application is the Composite Armored Vehicle (CAV), which is being developed by the U.S. Army. The main load bearing component of the upper hull is the thick section S-2 Glass/Vinyl Ester which experiences shock loading in the event of a ballistic impact at the external ceramic layers. It is imperative that the procedures to test these materials at high strain rate be fully developed and their response be completely understood through analytical and experimental approaches.

Sufficient work has been done on high strain rate testing of metals [1, 2 and 3]; however, a limited amount of work has been done on high strain rate testing of composite materials [4, 5, 6, 7 and 8]. One of the pioneers of this field, Nemat-Nasser [9, 10 and 11], has developed several Hopkinson bar experimental techniques. The stress-reversal momentum trap version of the compression split Hopkinson bar allows dynamic recovery experiments. The development of the tension split Hopkinson bar, copper pulse shaping, and several gas gun systems for plate impact and penetration experiments are some of the achievements, along with analytical and numerical modeling. Staab and Gilat [6] have used a tensile version of the Hopkinson bar to measure the rate dependent response of angle ply S-2 Glass composites. Dandekar, Green and Beaulieu [8] studied the effect of S-2 Glass/Polyester composites specimen geometry in quasi-static and medium strain rates. They found failure strains of S-2 Glass reinforced plastics to be much higher in the thickness direction than in the fill direction. Leber and Lifshitz [12] designed a new type of specimen for the static and high strain rate interlaminer shear behavior of plain-weave fiber reinforced laminates. They used the torsion split Hopkinson bar for experiment and modeled the experiment with Finite Element Methods. They found that the E-Glass/Epoxy material exhibits high sensitivity to the loading rate in respect to shear modulus, fracture strength and strain. Other researchers [13 and 14] used DYNA3D to model the composite material subjected to impact and/or high strain rate loading and used their material model to analyze the failure.

HOPKINSON BAR EXPERIMENTS

The FEA is based on Hopkinson bar experiments performed at Tuskegee University's Center for Advanced Materials (T-CAM). The material used for the experiments is plain weave S-2 Glass/Vinyl Ester composite, fabricated using the SCRIMP process. Test specimens are 8.89 mm (0.35 inch) square in cross-section, 8.23 mm (0.324 inch) in thickness and have 12 layers along the thickness. The test apparatus is a compression split Hopkinson bar with a momentum trap. Its incident and transmitter bars are each 1.524 meters (5 feet) long, with a diameter of 19.05 mm (0.75 inch), used in conjunction with a 228.6 mm (9 inch) striker bar.

Two different loading conditions are used, one in the thickness direction and the other in the fill direction of the composite specimens. The average strain rate in the thickness direction was 850 s^{-1}, and that in the fill direction was 1280 s^{-1}. Figure 1 shows examples of experimental stress vs. strain curves for both loading conditions (two specimens for each condition). The initial moduli of elasticity shown in the figure are the average values from the two test specimens for the corresponding loading condition. For the fill direction loading these values are much higher than the through thickness loading. This can be attributed to the fact that the material response is matrix dominated through the thickness and fiber dominated in the fill direction. The through thickness direction loaded specimens sustained higher stresses (as much as 640 MPa) and failure strains (approximately 10%) compared to specimens loaded in the fill direction, with maximum stresses of approximately 345 MPa and failure strains of about 1%. Figure 2 shows corresponding stress vs. time curves for the same specimens. Here, the time span from initial loading to failure is much greater through the thickness than in the fill direction. Both figures show that the responses for the two loading conditions are distinctively different from each other, and specimens loaded under the same conditions follow the same basic pattern, showing good repeatability.

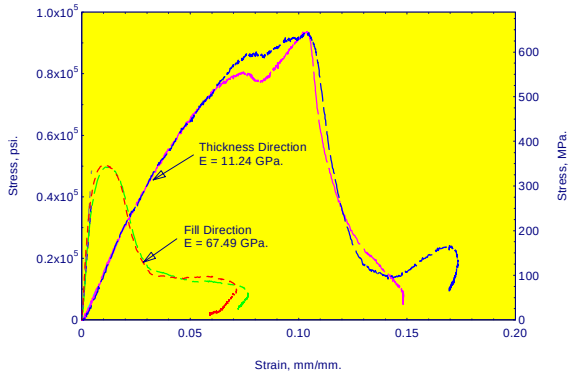

Fig. 1: Stress-Strain behavior of S-2 Glass/Vinyl Ester Composites

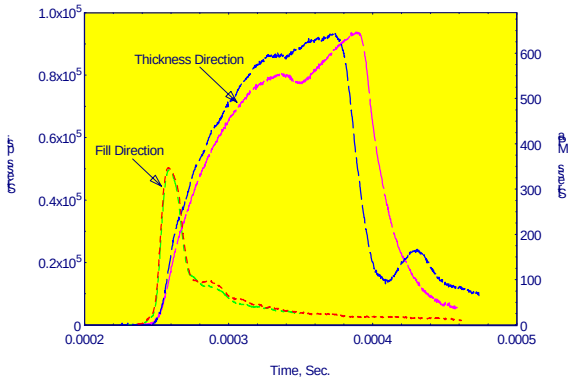

Fig. 2: Stress-Time curves for S-2 Glass/VinylEster Composite

Several specimens were tested to establish the baseline data for FEA. Figures 3 and 4 are the Scanning Electron Microscopy (SEM) micrographs for specimens loaded through the thickness and in the fill direction, respectively. These figures show that delamination due to interlaminar tension, and matrix cracks are the dominating failure modes in the through thickness loading. However, failure in the form of fiber buckling, edge cracks, matrix cracks and fiber breakage are dominant modes in the fill direction loading.

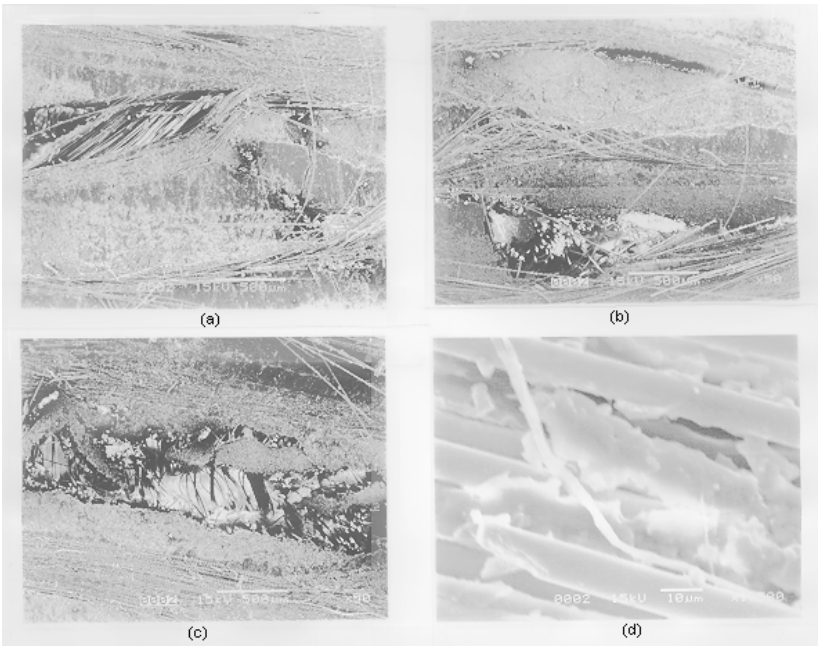

Fig. 3: SEM Micrographs for Loading in the Thickness Direction a) Matrix Crack b) & c) Delamination due to Interlaminaer Tension d) Matrix Crack

FINITE ELEMENT MODELING

In the current investigation, transient dynamic FEA is performed to model the high strain rate behavior of S-2 Glass/Vinyl Ester composites under compressive loading. Layered 3D solid elements (SOLID46) have been used to model the composite specimens. The element SOLID46 is based on the lamination theory, which considers the strain distribution in the thickness direction to be constant. Several elements through the thickness direction are employed in the FEA model to compensate for the non-linearity of strain along the thickness. Quasi-static properties of the laminate are used in the finite element program. The properties of the specimens, geometry, and FEA model are presented in Figure 5.

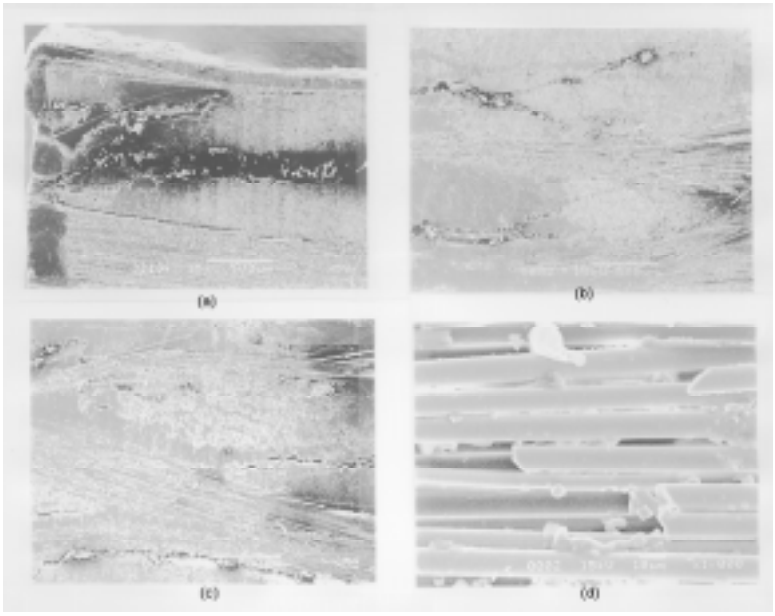

Fig. 4: SEM Micrographs for Loading in the Fill Direction a) Edge Crack b) & c) Matrix Crack d) Fiber Breakage

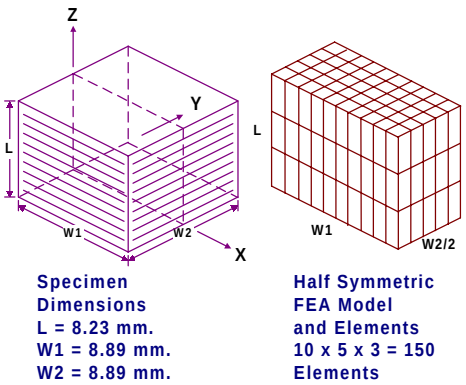

Quasi-Static Properties of S-2 Glass/Vinyl Ester
E_x = 20.2 GPa.
E_y = 20.2 GPa.
E_z = 8.62 GPa.
ν_{xy} = 0.273
ν_{yz} = 0.273
ν_{xz} = 0.273
G_{xy} = 7.93 GPa.
ρ = 1.75 gm/cc.

Fig. 5: Specimen Geometry, FEA model and Properties.

Time dependent loading similar to experiments is applied on the model as a distributed force on the loading surfaces. To simulate the experiment, the nodes on the surface of loading are coupled together to enforce equal displacement of all nodes on that surface. The displacement of the nodes opposite to the surface of loading is constrained in the direction of loading

RESULTS AND DISCUSSIONS

Loading in the Thickness Direction

Figure 6 shows the loading in the thickness direction. The comparison of the stress-strain response between experiment and FEA is presented in Figure 7. The FEA prediction of initial modulus is about 17% less than the experimental modulus. The correlation between experiment and FEA is good in the initial stage of loading. The FEA is unable to predict the post-yielding behavior of the material, because the stress calculation is based on linear elasticity.

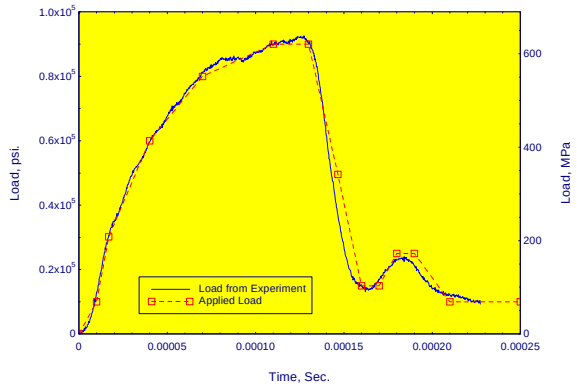

Fig. 6: Loading and Boundary Conditions, Thickness Direction.

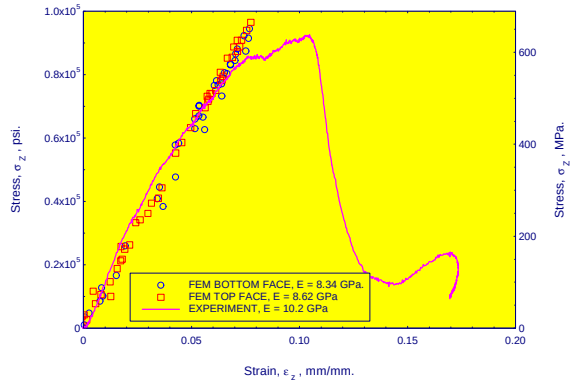

Fig. 7: Comparison of Stress-Strain Behavior between Experiment and FEA

The stress contours of the FEA model with respect to time have been analyzed to determine the location of maximum stresses. Contour plots of σ_z and τ_{xz} are presented in Figure 8, which show that the maximum σ_z occurs at X/W1 = 0.5 and the maximum τ_{xz} occurs at X/W1 = 0.3 and at 0.7 along the thickness. These locations are used to see the variation of different stresses with respect to time. The variation of σ_z (interlaminar normal stress) and τ_{xz} (interlaminar shear stress) with time are shown in figures 9 and 10 (at X/W1 = 0.5). The variation of σ_z is fluctuating in nature and becomes tensile at times 175.0×10^{-6} second and 230.0×10^{-6} second. Though the applied load was compressive, these interlaminar tensile stresses are tensile and may cause delamination in the specimen. Also, τ_{xz} changes its sign with time and becomes considerably high at times 175.0×10^{-6}, 205.0×10^{-6} and 230.0×10^{-6}

second. The interlaminar shear strength obtained through short beam shear test (ASTM D: 2344-84 (89)) is 27.66 MPa (4012 psi), which is more than twice the maximum τ_{xz} of 12.4 MPa. However, together with the interlaminar tensile stress, interlaminar shear stress can cause delamination and matrix crack opening.

The through thickness distributions of σ_z and τ_{xz} are plotted in Figures 11 and 12 at different time steps in the location of maximum interlaminar shear. In the initial stage of loading (at time 50.0×10^{-6} second), σ_z is compressive in nature, and the value is about 640 MPa at the bottom face of the specimen. From the experimental stress-time curve (Fig. 2), we can see that the failure stress is about 640 MPa at time 130.0×10^{-6} second. It is evident that the failure at the transmission (bottom) face initiates at 50.0×10^{-6} second and continues till 130.0×10^{-6} second. At time 175.0×10^{-6} second σ_z is tensile and is minimum (11.7 MPa) on the loading face and maximum (317 MPa) on the opposite face of the specimen. The tensile strength of the Vinyl Ester matrix is 69-82 MPa (10000-12000 psi). Therefore, matrix cracks and delamination will occur in the range of $0 < Z/L < 0.68$ along the thickness.

The τ_{xz} distribution shows two different peak locations, at Z/L = 0.33 and 0.67, which suggests that delamination is likely to occur at these locations. The maximum value of τ_{xz} (15.85 MPa) is much less than the interlaminar shear strength (27.66 MPa) of the specimen. However, τ_{xz} alone can not cause delamination. From this observation we conclude that compressive failure initiates at the bottom face of the specimen in the initial stage, followed by delamination in the later stages of loading

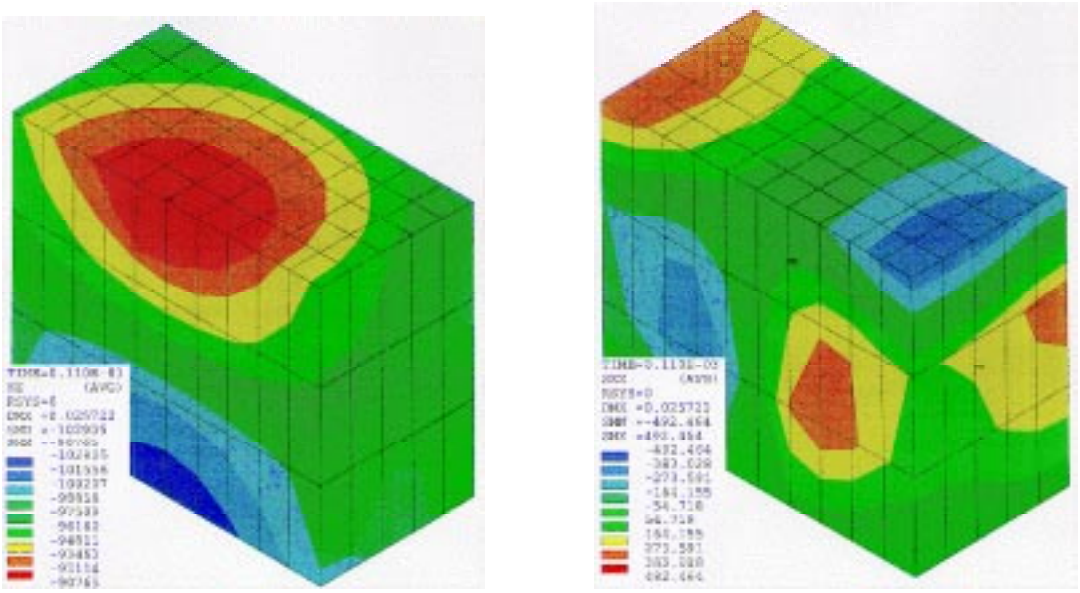

(a) (b)

Fig. 8: Contours of (a) Normal Stress (σ_z), (b) Interlaminar Shear Stress (τ_{xz})

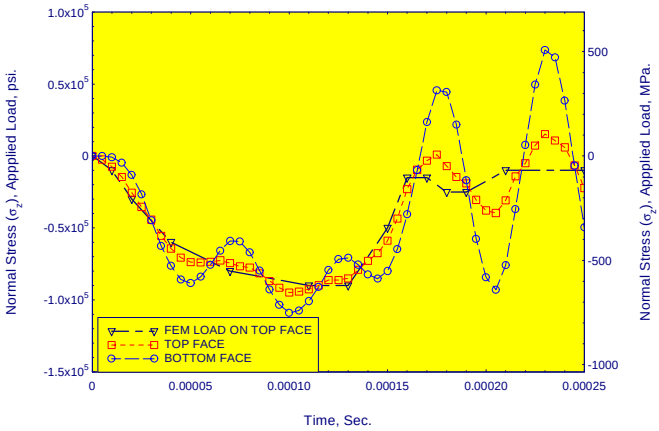

Fig. 9: Variation of Normal Stress (σ_z) *with Time*

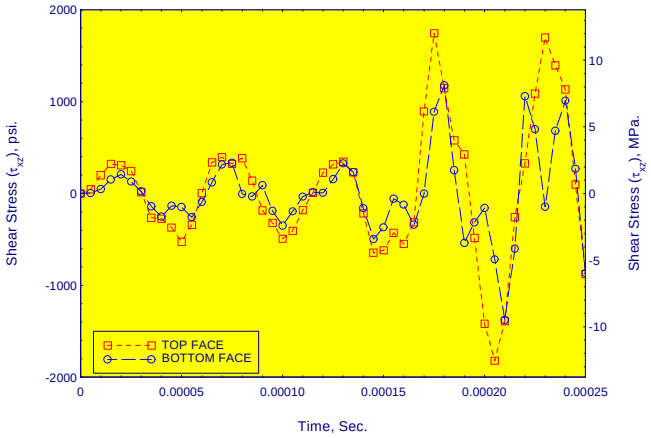

Fig. 10: Variation of Shear Stress (τ_{xz}) *with Time*

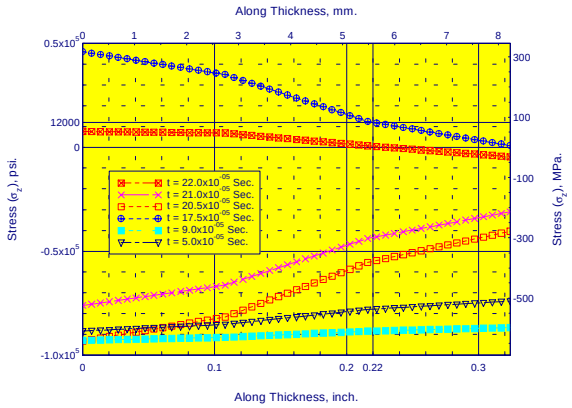

Fig. 11: Normal Stress (σ_z) *Distribution Along Thickness in Different Time Step*

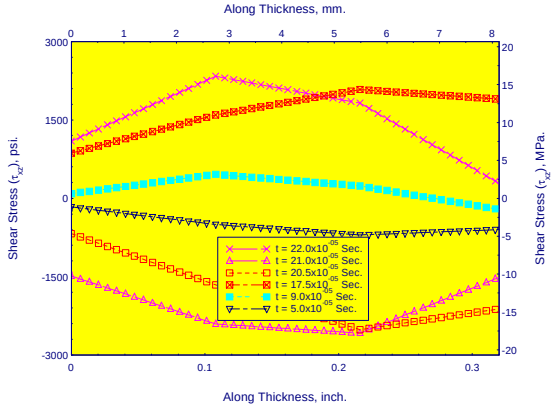

Fig. 12: Shear Stress (τ_{xz}) *Distribution Along Thickness in Different Time Step*

Loading in the Fill Direction

Figure 13 shows the loading in the fill direction. The comparison of the stress-strain response between experiment and FEA is presented in Figure 14. The FEA prediction of initial modulus is about 64% less than the experimental modulus. The correlation between experiment and FEA is not as good as in the case of the thickness direction loading. The reason for such discrepancy can be attributed to the fact that the constitutive equations used in the present investigation was limited to linear elasticity. During the pressure pulse loading one has to consider the separation of the thermodynamic response from the ability of the materials to convey shear loads. This calls for the modification of the constitutive equation and the equation of state. These modifications will be incorporated in future work.

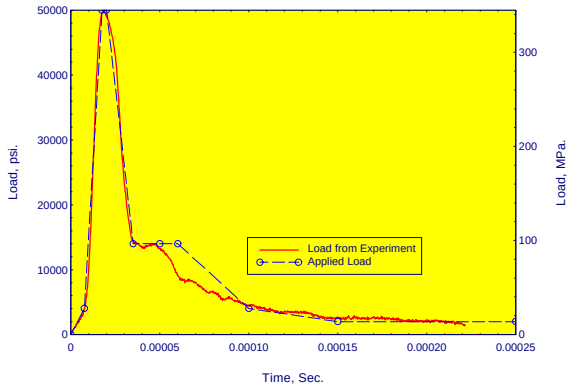

Fig. 13: Loading and Boundary Conditions, Fill Direction

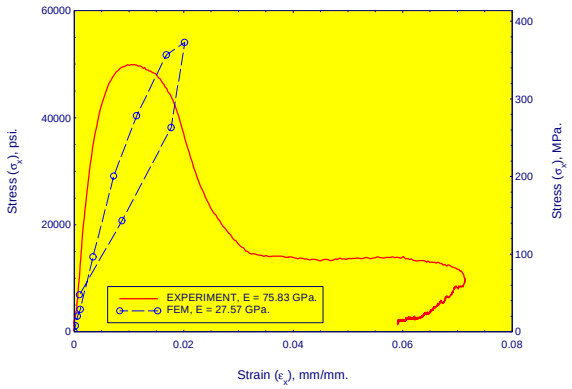

Fig. 14: Comparison of Stress-Strain Behavior between Experiment and FEA

Contour plots of σ_z and τ_{xz} at time 20.0x10^{-6} second are presented in Figure 15, which show that the maximum σ_z occur at Z/L = 0.33 and at 0.67, and the maximum τ_{xz} occurs at X/W1 = 0.7 along the thickness. These locations are used to see the variation of different stresses with respect to time.

The variation of σ_z (interlaminar normal stress) and τ_{xz} (interlaminar shear stress) with time are shown in figures 16 and 17 (at X/W1 = 0.5). The plot of σ_z indicates that from the early stage of loading it alternately becomes tensile and compressive. However, the maximum interlaminar tensile stress never exceeds 35 MPa. Compared to the tensile strength of the matrix (69-82 MPa) this interlaminar tensile stress will not cause delamination. Interlaminar shear stress, τ_{xz}, changes its sign with time from the very beginning. The maximum value is about 25 MPa. As compared to the experimental interlaminar shear strength of 27.66 MPa, the FEA prediction suggests no delamination. However, the repeated action of interlaminar tension and shear may cause stress concentration around any embedded flaw in the specimen and can cause delamination and matrix crack opening.

The through thickness distributions of σ_z and τ_{xz} are plotted in Figures 18 and 19 at different time steps in the location of maximum interlaminar shear. The locations of maximum interlaminar tensile stress are found to be at Z/L = 0.33 and 0.67. The maximum interlaminar tension (50 MPa) occurred at time 25.0x10^{-6} second. The plot of interlaminar shear stress, τ_{xz}, shows that the maximum shear stress (25 Mpa) occurs either at the incident (top) or transmission face of the specimen, which suggests that delamination and edge cracks may occur at these places. With the combined effect of interlaminar tensile and shear stress, the most possible locations for delamination are at Z/L = 0.33 and at 0.67.

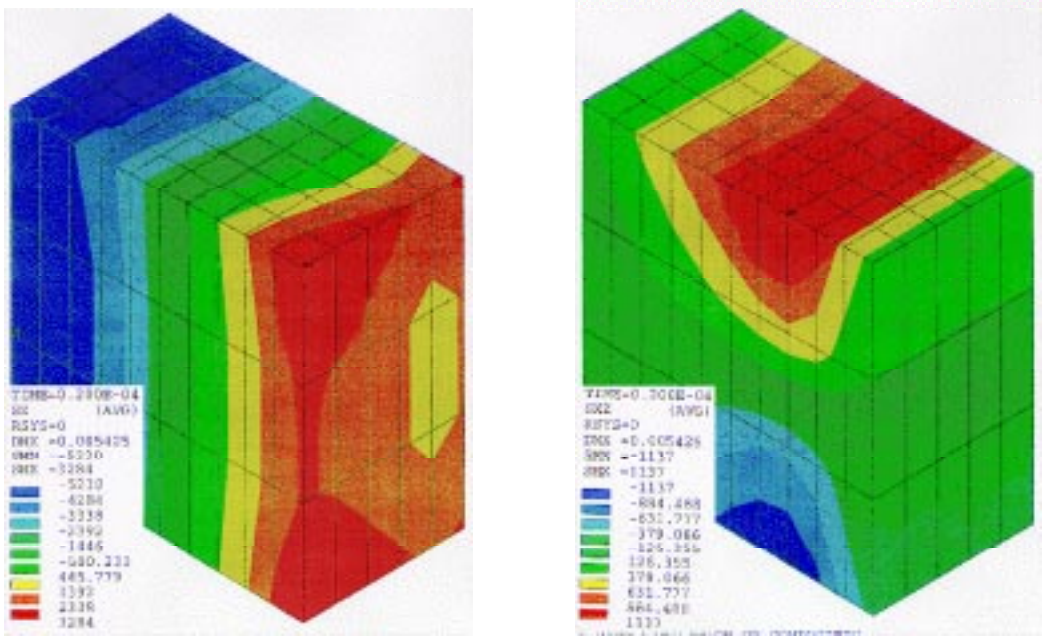

(a) (b)

Fig. 15: Contours of (a) Normal Stress (σ_z), (b) Interlaminar Shear Stress (τ_{xz})

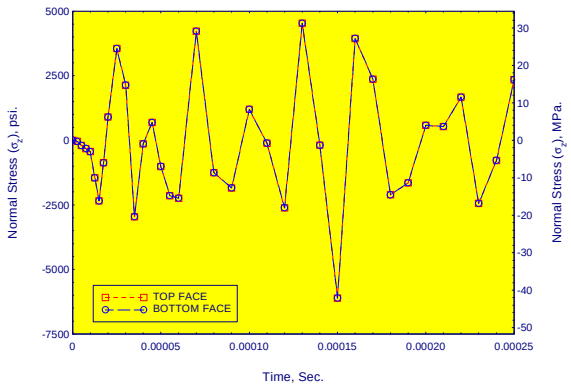

Fig. 16: Variation of Normal Stress (σ_z) *with Time*

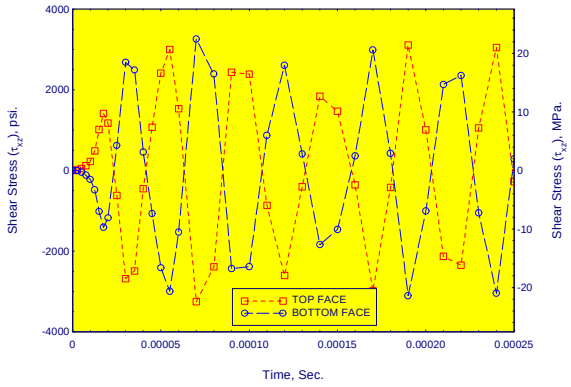

Fig. 17: Variation of Shear Stress (τ_{xz}) *with Time*

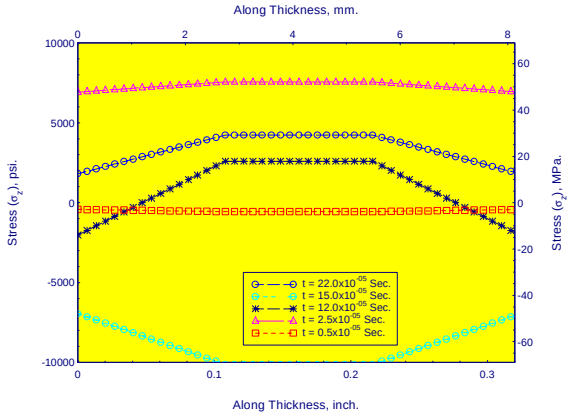

Fig. 18: Normal Stress (σ_z) *Distribution Along Thickness in Different Time Step*

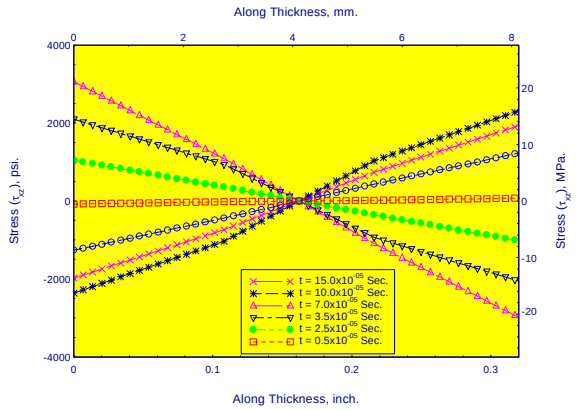

Fig. 19: Shear Stress (τ_{xz}) *Distribution Along Thickness in Different Time Step*

CONCLUSIONS

The following conclusions are made from the high strain rate experiment and modeling of S-2 Glass/Vinyl Ester composites.

- FEA can only predict the initial stage of high strain rate deformation of composites.
- The FEA stress-strain behavior correlates well with experiment in the case of thickness direction loading.
- Compressive failure initiates at the transmission face of the specimen in the initial stage, followed by delamination in the later stage of loading in the thickness direction.
- Delamination occurs due to interlaminar tension and repeated interlaminar shear in the initial stage of loading in the fill direction.
- Fiber buckling, edge cracks and disintegration of the specimen along the thickness are observed in the case of fill direction loading.

ACKNOWLEDGMENT

The financial support for this work provided by the Army Research Office (ARO), USA, is gratefully acknowledged

REFERENCES

1. Lankford, J., Conque, A., Bose, A. and Anderson, C.E., "Microstructure Dependence of High-Strain-Rate Deformation and Damage Development in Tungsten Heavy Alloys", *Shock-Wave and High-Strain-Rate Phenomena in Materials*, edited by M. Meyers, L. Murr, K. Staudhammer, Marcel Dekker, Inc., New York, 1992, pp. 137-145.
2. Gabelotaud, S., Nguy, C., Bensussan, P., Berveiller, M., and Lipinski P., "High-Strain-Rate Titanium Compression Experimental Results and Modelization", *Shock-Wave and*

High-Strain-Rate Phenomena in Materials, edited by M. Meyers, L. Murr, K. Staudhammer, , Marcel Dekker, Inc., New York, 1992, pp. 161-170.

3. Coates, R., Ramesh, K., "The Deformation of Tungsten Alloys at High Strain Rates", *Shock-Wave and High-Strain-Rate Phenomena in Materials*, edited by M. Meyers, L. Murr, K. Staudhammer, Marcel Dekker, Inc., New York, 1992, pp. 203-212.
4. Harding, J., "Mechanical Behavior of Composite Materials Under Impact Loading", *Shock-Wave and High-Strain-Rate Phenomena in Materials*, edited by M. Meyers, L. Murr, K. Staudhammer, Marcel Dekker, Inc., New York, 1992, pp. 21-34.
5. Newill, J. F. and Vinson, J. R., "Some High Strain Rate Effects on Composite Materials", *Proceedings of the Ninth International Conference on Composite Materials (ICCM9)*, Madrid, 12-16 July, 1993, pp. 269-277.
6. Staab, H. G. and Gilat, A., "High Strain Rate Characterization of Angle-Ply Glass/Epoxy Laminates", *Proceedings of the Ninth International Conference on Composite Materials (ICCM9)*, Volume V, 1993, pp. 278-285.
7. Harding, J. and Li, Y. L., "Determination of Interlaminar Shear Strength for Glass/Epoxy and Carbon/Epoxy at Impact Rates of Strain", *Composites Science and Technology*, 45, 1992, pp. 161-171.
8. Dandekar, D. P., Green, J. L. And Beaulieu, P., "Dynamic Characterization", *in Dynamic Response of S-2 Glass Reinforced Plastic Structural Armor*, A Progress Report, ARL-SR-5, Army Research Laboratory, December 1993, pp. 39-62.
9. Nemat-Nasser, S., Isaacs, J. B. And Starrett, J. E., "Hopkinson Techniques for Dynamic Recovery Experiments", *Proc. R. Soc. Lond.*, A, 1991, 435, pp. 371-391.
10. Nemat-Nasser, S., "New Frontiers in Dynamic Recovery Testing of Advanced Composites: Tailoring Microstructure for Optimal Performance", *JSME International Journal*, Series I, Vol. 34, No. 2, 1991, pp. 111-122.
11. Nemat-Nasser, S., " Dynamic Deformation and Failure", High Strain Rate Effects on Polymer, Metals and Ceramic Matrix Composites and Other Advanced Materials, Edited by Y. Rajapakse, J. Vinson, ASME, U.S.A, 1995, pp. 371-391.
12. Leber, H. and Lifshitz, J. M., "Interlaminar Shear Behavior of Plain-Weave GRP at Static and High Rates of Strain", *Composites Science and Technology*, 56, 1996, pp. 391-405.
13. Kerth, S. and Maier., "Numerical Simulation of the Crashing of Composite Tubes", *Computer Aided Design in Composite Material Technology IV*, Editors: Blain, W. R. and DeWilde, W. P., 1994, pp. 141-148.
14. Vinckier, D. and Thoma K., "Numerical Simulations High Velocity Impact Phenomena in Composite Structures", *Computer Aided Design in Composite Material Technology IV*, Editors: Blain, W. R. and DeWilde, W. P., 1994, pp. 183-190

DAMAGE DEVELOPMENT IN FILLED VISCOELASTIC MATRIX COMPOSITES

A. Meddad and B. Fisa

École Polytechnique de Montréal, Center for Applied Research on Polymers (CRASP)
Department of Mechanical Engineering, C.P. 6079, Montreal, Quebec, Canada, H3C 3A7

SUMMARY: This paper deals with the stress-strain behavior of two viscoelastic polymers, polypropylene and polyamide 6, filled with rigid particles in the range of axial strain of 0 to 8%. These materials, when subjected to a constant strain rate test lose stiffness via two mechanisms: filler-matrix debonding and the viscoelastic softening of the matrix. A model which combines the concepts of damage mechanics and the time dependence of the interfacial strength is described and compared to the experimental results of polypropylene and polyamide 6 filled with up to 50 *vol*.% of untreated and silane treated glass beads. The matrix behavior is described in terms of an empirical equation selected to fit the stress-strain behavior of neat polymers in the range of strain rates between 0.12 and 0.5% s^{-1} and strains between 0 and 8%. The stiffness of the damaged, partially debonded composite is calculated using the Kerner-Lewis equation assuming that debonded particles do not bear any load. The model is able to generate stress-strain curves which are in good agreement with the experimental data. The void volume attributable to debonding calculated using the model is much smaller than the experimental total determined void volume (which is a sum of several deformation mechanisms).

KEYWORDS: damage, interface, debonding, viscoelastic matrix

INTRODUCTION

When a second, rigid phase is dispersed in a polymer the most obvious effect is the substantial increase of the elastic (short term, small strain) stiffness. The effect on other properties is more complex to analyze. This is because, as a result of straining, the material properties change because of damage related to factors such as filler/matrix debonding but also due to the viscoelastic nature of the matrix. A number of attempts to model the debonding resulting from the tensile loading have been published (1). However, since only the rigid phase (the filler) is excluded from the load bearing as the debonding progresses, the material loses its stiffness not only from the reduction of the effective section but also from a reduction of the effective filler concentration in the remaining material [2,3].

This paper presents the model that can be used to calculate the stress-strain behavior of filled polymers, and to evaluate the debonding during the straining. The predicted results are compared to stress strain behavior of filled polypropylene and polyamide 6.

EXPERIMENTAL RESULTS

The materials investigated are polypropylene (PP) and polyamide 6 (PA6) filled with rigid particles (glass beads-GB, talc and calcium carbonate ($CaCO_3$). All the experimental details concerning the used, sample preparation and mechanical testing can be found in the previous paper [3].

Stress Versus Axial Strain Curves

Figure 1 shows the stress-strain curves of polypropylene and polypropylene filled with glass beads, talc and $CaCO_3$. In Table 1, the average values of several properties determined from the σ *vs* ε curves are listed: the initial modulus, E_0; the stress σ_0 and strain ε_0 at which the stress strain curve deviates from linearity; the stress and the strain at yield, (σ_y and ε_y).

The principal points of the experimental results are:

- All materials exhibit an elastic zone; the initial modulus E_o increases with the filler addition but is independent of the surface treatment for glass beads.
- The yield stress σ_y decreases with the filler addition: σ *vs* ε curves of all composites except those containing talc fall below that of neat PP well before yield.
- Both the stress and the strain at which the material ceases to be elastic (σ_0 and ε_0) decrease with filler addition. The values of σ_o and of ε_o are higher with treated beads.
- The platy irregular shape of talc particles leads to a definite reinforcing effect in PP, as evidenced by the high initial modulus and yield stress.
- Although the transition between the linear (elastic) stage and the constant stress plateau starts at a higher strain with treated beads the yield stress is independent of the surface treatment.
- The composite with talc (20 vol.%) broke at a relatively low axial strain of about 5%.

Filled polyamide 6 also has a linear zone at small strains and the initial modulus is unaffected by the surface treatment. Besides these similarities, there are significant differences between filled polypropylene and polyamide 6 filled with untreated beads, on the one hand, and polyamide 6 filled with treated beads (Fig. 2 and Table 1). With untreated beads, the curves fall below that of neat polyamide 6 but at higher strains than in filled polypropylene. The departure from linearity in untreated glass-polyamide 6 composites follows a similar pattern as in filled polypropylene i.e., the strain ε_0 decreases with increasing glass concentration. However, the stress σ_0 increases slowly with filler content. With treated glass, the strain ε_0 appears to be independent of the filler content. In fact, it is very close to the ε_0 value of the neat polyamide 6. The stress σ_0 increases substantially with the treated glass content. The stress-strain curves of polyamide 6 composites containing treated beads remain above the neat polyamide 6 curve.

Table 1:Summary of tensile properties of filled polypropylene GB: glass beads (T: treated beads)

Polymer-filler-*vol.%*	**E_0 (GPa)**	**ε_0 (%)**	**σ_0 (MPa)**	**ε_y (%)**	**σ_y (MPa)**
PP	1.57	0.75	11.9	7	32
PP-GB-20	2.4	0.30	7.3	4	22
PP-GB-20T	2.4	0.37	9.0	4	22
PP-Talc-20	4.96	0.24	11.9	2.4	30.7
PP-$CaCO_3$-20	3.1	0.20	6.2	2.9	22.7
PA6	0.92	0.73	6.8	2.7	18
PA6-GB-25	1.9	0.40	7.3	2.3	21
PA6-GB-25T	1.9	0.71	13.6	1.20	18

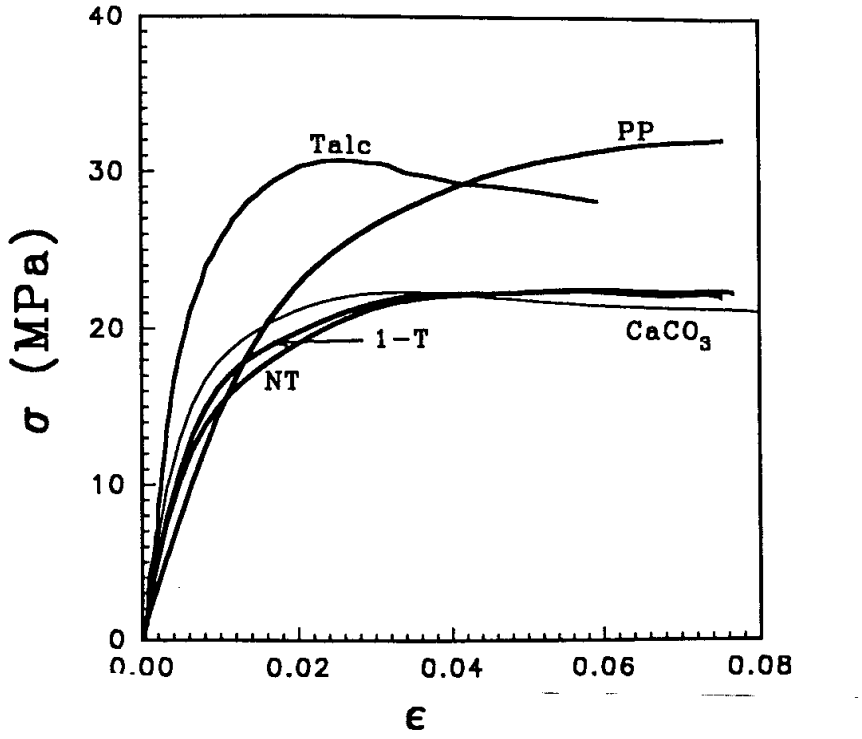

Fig. 1: Stress σ vs axial strain ε curves of PP filled with 20 vol.% of: silane treated glass beads(1-T), untreated glass(NT), talc and $CaCO_3$. . PP:unfilled polypropylene.

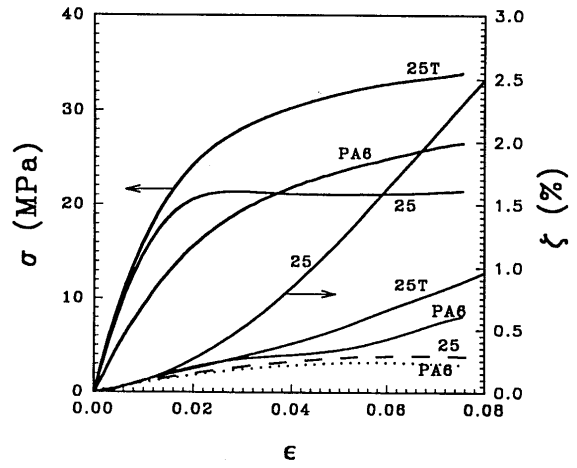

Fig. 2: PA6 filled with 25 vol.% glass beads. Stress σ and volume strain ζ vs axial strain ε (%). T- treated beads, dotted lines indicate dilational behavior(i.e. calculated using the initial Poisson ratio).

Tensile dilatometry

Figure 3 shows the volume strain versus axial strain (ζ vs ε) curves of polypropylene containing 0 and 20 *vol*.% of glass beads , talc and $CaCO_3$ respectively. The neat ζ *vs* ε polypropylene curve starts to deviate from linearity at about the same strain as the tensile stress-axial strain curve. The curves of filled polypropylene exhibit two linear parts, the first one being determined by the initial Poisson ratio, ν_{0c}. Beyond the first stage the increasing volume is an indication of the onset of debonding. As shown by curve 2 The talc filler behaves differently: the perpendicular to stress oriented platelets in the sample core start to debond at very low strain. The volume strain *vs* axial strain curves of neat and filled polyamide 6 ($\phi = 0.25$) are shown in Figure 2. The behavior of neat polyamide 6 is similar to that of polypropylene. At small strains, the ζ *vs* ε curves of polyamide 6, filled with treated or untreated glass coincide up to $\varepsilon \approx 1.5\%$ (for $\phi = 0.25$). The curves then diverge, the volume of untreated glass composite increases at a much higher rate than that of treated glass. It indicates that the fully debonded state is not reached treated beads.

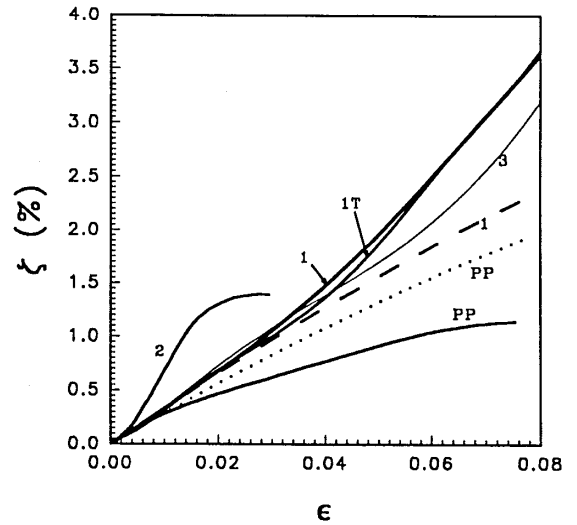

Fig. 3 Volume strain ζ vs axial strain ε of PP filled with 20 vol.% of : 1- glass beads, 2- talc and 3- $CaCO_3$. T: treated glass beads, dotted lines indicate dilational behavior

MODEL

The model is based on the following assumptions (see Fig. 4):

- Initially all filler particles (volume fraction ϕ) are well bonded to the matrix (bonded filler volume fraction $\phi_b = \phi$, Fig. 4a). The material behavior can be described by the Kerner-Lewis equation (see below).
- Upon straining the filler particles become progressively debonded ($\phi_b=\phi-\phi_d$, ϕ_d being the debonded filler volume fraction).The debonded particles do not bear any load (Fig. 4b).
- The completely debonded composite ($\phi_b=0$, $\phi_d=\phi$) behaves as a foam containing volume fraction of voids equal to ϕ_d (Fig. 4c). Its behavior can also be described by the Kerner-Lewis equation.
- The debonding rate ($d\phi_d/dt$) depends on the applied stress and the number of particles available for debonding ($\phi-\phi_d$) or (ϕ_b).

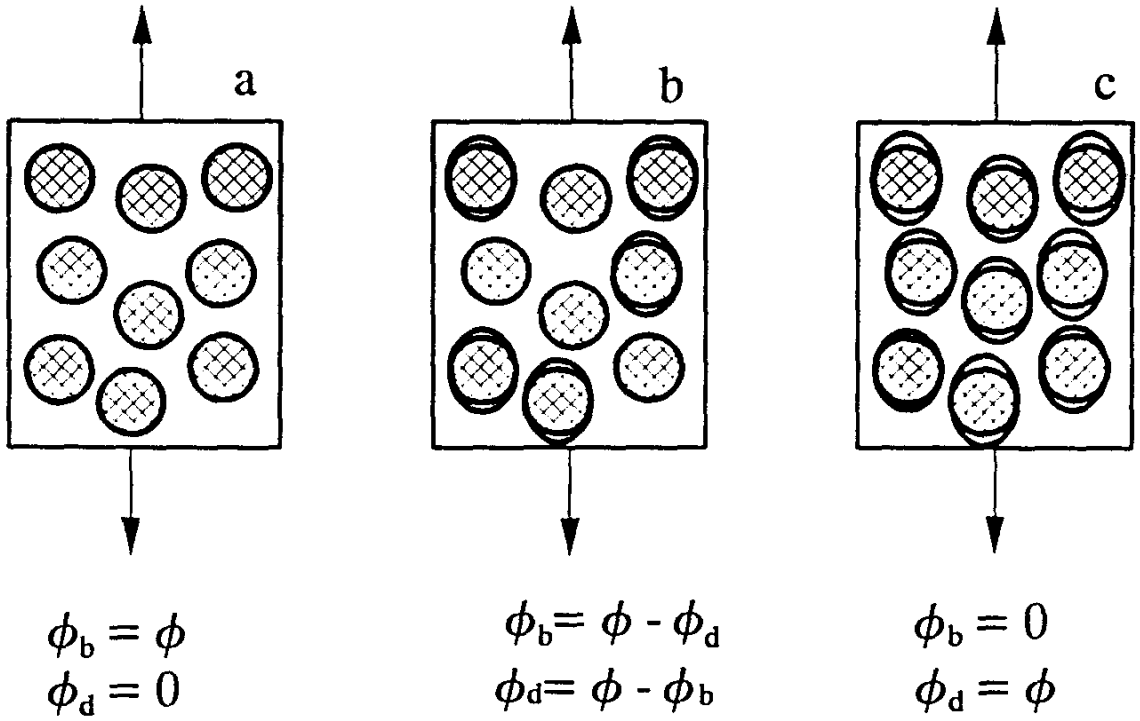

Fig. 4 Schematic representation of a filled polymer subjected to uniaxial tension. a- well-bonded composite, b- partially debonded composite and c- fully debonded composite.

During the constant strain rate tensile test ($d\epsilon/dt$ = const), the applied stress σ follows the relation:

$$\frac{d\sigma}{dt} = \frac{d(E_c \cdot \epsilon)}{dt} = \epsilon \cdot \frac{dE_c}{dt} + E_c \cdot \frac{d\epsilon}{dt} \qquad (1)$$

where E_c is the secant modulus of the composite. The modulus (E) decreases as debonding progresses. The partially debonded composite containing a volume fraction ϕ of the filler (of which ϕ_d is debonded : $0 \le \phi_d \le \phi$) is considered to consist of three components:

- matrix (modulus E_m)
- bonded filler (volume fraction $[\phi - \phi_d]$, modulus E_f)
- debonded filler - each vacuole containing a debonded filler particle behaves as a void.

The modulus of such hybrid material can be described by the Kerner-Lewis equation [5]:

$$E_c = E_m \cdot E_1 \cdot E_2 \qquad (2)$$

where E_1 represents the relative modulus of the still bonded filled material:

$$E_1 = \frac{1 + A_1 \cdot B_1 \cdot (\phi - \phi_d)}{1 - B_1 \cdot \psi \cdot (\phi - \phi_d)} \qquad (3)$$

with $A_1 = (7 - 5\nu)/(8 - 10\nu)$, $B_1 = (E_f/E_m - 1)/(E_f/E_m + A_1)$ and $\psi = 1 + \phi\,(1 - \phi_m)/\phi_m^2$, ν is the Poisson ratio of the matrix, ψ is a "crowding factor" which depends on ϕ_m - the maximum packing fraction of filler. The modulus E_2 is the relative modulus of the foam with a void fraction equal to ϕ_d. E_2 is then given by:

$$E_2 = \frac{1 - \phi_d}{1 - B_2 \cdot \psi \cdot \phi_d} \qquad (4)$$

with $B_2 = -1/A_1$. It is worth noting that the Kerner-Lewis equation and other expressions of this type have been successfully applied to hybrid materials [6] and to high density foams [7].

Considering the heterogeneous nature of materials under consideration it seems reasonable to adapt Bartenev's equation [8,9] for time to failure, t_f, of a material subjected to an effective stress, $\bar{\sigma}$. This equation, originally developed for materials containing defects, is written here in simplified form:

$$t_f = \frac{\exp\,(-B \cdot \bar{\sigma})}{K \cdot \bar{\sigma}} \qquad (5)$$

The constants B and K depend on the temperature, the material molecular structure and the nature and number of defects. It should be noted that this and other equations (e.g. Zhurkov-Bueche [10]) relating the time to failure to the applied stress have a theoretical basis and are often considered as interpolation formulas of a semi-empirical nature - useful for the mathematical expression of experimental data. Applying the Bartenev concept to a filled material, we assume that the time to failure of the filler/matrix interface can be described by equation 5. The probability of debonding is proportional to $1/t_f$. The debonding rate $d\phi_d/dt$ is then considered to

be proportional to $K\bar{\sigma}\exp(B\bar{\sigma})$ (the constants K and B are related to the overall behavior of the filled material rather than only to that of single particle/matrix interface, $\bar{\sigma}$ is the effective stress - see below) and to $(\phi - \phi_d)$:

$$\frac{d\phi_d}{dt} = (\phi - \phi_d) \cdot K \cdot \bar{\sigma} \exp(B \cdot \bar{\sigma}) \tag{6}$$

The effective stress, $\bar{\sigma}$, which acts only on the matrix and on the still bonded filler, can be related to the measured stress, σ (which is calculated using the entire sample cross section, including its debonded portion), using the strain equivalence principle [11]. A material containing a filler fraction $(\phi - \phi_d)$ but no voids will have a modulus E'_c:

$$E'_c = E_m \cdot E_1 \tag{7}$$

According to the strain equivalence principle:

$$\epsilon = \frac{\bar{\sigma}}{E'_c} = \frac{\sigma}{E_c} \tag{8}$$

This leads to:

$$\bar{\sigma} = \frac{\sigma}{E_2} \tag{9}$$

Since:

$$\frac{dE_c}{dt} = \frac{dE_c}{d\phi_d} \cdot \frac{d\phi_d}{dt} \tag{10}$$

a simultaneous solution of equations (1) and (6) can be obtained using known values of E_m, $d\epsilon/dt$ and ϕ, and using equations (2-4), (9) and (10). Solution of the equations (1) and (6) using the fourth order Runge Kutta method yields the value of the secant modulus E_c and of the debonded fraction ϕ_d. To determine the appropriate values of K and B, the calculated results are compared, with the help of the Marquardth-Levenberg algorithm, to the values of ϕ_d computed from the experimental stress-strain data using equation 2.

The volume increase due to debonding, ζ_d, can also be calculated assuming, for example, that each void created by debonding of a spherical particle (diameter d) is an ellipsoid with its two shorter axes equal to d and its longer axis equal to $d \cdot [1+(\epsilon - \epsilon_d)]$ where ϵ_d represents the strain at which the particle becomes debonded [2]. It follows that:

$$\zeta_d = \int_0^{\epsilon} \phi_d \, d\epsilon \tag{11}$$

RESULTS AND DISCUSSION

Having examined a number of more complex models for matrix behavior [4], we have finally adapted the following relation for the inelastic strain rate:

$$\dot{\varepsilon}_n = a \exp(b\,\sigma) + c\sigma + d = \dot{\varepsilon} - \frac{\dot{\sigma}}{E_{0m}}$$

with optimized constants a, b, c, d and E_{0m}.

The debonding process modeled with the help of equations 1, 2 and 6 using the materials constants of neat and filled polypropylene (Table 2) and several arbitrarily selected values of K and B leads to stress strain curves shown in Fig. 5. Two extreme cases are considered:

Table 2: Parameters used to calculate the initial composite modulus E_{0c} from equation 3. GB: glass beads.

Parameters	PP/GB	PP/Talc	PP/$CaCO_3$	PA6/GB
E_{0m} (GPa)	1.62	1.71	1.71	0.88
A_1	1.68	5.62	2.60	1.90
B_1	0.85	1.48	1.21	1.03
ψ	0.60	0.33	0.58	1.04

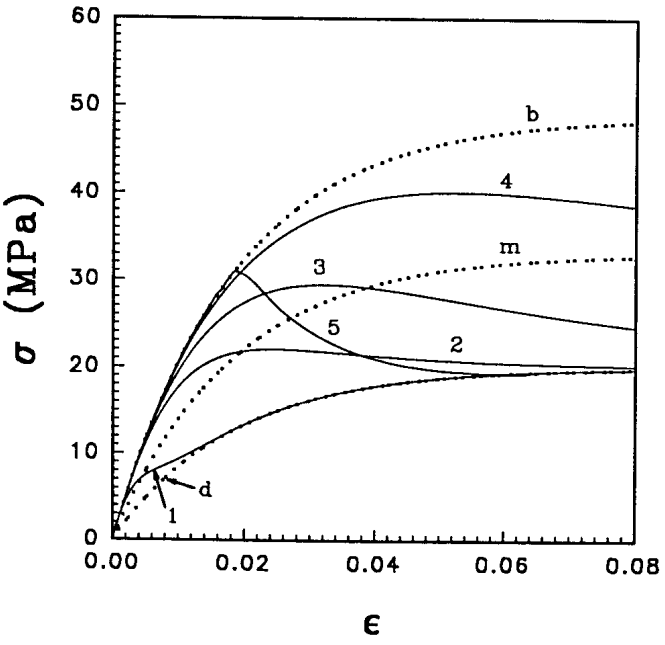

Fig. 5: Stress-strain curves calculated using equations 4.9 and 4.14 (see text): m: matrix, b: fully bonded composite, d: fully debonded composite. Curves 1 to 5 were calculated using following values of constants K and B, 1: K=3.04 10^{-2} MPa^{-1} s^{-1}, B= 0, 2: K= 2.03 10^{-3} MPa^{-1} s^{-1},B= 0,3: K= 6.80 10^{-4} MPa^{-1} s^{-1}, B= 0, 4: K= 1.2 10^{-4} MPa^{-1} s^{-1}, B= 0 and 5: K=2.03 10^{-14} MPa^{-1} s^{-1}, B= 1 MPa^{-1}.

When the value of the exponential term constant B is set to 0, the debonding rate is proportional to the effective stress $\bar{\sigma}$. The measured stress σ *vs* ε function deviates from that of the fully bonded composite at a relatively low strain and moves to the completely debonded state over a broad range of strains (see also Fig. 5 for the corresponding ϕ_d *vs* ε curves). With a high value of K (curve 1) the σ *vs* ε curve of the composite will cross that of the matrix when the matrix is still elastic and join that of the debonded composite at a strain well below the yield. The value of K used to draw curve 2 in Fig. 5 was selected so that the debonding process would be complete in the range of strains studied experimentally (0 to 8%). In this case the stress strain curve reaches a maximum at about 1.5% strain when about a third of all filler particles have debonded.

With a very high value of B the debonding will occur at nearly constant effective stress ($\bar{\sigma}$). Curve 5 corresponds to this case. The stress strain curve (σ *vs* ε) follows that of a well bonded composite until the onset of debonding (with the combination of K and B used at $\sigma = \bar{\sigma} \doteq 32$ MPa). With the reduction of the load bearing section the applied (measured) stress (σ) decreases (while $\bar{\sigma}$ = const) until the fully debonded state is reached at σ = 18 MPa and ε = 6%). The apparent "yield" of the composite (maximum of the value σ *vs* ε curve) corresponds to the onset of debonding rather than to the inherent yield of the matrix material. The corresponding ϕ_d *vs* ε curves are shown in Fig. 6.

The shapes of these curves suggest that the Bartenev type equation can cover the range of situations likely to occur in glass bead filled viscoelastic materials. The extreme case of the debonding occurring at constant effective stress (curves 5, Figs. 5-6) will certainly not be found in real materials where the dispersed phase distribution is at best uniformly random, particles are of different sizes, local stress fluctuations are caused not only by the material inherent heterogeneities but also by residual stresses which vary throughout the thickness, and where the debonding will therefore occur over a broader range of stress and strain.

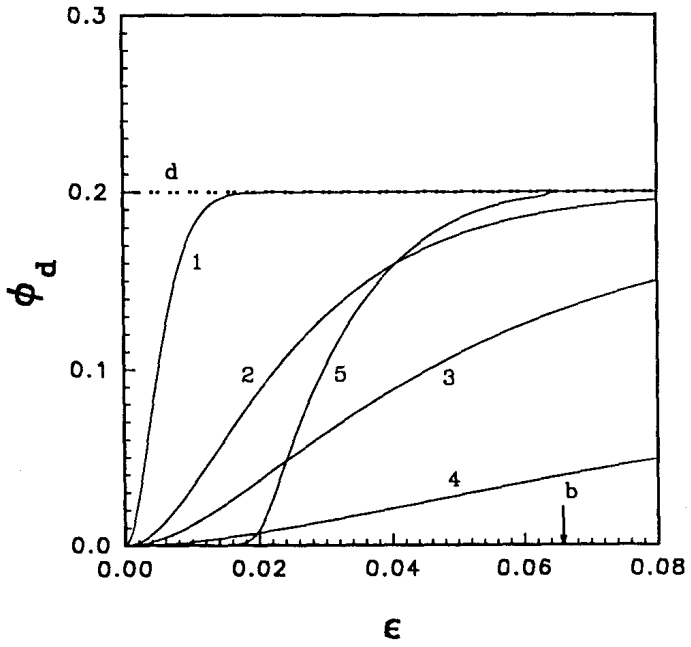

Fig. 6 Debonded filler fraction ϕ_d calculated using equations 1 and 6 as a function of strain ε. The curves are numbered as in Fig. 5.

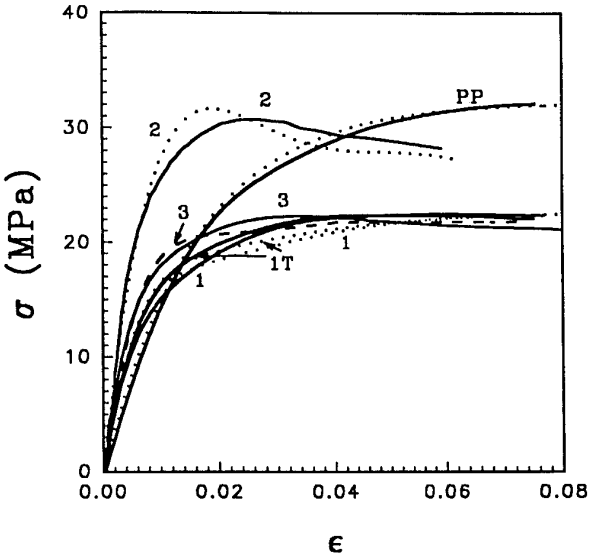

Fig. 7 Stress strain curves, predicted by the model and experimental (-----) of 20 vol. % filled PP. 1- glass beads, 2-talc and 3- $CaCO_3$. T- treated beads.

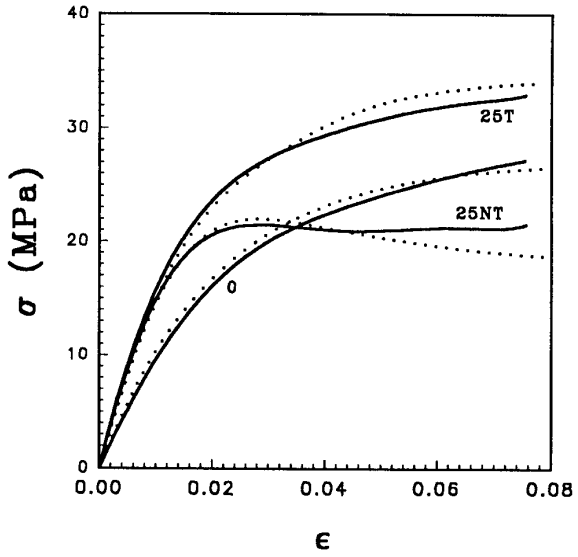

Fig. 8 Stress strain curves, predicted by the model and experimental (-----) of 25 vol. % filled PA6. T- treated beads.

The stress strain curve of filled material consisting of a matrix defined by equation 2 and undergoing the debonding process (eqs. 2 and 6) can be calculated and compared to experimental stress strain curves. Optimized values of K and B are listed in Table 3 for filled polypropylene and filled polyamide 6. The value of the constant K is affected by particle shape and traitment. On the other hand, the exponential term constant B also changes with the particle shape and treatment. The agreement between the experimental stress strain curves and those computed using the procedure described in this paper is quite good (Fig. 7 for polypropylene, glass beads, talc and $CaCO_3$, ϕ=0.2 and Fig. 8 for glass bead filled polyamide 6, ϕ=0.25). It confirms that the Bartenev equation can be used to describe the debonding process not only when the matrix is elastic [12] but also when the composite non-elasticity is caused by a combination of the debonding and of the matrix viscoelasticity. Moreover, the

Bartenev equation appears to be able to cover the cases of both complete and partial debonding (polypropylene and polyamide 6 respectively).

Table 3 : K and B values of 20vol. % filled polypropylene (PP) and 25vol. % filled polyamide 6 (PA6) .T-treated beads.

Parameters	PP/GB		PP/Talc	PP/$CaCO_3$	PA6/GB	
	NT	T			NT	T
$K \cdot 10^2$ ($GPa^{-1}\ s^{-1}$)	4.3	3.10	0.163	0.36	1.8	1.4
$B \cdot 10^2$ (GPa^{-1})	0.11	0.09	1.5	0.011	6.5	0.28

CONCLUSION

The stress-strain behavior of filled polymer is modeled by using a Bartenev type relation for the time dependence of the filler matrix interface strength and by considering the gradual transformation of the initially well-bonded composite into foam which take account the matrix viscoelasticity. A good agreement was achieved between calculated and experimental data.

REFERENCES

1 Anderson L.L. and Farris R.J., "A Predictive Model the Mechanical Behavior of Particulate Composites", *Polymer Engineering and Science*, Vol. 38, 1993, pp 1458-1465.

2 Zezin Yu P., "Damage Accumulation and Strength of Adhesion Bonds in Filled Polymeric Systems", *Mechanics of Composite Materials*, Vol. 30, 1994, pp. 131-135.

3 Meddad A. and Fisa B., "Stress-Strain Behavior and Tensile Dilatometry of Glass Bead-Filled Polypropylene and Polyamide 6", *Journal of Applied Polymer Science*, in press 1997.

4 Meddad A. and Fisa B., " A Model for Filler-Matrix Debonding in Glass Bead filled Viscoelastic Polymers", *Journal of Applied Polymer Science.*, in press 1997

5 Nielsen L.E. and Landel R.F, *Mechanical Properties of Polymers and Composites*, 2nd Ed., Marcel Dekker Inc. New York, 1994.

6 Jancar J. and DiBenedetto A.T., "The Mechanical Properties of Ternary Composites of Polyropylene with Inorganic Fillers and Elastomer Inclusions", *Journal of Materials Science*, Vol. 29, 1994, pp. 4651-4658

7 Collias I. and Baird D.G., "Tensile Toughness of Microcellular Foam of PS, SAN and PC", *Polymer Engineering and Science*, Vol. 35, 1995, pp. 1167-1177

8 Bartenev M.M. and Zuyev Yu. Z., *Strength and Failure of Viscoelastic Materials*, Pergamon Press, London, 1968.

9 Perepechko I.I., *An Introduction to Polymer Physics*, 1th Ed. Mir Publishers, Moscow (1981)

10 R.J. Crawford, *Plastics Engineering*, 2nd Ed. Pergamon Press London, 1987.

11 Lemaitre J. and Chaboche J.L., *Mécanique des matériaux solides*, 2nd Ed. Dunod Paris (1988)

12 Meddad A. and Fisa B., *Journal of Materials Science*, in press 1997

MODELLING OF THE PUSHING INSTALLATION OF OPTICAL FIBER CABLE IN URBAN AREA

Habiba Boulharts[1, 2], Jean-Louis Billoet[1], Jean Le Rouzic[2], Olivier Polit[1], Alain Pecot[2] and Jean-Luc Campion[2]

[1] LM2S /URA CNRS 1776, ENSAM Paris ,
151, boulevard de l'Hôpital, 75013 Paris, France
[2] FRANCE TELECOM - CNET Lannion , DTD/CAI ,
BP 40 , 22307 Lannion Cedex , France

SUMMARY : The spreading of whole optical access networks for the customers (FTTH , FFTB,...) connecting necessitates to master some mechanical parameters like optical fiber cable structure. The studied cable presents a multilayer cylindrical structure. The analytical constitutive equations have been obtained with homogenization techniques on multilayer cylindrical beam. A Timoshenko's approach is used without transverse shear correction. Some mechanical tests have been performed such as simple tensile tests , bending coupled with tension test and buckling tests. The cable buckling behavior is the first global approach studied in this paper. The buckling test results are provided by a bench test for pushing installation fully manufactured by the CNET. A modelling with finite elements using explicit method of ABAQUS software simulate the cable installation by pushing process. The stiffness matrix terms are validated by those experimental tests. The experimental buckling results are close to theoretical buckling results and 2-D numerical results.

KEYWORDS : linear elasticity, isotropic transverse beam, oriented composite layer, cable installation, pipe buckling, cable pushing bench test, finite element modelling.

INTRODUCTION

The fiber optical expansion is more and more important in access networks. The development of new cable structures must integrate the cable installation process constraints. In the urban area, the choice between a pulling and a pushing installation or a mixture of both depends on the length to install, the course dependent constraints, the nature of the ducts and the optical fiber cable mechanical characteristics. The pushing technique consists in applying a pushing effort on cable at the beginning of the duct. The optical cable flexional mode is the major mode occurring in this process. Our study is about the cable mechanical characteristics identification and its pushing installation process.

The studied optical fiber cable is considered like a composite material by its multilayer cylindrical structure and by its different components like hdPE, PCV, kelvar, glass-resin. The hdPE and PCV layers are transversely isotropic and the kevlar layer is anisotropic due to its helical twisted yarns (Fig. 1). The analytical constitutive equations are given for a multilayer cylindrical beam. The Hashin's model [1] is used to calculate the equivalent elastic constants

of kevlar and glass-resin layers. After writing the local behavior law for each layer in consecutive three-dimensional basis and reducing it in one dimension, the generalised behavior law is established with the help of integration techniques. The obtained stiffness matrix terms are compared with the stiffness moduli provided by tensile tests, bending and buckling tests.

A cable installation bench test is manufactured to understand the cable global behavior and to predict the cable buckling. The cable is introduced under a compressive axial load, inside translucent ducts. The buckling theories of pipes installed for the petrol drilling permit us to analyse the phenomena observed during the cable pushing process. The cable helix pitches in the helical configuration and the axial loads at the end-up of the duct are studied. Then a finite element modelling of cable pushing process is compared to the experimental data.

STRUCTURE CABLE STUDY

Homogenization techniques

The multilayer cable is supposed transversely isotropic in the axial direction. The local behavior law (Eqn 1) under transversely isotropic assumptions is expressed in the principal fiber direction (L,T,R) of each layer [2]. The Fig. 2 represents the three different basis (L,T,R), (X,R,θ),(X,Y,Z) used to express the constitutive equations. We have stress-strain relations in the (L,T,R) coordinate system :

$$\begin{vmatrix}\sigma_{LL}\\ \sigma_{TT}\\ \sigma_{RR}\\ \sigma_{TR}\\ \sigma_{LR}\\ \sigma_{LT}\end{vmatrix} = \begin{vmatrix}\psi E_L & 2\nu_{LT}K_T & 2\nu_{LT}K_T & 0 & 0 & 0\\ 2\nu_{LT}K_T & K_T+G_{TT} & K_T-G_{TT} & 0 & 0 & 0\\ 2\nu_{LT}K_T & K_T-G_{TT} & K_T+G_{TT} & 0 & 0 & 0\\ 0 & 0 & 0 & G_{TT} & 0 & 0\\ 0 & 0 & 0 & 0 & G_{LT} & 0\\ 0 & 0 & 0 & 0 & 0 & G_{LT}\end{vmatrix} \begin{vmatrix}\varepsilon_{LL}\\ \varepsilon_{TT}\\ \varepsilon_{RR}\\ \varepsilon_{TR}\\ \varepsilon_{LR}\\ \varepsilon_{LT}\end{vmatrix} \quad (1)$$

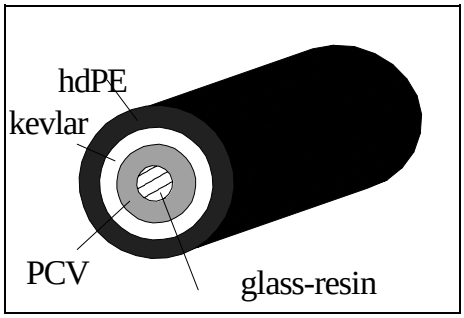

Fig.1 : Multilayer cable.

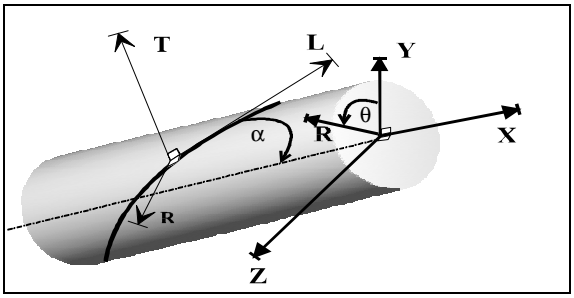

Fig. 2 : The three coordinate systems used.

This law is written in a common reference to the layers set, the local cylindrical (X,R,θ) coordinate system . The C16, C26, C36 et C45 coupling terms appear in the stiffness matrix (Eqn 2). The Cij terms depend on the cosines direction $(\cos\alpha, \sin\alpha)$ from the first coordinate transformation and the five independent elastic constants E_L, E_T, G_{LT}, G_{TT}, ν_{LT}, K_T of each homogenised layer. The twist angle of the kevlar yarn is α. We notice that the C16, C26, C36

et C45 coupling terms are null for the PCV, hdPE transversely isotropic layers and the glass-resin layer because there is no twist angle for those layers.

$$\begin{vmatrix}\sigma_{XX}\\ \sigma_{\theta\theta}\\ \sigma_{RR}\\ \sigma_{\theta R}\\ \sigma_{RX}\\ \sigma_{X\theta}\end{vmatrix} = \begin{vmatrix} C11 & C12 & C13 & 0 & 0 & C16\\ C12 & C22 & C23 & 0 & 0 & C26\\ C13 & C23 & C33 & 0 & 0 & C36\\ 0 & 0 & 0 & C44 & C45 & 0\\ 0 & 0 & 0 & C45 & C55 & 0\\ C16 & C26 & C36 & 0 & 0 & C66\end{vmatrix} \begin{vmatrix}\varepsilon_{XX}\\ \varepsilon_{\theta\theta}\\ \varepsilon_{RR}\\ \varepsilon_{\theta R}\\ \varepsilon_{RX}\\ \varepsilon_{X\theta}\end{vmatrix} \text{ with} \qquad (2)$$

$$C11 = C\ \psi\ E_L + K_T(4S^2C^2\nu_{LT} + S^4) + S^4G_{TT} + 4C^2S^2G_{LT}$$
$$C12 = S^2C^2\psi\ E_L + K_T(2\nu_{LT}(S^4 + C^4) + C^2S^2) + C^2S^2G_{TT} - 4C^2S^2G_{LT}$$
$$C13 = (2C^2\nu_{LT} + S^2)K_T - S^2G_{TT}$$
$$C22 = S^4\psi\ E_L + K_T(C^4 + 4C^2S^2\nu_{LT}) + C^4G_{TT} + 4S^2C^2G_{LT}$$
$$C23 = K_T(C^2 + 2S^2\nu_{LT}) - C^2G_{TT}$$
$$C33 = K_T + G_{TT}$$
$$C44 = C^2G_{TT} + S^2G_{LT}$$
$$C45 = -(G_{TT} - G_{LT})SC$$
$$C55 = S^2G_{TT} + C^2G_{LT}$$
$$C66 = S^2C^2\psi\ E_L + K_T(-4\nu_{LT}(S^2 + C^2) + C^2S^2) + C^2S^2G_{TT} + (C^2 - S^2)G_{LT}$$
$$C16 = (C^3S\ \psi\ E_L - K_T(2\nu_{LT}(C^3S - CS^3) - CS^3) - S^3C\ G_{TT} - 2C\ S\ (C^2 - S^2)G_{LT})$$
$$C26 = (C\ S^3\psi\ E_L - K_T(2\nu_{LT}(C\ S3 - C^3S) - CS^3) - S\ C^3G_{TT} + 2C\ S\ (C^2 - S^2)G_{LT})$$
$$C36 = \text{-}C\ S\ (K_T(1\text{-}2\nu_{LT})\text{-}G_{TT})$$

with $C = \cos\alpha; S = \sin\alpha$

The beam theory with Timoshenko's hypothesis including transverse shear is applied. The consequence on the constitutive equations is the neglecting of the following stresses components, $\sigma_{RR}, \sigma_{\theta\theta}, \sigma_{R\theta}$ in comparison with the other stresses components. The reduced local constitutive equations (Eqn 3) in the (X,R,θ) coordinate system are obtained with the $\overline{Cij}$ terms depending linearly on the preceding Cij terms.

$$\begin{vmatrix}\sigma_{XX}\\ 0\\ 0\\ 0\\ \sigma_{RX}\\ \sigma_{X\theta}\end{vmatrix} = \begin{vmatrix} C11 & C12 & C13 & 0 & 0 & C16\\ C12 & C22 & C23 & 0 & 0 & C26\\ C13 & C23 & C33 & 0 & 0 & C36\\ 0 & 0 & 0 & C44 & C45 & 0\\ 0 & 0 & 0 & C45 & C55 & 0\\ C16 & C26 & C36 & 0 & 0 & C66\end{vmatrix} \begin{vmatrix}\varepsilon_{XX}\\ \varepsilon_{\theta\theta}\\ \varepsilon_{RR}\\ \varepsilon_{\theta R}\\ \varepsilon_{RX}\\ \varepsilon_{X\theta}\end{vmatrix} \Leftrightarrow \begin{vmatrix}\sigma_{XX}\\ \sigma_{X\theta}\\ \sigma_{RX}\end{vmatrix} = \begin{vmatrix} \overline{C16} & \overline{C16} & 0\\ \overline{C16} & \overline{C16} & 0\\ 0 & 0 & \overline{C16}\end{vmatrix} \begin{vmatrix}\varepsilon_{XX}\\ \varepsilon_{X\theta}\\ \varepsilon_{RX}\end{vmatrix} \qquad (3)$$

The Eqn 3 are now expressed in the Cartesian (X, Y, Z) coordinate system. The new reduced local stiffness matrix is a function of the cosines direction $(\cos\theta, \sin\theta)$ from the second coordinate transformation. The stress-strain relations in the Cartesian (X, Y, Z) coordinate system are defined by the Eqn 4:

$$\begin{vmatrix}\sigma_{XX}\\ \sigma_{XY}\\ \sigma_{XZ}\end{vmatrix} = \begin{vmatrix} c\overline{C11} & s\overline{C16} & -c\overline{C16} \\ s\overline{C16} & c^2\overline{C55}+s^2\overline{C66} & c\ s(-\overline{C66}+\overline{C55}) \\ -c\overline{C16} & c\ s(-\overline{C66}+\overline{C55}) & s^2\overline{C55}+c^2\overline{C66}\end{vmatrix}\begin{vmatrix}\varepsilon_{XX}\\ \varepsilon_{XY}\\ \varepsilon_{XZ}\end{vmatrix} \text{ with } \begin{matrix} c = \cos\theta \\ s = \sin\theta \end{matrix} \quad (4)$$

The generalised efforts components (N,Ty,Tz) and generalised moments components (Mx,My,Mz) are obtained by the integration of the Eqn 4 in the circular cross section. We have the global reduced behavior law expressed by the relation (5). The $\overline{Ckl}'$ terms of the stiffness matrix is the summation of the $(R_k^x - R_{k-1}^x)$ thickness and $\overline{Cij}$ terms multiplication of each layer denoted by k. One can notice that the transverse shear correction obtained by the Hellinger-Reissner's functional mixed approach is not presented here. The matrix diagonal terms of the Eqn 5 are used to be compared to the experimental and numerical results.

$$\begin{vmatrix} N \\ Ty \\ Tz \\ Mx \\ My \\ Mz \end{vmatrix} = \begin{vmatrix} \overline{C11}' & 0 & 0 & \overline{C14}' & 0 & 0 \\ 0 & \overline{C22}' & 0 & 0 & \overline{C25}' & 0 \\ 0 & 0 & \overline{C22}' & 0 & 0 & \overline{C36}' \\ \overline{C14}' & 0 & 0 & \overline{C44}' & 0 & 0 \\ 0 & \overline{C25}' & 0 & 0 & \overline{C55}' & 0 \\ 0 & 0 & \overline{C36}' & 0 & 0 & \overline{C55}' \end{vmatrix} \begin{vmatrix} \varepsilon_X^0 \\ 2\varepsilon_{XY}^0 \\ 2\varepsilon_{XZ}^0 \\ \chi_X \\ \chi_Y \\ \chi_Z \end{vmatrix} \text{ with } \quad (5)$$

$$\overline{C11}' = \sum_k \overline{C11}^k p\,(R_k^2 - R_{k-1}^2)$$

$$\overline{C22}' = \sum_k (\overline{C66}^k + \overline{C55}^k) p\,(R_k^2 - R_{k-1}^2)/2$$

$$\overline{C44}' = \sum_k (\overline{C66}^k + \overline{C55}^k)\, p\,(R_k^4 - R_{k-1}^4)/4$$

$$\overline{C55}' = \sum_k \overline{C11}^k p\,(R_k^4 - R_{k-1}^4)/4$$

$$\overline{C14}' = \sum_k \overline{C16}^k 2p\,(R_k^3 - R_{k-1}^3)/3$$

$$\overline{C25}' = \sum_k \overline{C16}^k (-p)\,(R_k^3 - R_{k-1}^3)/3$$

$$\overline{C36}' = \sum_k \overline{C16}^k p\,(R_k^3 - R_{k-1}^3)/3$$

Global stiffness matrix validation

During the cable installation in the urban area, the stiffness moduli of traction $\overline{C11}'$, bending $\overline{C55}'$ and twist $\overline{C44}'$ are mainly involved. The validation of these terms in the global stiffness matrix (Eqn 5) is made in comparison with the same moduli obtained by numerical simulations, characterisation tests. At another level, those terms are also compared to the

results of another behavior law with orthotropic components [3]. These different comparisons are described below :

- Simple tests such as tensile test, bending tests and twist tests on a multilayer cylinder are modelled using finite element ABAQUS software. Several numerical cases are studied to validate the global stiffness matrix (Table 1). The case 1 is about a cylinder constituted by several isotropic layers. The case 2 concerns the simulation of a cylinder composed by isotropic and anisotropic layers without twist angle.

- The analytical comparison with [3] is about a configuration with a oriented kevlar yarn. The case 3 and the case 4 concern a cylinder with isotropic and anisotropic layers with respectively a kevlar yarn twist angle of 4° and 45°.

- The characterisation tests are made with optical fiber cable in which the kevlar yarn twist angle is 4°. The tensile test is realised with a length of 50 meters according to France Telecom standards. The bending test coupled with tensile effort realised at the ENSAM's Structure Laboratory necessitates a special devices setting (Fig. 3).

The Table 1 summarizes the stiffness moduli comparisons. Error percentages on the rigidity moduli are provided by the different configurations cited above and the values obtained by the global stiffness matrix (Eqn 5). For the case 3, the analytical values are $\overline{C11}'$ = 0.095 N.m^2, $\overline{C44}'$ = 1.7 10^{-8} N.m^4, $\overline{C55}'$ = 1.9 10^{-7} N.m^4 . Errors are inferior than 5 % excepted to the modulus $\overline{C44}'$ of case 4. One can conclude that with any geometrical and mechanical characteristics of each cable layer the diagonal terms of the global stiffness matrix can be calculated and used to simulate numerically the pushing installation process.

Table 1 : Error percentage of stiffness moduli.

Error in %		**case 1 : multilayer with isotropic materials**	**case 2 : multilayer without twist angle**	**case 3 : multilayer with kevlar layer at α =4°**	**case 4 : multilayer with kevlar layer at α=45°**
global matrix compared to	$\overline{Ckl}'$				
Numerical Simulations (ABAQUS)	$\overline{C11}'$	0,03	0,01	-	-
	$\overline{C44}'$	0,03	0,05	-	-
	$\overline{C55}'$	-1,71	0,02	-	-
Analytical Behavior from [3]	$\overline{C11}'$	-	-	0 ,5	-5 ,9
	$\overline{C44}'$	-	-	1,8	17,5
	$\overline{C55}'$	-	-	0,5	-5,9
Tensile Test	$\overline{C11}'$	-	-	-4,4	-
Bending Test	$\overline{C55}'$	-	-	-6,7	-

CABLE BUCKLING IN DUCT

Cable pushing bench test

A full-size bench test is realised at the C.N.E.T.'s facilities to understand the cable global behavior and to provide data to validate the pushing numerical simulations. It is composed by

a pusher engine, a motorised reel, translucent ducts and a computer (Fig. 4). Two effort sensors installed on either side of the pusher engine give the pushing effort Fpush, a counting wheel provides the introduced length, a third sensor placed at the up-end of the duct informs us on the stop effort, Fstop. This stop points out the up-end of the course. All data are recorded on the computer which pilots the test.

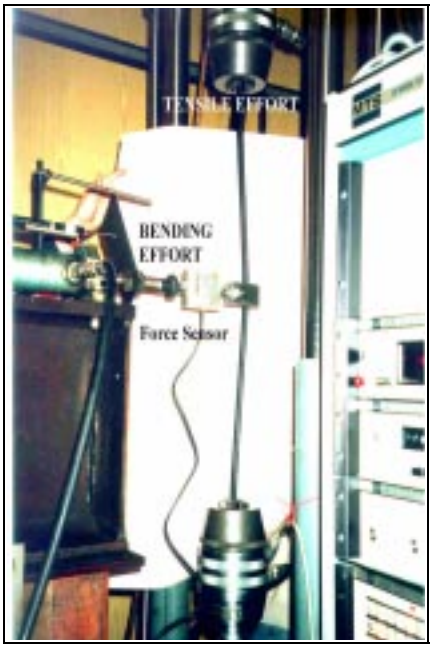

Fig. 3 : The bending test.

Fig. 4 : The pushing bench test.

The studied multilayer fiber optic cable is pushed on a length of 45 meters. During the pushing test, one can observe that first the cable keeps its pre-stressed configuration and lies inside the duct. Then lateral displacements in sinusoidal shape appear under a higher compressive load Fpush. If the compressive axial load Fpush gets more and more important, the cable buckles into a new helical shape. The Fig. 5 shows the buckled cable in a horizontal translucent PCV duct at the end of the test. The more the cable undulations increase, the more the contact force increases. The created frictional force provoked by this contact force also prevents the cable introduction. It's interesting to know how to predict this helical configuration. This study of the cable buckling is about the axial load influency on the helix pitch and the axial load distribution along the duct.

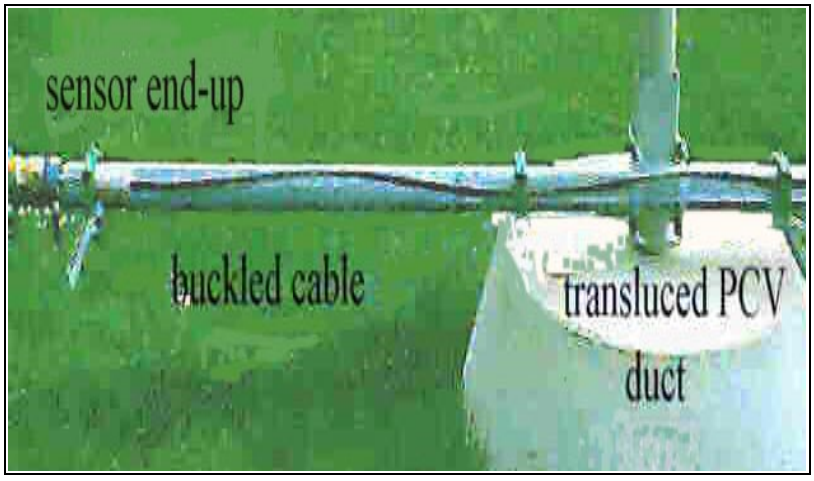

Fig. 5 : A buckled cable in a translucent PCV duct.

Theoretical study

Two formula express the compressive axial force Fpush as a function of the cable helix pitch P and its bending stiffness modulus EI. [4] discussed about their meaning. They differ by a factor of two .

$$\text{Fpush} = 8\pi^2 * \frac{(\text{E I})}{\text{P}^2} \quad \Leftrightarrow \quad \frac{\text{P}}{2} = \sqrt{2}\ \pi \sqrt{\frac{\text{E I}}{\text{Fpush}}} \tag{6}$$

$$\text{Fpush} = 4\pi^2 * \frac{(\text{E I})}{\text{P}^2} \quad \Leftrightarrow \quad \frac{\text{P}}{2} = \pi \sqrt{\frac{\text{E I}}{\text{Fpush}}} \tag{7}$$

According to [5], when the compressive axial load Fpush reaches a limiting value Fcr, the cable buckles into a sinusoidal shape. This first buckling load Fcr is given in the Eqn 8. If the axial load is greater than the critical load, the helical shape will be developed in a helix around the duct wall. The helical buckling load expression (Eqn 9) for a long cable in horizontal duct is a function of the cable bending modulus EI , the weight *w* and the clearance radius r in the duct.

$$\text{Fcr} = 2\ \sqrt{\frac{\text{E I}\ w}{\text{r}}} \tag{8}$$

$$\text{Fhel} = 2\sqrt{2}\ \sqrt{\frac{\text{E I}\ w}{\text{r}}} \tag{9}$$

The following differential equation for the axial load of a helically buckled weighty cable in a inclined duct is given in [4] and expresses in the Eqn 10 :

$$\frac{\text{dF}}{\text{dX}} = \mu\,(\,w \sin\beta + w_n\,) - w\cos\beta \quad \text{where} \ \ w_{\text{n}} = \frac{\text{r Fpush}^2}{4\,\text{EI}} \tag{10}$$

which is a function of the weight *w*, the friction coefficient μ, the contact force w_n, the incline angle β and the helical length X measured from down-up. The axial load F distribution for helically buckled cable in a horizontal duct under is written in the Eqn 11 :

$$\text{F}(\text{X}) = \sqrt{\frac{4\,\text{EI}\,w}{\text{r}}}\ \tan\left(\mu\ \text{X}\sqrt{\frac{\text{r}\,w}{4\,\text{EI}}} + \arctan\left(\text{Fpush}\sqrt{\frac{\text{r}}{4\,\text{EI}\ w}}\right)\right) \tag{11}$$

Experimental helical configuration study

A cable is pushed in a duct of 45 meters. When the test is finished, the helix pitches are collected. The cable helix pitches vary along the translucent duct. The Fig. 6 shows us several sets of helix pitches with the same value. There are 83 half periods. The graph can be divided by two parts or maybe more : the (1-39) set collection corresponds to a half helix pitch average of 36 cm, and the (40-83) set collection corresponds to a half helix pitch average of 68 cm. The whole half helix pitches average is about 53 cm. One can notice that the compressive axial load influences more the cable buckling on the down-up of the duct.

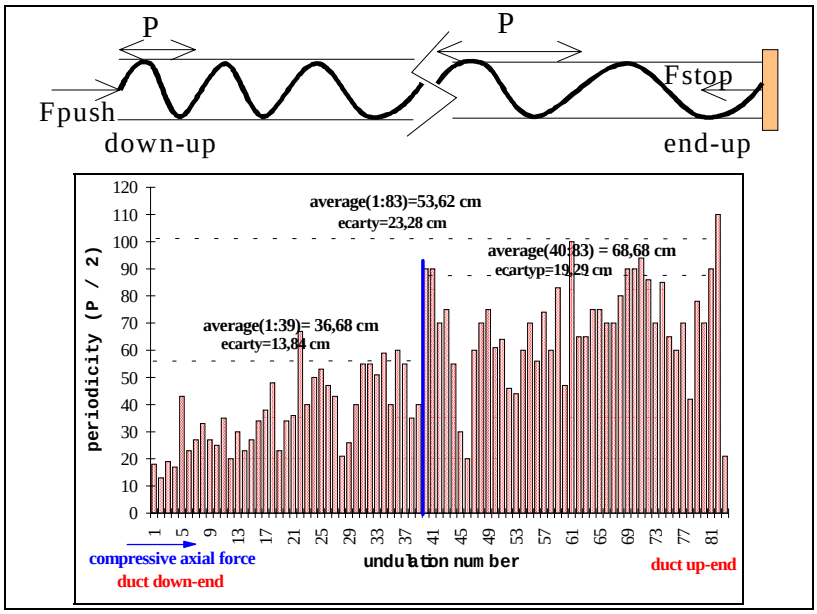

Fig. 6 : The cable periods collection in a duct of 45 meters.

It is interesting to extract the helix pitch P from the Eqns 6 and 7, and to compare it to the P experimental values. It is also an original way to validate the bending stiffness modulus from the Eqn 5.

Compressive axial load evolution

The Fig. 7 shows us the efforts Fpush and Fstop recordings during the test on 45 meters. This figure can be divided into three parts from the viewpoint of the Fpush increasing. In the part A, as the up-end cable extremity is free, the stop force Fstop remains stationary, also the compressive axial load Fpush does. In the part B, the cable reaches the stop. It's why the Fstop increases and remains stationary to 10 daN. The Fpush increases equally until the maximum cable length introduced in the duct is reached. There is a sharp peak at 140 daN which delimits the part C. In this last part, the dow-up cable extremity fords inside the duct under the excessive axial load. The Fpush decreasing corresponds to a new introduction of the folded cable. At the down-up of the duct, the cable forms a buckle in 8 shape. The pushing force limit is overflow. The cable is damaged after this test. Normally, we have to stop the cable introduction before reaching the helix configuration to conserve the cable optical functions.

We substitute these recorded Fpush data into Eqns 6 and 7 and obtain the curves P/2(6) and P/2(7) (Fig.7). These former inform us on the values before and after the cable reaches the stop at 44,8 meters. The helix pitch is inversely proportional to the compressive axial load. The smaller the axial load Fpush is, the higher the helix pitch P is as the curves P/2(6) and P/2(7) show us.

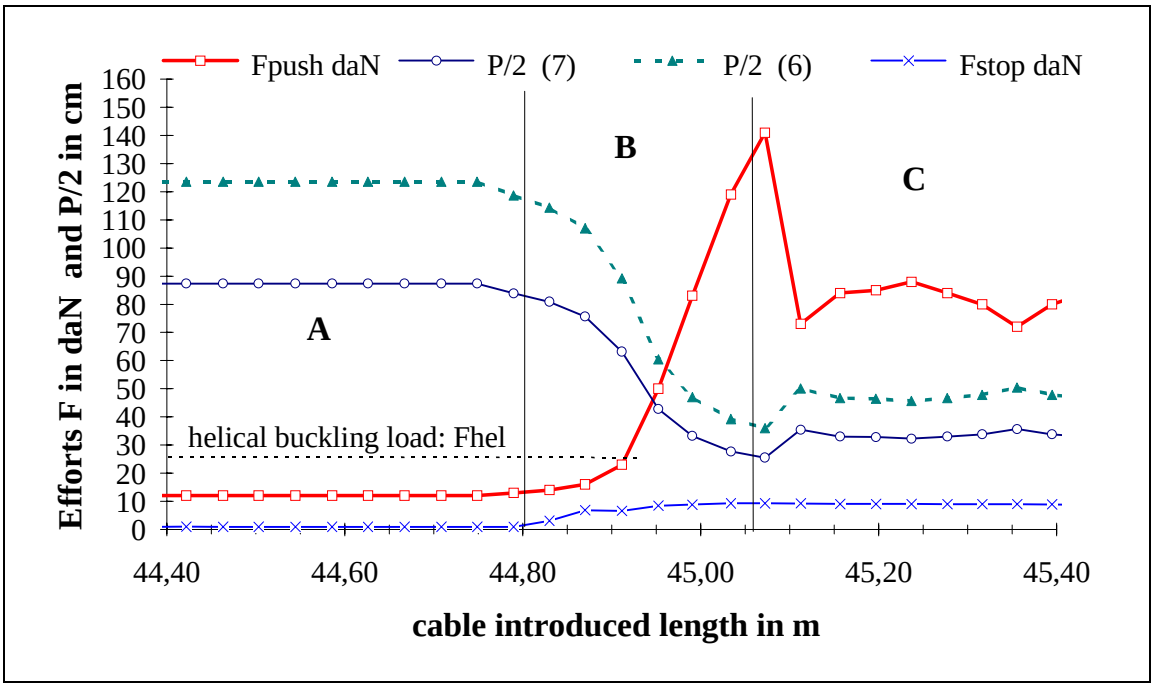

Fig. 7 : Efforts Fpush and Fstop recordings and P/2 deduced from Eqns 6 and 7.

According to Eqn 9, the helical buckling configuration appears for a Fpush minimum value of 25 daN :

$$\text{Fhel} = 2\sqrt{2}\ \sqrt{\frac{E\ I\ w}{r}} \cong \ 25\ \text{daN}$$

We can compare the P/2 values in the Figs. 6 and 7. We study the helix pitches when the cable starts buckling and when the test is stopped :

- The experimental P/2 values observed at the end-up of the duct are in relation with the beginning of the cable buckling (i.e. when the axial load Fpush reaches the buckling load, Fhel). For a buckling load value of 25 daN, the half helix pitches corresponding values are about 50 cm and 80 cm respectively for the P/2(7) and P/2(6) curves (Fig. 7). The experimental P/2 average is about 68 cm and is framed by the preceding values.

- The experimental P/2 values at the down-up of the duct correspond to the final helical configuration. For a Fpush value of 80 daN, the half helix pitches corresponding values are about 35 cm and 50 cm respectively for P/2(7) and P/2(6) curves. The experimental P/2 average is about 36 cm and is equally coherent with the theoretical values.

End-up axial load calculation

For a configuration of the bench test described below, we calculate the axial load distribution at the X=45 m from the Eqn 11. The cable/duct friction coefficient is 0.2. The effective weight is 0.12 kg/m. The cable Young modulus is 8. 10^9 N/m^2. The clearance radius is 0.038 m. We find a Fpush equal to 50 daN for a load F(X) given to 10 daN. According to the part B of the Fig. 7, the Fpush value is coherent. The stationary stage of the end -up load Fstop at 10 daN begins at a Fpush value of 40 daN.

Numerical simulations

A 2-D finite element modelling is used to simulate the cable pushing in a duct. Beam finite elements with two nodes at 3 degrees of freedom a node, using the Timoshenko's approach simulate the cable. Rigid elements simulate the duct. The simulation size is 12671 degrees of freedom. The explicit version on the ABAQUS software allows us to treat this non linear contact problem. The results of a cable pushing on a 5 meters long duct are compared to the numerical results for three duct diameters : 0.025 m, 0.040 m, 0.060 m (Fig. 8). The Table 2 represents the up-end force Fstop and the sinus and helix pitches comparisons. The numerical results are coherent for the pitch. But further they will have to be more improved as compared to the experimental compressive stop load.

Table 2 : Experimental and numerical comparisons on a 5meters duct.

Duct diameter m	Numerical results		Experimental results	
	Fstop N	sinus pitch m	Fstop N	helix pitch m
0.025	1015	0 ,50	670	0,57
0.040	646	0,72	450	0,73
0.060	357	0,85	210	0,89

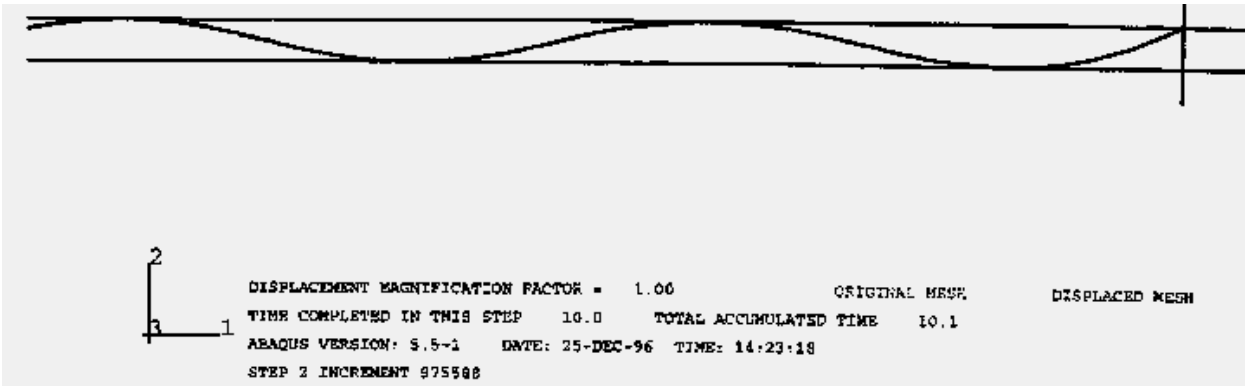

Fig 8 : Sinusoidal buckling configuration with 2D numerical simulation.

CONCLUSIONS

1. The analytical global stiffness matrix established for an oriented multilayer cylinder corresponds to the characteristic mechanics of the studied optical fiber cable. This stiffness matrix can be used for any isotropic transverse oriented multilayer cylinder. These calculated stiffness moduli are injected in the pushing numerical modelling.

2. The pushing experimental study permits us to understand the cable global behavior. The buckling theoretical relations applied to the pipes for petrol drilling afford us to understand the different configurations of cable buckling.

3. The 2-D finite element modelling of the cable pushing process is relatively close to the experimental values. Further this modelling will have to be more improved. A length representative of urban area configuration will be studied. The 3-D numerical approach using beam elements at 9 degrees of freedom a node for the cable and pipe elements for the duct will be studied. The numerical simulation will be a reliable tool to simulate the cable installation by pushing. This tool could be used to anticipate the conception of a new cable structure.

NOTATIONS

σ_{IJ} : stress component,
K_T : lateral shrinking modulus,
G_{TT} : Coulomb's transverse modulus,
G_{LT} : Coulomb's axial modulus,
ν_{LT} : Poisson's coefficient,
E_L : axial stiffness modulus,
ε_{IJ} : strain component,
C_{ij} : stiffness matrix component,
N : axial force,
Ti : transverse force in direction i,
Mi : moment in the direction i,
k : cylinder layer index,
α : twist angle,
θ : transformation angle,
Fpush : compressive axial load,
Fstop : axial effort in the up-end of the duct,
w : cable weight per unit length,
P : helix pitch,
μ : cable/duct friction coefficient,
r : clearance radius between cable and duct,
E I : cable bending modulus,
Fcr : sinusoidal buckling load,
Fhel: helical buckling load,
F(X) : up-end axial load at the distance X,
X : helically bucked length of a duct measured from down-up,
w_n :contact force resulting from helical buckling of weightless cable,
1 cm = 0.01 m .
1 daN = 10 N.

REFERENCES

1. Hashin, ''Analysis of properties of fiber composites with anisotropic constituents'', Journal of Applied Mechanics, sept 79, vol. 46, pp. 543-550.

2. Berthelot, J.M. , ''Composite materials '', Masson, Paris, 1992.

3. Noury T., '' Homogenization of composite beams with orthotropic components'', Thesis, Toulouse, France, dec. 1993.

4. Cheatham, J.B., ''Helical post-buckling configuration of a weightless column under the action of an axial load'', Society of Petroleum Engineers Journal, august 84, pp 467-472.

5. Wu, J., ''Helical buckling of pipe in extended reach and horizontal wells- Part2 : Frictional drag analysis'', Transactions of ASME, vol. 115, sept.1993, pp. 196-201.

SIMULATION OF FLEXURE IN OFF-AXIS THREE-POINT BENDING TEST BY A FINITE-ELEMENT CODE

A. D. Resnyansky

School of Mechanical and Manufacturing Engineering, UNSW, Sydney 2052, Australia

SUMMARY: The present paper is devoted to an application of a hierarchical model of unidirectional composite [1] to the finite element calculation of the three-point bending test in the quasi-static statement for a fibrous unidirectional composite. The finite element method (FEM) in use is based on the Hellinger-Reissner variational principle with assumed stress and displacement fields. Internal (structural) variables are calculated by the time increments where time is a load parameter. The arrangement of fibres and the component's debonding are not considered in the model. However, employing the structural parameters, the chances of the debonding between the constituents can be estimated. Numerical results confirm the conclusion of the beam theory that at the symmetrical loadings (the fibre direction is coincident with the load axis) and low span-to-depth ratio the shear failure prevails. At the same time, in the range of low span-to-depth ratios the influence of the fibre orientation is essential and provokes the mixed mode of fracture at the off-axis loading. Large span-to-depth ratio induces tensile fracture. However, again the off-axis loading destroys clearly defined boundaries of localised deformation and induces the peculiarities typical for the mixed mode of failure.

KEYWORDS: hierarchical model, homogenization approach, finite-element computation, three-point bending test, off-axis loading, fibrous unidirectional composite.

INTRODUCTION

The three-point bending test is one of the very popular tools for the study of the strength properties of material. The wide use of the method for composites faces peculiar features due to the non-isotropic and microstructural behaviour of composite beam, especially under the conditions of the off-axis loading. The complex stress state in the beam was understood for a long time. However, due to the convenience and availability of the test for mechanical assessment of the material properties, simple solutions of the beam theory [2] are widely used for acquisition of the shear and tensile stresses at failure in the three-point bending test.

In the case of the off-axis loading of composites the sample orientation is an essential parameter of the test. It is extremely important in this situation to understand which of the parameters, including the sample orientation and the span-to-depth ratio, are related to mechanical properties of the material and which ones are associated with the problem statement. Mathematical simulation is an invaluable tool in this situation.

The present paper is devoted to the numerical simulation of the problem in the quasi-static plane statement. A hierarchical model of unidirectional composite developed earlier [1,3] is

used for the development of a finite-element program and for numerical simulation. The Onzager principle is valid for the model and it enables us to construct the FEM algorithm with symmetrical stiffness matrix.

Numerical results for the graphite-epoxy composite at the variety of the off-axis angles (the angle between fibre and the load axis) and the span-to-depth ratios are compared with the experiment [4] in the critical load at failure. It is shown that the transition from the shear to the flexure depends not only on the span-to-depth ratio but on the off-axis angle as well.

MODEL OF THE COMPOSITE

The system of the constitutive equations of the model [1,3] contains evolutional relations for a rotation tensor determining the fibre orientation, a tensor of structural parameters Δ, which is responsible for the internal microstresses along fibres, and equations for elastic deformations (the tensor of elastic distortions a_{ij}). In the two-dimensional case the equations take the form:

$$\frac{da_{ij}}{dt} + a_{ik}\frac{\partial v_k}{\partial x_j} = -a_{ik}\psi_{kj}, \quad \frac{d\tilde{\Delta}}{dt} = -\tilde{\lambda}, \tag{1}$$

$$\frac{d\varphi}{dt} = \frac{a_{21}a_{22}\left(\psi_{11}-\psi_{22}\right)+\left(a_{22}^2-a_{21}^2\right)\psi_{12}}{a_{11}a_{22}-a_{12}a_{21}},$$

here fibres lie in the (x_1, x_2) - plane, φ is the angle between fibre and the x_1 - axis in the unloaded state, the tensor of structural parameters reduces to a sole parameter $\tilde{\Delta}$ - the difference between elastic strains in the constituents, which determines the internal stresses along the fibre, v_i - components of the velocity vector. Variables under tilde are associated with the local coordinate system connected with fibre. The tensor of elastic distortion A with components a_{ij} is linked with the standard tensor of elastic deformations ε^e by the rule: $\varepsilon^e = \left(I - A^T A\right)/2$, the superscript T denotes transposition. Combination of a_{ij} resulting in ε^e gives the following approximation of the constitutive equation for ε^e in the rectangular coordinate system associated with fibre:

$$\frac{d\tilde{\varepsilon}_{ij}^{e}}{dt} = \frac{d\tilde{\varepsilon}_{ij}}{dt} - \psi_{ij}, \tag{2}$$

here the rate of total deformation in the right side results from the components of the strain rate tensor $\partial v_i/\partial x_j$, ψ_{ij} are combinations of the state functions of constituents, which are responsible for the irreversible (plastic) deformation of composite and will be detailed later. Internal potential is expressed (for the isoentropic case) by the formula derived in details with the help of homogenization procedure in [3]: $E = \left(\sigma_{ij}\varepsilon_{ij}^{e} + \tilde{q}\tilde{\Delta}\right)/2$, here $\tilde{q} = E_{\tilde{\Delta}}$. In the coordinate system associated with fibre the stress tensor $\tilde{\sigma}$ is related to the elastic strain $\tilde{\varepsilon}^e$ by the Hooke's law:

$$\tilde{\sigma}_{11} = C_{11}\tilde{\varepsilon}^{e}_{11} + C_{12}\tilde{\varepsilon}^{e}_{22} + C_{12}\tilde{\varepsilon}^{e}_{33}\ , \quad \tilde{\sigma}_{22} = C_{12}\tilde{\varepsilon}^{e}_{11} + C_{22}\tilde{\varepsilon}^{e}_{22} + C_{23}\tilde{\varepsilon}^{e}_{33}\ ,$$

$$\tilde{\sigma}_{33} = C_{12}\tilde{\varepsilon}^{e}_{11} + C_{23}\tilde{\varepsilon}^{e}_{22} + C_{22}\tilde{\varepsilon}^{e}_{33}\ , \quad \tilde{\sigma}_{12} = C_{66}\tilde{\varepsilon}^{e}_{12}\ . \tag{3}$$

Effective elastic moduli C_{ij} result from the elastic moduli of composite constituents according to the homogenization procedure described in [1,3]. Differential consequences of the conservation laws are the governing equations of the model (the momentum and energy equations) for the fibrous composite and they have the standard form.

We reduce the model to the quasi-static case by the following simplifications. Firstly we consider t as a loading parameter similar to the loading parameter in the incremental theories of plasticity. The linkage of the load with t can be established from the given rate of loading $\dot{p}$. The given loading is reached in `time' by increments proportional to a step Δt. The inertial terms and the time derivative terms in the momentum equation are dropped.

We restrict ourselves by the isoentropic approximation. Therefore, the standard equations of equilibrium are valid. The stress-strain relations are obtained from the Hooke's law (3) and the `kinetic' laws (2) relating the elastic strain to the total deformation.

DESCRIPTION OF THE ALGORITHM

We consider the 2D-statement in the (x_1, x_2) - plane, where fibres are lying in the plane and $\varphi(x_1, x_2)$ is the angle between fibre and x_1. In the paper we assume the plane strain state, that is $\varepsilon_{33} = 0$, where ε - the tensor of total strain.

A method of study employed in the paper is two-dimensional finite element analysis based on a mixed stress-displacement formulation through the Hellinger-Reissner variational principle [5]. The formulation uses the four-node isoparametric quadrilateral element with assumed stress σ and displacement u linear distributions over the element.

The basic problem for the method design is the construction of the stress-strain linkage that can be expressed in increments by the general formula:

$$\Delta\sigma' = D\ \Delta\varepsilon' + G\ , \tag{4}$$

here σ' and ε' are 3-pseudovectors with components $\sigma_{11}, \sigma_{22}, \sigma_{12}$, etc. When the relation (4) is derived, the finite element theory for the Hellinger-Reissner principle gives the standard system of linear equations [5]:

$$H\bar{\sigma} + R\bar{u} = M\ , \quad R^T\bar{\sigma} = L\ , \tag{5}$$

here $\bar{\sigma}$ and $\bar{u}$ are assumed stresses and displacements for the given increment, H, R, M, L are assembled matrices. If D in (4) is a symmetrical matrix, then H in (5) is symmetrical along with the corresponding stiffness matrix $K = R^T H^{-1} R$. This fact is extremely important for the design of efficient and economic FEM algorithm.

In order to derive (4) we use constitutive equations of the model (1)-(3). Let us note that the first term in the equation for elastic strain is easy found from both the given displacements (they are connected with velocities by obvious formula $u = v\Delta t$) and coordinates. The second term is responsible for the inelastic behaviour of constituents and, as a consequence, of the composite. In the coordinate system related to fibre it takes the form [3]:

$$\begin{aligned}
&\tilde{\psi}_{11} = \alpha_{11}\tilde{\sigma}_{11} + \alpha_{12}\tilde{\sigma}_{22} + \alpha_{12}\tilde{\sigma}_{33} + \beta_1\tilde{q}, \\
&\tilde{\psi}_{22} = \alpha_{12}\tilde{\sigma}_{11} + \alpha_{22}\tilde{\sigma}_{22} + \alpha_{23}\tilde{\sigma}_{33} + \beta_2\tilde{q}, \\
&\tilde{\psi}_{33} = \alpha_{12}\tilde{\sigma}_{11} + \alpha_{23}\tilde{\sigma}_{22} + \alpha_{22}\tilde{\sigma}_{33} + \beta_2\tilde{q}, \\
&\tilde{\psi}_{12} = \alpha_{66}\tilde{\sigma}_{12}, \quad \tilde{\lambda} = \beta_1\tilde{\sigma}_{11} + \beta_2\tilde{\sigma}_{22} + \beta_2\tilde{\sigma}_{33} + \gamma\tilde{q},
\end{aligned} \tag{6}$$

The symmetry properties of the coefficients $\alpha_{ij}, \beta_i, \gamma$ in (6) follow from the Onzager principle proved for the model in [3]. Here $\tilde{q} = E_{\tilde{\Delta}}$, the coefficients in (6) are combinations of functions written out in [3] which describe the inelastic behaviour of constituents.

The initial step is the calculation of the rotation matrix B from the angle φ obtained on the previous increment step. The matrix connects a tensor F in the Cartesian system and that in the local coordinate system associated with fibre by the transformation rule:

$$\tilde{F} = B^T F B, \quad B = \begin{pmatrix} \cos(\varphi) & \sin(\varphi) \\ -\sin(\varphi) & \cos(\varphi) \end{pmatrix} \tag{7}$$

The system of constitutive equations (1) is used in increments, with the given time step Δt, which may be changed subject to the stability condition:

$$\begin{aligned}
&\Delta a_{ij} = -a_{ik}\frac{\partial \Delta u_k}{\partial x_j} - a_{ik}\psi_{kj}\Delta t, \\
&\Delta\varphi = \omega\Delta t, \\
&\Delta\tilde{\Delta} = -\tilde{\lambda}\Delta t,
\end{aligned} \tag{8}$$

here ω is the right-hand side in the third equation of the system (1).

Because the microstrains and, as a consequence, $\tilde{\Delta}$ are associated with internal processes in the composite so we consider this parameter separately from the set of the strain variables. It should be noted that from the point of view of the mathematical statement the variables σ and q, as well as ε and Δ are equivalent and they may be involved in the variational principle on the same rights. This becomes essential for the dynamic problem. In the present case we calculate ε and $\tilde{\Delta}$ separately.

For a given step equation (6) is written in increments as the following (in the matrix form):

$$\Delta \tilde{\Psi} = F\ \Delta\tilde{\sigma} + \tilde{\Psi}^0\ , \tag{9}$$

F is composed of the coefficients of (6), $\tilde{\Psi}^0$ is a value of the $\tilde{\Psi}$-dependence on the previous incremental step. From the Onzager principle F is a symmetrical matrix. The constitutive equation (2) for ε^e in the local system associated with fibre gives

$$\Delta\tilde{\varepsilon}^e = \Delta\tilde{\varepsilon} - \Delta\tilde{\Psi}\ .$$

Then the Hooke's law (3) is rewritten as

$$\Delta\tilde{\sigma} = C\ \Delta\tilde{\varepsilon}^e = C\left(\Delta\tilde{\varepsilon} - \Delta\tilde{\Psi}\right)\ .$$

Invoking (9), we have

$$C\ \Delta\tilde{\varepsilon} = \left(I + C\ F\right)\Delta\tilde{\sigma} + C\ \tilde{\Psi}^0 \qquad \text{or} \quad \Delta\tilde{\varepsilon} = \left(C^{-1} + F\right)\Delta\tilde{\sigma} + C\ \tilde{\Psi}^0\ . \tag{10}$$

Multiplying (10) on B from the left and on B^T from the right, we have one of the forms of (4).

It should be noted that due to both the symmetry of C (it means the material symmetriy of the transversally isotropic material) and the symmetry of F (it means the fulfillment of the Onzager principle) we have the symmetry of D in (4).

Thus, the finite element algorithm can be designed with the symmetrical matrix H in the basic system of linear equations (5) and, as a consequence, with the symmetrical stiffness matrix. It can be straightforward varified that the condition of the plane strain state $\varepsilon_{33} = 0$ leads to modifications of matrices C and F in (10) in such manner that their symmetry survives.

MATHEMATICAL STATEMENT OF THE PROBLEM

The three-point bending problem is approximated by the plane bending of the plate initially located in the following region of the space:

$$-S/2 < x_1 < S/2\ ,\quad -h < x_2 < 0\ ,\quad -\infty < x_3 < \infty\ .$$

Hereafter, we will refer to the crosssection $x_3 = 0$ of the plate. "Ends" ($x_1 = \pm S/2$) of the plate are clamped, i.e. $u = 0$ at $x_1 = \pm S/2, -h < x_2 < 0$.

The rest of the plate's boundary (except for the point of application of load) is free of normal stresses: $\sigma_{nn} = \sigma_{n\tau} = 0$, where n, τ are the normal and targent vectors to the boundary. At the point of loading (initially $x_1 = x_2 = 0$) a constant rate of the load is applied:

$$u_n = \dot{\varepsilon}_0 \cdot t, \tag{11}$$

t is a parameter of loading (time), $\dot{\varepsilon}_0$ is a given constant.

In the model, the composite elastic properties are determined by the properties of constituents: graphite fibres and epoxy matrix are assumed to have the following Young's moduli E_f, E_m, the shear moduli G_f, G_m and the Poisson's ratio ν_f, ν_m:

$$E_f = 300GPa, G_f = 125GPa, \nu_f = 02, E_m = 656GPa, G_m = 252GPa, \nu_m = 03.$$

The fracture properties of the constituents are expressed in the work by the stress limit. In the viscoelastic model the number of constants in a relevant dependence must correspond to the number of experimental points. As a dependence responsible for inelastic behaviour we choose the two-constant "thermal activation" function of the relaxation time τ_T on the shear sress in the following form: $\tau_T = \exp\left(U_0 - \gamma_0 J\right)$, here U_0, γ_0 are the material constants of constituents, the invariant of the stress tensor J:

$$J = \left[\left(\sigma_{11} - \sigma_{22}\right)^2 + \left(\sigma_{11} - \sigma_{22}\right)^2 + \left(\sigma_{11} - \sigma_{22}\right)^2 + 6\sigma_{12}^2\right]^{1/2} .$$

In order to construct this two-constant dependence for each constituent we must give two stress limits (σ_f^1, σ_f^2 for fibres and σ_m^1, σ_m^2 for matrix) at two strain rates ($\dot{\varepsilon}_1, \dot{\varepsilon}_2$). A method of the construction of the τ_T-dependence with the use of these data is described in [6]. As an example, the following data has been selected:

$$\sigma_f^1 = 23GPa \quad \text{at} \quad \dot{\varepsilon}_1 = 1m\,in^{-1}, \sigma_f^2 = 21GPa \quad \text{at} \quad \dot{\varepsilon}_2 = 001m\,in^{-1},$$

$$\sigma_m^1 = 013GPa \quad \text{at} \quad \dot{\varepsilon}_1 = 1m\,in^{-1}, \sigma_m^2 = 01GPa \quad \text{at} \quad \dot{\varepsilon}_2 = 001m\,in^{-1},$$

ANALYSIS OF RESULTS

On calculations the rate of loading in (11) has been chosen in accordance with the experiment [4] $\dot{\varepsilon}_o = 01\,m\,in^{-1}$ at $h = 5mm$, the fibre content $c = 0538$.

Our primary attention will be paid to the fulfilment of failure criterion. As the criterion we take the approaching of the stress limit. In the figures we draw the cross-section of the beam with dashed zones. They correspond to an excess in the stress limit for composite. Simultaneously we analyse the following parameters: the tensile stress along the plate surface (initially σ_{11}), the fibre stress in the coordinate system associated with fibre, the internal parameter $\tilde{\Delta}$ along the fibre, which is responsible for microstress (internal microstress may be the cause of debonding).

We approximate the constituents by isotropic materials so we restrict ourselves at the microstructural consideration by the stress along the fibres, although the graphite fibres may possess strong anisotropic properties. The limit in $\tilde{\Delta}$ can be assessed from the following reason: invoking the interlaminar shear stress for the composite [4] $006GPa$ as a basic point

for $\tilde{q}$ (see description of the model) we can find a critical value of $\tilde{\Delta}$ for the given constituents $\tilde{\Delta} \approx 0.02$. Keeping in mind that the debonding may be caused either the deformation of fibre or matrix this value can vary up to five times (according to the ratio of the Young's modulus of fibre to the matrix's one).

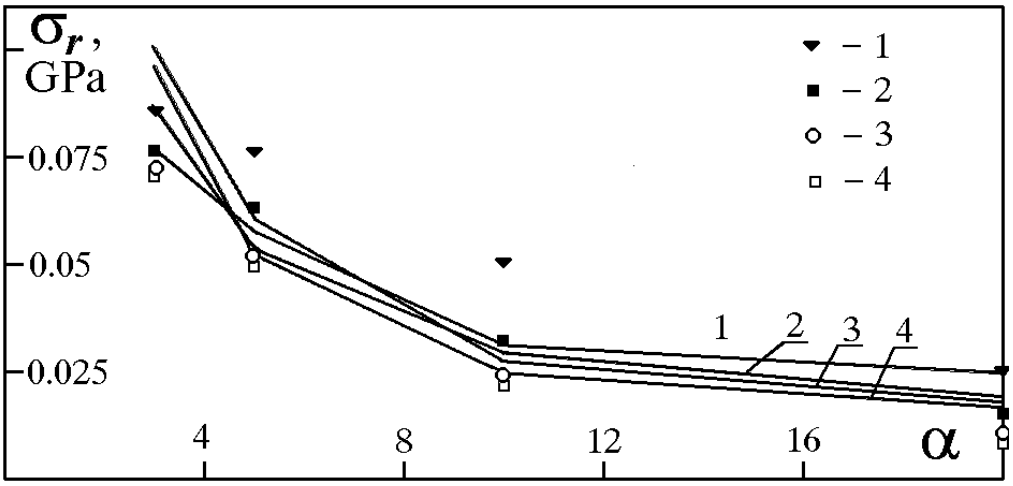

Fig. 1: The reduced load versus the span-to-depth ratio at the variety of the off-axis angles (curve 1- 0 deg , 2 - 15 deg , 3 - 30 deg , 4 - 45 deg), points are the corresponding experiment [4].

The simple beam theory [2] gives the following formulae for calculation of tensile $\sigma_{\tau\tau}$ and shear $\sigma_{n\tau}$ stresses:

$$\sigma_{\tau\tau} = \frac{3}{2}\sigma_r \alpha \ , \quad \sigma_{n\tau} = \frac{3}{4}\sigma_r \ , \tag{14}$$

here σ_r is a parameter associated with the real load in the experiment, the beam width and the beam depth. We reduce the applied load to the variable σ_r with the dimension of stress for convenience. $\alpha = S/h$ is the span-to-depth ratio. Analyses in the literature operate with the tensile and shear stress. In reality, an experiment gives only the value associated with the load at the failure. Therefore, using data from [4] we will employ only the values recalculated back from the reported tensile and shear stresses to the reduced load σ_r.

Fig. 1 shows the dependence of the load parameter on the span-to-depth ratio α for the variety of angles φ_0 between fibre and the the load axis from 0 up to 45 degress. Even keeping in mind the distinction in the simulated and experimental structures (the experiment [4] uses the fabric reinforced specimens, we calculate the unidirectional fibrous composite), the correlation is obvious.

The shear failure

Firstly we analyse the case of `short beam' with $S/h = 3$. Figure 2 shows the failure picture that exactly corresponds to the presentation about the shear mode [7]. The detachment of the failure zone from the outer layers of the beam (opposite to the point of application of the load) is clear seen. The concentration of the stress at the point of loading is natural. Due to the

crosswise compression with respect to the fibre direction in the failure zone, the debonding zone is not coincident with the fracture zone. The influence of the clamping effect on the debonding zone at periphery of the beam is out of our interest in the present paper.

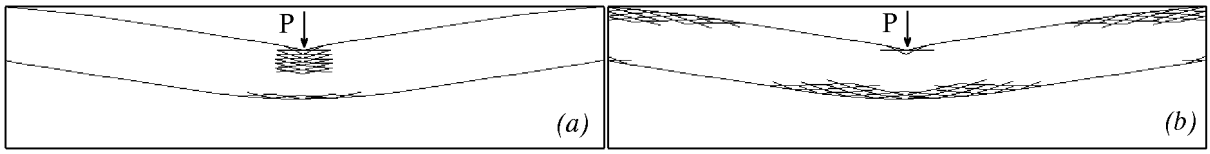

Fig. 2: The stress limit zones (a) and the possible debonding zone (the excess in the microstress - b) for the symmetrical loading; the span-to-depth ratio is 3.

In the case of the off-axis loading the picture is almost the same for the failure zones, but the zones, which are suspectied to be debonded, have some overlapping of the zones in the vicinity of the applied load and over the outer surface of the beam (Fig. 3, $\varphi_0 = 30^\circ$, the angle is countered in the counterclockwise direction from the vertical axis directed downward).

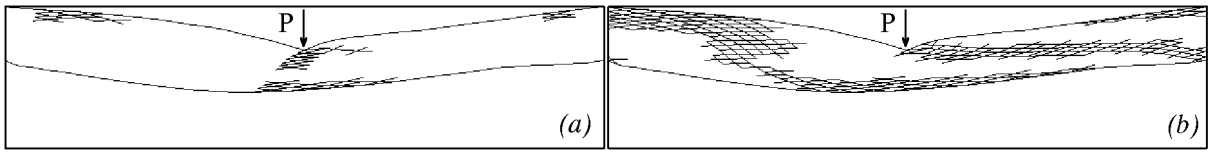

Fig. 3: The stress limit zones (a) and the possible debonding zone (b) for the off-axis loading (the angle is 30 deg); the span-to-depth ratio is 3.

Thus, in the case of $\alpha = 3$ the shear fracture occurs in the studied range of the angles. For the cases considered the tensile stress is low both in the composite as a whole and in fibres along the fibre direction.

It should be noted that even in the case of low span-to-depth ratio some influence of the fibre direction on the failure zone is noticeable in the outer (tensile) region opposite to the point of the load application.

Mixed mode of failure

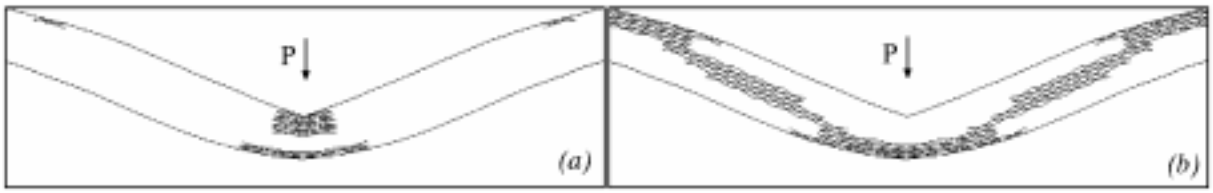

Fig. 4: The stress limit zones (a) and the possible debonding zone (b) for the symmetrical loading; the span-to-depth ratio is 5.

In the middle range of the span-to depth-ratio $S/h = 5$ for the symmetrical loadings ($\varphi_0 = 0^\circ$) the failure mode is still the shear one (Fig. 4). The widening of the tensile zone at the opposite surface to the load point becomes quite noticeable.

At $\varphi_0 = 30^0$ (Fig. 5) and more angles the mode can be considered to be changed to the mixed mode (in classification [7]) . In the failure zone the debonding is quite probable.

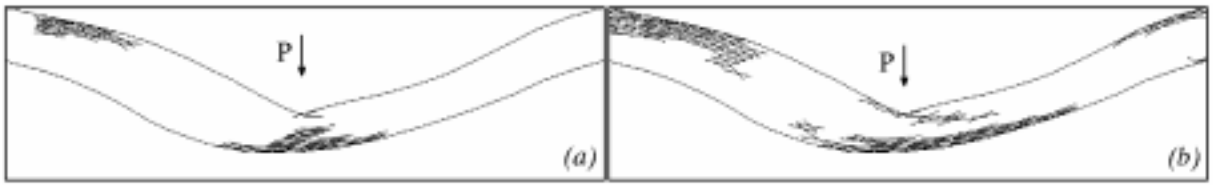

Fig. 5: The stress limit zones (a) and the possible debonding zone (b) for the off-axis loading (the angle is 30 deg); the span-to-depth ratio is 5.

The tensile failure

At large span-to-depth ratios ($\alpha = 10$ and 20 in this subsection) the influence of tension on the failure is obvious in the variety of angles. At the same time, some peculiarities take place.

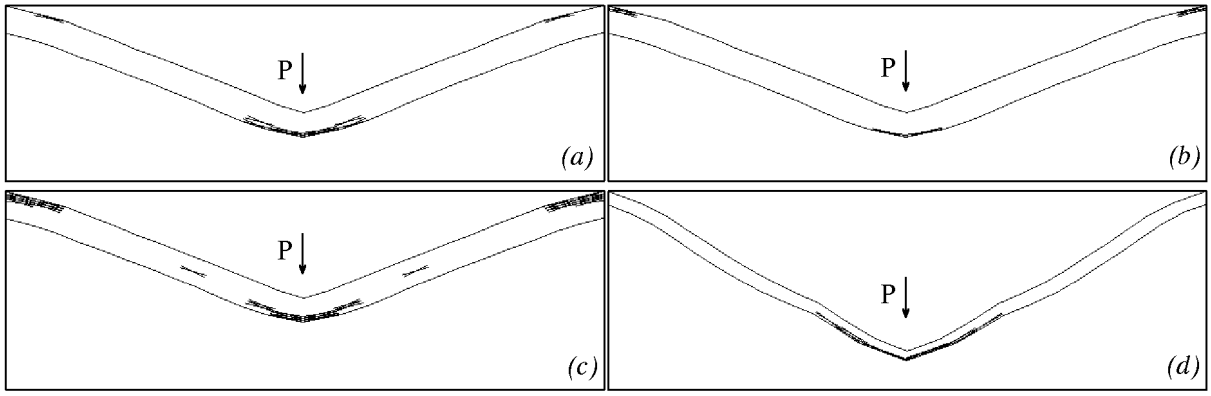

Fig. 6: The stress limit zones (a,d), the tensile stress limit zone (b), the possible debonding zone (c) for the symmetrical loading; the span-to-depth ratios are 10 (a,b,c) and 20 (d).

The case of symmetrical loading is drawn in Fig. 6, the failure starts on the opposite surface to the load point, the tensile stress and the debonding indicator are significant too. The appearence of the zones of localised deformation is seen especially clear at $S/h = 20$ (Fig. 6,d).

At these ratios the off-axis case is also characterised by the tensile failure. However, the features of the mixed failure mode are appeared, too. This is especially noticeable at the large off-axis angle (Fig. 7 a,b,c at $\varphi_0 = 45^0$).

Due to the specific fibre orientation in the given sample configurations, σ_f becomes significant at the large span-to-depth ratios and at the load with φ_0 more than 30° (in that part of the beam where orientation is in agreement with the load direction), the tensile stresses and the debonding zone are concentrated at the outer surface.

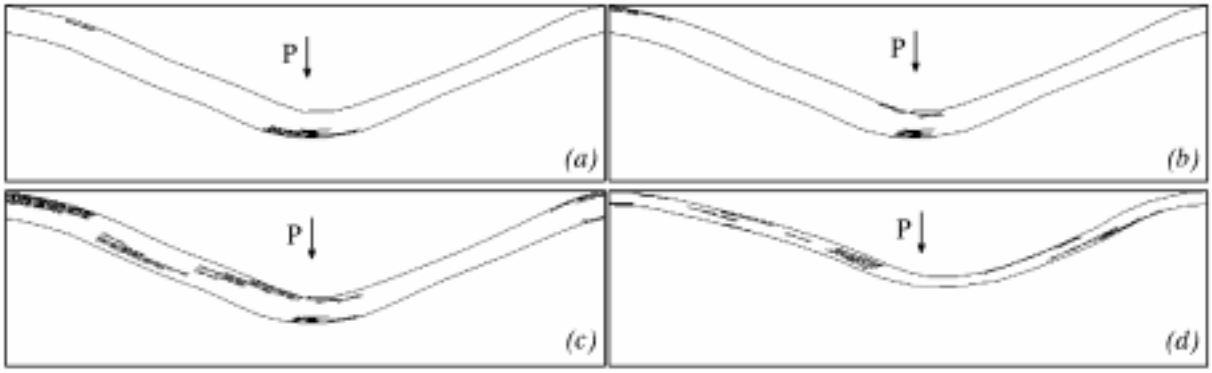

Fig. 7: The stress limit zones (a), the tensile failure zone (b), the possible debonding zone (c) and the fibre fracture zone (d) for the off-axis loading (the angle is 45 deg); the span-to-depth ratios are 10 (a,b,c) and 20(d).

CONCLUSION

The direct numerical simulation of the three-point bending test has shown that the load parameter correlates experiments quite adequately for the variety of the off-axis angles and span-to-depth ratios. At low span-to-depth ratios ($\alpha = 3$ for the given set of constituents) the shear failure mode is realised at the variety of the off-axis angles. However, even in the low range of span-to-depth ratios the influence of fibre orientation is essential. At $\alpha = 5$ the mixed failure mode takes place for the off-axis loading. At the large span-to-depth ratios ($\alpha = 10$ and 20 for the given composite) a steady tensile fracture takes place. Under these conditions, the fibre fracture is more probable at the off-axis test. At the symmetrical loading the areas of localised deformation are appeared clearly.

REFERENCES

1. Resnyansky, A.D. and Romensky, E.I., “Using a Homogenization Procedure for the Prediction of Material Properties and the Impact Response of Unidirectional Composite”, *The Present Proceedings.*

2. Timoshenko, S., *Strength of Materials. Part I,* Van Nostrand, New York, 1955.

3. Resnyansky, A.D. and Romensky, E.I., "Model of Dynamic Deformation of a Fibrous Thermoviscoelastic Composite", *Combustion, Explosion, and Shock Waves (Fizika Gorenia i Vzryva)*, Vol. 28, No. 4, 1992, pp. 430-436.

4. Birger, S., Moshonov, A. and Kenig S., "Failure Mechanisms of Graphite-Fabric Epoxy Composites Subjected to Flexural Loading", *Composites*, Vol. 20, No. 2, 1989, pp. 136-144.

5. Pian, T.H. and Tong, P., "Basis of Finite Element Methods for Solid Continua", *Int. Journal of Numerical Methods in Eng.*, Vol. 1, 1969, pp. 3-28.

6. Resnyansky, A.D. and Merzhievsky, L.A. "On Determination of Parametres of Dependence of The Shear-Stress-Relaxation Time", [In Russian], *Fizika Gorenia i Vzryva*, Vol. 28, No. 3, 1992, pp. 123-124.

7. Hanna, G.L. and Steingiser, S., "Defining the Adhesion Characteristics in Advanced Composites", *Composite Materials: Testing and Design, ASTM STP 460*, American Society for Testing and Materials, 1969, pp. 182-191.

FRACTURE MECHANICAL ANALYSIS OF PULL-OUT AND FRAGMENTATION TESTS

Christian Marotzke, Andreas Hampe

Federal Institute for Materials Research and Testing (BAM), Dept. VI
Unter den Eichen 87, 12205 Berlin, Germany

SUMMARY: The aim of this paper is a clarification of the failure process taking place in pull-out and fragmentation tests as well as a critical assessment of the common techniques for the evaluation of the experimental data. The fracture process is analysed by means of the finite element method. In the pull-out test, the mode ratio changes dramatically during the first phase of the crack from dominating mode I to mode II. The mixed mode energy release rate is calculated for glass fibers embedded in a thermoplastic matrix. It turns out that the strain energy stored during the cooling process, significantly increases the energy release rate in the pull-out test and has to be taken into account in the evaluation of the test data. In the fragmentation test, a mode II failure arises. Due to the existence of high radial compressive stresses in the interface, frictional shear stresses develop, which result in a strong decrease of the energy release rate and must not be neglected in the evaluation of the test data.

KEYWORDS: pull-out test, fragmentation test, energy release rate, finite element analysis

INTRODUCTION

For a long time, the micromechanical tests were used for the determination of the strength of the interface between fiber and matrix. However, for the determination of the strength, the stress state must be well defined. In the micromechanical tests, a complex, threedimensional stress state is encountered around the interface [1-3]. Severe stress concentrations arise at the fiber break in the fragmentation test and at the fiber end as well as at the fiber entry in the pull-out test. Within the linear theory of elasticity, singularities are found at these points, similar to a crack tip. Under those circumstances, it is not reasonable to conduct a stress analysis in order to calculate an interfacial strength, because the stresses at the critical points depend on the local geometry and on the local material properties, which may differ significantly from that of the bulk material. Moreover, not only one isolated stress component is found at these points but a superposition of radial and shear stresses. The ratio of the two components strongly depends on the material properties of fiber and matrix. In the past, ssubstantial simplifications concerning the stress field around the interface were used for the evaluation of the test data. One model, based on a plastic behaviour of the matrix [4], presumes an unbounded yielding of the matrix near the interface, leading to constant interfacial shear stresses (Kelly-Tyson formula). The two main inconsistencies inherent in this approach are the neglection of the other stress components and the unrealistic strains resulting from the unbounded yielding of the matrix. The other model simplifies the elastic stress field using the shear lag hypothesis [5,6]. This model is inconsistent in that it results in constant axial stresses in the matrix, violating the boundary conditions in the interface and, furthermore, underestimates the stress concentrations at the critical points [7]. A further

problem of the measurement of the strength with pull-out tests is the definition of the moment of failure initiation. Several studies have shown that the failure initiation arises long before the force maximum is reached [8,9].

In recent years, the characterisation of the interface by a fracture mechanical analysis leading to a fracture toughness or an energy release rate, becomes more and more accepted [1,10-15]. A fracture mechanical analysis is more adequate to the stress state arising in the interface with stress singularities at the critical points. However, not all problems encountered in the stress analysis are overcome. As a result of the superposition of radial and shear stresses, only a mixed mode fracture toughness can be measured directly. The discrimination of the modes requires a theoretical analysis [16]. In general, the fracture toughness can be determined experimentally, if the material behaves perfect linear elastically and if the variation of the compliance with the crack length can be measured with high precision. However, the determination of the crack length is not possible for all matrices and it is a rather complicated procedure [9]. Furthermore, polymeric matrices exhibit a more or less nonlinear behaviour. The linear elastic analysis, which is commonly utilised in the literature, gives a first approach and offers some insight into the main mechanisms of the fracture process, if the matrices are not too nonlinear.

FINITE ELEMENT MODEL

The pull-out test model consists of a fiber of ten microns in diameter embedded perpendicular into a halfsphere of matrix up to a length of 150 microns. The fragmentation test model of 400 microns in length corresponds to one half of a fragment, applying symmetry conditions at the edges. For both specimens, axisymmetrical finite element meshes are used (figs. 1a, 1b). The meshes are strongly refined around the interface with respect to the high stress gradients arising

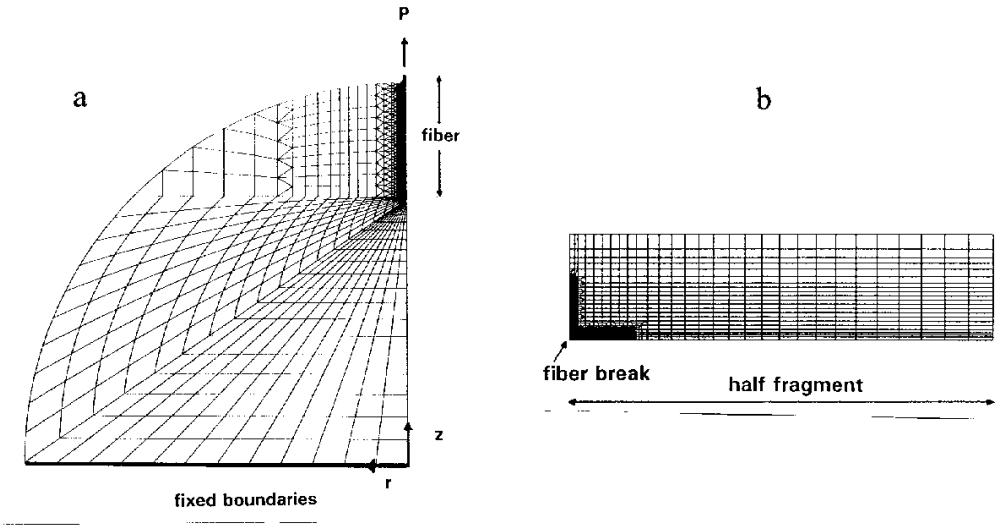

Fig. 1: Finite Element meshes (a: pull-out test, b: fragmentation test)

there. In the interface, contact elements are defined together with links between the two anticipated crack faces, which can be removed in order to simulate the crack propagation. The aim of the present analysis is to study of the variation of the interfacial stresses and of the energy release rate during interfacial failure. To this end, the propagation of an interface crack is simulated, however, not controlled by a failure criterion but prescribed externally.

FAILURE PROCESS IN PULL-OUT AND FRAGMENTATION TESTS

The process of interfacial failure is totally different in the pull-out and in the fragmentation test. If the initial stresses due to the thermal mismatch of fiber and matrix or due to curing are not taken into account, the interfacial stresses in the pull-out test build up continuously with the increase of the external force up to the initiation of the interface crack. In the fragmentation test, on the other hand, the loading of the interface starts abruptly with the breakage of the fiber. This is, the interface is loaded rather statically in the pull-out test while dynamically in the fragmentation test. A further essential difference between the respective tests is the correlation between the prescribed external load and the loading of the interface. While the load at failure initiation is correlated to the strength of the interface in the pull-out test, it is correlated to the fiber strength in the fragmentation test. This means that the onset of interfacial failure cannot be controlled by the external force in the fragmentation test. Therefore, the crack propagates unstably after the breakage of the fiber. Furthermore, the type of crack is different. In the pull-out test, a pure interface crack arises while in the fragmentation test it is often observed that the interface crack is preceded by short matrix cracks, both, in 90° and 45° direction [14].

STRESS FIELD AROUND THE INTERFACE

The stress field around the interface arising in the pull-out and fragmentation test is analysed for a glass fiber embedded in a polycarbonate matrix with a stiffness ratio of 32. The specimen is cooled down by 120°C, frictional stresses are not included at this stage. In the pull-out specimen, the thermal mismatch leads to an inhomogeneous stress field around the interface. The fiber is under axial compressive stresses reaching a maximum in the middle part (fig. 2).

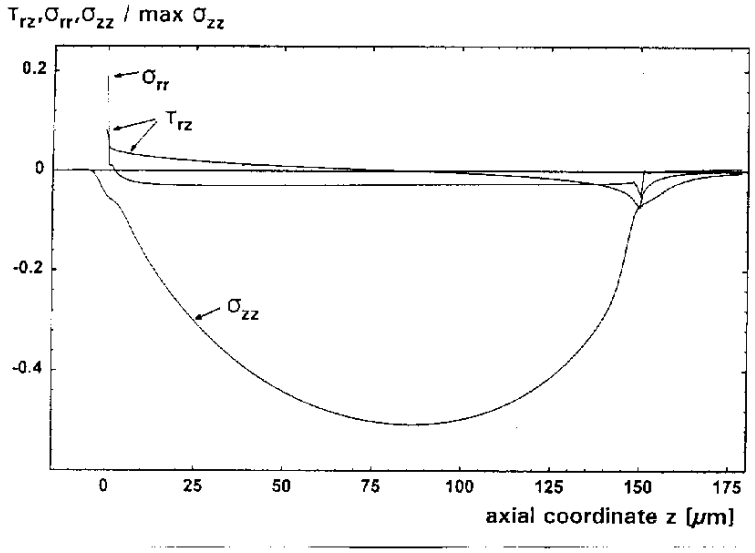

Fig. 2: Thermal stresses in fiber in interface in the pull-out test

The fiber stresses are accompanied by interfacial shear stresses which change their direction along the fiber. Two maxima occur, one at the fiber entry and a second one at the fiber end. In addition, compressive radial stresses arise in the interface except of the fiber entry, where a high tensile stress maximum is encountered. If the pull-out force is applied, the compressive

stress state is changed to tensile one, starting from the fiber entry (fig. 2, fig.3). However, during the first phase of the crack, still compressive stresses arise near the fiber end. With the further propagation of the crack, this zone decreases until the fiber is completely under tensile stresses.

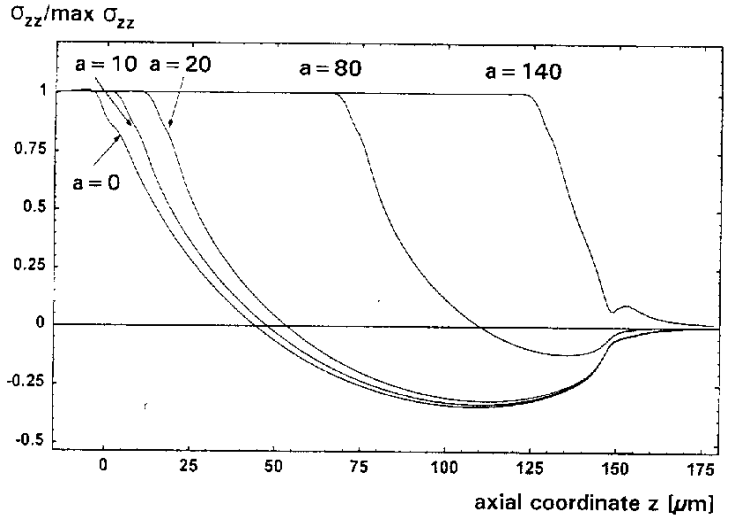

Fig. 3: Axial fiber stresses in pull-out specimen at different crack lengths a[μm]

By the application of the pull-out load, the shear stresses at the fiber entry are increased while they are decreased at the fiber end (fig. 2, fig. 4). With the initiation of the interface crack, the maximum at the fiber entry is further increased remaining almost constant during further crack propagation, while the average of the shear stresses grows due to the reduction of the stress transfer length. The radial tensile stress maximum at the fiber entry is also enhanced by the application of the external force (fig. 5). However, it drops by an order of magnitude by the initiation of the crack, again, remaining almost constant during further crack propagation. This is, while the radial tensile stresses are dominating before the onset of failure and are, accordingly, responsible for the crack initiation, the shear stresses are dominating during the further crack propagation. This is, the ratio of the failure modes changes with crack initiation.

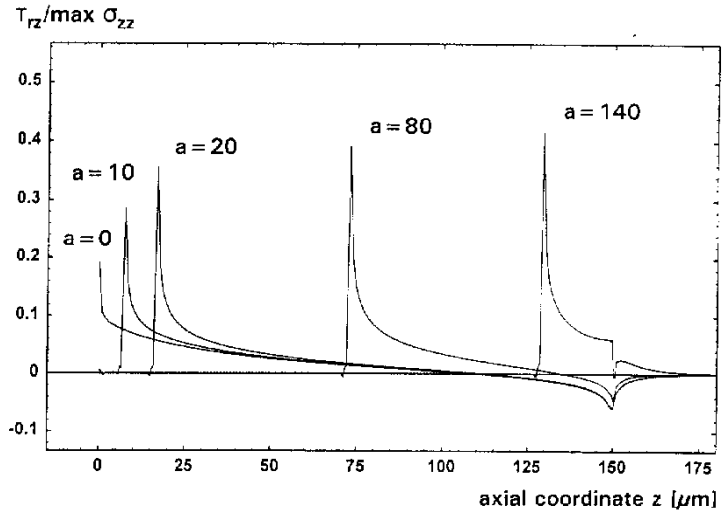

Fig. 4: Interfacial shear stresses in pull-out specimen at different crack lengths a[μm]

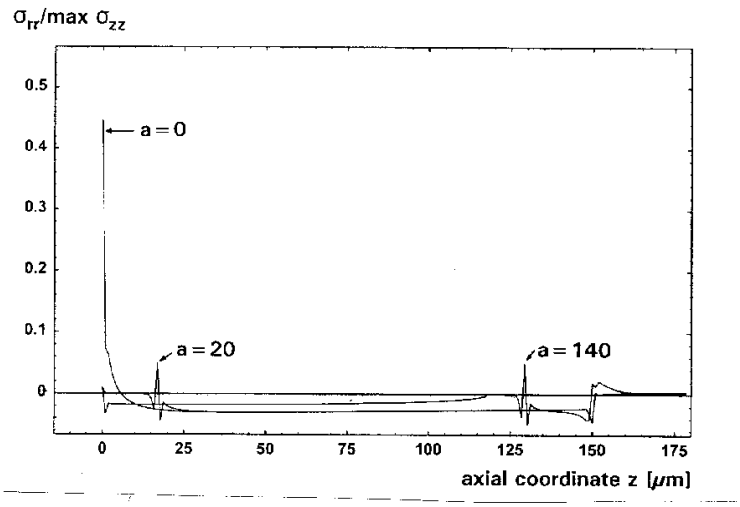

Fig. 5: Interfacial radial stresses in pull-out specimen at different crack lengths a[μm]

In the fragmentation specimen, the effect of the thermal mismatch on the stresses around the fiber is rather small. If the specimen is loaded, the fiber is under constant axial tensile stresses except of the ends of the specimen. After fiber breakage, the fiber stresses decrease very rapidly in the vicinity of the fiber break or, after crack initiation, at the crack tip, respectively (fig. 6). The maximum fiber stresses remain nearly unchanged by the crack extension.

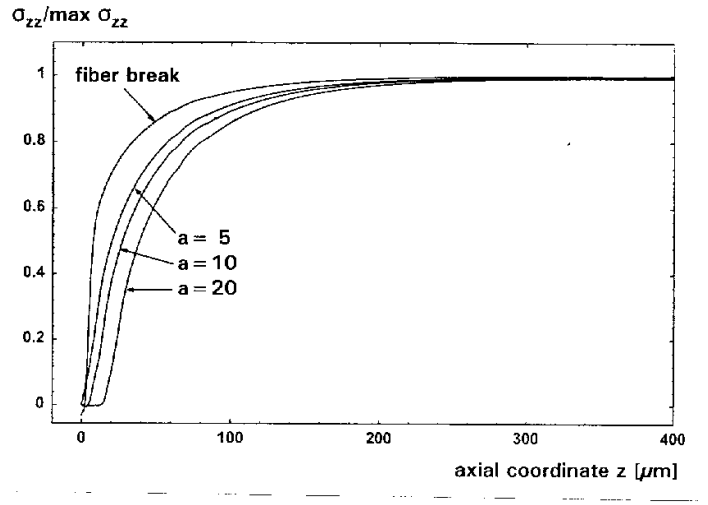

Fig. 6: Axial fiber stresses in the fragmentation specimen at different crack lengths a[μm]

Additionally, very high shear and radial compressive stresses arise in the interface near the break point (fig.7, fig.8). Both stress components are significantly decreased due to the initiation of the interface crack. Contrary to the pull-out specimen, the interfacial failure is governed by shear stresses in the fragmentation test since the radial stresses are compressive. These give rise to frictional shear stresses in the debonded zone, consuming a lot of released strain energy.

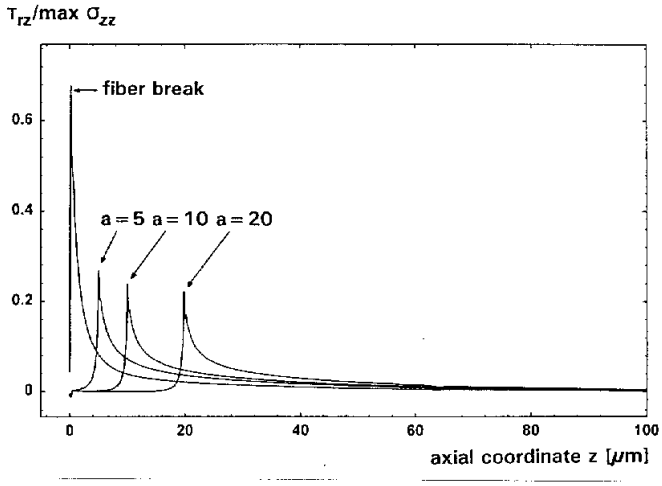

Fig. 7: Interfacial shear stresses in fragmentation specimen at different crack lengths a[μm]

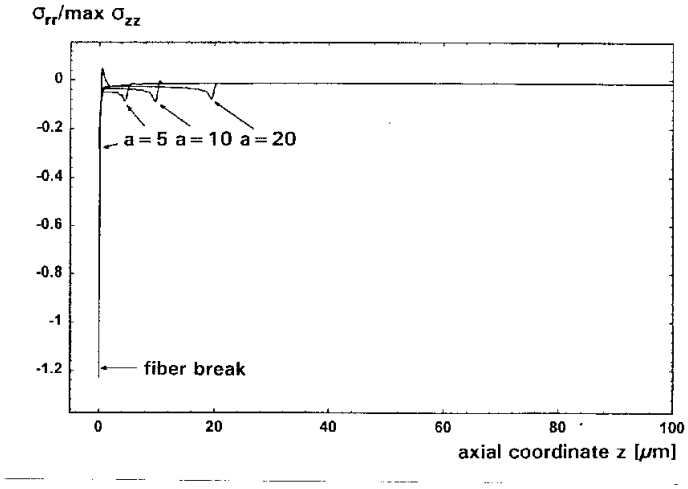

Fig. 8: Interfacial radial stresses in fragmentation specimen at different crack lengths a[μm]

ENERGY RELEASE RATE

In case of a perfect linear elastic material behaviour, the critical energy release rate does not depend on the crack length. If the course of the energy released during crack propagation, for example under fixed loads or fixed grips conditions, is known, the fracture process can be characterised, i. e. stable or unstable phases can be discriminated. To this end, the energy release rate arising in the pull-out and fragmentation test is calculated. In the pull-out test, fixed load conditions are prescribed, corresponding to the level at failure initiation as observed in the experiments. In the fragmentation test, fixed grips conditions are prescribed, corresponding to the strain to failure of the fiber. However, the unloading of the total specimen due to the propagation of the interface crack is very low, likewise resulting in an almost constant load. The force in the middle of the fiber decreases by only 0.7 % due to the fiber break and by 0.5% by a crack of two fiber diameters. This means, on the other hand, that the compliance of the fragmentation test specimen is rather insensitive against the crack length.

Pull-out Test

The energy release rate arising in a pull-out test increases very slowly over a large range of the crack in case of a frictionless interface, if thermal stresses not taken into account [17]. In case of a thermoplastic matrix, a large portion of energy is stored in the specimen as a result of the cooling process. The fiber is compressed while the matrix around the fiber is under tensile stresses. If the interface crack propagates, this energy is released. Furthermore, the external work done by the pull-out force acting at the fiber tip is increased by the additional displacement of the fiber tip as a result of the initial stresses. The energy release rate without thermal stresses increases slowly, until the crack approaches the fiber end, where the increase becomes very steep (fig. 9). Due to the thermal stresses, the energy release rate is enhanced significantly. This is, the initial stresses have to be taken into account, if pull-out experiments are evaluated. However, this part of stored energy is often neglected in the literature.

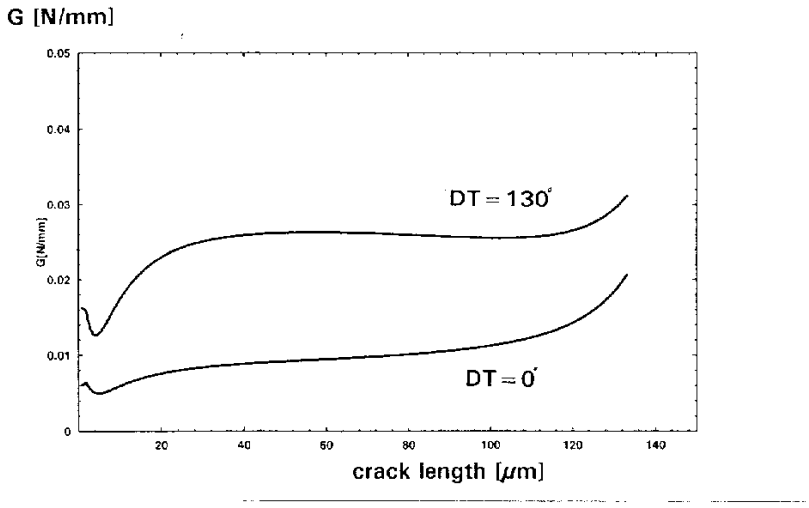

Fig.9: Energy release rate arising in pull-out test with and without thermal stresses

Fragmentation Test

The course of the energy release rate of a fragmentation test is totally different from that of a pull-out test. With the breakage of the fiber, a large amount of stored energy is released, which is much higher than that dissipated by the fiber break. The unused energy causes an unstable interface or matrix crack. In general, both cracks may develop simultaneously. The process occurring directly after fiber break is very complex and requires an analysis including dynamical effects. However, no reliable local material data are given at present for the respective matrices under high speed conditions. The present analysis, therefore, is confined to static conditions, which are valid for the second phase of stable crack propagation.

First, the released strain energy as a result of the fiber fracture and the interface crack is inspected. The total amount of released energy as well as the contributions of fiber and matrix are shown in figure 10. By the fracture of the fiber, the fiber is unloaded, releasing a large amount of strain energy. This value is represented by the starting point. At the same time, the matrix is stressed additionally, consuming energy. This process continues during the extension of the interface crack. The accumulated released energy increases due to crack propagation, however, with decreasing slope. Beyond a crack length of about one fiber radius,

the released energy grows rather linearly, resulting in an almost constant energy release rate, as shown below.

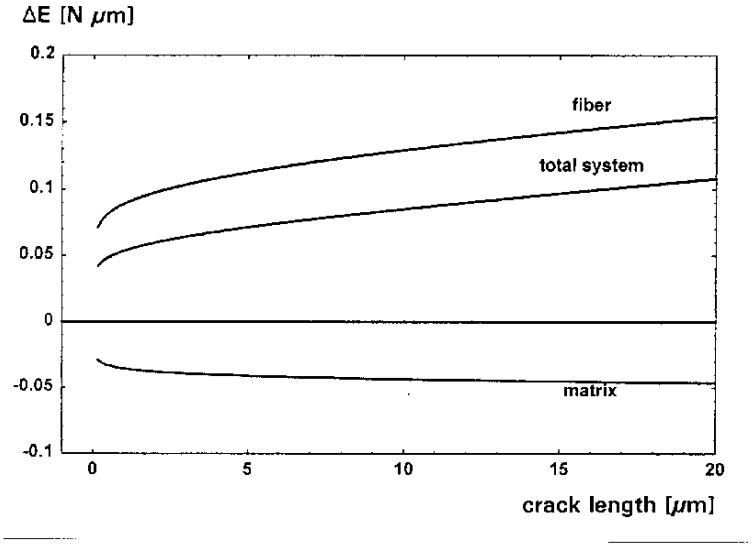

Fig. 10: Energy released by fiber and matrix in fragmentation test

The energy release rate of an interface crack is plotted in fig. 11 with and without interfacial friction. The first point represents the energy released by the fiber break per cross-section of the fiber. In the first phase of the interface crack, the energy release rate is extremely high. It drops, however, to about 20% of the maximum value within a crack length of only 20% of the fiber diameter. Beyond this region, the energy release rate slightly decreases, leading to a stable crack propagation. In order to get an estimation of the upper limit of the influence of friction, the same system is analysed allowing frictional stresses with a friction coefficient of 1.0 As a result of friction, the energy release rate decreases significantly to about one quarter of the original value. This shows that the evaluation of test data requires the knowledge of the work of friction.

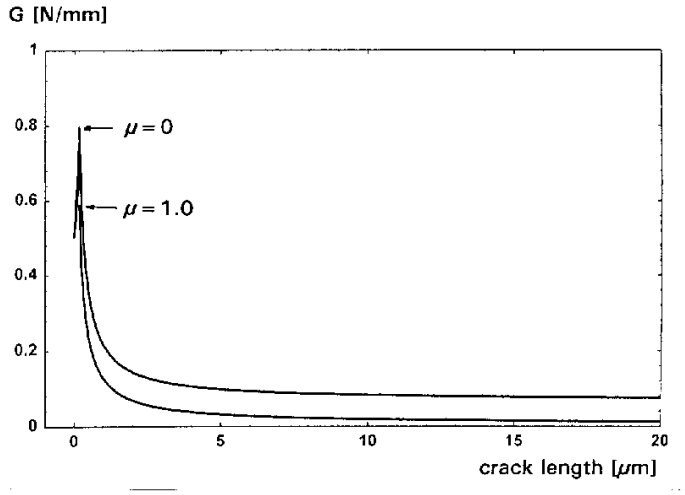

Fig. 11: Energy release rate arising in fragmentation test with and without friction

CONCLUSIONS

In general, the interfacial fracture toughness can be determined using pull-out and fragmentation tests. However, while in pull-out tests the compliance is sensitive against the crack length, this is not true in case of the fragmentation test. This means, the fracture toughness can be measured with an acceptable accuracy directly in the pull-out test, if the matrix is transparent and behaves rather brittle. In the fragmentation test, on the other hand, an additional theoretical analysis is needed. For such an analysis, the external force necessary to cause a stable crack propagation must be measured. This may be complicated due to the fact that multiple fiber fractures and, accordingly, multiple interface cracks usually are present in a fragmentation test. A further problem arising in the fracture mechanical evaluation is the existence of radial cracks.

REFERENCES

1. Atkinson, C., Avila, J., Betz, E. & Smelser, R. E., "The rod pull out problem, theory and experiment", *Journal of the Mechanics and Physics of Solids*, Vol. 30, 1982, pp. 97-120

2. Desarmot, G., Favre, J. P., "Advances in pull-out Testing", *Composites Science and Technology*, Vol. 42, 1991, pp. 151-187

3. Marotzke, C., "The elastic stress field arising in the single fiber pull-out test", *Composite Science and Technology*, Vol. 50, 1994, pp. 393-405

4. Kelly, A., Tyson, W. R., "Tensile properties of fibre reinforced metals: copper/tungsten and copper/molybdenium,", *Journal of the Mechanics and Physics of Solids*, Vol. 13, 1965, pp. 329-350

5. Piggott, M. R., *Load bearing fibre composites*, Pergamon Press, Oxford, 1980

6. Hsueh, C. H., "Elastic load transfer from partially embedded axially loaded fibre to matrix", *Journal of Materials Science Letters*, Vol. 7, 1988, pp. 487-500

7. Marotzke, C., "Influence of the fiber length on the stress transfer from glass and carbon fibers into a thermoplastic matrix in the pull-out test", *Composite Interfaces*, Vol. 1, 1993, pp. 153-166

8. Piggott, M. R., Xiong, Y. J., "Visualisation of debonding of fully and partially embedded glass fibres in epoxy resins", *Composite Science and Technology*, Vol. 52, 1995, pp. 535- 540

9. Hampe, A., Marotzke, C., "The fracture toughness of glass fibre/polymer matrix interfaces: measurement and theoretical analysis", *Proceedings of the third International Conference on Deformation and Fracture of Composites*, Surrey, 1995

10. Y. C. Gao, Y. W. Mai and B. Cotterell, "Fracture of fiber reinforced materials", *Journal of Applied Mathematics and Physics* (ZAMP), Vol. 39, 1988, pp. 550-572

11. Liu, H.-Y., Mai, Y.-W., Zhou, L.-M., Ye, L., "Simulation of the fibre fragmentation process by a fracture mechanics analysis", *Composites Science and Technology*, Vol. 52, 1994, pp. 253-260

12. Beckert, W., Lauke, B., "Fracture mechanics finite element analysis of debonding crack extension for a single-fibre pull-out specimen", *Journal of Materials Science Letters*, Vol. 14, 1995, pp. 333-336

13. Kerans, T. A. Parthasarathy, "Theoretical analysis of the fiber pullout and pushout tests", *Journal of the American Ceramic Society*, Vol. 74, 1991, pp. 1585-1596

14. Pegoretti, A., Accorsi, M. L., DiBenedetto, A.T., "Fracture toughness of fiber-matrix interface in glass-epoxy composites, *Journal of Materials Science*, Vol. 31, 1996, pp.6145-6153

15. Wagner, H. D., Nairn, J. A., Detassis, M., "Toughness of interfaces from initial fiber-matrix debonding in a single fiber composite fragmentation test", *Applied Composite Materials*, Vol. 2, 1995, pp. 107-117

16. Charalambides, M., Kinloch, A. J., Wang, Y., Williams, J. G., "On the analysis of mixed-mode failure", *International Journal of Fracture*, Vol. 54, 1992, pp. 269-291

17. Marotzke, C., Qiao, L., "Determination of the interfacial fracture toughness using micromechanical tests", *Proceedings of the seventh European Conference on Composite Materials*, London, 1996, Vol. 2, Woodhead Publishing Limited, Cambridge, pp. 17-22
crack was propagated fifty millimetres before the test specimen was unloaded. The foam-based systems E and F were not evaluated in this part of the study.

FINITE ELEMENT ANALYSIS OF TEST METHODS FOR THE DETERMINATION OF THROUGH-THICKNESS PROPERTIES INTENSION, COMPRESSION AND SHEAR OF LONG FIBRE REINFORCED COMPOSITES

S. Mespoulet[1], J.M. Hodgkinson[1], F.L. Matthews[1], D. Hitchings[2], P. Robinson[2]

[1] Centre for Composite Materials, [2] Department of Aeronautics
Imperial College of Science, Technology and Medicine
Prince Consort Road, London SW7 2BY, United Kingdom

SUMMARY: The detailed design of 3D laminated structures has shown the need for reliable methods for measuring the through-thickness mechanical properties of composite materials. In this work, finite element studies have been conducted in order to develop suitable test methods for the determination of the through-thickness strengths and elastic constants in tension, compression and shear. For these three loading cases, the specimens are loaded directly either normally or in shear. In both cases of direct normal and shear loading, two specimen designs are proposed: a parallel-sided block for the determination of the elastic constants only and an elliptically-waisted specimen for the determination of both the elastic constants and strength.

KEYWORDS: through-thickness, mechanical properties, test method, finite element, shear, tension, compression

INTRODUCTION

The structural design of laminated components is largely dependent on the accurate input of the material mechanical properties in tension, compression and shear. Standardised test methods exist for the evaluation of most of the in-plane elastic constants and strength parameters. As long as the design approach remains two-dimensional, this is sufficient. However, structures have become more complex 3D arrangements for the design of which the through-thickness (TT) material mechanical properties are also required. No recognised standards exist for TT tension or compression testing. So far as shear is concerned, the Iosipescu test technique [1] has out-of-plane possibilities [2,3] but, in that case, the determination of the shear strength is erroneous since failure is more due to transverse tension than to shear [4].

Numerous attempts at developing suitable TT test methods have been undertaken and these have been reviewed elsewhere [5-7]. A suitable TT test method should make use of simple specimens cut from laminates which are not too thick (thick laminates being difficult to manufacture), ensure a pure and uniform stress state in the gauge section which leads to the expected failure mode, rely on a direct and simple analysis and enable the determination of

both elastic and strength parameters. Based on an extensive literature search [5], the most promising methods have been short listed. These have been studied with finite element (FE) methods for optimisation and tested experimentally for complete validation. The experimental results from tensile [8] and compressive [9] testing have already been reported. The present article reports the results of the FE study for the investigated test methods. These are the direct normal test method which has tensile and compressive possibilities and the direct shear test method.

PRELIMINARY CONSIDERATIONS

Material Properties

The material properties used for the FE analysis are reported in table 1. They are those of Hexcel carbon/epoxy T300/914. The in-plane properties were determined by in-plane testing and, for these, the coefficients of variation are given in brackets in the table. The determination of the other properties is based on the assumption of material transverse isotropy. All the FE analyses were conducted on unidirectional (UD) material.

Table 1: Mechanical properties data for FE input (UD Carbon/Epoxy T300/914)

Elastic Properties		Strength Properties (MPa)	
E_1 (GPa)	129 (3.3%)	σ_{1t}^u	1434 (7.6%)
E_2 (GPa)	9.5 (1.6%)	σ_{1c}^u	1318 (7%)
E_3 (GPa)	9.5	σ_{2t}^u	48 (8.3%)
G_{12} (GPa)	4.7 (1.3%)	σ_{2c}^u	215 (9.1%)
G_{23} (GPa)	3.2	σ_{3t}^u	48
G_{31} (GPa)	4.7	σ_{3c}^u	215
ν_{12}	0.34 (6.4%)	τ_{12}^u	79 (8%)
ν_{23}	0.5^+	τ_{23}^u	79
ν_{13}	0.34	τ_{31}^u	79

$^+$ Data from references [11,12]

Finite Element Study

The FE package used for this study is FE77, the in-house system of the Department of Aeronautics at Imperial College. All the analyses were performed in the linear elastic region. The 2D and 3D meshes were built up with 8-noded and 20-noded brick elements respectively with parabolic-shaped interpolation functions. Output average stresses were interpolated from the stresses at the Gauss points. The 3D Hill failure criterion was introduced into the code in order to locate the failure initiation.

DIRECT NORMAL TEST METHOD

Several authors have investigated this technique for TT parameters determination [2,10-13]. In this method, a normal (tensile or compressive) load is applied in the TT direction of the laminated specimen. There are several advantages to this method: simplicity of analysis, potential application to multi-directional laminates, determination of both elastic constants and strength parameters. Its main drawback though is the use of fairly long specimens which means that thick laminates have to be manufactured. The main objective of the FE analysis has therefore been to reduce as much as possible the specimen length while keeping a pure and uniform tensile or compressive stress state in the gauge section. Two specimen shapes have been investigated: the parallel-sided block and the waisted specimen.

Parallel-Sided Block

The 3D FE model used is represented in figure 1. Since there are 3 planes of symmetry, only 1/8 of the set-up needs to be meshed. The top surface of the model is completely constrained in the (xy) plane and a displacement of 0.1mm is applied in the TT z-direction. The end block material properties are those of aluminium (E=72.4GPa, ν=0.3). The influence of the specimen length to width ratio (L/W) on the stress state purity and uniformity has been investigated.

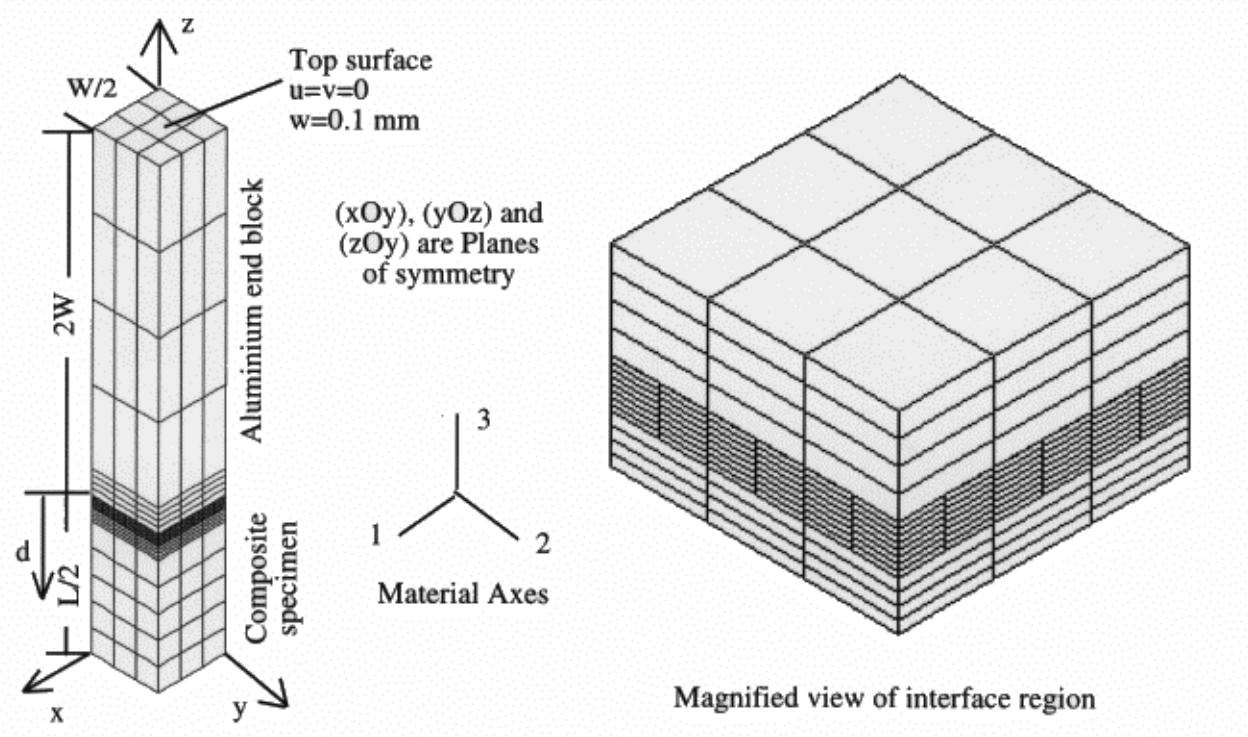

Fig. 1: Parallel-sided block 3D FE model for normal testing

The TT normal stress σ_{33} (equivalent to σ_{zz}) is highest at the interface between the specimen and the jig. Failure will therefore always occur at this location but the geometry may still be suitable for elastic constants determination, provided a sufficiently uniform σ_{33} can be achieved over an appropriate gauge length. The results also showed, that although secondary stresses (σ_{11}, σ_{22}, σ_{31} and σ_{23}) are high at the interface, they decrease very rapidly away from it and become significantly lower than σ_{33}. The stress state can therefore be considered pure at a short distance from the interface.

The uniformity of the stress state can be quantified by the parameter $C_u(d)$ defined as follows:

$$C_u(d) = \frac{\sigma_{33}^{min}}{\sigma_{33}^{max}}$$ on the (xy) plane at a distance d from the interface (see fig. 1)

with σ_{33}^{min} and σ_{33}^{max} being the minimum and maximum σ_{33} values respectively.

Figure 2 shows the curves $C_u(d)$ for different specimen dimensions. As can be seen in this figure, a good uniformity (i.e. $C_u>0.9$) is obtained for specimen length to width ratios (L/W) of at least 2. In that case, $C_u=0.9$ at d=1/3 of L.

Further study for a laminated specimen attached to an epoxy end block (E=3GPa and ν=0.3) showed that the specimen length can be reduced to one specimen width and still achieve a C_u value of 0.9 at a distance d=1/3 of L from the interface.

Waisted Specimen

As noted in the previous section, parallel-sided blocks fail at the bond line due to stress concentrations at this location. In order to avoid this problem, the specimen has to be waisted but the shape of the waisted section must be designed carefully so as to avoid significant stress concentrations at the transition to the gauge section (see location M in fig. 3). The design which proved the most successful for that purpose is an elliptically waisted specimen. The model is shown in figure 3. The parameter values are a=6mm, b=2mm, c=1mm, s=4mm and W=4mm.

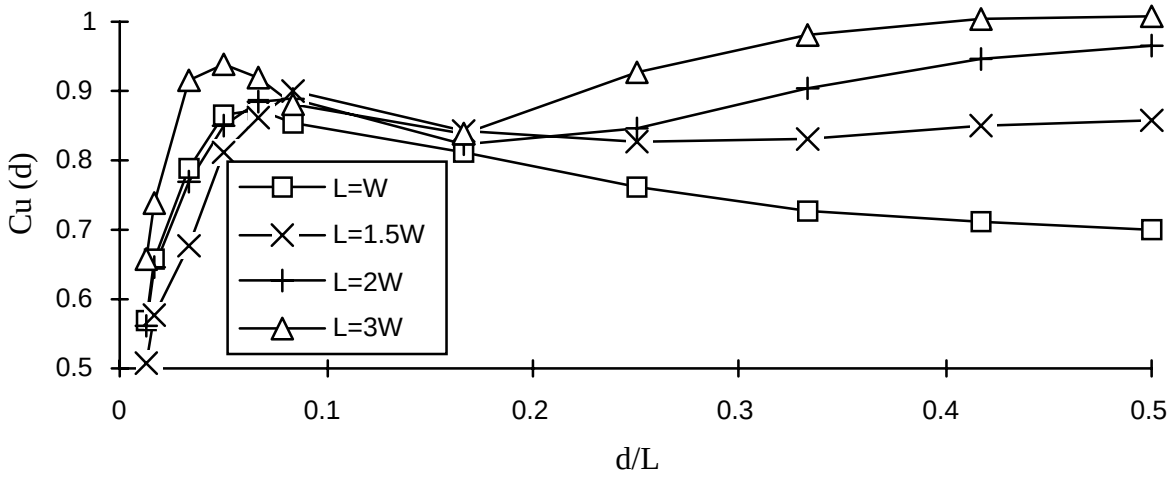

Fig. 2: Stress uniformity in parallel-sided blocks attached to aluminium end block

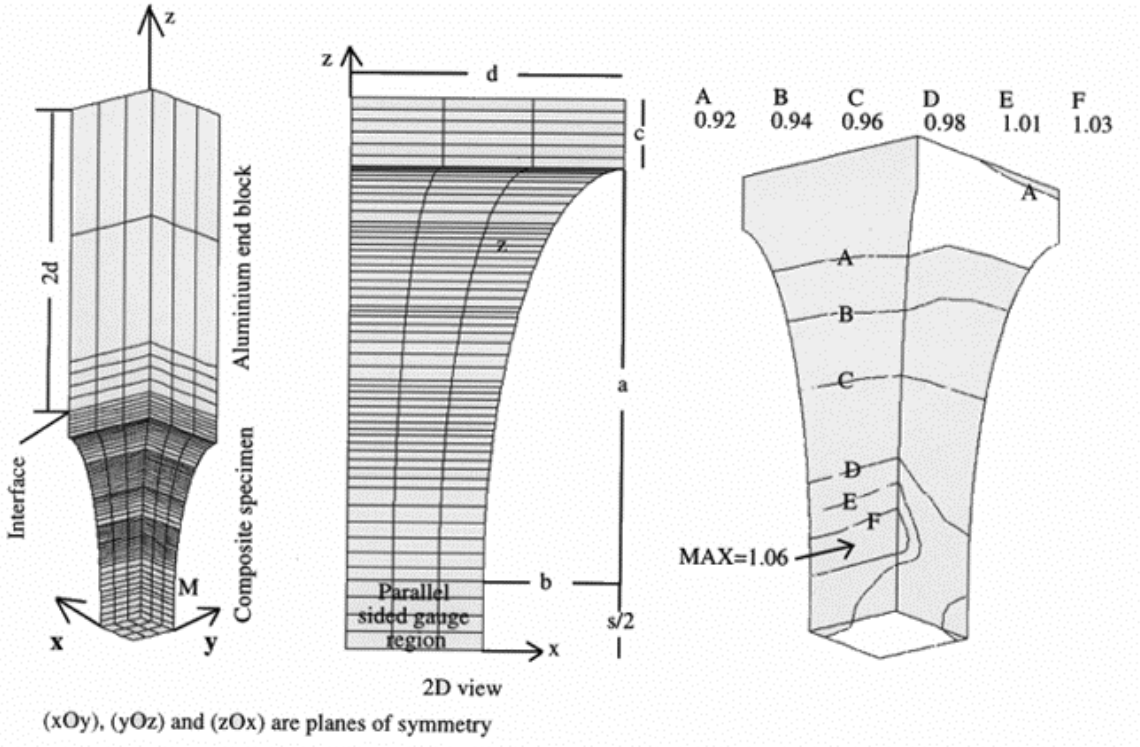

Waisted specimen for direct normal testing

Fig. 3 (left and centre): 3D FE Model *Fig. 4 (right): Normalised σ_{33} contour plot*

Figure 4 shows the normalised σ_{33} contour plot for this waisted specimen design (is carried out with regard to the average stress, σ_{33}^{av}, defined as the ratio of the reaction forces resultant to the cross-sectional area in the gauge section). The maximum occurs at M with σ_{33} at this location being 6% higher than σ_{33}^{av}. The Hill failure criterion is highest at the location of maximum σ_{33} with $\sigma_{33}/\sigma_{33}^{u}$, being the dominant term by far (σ_{33}^{u} is the composite tensile or compressive strength). This implies an essentially pure TT normal stress failure, i.e. the other stresses do not contribute to failure. The value of σ_{33} at the interface is approximately half the value in the gauge section. Provided the bond strength between the loading bar and the specimen is high enough, the failure will therefore occur within the specimen in pure tension or compression.

The influence of variations in the semi-major axis, a, of the elliptical waisting on the stress concentration at location M and at the interface has been investigated (leaving all the other parameters constant at the values given above). For that purpose, the stress concentration parameter C_C is introduced:

$$C_C=\frac{\sigma_{33}^{max}}{\sigma_{33}^{av}}$$ with σ_{33}^{max} the maximum TT normal stress at M or at the interface

Figure 5 shows the results of this study.

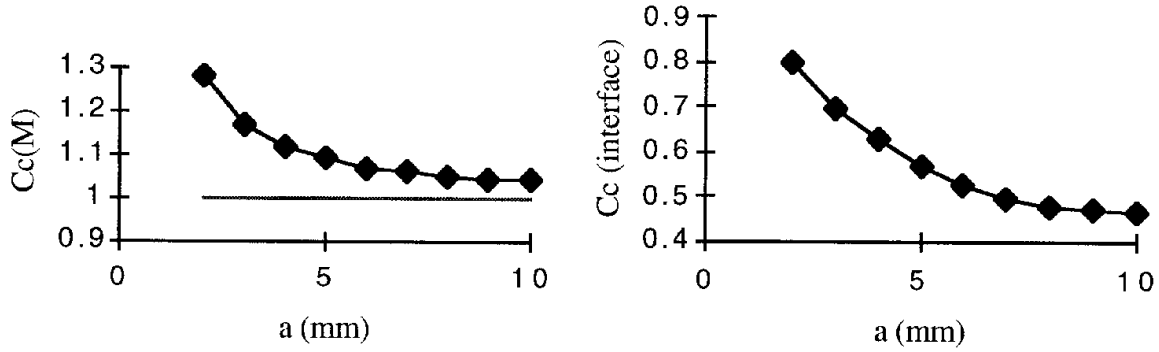

Fig. 5: Stress concentrations at location M and at the interface in waisted specimens

From these curves, it is clear that the σ_{33} concentrations decrease with increasing values of a. With a circular fillet (a=b=4mm), the stress concentrations at location M are 12% higher than the average stress. It is therefore advisable to use an elliptically shaped specimen.

A major subject of concern when devising a direct normal test method for strength determination is that of load misalignment. A simple calculation based on beam bending theory shows that a misalignment as low as 1/60 of the width, W, between the specimen and the load axes induces bending stresses on the outer face which amount to 10% of the average stress. This result has been confirmed numerically. The interested reader is invited to consult references [8,9] for the experimental applications of the present numerical study.

DIRECT SHEAR TEST METHOD

The principle of this method is shown in figure 6 where both the specimen (simple parallel-sided block) and the steel jig are represented (steel properties: E=207GPa, ν=0.3). The load axis coincides with the specimen axis so that no overall bending stresses are induced. Two orientations of the composite UD material have been used: type 'x' with the fibres in the x direction and type 'z' with the fibres in the z direction for the determination of the (31) and (32) properties respectively. Moreover, as for the direct normal test method, two designs have been investigated: the parallel-sided block and the waisted specimen. All the analyses in this section are two-dimensional.

Parallel-Sided Block

The objective here is to ensure that the measured strain at the centre of the specimen edge (point O, Fig. 6) is equal to the average strain so that the shear modulus can be measured accurately. For this study, the parameter C_O has been introduced. It is defined as follows:

$$Co=\frac{\tau_{3i}^{O}}{\tau_{3i}^{av}}$$ with τ_{3i}^{O} the shear stress at point O and τ_{3i}^{av} the average shear stress

τ_{3i}^{av} is defined as the ratio of the reaction forces resultant to the specimen cross-sectional area in the plane (xz). Suffix i takes the value 1 for type 'x' and 2 for type 'z' specimens.

First, let us take the simple case of a block, made of type (x) material, at the top surface of which a uniform displacement of 0.1 mm is applied in the x-direction, as shown on the left of figure 7. In the same figure, the curve on the right shows the variation of the parameter C_o with the ratio L/H. When this ratio is higher than 10, C_o is close to 1 and the shear modulus could therefore be determined accurately.

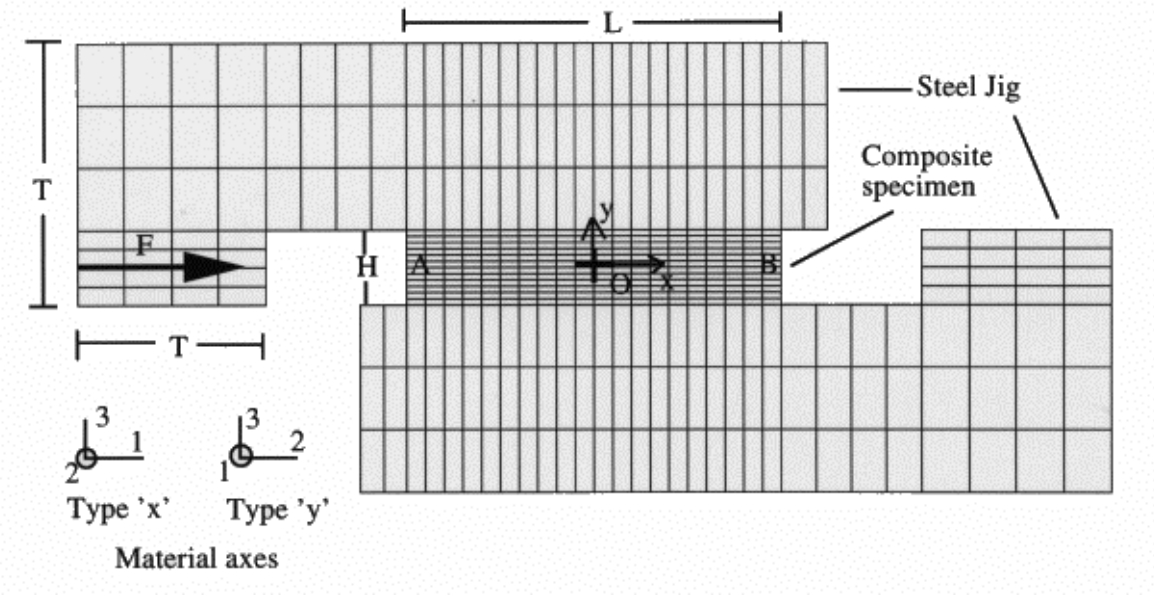

Fig. 6: Parallel-sided block 2D FE model for direct shear testing

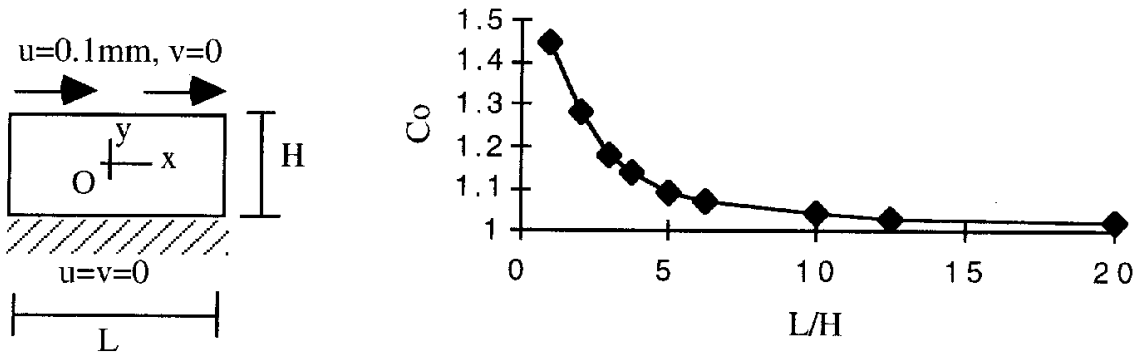

Fig. 7: C_o in type 'x' specimens of varying length subjected to uniform displacement

In practice however, the specimen will not be attached to an infinitely rigid material but to an elastic material. The edges will therefore be subjected to higher stresses than the middle. Figure 6 showed the model which accounts for this real situation. In this case, the specimen length, L, and height, H, and the jig thickness, T, all influence the shear stress distribution in the specimen. When L and T are kept constant, the shear stress uniformity along [AB] (see figure 6) increases with increasing values of H and C_o converges towards 1. For practical purposes, H was taken to be 8mm. This thickness enables strain gauges to be bonded at the centre of the specimen edge while keeping the laminate thickness from which the specimen will be cut relatively low. In this case, the influence of T and L on C_o was investigated. The results of this study are shown in figure 8. As clearly seen on this graph, the higher the L/T ratio, the closer C_o is to its converging value which is itself very close to the value calculated

in the simple case of figure 7. For relatively long specimens (80mm and over), an acceptable level of stress uniformity (i.e. C_o=0.95) is reached for high values of T (50mm and over). Practically, the steel jig thickness, T, should not be higher than 20mm for handling purposes. Therefore, shorter specimens have to be used.

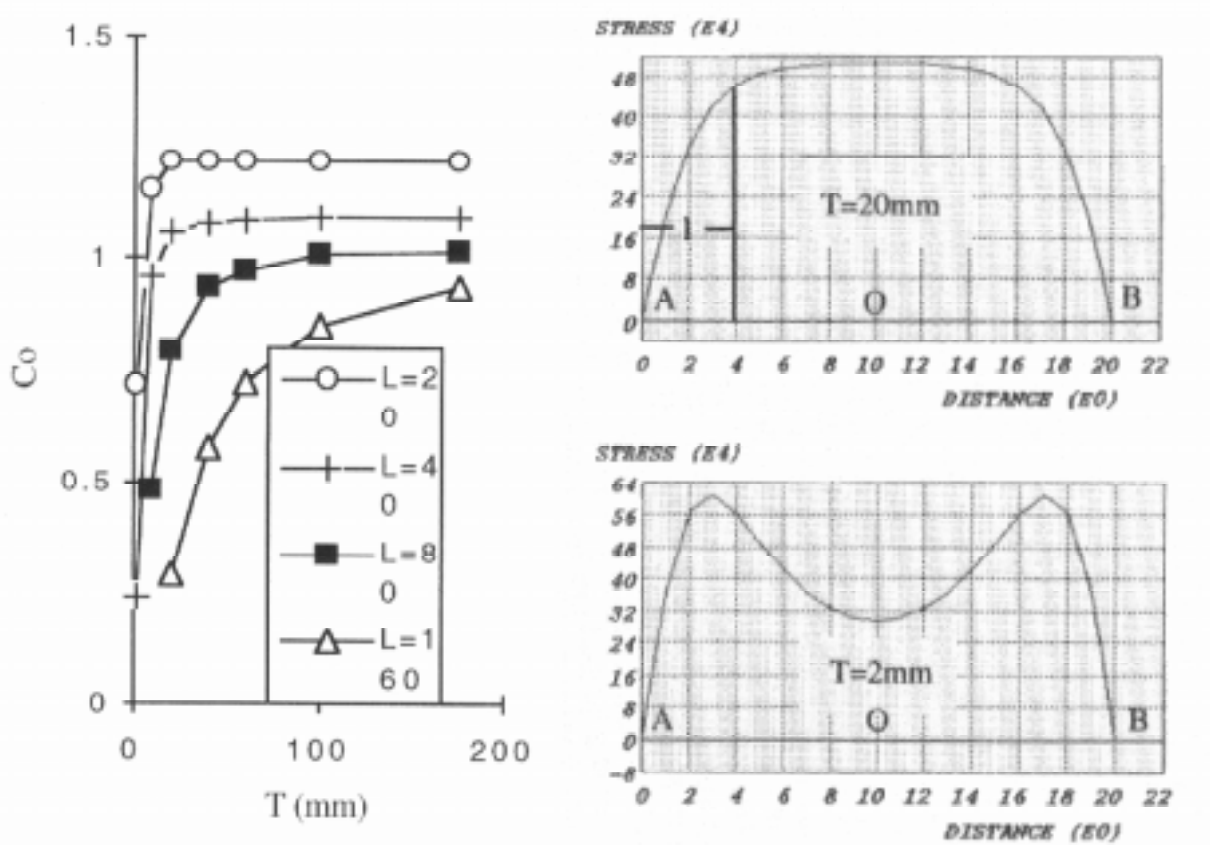

Fig. 8: Left, C_0 in type 'x' specimens attached to jig; and right, normalised shear stress distribution along the horizontal mid line [AB] of the specimen

On the right of figure 8, two characteristic shear stress distribution curves are shown for L=20mm. When T=20mm (top curve), the shear stress curve is a plateau whereas when T=2mm (bottom curve), the maximum shear stress occurs at a short distance from the edges and then decreases to a minimum at point O. For the measurement of the shear modulus, the top curve shape is more satisfactory. However, in this case, the value of the shear stress in the plateau region is higher than the average stress, τ_{31}^{av}. This is due to the fact that the stress increases progressively from 0 at the edge to its maximum value over a distance, l, which is not negligible compared to L. After, the detailed analysis of 'plateau shaped' stress distribution curves for L varying from 20 to 30mm and T=20mm, it has been found that l is constant and can be approximated to 4mm (when L<20mm, the curve has got a maximum at O but no plateau region). The modified average shear stress, τ_{31}^{av}(mod) can now be defined as F/(L-l) for an out-of-plane width equal to unity. Table 2 compares the values of C_o, calculated using τ_{31}^{av} and C_o(mod), calculated using τ_{31}^{av}(mod) for 3 different specimen length. From these results, it is clear that the use of l in the calculation of τ_{31}^{av}(mod) to account for the stress gradient at the edges enables the use of the simple type 'x' parallel-sided specimens for G_{31} measurement.

Table 2: Co and Co(mod) for parallel-sided specimens attached to jig (T=20mm, H=8mm)

	Type 'x'	**Specimens**		**Type 'z'**	**Specimens**
	C_o	C_o(mod)		C_o	C_o(mod)
L=20mm	1.21	0.97		1.35	1.02
L=25mm	1.16	0.98	L=16mm	1.23	1.00
L=30mm	1.12	0.97			

The results for type 'z' material are similar. However, being less stiff in the loading direction, the 'plateau-shaped' shear stress distribution occurs only for specimens with a length lower than 16mm (and higher than 12mm) and the length l is equal to 3mm. The values of C_o and C_o(mod) are given in table 2. Here again, C_o(mod) gives better results. Provided l can be estimated, the parallel-sided specimen provides therefore with an accurate measurement of G_{23}.

Waisted Specimen

The previous parallel-sided specimens fail at the corners where very high stress concentrations occur. It is necessary to reduce the specimen cross-section in the middle so as to avoid this phenomenon and achieve failure within the specimen. This will occur if the specimen is waisted as shown in figure 9. However, two other problems have to be tackled. Firstly, the shear stress concentrations in the region of high curvature are high. Secondly, the transverse tensile stress is still significant. The ratio of transverse tensile to shear stress is indeed close to unity for this type of geometry. As the transverse tensile strength is lower than the shear strength (see table 1), the specimen is more likely to fail in tension than in shear.

In order to lower the shear stress concentrations and reduce the transverse tensile stress, epoxy end blocks have been added to the composite specimen as shown in figure 9. However, this is not sufficient to reduce the tensile stresses to an acceptable level. Therefore, a TT compressive load has been applied together with the longitudinal load in order to "close" the specimen and this has been achieved by applying a force F inclined to the axis of the specimen as shown in figure 9.

For the study of this model, a shear stress concentration coefficient, C_{3i}, and a transverse tensile stress coefficient, C_{33}, are introduced. They are defined as follows:

$$C_{3i} = \frac{\tau_{3i}^{max}}{\tau_{3i}^{av}} \quad \text{and} \qquad C_{33} = \frac{\sigma_{33}^{max}}{\tau_{3i}^{av}}$$

with τ_{3i}^{max} and τ_{3i}^{av}, the maximum and average shear stress respectively, σ_{33}^{max}, the maximum TT tensile stress and suffix i takes the value 1 for type 'x' and 2 for type 'z' specimens. τ_{3i}^{av} is derived as follows:

$$\tau_{3i}^{av} = \frac{F_x}{WL_{eff}} \qquad \text{with} \quad L_{eff} = L + 2e\frac{G_{ep}}{G_{3i}}$$

where F_X is the applied longitudinal force, W, the out-of-plane specimen width, L_{eff}, the effective length along x and G_{ep}, the epoxy shear modulus.

After a thorough investigation of the geometrical and loading parameters, an acceptable design was found to be as follows: L=30mm, a=30mm, b=5mm, e=9mm, T=20mm and α=0.2. In this case, C_{31}=1.013 and C_{33}=0.401. Figure 10 shows the normalised shear stress contour plot. τ_{31}^{max} occurs in the region labelled 'MAX', at the interface between the composite and the epoxy (after a convergence study was carried out, it was found that the value was not singular). σ_{33}^{max} also occurs at the interface between the composite and the epoxy.

The sensitivity of the model to the different parameters has been studied. Table 3 shows the effect of increasing separately parameters L, a, e and α by 10% on the stress coefficients C_{31} and C_{33}. The maximum variation of C_{31} and C_{33} is 2%. Clearly, the maximum shear and transverse tensile stresses are not too sensitive to minor changes in the geometry and loading conditions. The determination of τ_{31}^{u} should therefore be accurate provided the bond of the epoxy to the composite is stronger than the composite and this strength will not be too sensitive to experimental imprecision.

For the measurement of the shear strength τ_{32}^{u}, the reference model has been run with type (z) material. The output of the FE analysis is: C_{32}=1.016 and C_{33}=0.279. Compared to the type (x) specimen, the determination of the shear strength is as accurate (less than 2% error) and the maximum transverse tensile stress in the composite is 30% lower. This specimen is therefore suitable for the determination of τ_{32}^{u}.

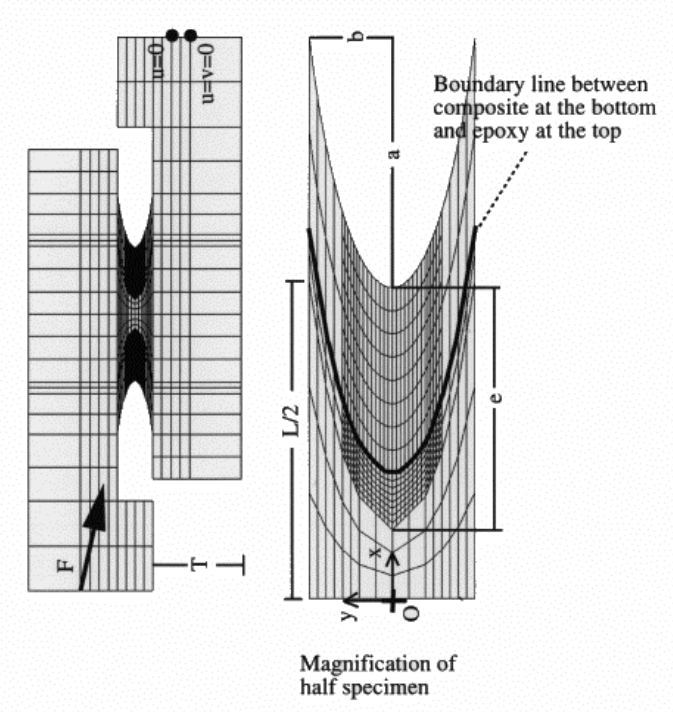

Fig. 9: Waisted specimen 2D FE model for direct shear testing

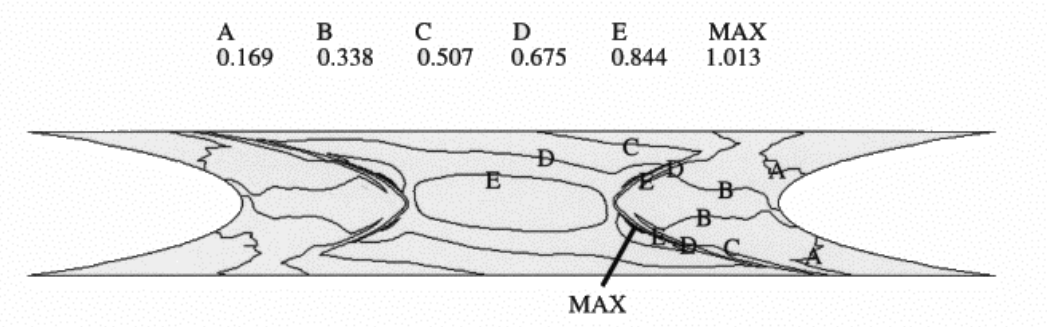

Fig. 10: Normalised τ_{31} contour plot in the shear waisted specimen

Table 3: Sensitivity study of the waisted specimen under direct shear loading

	L	**a**	**e**	**α**	**C_{31}**	**C_{33}**
Reference	30	30	9	0.2	1.013	0.401
Increase L (+10%)	33	30	9	0.2	1.031 (+1.8%)	0.405 (+1%)
Increase a (+10%)	30	33	9	0.2	1.012 (-0.1%)	0.396 (-1.2%)
Increase e (+10%)	30	30	9.9	0.2	1.015 (+2%)	0.409 (+2%)
Increase α (+10%)	30	30	9	0.22	1.013 (±0%)	0.393 (-2%)

CONCLUSIONS

FE analysis has been used to design suitably shaped specimens for through-thickness compression, tension and shear testing for the determination of elastic constants and strength of unidirectional laminated carbon fibre reinforced epoxy (Hexcel T300/914). The compression and tension test method, called the "direct normal test method", involves a specimen under direct normal loading. Two specimen designs are proposed. Firstly, a parallel-sided block with a square cross-section which allows only the determination of the elastic constants. Its length to width ratio depends on the material to which it is attached. If attached to a stiff material (e.g. aluminium), this ratio is 2. If attached to a soft material (e.g. epoxy), the ratio can be reduced to 1. Secondly, a waisted specimen design is proposed, allowing the measurement of both the elastic constants and the strength. It has a central gauge section of 4mm square cross-section widening to 8mm square at the ends via elliptically shaped fillets. Its total length is 16mm.

The shear test method, called the "direct shear test method", involves a specimen under direct shear loading. Only a 2D FE analysis has been carried out. Two specimen designs are again proposed. Firstly, as for the direct normal test method, a parallel-sided block specimen has been developed. It allows the determination of the shear moduli, provided the area under stress is corrected to account for stress gradients occurring at the specimen edges. The specimen thickness is 8mm while its length depends on the laminate orientation. For specimens with fibres in the loading direction, the length is between 20 and 30mm whereas for specimens with fibres normal to the loading direction, it is comprised between 12 and 16mm. Secondly, a waisted specimen is proposed for the determination of the shear strength (τ_{31}^{u} and τ_{32}^{u}). In order to minimise the shear stress concentrations and the transverse tensile stress, the design makes use of epoxy end blocks. Moreover, the loading involves a closing force, normal to the specimen longitudinal axis.

ACKNOWLEDGEMENTS

The authors wish to acknowledge the financial support of the EPSRC under grant number GR/K33705. Prepregs and autoclave consumables were gratefully received from Hexcel Composites and Westland Helicopters. The authors would also like to acknowledge useful discussions with Dr WR Broughton of the National Physical Laboratory, Dr K Sagoo of Westland Helicopters, Mr PE Brooks and Mr P Allen of Hexcel Composites and Dr J Lockett of the Polymer Engineering Group.

REFERENCES

1. "Standard Test Method for Shear Properties of Composite Materials by the V-Notched Beam Method", *Annual Book of ASTM Standards*, Section 15, Vol.15.03, 1993, ASTM D5379-93, ASTM, Philadelphia, PA, USA

2. Hodgkinson, J.M., Ayache, S., Matthews, F.L., "In-Plane and Out-of Plane Property Measurements on Thick Woven Glass/Polyester Laminates", *Proc. ECCM*, Amsterdam, European Association for Composite Materials, 1992

3. Hodgkinson, J.M., Bertholet, H., "Out-of-Plane Shear Property Measurements on CFRP Laminates", *Proc. 2nd Int. Conf. on Deformation and Fracture of Composites*, Manchester, UK, Institute of Materials, 1993

4. Morton, J., Ho, H., Tsai, M.Y., Farley, G.L., "An Evaluation of the Iosipescu Specimen for Composite Materials Shear Property Measurement", *J. Comp. Mat.*, Vol.26, No.5 1992, pp.708-750

5. Mespoulet, S., "Design, Development and Implementation of Through-Thickness Test Methods for Laminated Composite Materials", *MPhil/PhD Transfer Report*, Centre for Composite Materials, Imperial College, London, UK, 1995

6. Broughton, W.R., Sims, G.D., "An Overview of Through-Thickness Test Methods for Polymer Matrix Composites", *Report DMM(A)148*, National Physical Laboratory, Teddington, UK, 1994

7. Curtis, P.T., Broadley, B.P., "A Review of Test Methodology for the Measurement of the Through-Thickness Properties of Polymeric Composites", *Report DRA/MAT.STR/TR93065/1*, Defence Research Agency, Farnborough, UK, 1993

8. Mespoulet, S., Hodgkinson, J.M., Matthews, F.L., Hitchings, D., Robinson, P., "A Novel Test Method to Determine the TT Tensile Properties of Long Fibre Reinforced Composites", *Proc. ECCM-7*, Woodhead Publishing Ltd., London, UK, Vol.2, 1995, pp.131-137

9. Mespoulet, S., Hodgkinson, J.M., Matthews, F.L., Hitchings, D., Robinson, P., "The Development of a Through-Thickness Compression Test for Laminated CFRP", *Proc. 4th Int. Conf. on Deformation and Fracture of Composites*, Manchester, UK, Institute of Materials, 1997

10. Roy, A.K., Ran, Y.K., "Interlaminar Normal Stiffness and Strength of Thick Orthotropic Laminates: an Experimental Study", *J. Reinf. Plast. Comp.*, Vol. 13, 1994, pp.880-894

11. Kim, R.Y., Abrams, F., Knight, M., "Mechanical Characterization of a Thick Composite Laminate", *Integrated Comp..*, 3rd Inter. Technical Conf., Seattle, 1988

12. Daniel, I.M., Hsiao, H.M., Wooh, S.C., "Processing and Compressive Behavior of Thick Composites", *Mechanics of Thick Composites*, Symposium, ASME, Vol.162, 1993, pp. 107-126

13. Lagace, P.A., Weems, D.B., "A Through-the-Thickness Strength Specimen for Composites", ASTM STP, No.1003, CC Chamis, Ed., ASTM, Philadelphia, PA, USA, 1989, pp.197-207

LOOP TEST FOR THE STRENGTH OF MONOFILAMENTS

Horishi Fukuda Masayuki Yakushiji and Atsushi Wada

Department of Materials Science and Technology, Science University of Tokyo, Yamazaki, Noda, Chiba 278, Japan

SUMMARY: This paper presents the methodology to measure the strength of monofilaments used for composite materials. A loop test is adopted for the test. Because the loop test has some disadvantage to measure the strength, we combined it with an elastica theory by which the bending strength of monofilaments can be obtained. This method was applied to an optical fiber and a carbon fiber and it has been made clear that this method can be used to evaluate the strength.

KEYWORDS: strength of monofilaments, loop test combined with elastica theory, optical fiber, carbon fiber

INTRODUCTION

Composite materials are nowadays used in various fields because of their high stiffness- and/or strength-to-density ratios. Since most of loads in composite materials are carried by fibers, it becomes necessary to measure the strength of fibers. A tensile test is usually adopted to measure the strength of monofilaments and a so-called loop test is sometimes used. The work of Fidan et. al.[1] is one of them, although their primary concern is kink band or failure mode, rather than the strength. The work of Kitano et. al.[2] also dealt with the strength of monofilaments by means of the loop test where the strength is defined by their special way. This paper addresses the applicability of the loop test to evaluate the strength of monofilaments used for advanced composites.

PRINCIPLE OF PRESENT METHOD

Our idea for measuring the strength is first described. Figure 1 schematically shows the procedure of the loop test. By pulling both ends of the monofilament, the radius of curvature of the loop, ρ, decreases and eventually the filament breaks due to bending. Under the assumption of linear elasticity, the skin strain, ε, and the skin stress, σ, at point A of Fig.1 are calculated by

$$\varepsilon = \frac{D}{2\rho} \quad \text{and} \quad \sigma = E\varepsilon \qquad (1)$$

where D and E are the diameter and Young's modulus of the monofilament, respectively. Therefore, if we measure the radius of curvature at failure as well as D and E, we can calculate the

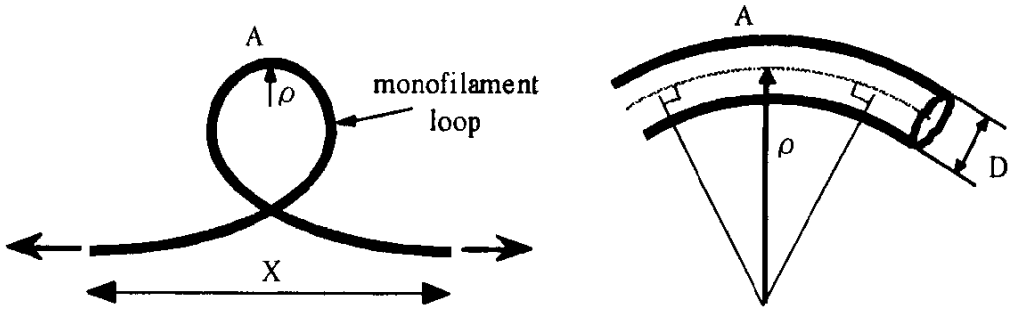

Fig.1: Loop test

bending strength.

The loop test is usually carried out on a microscope and photographs are taken at intervals to measure ρ. However, it is rather difficult to take a photograph at, or just before the failure because the failure of monofilament takes place suddenly.

To compensate for the above shortcoming, we tried to combine the loop test with the elastica theory[3]. Figure 2 shows the elastica deformation where one end is clamped and the other loading end is free. If the angle α at the free end exceeds $\pi/2$ and if it is close to π, it is the case of our present concern, although Fig.2 shows only the half part of our experiment.

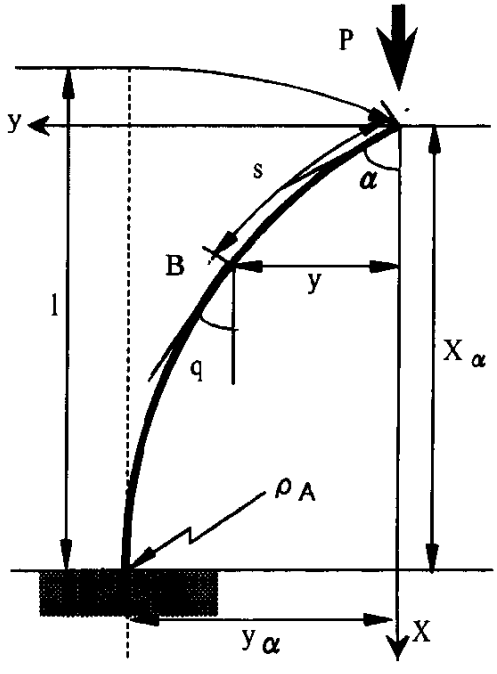

Fig.2: The Elastica

The fundamental equation of bending is, referring to Fig.2,

$$EI\frac{d\theta}{ds} = -Py \qquad (2)$$

where I is the moment of inertia of the cross section, P is the applied load, and θ , s, y are defined in Fig.2. After some calculation, this equation leads to

$$\rho_A = \frac{1}{2kp} \qquad (3)$$

where

$$k = \sqrt{\frac{P}{E \cdot I}} \quad , \quad p = \sin\left(\frac{\alpha}{2}\right) \qquad (4)$$

and

$$X\alpha = \frac{2}{k}E(p) - l \qquad (5)$$

In the above equation, E(p) is the second perfect elliptical integral.

Thus, if we measure the edge-to-edge distance, X of Fig.1, the radius of curvature, ρ , can be calculated with the aid of the parameter α .

PRELIMINARY EXPERIMENT USING OPTICAL FIBER

Before testing of carbon fiber which is the most popular fiber for composites, we first tried a preliminary test for an optical fiber. The reason why we selected optical fiber is because its diameter (125 μ m) is much larger than that of carbon fiber (7 μ m) and it is easy to operate for the skill training.

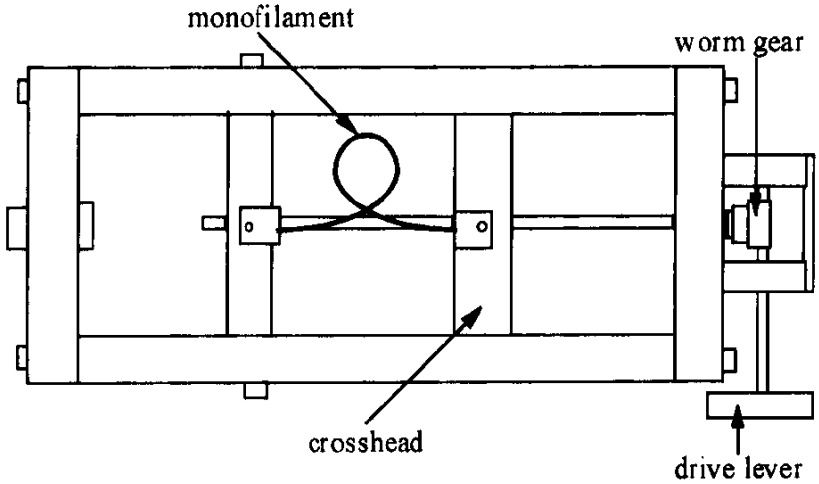

Fig.3: Loop test device

Test method

A multi-mode optical fiber made by Sumitomo Denko. Co. was used for evaluation. This fiber is made of glass and it is supplied in a form with plastic covering. The plastic protector was removed by mechanical way with a stripper and only the part of core and clad was evaluated. The clad diameter is 125 μ m.

Figure 3 is a hand-made testing machine which is mounted on an optical microscope. By rotating the drive lever manually, the crosshead slowly moves to the right and the size of the loop becomes small; eventually it leads to the break of the fiber. The crosshead movement was calculated from the rotation of the drive lever. One rotation of the drive lever corresponds to 0.05 mm of the crosshead movement.
It is necessary to make a loop the shape of which is close to the deformation of the elastica

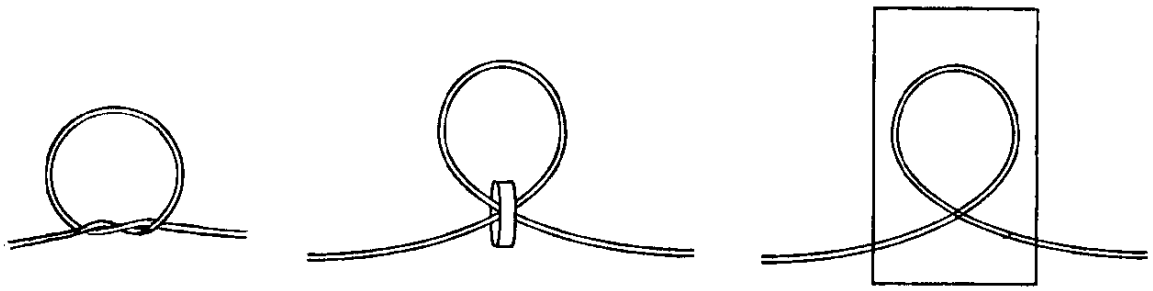

a.knotted b.passed through a ring c.sandwiched between glass plates

Fig.4: Three ways of making a loop

theory. In addition, it must be a possible method for experiment. For this purpose, we tried three ways as shown in Fig.4.
Both ends of a fiber should be rotation free. The fiber ends were glued on a pair of thin, square aluminum pieces (tabs) of the weight of about 300 mg. Each tab has a hole and it is mounted to the testing machine through a pin. The detail of the end tab will be described later again. Photographs were taken at intervals during the test.

Results and discussion

Figure 5 shows each one result for each way of making a loop. Young's modulus of the optical fiber, E, was measured separately to be 110 GPa and a catalog value was used for the diameter, D=125 μ m.
A series of squares in Fig.5 are experimental values in which the radius of curvature was

measured directly from a series of photographs. The dots are, on the other hand, the theoretical values where the elastica theory is incorporated.

According to Fig.5(a), there exists much difference between theory and experiment for the knotted loop. It is natural that this deviation occured because the shape of loop of this case is far from that predicted by the elastica theory. The cases of Fig.5(b) and (c) will be acceptable; between which (b) seems to be superior.

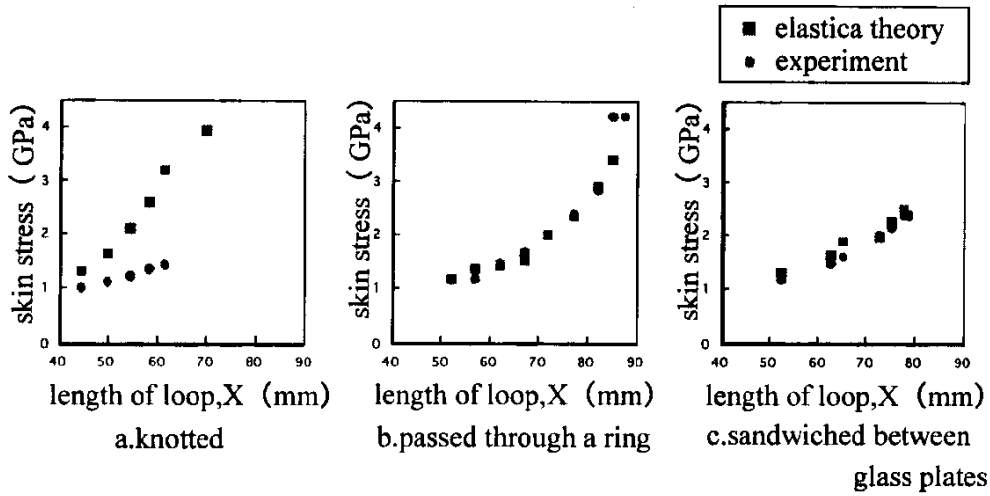

Fig.5: comparison of skin stress between experiment and theory (optical fiber)

STRENGTH MEASUREMENT OF CARBON FIBER

Test method

Torayca T300 carbon filaments were tested here where D and E were measured by separate experiments[4]. The procedure of testing is almost the same as the case of the optical fiber although some modifications were needed.

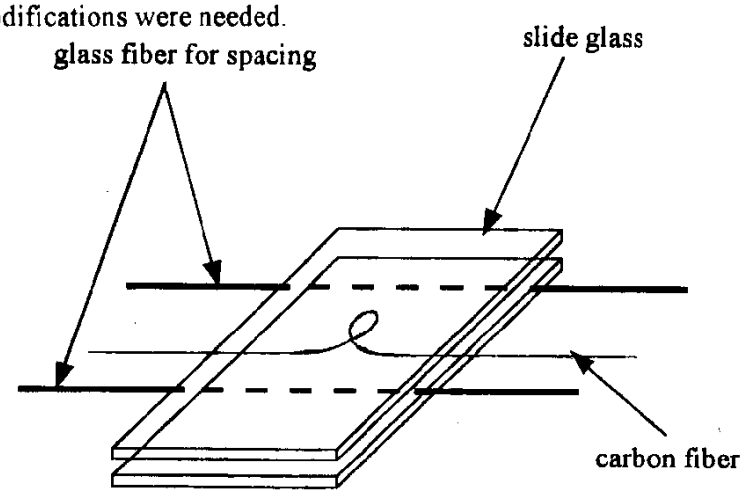

Fig.6: Modified method to making a loop(carbon fiber)

Concerning the way of making a loop, we could not find a very tiny ring of the size, say,20 μ m in diameter and 10 μ m of thickness. Then we had to choose the third way, glass plate.

If a slide glass is directly placed on a looped carbon fiber, the deformation of the fiber will be affected by the friction with the glass plate. Then we inserted a pair of glass fibers (13 μ m) for keeping the space, as shown in Fig.6.

In the case of an optical fiber, we used an aluminum tab for realizing rotation-free ends as shown in Fig.7(a). However, this tab seemed to be too heavy for a carbon monofilament; the scattering of measured data was pretty large, probably due to this undesirable end condition. After some trials, we finally chose a circular, thin paper for the end tab which is schematically shown in Fig.7(b). The weight of the circular sheet was about 20mg.

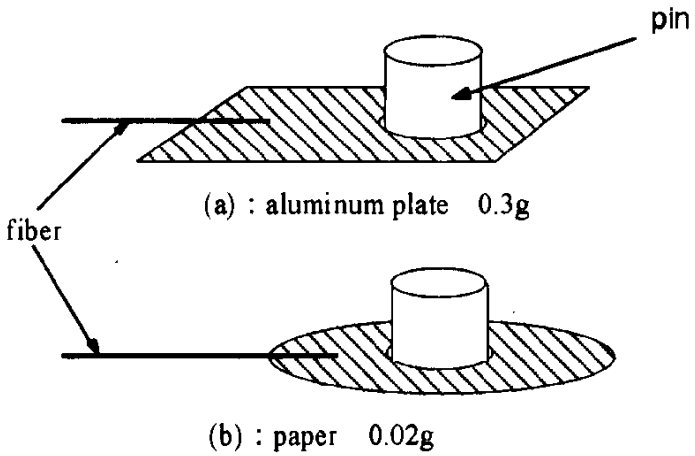

Fig.7: End tab

Results and discussion

Figure 8 is an example of the shape of a carbon monofilament during the test. This type of pictures was taken in a Macintosh computer and the radius of curvature was measured.

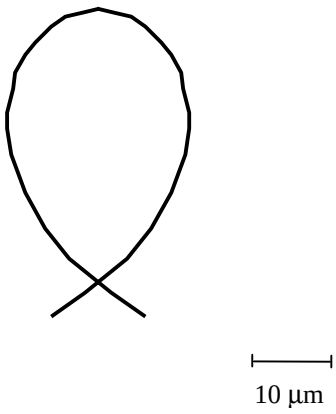

Fig. 8: Shape of carbon monofilament during the test

Figure 9 shows the skin stress which was calculated from the radius of curvature directly measured from photographs. Because the original length of the carbon fiber differs a little one by one, the abscissa was arranged in terms of the edge-to-edge distance, X of Fig. 1, minus the original length, 2l. Although there still remains some discrepancies among these experimental data, it looks acceptable.

Figure 10 demonstrates an example of the comparison between experimant and theory. Again the agreement is good. One point to be noted is that the experimental value is missing at the final point A where the fiber break took place. What we want to know is the bending stress at point A (bending strength) whereas we can not "measure" it by means of photograph because the fracture occurs suddenly. The elastica theory compensates for it.

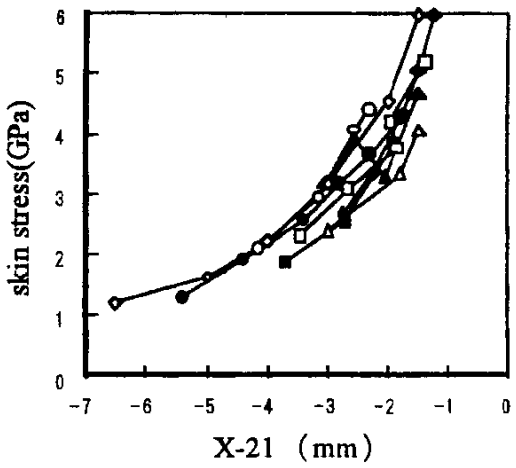

Fig.9: Bending stress vs. crosshead movement

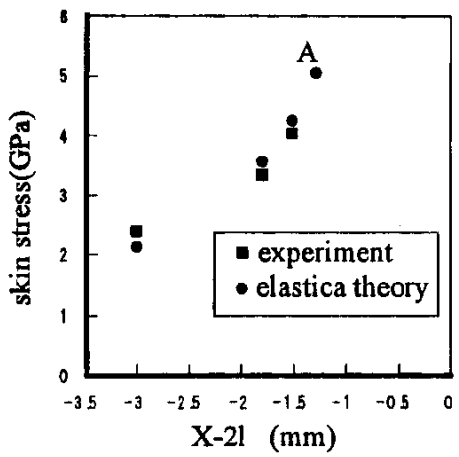

Fig.10: Comparison of skin stress between experiment and theory(carbon fiber)

According to Figs. 9 and 10, the strength of T300 carbon fiber is 5-6 GPa which is higher than the catalog value, 3.5 GPa. The catalog value is based on the tensile test of 25mm filament length. Since the fiber strength depends on the length of the test piece, it is important to describe the gage length. In our present method, however, it is rather difficult to identify the gage length. Assuming the half length of the loop corresponds to the gage length, it is estimated as about 0.5 mm.

In the previous paper[4], we measured the strength of the same T300 carbon fiber of 25mm length and the result was, in terms of the Weibull parameter, α =3.17 GPa and m=5.1. Substituting these data into two-parameter Weibull equation, the mean strength of 0.5 mm length is calculated as 6.8 GPa. This indirectly indicates that our methodology and measurements have been done successfully.

CONCLUSIONS

In the present paper we tried to develop the methodology to measure the strength of monofilaments by combining a so-called loop test and the elastica theory. The result showed that the present method can become an alternative of the tensile test, although there still remains some points to be overcome.

REFERENCES

1. Fidan, S., Palazotto, A., Tsai, C. T. and Kumar,S., "Compressive Properties of High-performance Polymeric Fibers," Composites Sci. Tech., Vol.49, 1993, pp.291-297.
2. Kitano, A., Norita, T. and Noguchi, K., "Compressive Strength of Fiber Reinforced Composite Materials - Effect of Fiber Properties," Proc. 12th Symp. Composite Mater., Japan Soc. Composite Mater., 1987, pp.125-128 (in Japanese).
3. Timoshenko, S. P. and Gere, J. M., "Theory of Elastic Stability," McGraw Hill, 1961, p.76.
4. Fukuda, H. and Miyazawa, T., "Micromechanical Approach to the Tensile Strength of Unidirectional Composites," Advanced Composite Mater, Vol.4, 1994,, pp.101-110 and pp.287-295.

A CRITICAL EVALUATION OF THROUGH-THICKNESS TEST METHODS

William R. Broughton

Composites and Polymers Properties Branch
Centre for Materials Measurement and Technology, National Physical Laboratory
Queens Road, Teddington, Middlesex, TW11 0LW, United Kingdom

SUMMARY: This paper critically evaluates a number of through-thickness test methods in terms of key factors relating to fibre format or architecture, matrix type, load introduction, specimen preparation and the potential for standardisation. Consideration is given to both the practicality of using a test method in an industrial environment, in terms of ensuring "fitness for purpose" and to the degree of uniformity of stress distributions throughout the test geometry. The evaluation is based on a comprehensive database obtained from tests conducted on a range fibre-reinforced plastic composites, including continuous and discontinuous, aligned, random and woven fabric fibre formats in thermoset and thermoplastic matrices. In order to meet the challenge, a number of new test geometries have been developed and experimentally evaluated.

KEYWORDS: polymer composites, through-thickness, test methods, tension, compression, elastic constants, strength, failure modes.

INTRODUCTION

An increasing demand for intrinsic through-thickness (T-T) strength and stiffness properties for use as input data for design and analysis of polymer matrix composite (PMC) structures has stimulated the development of T-T test methods. T-T tensile, compressive and shear properties are frequently required for both "thick" section applications and for "thin" sections where there is a concern that two-dimensional analysis is inadequate. There is a tendency to associate interlaminar stresses with "thick" sections, however, interlaminar stresses and strains may be induced in "thin" laminates through the application of membrane (ie in-plane) loads. In an attempt to generate this data, it has become apparent that methods applicable to conventional metallic materials are not suitable for testing PMCs. The unique and diverse nature of PMCs, introduces additional problems relating to anisotropy, low T-T tensile and shear properties, coupling effects and the relative difficulties of producing laminates of adequate thickness. These problems have provided a major challenge to researchers in finding solutions in order to generate reliable engineering data.

This paper critically evaluates a number of test methods for measuring T-T properties under tensile, compressive and shear loads. Each method is examined in terms of the level of standardisation, elastic and strength properties obtained, material suitability, material thickness requirements, specimen fabrication, test apparatus, methods of data measurement and data reduction procedures. The evaluation is based on a comprehensive database obtained from tests conducted on a range PMCs, including continuous and discontinuous, aligned, random and

woven fabric fibre formats in thermoset and thermoplastic matrices. In order to meet the challenge a number of new test geometries have been developed and experimentally evaluated.

The experimental results clearly demonstrate that many of the mechanical test methods evaluated produce reliable engineering data required for quality assessment and design. A number of these test methods are suitable for development into ISO standards. The paper contains recommendations and guidance as to the use of the remaining test methods.

THROUGH-THICKNESS TENSION AND COMPRESSION

This section provides a brief description of three directly loaded configurations that can be used to evaluate T-T tension and/or compression properties of PMCs:

- Rectangular (unwaisted) block
- Short waisted rectangular block with a plain radius gauge-section
- I-section

Waisted (Fig. 1) and unwaisted rectangular (ie parallel-sided) specimens can be loaded in either tension or compression, along the T-T axis. In tension, the load is introduced via reusable stainless steel or aluminium loading bars, adhesively bonded to the specimen. Compressive load is applied by placing the specimen between two hardened steel parallel platens with the specimen located at the centre of the platens in closely fitting recesses. A four pillar die set is often used to ensure uniform loading to the ends of the specimen. Commercial units are available at a reasonable price. The two geometries are complementary, with waisted and parallel-sided blocks providing strength and elastic property data, respectively.

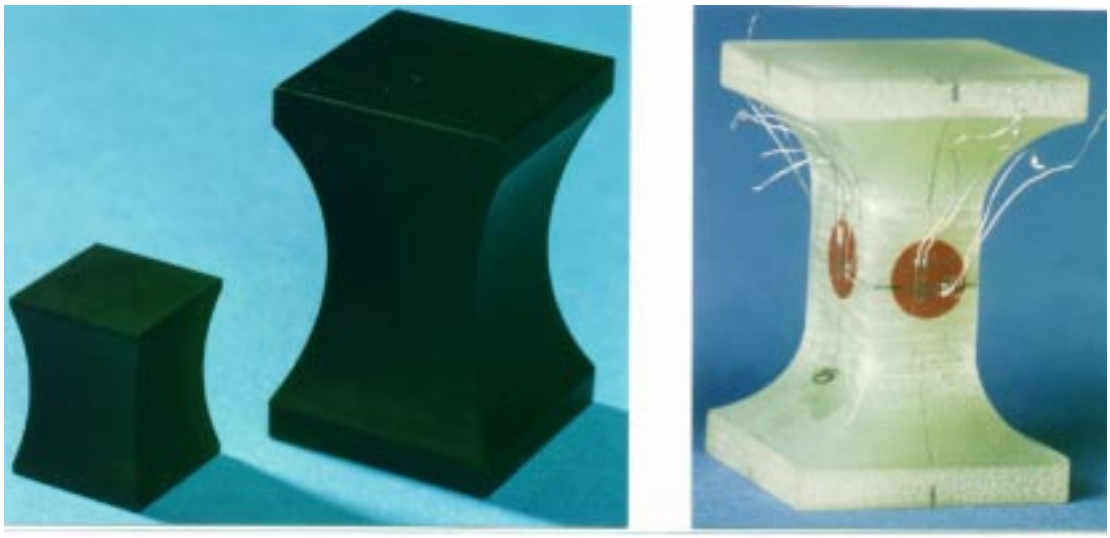

Fig. 1: Waisted block specimens: (left) plain radius; and (right) DERA.

Bonding loading bars to fibre-reinforced thermoplastics (eg glass-fibre reinforced polypropylene) is an extremely difficult task. Commercial grade adhesives proved ineffective. Although, surface treatments, such as corona discharge and flame treatment may enhance adhesion, these techniques require expensive equipment, an economic option unavailable to most mechanical test laboratories. An alternative approach, developed at the National Physical Laboratory (NPL), uses an I-section, where the load is applied to the specimen via the top and bottom flanges by two sets of hardened stainless steel stirrups (Fig. 2). The I-section is only suitable for measuring T-T tensile strengths.

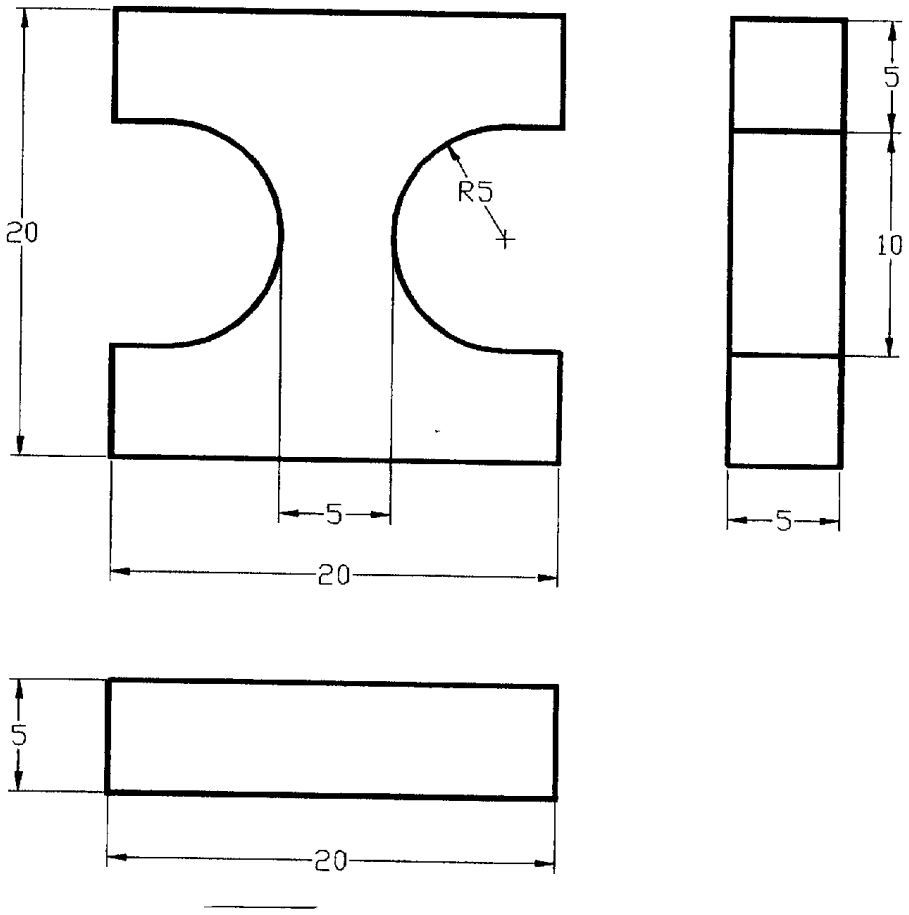

Fig. 2: I-section tensile specimen

Tables 1 and 2 compare T-T tensile and compressive data obtained from a diverse range of PMCs that have been tested by the three methods. Note that default values given in Tables 1 and 2 are bracketed (ie elastic properties assumed to be symmetric in the X-Z and Y-Z planes). Elastic and strength property measurements were in reasonable agreement with corresponding data [1] obtained from tests carried out by the Defence Evaluation Research Agency (DERA), using a waisted block specimen, developed at Fort Halstead. The DERA waisted block specimen (Fig. 1), which has a nominal T-T dimension of 38 mm, can be used to measure T-T elastic and strength properties in both tension and compression.

Rectangular Block

Square cross-section specimens, 15 mm square, with T-T dimensions (ie thickness) ranging from 18 to 40 mm were machined from a range of PMCs (see Tables 1 and 2). This test geometry provides consistent and reliable elastic property data for both monolithic and layered (ie sandwich constructions) materials, and is amenable to standardisation for this purpose. The test geometry is unsuitable for generating strength data. According to stress analysis [2], a length-to-width ratio of 2:1 should be sufficient to guarantee a relatively uniform stress state at the specimen mid-section (ie negligible end-effects), and prevent the possibility of buckling when loaded in compression. Elastic properties were approximately the same; independent of laminate thickness, test method or loading mode. The coefficient of variation (CV) for E_{zz} was generally less than 5.

Table 1: Through-thickness tensile measurements

Test Method	E_{zz} (GPa)	ν_{zx}	ν_{zy}	S_{zz} (MPa)
Aligned carbon-fibre/epoxy				
Rectangular Block (40 mm)	9.9 ± 0.1	0.019 ± .002	0.55 ± 0.01	N/A
Rectangular Block (20 mm)	9.9 ± 0.4	0.020 ± 0.002	0.51 ± 0.01	N/A
Plain Waisted Block (40 mm)	N/A	N/A	N/A	78 ± 7
DERA Waisted Block (38 mm)*	9.5 ± 0.1	0.020 ± 0.001	0.47 ± 0.01	71 ± 6
2/2 twill glass-fibre fabric/epoxy				
Rectangular Block (40 mm)	11.0 ± 0.4	0.19 ± 0.01	[0.19 ± 0.01]	N/A
DERA Waisted Block (38 mm)*	10.7 ± 0.3	0.18 ± 0.04	0.17 ± 0.01	36 ± 1
Discontinuous glass-fibre/nylon 66				
Rectangular Block (20 mm)	4.4 ± 0.1	0.27 ± 0.04	0.41 ± 0.02	N/A
I-section (20 mm)	N/A	N/A	N/A	69 ± 7
Random glass-fibre mat/polypropylene				
Rectangular Block (18 mm)	3.5 ± 0.1	0.16 ± 0.04	0.18	N/A
I-section (18 mm)	N/A	N/A	N/A	5.7 ± 1.6

Table 2: Through-thickness compression measurements

Test Method	E_{zz} (GPa)	ν_{zx}	ν_{zy}	S_{zz} (MPa)
Aligned carbon-fibre/epoxy				
Rectangular Block (40 mm)	10.0 ± 0.1	0.022 ± 0.001	0.52 ± 0.01	263 ± 3
Rectangular Block (20 mm)	9.9 ± 0.1	0.020 ± 0.001	0.56 ± 0.01	256 ± 6
Sandwich Block (40 mm)	10.0	0.02	0.52	258 ± 3
Plain Waisted Block (40 mm)	N/A	N/A	N/A	343 ± 7
Plain Waisted Block (20 mm)	N/A	N/A	N/A	344 ± 10
DERA Waisted Block (38 mm)*	10.3 ± 0.2	0.020 ± 0.005	0.47 ± 0.01	297 ± 5
2/2 twill glass-fibre fabric/epoxy				
Rectangular Block (40 mm)	12.4	0.21	0.21	588 ± 25
Plain Waisted Block	N/A	N/A	N/A	543 ± 5
DERA Waisted Block (38 mm)*	11.8 ± 0.2	0.19 ± 0.01	0.18 ± 0.01	545 ± 6
Discontinuous glass-fibre/nylon 66				
Rectangular Block (20 mm)	4.3	0.21	0.44	190 ± 8
Plain Waisted Block (20 mm)	N/A	N/A	N/A	195 ± 5
Random glass-fibre mat/polypropylene	4.2	0.21	[0.21]	181 ± 14
Rectangular Block (18 mm)	N/A	N/A	N/A	210 ± 9
Plain Waisted Block (18 mm)				

( ) denotes T-T dimension
* Data from Ref. 1.

A rectangular block is a relatively straightforward and economic specimen to test, requiring no special loading fixture. Although not essential, the use of a high precision die set will ensure

uniform axial compressive loading. Specimen fabrication is uncomplicated and economical. Caution needs to be exercised to ensure that misalignment, at both the fabrication and testing stages is minimised. Small misalignments will induce bending, resulting in differential strains on opposing faces of the specimen. Specimens were machined to the required profile by wet grinding.

Tensile specimens were adhesively bonded to the loading bars using a high strength, two part epoxy adhesive. For good alignment, it was essential that all faces were flat and parallel with the opposite surface, and perpendicular with adjacent surfaces. A room temperature curing adhesive was used to avoid residual stresses at the adherend interface. During the curing process, specimens were held in a gluing fixture to ensure accurate alignment between the loading blocks and the loading axis.

A major disadvantage is in the number of strain gauges (4 biaxial rosettes) required for the highest accuracy measurement of axial and transverse strain. A biaxial strain gauge with an active length of 2 mm was bonded on each face of the specimen at the mid-section, with gauges aligned parallel to and perpendicular to the loading direction. Strain averaging was used to account for possible bending strains. Strain gauge numbers could possibly be reduced if there was sufficient confidence in the quality and alignment of the specimen. Axial and transverse extensometers can also be used to measure the T-T elastic properties of 40 mm thick material loaded in tension (eg 2/2 twill fabric shown in Table 1). Extensometers are not particularly suitable for use with thin tensile specimens or compression specimens. Data reduction is straightforward with the applied stress, σ, given by:

$$\sigma = \frac{P}{A} \tag{1}$$

where P is the applied force and A is the specimen cross-sectional area.

As expected, rectangular tensile specimens failed consistently at the adhesive joints between the specimen and the metallic loading bars for all but the weakest materials, thus invalidating the strength data obtained. Strength values obtained from compression tests were consistent to within • 10%, and in reasonable agreement with the strength data obtained using the waisted block geometries. In compression, failure invariably initiates at the specimen ends, independent of material anisotropy and degree of homogeneity. The presence of stress concentrations in these regions causes premature failure, hence the lower strength value. This method is relatively insensitive to material flaws (eg porosity). A major problem with measuring T-T properties of relatively thin laminates (ie 10 mm thick) was surmounted, by adhesively bonding three layers of material together, to form a sandwich construction. A high strength, two part epoxy adhesive was used to bond the layers together. Compression data obtained from tests on aligned carbon-fibre/epoxy, demonstrated the effectiveness of this approach.

Waisted Block (Plain Radius)

As previously mentioned, short rectangular columns of uniform cross-section are unsuitable for generating T-T strength data, as failure invariably occurs at the specimen ends. An alternative approach, is to use waisted specimens with either a circular or elliptical profile extending along

the entire gauge-length of the specimen [2-4]. The reduction in cross-sectional area, promotes failure at the specimen mid-thickness. This relatively straightforward approach can be used to measure both T-T tensile and compressive strengths of monolithic and sandwich constructions. Compared to rectangular blocks, specimen fabrication is expensive and labour intensive.

A waisted specimen_with a plain radius along the entire gauge-length has been developed at the NPL (Fig. 1). This specimen has a nominal thickness of 40 mm, a fillet radius of 30 mm and 25 mm square ends. The gauge-section is 32 mm long, with a cross-section approximately 16 mm square at the specimen mid-thickness. The large fillet radius (ie 30 mm) reduces the stress concentration in the vicinity of the fillet root, although the stress state within the gauge-length is less uniform than an equivalent sized rectangular prism. This test geometry may be scaled down by a factor of 2, with minimal effect on compressive strength (Table 2). End effects increase slightly with a reduction of thickness (ie height).

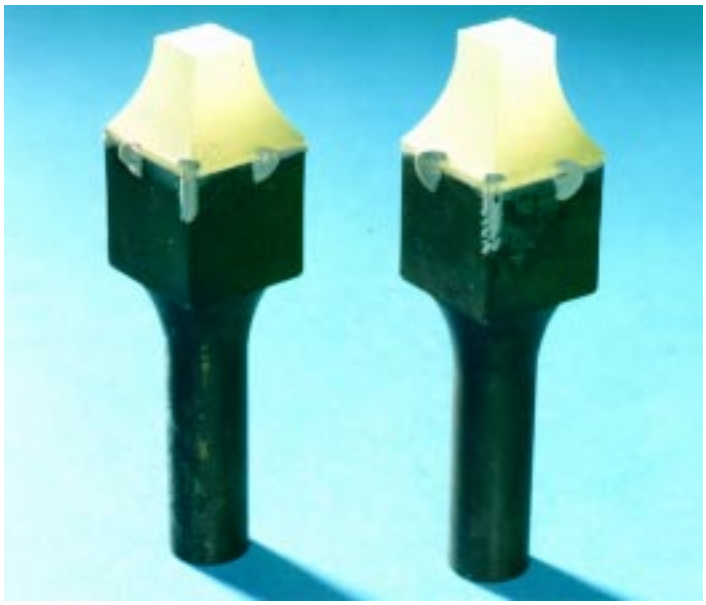

Fig. 3: Plain waisted block specimen

Specimen preparation, bonding procedure, loading configuration and test conditions are similar to those employed for rectangular block specimens. Alignment is critical for low-failure strain systems, as bending stresses produced through eccentric loading can result in premature failure. The applied stress, σ, is determined using Equation (1), where A in this case is the mid-thickness cross-sectional area of the specimen.

T-T tensile failure occurred in a plane orthogonal to the loading direction at the specimen mid-thickness. Shear is the predominant cause of failure in all fibre-reinforced plastic composites tested in compression; independent of the material microstructure. Failure is often instantaneous and catastrophic resulting in diagonal and interlaminar cracking, with failure modes generally remaining unaffected by a reduction in specimen size. For woven fabrics, two orthogonal fracture plains can be observed at 45^{o} to the T-T axis (Fig. 4).

Provided the adhesive joints have superior strength and fatigue performance than the composite material, waisted tensile specimens could be used under cyclic loading conditions. Environmental testing could also be performed with the same provision that the adhesive joints can withstand the environmental conditions. In compression, this test geometry is compatible

with both cyclic and environmental testing. The presence of frictional forces at the loading faces will probably result in fretting.

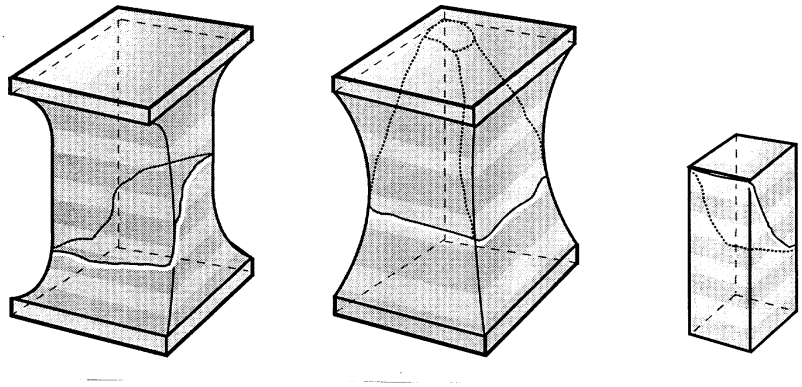

Fig. 4: Failed: (left) DERA; (centre) plain radius; and (right) rectangular blocks

I-Section

The test is simple and economic, and there are no major problems associated with alignment or adhesive bonding (Fig. 2). A special loading fixture is required (ie stirrups), however, the overall costs involved are relatively low compared with bonded configurations. Tests have been successfully conducted on glass-fibre reinforced nylon 66 and glass-fibre reinforced polypropylene. The load is applied to the specimen via the top and bottom flanges by two sets of stirrups, with the inside surfaces of the flanges resting directly on the stirrups.

Specimens have a nominal T-T dimension of 20 mm and a uniform thickness of 5 mm. The flange width and thickness are 20 mm and 5 mm, respectively. The 10 mm gauge-length has a plain waisted width. The radius of curvature of the gauge-length is 5 mm. The cross-section is 5 mm square at the specimen mid-thickness. Ideally, the fillet radius should be larger to minimise the high stresses and stress gradients in this region, however this is not a practicable option for thin laminates. The flange thickness was sufficient to ensure failure occurred within the gauge-length.

Table 3: Tensile and compression test methods suitable for standardisation

Method	**Elastic Properties**	**Strengths**
Tension		
Rectangular Block	Suitable.	Not suitable.
Plain Waisted Block	Not applicable.	Suitable -thermoset systems only.
I-Section	Not applicable.	Suitable - needs further development.
Compression		
Rectangular Block	Recommend.	QA only
Plain Waisted Block	Not applicable.	Suitable.

THROUGH-THICKNESS SHEAR

The number of test methods that can be used for T-T shear characterisation is limited, with all techniques demonstrating deficiencies. This section evaluates two methods that have been widely adopted for characterising T-T shear properties of PMCs, the double-notch and V-notched beam (Iosipescu) test methods. The V-notched beam method (ASTM D 5379 [5]) can provide in-plane and T-T shear moduli for all isotropic and anisotropic materials, and in many cases the shear strength. The double-notch method, which consists of loading a non-symmetrically notched coupon in uniaxial tension or compression is used to measure interlaminar shear strength. This method is available as ASTM D 3846 [6], and is quoted as an appendix to BS 4994 [7] and BS 6464 [8]. ASTM D 3846 specifies compressive loading, and the two BSI standards tensile loading. Typical T-T shear data obtained using these methods is shown in Table 4. Default values are bracketed (ie assumed material symmetry in the X-Z and Y-Z planes). Tests were conducted according ASTM specifications. Shear strengths obtained using the two test geometries were generally in good agreement [9].

Table 4: Through-thickness shear measurements (= non-shear failure)*

Test Method	G_{xz} (GPa)	G_{yz} (GPa)	S_{xz} (MPa)	S_{yz} (MPa)
Aligned carbon-fibre/epoxy				
V-Notched Beam	5.30 ± 0.31	2.93 ± 0.25	111 ± 2	64 ± 9*
V-Notched Beam (sandwich)	5.37	3.18	105	52*
Double-Notch	N/A	N/A	75 ± 12	N/A
2/2 twill glass-fibre fabric/epoxy				
V-Notched Beam	4.12 ± 0.14	[4.12 ± 0.14]	68.4 ± 0.9	[68.4 ± 0.9]
Double-Notch	N/A	N/A	64.9 ± 1.8	[64.9 ± 1.8]
Discontinuous glass-fibre/nylon 66				
V-Notched Beam	1.68 ± 0.06	-	56.9 ± 3.6*	58.4 ± 4.8*
Double-Notch	N/A	N/A	66.4 ± 4.8	[66.4 ± 4.8]
Random glass-fibre mat/polypropylene	1.04 ± 0.04	[1.04 ± 0.04]	22.7 ± 0.8	[22.7 ± 0.8]
V-Notched Beam	N/A	N/A	18.1 ± 3.3	[18.1 ± 3.3]
Double-Notch				

Double-Notch

Due to their simplicity, test geometries incorporating a double-notch have been widely employed in the measurement of interlaminar shear strength. The most reliable approach is to load a double-notch specimen in compression, with the specimen supported along its entire length to minimise out-of-plane deformation, as specified in ASTM D 3846 (Fig. 5). Tests were conducted using specimens 79.5 mm long and 10.0 mm wide (NB. ASTM D 3846 recommends 12.7 mm). Two parallel notches, one on each opposite face of the specimen and 6.4 mm (0.25 in) apart, were cut across the entire width of the specimen and centrally located along its length. The notch width was ± 1.5 mm and extended to the specimen mid-plane.

Linear-elastic stress analysis has shown that the shear stress distribution along the mid-plane between the notches is non-uniform with high shear stresses in the vicinity of the notches. Non-linear finite element analysis, conducted at the NPL, has indicated that the stress concentration at the notches is close to unity for an isotropic specimen loaded according to ASTM 3846. Data reduction is simple, with the applied stress determined using Equation (1), where A is the cross-sectional area between the notches.

The method specified in ASTM 3846 is relatively straightforward to perform, requiring a support fixture of moderate cost. This loading configuration provides consistent strength data with interlaminar failure regularly occurring along the mid-plane joining the two notches. T-T shear strength data is generally consistent with results obtained using the V-notched beam method, implying the shear stress concentration at the notches is close to unity (Table 3). Specimen preparation and testing is relatively straightforward, although the quality of machining the notches has a significant effect on strength data. Notch depth must be accurately machined to the required depth of half the specimen thickness (ie mid-plane). Fractographic examination of the failure surfaces reveals shear dominated mixed-mode failure. This method is particularly suited to testing thin laminates (ie 2.5 to 10 mm thick).

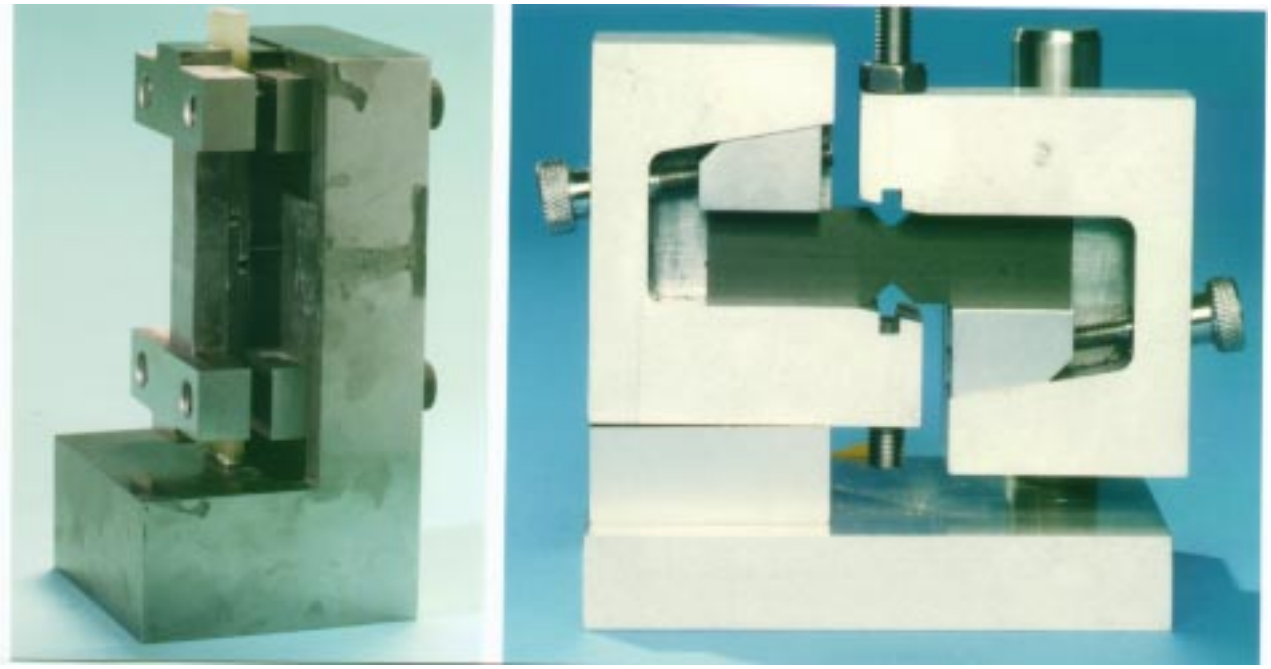

Fig. 5: Double-notch and V-notched beam tests

V-Notched Beam Shear

This test employs a double edge-notched, flat, rectangular specimen. Tests were carried out on monolithic materials, and a three-layered sandwich construction, according to ASTM D 5379 using the loading configuration shown in Fig. 5. Specimens were 76 mm in length, 20 mm wide (ie T-T dimension) and 5 mm thick (nominal). Two 90^o angle notches with a notch root radius of 1.3 mm were machined at the edge mid-length with faces oriented at $\pm 45^o$ to the longitudinal axis, to a depth of 20% of the specimen width (ie 4 mm). Shear strain was measured by bonding two biaxial strain gauges, one on each opposite face of the specimen at its centre in the area

between the notches. The strain gauges had an active gauge-length of 1 mm and were aligned at $\pm 45^{o}$ to the longitudinal axis of the specimen. Applied stress is determined from Equation (1), where A is the cross-sectional area between the notches.

Providing adequate material thickness is available (ie 10 mm), this method can be used to measure in-plane and T-T shear modulus and shear strength (Table 3) for a diverse range of composite materials. Differences between shear moduli, due to out-of-plane deformation, can be as high as 10% for a batch of nominally identical specimens. To ensure maximum accuracy, shear modulus is determined from the average response of back-to-back biaxial rosettes. At present the standard requires only one specimen from a batch to be tested in this manner provided the amount of twist for this test piece is no greater than 3%.

Table 5: Shear test methods suitable for standardisation

Method	Elastic Properties	Strengths
Double-Notch	Not applicable.	Strongly recommend.
V-Notched Beam	Strongly recommend.	Strongly recommend - caution on failure mode.

ACKNOWLEDGEMENTS

The research reported in this paper was carried out as part of the "Materials Measurement Programme", a programme of underpinning research financed by the United Kingdom Department of Trade and Industry. The author acknowledges the contributions his colleagues Dr Graham Sims and Miss Maria Lodeiro at the National Physical Laboratory, and Mr Robert Ferguson, Defence Research Agency at Fort Halstead.

REFERENCES

1. Ferguson, R.F., Hinton, M.J. and Wilson, C.J., private communication 1996.

2. Mespoulet, S., "Through-Thickness Test Methods for Laminated Composites", Centre for Composite Materials, Imperial College, London, United Kingdom, February 1995.

3. Mespoulet, S., Hodgkinson, J.M., Matthews, F.L., Hitchings, D. and Robinson, P., "A Novel Test Method to Determine the Through-Thickness Tensile Properties of Long Fibre Reinforced Composites", Proceedings of ECCM-7, Volume 2, London, 1996, pp 131-137.

4. Broughton, W.R. and Sims, G.D., "An Overview of Through-Thickness Test Methods for Polymer Matrix Composites", NPL Report DMM(A)148, October 1994.

5. ASTM D 5379/D 5379M - 93: "Standard test method for shear properties of composite materials by the V-notched beam method", Volume 15.03, Annual Book of ASTM Standards, Philadelphia, Pennsylvania, USA, 1996, 235-247.

6. ASTM D 3846: "Standard Test Method for In-Plane Shear of Reinforced Plastics", Volume 8.02, ASTM Standards, 1995, pp 435-439.

7. BS 4994: "Design and Construction Vessels and Tanks in Reinforced Plastics", 1987.

8. BS 6464: "Reinforced Plastics Pipes, Fittings and Joints for Process Plants", 1984.

9. Broughton, W.R., Lodeiro, M. and Sims, G.D., "Experimental Validation of Shear Test Methods for Through-Thickness Properties", Proceedings of ECCM-7, Volume 2, 1996, pp 125-130.

NEW TEST METHODS FOR CHARACTERISING SKIN-CORE DEBONDING IN COMPOSITE SANDWICH STRUCTURES

W.J. Cantwell[1], R. Scudamore[1], P. Davies[2] and J.-B. Ferrer[3]

[1] Dept. of Materials Science & Engineering, Univ. of Liverpool, Liverpool L69 3BX.
[2] Dept. of Ocean Engineering, IFREMER, Plouzan,, France.
[3] Dept. of Materials Science & Engineering, EPFL, Lausanne, Switzerland.

SUMMARY: The interfacial fracture properties of a series of fibre reinforced sandwich materials have been investigated using a number of different test techniques. The results have shown that relatively simple test geometries such as the single cantilever sandwich (SCS) specimen and the three point bend sandwich (TPBS) specimen are well suited to characterising the interfacial fracture properties of these lightweight materials. Both of these geometries also offer the advantage that they can be used to determine the interfacial fracture energy of sandwich materials at impact rates of strain.

KEYWORDS: sandwich materials, delamination, interfacial fracture, debonding.

INTRODUCTION

The use of high performance, light-weight sandwich materials has increased significantly in recent years. Typically, carbon and glass fibre reinforced plastics are bonded to low density cores to produce strong, stiff lightweight structures. The strength of the interface between the composite facing and the low density core is likely to be critical and needs to be optimised before these materials will achieve their full potential. To date, much of the work relating to skin-core adhesion in sandwich structures has involved the use of the climbing drum test where the skin is wrapped around a large radius cylinder mounted on one side of the specimen. The test suffers several limitations, however. One of these relates to the fact that the skins must be relatively thin and flexible. It is also difficult to undertake tests at high rates of loading, a loading condition that might result in a significant reduction in the fracture properties of these materials. Recently, Prasad and Carlsson [1,2] used a modified double cantilever beam specimen to evaluate debonding and crack kinking in foam core sandwich beams. In an earlier study, Carlsson et al [3] developed a cracked sandwich beam specimen to investigate shear failure in a GFRP-balsa sandwich structure. Their results indicated that the interfacial fracture toughness values of such materials can be much greater than those associated with traditional thermoset-based composite materials.

The authors recently developed a number of new tests to characterise skin-core adhesion in sandwich structures. These tests involve propagating a crack along the skin-core interface and determining an interfacial fracture energy. The objective of this work was to assess the interfacial fracture properties of sandwich materials using these tests and two traditional tests

used widely in industry. The advantages and limitations of the test procedures will be highlighted and discussed.

EXPERIMENTAL PROCEDURE

Materials

Four glass/polyester balsa systems (referred to as materials A to D) manufactured via a hand lay-up process were considered in this study. The skins in all materials were based on composites containing two layers of stitched quadriaxial E-glass fibre fabric in an isophthalic polyester resin and the core was an end-grain balsa having a density of 175 kg/m3 and a nominal thickness of 15 mm. Material A represents a standard system in which the skins were cured directly onto the balsa core. Prior to applying the composite skins, the cores in materials B to D were first sealed using a polyester resin. Material C contained a layer of chopped strand mat (CSM) at the skin-core interface and material D a layer of fabric based on a thermoplastic polyester fibre. Further details regarding the materials and manufacturing procedures can be found in refs 4 and 5.

Test Methods

Single Cantilever Sandwich Specimen

The interfacial fracture toughness of the sandwich materials was investigated using the single cantilever sandwich (SCS) geometry test shown in Fig. 1a. Here, one end of the beam was machined away leaving a tongue approximately 50 mm long. Prior to testing, the specimens were pre-cracked by loading the specimen in a vice and applying load to the end of the beam forcing a crack to propagate along the skin-core interface. Testing was carried out at a crosshead displacement rate of 5 mm/minute. In all tests, the crack was propagated 50 mm before the specimen was unloaded. Four specimens of each type were tested. The interfacial fracture energy was calculated using a compliance calibration procedure.

A finite element analysis was undertaken in order to determine the mode-mixity at the crack tip in the SCS geometry. Here, a 9000 node mesh based on eight-noded quadratic elements was used to model the specimen. Figure 2 shows the variation of GI/GII with crack length for material A. From the figure it is apparent that the degree of mode-mixity in this specimen does not vary with crack length, remaining constant over the range of crack lengths considered.

End-Loaded Sandwich Structure

The end-loaded sandwich structure (ELSS) is shown schematically in Fig. 1b. Here, a 200 x 20 mm pre-cracked sandwich beam was fixed to a movable chariot. Testing was again carried out on at a crosshead displacement rate of 5 mm/minute and a pre-crack length of approximately 50 mm was used throughout. Load was applied through a hinge bonded to the end of the pre-cracked region and crack advance monitored using a calibrated scale painted along the interfacial region. Typically, the crack was propagated fifty millimetres before the test specimen was unloaded.

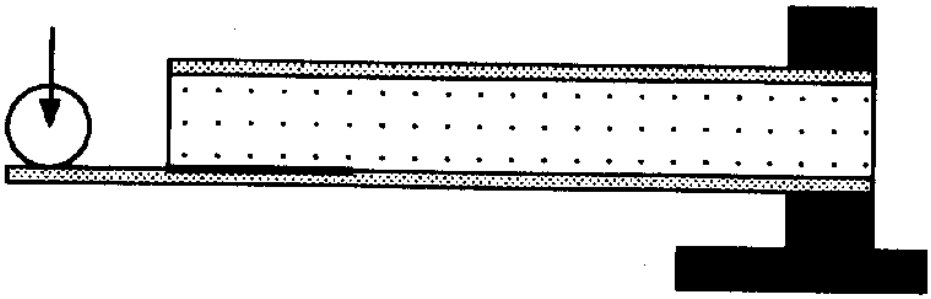

(a) Single cantilever sandwich specimen

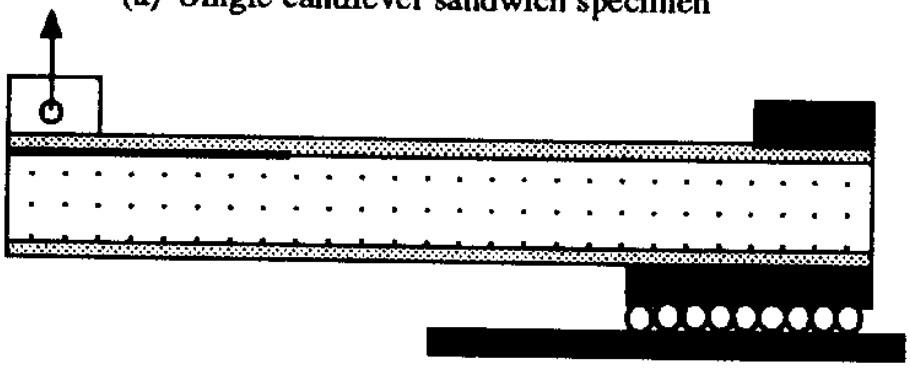

(b) End-loaded sandwich structure

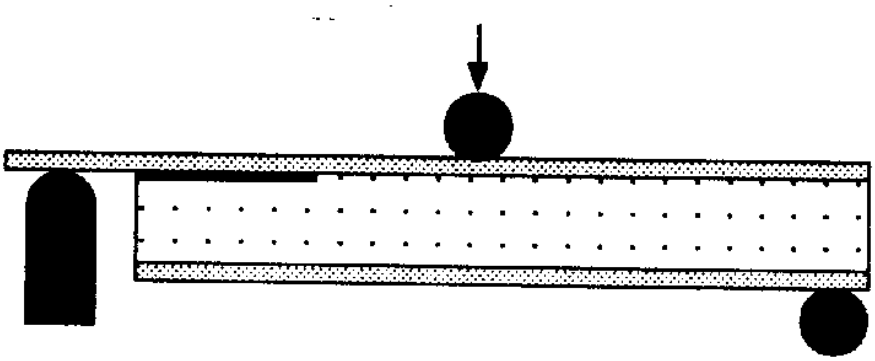

(c) Three point bend sandwich specimen

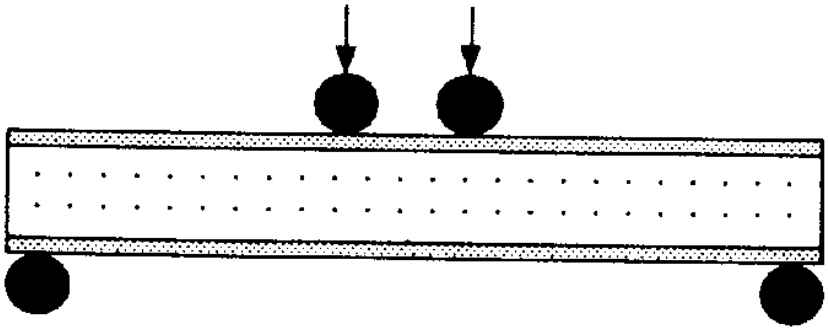

(d) Short beam shear test

Fig. 1: Schematic showing the test geometries evaluated in this programme.

Three Point Bend Sandwich Specimen

The three point bend sandwich (TPBS) specimen, Fig. 1c, is a simple flexural specimen similar in configuration to the mixed mode flexure (MMF) geometry used to characterise the interlaminar fracture toughness of high performance composites. The specimen consists of a simple beam from which the core and lower skin have been removed at one end. The specimen is then positioned on rollers (one of which is raised in order ensure than the specimen remains horizontal) and loaded at its mid-point. In this programme, specimens with dimensions 140 x 20 mm were supported on rollers positioned 120 mm apart. Once again, crack propagation is monitored optically using a calibrated scale and the fracture energy determined using a compliance calibration technique.

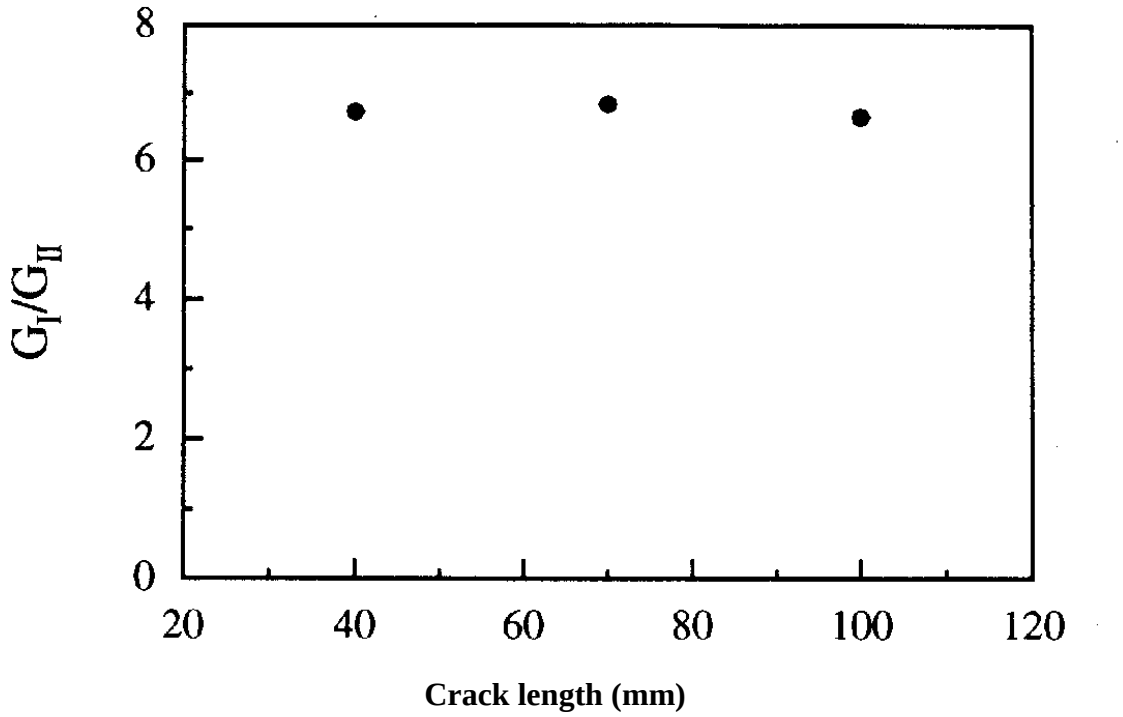

Fig. 2 The mode-mixity as a function of crack length for the SCS specimen geometry

Short Beam Shear Tests

A series of short beam shear tests based on the French standard NF T54-606 were undertaken on the four balsa materials in order to characterise their apparent shear strengths. In this part of the study, 50 mm wide beams were supported on cylindrical rollers positioned 200 mm apart. Load was applied by two central rollers rather than one, to avoid indentation, Fig. 1d. The crosshead displacement rate was 5 mm/min. The shear stress at rupture was determined from the expression:

$$\tau = \frac{P}{(h + h_c)B}$$

with P the maximum force, h the total sandwich thickness and hc the core thickness, B the beam width. Six beams of each type were tested.

Climbing Drum Peel Tests

A series of climbing drum tests were conducted according to the DIN 53 295. Here, 300 x 20 mm specimens were machined leaving 25 mm tongues at each end. One end of the specimen was held in steel grip and the other end fixed to the surface of a 100 mm external diameter drum. The subsequent movement of the drum relative to the lower end of the specimen resulted in the separation of the skin and core materials. The tests were undertaken at a crosshead speed of 25 mm/min.

RESULTS AND DISCUSSION

The following sections will consider the findings of each of the five test techniques individually.

Single Cantilever Sandwich Specimen

Crack propagation in all materials was found to be stable and the resulting load-displacement traces relatively smooth. The interfacial propagation fracture energies for the four materials are shown in Fig. 3. It is clear that all of the materials exhibit similar values of fracture energy. The standard system, material A, shows an average fracture energy of approximately 900 J/m2. Pretreating the balsa, material B, resulted in a small increase in the average fracture energy, however, it is probably not statistically significant. Material C containing a layer of chopped strand mat fibres at the skin-core interface exhibited an average fracture energy of approximately 800 J/m2. The interface between the polyester fibre interlayer and the balsa core in material D proved to be so strong that the crack propagated up through the thermoplastic fibre interlayer and then along the composite/interlayer interface. The fracture energy associated with the interlayer-balsa interfacial region is therefore likely to be greater than the value shown in the figure.

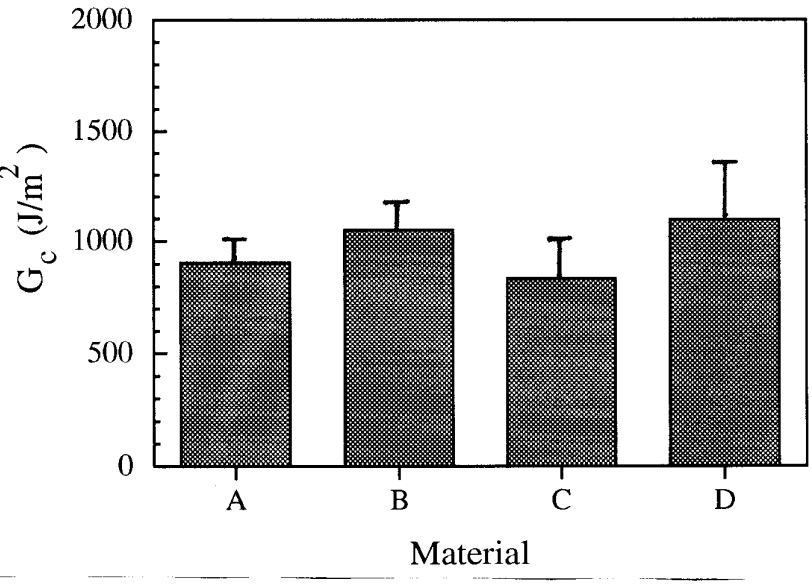

Fig. 3 Fracture data obtained using the single cantilever sandwich geometry.

End-Loaded Sandwich Structure

The modes of crack propagation observed in the balsa specimens were similar to those observed in the SCS geometry reported above. Figure 4 contains a summary of the mean interfacial fracture energies measured on the four materials examined in this study. From the figure, it is apparent that of the four sandwich structures, material A exhibited the highest value of interfacial fracture toughness. Here, a significant amount of fibre bridging occurring between the skin and core materials was observed.

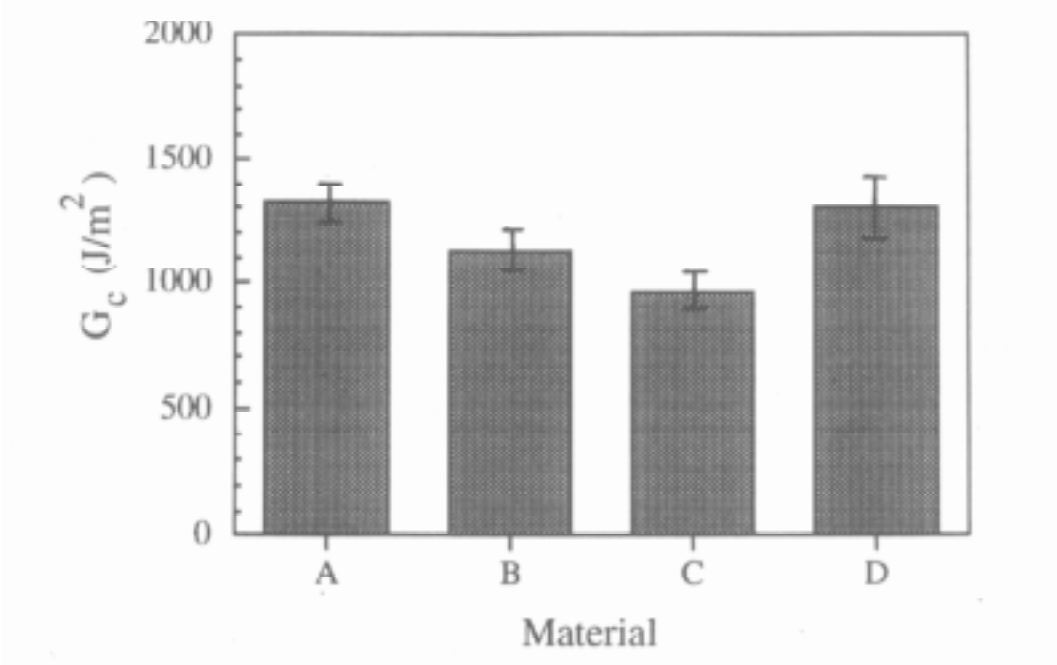

Fig. 4: Fracture data obtained using the end-loaded sandwich structure geometry.

Three Point Bend Sandwich Specimen

The load-displacement curves for the TPBS specimens were similar in appearance to those recorded during the SCS and ELSS tests with the exception that crack-propagation in material B occurred in a stick-slip mode. A subsequent optical examination of the failed sample indicated that fibre bridging was significant in materials A, C and D but limited in material B. This evidence suggests that fibre bridging has a significant influence on the stability of a propagating crack. The average fracture energies for the four balsa materials are presented in Fig. 5. From the figure it is clear that the fracture energies for materials A, C and D are similar to those determined using the SCS and ELSS geometries. Once again, material B proves to be the exception to this rule with the fracture energy being roughly fifty percent of the values measured using the other geometries. It is believed that this low value does not result from different loading conditions at the crack tip but is simply due to local variations in the quality of the skin-core interfacial region.

Short Beam Shear Tests

In all materials, initial failure occurred between the balsa blocks within the core material extending up to the skin-core interface at higher applied loads. Crack propagation in materials A, B and D occurred in an unstable manner whereas failure in system C containing a layer of chopped glass fibres was stable. The short beam shear shear strength data are summarised in

Fig. 6. From the figure, it is clear that the average shear strength values for these four systems are low (the interlaminar shear strength of the skins was around 30 MPa). It is also evident that the degree of scatter is quite large, probably a result of the fact that crack initiation depends on the position of joints between blocks. Material D containing the thermoplastic fibre interlayer yielded the highest value of shear strength.

The short beam shear test is often used as a quality control check in shipyards and can be employed to identify problems relating to the skin-core interface. Unfortunately, the tests on these balsa materials all yielded similar apparent shear strengths so this test is of limited use for more detailed studies of interface behaviour.

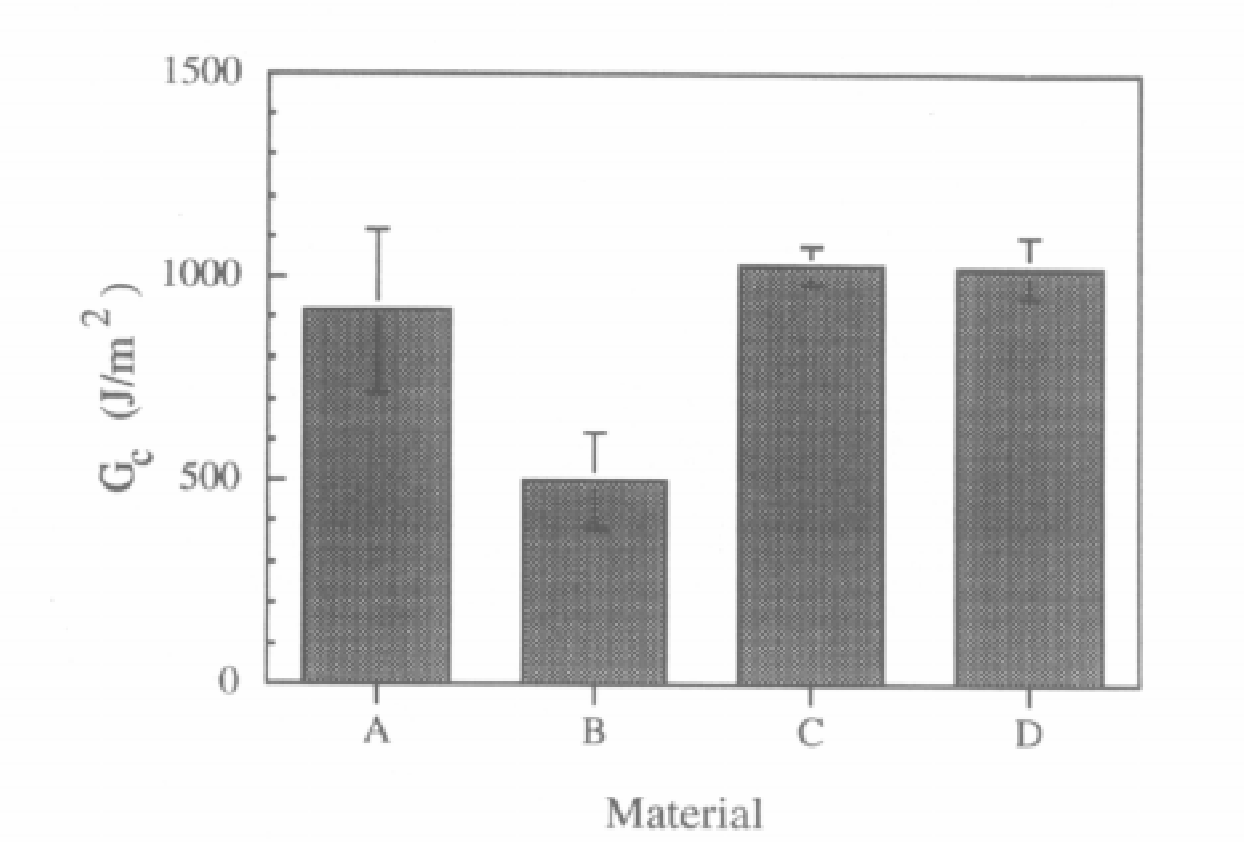

Fig. 5 : Fracture data obtained using the three point bend sandwich specimen.

Climbing Drum Peel Tests

Due to the high skin thicknesses of the balsa-based materials C and D, climbing drum peel tests were only undertaken on materials A and B. Both of these materials exhibited a stable mode of fracture in which the peel force remained roughly constant during the test. The specific moments for materials A and B were 88 and 91 Nm/m respectively. The major disadvantage of this technique is that it is only suited for the testing of relatively thin skinned systems.

Comparison of the Test Techniques

Comparing the experimental data yielded by the five test techniques enables several conclusions to be drawn. The short-beam shear test, although simple to use, is very sensitive to the quality of the balsa core and the measured shear strength depends on the position of the joints between the balsa blocks. The climbing drum peel test is a useful technique for characterising the interfacial fracture properties of sandwich materials but it is limited to the testing of thin-skinned materials. The end-loaded sandwich structure, the single cantilever sandwich and the three point bend sandwich specimen proved to be well suited to the testing of all four materials. For a given material system, different fracture energies were obtained using the specimens, Fig. 7. It is likely that the mode I/II mixity is different between the three tests and this is will result in different values of G. The ELSS test involves the use of a sliding chariot and is therefore slightly more cumbersome. The SCS and TPBS geometries offer several advantages including their ease of use and the possibility of undertaking tests at very high rates of strain. Problems do arise when testing very thin-skinned sandwich structures but these can be overcome by bonding a thicker substrate to the loading arm.

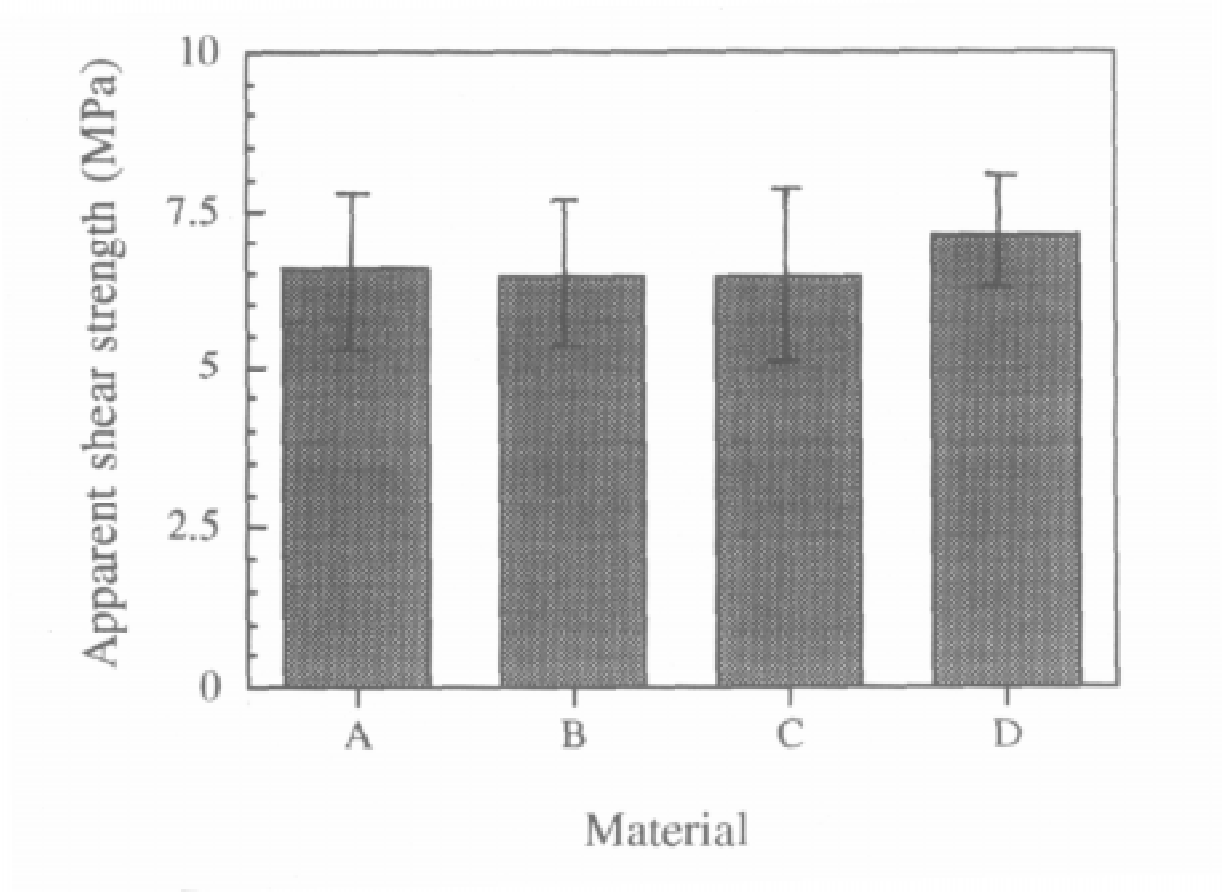

Fig. 6: Fracture data from the short beam shear tests

CONCLUSIONS

Five different test geometries have been used to characterise skin-core failure in a variety of balsa-based sandwich materials. The climbing drum peel test was found to be unsuitable for tests on thick-skinned structures such as the balsa-based materials C and D. The short-beam shear test, a technique frequently used as a quality control test in shipyards, failed to

differentiate between the various balsa systems and is deemed to be unsuitable for characterising materials of this nature. The end-loaded sandwich structure, the single cantilever sandwich specimen and the three point bend sandwich specimen were well suited for testing the range of systems examined in this study.

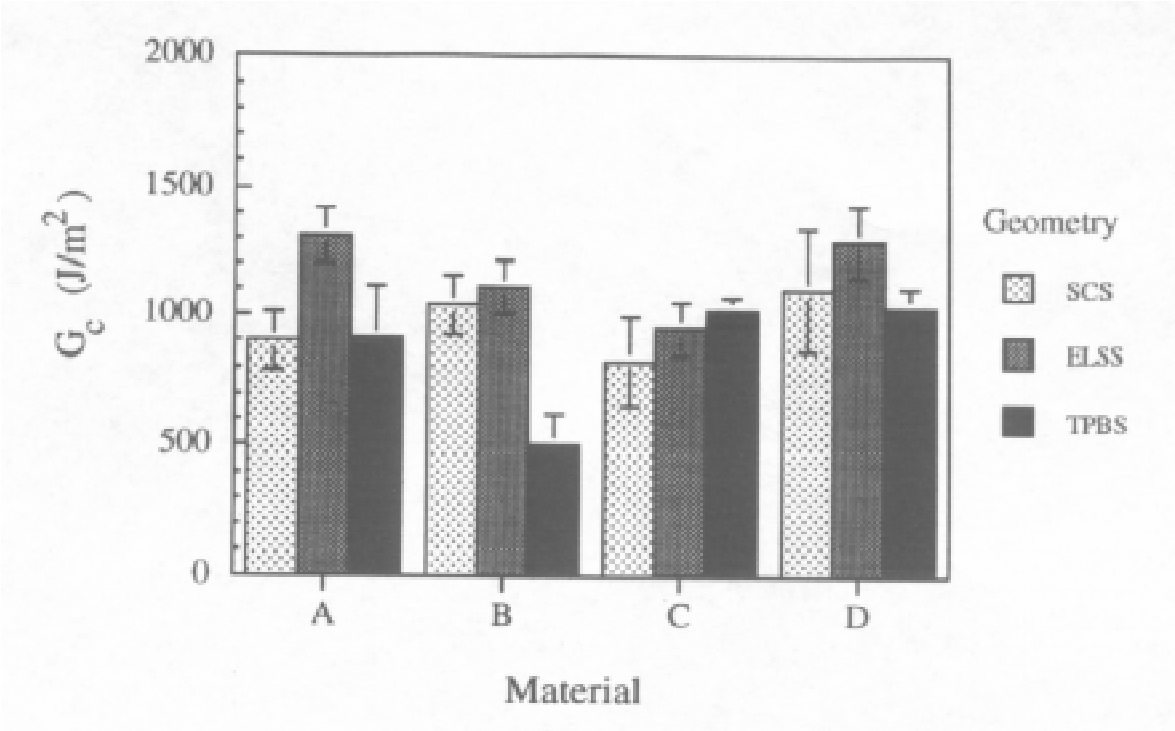

Fig.7: Comparison of the fracture energies determined using the SCS, ELSS and the TPBS geometries

REFERENCES

1. Prasad, S. and Carlsson, L.A., "Debonding and crack kinking in foam core sandwich beams - I. Analysis of fracture specimens", Engineering Fracture Mechanics, Vol. 47, 1994, pp. 813-824.
2. Prasad, S. and Carlsson, L.A., "Debonding and crack kinking in foam core sandwich beams - II. Experimental investigation", Engineering Fracture Mechanics, Vol. 47, 1994, pp. 825-841.
3. Carlsson, L.A., Sendlein, L.S. and Merry, S.L., "Characterization of face/core shear fracture of composite materials", Journal of Composite Materials, Vol. 25, 1991, pp. 101-116.
4. Cantwell, W.J., Broster, G., and Davies, P., "Skin-core-adhesion in GFRP-balsa sandwich structures", Journal of Reinforced Plastics and Composites, Vol. 15, 1996, pp. 1161-1172.
5. Cantwell, W.J. and Davies, P., "A study of skin-core adhesion in glass fibre reinforced sandwich materials", Applied Composite Materials, Vol. 3, 1996, pp. 407-420.

THE MEASUREMENT OF MODE III FRACTURE TOUGHNESS IN THICK COMPOSITE LAMINATES USING STRAIN GAGES

W. C. Liao and R. L. Tu

Department of Civil Engineering, Feng Chia University, Taichung Taiwan

SUMMARY： The edge crack torsion(ECT) specimen is used to measure the Mode III fracture toughness of thick laminates. In order to simplify the calculation of strain energy release rates, the thick laminate is homogenized as an orthotropic laminate using 3-D effective moduli and boundary collocation solution was derived. The in-plane shear strain and out-of-plane shear strain distributions calculated from the boundary collocation method are in good agreement with finite element results. A four-point torsion set-up is employed to measure the shear strain responses at two different locations. From the strain responses at two different positions, we are able to measure the in-situ shear moduli and interlaminar fracture toughness of ECT specimen. The difference between the measured global shear moduli and predictions is within 10% and is independent of the crack size. Several angle ply laminates are tested for the Mode III fracture toughness. The fracture toughness for Fibrite T300/976 material is measured from the strain responses.

KEYWORDS: edge crack torsion(ECT) specimen, mode III fracture toughness, boundary collocation method, strain energy release rates.

INTRODUCTION

The measurement of Mode III fracture toughness was first investigated by Donaldson's split cantilever beam method[1]. Subsequent finite element analysis and scanning electron microscope fractographs of the SCB specimens showed that significant Mode I and Mode II delaminations exist for such method[2,3]. In order to generate a pure Mode III fracture test, the edge crack torsion(ECT) specimen has been employed to measure the interlaminar fracture toughness of thick laminates[4,5]. In Lee's[4] method the effect of transverse shear was not taken into account. Li and Wang[6] developed a shear deformation theory to analyze the torsion of edge cracked specimens. However, the edge crack is limited to the mid-plane, and the linear shear deformation assumption in the thickness direction seems to be an insufficient candidate for the actual displacement field[5]. If the thick laminate is composed of repeated sublaminates, and the thickness of a typical subset is small compared to the total thickness of the laminate, then effective

moduli can be applied[7]. In this study, the thick laminate is homogenized as an orthotropic section, and boundary collocation solution for ECT specimen is derived.

In performing the torsion test of composite laminate, usually the global shear moduli have to be determined first. Conventionally, these global shear moduli are obtained from the coordinate transformation law[8]. There are substantial deviations in the measurements of material shear moduli G_{12} and G_{13} when using the $[\pm 45]_{NS}$ coupons. The nonlinear deformations are observed in the simple tension test of a $[\pm 45]_{NS}$ specimen. By measuring the strain responses of two gages under torsion loading, Tsai [9] et.al. was able to characterize the shear moduli G_{12}, G_{13} and G_{23} of AS4/3501-6 graphite/epoxy laminates. The nonlinearity phenomenon are reduced. The in-situ shear moduli for an edge-cracked composite bar have not been measured up-to-date. In this paper, we propose a method to measure the in-situ shear moduli of an ECT specimen. The strain responses are evaluated from the boundary collocation method. Data reduction method to yield the global shear moduli, torsional rigidity and fracture toughness are addressed.

TORSION THEORY OF AN ECT SPECIMEN

1. 3-D Effective moduli for thick laminates

In the manufacturing of thick composite laminates, usually the laminate is made of repeated sublaminates to avoid warping effect during curing cycles. If the thickness of a typical sublaminate is small compared to the total thickness of the laminate, then the inhomogeneity between each ply in a subset can be smeared out, and effective moduli applied. For a typical subset, if we assume that: 1) the in-plane strains are compatible, and 2) the out-of-plane stresses are continuous within each representative volume, then the effective moduli of a $\pm\theta$ type composite made of single material system can be expressed as[7]

$$\bar{c}_{ij} = \sum_{k=1}^{N} \mathrm{v}_k c_{ij}^k \qquad i,j = 1,2,3,6$$

$$\bar{c}_{pq} = \left[\sum_{k=1}^{N} \mathrm{v}_k c_{pq}^k / \Delta_k\right] \Big/ \Delta \quad , \qquad p,q = 4,5 \tag{1}$$

The definition of Δ and Δ_k and v_k can be seen in [7].

2. Boundary collocation method for edge cracked torsion (ECT) specimen

When the effective moduli are employed, a thick laminate can be homogenized as an orthotropic material. For an edge crack torsion (ECT) specimen with a crack located at arbitrary height e (or f) as shown in Fig. 1, the governing equation is given by[10]:

$$\frac{1}{G_{xz}}\frac{\partial^2 \psi}{\partial y^2} + \frac{1}{G_{xy}}\frac{\partial^2 \psi}{\partial z^2} = -2\Theta \tag{2}$$

In the above equation, G_{xy} and G_{xz} are the shear moduli in the xy and xz planes, respectively, Θ is the twisting angle per unit length, ψ is the stress potential with

$$\sigma_{xz} = -\frac{\partial \psi}{\partial y} \quad , \quad \sigma_{xy} = \frac{\partial \psi}{\partial z} \tag{3}$$

and other σ_{ij} =0. The boundary condition for the geometry shown in Fig. 1 is

$$\psi|_{\Gamma} = 0 \tag{4}$$

where Γ is the outer contour of this cross-section. Now, if we let

$$\psi = G_{xy}\Theta[-z^2 + \phi(y,z)]$$

$$p^2 = G_{xz} / G_{xy} \tag{5}$$

$$\bar{x} = py \quad , \quad \bar{y} = z$$

then Eqn. (2) can be transformed into

$$\frac{\partial^2 \phi}{\partial \bar{x}^2} + \frac{\partial^2 \phi}{\partial \bar{y}^2} = 0 \tag{6}$$

in associated with boundary condition

$$\phi|_{\Gamma} = \bar{y}^2 \tag{7}$$

The general form of ϕ is given as[11]

$$\phi(\bar{r}, \bar{\theta}) = \sum_{k=1}^{\infty} D_k \sin\left(0.5k(\pi + \bar{\theta})\right) \bar{r}^{0.5k} \tag{8}$$

where

$$\bar{r} = \sqrt{\bar{x}^2 + \bar{y}^2} \tag{9}$$

$$\bar{\theta} = \tan^{-1}(\bar{y} / \bar{x}) \tag{10}$$

In Eqn. (8), the D_k can be determined from the boundary conditions, i.e., Eqn. (7). The shearing strains γ_{xy} and γ_{xz} in the original system are

$$\gamma_{xy} = \sigma_{xy} / G_{xy} = \Theta\left[\sum_{k=1}^{\infty} D_k \frac{k}{2} \bar{r}^{\frac{k}{2}-1} \cos\left(\frac{k(\pi + \bar{\theta})}{2} - \bar{\theta}\right) - 2z\right] \tag{11}$$

$$\gamma_{xz} = \sigma_{xz} / G_{xz} = -\frac{1}{p}\Theta \sum_{k=1}^{\infty} D_k \frac{k}{2} \bar{r}^{\frac{k}{2}-1} \sin\left(\frac{k(\pi + \bar{\theta})}{2} - \bar{\theta}\right) \tag{12}$$

The torsional rigidity of this edge crack specimen is shown to be

$$GJ = T / \Theta = 2\frac{G_{xy}}{p}\left(-\frac{p^* 2b(e^3 + f^3)}{3} + \sum_{k=1}^{\infty} D_k E_k\right) \tag{13}$$

$$E_k = \frac{2}{k+2} \int_{-\pi}^{\pi} \bar{r}^{0.5k+2}(\bar{\theta}) \sin(0.5k(\pi + \bar{\theta}))\, d\bar{\theta} \tag{14}$$

In Eqn. (13), 2b is the width of the cross-section. The boundary collocation method is applied to solve Eqn. (7). In actual calculation, the infinite series coefficients D_k's are summed over finite terms. The least square method are employed to solve the overdetermined equations. The mode III stress intensity factor for this homogenized orthotropic thick laminate is

$$K_{III} = \lim_{r \to 0} \sqrt{2\pi r}\, \sigma_{xz}|_{\theta=0} = -\sqrt{p\pi/2}\; G_{xy}\Theta D_1 \tag{15}$$

in which D_1 is the first term of the coefficients D_k's. The corresponding Mode III strain energy release rate is given by:

$$G_{III} = \frac{K_{III}^2}{2G_{xy}} = \frac{\pi G_{xy}}{4p} \Theta^2 D_1^2 \qquad (16)$$

3. Illustrative examples

The $\pm 45]_{10s}$ laminate with interfacial crack located at the innermost interface (i.e., the 19/20th ply interface) is examined to evaluate the accuracy of the boundary collocation method. The material used assumes the following properties.

E_1=138 GPa, E_2=E_3=10.0 GPa

ν_{12}=ν_{13}=0.3, ν_{23}=0.45

G_{12} = G_{13}=6.9 GPa, G_{23}=3.45GPa

ply thickness=0.127mm, width of the laminate=5.08cm

The corresponding G_{xy} ,G_{xz} and shear anisotropy factor p for this laminate are calculated from Eqns. (1) and (5) as G_{xy}=35.76GPa, G_{xz}=4.60GPa, and p=0.357, respectively.

The stress and strain distributions at arbitrary position of the cross-section are evaluated through three kinds of methods. The detail of the finite element all local method and analytical series solution can be seen in[5]. Figure 3 shows the in-plane shear strain γ_{xy} distribution on the top surface (along z=h) for a/2b=0.2. It seems the differences between these three methods are small which is congruent with the basic assumption in 3-D effective moduli, i.e. in-plane strains are compatible. Figure 4 shows the variation of the out-of-plane shear strain γ_{xz} along the uncrack side(y=b) It seems these three methods differ little in the average sense. From Figs. 3 and 4, the boundary collocation method employing the 3-D effective moduli theory can be used to predict the in-plane shearing strain γ_{xy} at the top surface and the interlaminar shear strain γ_{xz} at uncrack side of ECT specimen. This suggests a method of measuring the in-situ shear moduli of thick laminates using strain gages. .

The G_{III} values are compared in Fig. 5. It is seen the boundary collocation method can yield good results when a/2b is greater than 0.1. The difference of G_{III} between the boundary collocation method and finite element approach is less than 2% in most cases. Figure 6 shows the torsional rigidities from three different approaches. Both boundary collocation method and analytical series solution yield larger GJs than finite element method. The difference is acceptable.

MEASUREMENT OF MODE III FRACTURE TOUGHNESS OF AN EDGE CRACK SPECIMEN

1 Measuring in-situ shear moduli of thick laminate using strain gages

The shearing strains for the ECT specimen are given in Eqns. (11) and (12). In torsion problem, the shearing strains are of major concern. The gages are located at the positions shown in Fig. 7. Gage A is attached on the top surface of the cross-section with 45° inclined to the loading axis to measure the in-plane shearing strain γ_{xy}. Gage B is placed on the thickness direction to measure the out-of-plane shearing strain γ_{xz}. Since the signals form these two gages represent the average strains over the grid area, the measured strains need to be modified according to the individual gage length and gage width.

(A) Gage A

Gage A is on the top surface of the specimen at height z=e(the origin of the cross-section is set on the crack tip), the in-plane shear strain along this surface is

$$\gamma_{xy}^{A} = \Theta\left[\sum_{k=1}^{\infty} D_k \frac{k}{2} \bar{r}^{\frac{k}{2}-1} \cos\left(\frac{k(\pi+\bar{\theta})}{2} - \bar{\theta}\right) - 2e\right] \tag{17}$$

The average shear strains over gage length $\bar{A}$, and gage width $\bar{B}$ can be evaluated from the following formula

$$\bar{\gamma}_{xy}^{A} = \frac{1}{\bar{A}\bar{B}} \int_{-\bar{A}/2}^{\bar{A}/2} \int_{-\bar{B}/2}^{\bar{B}/2} \gamma_{xy}^{A}(y+b-a)\, ds\, dt \tag{18}$$

in which , s and t(see Fig. 8) are the local coordinates(i.e. the gage width direction and gage length direction, respectively)[9] of the strain gage. The average in-plane shear strain $\bar{\gamma}_{xy}$ over torque T can be shown as:

$$\frac{\bar{\gamma}_{xy}}{T} = \frac{1}{\bar{A}\bar{B}GJ}\left[\sum_{k=1}^{\infty} D_k \frac{k}{2} F_k - 2eH\right] \tag{19}$$

Expression for F_k and H can refer [12].

(B) Gage B

Strain gage B is placed on the middle of the thickness direction to measure the out-of-plane shearing stress γ_{xz}. On this surface y=2b-a, we have

$$\gamma_{xz}^{B} = -\frac{1}{p}\Theta \sum_{k=1}^{\infty} D_k \frac{k}{2} \bar{r}^{\frac{k}{2}-1} \sin\left(\frac{k(\pi+\bar{\theta})}{2} - \bar{\theta}\right) \tag{20}$$

The relation of average shear strain $\bar{\gamma}_{xz}$ within gage length A^*, gage width B^* over applied torque T is :

$$\frac{\bar{\gamma}_{xz}^{B}}{T} = -\frac{1}{p A^* B^* GJ} \sum_{k=1}^{\infty} D_k \frac{k}{2} F_k^* \tag{21}$$

in which s^* and t^* are the local coordinate directions of the strain gage (see Fig. 8), and expression for F_k^* can refer [12].

From Eqns. (21) and (19), the $\bar{\gamma}_{xy}^{A}/T$ and $\bar{\gamma}_{xz}^{B}/T$ on the left hand side are recorded during the experiment, the width 2b, thickness 2h, crack size a and crack position e of a specimen are measured before the torque is applied. The only unknowns in these equations are the effective shear moduli G_{xy} and G_{xz}. These two unknowns can be solved by the Newton Raphson's method using nonlinear iteration scheme. These in-situ shear moduli will be compared to the shear moduli using 3-D effective moduli theory.

2. Characterization of Mode III fracture toughness

Once the in-situ shear moduli are determined form the strain responses of the two gages, the strain energy release rate and the torsional rigidity can be yielded from the boundary collocation method also. In the experiment, the torque is measured through the torque sensor or from the applied concentrated load[4]. If the critical load or torque is recorded, then the following formula is employed to evaluate the G_{IIIC} of thick laminate.

$$G_{IIIC} = G_{III}\left(\frac{T_{cr}}{T_o}\right)^2 \tag{22}$$

where T_o is seen to be equal the torsional rigidity when $\Theta = 1$rad/m, G_{III} can be evaluated from Eqn. (16). and T_{cr} is the measured critical torque.

EXPERIMENT

Several ECT specimens made from Fibrite T300/976 material are tested. The material has the following properties

$E_1 = 144.790$ GPa $E_2 = E_3 = 8.894$ GPa

$G_{12} = 4.876$ GPa, $G_{13} = 4.941$ GPa, $G_{23} = 3.233$GPa

$\nu_{12} = \nu_{13} = 0.3$, $\nu_{23} = 0.376$

The G_{12}, G_{13} and G_{23} are measured by the method proposed by Tsai et al.[9]. Several $[\pm 45]_{10s}$ laminates with different crack sizes are tested under torsion loading. The precrack is made by embedding a 1 mil (0.025mm) thin teflon film at the 19/20th interface during the hand lay-up. The dimensions, crack size, and measured gages responses for each specimen are shown in Table 1. The gage sizes for gage A and B are 2mm × 1.3mm and 0.2mm × 1.3mm, respectively. Figure 9 shows the torsion configuration[4]. During the experiment, the strain responses at gages A and B, as well as the torque is recorded. The in-situ shear moduli G_{xy} and G_{xz} listed in Table 1 are calculated from Eqns. (19) and (21). A typical shearing strain versus torque is shown in Fig. 10. For the specimens tested, the in-situ shear moduli are close to one another which are independent of the crack size. The average shear moduli are $G_{xy} = 33.65$ GPa, and $G_{xz} = 3.65$ GPa. According to 3-D effective moduli theory, the G_{xy} and G_{xz} for $[\pm 45]_{10s}$ laminate are $G_{xy} = 37.29$ GPa, and $G_{xz} = 3.82$ GPa, respectively. The difference between the theoretical prediction and measurement is less than 10%. This indicates this method can be used to measure the in-situ shear moduli of thick laminates, and the 3-D effective moduli theory can predict the engineering moduli of thick laminate with good accuracy. The fracture toughness is measured for four of the specimens, the critical torque and G_{IIIC} are listed in Table 1 also. The average G_{xy} and G_{xz} are used in the calculation of fracture toughness. The interlaminar fracture toughness ranges from 650 to 1000 J/m^2.

CONCLUSION

A method for measuring the Mode III fracture toughness of an ECT specimen is presented. The in-situ shear moduli can be determined from the strain gage responses. The boundary collocation method is employed to calculate the stress distributions, strain energy release rates and torsional rigidities of edge cracked thick laminates under torsion loading. Several $\pm 45]_{10s}$ angle-ply laminates with different crack sizes are tested to evaluate the proposed experimental method. Compared with the 3-D effective moduli theory, the difference between the in-situ shear moduli and prediction is less than 10%. The measured fracture toughness for Fibrite T300/976 material ranges from 650 to 1000 J/m^2.

ACKNOWLEDGMENTS

This work was partially supported by the National Science Council of the R.O.C. under Grant No. NSC 86-2211E035-11.

REFERENCES

1. Donaldson, S. L., Mode III Interlaminar Fracture Characterization of Composite Materials, *Composites Science and Technology*, **32** (1988) pp.225-249.
2. Martin, R. H., Evaluation of the Split Cantilever Beam for Mode III Interlaminar Delamination Testing, *Composite Materials: Fatigue and Fracture (third Volume), ASTM STP 1110*, T. K. O'Brien, Ed., American Society for Testing and Materials, 4. Lee, Shaw-Ming, An Edge Crack Torsion Method for Mode III Delamination Fracture Testing, *Journal of Composite Technology and Research*, **15**(3), Fall, (1993) pp.193-201.
3. Cicci, D., Sharif, F. and Kortschot, M. T., "Data Reduction for the Split Cantilever Meam Mode III Delamination Test," Proceedings of the ICCM-10, Whistler, B. C., Canada, Aug., 1995, vol.1, pp. 189-196.
4. Lee, Shaw-Ming, An Edge Crack Torsion Method for Mode III Delamination Fracture Testing, *Journal of Composite Technology and Research*, **15**(3), Fall, (1993) pp.193-201.
5. Liao, W. C., and Sun, C. T., "The Determination of Mode III Fracture Toughness in Thick Composite Laminates," Composite Science and Technology, 56, (1996) pp.489-499.
6. Li, Jian and Wang, Y., Analysis of a Symmetric Laminate with Mid-Plane Free Edge Delamination Under Torsion: Theory and Application to the Edge Crack Torsion (ECT) specimen for Mode III Toughness Characterization, *Engineering Fracture Mechanics*, **49** (2), (1994) pp.179-194.
7. Sun, C. T. and Li, S., Three-Dimensional Effective Elastic Constants for Thick Laminates, *Journal of Composite Materials*, **22** (1988) pp.629-639.
8. Jones, R. M. *Mechanics of Composite Materials*, Scripta Book Company, 1975.
9. Tsai, C. L., Daniel, I. M., and Yaniv, G., "Torsional Response of Rectangular Composite Laminates," Journal of Applied Mechanics, ASME, **57**, (1990) pp383-387.
10. Lekhnitskii, S. G., *Theory of Elasticity of an Anisotropic Body*, Mir Publishers, Moscow, 1981.
11. Cui, Z. Y. and Chen, Y. Z., "A Boundary Collocation Technique for Evaluating the Torsional Rigidity and Third Stress Intensity Factor of Cracked Bars," Sinica Solid Mechanica, 4, (1981) pp.503-511.
12. Liao, W. C., "The Torsional Response and Measurement of In-situ Shear Moduli of an Edge Cracked Thick Laminate," (in review)

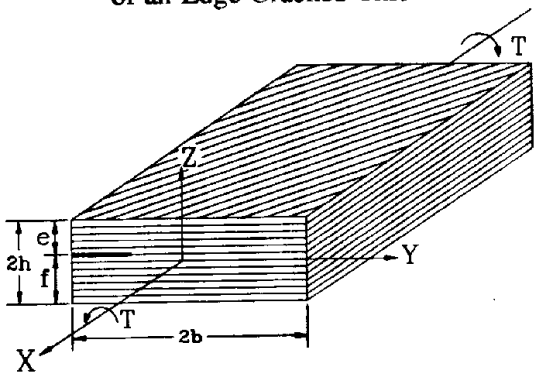

Fig. 1. Torsion of an edge crack thick laminate.

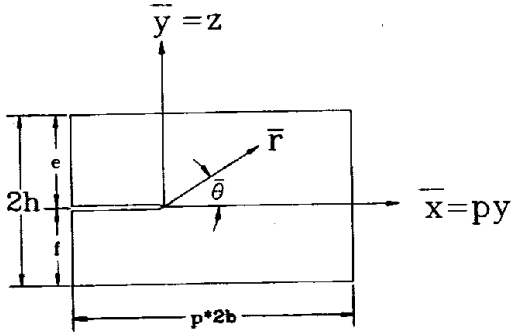

Fig. 2. Orthotropicalized cross-section of an edge cracked thick laminate.

Table 1 : The strain measurements and in-situ shear moduli of $\pm 45]_{10S}$ *laminates*

specimen cm	a/2b	$\bar{\gamma}^{A}_{xy}/T$ (1/Nm) measured	$\bar{\gamma}^{B}_{xz}/T$ (1/Nm) measured	G_{xy} (GPa)	G_{xz} (GPa)	T_{cr} (NM)	G_{IIIC} (J/m^2)
c_7 4.917×0.533	0.505	83.69e-6	319.11e-6	36.07	3.34	46.47	926
c_8 4.928×0.537	0.510	91.09e-6	253.14e-6	30.65	4.26		
c_9 4.485×0.538	0.149	91.88e-6	224.41e-6	34.41	3.39	56.59	654
c_11 4.905×0.529	0.534	87.15e-6	334.72e-6	33.96	3.52	45.62	998
c_12 4.014×0.529	0.650	120.87e-6	459.92e-6	33.93	3.91		
c_13 4.935×0.533	0.290	96.69e-6	237.55e-6	33.20	3.49	53.22	674
c_14 4.897×0.529	0.203	93.08e-6	213.82e-6	33.34	3.65		
				average 33.65±1.63	average 3.65±0.33		

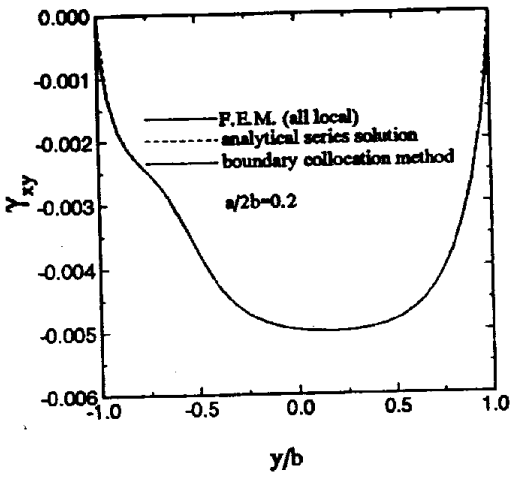

Fig. 3. The in-plane shear strain γ_{xy} *at top surface of a* $\pm 45]_{10S}$ *laminate(*Θ *=1 rad/m, 2b=5.08cm, e=0.2413cm, f=0.2667cm)*

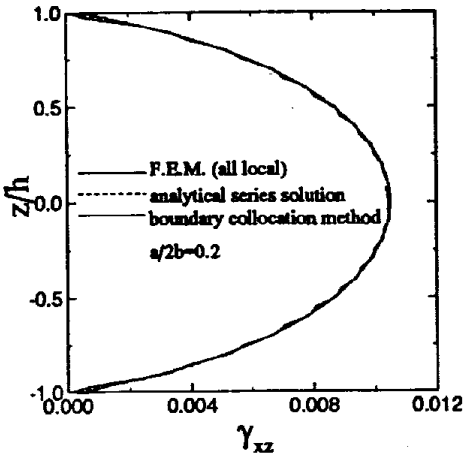

Fig. 4. The out-of-plane shear strain γ_{xz} *at uncracked side of a* $\pm 45]_{10S}$ *laminate(*Θ *=1 rad/m, 2b=5.08cm, e=0.2413cm, f=0.2667cm)*

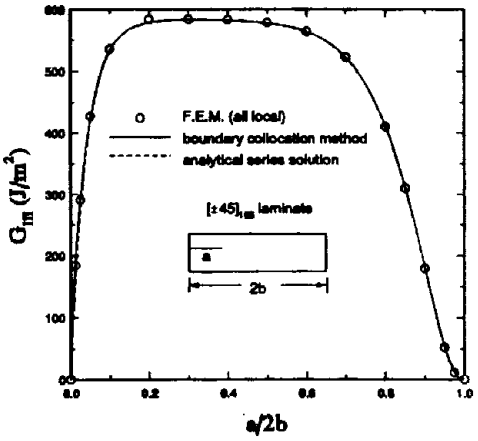

Fig. 5. Mode III strain energy release rate of a $\pm 45]_{10S}$ laminate(Θ =1 rad/m, 2b=5.08cm, e=0.2413cm, f=0.2667cm).

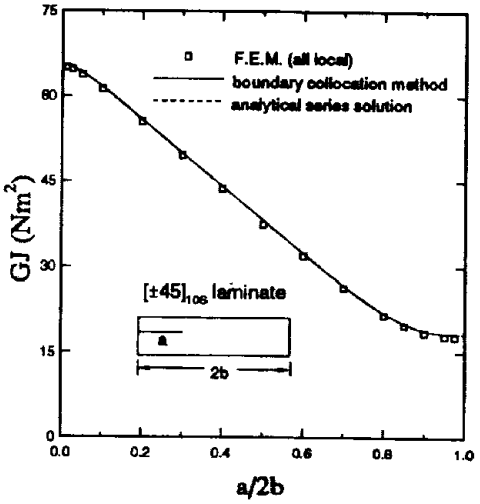

Fig. 6. The torsional rigidity of a $\pm 45]_{10S}$ laminate(2b=5.08cm, e=0.2413cm, f=0.2667cm).

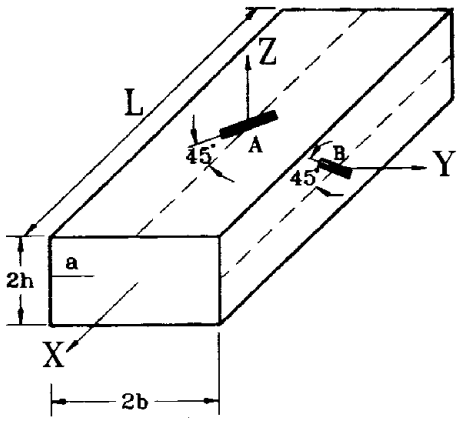

Fig. 7. The strain gage configuration of an ECT specimen.

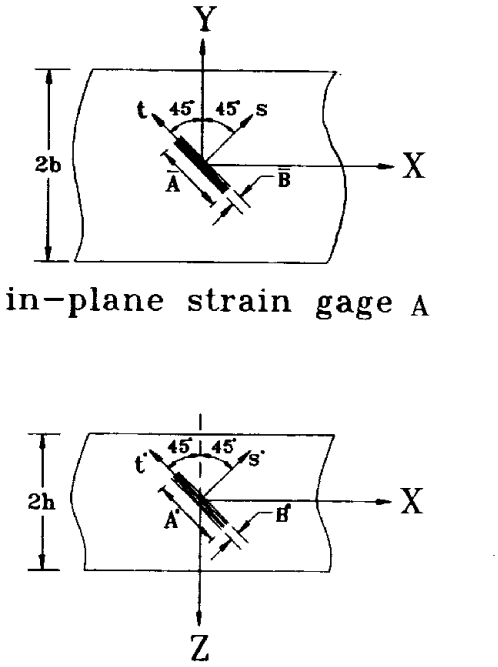

Fig. 8. The local coordinate system of gages A and B.

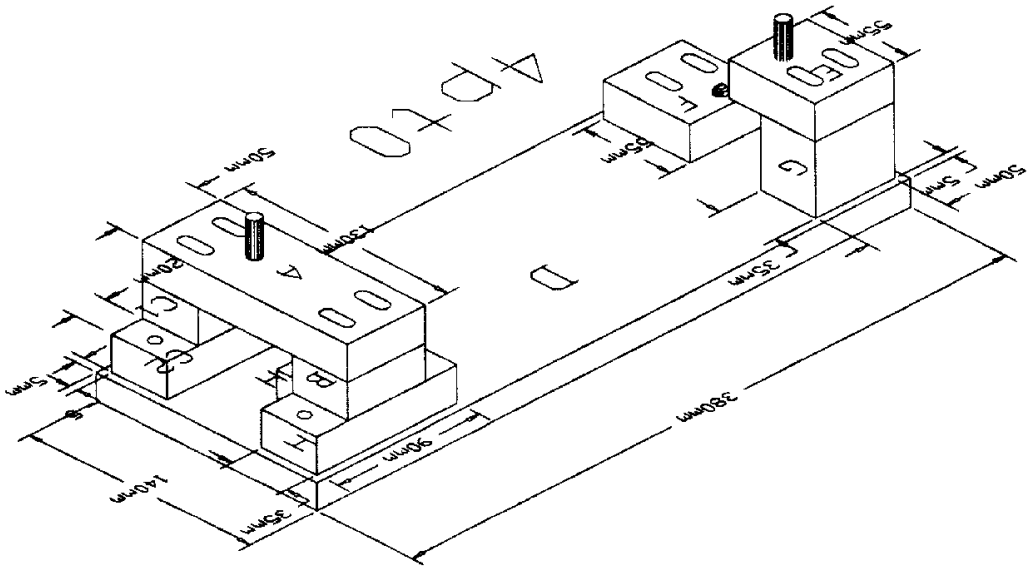

Fig. 9. The torsion machine set-up

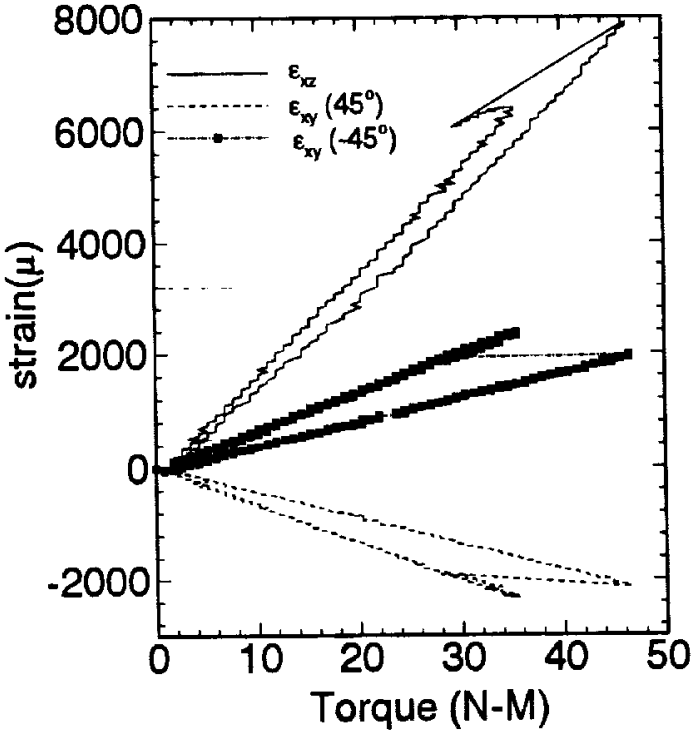

Fig. 10. The strain gage responses of a $\pm 45]_{10S}$ *laminate(specimen c_7).*

COMPARISON OF TENSILE PROPERTIES BETWEEN SPLIT DISK TEST AND TENSILE COUPON TEST

Sung-Ho Yoon[1] and Chun-Gon Kim[2]

[1] Department of Mechanical Engineering, Kumoh National University of Technology 188 Shinpyung-Dong, Kumi, Kyungbuk, 730-701, Korea
[2] Department of Aerospace Engineering, Korea Advanced Institute of Science and Technology, 373-1 Kusung-Dong, Yusong-Ku, Taejon, Korea

SUMMARY : The purpose of this study is to suggest an appropriate test method for the evaluation of tensile properties of filament wound structures. The split disk test using the ring specimen and the tensile coupon test using the conventional coupon specimen and the modified coupon specimen were considered. The tensile strength by the split disk test showed better agreement with the calculated value obtained from the rule of mixture than that by the tensile coupon test. With a suitable data reduction scheme, the measured tensile modulus of each test method agreed well with the calculated value obtained from the rule of mixture. According to the results, the split disk test was more useful than the tensile coupon tests in evaluating tensile properties of filament wound structures quantitatively.

KEYWORDS: tensile propeties, filament wound structures, split disk test, tensile coupon test, ring specimen, conventional coupon specimen, modified coupon specimen

INTRODUCTION

Filament winding is widely used for the fabrication of composite rocket motor cases, launcher tubes, high pressurized gas tanks, and aircraft fuselages due to the ease of fabrication and lower production costs. The netting theory is used for the preliminary design of filament wound structures, in which it is assumed that the applied load is taken only by reinforced fibers and the load bearing of the resin is negligible. The performance of filament wound structures is affected by tensile properties used for design. It is well known that tensile properties are influenced by the shape of the specimen and the continuity of reinforced fibers as well as constituents of the composite material. Filament wound structures are quite different from general flatwise composite structures in the shape and the continuity of reinforced fibers. One of the main concerns is to establish a quantitative test method for the evaluation of tensile properties which can be well reflected the effect of the filament winding. Several test methods were suggested for the evaluation of tensile properties of filament wound structures. Among these test methods, the internal pressurizing test with the ring specimen [1], the tensile coupon test with the flatwise specimen [2], and the split disk test with the ring specimen [3] are widely used. The internal pressurizing test with the ring specimen requires a complicated test fixture and a pressurizing device irrespective of the simple shape, the ease of

fabrication, and the testing of 'as wound' specimen. The tensile coupon test utilizes the flatwise coupon specimen which is manufactured by the filament winding. However, such a specimen may not be regarded as a representative of filament wound structures due to the discontinuity of reinforced fibers. The split disk test with the ring specimen has advantages such as no need of a complicated test fixture and a pressurizing device, in addition to the simple shape and the testing of 'as-wound' specimen. It has been reported that the split disk test with the ring specimen was not applicable to the measurement of the tensile modulus, but to the determination of an apparent tensile strength [4]. This was due to the local bending of the specimen around edges of the test fixture as well as the friction on contact surfaces between the test fixture and the specimen. According to the recent report [5], the split disk test with the ring specimen can be well adapted to evaluate the tensile modulus quantitatively if a suitable data reduction scheme is applied.

In this study, an appropriate test method for the evaluation of tensile properties of filament wound structures was suggested by comparing the results of the split disk test with those of the tensile coupon test using the conventional coupon specimen and the modified coupon specimen.

PREPARATION OF THE SPECIEMNS

Three types of the specimen such as the ring specimen, the conventional coupon specimen, and the modified coupon specimen were considered. All the specimens were manufactured by the filament winding. Fig. 1 shows configurations of the specimen used for this study. The ring specimen was cut from the filament wound tube with unidirectional reinforced fibers along the circumferential direction. The conventional coupon specimen and the modified coupon specimen were obtained from the filament wound flat plate with unidirectional reinforced fibers along the longitudinal direction. For the preparation of all the types of the specimen, processing variables such as reinforced fibers, resin, fiber ends, and winding tension were applied at the same conditions. Reinforced fibers were used as T300 carbon fiber of Toho besfight HTA-12K and resin as AD6005/HY906/DY062 of Ciba-Geigy epoxy. Fiber ends were 3 ends and winding tension was 19.6N per end.

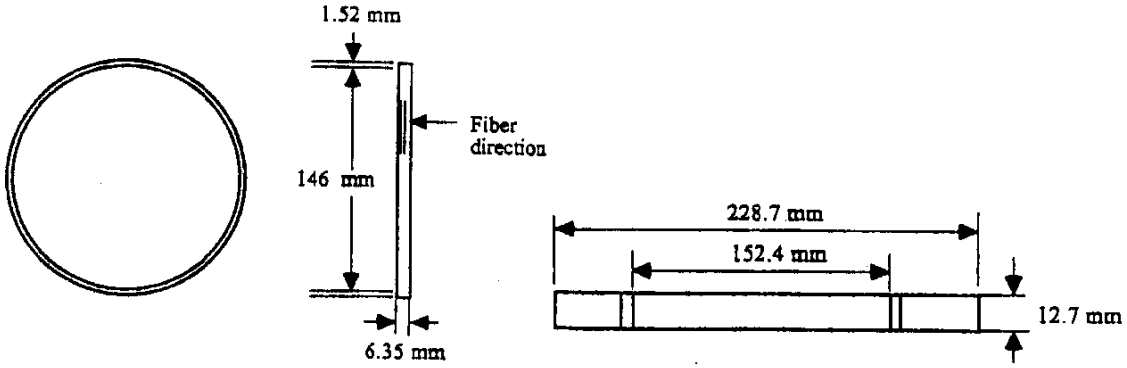

(a) Specimen for the split disk test (b) Specimen for the tensile coupon test

Fig. 1: Configurations of the specimen for this study.

The ring specimen was manufactured as follows: (i) cylindrical mandrel was installed on a winding machine (ii) the release agent of MS443 was treated on the surface of the mandrel (iii) resin-impregnated reinforced fibers were unidirectionally wound on the mandrel along the

circumferential direction to obtain the filament wound tube of 1.52mm thickness (iv) shrinkage tape was wrapped on the surface of the filament wound tube to squeeze out excessive resin (v) filament wound tube was cured into a rotating dry oven (vi) filament wound tube was removed from the mandrel and then reinstalled on the machining mandrel (vii) the ring specimen of 6.35mm width was cut using a diamond coated saw. The conventional coupon specimen was manufactured as follows: (i) flatwise mandrel was installed on a winding machine (ii) the release agent of MS443 was treated on the surface of the mandrel (iii) resin-impregnated reinforced fibers were unidirectionally wound on the mandrel along the hoop direction to obtain the filament wound flat plate of 2.1mm thickness (iv) steel molds were assembled on both sides of the mandrel to squeeze out excessive resin (v) the filament wound flat plate was cured into a dry oven (vi) the filament wound flat plate was removed from the mandrel by cutting both ends of the flat plate (vii) glass/epoxy reinforced tabs were attached on specified locations and the conventional coupon specimen of 12.7mm width was cut using a diamond coated saw. Although this procedure is typical to obtain the conventional coupon specimen of filament wound structures, it may result in the bending of the specimen due to the winding tension. The modified coupon specimen was manufactured in a similar way to the conventional coupon specimen, except that both ends of the flat plate were cut by a sharp knife before curing to prevent from inducing the bending of the specimen.

EVALUATION OF THE TENSILE STRENGTH

Fig. 2 shows the test set-up of the split disk test with the ring specimen. The load was applied with an Instron 1335 testing system at the crosshead speed of 1.0mm/min. Test was conducted by applying the load until fracture occurred. The specimen was aligned with an imaginary line joining the points of the test fixture by inserting pins into pin-holes around edges of the test fixture. The friction between the test fixture and the ring specimen was minimized by spreading the carbon powder onto contact surfaces. The tensile strength of the split disk test was obtained by Eqn 1.

$$\left(\sigma_m\right)_r = \frac{P_b}{2A_r} \tag{1}$$

where P_b is the load at fracture, A_r is the cross sectional area of the ring specimen around edges of the test fixture.

Fig. 3 shows the test set-up of the tensile coupon test with the conventional coupon specimen or the modified coupon specimen. The load was applied with an Instron 1335 testing system at the crosshead speed of 1.0mm/min. Test was conducted by applying the load until fracture occurred. The specimen was aligned with an imaginary line joining the points of grips. The tensile strength of the tensile coupon test was obtained by Eqn 2.

$$\left(\sigma_m\right)_t = \frac{P_b}{A_t} \tag{2}$$

where P_b is the load at fracture, A_t is the cross sectional area of the conventional coupon specimen or the modified coupon specimen.

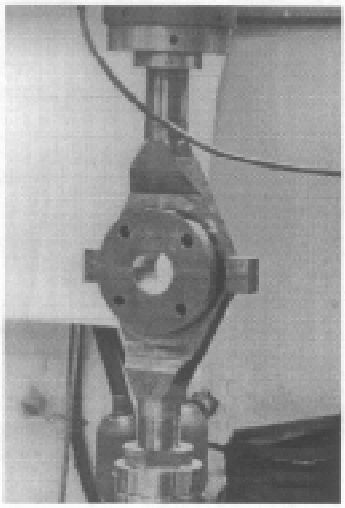

Fig. 2: Overview of the split disk test.

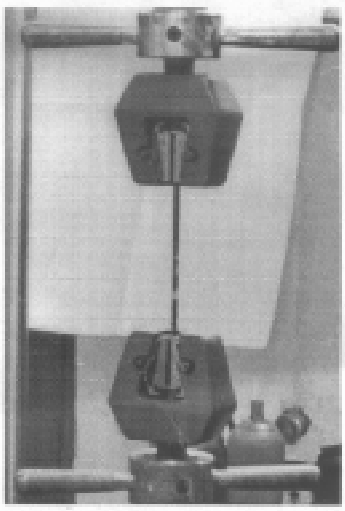

Fig. 3: Overview of the tensile coupon test

Table 1 shows the comparison of tensile strengths obtained from different types of specimen. From the view point of the continuity of reinforced fibers, the ring specimen reflected well the effect of filament winding rather than the conventional coupon specimen or the modified coupon specimen. The ring specimen initiated failure around edges of the test fixture and then fracture occurred abruptly. The measured tensile strength was 1921 MPa and the calculated value from the rule of mixture was 2378 MPa. In the conventional coupon specimen the bending remained initially due to the winding tension. In applying the load below the limit, the tensile strain on the convex part was different from that on the concave part. As the load was increasing further, the tensile strain on the convex part was nearly equal to that on the concave part. This resulted in less effect of the bending on the tensile strength. The measured tensile strength was 1480 MPa and the calculated value from the rule of mixture was 2085 MPa.

Table 1: Tensile strengths obtained from different types of the specimen.

	Number of Specimen	Fiber Volume Fraction (%)	Tensile Strength (MPa)	
			Measured (S_m)	Calculated (S_c)
Ring Specimen	7	65	1921	2378
Conventional Coupon Specimen	6	57	1480	2085
Modified Coupon Specimen	6	57	1521	2085

As the modified coupon specimen was obtained by cutting both edges of the filament wound flat plate before curing, there was little bending in the modified coupon specimen. When the load was applied to the specimen, tensile strain on each face was almost equal. The measured tensile strength was 1521 MPa and the calculated value from the rule of mixture was 2085 MPa.

According to the results, the ring specimen was more suitable than the conventional coupon

specimen or the modified coupon specimen for the evaluation of the tensile strength of filament wound structures.

EVALUATION OF THE TENSILE MODULUS

In the split disk test with the ring specimen, two strain gages (EA-13-062AP-120, Micro Measurement) were attached on the 15° and 40° locations of the specimen along the circumferential direction with respect to the horizontal axis. The friction on contact surfaces between the test fixture and the specimen was minimized by spreading the carbon powder uniformly. Load-strain relation under the loading path and that under the unloading path were required to eliminate the effect of friction on the tensile modulus. In applying the load to the specimen, the triangular wave under the displacement control of 1.0 mm/min was used as shown in Fig. 4. The tensile modulus of the split disk test was determined by averaging the tensile modulus of the loading path and that of the unloading path as shown in Eqn 3.

$$\left(E_g\right)_t = \frac{\left(E_g\right)_l + \left(E_g\right)_u}{2} \tag{3}$$

where $\left(E_g\right)_l$ is the tensile modulus of the loading path and $\left(E_g\right)_u$ is the tensile modulus of the unloading path.

In the tensile coupon test with the conventional coupon specimen or the modified coupon specimen, two strain gages (EA-05-062TT-120, Micro Measurement) were attached on the center of both faces. The load was applied under displacement control of 1.0mm/min. The tensile modulus of the conventional coupon specimen was determined by averaging the tensile modulus of the convex part and that of the concave part as shown in Eqn 4.

$$\left(E_g\right)_t = \frac{\left(E_g\right)_a + \left(E_g\right)_b}{2} \tag{4}$$

where $\left(E_g\right)_a$ is the tensile modulus of the convex part and $\left(E_g\right)_b$ is the tensile modulus of the concave part. The tensile modulus of the convex part or of the concave part was obtained by Eqn 5.

$$E_g = \frac{\Delta\sigma_g}{\Delta\varepsilon_g} \tag{5}$$

where $\Delta\varepsilon_g$ is the incremental strain at the gage location and $\Delta\sigma_g$ is the incremental stress defined as Eqn 6.

$$\Delta\sigma_g = \frac{\Delta P}{2A_g} \tag{6}$$

where ΔP is the incremental load, A_g is the cross sectional area at the gage location.

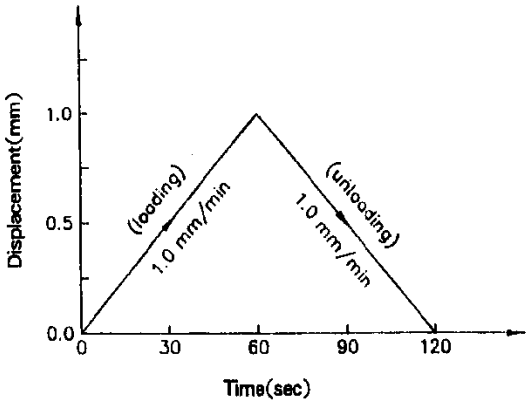

Fig. 4: Triangular wave for displacement control.

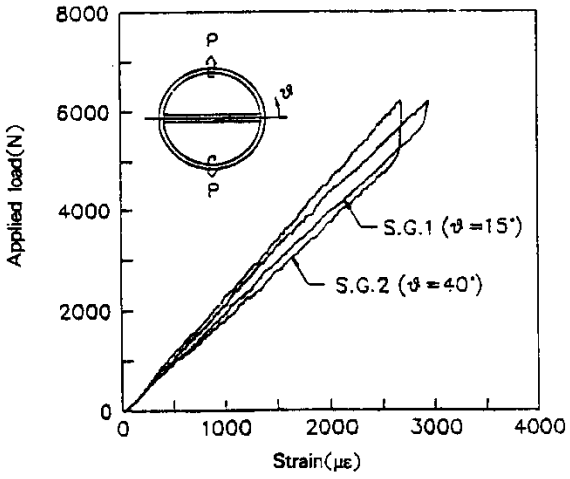

Fig. 5: Typical load-strain curves of the ring specimen.

Fig. 5 shows typical load-strain curves of the split disk test with the ring specimen. The hysteresis loop was formed due to the friction on contact surfaces between the test fixture and the ring specimen. This friction acts reverse to the direction of the relative sliding of the specimen to the test fixture, which results in the reduction of the load applied to the specimen as the applied load is increasing. The reverse is true when the applied load is decreasing. As the friction is the same in magnitude and the opposite in the sense during the loading path and the unloading path, it can be eliminated by averaging the tensile modulus of the loading path and that of the unloading path. Table 2 shows the measured tensile modulus of the split disk test. The tensile modulus of the loading path reveals higher value than that of the unloading path. The measured tensile modulus was 142.1 GPa and the calculated value from the rule of mixture was 141.2 GPa.

Table 2: Measured tensile modulus of the ring specimen.

Specimen	Gage Location	Measured Tensile Modulus (Gpa)		
		Loading Path $(E_g)_l$	Unloading Path $(E_g)_u$	Average $(E_g)_r$
RE-1	1	143.5	140.5	142.0
	2	153.9	134.1	144.0
RE-2	1	147.6	139.8	143.7
	2	157.1	130.6	143.9
RE-3	1	151.1	144.0	147.6
	2	151.4	129.6	140.5
RE-4	1	142.0	132.4	137.2
	2	146.3	128.8	137.6

* Calculated Tensile Modulus $(E_g)_c$: 141.2 GPa

Fig. 6 shows typical load-strain curves of the tensile coupon test with the conventional coupon specimen. The measured and calculated tensile modulus are shown in Table 3. As mentioned before, the conventional coupon specimen, which has initial bending due to winding tension, tends to be straight as the loading is increasing. However, until the certain limit of load was applied, the strain on the concave part induced higher than that on the convex part. This resulted that the tensile modulus on the convex part was higher than that on the concave part. The average of the measured tensile modulus was 123.6 GPa and the calculated value from the rule of mixture was 124.2 GPa.

Fig. 7 shows typical load-strain curves of the tensile coupon test with the modified coupon specimen. The measured and calculated tensile modulus are shown in Table 4. The bending of the modified coupon specimen is negligible, which makes strains on both sides of the specimen to be nearly equal in magnitude. The measured tensile modulus was 123.2 GPa and the calculated value from the rule of mixture was 124.2 GPa. Compared to the measurement of the tensile strength, the measured modulus agreed well with the calculated value from the rule of mixture through a suitable data reduction scheme.

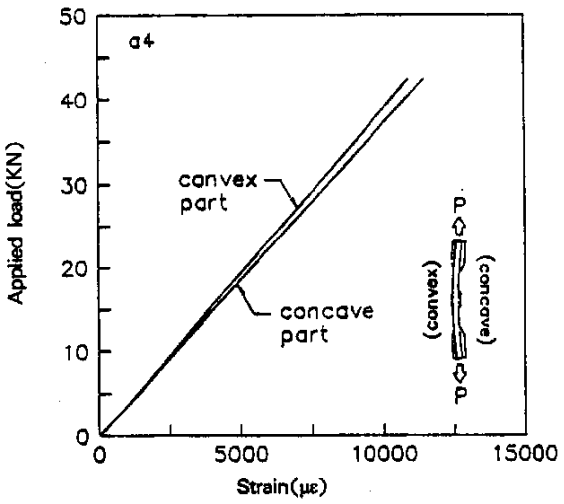

Fig. 6: Typical load-strain curves of the conventional coupon specimen.

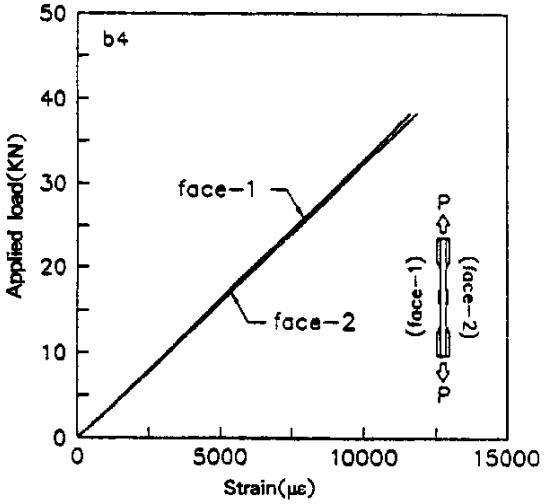

Fig. 7: Typical load-strain curves of the modified coupon specimen.

Table 3: Measured tensile modulus of the conventional coupon specimen.

Specimen	Measured Tensile Modulus (GPa)		
	Concave Part $(E_g)_a$	Convex Part $(E_g)_b$	Average $(E_g)_t$
CE-1	121.9	123.3	122.6
CE-2	120.0	127.1	123.6
CE-3	121.9	122.6	122.3
CE-4	123.0	128.9	126.0

* Calculated Tensile Modulus $(E_g)_c$: 124.2 GPa

Table 4: Measured tensile modulus of the modified coupon specimen.

Specimen	Measured Tensile Modulus (GPa)		
	Face-1 $(E_g)_a$	Face-2 $(E_g)_b$	Average $(E_g)_t$
ME-1	122.2	123.4	122.8
ME-2	121.0	123.5	122.3
ME-3	121.6	124.8	123.2
ME-4	124.3	-	124.3

* Calculated Tensile Modulus $(E_g)_c$: 124.2 GPa

CONCLUSIONS

It is necessary to establish a quantitative test method for the evaluation of tensile properties applicable to the design of filament wound structures. In this study, a suitable test method was suggested by comparing the results of the split disk test with those of the tensile coupon test. Compared to the tensile coupon test, the measured tensile strength of the split disk test showed better agreement with the calculated value obtained from the rule of mixture. The tensile modulus of each test method, with a suitable data reduction scheme, agreed well with the calculated value obtained from the rule of mixture. According to the results, the split disk test is more useful than the tensile coupon test in evaluating tensile properties of filament wound structures quantitatively.

REFERENCES

1. Erickson, P.W., Perry, H.A., and Barret, F.R., "Status of the NOL Ring Test for Glass Roving Reinforced Plastics," Proceedings of Filament Winding Conference, Society of Aerospace Materials and Process Engineers, March 1961.

2. Munjal, A.K., Kalkarni, S.B., and Starret, H.S., "Characterization of Filament Wound Kevlar and Glass Composites for Rocket Motor Applications," 29th National SAMPE Symposium, April 1984.

3. ASTM D2290-87, "Standard Test Method for Apparent Tensile Strength of Ring or Tubular Plastics and Reinforced Plastics by Split Disk Method," Annual Book of ASTM Standards, Vol.15.03, 1992.

4. Knight, C.E., Jr., "Failure Analysis of the Split-D Test Method," Composite Materials : Testing and Design (Fourth Conference), ASTM STP 617, American Society for Testing and Materials, July 1977, pp.201-214.

5. Yoon, S.H., Kim, C.G., and Cho, W.M., "New Aspects of Split Disk Test Method for Filament Wound Structures," Proceeding of the 10th International Conference on Composite Materials, Whistler, British Columbia, Canada, August 14th-18th, 1995.

APPROXIMATE STRESS ANALYSIS OF THE IOSIPESCU SHEAR SPECIMEN

James M. Whitney

Department of Civil & Environmental Engineering and Engineering Mechanics, University of Dayton, 300 College Park, Dayton, Ohio, 45469-0243,USA

SUMMARY: Use of higher order beam theories is investigated in conjunction with stress analysis of the Iosipescu (v-notch) shear test for composite materials. Higher order displacements are utilized which lead to a third order polynomial in the thickness coordinate for the inplane normal stress. Through-the-thickness shear and normal stresses are obtained by integrating the equilibrium equations from classical theory of elasticity. This procedure leads to a fourth order polynomial in the thickness coordinate for the transverse shear stress. The shear stress distribution at the notch cross-section as obtained from the higher order beam theory in conjunction with a graphite/epoxy unidirectional composite is compared to an available finite element solution. Discrepancies between these solutions are discussed. In addition, numerical results indicate that the transverse normal strain can have a significant influence on the shear stress distribution at the notch cross-section.

KEYWORDS: inplane shear, interlaminar shear, Iosipescu shear test, shear tests, higher order beam theory, stress analysis.

INTRODUCTION

The V-Notched beam (Iosipescu) shear test is now a standard test method under ASTM D5379. In addition to being widely accepted by the aerospace industry this test method is being utilized by other organizations, such as the Automotive Composites Consortium, as a standard for determining shear strength and modulus. The genesis of this test method can be found in a paper published by Iosipescu [1]. In this paper he proposed the test specimen shown in Fig. 1 for determining the shear properties of metals. Iosipescu argued that a 90° v-notch in the presence of a cross-section with zero moment would produce a state of pure shear which is uniformly distributed across the width, w, between the notches. Because the sides of the notches are parallel to the normal stress direction, Iosipescu also concluded that no stress concentration, at least for isotropic materials, existed at the bottom of the notch.

A considerable amount of work has been done in analyzing the shear stress distribution at the notch cross-section of the Iosipescu shear specimen. Most of these have been accomplished utilizing the finite element method. However, the geometry of the Iosipescu specimen presents a particular challenge to the finite element method. For example, it can be shown that stress distributions in the notch section of the specimen are very much influenced by the stress-free boundary conditions along the notch surface. Conventional finite element formulations, which are usually based on displacements, cannot directly satisfy traction-free boundary conditions, as these are natural conditions to be satisfied in the limit. Other difficulties can be encountered with the finite element method. Further complications arise with regard to stress analysis by the existence of a singularity at the notch tip for certain

material properties and laminate geometries [2]. In addition, load placement and distribution can have an effect on the shear stress at the notch cross-section [3-5].

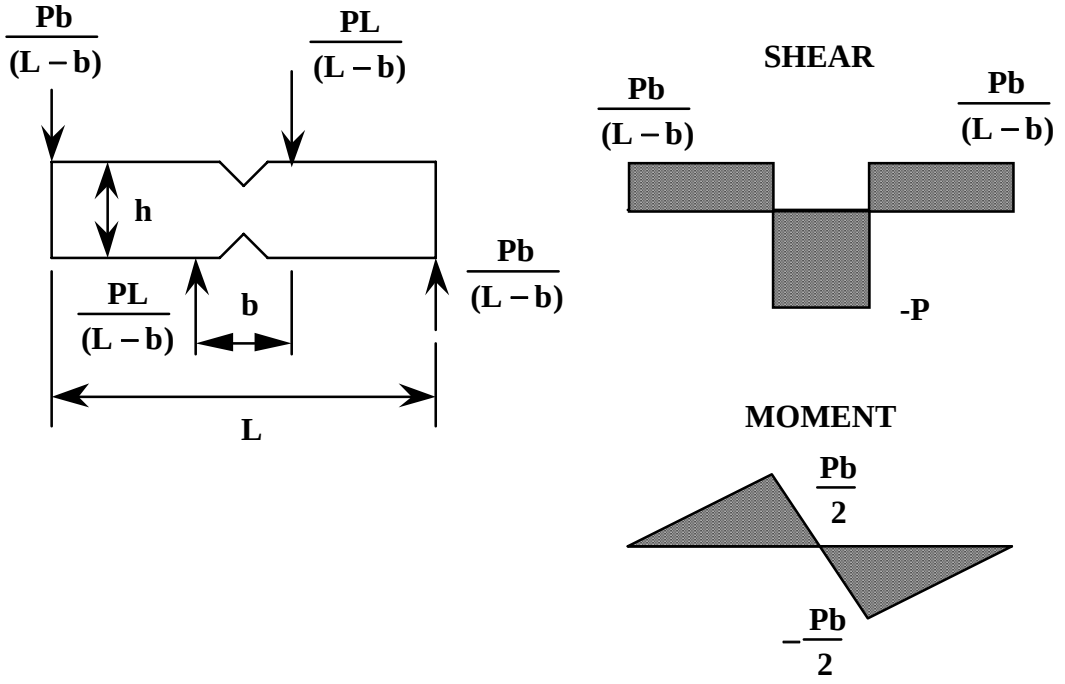

Fig. 1 : Iosipescu (v-notch) shear specimen

In the present paper two higher order plane stress models are presented for evaluating the stresses in the vicinity of the v-notches in the Iosipescu specimen, including the transverse normal stress. The models are based on an expansion of the displacements in the through-the-thickness coordinate, z, in the same fashion as higher order plate theories are often developed. Governing equations and boundary conditions are obtained from minimizing potential energy. Both approaches yield a third order polynomial in z for the through-the-thickness distribution of the inplane normal stress. Through-the-thickness shear and normal stresses are obtained by integrating the equilibrium equations from classical theory of elasticity.

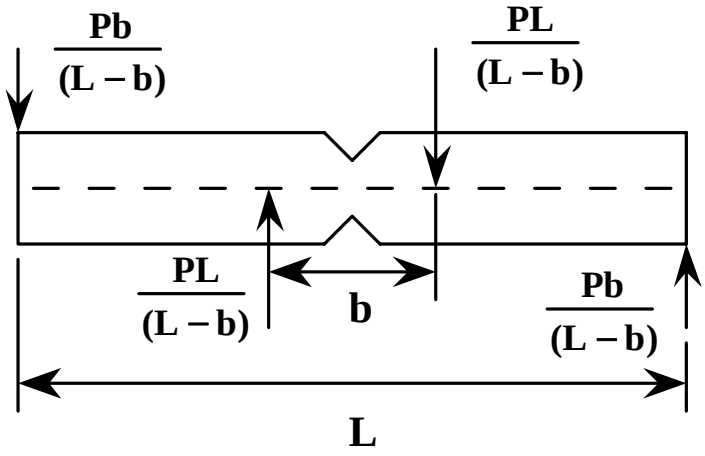

Fig. 2: Idealized loading with St. Venant effect dissipated

HIGHER ORDER BEAM ANALYSIS

In performing a higher order beam analysis we must assume that there is sufficient distance between the interior loads so that St. Venant's principle applies. In such a case the loading is idealized as shown in Figure 2. Under this condition we can consider a simplified analysis using the free-body diagrams shown in Figure 3. Using the free-body diagram on the left-hand side of Figure 3, we denote the beam depth by H(x). Thus,

$$H(x) = (h-2x) \tag{1}$$

In developing a higher order beam theory applicable to the Iosipescu shear test, we retain the usual assumptions associated with bending loads. In particular, the inplane normal stress, σ_x,

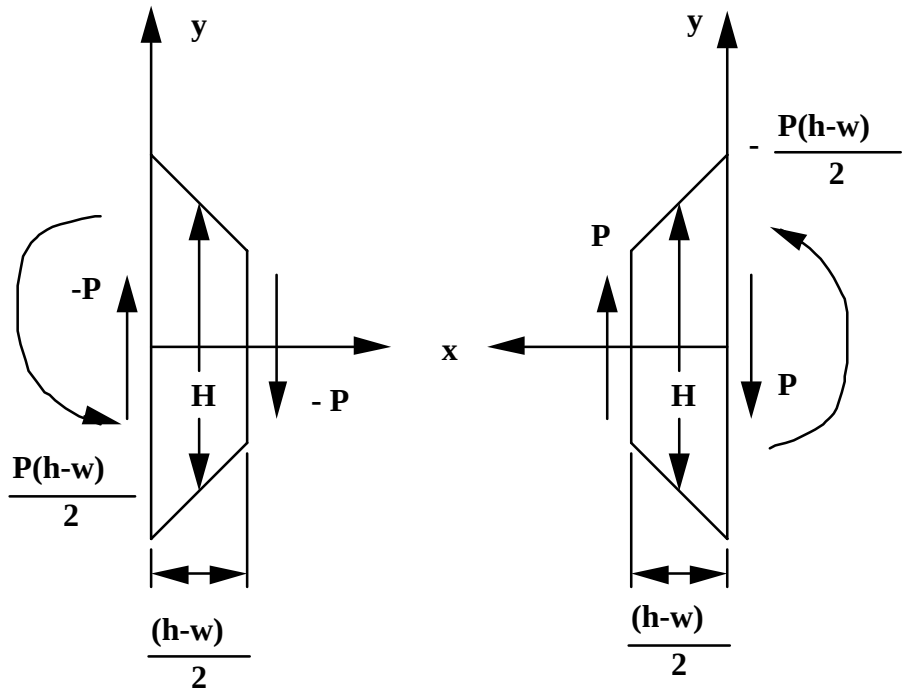

Fig. 3 : Free-body diagram for analytical model

is assumed to be anti-symmetric with respect to the through-the-thickness coordinate. For the present work we choose a displacement based theory which produces a third order polynomial for σ_x relative to the thickness coordinate, y. If a displacement based formulation is utilized, two approaches can be implemented in obtaining the desired distribution of σ_x . In the first case the effect of the thickness normal strain, ε_y, is neglected, which leads to the displacement field:

$$u = y\psi(x) + \frac{y^3}{3}\phi(x),\ v = v^o(x) \tag{2}$$

These displacements lead to the following normal stress, moment, and shear force resultants

$$\sigma_x = yE_1\left(\psi_{,x} + \frac{y^2}{3}\phi_{,x}\right)$$

$$M = t\int_{-H/2}^{H/2}\sigma_x y dy = E_1 t\frac{H^3}{12}(\psi_{,x} + \frac{H^2}{20}\phi_{,x})$$
$$Q = t\int_{-H/2}^{H/2}\tau_{xy}dy = G_{12}tH\left(\psi + v_{,x}^{o} + \frac{H^2}{12}\phi\right) \tag{3}$$

where a comma denotes partial differentiation, t denotes the beam thickness in the z direction, E_1 is the beam modulus in the x-direction, and G_{12} denotes the shear modulus relative to the x-y plane.

If we include the effect of the transverse normal strain, ε_y, the displacements in eq. (2) take the form

$$u = y\psi_x(x) + \frac{y^3}{3}\phi_x(x),\ v = v^0(x) + \frac{y^2}{2}\psi_y(x) + \frac{y^4}{4}\phi_y(x) \tag{4}$$

which leads to the following normal stress, moment, and shear force resultant

$$\sigma_x = y\left(Q_{11}\psi_{x,x} + Q_{12}\psi_y\right) + y^3\left(\frac{Q_{11}}{3}\phi_{x,x} + Q_{12}\phi_y\right)$$

$$M = Q_{11}\frac{tH^3}{12}\left[\psi_{x,x} + \frac{Q_{12}}{Q_{11}}\psi_y + \frac{H^2}{12}\left(\phi_{x,x} + \frac{Q_{12}}{Q_{11}}\phi_y\right)\right] \tag{5}$$

$$Q = G_{12}ht\left[\psi_x + v_{,x}^{0} + \frac{H^2}{12}\left(\phi_x + \frac{\psi_{y,x}}{2}\right) + \frac{H^4}{320}\phi_{y,x}\right]$$

where Q_{ij} are the reduced stiffnesses for plane stress.

Equation (4) contains all of the polynomial terms in the y coordinate which contribute to both a third order inplane stress, σ_x , and a fourth order transverse shear stress, τ_{xy}. Integration of the first of eqs. (5) in conjunction with the first equilibrium equation from classical theory of elasticity also produces a fourth order polynomial in y for the transverse shear stress, τ_{xy}. However, the expression for τ_{xy} obtained from assumed kinematic relations does not satisfy appropriate boundary conditions. This can only be accomplished by integrating the first equilibrium equation from classical theory of elasticity with the result

$$\tau_{xy} = -\int_{-H/2}^{y}\sigma_{x,x}d\zeta + \tau_{xy}(x,-H/2) \tag{6}$$

The second term in this relationship represents the value of τ_{xy} at the top of the cross-section, which in general does not vanish. Stresses relative to the x-y coordinate system along the

free boundary are shown in Fig. 4. These results along with a similar consideration of the lower notch boundary at y = - H(x)/2 lead to the conditions

$$\sigma_y(x,-H/2)=\sigma_x(x,-H/2),\ \tau_{xy}(x,-H/2)=\sigma_x(x,-H/2)$$
$$\sigma_y(x,H/2)=\sigma_x(x,H/2),\ \tau_{xy}(x,H/2)=-\sigma_x(x,H/2) \tag{7}$$

A major effect produced by the 90° notch is the introduction of a significant σ_y stress component. In conventional beam problems this stress component is not present except in the vicinity of a vertical surface traction. The distribution of σ_y can now be determined by

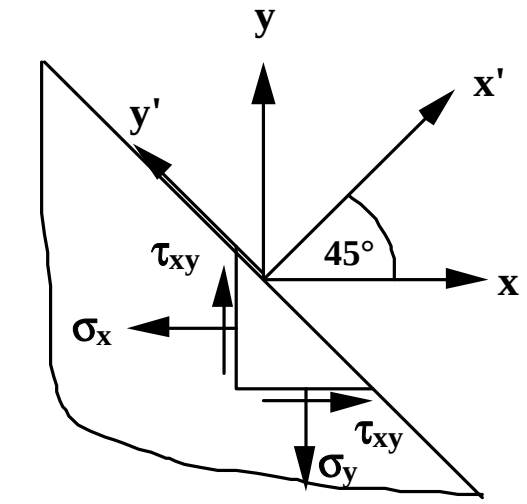

$$\sigma_y=\sigma_x,\ \tau_{xy}-\sigma_x,\ \sigma_x=\frac{M(x)H(x)}{2I(x)}$$

Fig. 4: Stresses along notch boundary in x - y coordinate system

integrating the second equation of equilibrium from classical theory of elasticity in conjunction with the resulting expression for τ_{xy} as determined from eq. (6), i.e.

$$\sigma_y=-\int_{-H/2}^{y}\tau_{xy,x}\,d\zeta+\sigma_y(x,-H/2) \tag{9}$$

It should be noted that eq. (9) will yield a third order polynomial in y when used in conjunction with axial strain effects only, while a fifth order polynomial will result when transverse strain effects are added. If σ_y is determined from kinematic assumptions, the resulting function will be of the same order in y as the corresponding function for σ_X.

For either kinematic relations, eq. (2) or eq. (4), two variables can be eliminated from the analysis by using M and Q as determined from the shear and moment diagrams, i.e.

$$M=\frac{P}{2}(h-w-2x),\ Q=-P \tag{10}$$

The remaining equilibrium equations in terms of displacement variables are determined from the principle of minimum potential energy. In order to conserve space the governing equations will not be presented here.

For the case of axial strain only, the governing equations can be reduced to a single non-homogeneous differential equation in the variable ϕ. The resulting solution is of the form

$$\phi = -\frac{420wh^2}{(9+35G_{12}/E_1)H^3} + \frac{630w^2h^3}{(9+35G_{12}/E_1)H^4} + \frac{A}{H^{\lambda}} + BH^{\lambda} \tag{11}$$

where $\pm\lambda$ are the roots of a quadratic equation involving geometric parameters and material properties. The undetermined coefficients A and B are determined from the following boundary conditions

$$\text{At } x = 0,\ \frac{(h-w)}{2}: \qquad \phi_{,x} = 0 \tag{12}$$

The variables ψ and v^0 are determined from the moment and shear force in conjunction with eq. (11).

When transverse strain is also included, three non-homogeneous, coupled, differential equations in the variables ϕ_x, ψ_y, and ϕ_y are obtained. In this case the solution is of the form

$$\begin{aligned}
\phi_x &= \sum_{i=1}^{6} A_i H^{\lambda_i} + L_1\frac{wh^2}{H^3} + L_2\frac{wh^3}{H^4} \\
\psi_y &= \sum_{i=1}^{6} F_{1i}A_i H^{\lambda_i} + L_3\frac{wh}{H^2} + L_4\frac{wh^2}{H^3} \\
\phi_y &= \sum_{i=1}^{6} F_{2i}A_i H^{\lambda_i} + L_5\frac{wh^3}{H^4} + L_6\frac{wh^4}{H^5}
\end{aligned} \tag{13}$$

where L_i are coefficients of a particular solution, while A_i are undetermined coefficients of the homogeneous solution. In addition λ_i are roots of a sixth order polynomial involving geometric parameters and material properties. The coefficients f_{ij} are eigenvector ratios. In this case the boundary conditions are of the form

$$\begin{aligned}
&\text{At } x = 0: && \phi_x = \phi_{x,x} = \phi_y = 0 \\
&\text{At } x = \frac{(h-w)}{2}: && \phi_{x,x} = \psi_y = \phi_y = 0
\end{aligned} \tag{14}$$

Conditions at the notch cross-section lead to vanishing of σ_x for both cases under consideration and continuity of v for the second case. Symmetry (or anti-symmetry) as dictated by Figs. 2 and 3 assure continuity of u and τ_{xy} at the notch cross-section. The

boundary conditions at the beginning of the notch region (x = 0 in Fig. 3) lead to linear distributions with respect to y for σ_x in both cases and for u in the second case.

NUMERICAL RESULTS

We now consider two examples, a unidirectional composite with the fibers oriented along the x-axis, [0°] composite, and a unidirctional composite with the fibers perpendicular to the x-axis, [90°] composite. Assumed material properties will be those typical of current graphite/epoxy composites. Before displaying the solutions, however, some discussion is in order relative to differences in behavior between these two cases. In particular, solutions for the [0°] case tend to be unstable for two reasons. First, there is a definite effect of assumed load placement and distribution on the stresses at the notch cross-section [3-5]. But even more importantly is the existence of a stress singularity at the notch tip [2]. In the case of [90°] graphite/epoxy unidirectional composites, the notch tip stresses are very insensitive to load placement and distribution [3, 5], and no singularity exists at the notch tip [2].

For the [0°] composite the following material properties are assumed:

$$\frac{E_1}{E_2} = 15.4, \quad \frac{G_{12}}{E_2} = 0.615, \quad \nu_{12} = 0.3 \tag{15}$$

where E_2 is the modulus in the y-direction. Here ν_{12} denotes the major Poisson's ratio as determined from a uniaxial tensile test in the x-direction while measuring contraction in the y-direction. When transverse strain effects are included in the kinematic relations, eq. (4), the reduced stiffnesses can be determined from the relationships

$$Q_{11} = \frac{E_1}{\left(1 - \nu_{12}^2 E_2 / E_1\right)}, \quad Q_{12} = \frac{\nu_{12} E_2}{\left(1 - \nu_{12}^2 E_2 / E_1\right)} \tag{16}$$

A comparison of shear stress distributions at the notch-tip for the two kinematic assumptions, eqs. (2) and (4), and classical beam theory are shown in Fig. 5. The notch depth is given by w/h = 0.5 and shear stress values are normalized by the average shear stress at the notch cross-section, i.e.

$$\tau_{xy}^* = \frac{wt\tau_{xy}}{P} \tag{17}$$

The shear stress distribution is determined from equilibrium consideration, i.e. eq. (6). For the case of a classical beam,

$$\sigma_x = \frac{M(x)y}{I(x)} = \frac{6Py(h - w - 2x)}{t(h - 2x)^3} \tag{18}$$

where I(x) is the moment of inertia of the cross-section with respect to the z-axis. Substituting this relationship into eq. (6) and performing the integration, we obtain the following expression for transverse shear stress

$$\tau_{xy} = -\frac{3P}{2t(h-2x)^2}[w + 4(2h - 3w - 4x)(\frac{y}{h-2x})^2] \tag{19}$$

At the notch cross-section this relationship yields the following normalized shear stress:

$$\tau^*_{xy} = -\frac{3}{2}[1 - 4(\frac{y}{w})^2] \tag{20}$$

Thus, the beam solution yields a classical parabolic shear stress distribution which is independent of material properties.

Results in Fig. 5 indicate a large effect of transverse normal strain as well as a significant departure from elementary beam theory. In fact these results indicate the type of instability alluded to at the beginning of this section and leaves serious doubt that any of the three cases represents an accurate solution.

For the [90°] composite the material properties relative to the x-y coordinates are as follows:

$$\frac{E_1}{E_2} = 0.065, \quad \frac{G_{12}}{E_2} = 0.04, \quad \nu_{12} = 0.0195 \tag{21}$$

A comparison of models for the shear stress distribution at the notch cross-section is shown in Fig. 6 for w/h = 0.5. As in the case of the [0°] composite considerable departure from elementary beam theory is displayed by the higher order theories. However, in this case similar results are obtained with and without transverse strain included. Thus, the solution appears to be more stable than for the case of the [0°] unidirectional composite. In addition, plane stress finite element results from Ref. [4] are included. The ABAQUS and PATRAN codes were used for calculations and pre-, post-processing, respectively.

A large discrepancy is quite evident between the shape of the shear stress distribution in Fig. 6 as obtained from the higher order beam theories and the finite element solution. It is difficult at this point to conclude which one of these two solutions is more accurate. As previously pointed out there are difficulties with the finite element procedure. In particular, a cursory examination of eq. (6) reveals that the boundary condition has a very important role to play in the shear stress distribution. Again, the exact boundary conditions are obtained only in the limit in conjunction with displacement based finite elements. It can be shown that in the absence of a singularity and load effects, which is the situation with the case displayed in Fig. 6, the shear stress at the notch tip must vanish. The finite element solution does not quite vanish at the notch tips. Some discrepancy between these finite element results and moiré data can be found in Ref. [5]. However the shape of the shear stress distribution as obtained from the moiré data is much closer to the finite element results than the higher order beam theory. It should also be noted that moiré data is difficult to interpret in the presence of high strain gradients.

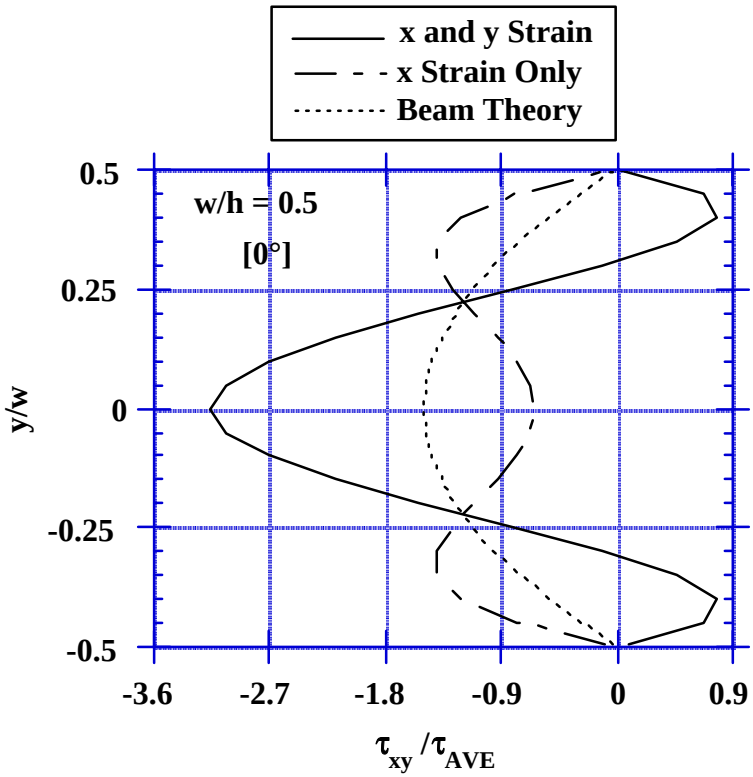

Fig. 5: Shear stress distribution at notch cross-section, [0°] composite

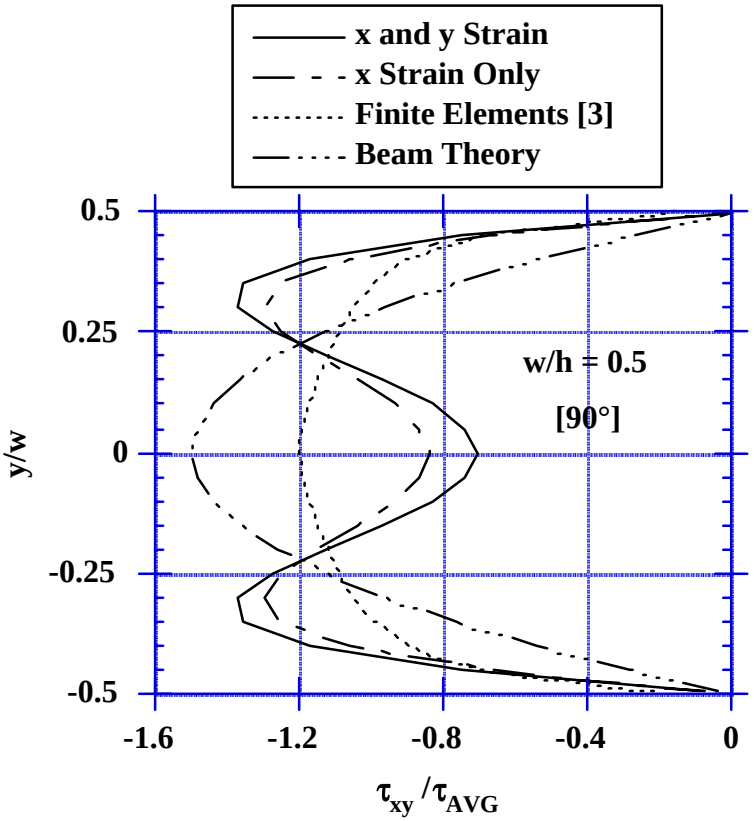

Fig. 6: Shear stress distribution at notch cross-section, [90°] composite

CONCLUSIONS

Results of the present study are inconclusive concerning the applicability of higher order beam theories to the stress analysis of the Iosipescu shear specimen. Because of the absence of a singularity, and insensitivity to load placement and distribution, the [90°] unidirectional graphite/epoxy specimen is ideal for this study.

To aid in resolving the discrepancies observed in Fig. 6, solutions from additional higher order beam theories need to be considered. Displacement based solutions of the following form are appropriate.

$$u = \sum_{i=odd}^{N} z^i \psi_x^{(i)}(x), \quad v = v^0(x) + \sum_{i=even}^{N+1} z^i \psi_x^{(i)}(x) \tag{22}$$

This will lead to an Nth order antisymmetric through-the-thickness distribution of σ_x and an N+1 even ordered distribution of τ_{xy}.

It would also seem appropriate that additional finite element approaches, utilizing other than constant strain elements, need to be explored.

ACKNOWLEDGMENT

The author wishes to acknowledge the Air Force Office of Scientific Research, Washington, D.C., and RDL, Culver City, California, for supporting part of this work under the Summer Faculty Program with Wright Laboratory, Wright-Patterson Air Force, Base, Ohio, USA. Additional support was provided by Wright Laboratory under an on-site contract with the University of Dayton Research Institute, Dayton, Ohio, USA.

REFERENCES

1. Iosipescu, N., "New Accurate Procedure for Single Shear Testing of Metals, "*Journal of Materials*, Vol. 2, No. 3, September, 1967, pp. 537-566.
2. Whitney, J. M., "Singularity Analysis of the Iosipescu Shear Specimen", *Proceedings of the Tenth International Conference on Composite Materials (ICCM X), Vol. IV, Characterization and Ceramic Matrix Composites*, Poursartip, A. and Street, K., Eds., Woodhead Publishing Ltd., Cambridge, England, 1995, pp. 219-226.
3. Ho, H., Tsai, M. Y., and Morton, J., "Numerical Analysis of the Iosipescu Specimen for Composite Materials," *Composite Science and Technology*, Vol. 46, No. 2, 1993, pp. 157-128.
4. Ho, H. and Morton, J., "Non-Linear Numerical Analysis of the Iosipescu Specimen for Composite Materials," *Composite Science and Technology*, Vol. 50, No. 4, 1994, pp. 355-365.
5. Whitney, J. M., "St. Venant Effect in the Iosipescu Shear Specimen," *Proceedings of the American Society for Composites, Eleventh Technical Conference*, Johnson, W. S., Ed., Technomic Publishing, Co., Lancaster, Pa., 1996, pp. 845-852.

SUBJECT INDEX

AUTHOR INDEX